Topics in Applied Physics
Volume 111

Topics in Applied Physics

Topics in Applied Physics is a well-established series of review books, each of which presents a comprehensive survey of a selected topic within the broad area of applied physics. Edited and written by leading research scientists in the field concerned, each volume contains review contributions covering the various aspects of the topic. Together these provide an overview of the state of the art in the respective field, extending from an introduction to the subject right up to the frontiers of contemporary research.

Topics in Applied Physics is addressed to all scientists at universities and in industry who wish to obtain an overview and to keep abreast of advances in applied physics. The series also provides easy but comprehensive access to the fields for newcomers starting research.

Contributions are specially commissioned. The Managing Editors are open to any suggestions for topics coming from the community of applied physicists no matter what the field and encourage prospective editors to approach them with ideas.

Managing Editor

Dr. Claus E. Ascheron

Springer-Verlag GmbH
Tiergartenstr. 17
69121 Heidelberg
Germany
Email: claus.ascheron@springer.com

Assistant Editor

Adelheid H. Duhm

Springer-Verlag GmbH
Tiergartenstr. 17
69121 Heidelberg
Germany
Email: adelheid.duhm@springer.com

Ado Jorio, Gene Dresselhaus,
Mildred S. Dresselhaus (Eds.)

Carbon Nanotubes

Advanced Topics in the Synthesis, Structure, Properties and Applications

With 250 Figures

Springer

Ado Jorio

Departamento de Física,
Universidade Federal de Minas Gerais
(UFMG),
Belo Horizonte, MG, 30.123-970
and
Divisão de Metrologia de Materiais,
Instituto Nacional de Metrologia,
Normalização e Qualidade Industrial
(INMETRO),
Duque de Caxias, RJ, 25250-020,
Brazil

Gene Dresselhaus

Francis Bitter Magnet Lab,
Massachusetts Institute of Technology,
Cambridge, MA, 02139-4307
USA

Mildred S. Dresselhaus

Department of Physics and Department of
Electrical Engineering and Computer Science,
Massachusetts Institute of Technology
Cambridge, MA, 02139-4307,
USA

Library of Congress Control Number: 2007930205

Physics and Astronomy Classification Scheme (PACS): 06.20.-f, 61.48.DE, 85.35.Kt, 78.67.Ch, 61.48.De

ISSN print edition: 0303-4216
ISSN electronic edition: 1437-0859
ISBN 978-3-540-72864-1 Springer Berlin Heidelberg New York
e-ISBN 978-3-540-72865-8 Springer Berlin Heidelberg New York
DOI 10.1071/978-3-540-72865-8

Typesetting: DA-TEX · Gerd Blumenstein · www.da-tex.de
Production: LE-TEX Jelonek, Schmidt & Voeckler GbR, Leipzig
Cover design: eStudio Calamar S. L., F. Steinen-Broo, Girona, Spain

Printed on acid-free paper 57/3180/YL 5 4 3 2 1 0

Foreword

The Story Behind the Nanotube Rush

Nanotubes have evolved into one of the most intensively studied materials and are held responsible for co-triggering the Nanotechnology Revolution. Why? This foreword attempts to provide a brief answer to "why" and "how" nanotubes have kept amazing both scientists and engineers over the past decades.

Even though nanotubes were commonly identified as contiguous hollow tubes in the core structure of carbon fibers in the 1970s [1], their popularity rose drastically following their observation on the cathode of a carbon arc used to produce fullerenes [2], the starting point of the Nanotube Rush era. Nanotubes, especially those of carbon, excite both fundamental scientists and engineers interested in applications due to the unique combination of their properties.

First, these molecular systems are nanometer-sized in diameter, but up to centimeters long, yielding an unprecedented length/diameter aspect ratio exceeding 10^7. Carbon nanotubes can be thought of as narrow strips of graphene [3] rolled up into seamless tubes. They form spontaneously and efficiently under well-defined conditions either as single-wall nanotubes (SWNTs) or nested multiwall nanotubes (MWNTs). Contiguous carbon nanotubes exhibit a high degree of atomic-scale perfection. This fact, along with their close relationship with graphene, makes nanotubes chemically inert. As for graphene under tension, nanotubes are two orders of magnitude stronger than steel at 1/6th of the weight. The melting point of nanotubes of about 4000 K in "ideal vacuum" [4], close to that of graphite, exceeds that of any metal. Depending on the atomic structure of nanotubes, including diameter, single-wall nanotubes act as ballistic conductors of electrons or show semiconducting behavior. Carbon nanotubes seem to be also excellent conductors of heat, expected to exceed the record thermal conductivity of isotopically pure diamond. Moreover, similar to the related graphite, carbon nanotubes appear to be biocompatible in many environments.

Nanotube Applications Guiding the Way

Due to the amazing combination of their properties, nanotubes appear ideal for a wide range of current or future applications. Their high mechanical strength, combined with high electrical/thermal conductivity, allows the formation of strong, transparent, yet electrically and thermally conductive composites – including electromagnetic shielding of cables and conductive coatings of aircraft components – at relatively low loading levels of very few weight percent. Nanotubes can also be spun into yarns with toughness competing with Kevlar. Nanotube yarns can be knotted, plied, braided and woven into conductive fabrics that remain tough even under ultraviolet radiation.

Due to the large aspect ratio, as near other "sharp" objects, the electric field is locally enhanced by two orders of magnitude close to the tip of nanotubes, thus significantly enhancing their field electron-emission properties. Since – unlike other cold cathodes – nanotubes have a high melting point and maintain their high aspect ratio over time, they have a future as successors of electron guns in cathode ray tube (CRT) displays with a significant advantage: nanotube arrays attached to a substrate make bright, ultraflat displays, with each pixel lit by the current from several gated nanotubes beneath it.

Due to their long electron mean-free path, single-wall carbon nanotubes are ballistic conductors of electrons and holes, which makes them appealing as building blocks of future molecular electronics circuits. Carbon-nanotube-based field-effect transistors surpass in all the relevant criteria current silicon-based devices at a small fraction of the size. Carbon nanotubes are also likely to play a key role in future electronics applications, including spintronics and quantum computing.

Nanotubes have found a large-scale application as an additive to the graphite component of Li-ion batteries. Forming an elastic filler, they absorb the slack and prevent reorientation of graphite crystallites during their expansion/contraction associated with the intercalation/deintercalation of Li ions, thus increasing energy delivery and the number of useful charge/discharge cycles. High conductivity combined with a high surface-to-volume ratio opens up an application of nanotube assemblies as electrodes in supercapacitors and fuel cells. Unusual arrangements of conductive and insulating nanotube yarns may yield electronic fabrics with supercapacitor functionality.

Under various conditions, nanotube arrays appear to be biocompatible with human tissue. The combination of their nanometer-size diameter, well-defined cylindrical shape, and lack of chemical reactivity offer promise for the use of nanotubes as efficient templates for the proliferation of neurons. With carbon nanotubes as an additive to nylon microcatheters used in surgery, the occurrence of thrombus formation appears to be efficiently suppressed.

Even though no longer at the forefront of potential applications, reversible hydrogen storage is likely to benefit from the light weight and large accessible surface area of nanotubes and related sp^2-bonded carbon nanostructures.

Reproducible measurements suggest the capability of carbon nanotubes to store up to 2% (weight) molecular hydrogen at room temperature.

Nanotubes as a Test Ground of Fundamental Science

Even though it was the applications of nanotubes that grabbed most of the media limelight, nanotubes themselves offer a unique possibility to explore fundamental properties of quasi-one-dimensional (1D) conductors and semiconductors. For example, any phase transition – including the onset of superconductivity or magnetic ordering – should be suppressed in strictly one-dimensional systems. Furthermore, free carriers in one-dimensional conductors have been postulated to behave as a Luttinger liquid rather than being subject to Fermi–Dirac statistics. The screening behavior of these 1D systems modifies the optical properties of nanotubes significantly. An important example is the large binding energy of excitons that, in semiconducting nanotubes, is two orders of magnitude larger than in 3D semiconductors and thus comparable to their bandgap in typical semiconductors.

Problem Solution by Hand-in-Hand Collaboration Between Experiment and Theory

Many initial problems have been solved since the beginning of the Nanotube Rush era. Intensive collaboration between theory and experiment, especially in the field of single-wall nanotubes, became the key to rapid progress, which continues until the present. Among the many examples, observed inconsistencies in nanotube conductivity measurements were reconciled by learning how to make good contacts reproducibly. Also, superconducting behavior in nanotubes was only observed after good contacts between nanotubes and leads were established. Still, many problems remain and await solution, including the controlled production of carbon nanotubes with a well-defined atomic *(n, m)* structure, which is a critical parameter in deciding whether a particular SWNT is metallic or semiconducting, and whether it will perform to the required specifications.

The entire arsenal of experimental and theoretical techniques that had been developed to characterize low-dimensional systems, ranging from nanoparticles to surfaces, has been applied to nanotubes. Nanotube metrology has matured to a well-established field affecting not only quality control, but also providing guidance regarding the likely behavior of particular samples. On the experimental side, most direct information about the morphology of individual single- and multiwall tubes, including diameter and interlayer spacing, has been provided by high-resolution transmission electron microscopy. Raman spectroscopy has proven especially valuable in providing information about the fraction of graphitic carbon in the sample and determining the

distribution of nanotube diameters by analyzing the diameter-dependent radial breathing mode. Photoluminescence spectra offer a powerful way to determine the chirality distribution among semiconducting nanotubes. These methods are often combined with scanning probe microscopy and other spectroscopic techniques to characterize nanotube samples in terms of uniformity, purity, chemical modifications, and defects.

Theoretical techniques used to investigate the relative stability and mechanical properties of nanotubes range from continuum elasticity theory to bond-order potentials. Since the electronic structure in carbon nanotubes is dominated by $2p\pi$ electronic states, the single $pp\pi$ band Hückel model has proven very useful in understanding the electronic structure and quantum transport in nanotubes. *Ab initio* density–functional theory (DFT) calculations, or their parameterized tight-binding counterparts, are the methods of choice to determine the electronic structure and stability of pristine and functionalized nanotubes and related structures in the electronic ground state. Description of the excited-state dynamics of nanotubes requires calculations beyond DFT, including combinations of time-dependent DFT with molecular dynamics, GW calculations of electronic spectra, and the Bethe–Salpeter equation to describe excitonic states.

Future of Carbon Nanotubes

In the first decade of the 21st century, almost two decades after the onset of the Nanotube Rush, the nanotube field is as vital as ever. The rate of publications and patent applications in the field of nanotubes still continues to increase. Whereas the stream of break-through discoveries has been holding up until the present, other outstanding problems, identified in this book, still await solution. Cross-fertilization with emerging related fields, such as graphene, will likely accelerate progress by providing insight from a different viewpoint. The continuing vitality of the nanotube field is unusual, when compared to other research areas that initially appeared at least as appealing, including the field of fullerenes and high-temperature superconductivity. Reasons for the unexpected evolution of the field in the recent past may bear hints about the future.

One feature that sets the field of nanotubes apart from other similarly appealing areas is the wide field of promising applications, ranging from molecular electronics and quantum computing to materials science and medicine. Fundamental interest in the properties of this unusual material, combined with an apparently unlimited potential for applications, have sparked off international, interdisciplinary collaborations on a previously unprecedented scale and demonstrated the benefits of such collaborations.

The intense need for communication among the disciplines has established sections dedicated to nanotube science at many conferences in different fields. The Internet offers web sites dedicated to nanotubes, linking the scientific

nanotube community together and providing advice to the interested novice. Conferences dedicated to nanotubes, including the NT series initiated by the NT99 workshop in 1999, attract hundreds of scientists every year to new venues and new countries. With their vision to provide access to information for all at minimum cost and to foster scientific collaboration between different disciplines and cultures around the globe, nanotube conferences fulfill several worthy missions at the same time. Another appeal is their educational mission, namely to give young aspiring scientists a fair chance for discussion with their senior colleagues. The inspiration coming from days of intense information exchange, where age differences are swept away in the heat of the discussion, is likely to fuel the nanotube field for many more years to come.

Acknowledgements

This work was partly supported by the NSF NIRT grant ECS-0506309, the NSF NSEC grant EEC-0425826, and the Humboldt Foundation Award.

References

[1] A. Oberlin, M. Endo, T. Koyama, Filamentous growth of carbon through benzene decomposition, J. Cryst. Growth **32**, 335 (1976).
[2] S. Iijima, Helical microtubules of graphitic carbon, Nature **354**, 56 (1991).
[3] Graphitic carbon is a layered structure. Graphene is a monolayer of graphite.
[4] Computer simulations suggest that the melting temperature of nanotubes should lie close to ≈4000 K, observed in high-purity graphite. The observed reduction of the melting point to above 3000 K has been linked to defects and residual oxygen under experimental conditions.

Michigan, December 2007 David Tománek

Preface

Over the past 15 years, carbon nanotubes have evolved into one of the most intensively studied materials of this decade. Now, it seems clear that the carbon nanotube field is on the verge of approaching a "phase transition critical point", which means the field is now mature for making the transition from nanoscience to nanotechnology. This is therefore an important time to review what we have learned in the past decade and, most important, to look into the future of carbon nanotubes and related fields. The general goal for this book is to review research highlights for the past decade and to point to research opportunities for the future. This book builds on the best-selling Springer publication of 2001 in the Topics in Applied Physics Series volume 80 on Carbon Nanotubes and features reviews of many topics that have evolved since that publication. The present book is directed to both the very large number of researchers now working in the field, as well as the many new entrants looking for useful applications of the special properties of carbon nanotubes. In the spirit of these goals, the present volume has sought to bring leaders in the field of carbon nanotube research to summarize, using a tutorial style, the important advances occurring during the past decade and to point to some promising future research directions for the carbon nanotube field. Most of the chapters are written by a collection of authors from different groups worldwide, guaranteeing a broad view of each topic, rather than reflecting the work of specific research groups. We are thankful to the authors who produced excellent chapters that will greatly benefit many readers interested in carbon nanotubes and related topics, and to Springer-Verlag for cooperating with us in implementing this project. A.J. personally acknowledges financial support from CNPq, Fapemig, CAPES, Rede Nacional de Pesquisa em Nanotubos de Carbono and Instituto de Nanotecnologia (CNPq and MCT), Brazil, and G.D. and M.S.D. acknowledge NSF-DMR 04-05538.

Belo Horizonte, December 2007

Ado Jorio
Gene Dresselhaus
Mildred S. Dresselhaus

Contents

Inorganic Nanotubes and Fullerene-Like Structures (IF)

R. Tenne[1], M. Remškar[2], A. Enyashin[3], and G. Seifert[3]

[1] Department of Materials and Interfaces, Weizmann Institute Rehovot 76100, Israel,
reshef.tenne@weizmann.ac.il
[2] Jozef Stefan Institute, Jamova 39, 1000 Ljubljana, Slovenia
maja.remskar@ijs.si
[3] Physical Chemistry, Technische Universität Dresden Bergstrasse 66b, 01062 Dresden, Germany
Gotthard.Seifert@chemie.tu-dresden.de

Abstract. Back in 1992 it was proposed that nanoparticles of layered compounds will be unstable against folding and will close up into fullerene-like structures (IF) and nanotubes. In the years that followed nanotubes and fullerene-like structures were synthesized from numerous compounds with layered structure. More recently, crystalline and noncrystalline nanotubes of compounds with a 3D, i.e., quasi-isotropic lattice have been intensively investigated. In view of their eminent applications potential, much effort and substantial progress has been achieved in the scaling-up of the synthesis of inorganic nanotubes and fullerene-like nanoparticles of WS_2 and MoS_2 and also other compounds. Early on it was suggested that hollow nano-octahedra consisting of a few hundred MoS_2 moieties make the true analogs of C_{60}, etc. This notion has been advanced considerably in recent years through a combined experimental–theoretical effort.

Substantial progress has been accomplished in the use of such nanoparticles for tribological applications and lately for impact resilient nanocomposites. These tests indicated that IF-MoS_2 and IF-WS_2 are heading for large-scale applications in the automotive, machining, aerospace, electronics, defense, medical and numerous other kinds of industries. A few products based on these nanoparticles have been recently commercialized by "ApNano Materials, Inc" ("NanoMaterials, Ltd.", see also www.apnano.com). Most recently, a manufacturing facility for the commercialization of these nanomaterials has been erected and sales of the product started. Novel applications of inorganic nanotubes and fullerene-like nanoparticles in the fields of catalysis; microelectronics; Li rechargeable batteries; medical and optoelectronics will be discussed.

1 Introduction

The last few years have seen a large growth in the scientific interest in inorganic nanotubes and fullerene-like nanoparticles. Numerous studies have been published in this area and a number of review papers and chapters in books (for a partial list see [1–5]) have been dedicated to the subject. As about half of this book is an update of a book published in 2001, the present

A. Jorio, G. Dresselhaus, M. S. Dresselhaus (Eds.): Carbon Nanotubes,
Topics Appl. Physics **111**, 631–671 (2008)

contribution will devote itself mostly to developments in the field of inorganic nanotubes in the last five years. Also, in order to make this chapter manageable in size and consistent with the rest of the book, which is dedicated to crystalline nanotubes made of carbon, a classification of the published studies will be made first. One of the most important developments in the area of inorganic nanotubes is the use of "chemie douce" – soft-chemistry (low-temperature) methods to synthesize inorganic nanotubes, mostly from oxide compounds. Here too, a distinction between multicrystalline [6] and crystalline nanotubes will have to be made. In analogy to bulk material where X-ray diffraction (XRD) is used to distinguish between crystalline and polycrystalline phases, here electron diffraction (ED) is the main tool. For example, crystalline nanotubes of VO_x-alkylamine [7] and $H_2Ti_3O_7$ [8], with well-defined ED patterns, were synthesized by hydrothermal synthesis in the past, and are being further studied in recent years. However, appreciable effort is currently being devoted to the study of arrays of polycrystalline titania (TiO_2) nanotubes [9–11], which are prepared by electrochemical anodization of titanium foils in a fluorine-containing solution. Such polycrystalline phases do not show sharp and ordered diffraction spots, but rather a smeared pattern. These polycrystalline nanotubes are studied in connection with applications in photocatalysis, dye-sensitized solar cells, rechargeable batteries, electrochromic devices and sensors, and they will be discussed only briefly, because their structure is only remotely related to carbon nanotubes. Hence, this chapter will devote itself mostly to inorganic nanotubes with highly crystalline order.

Crystalline nanotubes of inorganic compounds were first conceived in 2002 [12] (see Fig. 1). Building on the analogy between graphite and inorganic layered materials, it was proposed that nanoparticles of the layered compound WS_2 [13] first, and then MoS_2 [14, 15] and others, which appear in platelet form in the bulk, will suffer inherent instability and fold (wind) into hollow closed structures, i.e., fullerene-like structures (IF) and inorganic nanotubes (INT). Ever since this early observation was made, IFs of numerous other layered compounds were synthesized and studied. Early on, the structure and some properties of BN nanotubes [16–18] and fullerenes [19, 20] were studied both through theoretical calculations and experiment. This part will not be further reviewed here. Note also that MoS_2 nanoscrolls [21] and closed layers [22, 23] were observed before with no follow-up of this early work.

Recent advances in synthetic methodologies showed that it is possible to grow crystalline nanotubes also from quasi-isotropic (3D) materials, like ZnO [24,25], GaN [26] or In_2O_3 [27]. These materials crystallize in a diamond-related structure (sp^3-related bonding). Therefore nanoparticles of such compounds were not expected to fold or wind when grown in the nanoscale range, which is common to nanoparticles of 2D layered compounds. Indeed, such nanotubes, or perhaps one should call them hollow nanofibers, are not expected to be bona fida stable. Thus, they are likely to be less stable than

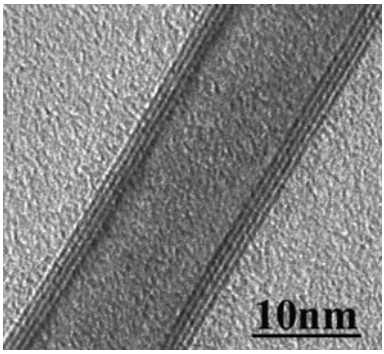

Fig. 1. TEM image of a typical 4-wall WS_2 nanotube produced by sulfurization of WO_3 powder at 840 °C [12]

the nonhollow nanofibers (if not surface passivated). They are usually highly faceted and frequently are grown with the help of a template, which can be later removed. In spite of that, nanotubes of 3D compounds could find numerous applications, as is briefly discussed below.

The structure of a monolayer of a 2D compound can be characterized in terms of a 2D lattice. It is possible to construct the infinite ensemble of the 2D lattices by the lengths of two translation vectors ($\boldsymbol{a}_1$ and $\boldsymbol{a}_2$) and the angle between them (φ). There are five types of the 2D Bravais lattices (Fig. 2): oblique ($\boldsymbol{a}_1 \neq \boldsymbol{a}_2$, $\varphi \neq 90°$), square ($\boldsymbol{a}_1 = \boldsymbol{a}_2$, $\varphi = 90°$), hexagonal ($\boldsymbol{a}_1 = \boldsymbol{a}_2$, $\varphi = 120°$), primitive rectangular ($\boldsymbol{a}_1 \neq \boldsymbol{a}_2$, $\varphi = 90°$), centered rectangular ($\boldsymbol{a}_1 \neq \boldsymbol{a}_2$, $\varphi = 90°$). Cylindrical surfaces may be constructed by rolling up these lattices. The walls of carbon nanotubes are composed of carbon hexagons with the same ordering as in the hexagonal graphenic layer. The basic principles of the structural specification of the "ideal" carbon nanotubes used at present are detailed in Chap. 1 of [28]. Many layered inorganic compounds, where tubular forms are known, also exhibit layers with a hexagonal atom arrangement. Examples of nonhexagonal layered structures, which may also form tubular structures are shown in Fig. 3. Using the basis vectors of the 2D lattice ($\boldsymbol{a}_1$, $\boldsymbol{a}_2$) one can define a "rolling" vector $\boldsymbol{c} = n\boldsymbol{a}_1 + m\boldsymbol{a}_2$ the integer indexes n and m may be used for the structural classification of the inorganic nanotubes in the same way as for carbon nanotubes – (n, m). For a 2D hexagonal lattice ($|\boldsymbol{a}_1| = |\boldsymbol{a}_2| \equiv |\boldsymbol{a}|$) the radius R of the corresponding tube is then given by: $R = \frac{|\boldsymbol{c}|}{2\pi} = \frac{|\boldsymbol{a}|}{2\pi}\sqrt{3(n^2 + m^2 + mn)}$.

Though inorganic nanotubes and fullerene-like structures have not been nearly as much studied as their carbon analogs, various properties and numerous applications for those nanomaterials were proposed and some have already been realized. The present review will attempt to delineate the unique properties of the INT and IF materials and in particular will attempt to show that the range of their potential applications is different and sometimes complementary to those of their carbon analogs, as discussed in the contribution by Endo et al.

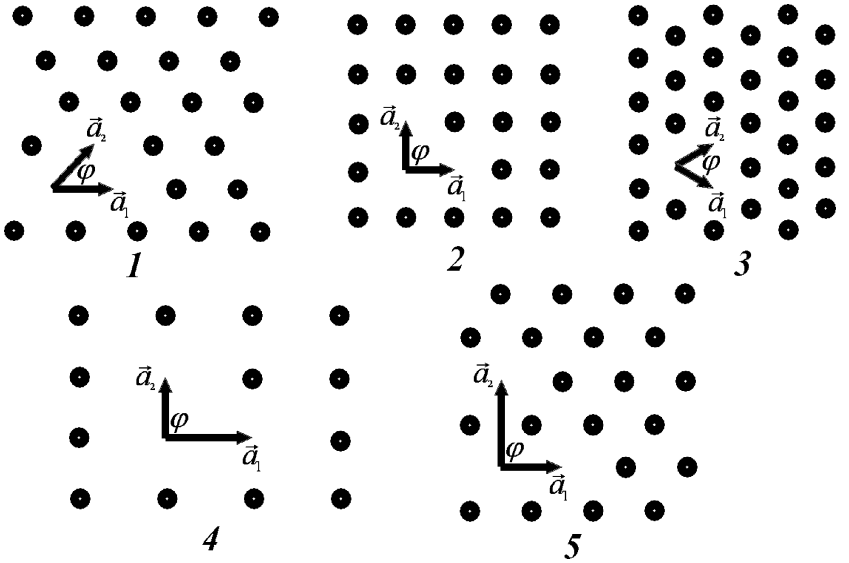

Fig. 2. The five 2D Bravais lattices: (**1**) – oblique; (**2**) – square; (**3**) – hexagonal; (**4**) – primitive rectangular; (**5**) – centered rectangular

2 Synthesis of INT and IF Materials

There is a whole range of synthetic strategies that have been developed for the preparation of inorganic nanotubes and fullerene-like nanoparticles. While the structure and shape control of IF and INT is not nearly as effective as in the case of carbon fullerenes and nanotubes, some of the successful methods demonstrated partial controllability. Furthermore, heuristic arguments derived from a combination of theory and experiment, allowed one to draw some far-reaching conclusions as to the propensity of a particular technique to produce certain nanostructures, as will be shown below. Despite some unique cases, unlike their carbon analogs, IF and INT prefer to come in multiwall structures. First-principles calculations provide a clue to this phenomenon, but far more work is needed on both the experimental and theoretical fronts to clarify the full complexity of IF structures and the INT. Remarkably though, chemistry provided some neat ways to produce various nanotubes, other than carbon, in large amounts (a few tons/day) and at affordable costs (< 100 dollars/kg).

2.1 Physical Techniques

Laser ablation and arc-discharge techniques, which played such a pivotal role in the discovery and furthering of the large-scale synthesis of carbon nanotubes and fullerenes, have been embraced only to a limited extent for the synthesis of IF and INT. Arc discharge of an MoS_2 target in water was shown to

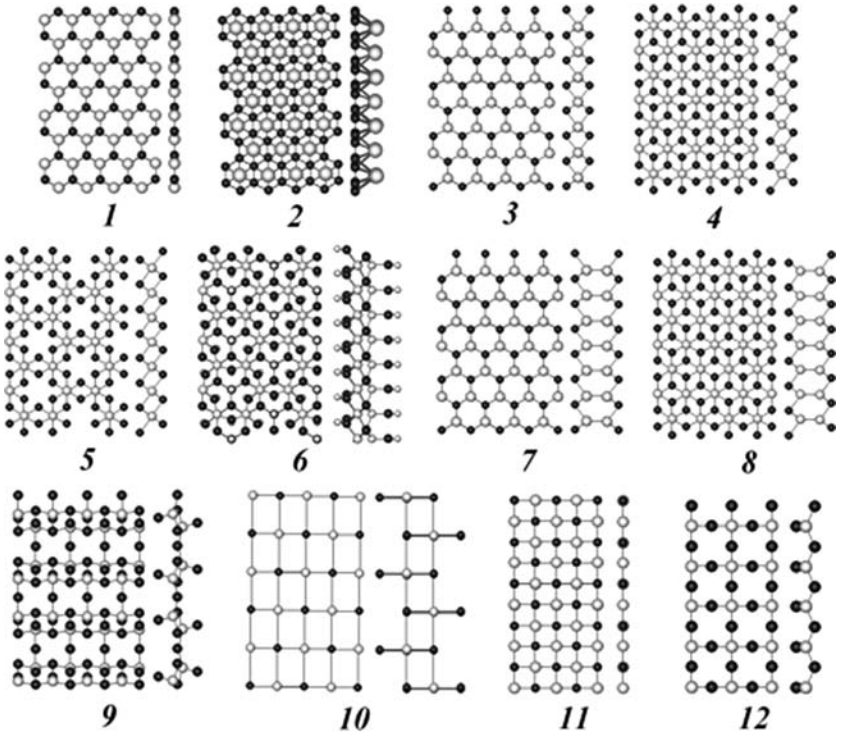

Fig. 3. Structures of the monolayers of some inorganic compounds: (**1**) – BN; (**2**) – AlB_2, MgB_2; (**3**) – MoS_2, WS_2, $NbSe_2$; (**4**) – TiS_2, ZrS_2, anatase TiO_2, $NiCl_2$; (**5**) – $FeCl_3$, MoO_3; (**6**) – imogolite $Al_2O_3(OH)_3Si(OH)$; (**7**) – GaS, GaSe; (**8**) – metastable InS with a hexagonal lattice, (**9**) – rectangular V_2O_5; **10** – centered rectangular lepidocrocite TiO_2; **11** – square MgO and **12** – SiO_2. The *empty circles* represent the metal atoms, while *full circles* stand for the nonmetal atoms

produce closed-cage nanoparticles consisting of 2–3 layers with a polyhedral topology and sizes between 5 and 15 nm [29]. The role of water is not fully clear but it seems to mend the violent reaction near the anode (temperatures reaching 3000 K), which would otherwise lead to excess sulfur evaporation. The authors used a 3-stage model to explain the formation of the closed-cage nanoparticles of that size and shape. In yet another set of experiments, arc discharge of IF-MoS_2 nanoparticles with a Mo core were reported [30]. Films of the nanoparticles were prepared and were found to provide superior tribological behavior as compared to films of 2H-MoS_2 prepared by pulsed laser ablation (vide infra).

Laser ablation is much more frequently used and allows for the direct determination of the cluster mass. Pulsed nitrogen laser (337 nm) ablation of a MoS_2 target combined with time-of-flight mass spectroscopy yielded peaks that could be assigned to stable $Mo_{13}S_{25}$ clusters. *Ab-initio* calculations con-

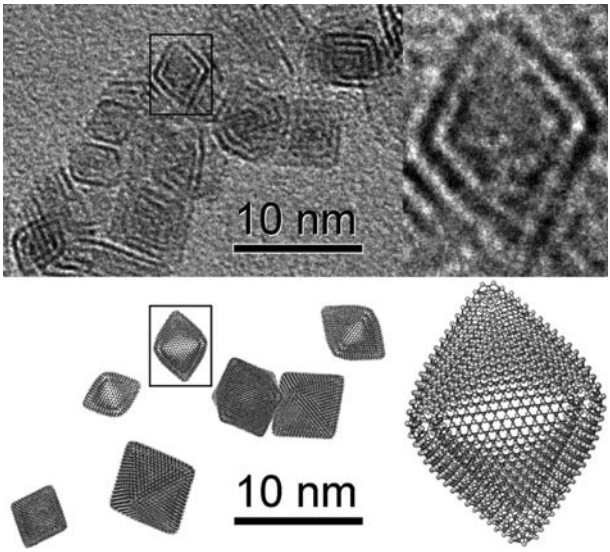

Fig. 4. *Left:* Nano-octahedra of MoS_2 prepared by laser ablation (see [34]). Exploded view of the framed nano-octahedron (*right*). The images in the *lower part* are structural models of the experimentally observed nano-octahedra

firmed that these structures are related to those of closed-cage MoS_2 polyhedra [31]. However, the portrayed structures with single- and double-bonded sulfur atoms protruding out from the cluster are not likely to be stable and further theoretical and experimental work is needed to confirm their exact structure. Using the second harmonics of a Nd:YAG laser (532 nm), multiwall polyhedral structures of 5–15 nm size of both MoS_2 and WS_2 were obtained [32]. Short multiwall WS_2 nanotubes were obtained, though at low yields. Nano-octahedra of MoS_2 were prepared by laser ablation [33, 34]. Figure 4 shows a TEM image of a typical product of the laser ablation (above) and their theoretical analogs modeled by density-functional tight-binding (DFTB) computations. Nano-octahedra and nanotetrahedra can be considered to be the ultimate closed-cage structure of MoS_2 (as well as many other layered compounds) – somewhat analogous to C_{60} in the carbon fullerene series. This specific issue is discussed in some detail below.

Nanostructured titanium oxide nanoparticles were produced in a pulsed microplasma cluster source in the presence of a helium-oxygen mixture as carrier gas [35]. Using HRTEM, isolated TiO_x cages that closely resemble carbon fullerenes were found in the deposit. The diameter of the cages ranges from about 0.9 to 2.7 nm. A fraction of the cages has irregular shapes, possibly induced by oxygen vacancies. It was proposed that the TiO_x fullerenoids grow in the gas phase, in a narrow temperature/pressure range within the cluster source, and that they are preserved through low-energy deposition.

In a series of experiments, ablation of the layered compound Cs_2O (with an anti-cadmium chloride structure) using the 532-nm line of a Nd:YAG laser [36], and subsequently with a focused solar beam [37], led to the formation of closed-cage fullerene-like nanoparticles. In contrast to the bulk material that comes in a platelet form and is extremely unstable in the ambient atmosphere, the IF-Cs_2O nanoparticles were found to be stable in the ambient for some time (< 1 h).

Electron-beam (e-beam) irradiation was found to produce closed-cage structures from various inorganic compounds and particularly those belonging to the layered metal-halide series. Early on, fullerene-like structures of MoS_2 were obtained by e-beam irradiation of MoS_2 within the TEM [38]. More recently, closed-cage polyhedral structures of layered $CdCl_2$ [39] were obtained by e-beam irradiation. Under ambient conditions, bulk 3R-$CdCl_2.H_2O$ comes as a layered monohydrate structure (the 3R symbol says that the unit cell of the compounds consists of 3 layers in a rhombohedral stacking). Unlike the bulk structure, the fullerene-like $CdCl_2$ was found to have no bound water molecules in their lattices. Furthermore, the nanoparticles were found to be stable in the ambient atmosphere for some time, before water started to dissolve the reactive corners, which suffer from excess strain. This observation is another manifestation of the kinetic stabilization achieved by the closed-cage IF structure. Faceted polyhedra and short nanotubes of CdI_2 [40] were also obtained by e-beam irradiation of the bulk materials. Interestingly, the TEM could resolve the two lines of the large iodine atoms in the individual closed monolayer. IF-$NiBr_2$ nanoparticles [41] were produced by sublimation-condensation in a furnace at 980 °C. The closed-cage nanoparticles were found to engulf a nonhollow core consisting of amorphous Ni. Alternatively, a $NiBr_2$-hydrate powder was first dried, and then laser ablated. The soot obtained by the laser ablation was placed on a TEM grid and was irradiated by focusing the e-beam on a spot for a few seconds, which resulted also in IF-$NiBr_2$ nanoparticles. In a few cases, nano-octahedra about 6 nm in size and consisting of 3 layers were observed. Closed polyhedra and short nanotubes of nickel perbromate hydrate $[Ni(BrO_4)_2(H_2O)_6]$ were also obtained, as a result of a reaction with residual humidity in the furnace.

2.2 Soft Chemistry "Chemie Douce"

Soft-chemistry methods are a canonical name for the low-temperature synthesis of materials, including among others hydrothermal (solvothermal) synthesis that is carried out in a high-pressure vessel (bomb reactor); intercalation-exfoliation method (of layered crystals); electrochemical synthesis, which in general yields polycrystalline nanotubes; solution-liquid solution (SLS), which is the low-temperature solution analog of the high-temperature vapor–liquid–solid (VLS) process, sol-gel, sonochemical methods, etc. Various kinds of nanotubes have been prepared using soft-chemistry methods, most of them being oxides. A number of examples of the synthesis of IF nanoparticles and

INT through soft-chemistry methods were described in the previous book [28] and they would not be further mentioned here.

Perhaps the most outstanding example of the success of soft-chemistry methods is the synthesis of the titanate nanoscrolls and the arrays of polycrystalline titania nanotubes. Back in 1998 a new method for the synthesis of titania nanotubes using first the sol-gel process and subsequently treating the product in an NaOH solution at 110 °C for 20 h was reported [42]. A more detailed structural analysis of the product revealed that the titania nanotubes are not of the anatase polytype, but are rather nanoscrolls obtained by the self-winding of molecular sheets of the hydrated layered titanate ($H_2Ti_3O_7$) compound [43]. Further study of the synthetic process [44] produced a plausible growth mechanism for the titanate nanotubes. First, titanate ($H_2Ti_3O_7$) nanocrystals are formed from the anatase (TiO_2) powder in the NaOH solution. Subsequently, the protons on the top surface of the crystal are neutralized in the highly basic solution. This reaction produces a charge imbalance between the top and lower sides of the $Ti_3O_7^{2-}$ layer leading to its exfoliation. Once exfoliated, the monomolecular sheet folds on itself due to interlayer (van der Waals) interactions. This work was followed by numerous other studies, where the growth mechanism was further studied and various potential applications, to be discussed below, have been proposed for such nanotubes. Crystalline nanotubes of very few other ternary compounds with layered structures have so far been reported. One such case is the hydrothermal synthesis of nanotubes of the layered compound $Bi_{24}O_{31}Br_{10}$ [45]. In a different kind of experiment, crystalline $PbCrO_4$ nanotubes were prepared by mixing lead acetate and sodium chromate in a mixture of aqueous and aprotic solvents in the presence of a surfactant and at room temperature [46]. This compound possesses a monoclinic unit cell and not a layered structure. Not surprisingly therefore, the rectangular cross section of the nanotubes reflected the unit-cell structure. Furthermore, the large diameter of the nanotubes (> 100 nm) far exceeds the typical value for nanotubes from layered compounds. Such compounds can wind around themselves, producing nanotubes with a characteristic diameter of 5 nm and above. Room-temperature synthesis of crystals of $K_5[(UO_2)_3(SeO_4)_5](NO_3)(H_2O)_{3.5}$ nanotubes (1.7 nm in diameter) were recently reported [47]. In another remarkable study, titanium phosphate ($Ti(HPO_4)_2 \times 0.5H_2O$ nanotubes were synthesized by a hydrothermal reaction in the presence of trioctylamine as the templating reactant [48].

In another remarkable experiment [9–11] arrays of polycrystalline titania (anatase polytype) were obtained by anodization of Ti foil in a fluoride-ion-containing solution. Anodization of Si, Al and various II–VI and III–V semiconductors is known to lead to the formation of a network of microporous holes with aspect ratios exceeding 10^3 for some three decades. These arrays and most particularly the alumina porous membrane serve to prepare numerous 1D nanostructures, which is mostly out of the scope of the present review. Recently, niobia and titania-niobia nanotubes were prepared by

the anodization of Nb and Ti45Nb foils in a hypophosphite-HF solution [49]. This advance allows the number of potential applications for such nanotube arrays to be extended considerably.

Template techniques for the fabrication of polycrystalline nanotube arrays have been used extensively in recent years. Thus, $Ni(OH)_2$ nanotubes were prepared by immersing a porous alumina membrane in hydrous nickel chloride and subsequently in ammonia solutions [50]. This study was motivated by the need for a high surface area material for the positive electrode of rechargeable Ni/Cd, Ni/Fe, Ni/metal–hydride and Ni/Zn batteries. Some other examples of the use of anodized (porous) alumina (AAO) membranes as templates for the synthesis of polycrystalline nanotubes are, for example, silica nanotubes [51], which were gold functionalized at their (open) tip. Such nanotubes can be used to bind specifically various biomolecules through the strong thiol–gold interaction. Another example is that of hydrous-RuO_2 nanotubes that can be potentially used for supercapacitors [52]. Polycrystalline nanotubes of the ferroelectric compound $PbTiO_3$ were also prepared using the same technique [53]. The ferroelectric transition temperature was found to be influenced by the crystallite size and not necessarily by the diameter of the nanotube or nanofibers. In another kind of study, hollow MoS_2 nanoparticles were obtained by the sonochemical reaction of $Mo(CO)_6$ and sulfur in isodurene with silica nanospheres used as a template [54]. After the sonochemical reaction was completed, the silica nanospheres were removed by light HF etching. The MoS_2 hollow nanoparticles showed a high reactivity and selectivity towards the decomposition of thiophene in a strongly reducing atmosphere, indicating that these nanomaterials could be very useful for the hydrodesulfurization of sulfur-rich gasoline. Elements of the pnictide series (P, As, Sb, and Bi) are able to form quasilayered puckered structure, with the lone pair of adjacent atoms oriented in opposite directions. A remarkably simple synthesis of Bi nanotubes by the room-temperature reduction of $BiCl_3$ solution with metallic zinc was proposed [55].

2.3 High-Temperature Reactions

This category includes IF and INT produced by reactions at $\sim 450\,^{\circ}C$ and above. The products of these reactions are in general of higher crystalline quality. Starting with the report on WS_2 nanotubes and fullerene-like structures, obtained by reacting thin films of WO_3 in a reducing atmosphere and under H_2S flow at $850\,^{\circ}C$ [13], a wealth of reports of new nanotubular structures has appeared in the literature. As for the previous paragraphs, the present review will concentrate mostly on recent developments in this field.

Viewing the substantial potential for applications, extensive work has been carried out on the synthesis of nanotubes from transition-metal dichalcogenides. One of the most important developments in recent years involves reacting volatile transition-metal dihalides or carbonyls and H_2S or other

sulfur-containing gases as precursors. The rationale for developing this reaction is that the synthesis of, e.g., IF-MoS_2, from the molybdenum oxide nanoparticles is a slow diffusion-controlled reaction, where the oxide core is gradually consumed by reaction with sulfur. Furthermore, some oxides like TiO_2 are very stable making the reaction with H_2S at $< 1200\,^{\circ}C$ practically unfeasible. Not least important is the fact that instead of the 750–950 °C used for the oxide to sulfide conversion, here, lower temperatures (below 750 °C) can be employed for the synthesis, though short annealing at higher temperatures is often needed. The first report of this new kind of reaction path was demonstrated for the synthesis of IF-NbS_2, which was obtained by reacting $NbCl_5$ vapors with H_2S in the range of temperatures between 400–550 °C [56]. Clear evidence was obtained that the reaction proceeds by a nucleation and growth mechanism, i.e., nucleation and then a layer-by-layer growth mode. When higher temperatures were used, the yield of the product became smaller, probably due to the fast self-decomposition of the niobium chloride vapors. This study was followed by a series of similar studies in which the metal-halide vapors were reacted with H_2S to yield fullerene-like nanoparticles and nanotubes (see for example [57, 58]). In another series of studies, vapors of metal carbonyls were used as the volatile precursor to react with H_2S, leading to IF-MX_2 (M = Mo, W; X = S, Se) nanoparticles [59]. Similarly, TiS_2 nanotubes were obtained by reacting $TiCl_4$ vapors with H_2S at 450 °C [60]. The nanotubes were subsequently used to demonstrate a rechargeable Li-intercalation battery [61].

Pyrolysis of ammonium thio-metallate was used on various occasions to synthesize nanotubes and fullerene-like nanoparticles of metal dichalcogenides compounds. In a remarkable experiment, WS_2 nested nanoparticles exhibiting a cuboid form of a rectangular parallelepiped, rather than the usual spherical morphology were obtained by spray pyrolysis of a 4×10^{-4} M $(NH_4)_2WS_4$ ethanolic solution at 900 °C [62]. Microwave-induced plasma reduction of WO_3 and ZrS_3 and HfS_3 at an effective plasma temperature > 1000 K yielded fullerene-like MS_2 (M = W, Zr, Hf) nanoparticles and nanotubes/nanorods [63]. The latter two were found to oxidize very rapidly, which was attributed to the imperfect structure of the nanotubes and fullerene-like nanoparticles. Bundles of single-wall $SbPS_4$ tubes each having 1.4 nm diameter were obtained by heating the respective elements to 650 °C in a sealed quartz tube for two days [64]. Partial Se to S substitution ($SbPS_{4-x}Se_x$; $0 \leq x \leq 3$) led to an increase in the diameter of the nanotubes and reduced the energy gap (from 2.57 to 1.9 eV). Templated ReS_2 nanotubes were synthesized by reacting $ReCl_3$-coated carbon nanotubes with H_2S gas at 1000 °C [65].

A most remarkable development of recent years is the synthesis of nanotubes with high crystalline order from compounds with a 3D (quasi-isotropic) lattice. Frequently, synthesis of such nanotubes involves a templating nanoobject. The first example was provided by the synthesis of an array of GaN nanotubes obtained by reacting trimethyl gallium and ammonia on the sur-

face of ZnO nanowires that served as a template and the subsequent removal of the template [26]. The nanotubes exhibited a hexagonal cross section following the contour of the ZnO nanowires, which grow along the [0001] growth axis with (100) and (110) facets. Likewise, In_2O_3 nanotubes with high crystalline order were obtained by heating a mixture of In and the above compound in an induction furnace to 1300 °C [27]. More recently, nanotubes and microtubes of 3D compounds, like InN were synthesized by a number of methods, like the carbothermal synthesis [66]. Furthermore, crystalline nanotubes of the ternary compound indium germanate ($In_2Ge_2O_7$) were synthesized by mixing In_2O_3, GeO_2 powders with active carbon and heating to 1000 °C in a sealed quartz ampoule [67]. The active carbon reduced the indium oxide into the volatile intermediate InO, which led to 1D axial growth of the nanotube. This, and similar germanate compounds, are being used as scintillating materials, e.g., for detecting solar neutrinos and as catalysts. $ZnAl_2O_4$ spinel nanotubes were obtained by first forming a core (ZnO) shell (Al_2O_3) 1D nanostructures. Subsequent annealing of the sample led to excessive outdiffusion of the ZnO core (Kirkendall effect) and spontaneous formation of the spinel nanotubes [68]. Similarly, $MgAl_2O_4$ nanotubes were obtained by conformal deposition of alumina on MgO nanowires. Following the annealing at 700 °C, the excess MgO core was removed by chemical etching, leaving behind the spinel structured nanotubes [69]. Heating $MnCl_2$ and Mg_2Si in excess of the former reactant at 650 °C led to a reaction of a molten-flux type that produced Mn_5Si_3 nanocages and bamboo-like nanotubes [70].

3 Structural Characterization and Stability

The largest inorganic tube was found in natural MoS_2 – molybdenite from quarries at Mont Saint-Hilaire, Quebec, Canada. The tube, 0.5 mm diameter by 6 mm long, is housed in the Canadian Museum of Nature as specimen No. 48756 [71]. It should be noted that the largest synthetic MoS_2 tube grown by chemical vapor transport was 11 μm in diameter and two millimeters in length. In this section, the structural aspects for the construction of inorganic nanotubes are considered.

3.1 General Considerations

Many different nanotube morphologies can coexist, sometimes even inside a particular nanotube. This includes, for example, faceted tubes, tubes with collapsed walls, periodically deformed cylindrical geometry – the so-called breathing tubes, tubes exhibiting transition from self-terminated layers to helical growth and vice versa, etc. Recently produced nanotubes with rectangular ($MgAl_2O_4$) [69] and hexagonal (GaN) [26] cross sections generalized the term of a tube even more, as an example of a hollow object possessing a high aspect ratio.

Most of the presently known inorganic nanotubes were synthesized based on layered – quasi-2D – compounds. The specific characteristic of these layered compounds is the pronounced anisotropy of the strong (covalent or ionic-covalent character) and weak (van-der-Waals') interactions within and between the layers, respectively. The structure of nanotubes can be complicated: they can have various numbers of cylindrical layers; open or closed ends; cylindrical, but also a scroll-like morphology. Nevertheless, the description of the tubular form of matter may be considerably simplified by using the classification developed for the single-wall carbon nanotubes, which can be constructed by rolling up of a monolayer in a seamless way.

The strain energy connected with the bending of the layered sheets to a tubular structure can be described in terms of classical elasticity theory, [72, 73]. The strain energy E_{strain} (per atom) of a tube with the radius R is given by:

$$E_{\text{strain}} = \frac{Yh^3}{24\rho R^2} \,. \tag{1}$$

Y is the Young's modulus of the layer, h is the layer thickness and ρ is the atom density of the layer.

There is one important difference in the structure of most known inorganic nanotubes compared with carbon nanotubes. The single-wall carbon nanotubes are based on a planar two-dimensional graphitic layer, which is just one carbon atom thick. In contrast, in most of the layered inorganic compounds, a single layer has a more complicated atomic arrangement and is several atoms thick. Therefore, inorganic single-wall tubes are composed of several concentric and interconnected cylinders of atoms. Due to their greater layer thickness, inorganic nanotubes of a given radius usually have higher strain energy than the corresponding carbon nanotubes. Also, the radii of stable inorganic nanotubes are considerably larger than those of carbon nanotubes – see Fig. 5.

Like their carbon-nanotube analogs, inorganic nanotubes may exist also in a multiwall tube structure, i.e., single shells are held together by weak van-der-Waals interactions. Another difference between carbon nanotubes and inorganic nanotubes is that the latter are often open ended, i.e., they do not possess a fullerene-like cap. However, caps can also be occasionally observed and atomistic models have been proposed for such caps in some cases (see, e.g., [76]).

Besides these general considerations, atomistic simulations of the structure and stability of a series of existing as well as hypothetical inorganic nanotubes were performed. (For an overview on the status of theoretical investigations of inorganic nanotubes see also [3].) The calculations were performed with empirical force fields, semiempirical quantum-mechanical methods and especially with density-functional-based methods, mainly using pseudopotentials and plane-wave (PW) basis expansions or within a tight-binding approach. Usually, periodic boundary conditions along the tube direction are

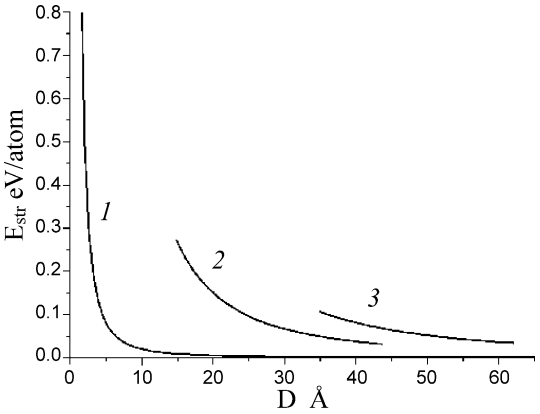

Fig. 5. Comparison of the calculated strain energies vs diameter of carbon nanotubes (*1*) and those of the inorganic nanotubes TiS_2 (*2*) and GaS (*3*) [74, 75]

used. A few studies were also published, using line-group symmetries [77], which allow the analysis of rather large tubes of any chirality. Generally, the unit cells of inorganic nanotubes contain considerably more atoms than carbon nanotubes, which increases the computational resources needed for calculations of inorganic nanotubes quite significantly.

3.2 Strain-Relaxation Mechanisms in the Nanotubes

WS_2 and MoS_2 adopt two kinds of stacking: a hexagonal polytype 2Hb with two molecular layers ($P6_3/mmc$) symmetry and a rhombohedral polytype 3R with three molecular layers per unit cell (R3m) symmetry [78]. Considering nanotubes with only two adjacent layers, the one with larger diameter contains a larger number of unit cells, but they have to be in the regular stacking order with the previous turn. Selected-area electron diffraction (SAED) of multiwall MoS_2 nanotubes produced by the chemical vapor transport technique reveals a rhombohedral (3R) stacking. This polytype is known to be stable at elevated pressure above 4 GPa. These results provide indirect evidence for the strain in the nanotube wall. The intensity of the strain increases towards the tube axis, causing the contraction of the interlayer distance and the instability of the inner molecular layers. It was observed that the relaxation of the strain produces edge dislocations or stacking faults. In nanotubes with diameters below 200 nm, the strain is partially relaxed, stabilizing the hexagonal (2H) stacking. The relaxation of the built-in strain was observed experimentally during the irradiation of the nanotubes with the electron beam [79]. The built-in strain in WS_2 nanotubes was recently confirmed by Raman spectroscopy [80].

The contraction of the interlayer distances caused by internal strain incorporated in the tube wall may influence the helicity of the nanotubes. The

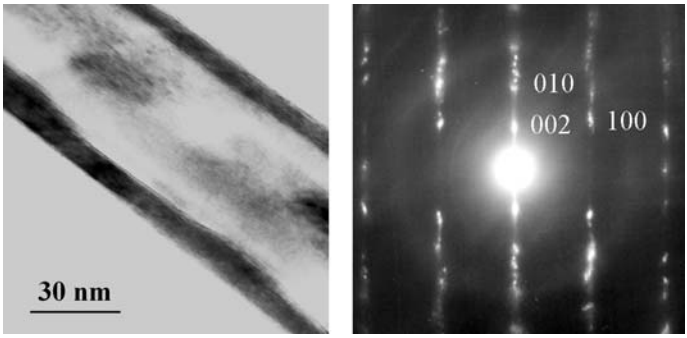

Fig. 6. TEM image of a NbS_2 nanotube (*left*) and its electron-diffraction pattern (*right*) [84]

method of synthesis is crucial for the observation of the strained nanotube walls. The nanotubes possessing incorporated strain were prepared by chemical transport reaction from the vapor phase at high temperature (1010 K) in a sulfur-rich atmosphere, where the sulfur adsorption/desorption, and the corresponding lattice relaxation dynamically coexist. Interlayer distances and chiral angles reveal the radial dependence of the strain and are strongly influenced by the wall thickness. While the separation among the outer layers is expanded, the interlayer distances closer to the inner core are contracted, even beyond the bulk value. The strain can be only partially relaxed by the change of chirality. Complete suppression of helicity is typical for MoS_2 and WS_2 nanotubes alloyed with gold and silver [81] as well as in nanotubes prepared in the presence of C_{70} [82]. Contrary to noble-metal-alloyed nanotubes, the Nb-doped WS_2 nanotubes did not show any extension of the interlayer distance [83].

Many inorganic NTs prepared by the decomposition process appear as an assembly of nanocrystallites forming the nanotube wall, e.g., of NbS_2 [84]. The crystallinity can be improved by additional annealing of the tubes, for example, or by increased in-situ temperature during the growth (see Fig. 6). Although the defects are a kind of relaxation and stabilization of the real system, they increase the free energy with regard to the perfect structure. Structures produced by gas-phase synthesis are more likely to be in equilibrium than those produced by diffusional transformations.

A different relaxation mechanism for ternary-alloyed nanotubes is by phase segregation [85]. Several distinct contributions to the nanotube energetics are: the internal and external surface energies, the energy of the interface between the different phases, the long-range van-der-Waals interactions between interfaces, and the elastic bending energy of the nanotube. For a two-layer system, like in the case of BN and C nanotubes, the material with the higher surface energy, in this case the BN, will preferentially lie on the tube interior where the surface area per unit length is smaller. For the

ternary system the C/BN/C three-layer tube structure is thermodynamically possible, while the BN/C/BN tube is unstable.

3.3 Studies of Some Specific Systems

The element most related to carbon is silicon, but the possibility of a synthesis of pure silicon nanotubes, which are topologically identical to carbon tubes, is questionable. For silicon, the sp^2 configuration with its layer stabilizing π-bonding is not stable. First, quantum-mechanical calculations on hypothetical silicon nanotubes based on hexagonal layers were published in 2000 [86]. The calculated strain energies of the silicon nanotubes are nearly the same as for the corresponding carbon tubes. The calculations agree that silicon tubulenes would be based on a buckled cyclohexane-type layer rather than on a planar honeycomb network [87, 88]. However, the overlap of the p_π-orbitals in the case of silicon is about ten times smaller than in carbon, i.e., any significant π-bonding contribution in such Si structures can be excluded. Therefore, the possible existence of Si nanotubes seems to be doubtful. Like silicon, germanium also crystallizes in the diamond structure. Germanium nanotubes based on graphitic-like layers were not investigated, but due to the missing π-bonding contribution, such structures should probably also be unstable.

Buckled hexagonal sheets and tubes of Si or Ge atoms could, however, be stabilized by saturation of the free valencies, e.g., with hydrogen atoms, as shown in refs. [89, 90] for silane SiH and germane GeH nanotubes. A stabilization of layered or tubular structures of silicon can also be accomplished by negative charging of the Si, as is the case in silicides (e.g., $CaSi_2$). The structure and stability of bundles of $CaSi_2$ nanotubes were calculated by density-functional calculations [91].

The most stable allotropes of phosphorus, arsenic, antimony, and bismuth are the layered modifications. These elements are isomorphic. Each atom connects pyramidally to the three neighboring atoms in the same layer. The structure of these layers looks similar to that of graphite, but the layers are "puckered" and the hexagonal rings appear like the chair cyclohexane conformation. The structural, electronic and mechanical properties of hypothetical nanotubes based on black phosphorus were calculated with a density-functional-based method [92]. The strain energy of phosphorous nanotubes varies proportionally to $1/R^2$, but it is higher than for carbon tubes with the same radii. This is caused by the increased repulsion of the lone pairs of the adjacent phosphorus atoms in the rolled-up layers. Calculations of bismuth nanotubes [93] also describe the properties of stable Bi tubes, which have been synthesized by a low-temperature controlled hydrothermal reduction method [94]. Both cluster and periodic theoretical models were applied to calculate the properties of boron nanotubes [95, 96]. The calculated strain energies of the boron nanotubes are comparable with the strain energy of other known – carbon and boron nitride – nanotubes. More recent calculations [96]

show that boron nanotubes may also have noncylindrical forms. The boron network may be stabilized by substitution with other elements. In this way, one can get the structure of the layered borides of the AlB_2 type. The stability and morphology of hypothetical diboride nanotubes were investigated using molecular mechanics [97] as well as first-principles DFT methods [98]. The structure, the nature of the chemical bonding, and the electronic properties of single- and multilayer tubes based on MgB_2, AlB_2, ScB_2 and TiB_2 were analyzed using the semiempirical extended Hückel (EHT) method (see for example [99]). The most stable tubes are those where the metal atoms are located inside the boron skeleton. The results of the first-principles calculations of the stoichiometric (6,0)TiB_2 and the composite (6,0)TiB_2@(12,0)B nanotubes were published in [100]. It was found that the strain energy of the (6,0)TiB_2 tube is $\sim 0.09\,\mathrm{eV/atom}$, which is comparable to the corresponding value in carbon nanotubes.

The layered modification of boron nitride (BN) was the first noncarbon compound predicted theoretically as suitable for the construction of inorganic nanotubes. With empirical force fields and quantum-mechanical methods, several important characteristics of these nanotubes were predicted, which have been confirmed experimentally. At present, BN nanostructures are being studied in nearly as much detail as the carbon nanotubes. The structural and thermal properties of BN nanotubes have been investigated by molecular dynamics simulations with empirical potentials. The Tersoff potential was employed to calculate strain energies, which agree semiquantitatively with the data of the first-principles calculations [101]. The study of the thermal properties shows that the temperature of the tube destruction depends distinctly on the configuration and the size of the tubes. The armchair tubes are stable at higher temperatures than the zigzag tubes of the same radii. Nanotubes with smaller radii disintegrate at lower temperatures, due to their higher strain energies. In analogy to the Stone–Wales defects in the carbon nanotubes, nonhexagonal rings play an important role in the process of thermal degradation of BN nanotubes. Evidently, the formation of these defects is a key step for the mechanical destructions of the BN nanotubes, as demonstrated by computer simulations [102].

Nanotubes based on other nitrides that possess a 3D structure but are isoelectronic to BN, i.e., AlN and gallium GaN, have been studied. The calculations show a big difference between the energies of the quasi-2D (BN) and the 3D (AlN, GaN) compounds. Nevertheless, the strain energy of the hexagonal AlN monolayer is smaller than that of the corresponding carbon nanotubes [103, 104]. From molecular dynamics simulations, it follows that AlN nanotubes could be stable at room temperature and begin to disintegrate at 600 K. Density-functional calculations were carried out also for graphitic-like monolayer GaN nanotubes. From these calculations, the same trends in the stability and characteristics are obtained as discussed above for AlN tubes. Molecular dynamics simulations with the empirical Tersoff potential were performed for the studies of the thermal properties of GaN tubes

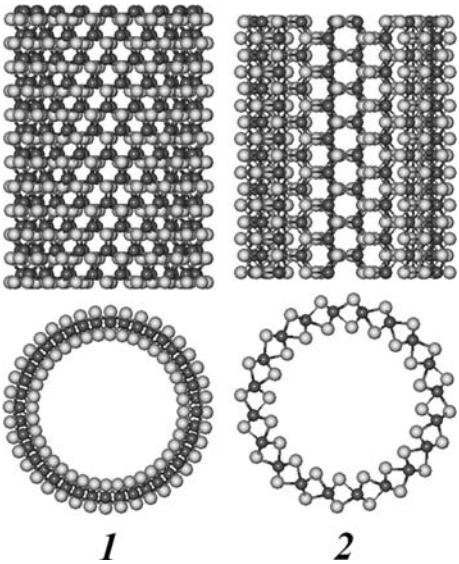

Fig. 7. The atomic structures of (***1***) zigzag (20,0) and (***2***) armchair (10,10) MoS_2 nanotubes (see [76]). *Upper drawings* show side views, while *lower drawings* show the top views of the nanotubes

and of their behavior under tension and fatigue [105, 106]. As for the BN nanotubes, a destruction of the GaN nanotubes starts after the formation of Stone–Wales-like defects.

The first quantum-mechanical calculations of metal sulfide nanotubes were performed with the DFTB (density functional tight binding) method for MoS_2 and WS_2 nanotubes (see, for example, [73, 76]). The layered dichalcogenides of Mo and W have a hexagonal structure and they are characterized by MX_6 units with a trigonal prismatic coordination of the metal. Due to the hexagonal structure of the layers, the tubes can be classified in the same way as carbon nanotubes, $n = m$ armchair tubes, $n > 0$, $m = 0$ zigzag tubes and $n \neq m$ chiral tubes. The calculated structures of an armchair and a zigzag MoS_2 nanotube are shown in Fig. 7. The strain energy of such triple-layer nanotubes is, as expected, clearly larger than for carbon nanotubes. Therefore, MS_2 tubes larger than 6 nm in diameter become more stable than the corresponding strips. This result is in accordance with the experimental finding that the smallest observed (inner) diameter of MoS_2 or WS_2 nanotubes is around 6–7 nm. Furthermore, the van der Waals interaction between the atomic layers in the stripes and between the shells in the multiwall nanotubes shift the stripe–tube transition to larger sizes with increasing number of atomic layers/shells. This may explain the great difficulty in the synthesis of single-wall MoS_2 and WS_2 nanotubes [12].

Nanotubes based on the semiconducting disulfides with octahedral coordination of the metal atoms (TiS_2 and ZrS_2) were studied with tight-binding methods (see for example [74]). The octahedral coordination of the Ti atoms was found to be more stable than the trigonal prismatic coordination for both the tubular and the layered form [75]. The stability and the energetics of the layered structure Ga chalcogenides (GaS, GaSe) were studied by density-functional-based calculations [75]. The calculated strain energies for these tubes are considerably larger than those of the transition-metal chalcogenides.

The tendency to form layered materials is much less pronounced for the metal oxides than for the respective chalcogenides, due largely to their higher ionicity. Correspondingly, the ability to form tubular structures should be less pronounced for the oxides. Nevertheless, a number of oxide-based tubes could be synthesized (see above) and were also studied theoretically. The first calculations of oxide nanotubes were carried out for TiO_2 nanotubes using the semiempirical EHT method [107]. For the construction of the tubular structures, an anatase monolayer was used. Beside anatase-based tubes, scroll-like nanotubes (nanorolls), and the nanotubes of the lepidocrocite modification of TiO_2 [108] were investigated with the DFTB method. It was shown that the cylindrical anatase nanotubes are the most stable ones among these nanostructures. This can be explained by the absence of dangling bonds and the smaller thickness of a layered compared with the lepidocrocite modification.

A very interesting type of inorganic nanotubes is the tubular structures based on vanadium oxide, VO_x. They differ from "classical" nanotubes in a number of ways. First, their composition depends on the procedure of synthesis and they intercalate organic molecules between the layers, forming thereby an organic–inorganic superlattice structure. Secondly, cylindrical nanotubes are rare among the VO_x tubes, but usually they occur as nanoscrolls. This structure leads to some difficulties in the construction of suitable models and computer simulations of these systems. Mainly due to the large size of such tubular structures, there are no semiempirical or first-principles quantum-mechanical studies available on the structural and energetic properties of these systems. Simple models based on the divanadium pentoxide V_2O_5, which has a quasilayered structure, have been proposed. The first attempts at modelling of the cylindrical and the scroll-like V_2O_5 nanotubes were performed with the EHT method [109], which can only give a first insight into the electronic properties, but does not allow an estimation of the energetics and the stabiliy of such structures.

Si–O nanotubes, based on a siloxene ($Si_6H_3(OH)_3$) layer, were considered first in [110]. Molecular dynamics simulations at 800 K confirm the stability of these tubes. A number of other oxide-based tubular structures are under investigation, including SiO_2, Al_2O_3, imogolite, ZnO, etc.

Another interesting class of tubular systems are the tubes based on layered halogenides, as for example $CdCl_2$ or $NiCl_2$. However, despite preliminary at-

tempts [111,112], the properties of these systems are not yet well understood, possibly because there exists no rational strategy for their synthesis.

4 Physical Properties

The availability of a new toolbox for the nanomanipulation of individual nanotubes and nanowires offered new opportunities for physical measurements and opened a whole range of issues to be addressed. Most interesting is the fact that nanotubes (nanowires) can be synthesized free of defects providing thereby a safe ground for quantitative comparisons with first–principles theoretical calculations, which was hitherto very difficult. Moreover, many physical properties show a remarkable size dependence in the transition from the bulk state to that of a single or few molecules. These changes can be systematically analyzed with the current technology. However, much of this physics is yet to be unraveled. While relatively much work has been done on the mechanical properties of inorganic nanotubes, the number of studies on the electronic, optical and magnetic properties of such nanotubes is very small and should be extended.

4.1 Mechanical Properties

The mechanical properties of WS_2 nanotubes are interesting not merely for academic reasons. These and similar inorganic nanotubes show extensive potential for becoming part of ultrahigh strength nanocomposites technology. A systematic and comprehensive study of the mechanical properties of WS_2 nanotubes was undertaken using scanning electron microcopy (SEM) and scanning probe microscopy (SPM) [113–115]. Several techniques for handling and mounting of individual nanotubes were used for these studies. Conceptually, performing similar experiments within the transmission electron microscope (TEM) could provide accurate atomistic pictures during the mechanical measurements, which could then be compared with quantitative computer simulations. However, technologically this is the most demanding and the least mature technique of all. Further developments in this direction are in progress. Another area, where progress is slow and much further work is needed, is the coupling between mechanical and electrical, thermal or optical effects in a single nanotube.

Figure 8 displays a series of micrographs taken during the tensile test of an individual WS_2 nanotube within the SEM. These experiments provided the full strain–stress curve of a nanotube. Repeating these experiments many times provides statistically averaged meaningful values for the Young's modulus (Y), the strength and the elongation to failure. In a limited series of about 10 nanotubes, the values of these parameters were found to be 150 GPa, 16 GPa and 12 %, respectively. The experimentally observed Young's modulus agrees very well with that of bulk WS_2 ($\perp$c). The strength of the nanotube

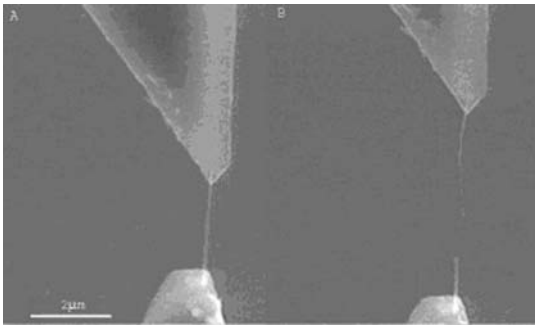

Fig. 8. SEM image of a WS_2 nanotube with both its edges glued to SiN cantilevers in a typical tensile test: before (*left*) and after (*right*) it has been broken (see [114])

is 11 % of the Young's modulus, which is rarely observed in bulk materials. First-principles calculations for single-wall MoS_2 nanotubes were performed and were generally in agreement with the experimental findings. The calculated stress and strain are 40 GPa and 17 % for the zigzag (22,0) tube, and 34 GPa and 19 % for the armchair (14,14) tube. The Young's modulus was found to be 230 GPa, which is the same as that of bulk MoS_2 ($\perp$c). The calculated strength results are equivalent to 17.4 % and 14.7 % (for the zigzag and armchair nanotubes, respectively) of the Young's modulus of MoS_2. Notwithstanding the differences between the Young's modulus of MoS_2 and WS_2, the agreement between the experimentally observed and the calculated values is very good. When the nanotube reaches its ultimate elongation, a single chemical bond in the middle of the nanotube breaks. This failure then leads to a stress concentration in the adjacent chemical bonds that become overstrained and consequently fail, leading to immediate destruction of the nanotube. The experimentally determined strength of the WS_2 nanotubes is 11 % of its Young's modulus, which is an exceedingly high value in comparison to high-strength materials. It is important to realize that the onset of failure of the nanotubes emerges from excessive distortion of a chemical bond, while the role of macroscopic failure mechanisms, like dislocation diffusion and propagation of cracks along grain boundaries seem not to be applicable here. A recent tensile test of a multiwall WS_2 nanotube within the TEM shows a telescopic failure, which confirms the notion that the strain is taken by the outermost layer of the nanotube [116].

The shear modulus of a beam is expressed as: $G = Y/2(1 + \nu)$, with ν the Poisson ratio. This expression shows that the three important mechanical parameters are not independent. In particular, if one assumes the value of 0.3 for the Poisson ratio of a WS_2 nanotube, G is found to be 57 GPa. DFTB calculations of the intralayer shear modulus yielded the values of 53 and 81.7 GPa for zigzag and armchair single-wall MoS_2 nanotubes, respectively. This value is significantly different from C_{44} values that were previously de-

termined by neutron and X-ray scattering of the linear compressibilities for bulk 2H–MoS_2 (15 GPa) [117]. Bending tests of ropes of single-wall MoS_2 nanotubes produced values of $Y = 120$ GPa and $G = 0.16$ GPa [118]. This data indicated that the interlayer shear of multiwall MoS_2, which is affected by the weak van der Waals interactions, is appreciably smaller than the one obtained within a layer.

To address this issue quantitatively, a bending test of an individual WS_2 nanotube was carried out by suspending the nanotube over a micrometer-wide trench [115]. An AFM tip approached the nanotube along the trench and produced a horizontal deflection. The net deflection of the nanotube was divided between axial strain and shear. This analysis produced a shear of 2 GPa, which is believed to reflect the slippage between adjacent WS_2 layers of the nanotubes and is designated as a sliding modulus. The DFTB calculation of the interlayer shear of two adjacent layers in 2H-MoS_2 resulted in a modulus of 4.09 GPa, which is in reasonable agreement with the experimental data for the multiwall WS_2 nanotubes (the van der Waals interaction between adjacent layers in the two materials is not likely to be very different).

Due to the strong C–C bond in sp^2 (graphitic) hybridization, the Young's and the shear moduli of carbon nanotubes are appreciably higher than those of most inorganic nano1tubes. (See the contribution by Yamamoto et al.). Furthermore, being made of carbon these nanotubes are very light. Nonetheless, carbon nanotubes, and especially the multiwall ones, which are very important, for example, in ultrahigh-strength nanocomposites, suffer from a number of disadvantages making the presently available inorganic (WS_2 or MoS_2) nanotubes suitable for a variety of mechanical applications. In particular, the C–C bond is unstable under compression and transforms easily into the sp^3 (diamond) bond. Contrarily, WS_2 or MoS_2 do not have a high-pressure phase and under high pressure they eventually break down, making their INT and IF nanoparticles much more robust under compression. Furthermore, the narrow scattering in the strength and elongation data of the WS_2 nanotubes [113–115] indicate that they are almost free of critical defects, permitting a predictable assessment of their mechanical behavior in a variety of media.

4.2 Electronic and Optical Properties

The electronic band structure of many inorganic nanotubes has been studied with semiempirical and density-functional based methods. In the latter the Kohn–Sham orbital energies were used for the representation of the band structures. Simple zone-folding schemes for the estimation of the nanotube band structure from the band structure of the corresponding layered structure is less meaningful for inorganic nanotubes than for carbon nanotubes. This is mainly due to the much more significant structural relaxation in the case of the rolled layer for inorganic tubes as compared to carbon nanotubes. This conjecture was nicely shown for the nanotubes of MoS_2 and WS_2. In

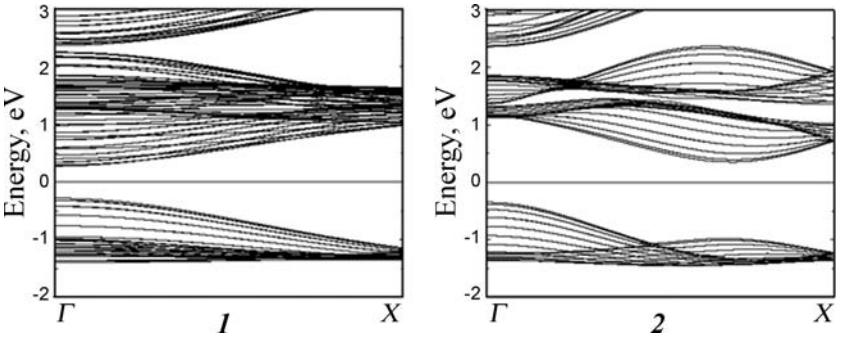

Fig. 9. The band structures of the MoS_2 nanotubes: (**1**) – (22,0) zigzag and (**2**) – (14,14) armchair configurations (see [76])

analogy to carbon nanotubes the qualitative picture of the band structure of armchair and zigzag MoS_2 can be derived from the band structure of the molecular MoS_2 layer with its hexagonal structure [76] – see Fig. 9. But there is a strong reduction of the gap size with decreasing radius of the tube. This reduction caused by the compression of the inner sulfur "shell" in the S–Mo–S triple layer in the tubular structure is compared with a flat triple layer in layered MoS_2. This calculated reduction is consistent with experimental observations of the optical-absorption spectra of MoS_2 nanotubes and inorganic fullerene-like structures and scanning tunnelling microscopy (STM) studies of WS_2 nanotubes [119]. A similar size dependence of the electronic gap was also predicted in the past for GaSe nanotubes. Many inorganic nanotubes investigated up to now are semiconductors or insulators and they show considerable dependence of the gap size on the tube diameter. This holds for hypothetical SiH– [89], GeH– [90] based nanotubes, hypothetical phosphorus tubes [92], Bi tubes [93], and many others. The diameter dependence of the gap size is in all cases nearly independent of the chirality of the nanotube. However, in many cases (MoS_2, BN, AlN, GaN), the zigzag nanotubes have a direct bandgap, whereas for the armchair nanotubes the gap is an indirect one.

For several tubular structures it has been shown that the semiconducting nanotubes can be transformed into metallic ones by intercalation or substitution. This has been demonstrated theoretically, e.g., for Si-based nanotubes in terms of silicide nanotubes ($CaSi_2$) [91], for BC-based nanotubes by intercalation with Li [120], and by partial substitution of Mo by Nb in MoS_2 nanotubes [121]. According to DFTB calculations NbS_2 nanotubes [122] should be metallic with the Fermi energy in the Nb electronic d-band, which is related to a rather high density of states at the Fermi energy. This could be of interest with respect to the superconducting properties of these nanotubes. Boron-based nanotubes [95, 96] and metal-boride nanotubes [97–100] should also be metallic.

The analysis of the optical properties of various kinds of inorganic nanotubes was undertaken in recent years. Many of the measurements were done on ensemble of nanoparticles with a few studies only dedicated to individual nanotubes.

Raman and IR spectroscopies were used to follow the structural transformation of TiO_2 powder into titanate nanotubes. Here, anatase/rutile titania (TiO_2) powder (Degussa P-25) was converted into the layered titanate ($H_xNa_{1-x}Ti_3O_7$) lattice by hydrothermal reflux in an NaOH solution. A subsequent HCl wash yielded $H_2Ti_3O_7$ nanotubes [123]. The conversion of the anatase/rutile nanoparticles (p-25 powder) to sodium titanate during the NaOH reflux was confirmed by the loss of the B_{2g} and the second order of the B_{1g} phonon mode at 398 cm^{-1} of anatase that individually peak at 516 and 784 cm^{-1}. Instead, a new peak appears at 906 cm^{-1}, which is typical for the short Ti–O bond stretching in the layered sodium titanate. The sodium–proton cation exchange during the HCl treatment was confirmed by the disappearance of this latter peak, as well as by the observation of new peaks at 266 and 822 cm^{-1}. The IR absorption peaks at 1618 and 3423 cm^{-1} are attributed to the bending and stretching modes of OH groups of physisorbed water molecules, which confirms the presence of such molecules in the titanate nanotubes. The shoulder at 3208 cm^{-1} was assigned to the Ti–OH bonds. This study confirmed the existence of the Ti–OH bonds in the nanotubes.

Optical absorption, photoluminescence (PL) and luminescence excitation of titanate nanotubes were undertaken [124]. The bandgap of the nanotubes (3.87 eV) is close to that of the layered sodium titanate (3.84 eV), but is appreciably higher than that of the anatase phase of titania (3.2 eV). Studies have shown that changing the internal diameter of TiO_2 nanotubes in the tube diameter range 2.5–5 nm does not lead to any changes in the position of absorption and emission bands, indicating small quantum size effects in this size range. This observation is not very surprising in view of the large effective mass of the exciton and the small Bohr radius (1.9 nm). It is concluded that the electronic structure of TiO_2 nanotubes is very close to that of TiO_2 nanosheets [124]. In yet another study strong and broad subbandgap photoluminescence with a peak at 570 nm was observed in samples consisting of titanate nanotubes. The PL was associated with the Ti–OH complex within the tubular structure [125].

The electronic structure and optical properties of VO_x-alkylamine nanotubes were investigated by absorption, photoelectron and electron energy-loss spectroscopies [126]. Photoemission and core-level electron energy-loss spectroscopies confirm the mixed-valence character of VO_x-alkylamine nanotubes. Indeed, the vanadium ion was found to have an average valency of 4.4+ in these nanotubes. The onset of the optical bandgap absorption was determined as 0.55 eV. A higher absorption peak at 1.25 eV was attributed to an internal d–d transition, which becomes optically allowed due to local symmetry breaking in the mixed (4,5) valency of the nanotube lattice. In another

study, the temperature dependence of the optical gap of VO_x-alkylamine nanotubes was determined [127]. The optical gap at 0.56 eV was found to be insensitive to the tube diameter. The feature above 3 eV was attributed to O_{2p} to V_{3d} charge-transfer excitations. A low-frequency mode is observed at 113 cm^{-1}, which is assigned as the radial breathing mode of the nanotube. The Raman spectrum of VO_x-alkylamine nanotubes was measured and the optical transitions were assigned to the various modes [128, 129]. Both studies indicated that the alkylamine template is very sensitive to the laser-beam damage. In the latter work [129] Cu ions were exchanged successfully with the alkylamine moiety (dodecylamine), which was followed by both Raman and IR spectroscopies.

The optical properties of MoS_2 nanotubes and fullerene-like nanoparticles have been reported in some detail before. More recently, the optical-limiting (OL) properties of MoS_2 nanotubes in aqueous suspensions were investigated [130]. The OL performance of MoS_2 nanotubes at 1064 and 532 nm was found to surpass that of the carbon-nanotubes sample.

The resonance Raman spectrum of individual WS_2 nanotubes was recorded [131]. The strongest peaks of the nanotubes were identified as 417 and 351 cm^{-1}, corresponding to the A_{1g} and E_{2g} modes, respectively. Both the A_{1g} and E_{2g} modes have the same polarization behavior with a strong signal in the ZZ geometry (Z denotes the tube axis) only and almost none for X-polarized incident or scattered light. From the orientation dependence of the nanotube's resonant Raman intensity, the ratio of the perpendicular to parallel polarizabilities α_{XX}/α_{ZZ} is estimated at 0.16, showing the strong polarization along the nanotube axis. Raman spectra of agglomerated WS_2 nanotubes were measured under hydrostatic pressure as well. The two main Raman modes shift linearly to higher energies with normalized pressure coefficients of $\omega_0^{-1}\,\mathrm{d}\omega/\,\mathrm{d}p = 4.5\,\mathrm{TPa}^{-1}$. The two-dimensional (inplane) Grüneisen parameter value of the WS_2 nanotubes is 0.45, as compared to the value of 2 for carbon nanotubes, which shows the softness of the WS_2 nanotube material. Another interesting observation is the blocking of the rigid-layer (E_{2g}) mode (33 cm^{-1}) in the IF nanoparticles. This observation indicates that the shear of the two layers with respect to each other in the unit cell is damped in the closed IF structure.

In a separate study [132], the IR reflectivity at room temperature and at 10 K of IF-WS_2 nanoparticles was studied. The IR-allowed modes in 2H-WS_2 are the XY-polarized (double degeneracy) E_{1u} and the Z-polarized A_{2u} modes at 356 and 437 cm^{-1}, respectively. It is found that the oscillator strength of the E_{1u} transition is appreciably stronger in the former (2H) material at both room temperature and 10 K. By analyzing the two modes at both the 2H (bulk) and IF-WS_2 nanoparticles it is concluded that the interlayer charge polarization, i.e., electron transfer from the metal to the sulfur atom, is appreciably smaller in the 2H as compared to the IF nanoparticles. On the other hand, the interlayer charge polarization between the layers is slightly

larger in the IF as compared to the 2H, indicative of the somewhat larger interlayer interaction in the IF as compared to the 2H-WS_2 particles.

5 Applications

The applications of inorganic nanotubes and fullerene-like nanoparticles can be divided between those that are expected to demonstrate significant potential in the foreseeable future and approaches that may lead to applications in the longer term. Early applications are already being commercialized.

5.1 Tribological Applications

Early on it was hypothesized that the spherical IF-MS_2 nanoparticles would behave like nanoball bearings thereby providing superior solid lubrication to the existing technology. Further work suggested that under mechanical stress the nanoparticles would slowly deform and exfoliate, transferring MS_2 nanosheets onto the underlying surfaces (third-body effect), and continue to provide effective lubrication until they are completely gone, or oxidize. The beneficial effect of the IF powder as an additive to lubricating fluids has been studied in quite some detail and this phenomenon is summarized in [133–135]. Work in progress indicates that this effect is particularly important when the clearance (gap) between the two mating surfaces and the surface roughness are approximately of the same order of magnitude as the nanoparticles themselves, i.e., 30–300 nm. More recently, IF-WS_2 nanoparticles were impregnated into metal and polymer films, endowing them with a self-lubricating character [136–138] and offering them a very large number of applications. Clearly, rolling and sliding friction of the nanoparticles is not possible in this case unless they are gradually released from the metal/polymer/ceramic matrix onto the surface. Here too, some of the beneficial effects of the IF nanoparticles can be attributed to their gradual exfoliation and the transfer of WS_2 nanosheets onto the asperities of the mating metal surface (third-body effect). Furthermore, the bare metal surface is shown to oxidize during the test, leading to a gradual increase in the friction coefficient to very high values (0.3–0.6). In contrast to this, the metal surface impregnated with IF nanoparticles does not seem to oxidize during the tribological test, although the coverage of the metal surface by the nanoparticles does not appear to exceed 20–30 %. This observation suggests that the temperature of the IF-WS_2-impregnated interface is lower than that of the pure metal surface during the tribological test. It, furthermore, suggests that the IF nanoparticles may act as a kind of "cathodic protection" against the oxidation of the metal surface, which prevents the oxidation of the metal surface. This technology offers numerous applications, among them various medical devices, like improved orthodontic practice [137]. In a related study, $Mo_6S_3I_6$ nanowires were also proclaimed as an excellent solid-state lubricant [139]. The authors suggest

that iodine loss during the test leads to a decomposition of the nanowires and the in-situ formation of lubricating MoS_2 nanosheets.

In order to capitalize on these applications "NanoMaterials, Ltd." recently constructed a manufacturing pilot plant with a production capacity of about 75 kg/batch and sales of their product under the title "NanoLub" have been launched. Toxicological tests indicated that the product is benign [140, 141].

5.2 Towards High-Strength Nanocomposites

The mechanical robustness of the WS_2 and MoS_2 nanotubes and the IF nanoparticles was studied in a series of papers [113–115]. Furthermore, Raman measurements of these nanoparticles indicated no degradation under hydrostatic pressures of 20 GPa, indicating again their high-pressure resilience [142]. In a series of experiments, fullerene-like WS_2 and MoS_2 nanoparticles were shown to withstand shockwaves of up to 25 and 30 GPa, respectively, with temperatures rising up to 1000 °C [143]. Significantly, the structural integrity of the nanoparticles was also confirmed by TEM, making these materials probably the strongest cage molecules known today and offering them a plethora of applications for the shielding of vehicles and in the future perhaps also as additives to strengthen construction materials. This work led to a surge of interest in fabricating nanocomposites with enhanced mechanical properties based on the fullerene-like nanoparticles and nanotubes of MoS_2, etc.

5.3 Li Intercalation and Hydrogen Sorption in MS_2 Nanotubes

Adsorption/desorption of hydrogen in MoS_2 nanotubes was investigated at room temperature [144]. The hydrogen-adsorption kinetics is nearly linear and it exhibits a saturation after about 30 min. Comparison of the gas adsorption (1.2 wt %) and electrochemical storage (0.97 wt %) suggests that the gas-adsorption process is the result of physisorption of the hydrogen in the MoS_2 nanotubes. TiS_2 nanotubes with open-ended tips, which were synthesized by a chemical transport reaction, can efficiently store 2.5 wt % of hydrogen at 298 K and under a hydrogen pressure of 4 MPa [145]. Detailed analysis showed that about 1 wt % of the hydrogen is chemisorbed while the rest of the hydrogen atoms are physisorbed to the nanotubes and can be easily recycled.

Li insertion into $MoS_2I_{0.3}$ nanotube bundles, which were prepared by chemical vapor transport was investigated [146]. Comparing their electrochemical properties with those of bulk 2H-MoS_2 powder, one finds a significant increase in the amount of inserted lithium and a decrease by about 0.7 V in the insertion potential for the electrodes made with the nanostructured material. Furthermore, EPR measurements showed that lithiated $MoS_2I_{0.3}$ nanotube bundles are less air sensitive than the lithiated bulk crystals. VS_2 nanotubes were prepared by reacting VO_x-alkylamine nanotubes with H_2S [147]. It is remarkable to note that the bulk phase of VS_2 with

lamellar structure is not known. Reversible electrochemical copper intercalation from an aqueous copper sulfate solution with a specific capacity of 314 mAh/g was demonstrated. The intercalation of lithium ions was studied also in SnO_2 nanotubes [148]. The capacity of the SnO_2 nanotube-based electrode was found to be very high (525 mAh/g) even after 80 cycles.

Lithium and iodine intercalation of VO_x-alkylamine nanotubes produced room-temperature ferromagnetic behavior [149], which is potentially important for spintronics. It was shown that the Li atoms donate electrons to the conduction band of the nanotube, while the iodine (electron-acceptor) atoms contribute holes to the valence band, removing the frustration in this spin-glass system. Furthermore, the doping shifts the Fermi level of the nanotubes from the middle of the energy gap into either the valence (iodine) or the conduction band (lithium), making this Mott–Hubbard insulator phase into a good conductor.

5.4 Solar Cells, Photocatalysis and Sensors

Titania (TiO_2) and titanate ($H_2Ti_3O_7$) tubes hold promise for a number of technologies. Dye-sensitized (Grätzel-type) solar cells made of an array of titania-nanotube photoanodes have been reported [150, 151]. The polycrystalline titania nanotubes are prepared by anodization of Ti films or foils. These cells hold great promise, mainly because the vectorial charge transfer along the nanotube walls is expected to favorably influence the collection of the carriers at the back contact. A detailed analysis [151] showed that the lifetime of the minority carriers and hence the photocurrent of the nanotube-based cells is larger than for the titania-nanoparticle-based cells. Nevertheless the open-circuit voltage and fill factor of such cells is somewhat inferior to the nanocrystalline-based titania cells. Similarly, a water photocleavage system that showed 7.9 % photoconversion efficiency in the 320–400 nm spectral range was demonstrated [152]. In another study by the same group, the resistivity of the nanotube array as a function of H_2 concentration in the gas atmosphere was monitored, showing perhaps the highest hydrogen sensitivity for any known hydrogen sensor with various possible medical and environmental applications [153]. Dopamine is an important marker for neurodegenerative diseases like Parkinsons, etc. A biosensor for this molecule was established by depositing titanate-nanotube films on a glassy carbon electrode [154]. The oxidation peak of the positively charged dopamine moieties in the current–voltage electrochemical plots was well separated from that of the negatively charged ascorbic and uric acids, which is not otherwise achievable in physiological solutions. This observation was attributed to the negative charge of the nanotubes in physiological buffered solutions (pH 7.4). Thus, the positively charged dopamine molecules are attracted to the electrode surface, while the negatively charged ascorbic and uric acid ions are repelled from the electrode surface, allowing the former to be oxidized under a milder (less-positive) bias.

Adding titanate nanotubes to the hole-transport layer – poly(vinylcarbazole) – in organic light-emitting diodes, led to improved luminosity and lower turn-on voltage. These effects were attributed to both the lower barrier for hole injection from the electrode to the organic semiconductor and to the improved hole transport in the organic film [155]. In another study, enhanced electrochromism was obtained in films made of titanate nanotubes [156]. The titanate nanotube films were shown to exhibit a faster proton diffusion and higher capacity than those made of TiO_2 (anatase) nanoparticles. This phenomenon arises from the creation of Ti^{3+} centers caused by the intercalation of protons into the nanotubes. The color change of these titanate nanotubes is more significant than that of TiO_2 anatase because of their layered nanostructure.

5.5 Biotechnology

A silica-nanotube-based nanofluidic device for the diagnostics of biomolecules has been reported [157]. Crystalline and very narrow ($< 20\,\text{nm}$) nanotubes were used as a platform for unipolar charge transport by integrating the nanotube in a metal-oxide-solution field-effect transistor (MOSolFET) (Fig. 10). The conductance of the potassium ion (KCI solution) within the p-type nanotube channel was modulated by controlling the gate voltage. The translocation of individual DNA molecules in subfemtoliter concentrations through the nanotube channel could be detected as a temporary current drop or rise. Careful control of the channel parameters may lead to the fabrication of a new nanobased diagnostic tool with the potential to uncover pathogenic DNA molecules. $(BiO)_2CO_3$ nanotubes were synthesized and were shown to play a strong anti-bacterial reactivity against helicobacter pylori, which is implicated in peptic ulcers and gastritis [158]. In another experiment, ferritin, cytochrome-*c*, streptavidin and glucose oxide were immobilized onto multiwall BN nanotubes [159]. This kind of functionalization can be the first step towards the application of such nanotubes in drug delivery, or as markers for pathogenic diseases.

5.6 Catalysis

Hollow nanoparticles of MoS_2 with imperfect crystallinity were prepared [160]. In the first report $Mo(CO)_6$ was reacted with sulfur in an aprotic solvent using an ultrasonic probe. Silica nanoparticles, which served as a template, were coated conformally by the molybdenum sulfide product. Subsequently, an HF etch was used to remove the template and a final annealing step produced the hollow nanoparticles of the MoS_2. These nanoparticles revealed high reactivity and selectivity towards the hydrodesulfurization of thiophene. In another study, Ni nanoparticles were deposited onto a MoS_2 nanotube support. This nanocomposite was found to serve as a very potent and selective catalyst for the hydrodesulfurization of thiophene and a few of its derivatives [161].

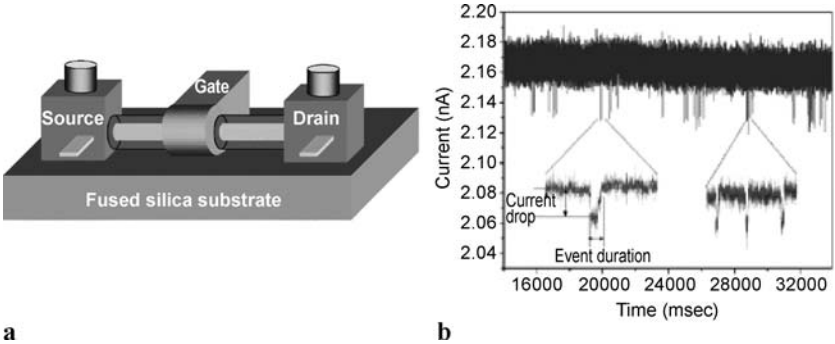

Fig. 10. A schematic drawing of the metal-oxide-solution field-effect transistor [157] (**a**) Electrical current vs time traces of the transistor (**b**). The sharp current drops indicate the passage of a single DNA molecule through the silica nanotube channel

Removal of nickel ions from municipal waste and seawater using a $Mg(OH)_2$ polycrystalline nanotube array was recently accomplished [162]. These few examples demonstrate the remarkable potential of inorganic nanotubes and fullerene-like nanoparticles in mitigating the environmental impact of sulfur-rich gasoline and in green chemistry.

6 Conclusions

Inorganic nanotubes and fullerene-like nanostructures are a generic form of inorganic layered (2D) compounds in the nanosize range. The synthesis of some kinds of nanotubes, like those of WS_2, MoS_2, BN, $H_2Ti_3O_7$ and V_2O_5 and some fullerene-like nanoparticles can be scaled up for commercial use, which provides a strong incentive for their study and eventually to their applications. However, size and shape control is still in its infancy. Crystalline nanotubes of various inorganic compounds with nonlayered structures, like oxides and nitrides were also prepared using various templates. Potential applications for such nanostructures in tribology, ultrastrong nanocomposites, as biosensors, catalysts for green chemistry, and renewable energy devices are being explored. Early sales of the products launched recently by "NanoMaterials Ltd." suggest a very wide field of applications.

While progress has been achieved in all fronts, numerous challenges face the field. Most daunting is the reproducible synthesis of inorganic nanotubes with well-controlled structural parameters, like single-wall ones. The structural characterization of such nanophases is in its infancy. Thus, determination of the chirality of each of the WS_2 layers in a multiwall nanotube, or the accurate structure determination of a MoS_2 ($NiCl_2$) nano-octahedra requires further work. The optical and electronic properties of such nanotubes have been hardly touched upon. New breathing modes of MoS_2 (WS_2)

nanotubes have been predicted by theory, but experimentally not verified as yet. Progress in this area will be possible only through close collaboration between experiment and theory. Chemical modifications of the nanotube surface should be studied systematically. The large variety of possible chemical compounds from which such nanotubes can be prepared and their inherent stability under harsh conditions suggest numerous applications in various fields, which is particularly important in view of the looming energy and environmental crisis facing mankind.

Acknowledgements

The authors are grateful to the German–Israeli Foundation (GIF), the Minerva Foundation (Munich), The G. M. J. Schmidt Minerva Center for Supramolecular Architectures and to "NanoMaterials Ltd." for their support of this research.

References

[1] R. Tenne: Inorganic nanotubes and fullerene-like nanoparticles (2006) 631
[2] M. Remskar: Inorganic nanotubes, Adv. Mater. **16**, 1497–1504 (2004) 631
[3] A. N. Enyashin, S. Gemming, G. Seifert: *Simulation of Inorganic Nanotubes* (Springer, Berlin, Heidelberg 2006) 631, 642
[4] F. Cheng, J. Chen: Storage of hydrogen and lithium in inorganic nanotubes and nanowires, J. Mater. Res. **21**, 2744–2757 (2006) 631
[5] C. N. R. Rao, M. Nath: Inorganic nanotubes, Dalton Trans. **1**, 1–25 (2003) 631
[6] B. C. Satishkumar, A. Govindaraj, E. M. Vogl, L. Basumallick, C. N. R. Rao: Oxide nanotubes prepared using carbon nanotubes as templates, J. Mater. Res. **12**, 604–606 (1997) 632
[7] M. E. Spahr, P. Bitterli, R. Nesper, M. Müller, F. Krumeich, H. U. Nissen: Redox-active nanotubes of vanadium oxide, Angew. Chem. Int. Ed. Engl. **37**, 1263–1265 (1998) 632
[8] G. H. Du, Q. Chen, R. C. Che, Z. Y. Yuan, L. M. Peng: Preparation and structure analysis of titanium oxide nanotubes, Appl. Phys. Lett. **79**, 3702–3704 (2001) 632
[9] V. Zwilling, E. Darque-Ceretti, A. Boutry-Forveille, D. David, M. Y. Perrin, M. Aucouturier: Structure and physicochemistry of anodic oxide films on titanium and TA6V alloy, Surf. Interface Anal. **27**, 629–637 (1999) 632, 638
[10] D. Gong, C. A. Grimes, O. K. Varghese, W. Hu, R. S. Singh, Z. Chen, E. C. Dickey: Titanium oxide nanotube arrays prepared by anodic oxidation, J. Mater. Res **16**, 3331–3334 (2001) 632, 638
[11] R. Beranek, H. Hildebrand, P. Schmuki: Self-organized porous titanium oxide prepared in H_2SO_4/HF electrolytes, Electrochem. Solid-State Lett. **6**, B12–B14 (2003) 632, 638
[12] G. Seifert, T. Köhler, R. Tenne: Stability of metal chalcogenide nanotubes, J. Phys. Chem. B **106**, 2497–2501 (2002) 632, 633, 647

[13] R. Tenne, L. Margulis, M. Genut, G. Hodes: Polyhedral and cylindrical structures of Tungsten disulphide, Nature **360**, 444–445 (1992) 632, 639
[14] L. Margulis, G. Salitra, R. Tenne, M. Talianker: Nested fullerene-like structures, Nature **365**, 113–114 (1993) 632
[15] Y. Feldman, E. Wasserman, D. J. Srolovitz, R. Tenne: High rate gas phase growth of MoS_2 nested inorganic fullerene-like and nanotubes, Science **267**, 222–225 (1995) 632
[16] A. Rubio, J. L. Corkill, M. L. Cohen: Theory of graphitic boron nitride nanotubes, Phys. Rev. B **49**, 5081–5084 (1994) 632
[17] N. G. Chopra, J. Luyken, K. Cherry, V. H. Crespi, M. L. Cohen, S. G. Louie, A. Zettl: Boron-nitride nanotubes, Science **269**, 966–967 (1995) 632
[18] E. J. M. Hamilton, S. E. Dolan, C. M. Mann, H. O. Colijn, C. A. McDonald, S. G. Shore: Science **260, 659** (1993) 632
[19] F. Jensen, H. Toftlund: Structure and stablitity of C_{24} and $B_{12}N_{12}$ isomers, Chem. Phys. Lett. **201**, 95–98 (1993) 632
[20] O. Stéphan, Y. Bando, A. Loiseau, F. Willaime, N. Shramchenko, T. Tamiya, T. Sato: Formation of small single-layer and nested BN cages under electron irradiation of nanotubes and bulk material, Appl. Phys. A **67**, 107–111 (1998) 632
[21] R. R. Chianelli, E. B. Prestridge, T. A. Pecorano, J. P. DeNeufville: Molybdenum disuflide in the poorly crystalline "rag" structure, Science **203**, 1105–1107 (1979) 632
[22] J. V. Sanders: High-resolution electron microscopy of some catalytic particles, Chem. Scr. **14**, 141–145 (1979) 632
[23] J. V. Sanders: Structure of catalytic particles, Ultramicroscopy **20**, 33–37 (1986) 632
[24] L. Vayssieres, K. Keis, A. Hagfeldt, S.-E. Lindquist: Three-dimensional array of highly oriented crystalline ZnO microtubes, Chem. Mater. **13**, 4395–4398 (2001) 632
[25] Y. Sun, G. M. Fuge, N. A. Fox, D. J. Riley, M. N. R. Ashfold: Synthesis of aligned arrays of ultrathin ZnO nanotubes on a Si wafer coated with a thin ZnO film, Adv. Mater. **17**, 2477–2481 (2005) 632
[26] J. Goldberger, R. He, Y. Zhang, S. Lee, H. Yan, H.-J. Choi, P. Yang: Single-crystal gallium nitride nanotubes, Nature **422**, 599–602 (2003) 632, 641
[27] Y. Li, Y. Bando, D. Golberg: Single-crystalline In_2O_3 nanotubes filled with In, Adv. Mater. **15**, 581–585 (2003) 632, 641
[28] R. Tenne, A. Zettl: Nanotubes from inorganic materials, in M. S. Dresselhaus, P. Avouris (Eds.): *Carbon Nanotubes*, Top. Appl. Phys. **80** (Springer, Berlin, Heidelberg 2000) pp. 81–112 633, 638
[29] N. Sano, H. Wang, M. Chhowalla, I. Alexandrou, G. A. J. Amaratunga, M. Naito, T. Kanki: Fabrication of inorganic molybdenum disulfide fullerenes by arc in water, Chem. Phys. Lett. **368**, 331–337 (2003) 635
[30] J. J. Hu, J. S. Zabinski: Nanotribology and lubrication mechanisms of inorganic fullerene-like MoS_2 nanoparticles investigated using lateral force microscopy (LFM), Tribol. Lett. **18**, 173–180 (2005) 635
[31] D. M. D. J. Singh, T. Pradeep, J. Bhattacharjee, U. V. Waghmare: Novel cage clusters of MoS_2 in the gas phase, J. Phys. Chem. A **109**, 7339–7342 (2005) 636

[32] R. Sen, A. Govindaraj, K. Suenaga, S. Suzuki, H. Kataura, S. Iijima, Y. Achiba: Encapsulated and hollow closed-cage structures of WS_2 and MoS_2 prepared by laser ablation at 450–1050 °C, Chem. Phys. Lett. **340**, 242–248 (2001) 636
[33] P. A. Parilla, A. C. Dillon, B. A. Parkinson, K. M. Jones, J. Alleman, G. Riker, D. S. Ginley, M. J. Heben: Formation of nanooctahedra in molybdenum disulfide and molybdenum diselenide using pulsed laser vaporization, J. Phys. Chem. B **108**, 6197–6207 (2004) 636
[34] A. N. Enyashin, S. Gemming, M. Bar-Sadan, R. Popovitz-Biro, S. Y. Hong, Y. Prior, R. Tenne, G. Seifert: Structure and stability of molybdenum sulfide fullerenes, Angew. Chem. Intl. Ed. **46**, 623–627 (2007) 636
[35] C. Ducati, E. Barborini, S. Vinati, P. Milani, P. A. Midgley: Titanium fullerenoid oxides, Appl. Phys. Lett. **87**, 201906 (2005) 636
[36] A. Albu-Yaron, T. Arad, R. Popovitz-Biro, M. Bar-Sadan, Y. Prior, M. Jansen, R. Tenne: Closed-cage (fullerene-like) structures of Cs_2O, Angew. Chem. Intl. Ed. **44**, 4169–4172 (2005) 637
[37] A. Albu-Yaron, T. Arad, R. Tenne, M. Levy, R. Popovitz-Biro, J. M. Gordon, D. Feuermann, E. A. Katz, M. Jansen, C. Mühle: Synthesis of fullerene-like Cs_2O nanoparticles by concentrated sunlight, Adv. Mater. **18**, 2993–2996 (2006) 637
[38] M. J. Yacaman, H. Lopez, P. Santiago, D. H. Galvan, I. L. Garzon, A. Reyes: Studies of MoS_2 structures produced by electron irradiation, Appl. Phys. Lett. **69**, 1065–1067 (1996) 637
[39] R. Popovitz-Biro, A. Twersky, Y. R. Hacohen, R. Tenne: Nanoparticles of $CdCl_2$ with closed cage structure, Isr. J. Chem. **41**, 7–14 (2001) 637
[40] R. Popovitz-Biro, N. Sallacan, R. Tenne: CdI_2 nanoparticles with closed-cage (fullerene-like) structures, J. Mater. Chem. **13**, 1631–1634 (2003) 637
[41] Y. Prior, R. Tenne, M. Bar-Sadan, R. Popovitz-Biro: Closed-cage (fullerene-like) structures of $NiBr_2$, Mater. Res. Bull. **41**, 2137–2146 (2006) 637
[42] T. Kasuga, M. Hiramatsu, A. Hoson, T. Sekino, K. Niihara: Formation of titanium oxide nanotube, Langmuir **14**, 3160–3163 (1998) 638
[43] G. H. Du, Q. Chen, R. C. Che, Z. Y. Yuan, L. M. Peng: Preparation and structure analysis of titanium oxide nanotubes, Appl. Phys. Lett. **79**, 3702–3704 (2001) 638
[44] S. Zhang, L.-M. Peng, Q. Chen, G. H. Du, G. Dawson, W. Z. Zhou: Formation mechanism of $H_2Ti_3O_7$ nanotubes, Phys. Rev. Lett. **91**, 256103 (2003) 638
[45] H. Deng, J. Wang, Q. Peng, X. Wang, Y. Li: Controlled hydrothermal synthesis of bismuth oxyhalide nanobelts and nanotubes, Chem. Eur. J. **11**, 6519–6524 (2005) 638
[46] D. Chen, K. Tang, Z. Liang, Y. Liu, H. Zheng: Fabrication of $PbCrO_4$ nanostructures: From nanotubes to nanorods, Nanotechnology **16**, 2619–2624 (2005) 638
[47] S. V. Krivovichev, V. Kahlenberg, R. Kaindl, E. Mersdorf, I. G. Tananaev, B. F. Myasoedov: Nanoscale tubules in uranyl selenates, Angew. Chem. Int. Ed. **44**, 1134–1136 (2005) 638
[48] Z. Yin, Y. Sakamoto, J. Yu, S. Sun, O. Terasaki, R. Xu: Microemulsion-based synthesis of titanium phosphate nanotubes via amine extraction system, J. Am. Chem. Soc. **126**, 8882–8883 (2004) 638

[49] A. Ghicov, S. Aldabergenova, H. Tsuchyia, P. Schmuki: TiO_2–Nb_2O_5 nanotubes with electrochemically tunable morphologies, Angew. Chem. Intl. Ed. **45**, 6993–6996 (2006) 639
[50] S. Chou, F. Cheng, J. Chen: Electrochemical deposition of $Ni(OH)_2$ and Fe-doped $Ni(OH)_2$ tubes, Eur. J. Inorg. Chem. pp. 4035–4039 (2005) 639
[51] S. J. Son, S. B. Lee: Controlled gold nanoparticle diffusion in nanotubes: Platfom of partial functionalization and gold capping, J. Am. Chem. Soc. **128**, 15974–15975 (2006) 639
[52] C.-C. Hu, K.-H. Chang, M.-C. Lin, Y.-T. Wu: Design and tailoring of the nanotubular arrayed architecture of hydrous RuO_2 for next generation supercapacitors, Nano Lett. **6**, 2690–2695 (2006) 639
[53] B. A. Hernandez-Sanchez, K.-S. Chang, M. T. Scancella, J. L. Burris, S. Kohli, E. R. Fisher, P. K. Dorhout: Examination of size-induced ferroelectric phase transitions in template synthesized $PbTiO_3$ nanotubes and nanofibers, Chem. Mater. **17**, 5909–5919 (2005) 639
[54] N. A. Dhas, K. S. Suslick: Sonochemical preparation of hollow nanospheres and hollow nanocrystals, J. Am. Chem. Soc. **127**, 2368–2369 (2005) 639
[55] B. Yang, C. Li, H. Hu, X. Yang, Q. Li, Y. Qian: A room-temperature route to bismuth nanotube arrays, Eur. J. Inorg. Chem. pp. 3699–3702 (2003) 639
[56] C. Schuffenhauer, R. Popovitz-Biro, R. Tenne: Synthesis of NbS_2 nanoparticles with (nested) fullerene-like structure (IF), J. Mater. Chem. **12**, 1587–1591 (2002) 640
[57] F. L. Deepak, A. Margolin, M. Bar-Sadan, R. Popovitz-Biro, R. Tenne: MoS_2 fullerene-like structures and nanotubes using the gas phase reaction with $MoCl_5$, Nano **1**, 167–180 (2006) 640
[58] X.-L. Li, J.-P. Ge, Y.-D. Li: Atmospheric pressure chemical vapor deposition: an alternative route to large-scale MoS_2 and WS_2 inorganic fullerene-like nanostructures and nanoflowers, Chem. Eur. J. **10**, 6163–6171 (2004) 640
[59] J. Etzkorn, H. A. Therese, F. Rocker, N. Zink, U. Kolb, W. Tremel: Metal-organic chemical vapor deposition synthesis of hollow inorganic-fullerene-type MoS_2 and $MoSe_2$ nanoparticles, Adv. Mater. **17**, 2372–2375 (2005) 640
[60] J. Chen, S.-L. Li, Z.-L. Tao, F. Gao: Low-temperature synthesis of titanium disulfide nanotubes, Chem. Commun. pp. 980–981 (2003) 640
[61] J. Chen, Z. L. Tao, S. L. Li: Lithium intercalation in open-ended TiS_2 nanotubes, Angew. Chem. Intl. Ed. **42**, 2147–2151 (2003) 640
[62] S. Bastide, D. Duphil, J.-P. Borra, C. Lévy-Clément: WS_2 closed nanoboxes synthesized by spray pyrolysis, Adv. Mater. **18**, 106–109 (2006) 640
[63] D. J. Brooks, R. E. Douthwaite, R. Brydson, C. Calvert, M. G. Measures, A. Watson: Synthesis of inorganic fullerene (MS_2 M=Zr,Hf and W) phases using H_2S and N_2/H_2 microwave-induced plasmas, Nanotechnology **17**, 1245–1250 (2006) 640
[64] C. D. Malliakas, M. G. Kanatzidis: Inorganic single wall nanotubes of $SbPS_{4-x}Se_x$ ($0< x <3$) with tunable band gap, J. Am. Chem. Soc. **128**, 6538–6539 (2006) 640
[65] M. Brorson, T. W. Hansen, C. J. H. Jacobsen: Rhenium(IV) sulfide nanotubes, J. Am. Chem. Soc. **124**, 11582–11583 (2002) 640
[66] L.-W. Yin, Y. Bando, D. Golberg, M.-S. Li: Growth of single-crystal indium nitride nanotubes and nanowires by a controlled-carboridation reaction route, Adv. Mater. **16**, 1833–1838 (2004) 641

[67] J. Zhan, Y. Bando, J. Hu, L. Yin, X. Yuan, T. Sekiguchi, D. Golberg: Hollow and polygonous microtubes of monocrystalline indium germanate, Angew. Chem. Int. Ed. **45**, 228–231 (2006) 641
[68] H. J. Fan, M. Knez, R. Scholz, K. Nielsch, E. Pippel, D. Hesse, M. Zacharias, U. Goesele: Monocrystalline spinel nanotube fabrication based on the Kirkendall effect, Nature Mater. **5**, 627–631 (2006) 641
[69] H. Fan, M. Knez, R. Scholz, K. Nielsch, E. Pippel, D. Hesse, U. Goesele, M. Zacharias: Single-crystalline $MgAl_2O_4$ spinel nanotubes using a reactive and removable MgO nanowire template, Nanotechnology **17**, 5157–5162 (2006) 641
[70] Z. Yang, Y. Gu, L. Chen, L. Shi, J. Ma, Y. Qian: Preparation of Mn_5Si_3 nanocages and nanotubes by molten salt flux, Solid State Commun. **130**, 347–351 (2004) 641
[71] J. A. Jaszczak: *Mesomolecules: From Molecules to Materials*, vol. 1 (Chapman & Hall 1995) 641
[72] G. G. Tibbetts: Why are carbon filaments tubular, J. Cryst. Growth **66**, 632–638 (1983) 642
[73] G. Seifert, T. Frauenheim: On the stability of non carbon nanotubes, J. Korean Phys. Soc. **37**, 89–92 (2000) 642, 647
[74] V. V. Ivanovskaya, G. Seifert: Tubular structures of titanium disulfide TiS_2, Solid State Commun. **130**, 175–180 (2004) 643, 648
[75] T. Köhler, T. Frauenheim, Z. Hajnal, G. Seifert: Tubular structures of GaS, Phys. Rev. B **69**, 193403 (2004) 643, 648
[76] G. Seifert, H. Terrones, M. Terrones, G. Jungnickel, T. Frauenheim: Structure and electronic properties of MoS_2 nanotubes, Phys. Rev. Lett. **85**, 146–149 (2000) 642, 647, 652
[77] I. Milosević, T. Vuković, M. Damnjanović, B. Nikolić: Symmetry based properties of the transition metal dichalcogenide nanotubes, Eur. Phys. J. B **17**, 707–712 (2000) 643
[78] C. C. Han, M. Y. Bai, J. T. Lee: A new and easy method for making Ni and Cu microtubules and their regularly assembled structures, Chem. Mater. **13**, 4260–4268 (2001) 643
[79] M. Remskar, A. Mrzel, F. Levy: Perspectives of fullerene nanotechnology, in E. Osawa (Ed.): *International Fullerenes Workshop* (Kluwer, Dordrecht, Boston, London 2001) 643
[80] M. Virsek, A. Jesih, I. Milosevic, M. Damnjanovic, M. Remskar: Raman scattering of the MoS_2 and WS_2 single nanotubes, Surf. Sci. **601**, 2868–2872 (2007) 643
[81] M. Remskar, Z. Skraba, P. Stadelmann, F. Levy: Structural stabilization of new compounds: MoS_2 and WS_2 micro- and nanotubes alloyed with gold and silver, Adv. Mater. **12**, 814–818 (2000) 644
[82] A. Mrzel, M. Remskar, D. Mihailovic: New organic-inorganic crystals grown by self-arrangement of C-70, Synth. Met. **135–136**, 725–726 (2003) 644
[83] Y. Q. Zhu, W. K. Hsu, S. Firth, M. Terrones, R. J. H. Clark, H. W. Kroto, D. R. M. Walton: Nb-doped WS_2 nanotubes, Chem. Phys. Lett **342**, 15–21 (2001) 644
[84] M. Remskar, A. Mrzel, A. Jesih, F. Lévy: Metal-alloyed NbS_2 nanotubes synthesized by the self-assembly of nanoparticles, Adv. Mater. **14**, 680–684 (2002) 644

[85] M. I. Mendelev, D. J. Srolovitz, S. A. Safran, R. Tenne: Equilibrium structure of multilayer van der Waals films and nanotubes, Phys. Rev. B **65**, 075402 (2002) 644
[86] S. B. Fagan, R. J. Baierle, R. Mota, A. J. da Silva, A. Fazzio: Ab initio calculations for a hypothetical material: Silicon nanotubes, Phys. Rev. B **61**, 9994–9996 (2000) 645
[87] R. Q. Zhang, S. T. Lee, C.-K. Law, W. K. Li, B. K. Teo: Silicon nanotubes: Why not?, Chem. Phys. Lett. **364**, 251–258 (2002) 645
[88] M. Zhang, Y. H. Kan, Q. J. Zang, Z. M. Su, R. S. Wang: Why silicon nanotubes stably exist in armchair structure?, Chem. Phys. Lett. **379**, 81–86 (2003) 645
[89] G. Seifert, T. Köhler, H. M. Urbassek, E. Hernandez, T. Frauenheim: Tubular structures of silicon, Phys. Rev. B **63**, 193409 (2001) 645, 652
[90] G. Seifert, T. Köhler, Z. Hajnal, T. Frauenheim: Tubular structures of germanium, Solid State Commun. **119**, 653–657 (2001) 645, 652
[91] S. Gemming, G. Seifert: Nanotube bundles from calcium disilicide: A density functional theory study, Phys. Rev. B **68**, 075416 (2003) 645, 652
[92] G. Seifert, E. Hernandez: Theoretical prediction of phosphorus nanotubes, Chem. Phys. Lett. **318**, 355–360 (2000) 645, 652
[93] C. Su, H.-T. Liu, J.-M. Li: Bismuth nanotubes: Potential semiconducting nanomaterials, Nanotechnology **13**, 746–749 (2002) 645, 652
[94] Y. Li, J. Wang, Z. Deng, Y. Wu, X. Sun, D. Yu, P. Yang: Bismuth nanotubes: A rational low-temperature synthetic route, J. Am. Chem. Soc. **123**, 9904–9905 (2001) 645
[95] I. Boustani, A. Quandt, E. Hernandez, A. Rubio: New boron based nanostructured materials, J. Chem. Phys. **110**, 3176–3185 (1999) 645, 652
[96] J. Kunstmann, A. Quandt: Constricted boron nanotubes, Chem. Phys. Lett. **402**, 21–26 (2005) 645, 652
[97] L. A. Chernozatonskii: Diboride bifullerenes and binanotubes, JETP Lett. **74**, 335–339 (2001) 646, 652
[98] A. Quandt, A. Y. Liu, I. Boustani: Density-functional calculations for prototype metal-boron nanotubes, Phys. Rev. B **64**, 125422 (2001) 646, 652
[99] V. V. Ivanovskaya, A. N. Enyashin, A. A. Sofronov, Y. N. Makurin, N. I. Medvedeva, A. L. Ivanovskii: Quantum chemical simulation of the electronic structure and chemical bonding in (6,6), (11,11) and (20,0)-like metal-boron nanotubes, J. Mol. Struct. **625**, 9–16 (2003) 646, 652
[100] S. Guerini, P. Piquini: Theoretical investigation of TiB_2 nanotubes, Microelectron. J. **34**, 495 (2003) 646, 652
[101] W. H. Moon, H. J. Hwang: Molecular-dynamics simulation of structure and thermal behaviour of boron nitride nanotubes, Nanotechnology **15**, 431–434 (2004) 646
[102] T. Dumitrica, H. F. Bettinger, G. E. Scuseria, B. I. Yakobson: Thermodynamics of yield in boron nitride nanotubes, Phys. Rev. B **68**, 085412 (2003) 646
[103] M. Zhao, Y. Xia, D. Zhang, L. M. Mei: Stability and electronic structure of AlN nanotubes, Phys. Rev. B **68**, 235415 (2003) 646

[104] M. Zhao, Y. Xia, Z. Tan, X. D. Liu, F. Li, B. D. Huang, Y. J. Ji, L. M. Mei: Strain energy and thermal stability of single-walled aluminum nitride nanotubes from first-principles calculations, Chem. Phys. Lett. **389**, 160–164 (2004) 646

[105] J. W. Kang, H. J. Hwang, K. O. Song, W. Y. Choi, K. R. Byun, O. K. Kwon, J. H. Lee, W. W. Kim: Structures, nanomechanics, and disintegration of single-walled gan nanotubes: Atomistic simulations, J. Korean Phys. Soc. **43**, 372–380 (2003) 647

[106] Y.-R. Jeng, P.-C. Tsai, T. H. Fang: Molecular dynamics investigation of the mechanical properties of gallium nitride nanotubes under tension and fatigue, Nanotechnology **15**, 1737–1744 (2004) 647

[107] V. V. Ivanovskaya, A. N. Enyashin, A. L. Ivanovskii: Nanotubes and fullerene-like molecules based on TiO_2 and ZrS_2: Electronic structure and chemical bond, Russian J. Inorg. Chem. **49**, 244–251 (2004) 648

[108] A. N. Enyashin, G. Seifert: Structure, stability and electronic properties of TiO_2 nanostructures, Phys. Stat. Sol. B **242**, 1361–1370 (2005) 648

[109] V. V. Ivanovskaya, A. N. Enyashin, A. A. Sofronov, Y. N. Makurin, N. I. Medvedeva, A. L. Ivanovskii: Electronic properties of single-walled V_2O_5 nanotubes, Solid State Commun. **126**, 489–493 (2003) 648

[110] G. Seifert, T. Frauenheim, T. Köhler, H. M. Urbassek: Tubular structures of siloxenes, Phys. Stat. Sol. B **225**, 393–399 (2001) 648

[111] Y. R. Hacohen, R. Popovitz-Biro, Y. Prior, S. Gemming, G. Seifert, R. Tenne: Synthesis of $NiCl_2$ nanotubes and fullerene-like structures by laser ablation: Theoretical considerations and comparison with MoS_2 nanotubes, Phys. Chem. Chem. Phys. **5**, 1644–1651 (2003) 649

[112] V. V. Ivanovskaya, A. N. Enyashin, N. I. Medvedeva, A. L. Ivanovskii: Electronic properties of $NiCl_2$ tubular nanostructures (2003) URL: `cond-mat/0304230` 649

[113] I. Kaplan-Ashiri, S. R. Cohen, K. Gartsman, R. Rosentsveig, G. Seifert, R. Tenne: Mechanical behavior of WS_2 nanotubes, J. Mater. Res. **19**, 454–459 (2004) 649, 651, 656

[114] I. Kaplan-Ashiri, S. R. Cohen, K. Gartsman, V. Ivanovskaya, T. Heine, G. Seifert, I. Kanevsky, H. D. Wagner, R. Tenne: On the mechanical behavior of WS_2 nanotubes under axial tension and compression, Proc. Natl. Acad. Sci. USA **103**, 523–528 (2006) 649, 650, 651, 656

[115] I. Kaplan-Ashiri, S. R. Cohen, N. Apter, Y. Wang, G. Seifert, H. D. Wagner, R. Tenne: J. Phys. Chem. C **111**, 8432 (2007) 649, 651, 656

[116] Y. Wang, I. Kaplan-Ashiri, H. D. Wagner, R. Tenne, L.-M. Peng: unpublished 650

[117] J. L. Feldman: Elastic constants of 2H-MoS_2 and 2H-$NBSe_2$ extracted from measured dispersion curves and linear compressibilities, J. Phys. Chem. Sol. **37**, 1141–1144 (1976) 651

[118] A. Kis, D. Mihailovic, M. Remskar, A. Mrzel, A. Jesih, I. Piwonski, A. J. Kulik, W. Benoit, L. Forro: Shear and Young's moduli of MoS_2 nanotube ropes, Adv. Mater. **15**, 733–736 (2003) 651

[119] L. Scheffer, R. Rosentzveig, A. Margolin, R. Popovitz-Biro, G. Seifert, S. R. Cohen, R. Tenne: Scanning tunneling microscopy study of WS_2 nanotubes, Phys. Chem. Chem. Phys. **4**, 2095–2098 (2002) 652

[120] O. Ponomarenko, M. W. Radny, P. V. Smith, G. Seifert: Properties of boron carbide nanotubes: Density-functional-based tight-binding calculations, Phys. Rev. B **67**, 125401 (2003) 652
[121] V. V. Ivanovskaya, T. Heine, S. Gemming, G. Seifert: Structure, stability and electronic properties of composite $Mo_{1-x}Nb_xS_2$ nanotubes, Phys. Stat. Sol. B **243**, 1757–1764 (2006) 652
[122] G. Seifert, H. Terrones, M. Terrones, T. Frauenheim: Novel NbS_2 metallic nanotubes,, Solid State Commun. **115**, 635–638 (2000) 652
[123] L. Qian, Z.-L. Dub, S.-Y. Yang, Z.-S. Jin: Raman study of titania nanotube by soft chemical process, J. Mol. Struct. **749**, 103–107 (2005) 653
[124] D. V. Bavykin, S. N. Gordeev, A. V. Moskalenko, A. A. Lapkin, F. C. Walsh: Apparent two-dimensional behavior of TiO_2 nanotubes revealed by light absorption and luminescence, J. Phys. Chem. B **109**, 8565–8569 (2005) 653
[125] L. Qian, Z.-S. Jin, S.-Y. Yang, Z.-L. Du, X.-R. Xu: Bright visible photoluminescence from nanotube titania grown by soft chemical process, Chem. Mater. **17**, 5334–5338 (2005) 653
[126] X. Liu, C. Täschner, A. Leonhardt, M. H. Rümmeli, T. Pichler, T. Gemming, B. Büchner, M. Knupfer: Structural, optical and electronic properties of vanadium oxide nanotubes, Phys. Rev. B **72**, 115407 (2005) 653
[127] J. Cao, J. Choi, J. L. Musfeldt, S. Lutta, M. S. Whittingham: Effect of sheet distance on the optical properties of vanadate nanotubes, Chem. Mater. **16**, 731–736 (2004) 654
[128] W. Chen, L. Mai, J. Peng, Q. Xu, Q. Zhu: Raman spectroscopic study of vanadium oxide nanotubes, J. Solid State Chem. **177**, 377–379 (2004) 654
[129] A. G. Souza Filho, O. P. Ferreira, E. J. G. Santos, J. Mendes Filho, O. L. Alves: Raman spectra in vanadate nanotubes, Nano Lett. **4**, 2099–2104 (2004) 654
[130] K. P. Loh, H. Zhang, W. Z. Chen, W. Ji: Templated deposition of MoS_2 nanotubules using single source precursor and studies of their optical limiting properties, J. Phys. Chem. B **110**, 1235–1239 (2006) 654
[131] P. M. Rafailov, C. Thomsen, K. Gartsman, I. Kaplan-Ashiri, R. Tenne: Orientation dependence of the polarizability of an individual WS_2 nanotube by resonant Raman spectroscopy, Phys. Rev. B **72**, 205436 (2005) 654
[132] R. D. Luttrell, S. Brown, J. Cao, J. L. Musfeldt, R. Rosentsveig, R. Tenne: Dynamics of bulk versus nanoscale WS_2: Local strain and charging effects, Phys. Rev. B **73**, 035410 (2006) 654
[133] L. Rapoport, N. Fleischer, R. Tenne: Applications of WS_2 (MoS_2) inorganic nanotubes and fullerene-like nanoparticles for solid lubrication and for structural nanocomposites, J. Mater. Chem. **15**, 1782–1788 (2005) 655
[134] L. Joly-Pottuz, F. Dassenoy, M. Belin, B. Vacher, J. M. Martin, N. Fleischer: Ultralow-friction and wear properties of IF-WS_2 under boundary lubrication, Tribol. Lett. **18**, 477–485 (2005) 655
[135] J. J. Hu, J. S. Zabinski: Nanotribology and lubrication mechanisms of inorganic fullerene-like MoS_2 nanoparticles investigated using lateral force microscopy (LFM), Tribol. Lett. **18**, 173–180 (2005) 655
[136] W. X. Chen, Z. D. Xu, R. Tenne, R. Rosenstveig, W. L. Chen, H. Y. Gan, J. P. Tu: Wear and friction of Ni-P electroless composite coating including inorganic fullerene-like WS_2 nanoparticles, Adv. Eng. Mater. **4**, 686–690 (2002) 655

[137] A. Katz, M. Redlich, L. Rapoport, H. D. Wagner, R. Tenne: Self-lubricating coatings containing fullerene-like WS_2 nanoparticles for orthodontic wires and other possible medical applications, Tribol. Lett. **21**, 135–139 (2006) 655
[138] H. Friedman, O. Eidelman, Y. Feldman, A. Moshkovich, V. Perfiliev, L. Rapoport, H. Cohen, A. Yoffe, R. Tenne: Fabrication of self-lubricating cobalt coatings on metal surfaces, Nanotechnology **18**, 115703 (2007) 655
[139] F. Dassenoy, L. Joly-Pottuz, J. M. Martin, D. Vrbanic, A. Mrzel, D. Mihailovic, W. Vogel, G. Montagnac: Tribological performances of $Mo_6S_3I_6$ nanowires, J. Eur. Ceram. Soc. **27**, 915–919 (2007) 655
[140] H. Tsabari: *Inorganic Fullerene-like WS_2 Nano-Spheres* (*IF-WS_2*), (Batch No.HP6) acute oral toxicity, acute toxic class method in the rat, final report, Harlan Biotech Israel (2005) 656
[141] I. Haist: *Test for Sensitization* (*Local Lymph Node Assay LLNA*) *with Inorganic Fullerene-like WS_2 Nano-Spheres*, Technical report, BSL Bioservice Project No. 052052 (2005) 656
[142] L. Joly-Pottuz, J. M. Martin, F. Dassenoy, M. Belin, G. Montagnac, B. Reynard, N. Fleischer: Pressure-induced exfoliation of inorganic fullerene-like WS_2 particles in a Hertzian contact, J. Appl. Phys. **99**, 023524 (2006) 656
[143] Y. Q. Zhu, T. Sekine, Y. H. Li, M. W. Fay, Y. M. Zhao, C. H. P. Poa, W. X. Wang, R. Martin, P. D. Brown, N. Fleischer, R. Tenne: Shock-absorbing and failure mechanism of WS_2 and MoS_2 nanoparticles with fullerene-like structure under shockwave pressures, J. Am. Chem. Soc. **127**, 16263–16272 (2005) 656
[144] J. Chen, S. L. Li, Z. L. Tao: Novel hydrogen storage properties of MoS_2 nanotubes, J. Alloys Compd. **356–357**, 413–317 (2003) 656
[145] J. Chen, S. L. Li, Z. L. Tao, Y. T. Shen, C. X. Cui: Titanium disulfide nanotubes as hydrogen-storage materials, J. Am. Chem. Soc. **125**, 5284–5285 (2003) 656
[146] R. Dominko, M. Gaberscek, D. Arcon, A. Mrzel, M. Remskar, D. Mihailovic, S. Pejovnik, J. Jamnik: Electrochemical preparation and characterization of Li_zMoS_{2-x} nanotubes, Electrochim. Acta **48**, 3079–3084 (2003) 656
[147] H. A. Therese, F. Rocker, A. Reiber, J. Li, M. Stepputat, G. Glasser, U. Kolb, W. Tremel: VS_2 nanotubes containing organic-amine templates from the NT-VO_x precursors and reversible copper intercalation in NT-VS_2, Angew. Chem. Int. Ed. **44**, 262–265 (2005) 656
[148] Y. Wang, J. Y. Lee, H. C. Zeng: Polycrystalline SnO_2 nanotubes prepared via infiltration casting of nanocrystallites and their electrochemical application, Chem. Mater. **17**, 3899–3903 (2005) 657
[149] L. Krusin-Elbaum, D. M. Newns, H. Zeng, V. Derycke, J. Z. Sun, R. Sandstrom: Room-temperature ferromagnetic nanotubes controlled by electron or hole doping, Nature **431**, 672–676 (2004) 657
[150] G. K. Mor, K. Shankar, M. Paulose, O. K. Varghese, C. A. Grimes: Use of highly-ordered TiO_2 nanotube arrays in dye-sensitized solar cells, Nano Lett. **6**, 215–218 (2006) 657
[151] K. Zhu, N. R. Neale, A. Miedaner, A. J. Frank: Enhanced charge-collection efficiencies and light scattering in dye-sensitized solar cells using oriented TiO_2 nanotubes arrays, Nano Lett. **7**, 69–74 (2007) 657

[152] C. M. Ruan, M. Paulose, O. K. Vargese, C. A. Grimes: Enhanced photoelectrochemical-response in highly ordered TiO_2 nanotube-arrays anodized in boric acid containing electrolyte, Sol. Energy Mater. Sol. Cells **90**, 1283–1295 (2006) 657
[153] G. K. Mor, M. A. Carvalho, O. K. Varghese, M. V. Pishko, C. A. Grimes: A room-temperature TiO_2-nanotube hydrogen sensor able to self-clean photoactively from environmental contamination, J. Mater. Res. **19**, 628–634 (2004) 657
[154] A. Liu, M. Wei, I. Honma, H. Zhou: Biosensing properties of titanate-nanotube films: Selective detection of dopamine in the presence of ascorbate and uric acid, Adv. Funct. Mater. **16**, 371–376 (2006) 657
[155] L. Qian, F. Teng, Z.-S. Jin, Z.-J. Zhang, T. Zhang, Y.-B. Hou, S.-Y. Yang, X.-R. Xu: Improved optoelectronic characteristics of light-emitting diodes by using a dehydrated nanotube titanic acid (DNTA)-polymer nanocomposites, J. Phys. Chem. B **108**, 13928–13931 (2004) 658
[156] H. Tokudome, M. Miyauchi: Electrochromism of titanate-based nanotubes, Angew. Chem. Int. Ed. **44**, 1974–1977 (2005) 658
[157] J. Goldberger, R. Fan, P. Yang: Inorganic nanotubes: A novel platform for nanofluidics, Acc. Chem. Res. **39**, 239–248 (2006) 658, 659
[158] R. Chen, M. H. So, J. Yang, F. Deng, C. M. Chea, H. Sun: Fabrication of bismuth subcarbonate nanotube arrays from bismuth citrate, Chem. Commun. pp. 2265–2267 (2006) 658
[159] C. Zhi, Y. Bando, C. Tang, D. Golberg: Immobilization of proteins on BN nanotubes, J. Am. Chem. Soc. **127**, 17144–17145 (2005) 658
[160] N. A. Dhas, K. S. Suslick: Sonochemical preparation of hollow nanospheres and hollow nanocrystals, J. Am. Chem. Soc. **127**, 2368–2369 (2005) 658
[161] F. Cheng, X. Gou, J. Chen, Q. Xu: Ni/MoS_2 nanocomposites as the catalysts for hydrodesulfurization of thiophene and thiophene derivatives, Adv. Mater. **18**, 2561–2564 (2006) 658
[162] S. Zhang, F. Cheng, Z. Tao, F. Gao, J. Chen: Removal of nickel ions from wastewater by $Mg(OH)_2/MgO$ nanostructures embedded in Al_2O_3 membranes, J. Alloys Compd. **426**, 281–285 (2006) 659

Index

Single-Wall Carbon Nanohorns and Nanocones

Masako Yudasaka[1,2], Sumio Iijima[1,2,3], and Vincent H. Crespi[4]

[1] Fundamental and Environmental Research Laboratories
NEC Corporation, Tsukuba, Japan
yudasaka@frl.cl.nec.co.jp
[2] Japan Sciene and Technology Agency c/o NEC, Tsukuba, Japan
[3] Department of Physics, Meijo University, Nagoya, Japan
iijimas@eiji-u.ac.jp
[4] Departments of Physics and Materials Science and Engineering
Pennsylvania State University, University Park, USA

Abstract. In addition to sheet structures with purely hexagonal carbon rings, which naturally form surfaces of zero Gaussian curvature such as sheets and tubes, a graphenic membrane can also assume a conical shape whose apex is defined by one or more disclinations taking the form of fivefold (or possibly smaller) rings. Geometrically, just as a sheet of paper with a wedge removed can be resealed to form a conical hat, a graphene sheet with a wedge removed (i.e., a disclination) can be resealed, notionally, to form a cone or horn. The single-wall carbon nanohorns (SWNH) form one class of such conical structures, with a particularly sharp apical angle, a well-characterized high-yield synthesis route, and a distinct aggregate microstructure. Conical graphenic structures with wider opening angles, corresponding to fewer pentagonal disclinations at the apex, also form, sometimes as multilayered structures. The pentagonal defects in carbon nanocones perturb the low-energy electronic structure both locally and globally, defining both a local region of enhanced reactivity and a global geometric phase relation with profound consequences for electron transport around the apex. The rapid variation in local sheet orientation around the cone and the two-dimensional nature of the electronic states within imply that uniform laboratory fields can generate highly nonuniform effective local fields for states in the cone.

1 Introduction

Carbon is unique among the elements in its ability to assume extended two-dimensional sheet structures in elemental form. Since the in-sheet bonding is extremely strong, these sheets are stable both as isolated objects (graphene), and when curved into cylindrical geometries (nanotubes) or quasispherical geometries (fullerenes) wherein, e.g., pentagonal rings provide the needed Gaussian curvature. Less well-ordered negative-curvature geometries can also be envisioned, and realized to some extent in the nanoporous carbons. An intermediate state between a sheet and a fullerene also exists, the carbon nanocone, wherein a single pentagonal ring or assembly of nearby pentagonal rings defines a conical apex, which is then extended by a pure-hexagon graphenic network into a larger conical structure. As it does for the nano-

A. Jorio, G. Dresselhaus, M. S. Dresselhaus (Eds.): Carbon Nanotubes,
Topics Appl. Physics **111**, 605–629 (2008)

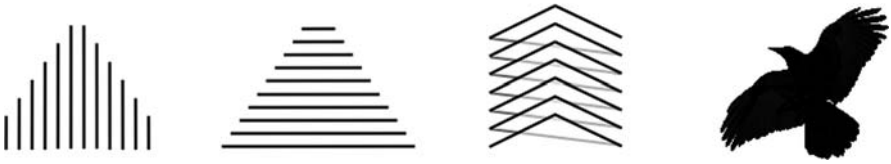

Fig. 1. Several carbon-based objects with overall conical nature are not covered here, including (from *left* to *right*) tubular cones, conical stacks of graphene sheets, helical graphitic whiskers, and ravens

tubes, fullerenes and graphene, the geometry of the nanocone defines a unique set of structural, mechanical, chemical, and electronic properties.

One major subclass of nanocones, nanohorns [1] formed by ablating graphite with a CO_2 laser, are distinguished by high yield, high purity and an aggregate microstructure, features that have facilitated the development of potential applications in the adsorption and release of small molecules. Cones can also be formed in vapor-phase carbon deposition onto graphite surfaces [2, 3] or in the pyrolysis of carbon-containing precursors such as hydrocarbons [4, 5] or CO [6]. Glassy carbons or naturally occurring graphite aggregates sometimes contain thicker conical structures [7, 8]. Such samples often contain heterogeneous mixtures of multilayered structures with nested cones. The end of a standard carbon nanotube also often forms a tapering structure, wherein a single pentagonal ring in a straight tube wall induces an inward taper, the tube eventually closing in a five-pentagon conical cap, with an opening angle of $\sim 20°$ [9]. An overall cone shape can also form in situations where it is not defined topologically by the presence of pentagons in the apex. These superficially cone-like objects are depicted schematically in Fig. 1: whisker-like conical helices [10–12] (wherein a single continuous graphene sheet wraps helically around a central axis), the progressive sharpening of a telescoping multiwall nanotube (a so-called tubular cone [13, 14]), and conical bumps formed as a result of self-organized heat flow around transition-metal inclusions in the laser sputtering of graphite [15]. Since we focus on cones and horns whose structure follows directly from the presence of pentagonal disclinations within a seamless graphene sheet, these alternative structures, (and other overall conical carbon objects with less-organized interior microstructures [16–19]) are not covered here.

2 Geometrical Definition of the Cone

Carbon cones can be classified at the coarsest level by the number of layers in the cone and the number of pentagonal disclinations defining the tip. Figure 2 shows schematically the construction of one-pentagon and two-pentagon cones in terms of wedges removed from a graphene sheet. More pentagons

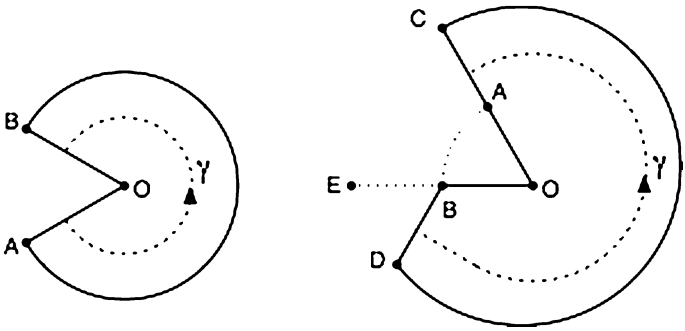

Fig. 2. The geometrical construction of a nanocone with one (*left*) and two (*right*) pentagons, in a continuum picture. One or two wedges are removed from a full sheet to form the opening B-O-A or C-A-O-B-D. This opening is then stitched back together by joining point A to point B and point C to point D to form the cone. Imagine making a party hat, except in graphene only discrete wedge angles are allowed. Adapted from [24]. The *dashed path* γ circumnavigates the apex

imply a sharper opening angle, in the sequence of approximately 113°, 84°, 60°, 39°, and 19° for one, two, three, four and five pentagonal disclinations within an ideal graphene lattice [20, 21]. Zero degrees corresponds to six pentagons, i.e., a nanotube. Strong deviations from these discrete angles suggest the formation of wrapped helices rather than continuous cones. In contrast, polygonal rings with more than six carbons induce negative curvature in the graphene sheet [22], and various combinations of n-fold rings embedded within a graphenic framework can generate a rich panoply of structures [23]. In this context, graphene, discussed in the contribution by *Charlier* et al., can be considered as a zero-pentagon carbon nanocone.

At a finer level, one may also consider the relative positions of the pentagons within the tip, classifiable by group theory [25]. These pentagonal rings affect both the mechanical and electronic response of the sp^2 carbon structure, both locally (through an enhanced local density of electronic states near the pentagonal rings) and globally (through new modes of mechanical response and geometrical phases associated with electron paths that circle the apex), as discussed in Sects. 7 and 8

3 Structure, Production, and Growth Mechanism of Single-Wall Carbon Nanohorns

The cone of narrowest opening angle has five pentagonal rings in its apex. One major class of such structures, typically forming as aggregates, is the single-wall carbon nanohorn (SWNH). In 1998, it was found that about 2000 single-wall carbon nanohorns assemble to form roughly spherical aggregates [1] of three types: dahlias (Fig. 3), buds (Fig. 4, top), and seeds (Fig. 4, bottom) [1].

We focus here mainly on the dahlia-type SWNH-aggregates, since they can be produced in large quantities with high purity [1,26,27] and so have several potential applications in methane storage [28], hydrogen–deuterium separation [29], fuel-cell electrodes [30], hydrogen generation from methane with steam [31], capacitors [32], and drug delivery [33–35], as described later. The dahlia-type aggregates have spherical forms with diameters of about 80–100 nm, as shown in Fig. 3 [1]. The magnified image of the dahlia-type aggregate surface (Fig. 3c) reveals that the horn-shaped tips of individual SWNHs have cone angles of about 20°, corresponding to five pentagonal rings at the tip, as indicated in Fig. 3d. The diameters of individual SWNHs are 1–2 nm at the horn tips and 4–5 nm in the tubule-body part. The wall-to-wall distances between adjacent SWNHs are about 0.4 nm [36]. Cone-shaped tips have also been found in other carbonaceous materials formed by arc discharge [37–40], suggesting that they have specific stability. The SWNH aggregate is robust and cannot be separated into individual SWNHs. However, objects that look like bundles of SWNHs (Fig. 5a) are occasionally seen when SWNHs are dispersed in solvents [41]. A similar bundle structure can be seen in high-resolution scanning electron microscopy images of the aggregate (Fig. 5b) by courtesy of Hitachi High-Technology Corporation, so the SWNH bundle could be the structural unit of the aggregate, as described in [1].

SWNHs are produced by CO_2 laser ablation of graphite at room temperature in Ar gas at about 760 Torr with a laser intensity of about 2 kW/cm^2 [1, 26, 27]. The production system has been steadily improved, recently reaching a production rate of 1 kg/day with a purity higher than 90 % [27]. The main impurities are graphitic particles with sizes on the order of micrometers [42], plus trace amounts of C_{60} [43]. The growth mechanism of SWNHs has been studied with in-situ optical measurements [44], and the mechanism is considered as follows [45]. The carbon clusters in the laser plume collide during propagation and form carbon droplets, which might have sizes of about 70 nm for the 100-nm dahlia aggregate, if we assume a carbon-droplet density of about 2 g/cm^3. The carbon in the droplets transforms into graphene sheets as the temperature decreases, and each graphene sheet spontaneously rolls up to form a tubule structure, as also seen in a theoretical calculation (Fig. 6) [46].

The structures of individual SWNHs and the aggregate sizes are influenced by the type and pressure of the ambient gas used in the laser ablation [1,26]. When SWNHs are produced at a low Ar pressure, the conical portion is shortened (bud-type aggregate, Fig. 4, top), and the tubule shapes become thin and bumpy (seed-type aggregate, Fig. 4, bottom). The same change is apparent when the gas is changed from Ar to He or N_2 [26]. The graphitization of the CO_2 laser ablation products is enhanced by an increase in the ambient pressure, and graphite balls are produced when the Ar gas pressure reaches about 4 atm [47, 48].

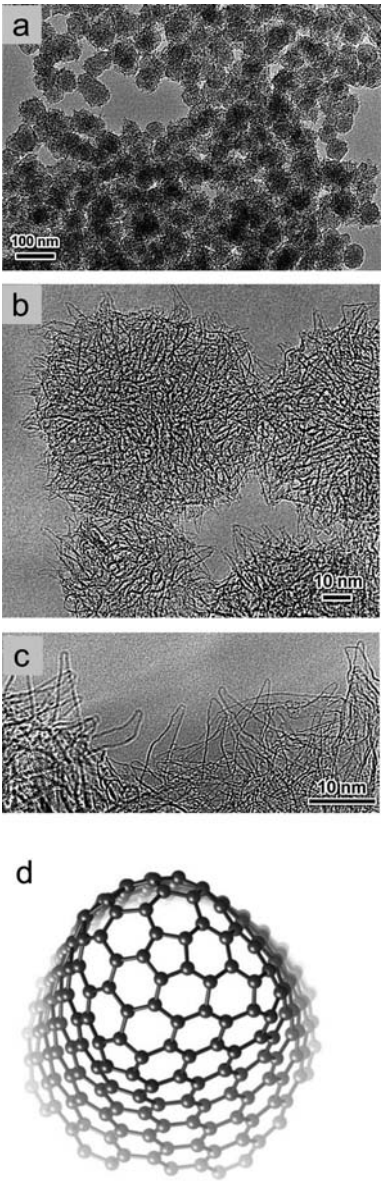

Fig. 3. TEM images of SWNHs at different scales of magnification (**a**–**c**) [1] and a computer graphic of the horn tip (**d**)

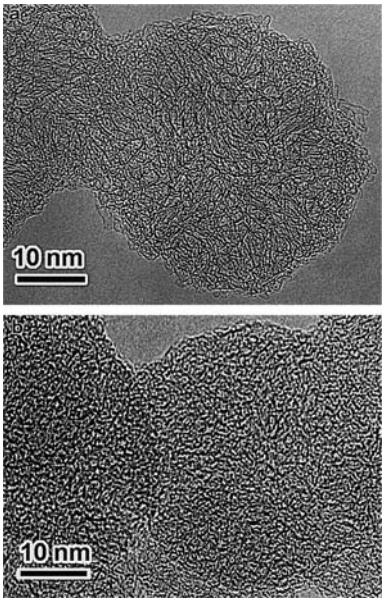

Fig. 4. TEM images of a bud-type aggregate (*top*) and a seed-type aggregate (*bottom*) [1]

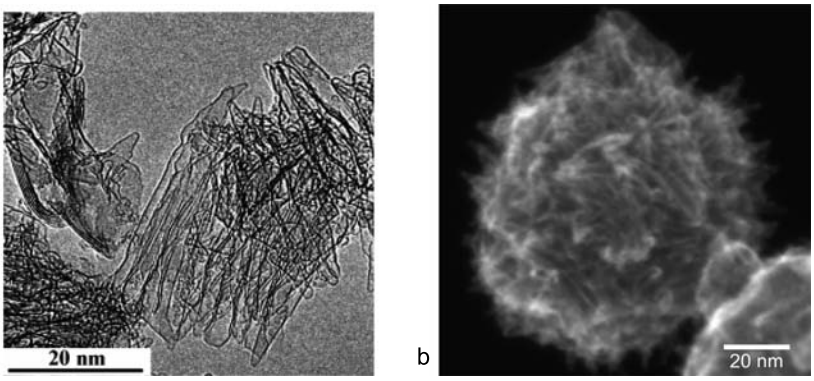

Fig. 5. (**a**) TEM images of bundle-like aggregates of SWNHs that were found when spherical SWNH aggregates were dispersed in an aqueous solution of the surfactant NaDDBS, after sonication [41]. (**b**) High-resolution SEM image of SWNH aggregates, showing the bundle-like arrangement of SWNH tubules. By courtesy of Hitachi High-Technology Corporation

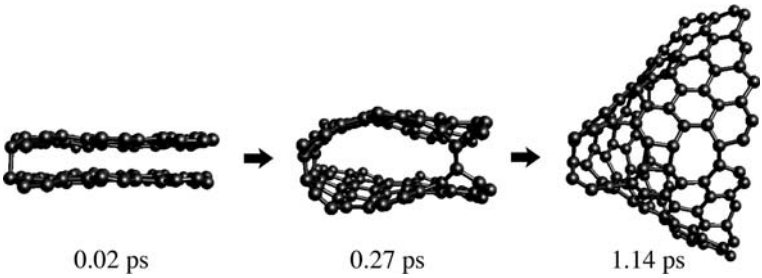

Fig. 6. Tight-binding molecular dynamics simulation of the reactive collision of two graphene sheets, suggesting that they can spontaneously roll up to form a SWNH tip structure [46]. The initial distance between graphene layers is small, 0.23 nm, and the temperature in the simulation is 2000 K. The simulation periods are shown below each structure

When the graphite target includes metal catalysts such as Ni–Y or Ni–Fe, the CO_2 laser ablation produces SWNTs together with SWNHs without heating the system [49–51]. Production methods not using the CO_2 laser ablation have also been reported, such as an arc-discharge method with carbon electrodes under various conditions [52–54].

4 Properties of Single-Wall Nanohorns

A SWNH is a closed tube in the as-grown state. The holes are easily opened by heat treatment in oxygen gas [55–57] or oxidative acids [58, 59]. The holes are visible with transmission electron microscopy (TEM) (Fig. 7, top), and the dominant hole diameters are 1–1.5 nm when the holes are opened by treatment in oxygen gas at 570 °C for 10 min (Fig. 7, bottom) [60]. The size and number of holes are changed by the oxidation conditions [55–58, 61]. Figure 8 shows that the opening of holes increases the surface area from 330 m^2/g in the as-grown SWNHs to 1300 m^2/g, and the pore volume also increases from 0.2 to 0.9 mL/g [55]. Analysis of nitrogen adsorption isotherms at 77 K suggests the existence of three deep potential sites: the deepest one is assumed to be an interstitial site among the SWNH tubules with a diameter of about 0.4 nm, followed by the inside surface of the SWNH wall and the central region of the hollow space inside the SWNHs [55].

The functional groups located at the hole edges are also controllable. The hole edges can have abundant carboxyl groups (and other oxygenated groups) when the holes are opened with H_2O_2 [59], or they can acquire further oxygenated functional groups, such as carbonyls, when the holes are opened by heat treatment in air or oxygen gas [57]. It is confirmed that carboxyl anhydrides and/or lactone groups are changed to carboxyl groups by immersion in water or methanol [62]. These oxygen-containing functional groups are re-

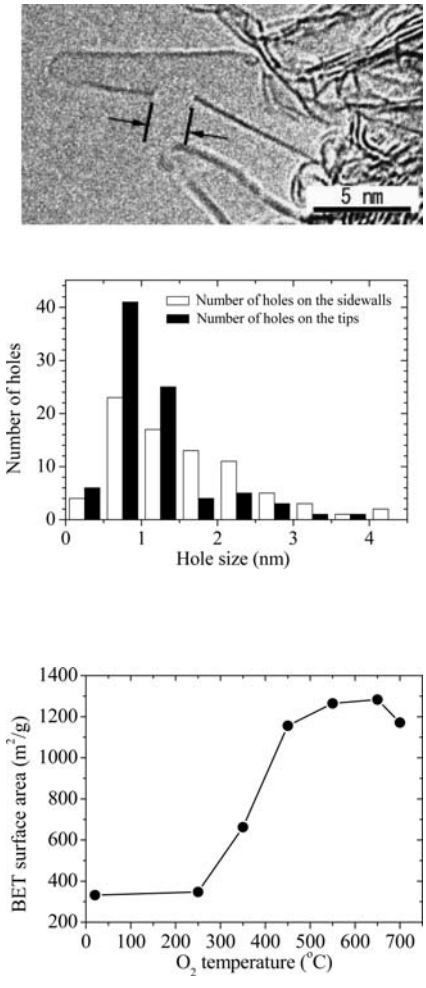

Fig. 7. TEM image of SWNHs with holes opened by heat treatment in oxygen gas at 570 °C (*top*) [60]. The hole sizes were measured as indicated with *bars* and *arrows* in the *top image*, and their histograms show typical hole sizes of 1 to 1.5 nm (*bottom*) [60]

Fig. 8. Surface area of as-grown SWNH and hole-opened SWNHox [61] estimated from the adsorption isotherm of nitrogen at 77 K, assuming adsorption follows the BET scheme. The obtained BET surface area depends on the heat-treatment temperature in oxygen gas [55–57]. The surface-area decrease for 700 °C heat-treatment is interpreted as indicating that many SWNH tubules are burned off

moved by heat treatment in hydrogen gas at, for example, 1200 °C, which probably replaces them with hydrogen [62, 63].

An interesting property of these hole is that those at the tips of the SWNH can be closed by heat treatment at 1200 °C in an Ar atmosphere, while those on the sidewalls, cannot be closed in this manner [64]. Magnetic [65–67] and electrical properties [65, 68–70] of SWNHs have also been studied. However, their details are not presented here.

5 Applications of Single-Wall Nanohorns

Due to the rough surface structure of the SWNH aggregate, catalysts are easily supported on the aggregate surface as small particles. An example is

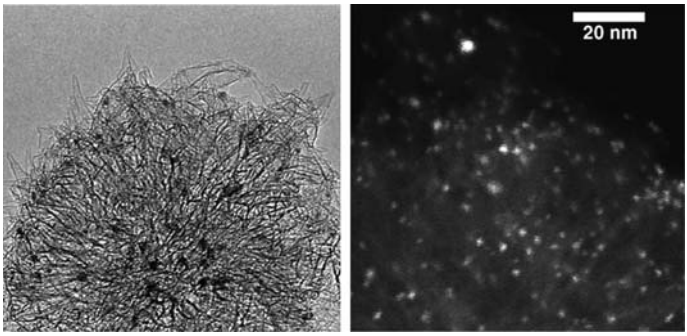

Fig. 9. TEM image of EuPt/SWNHs after treatment with methane and water at 500 °C for hydrogen generation (*left*), and its high-angle annular dark-field image (*right*). Pt particles appear as black spots in the left and white spots in the right. 60–70 % of the Pt particles have sizes 1–2 nm. The Eu particles are dispersed all over the aggregate, but are too small to be observed [31]

the use of catalysts for the decomposition of methane by steam to generate hydrogen [31]: Pt particles have sizes of 1–2 nm, while Eu particles form at extremely small sizes not visible to TEM, i.e., less than 1 nm (Fig. 9). It has also been reported that Pt-loaded SWNHs are potentially useful as electrodes in fuel cells [30].

Hole-opened SWNH (SWNHox) have additional promise for applications. It is possible to incorporate various molecules and clusters inside SWNHox from various solutions, even at room temperature [60, 71]. These incorporated molecules can also be released in a solvent; the release process usually exhibits both quick and slow processes with respective time constants in the range from minutes and hours to days [33, 34, 72]. These features are suitable for using SWNHox to carry and supply materials upon demand. One possible application would be drug delivery [33–35]. For example, cisplatin, an anticancer drug, can be incorporated inside SWNHox. The cisplatin can then be released from SWNHox to kill cultured cancer cells in vitro (Fig. 10) [34].

Since the hole size is controllable, as described above, SWNHox exhibit a molecular sieve effect: only molecules smaller than the hole diameter can enter the interior of the SWNHs [73].

Chemical modification of SWNHs is essential for various applications. Many reports show that chemical modifications of as-grown SWNHs are possible [74–77], and chemically modified SWNHs disperse well in aqueous solutions if the modification is designed to achieve this (Figs 11a,b). The chemical reactions are thought to occur at the dips and bumps on the sidewalls or horn tips, where pentagonal or heptagonal rings appear in the hexagonal graphene network.

The chemical modification of hole-opened SWNHox is also possible at their hole edges (Fig. 11c) [59, 78–80]. An interesting example is the attachment of Gd acetate to carboxylic groups or other groups at the hole edges,

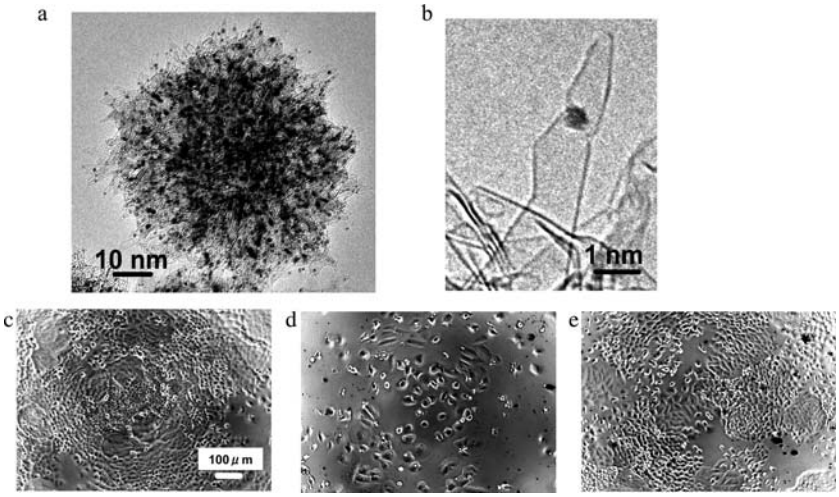

Fig. 10. A TEM image of cisplatin-incorporated SWNHox shows dark spots denoting cisplatin clusters inside SWNHs (**a**), and its magnified image (**b**). Photographs of cultured human lung-cancer cells (HR460) incubated for 48 h with no additions (control) (**c**), and addition of cisplatin@SWNHox (**d**) or SWNHox (**e**). Most of the cancer cells were terminated when cisplatin@SWNHox was added. No cytotoxity of SWNHox was apparent in (e) [34]

as confirmed with TEM (Fig. 12) [80]. Gd acetate plugs holes, which hinders both the entrance of C_{60} into a SWNHox [80] and the exit of C_{60} from inside a SWNHox [81]. This plugging and unplugging capability should reinforce the material supply functions of SWNHox.

The hollow space inside a SWNH provides a reaction chamber that is tolerant to very high temperatures, as expected for carbon-based materials. One advantage of a nanoreaction chamber with a high-temperature tolerance was demonstrated by the formation of magnetite nanoparticles from Fe acetate clusters confined inside SWNHox by heat treatment at 400 °C in Ar (Fig. 13). Magnetite-loaded SWNHs could be observed by magnetic resonance imaging (Fig. 13) [82]. When SWNHs are used as drug carriers, magnetite-loaded SWNHs could be useful to check whether they have arrived at the diseased part, or to move them to the diseased part by applying a magnetic field. This approach might be effectively combined with a hyperthermia system.

The toxicity of SWNHs has been studied intensively because it will be critical for fundamental studies and applications. No cytotoxicity has been found, and animal tests have shown no measurable toxicity [83]. Thus, no short-term toxicity has been found to date. The nature and amount of toxicity from long-term exposure is still unclear.

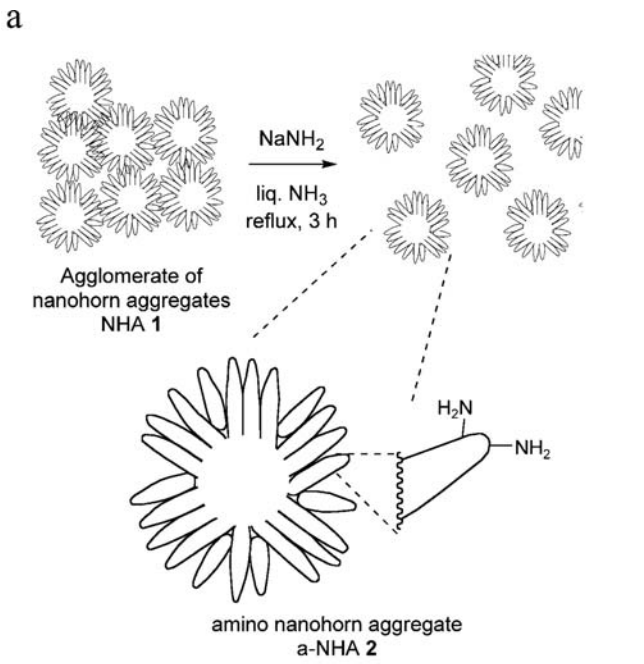

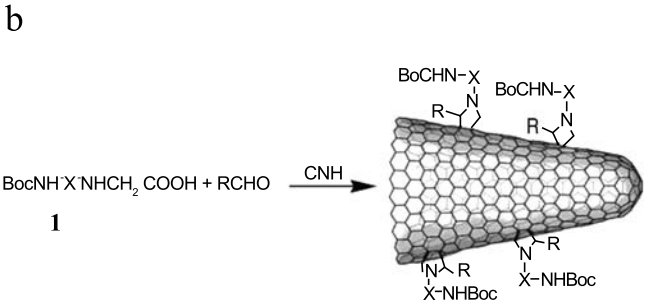

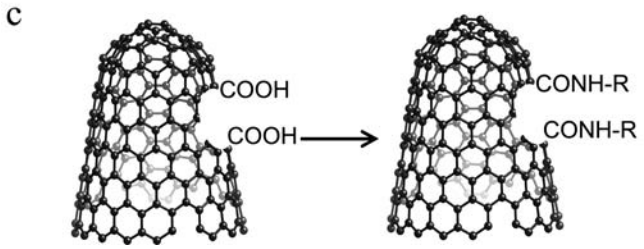

Fig. 11. Chemical modifications of SWNHs. Amination (**a**) [55] and addition of azomethine ylides (**b**) [74] on the sidewalls of as-grown SWNHs. Chemical modification of SWNHox by reaction of the carbocylic groups at the hole edges with amines through formation of amido conjugation (**c**) [78, 79]

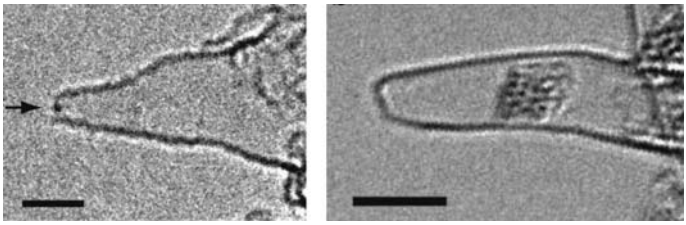

Fig. 12. SWNHox capturing a Gd acetate molecule at tip-hole (*left*), and Gd acetate clusters in the inside (*right*). Scale bars correspond to 2 nm (*left*) and 3 nm (*right*) [80]

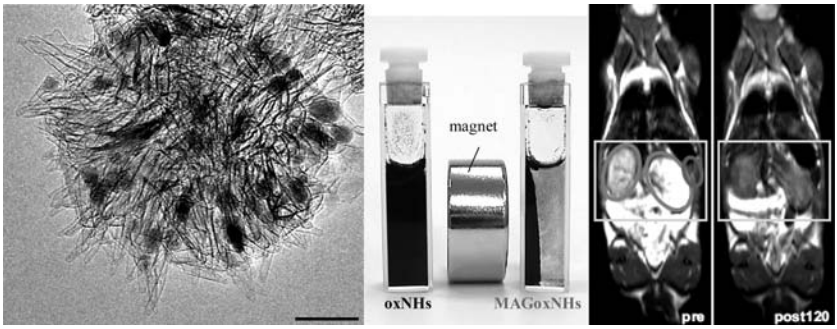

Fig. 13. TEM images of magnetite-SWNHox with an average magnetite particle size of 6 nm (*left*). The magnetite-SWNHox was attracted by the magnet but the SWNHox itself was not (*center*). In-vivo magnetic resonance imaging of magnetite-SWNHox intravenously administered from the tail vein of a mouse (*right*) [82]

6 Comparison of Single-Wall Nanohorns to Single-Wall Nanotubes

Both SWNHs and SWNTs are tubes made of single graphene sheets with hollow spaces inside. The diameter of a SWNT is small, and therefore molecules confined in SWNTs are arranged in a one-dimensional-like ordering, allowing detailed studies of their physics and chemistry in a highly constrained geometry. On the other hand, the diameter of an SWNH is large, so molecular movements, cluster formation and chemical reactions inside SWNHs are three-dimensional-like, which is useful for many applications in materials engineering.

The irregular tube structure of SWNHs has the advantage of opening holes not only at the tips but also on the sidewalls, and the large diameters of the tubules allow the hole sizes to be enlarged to 2 nm or larger. Due to the large diameters of holes and tubules, the incorporation and release of molecules are easy, which suggests that SWNHox can function as a carrier and supplier of materials. Unlike the bundle aggregates of SWNTs, the rough surface of

the SWNH spherical aggregates seems to be useful for holding catalysts or other materials and keeping their particle sizes small. The absence of metal-catalyst particles in SWNHs may be an additional advantage of SWNHs over SWNTs in practical use.

7 Mechanical Response of Carbon Nanocones

In the nanohorn, the graphenic carbon cone is generally connected seamlessly to a more cylindrical tubule-like region. We now focus our attention exclusively on the conical section and consider the mechanical (and in the next section, electronic) properties of a standalone carbon nanocone, as in Fig. 14. In a typical elastic response, all atoms in the material respond to the mechanical perturbation to a degree proportional to the perturbation, increasing their elastic energy quadratically in the magnitude of the distortion. Cones, however, are different. When pressed at the apex and held at the base, a blunt carbon nanocone with a single pentagon at its apex initially responds as a Hooke's law spring, but a sufficiently large distortion can induce a nonlinear mode of response, as part of the cone pops inside out to create a structure of mixed character, wherein one portion of the cone slopes upwards, the other downwards, as in Fig. 14. Since the local structures of both upward- and downward-sloping regions are local equilibrium states of an *undeformed* cone, essentially all of the elastic energy is concentrated in the transition region, i.e., the fold between upward and downward slopes. This fold maintains a similar shape, regardless of its circumference. Therefore, instead of responding elastically like a typical material, with an energy quadratic in the deformation and shared by all atoms, an axially compressed cone responds by imparting a fixed amount of the elastic energy per atom onto a finite subset of atoms, whose number varies linearly with the deformation. The cone's elastic energy then varies linearly with the deformation, so it acts as a constant-force spring, as shown in the central region of Fig. 14, starting from about 5 Å displacement [84]. The end result is similar to a displacive structural phase transition at constant pressure, although in a phase transition the number of affected atoms eventually encompasses the entire sample, whereas the fold of the nanocone eventually exits the structure. Cones with larger numbers of pentagons at the apices are more rigid and hence more difficult to invert; they may exhibit more complex modes of deformation that break azimuthal symmetry. Cones may also begin to invert from the base rather than the tip.

A fully inverted achiral cone recovers the initial undeformed state. However, if the cone is chiral, due to impurities, a ragged edge, or the placement of pentagon rings, then mechanical inversion also inverts the structure's chirality. A left-handed cone then becomes a right-handed cone, with atomic perfection, since the two sides of a clean graphenic sheet are essentially indistinguishable. This is a perfect chirality inversion of a nanometer-scale or

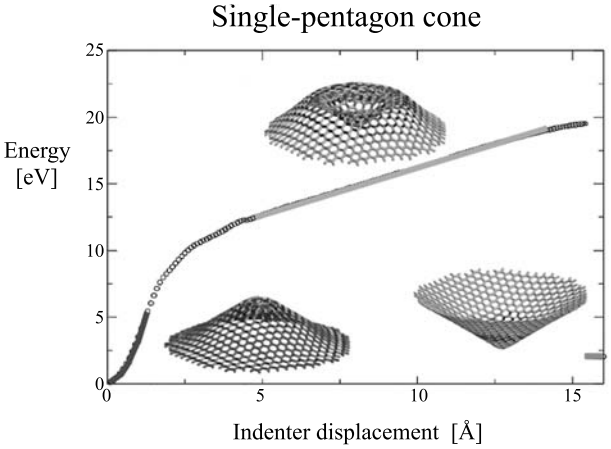

Fig. 14. Total energy of a single-pentagon nanocone pressed on the top by a spherical indenter and held at the base by a flat substrate with a hole at the center to accommodate complete inversion, within a Tersoff–Brenner treatment of the interatomic interaction. After a brief Hooke's-law regime, the tip of the cone inverts to define a constant-force regime, which is arrested by the final complete inversion of the cone as the folded region reaches the outer edge of the cone. Under alternative conditions, the cone may invert first at the base, the fold propagating upwards before escaping at the apex. See [84] for details

even micrometer-scale object, without breaking bonds. Macroscopically, a similar inversion can be performed by turning a glove inside out, but in this macroscopic case the two surfaces remain distinguishable, so the inversion is not perfect. This chirality inversion is a partner to the constant-force mechanical response, since both result from the degeneracy of the upward- and downward-sloping states. Theory predicts that breaking the local inversion symmetry of the graphene sheet by chemisorbing just a handful of hydrogen atoms onto the apical carbons will profoundly change the mechanical response. The precise form of the force–distance curve, whether the cone inverts first from the tip (constant-force) or the base, and whether any intermediate states are metastable [85] all depend on the detailed geometrical character of the system and its boundary conditions, but the overall mechanical response under axial deformations is governed by symmetry and the ability of a graphenic sheet to recover elastically after large deformations. Lower-symmetry deformations applied along nonaxial directions are more complex, but should maintain a propensity for nonlinear buckling distortions. Instabilities towards similar symmetry-lowering buckling distortions may be involved in limiting the sizes of cones formable in the synthesis of free-standing cones [86]. Experimental measurements of the mechanical response of carbon nanocones have, to our knowledge, not yet been performed.

8 Electronic Properties of Carbon Cones

The most salient feature of the carbon-nanocone electronic structure is an enhanced local density of electronic states in the vicinity of the pentagonal rings at the apex, as seen in first-principles [87–92], empirical tight-binding [85, 93–98], and continuum [24, 99] treatments. In some cases, these studies examined the conical endcaps [89, 94] or tapers [91, 93] of nanotubes rather than standalone cones. The precise position and size of these peaks in the density of states depend sensitively on the number and placement of the pentagons, which suggests that the phenomenon is not simply a recapitulation of the enhancements in the density of states seen around various defects in other forms of sp^2 carbon such as nanotubes or graphene, but may also involve a topological character. This enhancement, and a related increase in the electron density in the vicinity of the pentagons, has attracted considerable attention from the theoretical community, since it has possible application to field emission [85, 90] or scanning probes [88, 93]. Especially for sharp tapers, the conical shape naturally lends itself to electric-field enhancement. Also, graphene can be very robust structurally under punishing conditions of high field and high current.

This modification of the local density of states near the cone apex is not simply a local phenomenon: the global constraints on the phase of the low-energy electronic states as it wraps around the apical pentagons induce changes in the density of states, even within a continuum model of the electronic states [100], wherein the pentagons disappear into an infinitesimal apical disclination [24, 99]. If the pattern of phases of an electronic state at the Dirac point (i.e., Fermi point) of graphene is wrapped around a cone, it does not match onto itself around the circumference, so this state is not a proper low-energy state of the cone. For example, an apical disclination of 60° rotates one Fermi point into the other. In a continuum treatment, the disclinations can be shrunk to a point and represented as pure gauge fields, with associated geometrical phases, similar to the Aharonov–Bohm phases of nanotubes in an external axial magnetic field (see the contributions by *Ando* and by *Kono* et al.) or the effective A–B phases arising from elastic deformations that stretch or twist a nanotube (see the contribution of *Ando*). Since there are four distinct low-energy electronic states (two Dirac points and two sublattices), one obtains a multicomponent geometrical phase in a form first developed to describe large closed fullerenes [101]. In one-pentagon cones, these gauge fields generate a cusp in the local density of states near the cone apex as a function of energy, in contrast to the linear decrease to zero seen in flat graphene. The phase accumulated by translating between two pentagons does not commute with that from circumnavigating a single pentagon; therefore, the two opposing translations involved in a closed circuit about the apex of a cone with two pentagons do not cancel and the residual phase depends on the relative displacement between the two pentagons, following an "$n - m \pmod 3$ rule" for a two-pentagon cone [24], where (n, m)

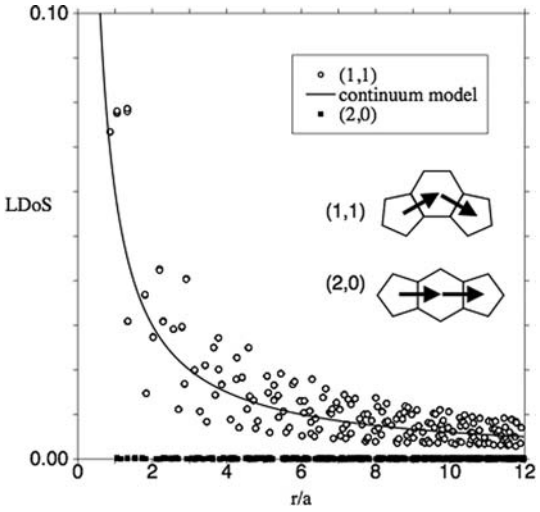

Fig. 15. Local density of electronic states (normalized per atom and per unit of nearest-neighbor hopping integral) as a function of distance from the apex for a tight-binding (*points*) and continuum model of one example from each of the two classes of two-pentagon carbon nanocones, showing the agreement between the atomistic and continuum models and the effect of the geometrical phase arising from the precise arrangement of the pentagonal disclinations. Adapted from [24]

measures the displacement between the pentagons in graphene lattice coordinates, as depicted in the inset to Fig. 15. The term "mod 3" means the remainder when dividing by three. This is the same expression as that used to classify carbon nanotubes, wherein (n, m) defines the circumference of the tube. Figure 15 compares tight-binding and continuum treatments of this phenomenon. For $n = m \pmod 3$, the density of states near the Fermi energy is nonzero in the vicinity of the apex; otherwise it drops to zero at the Fermi energy, as in graphene. These anomalies in the low-energy density of states decay upon moving away from the apex as a power law in the distance: the continuum model in which they appear contains no intrinsic length scale (to define, e.g., the e-folding length of an exponential falloff). The precise exponent of the power law depends on the number and arrangement of pentagons in the apex. There is also a slight difference in total energies between different arrangements of a given number of pentagons [102].

These geometrical phases have further effects more directly related to the electron phase, such as novel interference effects for waves that propagate around opposite sides of the apex and superlattice structures that could be visible in scanning tunneling microscopy [87]. Since geodesics emanating from a point on the surface of a cone can intersect on the opposite side of the apex, a single outgoing circular wave emitted from a point on the side of a cone can generate an interference pattern on the opposite side, where the

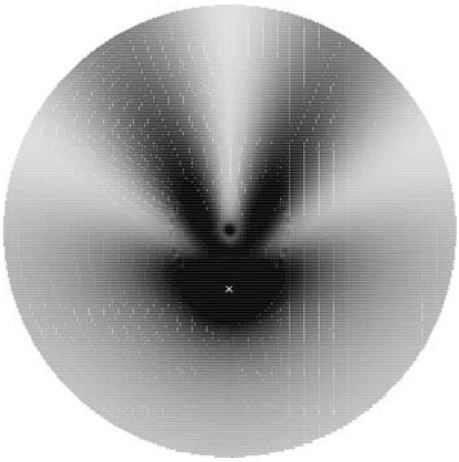

Fig. 16. Intensity pattern for a point source (*cross*) of electron waves emitting near the Fermi energy on the lower side of the apex (*central dot*) of a two-pentagon $n = m \pmod 3$ nanocone. Normally, for a point source of circular waves on a flat surface, one would not expect an interference pattern, since the outgoing wavefronts do not self-intersect. However, on a cone, the wavefront intersects itself on the opposite side of the apex from the point source. Even so, one might expect the line extending away from the apex exactly opposite the point source to be an antinode, since the path length around each side of the apex is identical. However, this line is actually a node due to the geometrical phase induced by the apex. Adapted from [24]

phase fronts of the wave self-intersect. This interference pattern is modified by the geometrical phase associated with the apex: for example, in a two-pentagon cone with $n - m = 0 \pmod 3$, the line directly opposite the point source is a node, not an antinode, even though the distances back to the source are equal for the two possible paths, as shown in Fig. 16 [24]. The response of the system to a magnetic field is also anomalous, with new Landau levels associated with Lissajous orbits that circle the apex multiple times. In contrast, the Landau levels of a carbon nanotube in a field perpendicular to the axis (the contribution by Kono et al.) do not pick out any single point in space as special. Since the perpendicular component of a magnetic field and the in-plane component of an electric field are those relevant to charge transport, a uniform magnetic field applied transverse to the cone axis, or a uniform electric field applied along the cone axis will generate transport phenomena governed by highly inhomogenous local fields [24] – similar effects may occur in bent or folded sheets of graphene. This field remains ripe for experimental investigation: to our knowledge, although some scanning tunneling microscopy work has been performed on pentagons in nanotubes [89], none of these fascinating consequences of geometric phase have yet been verified by direct observation in cones.

9 Conclusion

The wondrous flexibility of carbon chemistry, especially its ability to form robust low-dimensional networks, enables the formation of a plethora of carbon nanostructures, including fullerenes, nanotubes, and nanocones or nanohorns. Nanohorns in particular, with high-throughput synthesis and an adaptable and accommodating microstructure, have substantial promise for applications in the catalysis, storage and delivery of adsorbed substances largely complementary to applications of carbon nanotubes, as reviewed in the contribution by Endo et al. Animated by a range of possible global structural topologies, the unusual electronic structure of graphene, with linear dispersion and a Fermi surface confined to only two distinct points, generates an electronic system with a unique sensitivity to structure, whether the circumferential periodicity of a nanotube or the apical disclination of a nanocone. Aggregated nanohorns, having a facile synthesis route, have been studied experimentally, with a focus mainly on chemical properties related to catalysis, adsorption, release and functionalization. Isolated nanocones are much less thoroughly studied experimentally, perhaps due to issues related to synthesis, but they promise a rich variety of novel phenomena not observable in other carbon structures, both mechanical (related to their inversion symmetry) and electronic (related to the global topological phases associated with their apices).

Acknowledgements

V. H. Crespi thanks Paul E. Lammert for stimulating discussions and powerful insights into the geometrical interpretation of the electronic consequences of graphenic disclinations. M. Yudasaka and S. Iijima thank all the members of carbon nanotube projects conducted by SI for the collaborations on SWNHs and SWNTs.

References

[1] S. Iijima, M. Yudasaka, R. Yamada, S. Bandow, K. Suenaga, F. Kokai, K. Takahashi: Nano-aggregates of single-walled graphitic carbon nano-horns, Chem. Phys. Lett. **309**, 165 (1999) 606, 607, 608, 609, 610

[2] K. Sattler: Scanning tunneling microscopy of carbon nanotubes and nanocones, Carbon **33**, 915 (1995) 606

[3] M. Ge, K. Sattler: Observation of fullerene cones, Chem. Phys. Lett. **220**, 192 (1994) 606

[4] A. Krishnan, E. Dujardin, M. M. J. Treacy, J. Hugdahl, S. Lynum, T. W. Ebbesen: Graphitic cones and the nucleation of curved carbon surfaces, Nature **388**, 451 (1997) 606

[5] H. Terrones, T. Hayashi, M. Munoz-Navia, M. Terrones, Y. A. Kim, N. Grobert, R. Kamalakaran, J. Dorantes-Davila, R. Escudero, M. S. Dresselhaus, M. Endo: Graphitic cones in palladium catalysed carbon nanofibres, Chem. Phys. Lett. **343**, 241 (2001) 606
[6] D. D. Double, A. Hellawell: Cone-helix growth forms of graphite, Acta Metall. Mater. **22**, 481 (1974) 606
[7] J. A. Jaszczak, G. W. Robinson, S. Dimovski, Y. Gogotsi: Naturally occurring graphite cones, Carbon **41**, 2085 (2003) 606
[8] Y. Gogotsi, S. Dimovski, J. A. Libera: Conical crystals of graphite, Carbon **40**, 2263 (2002) 606
[9] S. Iijima: Growth of carbon nanotubes, Mater. Sci. Eng. **B19**, 172 (1993) 606
[10] S. Amelinckx, W. Luyten, T. Krekels, G. V. Tendeloo, J. V. Landuyt: Conical, helically wound, graphite whiskers: A limiting member of the "fullerenes"?, J. Cryst. Growth **121**, 543 (1992) 606
[11] Z. Lou, C. Chen, Q. Chen: Growth of conical carbon nanotubes by chemical reduction of $MgCO_3$, J. Phys. Chem. B **109**, 10557 (2005) 606
[12] Y. Kim, T. Hayashi, K. Osawa, M. Endo, M. S. Dresselhaus: Cone-type multishell in the hollow core of multi-wall carbon nanotube, Chem. Phys. Lett. **367**, 537 (2003) 606
[13] G. Zhang, X. Jiang, E. Wang: Tubular graphite cones, Science **300**, 472 (2003) 606
[14] P. Liu, Y. W. Zhanga, C. Lu: Molecular dynamics simulations of bending behavior of tubular graphite cones, Appl. Phys. Lett. **85**, 1778 (2004) 606
[15] D. J. Krajnovich, J. E. Vazquez, R. J. Savoy: Impurity-driven cone formation during laser sputtering of graphite, Science **259**, 1590 (1993) 606
[16] I.-C. Chen, L.-H. Chen, C. Orme, A. Quist, R. Lal, S. Jin: Fabrication of high-aspect-ratio carbon nanocone probes by electron beam induced deposition patterning, Nanotechnology **17**, 4322 (2006) 606
[17] N. Muradov, A. Schwitter: Formation of conical carbon structures on vapor-grown carbon filaments, Nano Lett. **2**, 673 (2002) 606
[18] C. K. Tana, K. P. Loha, J. T. L. Thongb, C. H. Sowc, H. Zhanga: Plasma synthesis of well-aligned carbon nanocones, Diam. Relat. Mater. **14**, 902 (2005) 606
[19] V. I. Merkulov, M. A. Guillorn, D. H. Lowndes, M. L. Simpson, E. Voelkl: Shaping carbon nanostructures by controlling the synthesis process, Appl. Phys. Lett. **79**, 1178 (2001) 606
[20] M. M. J. Treacy, J. Kilian: Designability of graphitic cones, Mater. Res. Soc. Symp. Proc. **675**, W2.6 (2001) 607
[21] T. W. Ebbesen: Cones and tubes: Geometry in the chemistry of carbon, Acc. Chem. Res. **31**, 558 (1998) 607
[22] S. Ihara, S. Itoh, K. Akagi, R. Tamura, M. Tsukada: Structure of polygonal defects in graphitic carbon sheets, Phys. Rev. B **54**, 14713 (1996) 607
[23] H. Terrones, M. Terrones: Curved nanostructured materials, New J. Phys. **5**, 126 (2003) 607
[24] P. E. Lammert, V. H. Crespi: Graphene cones: Classification by fictitious flux and electronic properties, Phys. Rev. B **69**, 035406 (2004) 607, 619, 620, 621
[25] D. J. Klein: Topo-combinatoric categorization of quasi-local graphitic defects, Phys. Chem. Chem. Phys. **4**, 2099 (2002) 607

[26] D. Kasuya, M. Yudasaka, K. Takahashi, F. Kokai, S. Iijima: Selective production of single-wall carbon nanohorn aggregates and their formation mechanism, J. Phys. Chem. B **106**, 4947 (2002) 608
[27] T. Azami, R. Yuge, D. Kasuya, T. Yoshitake, Y. Kubo, M. Yudasaka, A. Iijima: Large scale production of SWNH, in *The 32nd Fullerene-Nanotubes General Symposium* (2007) pp. 3–20 608
[28] E. Bekyarova, K. Murata, M. Yudasaka, D. Kasuya, S. Iijima, H. Tanaka, H. Kanoh, K. Kaneko: Single-wall nanostructured carbon for methane storage, J. Phys. Chem. B **107**, 4682–4684 (2003) 608
[29] H. Tanaka, H. Kanoh, M. Yudasaka, S. Iijima, K. Kaneko: Quantum effects on hydrogen isotope adsorption on single-wall carbon nanohorns, J. Am. Chem. Soc. **127**, 7511–7516 (2005) 608
[30] Y. T. Yoshitake, Y. Shimakawa, S. Kuroshima, H. Kimura, T. Ichihashi, Y. Kubo, D. Kasuya, K. Takahashi, F. Kokai, M. Yudasaka, S. Iijima: Preparation of fine platinum catalyst supported on single-wall carbon nanohorns for fuel cell application, Physica B **323**, 124 (2002) 608, 613
[31] K. Murata, M. Yudasaka, S. Iijima: Hydrogen production from methane and water at low temperature using EuPt supported on single-wall carbon nanohorns, Carbon **44**, 818 (2006) 608, 613
[32] C.-M. Yang, Y.-J. Kim, M. Endo, H. Kanoh, M. Yudasaka, S. Iijima, K. Kaneko: Nanowindow-regulated specific capacitance of supercapacitor electrodes of single-wall carbon nanohorns, J. Am. Chem. Soc. **129**, 20–21 (2007) 608
[33] T. Murakami, K. Ajima, J. Miyawaki, M. Yudasaka, S. Iijima, K. Shiba: Drug-loaded carbon nanohorns: Adsorption and release of dexamethasone in vitro, Mol. Pharm. **1**, 399 (2004) 608, 613
[34] K. Ajima, M. Yudasaka, T. Murakami, A. Maigne, K. Shiba, S. Iijima: Carbon nanohorns as anticancer drug carriers, Mol. Pharm. **2**, 475 (2005) 608, 613, 614
[35] T. Murakami, J. Fan, M. Yudasaka, S. Iijima, K. Shiba: Solubilization of single-wall carbon nanohorns using a PEG-doxorubicin conjugate, Mol. Pharm. **3**, 408–414 (2006) 608, 613
[36] S. Bandow, F. Kokai, K. Takahashi, M. Yudasaka, L. Qin, S. Iijima: Interlayer spacing anomaly of single-wall carbon nanohorn aggregate, Chem. Phys. Lett. **321**, 514–519 (2000) 608
[37] S. Iijima: Growth of carbon nanotubes, Mater. Sci. Eng. **B19**, 172–180 (1993) 608
[38] P. J. F. Harris, S. C. Tsang, J. B. Claridge, M. L. H. Green: High-resolution electron microscopy studies of a microporous carbon produced by arc-evaporation, J. Chem. Soc. Faraday Trans. **90**, 2799–2802 (1994) 608
[39] Y. Saito, K. Nishikubo, K. Kawabata, T. Matsumoto: Carbon nanocapsules and single-layered nanotubes produced with platinum-group metals (Ru, Rh, Pd, Os, Ir, Pt) by arc discharge, J. Appl. Phys. **80**, 3062 (1996) 608
[40] S. Iijima, T. Wakabayashi, Y. Achiba: Structures of carbon soot prepared by laser ablation, J. Phys. Chem. **100**, 5839 (1996) 608
[41] M. Zhang, M. Yudasaka, J. Miyawaki, J, Fan, S. Iijima: Isolating single-wall carbon nanohorns as small aggregates through a dispersion method, J. Phys. Chem. B **109**, 22201–22204 (2005) 608, 610

[42] J. Fan, M. Yudasaka, D. K. T. Azami, R. Y. H. Imai, Y. K. S. Iijima: Micrometer-sized graphitic balls produced together with single-wall carbon nanohorns, J. Phys. Chem. B **109**, 110756–10759 (2005) 608
[43] D. Kasuya, M. Yudasaka, K. Takahashi, F. Kokai, S. Iijima: Formation of C_{60} by CO_2 laser vaporization of graphite at room temperature, Chem. Phys. Lett. **337**, 25 (2001) 608
[44] F. Kokai, K. Takahashi, M. Yudasaka, S. Iijima: Emission imaging spectroscopic and shadowgraphic studies on the growth dynamics of graphitic carbon particles synthesized by CO_2 laser vaporization, J. Phys. Chem. B **103**, 8686–8693 (1999) 608
[45] T. Kasuya, M. Yudaska: Growth mechanism of SWNT and SWNH, New Diam. **73**, 2 (2004) in Japanese 608
[46] T. Kawai, Y. Miyamoto, O. Sugino, Y. Koga: Nanotube and nanohorn nucleation from graphitic patches: Tight-binding molecular-dynamics simulations, Phys. Rev. B **66**, 033404 (2002) 608, 611
[47] F. Kokai, K. Takahashi, D. Kasuya, A. Nakayama, Y. Koga, M. Yudaska, S. Iijima: Laser vaporization synthesis of polyhedral graphite, Appl. Phys. A **77**, 69–71 (2001) 608
[48] A. Nakayama, S. Iijima, Y. Koga, K.Shimizu, K. Hirahara, F. Kokai: Compression of polyhedral graphite up to 43 GPa and X-ray diffraction study on elasticity and stability of the graphite phase, Appl. Phys. Lett. **84**, 5112–5114 (2004) 608
[49] W. K. Maser, E. Munoz, A. Beito, M. T. Martinez, G. P. Fuente, Y. Maniette, E. Anglaret, J. L. Sauvajol: Chem. Phys. Lett. **292**, 587 (1998) 611
[50] M. Yudasaka, F. Kokai, K. Takahashi, R. Yamada, N. Sensui, T. Ichihashi, S. Iijima: Formation of single-wall carbon nanotubes: Comparison of CO_2 laser ablation and Nd:YAG laser ablation, J. Phys. Chem. B **103**, 3576–3581 (1999) 611
[51] F. Kokai, K. Takahashi, D. Kasuya, M. Yudasaka, S. Iijima: Growth of single-wall carbon nanotubes dependent on laser power density and ambient gas pressure during room-temperature CO_2 laser vaporization, Appl. Phys. A **73**, 401–407 (2001) 611
[52] H. Takikawa, M. Ikeda, K. Hirahara, Y. Hibi, Y. Tao, P. A. Ruiz, Jr., T. Sakakibara, S. Itoh, S. Iijima: Fabrication of single-walled carbon nanotubes and nanohorns by means of a torch arc in open air, Physica B **323**, 277–279 (2002) 611
[53] T. Yamaguchi, S. Bandow, S. Iijima: Synthesis of carbon nanohorn particles by simple pulsed arc discharge ignited between pre-heated carbon rods **389**, 181–185 (2004) 611
[54] H. Wang, M. Chhowalla, N. Sano, S. Jia, G. A. J. Amaratunga: Large-scale synthesis of single-walled carbon nanohorns by submerged arc, Nanotechnology **15**, 546–550 (2004) 611
[55] K. Murata, K. Kaneko, W. Steele, F. Kokai, K. Takahashi, D. Kasuya, K. Hirahar, M. Yudasaka, S. Iijima: Molecular potential structures of heat-treated single-wall carbon nanohorn assemblies, J. Phys. Chem. B **105**, 10210 (2001) 611, 612, 615

[56] S. Utsumi, J. Miyawaki, H. Tanaka, Y. Hattori, T. Itoi, N. Ichikuni, H. Kanoh, M. Yudasaka, S. Iijima, K. Kaneko: Opening mechanism of internal nanoporosity of single-wall carbon nanohorn, J. Phys. Chem. B **109**, 14319 (2005) 611, 612
[57] J. Fan, M. Yudasaka, J. Miyawaki, K. Ajima, K. Murata, S. Iijima: Control of hole opening in single-wall carbon nanotubes and single-wall carbon nanohorns using oxygen, J. Phys. Chem. B **110**, 1587 (2006) 611, 612
[58] C.-M. Yang, H. Noguchi, K. Murata, M. Yudasaka, A. Hashimoto, S. Iijima, K. Kaneko: Highly ultramicroporous single-walled carbon nanohorn assemblies, Adv. Mater. **17**, 866–870 (2005) 611
[59] M. Zhang, M. Yudasaka, K. Ajima, S. Iijima: Light assisted oxidation for opening holes of SWNHs, *The* 32*nd Fullerene-Nanotubes General Symposium*, pp. 2–14 (2007) 611, 613
[60] K. Ajima, M. Yudasaka, K. Suenaga, D. Kasuya, T. Azami, S. Iijima: Materials storage mechanims in porous nanocarbons, Adv. Mater. **16**, 397 (2004) 611, 612, 613
[61] Unpublished data (2003) 611, 612
[62] J. Miyawaki, M. Yudasaka, S. Iijima: Solvent effects on hole-edge structure for single-wall carbon nanotubes and single-wall carbon nanohorns, J. Phys. Chem. B **108**, 10732 (2004) 611, 612
[63] E. Bekyarova, K. Kaneko, M. Yudasaka, D. Kasuya, S. Iijima, A. Huidobro, Rodriguez-Reinoso: Controlled opening of single-wall carbon nanohorns by heat treatment in carbon dioxide, J. Phys. Chem. B **107**, 4479 (2003) 612
[64] J. Miyawaki, R. Yuge, T. Kawai, M. Yudasaka, S. Iijima: Evidence of thermal closing of atomic-vacancy holes in single-wall carbon nanohorns, J. Phys. Chem. C **111**, 1553–1555 (2007) 612
[65] S. Garaj, L. Thien-Nga, G. Gaa, L. Forro, K. Takahashi, F. Kokai, M. Yudasaka, S. Iijima: Electronic properties of carbon nanohorns studied by ESR, Phys. Rev. B **62**, 17115–17119 (2000) 612
[66] S. Bandow, F. Kokai, K. Takahashi, M. Yudasaka: Unique magnetism observed in single-wall carbon nanohorns, Cryst. Appl. Phys. A **73**, 281–285 (2001) 612
[67] H. Imai, P. K. Babu, E. Oldfield, A. Wieckosdki, D. Kasuya, T. Azami, Y. Shimakawa, M. Yudasaka, Y. Kubo, S. Iijima: 13C NMR spectroscopy of carbon nanohorns, Phys. Rev. B **73**, 125405 (2006) 612
[68] S. Bandow, A. Rao, G. Sumanasekera, P. C. Eklund, F. Kokai, K. Takahashi, M. Yudasaka, S. Iijima: Evidence for anomalously small charge transfer in doped single-wall carbon nanohorn aggregates with Li, K and Br, Appl. Phys. A **71**, 561–564 (2000) 612
[69] J.-M. Bonard, R.Gaal, S. Garaj, L. Thien-Nga, L. Forro, K. Takahashi, F. Kokai, M. Yudasaka, S. Iijima: Field emission properties of carbon nanohorn films, J. Appl. Phys. **91**, 10107–10109 (2002) 612
[70] K. Urita, S. Seki, S. Utsumi, D. Noguchi, H. Kanoh, H. Tanaka, Y. Hattori, Y. Ochiai, N. Aoki, M. Yudasaka, S. Iijima, K. Kaneko: Effects of gas adsorption on the electrical conductivity of single-wall carbon nanohorns, Nano Lett. **6**, 1325–1328 (2006) 612
[71] M. Yudasaka, K. Ajima, K. Suenaga, T. Ichihashi, A. Hashimoto, S. Iijima: Nano-extraction and nano-condensation for c_{60} incorporation into single-wall carbon nanotubes in liquid phases, Chem. Phys. Lett. **380**, 42 (2003) 613

[72] R. Yuge, M. Yudasaka, J. Miyawaki, Y. Kubo, T. Ichihashi, H. Imai, E. Nakamura, H. Isobe, H. Yorimitsu, S. Iijima: Controlling the incorporation and release of c_{60} in nanometer-scale hollow spaces inside single-wall carbon nanohorns, J. Phys. Chem. B **109**, 17861 (2005) 613
[73] K. Murata, K. Hirahara, M. Yudasaka, S. Iijima, D. Kasuya, K. Kaneko: Nanowindow-induced molecular sieving effect in a single-wall carbon nanohorn, J. Phys. Chem. B **109**, 12668–12669 (2002) 613
[74] N. Tagmatarchis, A. Maigne, M. Yudasaka, S. Iijima: Functionalization of carbon nanohorns with azomethine ylides: towards solubility enhancement and electron-transfer processes, Small **2**, 490 (2006) 613, 615
[75] C. Cioffi, S. Campidelli, F. G. Brunetti, M. Meneghetti, M. Prato: Functionalization of carbon nanohorns, Chem. Commun. p. 2129 (2006) 613
[76] I. D. Petsalakis, G. Pagona, G.Theodorakopoulos, N. Tagmatarchis, M. Yudasaka, S. Iijima: Unbalanced strain-directed functionalization of carbon nanohorns: A theoretical investigation based on complementary methods, Chem. Phys. Lett. **429**, 194–198 (2006) 613
[77] H. Isobe, T. Tanaka, R. Maeda, E. Noiri, N. Solin, M. Yudasaka, S. Iijima, E. Nakamura: Preparation, purification, characterization, and cytotoxicity assessment of water-soluble, transition-metal-free carbon nanotube aggregates, Angew. Chem. Int. Ed. **45**, 6676 (2006) 613
[78] G. Pagona, N. Tagmatarchis, J. Fan, M. Yudasaka, S. Iijima: Cone-end functionalization of carbon nanohorns, Chem. Mater. **18**, 3918 (2006) 613, 615
[79] C. Cioffi, S. Campidelli, C. Sooambar, M. Marcaccio, G. Marcolongo, M. Meneghetti, D. Paolucci, F. Paolucci, C. Ehli, G. Rahman, V. Sgobba, D. Guldi, M. Prato: Synthesis, characterization, and photoinduced electron transfer in functionalized single wall carbon nanohorns, J. Am. Chem. Soc. **129**, 3938–3945 (2007) 613, 615
[80] A. Hashimoto, H. Yorimitsu, K. Ajima, K. Suenaga, H. Isobe, J. Miyawaki, M. Yudasaka, S. Iijima, E. Nakamura: Selective desporition of a gadolinium(iii) cluster in a hole opening of single-wall carbon nanohorn, Proc. Roy. Acad. Sci. **101**, 8527 (2004) 613, 614, 616
[81] R. Yuge, M. Yudasaka, J. Miyawaki, Y. Kubo, H. Isobe, H. Yorimitsu, E. Nakamura, S. Iijima: Plugging and unplugging holes of sigle-wall carbon nanohorns, J. Phys. Chem. C, in press 614
[82] J. Miyawaki, M. Yudasaka, H. Imai, H. Yorimitsu, H. Isobe, E. Nakamura, S. Iijima: In vivo magnetic resonance imaging of single-wall carbon nanohorns by labeling with magnetite nanoparticles, Adv. Mater. **18**, 1010 (2006) 614, 616
[83] J. Miyawaki, M. Yudasaka, T. Azami, Y. Kubo, S. Iijima: Toxicological study of single-wall carbon nanohorns, Fullerene-Nanotube Symposium (2007) 614
[84] S. P. Jordan, V. H. Crespi: Theory of carbon nanocones: Mechanical chiral inversion of a micron-scale three-dimensional object, Phys. Rev. Lett. **93**, 255504 (2004) 617, 618
[85] O. A. Shenderova, B. L. Lawson, D. Areshkin, D. W. Brenner: Predicted structure and electronic properties of individual carbon nanocones and nanostructures assembled from nanocones, Nanotechnology **12**, 191–197 (2001) 618, 619

[86] S. Zhanga, Z. Yao, S. Zhao, E. Zhang: Buckling and competition of energy and entropy lead conformation of single-walled carbon nanocones, Appl. Phys. Lett. **89**, 131923 (2006) 618
[87] K. Kobayashi: Superstructure induced by a topological defect in graphitic cones, Phys. Rev. B **61**, 8496 (2000) 619, 620
[88] J.-C. Charlier, G.-M. Rignanese: Electronic structure of carbon nanocones, Phys. Rev. Lett. **86**, 5970 (2001) 619
[89] D. L. Carroll, P. Redlich, P. M. Ajayan, J. C. Charlier, X. Blase, A. D. Vita, R. Car: Electronic structure and localized states at carbon nanotube tips, Phys. Rev. Lett. **78**, 2811 (1997) 619, 621
[90] S. Berber, Y.-K. Kwon, D. Tomanek: Electronic and structural properties of carbon nanohorns, Phys. Rev. B **62**, R2291 (2000) 619
[91] Y.-W. Son, S. B. Lee, C.-K. Lee, J. Ihm: Electronic structure of straight semiconductor-semiconductor carbon nanotube junctions, Phys. Rev. B **71**, 205422 (2005) 619
[92] S. Compernolle, B. Kiran, L. F. Chibotaru, M. T. Nguyen, A. C. and: Ab initio study of small graphitic cones with triangle, square and pentagon apex, J. Chem. Phys. **121**, 2326 (2004) 619
[93] V. Meunier, M. B. Nardelli, C. Roland, J. Bernholc: Structural and electronic properties of carbon nanotube tapers, Phys. Rev. B **64**, 195419 (2001) 619
[94] R. Tamura, M. Tsukada: Electronic states of the cap structure in the carbon nanotube, Phys. Rev. B **52**, 6015 (1995) 619
[95] R. Tamura, M. Tsukada: Disclinations of monolayer graphite and their electronic states, Phys. Rev. B **49**, 7697 (1994) 619
[96] M. Muñoz-Navia, J. Dorantes-Dávila, M. Terrones, H. Terrones: Ground-state electronic structure of nanoscale carbon cones, Phys. Rev. B **72**, 235403 (2005) 619
[97] A. T. Balaban, D. J. Klein, X. Liu: Graphitic cones, Carbon **32**, 357 (1994) 619
[98] R. Tamura, K. Akagi, M. Tsukada, S. Itoh, S. Ihara: Electronic properties of polygonal defects in graphitic carbon sheets, Phys. Rev. B **56**, 1404 (1997) 619
[99] P. E. Lammert, V. H. Crespi: Topological phases in graphitic cones, Phys. Rev. Lett. **85**, 5190 (2000) 619
[100] C. L. Kane, E. J. Mele: Size, shape, and low energy electronic structure of carbon nanotubes, Phys. Rev. Lett. **78**, 1932 (1997) 619
[101] J. Gonzalez, F. Guinea, M. A. H. Vozmediano: Continuum approximation to fullerene molecules, Phys. Rev. Lett. **69**, 172 (1992) 619
[102] J. Han, R. Jaffe: Energetics and geometries of carbon nanoconic tips, J. Chem. Phys. **108**, 2817 (1998) 620

Index

Electrochemistry of Carbon Nanotubes

Ladislav Kavan[1] and Lothar Dunsch[2]

[1] J. Heyrovsky Institute of Physical Chemistry, v.v.i
Academy of Sciences of the Czech Republic
Dolejskova 3, 182 23 Prague 8, Czech Republic
kavan@jh-inst.cas.cz
[2] Leibniz Institute of Solid State and Materials Research
Helmholtzstr. 20, 01069 Dresden, Germany
l.dunsch@ifw-dresden.de

Abstract. The electrochemistry of carbon nanotubes is reviewed with the aim of summarizing what we can learn using these techniques, and what are the potential applications of nanotubes as electrode materials. Electrochemical charging changes the electronic structure. Consequently, electrochemistry and in-situ spectroelectrochemistry provide versatile tools for the investigation of fundamental effects related to the electronic structure of carbon nanotubes. This approach is compatible with chemical doping, but the electrochemical charging of nanotubes allows for precise control of the doping conditions. Salient (spectro)electrochemical data accumulated during the last ten years on SWNTs, DWNTs and fullerene peapods are here reviewed.

1 Electrochemistry of Nanotubes: Fundamentals

1.1 Introduction

Electrochemistry is an effective technique for the doping of carbon nanotubes. As a method for the creation of charged states in nanocarbons, it offers precise control of the doping level. Another advantage of electrochemical charging is the broad selection of compensating counterions, which occur in media ranging from aqueous and aprotic electrolyte solutions to ionic liquids. Electrochemical doping can be carried out under conditions where any chemical modification or breakdown of nanotubes can be safely excluded. These features become explicitly beneficial compared to chemical doping via reactions of nanotubes with redox-active molecules (cf. contribution by Terrones et al.). Especially in the p-doping regime, a larger potential range is accessible without any chemical follow-up reactions. The electrochemistry of nanotubes has, furthermore, turned out to be applicable to many practically attractive areas ranging from energy storage, sensing, actuators and nanoelectronics (cf. Sect. 3.2 and contribution by Endo et al.).

In the spectroelectrochemistry of nanotubes, the two leading techniques, viz. optical (Vis-NIR) and Raman spectroelectrochemistry, supply significant information, that is, to a great extent, unique and compatible. The point is that optical spectroelectrochemistry provides a "macroscopic" picture of the

A. Jorio, G. Dresselhaus, M. S. Dresselhaus (Eds.): Carbon Nanotubes,
Topics Appl. Physics **111**, 567–603 (2008)

sample, i.e., all tubes and all allowed transitions are addressed in one single experiment. Raman spectroelectrochemistry, on the other hand, provides a "microscopic" picture, by selecting solely the resonating tubes from the sample, and by a possibility of addressing just one isolated tube for spectroelectrochemical experiments. It is obvious that spectroelectrochemistry benefits from the precise control of the doping conditions. It upgrades the spectroscopic studies of chemically redox-doped nanotubes, while it may or may not provide compatible data on certain systems. In view of the great impact of spectroelectrochemistry on nanotube science, these issues will be discussed separately in Sect. 2.

1.2 Potential-Dependent Reactions

The electrochemical reaction at the interphase of a solid electrode material with an ion-conducting medium is driven by the application of a voltage to force the transport of electrons across this interphase. The latter is structured by the electrochemical double layer. Electrochemistry can control the position of the Fermi level (E_F) in an electrode material (metal or semiconductor) by varying the potential. The position of the Fermi level in relation to the energies of the highest occupied and lowest unoccupied molecular orbitals (HOMO and LUMO) of a redox system (molecule) in solution controls the thermodynamically possible reaction to reduce/oxidize such a species in solution [1, 2]. The rate of the electrode reaction is expressed by the current density, i. It is dependent on the electrode potential U (related to the equilibrium potential U_0) exponentially according to the Butler–Volmer equation:

$$i = i_0 \left[\exp \frac{-\alpha n F (U - U_0)}{RT} - \exp \frac{(1-\alpha) n F (U - U_0)}{RT} \right] . \tag{1}$$

The quantity $(U - U_0)$ is an expression of the activation energy of the electron transport across the interphase, the transfer coefficient α reflects the symmetry of the potential influence on the activation barrier and is, in a symmetric situation, equal to 0.5; R is the gas constant, T is the temperature and n is the number of electrons transferred. The transfer coefficient α is a measure of the influence of the electrode potential on the rate (and preference) of the forward and backward electrode reactions, respectively. If the free energy of the system is a nonlinear function of the potential, then α is dependent on the potential. For carbon nanotubes, the reference equilibrium potential U_0 can be defined as a situation when all bonding orbitals are filled and all antibonding orbitals are empty. This provides one occupied π orbital per C atom [3].

Assuming solely the effect of the potential, the electron transfer rate would increase to very large values (1) but there is a second effect limiting the rate of electrode reactions. Due to the phase-boundary geometry, the mass transport defines the concentration of the redox species at the electrode. Consequently,

the rate of mass transport to the surface controls the overall electrode reaction at higher electrode potentials.

The electrode reaction is anodic (oxidation) or cathodic (reduction) depending on the position of the Fermi level in the solid phase of the electrode relative to the positions of the HOMO and LUMO of the redox species in the electrolyte solution. The current is cathodic if the LUMO of the redox molecule is lower than the Fermi level and then the electron transport is energetically favored to the redox species leading to the electrochemical reduction. Contrarily, the current is anodic if the HOMO of the redox molecule is higher than the Fermi level to favor the electron transport from the redox species to the electrode leading to the electrochemical oxidation. In both cases, the electronic state of the redox species is changed and thus a new chemical entity is formed. Any electron transfer causing chemical changes of the redox species at the electrode surface is called a Faradaic reaction.

A charge transfer can also occur that does not result in a chemical change, but rather in a change of the electrical properties of the double layer at the electrochemical interface. This double layer can be considered as a capacitor and the charge distribution of both parts of the capacitor can be changed by a charge transport. In this case, the current is called non-Faradaic.

The electrochemical behavior of single redox-active molecules like fullerenes in solution is characterized as Faradaic processes. However, the situation at carbon nanotubes is more complex. Since virgin carbon nanotubes are not soluble in any usual solvent, their electrochemical behavior can only be studied in the solid state, for instance as a thin layer at an electrode surface [4–10] in contact with an electrolyte solution. This carbon layer overlaps the double layer on the electrode substrate and may form a second double layer at the interphase. The nanocarbon layer consists of two interfaces, the electrical properties of which are changed depending on the electrode potential. A similar situation exists for free-standing buckypapers [11–16] where both surfaces of this sheet are in contact with the electrolyte solution to form a double layer.

1.3 Faradaic and Non-Faradaic Processes in Nanocarbons (Nanotubes, Fullerenes)

To illustrate the Faradaic and non-Faradaic processes at nanocarbons the situation at fullerenes and nanotubes is compared. In the C_{60} fullerene, the HOMO is filled by 10 electrons at a h_u state, while the LUMO consists of the t_{1u} state with the t_{1g} state as the next higher one. The negative energies of the t_{1u} LUMO causes the large electron affinity. The t_{1u} and t_{1g} levels are accessible for an uptake of up to 12 electrons. Electrochemical studies have demonstrated that C_{60} and C_{70} can be reduced up to the hexa-anions in solution [17, 18]. Each of the anion states of the fullerene can be reached in a single Faradaic electron-transfer reaction, resulting in a defined chemical species.

The electrochemical behavior of single-walled carbon nanotubes (SWNTs) is similar to that of graphite, but there are additional effects caused by the specific electronic structure of the rolled graphene. The density of electronic states in SWNTs exhibits distinct singularities that are typical of a one-dimensional nanostructure. These van Hove singularities (vHSs) originate from the size-dependent quantization of the electronic wave-functions around the circumference of the SWNT. The diameter of the SWNT controls the energy spacing between the corresponding vHSs.

As mentioned in Sect. 1.2, SWNTs can be employed either as a surface layer at a working electrode (Fig. 1), a free-standing buckypaper or even an individual SWNT in contact with an electrolyte solution. If an electrode potential U is applied to a covered electrode, a net charge is built up in the SWNT layer, determined by the charge in both the electrical double layers in contact with the solution and with the solid substrate. Furthermore, a certain resistance (R) of the SWNT layer causes an iR drop in that layer. As the electrode potential is controlled by a reference electrode in solution (Fig. 1), the potential is defined for the SWNT/electrolyte solution interface. The capacitance of the electrical double layer C_{dl} can be modeled as that of a parallel-plate capacitor:

$$C_{\mathrm{dl}} \cong \frac{\varepsilon_0 \varepsilon A}{d_{\mathrm{OHP}}} \,. \tag{2}$$

Here ε_0 is the permittivity of free space, ε is the dielectric constant of the electrolyte solution, A is the area of the SWNT layer, and d_{OHP} is the distance to the outer Helmholtz plane (Fig. 2). C_{dl} is dependent on the potential but is often assumed to be independent of the Fermi level of the electrode. The thickness of the outer Helmholtz layer, d_{OHP} is about 0.5 nm. Here, most of the potential drop occurs, but for detailed descriptions of the electrochemical interface, the diffusive layer must be taken into consideration as well (see Fig. 2). The capacitance C_{dl} of an isolated SWNT is of the order of 10 fF/μm of the tube length [3], but the capacitance of a SWNT bundle is more difficult to evaluate since the double layer is usually formed solely at the outer surface of the bundle.

SWNTs have a rather low density of electronic states around the Fermi level. When the applied electrode potential, U_{appl} at the SWNT/electrolyte interface moves into the anodic or cathodic directions, raising or lowering of the Fermi level will overcome this energy spacing to fill or deplete each subsequent state (Fig. 3). In this way, a significant part of the electrode potential causes a change of the chemical potential of the SWNT (eU_{ch}) instead of an electrostatic change of the double layer (eU_{dl}) [3,19]. This is analogous to the situation at semiconductor electrodes, where the band bending at the surface of the semiconductor is changed by the applied electrode potential to appear as a chemical potential.

The contribution of the chemical potential in the SWNT electrode is modeled by a second capacitance in series with the double-layer capacitance [3,19],

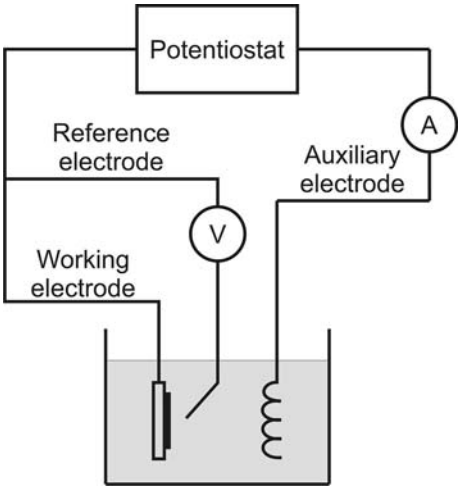

Fig. 1. Scheme of a three-electrode electrochemical cell for the exact control of the electrode potential

the quantum capacitance C_q, which is related to the change of the occupation of the DOS in the SWNT (Fig. 3). Although the quantum capacitance C_q, is formally related to a double-layer situation, it is an expression of the chemical potential of the material. Therefore, its change can be considered a Faradaic process based on the change in the charge on the SWNT.

The current flowing at a SWNT electrode splits into an electrostatic part over the double-layer capacitance, C_{dl} and a chemical part over the quantum capacitance, C_q. The latter is estimated to be of the order of 1 fF/μm of a single SWNT [3]. A qualitative difference exists between a classical metal electrode in contact with an electrolyte solution and a SWNT electrode. Since the C_q and C_{dl} are in series (Fig. 3a) the total capacitance is dominated by the smaller one. The classical metal electrode behaves like a net double-layer capacitor, because $C_q \gg C_{dl}$. Here, the applied potential moves the bands by eU_{dl} without changing the relative position of the Fermi level against the band edges (Fig. 3b). On the other hand, a SWNT is characterized by the effect of a finite DOS ($C_q \ll C_{dl}$). Hence, it is quantum-capacitance dominated. In this case, the Fermi level moves by eU_{ch}, but the bands remain intact (Fig. 3b). This description can be applied to metallic and semiconducting nanotube structures, but the actual values of C_q and their potential dependencies vary according to the particular band structure of the SWNT.

1.4 Doping of Nanocarbons

The term "doping" was introduced into electrochemical terminology via materials physics. Here, it denotes the insertion of holes or electrons into a semiconductor at very low concentrations via "impurities" (cf. contribution

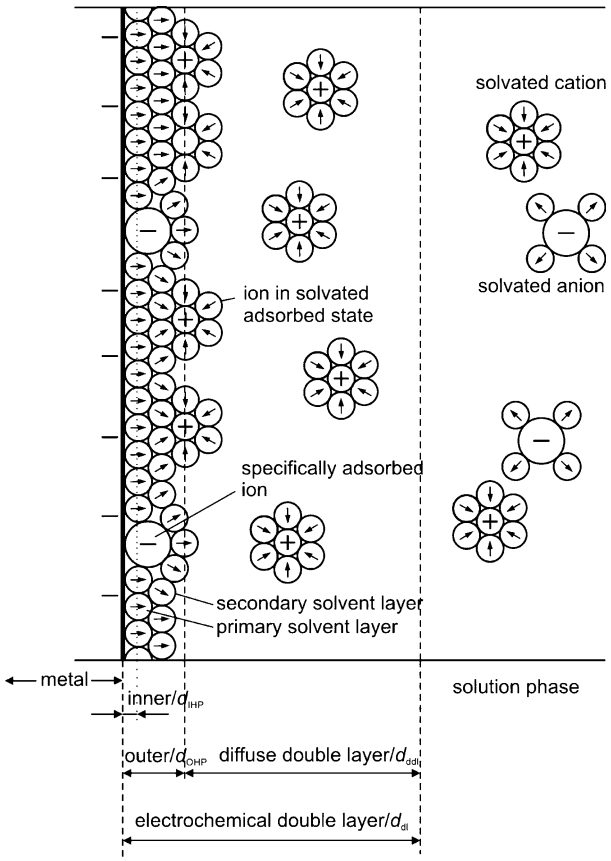

Fig. 2. Scheme of the electrochemical double layer at an electrode. The solvent molecule is assumed to have a permanent dipole moment as labeled by an *arrow*. The solution phase nearby the solid surface is modeled by several layers. The closest layer (called the compact layer) contains oriented solvent molecules and sometimes also specifically adsorbed ions or molecules. The next layer is composed of non-specifically adsorbed solvated ions. These propagate into the bulk solution in the diffuse layer

by Terrones et al.). However, starting with conducting polymers as a special type of semiconductors, the term "doping" has been used in a broader sense. It denotes charging of the polymer up to high concentrations of free carriers by redox reactions [20]. Nowadays, for many π-conjugated systems like nanocarbons, the terms p-/n-doping often replace the traditional terms, oxidation/reduction.

In general, the charging of a SWNT can be carried out either chemically or electrochemically [21]. In both cases, the charging of a SWNT is amphoteric, i.e., the tubes accommodate extra holes or electrons (p- or n- dop-

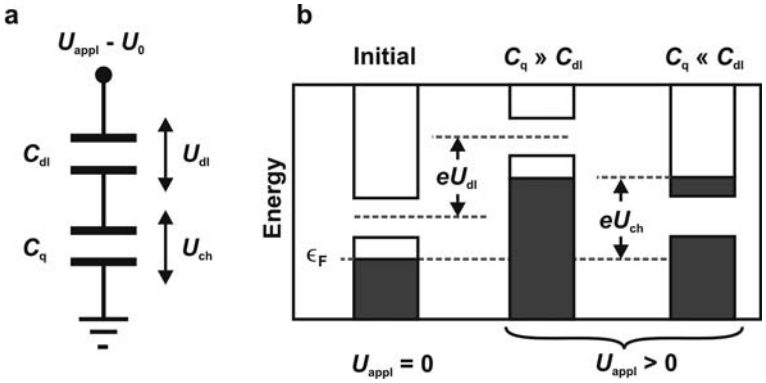

Fig. 3. Scheme of the serial arrangement of the capacities of a nanotube layer, where C_{dl} and C_q are the double-layer capacitance and the quantum capacitance, respectively (**a**). Changes in the Fermi level at the electrode and its influence on the double layer and the quantum capacitance (**b**). Adapted with permission from [3]. Copyright 2006 American Chemical Society

ing). The process depends on the selection of the particular redox reactant ("dopant") or on the applied electrode potential. The extra electrons/holes in the solid have to be compensated by counterions (donors or acceptors; D_c^+/A_c^-), which are produced in the chemical redox process using redox active molecules D_c/A_c or that are simply available in the electrolyte solution ("electrochemical counterions"; D_e^+/A_e^-) [21, 22]. In the case of chemical redox doping, the control of the doping reaction is rather poor with respect to the amount of e^-/h^+ states in nanocarbons and their homogeneous distribution in the sample volume. Also, the selection of "chemical" counterions D_c^+/A_c^- is very limited; in most reported studies of SWNTs, D_c^+ was K^+ and A_c^- was Br^- (cf. with the contribution by Terrones et al.). These counterions were also frequently used in earlier studies of graphite.

Electrochemistry is the method of choice to avoid the mentioned drawbacks of chemical doping. The counterions D_e^+/A_e^- can be selected from a large variety of common electrolytes. More importantly, the doping level of the nanostructure is precisely adjustable by the electrode potential. Doping can be depicted by general reactions:

$$\text{electrochemical n-doping:} \qquad nC + e^- + D_e^+ \rightarrow [nC]^- D_e^+ , \tag{3a}$$

$$\text{electrochemical p-doping:} \qquad nC + h^+ + A_e^- \rightarrow [nC]^+ A_e^- , \tag{3b}$$

where n is the number of carbon atoms in a hypothetical SWNT unit accepting one electron or hole. At first, the compensating counterions (A_e^-/D_e^+) must be transported to the SWNT. The ion transport is diffusion controlled both in the electrolyte solution as well as in the nanotube layer, and the counterions are solvated in all cases (except for ionic liquids). This contrasts

chemical-doping reactions in the gas phase where the "naked" counterions D_c^+/A_c^- (produced by the redox reaction) interact with the carbon structure:

$$\text{chemical n-doping:} \qquad nC + D_c \rightarrow [nC]^- D_c^+ , \tag{4a}$$

$$\text{chemical p-doping:} \qquad nC + A_c \rightarrow [nC]^+ A_c^- . \tag{4b}$$

This difference must be taken into consideration when the positions of the counterions are discussed. In doped nanotubes the counterions can be located at: 1. the external surface of a tubular rope (or at the single nanotube's surface), 2. the interstitial channels between tubes in a rope (internal surfaces) or 3. in the interior of an individual tube. (For the sake of completeness, we should also mention the inplane or substitutional doping, as a special category of doping, cf. with contributions by Terrones et al.). For electrochemical doping, the external 1. and internal 2. attachment of counterions were distinguished by the electrochemical impedance [23, 24]. This is important for the Li^+ cation accumulation at the internal surface due to its possible application in Li-ion batteries [25] (cf. Sect. 3.2).

The penetration of the counterions into the interior of SWNTs is the most exceptional case, as it requires larger defect sites at a SWNT wall and/or SWNTs opened by decapping [26, 27]. The peapod-like "doped" structure can be prepared via solid/gas reactions (chemical doping) [26], while electrochemical charge transfer [27] does not result in intratubular counterions. However, *Iijima* and coworkers [28] claimed to have aqueous electrolyte solutions in the interior of opened SWNTs, too.

The electrochemical doping causes a change in the Fermi level ΔE_F proportional to the electrode potential. *Cronin* et al. [29] estimated a proportionality constant between ΔE_F and the electrode potential to be (0.4 to 0.7) eV/V. As discussed in Sect. 1.3, the more detailed description of doping by *Heller* et al. [3, 19] using quantum capacitance in series with the classical double-layer capacitance provides a differentiation of the Faradaic and non-Faradaic processes upon the doping of nanocarbons.

The (electrochemical) doping of nanotubes results in a change of the C–C bond length similarly to graphite [30, 31]. The doping-induced contraction/elongation of the C–C bond is the result of three effects: 1. the modification of the population of the π orbitals (bond order); 2. the modification of the matrix elements between p_π orbitals (effective atomic potential); and 3. the Coulomb repulsion between extra charges. Thus, the C–C bond length in doped graphene scales with the number of extra electrons transferred to a carbon atom [31, 32]. This graphene expansion/shrinkage by extra electrons/holes in π orbitals is just opposite to the effect expected in simple alternation of the π bond order (cf. Sect. 4.2 for further discussion). In nanotubes the charge transfer to the carbon structure via doping creates a strain in the tube exceeding by orders of magnitude the effect in ordinary ferroelectrics [33]. The doping-induced dimensional changes in SWNTs

are applicable in electrochemical (electromechanical) actuators [12,13,33–37] (see Sect. 3.2).

2 Experimental Techniques

2.1 Materials in Electrochemical Studies of Nanotubes

The electrochemistry of a SWNT is done either at a supported thin layer of nanotubes, a supported single isolated tube, a free-standing buckypaper or even a free-standing single tube. A carbon paste electrode is also sometimes used, especially for sensors [38]. Metals like Pt, Au, and Hg or metal oxides like indium tin oxide (ITO) are applied as the electrode-supporting materials. Metals also serve for contacting the free-standing buckypaper [11–16]. The nanotube layer is usually deposited from sonicated suspensions, but organized arrays of tubes can also be grown directly on the support [38]. The use of mercury as a support is restricted to cathodic potentials only. It offers a huge overvoltage of hydrogen evolution, which, in principle, allows rather deep n-doping to be studied even in aqueous media [4]. The ITO electrode is unstable at larger cathodic potentials, but its main advantage is for optical transparency, applicable in spectroelectrochemistry (Sect. 4.1).

The electrolyte solution is usually the limiting component in terms of the overall stability of the electrochemical system. Because the unmodified nanotubes are insoluble in all the usual solvents, the selection of the electrolyte solution is only restricted by its electrochemical stability. Aqueous media have been used in many studies of nanocarbons [4, 8, 9, 11–14, 16, 35, 39–41]. Among the organic solvents, acetonitrile [7, 9, 42, 43] tetrahydrofuran [15] or ethylene carbonate/dimethylcarbonate [15] allow larger electrochemical potentials both in the anodic and cathodic ranges. The largest potentials are accessible in ionic liquids [44]. While the ionic liquids are sufficiently conducting, any solvent requires the addition of a supporting electrolyte to get sufficiently conductive solutions. Its selection makes the electrochemical doping of nanocarbons advantageous, since many salts are available for doping. The composition of an electrochemical system determines the so-called "potential window", i.e., the range of electrode potentials at which the electrochemical study of any material like a SWNT is not perturbed by the electrochemical current caused by parasitic electrolytic reactions of the sole solvent and/or the electrolyte. For instance, the potential window of aqueous electrolyte solutions is determined by the evolution of hydrogen and oxygen at the cathode or anode, respectively [45].

2.2 Voltammetry

As stated in Sect. 1.2, the electrode potential U is the most important parameter in electrochemistry to control the direction and the extent of a heterogeneous electron-transfer reaction at the electrode surface. Therefore, the exact

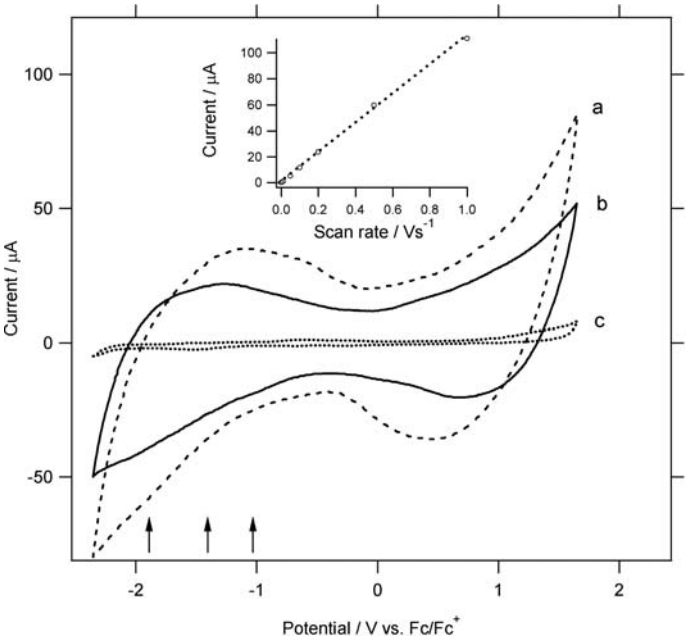

Fig. 4. Cyclic voltammogram of (**a**) SWNT (*dashed line*) and (**b**) C_{60}@SWNT (*full line*) deposited on a Pt electrode in 1-butyl-3-methylimidazolium tetrafluoroborate; scan rate 0.1 V/s. The mass of carbon material is not specified. Also shown is the voltammogram of a blank Pt electrode under the same conditions (*dotted line*, **c**). *Arrows* indicate the expected formal potentials corresponding to C_{60}/C_{60}^{-} , C_{60}^{-}/C_{60}^{2-} and C_{60}^{2-}/C_{60}^{3-} redox couples. *Inset:* anodic voltammetric current at 0 V plotted vs. the scan rate for C_{60}@SWNT. Reprinted with permission from [10]

control of the electrode potential is the precondition of any electrochemical experiment to follow the electrochemical reaction. Such measurements are done by voltammetry where the electrode potential is scanned at a rate $v = \mathrm{d}U/\,\mathrm{d}t$, and the resulting current (i) is monitored (cf. Figs. 4 and 5). The current flows through the electrochemical cell and changes the concentration of the electroactive species at the electrode surface by reduction (n-doping) or oxidation (p-doping) [46].

Such an electrochemical cell consists of a three-electrode arrangement of a working (indicator) electrode, a reference electrode, and a counter (auxiliary) electrode (cf. Fig. 1). The potential of the working electrode is controlled by a potentiostat that holds the electrode potential at a given value referred to the (stable and known) potential of a reference electrode [47]. The reference in an aqueous medium is a certain electrode of the second type, like the standard hydrogen electrode (the potential of which is set by definition to zero), the calomel electrode or the silver/silver chloride electrode. In aprotic media, the reference electrodes are less defined, which can be circumvented by choosing

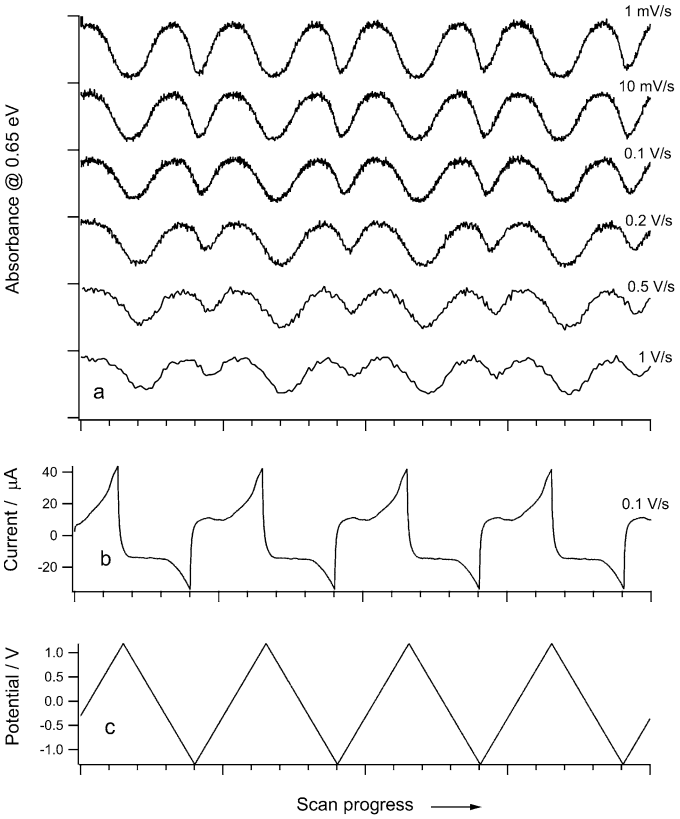

Fig. 5. Cyclic voltammetry of C_{60}@SWCNT peapods deposited on an ITO electrode in 1-butyl-3-methylimidazolium tetrafluoroborate. The applied potential was scanned between −1.35 and 1.15 V vs. Fc/Fc^+. The NIR absorbance at a fixed photon energy of 0.65 eV is plotted as a function of scan progress for various rates between 1 mV/s to 1 V/s (**a**). The *curves* in (a) are offset for clarity, but the absorbance scale is identical for all curves. (**b**) Shows an example of the current response for one scan rate, 0.1 V/s. The origin of scan progress is identical for all *plots*. (**c**) The potential ramp, which was applied in (a) and (b). Reprinted with permission from [10]

the potential of a certain redox couple like ferrocene/ferrocenium (Fc/Fc^+) as an alternative reference. The electrode potential can be referenced to the energy of the electron at the vacuum level and here a reference value for the standard hydrogen electrode is usually considered to be 4.5 eV.

Some studies on carbon nanotubes employed electrochemical cells with only two electrodes, but in this case the control of the electrode potential is difficult in principle [45]. The second electrode is used both as the counter and the reference electrode and its potential must be constant independent of the current following through the cell. Furthermore, the iR drop across

the cell would cause a different value of the real working electrode potential, which, moreover, changes during the potential scan. Therefore, for an exact evaluation of the Fermi level of the nanotube layer, the two-electrode setup has to be avoided. The potentiostatic three-electrode technique (Fig. 1) should become a standard in all electrochemical studies of nanotubes.

At an applied electrode potential, the current, i consists of two contributions in accordance with the type of the reaction: a Faradaic current i_{f} attributed for carbon nanostructures to the charging of the quantum capacitance C_{q} and the non-Faradaic current i_{nf} caused by the charging of the electrical double layer C_{dl} in the nanotube layer (or at a single nanotube). The total current is:

$$i = i_{\mathrm{f}} + i_{\mathrm{nf}}\,. \tag{5}$$

As the film of the nanotubes at an electrode represents a thin-layer condition in voltammetry, the response is a current peak. The peak maximum i_{p} is expressed as:

$$i_{\mathrm{p}} = i_{\mathrm{f}} = \frac{n^2F^2\nu V c_0}{4RT}\,, \tag{6}$$

where c_0 is the concentration of all states in a vHS and V is the volume of the nanotube film. The non-Faradaic charging results in a linear dependence of the current, i_{nf} on the scan rate ν:

$$i_{\mathrm{inf}} = \frac{\mathrm{d}Q}{\mathrm{d}t} = mC_{\mathrm{dl}}\frac{\mathrm{d}U}{\mathrm{d}t} = mC_{\mathrm{dl}}\nu\,, \tag{7}$$

where Q is the double-layer charge and m is the mass of electroactive material. As both contributions to the current are linearly dependent on the scan rate, ν, it is not possible to differentiate between both partial currents by voltammetric techniques (cf. Fig. 4, inset). Only spectroelectrochemistry makes the determination of the quantum capacitance, C_{q} possible by the depletion or filling of the van Hove singularities (see Sect. 4).

A further advantage of the voltammetric techniques is the study of the complementary redox reactions by reversing the electrode potential. Thus, by cyclic voltammetry the reduction or oxidation of a nanotube film at the surface of a working electrode can be checked for its chemical reversibility. (The electrochemical reversibility cannot be discussed since the voltammetric response of a nanotube is not sufficiently resolved). Furthermore, since the electrode potential can be scanned in both the anodic and the cathodic directions, it is possible to follow the oxidation (p-doping) and reduction (n-doping) in one single experiment.

2.3 Methods of Spectroelectrochemistry

In spectroelectrochemistry, the SWNT sample is either a self-standing buckypaper [11–16] or a supported thin layer of nanotubes [4–10, 39–41]. The latter

can even be so sparse that just one individual single nanotube occurs in the area of ca. $1\,\mu m^2$, which allows its optical addressing by a confocal microscope [39–41]. In all cases, the SWNT constitutes the working electrode, and is surrounded by an ionically conducting medium, i.e., the electrolyte (solution). For precise electrochemical control of a SWNT, the three-electrode setup is essential [45]. Hence the experimental cell is completed with a reference and counter electrodes and the electrodes are connected to a conventional potentiostat (see Fig. 1).

The cell must further allow the in-situ acquisition of spectra of the working electrode, which is achieved either by an appropriate cell geometry or by using a suitable window(s). In particular, the measurements of transmission optical spectra in the visible-near-infrared region (Vis-NIR) requires optically transparent conductive substrates like ITO (indium-tin-oxide) [4, 6, 7, 10] or a thin semitransparent film of Pt [42, 43]. Raman spectroelectrochemistry requires only one optical window and the substrate does not need to be transparent. Single-nanotube spectroelectrochemistry is carried out with a confocal Raman microscope, employing an immersion objective and surfactant-separated tubes on a metal support [39–41] or a "truly" isolated individual SWNT on a SiO_2/Si substrate with a patterned metal contact [29] (Sect. 4.4).

In most cases, the spectra are recorded in a quasi-equilibrium state at a constant applied electrode potential. Occasionally, the spectra were also recorded during slow cyclovoltammetric scans [7, 10] or upon galvanostatic charging with small currents [48]. Electrochemistry is most often combined with Raman spectroscopy and optical (Vis-NIR) spectroscopy. Other techniques, like electron spin resonance (ESR), are still infrequently used in spectroelectrochemistry [48, 49].

3 Practical Applications of Charge Transfer at Nanotubes

3.1 Electrochemical Synthesis and Behavior of Nanotubes

Electrochemistry is applied for both the synthesis and characterization of nanotubes. In 1995, *Hsu* et al. [50] discovered an electrochemical method for the synthesis of nanotubes [51] involving an electrolysis in molten alkali halides using two graphite electrodes. By destroying the graphitic electrode material, nanotubes were produced. However, the electrolytic synthesis of nanotubes remained a curiosity, similar to the electrochemical synthesis of other forms of carbon, the so-called "electrochemical carbon" [52]. The room-temperature synthesis of nanotubes and fullerenes, reported by *Kavan* and *Hlavaty* [53] also employed this methodology.

Early electrochemical studies of carbon nanotubes have dealt with tubes of rather large diameters. Electrochemical application of a carbon nanotube as an individual microelectrode has been pioneered by *Campbell* et al. [54].

They fixed CVD-grown nanotubes (50–200 nm in diameter; CVD denotes chemical vapor deposition) on Pt, and investigated the basic electrochemical feedback of the tip part of the partially insulated carbon-nanotube electrode. An alternative experimental geometry employs the configuration of a field-effect transistor (FET) in which the SWNT is surrounded by electrolyte solution, allowing electrochemical gating. This idea is applicable not only in transistors, but also in sensing, but more generally, an electrochemically gated FET actually presents a nanoscale reference electrode, which is sensitive to the electrostatic potential in the electrolyte solution [29, 55] (cf. Sect. 3.2).

The first electrochemical study of a SWNT deposited on Pt or Au electrodes was presented by *Bard* and coworkers [56]. They reported a featureless cyclic voltammogram exhibiting just capacitive-like double-layer charging. The specific capacitance of a SWNT was 283 F/g, which seems to be too high in view of other studies in the field [57, 58]. In general, the capacitance is also due to a quantum capacitance and the charge used in cyclovoltammetric studies is partly used for the filling or depletion of the van Hove singularities (Sect. 1.3). The featureless voltammetric response of SWNTs [4, 7, 56–58] can also be caused by many charge-transfer reactions to a variety of nanotubes contained in the bundles differing from one another in the positions of their vHSs due to their different diameters and chiralities (cf. Fig. 4).

The first electrochemical study of an individual SWNT electrode was presented in 2005 by *Heller* et al. [19] Here, the SWNT behaved like a common microelectrode, and, surprisingly, the electrochemical behavior of metallic and semiconducting tubes was identical [19]. The same group [3] later analyzed the electrochemistry of the SWNT in terms of its electron-transfer kinetics. They predicted that distinct vHSs can be resolved by voltammetry. Another electrochemical technique is the spatially resolved functionalization of single-walled carbon nanotubes using an FET structure, and a microelectrode for modification of the nanotube at selected positions [59]. This chemical modification is analogous to the electrodeposition of metals at nanotubes that occurs preferentially at imperfections [38, 60]. Such a deposition can even be used to close nanotubes via electrodeposited nanoplugs [61].

3.2 Practical Devices

The redox doping of nanotubes [21] finds applications in different fields and different electrochemical devices [38, 62–65]. Here, the main directions of the applications of doped nanotubes and the pertinent electrochemical background are given. A detailed treatment can be found in special reviews and also in other parts of this book (contributions by Endo et al. and by Terrones et al.). The electrochemistry of carbon nanotubes has been mostly focused on practical issues of energy storage [58]. This theme splits into three subtopics: hydrogen storage [66, 67], batteries [24, 68, 69] and supercapacitors [57, 58]. Additional electrochemical applications of SWNTs can be traced in the area

of sensors and actuators [38, 62]. Also, the electrochemical gating in an FET is of potential use in nanoelectronics [29, 55, 59, 70].

The electrochemical hydrogen storage in SWNTs is attractive by a possible combination of the electrolytic production of hydrogen with its simultaneous accumulation in the electrode material. Storage capacities between 10 to 130 mAh/g are typically found in the recent literature [67]. The lithium insertion into nanotubes is characterized by a larger capacity compared to that of graphite (372 mAh/g for LiC_6), a faster kinetics and the absence of staging [24]. Since the intercalation between graphene layers is ruled out in a SWNT (because of a lack of adjacent layers), lithium is accommodated in the nanochannels occurring inside the SWNT bundles [24]. The possibility of free-standing sheets of carbon nanotubes offered encouraging opportunities of charge storage from the very beginning of the search for applications [71]. Both carbon-nanotube membranes as well as layers at substrates or composites have been studied for electrochemical energy storage via lithium insertion [72]. Also, highly flexible batteries can be produced using a polypyrrole cathode and a carbon-nanotube anode [73]. A further route for the improvement of the Li storage in nanotubes and their application to rechargeable lithium batteries is to functionalize them electrochemically [74].

Carbon nanotubes are competitive to activated carbon for supercapacitors, as they typically achieve capacitances of ca. 15–100 F/g [57, 58, 75]. The progress in the application of carbon nanotubes in supercapacitors is determined both by improved methods to form the carbon-nanotube layers, e.g., by electrophoretic deposition [76] and by the development of hybrid supercapacitors, e.g., with a TiO_2-nanowire anode [77] or $Ni(OH)_2$ composites [78]. For reviews of nanotube-based supercapacitors see the contribution by Endo et al. and [57, 58]. Nanotubes are used as an electrocatalyst support in anode catalysis in fuel cells and the results in this special field have already been reviewed [79]. Different carbon-nanotube nanocomposites are applied as electrocatalysts for low-temperature fuel cells [80] while the catalytic properties of the nanotube itself (not of impurities from the catalyst) are not elucidated clearly.

The nanotube-based gas ionization sensor was demonstrated in 2003 by *Modi* et al. [81]. The field-effect transistor (FET) based on a carbon nanotube was discovered in 1998 by *Dekker* and coworkers [82]. In 2002, *McEuen* and coworkers [70] have shown that the electrochemical processes can be used as the gating method. The electrochemically gated SWNT-FET [29, 55, 59, 70] turned out to be an attractive device both for electronic applications and for sensing. In principle, the electrochemical FET can monitor the changes in chemical potential of a solution due to any potential-determining redox couple [55]. This provides interesting opportunities in chemical and biological sensing [38, 62].

The application of carbon nanotubes in electrochemical sensors benefits from their modification to make them specific for the detection of selected molecules via electron-transfer reactions (for general reviews see [38, 62, 83,

84]). Therefore, most of the SWNT-based electrochemical sensors operate amperometrically, i.e., the current at the nanotube electrode is proportional to the concentration of the analyte, like in a methanol sensor for fuel cells [85]. Among the electrochemical sensors based on SWNTs, the field-effect transistors (also called ChemFETs) and chemiresistors are used especially for the detection of glucose, cholesterol, dopamine and other biomolecules (for a review see [38, 62, 84, 86]). For instance, an electrostatic assembly of DNA on nanotube-modified gold electrodes is controlled by a piezoelectric quartz crystal impedance technique for an improved detection of purines, nucleic acids and DNA.

Baughman et al. [37] discovered that the electrochemical doping of a SWNT causes a very strong alteration of its C–C bond length. Therefore, carbon-nanotube actuators are among the best candidates for such devices. Even the use of a single carbon nanotube has been shown to work in an actuator design [87]. The SWNT actuators can be fabricated in contact with aqueous solutions, organic solvents and ionic liquids as electrolytes. In particular the latter electrolyte solution offers a very broad potential window to get a large change of the nanotube structure [88].

4 Spectroelectrochemistry of Nanotubes

Electrochemical charge-transfer processes influence the electronic structure, as well as the optical, vibrational and other spectra of a SWNT, which follow the variations in the concentration of electrons/holes in the solid. Analogous doping effects occur upon chemical redox reactions [89], but electrochemical doping benefits from easy control of the doping level and a broad selection of compensating counterions (Sect. 1.4). This strategy was pioneered in 1999 by *Eklund* and coworkers [90] and during the subsequent years, several tens of papers came out dealing with this subject.

4.1 Vis-NIR Spectroelectrochemistry

In 1999, two independent groups [91, 92] pioneered the investigation of optical (Vis-NIR) spectra of redox-doped SWNT. They used gaseous Br_2 or I_2 as electron acceptors (p-doping) and K, Cs or organic radical anions as electron donors (n-doping). The chemical redox doping was amphoteric, and it manifested itself as disappearance of optical bands of transitions between van Hove singularities: E_{11}^{S}, E_{22}^{S} and E_{11}^{M} (the superscripts S and M denote semiconducting and metallic tubes, respectively). There was also a secondary effect, called doping-induced absorption [91], which consists of the appearance of a new absorption band at deeper doping. This band was tentatively assigned to transitions within partly filled valence (p-doping) or conduction (n-doping) bands [91, 93], modification of the π-plasmon background [94] or

to the creation of new free-charge-carrier plasmons [95]. Most previous studies did not consider excitonic effects (Sect. 4.2), i.e., the spectral bands were assigned to simple excitations within allowed optical transitions between vHS (noninteracting e^-/h^+).

In 2000, the Vis-NIR spectroelectrochemistry of SWNTs was pioneered by *Kavan* et al. [4]. The observed effects were very similar to those for chemical redox doping. The bleaching of optical transitions E_{11}^{S}, E_{22}^{S} and E_{11}^{M} was traceable upon adjusting the electrochemical potential of a thin semitransparent film of SWNTs on ITO [4,7,10] or Pt [42,43] electrodes in aqueous [4] or acetonitrile [7, 42, 43] electrolyte solutions or in ionic liquids [10]. In the latter case, tetrafluoroborate or hexafluoroborate salts of 1-butyl-3-methylimidazolium turned out to be particularly suitable "solvent-free" media, for optical and Raman (Sect. 4.2) spectroelectrochemistry studies of nanotubes [10]. The main advantage of aprotic media, especially the ionic liquids, is their broader potential window (Fig. 4). Strictly speaking, the use of aqueous electrolyte solutions is limited by the redox couples H^+/H_2 and O_2/H_2O whose standard redox potentials are 0 and 1.229 V, respectively. This window can only be extended if we assume certain overvoltages of H_2 or O_2 evolution at the SWNT surface. However, since this overvoltage is unknown, we should consider all experiments outside the stability window of water [96] with care [45].

The charging-induced attenuation of optical bands is reversible and fast (in seconds) [7, 10]. Figure 5a illustrates this effect for the E_{11}^{S} transition. The analogy of chemical and electrochemical doping extended even to the appearance of doping-induced transitions for heavy electrochemical doping in acetonitrile solutions [7] and in ionic liquids [10].

The Fermi-level position E_F in pristine (undoped) material is assumed to be in the middle of the gap between vHS, and scales linearly with the bandgap [40, 97]. Real solid samples are composed of contacting tubes in bundles, where the Fermi levels are aligned. If we further assume that doping by charge transfer does not change the band structure (DOS) but only causes a Fermi-level shift, ΔE_F then the optical electronic transitions disappear as a result of either pumping electrons into the valence band vHS (n-doping) or holes into the conduction band vHS (p-doping). Then, the optical band starts to bleach for:

$$\Delta E_F \geq \left[\frac{E_{ii}}{2} - \frac{\Delta E_c + \Delta E_v}{4} \right], \tag{8}$$

where E_{ii} is the energy separation between vHSs and ΔE_c and ΔE_v are the widths of energy distribution of states in the conduction and valence bands, respectively [40]. These widths are influenced significantly by solvation [40]. The number of extra charges (electrons or holes), f_C introduced by charging

between the open-circuit potential, U_{OCP} and a certain applied electrochemical potential, U, is:

$$f_{\mathrm{C}} = \frac{M_{\mathrm{C}}}{F} \int_{U_{\mathrm{OCP}}}^{U} C \, \mathrm{d}U \,, \tag{9}$$

where M_{C} is the atomic weight of carbon, and F is the Faraday constant (96,485 C/mol).

For graphite, $C_{\mathrm{gr}} \cong 3\,\mu\mathrm{F cm}^{-2}$ both for aqueous and acetonitrile electrolyte solutions around a potential of zero charge [98–100]. The theoretical surface area of a SWNT can be modeled as that of a one-sided graphene sheet ($S_{\mathrm{theo}} = 1315\,\mathrm{m}^2/\mathrm{g}$) [101], which would predict:

$$C \cong C_{\mathrm{gr}} S_{\mathrm{theo}} \cong 39\,\mathrm{F/g}\,. \tag{10}$$

Surprisingly similar values (31–39 F/g) were found for SWNT bundles exhibiting a BET surface area of only $285\,\mathrm{m}^2/\mathrm{g}$ [13]. The latter value supports the idea that only the outer surface of a SWNT bundle is involved in the N_2 adsorption [13, 101]. *Smalley* and coworkers [24] assumed $C_{\mathrm{gr}} \cong 10\,\mu\mathrm{F cm}^{-2}$ (note a typo in this entry in [24]) from where we get a better agreement of the BET and electrochemical data. If we suppose C to be independent of potential, a typical value of $C \cong 40\,\mathrm{F/g}$ for SWNT bundles, and $|U - U_{\mathrm{OCP}}| = 1\,\mathrm{V}$ would give $f_{\mathrm{C}} \cong 0.005\,\mathrm{e}^-/\mathrm{C}$ atom (9), which translates into a Fermi-level shift, ΔE_{F} of ca. 0.3 to 0.7 eV [11, 29]. (The ΔE_{F} is proportional to the electrochemical potential, but, depending on the actual electrochemical system, the proportionality constant need not necessarily be unity [9, 29, 102]). For typical SWNTs of diameters around (1.3 to 1.4) nm, a shift of $\Delta E_{\mathrm{F}} \cong 0.7\,\mathrm{eV}$ is sufficient to quench the first two transitions in semiconducting tubes (E_{11}^{S}, E_{22}^{S}), but the first transition in metallic tubes (E_{11}^{M}) remains intact.

Fullerene peapods, viz. C_{60}@SWNT and C_{70}@SWNT showed a similar spectroelectrochemical behavior to that of empty tubes [10,103,104]. The Vis-NIR spectra of peapods were dominated by the tube-related transitions, but the fullerene-specific optical transitions were not traceable [10, 103, 104]. As expected, the spectroelectrochemistry of peapods confirms gradual intensity attenuation of optical bands assigned to E_{11}^{S}, E_{22}^{S}, E_{11}^{M}, as well as the onset of doping-induced transitions in heavily doped samples [10, 103, 104].

Double-wall carbon nanotubes (DWNTs) were grown by pyrolysis of C_{60} or C_{70} peapods (cf. contribution by *Pfeiffer* et al.), and were studied by Vis-NIR spectroelectrochemistry in acetonitrile solution and in ionic liquids [105]. The optical transitions in the outer tubes (diameters ca. 1.3–1.4 nm) are $E_{11}^{\mathrm{So}} \approx 0.6\,\mathrm{eV}$, $E_{22}^{\mathrm{So}} \approx 1.2\,\mathrm{eV}$, $E_{11}^{\mathrm{Mo}} \approx 1.8\,\mathrm{eV}$ and those in the inner tubes (diameter ca. 0.7 nm) are $E_{11}^{\mathrm{Si}} \approx 1.2\,\mathrm{eV}$, $E_{22}^{\mathrm{Si}} \approx 2.4\,\mathrm{eV}$. (The superscripts in our symbols denote S – semiconducting, M – metallic, o – outer, i – inner). Hence, only the first Vis-NIR band ($E_{11}^{\mathrm{So}} \approx 0.6\,\mathrm{eV}$) can be safely assigned, but the transitions E_{11}^{Si} and E_{22}^{So} overlap between 1 and 1.5 eV, and the same is true for E_{11}^{Mo} and E_{22}^{Si} between 1.8–2.5 eV. Electrochemical charging causes

a reversible bleaching of optical transitions, while the behavior of the outer tube resembles that of SWNTs. The most characteristic feature of DWNTs is a sluggish feedback of the inner tubes to electrochemical charge transfer. Obviously, the formation of an electrochemical double layer influences primarily the outer tube, while the inner tube is screened from direct electrochemical charging [105]. The doping-induced transitions can also emerge in the region of E_{11}^{Si} and E_{22}^{So}. Due to the spectral overlaps and coexistence of several effects influencing the spectra, the interpretation of the optical spectroelectrochemistry of DWNTs is quite complicated at progressive doping.

4.2 Raman Spectroelectrochemistry

The investigation of Raman spectra of redox-doped SWNTs (without using electrochemistry) was pioneered in 1997 by *Rao* et al. [89]. The chemical p-doping (with I_2 or Br_2) or n-doping (with K or Rb) manifested itself as frequency shifts of the tangential displacement mode (G-mode, also coded TM or T-mode; cf. contribution by Saito et al.). This band is suitable for the investigation of doping-induced changes of the C–C bond length, Fano broadening and some other more subtle effects, like the Peierls-like transition in metallic SWNTs [11]. Unfortunately, the doping-induced frequency changes, $\Delta\omega_{\mathrm{G}}$ are far from being clearly understood, especially for n-doping, where the G-band sometimes shows opposite and/or nonmonotonic frequency shifts [7, 15, 48, 89, 94, 106–108]

Besides the frequency shifts, doping causes the attenuation of the Raman intensity of all SWNT bands. The obvious interpretation follows from the suppression of resonance enhancement due to quenching of optical absorptions between vHSs (Sect. 4.1). Within this approximation, the intensity of Stokes–Raman scattering, I_{Raman} scales with the transition energy, E_{ii}:

$$I_{\mathrm{Raman}} \cong |(E_{\mathrm{L}} - E_{ii} - i\gamma)(E_{\mathrm{L}} - E_{ii} - E_{\mathrm{ph}} - i\gamma)|^{-2}\,, \tag{11}$$

where E_{L} is the laser photon energy, E_{ph} is the phonon energy and γ is the damping constant, describing the relaxation of the excited state. The Raman spectra of typical SWNTs with diameters around 1.2–1.4 nm are resonantly enhanced through the E_{33}^{S} transition (for the green and blue lasers) as well as through the E_{11}^{M} (for red lasers). Consequently, these spectra should not be influenced by electrochemical charging at ca. ($U_{\mathrm{OCP}} \pm 1\,\mathrm{V}$), since ΔE_{F} is not sufficient to quench the E_{33}^{S} and E_{11}^{M} transitions (cf. Sect. 4.1). However, we do observe significant (albeit not complete) intensity bleaching of Raman modes resonating with E_{33}^{S} and E_{11}^{M} even under the conditions of mild charging [4, 7, 11, 12, 109, 110].

Earlier studies of optical and Raman spectroelectrochemistry did not consider explicitly the excitonic absorptions in SWNT. Recently, *Wang* et al. [96] suggested that the attenuation of RBM intensity (enhanced via E_{22}^{S}) can be used for the determination of the exciton binding energy. Reportedly, the

electronic energy gap, in which the RBM intensity is not attenuated, is a superposition of the exciton binding energy and the energy of an incident or scattered photon, causing the resonance enhancement [cf. (11)]. We should note, however, that the extremely large Raman plateau observed in [96] and no frequency shifts of the G- and D-modes contradict other studies on the subject [45]. Eventually, *Wang* et al. [111] suggested a different interpretation that the electronic energy gap is a superposition of the exciton binding energy with the $\Delta E_{11}^{\mathrm{S}}$. Detailed analysis of excitonic effects remains a challenge for future efforts.

4.2.1 SWNTs

The first study of SWNTs by using Raman spectroscopy in combination with electrochemical doping was presented in 1999 by *Eklund* and coworkers [90]. This study actually dealt with combined chemical/electrochemical doping because the medium (concentrated H_2SO_4) that was used also caused parallel chemical redox doping (cf. Sect. 1.4). In 2000, two groups, viz. *Kavan* et al. [4] and *Fischer* and coworkers [48] studied Raman spectroelectrochemistry in conventional electrolyte solutions, both aqueous [4] and aprotic (tetrahydrofuran) [48]. In subsequent years, Raman spectroelectrochemistry in aqueous media progressed considerably [8,9,11–14,16,29,34,35,39–41,96,110], and the palette of aprotic solvents was extended by using acetonitrile [5–7, 112, 113] ethylene carbonate/dimethyl carbonate solutions [15] ethylene, carbonate/diethyl carbonate [25]. In 2003, the advantageous properties of ionic liquids were first demonstrated for applications as the electrolyte medium in Raman and Vis-NIR (Sect. 4.1) spectroelectrochemistry [10].

The radial breathing mode (RBM) of SWNTs is suitable for investigations of tube-specific effects (see the contributions by Jorio et al. and by Saito et al.). In particular, the tubes made by the HiPCO process are favored for fundamental spectroelectrochemical studies. Due to their small diameters, they exhibit sharp and well-separated RBM peaks [5–7, 113]. We may even acquire data on certain (n, m)-identified tubes [5, 96, 113], which are, otherwise, accessible only through demanding experiments at the single-nanotube level (Sect. 4.4). There has been some controversy in the literature regarding the "diameter selectivity" of the attenuation of Raman intensity upon doping [6, 114–116]. Recent studies of index-identified HiPCO tubes, both semiconducting [5] and metallic [113] revealed that the actual reason for the variable doping sensitivity of the individual RBMs is not the tube diameter, but the relative deviation of each particular tube from the condition of ideal resonance (11). This empirical "resonance rule" [5, 113] says that the well-resonating tubes are also highly doping sensitive and vice versa. Figure 6 shows the illustrative data for index-identified HiPCO tubes according to the experimental Kataura plot. For instance, the tube (11,0) is almost intact by doping at the 1.56 eV excitation (out of resonance), but it becomes doping sensitive at 1.65 eV, when it is in perfect resonance. This general rule is valid

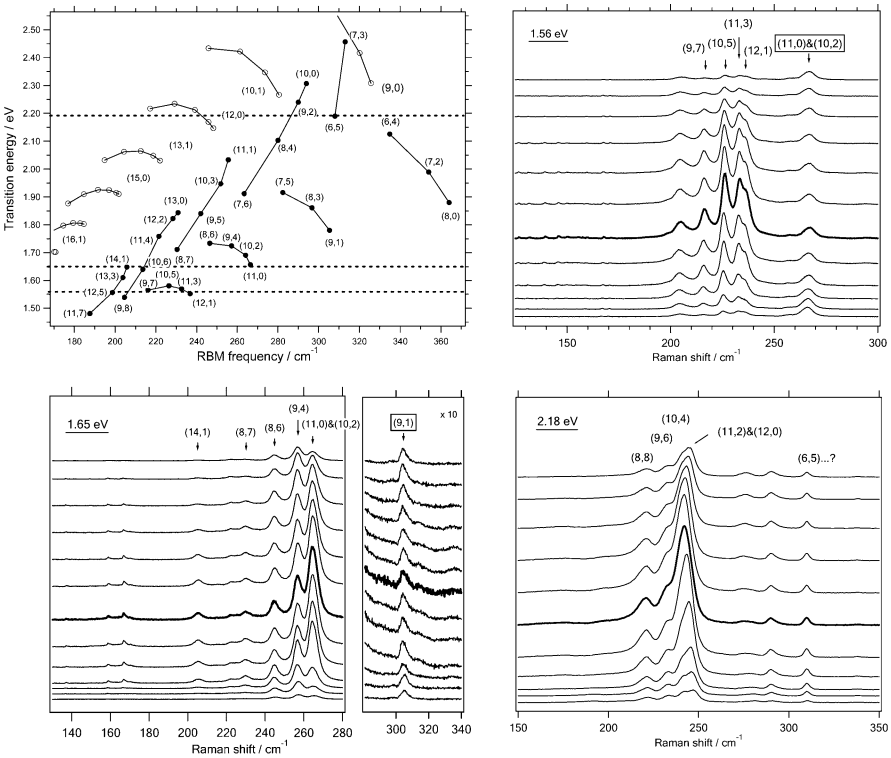

Fig. 6. *Left upper chart:* Experimental Kataura plot for selected nanotubes with the energies of transitions E_{22}^{S} (*full points*) and E_{11}^{M} (*open points*). Lines connect the corresponding nanotubes families ($2n+m=$ const). Data were compiled from [5, 117–120] and from calculation results, which were kindly provided by Prof. Jorio (see also [121]). Reprinted with permission from [121]. 2006 by the American Physical Society. The remaining charts show the potential-dependent Raman spectra of SWNTs on a Pt electrode in 0.2 M $LiClO_4$ + acetonitrile. The spectra were excited by a Ti-sapphire laser at 1.56 eV and 1.65 eV and by a Kr^+ laser at 2.18 eV (cf. the *dashed lines* in the experimental Kataura plot). The spectrum at nearly no doping is highlighted by a *bold curve*. The remaining spectra were measured at potentials changing in steps of 0.3 V towards negative or positive values, respectively, for *curves* arranged upwards or downwards, respectively, from the *bold curve*. Spectra are offset for clarity, but the intensity scale is identical in the respective chart. The tubes with large positive deviation from the resonance condition are highlighted by *box-framed* annotation. Adapted with permission from [5]. 2005 American Chemical Society

for many other tubes [5], but there are also some exceptional cases, like the tube (6,5), whose doping behavior at 2.18 eV is not well understood yet [113] (Fig. 6).

The frequency of the G-mode in doped SWNTs brings valuable structural information, but the complicated (nonunique) trends for n-doping [7, 15, 25, 48, 89, 94, 96, 106–108] do not allow an easy interpretation of all spectroelectrochemical data. Monotonic and expected trends (blueshift of the G-mode) are regularly observed for anodic charging (p-doping). It is tempting to discuss these shifts in terms of mechanical strain upon pumping of extra holes into SWNT. In analogy to graphite intercalation compounds [31, 32] the contraction of C–C bond length, $-\Delta a_{CC}$ is expressed as:

$$-\Delta a_{CC} = 0.157 f_C + 0.146 |f_C|^{\frac{3}{2}} + 0.236 f_C^2 \cong 0.157 f_C$$
$$= 0.157 \frac{M_C}{F} \int_{U_{OCP}}^{U} C \, dU \,, \tag{12}$$

where f_C is the number of holes per C atom; cf. (9). (Since $f_C \ll 1$ we can neglect the high-power terms in 12.) Obviously, both mechanical strain and electrochemical charging can be modeled using the same philosophy [12, 13], which provides a basis for the discussion of electrochemical actuators (Sect. 3.2). The observed G-mode shifts, $\Delta\omega_G$ were reported to be [7, 9, 13, 90]:

$$\Delta\omega_G / f_C \approx (250 \text{ to } 423) \text{ in } \mathrm{cm}^{-1}/\text{hole/C atom}, \tag{13}$$

which is similar to the value of chemically p-doped graphite: 460 cm^{-1}/hole/C atom [89]. These shifts actually relate to the main peak of the G-mode (G^+-mode); individual shifts for the G^+- and G^--modes, respectively, were reported to be 260 and 320 cm^{-1}/electron/C atom, respectively [13].

In cathodically n-doped SWNTs, the "normal" redshift of the G-mode is observed in solutions with compensating counterions NR_4^+ (R = methyl, butyl, octyl) in acetonitrile [6] and Li^+ in acetonitrile [7], ethylene carbonate/dimethyl carbonate [15] and ethylene carbonate/diethyl carbonate [25]. (In the latter case, the trends were not strictly monotonic at deeper n-doping.) The "normal" redshift occurs also for most aqueous electrolyte solutions [4, 8, 11, 14], except for 1 mM aqueous H_2SO_4, where an anomalous blueshift was traced [29]. Such an anomalous blueshift was most explicitly expressed in ionic liquids, where the counterion was 1-butyl-3-methylimidazolium [10]. Non-monotonic trends [15, 48] were reported in K^+-containing aprotic electrolyte solutions. This seems to indicate that the compensating cations have some influence on the Raman shift, but a deeper physical interpretation was not yet given. Recently, *Rauf* et al. [122] suggested a simple mechanical model based on Coulomb interaction and C–C bond-length oscillations in a hypothetical C–C molecule. Although the model seems to outline the non-monotonic shifts in K-doped tubes, the effect of the counterion is not elucidated.

The spectroelectrochemical behavior of the second-order Raman bands G′- and D-modes resembles that of the G-mode [8, 9, 15, 25]. However, the understanding of the similar trends in intensity attenuation and frequency shifts also need to consider other effects, such as the $\boldsymbol{k}$-vector dependence [12].

At heavy electrochemical charging, the D-band reflects the expected growth due to defects, such as the population of interstitial channels in a SWNT bundle [15, 25] and an irreversible chemical modification [15, 25]. The spectroelectrochemical studies of the intermediate-frequency region (IFM) 600–1200 cm^{-1} are still scarce due to their low intensity and a difficult assignment of certain bands in this spectral region [112, 123].

4.2.2 Fullerene Peapods

Whereas the tube-related bands (RBM and G-mode) in peapods (C_{60}@SWNT and C_{70}@SWNT) exhibit similar spectroelectrochemistry to that of empty tubes [10,103,104,124,125], valuable information comes from the region of the intratubular fullerene bands. Figure 7 shows an example of C_{60}@SWNT. The most striking effect is the so-called "anodic Raman enhancement", occurring exclusively for anodically p-doped C_{60}@SWNTs [10, 103, 104]. This enhancement affects all C_{60}-related bands in aprotic electrolyte solutions [103, 104] and in ionic liquids [10], but, surprisingly, it is absent, if the same peapods are p-doped chemically with F_2 [125] or $FeCl_3$ [126]. The anodic Raman enhancement is not detected for the anodically treated C_{70} peapods, either [104]. The latter peculiarity was tentatively attributed to the hybridization of π-orbitals of fullerene and SWNTs and to the standing/lying allotropy of C_{70}@SWNT [104].

The frequency of fullerene-related bands remains intact in the electrochemical charging of peapods (cf. Fig. 7), which show a negligible charge transfer towards intratubular species [10, 103, 104]. This is supported by the absence of any voltammetric peaks in cyclic voltammograms of peapods even at the potentials when triply charged anions C_{60}^{3-} and C_{70}^{3-} would be formed (cf. Fig. 4) [10, 103, 104]. The intratubular fulleride is, however, observed in chemically n-doped peapods by K vapor [124–128], because K atoms (in contrast to solvated electrolyte cations) penetrate through defects in a peapod wall (cf. Sect. 4.3) [124, 127]. But it is obvious that we are far from a clear understanding of the unexpectedly complex response of intratubular C_{60} and C_{70} in peapods towards electrochemical and chemical doping.

4.2.3 Double-Walled Carbon Nanotubes

Raman spectroelectrochemistry of DWNTs made by the pyrolysis of peapods [105, 123, 127, 129] and via CVD [25] provides an elegant distinction of outer/inner tubes of DWNT in the region of the RBM bands (for a general discussion of DWNTs see the contribution by Pfeiffer et al.). This distinction turned out to be a problem in Vis-NIR spectroelectrochemistry (Sect. 4.1). Figure 8 shows an example of a Raman spectroelectrochemical plot of DWNTs made from C_{70}@SWNT. In general, the sluggish spectroelectrochemical feedback of inner tubes mimics that of intratubular fullerene in peapods (cf. Fig. 7), because the formation of an electrochemical double

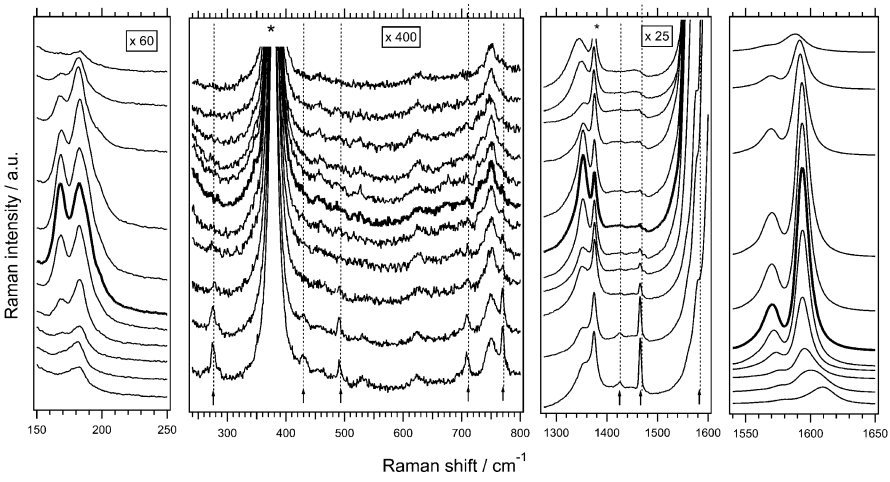

Fig. 7. Potential-dependent Raman spectra of C_{60}@SWNT (peapods) on a Pt electrode (excited at 2.54 eV) in 0.2 M $LiClO_4$ + acetonitrile. The electrode potential varied by 0.3 V from −1.75 V to 1.25 V vs. Fc/Fc^+ for *curves* from *top* to *bottom*. *Bold curve* corresponds to the Raman spectrum of a nearly undoped sample. Spectra are offset for clarity, but the intensity scale is identical for all spectra in the respective window. The intensities are zoomed in the first three windows as indicated. *Arrows* and *dashed lines* indicate the expected Raman lines of C_{60}. Peaks at 378.5 and 1374.5 cm^{-1} (labeled by *asterisk*) belong to acetonitrile. Reprinted with permission from [104]. 2003 American Chemical Society

layer on DWNT primarily affects the outer tube [25, 105, 123, 127, 129]. There was some confusion in the earlier literature as to the (n, m) assignment of the RBM of inner tubes [122, 130–132]. The central problem was that there were more RBM peaks than the geometrically possible inner tubes [122, 132]. This paradox was rationalized assuming that there is a palette of DWNTs, in which the given (n, m) inner tube can be accommodated in several possible outer tubes. Consequently, the tube–tube distance may deviate slightly from the ideal configuration, thus creating some strain in the system, and eventually, splitting of RBMs [122, 132]. A detailed spectroelectrochemical study of chirality-resolved inner tubes has not yet been given. It would have to consider the "resonance rule" (Sect 4.2.1) along with the strain in the nonideal combinations of inner/outer tubes.

In contrast to the RBM, the G-bands of inner/outer tubes overlap in pristine DWNTs (cf. Fig. 8) [105, 122, 123, 127, 129, 133]. In 2003, *Eklund* and coworkers [133] discovered that p-doping with Br_2 selectively upshifts the G-bands of the outer tubes only, while the G-bands of the inner tubes remain intact [133]. In 2004, *Kavan* et al. [129] observed the same effect for anodic charging of DWNTs in acetonitrile solution. An advantage of the electrochemical "deconvolution" of the G-band consists in an easy tuning of the doping

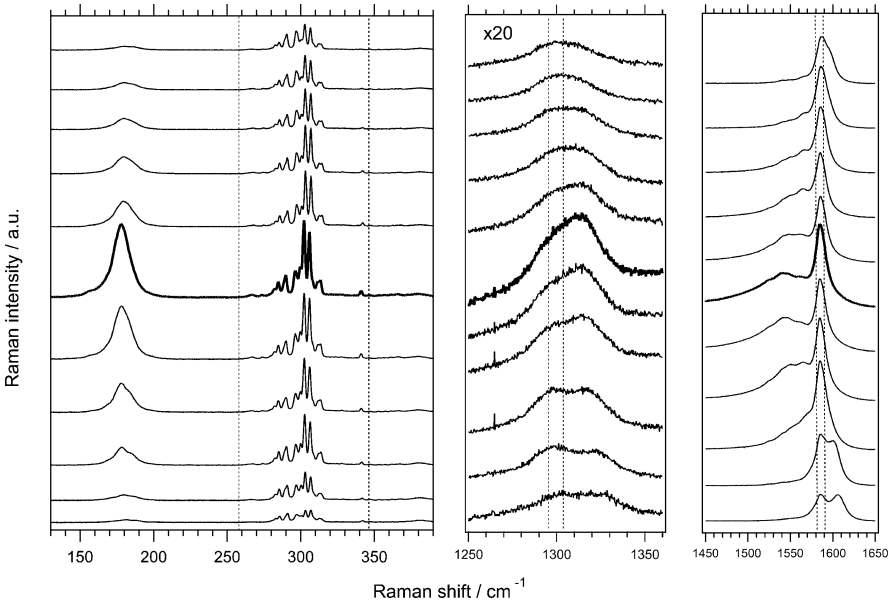

Fig. 8. Potential-dependent Raman spectra of ex-peapod DWNT on a Pt electrode (excited at 1.83 eV) in 0.2 M $LiClO_4$ + acetonitrile. The electrode potential varied in steps of 0.3 V from −1.85 V to 1.15 V vs. Fc/Fc^+ for *curves* from *top* to *bottom*. *Bold curve* corresponds to the Raman spectrum of a nearly undoped sample. Spectra are offset for clarity, but the intensity scale is identical for all spectra in the respective window. The intensities are zoomed by a factor of 20 in the *second window*. *Dashed lines* show the intervals of wave numbers within which the Raman features of the inner tubes are expected. Adapted with permission from [105]. 2005 American Chemical Society

conditions, i.e., progressive movement of the G-band can be monitored by simple adjustment of the electrode potential. [105, 129]. A similar effect is also traceable during a cathodic sweep in media such as ionic liquids, where the "anomalous" blueshift (cf. Sect. 4.2.1) of the outer tubes is well expressed, and the deeply cathodic potentials are accessible without irreversible parasitic reactions [105]. Also, the K-vapor n-doping causes an analogous blueshift in the outer tubes [122]. A mechanical model was suggested based on Coulombic tuning of the C–C bond length in K-doped DWNTs, and was applied also for the inner tubes [122]. As mentioned above (Sect. 4.2.1) this model does not explain the effect of counterions causing redshifts of the G-mode. By careful inspection of the spectra of cathodically doped outer tubes in [105] we may even note that the G-mode shifts to the blue for the 1.83-eV excitation, but to the red for the 2.41-eV excitation. The effects are obviously more complex because of competing interactions.

The second-order Raman scattering in DWNTs is very useful, because the inner/outer tubes exhibit distinct G′-mode bands already in pristine samples, both for the ex-peapod [134] and CVD-grown [25] DWNTs. In both cases, the higher-frequency component is assignable to the outer tube, and it bleaches more rapidly upon electrochemical charging [25, 134]. Qualitatively, the same pattern is traced also for the D-mode: the higher-frequency and doping-sensitive component belongs to the outer tube [105] (cf. Fig. 8). Spectroelectrochemistry thus brings solid arguments for the existence of the "defect-induced" D-mode in inner tubes. This is a bit surprising for the ex-peapods inner tubes, which are assumed to be defect free. Hence, the only "defect" of inner tubes is their finite length, which enhances the D-band intensity [105].

4.3 Combined Chemical/Electrochemical Doping

The first Raman spectroelectrochemical study of SWNTs by *Eklund* and coworkers [90] (cf. Sect. 4.2) was, in fact, also the first study of combined chemical/electrochemical doping. The anodic oxidation of SWNTs in concentrated sulfuric acid starts from a charge-transfer complex:

$$(\mathrm{SWNT})^{+}\mathrm{HSO_4^-}\ \ n\mathrm{H_2SO_4}\,,$$

which is formed via a spontaneous chemical oxidation of SWNTs by H_2SO_4 analogously to the reaction of graphite with H_2SO_4.

Valuable information follows from the spectroelectrochemical behavior of the G-mode in K-doped nanotubes and peapods, i.e., in materials that have been pretreated (chemically n-doped) with K vapor [124, 127, 135]. The reaction with K vapor causes n-doping of the carbon skeleton, and the K^+ counterions decorate either the outer surface of the tube or penetrate also into the interior of a tube. The G-mode serves as an interesting indicator of the location of the K^+ counterion in K-doped nanostructures. For obvious reasons, the anodic charging is preferential, as it causes regular and large blueshifts in ordinary (K-free) materials (cf. Sect. 4.2).

If the K^+ ions in n-doped tubes decorate solely the external surface, they are easily released upon contact with water and air, and the anodic spectroelectrochemistry confirms the "normal" behavior like for K-free tubes [127]. However, if the K^+ ions reside also in the interior of a tube, the n-doping is distinctly more irreversible. In this case, the intratubular K^+ survives contact to air, washing with water, and even anodic electrochemistry [124, 135]. Consequently, the G-mode position is "frozen" during an anodic spectroelectrochemical sweep, because the intratubular K^+ ions effectively screen out the effect of electrolyte anions, accumulated at the external tube surface as a result of anodic charging.

The first scenario is typical for SWNTs and DWNTs [127]; in other words, no intratubular K^+ is found spectroelectrochemically in these structures.

(We may note that deliberate encapsulation of KI into SWNTs mimics the effects of charge transfer in electrochemical doping [136].) The second scenario takes place in peapods. Both C_{60}@SWNT and C_{70}@SWNT, show an arrested G-mode after K doping and subsequent anodic spectroelectrochemistry [124, 135]. The presence of intratubular K^+ is further confirmed by the spectroelectrochemical behavior of the $A_g(2)$ mode in the intratubular C_{60}: It remains at the position typical for the K_nC_{60} fulleride ($n \approx 4$) even at heavy anodic charging [124]. The final confirmation of the structure K_nC_{60}@SWNT came later from direct imaging by transmission electron microscopy [137]. The residual irreversible doping with intratubular K^+ was also found for C_{70}@SWNT, although the intratubular fulleride K_nC_{70} is not that easily traceable by Raman spectroscopy like that for K_nC_{60} [135]. However, convincing arguments are still to be found as to why K_nC_{60}@SWNT and K_nC_{70}@SWNT are formed via K-vapor treatment, but the insertion of K occurs neither into SWNTs nor DWNTs under the same conditions.

4.4 Single-Nanotube Studies

There are not many spectroelectrochemical studies at the single-nanotube level, which is obviously due to technical difficulties in the SWNT sample preparation, and its Raman measurement under electrochemical control. The potentiostatic setup and the cell geometry may not be at optimum conditions, and special care should be taken, if only a two-electrode configuration (instead of the classical three-electrode configuration) was used for the electrochemical charging of tubes [29, 45, 96]. Also, the deposition of non-bundled SWNTs on the metal working electrode usually requires surfactants and sonication, which is not without principal objections, either. An amazingly simple technique for the deposition of SWNTs, DWNTs and peapods on Au(111) directly from a dry buckypaper was developed recently [138]. However, this general method provides isolated nanoribbons rather than individual tubes, and no spectroelectrochemical tests of these assemblies have been reported as yet.

Electrochemical addressing of single nanotubes was first demonstrated in 2003 by *Murakoshi* and coworkers [40]. An individual SWNT wrapped with sodium dodecyl sulfate (SDS) was deposited on an Au electrode and charged electrochemically in an aqueous electrolyte solution [39–41]. The absolute E_F positions (and the work functions) of individual isolated SWNTs are not identical, but they scale linearly with the gap energy [40]. This conclusion was also reproduced for chemical doping [97]. The isolated SWNT exhibits sharper Raman intensity vs. electrode potential profiles compared to those of bundled tubes. The width of such profiles (FWHM) was between 0.6 to 0.9 V for isolated metallic SWNTs and 0.3 to 0.7 V for isolated semiconducting SWNTs [40]. However, bundled tubes show FWHMs of ca. 1 to 2 V [4, 5, 7].

In general, the surfactant (SDS) may influence the charging state of the electrochemical interface, and spectroelectrochemical experiments on “truly”

isolated (SDS-free) nanotubes would be preferential. Such a "cleaner" approach was first demonstrated by *Cronin* et al. [29] in 2004. Their experimental configuration was typical of the FET application, i.e., a SWNT was deposited on SiO_2/Si between two patterned Au contacts, and Raman spectroelectrochemistry of the G-mode in an individual SWNT was studied in diluted H_2SO_4 [29]. This work demonstrated electrochemical gating, if the SWNT was charged against the silver reference electrode. However, rapid degradation limited the sample life and the maximum gate voltage that could be applied [29]. We are not aware that others were later able to prepare a fine stable sample of this kind.

5 Summary and Outlook

During the last ten years, the electrochemical and spectroelectrochemical methods have supplied fundamentally new information about carbon nanotubes, as well as about prospective practical applications. This acquired knowledge is far from being comprehensive and free from open questions. We predict that the future development will progress in three directions:

1. New inputs will come from refined synthetic and purification methods. They will provide macroscopic amounts of well-defined samples of SWNTs for fundamental (spectro)electrochemical studies. Also, new structures will be studied, such as peapods from less-common fullerenes, DWNTs, as well as nanostructures containing heteroatoms.
2. The experimental progress will influence not only the sample synthesis, but also the development of new (spectro)electrochemical techniques. For instance, the combination of Raman spectroscopy with advanced scanning probe imaging will be further upgraded by electrochemical control of the sample. We expect considerable progress in single nanotube studies, both in the area of fundamental electrochemistry and in Raman spectroelectrochemistry. Eventually, the details of the electronic structure of SWNTs will be traceable by cyclic voltammetry or similar techniques.
3. The theoretical interpretation of electronic and spectral changes upon electrochemical charge transfer will develop towards elucidating some persistent open points and contradictions. We predict that new knowledge will be acquired by deeper interpretation of excitonic effects. There are some other phenomena whose clear understanding still requires fundamental studies; they include G-mode shifts, doping-induced transitions and "anodic Raman enhancement" in C_{60}@SWNTs. The combination of experiment and theory should elucidate the rich phenomena seen in the Raman spectra as illustrated in Figs. 6–8.

Acknowledgements

This work was supported by the Czech Ministry of Education Youth and Sports (contract No. LC-510) and by IFW Dresden.

References

[1] A. J. Bard, L. R. Faulkner: *Electrochemical Methods Fundamentals and Applications*, 2nd ed. (Wiley, New York 2001) 568
[2] L. Dunsch: *Vom Ion zur Elektrode*, 2nd ed. (DVG, Leipzig 1988) 568
[3] I. Heller, J. Kong, K. A. Williams, C. Dekker, S. G. Lemay: Electrochemistry at single walled carbon nanotubes, J. Am. Chem. Soc. **128**, 7353–7359 (2006) 568, 570, 571, 573, 574, 580
[4] L. Kavan, P. Rapta, L. Dunsch: In situ Raman and Vis NIR spectroelectrochemistry at single-walled carbon nanotubes, Chem. Phys. Lett. **328**, 363–368 (2000) 569, 575, 578, 579, 580, 583, 585, 586, 588, 593
[5] L. Kavan, M. Kalbac, M. Zukalova, L. Dunsch: Electrochemical doping of chirality-resolved carbon nanotubes, J. Phys. Chem. B **109**, 19613–19619 (2005) 569, 578, 586, 587, 593
[6] L. Kavan, L. Dunsch: Diameter selective electrochemical doping of HiPCO single wall carbon nanotubes, Nano Lett. **3**, 969–972 (2003) 569, 578, 579, 586, 588
[7] L. Kavan, P. Rapta, L. Dunsch, M. J. Bronikowski, P. Willis, R. E. Smalley: Electrochemical tuning of electronic properties of single walled carbon nanotubes: In-situ Raman and Vis-NIR study, J. Phys. Chem. B **105**, 10764–10771 (2001) 569, 575, 578, 579, 580, 583, 585, 586, 588, 593
[8] P. Corio, A. Jorio, N. Demir, M. S. Dresselhaus: Spectroelectrochemical studies of single wall carbon nanotubes films, Chem. Phys. Lett. **392**, 396–402 (2004) 569, 575, 578, 586, 588
[9] P. Corio, P. S. Santos, V. W. Brar, G. G. Samsonidze, S. G. Chou, M. S. Dresselhaus: Potential dependent surface Raman spectroscopy of carbon nanotubes, Chem. Phys. Lett. **370**, 675–682 (2003) 569, 575, 578, 584, 586, 588
[10] L. Kavan, L. Dunsch: Ionic liquids for in-situ Vis-NIR and Raman spectroelectrochemistry: Doping of carbon nanostructures, Chem. Phys. Chem. **4**, 944–950 (2003) 569, 576, 577, 578, 579, 583, 584, 586, 588, 589
[11] P. M. Rafailov, J. Maultzsch, C. Thomsen, H. Kataura: Electrochemical switching of the Peierls-like transition in metallic single-walled carbon nanotubes, Phys. Rev. B **72**, 045411 (2005) 569, 575, 578, 584, 585, 586, 588
[12] P. M. Rafailov, C. Thomsen: Raman spectroscopy of electrochemically doped carbon nanotubes, J. Optoelect. Adv. Mater. **7**, 461–464 (2005) 569, 575, 578, 585, 586, 588
[13] M. Stoll, P. M. Rafailov, W. Frenzel, C. Thomsen: Electrochemical and Raman measurements on single walled carbon nanotubes, Chem. Phys. Lett. **375**, 625–631 (2003) 569, 575, 578, 584, 586, 588
[14] C. P. An, Z. V. Vardeny, Z. Iqbal, G. Spinks, R. H. Baughman, A. A. Zakhidov: Raman scattering study of electrochemically doped single-wall carbon nanotubes, Synth. Met. **116**, 411–414 (2001) 569, 575, 578, 586, 588

[15] A. Claye, S. Rahman, J. E. Fischer, A. Sirenko, G. U. Sumanasekera, P. C. Eklund: In-situ Raman scattering in alkali-doped single-wall carbon nanotubes, Chem. Phys. Lett. **333**, 16–22 (2001) 569, 575, 578, 585, 586, 588, 589
[16] S. Gupta, J. Robertson: Ion transport and electrochemical tuning of Fermi level in single-wall carbon nanotubes, J. Appl. Phys. **100**, 083711–0837119 (2006) 569, 575, 578, 586
[17] Q. Xie, E. Perez-Codero, L. Echegoyen: Electrochemical detection of C_{60}^{6-} and C_{70}^{6-}, J. Am. Chem. Soc. **114**, 3978–3980 (1992) 569
[18] C. A. Reed, R. D. Bolskar: Discrete fulleride anions and fullerenium cations, Chem. Rev. **100**, 1075–1120 (2000) 569
[19] I. Heller, J. Kong, H. A. Heering, K. A. Williams, S. G. Lemay, C. Dekker: Individual single-wall carbon nanotubes as nanoelectrodes for electrochemistry, Nano Lett. **5**, 137–142 (2005) 570, 574, 580
[20] S. Roth: *One-Dimensional Metals* (Wiley-VCH, Weinheim 1995) 572
[21] L. Duclaux: Review on doping of nanotubes, Carbon **40**, 1751–1764 (2002) 572, 573, 580
[22] M. Burghard: Electronic and vibrational properties of carbon nanotubes, Surf. Sci. Rep. **58**, 1–109 (2005) 573
[23] A. Claye, J. E. Fischer, A. Metrot: Kinetics of alkali insertion into single-wall carbon nanotubes, Chem. Phys. Lett. **330**, 61–67 (2000) 574
[24] A. S. Claye, J. E. Fischer, C. B. Huffman, A. G. Rinzler, R. E. Smalley: Li insertion electrochemistry at single wall carbon nanotubes, J. Electrochem. Soc. **147**, 2845–2852 (2000) 574, 580, 581, 584
[25] Y. A. Kim, M. Kojima, H. Muramatsu, S. Umemoto, T. Watanabe, K. Yoshida, K. Sato, T. Ikeda, T. Hayashi, M. Endo, M. Terrones, M. S. Dresselhaus: In situ Raman study of single- and double-walled carbon nanotubes, Small **2**, 667–676 (2006) 574, 586, 588, 589, 590, 592
[26] T. Takenobu, T. Takano, M. Shiraishi, Y. Murakami, M. Ata, H. Kataura, Y. Achiba, Y. Iwasa: Stable and controlled amphoteric doping by encapsulation of organic molecules inside carbon nanotubes, Nature Mater. **2**, 683–688 (2003) 574
[27] L. Duclaux, J. P. Salvetat, P. Lauginie, T. Cacciaguera, A. M. Faugere, C. Goze-Bac, P. Bernier: Synthesis and characterization of SWCNT-heavy alkali metal intercalation compounds, effect of host SWCNTs materials, J. Phys. Chem. Solids **64**, 571–581 (2003) 574
[28] M. Zheng, M. Yudasaka, S. Iijima: Dissociation of electrolytes in nano-aqueous system within single-wall carbon nanotubes, J. Phys. Chem. B **109**, 6037–6039 (2005) 574
[29] S. B. Cronin, R. Barnett, M. Tinkham, S. G. Chou, O. Rabin, M. S. Dresselhaus, A. K. Swan, M. S. Unlu, B. B. Goldberg: Electrochemical gating of individual single wall carbon nanotubes, Appl. Phys. Lett. **84**, 2052–5054 (2004) 574, 579, 580, 581, 584, 586, 588, 593, 594
[30] J. Sandler, M. S. P. Shaffer, A. H. Windle, M. P. Halsall: Variations in the Raman peak shift as a function of hydrostatic pressure, Phys. Rev. B **67**, 035417 (2003) 574
[31] C. T. Chan, W. A. Kamitakahara, K. M. Ho, P. C. Eklund: Charge transfer effects in graphite intercalates, Phys. Rev. Lett. **58**, 1528–1531 (1987) 574, 588

[32] L. Pietronero, S. Strassler: Bond-length change as a tool to determine charge transfer, Phys. Rev. Lett. **47**, 593–596 (1981) 574, 588
[33] Y. N. Garstein, A. A. Zakhidov, R. H. Baughman: Charge induced anisotropic distortion of carbon nanotubes, Phys. Rev. Lett. **89**, 045503 (2002) 574, 575
[34] S. Gupta, M. Hughes, A. H. Windle, J. Robertson: Charge transfer in carbon nanotube actuators, J. Appl. Phys. **95**, 2038–2048 (2004) 575, 586
[35] S. Gupta: Electrochemical tuning and investigation on actuator mechanism of nanotubes, Diam. Rel. Mater. **15**, 378–384 (2006) 575, 586
[36] P. Puech, E. Flahaut, A. Sapelkin, H. Hubel, D. J. Dunstan, G. Landa, W. S. Bacsa: Nanoscale pressure effects in double walled carbon nanotubes, Phys. Rev. B **73**, 233408 (2006) 575
[37] R. H. Baughman, C. X. Cui, A. A. Zakhidov, Z. Iqbal, J. N. Barisci, G. M. Spinks, G. G. Wallace, A. Mazzoldi, D. D. Rossi, A. G. Rinzler, O. Jaschinski, S. Roth, M. Kertesz: Carbon nanotube actuators, Science **284**, 1340–1344 (1999) 575, 582
[38] K. Balasubramanian, M. Burghard: Biosensors based on carbon nanotubes, Anal. Bioanal. Chem. **385**, 452–468 (2006) 575, 580, 581, 582
[39] K. Murakoshi, K. Okazaki: Electrochemical potential control of isolated carbon nanotubes, Electrochim. Acta **50**, 3069–3075 (2005) 575, 578, 579, 586, 593
[40] K. Okazaki, Y. Nakato, K. Murakoshi: Absolute potential of the Fermi level of isolated SWCNT, Phys. Rev. B **68**, 035434 (2003) 575, 578, 579, 583, 586, 593
[41] K. Okazaki, Y. Nakato, K. Murakoshi: Characteristics of Raman features of isolated single wall carbon nanotubes under electrochemical control, Surf. Sci. **566-568**, 436–442 (2004) 575, 578, 579, 586, 593
[42] S. Kazaoui, N. Minami, H. Kataura, Y. Achiba: Absorption spectroscopy of single-wall carbon nanotubes, Synth. Met. **121**, 1201–1202 (2001) 575, 579, 583
[43] S. Kazaoui, N. Minami, N. Matsuda, H. Kataura, Y. Achiba: Electrochemical tuning of electronic properties in single-wall carbon nanotubes, Appl. Phys. Lett. **78**, 3433–3435 (2001) 575, 579, 583
[44] M. C. Buzzeo, R. G. Evans, R. G. Compton: Non-haloaluminate room-temperature ionic liquids in electrochemistry – a review, Chem. Phys. Chem. **5**, 1106–1120 (2004) 575
[45] L. Kavan, M. Kalbac, M. Zukalova, L. Dunsch: Comment on determination of the exciton binding energy in single-walled carbon nanotubes, Phys. Rev. Lett. **98**, 019701 (2007) 575, 577, 579, 583, 586, 593
[46] E. R. Brown, J. R. Sandifer: Electrochemical methods, in *Physical Methods of Chemistry*, vol. II, 2nd ed. (Wiley, New York 1986) Chap. 2 576
[47] P. T. Kissinger, W. R. Heineman: *Laboratory Techniques in Electroanalytical Chemistry*, 2nd ed. (M. Dekker, New York 1996) 576
[48] A. Claye, N. M. Nemes, A. Janossy, J. E. Fischer: Structure and electronic properties of K doped single-wall carbon nanotubes, Phys. Rev. B **62**, R4845–R4848 (2000) 579, 585, 586, 588
[49] J. Tarabek, L. Kavan, M. Kalbac, P. Rapta, M. Zukalova, L. Dunsch: In situ EPR spectroelectrochemistry of single-walled carbon nanotubes and C_{60} fullerene peapods, Carbon **44**, 2147–2154 (2006) 579

[50] W. K. Hsu, J. P. Hare, M. Terrones, H. W. Kroto, D. R. M. Walton, P. J. F. Harris: Condensed-phase nanotubes, Nature **377**, 687–687 (1995) 579
[51] W. K. Hsu, M. Terrones, J. P. Hare, H. Terrones, H. W. Kroto, D. R. M. Walton: Electrochemical formation of carbon nanostructures, Chem. Phys. Lett. **262**, 161–166 (1996) 579
[52] L. Kavan: Electrochemical carbon, Chem. Rev. **97**, 3061–3082 (1997) 579
[53] L. Kavan, J. Hlavaty: Carbon nanostructures from perfluorinated hydrocarbons, Carbon **37**, 1863–1865 (1999) 579
[54] J. K. Campbell, L. Sun, R. M. Crooks: Electrochemistry using single carbon nanotubes, J. Am. Chem. Soc. **121**, 3779–3780 (1999) 579
[55] L. Larrimore, S. Nad, X. Zhou, H. Abruna, P. L. McEuen: Probing electrostatic potentials in solutions with carbon nanotube transistors, Nano Lett. **6**, 1329–1333 (2006) 580, 581
[56] C. Liu, A. J. Bard, F. Wudl, I. Weitz, J. R. Heath: Electrochemical characterization of films of single-walled carbon nanotubes and their possible use as supercapacitors, Electrochem. Solid-State Lett. **2**, 577–578 (1999) 580
[57] E. Frackowiak, F. Béguin: Carbon materials for supercapacitors, Carbon **39**, 937–950 (2001) 580, 581
[58] E. Frackowiak, F. Béguin: Electrochemical storage of energy in carbon nanotubes, Carbon **40**, 1775–1787 (2002) 580, 581
[59] B. R. Goldsmith, J. G. Coroneus, V. R. Khalap, A. A. Kane, G. A. Weiss, P. G. Collins: Conductance-controlled point functionalization of single-walled carbon nanotubes, Science **315**, 77–81 (2007) 580, 581
[60] L. Dunsch, P. Janda, K. Mukhopadhyay, H. Shinohara: Electrochemical metal deposition on carbon nanotubes, New Diam. Front. Carb. Technol. **11**, 427–435 (2001) 580
[61] G. G. Wildgoose, C. E. Banks, R. G. Compton: Metal nanoparticles and related materials supported on carbon nanotubes: Methods and applications, Small **2**, 182–193 (2006) 580
[62] G. G. Wildgoose, C. E. Banks, H. C. Leventis, R. G. Compton: Chemically modified carbon nanotubes for electroanalysis, Microchim. Acta **152**, 187–214 (2006) 580, 581, 582
[63] K. Gong, Y. Yan, M. Zhang, L. Su, S. Xiong, L. Mao: Electrochemistry and electroanalytical applications of carbon nanotubes: A review, Anal. Sci. **21**, 1383–1393 (2005) 580
[64] J. Gooding: Nanostructuring electrodes with carbon nanotubes, Electrochim. Acta **50**, 3049–3060 (2005) 580
[65] B. S. Sherigara, W. Kutner, F. D'Souza: Electrocatalytic properties and sensor applications of fullerenes and carbon nanotubes, Electroanalysis **15**, 753–772 (2003) 580
[66] N. Rajalakshmi, K. S. Dhathathreyan, A. Govindaraj: Electrochemical investigation of single-walled carbon nanotubes for hydrogen storage, Electrochim. Acta **45**, 4511–4515 (2000) 580
[67] R. A. H. Niessen, J. de Jonge, P. H. L. Notten: The electrochemistry of carbon nanotubes I Aqueous electrolytes, J. Electrochem. Soc. **153**, A1484–A1491 (2006) 580, 581

[68] G. T. Wu, C. S. Wang, X. B. Zhang, H. S. Yang, Z. F. Qi, P. M. He, W. Z. Li: Structure and lithium insertion properties of carbon nanotubes, J. Electrochem. Soc. **146**, 1696–1701 (1999) 580
[69] E. Frackowiak, S. Gautier, H. Gaucher, S. Bonnamy, F. Béguin: Electrochemical storage of lithium in multiwalled nanotubes, Carbon **37**, 61–69 (1999) 580
[70] S. Roseblatt, Y. Yaish, J. Park, J. Gore, V. Sazonova, P. L. McEuen: High performance electrolyte gated carbon nanotube transistor, Nano Lett. **2**, 869–872 (2002) 581
[71] G. Che, B. B. Lakshmi, E. R. Fisher, C. R. Martin: Carbon nanotube membranes for electrochemical energy storage and production, Nature **393**, 346–349 (1998) 581
[72] B. Gao, A. Kleinhammes, X. P. Tang, C. Bower, L. Fleming, Y. Wu, O. Zhou: Electrochemical intercalation of SWCNT with lithium, Chem. Phys. Lett. **307**, 153–157 (1999) 581
[73] J. Wang, C. Y. Wang, C. O. Too, G. G. Wallace: Highly-flexible fibre battery incorporating polypyrrole cathode and carbon nanotubes anode, J. Power Sources **161**, 1458–1462 (2006) 581
[74] M. Baibarac, M. Lira-Cantu, J. Oro-Sole, N. Casan-Pastor, P. Gomez-Romero: Electrochemically functionalized carbon nanotubes and their application to rechargeable lithium batteries, Small **2**, 1075–1082 (2006) 581
[75] F. Wu, B. Xu: Progress on the application of carbon nanotubes in supercapacitors, New Carbon Mater. **21**, 176–184 (2006) 581
[76] C. S. Du, N. Pan: High power density supercapacitor electrodes of carbon nanotube films by electrophoretic deposition, Nanotechnology **17**, 5314–5318 (2006) 581
[77] Q. Wang, Z. H. Wen, J. H. Li: A hybrid supercapacitor fabricated with a carbon nanotube cathode and a TiO2-B nanowire anode, Adv. Funct. Mater. **16**, 2141–2146 (2006) 581
[78] Y. G. Wang, L. Yu, Y. Y. Xia: Electrochemical capacitance performance of hybrid supercapacitors based on NiO_2 carbon nanotube composites and activated carbon, J. Electrochem. Soc. **153**, A743–A748 (2006) 581
[79] H. S. Liu, C. J. Song, L. Zhang, J. J. Zhang, H. J. Wang, D. P. Wilkinson: A review of anode catalysis in the direct methanol fuel cell, J. Power Sources **155**, 95–110 (2006) 581
[80] Y. H. Lin, X. L. Cui, C. C. Yen, M. Wai: Platinum/carbon nanotube nanocomposite synthesized in supercritical fluid as electrocatalysts for low-temperature fuel cells, J. Phys. Chem. B **109**, 14410–14415 (2005) 581
[81] A. Modi, N. Koratkar, E. Lass, B. Wei, P. M. Ajayan: Miniaturized gas ionization sensors using carbon nanotubes, Nature **424**, 171–174 (2003) 581
[82] S. J. Tans, R. M. Verschueren, C. Dekker: Transistor based on single walled carbon nanotubes, Nature **393**, 49–51 (1998) 581
[83] N. Sinha, J. Z. Ma, J. T. W. Yeow: Carbon nanotube-based sensors, J. Nanosci. Nanotechnol. **6**, 573–590 (2006) 581
[84] J. S. Ye, F. S. Sheu: Functionalization of CNT: New routes towards electrochemical sensors, Curr. Nanosci. **2**, 1–9 (2006) 581, 582
[85] D. W. Kim, J. S. Lee, G. S. Lee, L. Overzet, M. Kozlov, A. E. Aliev, Y. W. Park, J. Yang: Carbon nanotubes based methanol sensor for fuel cells application, J. Nanosci. Nanotechnol. **6**, 3608–3613 (2006) 582

[86] Y. H. Lin, W. Yantasee, J. Wang: Carbon nanotubes (CNTs) for the development of electrochemical biosensors, Front. Biosci. **10**, 492–505 (2005) 582
[87] S. Roth, R. H. Baughman: Actuators of individual carbon nanotubes, Curr. Appl. Phys. **2**, 311–314 (2002) 582
[88] J. N. Barisci, G. G. Wallace, D. R. MacFarlane, R. H. Baughman: Investigation of ionic liquids as electrolytes for carbon nanotube electrodes, Electrochem. Commun. **6**, 22–27 (2004) 582
[89] A. M. Rao, P. C. Eklund, S. Bandow, A. Thess, R. E. Smalley: Evidence for charge transfer in carbon nanotube bundles from Raman scattering, Nature **388**, 257–259 (1997) 582, 585, 588
[90] G. U. Sumanasekera, J. L. Allen, S. L. Fang, A. L. Loper, A. M. Rao, P. C. Eklund: Electrochemical oxidation of single-wall carbon nanotubes in sulfuric acid, J. Phys. Chem. B **103**, 4292–4297 (1999) 582, 586, 588, 592
[91] S. Kazaoui, N. Minami, R. Jacquemin, H. Kataura, Y. Achiba: Amphoteric doping of single-wall carbon nanotubes, Phys. Rev. B **60**, 13339–13342 (1999) 582
[92] P. Petit, C. Mathis, C. Journet, P. Bernier: Tuning and monitoring of electronic structure of single-wall carbon nanotubes, Chem. Phys. Lett. **305**, 370–374 (1999) 582
[93] R. Jacquemin, S. Kazaoui, D. Yu, A. Hassanien, N. Minami, H. Kataura, Y. Achiba: Doping mechanism of single-wall carbon nanotubes studied by optical absorption, Synth. Met. **115**, 283–287 (2000) 582
[94] N. Bendiab, E. Anglaret, J. L. Bantignies, A. Zahab, J. L. Sauvajol, P. Petit, C. Mathis: Stoichiometry dependence of the Raman spectrum of alkali doped single-wall carbon nanotubes, Phys. Rev. B **64**, 245424 (2001) 582, 585, 588
[95] X. Liu, T. Pichler, M. Knupfer, J. Fink, H. Kataura: Electronic properties of K-intercalated peapods, Phys. Rev. B **69**, 0754171 (2004) 583
[96] Z. Wang, H. Pedrosa, T. Krauss, L. Rothberg: Determination of the exciton binding energy in single walled carbon nanotubes, Phys. Rev. Lett. **96**, 047403 (2006) 583, 585, 586, 588, 593
[97] M. J. O'Connell, E. E. Eibergen, S. K. Doorn: Chiral selectivity in the charge-transfer bleaching of single-walled carbon-nanotube spectra, Nature Mater. **4**, 412–418 (2005) 583, 593
[98] H. Gerischer: Density of electronic states of graphite from differential capacitance, J. Phys. Chem. **91**, 1930–1935 (1987) 584
[99] H. Gerischer: Double layer capacity of graphite, J. Phys. Chem. **89**, 4251–4256 (1985) 584
[100] J. P. Randin, E. Yeager: Differential capacitance study of stress annealed pyrolytic graphite electrodes, J. Electrochem. Soc. **118**, 711–714 (1971) 584
[101] A. Peigney, C. Laurent, E. Flahaut, R. R. Bacsa, A. Rousset: Specific surface area of carbon nanotubes, Carbon **39**, 507–514 (2001) 584
[102] J. C. Rubim, P. Corio, M. C. C. Riberiro, M. Matz: Surface enhanced Raman on electrode surface, J. Phys. Chem. **99**, 15765–15774 (1995) 584
[103] L. Kavan, L. Dunsch, H. Kataura: In situ Vis-NIR and Raman spectroelectrochemistry at fullerene peapods, Chem. Phys. Lett. **361**, 79–85 (2002) 584, 589

[104] L. Kavan, L. Dunsch, H. Kataura, A. Oshiyama, M. Otani, S. Okada: Electrochemical tuning of electronic structure of C_{60} and C_{70} fullerene peapods: In-situ Vis-NIR and Raman study, J. Phys. Chem. B **107**, 7666–7675 (2003) 584, 589, 590

[105] M. Kalbac, L. Kavan, M. Zukalova, L. Dunsch: In situ Vis-NIR and Raman spectroelectrochemistry of double wall carbon nanotubes, Adv. Funct. Mater. **15**, 418–426 (2005) 584, 585, 589, 590, 591, 592

[106] G. Chen, C. A. Furtado, S. Bandow, S. Iijima, P. C. Eklund: Anomalous contraction of the C-C bond length in semiconducting carbon nanotubes observed during Cs doping, Phys. Rev. B **71**, 045408 (2005) 585, 588

[107] G. Chen, C. A. Furtado, U. J. Kim, P. C. Eklund: Alkali metal doping dynamics and anomalous lattice contraction of individual debundled carbon nanotubes, Phys. Rev. B **72**, 155406 (2005) 585, 588

[108] N. Bendiab, L. Spina, A. Zahab, P. Poncharal, C. Marliere, J. L. Bantignies, E. Anglaret, J. L. Sauvajol: Combined in-situ conductivity and Raman studies of Rb doping of single-wall carbon nanotubes, Phys. Rev. B **63**, 153407 (2001) 585, 588

[109] S. Gupta, M. Hughes, A. H. Windle, J. Robertson: In situ Raman spectroelectrochemistry of nanotubes, Diam. Rel. Mater. **13**, 1314–1321 (2004) 585

[110] S. Ghosh, A. K. Sood, C. N. R. Rao: Electrochemical tuning of band structure of single-wall carbon nanotubes, J. Appl. Phys. **92**, 1165–1167 (2002) 585, 586

[111] Z. Wang, H. Pedrosa, T. Krauss, L. Rothberg: Reply to the comment on determination of the exciton binding energies, Phys. Rev. Lett. **98**, 019702 (2007) 586

[112] M. Kalbac, L. Kavan, M. Zukalova, L. Dunsch: The identification of dispersive and non-dispersive intermediate frequency modes of HiPCO single walled carbon nanotubes by in situ Raman spectroelectrochemistry, Phys. Stat. Sol. (b) **243**, 3134–3137 (2006) 586, 589

[113] L. Kavan, M. Kalbac, M. Zukalova, L. Dunsch: Raman spectroelectrochemistry of index-identified metallic carbon nanotubes: The resonance rule revisited, Phys. Stat. Sol. B **243**, 3130–3133 (2006) 586, 587

[114] A. Kukovecz, T. Pichler, R. Pfeiffer, H. Kuzmany: Diameter selective charge transfer in p- and n-doped single-wall carbon nanotubes, Chem. Commun. pp. 1730–1731 (2002) 586

[115] A. Kukovecz, T. Pichler, C. Kramberger, H. Kuzmany: Diameter selective doping of single-wall carbon nanotubes, Phys. Chem. Chem. Phys. **5**, 582–587 (2003) 586

[116] W. Zhou, J. Vavro, N. M. Nemes, J. E. Fischer, F. Borondics, K. Kamaras, D. B. Tanner: Charge transfer and Fermi level shift in p-doped single-walled carbon nanotubes, Phys. Rev. B **71**, 205423 (2005) 586

[117] H. Telg, J. Maultzsch, S. Reich, F. Hennrich, C. Thomsen: Chirality distribution and transition energies of carbon nanotubes, Phys. Rev. Lett. **93**, 177401 (2004) 587

[118] A. Jorio, C. Fantini, M. A. Pimenta, R. B. Capaz, G. G. Samsonidze, G. Dresselhaus, M. S. Dresselhaus, J. Jiang, N. Kobayashi, A. Gruneis, R. Saito: Resonance Raman spectroscopy (n,m)-dependent effects in small diameter single-wall carbon nanotubes, Phys. Rev. B **71**, 075401 (2005) 587

[119] R. B. Weisman, S. M. Bachilo: Dependence of optical transition energies on structure for single-walled carbon nanotubes, Nano Lett. **3**, 1235–1238 (2003) 587

[120] C. Fantini, A. Jorio, M. Souza, M. S. Strano, M. S. Dresselhaus, M. A. Pimenta: Optical transition energies for carbon nanotubes from resonant Raman spectroscopy, Phys. Rev. Lett. **93**, 147406 (2004) 587

[121] H. Son, A. Reina, G. G. Samsonidze, R. Saito, A. Jorio, M. S. Dresselhaus, J. Kong: Raman characterization of electronic transition energies of metallic single-wall carbon nanotubes, Phys. Rev. B **74**, 073406 (2006) 587

[122] H. Rauf, T. Pichler, R. Pfeiffer, F. Simon, H. Kuzmany, V. N. Popov: Detailed analysis of the Raman response of n-doped double-wall carbon nanotubes, Phys. Rev. B **74**, 235419 (2006) 588, 590, 591

[123] M. Kalbac, L. Kavan, M. Zukalova, L. Dunsch: The intermediate frequency modes of single- and double-walled carbon nanotubes: A Raman spectroscopic and in situ spectroelectrochemical study, Chem. Eur. J. **12**, 4451–4457 (2006) 589, 590

[124] M. Kalbac, L. Kavan, M. Zukalova, L. Dunsch: Two positions of potassium in chemically doped C_{60} peapods: An in situ spectroelectrochemical study, J. Phys. Chem. B **108**, 6275–6280 (2004) 589, 592, 593

[125] L. Kavan, M. Kalbac, M. Zukalova, L. Dunsch: Electrochemical and chemical redox doping of fullerene (C_{60}) peapods, Carbon **44**, 99–106 (2006) 589

[126] T. Pichler, A. Kukovecz, H. Kuzmany, H. Kataura, Y. Achiba: Quasicontinuous electron and hole doping of C_{60} peapods, Phys. Rev. B **67**, 125416 (2003) 589

[127] M. Kalbac, L. Kavan, M. Zukalova, L. Dunsch: Spectroelectrochemical recognition of chemical dopants in the inner space of carbon nanostructures, Nano **1**, 219–227 (2006) 589, 590, 592

[128] T. Pichler, H. Kuzmany, H. Kataura, Y. Achiba: Metallic polymers of C_{60} inside single-wall carbon nanotubes, Phys. Rev. Lett. **87**, 267401–267414 (2001) 589

[129] L. Kavan, M. Kalbac, M. Zukalova, M. Krause, L. Dunsch: Electrochemical doping of double wall carbon nanotubes: An in situ Raman spectroelectrochemical study, Chem. Phys. Chem. **5**, 274–277 (2004) 589, 590, 591

[130] L. Kavan, M. Kalbac, M. Zukalova, M. Krause, L. Dunsch, H. Kataura: Redox doping of double-wall carbon nanotubes and C_{60} peapods, Full. Nanotub. Carb. Nanostr. **13**, 115–119 (2005) 590

[131] R. Pfeiffer, H. Kuzmany, C. Kramberger, C. Schaman, T. Pichler, H. Kataura, Y. Achiba, J. Kürti, V. Zolyomi: Unusual high degree of unperturbed environment in the interior of single wall carbon nanotubes, Phys. Rev. Lett. **90**, 225501 (2003) 590

[132] R. Pfeiffer, F. Simon, H. Kuzmany, V. N. Popov: Fine structure of the RBM of double wall carbon nanotubes, Phys. Rev. B **72** (2005) 590

[133] G. Chen, S. Bandow, E. R. Margine, C. Nisoli, A. N. Kolmogorov, V. H. Crespi, R. Gupta, G. U. Sumanasekera, S. Iijima, P. C. Eklund: Chemically doped double walled carbon nanotubes, Phys. Rev. Lett. **90**, 257403 (2003) 590

[134] M. Kalbac, L. Kavan, M. Zukalova, L. Dunsch: Electrochemical tuning of high energy phonon branches of double wall carbon nanotubes, Carbon **42**, 2915–2920 (2004) 592

[135] M. Kalbac, L. Kavan, M. Zukalova, L. Dunsch: The influence of an extended fullerene cage: A study of chemical and electrochemical doping of C_{70} peapods by in situ Raman spectroelectrochemistry, J. Phys. Chem. C **111**, 1079–1085 (2007) 592, 593
[136] A. Ilie, J. S. Bendall, D. Roy, E. Philip, M. L. H. Green: Effects of KI encapsulation in single walled carbon nanotubes by Raman and optical spectroscopy, J. Phys. Chem. B **110**, 13848–13857 (2006) 593
[137] L. Guan, K. Suenaga, Z. Shi, Z. Gu, S. Iijima: Direct imaging of alkali metal site in K-doped fullerene peapods, Phys. Rev. Lett. **94**, 045502 (2005) 593
[138] M. Kalbac, L. Kavan, M. Zukalova, H. Pelouchova, P. Janda, L. Dunsch: Isolated nanoribbons of carbon nanotubes and peapods, Chem. Phys. Chem. **6**, 426–430 (2005) 593

Index

Doped Carbon Nanotubes: Synthesis, Characterization and Applications

Mauricio Terrones, Antonio G. Souza Filho, and Apparao M. Rao

[1] Advanced Materials Department, IPICYT
Camino a la Presa San José 2055, San Luis Potosí, SLP, México
mterrones@ipicyt.mx.edu
[2] Departamento de Fisica, Universidade Federal do Ceara
P.O. Box 6030, 60455-900 Fortaleza, CE, Brazil
agsf@fisica.ufc.br
[3] Department of Physics and Astronomy, Clemson University
Clemson, South Carolina 29634, USA
arao@clemson.edu

Abstract. Various applications of carbon nanotubes require their chemical modification in order to tune/control their physicochemical properties. One way for achieving this control is by carrying out doping processes through which atoms and molecules interact (covalently or noncovalently) with the nanotube surfaces. The aim of this chapter is to emphasize the importance of different types of doping in carbon nanotubes (single-, double- and multiwall). There are three main categories of doping: exohedral, endohedral and inplane doping. We will review the most efficient ways to dope carbon nanotubes and discuss the effects on the electronic, vibrational, chemical, magnetic and mechanical properties. In addition, we will discuss the different ways of characterizing these doped nanotubes using spectroscopic techniques, such as resonant Raman, X-ray photoelectron, electron energy loss spectroscopy and others. It will be demonstrated that doped carbon nanotubes could be used in the fabrication of nanodevices (e.g., sensors, protein immobilizers, field emission sources, efficient composite fillers, etc.). We will also present results related to the importance of inplane-doped nanotubes for attaching various metal clusters and polymers covalently using wet chemical routes.

1 Introduction

We have witnessed that pure carbon nanostructures and especially nanotubes possess fascinating electronic and mechanical properties depending on the diameter and chirality ([1, 2] and contributions by Tomanek et al., by Jorio et al., and by Lefebvre et al. in this book). However, in layered sp^2 carbon nanosystems, it is possible to tailor the electronic, vibrational, chemical and mechanical properties by introducing either noncarbon atoms or molecules and compounds in different manners at small concentrations (from parts per million to small weight percentages). We define this phenomenon as doping.

In the following sections, we will review different ways of doping carbon nanotubes. For the sake of clarity, we will define three main doping categories: 1. exohedral doping or intercalation, 2. endohedral doping or encapsulation

A. Jorio, G. Dresselhaus, M. S. Dresselhaus (Eds.): Carbon Nanotubes,
Topics Appl. Physics **111**, 531–566 (2008)
Springer-Verlag Berlin Heidelberg 2008

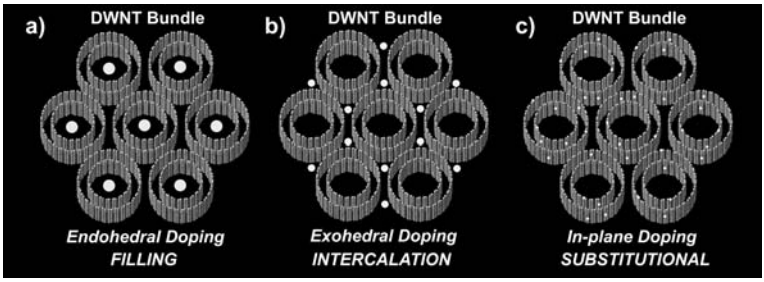

Fig. 1. Molecular models representing schematically (**a**) endohedral doping; (**b**) exohedral doping or intercalation, and (**c**) inplane doping (substitutional) in DWNT bundles

and 3. inplane or substitutional doping (Fig. 1). In the contribution by Kavan and Dunsch, electrochemical doping will be discussed in detail, and therefore this topic is not presented in this chapter.

Although some work has reported the doping of multiwall carbon nanotubes (MWNTs), little work has addressed the doping of single- and double-wall carbon nanotubes (SWNTs and DWNTs, respectively). We believe that these doped systems could reveal unexpected quantum effects, and it should be possible to tailor the bandgaps of carbon nanotubes when doping at very low concentration levels. There are numerous challenges that we must overcome before producing in a controlled way different types of doped SWNTs, DWNTs and MWNTs, but it is clear that these materials will be important in the fabrication of nanotube composites, electronic devices, sensors, composites, nanorobots, etc.

2 Exohedral Doping or Intercalation

By analogy with graphite and bulk C_{60}, the "bundled" form of as-prepared SWNTs can serve as a host lattice whose electronic properties can be tailored by doping with electron-donating, or electron-accepting guest atoms and small molecules that reside in the interstitial channels. Chemical doping is expected to substantially increase the density of free charge carriers and thereby to enhance the electrical and thermal conductivity in the SWNT bundles. In a series of Raman scattering [3] and electrical resistivity studies [4], the amphoteric nature of the SWNT bundles was uncovered for the first time. A material is "amphoteric" when it possesses the ability to accept (or donate) electrons from (to) dopant atoms or molecules. *Lee* et al. [4] found that the room-temperature resistance decreased by several orders of magnitude in potassium-doped SWNT bundles relative to undoped bundles.

The intercalated alkali-metal atoms act as electron donors and this charge transfer weakens the C–C bonds in the SWNTs, as electrons have been known

to soften the C–C bond in all sp^2-bonded carbon materials [5]. Using Raman spectroscopy, doping-induced shifts in the high-frequency vibrational modes were observed and are discussed later in this chapter. Donor alkali metals (e.g., K or Rb) were observed to downshift certain Raman-active mode frequencies, whereas acceptor halogens (e.g., Br_2) were found to upshift these mode frequencies. Similar softening (stiffening) in the Raman-active mode frequencies were observed in graphite intercalation compounds and are associated with an expansion (contraction) in the carbon hexagons [5].

Optical absorption spectra of doped SWNT thin films can provide insight into which electronic states are primarily influenced by charge-transfer interaction with the dopants. *Kazaoui* et al. [6] have separately monitored the doping behavior of semiconducting and metallic SWNTs in a combined optical absorption and dc-resistance measurement study. Both electron acceptors (Br_2, I_2) and donors (K, Cs) were used as dopants with controlled stoichiometry. Disappearance of absorption bands at 0.68 and 1.2 eV (assigned to semiconductor SWNTs), and 1.8 eV (assigned to metallic SWNTs) in pristine SWNTs with a concomitant decrease in the electrical resistance upon doping has been attributed to electron depletion from or filling of specific bands in semiconducting or metallic SWNTs.

3 Endohedral Doping or Encapsulation

The discovery of capillarity in carbon nanotubes opened up a new research area because it is now possible to encapsulate atoms, molecules or crystalline materials inside nanotubes. This field started with the theoretical work of *Pederson* and *Broughton* [7] claiming the nanocapillarity of carbon nanotubes. From the experimental standpoint, *Ajayan* and *Iijima* [8] were the first to report the filling of MWNT cores with lead or lead oxide by heating the tubes in air together with metallic lead. The filling of carbon nanotubes has been a very active field and has been reviewed elsewhere [2, 9–21].

The discovery of C_{60}@SWNTs (peapods) is another very important advance in carbon-nanotube science. The control and high yield of C_{60} filling could lead to double-wall carbon nanotubes (DWNTs) after heat treatments (see the contribution by Pfeiffer et al. on DWNTs and electron microscopy in this volume). Furthermore, this system allowed the observation in real time using an electronic microscope of nanoscale phenomena such as dimerization, diffusion and coalescence [22, 23]. 1D crystals have been synthesized using the encapsulation of metallofullerenes [24]. DWNTs have also been reported as effective containers for special arrays of C_{60} molecules leading to crystalline (with and without helicoidal symmetry) and amorphous 1D systems [25].

The dynamics of water in 1D nanochannels, such as inside carbon nanotubes, is of great interest for biology and nanofluidics as an example of proton transport in a restricted environment. Furthermore, the possibility of having water molecules in the cavity opens up the possibility of having chemical

reactions in the interior of nanotubes, thus leading to a unique nanoreactor [26]. Neutron-diffraction and neutron-scattering experiments combined with molecular dynamics simulations allowed the identification of water inside nanotubes and its soft dynamics [27]. Interestingly, encapsulation of organic molecules, such as metallocenes inside SWNTs, has led to a hybrid system with modified electronic and optical properties [28]. It is important to note that there are still some difficulties in preparing very homogeneous samples of filled nanotubes. Therefore, TEM measurements are sometimes difficult to perform. In this context, metrology based on the Raman scattering technique has been proposed to study such samples [29].

4 Inplane or Substitutional Doping

4.1 Substitutional Doping in Graphite

It has been demonstrated that graphite can be doped substitutionally with B atoms in order to enhance its degree of crystallinity (e.g., reduction of the interlayer spacing and slight increase in the inplane distances) [30, 31]. However, B concentrations in excess of 5 at % within graphitic systems can also result in the formation of B_4C as a byproduct when high temperatures are used [32]. From the electronic standpoint, it was demonstrated that the electronic properties of bulk graphites doped with B behave like p-type conductors [33, 34]. In particular, scanning tunneling microscopy (STM) studies revealed that B-doped highly oriented pyrolytic graphite (HOPG) exhibits areas of extreme intensity (of ca. 1 nm in diameter), where B atoms have substituted C atoms within the hexagonal carbon network.

More than 30 years ago, researchers also showed that N atoms are able to induce crystalline disorder in the graphene sheets, when using concentrations of N lower than 6.5 wt % [35–37]. More recently [38] the synthesis of N-doped carbons produced at high temperatures ($> 2500\,^{\circ}C$) was reported. These authors were able to introduce N within sp^2-like carbons ranging from 0.7 to 4.5 at %. From an electronic point of view, one would expect an excess of donors on the N-rich areas, thus being more reactive when compared to crystalline graphite. It is expected that the recently developed ability of preparing and manipulating single and double graphene layers will open up opportunities for studying the doping in these systems that are more closely related to nanotubes than HOPG (see also the contribution by Charlier et al.).

4.2 Substitutional Doping in Nanotubes

It is noteworthy that substitutional doping of B and N within graphene nanocylinders will introduce strongly localized electronic features in the valence or conduction bands, respectively, and will enhance the number of electronic

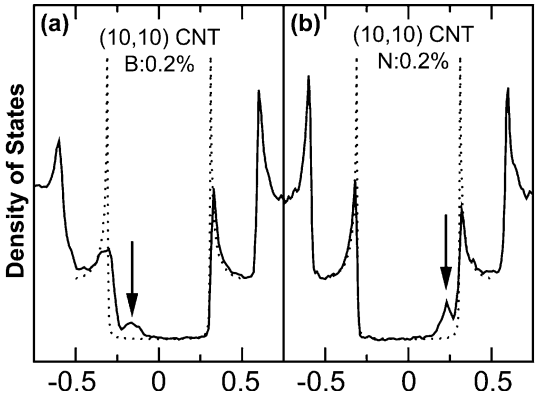

Fig. 2. Calculated densities of states (DOS) using tight-binding parameters fitted with *ab initio* calculations for: (**a**) an armchair (10,10) B-doped carbon nanotube (B = 0.2 at %, *solid line*) exhibiting a clear peak in the valence band (see *arrow*), and (**b**) an armchair (10,10) N-doped carbon nanotube (N = 0.2 at %, *solid line*), in which a sharp and localized peak arises in the conduction band (see *arrow*). *Solid lines* correspond to the doped materials, whereas *dotted lines* are related to the pure C nanotubes (undoped). Note that for all cases the presence of B introduces states in the valence band (holes), whereas N injects electrons in the conduction band (donors). Because of the quantum confinement within the nanotube, electrons can only propagate along the nanotube axis, and so their wavevectors point in this direction. The spikes shown in the DOS of the tubules are called "van Hove" singularities and are the typical signature of one-dimensional quantum conduction, which is not present in an infinite graphite crystal (calculations performed by S. Latil; courtesy of S. Latil)

states at the Fermi level (E_f) depending on the location and concentration of dopants (Fig. 2).

Boron has one electron less than C, and when it substitutes for C atoms within a SWNT (three-coordinated B) sharp localized states below the Fermi level (valence band) appear (Fig. 2a). These states are caused by the presence of holes in the structure, and the tube could be considered as a p-type nanoconductor. From the chemical standpoint, this structure would be more likely to react with donor-type molecules.

For N-doped SWNTs, two types of C–N bonds could occur in carbon nanotubes (Fig. 3a). The first is a three-coordinated N atom within the sp^2-hybridized network, which induces sharp localized states above the Fermi level due to the presence of additional electrons (Fig. 2b). These doped tubes exhibit n-type conduction, and are more likely to strongly react with acceptor molecules. The second type of substitutional N doping is the pyridine-type (two-coordinated N), which can be incorporated in the SWNT lattice, provided that an additional carbon atom is removed from the framework (Fig. 3a). This type of defect induces the presence of localized states below

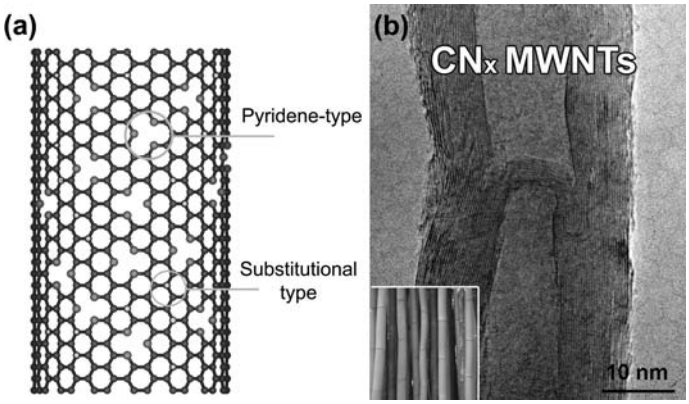

Fig. 3. (**a**) Molecular model of N-doped carbon nanotubes, exhibiting two types of nitrogen: 1. Pyridine-type in which each N atom is bonded to two carbon atoms, responsible for creating cavities and corrugation in the nanotube structure, and 2. Substitutional N atoms, which are bonded to three carbon atoms; (**b**) HRTEM image of an N-doped MWNT exhibiting the bamboo-type morphology; *inset* shows an image of bamboo trees that exhibit a similar morphology to that of N-doped MWNTs

and above the Fermi level. Therefore, substitutional N doping in SWNTs should result in n-type conducting behavior, whereas pyridine-type N may produce as either a p- or n-type conductor, depending on the level of doping, the number of N atoms and the number of removed C atoms within the hexagonal sheet.

Hernández and coworkers [39, 40] described the mechanical properties of individual CN_x and CB_x nanotubes, demonstrating that high concentrations of B and/or N within SWNTs lower the Young's modulus. Interestingly, the Young's modulus still remains on the order of 0.5–0.8 TPa. This phenomenon has been experimentally confirmed in pristine and N-doped MWNTs [41]. In this context, the Young's modulus for pure carbon and N-doped MWNTs are 0.8–1 TPa and $\sim$ 30 GPa, respectively. We believe that the lower values observed for N-doped nanotubes are due to the relatively high N concentration (e.g., 2–5 %) within the carbon tubes, which introduces defects and significantly lowers the mechanical strength. However, if the N concentration is < 0.5 %, one would expect that the mechanical properties will not be substantially altered.

It is also important to mention that besides N and B, other elements such as Si and P could also dope SWNTs [42, 43]. Theoretical work has pointed out that substitutional Si induces a strong deformation of the cylindrical surface (outward) of the tubes and this bump site leads to a more reactive surface that when it is otherwise undoped [42, 44].

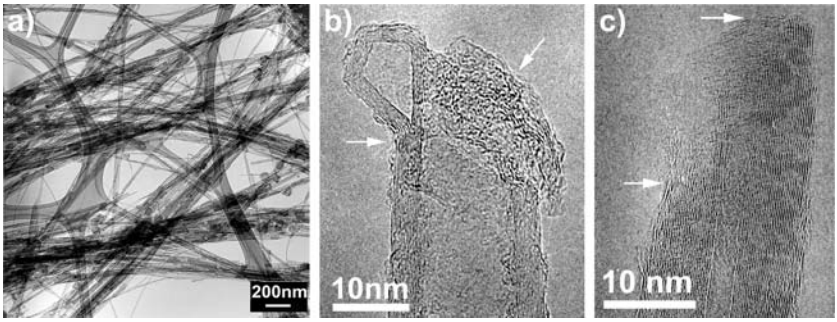

Fig. 4. (**a**) Low-magnification TEM image of B-doped carbon nanotubes produced by the arc-discharge technique. Note that the amount of polyhedral particles is significantly reduced; (**b**–**c**) HRTEM images of ill-formed nanotube caps showing irregular closings of the tube ends; note the amorphous material around the tip in (b) [47]

4.3 Synthesis Methods for Substitutional Doped Nanotubes

Over the past decade various authors have reported the production of B or N substitutionally doped carbon nanotubes using processes far from thermodynamical equilibrium. These techniques are briefly discussed below.

4.3.1 Arc-Discharge Method

B-doped MWNTs can be produced when arcing either BN/graphite or B/graphite electrodes in an inert atmosphere (e.g., He, N_2). Here, large amounts of crystalline and long carbon nanotubes ($\leq 100\,\mu m$) can be obtained. In some cases, ill-formed caps containing B occasionally open or exhibit negative curvature regions (Fig. 4) [45–47]. We should point out that when using this technique, it has been difficult to produce B-doped SWNTs, because B appears to frustrate the tubule growth. Arc experiments using pure graphite electrodes in an NH_3 atmosphere indicate that it is also difficult to produce N-doped SWNTs and MWNTs, possibly because N_2 molecules are easily created and do not react with the carbon [48]. *Glerup* et al. [49] reported the possibility of growing N-doped SWNTs by arcing composite anodes containing graphite, melamine, Ni and Y. These authors also revealed using EELS, that the tubes possess low concentrations of N ($< 1\,\%$), and sometimes the tubes are corrugated due to the presence of N atoms in the hexagonal network.

4.3.2 Laser-Ablation Method

Zhang et al. [50] were the first to report sandwich-like C-BN nanotubes by laser vaporization of graphite-BN targets. These researchers showed evidence

of BC_7N layers within the MWNTs as well as areas of segregated B and C. Subsequently, *Rao* and colleagues [51] demonstrated that it is possible to generate B-doped SWNTs, using laser vaporization of B-graphite-Co-Ni targets. The authors characterized the samples using HRTEM and EELS, and found SWNTs in the products when the B content in the target material was up to 3 at %. For higher B concentrations in the graphite target (e.g., > 3.5 at %), graphite and metal-encapsulated particles were mainly generated and only small quantities of SWNTs were obtained under these conditions.

4.3.3 Chemical Vapor Deposition

The thermal decomposition of N-containing hydrocarbons over metal particles (e.g., Fe, Co, Ni) results in the formation of N-doped MWNTs (also termed CN_x nanotubes). The first reports on the formation of aligned arrays of N-doped MWNTs (< 1–2 %) involved the pyrolysis of aminodichlorotriazine and triaminotriazine over laser-etched Co thin films at 1050 °C [52, 53]. These results indicated that it is very difficult to produce crystalline and highly ordered structures containing large concentrations of N within the hexagonal carbon lattice. CN_x nanotubes with low nitrogen concentrations were subsequently generated via pyrolysis of pyridine and methylpyrimidine [54]. The degree of perfection within graphene sheets is highly dependent upon the nitrogen concentration (i.e., the lower the nitrogen content, the more crystalline and the straighter the nanotubes become). It is also important to note that the morphology of N-doped MWNTs exhibits a bamboo-type structure (see Fig. 3b).

Keskar et al. have prepared isolated N-doped SWNTs from a thermal decomposition of xyelene-acetonitrile mixture over nanosized Fe catalyst particles [55]. Very recently, long strands of N-doped SWNT bundles were successfully produced by pyrolyzing ferrocene:ethanol solutions containing small weight ratios of benzylamine (e.g., from 1 to 22 wt % in ethanol) at 950 °C in an Ar atmosphere [56]. These authors demonstrated that the electron conduction in N-doped SWNT ropes is very different when compared to pure carbon SWNTs, especially at temperatures lower than 20 K [56]. It is important to note that N-doped SWNTs do not exhibit the bamboo-type morphology (Fig. 3b), and it is believed that either B- and N-doped SWNTs contain mainly substitutional-type doping, and in lower concentration when compared to MWNTs. The latter is because the single-shell cylinders would then collapse (would not grow) if a large amount of foreign atoms is being introduced into the hexagonal carbon lattice.

4.3.4 B and N Substitution Reactions

B- and N-doped SWNTs can also be produced using partial substitution in the presence of B_2O_3 vapor and N_2 at 1500–1700 K [57]. In these experiments, B-doped tubes exhibited a B/C ratio of < 0.1. However, lower amounts of

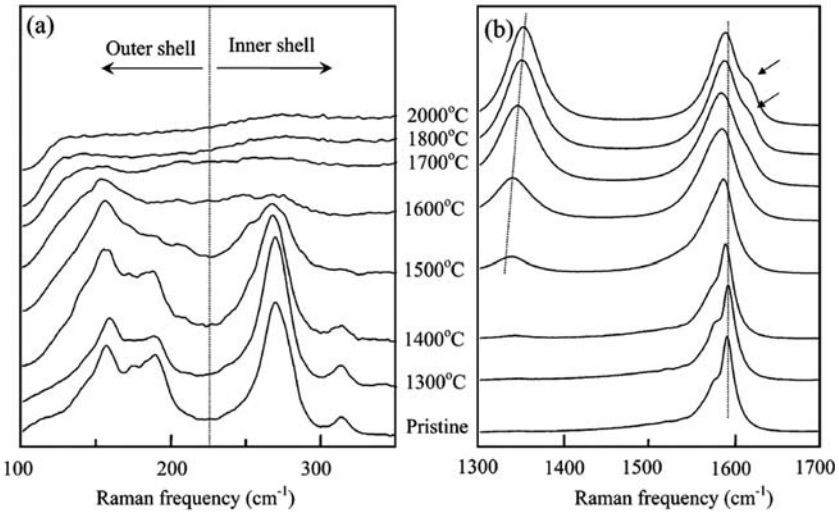

Fig. 5. (**a**) Low-frequency and (**b**) high-frequency Raman spectra of B-DWNTs pristine and heat treated at temperatures ranging from 1300 to 2000 °C. The disappearance of the RBM frequency is a direct indicator of the destruction of the original DWNTs and the formation of diameter-enlarged DWNTs. It is clear that above 1500 °C, B gets incorporated into the carbon lattice, making the D-band intensity (at ca. 1340 cm^{-1}) very significant in all spectra [59]; note that amorphous carbon is not produced during heat treatments. Also note the arrows in (**b**) pointing to the development of the disorder-induced D′ band (at 1620 cm^{-1}) at high heat treatment temperature

N (N/C < 0.01) were also incorporated within the hexagonal framework. In contrast to B-doped MWNTs, SWNTs do not exhibit preferred chiralities, possibly because the dopants only substitute individual C atoms within the framework, thus preserving the tubule chirality. It is noteworthy that either B- or N-doped SWNTs show corrugation, which could be attributed to defects created on the C surface or to electron-irradiation effects. Other synthesis methods for high B-doped SWNTs [58] in which 15 % of the C atoms are replaced by B have been reported. However, further studies are needed to confirm this unexpected level of B solubility in carbon.

More recently, *Endo* and coworkers [59] reported the synthesis of B-doped DWNTs by annealing B powders together with pure DWNTs at different temperatures (ranging from 1200–2600 °C). These authors demonstrated by Raman spectroscopy that above 1600 °C, B gets incorporated into the carbon-tube lattice (Fig. 5). In addition, B served as an efficient trigger for coalescing nanotubes (Fig. 6). Theoretical work showed that interstitial B atoms function as atomic welders and eventually get incorporated into the tube lattice (Fig. 6).

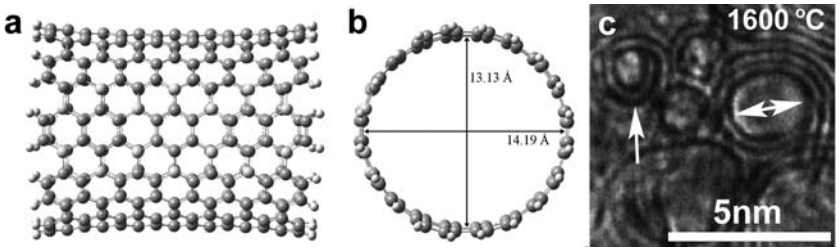

Fig. 6. (**a**,**b**) Effect of substitutional B on the cylindrical shape of a carbon nanotube, using molecular models calculated from the front and side view of the optimized (10,10) open carbon nanotubes containing 14 substituted boron atoms along the nanotube axis in a BC_3 pattern, with the indication of the nanotube diameter (Å) in opposite directions [59]. (**c**) HRTEM image of the cross sections of DWNTs treated with B at 1600 °C revealing clear differences in diameter, possibly due to the presence of B atoms in the nanotube lattice (see **arrows**). Also note the appearance of narrow-diameter tubes

4.3.5 Plasma-Assisted CVD

The microwave plasma-enhanced chemical vapor deposition (PECVD) technique has been used to produce large areas of aligned N-doped MWNTs [60–62]. These experiments involve catalytic particles of Fe and/or Ni dispersed on silica substrates. During growth at 500 °C, acetylene or CH_4 and N_2 or NH_3 can be used. For producing B- or BN-doped MWNTs, other gases such as B_2H_6 in conjunction with H_2 and CH_4 could be used as a reacting gas in the PECVD process [63]. However, these methods have not yet been exploited to produce substitutionally doped SWNTs.

5 Characterization Techniques for Studying Doped Nanotubes

5.1 Morphological and Structural Characterization

The most useful techniques to study the structure and morphology of MWNTs, DWNTs and SWNTs are: 1. high-resolution transmission electron microscopy (HRTEM); 2. scanning electron microscopy (SEM), and 3. scanning tunneling microscopy (STM). In order to determine the overall crystalline structure of nanotubes, X-ray powder diffraction (XRD) becomes a powerful route. Electron diffraction (ED) has also proven useful in determining the chirality of tubes (the orientation of the hexagonal rings along the tube axis; zigzag, armchair or chiral). An alternative route used to determine the chirality of individual SWNTs is Raman spectroscopy, in which each SWNT has a characteristic radial breathing mode (RBM) associated with a particular diameter and, depending on the Raman laser line, it is possible

to obtain resonance for particular tubules with specific electronic transitions (see the contributions by Jorio et al. and by Saito et al.). Because of the special relation between the geometric structures and the electronic structure, resonance Raman spectroscopy can be used to obtain the (n, m) geometric structure of isolated SWNTs [64].

In order to estimate the dopant concentration within SWNTs, DWNTs and MWNTs, analytical techniques associated with HRTEM can be used. In this context, electron energy-loss spectroscopy (EELS) becomes a useful and powerful tool to determine the stoichiometry of elements in individual nanotubes, as well as the nature of the chemical bond. Similarly, X-ray photoelectron spectroscopy (XPS) could be used to determine stoichiometries of elements and their corresponding binding energies. However, these techniques are generally only accurate and sensitive to elements when concentrations are above 1 at %. Therefore, Raman spectroscopy, which is also sensitive to the incorporation of foreign elements, may provide an efficient route to determine dopant concentrations between 0.1 and 1.0 at % in SWNTs and MWNTs (see below).

5.1.1 Atomic Structure of N-Doped MWNTs

In general these tubular structures (produced using the CVD process) reveal: 1. unusual stacked-cone or compartmentalized morphologies (bamboo-type) (Fig. 3), and 2. the degree of tubular perfection decreases as a result of the N incorporation into the hexagonal carbon lattice. EEL spectra of the CN_x nanofibers indicates the presence of ionization edges at ca. 284.5 eV and 400 eV, corresponding to the C and N K-edges. In some samples, a splitting in the π^*-type peak of the nitrogen K edge exhibits two features at ca. 398.7 and 400.7 eV (note that these energies have also been observed in XPS). This has suggested two bonding types between N and C, within the hexagonal network: highly coordinated N atoms replacing C atoms within the graphene sheets (ca. 401–403 eV), and to pyridinic-type nitrogen (ca. 399 eV; Fig. 3). It has been found that as the overall N content increases within these structures, the number of graphitic walls within the nanofibers decreases and the proportion of pyridine-like N increases (remaining almost constant with the number of three-coordinated N atoms). From EEL and XP spectra, it has been estimated that the N content within the tubes is ca. ≤ 10 %, commensurate with C_9N_x ($x \leq 1$) stoichiometries.

More recently, *Koziol* et al. [65] reported an astonishing result that consists of the production of highly crystalline thick multiwall carbon nanotubes (MWNTs) with 3-dimensional order (the concentric cylinders adopt the crystal structure of perfect graphite). These tubes were produced using a CVD process involving the thermolysis of toluene/1,4-diazine ($C_7H_8/C_4H_4N_2$) solutions containing 2 wt % ferrocene ($FeCp_2$) under an Ar atmosphere at 760 °C. Subsequent crystallographic studies confirmed that these samples were indeed highly crystalline [66], and N, which seems to be responsible for

the dramatic structural order, was found to segregate preferentially within the core of the nanotubes.

5.1.2 Atomic Structure of B-Doped MWNTs

These tubes are mainly produced using the arc-discharge method because in the CVD technique, the B precursors tend to frustrate the nanotube growth at temperatures below 900 °C. Although it has been difficult to determine the correct binding energy for B using either EELS or XPS on these systems, it is likely that substitutional B (three-coordinated) is incorporated in the hexagonal C lattice. In this context, careful EELS studies (using first- and second-derivative spectra) have shown that minute B traces ($< 1\,\%$) are present within the body of tubules [67]. Electron-diffraction studies have shown that these long B-doped CNTs exhibit a preferred zigzag or near-zigzag chirality (e.g., zigzag $\pm 3°$) [68, 69]. Static and dynamic *ab initio* and tight-binding calculations carried out by *Blase* et al. and *Hernández* et al., respectively [68, 70], demonstrated that B atoms act as a surfactant during the growth of long tubes, and inhibits tube closure during its formation. Therefore, inplane doping during nanotube growth may well control the tube chirality.

Bulk XRD studies on B-doped MWNTs reveal the presence of highly ordered three-dimensional graphite crystals, attributed to AB... stacking. This ordering has never been observed in conventional pure carbon MWNTs and nanoparticles. From the (00l) reflections (caused by the presence of parallel layers), two different average interlayer spacings were observed in these samples (Fig. 7). It was proposed that one family of these spacings correspond to standard CNTs/nanoparticles (ca. 3.42 Å) and the other type of spacing to AB-stacked graphite (ca. 3.35 Å). The AB stacking observed in nanotubes could arise from concentric B-doped zigzag tubes exhibiting AB... stacking or flattened tube domains (also confirmed by the interlayer spacing irregularities) [71].

5.1.3 Atomic Structure of Doped SWNTs

The structure of SWNT bundles doped with B and N has been recently reported [51, 56, 72]. However, it was difficult to observe clear morphological changes on the doped tubules when compared with their undoped counterparts. For example, the bamboo-type morphology observed in N-doped MWNTs was never seen in N-doped SWNTs (note that bamboo-structure effects would prevent SWNTs from growing continuously). Therefore, it is expected that only substitutional N atoms (three-coordinated N in the carbon lattice) are present in N-doped SWNTs so that continuous nanotube growth is achieved [56]. For B-doped SWNTs, continuous tubules were also produced and B coordinated into three carbon atoms is expected [72].

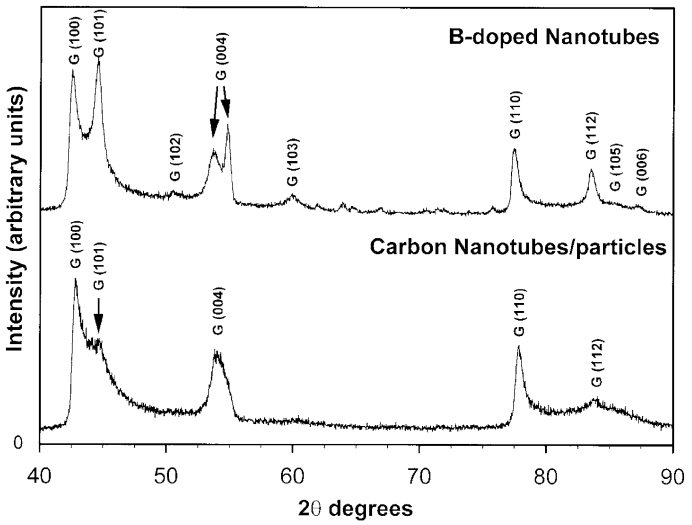

Fig. 7. XRD patterns from the inner-core deposits obtained from the BN/graphite arc-discharge experiments compared to undoped MWNTs and nanoparticles produced using the arc-discharge technique. The XRD pattern from 40–90 (2θ) degrees clearly shows the high degree of crystallinity of the B-doped sample [note the (101), (103) and (112) reflections, which denote a 3D order and AB... stacking of the layers]. Also note that the (00l) reflection exhibits two peaks corresponding to 3.35 Å and 3.42 Å, thus confirming the presence of two different "graphitic" structures (graphite-like AB... possibly from faceted areas of polygonized nanotubes and turbostratic graphite arising from concentric graphene cylinders – MWNTs) [71]

TEM observations of N-doped SWNTs revealed tube diameters around 1.6 nm, a result that is also consistent with the Raman measurements [56]. It is also important to mention that in these materials, it was difficult to detect traces of N using EELS or XPS. This is because N levels below 1–2 % are below the detection limit of these instruments.

For B- and N-doped SWNTs, it was noted that as the B or N content was increased in the laser target or the precursor solution, respectively, the production of SWNTs was inhibited. Therefore, only low concentrations (below 2 wt %) of dopants could be embedded in the hexagonal cylinders. The chirality determination of doped SWNTs and bundles using electron diffraction has been difficult to carry out, and novel strategies to determine the chirality of individual SWNTs are being developed.

5.2 Electronic and Transport Characterization

Microwave conductivity studies on bulk B-doped MWNTs (produced using the arc-discharge method) reveal that these structures are intrinsically metallic [73], which differs from standard pure CNTs, which show thermally acti-

vated transport. Subsequently, *Carroll* et al. [74] detected for the first time characteristic peaks in the density of states (DOS) using scanning tunneling spectroscopy (STS) on B-doped MWNTs produced using the arc-discharge method. Peaks appearing in the valence band were caused by the introduction of B (which acts as an acceptor) in the carbon lattice (Fig. 8a). These authors suggested that BC_3 islands, distributed within the tubules, significantly alter the local density of states (LDOS) from a semimetal to an intrinsic metal. The results were confirmed using *ab initio* calculations, indicating that the changes in the electronic structure are mainly due to the presence of dopant-rich islands and not to isolated substitutional B atoms [74].

STM and STS studies have revealed that N-doped MWNTs are metallic and exhibit a characteristic peak in the conduction-band DOS (Fig. 8b). For pure CNTs, the valence- and conduction-band features appear to be symmetric about the Fermi level, whereas for the N-doped MWNT (Fig. 8b) an additional electronic feature occurs at ca. 0.18 eV indicated by the vertical line. This result is in contrast to the B-doped case [75]. Both two- and three-coordinated N (substitutional and pyridinic, respectively), randomly distributed within armchair and zigzag CNTs, should lead to these prominent donor peaks just above the Fermi energy (at ca. 0.18 eV). More recently, it has been demonstrated that CN_x nanotubes exhibit a metallic-like behavior [77].

Electronic transport measurements on individual B-doped MWNTs reveal a metallic behavior above 30 K, due to an enhancement in conduction channels without experiencing strong backscattering [76]. In addition, the $\mathrm{d}I/\mathrm{d}V$ vs. V curves of MWNTs exhibit a small peak close to the Fermi level, E_f, which is associated with the presence of acceptor states caused by BC_3 islands (Fig. 8c). At lower temperatures, the resistance starts to increase. The results suggest that B doping induces a p-type behavior within MWNTs [76].

Four-probe measurements carried out in long strands of pure carbon SWNTs and N-doped SWNTs have been reported recently [56]. The undoped SWNT sample (0 % N) showed a semiconducting behavior over the whole temperature range (Fig. 8d); the conductivity decreased exponentially with temperature. However, for strands of SWNTs containing different nitrogen-precursor concentrations (2 %, 13 % and 26 %), the relative conductivity ($r/r\mathrm{RT}$, where RT refers to room temperature = 300 K) at very low temperatures gets higher as the dopant concentration is increased (Fig. 8d and inset). In contrast to the pristine case, the conductivity of the doped samples did not continue dropping all the way to zero. In this context, *Latil* et al. [78] performed calculations on B- and N-doped nanotubes and reported that the mean free path of charge carriers decreases (increases) linearly with dopant concentration (tube diameter) at low doping levels. These authors also demonstrated that the electron conduction could also be enhanced if the amount of foreign atoms is less than 0.5 %. It should be mentioned that the electron spin resonance (ESR) studies have also confirmed the intrinsic metallic behavior of bulk B-doped MWNTs [79].

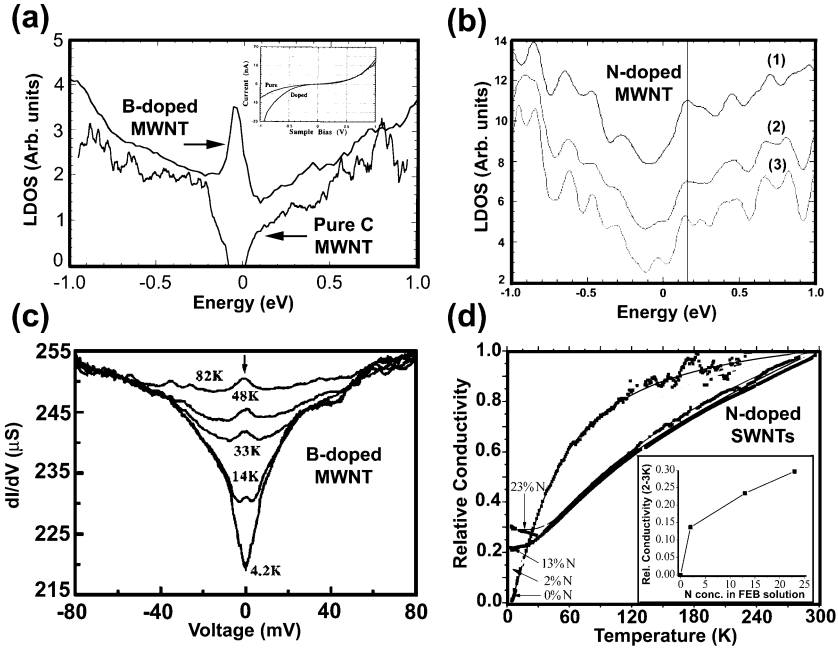

Fig. 8. (**a**) LDOS of a boron-doped MWNT measured with STS showing a clear peak on the valence band caused by the presence of B atoms within the tube [74]. A possible explanation is based upon the existence of BC_3 islands within the carbon hexagonal network (courtesy of Ajayan and Carroll); (**b**) STS acquired on a straight and clean section of a CN_x nanotube. Spectra (1)–(3) were taken at different locations along the surface but close to a "hole". Note the peak at 0.18 eV (conduction band) in all spectra [75]; (**c**) $\mathrm{d}I/\mathrm{d}V$ vs. V curves of an individual MWNT doped with B, exhibiting a small peak close to the E_f, which is associated with the presence of an acceptor (B): peak due to B indicated by an *arrow* [76]; (**d**) Experimental conductivity (*squares*) data points and their corresponding fitting results (*continuous lines*) as a function of temperature for SWNT fibers synthesized with different initial nitrogen precursor (benzylamine) concentrations (% wt) in the ferrocene:ethanol:benzylamine (FEB) solution [56]. The parameters used to obtain the values for the donor energy levels and the carrier concentrations were derived from the fitting parameters contained in these curves (*continuous lines*). The *inset* shows the relative conductivity behavior of the SWNT strands as a function of the nitrogen-precursor (benzylamine) concentration (wt %) in the FEB solution at low temperatures (2–3 K)

Thermoelectric power measurements (TEP) are sensitive to the carrier sign of any material. Since the TEP is a zero-current transport coefficient, it is able to probe the intrinsic conduction properties of individual nanotubes, being less influenced by randomly entangled morphologies and imperfections in the measured mats as compared to standard conductivity measurements. TEP studies of mats of B- and N-doped MWNTs have been carried out [80]. These studies indicate that the TEP of B-doped MWNTs is positive, thus indicating hole-like carriers (Fig. 9b). In contrast, the N-doped tubes exhibit negative TEP over the same temperature range (Fig. 9c), suggesting electron-like conduction [80]. These results could be correlated with the DOS for B- and N-doped MWNTs. It is important to note that as-produced pure-carbon MWNTs exhibit positive TEP, which has been attributed to the presence of oxygen dopants within the tube mats (Fig. 9a). If the sample is left in vacuum for 94 h, the TEP signal decreases considerably [80]. In this context, it is important to note that TEP studies for SWNTs have been able to clearly indicate alkali-metal intercalation [81] and O contamination (or doping) [82]. Recently, *Rao* and coworkers [72] demonstrated that B-doped SWNTs (produced using the laser-ablation technique) display positive TEP values (Fig. 10), thus implying the presence of holes (as for B-doped MWNTs). One should emphasize that these clear changes in the TEP occurred for very low B concentrations (e.g., 0.05–0.1 at % B), too low to be detected with EELS or XPS. Therefore, TEP measurements are extremely sensitive to low doping levels of B (or N) within SWNTs and MWNTs.

5.3 Raman Characterization

Raman characterization is an important technique for characterizing both undoped and doped carbon nanotubes [83–88, in the contribution by Saito et al. in this volume]. The dopant-induced interactions (whether it is an inorganic species such as an alkali-metal donor or a halogen acceptor, or an organic polymer chain or a DNA strand) with the sidewall of a nanotube will perturb the Fermi level of the nanotube through charge-transfer interactions. Since electrons and phonons are strongly coupled to each other, these perturbations will influence the various Raman modes present in carbon nanotubes, similar to what has been observed in the sp^2-hybridized carbon (graphite) intercalation compounds [5]. Next, we discuss some clear examples of how this technique is used for probing modifications of the nanotube surface, such as by the introduction of surface species and the charge-transfer effects resulting from the doping.

5.3.1 Nonsubstitutional n-Type Doped Nanotubes

The doping with alkali metals like K, Rb, and Cs leads to a softening (or downshift) of 35 cm^{-1} (saturated regime) of the G-band frequencies, and is accompanied by dramatic changes in its lineshape (Fig. 11) [3, 83–90].

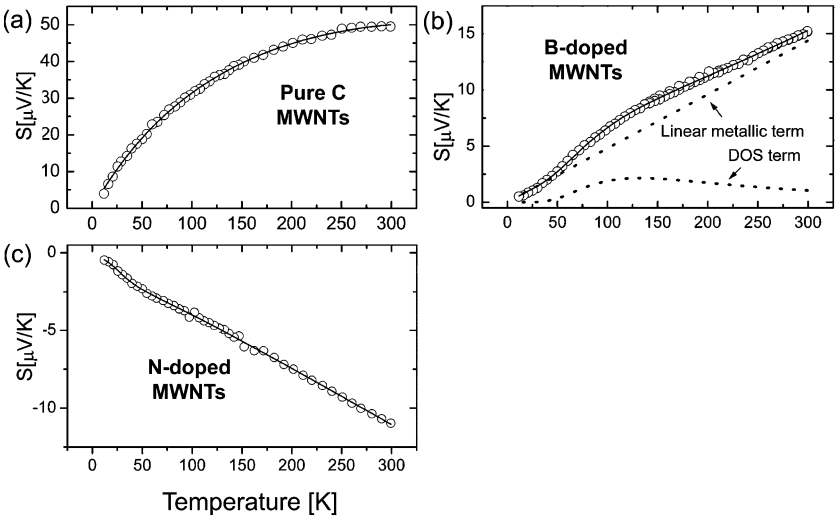

Fig. 9. Thermopower plots for pure carbon and doped MWNT mats. (**a**) TEP of a pure C MWNT mat fit by heterogeneous model (*solid line*); (**b**) TEP of a B-doped MWNT mat and fit (*solid line*) indicating positive (hole) carriers. The *dotted lines* show the effect of the linear metallic term (*straight line*) and the DOS term, and (**c**) TEP of a N-doped MWNT mat indicating negative (electron) carriers and fit (*solid line*) [80]

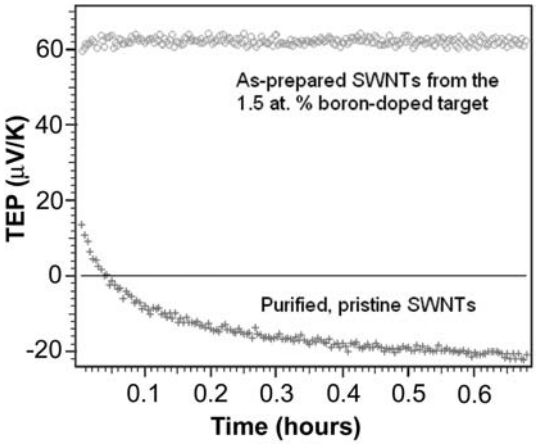

Fig. 10. Comparison of the TEP data for the purified, pristine SWNT material and the SWNTs produced from the nominal 1.5 at % boron-doped target. In both data sets the sample was held at 500 K and 10^{-6} torr vacuum [72]

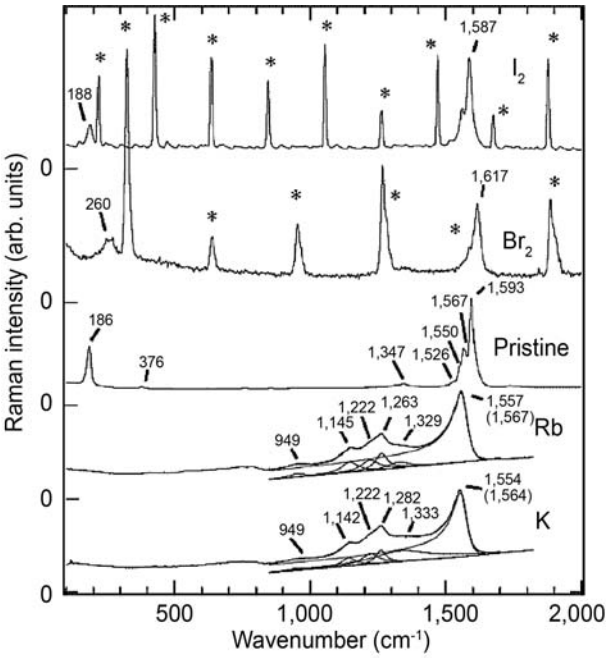

Fig. 11. Raman spectra of SWNT bundles reacted with various donor and acceptor reagents. A Raman spectrum of pristine SWNT bundles is included for comparison. The *asterisks* label the harmonic series of peaks associated with the fundamental stretching frequency for I_2 ($220\,cm^{-1}$) and Br_2 ($242\,cm^{-1}$) [3]

The downshifts in Raman frequencies provide evidence for charge transfer between the dopants and SWNT bundles. First-principles calculations based on a frozen-phonon model support the experimentally observed downshift in the phonon frequencies of alkali-metal-doped SWNTs [91].

The intercalation of other metals such as silver (Ag) into SWNT bundles has also been studied [92]. In Fig. 12a we show the Raman spectra of both pristine SWNT and SWNT/Ag obtained with an excitation energy of 2.41 eV [93]. The downshift in the tangential G^+-mode from 1582 to $1575\,cm^{-1}$ and in the G′-band from 2650 to $2640\,cm^{-1}$ indicates that electrons are transferred from the silver atoms to the SWNTs. Besides the shift of the G-band mode frequencies, further confirmation for the charge transfer between the chemical species and the SWNTs can be gathered by analyzing the profile of the G^--band. The profile of this band tells us about the metallic and semiconducting behavior of the SWNTs. The lower trace in Fig. 12a shows a G-band profile typical of contributions mainly coming from semiconducting SWNTs. The G^--band for the SWNT/Ag system (upper trace in Fig. 12a), however, exhibits a strong Breit–Wigner–Fano profile, which is typical of metallic SWNTs (see the contribution by Saito et al.). The change

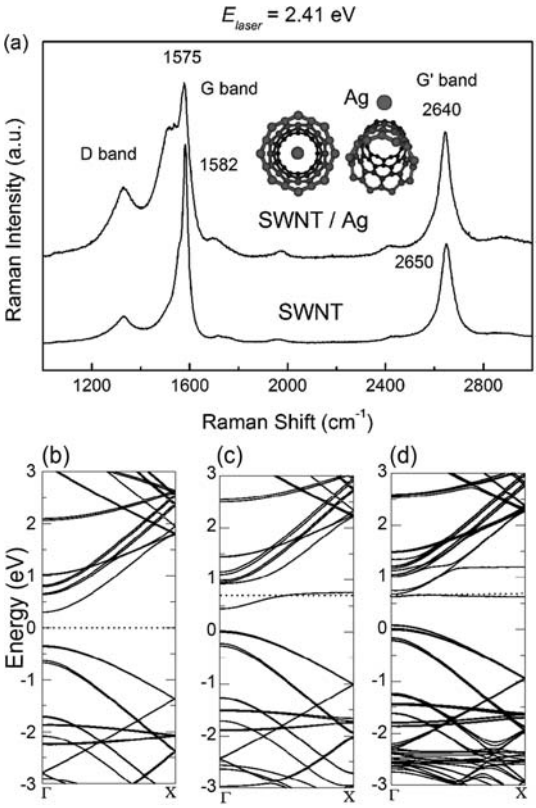

Fig. 12. (**a**) Raman spectra of pristine and SWNT/Ag samples. Electronic band structure for a pristine (8,0) SWNT (**b**) and for an Ag atom interacting with the SWNT through the (**c**) inner and (**d**) outer surface. The *horizontal dashed lines* correspond to the Fermi level [92, 93]

from a semiconductor to metallic-like profile observed for the SWNT/Ag samples indicates that the conduction-band states are being populated by charge-transferred electrons from the Ag atoms to the SWNT, thus moving the Fermi level up in energy, which allows the coupling between free carriers and the phonons, enhancing the BWF profile. The *ab initio* calculations of electronic band structure for the SWNT/Ag (Fig. 12b–d) system shows a half-filled level in agreement with experiments.

We should note that the effects of doping on the phonon frequencies of carbon nanotubes are similar to graphite only for high doping levels. Recent studies showed that for both isolated and bundled SWNTs, there is an anomalous change in the C–C bond length upon doping with alkali metals [94, 95] and four regimes have been identified. For low dopant content, intercalant adsorption mainly occurs on the outside surface of the bundle and the frequencies do not change. In the second regime of dopant concentration, the

G-band frequencies increase and the RBM intensity is suppressed. In the third regime, the frequency of the G-band decreases with a continuous loss in intensity. Finally, in the fourth regime, the G-band frequency remains constant, thus indicating the saturation regime. These results are different from GICs for which the downshift is monotonic and this difference in behavior should be related to curvature effects of nanotubes and to the bundling effect. The C–C bond lengths along the nanotube axis and along the circumference are affected differently by the doping and they have a nonlinear behavior, thus exhibiting either lattice contraction or expansion, depending on the doping concentration [96].

5.3.2 Nonsubstitutional p-Type Doped Nanotubes

For SWNT bundles doped with halogens (for example, Br_2), an upshift in the Raman-mode frequencies was observed relative to the corresponding frequencies in the pristine bundles (Fig. 11) [3, 83]. Doping with acceptors creates hole carriers in the SWNTs. Similar to graphite [5], the $FeCl_3$ acts as an electron acceptor in the presence of SWNTs [91, 97]. This behavior is observed through the suppression of the optical transition in the absorption spectra because the depletion of valence states of the SWNTs. Upshifts in the Raman frequencies were observed [97]. *Ab-initio* calculations confirm the acceptor nature of $FeCl_3$ when adsorbed by SWNTs [98].

An opposite scenario, compared with the SWNT/Ag system, was observed for SWNT/CrO_3. The upshift observed for the G^+-band and the G′-band frequencies for SWNT/CrO_3 indicates an effective stiffening of the C–C bonds due to charge transfer from the SWNT to the oxidizing CrO_3 species. When the CrO_3 is attached to the SWNT sidewall, the translational symmetry is broken and this contributes to enhancing the D-band intensity and linewidth when compared with the pristine SWNT. The linewidth of all the modes increases, thus indicating that the system becomes disordered due to the CrO_3 attachment to the tube walls. Calculations indicated that the binding energy between SWNTs and CrO_3 is typical of covalent bonds [92]. Thus, the carbon atom to which the Cr is bonded exhibits a sp^3-like hybridization, breaking the symmetry and enhancing the D-band intensity. These results are often discussed within the framework of a rigid-band model, whereby it is assumed that there is no modification to the E_{ii} values of a SWNT through the doping process, but the Fermi level is shifted very significantly by the addition of electrons and holes [3, 99].

Resonant Raman scattering data of Br_2 adsorbed by high-purity bundled DWNTs were analyzed by considering the effect of doping on the electronic transitions [100]. For some excitation laser energies it is possible to get the resonance Raman spectra of both the DWNTs and the Br_2. Both decreases and increases in the radial breathing mode (RBM) intensity due to bromination are observed and are attributed to the shift of electronic transition

values E_{ii}. Upshifts in the G^+ band frequency are observed when the inner tube is metallic.

5.3.3 Raman Spectroscopy for Inplane Doped Nanotubes

As described earlier the xylene-injection chemical vapor deposition (CVD) method for synthesizing nitrogen-doped isolated SWNTs resulted in nitrogen-doped SWNTs [55]. Figure 13 shows the Raman spectra of isolated SWNTs as a function of increasing nitrogen concentration in the injected feed (doping concentrations listed in the figure correspond to the concentration of nitrogen in the xylene-acetonitrile feed). As the nitrogen concentration in the feed was increased from 1–33 at %, the RBM intensity decreased dramatically relative to the 303-cm^{-1} peak of Si (Fig. 13). Concomitantly, the intensity of the disorder-induced D-band at $\sim 1350\,cm^{-1}$ grows in intensity (relative to the G-band intensity) hinting that the increasing presence of nitrogen in the feed is in fact bringing about a noticeable change in the degree of long-range ordering in the hexagonal lattice of the nanotube. This increase in the intensity of the D-band is attributed to the activation of off-zone-center phonons due to relaxation of the strict selection rules for Raman scattering due to a double-resonance process [85]. Interestingly, the D′-band at $\sim 1610\,cm^{-1}$ (Fig. 13) was observed for the first time in the Raman spectrum of carbon nanotubes when the nitrogen concentration reached $\sim$ 2–3 at %. Both the D and D′ bands were previously observed in vapor-grown carbon fibers and have been attributed to the activation of zone-edge and midzone phonons [101].

The Raman characterization of long-strand N-doped SWNTs has been recently reported and the RBM spectra are shown in [56]. By observing the RBM evolution it was concluded that the formation of large-diameter tubes is prevented by the amount of N precursor. The D-band to G-band ratio increases as the amount of N precursor increases [56]. Since it is not possible to separate in the D-band profile the contribution of specific defects, the I_D/I_G result indicates that the nanotube wall is getting more disordered and in part this effect should be related to the incorporation of N atoms in the carbon lattice [56]. For inplane doping, extracting the information on charge transfer from the G-band frequency shifts is more complicated than for intercalated systems. This is because for the substitutional doping, the carbon-nanotube atomic structure and electronic bands are strongly affected and the phonon frequency is affected also by the lattice distortion because of the different chemical nature of the dopant.

The Raman features that are most affected due to the nitrogen doping are: 1. the intensity of RBM, which is much lower in nitrogen-doped SWNTs as compared to that in pristine SWNTs. The nitrogen dopant most likely hinders the collective in-and-out movement of the carbon atoms (breathing mode) in the nanotube. 2. The modes associated with defects in the lattice, i.e., D-band and D′-bands become strongly Raman active with increasing nitrogen concentration in the feed.

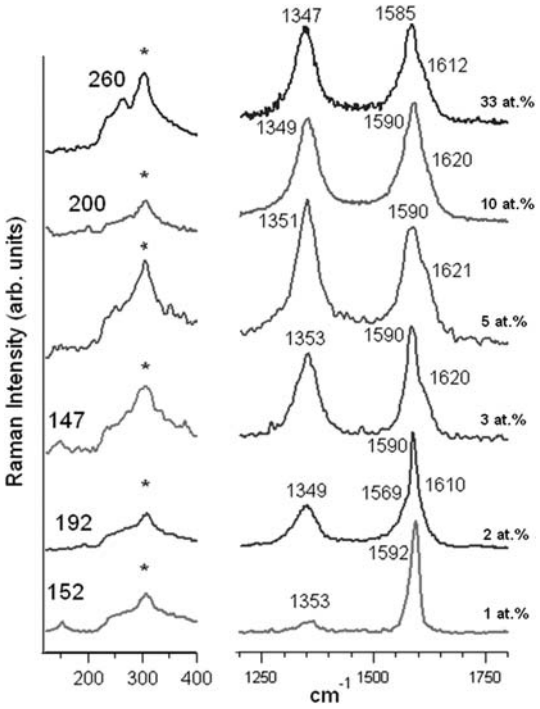

Fig. 13. Systematic changes in the micro-Raman spectra of isolated SWNTs as the atomic per cent of nitrogen in the injected mixture is increased from 1–33 at % [55]

For B-doped SWNTs produced using the laser technique that was described above [72], the overall effect of the boron incorporation primarily leads to: 1. a systematic increase in intensity of the disorder-induced band (D-band) upon boron doping, with increasing D-band intensity observed for higher doping levels, 2. a systematic downshift in the G'-band frequency due the relatively weaker C–B bond, and 3. a nonlinear variation in the RBM and G'-band intensities that is attributed to shifts in resonance conditions in the doped tubes [72]. Resonant Raman spectroscopy thus provides large changes in the intensity of prominent features even when the dopant concentration is below the detectable limit of EELS (0.05–0.1 at %). As mentioned earlier, thermoelectric (TEP) data also provided complementary evidence for the presence of a small boron concentration in the SWNT lattice that transforms the SWNTs into a permanently p-type material.

The doped nanotubes are also important for unveiling new features of the Raman spectra of nanocarbon-based systems. [102]. When DWNTs are annealed at high temperatures, a very sharp mode is observed at about $1850\,\mathrm{cm}^{-1}$ and is called the coalescence-induced mode [103]. The CIM feature is associated with short chains of 1D carbon atoms with an odd number of

atoms, interconnecting the nanotube surfaces and promoting the coalescence of DWNTs.

6 Applications of Doped Nanotubes

In the following paragraphs we will briefly review some possible applications of different types of doped carbon nanotubes in diverse areas such as electronics, biology, composites and catalysis (see also the contribution by Endo et al.). Since the preparation methods are not yet able to selectively produce metallic nanotubes upon demand, the development of efficient purification and separation methods is a very important step in nanotube-based technology at the present time [104–107].

Field Emission Sources

Charlier et al. [108] demonstrated experimentally and theoretically that B-doped MWNTs exhibit enhanced field emission (turn-on voltages at ca. 1.4 V/μm) when compared to pure carbon MWNTs (turn-on voltages at ca. 3 V/μm). This phenomenon is thought to be due to the presence of B atoms at the nanotube tips, which results in an increased density of states close to the Fermi level. Theoretical tight-binding and *ab-initio* calculations demonstrate that the work function of B-doped SWNT is much lower (1.7 eV) than that observed in pure-carbon MWNTs. Similarly, it has been demonstrated that bundles of N-doped MWNTs are able to emit electrons at relatively low turn-on voltages (2 V/μm) and high current densities (0.2–0.4 A/cm^2) [77]. More recently, individual N-doped MWNTs have also shown excellent field emission properties at 800 K; experimental work functions of 5 eV and emission currents of ca. 100 nA have been obtained at ±10 V [109].

Li-Ion Batteries

At present, several electronic companies commercialize these batteries in portable computers, mobile telephones, digital cameras, etc. Interestingly, *Endo* and coworkers [110] demonstrated that B-doped vapor-grown carbon fibers (VGCFs) and carbon nanofibers are by far superior compared with any other carbon source present in the graphitic anode inside Li-ion batteries. This effect could be due to the fact that the population of Li ions has a stronger affinity in the B-doped sites, thus resulting in a higher storage efficiency. N-doped CNTs and nanofibers have also shown efficient reversible Li storage (480 mAh/g); much higher when compared to commercial carbon materials used for Li^+ batteries (330 mAh/g) [111].

Gas Sensors

Since 1998, it has been demonstrated by various groups [112–114] that pure carbon SWNTs and MWNTs can be used to detect toxic gases and other species [112]. However, N-doped MWNTs appear to be more efficient in this context because they are able to display a fast response (order of milliseconds) when toxic gases and organic solvents are introduced [115]. From a theoretical standpoint, a decrease in the density of states at E_f is observed, indicative of lower conduction and chemisorption.

Polymer Composites with Doped Nanotubes

In order to fabricate nanotube composites exhibiting high performance, the formation of stable tube-surface/polymer interfaces is crucial. In this case, the surface of highly crystalline MWNTs tends to be similar to graphite, and chemically "inert". Therefore, surface-modification treatments are required so that efficient tube–matrix interactions need to be established [116]. In this context, the creation of nanotubes containing a small number of foreign atoms in the hexagonal network such as N or B, could circumvent this problem. In some cases, the mechanical properties would not be altered significantly because these "doped" structures would preserve their outstanding mechanical properties since the level of doping is low ($<$ 1–2 %). Preliminary studies on the preparation of epoxy composites using N-doped MWNTs revealed an increase of 20 °C in the glass-transition temperature with incorporation of 2.5 wt % of CN_x MWNT using dynamic mechanical thermal analysis (DMTA) [117]. More recently, it has been demonstrated that it is possible to grow polystyrene (PS) on the surface of N-doped MWNTs using atomic transfer radical polymerization (ATRP) [118] and nitroxide-mediated radical polymerization [119] without using any acid treatment. Recent mechanical and electrical tests have demonstrated that PS-grafted CN_x nanotubes exhibit enhanced properties when compared to mixtures of PS and pristine CN_x tubes [120]. The charge transfer between carbon nanotubes and pendant ferrocene groups is used for converting solar energy into electric current via photoexcitation process [121].

Efficient Metal Surfaces for Anchoring Molecules

Recently, it has been possible to create active nitrogen-rich sites for the efficient covalent anchoring of proteins [122], Au [123], Ag [124], Fe and Pt clusters [125] to the surfaces of N-doped MWNTs (Fig. 14). It has been demonstrated that the doped tubes are much more efficient for anchoring molecules when compared to pure carbon nanotubes.

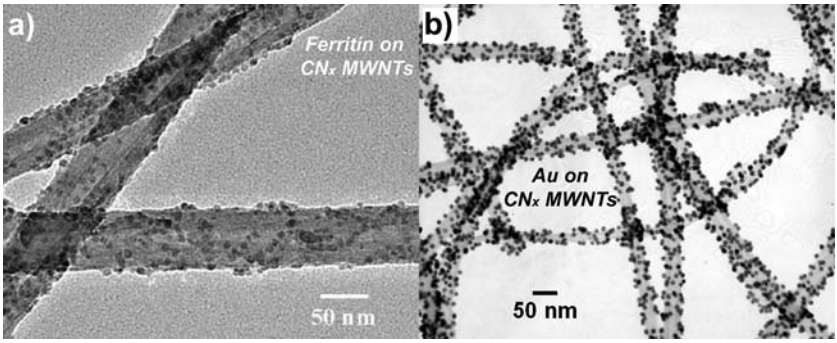

Fig. 14. (**a**) TEM image of ferritin-CN_x MWNT conjugates [122], and (**b**) TEM photograph of gold nanoparticle-CN_x nanotube hybrid structures [123]

Toxicity of Doped Carbon Nanotubes

In comparison with previous toxicological studies using SWNTs, new results demonstrated that CN_x [126] tubes appear to be far less harmful. For example, using extremely high doses of CN_x nanotubes (e.g., 5 mg/kg), no lethal effects were observed on the mice, which is in contrast to previous reports using undoped MWNTs or SWNTs [127]. The pathological changes induced by pure MWNTs are more severe than CN_x MWNTs; in both, these pathological changes were dose and time dependent [126]. CN_x tubes could then be used as agents for drug delivery, supports for enhanced enzyme activities, biofilters, virus inhibitors, gene transfers, etc. However, additional and strict biosafety measures need to be developed for the production and processing of these nanotubes into new materials. In addition, the toxicological effects of other types of doped nanotubes should also be studied in the near future.

Very recently, *Elias* et al. [128] carried out a detailed cell viability study with amoeba and different types of nanotubes (pure-carbon MWNTs and N-doped MWNTs). The authors noted that when the cells were incubated with CN_x MWNTs, they survived and there were no changes in their behavior or morphology, at all doses tested. In contrast, most of the ameba populations died after 8 h of incubation with undoped MWCNTs (100 μg) (Fig. 15). These results imply that nitrogen addition increases biocompatibility (as mentioned earlier) and that they should be tested for their usage in various applications, such as cell transporters and drug-delivery systems.

7 Perspectives and Challenges

In this review, we have discussed the current state of carbon-nanotube doping through some examples. It was clear that these hybrid materials (doped nanotubes) are attractive for developing both basic science and nanotube-based technology. Although there are special interesting effects in doped

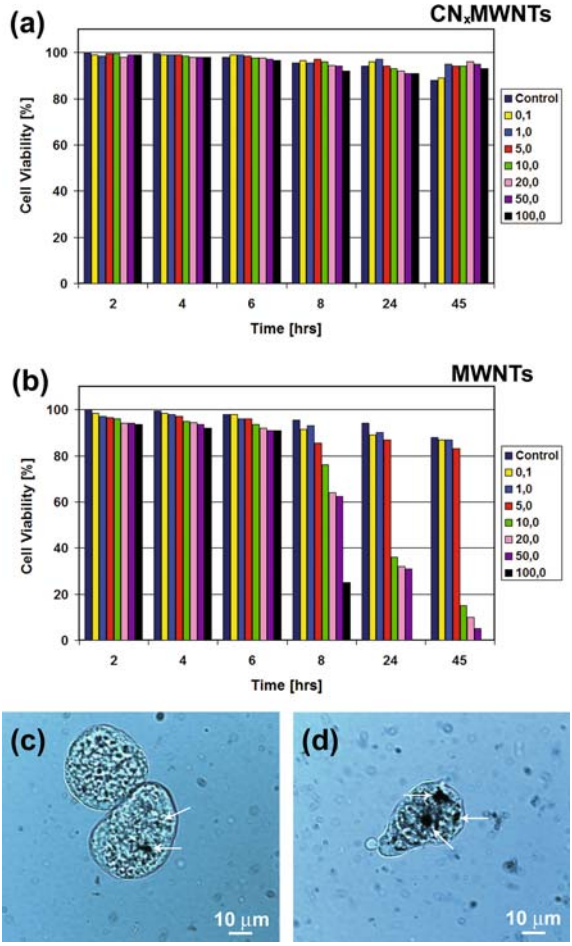

Fig. 15. Cell viability of Entamoeba histolytica cells incubated with: (**a**) CN_x MWNTs; (**b**) undoped MWNTs. *Dark blue color* is associated with the control experiment, where pure phosphate buffer solution (PBS) was added to the cell medium. *Yellow color* is associated with the lowest concentration used (0.1 μg), while *black* is linked to the highest concentration (100 μg). Cell viability decreases with time naturally, as can be observed in the column corresponding to 24 h. Note that for undoped MWNTs, doses of 100 mg drastically reduced cell viability after 6 h of incubation, and the results were absolutely lethal after 24 h. Low concentrations of undoped MWNTs (0.1, 1.0 and 5.0 μg), did not reveal important viability effects. However, and more interestingly, longer incubation times of CN_x MWNTs resulted in an increase of cell viability when compared to the control sample. Optical microscope images of living amoebas incubated with CN_x MWNTs for (**c**) 45 min and (**d**) 22 h. In both images, it is possible to observe black agglomerates inside cells (see *arrows*). It is not possible to determine whether these are carbon nanotubes or not, but those black spots were not present in the control sample (courtesy of Elias)

nanotubes with specific elements, further studies should continue using different elements. However, and in order to exploit fully these novel properties, low concentrations of dopants (e.g., $< 0.5\,\%$) should be incorporated within these tubes. In this way, the electronic conductance would be significantly enhanced and the mechanical properties would not be altered. The illustrated examples and phenomena clearly demonstrate that the science of doping carbon nanotubes should be developed further with more emphasis given to interdisciplinary aspects of research. It is easy to see that physics, chemistry, biochemistry and materials science are working together in their mutual benefit developing the basic science that is beginning to find significant potential for applications to technology. We should point out that the physicochemical properties of endohedral- and exohedral-doped tubes should continue to be studied, as these materials may also show useful opportunities in various technological arenas. This review is also intended to motivate new ways of characterizing these complex systems as the current analytical techniques appear to be limiting the way we could identify low dopant concentration within doped tubes. It seems that Raman spectroscopy, TEP studies and electron transport are very sensitive to low doping concentrations. In addition, reliable methods for producing doped nanotube samples in a reproducible way are required. We also envisage that doped carbon systems may exhibit unusual magnetic properties that need to be carefully tested, since recent theoretical work has proposed this possibility. Finally, it is expected that doped nanotubes may replace pure-carbon nanotubes for specific applications, but further developments are needed for many of the potential applications areas that have been identified.

Researchers should be aware that doping of carbon nanotubes may also occur unintentionally, and this will result in significant changes of the electronic, transport, chemical and vibrational properties. Therefore, one should be careful when carrying out synthesis and purification experiments involving noncarbon elements, because these may get embedded into the hexagonal network of nanotubes, and would then modify the physicochemical response.

Acknowledgements

We are in debted to P. M. Ajayan, Y. Bando, X. Blase, J. Y. Cavallié, J. C. Carrero-Sánchez, D. L. Carroll, J. C. Charlier, A. K. Cheetham, P. Corio, E. Cruz-Silva, R. Czerw, M. De Honor, M. S. Dresselhaus, A. L. Elías, M. Endo, S. B. Fagan, B. Fragneaud, P. L. Gai, D. Golberg, A. González-Montiel, N. Grobert, T. Hayashi, A. Jorio, R. Kamalakaran, Y. A. Kim, J. P. Laclette, F. López-Urías, Karine Masenelli-Varlot, J. Mendes Filho, E. Muñoz-Sandoval, H. Muramatsu, K. McGuire, L. Noyola-Cherpitel, Ph. Redlich, J. M. Romo-Herrera, J. A. Rodríguez-Manzo, M. Rhle, R. Saito, H, Terrones, E. B. Barros, F. Villalpando-Páez and A. Zamudio for stimulating discussions and valuable assistance in some of the work reviewed here. M. Terrones is grateful to CONACYT-México (45772 (MT), 41464-Inter Amer-

ican Collaboration (MT), 2004-01-013/SALUD-CONACYT (MT), PUE-2004-CO2-9 Fondo Mixto de Puebla (MT), and the MIT-CONACYT collaboration project) for financial support. A. G. Souza Filho acknowledge the support from Brazilian agencies FUNCAP (grant 985/03), CNPq (grants 556549/2005-8, 475329/2006-6, 307417/2004-2), Rede Nacional de Pesquisa em Nanotubos de Carbono, Rede Nacional de Nanobiotecnologia e sistemas nanoestruturados, Instituto do Milênio de Nanotecnologia, and Instituto do Milênio de Materiais Complexos (CNPq/MCT-Brazil). A. M. Rao gratefully acknowledges support from NSF through grants 0304019, 0244290, and 0216307.

References

[1] M. S. Dresselhaus, G. Dresselhaus, P. C. Eklund: *Science of Fullerenes and Carbon Nanotubes* (Academic Press, New York 1996) 531

[2] J. Sloan, M. Terrones, S. Nufer, S. Friedrichs, S. R. Bailey, H. G. Woo, M. Ruhle, J. L. Hutchison, M. L. H. Green: Metastable one-dimensional $AgCl_{1-x}I_x$ solid-solution wurzite "tunnel" crystals formed within single-walled carbon nanotubes, J. Am. Chem. Soc. **124**, 2116 (2002) 531, 533

[3] A. M. Rao, P. C. Eklund, S. Bandow, A. Thess, R. E. Smalley: Evidence for charge transfer in doped carbon nanotube bundles from Raman scattering, Nature **388**, 257 (1997) 532, 546, 548, 550

[4] R. S. Lee, H. J. Kim, J. E. Fischer, A. Thess, R. E. Smalley: Conductivity enhancement in single-walled carbon nanotube bundles doped with K and Br, Nature **388**, 255 (1997) 532

[5] M. S. Dresselhaus, G. Dresselhaus: Intercalation compounds of graphite, Adv. Phys. **30**, 139 (1981) 533, 546, 550

[6] S. Kazaoui, N. Minami, R. Jacquemin, H. Kataura, Y. Achiba: Amphoteric doping of single-wall carbon-nanotube thin films as probed by optical absorption spectroscopy, Phys. Rev. B **60**, 13339 (1999) 533

[7] M. R. Pederson, J. Q. Broughton: Nanocapillarity in fullerene tubules, Phys. Rev. Lett. **69**, 2689 (1992) 533

[8] P. M. Ajayan, T. W. Ebbesen, T. Ichihashi, S. Iijima, K. Tanigaki, H. Hiura: Opening carbon nanotubes with oxygen and implications for filling, Nature **362**, 522 (1993) 533

[9] M. Monthioux: Filling single-wall carbon nanotubes, Carbon **40**, 1809 (2002) 533

[10] D. Tasis, N. Tagmatarchis, A. Bianco, M. Prato: Chemistry of carbon nanotubes, Chem. Rev. **106**, 1105 (2006) 533

[11] Z. Y. Wang, Z. B. Zhao, J. S. Qiu: Development of filling carbon nanotubes, Prog. Chem. **18**, 563 (2006) 533

[12] M. Terrones, N. Grobert, W. K. Hsu, Y. Q. Zhu, W. B. Hu, H. Terrones, J. P. Hare, H. W. Kroto, D. R. M. Walton: Advances in the creation of filled nanotubes and novel nanowires, Mater. Res. Soc. Bull. **24**, 43 (1999) 533

[13] S. Iijima, T. Ichihashi: Single-shell carbon nanotubes of 1 nm diameter, Nature **363**, 603 (1993) 533

[14] D. S. Bethune, C. H. Kiang, M. S. D. Vries, G. Gorman, R. Savoy, J. Vazquez, R. Beyers: Cobalt-catalyzed growth of carbon nanotubes with single-atomic-layerwalls, Nature **363**, 605 (1993) 533
[15] B. W. Smith, M. Monthioux, D. E. Luzzi: Encapsulated C_{60} in carbon nanotubes, Nature **296**, 323 (1998) 533
[16] J. Sloan, J. Hammer, M. Z. Sibley, M. L. H. Green: The opening and filling of single walled carbon nanotubes (SWTs), Chem. Commun. **3**, 347 (1998) 533
[17] C. H. Kiang, J. S. Choi, T. T. Tran, A. D. Bacher: Molecular nanowires of 1 nm diameter from capillary filling of single-walled carbon nanotubes, J. Phys. Chem. B **103**, 7449 (1999) 533
[18] P. Corio, A. P. Santos, M. L. A. Temperini, V. W. Brar, M. A. Pimenta, M. S. Dresselhaus: Chem. Phys. Lett. **383**, 475 (2004) 533
[19] A. Govindaraj, B. C. Satishkumar, M. Nath, C. N. R. Rao: Metal nanowires and intercalated metal layers in single-walled carbon nanotube bundles, Chem. Mater. **12**, 205 (2000) 533
[20] J. Sloan, D. M. Wright, H. G. Woo, S. R. Bailey, G. Brown, A. P. E. York, K. S. Coleman, J. L. Hutchison, M. L. H. Green: Capillarity and silver nanowire formation observed in single walled carbon nanotubes, Chem. Commun. **700**, 699 (1999) 533
[21] R. R. Meyer, J. Sloan, R. E. Dunin-Borkowski, A. Kirkland, M. C. Novotny, S. R. Bailey, J. L. Hutchison, M. L. H. Green: Discrete atom imaging of one-dimensional crystals formed within single-walled carbon nanotubes, Science **289**, 1324 (2000) 533
[22] D. E. Luzzi, B. W. Smith: Carbon cage structures in single wall carbon nanotubes: a new class of materials, Carbon **38**, 1751 (2000) 533
[23] E. Hernández, V. Meunier, B. W. Smith, R. Rurali, H. Terrones, Buongiorno, N. Nardelli, M. Terrones, D. E. Luzzi, J. C. Charlier: Fullerene coalescence in nanopeapods: A path to novel tubular carbon, Nano Lett. **3**, 1037 (2003) 533
[24] K. Hirahara, K. Suenaga, S. Bandow, H. Kato, T. Okazaki, H. Shinohara, S. Iijima: One-dimensional metallofulerene crystal generated inside single-walled carbon nanotubes, Phys. Rev. Lett. **85**, 5384 (2000) 533
[25] A. Khlobystov, D. A. Britz, A. Ardavan, G. A. D. Briggs: Observation of ordered phases of fullerenes in carbon nanotubes, Phys. Rev. Lett. **92**, 245507 (2004) 533
[26] D. Ugarte, T. Stockli, J. M. Bonard, A. Chatelain, W. A. D. Heer: Filling carbon nanotubes, Appl. Phys. A **67**, 101 (1998) 534
[27] A. Kolesnikov, J. M. Zanotti, C. K. Loong, P. Thiyagarajan, A. P. Moravsky, R. O. Loutfy, C. J. Burnham: Anomalously soft dynamics of water in a nanotube: A revelation of nanoscale confinement, Phys. Rev. Lett. **93**, 035503 (2004) 534
[28] L. J. Li, A. N. Khlobystov, J. G. Wiltshire, G. A. Briggs, R. J. Nicholas: Diameter-selective encapsulation of metallocenes in single-walled carbon nanotubes, Nature Mater. **4**, 481 (2005) 534
[29] H. Kataura, Y. Maniwa, T. Kodama, K. Kikuchi, K. Hirahara, S. Iijima, S. Suzuki, W. Krätschmer, Y. Achiba: Fullerene-peapods: Synthesis, structure, and Raman spectroscopy, in H. Kuzmany, J. Fink, M. Mehring, S. Roth

(Eds.): *Electronic Properties of Molecular Nanostructures*, AIP Proc. **591** (2001) p. 251 534
[30] C. E. Lowell: Solid solution of boron in graphite, J. Am. Ceram. Soc. **50**, 142 (1966) 534
[31] C. T. Hach, L. E. Jones, C. Crossland, P. A. Thrower: An investigation of vapor deposited boron rich carbon – a novel graphite-like material – part I: the structure of BC_x (C_6B) thin films, Carbon **37**, 221 (1999) 534
[32] A. Oya, R. Yamashita, S. Otani: Catalytic graphitization of carbons by borons, Fuel **58**, 495 (1979) 534
[33] M. Endo, T. Hayashi, S. H. Hong, T. Enoki, M. S. Dresselhaus: Scanning tunneling microscope study of boron-doped highly oriented pyrolytic graphite, J. Appl. Phys. **90**, 5670 (2001) 534
[34] M. Endo, C. Kim, T. Karaki, Y. Nishimura, M. J. Matthews, S. D. M. Brown, M. S. Dresselhaus: Anode performance of a Li ion battery based on graphitized and B-doped milled mesophase pitch-based carbon fibers, Carbon **37**, 561 (1999) 534
[35] A. Marchand, J. V. Zanchetta: Proprietes electroniques d'un carbone dope a l'azote, Carbon **3**, 483 (1966) 534
[36] K. Takeya, K. Yazawa: Unusual galvanomagnetic properties of pyrolytic graphite, J. Phys. Soc. Jpn. **19**, 138 (1964) 534
[37] K. T. K. Yazawa, N. Okuyama, H. Akutsu: Evidence for existence of extremely light carriers in pyrolytic carbons, Phys. Rev. Lett. **15**, 111 (1965) 534
[38] T. Belz, A. Baue, J. Find, M. Günter, D. Herein, H. Möckel, N. Pfänder, H. Sauer, G. Schulz, J. Schütze, O. Timpe, U. Wild, R. Schlögi: Structural and chemical characterization of N-doped nanocarbons, Carbon **36**, 731 (1998) 534
[39] E. Hernández, C. Goze, P. Bernier, A. Rubio: Elastic properties of C and $B_xC_yN_z$ composite nanotubes, Phys. Rev. Lett. **80**, 4502 (1999) 536
[40] E. Hernández, C. Goze, P. Bernier, A. Rubio: Elastic properties of single-wall nanotubes, Appl. Phys. A. Mater **68**, 287 (1999) 536
[41] R. P. Gao, Z. L. Wang, Z. G. Bai, W. A. de Heer, L. M. Dai, M. Gao: Nanomechanics of individual carbon nanotubes from pyrolytically grown arrays, Phys. Rev. Lett. **85**, 622 (2000) 536
[42] R. J. Baierle, S. B. Fagan, R. Mota, A. J. R. da Silva, A. Fazzio: Electronic and structural properties of silicon-doped carbon nanotubes, Phys. Rev. **64**, 085413 (2001) 536
[43] E. Cruz-Silva, D. Cullen, L. Gu, J. M. Romo-Herrera, E. Muñoz-Sandoval, F. López-Urías, D. J. Smith, H. Terrones, M. Terrones: Hetero-doped nanotubes: Theory, synthesis and characterization of phosphorous-nitrogen doped multiwalled carbon nanotubes submitted 536
[44] S. B. Fagan, R. Mota, R. J. Baierle, A. J. R. da Silva, A. Fazzio: Ab initio study of an organic molecule interacting with a silicon-doped carbon nanotube, Diam. Relat. Mater. **12**, 861 (2003) 536
[45] O. Stephan, P. M. Ajayan, C. Colliex, P. Redlich, J. M. Lambert, P. Bernier, P. Lefin: Doping graphitic and carbon nanotube structures with boron and nitrogen, Science **266**, 1683 (1994) 537

[46] P. Redlich, L. Loeffler, P. M. Ajayan, J. Bill, F. Aldinger, M. Ruhle: B-C-N nanotubes and boron doping of carbon nanotubes, Chem. Phys. Lett. **260**, 465 (1996) 537
[47] M. Terrones, W. K. Hsu, S. Ramos, R. Castillo, H. Terrones: The role of boron nitride in graphite plasma arcs, Full. Sci. Tech. **6**, 787 (1998) 537
[48] W. K. Hsu, M. Terrones: unpublished results 537
[49] M. Glerup, J. Steinmetz, D. Samaille, O. Stephan, S. Enouz, A. Loiseau, S. Roth, P. Bernier: Synthesis of N-doped SWNT using the arc-discharge procedure, Chem. Phys. Lett. **387**, 193 (2004) 537
[50] Y. Zhang, H. Gu, K. Suenaga, S. Iijima: Heterogeneous growth of B–C–N nanotubes by laser ablation, Chem. Phys. Lett. **279**, 264 (1997) 537
[51] P. Gai, O. Stephan, K. McGuire, A. M. Rao, M. S. Dresselhaus, G. Dresselhaus, C. Colliex: Structural systematics in boron-doped single wall carbon nanotubes, J. Mater. Chem. **14**, 669 (2004) 538, 542
[52] M. Terrones, N. Grobert, J. Olivares, J. P. Zhang, H. Terrones, K. Kordatos, W. K. Hsu, J. P. Hare, P. D. Townsend, K. Prassides, A. K. Cheetham, H. W. Kroto, D. R. M. Walton: Controlled production of aligned-nanotube bundles, Nature **388**, 52 (1997) 538
[53] M. Terrones, P. Redlich, N. Grobert, S. Trasobares, W. K. Hsu, H. Terrones, Y. Q. Zhu, J. P. Hare, C. L. Reeves, A. K. Cheetham, M. Ruhle, H. W. Kroto, D. R. M. Walton: Carbon nitride nanocomposites: Formation of aligned C_xN_y nanofibers, Adv. Mater. **11**, 655 (1999) 538
[54] R. Sen, B. C. Satishkumar, S. Govindaraj, K. R. Harikumar, M. K. Renganathan, C. N. R. Rao: Nitrogen-containing carbon nanotubes, J. Mater. Chem. **7**, 2335 (1997) 538
[55] G. Keskar, R. Rao, J. Luo, J. Hudson, A. M. Rao: Growth, nitrogen doping and characterization of isolated single-wall carbon nanotubes using liquid precursors, Chem. Phys. Lett. **412**, 269 (2005) 538, 551, 552
[56] F. Villalpando-Paez, A. Zamudio, A. L. Elias, H. Son, E. B. Barros, S. Chou, Y. A. Kim, H. Muramatsu, T. Hayashi, J. Kong, H. Terrones, G. Dresselhaus, M. Endo, M. Terrones, M. S. Dresselhaus: Synthesis and characterization of long strands of nitrogen-doped single-walled carbon nanotubes, Chem. Phys. Lett. **424**, 345 (2006) 538, 542, 543, 544, 545, 551
[57] D. Golberg, Y. Bando, L. Bourgeois, K. Kurashima, T. Sato: Large-scale synthesis and HRTEM analysis of single-walled B- and N-doped carbon nanotube bundles, Carbon **38**, 2017 (2000) 538
[58] E. Borowiak-Palen, T. Pichler, G. G. Fuentes, A. Graff, R. J. Kalenczuk, M. Knupfer, J. Fink: Efficient production of B-substituted single-wall carbon nanotubes, Chem. Phys. Lett. **378**, 516 (2003) 539
[59] M. Endo, H. Muramatsu, T. Hayashi, Y. A. Kim, G. V. Lier, J. C. Charlier, H. Terrones, M. Terrones, M. S. Dresselhaus: Atomic nanotube welders: Boron interstitials triggering connections in double-walled carbon nanotubes, Nano Lett. **5**, 1099 (2005) 539, 540
[60] E. G. Wang, Z. G. Guo, J. Ma, M. M. Zhou, Y. K. Pu, S. Liu, G. Y. Zhang, D. Y. Zhong: Optical emission spectroscopy study of the influence of nitrogen on carbon nanotube growth, Carbon **41**, 1827 (2003) 540

[61] K. Teo, M. Chhowalla, G. A. J. Amaratunga, W. I. Milne, D. G. Hasko, G. Pirio, P. Legagneux, F. Wyczisk, D. Pribat: Uniform patterned growth of carbon nanotubes without surface carbon, Appl. Phys. Lett. **79**, 1534 (2001) 540

[62] K. Teo, D. B. Hash, R. G. Lacerda, N. L. Rupesinghe, M. S. Bell, S. H. Dalal, D. Bose, T. R. Govindan, B. A. Cruden, M. Chhowalla, G. A. J. Amaratunga, J. M. Meyyappan, W. I. Milne: The significance of plasma heating in carbon nanotube and nanofiber growth, Nano Lett. **4**, 921 (2004) 540

[63] J. Yu, X. D. Bai, J. Ahn, S. F. Yoon, E. G. Wang: Highly oriented rich boron B–C–N nanotubes by bias-assisted hot filament chemical vapor deposition, Chem. Phys. Lett. **323**, 529 (2000) 540

[64] A. Jorio, M. A. Pimenta, A. G. Souza Filho, R. Saito, M. S. Dresselhaus, G. Dresselhaus: Characterizing carbon nanotube samples with resonance Raman scattering, New J. Phys. **5**, 137 (2003) 541

[65] K. Koziol, M. S. Shaffer, A. H. Windle: Three-dimensional internal order in multiwalled carbon nanotubes grown by chemical vapor deposition, Adv. Mater. **17**, 760 (2005) 541

[66] C. Ducati, K. Koziol, S. Friedrichs, T. J. V. Yates, M. S. Shaffer, P. A. Midgkey, A. H. Windle: Crystallographic order in multi-walled carbon nanotubes synthesized in the presence of nitrogen, Small **2**, 774 (2006) 541

[67] P. Kohler-Redlich, M. Terrones: Detection of B using EELS within B-doped carbon nanotubes, Unpublished results 542

[68] X. Blase, J.-C. Charlier, A. D. Vita, R. Car, P. Redlich, Ph, M. Terrones, W. K. Hsu, H. Terrones, D. L. Carroll, P. M. Ajayan: Boron-mediated growth of long helicity-selected carbon nanotubes, Phys. Rev. Lett. **83**, 5078, (1999) 542

[69] W. Hsu, S. Firth, P. Redlich, M. Terrones, H. Terrones, Y. Q, Zhu, N. Grobert, A. Schilder, R. J. H. Clark, H. W. Kroto, D. R. M. Walton: Boron doping effects in carbon nanotubes, J. Mater. Chem. **10**, 1425 (2000) 542

[70] E. Hernández, P. Ordejón, I. Boustani, A. Rubio, J. A. Alonso: Tight binding molecular dynamics stuides of boron assisted nanotube growth, J. Chem. Phys. **113**, 3814 (2000) 542

[71] M. Terrones, N. Grobert, H. Terrones: Synthetic routes to nanoscale $B_xC_yN_z$ architectures, Carbon **40**, 1665 (2002) 542, 543

[72] K. McGuire, N. Gothard, P. Gai, M. Dresselhaus, G. Sumanasekera, A. Rao: Synthesis and Raman characterization of boron-doped single-walled carbon nanotubes, Carbon **43**, 219 (2005) 542, 546, 547, 552

[73] M. Terrones, W. K. Hsu, A. Schilder, H. Terrones, N. Grobert, J. P. Hare, Y. Q. Zhu, M. Schwoerer, K. Prassides, H. W. Kroto, D. R. M. Walton: Novel nanotubes and encapsulated nanowires, Appl. Phys. A-Mater. **66**, 307 (1998) 543

[74] D. Carroll, P. Redlich, X. Blase, J. C. Charlier, S. Curran, P. M. Ajayan, S. Roth, M. Ruhle: Effects of nanodomain formation on the electronic structure of doped carbon nanotubes, Phys. Rev. Lett. **81**, 2332 (1998) 544, 545

[75] R. Czerw, M. Terrones, J. C. Charlier, X. Blase, B. Foley, R. Kamalakaran, N. Grobert, H. Terrones, D. Tekleab, P. M. Ajayan, W. Blau, M. Ruhle, D. L. Carroll: Identification of electron donor states in N-doped carbon nanotubes, Nano Lett. **1**, 457 (2001) 544, 545

[76] K. Liu, P. Avouris, R. Martel, W. K. Hsu: Electrical transport in doped multiwalled carbon nanotubes, Phys. Rev. B **63**, 161404 (2001) 544, 545

[77] D. Golberg, P. S. Dorozhkin, Y. Bando, Z. C. Dong, C. C. Tang, Y. Uemura, N. Grobert, M. Reyes-Reyes, H. Terrones, M. Terrones: Structure, transport and field-emission properties of compound nanotubes: CN_x vs. BNC_x ($x < 0.1$), Appl. Phys. A-Mater. **76**, 499 (2003) 544, 553

[78] S. Latil, S. Roche, D. Mayou, J.-C. Charlier: Mesoscopic transport in chemically doped carbon nanotubes, Phys. Rev. Lett. **92**, 256805 (2004) 544

[79] W. K. Hsu, S. Y. Chu, E. Munoz-Picone, J. L. Boldu, S. Firth, P. Franchi, B. P. Roberts, A. Schilder, H. Terrones, N. Grobert, Y. Q. Zhu, M. Terrones, M. E. McHenry, H. W. Kroto, D. R. M. Walton: Metallic behaviour of boron-containing carbon nanotubes, Chem. Phys. Lett. **323**, 572 (2000) 544

[80] Y. M. Choi, D. S. Lee, R. Czerw, P. W. Chiu, N. Grobert, M. Terrones, M. Reyes-Reyes, H. Terrones, J. C. Charlier, P. M. Ajayan, S. Roth, D. L. Carroll, Y. W. Park: Nonlinear behavior in the thermopower of doped carbon nanotubes due to strong, localized states, Nano Lett. **3**, 839 (2003) 546, 547

[81] L. Grigorian, G. U. Sumanasekera, A. L. Loper, S. Fang, J. L. Allen, P. C. Eklund: Transport properties of alkali-metal-doped single-wall carbon nanotubes, Phys. Rev. B **58**, 4195 (1998) 546

[82] K. Bradley, S. Jhi, P. G. Collins, J. Hone, M. L. Cohen, S. G. Louie, A. Zettl: Is the intrinsic thermoelectric power of carbon nanotubes positive?, Phys. Rev. Lett. **85**, 4361 (2000) 546

[83] S. Bandow, A. M. Rao, G. U. Sumanasekera, P. C. Eklund, F. Kokai, K. Takahashi, S. Iijima: Evidence for anomalously small charge transfer in doped single-wall carbon nanohorn aggregates with Li, K and Br, Appl. Phys. A-Mater. **71**, 561 (2000) 546, 550

[84] M. S. Dresselhaus, P. C. Eklund: Phonons in carbon nanotubes, Adv. Phys. **40**, 705 (2000) 546

[85] M. S. Dresselhaus, G. Dresselhaus, A. Jorio, A. G. Souza Filho, R. Saito: Raman spectroscopy on isolated single wall carbon nanotubes, Carbon **40**, 2043 (2002) 546, 551

[86] A. Kukovecz, T. Pichler, R. Pfeiffer, H. Kuzmany: Diameter selective charge transfer in p- and n-doped single wall carbon nanotubes synthesized by the HiPCO method, Chem. Commun. **5**, 1730 (2002) 546

[87] A. Jorio, R. Saito, J. H. Hafner, C. M. Lieber, M. Hunter, T. McClure, G. Dresselhaus, M. S. Dresselhaus: Structural (n, m) determination of isolated single-wall carbon nanotubes by resonant Raman scattering, Phys. Rev. Lett. **86**, 1118 (2001) 546

[88] A. G. Souza Filho, A. Jorio, G. G. Samsonidze, G. Dresselhaus, R. Saito, M. S. Dresselhaus: Raman spectroscopy for probing chemically/physically induced phenomena in carbon nanotubes, Nanotechnol. **14**, 1130 (2003) 546

[89] Y. A. Kim, M. Kojima, H. Muramatsu, S. Umemoto, T. Watanabe, K. Yoshida, K. Sato, T. Ikeda, T. Hayashi, M. Endo, M. Terrones, M. S. Dresselhaus: In situ Raman study on single- and double-walled carbon nanotubes as a function of lithium insertion, Small **2**, 667–676 (2006) 546

[90] B. Akdim, X. Duan, D. A. Shiffler, R. Pachter: Theoretical study of the effects of alkali-metal atoms adsorption on Raman spectra of single-wall carbon nanotubes, Phys. Rev. B **72**, 121402 (2005) 546
[91] H. Kuzmany, A. Kukovecz, F. Simon, M. Holzweber, C. Kramberger, T. Pichler: Functionalization of carbon nanotubes, Synth. Met. **141**, 113 (2004) 548, 550
[92] S. B. Fagan, A. G. Souza Filho, J. Mendes Filho, P. Corio, M. S. Dresselhaus: Electronic properties of Ag- and CrO_3-filled single-wall carbon nanotubes, Chem. Phys. Lett. **456**, 54 (2005) 548, 549, 550
[93] P. Corio, A. P. Santos, M. L. A. Temperini, V. W. Brar, M. A. Pimenta, M. S. Dresselhaus: Characterization of single wall carbon nanotubes filled with silver and with chromium compounds, Chem. Phys. Lett. **383**, 475 (2004) 548, 549
[94] G. Chen, C. A. Furtado, U. J. Kim, P. C. Eklund: Alkali-metal-doping dynamics and anomalous lattice contraction of individual debundled carbon nanotubes, Phys. Rev. B **72**, 155406 (2005) 549
[95] G. Chen, C. A. Furtado, S. Bandow, S. Iijima, P. C. Eklund: Anomalous contraction of the C–C bond length in semiconducting carbon nanotubes observed during Cs doping, Phys. Rev. B **71**, 045408 (2005) 549
[96] L. Terrazos, R. B. Capaz: unpublished results 550
[97] T. Pichler, A. Kukovecz, H. Kuzmany, H. Kataura: Charge transfer in doped single wall carbon nanotubes, Synth. Met. **135-136**, 717 (2003) 550
[98] S. Guerini, A. G. Souza Filho, J. M. Filho, O. L. Alves, S. B. Fagan: Electronic properties of $FeCl_3$-adsorbed single-wall carbon nanotubes, Phys. Rev. B **72**, 233401 (2005) 550
[99] A. Rakitin, C. Papadopoulos, J. M. Xu: Carbon nanotube self-doping: Calculation of the hole carrier concentration, Phys. Rev. B **67**, 033411 (2003) 550
[100] A. G. Souza Filho, M. Endo, H. Muramatsu, T. Hayashi, Y. A. Kim, E. B. Barros, N. Akuzawa, G. G. Samsonidze, R. Saito, M. S. Dresselhaus: Resonance Raman scattering studies in Br-2-adsorbed double-wall carbon nanotubes, Phys. Rev. B **73**, 235413 (2006) 550
[101] T. C. Chieu, M. S. Dresselhaus, M. Endo: Raman studies of benzene-derived graphite fibers, Phys. Rev. B **26**, 5867 (1982) 551
[102] M. Endo, Y. A. Kim, T. Hayashi, H. Muramatsu, M. Terrones, R. Saito, F. Villalpando-Paez, S. G. Chou, M. S. Dresselhaus: Nanotube coalescence-inducing mode: A novel vibrational mode in carbon systems, Small **2**, 1031 (2006) 552
[103] C. Fantini, E. Cruz, A. Jorio, M. Terrones, H. Terrones, G. V. Lier, J. C. Charlier, M. S. Dresselhaus, R. Saito, Y. A. Kim, T. Hayashi, H. Muramatsu, M. Endo, M. A. Pimenta: Resonance Raman study of linear carbon chains formed by the heat treatment of double-wall carbon nanotubes, Phys. Rev. B **73**, 193408 (2006) 552
[104] V. Georgakilas, D. Voulgaris, E. Vazquez, M. Prato, D. M. Guldi, A. Kukovecz, H. Kuzmany: Purification of HiPCO carbon nanotubes via organic functionalization, J. Am. Chem. Soc. **124**, 14318 (2002) 553
[105] M. Zheng, A. Jagota, E. D. Semke, B. A. Diner, R. S. Mclean, S. R. Lustig, R. Richardson, N. G. Tassi: DNA-assisted dispersion and separation of carbon nanotubes, Nature Mater. **2**, 338 (2003) 553

[106] M. Zheng, A. Jagota., M. S. Strano, A. P. Santos, P. Barone, S. G. Chou, B. A. Diner, M. S. Dresselhaus, R. S. Mclean, G. B. Onoa, G. G. Samsonidze, E. D. Semke, M. Ursey, D. J. Walls: Structure-based carbon nanotube sorting by sequence-dependent DNA assembly, Science **302**, 1545 (2003) 553

[107] D. A. Heller, E. S. Jeng, T. K. Yeung, B. M. Martinez, A. E. Moll, J. B. Gastala, M. S. Strano: Optical detection of DNA conformational polymorphism on single-walled carbon nanotubes, Science **311**, 508 (2006) 553

[108] J.-C. Charlier, M. Terrones, M. Baxendale, V. Meunier, T. Zacharia, N. L. Rupesinghe, W. K. Hsu, N. Grobert, H. Terrones, G. A. J. Amaratunga: Enhanced electron field emission in B-doped carbon nanotubes, Nano Lett. **2**, 1191 (2002) 553

[109] M. Doytcheva, M. Kaiser, M. Reyes-Reyes, M. Terrones, N. de Jonge: Electron emission from individual nitrogen-doped multi-walled carbon nanotubes, Chem. Phys. Lett. **396**, 126 (2004) 553

[110] M. Endo, Y. A. Kim, T. Hayashi, K. Nishimura, T. Matusita, K. Miyashita, M. S. Dresselhaus: Vapor-grown carbon fibers (VGCFs) – Basic properties and their battery applications, Carbon **39**, 1287 (2001) 553

[111] D. Y. Zhang, G. Y. Zhang, S. Liu, E. G. Wang, Q. Wang, H. Li, X. J. Huang: Lithium storage in polymerized carbon nitride nanobells, Appl. Phys. Lett. **79**, 3500 (2001) 553

[112] J. Kong, N. R. Franklin, C. W. Zhou, M. G. Chapline, S. Peng, K. J. Cho, H. J. Dai: Nanotube molecular wires as chemical sensors, Science **287**, 622–625 (2000) 554

[113] S. S. Wong, E. Joselevich, A. T. Woolley, C. L. Cheung, C. M. Lieber: Covalently functionalized nanotubes as nanometre-sized probes in chemistry and biology, Nature **394**, 52–55 (1998) 554

[114] P. Collins, K. Bradley, M. Ishigami, A. Zettl: Extreme oxygen sensitivity of electronic properties of carbon nanotubes, Science **287**, 1801–1804 (2000) 554

[115] F. Villalpando-Páez, A. H. Romero, E. Munoz-Sandoval, L. M. Martinez, H. Terrones, M. Terrones: Fabrication of vapor and gas sensors using films of aligned CN_x nanotubes, Chem. Phys. Lett. **386**, 137 (2004) 554

[116] P. Calvert: Nanotube composites – a recipe for strength, Nature **399**, 210 (1999) 554

[117] A. Eitan, L. S. Schadler, J. Hansen, P. M. Ajayan, R. W. Siegel, M. Terrones, N. Grobert, M. Reyes-Reyes, M. Mayne, H. Terrones: Processing and thermal characterization of nitrogen doped MWNT/epoxy composites, in *Proc. Tenth US–Japan Conf. Compos. Mater.* (2002) pp. 634–640 554

[118] B. Fragneaud, K. Masenelli-Varlot, A. González-Montiel, M. Terrones, J. Y. Cavaillé: Efficient coating of N-doped carbon nanotubes with polystayrene using atomic transfer radical polymerization, Chem. Phys. Lett. **419**, 567 (2005) 554

[119] M. Dehonor, K. Masenelli-Varlot, A. González-Montiel, C. Gauthier, J. Y. Cavaillé, H. Terrones, M. Terrones: Nanotube brushes: Polystyrene grafted covalently on CN_x nanotubes by nitroxide-mediated radical polymerization, Chem. Commun. **42**, 5349 (2005) 554

[120] B. Fragneaud, K. Masenelli-Varlot, A. González-Montiel, M. Terrones, J.-Y. Cavaillé: Electrical behavior of polymer grafted nanotubes/polymer nanocomposites using N-doped carbon nanotubes, Chem. Phys. Lett. **444**, 1 (2007) 554
[121] D. M. Guldi, M. Marcaccio, D. Paolucci, F. Paolucci, M. Tagmatarchis, D. Tasis, E. Vasquez, M. Prato: Angew. Chem. Int. Ed. **42**, 4206 (2003) 554
[122] K. Jiang, L. S. Schadler, R. W. Siegel, X. J. Zhang, H. F. Zhang, M. Terrones: Protein immobilization on carbon nanotubes via a two-step process of diimide-activated amidation, J. Mater. Chem. **14**, 37 (2004) 554, 555
[123] K. Jiang, A. Eitan, L. S. Schadler, P. M. Ajayan, R. W. Siegel, N. Grobert, M. Mayne, M. Reyes-Reyes, H. Terrones, M. Terrones: Selective attachment of gold nanoparticies to nitrogen-doped carbon nanotubes, Nano Lett. **3**, 275 (2003) 554, 555
[124] A. Zamudio, A. L. Elías, J. A. Rodríguez-Manzo, F. López-Urías, G. Rodríguez-Gattorno, F. Lupo, M. Rühle, D. J. Smith, H. Terrones, D. Díaz, M. Terrones: Efficient anchoring of silver nanoparticles on N-doped carbon nanotubes, Small **2**, 346 (2005) 554
[125] X. Lepró, Y. Vega-Cantú, F. J. Rodríguez-Macías, Y. Bando, D. Golberg, M. Terrones: Production and characterization of co-axial nanotube junctions and networks of CNx/CNT, Nano Letters **7**, 2220 (2007) 554
[126] J. L. Carrero-Sánchez, A. L. Elías, R. Mancilla, G. Arellín, H. Terrones, J. P. Laclette, M. Terrones: Biocompatibility and toxicological studies of carbon nanotubes doped with nitrogen, Nano Lett. **6**, 1609 (2006) 555
[127] D. B. Warheit, B. R. Laurence, K. L. Reed, D. H. Roach, G. A. M. Reynolds, T. R. Webb: Comparative pulmonary toxicity assessment of single-wall carbon nanotubes in rats, Toxicol. Sci. **77**, 117 (2004) 555
[128] A. L. Elias, J. Carrero-Sánchez, H. Terrones, M. Endo, J. Laclette, M. Terrones: Comparative viability studies of pure carbon and nitrogen-doped multi walled carbon nanotube with amoeba cells: From amoebicidal to biocompatible structures, Small **3**, 1723 (2007) 555

Index

Double-Wall Carbon Nanotubes

Rudolf Pfeiffer[1], Thomas Pichler[2], Yoong Ahm Kim[3], and Hans Kuzmany[1]

[1] Faculty of Physics, University of Vienna, Austria
rudolf.pfeiffer@univie.ac.at
hans.kuzmany@univie.ac.at
[2] Institut für Festkörperphysik und Werkstoffforschung, Dresden, Germany
t.pichler@ifw-dresden.de
[3] Faculty of Engineering, Shinshu University, Nagano, Japan
yak@endomoribu.shinshu-u.ac.jp

Abstract. Double-wall carbon nanotubes (DWNTs) are the simplest archetypical manifestation of MWNTs and as such combine the outstanding properties of SWNTs with the possibility to study concentric intertube interactions with high precision. Two complementary routes for the efficient growth of DWNTs are discussed. Firstly, SWNTs filled with various carbon sources, such as fullerenes or acenes can form inner-shell tubes by a high-temperature treatment under clean-room conditions. Inner–outer tube pairs can be identified with a well-defined mutual chirality. Isotope labeling and full isotope substitution is possible. Using different carbon sources, DWNTs with intrinsic functionality and special electronic and magnetic properties can be grown. Alternatively, a direct growth using chemical vapor deposition and subsequent purification is described. Large-scale growth of very long continuous DWNTs for application in composites and as advanced field emission sources are straightforward for this technique. The two techniques for growth of DWNTs are evaluated with respect to their scientific novelty and application potential. Stability, electronic structure, transport and mechanical properties are reviewed.

1 Introduction

Double-wall carbon nanotubes (DWNTs), being the simplest example of MWNTs, provide the ideal model for studying the influence of interlayer interaction on the physical and chemical properties of nanotube systems. The DWNTs have several advantages over simple SWNTs. In general, they exhibit higher stability, which can be a substantial help in high-current and high-field experiments as, e.g., in field emission applications. The small diameters of the inner tubes enable the study of high-curvature effects. The characteristic geometry of the systems allows growth of heterotubes, e.g., a boron-nitride tube outside and a carbon nanotube inside [1], or a ^{12}C tube outside and a ^{13}C tube inside [2]. The higher stiffness combined with a small diameter provide an advantage if used as a mechanical sensor. The concentric nature of the system suggests its use for nanoscale machines [3]. Finally, independent doping or functionalization of inner and outer tubes is possible. In detail semiconductor@metallic tubes or metallic@semiconductor tubes can

A. Jorio, G. Dresselhaus, M. S. Dresselhaus (Eds.): Carbon Nanotubes,
Topics Appl. Physics **111**, 495–530 (2008)

be expected. The latter represent a molecular wire covered by an insulator for use as connectors in nanoelectronic systems or as a molecular capacitor in memory devices.

Calculations [4] demonstrated that the interlayer distance between the inner and outer tubes of the DWNT can vary from 0.33 to 0.41 nm, which is quite different from that of the normal MWNTs (0.34 nm). Since the interlayer interaction between adjacent layers is very weak, but depends on the relative (n, m) values of the two constituent tubes, the ease and direction of the intertube sliding motion were expected to depend on the chirality of the constituent layers [5].

With respect to electronic structure the electron transport in incommensurate MWNTs can be either diffusive, ballistic, or intermediate between them [6]. Calculations on the conductance of very long clean incommensurate DWNTs based on the Landauer formula were reported [7] and revealed that the quantized conductance of $1G_0$ [$G_0 = 2e^2/h \approx 1/(12.9\,\mathrm{k\Omega})$] in the very low voltage range could be retained for tube lengths up to about 10 µm.

Generally, there are three different ways to prepare DWNTs: arc discharge, a catalytic chemical vapor deposition (CCVD) process, and thermal treatment of precursor systems where a carbon source, in general C_{60} fullerenes, is encapsulated into SWNTs.

1.1 Fingerprints of Double-Wall Carbon Nanotubes

Like for all other forms of carbon nanophases, high-resolution transmission electron microscopy (HRTEM) is a crucial technique to detect and identify DWNTs. Figure 1a depicts an example of an individual and some bundled DWNTs. The analysis of such images allows us to determine the diameters and the wall-to-wall distance in these tube systems.

On the other hand, HRTEM requires a very careful sample preparation and is highly selective of local areas (see contribution by *Jorio* et al.). Therefore, for general materials characterization, high-resolution Raman scattering of the radial breathing mode (RBM) has proven to be an excellent method to identify the structure and concentration of DWNTs, at least in a qualitative manner. Since the RBM frequency scales inversely to the tube diameter (see contribution by *Saito* et al.), the response of the inner-shell tubes in the DWNTs system appears as a set of sharp lines just above the RBM response of the outer-shell tubes (see Sect. 3.2). Such spectra were first reported by *Bandow* et al. [9]. An example is depicted in Fig. 1b. The Raman signature of the inner-tube RBMs is now widely used to check for the successful growth of the DWNTs.

2 Preparation of Double-Wall Carbon Nanotubes

Besides the arc-discharge process there are two mainly used and basically different possibilities to grow DWNTs. From a historical point of view the first

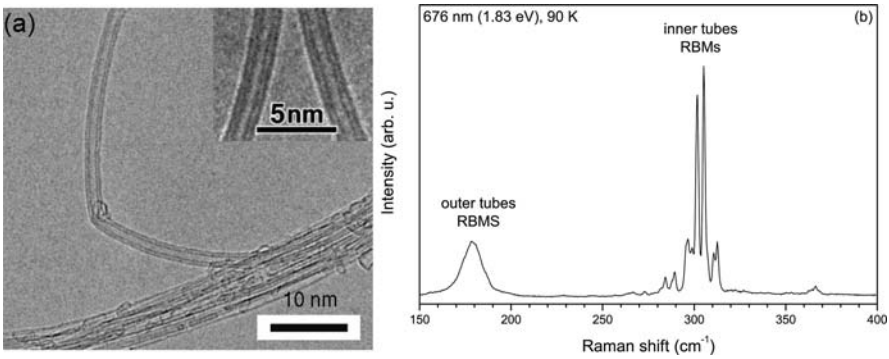

Fig. 1. (**a**) High-resolution TEM of DWNTs grown from fullerene peapods [8] and (**b**) Raman response of DWNTs after transformation of C_{60} peapods at 1250 °C. The *insert* in (a) is adapted from [9]

technique was based on a precursor material consisting of C_{60} fullerenes that were filled into opened tubes, or were there incidentally from the growth process [10]. More generally, this route has now been demonstrated to work with several carbon-rich fillers such as higher fullerenes, ferrocene, anthracene, or even toluene. This method has the advantage of providing very clean DWNTs except for some SWNTs where the filler material could not enter. However, due to the limited carbon supply on the inside, one inner tube cannot fill the whole outer tube.

The other route to DWNTs uses a CCVD process. From this process a very high yield and large-scale DWNTs could be obtained recently by specific tuning of the growth parameters [11].

2.1 DWNT Growth from Chemical Vapor Deposition

The currently adopted method to synthesize carbon nanotubes is by a catalytic decomposition of hydrocarbons using nanometer-size catalytic metals. When compared to the arc-discharge and laser-ablation methods, the CVD technique is a very controllable and cost-effective technique [12]. A description of this growth technique and its advantages is given in contribution by *Joselevich* et al.

To our knowledge, *Hafner* et al. [11] were the first to produce DWNTs intentionally as the main growth product using this technique. Specifically, they synthesized a mixture of SWNTs and DWNTs by the catalytic decomposition of C_2H_4 at 700–850 °C over Mo- and Fe/Mo-Al_2O_3 catalysts, and reported that the DWNT proportion increased from 30 % at 700 °C to 70 % at 850 °C. Porous materials have been utilized to prepare small-sized metal particles for growing nanotubes with the CVD technique because the nanopores in support materials could hold a homogeneous dispersion of metal particles

during nanotube growth, resulting in a more homogeneous nanotube diameter. *Colomer* et al. [13] reported the synthesis of well-crystallized DWNT bundles forming rings by reducing a $Mg_{0.9}Co_{0.1}O$ solid solution in an H_2:CH_4 atmosphere at 1000 °C. In addition, many groups [14–20] have used MgO as a support material for the DWNT growth, because MgO is easily removed by hydrochloric acid treatment. *Cumings* et al. [21] used fumed alumina as a support material by flowing methane at 900 °C for 10 min. In contrast, the *Shinohara* group has utilized zeolites [22] and mesoporous silica [23] as support materials for obtaining DWNTs using the CVD technique. Similarly, *Zhu* et al. [24] synthesized DWNTs using a Fe/Co metal catalyst and a mesoporous silica support material. Very recently, *Yamada* et al. [25] reported the fabrication of a high-purity DWNT forest by controlling the catalyst Fe film thickness via a water-assisted CVD technique. Unfortunately, according to these reports usually mixtures of DWNTs and SWNTs are generated, in addition to metal particles, amorphous carbon and multilayered carbon nanotubes.

Recently, *Endo* et al. [26] reported the fabrication of highly purified DWNTs through an optimized combination of a catalytic CVD method with an optimized two-step purification process. The synthesis of DWNTs was carried out by a catalytic chemical vapor deposition method utilizing a conditioning catalyst (Mo/Al_2O_3) at one end of the furnace, and the nanotube catalyst (Fe/MgO) in the middle part of the furnace. Subsequently, a CH_4:Ar (1 : 1) mixture was fed into the reactor typically for 10 min at 875 °C [26]. Subsequently, in order to obtain high-purity DWNTs, a purification process was applied to synthesize these products. Firstly, an oxidation process (500 °C, 20 min) was carried out to reduce the amount of the chemically active SWNTs. Secondly, a hydrochloric acid (18 %, 100 °C, 10 h) treatment was carried out in order to remove magnesium oxide and iron catalysts, followed by air oxidation at 500 °C for 10 min in order to remove carbonaceous impurities. Based on a detailed in-situ Raman study, *Osswald* et al. [27, 28] very recently confirmed that the optimized oxidative conditions for obtaining high-purity and crystalline DWNTs was via a complete removal of amorphous deposited carbon and defective MWNTs using a temperature above 480 °C. Magnetic susceptibility studies confirmed the high DWNT sample purity through their diamagnetic behavior. In addition, detailed high-resolution TEM images confirmed the high yield of DWNTs (above 95 %) in bundles and, furthermore, with relatively homogeneous and small-sized inner tubes of mainly ca. 0.9 nm diameter and outer diameters of ca. 1.5 nm (see diameter distribution of high-purity DWNTs in Fig. 2).

Figure 3 shows Raman spectra in the low-frequency (RBM), and high-frequency (tangential G-band mode) ranges, respectively. The low-frequency Raman spectra confirm the presence of inner tubes from the Raman response around 260 cm^{-1}. The disappearance of RBMs assigned to SWNTs (see short arrows around 180, 210 and 240 cm^{-1} in Fig. 3a) after purification indicates the effective removal of chemically active (small-diameter) SWNTs.

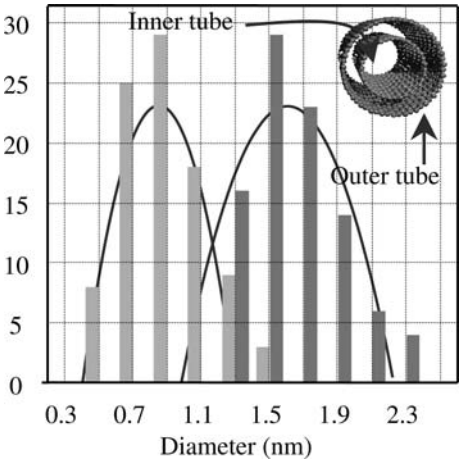

Fig. 2. Diameter distribution of highly purified DWNTs based on detailed high-resolution transmission electron microscope observations [26]

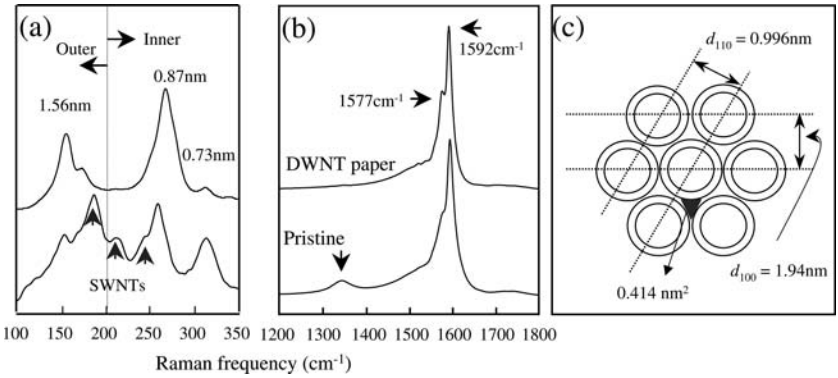

Fig. 3. (**a**) The low-frequency and (**b**) high-frequency Raman spectra for as-grown and purified DWNTs, respectively as excited by a 532 nm laser. (**c**) Schematic stacking model of the bundled DWNTs from their X-ray diffraction pattern [26]

In addition, the effective removal of deposited carbon on the outer surface of carbon nanotubes is confirmed from the greatly reduced intensity of the D-band (defect-induced, double-resonance Raman scattering feature [29]), as shown in Fig. 3b. It is noteworthy that the D-band for DWNTs is negligible in the Raman spectra. The DWNTs exhibit well-developed (100) and (110) diffraction lines from X-ray diffraction (XRD) measurements, which indicates a high crystallinity (see Fig. 3c). The numbers in Fig. 3a indicate the calculated tube diameters using the equation $\omega_{\mathrm{RBM}} = 218.3/d_{\mathrm{t}} + 15.9$, where d_{t} is the tube diameter (nm) and ω_{RBM} is the RBM frequency (cm^{-1}) [30]. For 532-nm laser excitation, the E_{33}^{S} transition energy of the semiconducting outer tubes (1.41 and 1.56 nm), the E_{11}^{M} of the metallic inner tubes (0.9 nm)

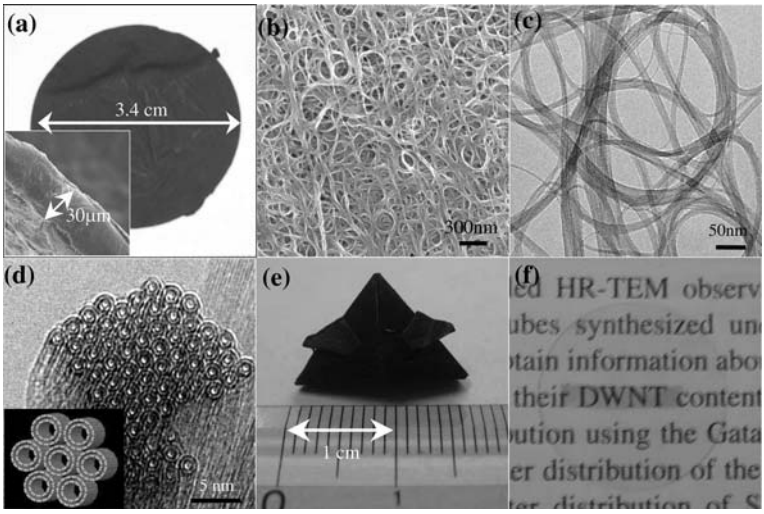

Fig. 4. (**a**) Photographs of round and thin DWNT-derived buckypaper (*inset*, thickness is approximately 30 μm). (**b**) Low-resolution transmission electron microscope and (**c**) field emission electron microscope images indicate a bundled structure. (**d**) Cross-sectional high-resolution TEM image of a bundle of DWNTs. (The *inset* is its schematic model with two concentric shells regularly packed in a hexagonal array). (**e**) DWNT-derived buckypaper is flexible and mechanically strong and (**f**) semitransparent

and the E_{22}^{S} of the semiconducting inner tubes (0.76 nm) all match resonance with E_{laser} well.

Nanosized carbon nanotubes have a high tendency toward self-aggregation due to strong van der Waals forces. By utilizing this intrinsic property of carbon nanotubes, paper-like sheets (so-called buckypaper) were easily fabricated from carbon nanotubes dispersed in solution [31]. This holds also for DWNTs. At first, a stable suspension of DWNTs was prepared with the help of ultrasonication (30 min) but without any surfactant. The preparation without surfactant is very important for fabricating high-purity buckypaper. Then, by very carefully pouring a stable suspension of nanotubes into a PTFE filter-attached funnel, very thin (ca. 30 μm), round (diameter = 3.4 cm), (light-weight mass = ca. 15 mg) and black buckypaper was produced (see Fig. 4a). As expected, buckypaper is the result of the physical entanglement of DWNT bundles (10–30 nm) (Fig. 4b). From the cross-sectional HRTEM image (Fig. 4d), these tubes consist of two relatively round, small and homogeneous-sized (below 2 nm in the outer shell) concentric individual tubules. Furthermore, these coaxial tubes are packed in a hexagonal array. This DWNT buckypaper is highly flexible and is mechanically strong (see Fig. 4e). The high structural integrity in DWNT-derived buckypapers is thought to be derived mainly from their long lengths (up to μm), because

the longer the tubes, the greater is the mechanical robustness of the intermingled bundle. Also, semitransparent films (see Fig. 4f) can be fabricated by utilizing a very small amount of DWNTs.

2.2 DWNT Growth from Precursor Material

Historically, the first demonstration of DWNT growth was from C_{60} peapods under intensive electron radiation in a TEM [32]. Subsequently, *Smith* and *Luzzi* [33] and especially *Bandow* et al. [9] demonstrated how C_{60} peapods can be transformed into DWNTs in macroscopic amounts by annealing at temperatures of around 1000 °C. Such transformations can be performed at temperatures as low as 800 °C but the transformation takes literally weeks in this case [9]. Since these first experiments, C_{60} and also higher fullerenes@SWNTs are very frequently used as a precursor to prepare DWNTs, whereas other precursors such as ferrocene or anthracene were used only recently.

2.2.1 DWNT Growth from Fullerene Peapods

C_{60} can be filled into the nanotubes either from the gas phase [34] or from solution [35, 36] after the tubes were opened by mild oxidation in air. A high degree of filling can be obtained, as determined from electron energy-loss spectroscopy on the C_{1s} edge. The matrix element weighted density of states of the conduction band yields the bulk filling factor by comparing the C_{60} and the SWNTs density of states [37]. Alternatively, the relative Raman intensity of the pentagonal pinch – or $A_g(2)$ – mode of the encapsulated fullerenes at $1465\,cm^{-1}$ to the G^+ mode of the tubes at $1590\,cm^{-1}$ can be used as a signature for the filling. For 1.4 nm tubes and 488 nm laser excitation, this ratio is 0.004 for 60 % filling [38]. Substantial tube filling can be obtained down to a tube diameter of 1.2 nm [39]. Figure 5 depicts Raman spectra of the pristine SWNTs, of nanotubes after filling with C_{60} and of the system after transformation at 1250 °C to DWNTs. In the latter spectra the response from the inner-shell RBMs is clearly visible.

To unravel details one has to study the intermediate stages of the inner-tube growth, together with the decay – or modulation – of the precursor molecules. The latter can be studied by the decrease of the $A_g(2)$ mode with heating time. From such measurements the half-lifetime of the unmodulated fullerenes at 1250 °C annealing was observed to be only 2.9 ± 0.5 min [41].

C_{60} fullerenes are arranged in the tubes periodically in a 1D linear chain. This periodicity is best observed by XRD. Figure 6a depicts the XRD patterns after various exposure times at 1250 °C. The intrinsically asymmetric peak around $q \approx 6.6\,nm^{-1}$ is the fingerprint of the 1D chain. The half-lifetime of the chain was evaluated as 14 ± 2 min, which is almost five times longer than the decay of the fullerenes [41]. Thus, the fullerenes transform into an intermediate phase, which has the same periodicity as the starting molecules.

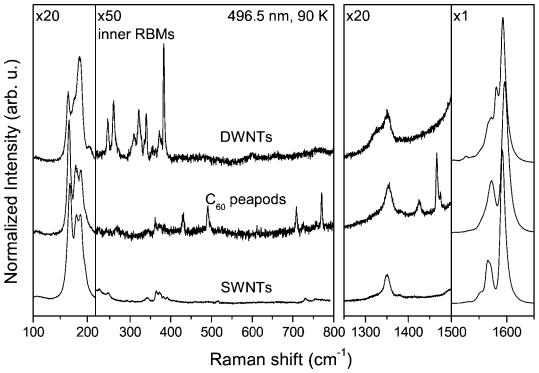

Fig. 5. Raman spectra of pristine SWNTs (*bottom*), C_{60} peapods (*center*), and DWNTs (*top*); after [40]

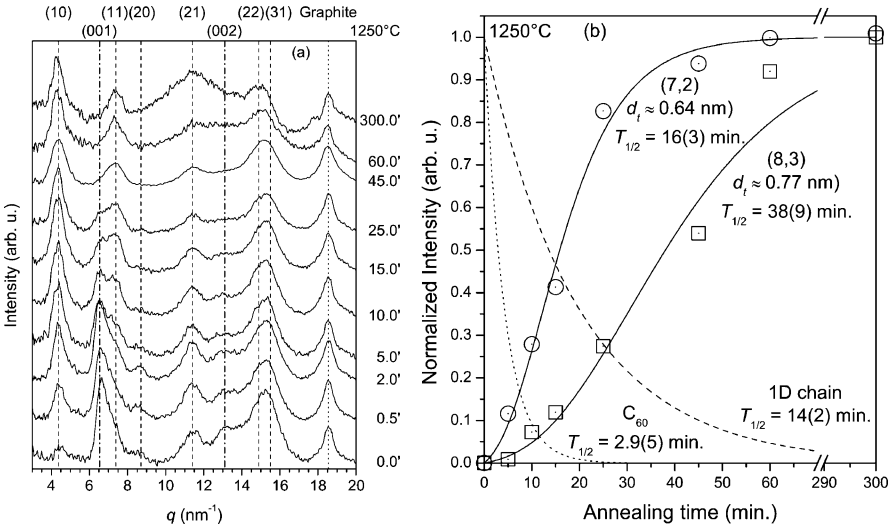

Fig. 6. (**a**) X-ray diffraction pattern as recorded after various exposure times of peapod samples at 1250 °C. (**b**) The decay of the C_{60} pentagonal-pinch mode (*dotted*), the decay of the periodic structure observed by X-ray diffraction (*dashed*) and the relative increase of the Raman response from the $(7, 2)$ and $(8, 3)$ inner-shell tubes; adapted from [41]

This rules out the possibility that the fullerenes decay into small parts, e.g., C_2 units, from which the inner tubes grow.

The growth of the inner tubes can be monitored by the intensity of their RBM response [42, 43]. The volume fraction of a tube follows an S-shaped curve with time. Figure 6b compares such growth curves for the $(7, 2)$ and

(8, 3) inner tubes, which can be observed simultaneously with 676-nm laser excitation. The (7, 2) tube ($d_t \approx 0.64$ nm) grows to half of its maximum volume fraction in 16 min. For the (8, 3) tube ($d_t \approx 0.77$ nm) it takes about twice as long to reach half of its maximum volume fraction. For tubes with diameters between the (7, 2) and (8, 3) tubes, the growth curves are similar and the growth half-times depend primarily on the inner-tube diameter. The growth of the (7, 2) tube corresponds reasonably well to the decay of the 1D chain inside the tubes but the growth rate of the (8, 3) tube is much lower than the decay of the 1D chain [41]. The time gap between the disappearance of the C_{60} modes and the appearance of the tube modes indicates the existence of an intermediate phase that is unobserved in the Raman spectra.

The transformation of peapods into DWNTs is usually done in a dynamic or static vacuum. *Fujita* et al. [44] performed transformation experiments at 1100 °C in inert-gas environments at pressures of about 1 mbar. Remarkably, the inner-tube formation is accelerated in Ar and especially in He atmospheres by more than a factor of 5. However, in a H_2 atmosphere there was equal if not less growth than in vacuum [45].

2.2.2 DWNT Growth from Ferrocene

Recently, the growth of DWNTs from other precursor structures was reported. Most spectacular is the growth from catalytic particles derived from metallocenes that were filled into the tubes. Transformation to DWNTs can be performed at temperatures as low as 600 °C [46–48]. An especially interesting system is ferrocene@SWNTs [48, 49] where the ferrocene ($FeCp_2$) can act both as catalyst and carbon source [50].

In a recent study by *Shiozawa* et al. [49] the different steps of the temperature-driven chemical reaction inside $FeCp_2$-filled SWNTs upon the formation of inner tubes were traced and analyzed by Raman spectroscopy and photoemission (PE). Detailed information was obtained from a comparison to the growth from noncatalytic C_{60} precursors. One difference between the two systems regards the charge transfer to the outer-wall tube. The shift of the van Hove singularities in the valence band as observed by He I ultraviolet PE can be used to determine this shift accurately. Whereas for pristine C_{60} peapods no charge transfer is observed [51], a small but significant charge transfer of about 0.19 electrons per ferrocene and a shift of the Fermi level by about 0.1 eV towards the conduction band was measured for the ferrocene system. This is consistent with a charge transfer of 0.35–0.55 electrons predicted for cobaltocene using LDA methods [52]. In addition, the bulk filling factor of SWNTs with 1.4 nm mean diameter, as analyzed by the relative carbon to iron PE intensity, is only 12 % in the case of ferrocene filling and is thus significantly lower than the 78 % [37] achieved for the C_{60} filling.

The second difference concerns the DWNT growth. The catalytic growth from the $FeCp_2$ precursor was observed at temperatures as high as 1150 °C and down to 600 °C. The charge transfer between the inner and outer tubes

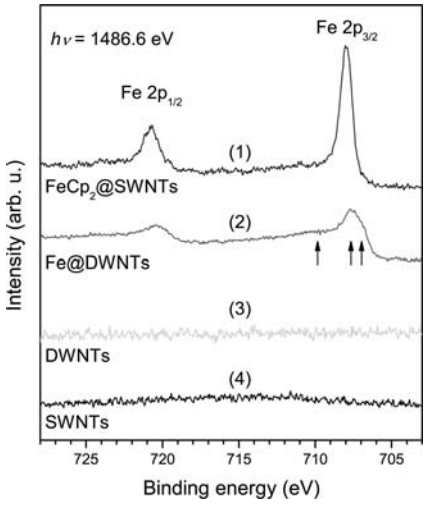

Fig. 7. (**1**) XPS response of ferrocene filled into SWNTs, (**2**) after the system was transformed to DWNTs at 600 °C, and (**3**) after heating the filled tubes for 2 h at 1150 °C. Spectrum (**4**) is for pristine SWNTs; adapted from [49]

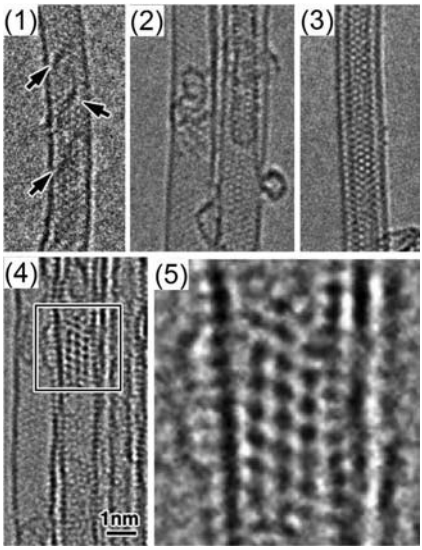

Fig. 8. HRTEM of (**1**) ferrocene in the tubes, (**2**) growing inner-shell tubes, (**3**) DWNTs grown at 1150 °C, (**4**) Fe_3C nanoparticle, and (**5**) blow up of the particle pattern; adapted from [49]

depends critically on the reaction time and reaction temperature. When the reaction takes place at 600 °C for 2 h a charge transfer leading to an upshift of the Fermi level of about 0.05 eV is observed. On the other hand, for the high-temperature reaction at 1150 °C no charge transfer is observed, as in the case of the peapod precursor.

More information is obtained from X-ray PE (XPS). Examples are depicted in Fig. 7. The XPS pattern of ferrocene inside the tubes is almost the same as for free iron. After the first two hours annealing at 600 °C the

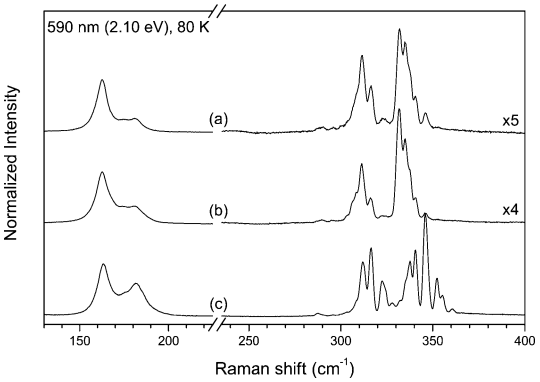

Fig. 9. Raman spectra of the radial breathing mode for DWNTs as excited with 590-nm laser radiation. Ferrocene-derived DWNTs after transformation at (**a**) 1150 °C and (**b**) 600 °C, respectively. (**c**) Peapod-derived DWNTs after transformation at 1150 °C. The SWNT starting material was the same in all cases; adapted from [49]

Fe $2p_{3/2}$ peak is upshifted and broken up into three structures indicated by arrows in Fig. 7. This obviously reflects a significant change in the chemical environment of the iron atoms and is a clear sign of the decomposition of the ferrocene inside the SWNTs. HRTEM identified a staggered structure of the ferrocene in the tubes as depicted in Fig. 8(1). By heat treatment, the inner tubes grow and eventually develop the DWNTs structure [Fig. 8(2),(3)]. The iron was observed to reassemble as Fe_3C, as depicted in Fig. 8(4,5). In contrast to the transformation at 600 °C the Fe is completely released from the tubes for transformation at 1150 °C as demonstrated in Fig. 7(3).

The third difference was observed regarding the RBM Raman pattern of the inner tubes thus produced. Results are depicted in Fig. 9. After vacuum annealing and successful transformation to DWNTs the response from the inner-shell tubes appears as sharp lines in the range of 305–360 cm^{-1} that can be assigned to the RBM signals mainly from the $(6, 4)$ and $(6, 5)$ inner tubes. Line positions and line intensities are almost independent of transition temperature. Interestingly, as compared to the samples using a fullerene precursor, there is a distinct difference in the pattern of the inner tubes. Although the line positions are exactly the same in both cases, the intensity distribution of the lines is different. In the case of fullerene-grown inner tubes, the line pattern is upshifted to higher frequencies or smaller interwall distances. This means the growth mechanism is the same for the catalytic growth at any temperature but different from the noncatalytic fullerene-controlled growth. Additionally, for the growth from ferrocene precursors, RBM lines with frequencies as high as 465 cm^{-1} of much smaller inner tubes were observed. This corresponds to $(6, 0)$ and $(4, 3)$ tubes with diameters around 0.485 nm. Using a typical van der Waals distance of 0.34 nm as an intratube distance for the

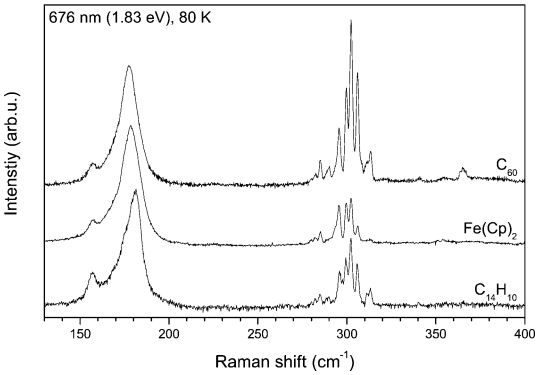

Fig. 10. RBM Raman response from double-wall carbon nanotubes as grown from anthracene-filled tubes (*bottom*) in comparison to tubes filled with ferrocene (*center*) and C_{60} (*top*)

DWNTs, the outer-tube diameter filled with the ferrocene is estimated to be as small as 1.165 nm, which is much smaller than for the C_{60} peapods [37].

The characteristically different line distributions suggest two significantly different growth mechanisms. For ferrocene-based inner-tube growth, the presence of the Fe_3C nanocrystals suggests that these particles act as a catalyst, at the moderate temperature the ferrocene decomposes and Fe_3C nanocrystals grow. The liberated carbon particles dissolve in the carbide and eventually precipitate from there to form the inner-shell tube. Since in this process each inner tube is grown from scratch, the diameter can be well adapted to the outer-tube diameter and an optimum diameter difference can be established. In contrast, in the case of the growth of inner tubes from fullerenes, caps are already available and they apparently have a strong influence on the diameter of the eventually grown inner tubes.

2.2.3 DWNT Growth from Other Carbon Precursors

It was certainly interesting to see whether DWNTs can also be grown from other precursor systems that contain neither catalytic particles nor preformed cap structures. Small hydrocarbon molecules could be filled into the tubes but were shown to escape during the process of transformation to DWNTs. On the other hand, the carbons of toluene were shown from isotope-substitution experiments to enter the inner-tube walls if the toluene was filled into the tubes simultaneously with C_{60} [53]. Explicit transformation to DWNTs was demonstrated for anthracene as depicted in Fig. 10. The concentration of the inner-shell tubes is comparable to the concentration of the ferrocene-grown tubes but exhibits the line pattern of the peapod-grown tubes.

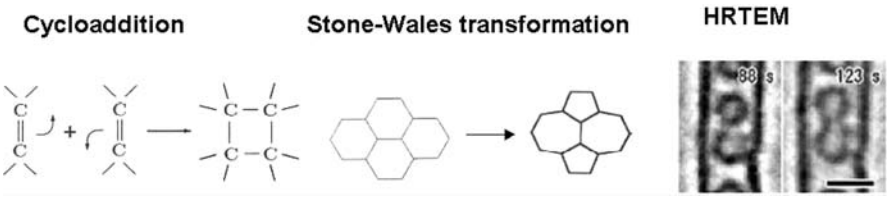

Fig. 11. Bond-breaking schemes for the cycloaddition process and for the Stone–Wales transformation. *Right panel:* HRTEM images of a coalescence of two C_{60} cages to form a short C_{120} tube; adapted from [55]

2.2.4 Theoretical Models for the Fullerene Coalescence

Since the very recent XRD [41] and ^{13}C Raman experiments [54] rule out a growth model where the fullerenes are first disintegrated into small carbon particles, we will only review the coalescence model.

A large number of calculations have been performed on levels extending from simple molecular dynamics using Brenner potentials to sophisticated *ab-initio* procedures. Two basic concepts are involved in these calculations: the cycloaddition process (CA) and the Stone–Wales (SW) transformation. Both processes involve covalent-bond breaking as depicted in Fig. 11 and are therefore very energy expensive.

Whereas the CA is very well known and plays a crucial role in the formation of fullerene polymer generation, the SW transformation has not been observed explicitly in experiments, even though it is assumed to play the fundamental role in the fullerene coalescence. The CA has been observed in fullerenes under high pressure at moderate temperatures, by photoexcitation, or in fullerene charge-transfer systems. Since the tetraphenyl configuration is not very temperature stable, this configuration can only be an intermediate state in the coalescence process. In contrast, the SW transformation enables the adjustment from an initial seed with a highly necked structure to the final perfect inner-shell tube.

The SW is established by a $\pi/2$ rotation of a covalent bond in the hexagonal lattice. Thus, it transforms four fused hexagons into a pair of fused pentagons and heptagons. Conceptually this configuration represents a dislocation dipole. Each of the two dislocations consist of a 5/7 defect on the rolled-up graphene sheet. The heptagons enable the concave curvatures on the necking transitions during the fullerene coalescence. The fusion process between two (or more) fullerenes is exothermic but it needs to overcome a set of energy barriers provided by the SW transformations. Each barrier is about 5 eV high. Thus, a simple bond rotation can not be activated at the temperatures of the DWNT growth. It may be collective processes that enable the SW transformation. By molecular dynamical calculations it was explicitly demonstrated that two C_{60} fullerenes can be fused to a C_{120} fullerene

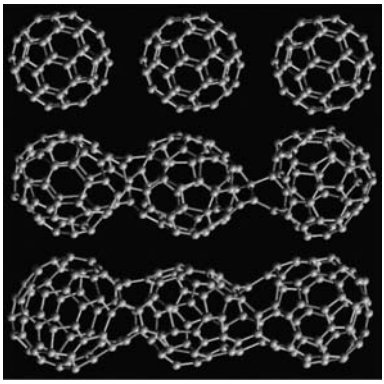

Fig. 12. Structures of intermediate phases during the fullerene coalescence inside SWNTs as obtained from calculations for constant carbon content; adapted from [57]

or a very short $(5, 5)$ tube by an initial CA and 20 subsequent SW transformations [56]. Experimentally, this coalescence process was demonstrated by HRTEM, as depicted in Fig. 11.

Even more important, the existence of a coalescence process for an extended set of fullerenes was demonstrated recently from *ab-initio* calculations [57]. The calculations exhibit explicitly intermediate phases consisting of necked tubular structures. The periodicity of such structures remains the same as the periodicity of the linear chains in the original peapod material. A result of such behavior is depicted in Fig. 12. The conservation of periodicity is fully consistent with the experimental results depicted in Fig. 6. Only if one or several C_2 units are expelled from the fullerenes is the periodicity reduced.

3 Properties and Applications of DWNTs

As already mentioned in the introduction, the tube–tube interaction leads to a characteristic change of the electronic structure of the DWNTs. This interaction also determines the mechanical properties of the systems and gives rise to several interesting mechanical applications.

3.1 Electronic and Optical Properties, Transport

Since DWNTs consist of two concentric SWNTs their electronic and optical properties are strongly related to those of the participating SWNTs. However, the concentric tube–tube interaction modulates these properties regarding their dependence on the interwall distances. In addition and more seriously, the high curvature of the inner-shell tubes leads to considerable deviations from the properties known for conventional SWNTs due to a change in σ–π hybridization. Theoretical models as described below were developed to find the lowest interaction energy between concentric tubes with respect to their interwall distance and tube–tube orientation.

3.1.1 Model Calculations

As a consequence of the general incommensurability between the inner- and outer-shell tubes, the unit cells of the DWNTs can be very large. Thus, first-principles calculations, such as from DFT, can only be applied to selected tube pairs such as armchair–armchair or zigzag–zigzag tubes where commensurability is provided. In other cases, empirical potentials are used such as Lennard-Jones potentials for the intertube interaction and Brenner potentials or Tersoff potentials [58] for the covalent carbon–carbon interaction. Often, as for example in [5], the parameters for the covalent-bonding potentials are used as evaluated from first-principles calculations. Besides this, scaling parameters are still needed for the cutoff potentials and to better match experimental results for the sp^2 bond lengths. With this background, molecular dynamical calculations have been performed to obtain the interaction potentials, the total energies and eventually the stable state with respect to tube–tube pairing. In the above-cited work a minimum energy was observed for a wall-to-wall distance (WtWD) of 0.34 ± 0.01 nm with a rather flat shape and a minimum energy value of -35 meV/atom. There is almost no chirality dependence on the total energy. However, the orientation of the potential shape does depend on the relative chiral angle between the two tubes. In general, except for armchair and zigzag tubes, the potential shapes are inclined to the tube axis. This means that the easy or minimum friction motion has a longitudinal (translational) and circumferential (rotational) component.

From other calculations, barrier heights were evaluated to be 0.52 and 0.23 meV/atom [4]. These values were obtained for commensurate, i.e., armchair or zigzag pairs, respectively. For incommensurate pairs, even lower values on the order of 0.1 meV/atom were reported [59]. There is so far general agreement from several calculations and from some experiments (see below) that the WtWD in the DWNTs is slightly larger than the graphite interlayer distance (0.34 nm for HOPG, 0.35 nm for turbostratic graphite). This is attributed to the difference in the π-stacking interaction in the curved as compared to the planar structures.

In a more recent calculation, the dependence of the ground-state energy for DWNT pairs was explicitly formulated with respect to WtWD and chiral-angles $\theta_{1,2}$ or a chiral-angle difference $\Delta\theta$ [60]. Explicit relations are given for the ground-state energy and, in agreement with previous calculations, the dependence on chiral angles turned out to be weak.

The intertube interaction has interesting consequences on the electronic structure of DWNTs. Again, calculations can be performed at a first-principles level (like LDA in DFT) only for commensurate pairs. In some early work, *Okada* and *Oshiyama* [61] calculated ground-state energies for zigzag tubes $[(7,0),\ (8,0),\ (10,0)]$ in various outer zigzag tubes. Minimum ground-state energies were again found for WtWD to be slightly larger than the interlayer distance in graphite. For example, for a $(7,0)$ inner tube, the lowest energy was found for 0.35 nm WtWD for a $(16,0)$ outer tube. While the $(7,0)$ and

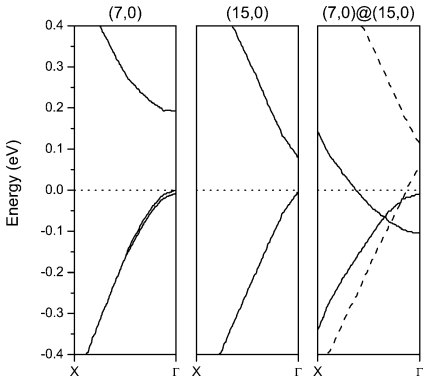

Fig. 13. Band structure of two SWNTs and the combined DWNT in high resolution; adapted from [63]. The *dashed bands* in the *right part* of the figure are derived from the outer-tube bands, while the *solid bands* are derived from the inner-tube bands

the $(16,0)$ tubes were semiconducting, the combination $(7,0)@(16,0)$ turned out to be metallic. This metallization was due to a difference in the downshifts of energy bands between the inner-shell and outer-shell tubes. Due to a stronger σ-π rehybridization, the inner tubes, in particular the π^*-band, exhibits a stronger downshift, leading eventually to a finite DOS at the Fermi level.

More recent calculations [62–64] confirmed these results. Figure 13 depicts electronic bands for $(7,0)$, $(15,0)$ and for $(7,0)@(15,0)$ close to the Fermi level. Both isolated tubes exhibit a gap that for $(15,0)$ is curvature induced. Due to different energy-level downshifts in the combination of the two tubes, the Fermi level is crossed by two bands. In this particular case the valence band and the conduction band from the inner tube become overlapping. The formation of the DWNTs is shown to be endothermic by 7.5 meV/atom but the WtWD was only 0.313 nm in the above case. A charge of 0.3 electrons/cell was transferred from $(15,0)$ to $(7,0)$. For larger WtWD, the different shifts of the inner tube π and π^* bands become weaker so that they no longer overlap. For larger-diameter inner tubes such as $(8,0)$, the downshift of the bands was smaller and did not lead to a metallic state. In [62] a similar result was obtained for the $(8,0)@(17,0)$ system, but for the $(7,0)@(16,0)$ DWNT a metallic state was reached. Using an intermolecular Hückel Hamiltonian a systematic charge transfer from the outer tubes to the inner tubes was observed for 65 different DWNTs.

The above results consistently show that intertube interactions drive the systems to a metallic state or at least noticeably reduce the gap energy. This is consistent with the experimentally observed metallization described below for the ^{13}C NMR experiments. On the other hand, it is also consistent with the downshift of the electronic transitions as described below for the resonance Raman scattering of the RBM of an inner tube within different outer tubes, as depicted in Fig. 14.

3.1.2 Experimental Results for Electronics and Structure

Experimental values for the WtWD were observed by HRTEM between 0.32 [65] and 0.42 nm [66]. The values given below for the Raman analysis of the inner-tube RBM are between 0.32 and 0.34 nm, which are slightly smaller than the calculated values. XRD from DWNT bundle samples revealed a WtWD of 0.36 ± 0.1 nm [67].

Electron diffraction provides another possibility to identify the two components of DWNTs, even with respect to chirality. This was first demonstrated by *Zuo* et al. [68] for a rather large DWNT system with inner- and outer-tube diameters of 3.33 and 4.04 nm, respectively. More recently, handedness was investigated by TEM electron diffraction [69]. In these experiments no correlation between the handedness of inner and outer tubes was found. In [70] and later in [71], an iterative method of image simulation was worked out to yield the individual chiralities of the two components in the DWNT. Results were obtained for tubes grown from the peapod and arc-discharge methods. A wide range of relative chiral angles between 0 and 60° was observed that supports the above-described theoretical results concerning the independence of the interaction potential from the chiral angles. The average WtWD was 0.365 ± 0.02 nm and 0.38 ± 0.035 nm for the peapod-grown DWNTs and for the laser-ablation-grown DWNTs, respectively. The smallest diameter DWNTs observed were $(15, 3)@(8, 0)$ with outer/inner-tube diameters of 1.31/0.68 nm.

In addition to the evaluation of the WtWD for the concentric tubes, in some cases also offcenter tubes were observed with a rather large asymmetry in the WtWD. WtWDs were also observed to change along the tube axis with a partly commensurate correlation between generally incommensurate tube pairs [71].

Photoluminescence is another important experimental tool to characterize carbon nanotubes. In a recent study by *Okazaki* et al. [72], photoluminescence quenching was reported for peapod-grown DWNTs. Reduced luminescence emission from either inner-shell or outer-shell tubes was observed as long as the diameters were large enough to enable filling with fullerenes. Since 100 % filling of nanotubes with fullerenes leads only to about 80 % filling of the tubes with inner-shell tubes the remaining unfilled part of the tubes contributed to the luminescence emission. Smaller tubes with diameters below 1.28 nm remained single wall and contributed fully to the emitted luminescence. On the other hand, photoluminescence from inner-shell tubes was reported for DWNTs grown by CVD [73]. However, luminescence from a small fraction of SWNTs in the samples could not be excluded in this case.

3.1.3 Transport

Electrical transport in MWNTs (see the contribution by Biercuk et al.) was often observed to occur only in the outermost shells and quantum conductance was reported. Therefore, once more DWNTs are appropriate model

materials. Since most DWNTs have an incommensurate structure, calculations have been concentrated on such systems. In [6] the distribution of the level spacings originating from the disordered structure was analyzed. Transport was found to be either diffusive, ballistic or intermediate, depending on the position of the Fermi level.

In a recent paper, *Chen* et al. [7] calculated the transport through several DWNTs with incommensurate structure. The conductance was found to depend on the position of the Fermi level and on the length of the tubes. For not too long tubes, the transport was ballistic and could be evaluated from the Landauer formula. Explicit results were given for the case of $(9,0)@(10,10)$. For short tubes $2G_0$ is the dominant conductance. With increasing tube length (up to 24.6 µm), more and more energy levels adopt a $1G_0$ transport. Finally, for tube lengths increasing to 36.9 µm almost all energy positions exhibit $1G_0$ and for some positions even nonballistic transport is obtained.

In DWNTs, only very few transport experiments were reported so far. In [74] tubes were deposited on a gold substrate and piezoelectrically moved to another gold electrode that was covered with a Hg droplet. The current as a function of the bias voltage was recorded. Before the transport experiment, electron diffraction was used to determine the inner-shell and outer-shell tube chiralities. The DWNT system discussed was $(51,34)@(53,43)$. For small voltages the I–V curve was linear, indicating a finite density of states at the Fermi level. For higher voltages the relation became nonlinear, probably as a consequence of additional transport channels being opened on the inner tubes.

More recently, transport experiments were carried out with the field-effect transistor (FET) geometry [75]. In this case, tube diameters were much smaller, of the order of 4 nm, but this is still considerably larger than diameters for conventional DWNTs. Pristine tubes of this type exhibited ambipolar conduction for a gate voltage range of −40 to 40 V. After filling the tubes with Cs atoms by a special plasma-irradiation process [76], only n-type FETs could be observed with on-off ratios in the source–drain current as high as 10^6. The filling level can be controlled by the acceleration voltage of the plasma and allowed to detect the continuous transition from an ambipolar to an n-type FET. At temperatures lower than 40 K, Coulomb-blockade oscillations determined the current profile.

3.2 Raman Scattering

Raman scattering is the main analytical tool to study structural bulk effects in DWNTs. Due to its proportionality to the inverse tube diameter, the RBM is particular attractive since the response from the inner-shell and from the outer-shell tubes is well separated in frequency. In contrast, the tangential modes of the two tubes overlap strongly unless very narrow inner tubes are considered [77]. The overtones, in particular the overtone of the D-band, are sensitive to small frequency shifts introduced by external disturbances.

3.2.1 The Nature of the Radial Breathing Mode Response

Comparing the RBM response of the same tubes once as inner tubes and once as bundled tubes (e.g., in a HiPco buckypaper) yields several interesting results. For the same excitation energy and frequency range, the HiPco spectra exhibit fewer peaks than the corresponding inner tubes. By considering a general shift of about $1\,\mathrm{cm}^{-1}$, one can assign some – but not all – of the inner-tube peaks to the HiPco peaks. In addition, the widths of the HiPco peaks are about $12\,\mathrm{cm}^{-1}$, whereas the inner-tubes peaks are more than a factor of 10 narrower. In fact, the intrinsic linewidth of the inner tubes can be as small as $0.4\,\mathrm{cm}^{-1}$ [78]. This indicates rather long phonon lifetimes and thus remarkably defect-free inner tubes. Hence, the outer tube can be regarded as providing a nanocleanroom in which the inner tubes grow.

For the unique assignment of an RBM peak to a specific tube chirality (n, m), the RBM frequencies and the optical transition energies must be considered. Several groups recorded Raman maps – i.e., contour plots of the RBM intensity vs. frequency and excitation energy – of individual SWNTs dispersed in SDS [79, 80]. A similar Raman map of buckypaper DWNTs was reported recently [81], as depicted in Fig. 14.

As compared to the maps of SWNTs, there is one important difference: A specific inner tube gives rise to a whole cluster of peaks with almost the same resonance energy. This reflects the above observation that there are many more peaks in the inner tubes RBM spectra than geometrically allowed tubes. The clusters originate from the same inner-tube type accommodated in several different outer tubes. The inner–outer tube interaction depends on the diameter difference of the two concentric shells. The stronger the interaction, the further the inner-tube RBM shifts to higher frequencies [84]. This issue has been confirmed from a continuum model calculation in which a Lennard-Jones potential was used to take care of the tube–tube interaction. As depicted in Fig. 15 the rather good agreement between calculated and observed Raman response strongly supports the above interpretation and explains the many narrow lines in the RBM response of the inner-shell tubes as pair spectra. Since the experimental spectrum was constructed as described in the figure caption, the individual peak heights represent effective pair occupations.

3.2.2 Tangential Modes and Overtones

Several attempts were made to reveal the G-line components from the inner-shell tubes. Due to their weak dependence on the tube diameter, they strongly overlap with the response from the outer-shell tubes. Only the G^+ component of the inner tubes is easily assigned to a peak at $1580\,\mathrm{cm}^{-1}$. A more efficient procedure was reported by *Simon* et al. [2] where ^{13}C isotope substitution for the inner-shell tubes was used to separate the G-lines from the inner and outer tubes.

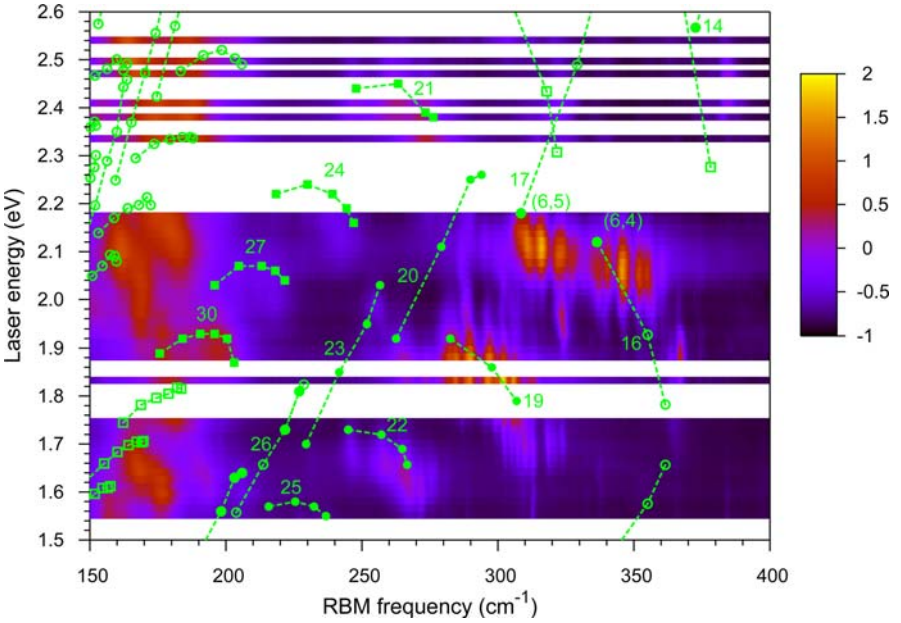

Fig. 14. Raman map for DWNTs. The color-coded Raman intensities represent the response from the outer-shell tubes (low-frequency side) and from the inner-shell tubes (*main part* of the figure). The *open symbols* depict values for individual tubes as calculated from a symmetry-adapted nonorthogonal tight-binding model [82] corrected for many-body effects after [83]. The *full symbols* represent experiments recorded for HiPco tubes. The *dashed lines* connect tube families $2m + n = \text{const}$. Adapted from [81]

An analysis of the D-band overtone (D*- or G′-band around 2560 cm^{-1}) for DWNTs revealed a downshift of the response from the inner-shell tubes [85]. This was expected from previous results on HiPco tubes with varying diameter (see the contribution by Saito et al.). However, the downshift was much stronger than predicted from the SWNT experiments and was considered as a fingerprint of the high curvature of the inner-shell tubes.

The recording of the D* Raman line turned out to be very useful for small externally induced lineshifts as for the same relative change the absolute shifts are enhanced. Use of this effect was, for example, made in [86] where an electrochemical doping-induced shift of the D* line was studied.

3.2.3 Temperature, Pressure, and Doping Effects

Raman spectroscopy cannot only be used to measure the optical transition energies between the van Hove singularities or their related exciton states but also to determine the lifetime of the excited states. This was demonstrated

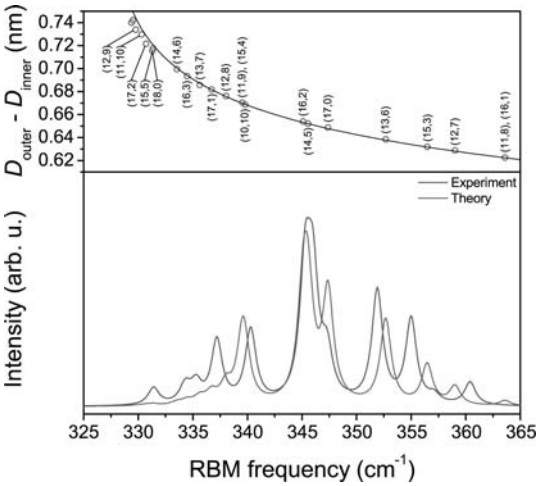

Fig. 15. Calculated RBM frequencies of inner-shell tubes as a function of wall-to-wall distance (*top*) and the constructed Raman response for the (6, 4) cluster and the spectrum obtained from the calculation with the frequencies dressed with Lorentzian lines (*bottom*). Constructed means the height of each peak was normalized to the maximum scattering intensity from the Raman map. After [84]

in a recent paper where the transition energies and the electronic damping Γ was measured as a function of temperature for DWNTs [87]. Electron–phonon coupling was found to be the reason for the temperature dependence. At low temperatures the damping constant for the inner-shell excitation was only 30 meV, and thus a factor of two smaller than the electronic damping of SWNTs with comparable diameter.

The RBM and G-mode regions of DWNTs remain practically unchanged after heat treatments up to 2000 °C [88]. However, after heating to about 1500 °C a sharp peak around 1855 cm^{-1} – attributed to vibrations of linear carbon chains – can be observed. Since this peak arises at temperatures just below the temperature needed for the coalescence of DWNTs, it was called the coalescence-induced mode (CIM) [88–90].

With respect to high-pressure effects, interesting differences have been reported between the response from inner-shell and outer-shell tubes [91, 92]. Whereas the pressure coefficient for the latter follow basically the behavior known from SWNTs, which means frequencies increase and lines broaden significantly with hydrostatic pressure, the frequencies from the former remain essentially unaltered. The pressure-induced decrease of frequencies has been ascribed to a faceting effect valid only for the outer tubes in the bundles, whereas in contrast the inner tubes do not suffer from this deformation. Interestingly, while the inner-shell tube-pressure coefficient decreases with decreasing tube diameter, locally, for selected frequencies this trend is inverted, at least for the RBM. Understanding for this anomaly comes from

the fact that clustered lines originate from the same inner tube in different outer tubes.

Doping of DWNTs with alkali metals has been reported in several papers [93–95]. Both the outer-shell and the inner-shell tubes can accept electrons from the alkali-metal donors. The response of the DWNT system to doping is visualized by Raman scattering from the G^+ band and from the D^* band [86]. For weak doping, the G^+ band shifts a few wave numbers upwards but eventually, for strong doping, it softens by as much as $30\,\mathrm{cm}^{-1}$.

3.3 13 C Substitution and Nuclear Magnetic Resonance

The peapod-grown DWNTs allow for a selective ^{13}C substitution of the inner tubes by using ^{13}C-enhanced fullerenes as a filling material. This enables growth of DWNTs where the inner-shell tubes are highly ^{13}C-enriched, whereas the outer-shell tubes and all carbonaceous contaminations remain with the natural ^{13}C concentration of only 1.1 %. This allows for a selective spectroscopy from the inner-shell tubes with respect to vibrations and, even more important, with respect to nuclear magnetic resonance (NMR).

Evidence for a successful filling with ^{13}C can be provided by Raman experiments. The downshift of the RBM pattern gives quantitative information on the substitution from $\omega = \omega_0\sqrt{(12 + c_0)/(12 + c)}$, where c_0 is 0.011 and c is the concentration of the ^{13}C atoms on the inner-shell tubes. In cases where the Raman response from the outer-shell and inner-shell tubes is strongly overlapping, as for example in the case of the D-line, the isotope substitution provides a clear separation of the Raman response. An observed substantial intensity of the inner-shell D-line in peapod-grown DWNTs is surprising on account of the very long lifetime of the RBMs. Curvature-enhanced electron–phonon coupling and details from the transformation process may be responsible for this observation. A line broadening for the RBMs yields evidence for a statistical distribution of the ^{13}C atoms [2]. Detailed calculations revealed that the ^{13}C atoms do not diffuse around but rather remain localized during the transformation process [54].

NMR spectra for ^{13}C-enriched NTs in a DWNT system were recently reported by *Simon* et al. [2] and by *Singer* et al. [96]. For the highly enriched material (89 % ^{13}C), the NMR signal was enhanced by two orders of magnitude. Static and magic-angle spinning NMR revealed deviations from studies on conventional SWNTs with respect to lineshape and linewidth. This is attributed to the high curvature of the inner-shell tubes and the concomitant broader σ–π hybridization.

The enhanced signals also facilitated the determination of the temperature- and magnetic-field dependence of the magnetization relaxation $M(t)$ after $\pi/2$ pulse excitation to saturation. The relaxation was found to follow a stretched exponential law that reflects the influence of the diameter distribution and the powder average for the DWNT system. From the temperature

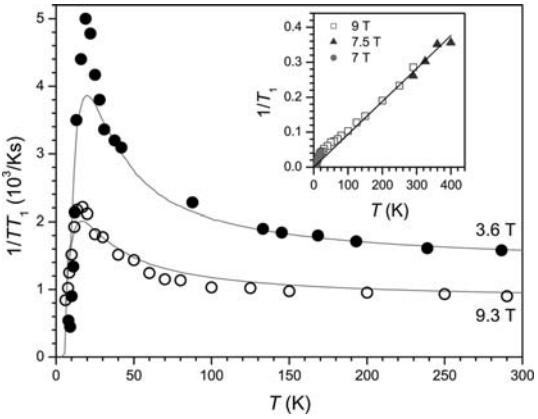

Fig. 16. Temperature dependence of $1/TT_1$ between 300 K and 20 K for two different fields B. The *full drawn lines* are as calculated for a 1D density of states with a gap at the Fermi level. The *insert* depicts the linear relation between $1/T_1$ and T for temperatures above 150 K; adapted from [96]

dependence of $M(t, T, B)$ the longitudinal relaxation times T_1 were determined and analyzed as $1/TT_1$. With respect to magnetic field dependence, $1/TT_1$ followed a linear dependence on $B^{-1/2}$, which indicates a 1D spin diffusion behavior. The temperature dependence of $1/TT_1$ is depicted in Fig. 16.

The system exhibits Korringa behavior ($1/TT_1$ independent of temperature) for temperatures down to 150 K. From this it is claimed that essentially all inner-shell tubes are metallic, consistent with the above-described calculated metallization of the DWNT band structure. Also, the quenching of the luminescence as found in [72] supports the NMR findings as far as the metallization of the inner-shell tubes is concerned.

For temperatures lower than 150 K the spin relaxation first decreases and then, below 20 K a gap of $2\Delta = 3.7$ meV appears in the spin-excitation spectrum. The full drawn lines in Fig. 16 are as calculated from

$$\frac{1}{TT_1} = \alpha^2 \int_{\Delta}^{\infty} n(\epsilon) n(\epsilon + \omega_n) \left(-\frac{\partial f}{\partial \epsilon} \right) \mathrm{d}\epsilon$$
$$n(\epsilon) = \frac{\epsilon}{\sqrt{\epsilon^2 - \Delta^2}} \quad \text{for} \quad |\epsilon| > \Delta\,, \quad \text{and 0 otherwise,} \tag{1}$$

where α is a constant derived from the field dependence of $1/TT_1$ and $n(\epsilon)$ is a gapped 1D density of states. Various possibilities for the origin of this gap are discussed in terms of Luttinger-liquid behavior or a Peierls distortion.

3.4 Thermal and Chemical Stability, Mechanical Properties

It is expected that the coaxial structure of DWNTs makes them very stable versus heat treatment under an argon atmosphere. Similarly, a high chemical

stability can be anticipated due to the shielding effect of the outer walls. Interesting mechanical properties can be expected with respect to kinking resistance, stiffness, and intertube gliding.

3.4.1 Thermal Stability

Structural transformation of carbon nanostructures was first observed at ca. 800 °C for nanohorns, and at ca. 1200 °C for catalytic CVD-derived SWNTs [97]. For a comparative study of the thermal stability of DWNTs, arc-discharge-derived high-purity SWNTs (Iljin Company, Korea) were used because these tubes are believed to exhibit high structural integrity. Both samples were thermally treated at a temperature of 2000 °C for 30 min using a graphite-resistance furnace. No changes in the Raman spectra could be observed for thermally treated DWNT buckypaper. On the other hand, a reduced width of the RBM and a slightly intensified D-band were observed for SWNTs [98].

From cross-sectional TEM images of SWNTs, a large portion of round and small-sized (ca. 1.4 nm) SWNTs in a single SWNT bundle were structurally transformed into distorted and large-sized (ca. 4–5 nm) tubes via the well-known coalescence process [99]. Therefore, it is certain that the Raman signals from the thermally treated SWNT buckypaper are derived from the resonance scattering of the remaining SWNTs. The appearance of a shoulder at 180 cm^{-1} and an increased D-band intensity for thermally treated SWNT bundles indirectly indicates the structural transformation from less-stable small-sized tubes to more-stable large-sized tubes through the zipping mechanism [99].

The lack of changes for DWNT buckypaper treated at 2000 °C suggests among others that these samples will exhibit highly stable emitting performance along with a low threshold voltage when they are fabricated into a field emission display.

3.4.2 Pore Structure and Oxidative Stability of the Bundled DWNTs

It is well known that the surface properties, including the pore texture, in carbon nanotubes directly affect their performance in widespread applications. Up to now, SWNT-derived buckypaper has exhibited possible uses as a hydrogen-storage material, as anode materials in lithium-ion batteries, and as actuators or artificial muscles and sensors [86, 100–103]. This is due to an intrinsic highly accessible surface area (derived from their nanosized diameter), and the ability to handle and manipulate DWNTs. In this sense, it was very important to evaluate the surface properties of DWNT buckypaper, including its oxidation stability as compared with that of SWNTs, with an eye toward understanding the structural differences between bundles of single graphene tubules and DWNT ropes.

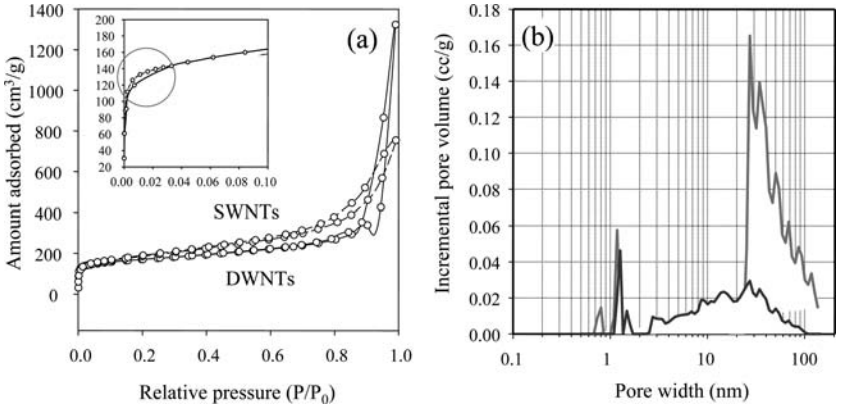

Fig. 17. (**a**) Adsorption isotherm of SWNT- and DWNT-derived buckypapers (*inset* shows a comparative plot of the adsorption on both samples below $P/P_0 = 0.1$), (**b**) micropore-size distribution of SWNT- and DWNT-derived buckypapers using the DFT method. The *light line* indicates DWNTs, whereas the *dark line* indicates SWNTs. Note that small micropores below 0.8 nm, corresponding to interstitial pores, were observed in the bundled DWNTs. After [31]

A comparative study of the pore structure and the oxidation stability between DWNT- and SWNT-derived buckypapers yields such information. Figure 17 shows the N_2 adsorption isotherms for SWNT- and DWNT-derived buckypapers, respectively. DWNTs exhibited a steady uptake of N_2 at a medium relative pressure (P/P_0) and an abrupt uptake of N_2 at high relative pressure (above 0.9), similar to a typical type II isotherm, whereas the adsorption isotherms for SWNT-derived buckypaper shows a hysteresis loop at high relative pressure, corresponding to a typical type IV isotherm [104]. An abrupt increase in the N_2 uptake below $P/P_0 = 0.1$ (see inset to Fig. 17a) strongly suggests the presence of micropores smaller than 1.5 nm for DWNTs. Furthermore, below $P/P_0 < 0.02$, the higher uptake of N_2 in DWNTs when compared to SWNTs is directly related to the three-times larger micropore volume observed in DWNTs, although the total specific surface area of DWNTs (568.7 m^2/g) is lower than that of SWNTs (641.7 m^2/g) [31].

The pore-size distributions for both DWNT and SWNT samples were obtained from N_2 adsorption isotherms using the density-functional theory (DFT) method, as shown in Fig. 17b. From this figure, both samples exhibit similar micro- and mesopore distributions. But, the clearly observed small micropores (ca. 0.8 nm) and the three-times larger micropore volume in DWNTs are ascribed to well-developed intertube (or interstitial) cavities due to the high hexagonal stacking order. In addition, a large portion of the pores ranging from 20 to 100 nm in DWNTs (Fig. 17b) is thought to be caused by the empty spaces created by the highly intermingled long bundles.

Also, a comparative study of the resistance to oxidation was carried out for both types of buckypapers using a thermal gravimetric analysis in an argon and oxygen (1 %) gas mixture. The results demonstrate that DWNTs are oxidized at a significantly higher temperature (ca. 717 °C) when compared to SWNTs (ca. 541 °C). The high resistance to oxidation of DWNTs is derived from their "coaxial structure" as well as the high crystallinity of the bundles. Since DWNTs exhibit a high thermal stability, and DWNTs are also structurally stable, it will be very important to compare the structural and oxidation stability of nanotubes as a function of the number of concentric walls within MWNTs.

3.4.3 Mechanical Properties

Mechanical properties must be considered as particularly important for DWNTs as the stiffness and the tensile strength are expected to have higher values due to the inner-shell tubes. Unfortunately, neither theoretical nor experimental results are available so far. On the other hand, several theoretical end experimental papers reported on the intertube sliding properties that may be relevant for nanobearings, nanosprings or nano-oscillators applications [3, 105–107].

The weak intertube interaction in DWNTs described above tempted several authors to evaluate rotational bearings by molecular dynamical methods. In [3] frictional forces were determined from the heat dissipation to the bath. Explicit results were obtained for $(9,9)@(14,14)$ and $(9,9)@(22,4)$ DWNTs. Brenner potentials were used for the intralayer interaction and the Kolmogorov–Crespi potential [59] for the van der Waals interaction between the layers. The energy barrier for the rotation was found to decrease with increasing periodicity in the circumferential direction. Since the periodicity for the $(14,14)$ sleeve (outer tube) is much higher than for the $(22,4)$ sleeve the barrier height was only 0.002 meV/carbon for the former case and thus much smaller than 0.06 meV as for the latter case. For very high rotation rates, the dissipation increased nonlinearly until beyond 0.5 rotations/ps the shaft (inner-shell tube) deformed and eventually for 0.75 rotations/ps the bearing failed by the collapsing of the shaft. As an extension to the above-described sliding and rotary motion, *Tu* et al. [106] even proposed concepts for an ac-voltage-driven DWNT motor.

Experimental results were mostly reported so far for sliding friction in MWNTs [107–109]. Since the basic functions of the intertube sliding goes back to DWNTs, such experiments should be mentioned here. In the work of *Kis* et al. [107] cyclic telescoping motion was studied for MWNTs suspended between an AFM tip and a platinum wire. The telescoping motion was driven with frequencies of 0.1–100 Hz from the Pt wire and observed by TEM. Forces were measured by the AFM tip. Before starting the experiment the outer layers of the MWNTs were burned away to liberate the core part of the tube. Frictional forces were below the measurement limit of 1.4×10^{-15} N/atom

with a total dissipation per cycle lower than 0.4 meV/atom. Intentionally introduced defects led to temporary mechanical dissipation, but this could be removed by self-healing so that the original smooth motion could be retained.

4 Summary and Outlook

Double-wall carbon nanotubes must be considered as a new species in the field of carbon nanophases. Many of the physical properties are basically a superposition of the properties of the two constituting concentric tubes but intertube interaction can noticeably perturb the properties of both tubes. Raman scattering and HRTEM are the main analytical tools to study the growth and the structure of the DWNTs.

For the preparation of DWNTs two routes are now established. One is a large-scale method using a catalytical CVD process with especially selected growth parameters. It can produce DWNTs with high efficiency. The other route uses precursor materials, such as either fullerene peapods or encapsulated metallocenes. It produces exclusively DWNTs with a high degree of perfection. There is a fundamental difference between the two precursor systems. Whereas the fullerene precursor route needs rather high temperatures up to 1250 °C, the growth of DWNTs from metallocenes can already be performed at 600 °C. This is possible since the metallocenes, in particular ferrocene, are transformed to Fe_3C that acts as a catalyst. The final product of the DWNT material is different for catalyst-grown material and peapod-grown material. The high temperature is needed in the peapod-grown material to activate the coalescence mechanism. There is a yet unrevealed intermediate phase between the starting peapod system and the final DWNT product.

Calculations of the electronic ground state reveal an optimum wall-to-wall distance between 0.34 and 0.36 nm, slightly larger than the interlayer spacing of graphite. However, in the range of its minimum, the total-energy curve vs intertube distance is rather flat, allowing for several combinations of inner–outer tube pairs. Experimental results from XRD, HRTEM, Raman scattering and electron diffraction confirm this result. Due to the tube–tube interaction, the conduction-band states of the inner-shell tubes are downshifted, which leads in many cases to bands crossing over the Fermi level. This means DWNTs tend to have a metallic inner tube.

The RBM observed in Raman experiments turned out to be an excellent analytical tool to reveal the success of DWNT growth on a bulk scale, to study the transition from peapods to DWNTs and to unravel the details of the Raman spectra for the inner–outer tube constituents. A very narrow linewidth observed at least for the peapod-grown material shows evidence for a very high degree of tube perfection. The D^* (or G') band is a very sensitive indicator for any small changes of the DWNT structure.

^{13}C substitution of the fullerene precursor material opens a new dimension in DWNT research. DWNT systems can be grown where the inner-shell tube

is ^{13}C whereas the outer-shell tubes remain ^{12}C. Measurements of the temperature dependence of the longitudinal relaxation time T_1 in such systems revealed a general Korringa behavior.

Double-wall carbon nanotubes exhibit an enhanced thermal and chemical stability as compared to SWNTs. Under inert conditions, they can survive 2000 °C without reaction. The tubes like to crystallize into DWNT bundles that provide a selective pore structure appropriate for gas storage. The strong bundling also reduces oxidative attack.

4.1 Outlook

Even though DWNTs can now be prepared in a well-defined manner, either by CCVD or from various precursor routes, very few experiments have been reported on the particular properties of such systems. Experiments and theoretical analyses are needed for optical absorption, transport, mechanical strength and stiffness. Only very few single-tube experiments have been reported so far.

The higher thermal and chemical stability calls for application in charge-storage devices and field emission.

High-curvature effects for the inner tubes and the unraveling of the secret about the transient phase in the case of the structural transformation from the peapods to DWNTs are other challenging problems. They include the understanding of the importance of the Stone–Wales transformations to the fullerene or other precursor coalescence.

Concerning the Raman experiments, the fine structure of the RBM is understood but the noticeable intensity of the D-line from the inner-shell tubes as it is observed, in spite of the long lifetime of the RBM phonons, calls for a better understanding of this effect.

A very rich field of further and detailed research has been opened for magnetic resonance experiments, in particular for NMR where the DWNTs with ^{13}C on the inner tubes and ^{12}C on the outer tubes provide an excellent system. Doping effects or outer-tube functionalization are challenging questions that should be studied for this system. Conduction electron spin resonance of the metallized inner-shell tubes is already a challenge for ESR. More challenges will follow once spins are introduced into the inner-shell walls by, e.g., using $C_{59}N$ for filling.

Acknowledgements

The authors acknowledge valuable discussion with Hide Shiozawa, Ferenc Simon and Valentin N. Popov. Work supported by the Austrian Science Foundation, projects P17345 and I83-N20 (ESF-IMPRESS), the Deutsche Forschungsgemeinschaft, project PI440/3/4, and a Grant-in-Aid from the Ministry of Education, Culture, Sports, Science and Technology of Japan (No. 18710084).

References

[1] W. Mickelson, S. Aloni, W.-Q. Han, J. Cumings, A. Zettl: Packing C_{60} in boron nitride nanotubes, Science **300**, 467–469 (2003) 495

[2] F. Simon, C. Kramberger, R. Pfeiffer, H. Kuzmany, V. Zólyomi, J. Kürti, P. M. Singer, H. Alloul: Isotope engineering of carbon nanotube systems, Phys. Rev. Lett. **95**, 017401 (2005) 495, 513, 516

[3] S. Zhang, W. K. Liu, R. S. Ruoff: Atomistic simulations of double-walled carbon nanotubes (DWCNTs) as rotational bearings, Nano Lett. **4**, 293–297 (2004) 495, 520

[4] J.-C. Charlier, J.-P. Michenaud: Energetics of multilayered carbon tubules, Phys. Rev. Lett. **70**, 1858–1861 (1993) 496, 509

[5] R. Saito, R. Matsuo, T. Kimura, G. Dresselhaus, M. S. Dresselhaus: Anomalous potential barrier of double-wall carbon nanotube, Chem. Phys. Lett. **348**, 187–193 (2001) 496, 509

[6] K.-H. Ahn, Y.-H. Kim, J. Wiersig, K. J. Chang: Spectral correlation in incommensurate multiwalled carbon nanotubes, Phys. Rev. Lett. **90**, 026601 (2003) 496, 512

[7] J. Chen, L. Yang, H. Yang, J. Dong: Electron transport properties of incommensurate double-walled carbon nanotubes, Chem. Phys. Lett. **400**, 384–388 (2004) 496, 512

[8] H. Kuzmany, R. Pfeiffer, C. Kramberger, T. Pichler: The nanospace inside single wall carbon nanotubes, in E. Buzaneva, E. Scharff (Eds.): *Frontiers of Multifunctional Integrated Nanosystems* (Kluwer Academic Publishers 2004) pp. 171–184 497

[9] S. Bandow, M. Takizawa, K. Hirahara, M. Yudasaka, S. Iijima: Raman scattering study of double-wall carbon nanotubes derived from the chains of fullerenes in single-wall carbon nanotubes, Chem. Phys. Lett. **337**, 48–54 (2001) 496, 497, 501

[10] B. W. Smith, M. Monthioux, D. E. Luzzi: Encapsulated C_{60} in carbon nanotubes, Nature **396**, 323–324 (1998) 497

[11] J. H. Hafner, M. J. Bronikowski, B. R. Azamian, P. Nikolaev, A. G. Rinzler, D. T. Colbert, K. A. Smith, R. E. Smalley: Catalytic growth of single-wall carbon nanotubes from metal particles, Chem. Phys. Lett. **296**, 195–202 (1998) 497

[12] A. Oberlin, M. Endo, T. Koyama: Filamentous growth of carbon through benzene decomposition, J. Cryst. Growth **32**, 335–349 (1976) 497

[13] J.-F. Colomer, L. Henrard, E. Flahaut, G. Van Tendeloo, A. A. Lucas, P. Lambin: Rings of double-walled carbon nanotube bundles, Nano Lett. **3**, 685–689 (2003) 498

[14] E. Flahaut, R. Bacsa, A. Peigney, C. Laurent: Gram-scale CCVD synthesis of double-walled carbon nanotubes, Chem. Commun. pp. 1442–1443 (2003) 498

[15] W. Z. Li, J. G. Wen, M. Sennett, Z. F. Ren: Clean double-walled carbon nanotubes synthesized by CVD, Chem. Phys. Lett. **368**, 299–306 (2003) 498

[16] A. Grüneis, M. H. Rümmeli, C. Kramberger, A. Barreiro, T. Pichler, R. Pfeiffer, H. Kuzmany, T. Gemming, B. Büchner: High quality double wall carbon nanotubes with a defined diameter distribution by chemical vapor deposition from alcohol, Carbon **44**, 3177–3182 (2006) 498

[17] H. Ago, K. Nakamura, S. Imamura, M. Tsuji: Growth of double-wall carbon nanotubes with diameter-controlled iron oxide nanoparticles supported on MgO, Chem. Phys. Lett. **391**, 308–313 (2004) 498
[18] S. C. Lyu, T. J. Lee, C. W. Yang, J. C. Lee: Synthesis and characterization of high-quality double-walled carbon nanotubes by catalytic decomposition of alcohol, Chem. Commun. pp. 1404–1405 (2003) 498
[19] S. C. Lyu, B. C. Liu, C. J. Lee, H. K. Kang, C.-W. Yang, C. Y. Park: High-quality double-walled carbon nanotubes produced by catalytic decomposition of benzene, Chem. Mater. **15**, 3951–3954 (2003) 498
[20] S. C. Lyu, B. C. Liu, S. H. Lee, C. Y. Park, H. K. Kang, C.-W. Yang, C. J. Lee: Large-scale synthesis of high-quality double-walled carbon nanotubes by catalytic decomposition of n-hexane, J. Phys. Chem. B **108**, 2192–2194 (2004) 498
[21] J. Cumings, W. Mickelson, A. Zettl: Simplified synthesis of double-wall carbon nanotubes, Solid State Commun. **126**, 359–362 (2003) 498
[22] T. Hiraoka, T. Kawakubo, J. Kimura, R. Taniguchi, A. Okamoto, T. Okazaki, T. Sugai, Y. Ozeki, M. Yoshikawa, H. Shinohara: Selective synthesis of double-wall carbon nanotubes by CCVD of acetylene using zeolite supports, Chem. Phys. Lett. **382**, 679–685 (2003) 498
[23] P. Ramesh, T. Okazaki, R. Taniguchi, J. Kimura, T. Sugai, K. Sato, Y. Ozeki, H. Shinohara: Selective chemical vapor deposition synthesis of double-wall carbon nanotubes on mesoporous silica, J. Phys. Chem. B **109**, 1141–1147 (2005) 498
[24] J. Zhu, M. Yudasaka, S. Iijima: A catalytic chemical vapor deposition synthesis of double-walled carbon nanotubes over metal catalysts supported on a mesoporous material, Chem. Phys. Lett. **380**, 496–502 (2003) 498
[25] T. Yamada, T. Namai, K. Hata, D. N. Futaba, K. Mizuno, J. Fan, M. Yudasaka, M. Yumura, S. Iijima: Size-selective growth of double-walled carbon nanotube forests from engineered iron catalysts, Nature Nanotechnol. **1**, 131–136 (2006) 498
[26] M. Endo, H. Muramatsu, T. Hayashi, Y. A. Kim, M. Terrones, M. S. Dresselhaus: Nanotechnology: 'buckypaper' from coaxial nanotubes, Nature **433**, 476 (2005) 498, 499
[27] S. Osswald, E. Flahaut, H. Ye, Y. Gogotsi: Elimination of D-band in Raman spectra of double-wall carbon nanotubes by oxidation, Chem. Phys. Lett. **402**, 422–427 (2005) 498
[28] S. Osswald, E. Flahaut, Y. Gogotsi: In situ Raman spectroscopy study of oxidation of double- and single-wall carbon nanotubes, Chem. Mater. **18**, 1525–1533 (2006) 498
[29] C. Thomsen, S. Reich: Double resonant Raman scattering in graphite, Phys. Rev. Lett. **85**, 5214–5217 (2000) 499
[30] A. Jorio, M. A. Pimenta, A. G. Souza Filho, R. Saito, G. Dresselhaus, M. S. Dresselhaus: Characterizing carbon nanotube samples with resonance Raman scattering, New J. Phys. **5**, 139 (2003) 499
[31] H. Muramatsu, T. Hayashi, Y. A. Kim, D. Shimamoto, Y. J. Kim, K. Tantrakarn, M. Endo, M. Terrones, M. S. Dresselhaus: Pore structure and oxidation stability of double-walled carbon nanotube-derived bucky paper, Chem. Phys. Lett. **414**, 444–448 (2005) 500, 519

[32] B. W. Smith, M. Monthioux, D. E. Luzzi: Carbon nanotube encapsulated fullerenes: A unique class of hybrid materials, Chem. Phys. Lett. **315**, 31–36 (1999) 501
[33] B. W. Smith, D. E. Luzzi: Formation mechanism of fullerene peapods and coaxial tubes: A path to large scale synthesis, Chem. Phys. Lett. **321**, 169–174 (2000) 501
[34] H. Kataura, Y. Maniwa, T. Kodama, K. Kikuchi, K. Hirahara, K. Suenaga, S. Iijima, S. Suzuki, Y. Achiba, W. Krätschmer: High-yield fullerene encapsulation in single-wall carbon nanotubes, Synth. Met. **121**, 1195–1196 (2001) 501
[35] M. Yudasaka, K. Ajima, K. Suenaga, T. Ichihashi, A. Hashimoto, S. Iijima: Nano-extraction and nano-condensation for C_{60} incorporation into single-wall carbon nanotubes in liquid phases, Chem. Phys. Lett. **380**, 42–46 (2003) 501
[36] F. Simon, H. Kuzmany, H. Rauf, T. Pichler, J. Bernardi, H. Peterlik, L. Korecz, F. Fülöp, A. Jánossy: Low temperature fullerene encapsulation in single wall carbon nanotubes: Synthesis of $N@C_{60}$@SWCNT, Chem. Phys. Lett. **383**, 362–367 (2004) 501
[37] X. Liu, T. Pichler, M. Knupfer, M. S. Golden, J. Fink, H. Kataura, Y. Achiba, K. Hirahara, S. Iijima: Filling factors, structural, and electronic properties of C_{60} molecules in single-wall carbon nanotubes, Phys. Rev. B **65**, 045419 (2002) 501, 503, 506
[38] H. Kuzmany, R. Pfeiffer, C. Kramberger, T. Pichler, X. Liu, M. Knupfer, J. Fink, H. Kataura, Y. Achiba, B. W. Smith, D. E. Luzzi: Analysis of the concentration of C_{60} fullerenes in single wall carbon nanotubes, Appl. Phys. A **76**, 449–455 (2003) 501
[39] M. Melle-Franco, H. Kuzmany, F. Zerbetto: Mechanical interactions in all-carbon peapods, J. Phys. Chem. B **107**, 6986–6990 (2003) 501
[40] R. Pfeiffer: *Dispersion of Raman Lines in Carbon Nanophases*, Ph.D. thesis, University of Vienna (2004) 502
[41] R. Pfeiffer, M. Holzweber, H. Peterlik, H. Kuzmany, Z. Liu, K. Suenaga, H. Kataura: Dynamics of carbon nanotube growth from fullerenes, Nano Lett. **7**, 2428–2434 (2007) 501, 502, 503, 507
[42] S. Bandow, T. Hiraoka, T. Yumura, K. Hirahara, H. Shinohara, S. Iijima: Raman scattering study on fullerene derived intermediates formed within single-wall carbon nanotube: From peapod to double-wall carbon nanotube, Chem. Phys. Lett. **384**, 320–325 (2004) 502
[43] C. Kramberger, A. Waske, K. Biedermann, T. Pichler, T. Gemming, B. Büchner, H. Kataura: Tailoring carbon nanostructures via temperature and laser irradiation, Chem. Phys. Lett. **407**, 254–259 (2005) 502
[44] Y. Fujita, N. Niwa, S. Bandow, S. Iijima: Enhancement of inner tube formation from peapods in de-pressurized inert gas environment, Appl. Phys. A **85**, 307–310 (2006) 503
[45] Y. Fujita, S. Bandow, S. Iijima: Effect of hydrogen on polymerizing the fullerene molecules in the single-wall carbon nanotubes, Chem. Lett. **36**, 94 (2007) 503
[46] L.-J. Li, A. N. Khlobystov, J. G. Wiltshire, G. A. D. Briggs, R. J. Nicholas: Diameter-selective encapsulation of metallocenes in single-walled carbon nanotubes, Nature Mater. **4**, 481–485 (2005) 503

[47] L. Guan, Z. Shi, M. Li, Z. Gu: Ferrocene-filled single-walled carbon nanotubes, Carbon **43**, 2780–2785 (2005) 503
[48] Y. Li, R. Hatakeyama, T. Kaneko, T. Okada: Nano sized magnetic particles with diameters less than 1 nm encapsulated in single-walled carbon nanotubes, Jpn. J. Appl. Phys. **45**, L428–L431 (2006) 503
[49] H. Shiozawa, T. Pichler, A. Grüneis, R. Pfeiffer, H. Kuzmany, Z. Liu, K. Suenaga, H. Kataura: Catalytic reaction inside a single-wall carbon nanotube, accepted by Adv. Mater. 503, 504, 505
[50] A. Barreiro, S. Hampel, M. H. Rümmeli, C. Kramberger, A. Grüneis, K. Biedermann, A. Leonhardt, T. Gemming, B. Büchner, A. Bachtold, T. Pichler: Thermal decomposition of ferrocene as a method for production of single-walled carbon nanotubes without additional carbon sources, J. Phys. Chem. B **110**, 20973–20977 (2006) 503
[51] H. Rauf, H. Shiozawa, T. Pichler, M. Knupfer, B. Büchner, H. Kataura: Influence of the C_{60} filling on the nature of the metallic ground state in intercalated peapods, Phys. Rev. B **72**, 245411 (2005) 503
[52] V. M. García-Suárez, J. Ferrer, C. J. Lambert: Tuning the electrical conductivity of nanotube-encapsulated metallocene wires, Phys. Rev. Lett. **96**, 106804 (2006) 503
[53] F. Simon, H. Kuzmany: Growth of single wall carbon nanotubes from ^{13}C isotope labelled organic solvents inside single wall carbon nanotube hosts, Chem. Phys. Lett. **425**, 85–88 (2006) 506
[54] V. Zólyomi, F. Simon, Á. Rusznyák, R. Pfeiffer, H. Peterlik, H. Kuzmany, J. Kürti: Inhomogeneity of ^{13}C isotope distribution in isotope engineered carbon nanotubes: Experiment and theory, Phys. Rev. B **75**, 195419 (2007) 507, 516
[55] K. Urita, Y. Sato, K. Suenaga, S. Iijima: HR-TEM study of atomic defects in carbon nanostructures, in H. Kuzmany, J. Fink, M. Mehring, S. Roth (Eds.): *Electronic Properties of Novel Nanostructures*, AIP Conference Proceedings **786** (2005) pp. 109–113 507
[56] S. Han, M. Yoon, S. Berber, N. Park, E. Osawa, J. Ihm, D. Tománek: Microscopic mechanism of fullerene fusion, Phys. Rev. B **70**, 113402 (2004) 508
[57] E. Hernández, V. Meunier, B. W. Smith, R. Rurali, H. Terrones, M. Buongiorno Nardelli, M. Terrones, D. E. Luzzi, J.-C. Charlier: Fullerene coalescence in nanopeapods: A path to novel tubular carbon, Nano Lett. **3**, 1037–1042 (2003) 508
[58] J. Tersoff: Empirical interatomic potential for carbon, with applications to amorphous carbon, Phys. Rev. Lett. **61**, 2879–2882 (1988) 509
[59] A. N. Kolmogorov, V. H. Crespi: Smoothest bearings: Interlayer sliding in multiwalled carbon nanotubes, Phys. Rev. Lett. **85**, 4727–4730 (2000) 509, 520
[60] L. Bellarosa, E. Bakalis, M. Melle-Franco, F. Zerbetto: Interactions in concentric carbon nanotubes: The radius vs. the chirality angle contributions, Nano Lett. **6**, 1950–1954 (2006) 509
[61] S. Okada, A. Oshiyama: Curvature-induced metallization of double-walled semiconducting zigzag carbon nanotubes, Phys. Rev. Lett. **91**, 216801 (2003) 509

[62] V. Zólyomi, J. Koltai, A. Rusznyák, J. Kürti, A. Gali, F. Simon, H. Kuzmany, A. Szabados, P. R. Surján: Inter-shell interaction in double walled carbon nanotubes: Charge transfer and orbital mixing, arXiv:cond-mat/0603407 510
[63] W. Song, M. Ni, J. Lu, Z. Gao, S. Nagase, D. Yu, H. Ye, X. Zhang: Electronic structures of semiconducting double-walled carbon nanotubes: Important effect of interlay interaction, Chem. Phys. Lett. **414**, 429–433 (2005) 510
[64] S.-D. Liang: Intrinsic properties of electronic structure in commensurate double-wall carbon nanotubes, Physica B: Condens. Matter **352**, 305–311 (2004) 510
[65] M. Xia, S. Zhang, X. Zuo, E. Zhang, S. Zhao, J. Li, L. Zhang, Y. Liu, R. Liang: Assignment of the chiralities of double-walled carbon nanotubes using two radial breathing modes, Phys. Rev. B **70**, 205428 (2004) 511
[66] J. Wei, B. Jiang, X. Zhang, H. Zhu, D. Wu: Raman study on double-walled carbon nanotubes, Chem. Phys. Lett. **376**, 753–757 (2003) 511
[67] M. Abe, H. Kataura, H. Kira, T. Kodama, S. Suzuki, Y. Achiba, K.-I. Kato, M. Takata, A. Fujiwara, K. Matsuda, Y. Maniwa: Structural transformation from single-wall to double-wall carbon nanotube bundles, Phys. Rev. B **68**, 041405 (2003) 511
[68] J. M. Zuo, I. Vartanyants, M. Gao, R. Zhang, L. A. Nagahara: Atomic resolution imaging of a carbon nanotube from diffraction intensities, Science **300**, 1419–1421 (2003) 511
[69] Z. Liu, K. Suenaga, H. Yoshida, T. Sugai, H. Shinohara, S. Iijima: Determination of optical isomers for left-handed or right-handed chiral double-wall carbon nanotubes, Phys. Rev. Lett. **95**, 187406 (2005) 511
[70] M. Kociak, K. Hirahara, K. Suenaga, S. Iijima: How accurate can the determination of chiral indices of carbon nanotubes be? An experimental investigation of chiral indices determination on DWNT by electron diffraction, Eur. Phys. J. B **32**, 457–469 (2003) 511
[71] A. Hashimoto, K. Suenaga, K. Urita, T. Shimada, T. Sugai, S. Bandow, H. Shinohara, S. Iijima: Atomic correlation between adjacent graphene layers in double-wall carbon nanotubes, Phys. Rev. Lett. **94**, 045504 (2005) 511
[72] T. Okazaki, S. Bandow, G. Tamura, Y. Fujita, K. Iakoubovskii, S. Kazaoui, N. Minami, T. Saito, K. Suenaga, S. Iijima: Photoluminescence quenching in peapod-derived double-walled carbon nanotubes, Phys. Rev. B **74**, 153404 (2006) 511, 517
[73] T. Hertel, A. Hagen, V. Talalaev, K. Arnold, F. Hennrich, M. Kappes, S. Rosenthal, J. McBride, H. Ulbricht, E. Flahaut: Spectroscopy of single- and double-wall carbon nanotubes in different environments, Nano Lett. **5**, 511–514 (2005) 511
[74] M. Kociak, K. Suenaga, K. Hirahara, Y. Saito, T. Nakahira, S. Iijima: Linking chiral indices and transport properties of double-walled carbon nanotubes, Phys. Rev. Lett. **89**, 155501 (2002) 512
[75] Y. F. Li, R. Hatakeyama, T. Kaneko, T. Izumida, T. Okada, T. Kato: Electronic transport properties of Cs-encapsulated double-walled carbon nanotubes, Appl. Phys. Lett. **89**, 093110 (2006) 512

[76] G. H. Jeong, A. A. Farajian, R. Hatakeyama, T. Hirata, T. Yaguchi, K. Tohji, H. Mizuseki, Y. Kawazoe: Cesium encapsulation in single-walled carbon nanotubes via plasma ion irradiation: Application to junction formation and ab initio investigation, Phys. Rev. B **68**, 075410 (2003) 512
[77] O. Dubay, G. Kresse, H. Kuzmany: Phonon softening in metallic nanotubes by a Peierls-like mechanism, Phys. Rev. Lett. **88**, 235506 (2002) 512
[78] R. Pfeiffer, H. Kuzmany, C. Kramberger, C. Schaman, T. Pichler, H. Kataura, Y. Achiba, J. Kürti, V. Zólyomi: Unusual high degree of unperturbed environment in the interior of single-wall carbon nanotubes, Phys. Rev. Lett. **90**, 225501 (2003) 513
[79] C. Fantini, A. Jorio, M. Souza, M. S. Strano, M. S. Dresselhaus, M. A. Pimenta: Optical transition energies for carbon nanotubes from resonant Raman spectroscopy: Environment and temperature effects, Phys. Rev. Lett. **93**, 147406 (2004) 513
[80] H. Telg, J. Maultzsch, S. Reich, F. Hennrich, C. Thomsen: Chirality distribution and transition energies of carbon nanotubes, Phys. Rev. Lett. **93**, 177401 (2004) 513
[81] R. Pfeiffer, F. Simon, H. Kuzmany, V. N. Popov: Fine structure of the radial breathing mode of double-wall carbon nanotubes, Phys. Rev. B **72**, 161404 (2005) 513, 514
[82] V. N. Popov: Curvature effects on the structural, electronic and optical properties of isolated single-walled carbon nanotubes within a symmetry-adapted non-orthogonal tight-binding model, New J. Phys. **6**, 17 (2004) 514
[83] A. Jorio, C. Fantini, M. A. Pimenta, R. B. Capaz, G. G. Samsonidze, G. Dresselhaus, M. S. Dresselhaus, J. Jiang, N. Kobayashi, A. Grüneis, R. Saito: Resonance Raman spectroscopy (n, m)-dependent effects in small-diameter single-wall carbon nanotubes, Phys. Rev. B **71**, 075401 (2005) 514
[84] R. Pfeiffer, C. Kramberger, F. Simon, H. Kuzmany, V. N. Popov, H. Kataura: Interaction between concentric tubes in DWCNTs, Eur. Phys. J. B **42**, 345–350 (2004) 513, 515
[85] R. Pfeiffer, H. Kuzmany, F. Simon, S. N. Bokova, E. Obraztsova: Resonance Raman scattering from phonon overtones in double-wall carbon nanotubes, Phys. Rev. B **71**, 155409 (2005) 514
[86] M. Kalbáč, L. Kavan, M. Zukalová, L. Dunsch: Electrochemical tuning of high energy phonon branches of double wall carbon nanotubes, Carbon **42**, 2915–2920 (2004) 514, 516, 518
[87] F. Simon, R. Pfeiffer, H. Kuzmany: Temperature dependence of the optical excitation lifetime and band gap in chirality assigned semiconducting single-wall carbon nanotubes, Phys. Rev. B **74**, 121411 (2006) 515
[88] M. Endo, Y. A. Kim, T. Hayashi, H. Muramatsu, M. Terrones, R. Saito, F. Villalpando-Paez, S. G. Chou, M. S. Dresselhaus: Nanotube coalescence-inducing mode: A novel vibrational mode in carbon systems, Small **2**, 1031–1036 (2006) 515
[89] M. Jinno, Y. Ando, S. Bandow, J. Fan, M. Yudasaka, S. Iijima: Raman scattering study for heat-treated carbon nanotubes: The origin of ≈ 1855 cm^{-1} Raman band, Chem. Phys. Lett. **418**, 109–114 (2006) 515

[90] C. Fantini, E. Cruz, A. Jorio, M. Terrones, H. Terrones, G. Van Lier, J.-C. Charlier, M. S. Dresselhaus, R. Saito, Y. A. Kim, T. Hayashi, H. Muramatsu, M. Endo, M. A. Pimenta: Resonance Raman study of linear carbon chains formed by the heat treatment of double-wall carbon nanotubes, Phys. Rev. B **73**, 193408 (2006) 515

[91] P. Puech, H. Hubel, D. J. Dunstan, R. R. Bacsa, C. Laurent, W. S. Bacsa: Discontinuous tangential stress in double wall carbon nanotubes, Phys. Rev. Lett. **93**, 095506 (2004) 515

[92] J. Arvanitidis, D. Christofilos, K. Papagelis, T. Takenobu, Y. Iwasa, H. Kataura, S. Ves, G. A. Kourouklis: Double-wall carbon nanotubes under pressure: Probing the response of individual tubes and their intratube correlation, Phys. Rev. B **72**, 193411 (2005) 515

[93] H. Rauf, T. Pichler, R. Pfeiffer, F. Simon, H. Kuzmany, V. N. Popov: Detailed analysis of the Raman response of n-doped double-wall carbon nanotubes, Phys. Rev. B **74**, 235419 (2006) 516

[94] A. Rahmani, J.-L. Sauvajol, J. Cambedouzou, C. Benoit: Raman-active modes in finite and infinite double-walled carbon nanotubes, Phys. Rev. B **71**, 125402 (2005) 516

[95] W. Ren, F. Li, P. Tan, H.-M. Cheng: Raman evidence for atomic correlation between the two constituent tubes in double-walled carbon nanotubes, Phys. Rev. B **73**, 115430 (2006) 516

[96] P. M. Singer, P. Wzietek, H. Alloul, F. Simon, H. Kuzmany: NMR evidence for gapped spin excitations in metallic carbon nanotubes, Phys. Rev. Lett. **95**, 236403 (2005) 516, 517

[97] M. Yudasaka, T. Ichihashi, D. Kasuya, H. Kataura, S. Iijima: Structure changes of single-wall carbon nanotubes and single-wall carbon nanohorns caused by heat treatment, Carbon **41**, 1273–1280 (2003) 518

[98] Y. A. Kim, H. Muramatsu, T. Hayashi, M. Endo, M. Terrones, M. S. Dresselhaus: Thermal stability and structural changes of double-walled carbon nanotubes by heat treatment, Chem. Phys. Lett. **398**, 87–92 (2004) 518

[99] M. Terrones, H. Terrones, F. Banhart, J.-C. Charlier, P. M. Ajayan: Coalescence of single-walled carbon nanotubes, Science **288**, 1226–1229 (2000) 518

[100] C. Liu, Y. Y. Fan, M. Liu, H. T. Cong, H. M. Cheng, M. S. Dresselhaus: Hydrogen storage in single-walled carbon nanotubes at room temperature, Science **286**, 1127–1129 (1999) 518

[101] A. S. Claye, J. E. Fischer, C. B. Huffman, A. G. Rinzler, R. E. Smalley: Solid-state electrochemistry of the li single wall carbon nanotube system, J. Electrochem. Soc. **147**, 2845–2852 (2000) 518

[102] G. U. Sumanasekera, C. K. W. Adu, S. Fang, P. C. Eklund: Effects of gas adsorption and collisions on electrical transport in single-walled carbon nanotubes, Phys. Rev. Lett. **85**, 1096–1099 (2000) 518

[103] R. H. Baughman, C. Cui, A. A. Zakhidov, Z. Iqbal, J. N. Barisci, G. M. Spinks, G. G. Wallace, A. Mazzoldi, D. De Rossi, A. G. Rinzler, O. Jaschinski, S. Roth, M. Kertesz: Carbon nanotube actuators, Science **284**, 1340–1344 (1999) 518

[104] C.-M. Yang, K. Kaneko, M. Yudasaka, S. Iijima: Effect of purification on pore structure of HiPco single-walled carbon nanotube aggregates, Nano Lett. **2**, 385–388 (2002) 519

[105] K. Sohlberg, R. E. Tuzun, B. G. Sumpter, D. W. Noid: Application of rigid-body dynamics and semiclassical mechanics to molecular bearings, Nanotechnol. **8**, 103–111 (1997) 520
[106] Z. C. Tu, X. Hu: Molecular motor constructed from a double-walled carbon nanotube driven by axially varying voltage, Phys. Rev. B **72**, 033404 (2005) 520
[107] A. Kis, K. Jensen, S. Aloni, W. Mickelson, A. Zettl: Interlayer forces and ultralow sliding friction in multiwalled carbon nanotubes, Phys. Rev. Lett. **97**, 025501 (2006) 520
[108] M.-F. Yu, B. I. Yakobson, R. S. Ruoff: Controlled sliding and pullout of nested shells in individual multiwalled carbon nanotubes, J. Phys. Chem. B **104**, 8764–8767 (2000) 520
[109] J. Cumings, A. Zettl: Low-friction nanoscale linear bearing realized from multiwall carbon nanotubes, Science **289**, 602–604 (2000) 520

Index

New Techniques for Carbon-Nanotube Study and Characterization

Achim Hartschuh[1,2]

[1] Department Chemie und Biochemie, Ludwig-Maximilians-Universität München München, Germany
[2] Center for Nanoscience CeNS, München, Germany
achim.hartschuh@cup.uni-muenchen.de

Abstract. This chapter reviews three new experimental techniques for the study and characterization of carbon nanotubes and the exploration of novel phenomena. First, imaging and spectroscopy on the nanoscale is presented using near-field optical microscopy. Secondly, phonon spectroscopy with atomic resolution is demonstrated based on inelastic electron tunneling. Finally, coherent phonon generation by ultrashort laser pulses is reviewed.

1 Introduction

Progress in science is and was often triggered by novel techniques and new instrumentation. Within the past few years several spectroscopic techniques have emerged that provide fascinating new insights into the properties of carbon nanotubes. Besides giving answers to existing physical problems, these techniques provide access to the formulation of fundamentally new questions and the exploration of new phenomena. In this chapter we review results achieved by the application of three different experimental techniques and discuss their potential for future studies. Nanoscale spatial resolution is achieved with scanning near-field optical microscopy and scanning tunneling microscopy, permitting us to interact with a single nanotube by optical or electrical means. We review examples showing that highly confined optical and electrical interactions can be used to generate and probe localized phonon modes in the vicinity of structural defects and external perturbations. Finally, ultrashort femtosecond laser pulses are utilized to initiate coherent phonons, i.e., synchronized lattice vibrations of nanotubes within an ensemble that follow a single-molecule trajectory. Real-time observations of these trajectories unravel phonon-mode coupling, guiding the way for phonon control through phase-controlled optical excitation.

2 Near-Field Optical Microscopy

Photoluminescence and Raman spectroscopy are powerful tools for studying the electronic and vibronic properties of single-wall carbon nanotubes

A. Jorio, G. Dresselhaus, M. S. Dresselhaus (Eds.): Carbon Nanotubes,
Topics Appl. Physics **111**, 371–392 (2008)

(SWNTs). Experiments on individual SWNTs, in particular, remove ensemble averaging involving different nanotube chiralities and can help to refine our understanding of nanotube physics. The spatial resolution achieved in conventional microscopy, on the other hand, is limited by diffraction to about half the wavelength of the excitation light. Thus, the spectroscopic data obtained results from spatial averaging over 300 nm along the investigated nanotube.

Near-field optical techniques overcome the diffraction limit and can provide new insights into material properties on the nanometer scale. Several schemes have been suggested in the past and have been implemented experimentally. The widely adapted aperture approach is based on an aluminum-coated fiber tip of which the foremost end is left uncoated to form a small aperture (see, e.g., [1–3]). Unfortunately, only a tiny fraction ($\leq 10^{-4}$ for a 100-nm aperture) of the light coupled into the fiber is emitted by the aperture because of the cutoff of propagation of waveguide modes. In practice, the spatial resolution of aperture probes is limited to about 50 nm.

Alternatively, laser-illuminated metal probes are utilized to locally enhance electromagnetic fields, thereby enhancing the spectroscopic response of the system studied within a small sample volume (see, e.g., [4–10]). This very general approach allows the study of a variety of spectroscopic signals. So far, tip-enhanced microscopy has been applied to investigate Raman scattering and photoluminescence of SWNTs (see, e.g., [9–15]). The highest spatial resolution achieved up to now is about 10 nm, essentially limited by the tip size. In addition to superior resolution, near-field optical microscopy also provides significant signal enhancement by several orders of magnitude. Given the tiny probe volume of about $(10\,\mathrm{nm})^3 = 10^{-21}$ liter that is associated with the spatial resolution, this signal enhancement is crucial for efficient sample detection. The combination of nanoscale resolution and signal amplification makes this technique ideally suited for investigations of localized perturbations caused by defects or a nonuniform environment. In short, near-field measurements can extract optical signals that would be averaged out in conventional optical microscopy.

2.1 Experimental

Tip-enhanced optical microscopy is based on the local field enhancement at a laser-illuminated metal probe. The enhancement originates from a combination of the electrostatic lightning-rod effect, which is due to the geometric singularity of sharply pointed structures, and localized surface plasmon resonances that depend sensitively on the excitation wavelength. To exploit short-ranged near-field interactions, the tip needs to be scanned in close proximity to the sample surface. The tip–sample distance control is achieved as in atomic force microscopy by probing interatomic forces and using a feedback control for constant-force conditions. In an image scan, topography and

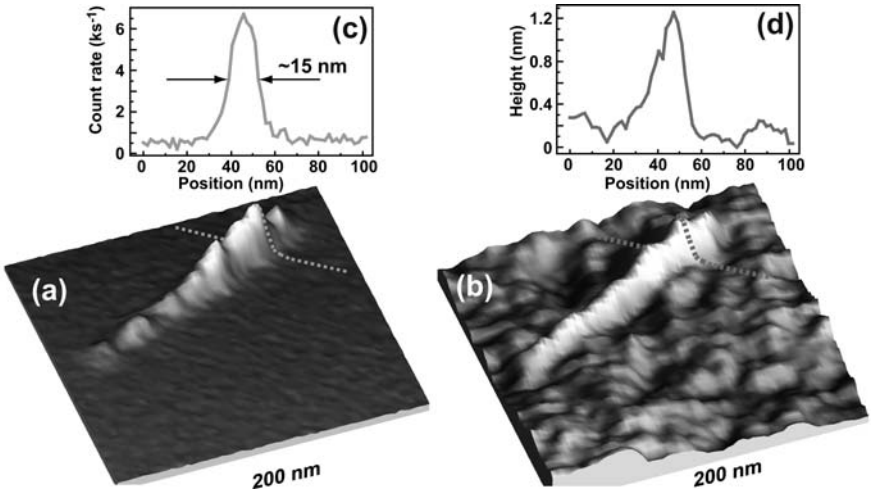

Fig. 1. Simultaneous near-field Raman image (**a**) and topographic image (**b**) of a SWNT on glass. Scan area $200 \times 200\,\mathrm{nm}^2$. The Raman image is acquired by detecting the intensity of the G-band upon laser excitation at 632.8 nm. Besides the nanotube, the topographic image shows the roughness of the glass surface. (**c**) Cross section taken along the indicated *dashed line* in the Raman image. (**d**) Cross section taken along the indicated *dashed line* in the topographic image. The height of the individual nanotube is $\approx 1.0\,\mathrm{nm}$. Vertical units are photon counts per second for (c) and per nanometer for (d)

optical information are recorded simultaneously, allowing for a direct correlation between structural and optical properties. As in any scanning probe technique, the spatial resolution achieved in the experiment is determined essentially by the diameter of the tip apex. In general, near-field optical images exhibit an increased resolution compared to the topographic image because of the dependency of the signal enhancement on higher orders of the electromagnetic fields [3, 16].

2.2 Results

In this section, the key applications of near-field optical microscopy are reviewed: 1. spectrally selective imaging with nanoscale spatial resolution, and 2. Raman and PL spectroscopy of SWNTs on a length scale of 10 nm.

2.2.1 Nanoscale Optical Imaging

Figure 1a shows a near-field Raman image of a SWNT on a glass substrate together with the simultaneously acquired topographic image of the same sample area in Fig. 1b. The Raman image was acquired by detecting the

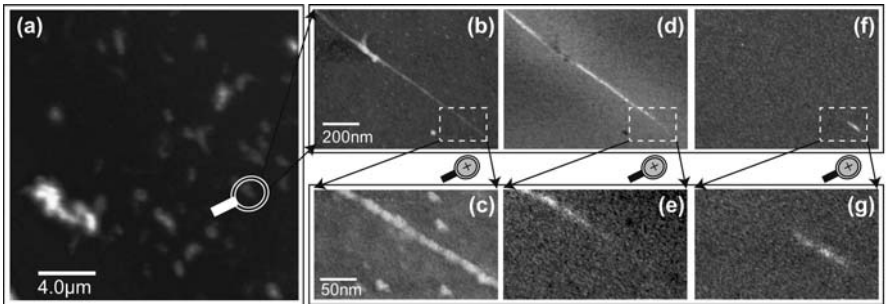

Fig. 2. Imaging of DNA-wrapped SWNTs at different magnifications: (**a**) Confocal Raman image using an excitation wavelength of 632.8 nm. Topographic images in (**b**) and (**c**) indicate a periodic height modulation expected for wrapping with short DNA segments. (DNA wrapping of nanotubes was carried out following the procedure described in [20].) Near-field Raman images (**d**) and (**e**) show the G-band intensity around 700 nm and in photoluminescence images (**f**) and (**g**) the intensity around 950 nm. PL occurs only in the lower section of the nanotube with the emission wavelength of an (8, 3) nanotube, while the Raman intensity is significantly weaker. The abrupt transition from strong to weak Raman scattering combined with the appearance of PL is interpreted as a local change in the nanotube chirality

intensity of the G-band around 1600 cm^{-1} after laser excitation at 632.8 nm while raster scanning the sample. The topographic image was acquired in the shear-force mode (noncontact mode) by applying small forces of a few tens of pN for which the soft gold probes used are not damaged. The spatial resolution can be determined from the width of the signals (FWHM) presented as linescans in Figs. 1c and d to be about 20 nm, far below the diffraction limit of conventional microscopy. The sharpest images of SWNTs observed up to now feature an optical resolution of about 10 nm, limited by the tip diameter [13].

Simultaneous near-field Raman and photoluminescence (PL) imaging have been demonstrated in [14]. For SWNTs grown by arc discharge on glass, highly confined PL from short segments of about 20 nm in length has been observed. The PL from micelle-encapsulated SWNTs on mica typically stems from longer segments of up to several hundreds of nanometers. Figure 2 shows imaging of a DNA-wrapped nanotube at different magnifications. In the present case, photoluminescence occurs only within about 75 nm in the lower part of the nanotube (Fig. 2g). The intensity of the Raman signal, on the other hand, drops exactly at the position at which PL starts to occur, indicating a change in nanotube chirality (Fig. 2e) [17–19].

In general, the resulting signal enhancement for Raman scattering and photoluminescence will be different. For Raman scattering, the electromagnetic signal enhancement is caused by the enhancement of both incident field

E_{incident} and scattered field and scales approximately as $\approx [E_{\text{local}}/E_{\text{incident}}]^4$, where E_{local} is the local electric field [21].

For photoluminescence, on the other hand, three contributions occur that can be discussed in terms of the corresponding transition rates. First, the enhancement of the incident field is linked to an enhanced excitation rate proportional to $[E_{\text{local}}/E_{\text{incident}}]^2$. Secondly, tip-induced modifications of the local photonic mode density can increase the spontaneous emission rate and hence the PL quantum yield (Purcell effect). Finally, the nonradiative decay rate can be increased due to quenching by the metal tip. The relative contributions of the three effects depend on the distance between tip and sample and the mutual orientation of the tip and transition dipole [8, 22–24]. Since the PL quantum yield is very low for SWNTs on substrates, typically about 10^{-4}, it could be increased substantially by an enhanced radiative rate. Remarkably, the observed enhancement of the PL signal will depend on the PL quantum yield of the nanotube in the absence of the metal tip. On the basis of simultaneously recorded Raman scattering images with and without a metal tip, signal enhancements for PL and Raman scattering have been determined quantitatively in [14]. Near-field enhancement was found to be much stronger for PL than for Raman scattering, indicating that it is possible to increase the PL quantum yield of SWNTs using metallic nanoparticles.

2.2.2 Nanoscale Optical Spectroscopy

The optical resolution apparent in Fig. 1 shows that the enhanced field is laterally confined to the size of the metal tip, i.e., within 20 nm. Hence, the near-field signal detected on top of a nanotube results from a very short section of about 20 nm in length, giving an insight into the local electronic and structural properties. Near-field spectroscopic Raman imaging has been utilized to visualize variations of the RBM frequency along nanotubes on the nanoscale. Figure 3 shows high-resolution images of nanotubes grown by arc discharge, Fig. 3a, and by CVD, Fig. 3c. Near-field Raman spectra taken along the nanotube at positions 1–4 are presented in Figs. 3b and 3d, respectively. While the RBM frequency of the arc-discharge nanotube varies strongly by up to 15 cm^{-1} on a length scale of several 10 nm, uniform characteristics are observed for the CVD nanotube, indicating a more uniform growth process [13].

Near-field photoluminescence spectra taken along a nanotube in steps of 30 nm are presented in Fig. 4 [14]. The spectral position and shape of the photoluminescence is found to vary significantly on the nanoscale. From the spectra it is clear that the observed photoluminescence emission is in fact composed of multiple emission bands with different emission energies and varying relative contributions. Due to its limited spatial resolution, standard confocal spectroscopy would only show a single broadened luminescence peak resulting from a superposition of individual bands. The observed local ener-

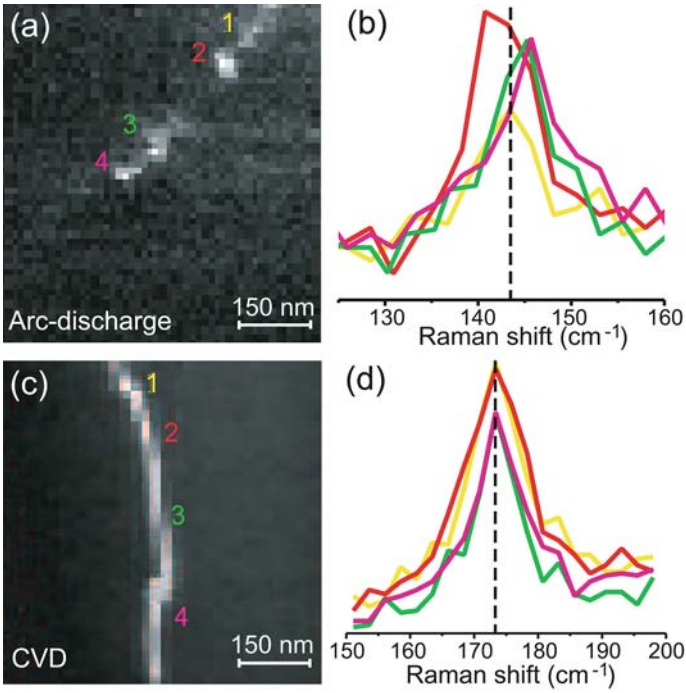

Fig. 3. Near-field Raman spectroscopy: (**a**) and (**c**): Near-field spectral images for the RBM of an arc-discharge-grown SWNT ($\omega_{\mathrm{RBM}} = 143\,\mathrm{cm}^{-1}$) and a SWNT grown via CVD ($\omega_{\mathrm{RBM}} = 173\,\mathrm{cm}^{-1}$), respectively. The integration time was 210 ms per pixel. (**b**) and (**d**): Corresponding RBM spectra for several locations along the length of the SWNTs as marked. The most notable feature is the spectral wandering of the RBM peak for the arc-discharge-grown nanotube and the variation in intensity. In comparison, RBM scattering for the CVD-grown nanotube shows no such variations (from [13])

getic fluctuations are most likely related to changes of the dielectric function of the environment and the presence of charged adsorbates.

Other examples for tip-enhanced near-field spectroscopy on SWNTs include the investigation of intramolecular junctions based on RBM and G-band variations [19] and the observation of highly localized phonon modes at the end of a nanotube [25]. Diameter-selective near-field Raman analysis and imaging of isolated carbon-nanotube bundles was shown in [15]. In [26], nanoscale uniaxial pressure effects on a carbon-nanotube bundle were studied. Upon applying large forces of up to 2.4 nN using contact-mode AFM, significant spectral shifts in the RBM frequencies and variations in the G-band frequencies have been observed.

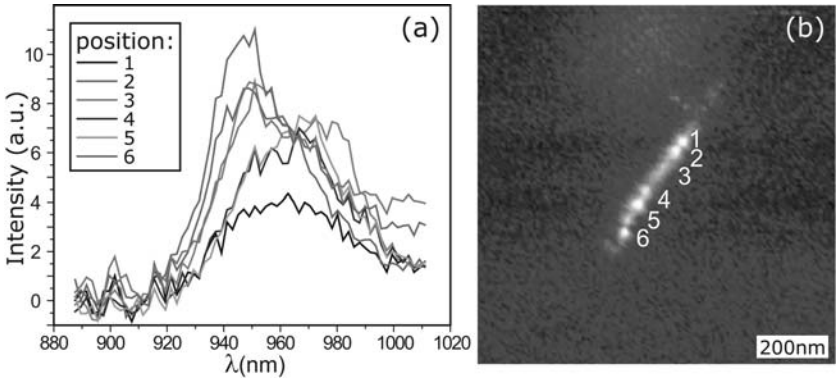

Fig. 4. (**a**) Near-field photoluminescence spectra taken along positions 1–6 in steps of 30 nm indicated in the near-field photoluminescence image of the SWNT in (**b**). The spectral position and shape of the photoluminescence is found to vary significantly on the nanoscale (from [14])

2.3 Outlook

Near-field optical spectroscopy provides a unique tool to study the correlation between local structural and electronic properties that determine Raman and photoluminescence spectra. In addition, near-field PL spectroscopy allows study of the influence of the local dielectric environment on the emission properties of SWNTs. Combined with the powerful toolbox of laser spectroscopy, such as impulsive coherent phonon generation presented in the third part of this chapter and other time-resolved techniques (see the contribution by *Ma* et al.), real-time observations of exciton dynamics and propagation along a single nanotube could come within reach.

At present, we have to improve our understanding of the image formation and signal-enhancement processes that are known to differ for Raman scattering and photoluminescence. In particular, radiative rate enhancement and photoluminescence quenching, known to be crucial for single-molecule fluorescence studies [23, 24], have to be quantified for SWNTs. Near-field optical images and spectra feature not only higher spatial resolution compared to data achieved by conventional microscopy, but they also result from a different type of interaction. More specifically, high spatial resolution results from field confinement that requires the presence of evanescent fields with k-vectors that exceed the k-vectors of propagating waves by more than an order of magnitude. Far-field optical transitions in the visible occur only within the light cone formed by k-vectors that obey $k = 2\pi/\lambda \approx 0.01\,\mathrm{nm}^{-1}$ and these k-vectors are thus far smaller than the range of k-vectors in the Brillouin zone of nanotubes for which $k \approx 1\,\mathrm{nm}^{-1}$. In the optical near-field it could be possible to initiate "nonvertical" electronic transitions connecting states with different k-vectors within the whole Brillouin zone (see, e.g., [27, 28]).

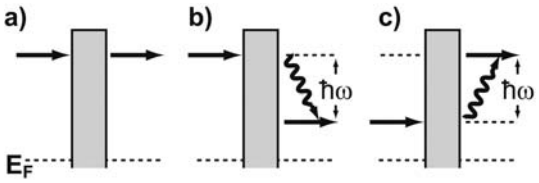

Fig. 5. Energy diagram for elastic tunneling (**a**), inelastic tunneling by phonon emission (**b**) and by phonon absorption (**c**). Fermi energy E_F and phonon energy $\hbar\omega$ are indicated

Besides giving access to a new class of optical transitions that could be used to characterize the electronic band structure of nanotubes, such knowledge would guide the way to design schemes for "nanotube photonics" utilizing efficient coupling of electromagnetic radiation to nanotubes.

3 Phonon Spectroscopy Using Inelastic Electron Tunneling

Scanning tunneling microscopy (STM) has been used extensively to visualize carbon nanotubes with atomic-scale resolution (see, e.g., [29, 30] and the contribution by *Jorio* et al. in this book). Spectroscopy, performed by taking the first derivative of the tunneling current $\mathrm{d}I/\mathrm{d}V(V)$, reveals the local density of states (LDOS) leading to the well-known curves for metallic and semiconducting nanotubes characterized by van Hove singularities (vHS). In this section we review recent results achieved by inelastic electron tunneling spectroscopy (IETS). Combined with scanning tunneling microscopy (IETS-STM), vibrational maps of individual nanostructures and molecules can be recorded with atomic-scale resolution (see, e.g., [31]).

In IETS, peaks in the second derivative of the current–voltage characteristics ($\mathrm{d}^2I/\mathrm{d}V^2(V)$) appear at voltages V_i given by the quantum relation $eV_i = \hbar\omega_i$, where ω_i are the vibrational frequencies of the nanotube. The peaks occur because of a small increase in the conductance of the junction formed by the STM tip and the nanotube due to the presence of additional tunneling channels when the bias voltage V exceeds the inelastic threshold. When $eV \geq eV_i = \hbar\omega_i$ electrons can tunnel inelastically, losing energy to a vibrational excitation (Fig. 5).

3.1 Experimental

Current–voltage (I–V) spectroscopy is performed by keeping the STM tip stationary above the nanotube, switching off the feedback, and recording the current as a function of the voltage applied to the sample. Within several approximations, the first derivative is proportional to the local density of states $\rho(r_0, E)$ at the location of the tip apex r_0 according to

$\mathrm{d}I/\mathrm{d}V(V) \propto \rho(r_0, E_\mathrm{F} + eV)$, where E_F is the Fermi energy. Experimentally, $\mathrm{d}I/\mathrm{d}V(V)$ curves are measured by superimposing a sinusoidal voltage ΔV with frequency f on the bias voltage followed by signal demodulation at f. In inelastic tunneling spectroscopy, the second derivative $\mathrm{d}^2I/\mathrm{d}V^2(V)$ is extracted by signal demodulation at $2f$ [31–34]. Local IETS spectra are measured by ramping the bias voltage V at a fixed sample position while recording $\mathrm{d}^2I/\mathrm{d}V^2(V)$ (see Fig. 7b). Alternatively, images of specific vibrational modes can be obtained by raster scanning the tip at constant bias voltage V in the constant-current mode to record the surface topography while recording $\mathrm{d}^2I/\mathrm{d}V^2(V)$ (see, e.g., [33]).

In order to observe transitions involving phonons in carbon nanotubes, electron energies eV have to be in the range of vibrational energies, e.g., $\hbar\omega_\mathrm{RBM}$, requiring measurements at low bias voltages V. To avoid thermal excitation, the sample has to be cooled down to low temperatures. For STM measurements, nanotubes have to be in direct contact with a conductive substrate, while the resistance of the junction formed by the nanotube and the metal substrate can typically be neglected compared to the tunneling gap. Alternatively, partly suspended nanotubes bridging trenches can be studied. In this case, the nanotube establishes current flow to contacts on either side of the trench.

3.2 Results

Vitali et al. [32,34] presented the first inelastic tunneling images of nanotubes and demonstrated the enormous potential of IETS-STM for the investigation of localized perturbations in carbon nanotubes. In a first step, the signatures of the radial breathing mode (RBM) have been identified in IETS spectra. Figure 6 shows $\mathrm{d}^2I/\mathrm{d}V^2(V)$ spectra obtained for eight nanotubes with different structural parameters (n, m). Direct chirality identification results from atomic-scale STM images reflecting both nanotube diameter d_t and chirality. Additionally, nanotube diameters are determined using the known relation to the energy separation of the vHS measured by $\mathrm{d}I/\mathrm{d}V$ curves. Based on this data the linear relation between the radial breathing mode frequency and the inverse nanotube diameter $\omega_\mathrm{RBM} = \alpha/d_\mathrm{t}$ was verified and the scaling factor α was determined to be $262\,\mathrm{meV/\AA} \approx 210\,\mathrm{cm}^{-1}$ nm in good agreement with Raman scattering and photoluminescence data (see the contributions by *Saito* et al. and by *Lefebvre* et al.).

In a series of experiments, phonon modes in the vicinity of localized defects and perturbations have been imaged and investigated spectroscopically. Figure 7b shows vibrational spectra taken along the white dotted line in Fig. 7a [32].

From the topographic image in Fig. 7a three different regions can be distinguished, labeled (1)–(3), featuring clearly different phonon characteristics. In region (1) up to about 160 Å, a metallic (17, 14) nanotube is identified exhibiting an RBM energy of 12 meV (Fig. 7b). In region (2) at position 170 Å,

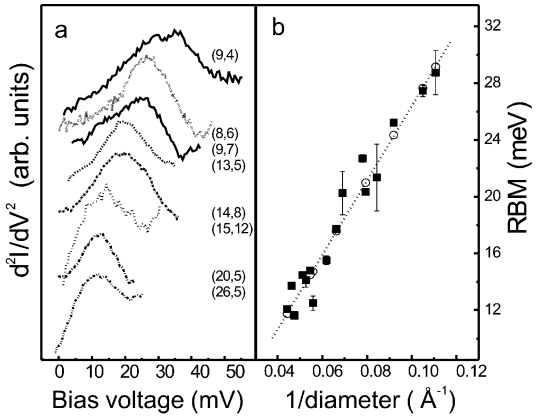

Fig. 6. (**a**) IETS-STM spectra of eight different isolated SWNTs, obtained at 6 K as the $\mathrm{d}^2I/\mathrm{d}V^2(V)$ lock-in signal with a bias modulation of $\Delta V = 10\,\mathrm{meV}$ at a frequency of $f = 2.7\,\mathrm{kHz}$ in the energy range of the RBM. Each spectrum is labeled by the (n, m) pair of the respective nanotube. (**b**) Frequency of the RBM of isolated SWNTs plotted against the inverse nanotube diameter together with the linear scaling relation $\omega_{\mathrm{RBM}} = \alpha/d_{\mathrm{t}}$. The experimentally observed peak energies in the IETS and the theoretically calculated phonon energies are shown as *solid squares* and *open circles*, respectively (from [32])

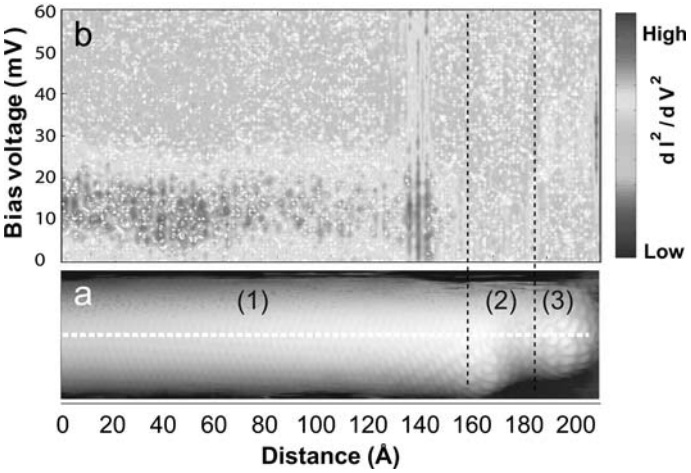

Fig. 7. Changes in the local vibrational properties of a SWNT associated with the presence of local defects. (**a**) Topographic image of a $(17, 14)$ nanotube containing an intramolecular junction and a closed end. The transitions between the corresponding regions (1) to (3) are highlighted by *black dashed lines*. (**b**) Color scale map of the $\mathrm{d}^2I/\mathrm{d}V^2(V)$ spectra as a function of energy and position along the nanotube. The *white dotted line* in (**a**) indicates the sampling positions along the nanotube axis where the IETS spectra were taken (from [32])

the diameter abruptly decreases from 21.2 to 9.7 Å while the chiral angle is preserved. Surprisingly, no radial breathing mode is observed. Region (3) contains the closed ending of a semiconducting nanotube ((8, 6) or (8, 7)) with a phonon energy of 29 meV. The absence of the RBM in section (2) indicates that a minimum nanotube length of about 3 nm is necessary to sustain an RBM vibration.

Imaging of higher-energy modes at 200 meV corresponding to the Raman G-band modes was demonstrated in [34]. Investigations of a crossed junction between nanotubes revealed a pressure-induced metallization at the junction associated with pronounced spatial variations of phonon properties.

In a different type of experiment, *LeRoy* et al. [35] demonstrated that phonons in nanotubes can be generated and controlled by inelastic electron tunneling. The experimental configuration is shown schematically in Fig. 8d. At lower tunneling currents ($I_{\mathrm{set}} = 100\,\mathrm{pA}$), $\mathrm{d}I/\mathrm{d}V$ curves of partially suspended nanotubes were found to exhibit the well-known Coulomb staircase with Coulomb peaks resulting from single-electron charging (Fig. 8a). For higher currents exceeding 300 pA, additional peaks occurred on either side of the Coulomb peaks. These peaks, marked by "Em" and "Abs" for emission and absorption, respectively, in Fig. 8e, increase in intensity with increasing current and can become even stronger than the Coulomb peak "C" for high currents. The energy difference between the main and side peaks, on the other hand, remains constant, being equal to the energy of the radial breathing mode of the investigated nanotube.

The appearance of equidistant side peaks reflects additional tunneling channels caused by the electronic generation of phonons. More specifically, peaks on the side towards lower voltages, corresponding to tunneling electrons with smaller energies, indicate phonon-assisted tunneling by the absorption of a phonon (Fig. 5e). Phonon emission, on the other hand, allows tunneling of electrons with higher energies. Phonon absorption at the extremely low temperature of the experiment (5 K) is surprising and can only be explained by a current-induced nonequilibrium phonon population. Current-induced heating is also responsible for the enhancement of the peaks on the high-energy side through stimulated phonon emission.

The new peaks that are observed for increased values of the current allow estimation of the lifetime of the phonon in an individual SWNT. The fact that side peaks on the low-energy side are visible only for higher currents, i.e., faster rates of electron-tunneling, implies that the decay time for the phonon mode in this SWNT is longer than the average time between electron-tunneling events at these rates. For example, for the case of Fig. 8b, the current for the first absorption peak visible at −0.15 V gives an average rate of electron-tunneling events of $1.44 \times 10^8\,\mathrm{s}^{-1}$. From this, a phonon decay time of at least $\tau = 7\,\mathrm{ns}$ is deduced that is much longer than the typical times extracted from Raman experiments [36]. Remarkably, this decay time corresponds to a lower bound for the quality factor $Q = \tau\nu_{\mathrm{RBM}}$ of 20 000 for the RBM in these suspended nanotubes.

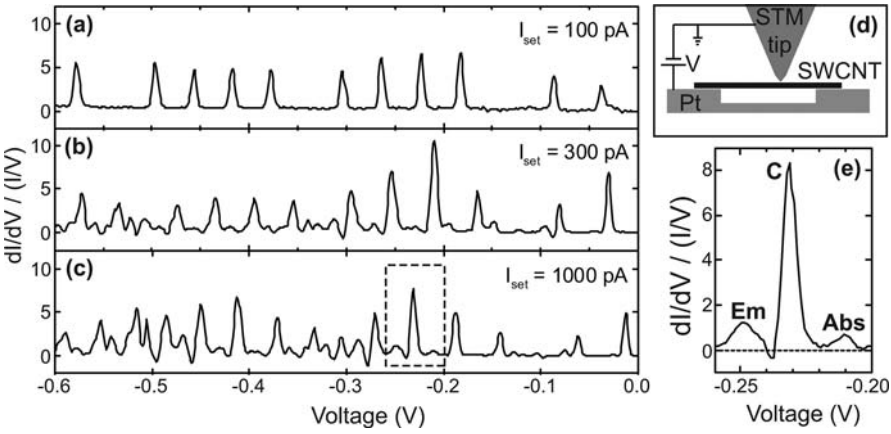

Fig. 8. Current dependence of phonon-assisted tunneling. (**a**) Normalized differential conductance of a metallic SWNT as a function of sample voltage taken with a low setpoint current I set at -0.6 V. The tip is located at the center of the suspended SWNT shown schematically in (**d**). A series of sharp peaks is visible due to the Coulomb staircase as the Fermi level of the substrate aligns with unoccupied states of the SWNT. (**b**) and (**c**): Same as (**a**) with increasing setpoint current. A series of side peaks has appeared near the main Coulomb staircase peaks due to the absorption and emission of phonons. (**e**) Zoom-in on one of the peaks marked in (**c**) showing side peaks corresponding to the emission (Em) and absorption (Abs) of phonons (from [35])

3.3 Outlook

Inelastic electron tunneling spectroscopy is a powerful tool for in depth investigations of electronic and vibrational properties in the vicinity of defects and external perturbations. Atomic-scale resolution gives access to new questions such as the minimum structural length required to sustain a phonon mode in nanostructures.

As for any novel technique, open questions remain regarding the details of the signal formation, i.e., the local requirements for electron tunneling and the interaction between tunneling electrons and phonons in the particular sample material. Selection rules for phonon generation by inelastic electron tunneling have been developed for different molecular systems (see, e.g., [37]) and need to be refined for nanotubes. In general, both optically active and inactive phonon modes are observable in IETS although with varying signal contributions [38, 39]. Furthermore, recent investigations on HOPG revealed that phonon generation is not limited to phonons with small k-vectors, and phonons with large momentum can be excited as well [38]. The geometrical configuration of the tunneling system, on the other hand, could lead to restrictions to phonons in certain regions of the Brillouin zone. For a quan-

titative analysis of IETS-STM data, the properties of the tip, such as its density of states and shape, will become relevant.

4 Coherent Phonon Generation and Detection

Phonons in SWNTs are usually studied by resonant Raman spectroscopy providing a wealth of information on the most fundamental properties including the vibronic and electronic structure as well as electron–phonon coupling. In conventional continuous wave (cw) Raman scattering, on the other hand, only ground-state vibrations can be studied, whereas photoexcited-state vibrational dynamics and energies remain largely unknown. With the advent of ultrafast laser spectroscopy, it became possible to monitor photo-induced electronic and vibrational dynamics on a femtosecond timescale (see also the contribution by *Ma* et al.). In general, time-domain observations of phonon dynamics require the generation of coherent phonons (CP), i.e., inphase lattice vibrations of an ensemble of the same species that add up constructively to generate a detectable signal. Coherent phonons have been observed in a variety of different systems including thin films, semiconductor nanostructures and fullerenes (see, e.g., [40–42]).

Coherent phonon generation in nanotubes can be described by the mechanism of displacive excitation (DECP) [43–45]. After excitation by an ultrashort pump pulse, the electronically excited system rapidly reaches quasiequilibrium in a time short compared to nuclear response times. If the excited-state electronic configuration is associated with a different equilibrium nuclear configuration, the system will start to oscillate around the new energetic minimum (Fig. 9). The frequency of the oscillation is given by the vibronic frequency associated with the modified configurational coordinate. Besides the formation of wavepackets in the excited state, this process also generates ground-state coherence. In the case of redshifted excitation for example, the pump pulse leaves a hole in the ground state near the region for larger displacements with respect to equilibrium (Fig. 9b). The nuclear distribution is therefore effectively centered at smaller displacements corresponding to an oscillating ground state wavepacket.

These oscillating wavepackets induce a periodic modulation of the Frank–Condon envelope of the involved electronic transitions, namely ground-state absorption and stimulated emission, which is reflected into transmission modulation at both ground- and excited-state vibrational frequencies. Once CPs are created, the vibrational motion of an ensemble of nanotubes is that of a single-molecule trajectory until the coherence of the wave packets is destroyed by intra- and/or inter-tube processes.

Within the DECP model, coherent phonon generation is possible only for A_1 symmetry Raman-active vibrational modes for which the quasiequilibrium nuclear coordinate is displaced with no change in lattice symmetry. In the

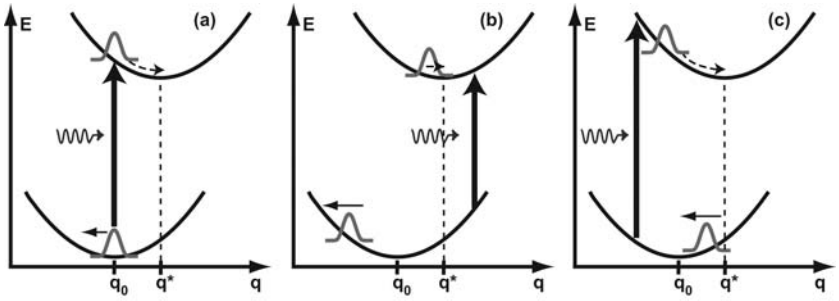

Fig. 9. Schemes illustrating the generation of wavepackets formed by coherent phonons upon displacive excitation (DECP) for three different pump carrier frequencies. Excitation at the absorption maximum (**a**), redshifted (**b**) and blueshifted excitation (**c**). Wavepackets in the electronic ground and excited state evolve in time, following the *arrows* driven by different nuclear equilibrium configurations described by the coordinates q_0 and $q*$, respectively [46, 47]

case of nanotubes, these are the radial breathing mode (RBM) and the high-energy C–C stretching modes that are part of the G-band.

4.1 Results

A theoretical description of coherent phonons in carbon nanotubes and their role in selective cap opening of finite-length nanotubes has been presented in [45, 48]. Experimentally, coherent phonons in SWNTs have only recently been studied for the first time [49–51]. The results presented in the following demonstrate that ultrafast laser spectroscopy allows us to selectively prepare vibrational wavepackets in nanotubes and to monitor their dynamics and coupling to different modes in real time.

Coherent phonons are studied experimentally using optical pump-probe techniques [49–51]. In these techniques, the observed quantity is the differential transmission ($\Delta T(\tau)/T = (T^*(\tau) - T)/T$), i.e., the normalized ratio between the transmission T^* after pulse excitation at time τ and without pulse excitation T (see also the contribution by *Ma* et al.). Coherent modes manifest themselves as a temporal modulation of the transmission with the frequency of the coherent mode. To excite such modes, laser pulses with a duration shorter than the inverse of the fundamental vibrational frequency are a prerequisite.

The publication by *Lim* et al. [51] is focused on the comparison of coherent phonon (CP) and resonant Raman scattering (RRS) data and on the dependency of the CP signal intensity on excitation energies. *Lim* et al. used a degenerate pump-probe scheme in which excitation and probe pulses have the same wavelength with a pulse duration of 50 fs. Figure 10a shows the pump-probe time trace ($\Delta T/T$) acquired within the first 16 ps after pulse excitation at 800 nm. The decay of the pump-probe signal occurs within a

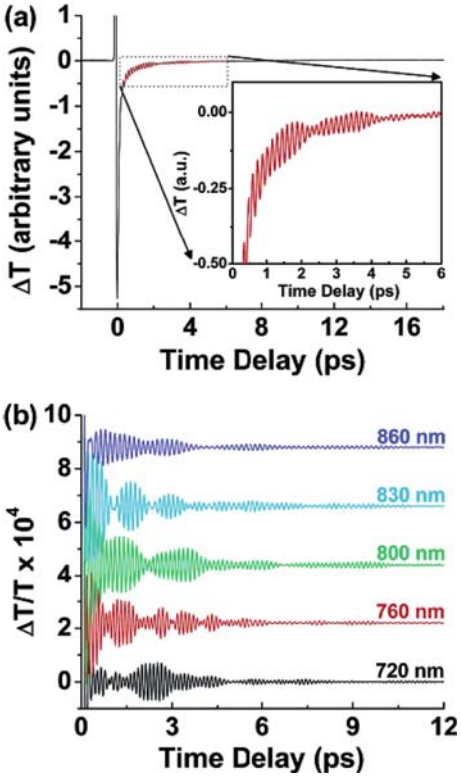

Fig. 10. (**a**) Pump-probe time-domain data taken at a center wavelength of 800 nm. The decay of the pump-probe signal within several picoseconds reflects the decay of the excited-state population. The inset is a zoom-in of the data between 0.3 and 6 ps, highlighting the CP contribution to the signal. (**b**) Coherent phonon oscillations excited and measured at five different photon energies. The individual traces are offset for clarity. The slower decay of the excited-state population has been subtracted (from [51])

few picoseconds and reflects the decay of the excited-state population. In addition, the time trace exhibits high-frequency modulations that are clearly seen in the inset showing a magnified view.

For different pump-probe wavelengths beating patterns with different modulation frequencies occur, as shown in Fig. 10b. To determine the frequencies of these oscillations, the Fourier transform of the time-domain data are calculated. As an example, the resulting CP spectrum for 765 nm is presented in Fig. 11. Based on the pulse length of 50 fs used in the experiment, frequencies up to $1/100\,\mathrm{fs}^{-1}$ corresponding to $330\,\mathrm{cm}^{-1}$, the regime of the radial breathing mode, are accessible. Also shown are resonant Raman scattering data obtained after cw excitation at the same wavelength. CP and RRS feature very similar peak positions. Obviously, the modulations observed in

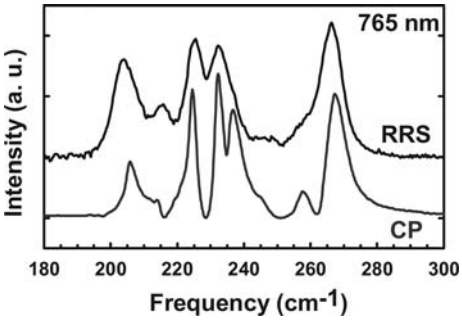

Fig. 11. Phonon spectrum detected at a center wavelength of 765 nm obtained from resonant Raman scattering (RRS) and coherent phonon (CP) measurements in the frequency range of the RBM (from [51])

Fig. 10 result from coherent oscillations of the radial breathing mode coordinate, i.e., the diameter of the nanotubes. In other words, upon short-pulse laser excitation, all nanotubes of a certain species within the sample breathe in phase.

Upon close examination, the authors found three noticeable differences between the CP and RRS data sets established for the same sample. First, the spectral width of the phonon bands in the CP spectra is decreased from 5–6 cm^{-1} to 3 cm^{-1} as compared to RRS spectra. Remarkably, this value is identical to the homogeneous linewidth derived from Raman scattering spectra for individual SWNTs in [36] after correcting for instrumental broadening and substrate effects. Secondly, while the chirality dependencies of the signal intensities feature similar family behavior for $(n - m) \bmod 3 = 1, 2$ suggesting the same role of electron–phonon coupling, different trends for $(2n + m) = \text{const}$ are observed. Namely, in Raman scattering, the signal strength decreases as $(2n + m)$ increases, whereas the CP signal increases with increasing $(2n + m)$. At present, no explanation is available for this result. Furthermore, intensity maps of the CP and RRS signal vs. excitation energy exhibit similar main-peak positions indicating that CPs and phonons from spontaneous Raman scattering are generated efficiently for the same energies. CP excitation spectra, however, exhibit a symmetric double peak with an intensity minimum at the energy with maximum absorption strength. This is a typical feature of coherent phonon signals reflecting the dependency of the nuclear displacement on the derivative of the optical lineshapes [46,47].

Gambetta et al. [50] studied coherent phonon generation in a nondegenerate pump-probe scheme using a time resolution better than 10 fs. The short pulse duration allows for observing high-frequency phonons up to approximately 2200 cm^{-1} covering the range of the radial breathing mode and the G-band modes. The time trace of the differential transmission detected, shown in Fig. 12, exhibits slow and fast modulations with periods of 132 fs and 21 fs resulting from RBM and G-band vibrations, respectively. The modulation

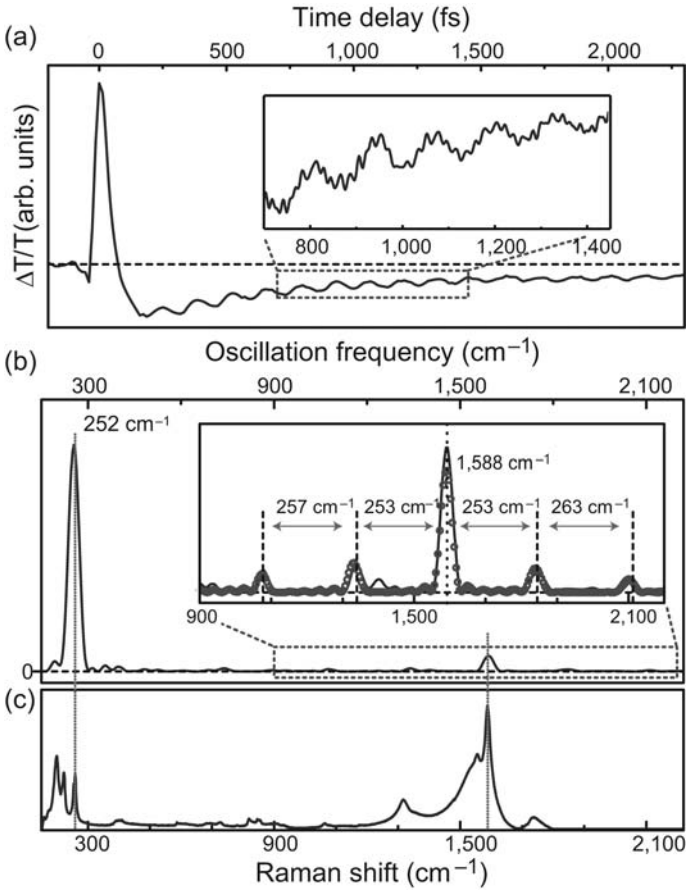

Fig. 12. Differential transmission ($\Delta T/T$) dynamics of SWNTs. (**a**) Excitation and probing by a sub-10 fs visible pulse; probe energy is 2.1 eV. The *inset* shows a portion of the trace acquired with a higher sampling rate, to fully resolve the high-frequency modulation. (**b**) Fourier transform (FT) power spectrum of the time trace shown in (a). *Inset:* the *solid line* is the zoom of the FT power spectrum, showing sidebands around the G mode. Regular spacing between the modes is indicated by *labels* and *double-headed arrows*. (**c**) Continuous-wave Raman spectrum obtained with HeNe excitation (from [50])

depth decays slowly, with a time constant of $T_2 \approx 1.6$ ps, allowing more than 20 RBM oscillations to be detected.

Figure 12b shows the coherent phonon spectrum achieved by taking the Fourier transform of the time trace together with the cw Raman spectrum in Fig. 12c. In the CP spectrum the contributions from the RBM around 250 cm^{-1} and the G mode at 1588 cm^{-1} are clearly identified. In addition to the dominant RBM and G-band, the CP spectrum contains small peaks

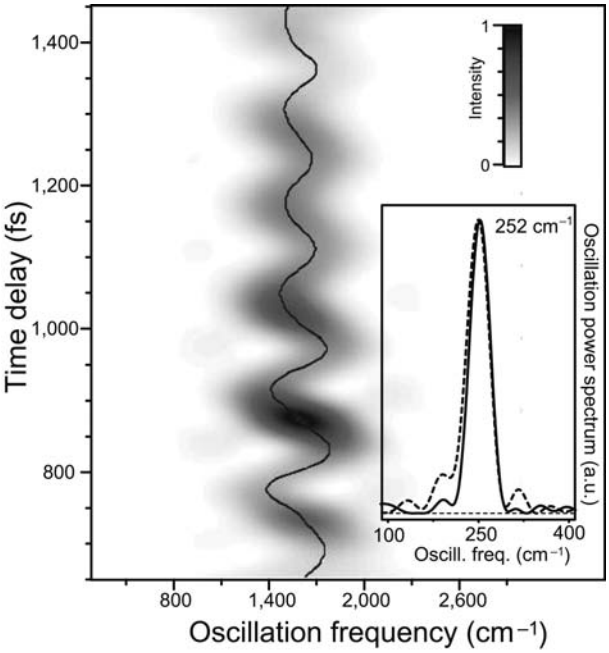

Fig. 13. Analysis of the frequency modulation of the G mode. Sliding-window Fourier transformation analysis of the data in the *inset* of Fig. 12. The measured G-band mode peak position is plotted as a *thin solid line*. *Inset:* FT power spectrum of the time dependence of the band peak position from (**a**) (*dashed line*); *solid line:* FT power spectrum of the time trace shown in Fig. 12a (from [50])

that do not correspond to any feature in the Raman spectrum. These small peaks are almost equally spaced with the frequency of the RBM, as can be seen from the inset in Fig. 13b. Analysis of the instantaneous frequencies and amplitudes of the G-band vibration using a sliding-window Fourier transformation analysis are shown in Fig. 13a. The frequency of the G-band vibration is clearly modulated in time at the frequency of the RBM. Hence, after pulsed excitation, the G-band mode frequency depends on the RBM configuration; in other words, the high-frequency mode follows the low-frequency mode adiabatically.

From the amplitude ratio between the central peak and anharmonic sidebands, the anharmonic coupling constant can be derived based on a simple model of coupled harmonic oscillators. From the experimental data, *Gambetta* et al. estimate a coupling constant of $2\,\mathrm{cm}^{-1}$ in agreement with theoretical predictions for the excited-state. For the electronic ground state, on the other hand, theoretical calculations predict nearly zero coupling between G-band mode and RBM. *Gambetta* et al. describe the excited-state nuclear configuration by a localized corrugation of the nanotube connected to a di-

ameter increase of about 4×10^{-4} nm. A similar trend with a somewhat larger displacement of about 1 to 2 % has been predicted by [45].

4.2 Outlook

Up to now, experimental studies report only on CP in semiconducting nanotubes. The lack of RBM modes of metallic nanotubes indicates that coherence is either not generated or not preserved in these types of nanotubes. In agreement with the DECP model, generation of coherent phonons appears to be limited to A_1-symmetry modes with zero momentum such as the RBM and G-band modes. At present, several open questions remain regarding the details of the generation process. In particular, an *a-priori* distinction between ground- and excited-state coherent phonons is not possible. Experimentally, the different contributions can only be distinguished by the detailed investigation of the initial phase and the temperature dependence of the signal [46]. A general description of coherent phonon generation showed that DECP is not a distinct mechanism, but a particular case of stimulated Raman scattering [52].

In summary, real-time observations of coherent phonon dynamics provide information on the vibrational properties of SWNTs that are not achievable by conventional Raman spectroscopy. In particular, photoexcited modes and coupling between different modes can be studied with great flexibility. Given the enormous versatility of tools provided by today's ultrafast laser spectroscopy, optical control of vibrational states in SWNTs could be envisaged [53, 54]. In addition, combined with near-field optical microscopy, phonon populations in nanotubes could be generated and manipulated by adaptive pulse shaping on the nanoscale [55].

References

[1] D. W. Pohl, W. Denk, M. Lanz: Optical stethoscopy: Image recording with resolution $\lambda/20$, Appl. Phys. Lett. **44**, 651–653 (1984) 372

[2] E. Betzig, J. K. Trautman: Near-field optics: Microscopy, spectroscopy, and surface modification beyond the diffraction limit, Science **257**, 189–195 (1992) 372

[3] L. Novotny, B. Hecht: *Principles of Nano-Optics* (Cambridge University Press, Cambridge 2006) 372, 373

[4] J. Wessel: Surface-enhanced optical microscopy, J. Opt. Soc. Am. B **2**, 1538–1541 (1985) 372

[5] E. J. Sánchez, L. Novotny, X. S. Xie: Near-field fluorescence microscopy based on two-photon excitation with metal tips, Phys. Rev. Lett. **82**, 4014–4017 (1999) 372

[6] S. M. Stöckle, Y. D. Suh, V. Deckert, R. Zenobi: Nanoscale chemical analysis by tip-enhanced Raman spectroscopy, Chem. Phys. Lett. **318**, 131–136 (2000) 372

[7] N. Hayazawa, Y. Inouye, Z. Sekkat, S. Kawata: Near-field Raman scattering enhanced by a metallized tip, Chem. Phys. Lett. **335**, 369–374 (2001) 372
[8] H. G. Frey, S. Witt, K. Felderer, R. Guckenberger: High-resolution imaging of single fluorescent molecules with the optical near-field of a metal tip, Phys. Rev. Lett. **93**, 200801–200804 (2004) 372, 375
[9] A. Hartschuh, E. J. Sánchez, X. S. Xie, L. Novotny: High-resolution near-field Raman microscopy of single-walled carbon nanotubes, Phys. Rev. Lett. **90**, 095503–095506 (2003) 372
[10] S. Kawata, V. M. Shalaev (Eds.): *Tip Enhancement*, Advances in Nano-Optics and Nano-Photonics (Elsevier, Amsterdam 2007) 372
[11] N. Hayazawa, T. Yano, H. Watanabe, Y. Inouye, S. Kawata: Detection of an individual single-wall carbon nanotube by tip-enhanced near-field Raman spectroscopy, Chem. Phys. Lett. **376**, 174–180 (2003) 372
[12] T. Ichimura, N. Hayazawa, M. Hashimoto, Y. Inouye, S. Kawata: Tip-enhanced coherent anti-stokes Raman scattering for vibrational nanoimaging, Phys. Rev. Lett. **92**, 220801–220804 (2004) 372
[13] N. Anderson, A. Hartschuh, L. Novotny: Nanoscale vibrational analysis of single-walled carbon nanotubes, J. Am. Chem. Soc. **127**, 2533–2537 (2005) 372, 374, 375, 376
[14] A. Hartschuh, Q. Huihong, A. J. Meixner, N. Anderson, L. Novotny: Nanoscale optical imaging of excitons in single-walled carbon nanotubes, Nano Lett. **5**, 2310–2313 (2005) 372, 374, 375, 377
[15] T. Yano, P. Verma, S. Kawata, Y. Inouye: Diameter-selective near-field Raman analysis and imaging of isolated carbon nanotube bundles, Appl. Phys. Lett. **88**, 093125–093127 (2006) 372, 376
[16] A. Hartschuh, M. R. Beversluis, A. Bouhelier, L. Novotny: Tip-enhanced optical spectroscopy, Phil. Trans. R. Soc. Lond. A **362**, 807–819 (2004) 373
[17] L. Chico, V. H. Crespi, L. X. Benedict, S. G. Louie, M. L. Cohen: Pure carbon nanoscale devices: Nanotube heterojunctions, Phys. Rev. Lett. **76**, 971–974 (1996) 374
[18] S. K. Doorn, M. J. O'Connell, L. Zheng, Y. T. Zhu, S. Huang, J. Liu: Raman spectral imaging of a carbon nanotube intramolecular junction, Phys. Rev. Lett. **94**, 016802–016805 (2005) 374
[19] N. Anderson, A. Hartschuh, L. Novotny: Chirality changes in carbon nanotubes studied with near-field Raman spectroscopy, Nano Lett. **7**, 577–582 (2007) 374, 376
[20] M. Zheng, A. Jagota, M. S. Strano, A. P. Santos, P. Barone, S. G. Chou, B. A. Dinder, M. S. Dresselhaus, R. S. Mclean, G. B. Onoa, G. G. Samsonidze, E. D. Semke, M. Usrey, D. J. Walls: Structure-based carbon nanotube sorting by sequence-dependent DNA assembly, Science **302**, 1545–1548 (2003) 374
[21] M. Moskovits: Surface-enhanced spectroscopy, Rev. Mod. Phys. **57**, 783–826 (1985) 375
[22] M. Thomas, R. Carminati, J. R. Arias-Gonzalez, J.-J. Greffet: Single-molecule spontaneous emission close to absorbing nanostructures, Appl. Phys. Lett. **85**, 3863–3865 (2004) 375
[23] P. Anger, P. Bharadwaj, L. Novotny: Enhancement and quenching of single-molecule fluorescence, Phys. Rev. Lett. **96**, 113002–113006 (2006) 375, 377

[24] S. Kühn, U. Hakanson, L. Rogobete, V. Sandoghdar: Enhancement of single-molecule fluorescence using a gold nanoparticle as an optical nanoantenna, Phys. Rev. Lett. **97**, 017402–017405 (2006) 375, 377
[25] A. Hartschuh, A. J. Meixner, L. Novotny: Local phonon modes of single-walled carbon nanotubes observed by near-field Raman spectroscopy, Proc. AIP **723**, 63–66 (2004) 376
[26] T. Yano, Y. Inouye, S. Kawata: Nanoscale uniaxial pressure effect of a carbon nanotube bundle on tip-enhanced near-field Raman spectra, Nano Lett. **6**, 1269–1273 (2006) 376
[27] S. Savasta, G. Martino, R. Girlanda: Near-field optical spectroscopy of an extended interacting electron system, Phys. Rev. B **61**, 13852 (2000) 377
[28] J. R. Zurita, L. Novotny: Multipolar interband absorption in a semiconductor quantum dot. I. Electric quadrupole enhancement, J. Opt. Soc. Am. B **19**, 1355–1362 (2002) 377
[29] T. W. Odom, J.-L. Huang, P. Kim, C. M. Lieber: Atomic structure and electronic properties of single-walled carbon nanotubes, Nature **391**, 62–64 (1998) 378
[30] L. C. Venema, J. W. G. Wildöer, J. W. Janssen, S. J. Tans, H. L. J. T. Tuinstra, L. P. Kouwenhoven, C. Dekker: Imaging electron wave functions of quantized energy levels in carbon nanotubes, Science **283**, 52–55 (1999) 378
[31] B. C. Stipe, M. A. Rezaei, W. Ho: Single-molecule vibrational spectroscopy and microscopy, Science **280**, 1732–1735 (1998) 378, 379
[32] L. Vitali, M. Burghard, M. A. Schneider, L. Liu, C. S. Jayanthi, K. Kern: Phonon spectromicroscopy of carbon nanostructures with atomic resolution, Phys. Rev. Lett. **93**, 136103–136106 (2004) 379, 380
[33] M. Grobis, K. H. Khoo, R. Yamachika, X. Lu, K. Nagaoka, S. G. Louie, M. F. Crommie, H. Kato, H. Shinohara: Spatially dependent inelastic tunneling in a single Metallofullerene, Phys. Rev. Lett. **94**, 136802–136805 (2005) 379
[34] L. Vitali, M. Burghard, P. Wahl, M. A. Schneider, K. Kern: Local pressure-induced metallization of a semiconducting carbon nanotube in a crossed junction, Phys. Rev. Lett. **96**, 086804–086807 (2006) 379, 381
[35] B. J. LeRoy, S. G. Lemay, J. Kong, C. Dekker: Electrical generation and absorption of phonons in carbon nanotubes, Nature **432**, 371–374 (2004) 381, 382
[36] A. Jorio, C. Fantini, M. S. S. Dantas, M. A. Pimenta, A. G. Souza Filho, G. G. Samsonidze, V. W. Brar, G. Dresselhaus, M. S. Dresselhaus, A. K. Swan, M. S. Ünlü, B. B. Goldberg, R. Saito: Linewidth of the Raman features of individual single-wall carbon nanotubes, Phys. Rev. B **66**, 115411–115418 (2002) 381, 386
[37] N. Lorente, M. Persson, L. J. Lauhon, W. Ho: Symmetry selection rules for vibrationally inelastic tunneling, Phys. Rev. Lett. **86**, 2593–2597 (2001) 382
[38] L. Vitali, M. A. Schneider, K. Kern: Phonon and plasmon excitation in inelastic electron tunneling spectroscopy of graphite, Phys. Rev. B **69**, 121414(R)–121417(R) (2004) 382
[39] S. Sapmaz, P. Jarillo-Herrero, Y. M. Blanter, C. Dekker, H. S. J. van der Zant: Tunneling in suspended carbon nanotubes assisted by longitudinal phonons, Phys. Rev. Lett. **96**, 026801–026804 (2006) 382

[40] C. Thomsen, J. Strait, Z. Vardeny, H. J. Maris, J. Tauc, J. J. Hauser: Coherent phonon generation and detection by picosecond light pulses, Phys. Rev. Lett. **53**, 989–992 (1984) 383
[41] S. B. Fleischer, B. Pevzner, D. J. Dougherty, H. J. Zeiger, G. Dresselhaus, M. S. Dresselhaus, E. P. Ippen, A. F. Hebard: Coherent phonons in alkali metal-doped C60, Appl. Phys. Lett. **71**, 2734–2736 (1997) 383
[42] Ü. Özgür, C. W. Lee, H. O. Everitt: Control of coherent acoustic phonons in semiconductor quantum wells, Phys. Rev. Lett. **86**, 5604–5607 (2001) 383
[43] H. J. Zeiger, J. Vidal, T. K. Cheng, E. P. Ippen, G. Dresselhaus, M. S. Dresselhaus: Theory for displacive excitation of coherent phonons, Phys. Rev. B **45**, 768–778 (1992) 383
[44] A. V. Kuznetsov, C. J. Stanton: Theory of coherent phonon oscillations in semiconductors, Phys. Rev. Lett. **73**, 3243–3246 (1994) 383
[45] M. E. Garcia, T. Dumitrica, H. O. Jeschke: Laser-induced coherent phonons in graphite and carbon nanotubes: Model and simulations, Appl. Phys. A **79**, 855–857 (2004) 383, 384, 389
[46] A. T. N. Kumar, F. Rosca, A. Widom, P. M. Champion: Investigations of amplitude and phase excitation profiles in femtosecond coherence spectroscopy, J. Chem. Phys. **114**, 701–724 (2001) 384, 386, 389
[47] A. T. N. Kumar, F. Rosca, A. Widom, P. M. Champion: Investigations of ultrafast nuclear response induced by resonant and nonresonant laser pulses, J. Chem. Phys. **114**, 6795–6815 (2001) 384, 386
[48] T. Dumitrica, M. E. Garcia, H. O. Jeschke, B. I. Yakobson: Selective cap opening in carbon nanotubes driven by laser-induced coherent phonons, Phys. Rev. Lett. **92**, 117401–11704 (2004) 384
[49] C. Manzoni, A. Gambetta, E. Menna, M. Meneghetti, G. Lanzani, G. Cerullo: Intersubband exciton relaxatio dynamics in single-walled carbon nanotubes, Phys. Rev. Lett. **94**, 27401–27404 (2005) 384
[50] A. Gambetta, C. Manzoni, E. Menna, M. Meneghetti, G. Cerullo, G. Lanzani, S. Tretiak, A. Piryatinski, A. Saxena, R. L. Martin, A. R. Bishop: Real-time observation of nonlinear coherent phonon dynamics in single-walled carbon nanotubes, Nature Phys. **2**, 515–520 (2006) 384, 386, 387, 388
[51] Y. S. Lim, K. J. Yee, . H. Kim, E. H. Haroz, J. Shaver, J. Kono, S. K. Doorn, R. H. Hauge, R. E. Smalley: Coherent lattice vibrations in single-walled carbon nanotubes, Nano Lett. **6**, 2696–2700 (2006) 384, 385, 386
[52] T. E. Stevens, J. Kuhl, R. Merlin: Coherent phonon generation and the two stimulated Raman tensors, Phys. Rev. B **65**, 144304–144307 (2002) 389
[53] T. Feurer, J. C. Vaughan, K. A. Nelson: Spatiotemporal coherent control of lattice vibrational waves, Science **299**, 374–377 (2003) 389
[54] G. P. Zhang, T. F. George: Controlling vibrational excitations in C60 by laser pulse durations, Phys. Rev. Lett. **93**, 147401–147404 (2004) 389
[55] T. Brixner, F. J. Garcia de Abajo, J. Schneider, W. Pfeiffer: Nanoscopic ultrafast space-time-resolved spectroscopy, Phys. Rev. Lett. **95**, 093901–093904 (2005) 389

Index

High Magnetic Field Phenomena in Carbon Nanotubes

Junichiro Kono[1], Robin J. Nicholas[2], and Stephan Roche[3]

[1] Department of Electrical & Computer Engineering, Rice University, Houston, TX 77005, USA
kono@rice.edu
[2] Physics Department, Oxford University, Clarendon Laboratory, Parks Road, Oxford OX1 3PU, UK
r.nicholas@physics.ox.ac.uk
[3] CEA/DSM/DRFMC/SPSMS/GT, 17 avenue des Martyrs, 38054 Grenoble, France
stephan.roche@cea.fr

Abstract. We review recent progress in the theoretical and experimental studies of single-wall carbon nanotubes in high magnetic fields. Low-temperature magneto-transport experiments demonstrate the influence of quantum interference, disorder, and band-structure effects. Magneto-optical spectroscopy has been used to show the effects of the Aharonov–Bohm phase on the band structure and on the excitonic properties of carbon nanotubes.

1 Introduction

Single-wall carbon nanotubes (SWNTs) in magnetic fields provide a wide range of new scientific opportunities [1–5]. In a magnetic field parallel to the nanotube axis, their band structure is predicted to change dramatically due to the Aharonov–Bohm (AB) phase generated around the nanotube circumference (see the contribution by Ando in this volume). The bandgap is expected to oscillate between zero and a finite value as a function of the magnetic flux ϕ threading the nanotubes with a period $\phi_0 = e/h$, the magnetic flux quantum, where e is the electronic charge and h is the Planck constant. A perpendicular magnetic field leads to a distinctly different behavior: the zero-field band structure with one-dimensional (1D) van Hove singularities (VHSs) gradually changes into a Landau-level spectrum as the magnetic field increases. The large diamagnetic susceptibility for magnetic fields perpendicular to graphene sheets leads to highly anisotropic magnetic susceptibilities for nanotubes, which in turn causes magnetic alignment. These effects are expected to lead to novel magnetic, magneto-transport, and magneto-optical phenomena, some of which have been observed in recent experiments. Low-temperature magneto-transport experiments have found a variety of new phenomena, which are the combined result of quantum interference, disorder, and band-structure effects. Magneto-optical spectroscopy has been demonstrated to be an extremely powerful tool for investigating magnetic-field effects on

A. Jorio, G. Dresselhaus, M. S. Dresselhaus (Eds.): Carbon Nanotubes,
Topics Appl. Physics **111**, 393–421 (2008)

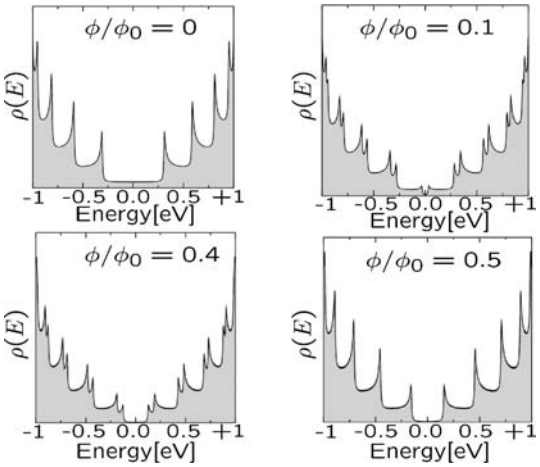

Fig. 1. Density of states of the $(10, 10)$ nanotube for several magnetic flux values

the band structure and excitonic properties of carbon nanotubes. This research field is evolving rapidly, and we present here a personal overview of the current situation.

2 Band Structure in Magnetic Fields

2.1 Parallel Field: Role of the Aharonov–Bohm Phase

As fully described in [1], the AB effect [6] of a parallel magnetic field (B) has a profound influence on the band structure of carbon nanotubes through field-dependent modulations of the phase of the electronic states. In particular, an energy gap opens up in a metallic tube and oscillates with B. A magnetic field can thus transform a metallic system into a semiconducting one and vice versa [2, 3, 7, 8]. See Fig. 1 for the density of states (DOS) for a (10,10) tube for several values of magnetic flux ϕ/ϕ_0.

An expression for the energy gap for (n, m) tubes with $n - m = 3\ell$ (ℓ: integer) can be derived as $E_g = 3E_0\phi/\phi_0$ $(0 \le \phi \le \phi_0/2)$ and $3E_0\,|1 - \phi/\phi_0|$ $(\phi_0/2 \le \phi \le \phi_0)$, where $E_0 \equiv 2\pi a_{c-c}\gamma_0/|\boldsymbol{C}_h|$, where $\boldsymbol{C}_h$ is the chiral vector, $a_{C\text{–}C}$ is the C–C bond length (0.142 nm), and γ_0 is the C–C transfer integral (≈ 3 eV). Numerically, $E_g \approx 40$ meV at 60 T for the $(10, 10)$ tube (diameter $d_t = 1.4$ nm), and $E_g \approx 75$ meV at 50 T for the $(22, 22)$ tube ($d_t \approx 3$ nm). To achieve $\phi = \phi_0$ in nanotubes with d_t of 1 nm, 10 nm, 20 nm, and 40 nm, one needs, respectively, magnetic fields of 5325 T, 53 T, 13 T, and 3 T.

Semiconducting tubes [i.e., (n, m) tubes with $n - m = 3\ell \pm 1$] are affected in a similar way, but the gap expression is slightly different. One finds that $E_g = E_0\,|1 - 3\phi/\phi_0|$ for $(0 \le \phi \le \phi_0/2)$ and $E_0\,|2 - 3\phi/\phi_0|$ for $(\phi_0/2 \le \phi \le \phi_0)$. Hence, the initially finite gap (E_0) continuously decreases with

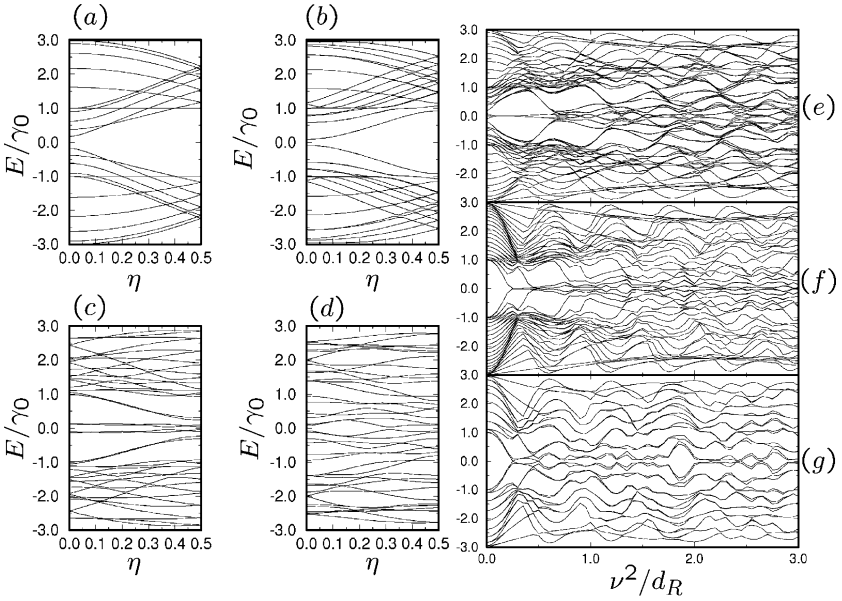

Fig. 2. Energy dispersions of the $(10, 0)$ tube in a perpendicular field plotted versus dimensionless wavevector $\eta = k_{\parallel}|\boldsymbol{T}|/2\pi$ for several values of the dimensionless inverse magnetic length ν: (**a**) 0.0, (**b**) 1.0, (**c**) 2.0, and (**d**) 3.0. Energy at $k_{\parallel} = 0$ as a function of ν^2/d_R [d_R: highest common divisor of $(2n+m, n+2m)$] for (**e**) (20,0), (**f**) (20,20), and (**g**) (9,9) tubes, using $\gamma_0 = 2.9\,\mathrm{eV}$. Adapted from [4]

increasing ϕ, reaching zero at $\phi = \phi_0/3$. The gap further opens as ϕ increases from $\phi_0/3$, reaching a local maximum $(E_0/2)$ at $\phi = \phi_0/2$, before closing again at $\phi = 2\phi_0/3$ and finally recovering its original value of E_0 at $\phi = \phi_0$.

These theoretical predictions have been partially verified by recent interband magneto-optical studies on semiconducting SWNTs [9–12], as described in Sect. 5. In addition, recent experimental magneto-transport studies have shown various manifestations of the AB effect, including band structure and quantum interference effects [13–20], as described in Sect. 4.

2.2 Perpendicular Field: Onset of Landau Levels

When a perpendicular B is applied, the 2D vector potential in the Landau gauge for the nanotube surface is given by $\boldsymbol{A} = (0, (|\boldsymbol{C}_h|B/2\pi)\sin(2\pi\tilde{x}/|\boldsymbol{C}_h|))$, with $(\tilde{x}, \tilde{y})$ being unit vectors in the circumferential and axial directions, respectively. Energy dispersions can then be calculated at different values of B [2, 7]. In Fig. 2, the energy E/γ_0 is shown as a function of the dimensionless wavevector $k_{\parallel}|\boldsymbol{T}|/2\pi$ for several values of the dimensionless inverse magnetic length $\nu = |\boldsymbol{C}_h|/2\pi\ell_{\mathrm{m}}$, where $k_{\parallel}$ is the 1D wavevector along the tube axis, $\boldsymbol{T}$ is the fundamental 1D translational vector, and $\ell_{\mathrm{m}} = \sqrt{\hbar/eB}$.

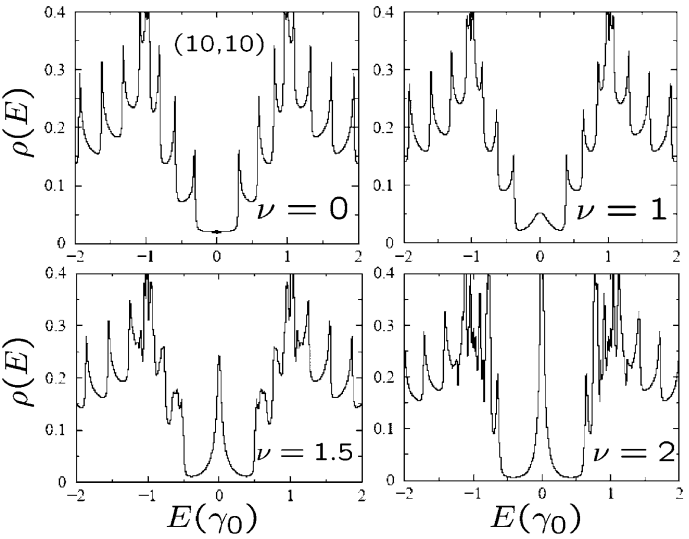

Fig. 3. Density of states of the $(10, 10)$ tube in a perpendicular magnetic field. The field strength is expressed in terms of the dimensionless parameter $\nu = |\boldsymbol{C}_h|/2\pi\ell_{\mathrm{m}}$, where $\ell_{\mathrm{m}} = \sqrt{\hbar/eB}$ is the magnetic length. Adapted from [21]

As seen in Fig. 2, as B increases, subband dispersions are suppressed, particularly in the vicinity of the charge-neutrality point (CNP). Using the $\boldsymbol{k}\ \boldsymbol{p}$ method, an expression for the eigenstates close to the $\boldsymbol{K}$ points can be derived analytically for metallic tubes in a B field. The $\boldsymbol{k}\ \boldsymbol{p}$ equation at the CNP ($\delta\boldsymbol{k} = 0$) in a perpendicular B field is decoupled into two equations [7]

$$\left(-\frac{\partial}{\partial\tilde{x}} + \frac{|\boldsymbol{C}_h|}{2\pi\ell_{\mathrm{m}}^2}\sin\left(\frac{2\pi\tilde{x}}{|\boldsymbol{C}_h|}\right)\right)\mathcal{F}_A^k(\tilde{x}) = 0\,, \tag{1}$$

$$\left(+\frac{\partial}{\partial\tilde{x}} + \frac{|\boldsymbol{C}_h|}{2\pi\ell_{\mathrm{m}}^2}\sin\left(\frac{2\pi\tilde{x}}{|\boldsymbol{C}_h|}\right)\right)\mathcal{F}_B^k(\tilde{x}) = 0\,, \tag{2}$$

from which two independent solutions can be obtained

$$\Psi_A(\tilde{x}) = \begin{pmatrix}1\\0\end{pmatrix}\mathcal{F}_A(\tilde{x})\,, \qquad \Psi_B(\tilde{x}) = \begin{pmatrix}0\\1\end{pmatrix}\mathcal{F}_B(\tilde{x})\,,$$

$$\mathcal{F}_A(\tilde{x}) = \frac{1}{\sqrt{|\boldsymbol{C}_h|I_0(2\nu^2)}}\exp\left[-\nu^2\cos\left(\frac{2\pi x}{|\boldsymbol{C}_h|}\right)\right],$$

$$\mathcal{F}_B(\tilde{x}) = \frac{1}{\sqrt{|\boldsymbol{C}_h|I_0(2\nu^2)}}\exp\left[+\nu^2\cos\left(\frac{2\pi x}{|\boldsymbol{C}_h|}\right)\right],$$

where $I_0(2\nu^2)$ is the modified Bessel function of the first kind. For sufficiently large B ($\nu \gg 1$), these wavefunctions become strongly localized in the circumferential direction; i.e., $\Psi_A(\tilde{x})$ is localized around $\tilde{x} = \pm|\boldsymbol{C}_h|/2$ at the bottom

side of the cylinder, whereas $\Psi_B(\tilde{x})$ is localized around the top side $\tilde{x} = 0$. As a result, the boundary condition on the wavefunction becomes irrelevant, and the resulting band structure, starting from an initially metallic or semiconducting nanotube, becomes identical. For a small $\delta\boldsymbol{k}$ around the $\boldsymbol{K}$ points, the low-energy properties are described by an effective Hamiltonian that can be determined by the two degenerate states Ψ_A and Ψ_B as [7]

$$\mathcal{H}_{\text{eff}} = \begin{pmatrix} 0 & -i\gamma_0 \delta k I_0^{-1}(2\nu^2) \\ +i\gamma_0 \delta k I_0^{-1}(2\nu^2) & 0 \end{pmatrix}, \tag{3}$$

whose eigenvalues are $E^{\pm}_{q=0} = \pm\gamma_0|\delta\boldsymbol{k}|/I_0(2\nu^2)$, with group velocity $v = \gamma_0/\hbar I_0(2\nu^2)$, while the DOS becomes $\rho(E_{\text{F}}) \sim I_0(2\nu^2)/\pi\gamma_0 \sim \mathrm{e}^{\nu^2}/\sqrt{4\pi\nu^2}$ $(\nu \gg 1)$. The DOS at the CNP thus diverges exponentially with increasing B. This is shown in Fig. 3 for the $(10, 10)$ tube for several values of B expressed in terms of the dimensionless inverse magnetic length ν.

Given the diameter-dependent scaling property of the band structure, the larger the diameter, the smaller the required B to fully develop such a Landau subband at the CNP. This effect has been also studied analytically using the supersymmetry framework [22]. The appearance of the so-called Hofstadter butterfly was further explored numerically for large-diameter nanotubes [23]. As already seen in the field-dependent band structures (Fig. 2), the whole DOS also progressively degrades as the Landau subbands start to emerge within the whole spectrum, although a strong mixing between high-energy subbands remains (Fig. 3). As soon as $\nu = |\boldsymbol{C}_h|/2\pi\ell_{\text{m}} \geq 1$ is satisfied, the electronic spectrum becomes fully dominated by Landau levels. One finds that for tubes with d_{t} of 1 nm, 10 nm, 20 nm, and 40 nm, the condition $\nu = 1$ corresponds to B of 2635 T, 26 T, 6.6 T, and 1.6 T, respectively.

3 Magnetization

3.1 Theory of the Magnetic Susceptibility

The strong B dependence of the band structure suggests a large orbital magnetic susceptibility, χ, like that seen in graphite. Calculations show that the orbital χ is indeed several orders of magnitude larger than the paramagnetic (or Pauli) contribution due to the electron spin [3, 24–27]. At zero temperature, the orbital part of χ can be computed from the second derivative of the free energy, which is in turn related to the band dispersion, i.e.,

$$\chi = k_{\text{B}}T \frac{\partial^2}{\partial B^2} \sum_{nk} \ln\left[1 + \exp\left(-\frac{\varepsilon_n(k,\phi) - \mu}{k_{\text{B}}T}\right)\right]. \tag{4}$$

The magnetic susceptibility χ of SWNTs has been theoretically studied. *Ajiki* and *Ando* [28] calculated χ for isolated SWNTs [24] as well as for

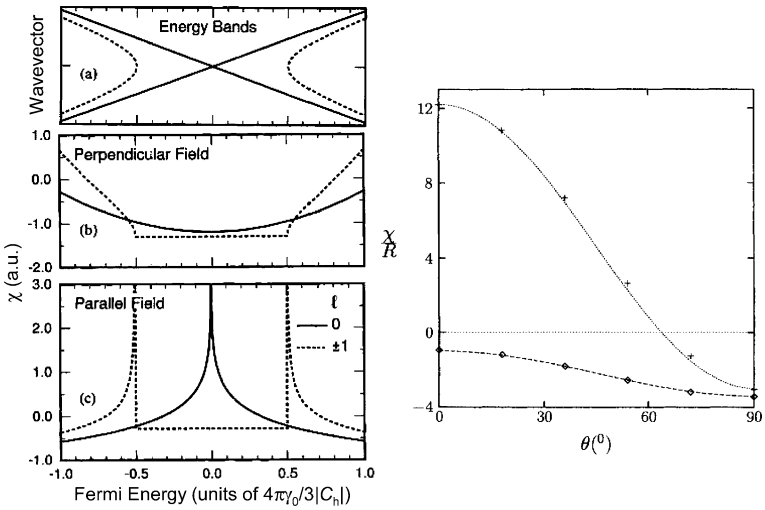

Fig. 4. (*Left*) The (**a**) band structure, (**b**) $\chi_\perp$, and (**c**) $\chi_\parallel$ of metallic ($\ell = 0$, *solid lines*) and semiconducting ($\ell = \pm 1$, *dashed lines*) SWNTs calculated by *Ajiki* and *Ando* (adapted from [28]). (*Right*) Scaled magnetic susceptibility χ/R as a function of the angle between the tube and axis and the applied magnetic field for metallic (*pluses* and *dotted line*) and semiconducting (*diamonds* and *dashed line*) SWNTs calculated by *Lu*, where R is the tube radius (adapted from [25])

ensembles (bundles) of SWNTs using the $\boldsymbol{k}\ \boldsymbol{p}$ perturbation method, while almost simultaneously *Lu* [25] performed a numerical study using a tight-binding approach within the London approximation. In both calculations, χ was found to scale linearly with the nanotube diameter. Furthermore, for an applied B parallel to the tube axis, $\chi_\parallel$ was paramagnetic for tubes with $\ell = 0$, while for tubes with $\ell = 1$ or 2, $\chi_\parallel$ was found to be diamagnetic. In contrast, for a perpendicular B, all nanotubes were found to be diamagnetic. Finally, it was found that the χ of the tubes with $\ell = 1$ and $\ell = 2$ was almost identical.

An interesting aspect is the magnetic anisotropy, i.e., $\chi_\parallel - \chi_\perp$ (see Fig. 4). It has been theoretically found that for undoped metallic tubes (i.e., the Fermi energy exactly at the CNP) $\chi_\parallel$ is positive (paramagnetic), whereas $\chi_\perp$ is negative (diamagnetic); $\chi_\parallel$ rapidly decreases as the Fermi energy deviates from the CNP, exhibiting a logarithmic divergence, while $\chi_\perp$ remains almost constant as a function of Fermi energy near the CNP [see Fig. 4b]. For undoped semiconducting tubes, both $\chi_\parallel$ and $\chi_\perp$ are negative (diamagnetic) and $|\chi_\perp| > |\chi_\parallel|$ [see Fig. 4 (right)]. As the Fermi energy is varied in a semiconducting tube, both $\chi_\parallel$ and $\chi_\perp$ remain constant as long as the Fermi energy lies within the bandgap; however, a square-root-like divergence appears in $\chi_\parallel$ when the Fermi energy enters the band edges, as shown in Fig. 4c. In contrast, $\chi_\perp$ does not exhibit any divergence and is diamagnetic around the CNP region for both metallic and semiconducting tubes. In all

cases, χ increases linearly with d_t, which makes it possible to define universal relations for $\chi_\perp$ and $\chi_\parallel$. With increasing temperature (T), $\chi_\parallel$ is predicted to decrease (increase) for metallic (semiconducting) tubes, while $\chi_\perp$ is predicted to increase for both metallic and semiconducting nanotubes [28].

In contrast with these earlier $\boldsymbol{k}\ \boldsymbol{p}$ [24, 28] and tight-binding [25] results, a recent *ab-initio* study predicts different results for the two families of semiconducting zigzag tubes [29]. For zigzag tubes with $\ell = 2$, $\chi_\parallel/d_t$ is very weakly dependent on n, while for those with $\ell = 1$, $|\chi_\parallel/d_t|$ decreases slowly with d_t [29]. An opposite behavior is found for $\chi_\perp$, i.e., $\chi_\parallel/d_t$ is almost independent of n for $\ell = 1$, whereas its absolute value decreases monotonically for $\ell = 2$. For $d_t \to \infty$, the *ab-initio* calculations are consistent with the tight-binding results [25]. Finally, for nanotubes with $d_t = 1\,\text{nm}$, the computed anisotropy $\chi_\parallel - \chi_\perp$ values are between 1.2 and 1.8×10^{-5} emu/mol depending on the tube chirality [29], similar to the predicted values of 1.9×10^{-5} emu/mol [28] and 1.5×10^{-5} emu/mol [25].

3.2 Magnetic-Susceptibility Measurements

Heremans and coworkers [30, 31] measured the χ of diamond, graphite, C_{60}, and multiwall carbon nanotubes as a function of T and B. It was found that the χ of nanotubes was about half that of graphite, which is known to be very large ($\approx -3 \times 10^5$ emu/g for $H \parallel c$-axis below 100 K) due to the existence of the aromatic-like π-electrons that are absent in diamond; their results showed similar T and B dependences to graphite [see Fig. 5 (left)]. *Ramirez* et al. [32] reported that the χ of nanotube bundles is even larger than that of graphite on a per carbon basis. More recent studies on aligned multiwall nanotubes [33–35] showed the predicted anisotropic behavior, $|\chi_\parallel| < |\chi_\perp|$ [see, e.g., Fig. 5 (right)]. Furthermore, through magneto-transport measurements on small-gap nanotubes, *Minot* et al. [17] showed that states near the bandgap have an orbital magnetic moment much larger than the Bohr magneton, quantitatively consistent with predicted values, indicating that the motion of electrons around the nanotube circumference indeed plays an important role in determining χ.

Anisotropic χ naturally leads to magnetic alignment [36, 37]. *Fujiwara* et al. [33] fabricated magnetically aligned multiwall nanotube films by drying nanotubes dispersed in methanol in a B field of 7 T. *Kimura* et al. [38] used a similar technique to obtain electrically and mechanically anisotropic multiwall nanotube/polymer composites. Furthermore, *M. Fujiwara* et al. [39, 40] succeeded in magnetically aligning individual multiwall nanotubes and estimated $\chi_\parallel - \chi_\perp$ to be $\sim (9 \pm 5) \times 10^{-6}$ emu/mol.

More recently, SWNTs have been magnetically aligned [9, 10, 41–43]. *Walters* and coworkers [41, 42] produced thin membranes comprised of highly aligned SWNTs by producing a SWNT suspension, placing the suspension in B as high as 25 T, and filtering the suspension in the field. *Zaric* et al. [9, 10]

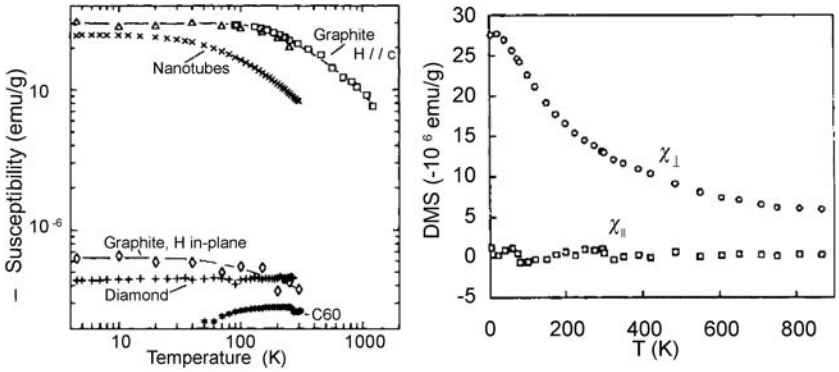

Fig. 5. (*Left*) Temperature dependence of the magnetic susceptibility of various carbon materials, including bundles of multiwall carbon nanotubes. Adapted from [30]. (*Right*) The parallel and perpendicular magnetic susceptibility of aligned multiwall carbon nanotubes. Here, DMS refers to the diamagnetic susceptibility. Adapted from [34]

demonstrated magnetic alignment of SWNTs of specific chiralities using individually suspended SWNTs in aqueous solutions. Through analysis of the photoluminescence and absorption spectra in B, in conjunction with atomic force microscopy to determine the length distribution, they were able to estimate $\chi_{\parallel} - \chi_{\perp}$ to be $\sim 1.4 \times 10^{-5}$ emu/mol for 1-nm diameter semiconducting nanotubes. This value is similar to the predicted values, i.e., 1.9×10^{-5} emu/mol [24] and 1.5×10^{-5} emu/mol [25]. Furthermore, the extracted degree of alignment showed that tubes of larger d_{t} align better, which is in qualitative agreement with the prediction, i.e., $|\chi_{\parallel} - \chi_{\perp}| \propto d_{\mathrm{t}}$ [24, 25]. *Islam* et al. [43] compared magnetically purified and raw samples in their magnetic alignment experiments and demonstrated that residual magnetic impurities significantly influence low-field magnetic alignment behaviors.

To summarize the experimental situation, polarized magneto-optical spectroscopy studies in high magnetic fields have allowed researchers to estimate the diamagnetic anisotropy, $\chi_{\parallel} - \chi_{\perp}$, of semiconducting SWNTs with diameters ~ 1 nm, which is quantitatively consistent with the values predicted by $\boldsymbol{k}\ \boldsymbol{p}$ [24, 28] and tight-binding [25] calculations. However, experimental determination of χ for metallic SWNTs has not been reported. Moreover, the family ($\ell = 1$ or 2) dependence of χ for smaller-diameter semiconducting SWNTs, predicted by a recent *ab-initio* calculation [29], has not yet been experimentally confirmed.

4 Magneto-transport

Magneto-transport exhibits a rich variety of phenomena arising from the interplay of localization, quantum interference, and band-structure effects.

One thus has to carefully examine how each of these ingredients changes with magnetic field, temperature, and the degree of disorder.

4.1 Disorder and Quantum Interference

For a general understanding of disorder effects on transport properties, an evaluation of the elastic mean free path ℓ_e is crucial. For sufficiently weak disorder, a perturbative treatment can be employed with the Fermi golden rule. This was first performed by *White* and *Todorov* [44] within a model of two bands degenerate at the CNP for armchair tubes. If the disorder is described by Anderson-type random fluctuations of onsite energies with a uniform probability $1/W$, a straightforward calculation gives [21, 44] $\ell_e = (18a_{C\text{–}C}\gamma_0^2/W^2)\sqrt{n^2+m^2+nm} \propto d_t/W^2$. Numerical studies have confirmed this behavior [45]. For semiconducting tubes, $\ell_e \propto 1/W^2$ is still satisfied, but ℓ_e is much smaller and does not scale with d_t.

As theoretically discussed by *Ando* et al. [46], in the case of long-range disorder, severe selection rules yield a complete suppression of backscattering at the CNP with an anomalously long ℓ_e. However, this property vanishes as soon as massive higher subbands are involved in conduction, or equivalently, when a magnetic field is applied parallel to the tube axis. As shown in Sect. 2.1, the opening of a bandgap will strongly change the dispersion relation in the vicinity of the CNP, enhancing the backscattering efficiency of the underlying disorder, irrespective of its range. In the case of a perpendicular magnetic field, the band structure changes discussed in Sect. 2.2 result in an appearance of strong backscattering at the CNP [7].

4.2 Weak Localization and Magnetoresistance Oscillations

Quantum interference between clockwise and counterclockwise backscattering paths exists in the coherent regime, which increases the return probability to the origin for propagating wavepackets. Within the framework of weak localization theory, it is possible to derive perturbatively the relation between the measured conductance $G(E)$, its quantum correction $\delta G_{WL}(E)$, and the coherence length L_ϕ. The scaling properties of $\delta G_{WL}(E)$ and L_ϕ for carbon nanotubes have been theoretically investigated in the coherent regime by solving the time-dependent Schrödinger equation [47, 48].

Depending on the relative magnitudes of ℓ_e, L_ϕ, and $|\mathcal{C}_h|$, different types of magneto-transport phenomena are observed. First, for illustration purposes, we discuss numerical results [49] for the metallic $(9,0)$ tube in various transport regimes. In Fig. 6, the B dependence of the diffusion coefficient, $\mathcal{D}$, is shown, and several cases of interest can be explored. First, the weak localization regime [50] is analyzed under the condition $\ell_e < |\mathcal{C}_h| < L_\phi$. Figure 6 shows that $\mathcal{D}$ increases at low B (negative magnetoresistance) and $\phi_0/2$-periodic AB oscillations are seen, i.e., $\mathcal{D}(\phi + \phi_0/2) = \mathcal{D}(\phi)$, in agreement with weak localization theory. In contrast, when $\ell_e > |\mathcal{C}_h|$

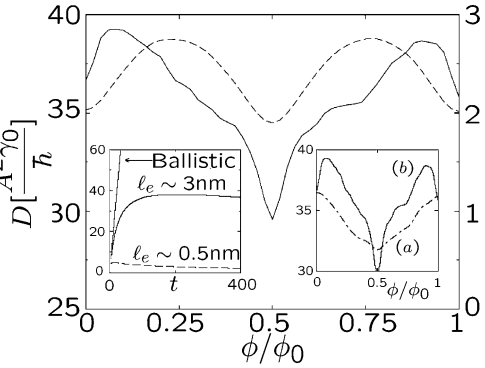

Fig. 6. Diffusion coefficient $\mathcal{D}$ for the (9,0) nanotube for two disorder strengths, $W/\gamma_0 = 3$ and 1, such that the mean-free path ($\ell_e \sim 0.5$ and 3 nm, respectively) is either shorter (*dashed line*) or longer (*solid line*) than the nanotube circumference ($|\mathcal{C}_h| \sim 2.3$ nm). The right y-axis is for the *dashed line* and the left y-axis is for the *solid line*. *Inset:* $\mathcal{D}(\tau_\phi, \phi/\phi_0)$ for $\ell_e = 3$ nm and $L(\tau_\phi) < 2\ell_e$

and $L_\phi < 2\ell_e$, the system exhibits a positive magnetoresistance associated with $\mathcal{D}(\phi + \phi_0) = \mathcal{D}(\phi)$. When $\ell_e > |\mathcal{C}_h|$ and $L_\phi > 2\ell_e$, negative magnetoresistance and AB oscillations with a period ϕ_0 are obtained. However, it is important to note that the field required to observe conventional weak localization also strongly modifies the band structure, with ϕ_0-periodic oscillations as discussed in Sect. 2.1. Although the bandgap opening and oscillations, as well as VHS splitting and shifting, are likely to be smoothed by disorder, magneto-fingerprints will likely come from entangled multiple sources, which goes far beyond the conventional theory of weak localization [49].

Roche and *Saito* [51] theoretically found that for a fixed disorder strength, magnetotransport fingerprints show strong fluctuations as a function of Fermi-level position, tube diameter, and the orientation of B with respect to the tube axis. In Fig. 7, the field-dependent DOS and conductance are shown for (22,22) metallic nanotubes with 3 nm diameter with (c) or without (a,b) superimposed elastic disorder (still Anderson type). First, the evolution of the DOS and conductance for a parallel field are shown for varying Fermi energy and magnetic flux from zero to one flux quantum. The VHS splitting and shifts are clearly observed (Figs. 7a and b). The presence of elastic disorder clearly degrades the conductance value (Fig. 7d). However, as long as $W \leq \gamma_0/5$, although the transport regime becomes diffusive with contributions from quantum interference, the main field-dependent band-structure features are expected to be robust to disorder.

The first experimental magnetotransport study of carbon nanotubes was performed by *Langer* et al. [52] on large-diameter multiwall nanotubes, with fields applied perpendicular to the tube axis. The observation of negative magnetoresistance together with universal conductance fluctuations were analyzed in terms of quantum interference in the weak localization regime.

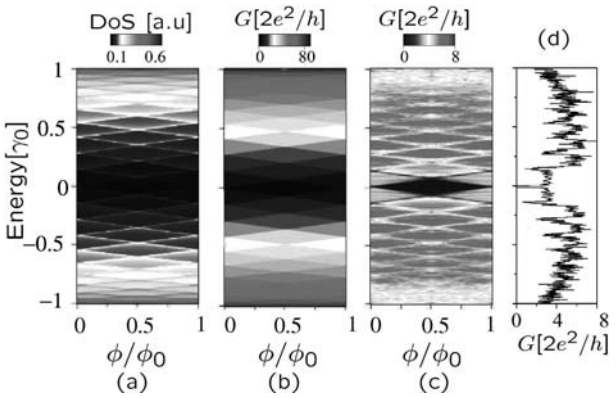

Fig. 7. Contour plots of the (**a**) DOS and conductance of a (**b**) clean and (**c**) disordered (22,22) nanotube, as a function of Fermi energy and magnetic flux. Disorder is of the Anderson type with $W = \gamma_0/5$. The conductance at zero flux for one disorder configuration is given in (**d**)

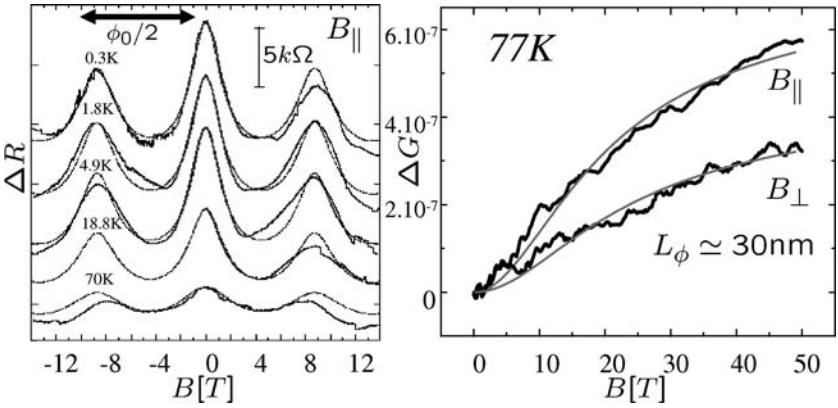

Fig. 8. (*Left*) Magnetoresistance of a multiwall nanotube measured in the parallel configuration [13]. (*Right*) Magnetoconductance $\Delta G(B)$ up to 50 T for $B_\parallel$ and $B_\perp$ with a bias voltage of 300 mV and zero gate voltage at 80 K. *Solid lines* represent the quasi-2D weak localization fits for both configurations [19]

Bachtold et al. [13] further investigated weak localization in multiwall nanotubes, and observed negative magnetoresistance and $\phi_0/2$-periodic AB oscillations in a parallel B (see Fig. 8). The value of ℓ_e extracted in the diffusive regime was found to be of the order of $|\mathcal{C}_h|$ and a few times smaller than the estimated L_ϕ, which was attributed to weak electron–electron interactions. They also observed, in a different sample, small-amplitude oscillations of much smaller period ($\phi_0/10$) that were superimposed on the main $\phi_0/2$-oscillations. Furthermore, other groups [14–16] reported different oscillation

periods as well as changes from positive to negative magnetoresistance under a change in B orientation. Different interpretations were proposed, based on field-dependent band-structure effects and quantum interference effects. It should be noted that in one of the devices studied in [13] ℓ_e was estimated to be $\sim 10\ |\mathcal{C}_h|$, which jeopardizes a strict application of weak localization theory. Similarly, other experiments [14] have been obtained in a regime in which weak localization theory does not apply. Finally, it should be noted that if $\phi_0/2$ oscillations are observed in a magneto-transport experiment, the modifications of the band structure are also expected to impact significantly, and thus, the whole theory should simultaneously take into account disorder, quantum interference, and band-structure effects, as proposed in [51].

4.3 Most Recent Experiments

Very recently, several groups have further performed novel magneto-transport experiments. *Coskun* et al. [18] studied magneto-transport in the Coulomb blockade regime, where evidence for ϕ_0-periodic oscillations of the bandgap was given for large d_t multiwall nanotubes weakly coupled to Au/Cr metallic contacts. In addition, more recently, by achieving a good ohmic contact between a single-wall metallic nanotube and Pt electrodes, *Cao* et al. [53] observed B-dependent modulations of Fabry–Perot interference patterns in the ballistic transport regime. Furthermore, *Fedorov* et al. [19] have measured magnetotransport in double-wall nanotubes with 3 nm diameter while varying the B-orientation and applied gate voltage (see Fig. 8). With an estimated modulation of the position of the Fermi level by about 50 meV, the magnetotransport fingerprints were shown to switch from a regime fully dominated by weak localization (negative magnetoresistance) to a more complex regime where both weak localization and band-structure effects were contributing.

Finally, the respective contributions of band-structure effects and quantum interference phenomena were recently disentangled [54]. In Fig. 9, the DOS of a clean (260,260) nanotube ($d_t = 35$ nm) is shown as a function of gate voltage and magnetic flux ϕ in the interval $[0,\ h/e]$. For theory–experiment comparison, the energy scale E was converted into an equivalent gate voltage scale U_{gate}. This was done successfully by assuming a constant capacitive coupling $C_{gate} \simeq 300$ aF/μm between the gate and the tube. In a color plot, a diamond-shaped structure is clearly visible that shows the splitting and shift of the VHS, driven by the B (Sect. 2.1). The DOS increases from the CNP to the higher electronic subbands. Some diamonds are highlighted with dashed lines. Figure 9 (right) shows the experimental data with ϕ ranging from 0 to h/e. The measured conductance indeed reveals diamond-like ridges of high conductance (highlighted by dashed lines) on which an additional conductance valley at $\phi = h/2e$ is superimposed. The latter is caused by the coherent backscattering in the disorder potential. Although these similarities are not sufficient for a one-to-one assignment of calculation and experiment, they demonstrate that the position, shape, and size of the diamonds agree

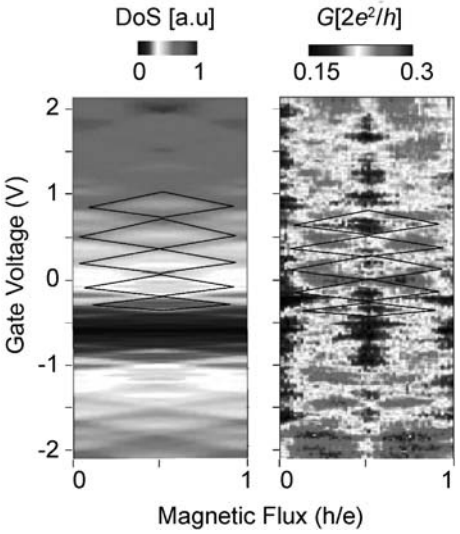

Fig. 9. (*Left*) Color representation of the calculated DOS for a (260,260) nanotube as a function of gate voltage and coaxial magnetic flux. The *solid lines* indicate ridges of high DOS induced by the h/e-periodic splitting of van Hove singularities. (*Right*) First h/e-period of the experimental data, with *solid lines* indicating diamond-like ridges of high conductance. Adapted from [54]

well and give the first evidence of the joint contributions of DOS and quantum interference effects in the measured magnetoresistance of carbon nanotubes.

To date, no experiment has been able to provide clear evidence for the predicted peculiar energy-dependent backscattering phenomena [21, 44, 46]. This is because close to the CNP, where the energy dispersion is linear (massless subbands), the anomalously large elastic mean free path at the CNP should hinder the observation of any weak localization phenomena. Indeed, no clear signatures of weak localization have been reported in SWNTs, for which the linear energy dispersion extends over a large energy range around the CNP. Differently, MWNTs offer an interesting playground to challenge the different physics between massless and massive subbands, but the predicted magneto-transport anomalies [51] remain to be confirmed experimentally.

5 Magneto-Optics

Consequences of the band-structure modifications in SWNTs induced by a magnetic field are expected to directly influence interband optical properties. Both absorption and emission spectra are expected to exhibit AB-phase-induced peak shifts and splittings [3, 21, 55].

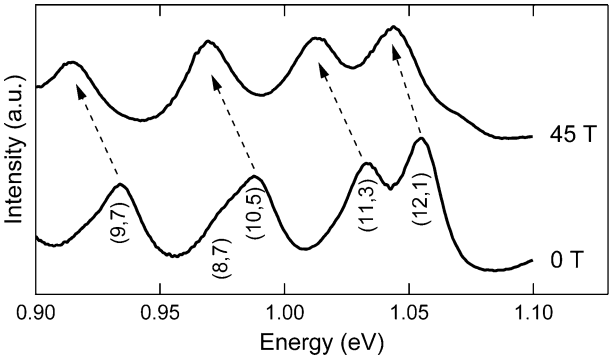

Fig. 10. Room-temperature PL spectra for 5 types of semiconducting SWNTs at 0 T and 45 T with 795 nm (1.56 eV) excitation. All peaks show redshifts with magnetic field, consistent with field-induced bandgap shrinkage [9, 10]

5.1 Bandgap Shrinkage and Aharonov–Bohm Splitting

The first magneto-optical studies of SWNTs were performed on micelle-suspended HiPco samples in dc high magnetic fields up to 45 T at room temperature [9–12]. Both photoluminescence (PL) and absorption measurements were carried out in the near-infrared and visible ranges, covering both the E_{11} and E_{22} transition ranges of semiconducting SWNTs. Figure 10 shows typical PL spectra at 0 T and 45 T, taken with an excitation wavelength of 795 nm (1.56 eV), which are dominated by 5 different chirality types of semiconducting SWNTs. As B increases from 0 T to 45 T, all the peaks are seen to redshift, indicating that the bandgap (E_g) of semiconducting SWNTs indeed shrinks with increasing B. The size of the redshifts is also consistent with theoretical expectations based on the AB effect, including the fact that the shift is more obvious for lower-energy peaks (larger-diameter tubes).

More detailed comparison of the peak shifts with theory can be made by performing low-temperature PL, and in particular by taking PL excitation (PLE) maps in steady B fields [56]. This allows the shifts of different individual nanotube species to be measured independently. The redshifts observed in a field of 19.5 T are shown in Fig. 11a and are found to compare well with the theoretical shifts expected of $\delta E_g/E_g = \pm 3\phi/\phi_0 = \pm 3\pi d_t^2 B/4\phi_0$, which demonstrates the expected diameter dependence of the shift. Data taken in pulsed fields up to 58 T are also shown in Fig. 11b and give good agreement with theory when account is taken of the fact that unpolarized light was used, leading to averaging over randomly oriented nanotubes.

Absorption spectra typically consist of many overlapping peaks due to the presence of multiple species of SWNTs in the sample, which makes absorption less ideal than PL for searching for signatures of the AB phase. Nevertheless, field-induced broadening indicative of splitting was observed in dc B fields up to 45 T [9] and clear splittings were observed in pulsed B fields above

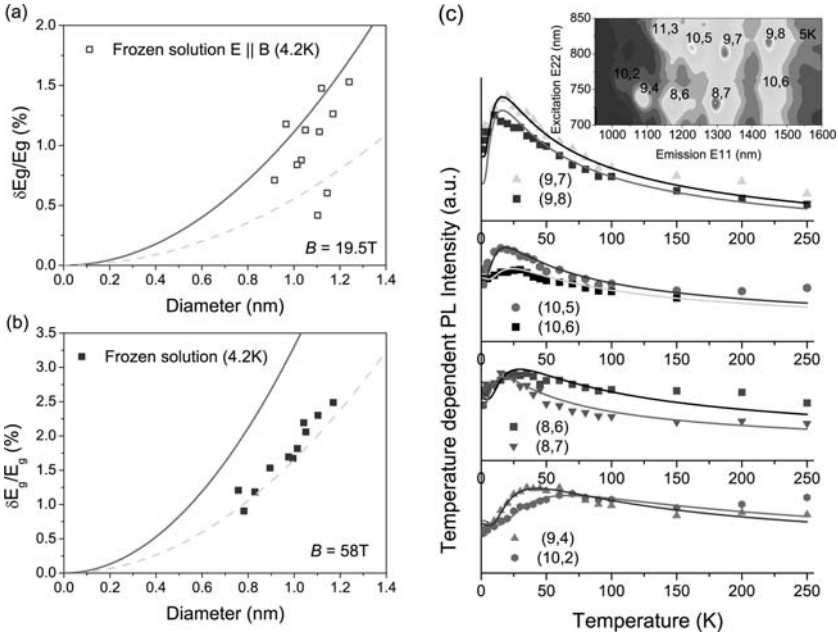

Fig. 11. (**a**) Relative energy shifts ($\delta E_g/E_g$) in PL from 0 to 19.5 T versus tube diameter for SWNT solutions at 4.2 K, measured using polarized excitation and collection in the Voigt ($k \perp B$) configuration. (**b**) Relative energy shift in PL from 0 to 58 T, using unpolarized light in the Voigt configuration. Full theoretical shifts as expected for polarized excitation and collection (*solid lines*) and averaged shifts, assuming random nanotube orientation (*broken lines*). Adapted from [56]. (**c**) Temperature dependence of the PL intensities deduced for specific nanotube species. The *inset* shows a typical PLE map measured at 5 K. Adapted from [57]

55 T [12]. Figure 12 shows B-dependent absorption spectra in the E_{11} region up to 71.4 T. Three main peaks are dominant at zero B, and are labeled A, B, and C. At fields above ~ 55 T, each of these peaks splits into two clearly resolved peaks (e.g., peaks A^+ and A^-). The observation of clear absorption-peak splittings at high B provides direct evidence of the expected K–K' splitting due to the B-induced symmetry breaking, where K and K' label the corners of the hexagonal Brillouin zone.

5.2 Magnetic Brightening of "Dark" Excitons: Theory

Coulomb interactions among photocreated carriers significantly influence optical properties, especially in low-dimensional systems [58], and thus, one has to take into account both the AB effect and excitonic effects on an equal footing. Excitons in SWNTs have been the subject of numerous theoretical studies over the last decade [59–69, and in the contributions by Ando and by Spataru et al. in this volume]. Experimental studies in recent years (e.g., two-photon

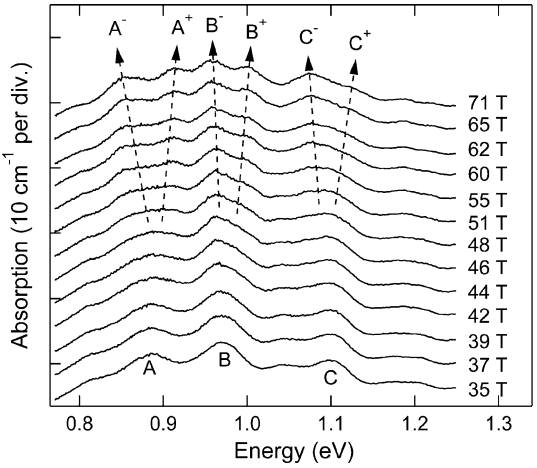

Fig. 12. Magnetoabsorption spectra for micelle-suspended SWNTs in D_2O in the spectral range of the first subband (E_{11}) transitions, clearly showing field-induced Aharonov–Bohm splittings. Adapted from [12]

PL studies [70,71]) convincingly demonstrated the excitonic nature of optical processes in semiconducting SWNTs. These theoretical studies [59–69, and the contribution by Spataru et al. in this volume] have not only confirmed earlier predictions for 1D excitons in general [72–78] but also raised new issues specific to SWNT excitons, including the existence of "dark" excitons (see the contribution by Spataru et al. in this volume).

An optically inactive, or "dark," exciton state arises due to K–K' Coulomb mixing. In the presence of time-reversal symmetry, i.e., without B, exchange-interaction-induced intervalley mixing results in a set of excitonic states, only one of which is optically active [62,63,66–69, and the contribution by Spataru et al. in this volume]. This predicted bright state, however, is not the lowest in energy. The lowest two singlet exciton states, shown in the upper right panel of Fig. 13, are the bonding-like and antibonding-like linear combinations of the K-point and K'-point exciton states, which are expected to split by an amount Δ_x determined by the strength of the electron–hole exchange interaction [66]. The higher state ($1u$, solid line) is bright, while the lower state ($1g$, dashed line) is dark.

Recently, *Ando* investigated the effects of B applied along the tube axis on these low-lying exciton states [1, 68]. The magnetic field lifts the K–K' degeneracy (see the left panels of Fig. 13), with the amount of single-particle state splitting (Δ_{AB}) determined by the AB phase, as described in Sect. 2. As B increases, the relative importance of the Coulomb mixing gradually decreases. At high enough B where $\Delta_{AB} \gg \Delta_x$, both states become bright and two peaks with an equal oscillator strength are expected, which is consistent with the magnetoabsorption data obtained by *Zaric* et al. [12].

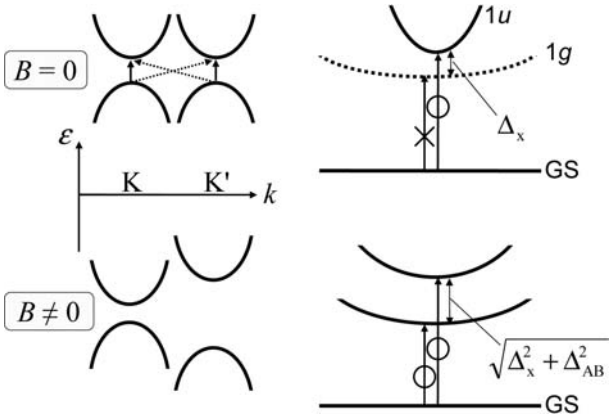

Fig. 13. The expected magnetic-field evolution of K–K' intervalley mixing and splitting in a single-particle picture (*left*) and in an excitonic picture (*right*). $1u$ ($1g$) is the bonding (antibonding) superposition state of the K and K' exciton states. The *solid* (*dashed*) *line* represents a bright (dark) exciton state. $\Delta_{\rm x}$: Coulomb-induced splitting; $\Delta_{\rm AB}$: Aharonov–Bohm-induced splitting. Both states become optically allowed in a magnetic field, suggesting "magnetic brightening" of the $1g$ state. Here, GS refers to the ground state

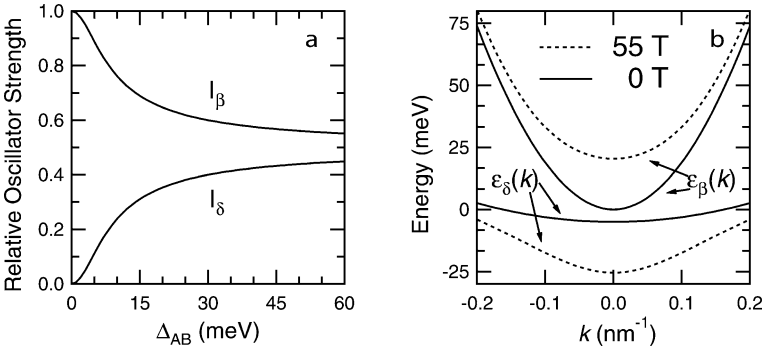

Fig. 14. Magnetoexciton bands and magnetic-field dependence of relative oscillator strengths. (**a**) Calculated relative oscillator strength of the dark (I_δ) and bright (I_β) excitons vs. Aharonov–Bohm splitting, $\Delta_{\rm AB}$, for a 1-nm diameter pristine nanotube in a parallel field. Both I_δ and I_β approach ~ 0.5 at $\Delta_{\rm AB}$ greater than ~ 50 meV. (**b**) Calculated dispersions for bright and dark exciton bands at 0 and 55 T for a perfectly aligned nanotube. At 0 T the higher-energy, lower-mass ($0.02m_{\rm e}$), bright exciton is separated from the lower-energy, higher-mass ($0.2m_{\rm e}$), dark exciton by 5.5 meV. At 55 T both peaks are bright and approach similar mass values, separated by 55 meV. Adapted from [79]

More recently, *Shaver* et al. [79] proposed a more phenomenological model to explain their B- and T-dependent PL data. Within a two-band model for a perfectly aligned nanotube, they calculated the relative oscillator strengths for the dark (δ) and bright (β) states in the presence of B. Figure 14a plots the calculated evolution of the relative intensities, I_δ and I_β, as a function of Δ_{AB}. As Δ_{AB} increases, the lower-energy state gains oscillator strength at the expense of the higher, until both reach equal values at very high B where $\Delta_{\mathrm{AB}} \gg \Delta_x$. Two bright states of approximately equal oscillator strength appear in high B. PL intensities are not only dependent on oscillator strengths but also on the thermal distribution of the exciton population. In order to model the T- and B-dependent exciton population within and between the exciton bands, *Shaver* et al. [79] calculated exciton dispersions both in the absence and presence of B, as plotted for 0 T and 55 T in Fig. 14b. At 0 T, the dark and bright bands have different effective masses ($m_\delta > m_\beta$ [66]) and are separated by an energy of Δ_x at $k = 0$. At 55 T, the bands are now separated by energy $(\Delta_x^2 + \Delta_{\mathrm{AB}}^2)^{1/2}$ at $k = 0$ and are closer to each other in effective mass. PL simulations based on this model are shown in Fig. 16, as discussed below.

5.3 Magnetic Brightening of "Dark" Excitons: Experiment

Recently, two groups independently reported the first clear experimental evidence of dark excitons [57, 79, 80]. They demonstrate that a B field can significantly increase the PL intensity of semiconducting SWNTs by brightening the dark exciton state through T- and B-dependent PL of prealigned, static films of individualized SWNTs. The PL intensity increased with B and the amount of brightening increased as T was decreased.

The splitting of dark and bright exciton states can be measured from an analysis of the T dependence of the radiative decay rate. Calculations of the decay rate by *Spataru* et al. [67] and *Perebeinos* et al. [66] have shown that the decay is dominated by two factors: 1. for a single 1D exciton with a parabolic dispersion, the radiative lifetime is known to vary as $\tau_r \propto T^{1/2}$ [78], and 2. the thermal distribution of the excitons between the different bright and dark exciton states depends on T and B. The initial optical excitation creates excitons in the optically active states that are spin singlets with odd parity. The application of B leads to brightening of the dark exciton although some emission from the dark state occurs even at zero field due to effects such as disorder, defects, environmental coupling or impurities.

The T dependence of the intensity (I) seen in Fig. 11 can be modeled with the relation [57]

$$I \propto \frac{1}{(T^2 + T_0^2)^{\frac{1}{4}}} \times \frac{\eta + e^{-\Delta_x/kT}}{1 + e^{-\Delta_x/kT}}\,, \tag{5}$$

which is based on the simplification that recombination is dominated by radiative emission from two 1D parabolic excitons, one dark and at a lower

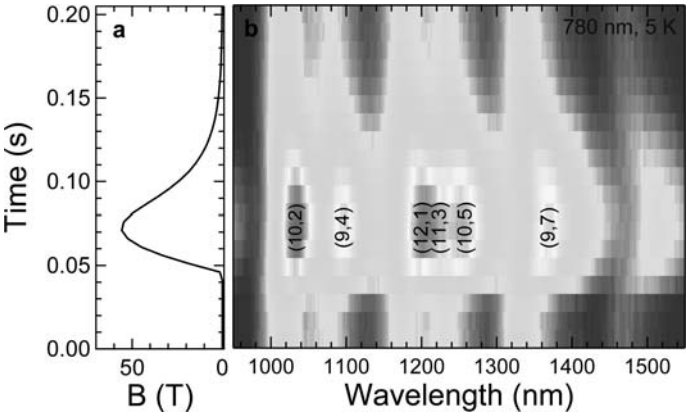

Fig. 15. Magnetic brightening in single-wall carbon nanotubes in a pulsed magnetic field. (**a**) Temporal profile of the applied pulsed magnetic field. (**b**) Contour map of near-infrared photoluminescence intensity for a single-wall carbon nanotube film as a function of time and emission wavelength. Each peak is labeled by its assigned nanotube chirality index (n,m). The photoluminescence intensity increases with increasing magnetic field strength. Also, note the Aharonov–Bohm-effect-induced redshift of each emission peak with field intensity. The excitation wavelength was 780 nm and the sample temperature was 5 K. Adapted from [79]

energy and one bright, corresponding to the two lowest-energy singlet states. The energy separation is Δ_x, and there is a finite mixing of the spectral weight between the even and odd parity states of magnitude $\eta = I_\delta / I_\beta$. This uses the same assumptions as in *Spataru* et al. [67] that thermalization occurs only within the singlet states. The $T^{-1/2}$ divergence at low T is removed by the addition of a small Lorentzian broadening term of $T_0 = 1\,\text{meV}$, which is comparable to the broadening observed in measurements on individual nanotubes [81]. Figure 11 shows fits to (5) for 8 strong nanotube species. These show typical values for Δ_x in the range 1–5 meV for nanotubes with diameters from 1.2 to 0.8 nm [57].

Figure 15 shows PL data at 5 K taken in a pulsed high B field [79]. The pulsed B and PL spectra are recorded as a function of time, showing an intensity increase (magnetic brightening) and a peak-position redshift (AB effect) tracking the B magnitude. Figure 16 shows three sets of PL data taken at different temperatures plotted on the same scales. This figure dramatically demonstrates the difference in intensity increase at different T values. Figure 16a shows 5 K spectra. At this lowest T, the overall intensity increases ~ 4 to 5 times over the utilized field range. Figure 16b shows PL spectra at 80 K taken at the same five B values. Here, we see the amount of brightening to be less than in the 5 K experiment. Lastly, 260 K spectra are shown in Fig. 16c; the amount of intensity increase is negligible, but there is a slight

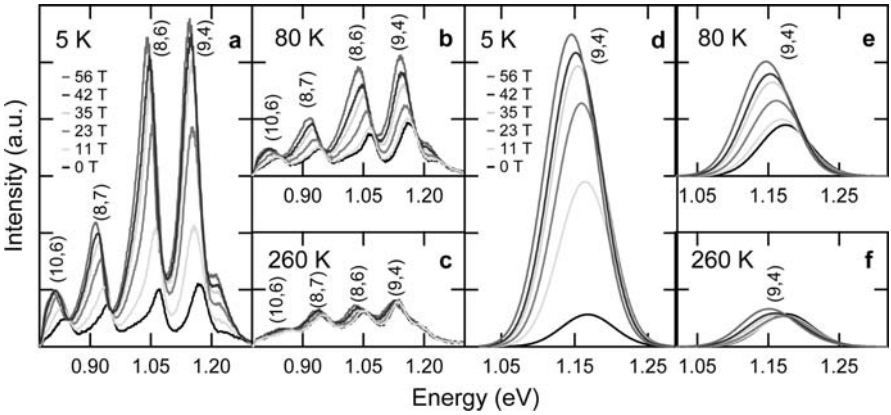

Fig. 16. Temperature dependence of magnetic brightening. PL spectra taken with 740-nm excitation at various magnetic fields (0 T, 11 T, 23 T, 35 T, 42 T and 56 T) at (**a**) 5 K, (**b**) 80 K, and (**c**) 260 K. The amount of brightening is shown to be dramatically higher at lower temperature (scales are equal). All peaks shift to lower energy with increasing magnetic field at all temperatures, due to the Aharonov–Bohm effect. Simulated photoluminescence spectra for the (9,4) nanotube at (**d**) 5 K, (**e**) 80 K, and (**f**) 260 K at the same fields. All essential features in the experimental spectra are reproduced: the peak intensity increases (or brightens) with increasing magnetic field, and the amount of brightening is larger at lower temperature. Adapted from [79]

change in the lineshape, indicating the presence of the higher energy peak, as previously observed in magneto-absorption data [9, 12].

Calculated spectra are shown for 5 K (Fig. 16d), 80 K (Fig. 16e), and 260 K (Fig. 16f) at the same B as the corresponding experimental traces in Figs. 16a–c. The B- and T-dependent exciton bands with relative oscillator strengths and populations, as well as acoustic phonon and impurity scattering, are taken into account to simulate the lineshape [79]. The 5 K spectra in Fig. 16d successfully reproduce the relative increase in PL intensity as well as the redshift observed as B is increased. The 80 K spectra in Fig. 16e exhibit the same behavior as 5 K but with less brightening due to a significant population in $k \approx 0$ states of the bright exciton band before the field is applied. The 260 K spectra in Fig. 16f only show weak brightening and an asymmetric lineshape at high fields, indicating that at high temperatures excitons are partially populating the higher state.

Table 1 shows the parameters deduced from fitting B- and T-dependent data for a series of peaks [79] with chiral indices, (n, m), giving values for the dark–bright splitting in the range of 5–8 meV. By contrast, fitting of the full T dependence in a magnetic field [57] shown in Fig. 17, using low excitation density B-dependent PLE maps leads to significantly lower values of Δ_x for larger-diameter tubes and shows that there is no observable magnetic-field

Table 1. Integrated photoluminescence intensity at 56 T [$I(56\,\mathrm{T})$] normalized to the integrated photoluminescence intensity at 0 T [$I(0\,\mathrm{T})$] and peak-position change $E(56\,\mathrm{T}–0\,\mathrm{T})$ from 0 T to 56 T compiled from Voigt fits of 5 K spectra for a series of nanotubes with chiral indices n and m. The bright–dark splitting, Δ_x, calculated from fitting the temperature dependence at various fields is also shown. *Bold-faced numbers* indicate the four main photoluminescence features, while the *normal-faced numbers* are for shoulder features in the spectra. Adapted from [79]

n	m	Diameter (nm)	$I(56\,\mathrm{T})/I(0\,\mathrm{T})$	$\Delta E(56\,\mathrm{T}–0\,\mathrm{T})$ (meV)	Δ_x (meV)
10	**6**	**1.11**	**2.13**	**26.9**	**7.7**
10	5	1.05	2.95	27.9	–
8	**7**	**1.03**	**3.39**	**29.1**	**8.1**
11	3	1.01	4.19	16.9	–
8	**6**	**0.96**	**6.08**	**27.0**	**7.9**
9	**4**	**0.91**	**5.48**	**24.0**	**5.5**
10	2	0.88	7.68	22.7	–

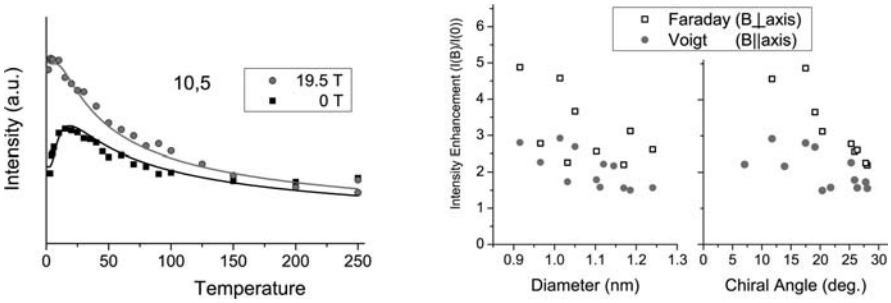

Fig. 17. (*Left*) The temperature dependence of the PL intensity for a (10,5) tube at 0 and 19.5 T, fitted with (5), with an increase in the mixing parameter η from 0.23 to 0.64 caused by the field. (*Center* and *right*) The increase in intensity produced by a magnetic field of 19.5 T for both the Voigt and Faraday geometries as a function of nanotube diameter and chiral angle. Adapted from [57]

dependence of Δ_x. These measurements show a similar diameter dependence of the magnetic brightening, which is largest for the smallest diameter tubes, as can be seen in Fig. 17, and the data interestingly also show a strong dependence on the chiral angle of the nanotubes.

The observations and calculations of magnetic brightening clearly demonstrate the existence of previously unobserved dark excitons and their significant influence on the PL quantum yield. In addition, these studies show that careful symmetry manipulation by a B field, accompanied by a modification of the electronic wavefunctions by the AB effect, significantly increases the PL intensity at low temperatures. Considering the fact that dark excitons

are already partially brightened by disorder, we expect the observed signal increase to be even more drastic in disorder-free SWNT samples.

5.4 Perpendicular Field Effects

For B fields applied perpendicularly to the tube axis, we expect no E_g shifts associated with the AB-phase. For SWNTs aligned at an angle θ to an applied B field, *Lu* [25] predicts a scaling of E_g showing a redshift in energy decreasing drastically from a maximum for fields parallel to a minimum for fields perpendicular to the tube axis. *Ajiki* and *Ando* [82] predict only small perturbations in the electronic levels in the low-field regime. For large perpendicular fields (of the order of 100s of T), however, they predict the formation of 2D Landau levels on the cylinder surface that will reduce the bandgap (see Sect. 2.2). By contrast, *Ajiki* [83] predicts that depolarization-field effects will lead to a blueshift at very high B. It is therefore surprising that the experimental picture shows large effects, although none of the above calculations take into account excitonic interactions, which may be highly significant.

PLE mapping [56, 57] in the Faraday geometry, where the excitation light is orientated with $k \| B$ and preferentially selects tubes orientated perpendicular to the B field shows two main phenomena: 1. very strong magnetic brightening and 2. unexpectedly large redshifts in E_g. The intensity changes shown in Fig. 17 demonstrate even larger brightening than seen in the Voigt geometry, with the greatest enhancements seen for small-diameter tubes, or tubes with a small chiral angle. The B-induced fractional bandgap shifts for the PL taken in the Faraday geometry are of a similar order ($\sim 1\%$) to those observed for tubes predominantly perpendicular to B – not expected from current theory. The overall δE_g dependence with diameter also shows the opposite trend with diameter to that associated with an AB-phase-induced shift – the magnitude of the shift decreases with increasing diameter, suggesting that some other mechanism may be responsible.

The strong magnetic brightening suggests that an explanation of this behavior is likely to involve mixing of energy levels due to the symmetry breaking from the magnetic field, as found for the Voigt geometry. A good potential candidate for this is the role of spin, since the theoretical treatments [66–68] show that there is a near degeneracy between the lowest (dark) singlet exciton state and the highest triplet state due to a vanishingly small exchange energy. Under these circumstances a magnetic-field-induced spin splitting, of the order of 2.3 meV at 19.5 T, will produce a considerable mixing of the two dark $m_S = 0$ singlet and triplet states. Since the dark and bright singlet levels are very close in energy to each other and are also mixed, all three levels are expected to be within a few meV [57]. As a result, the singlet family can mix with the triplet states, opening up the possibility for recombination for any excitons that may have been scattered into the triplet states, which will also have a significantly high density of states, due to their larger exciton masses [66]. Until a detailed theoretical treatment of this situation is

given, this explanation must remain speculative, however. Further discussion about effects connected with a perpendicular magnetic field is given in the contribution by Ando.

6 Summary and Remaining Problems

In this chapter the critical changes of the electronic band structure in high magnetic fields were reviewed. First, the theoretical basis underlying the Aharonov–Bohm effect was analyzed defining the main effects of bandgap opening and flux-dependent oscillations for the axial field case. The occurrence of Landau levels was further discussed, for the case of a perpendicular applied field to the nanotube axis. The impact of magnetic field on quantum interference phenomena was scrutinized within the weak-localization regime, and past controversies were shown to result from an incomplete description of the joint contributions of field-dependent band structures and field-dependent modulations of quantum interference effects.

Magnetoconductance experiments performed in either the Coulomb-blockade or in the weak-localization regime [20] have demonstrated the possibility of tuning the Fermi level by several tens of meV, opening new horizons for exploring the physics through several subbands. Some first experimental indications of Landau-level formation have been reported [84], but not confirmed so far by more sophisticated experiments. Some spectacular magnetoresistance oscillatory features such as a metal–insulator transition have been theoretically predicted in chemically modified nanotubes, but to date no experiments have tackled these challenges.

Magneto-optical spectroscopy has revealed a variety of signatures of the Aharonov–Bohm effect. Both absorption and emission processes have been shown to critically depend on the amount of magnetic flux threading the tube. Such tube-threading magnetic flux breaks time-reversal symmetry, lifting the degeneracy between the two otherwise equivalent valleys. This symmetry breaking has a profound influence on the low-lying exciton states in semiconducting SWNTs. The so-called dark (or optically inactive) exciton state, which lies below the first bright (optically active) exciton state, is brightened by a tube-threading magnetic flux. At high enough magnetic fields where the field-induced valley splitting is much larger than the exchange-induced valley splitting, two equally bright exciton states arise. These studies have shown the importance of symmetry breaking in order to manipulate and improve the optical properties of SWNTs, but further work is needed in this direction.

An important open question, where high-field studies would be interesting, is how to experimentally distinguish between the weak- and strong-localization regimes. The experimental observation of strongly localized wavefunctions should correspond to a measured exponential decrease of the conductance above a certain nanotube length L, i.e., $G \simeq (2e^2/h)\exp(-L/\xi)$, with the localization length $\xi(E)$ predicted to be energy dependent. The

conductance should decrease at each onset of new subbands, following the mean-free path pattern [21], independent of the nature of the disorder. Recently, *Gómez-Navarro* et al. [85] reported on an exponential increase of the resistance, in Ar^+-irradiated nanotubes. The unknown effect of B in strongly localized regimes remains to be explored.

In all the known magneto-transport and magneto-optical experiments, the nature of the disorder has been poorly characterized, precluding the identification of specific magnetic-dependent transport signatures. Recent low-temperature magneto-PL studies [57, 79] suggested a finite amount of disorder-induced brightening of dark excitons, but a quantitative understanding of the nature and degree of disorder is missing. This situation could be overcome by intentionally doping or functionalizing conducting nanotubes, and by a close collaboration between theory and experiment.

Finally, spectroscopy of metallic SWNTs in high magnetic fields is an open field of research with the expectation that such studies would be fruitful in elucidating the fundamental dynamical properties of interacting 1D electrons. Both charge and spin excitations in such systems are expected to be collective in nature, and high-field spectroscopic studies in combination with many-body theory are needed.

Acknowledgements

This work was supported in part by the Robert A. Welch Foundation (Grant C-1509) (J. Kono), the National Science Foundation (Grants DMR-0134058, DMR-0325474, and OISE-0437342) (J. Kono), and EuroMagNET under the EU Contract RII3-CT-2004-506239 of the 6th Framework "Structuring the European Research Area, Research Infrastructures Action" (R. J. Nicholas and J. Kono). A portion of this work was performed at the National High Magnetic Field Laboratory, which is supported by NSF cooperative agreement No. DMR-0084173, by the State of Florida, and by the U.S. Department of Energy. The authors would like to thank Tsuneya Ando, Rémi Avriller, Xavier Blase, Jean-Christophe Charlier, Scott A. Crooker, Gianaurelio Cuniberti, David J. Hilton, Vojislav Krstić, Sylvain Latil, Lance Li, Shigeo Maruyama, Yuhei Miyauchi, Ian Mortimer, Norbert Nemec, Vasili Perebeinos, Oliver Portugall, Bertrand Raquet, Geert L. J. A. Rikken, Riichiro Saito, Thomas A. Searles, Jonah Shaver, Christoph Strunk, Francois Triozon, Xing Wei, and Sasa Zaric for fruitful collaborations and discussions.

References

[1] T. Ando: Role of the Aharonov–Bohm phase in the optical properties of carbon nanotubes, in *Topics in Applied Physics*, vol. 111 (Springer, Heidelberg 2008)

p. 213 393, 394, 408
[2] H. Ajiki, T. Ando: Electronic states of carbon nanotubes, J. Phys. Soc. Jpn. **62**, 1255 (1993) 393, 394, 395
[3] H. Ajiki, T. Ando: Aharonov–Bohm effect in carbon nanotubes, Physica B **201**, 349 (1994) 393, 394, 397, 405
[4] R. Saito, G. Dresselhaus, M. S. Dresselhaus: *Physical Properties of Carbon Nanotubes* (Imperial College Press, London 1998) 393, 395
[5] J. Kono, S. Roche: Magnetic properties, in M. J. O'Connell (Ed.): *Carbon nanotubes: Properties and applications* (CRC Press, Boca Raton 2006) Chap. 5, pp. 119–151 393
[6] Y. Aharonov, D. Bohm: Significance of electromagnetic potentials in the quantum theory, Phys. Rev. **115**, 485 (1959) 394
[7] H. Ajiki, T. Ando: Energy bands of carbon nanotubes in magnetic fields, J. Phys. Soc. Jpn. **65**, 505 (1996) 394, 395, 396, 397, 401
[8] W. Tian, S. Datta: Aharonov–Bohm-type effect in graphene tubules: A Landauer approach, Phys. Rev. B **49**, 5097 (1994) 394
[9] S. Zaric, G. N. Ostojic, J. Kono, J. Shaver, V. C. Moore, M. S. Strano, R. H. Hauge, R. E. Smalley, X. Wei: Optical signatures of the Aharonov–Bohm phase in single-walled carbon nanotubes, Science **304**, 1129 (2004) 395, 399, 406, 412
[10] S. Zaric, G. N. Ostojic, J. Kono, J. Shaver, V. C. Moore, R. H. Hauge, R. E. Smalley, X. Wei: Estimation of magnetic susceptibility anisotropy of carbon nanotubes using magneto-photoluminescence, Nano Lett. **4**, 2219 (2004) 395, 399, 406
[11] S. Zaric, G. N. Ostojic, J. Shaver, J. Kono, X. Wei, M. Furis, S. A. Crooker, O. Portugall, P. H. Frings, G. L. J. A. Rikken, V. C. Moore, R. H. Hauge, R. E. Smalley: Magneto-optical spectroscopy of carbon nanotubes, Physica E **29**, 469 (2005) 395, 406
[12] S. Zaric, G. N. Ostojic, J. Shaver, J. Kono, O. Portugall, P. H. Frings, G. L. J. A. Rikken, M. Furis, S. A. Crooker, X. Wei, V. C. Moore, R. H. Hauge, R. E. Smalley: Excitons in carbon nanotubes with broken time-reversal symmetry, Phys. Rev. Lett. **96**, 016406 (2006) 395, 406, 407, 408, 412
[13] A. Bachtold, C. Strunk, J.-P. Salvetat, J.-M. Bonard, L. Forró, T. Nussbaumer, C. Schönenberger: Aharonov–Bohm oscillations in carbon nanotubes, Nature **397**, 673 (1999) 395, 403, 404
[14] A. Fujiwara, K. Tomiyama, H. Suematsu, M. Yumura, K. Uchida: Quantum interference of electrons in multiwall carbon nanotubes, Phys. Rev. B **60**, 13492 (1999) 395, 403, 404
[15] J.-O. Lee, J.-R. Kim, J.-J. Kim, J. Kim, N. Kim, J. W. Park, K.-H. Yoo, K.-H. Park: Magnetoresistance and differential conductance in multiwalled carbon nanotubes, Phys. Rev. B **61**, R16362 (2000) 395, 403
[16] J.-O. Lee, J.-R. Kim, J.-J. Kim, J. Kim, N. Kim, J. W. Park, K.-H. Yoo: Observation of magnetic-field-modulated energy gap in carbon nanotubes, Solid State Commun. **115**, 467 (2000) 395, 403
[17] E. D. Minot, Y. Yaish, V. Sazonova, P. L. McEuen: Determination of electron orbital magnetic moments in carbon nanotubes, Nature **428**, 536 (2004) 395, 399

[18] U. C. Coskun, T.-C. Wei, S. Vishveshwara, P. M. Goldbart, A. Bezryadin: *h/e* magnetic flux modulation of the energy gap in nanotube quantum dots, Science **304**, 1132 (2004) 395, 404
[19] G. Fedorov, B. Lassagne, M. Sagnes, B. Raquet, J.-M. Broto, F. Triozon, S. Roche, E. Flahaut: Gate-dependent magnetoresistance phenomena in carbon nanotubes, Phys. Rev. Lett. **94**, 066801 (2005) 395, 403, 404
[20] B. Stojetz, C. Miko, L. Forró, C. Strunk: Effect of band structure on quantum interference in multiwall carbon nanotubes, Phys. Rev. Lett. **94**, 186802 (2005) 395, 415
[21] S. Roche, G. Dresselhaus, M. S. Dresselhaus, R. Saito: Aharonov–Bohm spectral features and coherence lengths in carbon nanotubes, Phys. Rev. B **62**, 16092 (2000) 396, 401, 405, 416
[22] H.-W. Lee, D. S. Novikov: Supersymmetry in carbon nanotubes in a transverse magnetic field, Phys. Rev. B **68**, 155402 (2003) 397
[23] N. Nemec, G. Cuniberti: Hofstadter butterflies of carbon nanotubes: Pseudo-fractality of the magnetoelectronic spectrum, Phys. Rev. B **74**, 165411 (2006) 397
[24] H. Ajiki, T. Ando: Magnetic properties of carbon nanotubes, J. Phys. Soc. Jpn. **62**, 2470 (1993) 397, 399, 400
[25] J. P. Lu: Novel magnetic properties of carbon nanotubes, Phys. Rev. Lett. **74**, 1123 (1995) 397, 398, 399, 400, 414
[26] L. Wang, P. S. Davids, A. Saxena, A. R. Bishop: Quasiparticle energy spectra and magnetic response of certain curved graphitic geometries, Phys. Rev. B **46**, 7175 (1992) 397
[27] P. S. Davids, L. Wang, A. Saxena, A. R. Bishop: Magnetic ordering transition of electrons on mesoscopic tubes, Phys. Rev. B **48**, 17545 (1993) 397
[28] H. Ajiki, T. Ando: Magnetic properties of ensembles of carbon nanotubes, J. Phys. Soc. Jpn. **64**, 4382 (1995) 397, 398, 399, 400
[29] M. A. L. Marques, M. d'Avezac, F. Mauri: Magnetic response and NMR spectra of carbon nanotubes from *ab-initio* calculations, Phys. Rev. B **73**, 125433 (2006) 399, 400
[30] J. Heremans, C. H. Olk, D. T. Morelli: Magnetic susceptibility of carbon structures, Phys. Rev. B **49**, 15122 (1994) 399, 400
[31] J.-P. Issi, L. Langer, J. Heremans, C. H. Olk: Electronic properties of carbon nanotubes: Experimental results, Carbon **33**, 941 (1995) 399
[32] A. P. Ramirez, R. C. Haddon, O. Zhou, R. M. Fleming, J. Zhang, S. M. McClure, R. E. Smalley: Magnetic susceptibility of molecular carbon: Nanotubes and fullerite, Science **265**, 84 (1994) 399
[33] A. Fujiwara, F. Katayama, K. Tomiyama, H. Ootoshi, H. Suematsu: *Electronic Transport and Magnetic Properties of Carbon Nanotubes*, Molecular Nanostructures (World Scientific, Singapore 1998) p. 439 399
[34] A. S. Kotosonov: Texture and magnetic anisotropy of carbon nanotubes in cathode deposites obtained by electric-arc method, JETP Lett. **70**, 476 (1999) 399, 400
[35] F. Tsui, L. Jin, O. Zhou: Anisotropic magnetic susceptibility of multiwalled carbon nanotubes, Appl. Phys. Lett. **76**, 1452 (2000) 399
[36] P. de Rango, M. Lees, P. Lejay, A. Sulpice, R. Tournier, M. Ingold, P. Germi, M. Pernet: Texturing of magnetic materials at high temperature by solidification in a magnetic field, Nature **349**, 770 (1991) 399

[37] M. Fujiwara, N. Fukui, Y. Tanimoto: Magnetic orientation of benzophenone crystals in fields up to 80.0 KOe, J. Phys. Chem. B **103**, 2627 (1999) 399
[38] T. Kimura, H. Ago, M. Tobita, S. Ohshima, M. Kyotani, M. Yumura: Polymer composites of carbon nanotubes aligned by a magnetic field, Adv. Mater. **14**, 1380 (2002) 399
[39] M. Fujiwara, E. Oki, M. Hamada, Y. Tanimoto, I. Mukouda, Y. Shimomura: Magnetic orientation and magnetic properties of a single carbon nanotube, J. Phys. Chem. A **105**, 4383 (2001) 399
[40] M. Fujiwara, K. Kawakami, Y. Tanimoto: Magnetic orientation of carbon nanotubes at temperatures of 231 K and 314 K, Mol. Phys. **100**, 1085 (2002) 399
[41] D. A. Walters, M. J. Casavant, X. C. Qin, C. B. Huffman, P. J. Boul, L. M. Ericson, E. H. Haroz, M. J. O'Connell, K. Smith, D. T. Colbert, R. E. Smalley: In-plane-aligned membranes of carbon nanotubes, Chem. Phys. Lett. **338**, 14 (2001) 399
[42] M. J. Casavant, D. A. Walters, J. J. Schmidt, R. E. Smalley: Neat macroscopic membranes of aligned carbon nanotubes, J. Appl. Phys. **93**, 2153 (2003) 399
[43] M. F. Islam, D. E. Milkie, O. N. Torrens, A. G. Yodh, J. M. Kikkawa: Magnetic heterogeneity and alignment of single wall carbon nanotubes, Phys. Rev. B **71**, 201401(R) (2005) 399, 400
[44] C. T. White, T. N. Todorov: Carbon nanotubes as long ballistic conductors, Nature **393**, 240 (1998) 401, 405
[45] F. Triozon, S. Roche, A. Rubio, D. Mayou: Electrical transport in carbon nanotubes: Role of disorder and helical symmetries, Phys. Rev. B **69**, 121410(R) (2004) 401
[46] T. Ando, T. Nakanishi, R. Saito: Berry's phase and absence of back scattering in carbon nanotubes, J. Phys. Soc. Jpn. **67**, 2857 (1998) 401, 405
[47] S. Roche, J. Jiang, F. Triozon, R. Saito: Quantum dephasing in carbon nanotubes due to electron–phonon coupling, Phys. Rev. Lett. **95**, 076803 (2005) 401
[48] S. Roche, J. Jiang, F. Triozon, R. Saito: Conductance and coherence lengths in disordered carbon nanotubes: Role of lattice defects and phonon vibrations, Phys. Rev. B **72**, 113410 (2005) 401
[49] S. Roche, F. Triozon, A. Rubio, D. Mayou: Conduction mechanisms and magneto-transport in multiwalled carbon nanotubes, Phys. Rev. B **64**, 121401(R) (2001) 401, 402
[50] B. L. Al'tshuler, A. G. Aronov, B. Z. Spivak: The Aharonov–Bohm effect in disordered conductors, JETP Lett. **33**, 94 (1981) 401
[51] S. Roche, R. Saito: Magnetoresistance of carbon nanotubes: From molecular to mesoscopic fingerprints, Phys. Rev. Lett. **87**, 246803 (2001) 402, 404, 405
[52] L. Langer, V. Bayot, E. Grivei, J.-P. Issi, J. P. Heremans, C. H. Olk, L. Stockman, C. van Haesendonck, Y. Bruynseraede: Quantum transport in a multiwalled carbon nanotube, Phys. Rev. Lett. **76**, 479 (1996) 402
[53] J. Cao, Q. Wang, M. Rolandi, H. Dai: Aharonov–Bohm interference and beating in single-walled carbon-nanotube interferometers, Phys. Rev. Lett. **93**, 216803 (2004) 404
[54] C. Strunk, B. Stojetz, S. Roche: Quantum interferences in multiwall carbon nanotubes, Semicond. Sci. Technol. **21**, S38 (2006) 404, 405

[55] F. L. Shyu, C. P. Chang, R. B. Chen, C. W. Chiu, M. F. Lin: Magnetoelectronic and optical properties of carbon nanotubes, Phys. Rev. B **67**, 045405 (2003) 405
[56] I. B. Mortimer, L.-J. Li, R. A. Taylor, G. L. Rikken, O. Portugall, R. J. Nicholas: Magneto-optical studies of single-wall carbon nanotubes, Phys. Rev. B **76**, 085404 (2007) 406, 407, 414
[57] I. B. Mortimer, R. J. Nicholas: Role of bright and dark excitons in the temperature-dependent photoluminescence of carbon nanotubes, Phys. Rev. Lett. **98**, 027404 (2007) 407, 410, 411, 412, 413, 414, 416
[58] C. D. Spataru, S. Ismail-Beigi, R. B. Capaz, S. G. Louie: Quasiparticle and excitonic effects in the optical response of nanotubes and nanoribbons, in A. Jorio, G. Dresselhaus, M. Dresselhaus (Eds.): *Topics in Applied Physics*, vol. 111 (Springer, Heidelberg 2008) p. 183 407
[59] T. Ando: Excitons in carbon nanotubes, J. Phys. Soc. Jpn. **66**, 1066 (1997) 407, 408
[60] C. D. Spataru, S. Ismail-Beigi, L. X. Benedict, S. G. Louie: Excitonic effects and optical spectra of single-walled carbon nanotubes, Phys. Rev. Lett. **92**, 077402 (2004) 407, 408
[61] E. Chang, G. Bussi, A. Ruini, E. Molinari: Excitons in carbon nanotubes: An *ab-initio* symmetry-based approach, Phys. Rev. Lett. **92**, 196401 (2004) 407, 408
[62] V. Perebeinos, J. Tersoff, P. Avouris: Scaling of excitons in carbon nanotubes, Phys. Rev. Lett. **92**, 257402 (2004) 407, 408
[63] H. Zhao, S. Mazumdar: Electron–electron interaction effects on the optical excitations of semiconducting single-walled carbon nanotubes, Phys. Rev. Lett. **93**, 157402 (2004) 407, 408
[64] T. Ando: Excitons in carbon nanotubes revisited: Dependence on diameter, Aharonov–Bohm flux, and strain, J. Phys. Soc. Jpn. **73**, 3351 (2004) 407, 408
[65] E. Chang, G. Bussi, A. Ruini, E. Molinari: First-principles approach for the calculation of optical properties of one-dimensional systems with helical symmetry: The case of carbon nanotubes, Phys. Rev. B **72**, 195423 (2005) 407, 408
[66] V. Perebeinos, J. Tersoff, P. Avouris: Radiative lifetime of excitons in carbon nanotubes, Nano Lett. **5**, 2495 (2005) 407, 408, 410, 414
[67] C. D. Spataru, S. Ismail-Beigi, R. B. Capaz, S. G. Louie: Theory and *ab-initio* calculation of radiative lifetime of excitons in semiconducting carbon nanotubes, Phys. Rev. Lett. **95**, 247402 (2005) 407, 408, 410, 411, 414
[68] T. Ando: Effects of valley mixing and exchange on excitons in carbon nanotubes with Aharonov–Bohm flux, J. Phys. Soc. Jpn. **75** (2006) 407, 408, 414
[69] E. Chang, D. Prezzi, A. Ruini, E. Molinari: Dark excitons in carbon nanotubes, arXiv URL: `cond-matt/0603085` 407, 408
[70] F. Wang, G. Dukovic, L. E. Brus, T. F. Heinz: The optical resonances in carbon nanotubes arise from excitons, Science **308**, 838 (2005) 408
[71] J. Maultzsch, R. Pomraenke, S. Reich, E. Chang, D. Prezzi, A. Ruini, E. Molinari, M. S. Strano, C. Thomsen, C. Lienau: Exciton binding energies in carbon nanotubes from two-photon photoluminescence, Phys. Rev. B **72**, 241402 (2005) 408
[72] R. Loudon: One-dimensional hydrogen atom, Am. J. Phys. **27**, 649 (1959) 408

[73] R. J. Elliot, R. Loudon: Theory of fine structure on the absorption edge in semiconductors, J. Phys. Chem. Solids **8**, 382 (1959) 408
[74] R. J. Elliot, R. Loudon: Theory of the absorption edge in semiconductors in a high magnetic field, J. Phys. Chem. Solids **15**, 196 (1960) 408
[75] T. Ogawa, T. Takagahara: Interband absorption spectra and Sommerfeld factors of a one-dimensional electron–hole system, Phys. Rev. B **43**, 14325 (1991) 408
[76] T. Ogawa, T. Takagahara: Optical absorption and Sommerfeld factors of one-dimensional semiconductors: An exact treatment of excitonic effects, Phys. Rev. B **44**, 8138 (1991) 408
[77] S. Glutsch, F. Bechstedt: Effects of the Coulomb interaction on the optical spectra of quantum wires, Phys. Rev. B **47**, 4315 (1993) 408
[78] D. S. Citrin: Long intrinsic radiative lifetimes of excitons in quantum wires, Phys. Rev. Lett. **69**, 3393 (1992) 408, 410
[79] J. Shaver, J. Kono, O. Portugall, V. Krstic, G. L. J. A. Rikken, Y. Miyauchi, S. Maruyama, V. Perebeinos: Magnetic brightening of carbon nanotube photoluminescence through symmetry breaking, Nano Lett. **7**, 1851 (2007) 409, 410, 411, 412, 413, 416
[80] J. Shaver, J. Kono, O. Portugall, V. Krstic, G. L. J. A. Rikken, Y. Miyauchi, S. Maruyama, V. Perebeinos: Magneto-optical spectroscopy of excitons in carbon nanotubes, Phys. Stat. Sol. (b) **243**, 3192 (2006) 410
[81] H. Htoon, M. J. O'Connell, P. J. Cox, S. K. Doorn, V. I. Klimov: Low temperature emission spectra of individual single-walled carbon nanotubes: Multiplicity of subspecies within single-species nanotube ensembles, Phys. Rev. Lett. **93**, 027401 (2004) 411
[82] H. Ajiki, T. Ando: Lattice distortion with spatial variation of carbon nanotubes in magnetic fields, J. Phys. Soc. Jpn. **65**, 2976 (1996) 414
[83] H. Ajiki: Magnetic-field effects on the optical spectra of a carbon nanotube, Phys. Rev. B **65**, 233409 (2002) 414
[84] A. Kanda, S. Uryu, K. Tsukagoshi, Y. Ootuka, Y. Aoyagi: Magnetic field dependence of Coulomb oscillations in metal/multi-wall carbon nanotube/metal structures, Physica B **323**, 246 (2002) 415
[85] C. Gómez-Navarro, P. J. D. Pablo, J. Gómez-Herrero, B. Biel, F.-J. Garcia-Vidal, A. Rubio, F. Flores: Tuning the conductance of single-walled carbon nanotubes by ion irradiation in the anderson localization regime, Nature Mater. **4**, 534 (2005) 416

Index

Carbon-Nanotube Optoelectronics

Phaedon Avouris, Marcus Freitag, and Vasili Perebeinos

IBM Research Division, T. J. Watson Research Center,
Yorktown Heights, NY 10598, USA {avouris,mfreitag,vperebe}@us.ibm.com

Abstract. Semiconducting single-walled carbon nanotubes are direct-gap materials that provide ideal systems for the study of photophysics in one-dimension. While their excited states involve strongly bound 1D excitons, their single atomic layer structure makes their optical properties especially sensitive to their environment and external fields, thus allowing for their controlled modification. In this chapter we review the properties of the excited states of nanotubes, the mechanisms of their production and detection, focusing particularly on electrically-induced excitation by ambipolar electron-hole recombination and impact excitation by hot carriers. Radiative decay of photo-excited and electron-excited (electroluminescence) emission as well as the non-radiative decay to free carriers leading to photoconductivity are discussed. The influence of external electric fields and of environmental interactions on excited nanotubes is considered. Finally, the possible technological uses of carbon nanotubes as nanometer scale light sources and photocurrent and photovoltage detectors are discussed.

1 The Nature of the Optically Excited State

The simple, single-particle, tight-binding model (TBM) and its refinements to include curvature effects [1, 2] and trigonal distortions [3–5] has been very successful in describing qualitative trends in a large array of phenomena involving carbon nanotubes CNTs. Inclusion of electron–electron interactions is, however, essential for a quantitative analysis and even for the correct qualitative understanding of the physics of nanotubes. This is particularly true when it comes to understanding the nature of the excited states of CNTs. Early on, theoretical work by *Ando* [6] pointed out the importance of e–e interactions in nanotube excited states. He indicated that such interactions in semiconducting CNTs would, in general, open up a wider bandgap than that predicted by the TBM, while the electron–hole attraction will lead to bound excitons and partially compensate for the excitation blueshift. A number of additional theoretical studies incorporating e–e interactions supported and clarified the excitonic nature of the excited states of CNTs [6–13]. However, because of the similarity of the interband excitation energies predicted by the TBM and the experimentally observed transition energies, the exciton picture was slow to be generally adapted. Eventually, convincing evidence came from a variety of experiments. For example, absorption and fluorescence spec-

A. Jorio, G. Dresselhaus, M. S. Dresselhaus (Eds.): Carbon Nanotubes,
Topics Appl. Physics **111**, 423–454 (2008)

troscopy uncovered the anomalous "ratio problem", i.e., that the ratio of the second, E_{22}^S, to the first excitation energy, E_{11}^S, is not 2, as predicted by single-particle models, but is closer to 1.8 when extrapolated to large CNT diameters, or zero energy [12, 14]. See also contributions by Ando and by Lefebvre et al. While, because of the dipole selection rule, single-photon spectroscopy probes odd-parity excited states, two-photon spectroscopy probes even-parity states. In chiral CNTs the exciton states resulting from a given band-to-band transition have even (g), or odd (u) symmetry with respect to a two-fold axis (U-axis) perpendicular to the tube axis. Indeed, comparison of one- and two-photon fluorescence spectroscopy results [15, 16] showed an energy splitting of about 300 meV for the lowest u and first excited g-exciton states of 0.8 nm CNTs. Resonant photoconductivity studies [17] and later fluorescence studies [18–22] found phonon sidebands to the purely electronic transitions (zero-phonon lines) whose energy and intensity could only be accounted for within the excitonic model [23].

The excitons in single-wall CNTs are Wannier-type excitons [24], which because of the circumferential electron confinement and their 1D character have unusually high binding energies; typically $E_b \sim 0.3$–0.5 eV. The exciton binding energy depends on the diameter and chirality of the semiconducting CNT. Increasing the diameter decreases the confinement and decreases E_b. The Coulombic coupling between the electron and hole forming the 1D CNT exciton, as in the case of bulk excitons, depends on dielectric screening. In bulk excitons $E_b \sim 1/\varepsilon^2$. In nanotubes, when the exciton size is larger than the tube diameter, most of the electric-field lines between charges penetrate the surrounding medium and this makes E_b (as well as the bandgap E_g) a function of the dielectric constant of the surrounding environment. *Perebeinos* et al. [9] gave the following expression for the dependence E_b on CNT diameter (d_t), chirality through the effective mass (m^*) and dielectric constant (ε): $E_b = C d_t^{\alpha-2} m^{*\alpha-1} \varepsilon^{-\alpha}$, where $\alpha = 1.4$. An example is given in Fig. 1, which shows the computed absorption spectra of a (19,0) CNT as a function of the dielectric environment. Figure 1a gives both the exciton (E_{11}^S, E_{22}^S) and interband transition (Δ_{11}, Δ_{22}) spectra, while in Fig. 1b the excitonic contributions are subtracted [25]. It is clear that in CNTs most of the oscillator strength is transferred from the interband to the excitonic transitions, which dominate their optical absorption and emission spectra [7–9]. Only in CNTs embedded in high dielectric constant media, where the e–h interaction is effectively screened, do the interband transitions become strong.

Including the effect of electron–electron interactions changes more than the energies of the electronic excitations of nanotubes; it removes the degeneracies present in the single-particle model, as shown in Fig. 2.

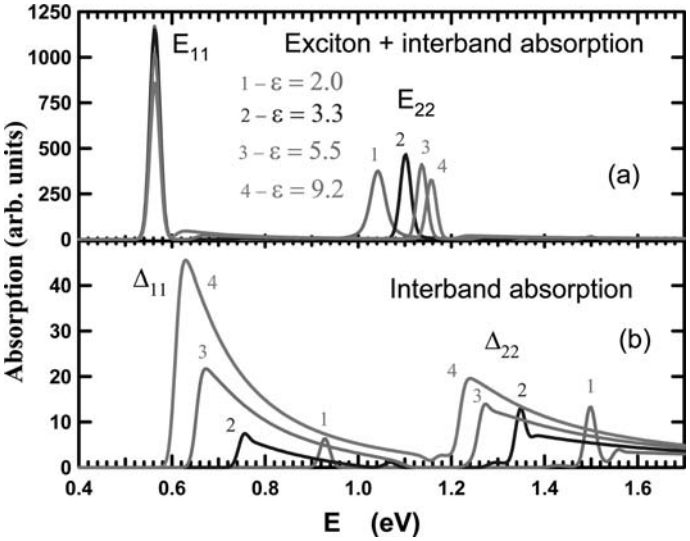

Fig. 1. Absorption spectra of a (19,0) CNT (with diameter $d_t = 1.5\,\text{nm}$) as a function of the dielectric response [25]:*curve* (1): $\varepsilon = 2.0$, models the CNT response in vacuum [7, 8]; *curve* (2): $\varepsilon = 3.3$, models the CNT response in solution [26]; *curve* (3): $\varepsilon = 5.5$; *curve* (4): $\varepsilon = 9.2$. (**a**) Total absorption due to both excitons and interband contributions. The E_{11}^S energy is kept constant. (**b**) Interband absorption with the exciton contribution of E_{11}^S and E_{22}^S being subtracted out. Note the difference in scales in (a) and (b) ($\times 25$)

2 Exciton Properties

2.1 Low-Energy Exciton Bandstructure – Dark and Bright Excitons

The doubly degenerate valence and conduction bands of the nanotubes give rise to the four lowest-energy excitons [9, 13, 27–30], as shown in Fig. 3. The lowest-energy exciton has zero circumferential angular momentum and consists of the symmetric linear combination of electron–hole pairs originating from the K and K' points of the graphene Brillouin zone. This exciton can not decay radiatively to the ground state, because it has even spatial parity. The odd-symmetry exciton has a higher energy due to exchange interactions and it couples to the light field in the dipole approximation. The remaining two excitonic states have finite circumferential angular momenta, because they originate from an electron and hole from different valleys, K and K', and, thus, they cannot be excited by light, as is further discussed in the contribution by Spataru et al.

As a specific example, the band structure of the (19,0) CNT is shown in Fig. 2. Figure 2a gives the single-particle picture, while Fig. 2c shows the two-particle structure.

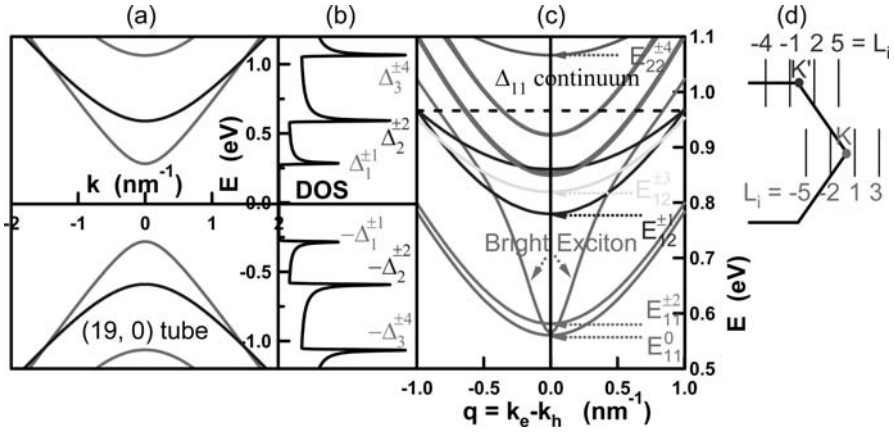

Fig. 2. Electronic structure of a (19,0) tube based on the π-tight-binding model: (**a**) dispersion of the doubly degenerate valence and conduction bands; (**b**) density of states with peaks corresponding to the bottom of the first, second, and third bands with energies $\pm\Delta_1^L$, $\pm\Delta_2^L$, and $\pm\Delta_3^L$, respectively. The superscript L is the angular momentum measured as a minimum distance from the K or K' graphene points in units of $2/3d_t$, as shown in (**d**). (**c**) Exciton dispersion calculated with $\varepsilon = 2$ [9, 25] for different angular momenta: $L = 0$ to 4. The *arrows* indicate the minimum energies of excitons for a given angular momentum and the *horizontal line* shows the onset of the intraband continuum

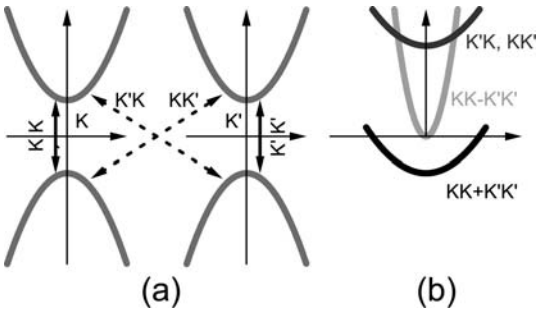

Fig. 3. (**a**) Single-particle electronic structure of the doubly degenerate valleys around the K and K' points of the graphene Brillouin zone shown in *red*. The four possible electron–hole combinations give rise to fourfold degenerate states. (**b**) Coulomb interaction partly lifts this degeneracy, giving rise to four excitonic bands two of zero angular momenta ($KK \pm K'K'$) and two degenerate excitons with a finite, but opposite sign angular momenta ($KK', K'K$)

2.2 Exciton Radiative and Nonradiative Lifetimes

The potential usefulness of carbon nanotubes as an optical material depends on their luminescence efficiency, which in turn depends on their radiative and nonradiative lifetime. Most studies of bulk, surfactant-coated nanotubes have given low fluorescence quantum yields of the order of 10^{-3} to 10^{-4} [19, 31–33]. Although these yields may have significant uncertainties due to the presence of both semiconducting and metallic (nonemitting) nanotubes, different orientations in solutions and not accurately known absorption strengths, it is clear that efficient nonradiative processes are present. (Very recent single-molecule fluorescence studies have suggested higher yields of up to 7 in section 3.3 of Lefebvre et al they use 7 % [34], as further discussed in the contribution by Lefebvre et al.)

To properly describe the radiative decay process one has to consider the band structure of the lowest exciton bands and know how they are populated (see also the contribution by *Spataru* et al. in this volume). In the following discussion we assume an efficient thermalization of excitons within the band. First, we consider a 0D molecular two-level system with a dark state lower in energy by δE than a bright state. The radiative lifetime of the bright state, τ_{r}, is inversely proportional to the dipole oscillator strength, which in turn scales linearly with the size of the molecule. The measured radiative lifetime τ^* would be the ensemble average, $\tau^* = \tau_{\mathrm{r}} Z$, where the statistical sum Z for the two-level system is given by $Z(T) = 1 + \exp(\delta E / k_{\mathrm{B}} T)$. For two-band 1D excitons with a parabolic band structure characterized by an effective mass m_{exc}, a similar expression holds for the radiative lifetime except that the statistical sum should be now modified to: $Z \sim \sqrt{m_{\mathrm{exc}} k_{\mathrm{B}} T}(1 + \exp(\delta E / k_{\mathrm{B}} T))$. As has been discussed above, there are four low-energy excitonic bands that contribute to the statistical sum, and the dispersion of the bright exciton is predicted to be much stronger than other dark excitonic bands. This complicates the calculation of the temperature dependence of the radiative lifetime from the above expression. However, as shown in [27] the results of the full calculations of the radiative lifetime can be fairly well fitted to a very simple expression for tubes with diameters in the range of experimental interest, $1.0\,\mathrm{nm} < d_t < 2.5\,\mathrm{nm}$, as follows:

$$\tau^* = \tau_{\min}(T/T_{\min}) \exp[(T_{\min} - T)/T]\,, \tag{1}$$

where $T_{\min}$ and $\tau_{\min}$ are the only two diameter dependent parameters, standing, respectively, for the temperature at which the radiative lifetime has its minimum and the corresponding minimum value of the radiative lifetime. At very low temperatures the dark-state population dominates and no emission is, in principle, expected. As the temperature increases, the population of the bright state also increases and the radiative lifetime decreases. At higher temperatures excitonic states with large momentum are occupied, which do not contribute to the light emission and, as a result, the radiative lifetime should again increase. Both the minimum radiative lifetime ($\sim$ 2–5 ns) and

the temperature (∼40–100K) where this minimum occurs depend on the energy splitting δE, and both of them are inversely proportional to the tube diameter. In cases where thermalization between the singlet and the triplet states becomes efficient (for example by increasing the spin-orbit coupling through magnetic or high-Z impurities), a temperature dependence of the radiative lifetime (∼ 30–70 ns) similar to that of (1) is found, except that both the minimum radiative lifetime and $T_{\min}$ (∼ 100–300 K) increase by an order of magnitude due to the larger singlet–triplet splitting compared to the dark–bright energy splitting in the singlet manifold.

Finally, it is predicted that the τ_{r} behavior would be sensitive to deviations from ideality, such as symmetry breaking and phonons. Indeed, any symmetry breaking mixes the wavefunctions of the dark and bright excitons and leads to a partial transfer of spectral weight to the dark exciton [27]. Therefore, observation of an emission peak at a lower energy than the dipole-allowed transition implies some type of symmetry breaking. Single-nanotube spectroscopy at low temperatures allows us to probe such effects. Recent fluorescence measurements are suggestive of such behavior by showing multiple peaks, with spectral weight shifting from high- to low-energy peaks with decreasing temperature [35–37]. In addition, time-reversal symmetry can be broken by the external perturbation, such as a high magnetic field ([38], see also the contribution by Kono et al. in this volume). This leads to the "brightening" of the dark state and increased optical quantum yield.

In accord with the observed low fluorescence quantum yield, the measured fluorescence lifetime of semiconducting nanotubes is short, of the order of 10–100 ps, while the radiative lifetime is estimated to be of the order of 10 ns (for a detailed discussion and references see in this volume the contribution by Ma et al.). The existence of the dark exciton states cannot account for the small yield and fast decay because the dark–bright splitting is rather small, of the order of 10 meV [27], so thermal equilibrium would leave a significant (∼ 40 %) exciton population in the bright state. Bimolecular decay processes could not be the determining factor either because the short lifetime is observed at even low excitation levels. We have to conclude, therefore, that another intrinsic energy-dissipation channel controls the relaxation of the lowest exciton state. Undoubtedly, electron–phonon coupling between the E_{11} exciton and the ground state plays a key role [25].

2.3 Exciton–Optical Phonon Sidebands in Absorption Spectra

Fine structure in the optical data can provide a distinctive signature of excitonic transitions in semiconducting carbon nanotubes. In zero-dimensional systems (0D) phonon sidebands show up in optical spectra as replicas of the main electronic transition and are used to determine the strength of the exciton–phonon interaction. On the other hand, in bulk 3D semiconductors where band-to-band absorption dominates the optical spectrum, typically no distinct phonon sidebands are observed. In 1D systems the zero-phonon line

has an excitonic origin and optical phonon sidebands are clearly observed. Unlike in molecules, the spectral lineshape of this phonon replica is significantly broader than that of the zero-phonon line due to the 1D exciton dispersion, which is much larger than the phonon dispersion. In addition, the exciton dispersion makes the phonon sideband intensity in carbon nanotubes significantly smaller than that in a 0D system with the same strength of the exciton–phonon interaction. Thus, in a molecular system the phonon sideband intensity is given by the Huang–Rhys factor $S = (g/\hbar\omega)^2$, where g is the strength of the exciton–phonon interaction and $\hbar\omega$ is the phonon energy, which coincides with the position of the sideband replica. In 1D carbon nanotubes, on the other hand, the measured phonon sideband intensity $S' = (g/\hbar\bar{\omega})^2$ is smaller than the molecular limit result, due to the larger average energy position of the phonon sideband $\hbar\bar{\omega} = \langle\hbar\omega_{-q} + E_q - E_{q=0}\rangle$, where $\hbar\omega_{-q}$ and E are phonon and exciton energies, respectively.

To calculate the phonon sidebands in the absorption spectra of carbon nanotubes we need to know the exciton–phonon coupling between the optically bright excitons and all possible phonons in the carbon-nanotube structure. The latter is given by a linear combination of the electron–phonon interactions [39] with weights determined by the exciton wavefunction from the two-particle Bethe–Salpeter equation solution [9]. The resulting exciton–phonon interaction is typically a few per cent stronger than the ground-state electron–phonon coupling because of the confinement of the optically active exciton [23]. The resulting optical absorption is given by the following expression [40]:

$$\sigma(E) = \sum_{\alpha} \frac{I_\alpha}{\pi} \frac{\gamma_\alpha(E)}{[E - \varepsilon_\alpha]^2 + \gamma_\alpha^2(E)}\,, \tag{2}$$

where I_α, ε_α, and γ_α are the oscillator strength, energy, and the imaginary part of self-energy of exciton α. The exciton self-energy can be calculated using the random-phase approximation [23]:

$$\gamma_\alpha(E) = \pi \sum_{\eta} |B_{\alpha\eta}|^2 \delta(E - E_{\alpha' q} - \hbar\omega_{-q\mu})\,, \tag{3}$$

where index η stands for the $(\alpha' q\mu)$ variables, $B_{\alpha\eta}$ is the exciton–phonon coupling, $E_{\alpha' q}$ and $\hbar\omega_{-q\mu}$ are the exciton and phonon energies, respectively.

An example of a computed spectrum is shown in Fig. 4. Most of the spectral weight is transferred to the optical-phonon sideband with energy of ~ 200 meV. Unlike the sidebands in molecular systems, the phonon sidebands in CNTs are expected to be much broader due to the exciton dispersion. Indeed, a phonon with momentum $\boldsymbol{q}$ can assist an exciton transition with the opposite momentum $-\boldsymbol{q}$, giving rise to a phonon-sideband peak with energy $E_{-q} + \hbar\omega_q - E_{11}^S$, so that the spectral lineshape of the phonon sideband resembles a convoluted density of exciton and phonon states. Most importantly, the phonon sideband in Fig. 4 peaks at an energy of 210 meV, which

is larger than any of the single phonon energies of the CNT. This energy shift is due to the fact that the dark states with finite angular momentum have the strongest exciton–phonon coupling with the K-point optical phonon with an energy of 180 meV giving a dark–bright exciton splitting of 30 meV (the splitting depends on CNT diameter), which accounts for the shift of the sideband at about 210 meV [17]. Therefore, the energy position of the phonon sidebands gives information about the electronic states of carbon nanotubes that cannot be directly accessed. Optical-phonon sidebands have also been observed in many other optical studies [18–22]. We have also predicted a weaker RBM replica in the absorption spectra. As the CNT diameter is reduced, the exciton–phonon coupling to both RBM and optical phonons increases resulting in stronger phonon replicas, which can have up to 15 % of the oscillator strength in $d_t = 1$ nm diameter CNTs. The modification of the exciton transition energy due to the phonon coupling can reach up to 70 meV. At the same time, the electron-phonon interaction renormalizes the phonon energy. This effect is typically an order of magnitude smaller. However, in metals with strong electron-optical phonon coupling strength, and in cases like graphene where the phonons have energies comparable to or larger than the gap, the dynamic effect can be especially large (see the contribution by *Charlier* et al in this volume). The energy renormalization in perturbation theory reduces the phonon energy, that is, has a negative sign, and is maximum in undoped (intrinsic) graphene and CNTs. Therefore, reducing the energy renormalization by changing the carrier density can induce a blue shift in the Raman frequency. A similar situation may be expected in the case of 1D metallic nanotubes, although the effect becomes even stronger due to the reduced dimensionality of the system. Finally, and most importantly, we found that the renormalization of the phonon energy by carriers in semiconducting CNTs also results in a blue shift due, in this case, to the coupling of the Raman active phonons to virtual electron-hole pairs [41].

Although the acoustic-phonon coupling strength is much weaker than the coupling to optical phonons, it nevertheless plays an important role in determining the intrinsic linewidth of the dipole active (E_{11}^S) exciton. The experimentally observed linear dependence of the excitonic linewidth in the fluorescence data by the *Lefebvre* group [36] of FWHM $= 0.29 k_B T$, in 1-nm diameter CNT, can readily be reproduced assuming a reasonable strength of the exciton–acoustic-phonon coupling [23] and the bright-exciton dispersion [27].

2.4 Impact Excitation, Auger Recombination and Exciton Annihilation

Excited states of carbon nanotubes can be produced by photoexcitation, electron–hole recombination (see Sect. 1), or through internal excitation by energetic ("hot") carriers flowing through the CNT. The excitation mechanism involves the Coulombic interactions between electrons, i.e., an impact

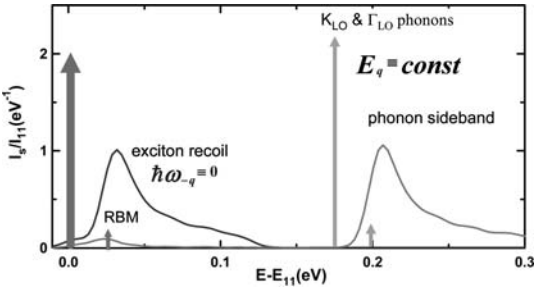

Fig. 4. First exciton absorption in a (17, 0) tube $d_t = 1.4\,\text{nm}$ calculated in a dielectric environment with $\varepsilon = 2$ [23] including the exciton–phonon coupling. The *phonon sideband curve* shows absorption spectra according to (2), the *vertical lines* shows the corresponding molecular limit calculated with flat exciton dispersion E_q = const, and the *exciton recoil curve* was calculated with the phonon energies set to zero to show the contribution to the phonon-sideband width from the exciton dispersion. The zero-phonon line is centered at zero energy and it has approximately 92 % of the spectral weight with the strongest optical-phonon sideband having approximately 8 % intensity

scattering mechanism. Electron–electron interactions are very strong in 1D materials such as CNTs. Indeed, calculations suggest, see Fig. 5, that impact excitation processes in CNTs, are much more efficient (4–5 orders of magnitude stronger) than in conventional bulk semiconductors [42].

Conservation of circumferencial angular momentum plays a critical role in determining the threshold energy, E_{th}, for the impact ionization and excitation in carbon nanotubes. Due to the hyperbolic dispersion of the electrons and holes, the first and second electronic bands in perfect-symmetry tubes are not impact-ionization active at low energies. On the other hand, the third and fourth bands become impact-ionization active at the bottom of the band, because the energies of the bands are proportional to the angular momenta, such that it is easy to conserve both of them, whereas the longitudinal momentum along the tube axis is zero in both the initial and final states. Furthermore, the impact-excitation rate is higher in nanotubes than the impact-ionization rate, neglecting the strong electron–hole interaction in the produced electron–hole pair. The Coulomb interaction between the electron and hole composing an exciton increases the effective mass of the exciton, which helps to conserve both energy and momentum and to substantially reduce the impact-excitation threshold in the first and the second band.

The energy necessary for the electronic excitation must come from the hot carriers. The carriers are accelerated by the field but can lose energy to both phonons, particularly high-energy optical phonons (strongest electron–phonon coupling), and electronic transitions. The problem can be treated by solving the corresponding Boltzmann equation [42]. It is thus found that the

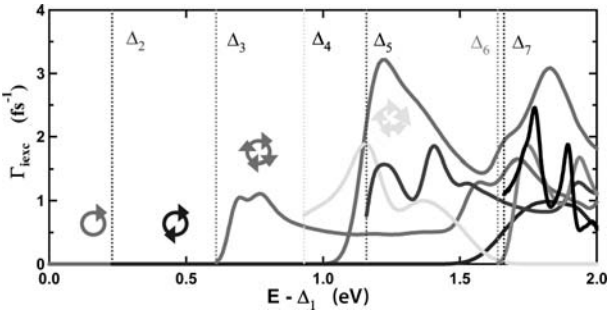

Fig. 5. Impact-excitation rates for a (25,0) nanotube $d = 2.0\,\mathrm{nm}$ as a function of energy measured from the bottom of the first conduction band Δ_1, for the first seven conduction bands. The *vertical dashed lines* correspond to the bottoms of the conduction bands Δ_i, $i = 2, 3, \ldots, 7$ relative to Δ_1. After [42]

exciton production rate P varies exponentially with the applied field F as $P \sim \exp(-E_{\mathrm{th}}/eF\lambda_{\mathrm{op}})$, where E_{th} is the excitation threshold and λ_{op} ($\sim$ 20–40 nm) is the electron mean-free path due to optical-phonon scattering (see also the contribution by *Biercuk* et al. in this volume). Optical phonons can efficiently decay into the heat bath provided by the substrate. However, in the case of suspended nanotubes evidence has been presented of the development of a nonequilibrium optical phonon distribution [43, 44]. In our model we have included this possibility by having the optical phonons at different temperatures, T_{op}, while keeping the other phonons at ambient temperature. The resulting exciton production rate could be well fitted by an exponential dependence with an effective temperature, T_{eff} [42]:

$$P = P_0 \exp(-E_{\mathrm{th}}/k_{\mathrm{B}}T_{\mathrm{eff}})\,; \qquad k_{\mathrm{B}}T_{\mathrm{eff}} = \sqrt{(k_{\mathrm{B}}T_{\mathrm{op}})^2 + (eF\lambda_{\mathrm{op}})^2}\,. \tag{4}$$

The angular-momentum conservation law can also help to understand why the reverse process, i.e., the Auger recombination of a small longitudinal momentum E_{11}^S exciton and a free carrier is not important. Indeed, the free carrier in the first band must accept the entire E_{11}^S exciton energy without changing its own momentum, which is not possible. Another exciton decay channel is the exciton–exciton annihilation process in which the angular momenta of the two colliding low-energy E_{11}^S excitons add up to zero is probable. In this process, a second E_{22}^S exciton of zero angular momentum can be created, whose energy is roughly twice the E_{11}^S energy at the bottom of the band. This decay channel can be efficient, provided the exciton density is high. This condition has recently been experimentally realized in impact-excitation electroluminescence [45] and under high-intensity laser ablation [46–48], as is also discussed in the contribution by Ma et al.

2.5 Franz–Keldysh, Stark Effects and Exciton Ionization by Electric Fields

In electroluminescence, photoconductivity and impact-excitation experiments an electric field parallel to the CNT axis is applied. Such a field can modify both the spectral properties and excited-state decay dynamics of CNTs. The electro-optical response of 3D semiconductors was discussed almost fifty years ago by *Franz* [49] and *Keldysh* [50, 51]. They showed that in the presence of the field, the absorption coefficient decays exponentially for photon energies below the semiconductor bandgap and becomes oscillatory for photon energies above the bandgap. The interest in electroabsorption was revived about three decades later after the discovery of the quantum-confined Stark effect in 2D quantum-well structures [52, 53], where large Stark shifts were observed in fields directed perpendicular to the 2D planes.

An electric field leads to several modifications of the absorption spectrum: 1. modulation of the absorption coefficient; 2. growth of the band-to-band absorption spectral weight; 3. shift of the absorption peak, known as the Stark effect; and 4. dissociation of the bound exciton. In bulk 3D semiconductors the exciton binding energy is small and most of the theoretical and experimental focus has been on the field-induced absorption in the region below the bandgap and on the quantum-confined Stark effect in 2D structures [24]. In carbon nanotubes, the binding energy is large and the oscillator strength of the higher-lying Rydberg states is very small, so that relatively large changes in the absorption at the first excitonic peak and the first band-to-band absorption are to be expected.

The influence of an external electric field on the absorption spectra of CNTs was studied theoretically by *Perebeinos* and *Avouris* who solved the Bethe–Salpeter equation for excitons in an external dc electric field directed along the tube axis [54]. At zero field, there is no absorption in the energy range between the first exciton and the onset of the band-to-band absorption (Fig. 6). In the presence of the field, however, an absorption peak develops in the optically forbidden region, i.e., below the bandgap at about 0.7 eV (Fig. 6). With increasing field strength, spectral weight is transferred from the excitonic peak to the band-to-band absorption. At some critical field F_c, the band absorption merges with the first-exciton absorption peak. In contrast, in the absence of excitons the band-to-band absorption simply decays exponentially below the bandgap edge. The same authors found quadratic field dependences of both the spectral weight growth of the band-to-band absorption and of the Stark shift. The effects are most pronounced in large-diameter tubes with large excitonic radii, since the field coupling of the bound exciton to the free electron–hole continuum states is proportional to the exciton radius [9]. Specifically, they found the spectral weight shift to be proportional to $\sim d_t^4 F^2$ and that it can be as large as 10 % at 15 V/μm in $d_t = 1.5$ nm, while the Stark shift is proportional to $\sim d_t^3 F^2$ and can be as large as 10 meV at 15 V/μm in a $d_t = 1.5$ nm tube. Analogous results were obtained in [55].

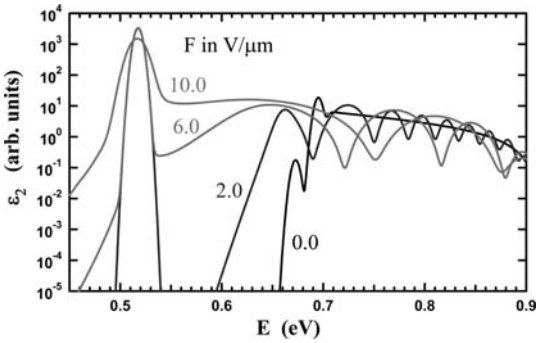

Fig. 6. Absorption spectra of a (16,8) nanotube, $d_t = 1.7\,\mathrm{nm}$, in applied electric fields of $F(\mathrm{V/m}) = 0.0, 2.0, 6.0, 10.0$. The first optically active exciton in zero field is at 0.5 eV, while the band-to-band absorption is at about 0.2 eV higher energy

The presence of the field can also lead to the ionization (dissociation) of the exciton. This is essential for the observation of CNT photoconductivity upon excitation of the low-energy (E_{11}^S) bound-exciton state. On the other hand, the higher-energy E_{22}^S state is autoionizing because it is embedded in the lowest-energy free-particle continuum. The ionization lifetime of the bound exciton can be written as the product of the tunneling probability into the free electron–hole continuum and the attempt frequency. From the uncertainty principle it can be shown that the attempt frequency is proportional to the exciton binding energy E_b, while the tunneling probability can be described by a single parameter F_0 [56], so that the dissociation rate can be written as:

$$\Gamma_0(F) = \alpha E_\mathrm{b}(F_0/F)\exp[-(F_0/F)]\,, \tag{5}$$

where F_0 is proportional to $\sim E_\mathrm{b}^{3/2} m^{1/2} \sim 1/d_t^2$, where m is a reduced exciton mass. We solve numerically for the exciton tunneling rate $\Gamma_0(F)$ [54] and the results can be well fitted to (5) at low fields with $F_0 \approx 90\,\mathrm{V/\mu m}$ in a $d_t = 1.5\,\mathrm{nm}$ tube, and $\alpha \approx 4$ being almost diameter independent. At fields above half the critical field $F_\mathrm{c} \approx 0.5F_0$, the numerical solutions start to deviate from (5). Since the binding energy in large-diameter tubes is typically less than the optical-phonon energy of 180–200 meV, the bound exciton can be dissociation by a phonon-assisted mechanism. The probability to absorb an optical phonon is proportional to the phonon occupation number n_ph, which is small at room temperature, but can be large in optoelectronic CNT devices operating at high biases [43]. The bound-exciton dissociation rate in this regime [54] becomes $\Gamma_1 \approx \Gamma_0 + n_\mathrm{ph}/\tau_\mathrm{ph}$, where $\tau_\mathrm{ph} = 30$–$100\,\mathrm{fs}$ is the exciton–optical-phonon scattering rate [23, 57].

3 Overview of CNT Electronics – Unipolar and Ambipolar FETs

Before we discuss electro-optic experiments, which are based on the carbon-nanotube field-effect transistor (CNTFET), we give a brief review of the switching mechanism in this fundamental electronic device [58]. An electric current through a semiconducting carbon nanotube that is contacted by two metal electrodes (source and drain) and capacitively coupled to a third electrode (the gate) can be switched on and off by applying a voltage at the gate [59, 60]. This device geometry is similar to that of a silicon metal-oxide-semiconductor field-effect transistor (MOSFET), with the inversion layer (channel) in the silicon replaced by the carbon nanotube. Switching of the carbon-nanotube field-effect transistor (CNTFET) however, is generally dominated by the response of the contact region and the device acts as a Schottky-barrier (SB) transistor rather than a bulk-switching transistor [61–64], as also discussed in the contribution by Biercuk et al.

The height of the Schottky barriers for electrons and holes determines the polarity of the device (n- or p-type). At roughly equal SB heights, both carriers can be injected equally well into the CNT and ambipolar conduction is observed [64–67]. This means at a positive gate voltage electrons carry the current in the CNT, and at a negative gate voltage holes carry the current. Tunneling through the 1-dimensional SB in a carbon nanotube is much more pronounced than in 3D Schottky-barrier devices because of the nanometer-scale width of the Schottky barriers. The SB width is strongly dependent on the gate oxide thickness and dielectric constant and to a lesser degree on the diameter of the CNT. As a rule of thumb, the SB width scales with the gate oxide thickness [65, 67] and thermally assisted tunneling is important for carrier injection in CNTFETs [68].

While scaling the oxide thickness improves operating characteristics such as the subthreshold slope by decreasing the SB width [69], it also leads to ambipolar characteristics that are undesirable in logic applications: The device does not turn off for either large positive or negative voltages because the Schottky barriers become leaky due to tunneling. There has been a lot of interest in finding ways to maintain unipolar characteristics in scaled CNTFETs [70]. One way to do this is through modulation doping, either by a second gate that electrostatically dopes the contact region of the device or through chemical doping.

On the other hand, ambipolar CNTFETs enable novel electrooptic devices that are impossible to achieve with unipolar transistors. In ambipolar devices, the minimum of the current is produced at a gate voltage halfway between source and drain voltages: $V_g = 1/2(V_d - V_s)$. At this voltage equal amounts of electrons and holes are injected from opposite contacts into the CNT. When these carriers associate they can recombine radiatively within the CNT leading to electroluminescence [71]. The opposite effect, where light excites

carriers in the CNTs and a photocurrent is measured is also possible [72]. In the following two sections, we will review these topics.

4 Photoconductivity and Light Detection

4.1 Types of Nanotube Photodetectors

Photodetectors can be based on a variety of physical effects, some of which have been demonstrated using carbon nanotubes. In thermal detectors, a change in temperature due to the illumination with visible or infrared light produces an electrical response. Thermopiles, bolometers, and pyroelectric detectors fall in this regime. In photon detectors, the photons are absorbed by a semiconducting material and the photogenerated electrons and holes produce a current or voltage across the device. Photoconductive detectors, p–n junctions, and Schottky barrier diodes are members of this group.

In CNTFETs, oxygen is known to turn unprotected nanotubes p-type by lowering Schottky-barrier heights for holes [73]. This effect is responsible for a photoresponse of CNTFETs upon UV illumination, because photons of sufficient energy can photodesorb molecular oxygen from the carbon nanotube and the metal electrodes and thus change the FET characteristics [74]. In air, the recovery to the initial conductance state takes on the order of tens of seconds. In vacuum no recovery is observed. The high sensitivity of CNTFETs to changes in their environment is the main reason they are actively explored as sensors for trace amounts of gases and molecules.

Photons with energy greater than the direct silicon bandgap (and to a lesser degree the indirect gap) can be absorbed in the silicon backgate of a CNTFET. They produce a photovoltage at the silicon/SiO_2 interface because the band bending in the silicon separates electrons and holes. This photovoltage acts as an additional gate voltage and shifts the gate-voltage characteristics of the CNTFET [72]. Depending on the biasing conditions, this can lead to an increase or decrease in transport current.

In a nanotube bolometer, the incident radiation heats the CNT and the change in temperature affects the resistivity of the device, i.e., it is based on the nonradiative decay of the excited CNT. FETs made from individual CNTs that are well heat sunk to the underlying substrate usually do not show an appreciable increase in temperature for incident power densities up to $100\,\mathrm{kW/cm^2}$ even when the laser is focused to a diffraction-limited spot. However, in films of carbon nanotubes that are suspended between two electrodes, heating is observed, and the film acts as a bolometer [75]. In the suspended-film geometry in vacuum, heat can only escape through the contacts, which are centimeters apart, or radiatively, which is very inefficient. Along the film, the heat and current flow is strongly limited by tube–tube junctions. In addition, CNTs have a very small heat capacity, which means that temperature increases are large. For best performance as a bolometric

detector, the nanotube film is cooled to a temperature around 200 K, where the electrical response is semiconducting (e.g., the resistance decreases for increasing temperature). There is hope that this kind of device might be competitive with existing bolometer materials, especially when metallic and semiconducting CNTs could effectively be separated.

Finally, there are several types of devices based on direct photon detection that have been realized recently with carbon nanotubes and that are the subject of the remainder of this section. They include photoconductors [72], Schottky-barrier diodes [70], and p–n junctions [76]. In these devices a photon produces an exciton within the carbon nanotube, which then decays to a free electron and hole at the valence- and conduction-band edges. These carriers are separated by an externally applied electric field, or by internal fields and lead to a photocurrent or photovoltage.

4.2 CNT Photoconductor

The photocurrent generated by the resonant excitation of a CNT allows CNTFETs to be used as nanosized, polarized photodetectors [72]. Excitation of higher exciton states, such as the E_{22}^{S} state that is autoionizing because it is embedded in the first free-particle continuum, directly leads to free electron–hole pairs. These are separated by the applied field. An example of a photoconductivity measurement in a CNTFET configuration is shown in Fig. 7. The increase in the off-state current in both the unipolar and ambipolar cases arises from the photogenerated electron–hole pairs in the CNT. The shift in gate-voltage characteristics is due to the previously discussed photovoltage generated at the silicon backgate/SiO_2 interface. One has to be careful to bias the device well in the off state to eliminate the large and non-CNT-specific contribution of the backgate photovoltage.

Guo et al. [77]. have modeled the photocurrent generated in an ambipolar CNTFET under illumination with infrared light with energy close to the energy of the CNT bandgap. The model showed that the gate-voltage characteristic under illumination evolves as we observe in the experiment of Fig. 7b (i.e., the off state increases monotonically with increasing light intensity). The authors point out that contrary to intuition, optical-phonon scattering increases the measured photocurrent. Once a photogenerated electron or hole has traveled far enough in the applied field, it can lose the energy of 180 meV by emitting an optical phonon. After this scattering event, it can not return to the position where it was created because the bandgap now poses an energy barrier. This helps prevent recombination of electrons and holes and thus increases the current that is collected at the electrodes.

4.3 Photocurrent Spectroscopy and Quantum Efficiency

To show that the photocurrent in a CNTFET is intrinsic to the CNT, both the wavelength and polarization dependence of the photocurrent are measured.

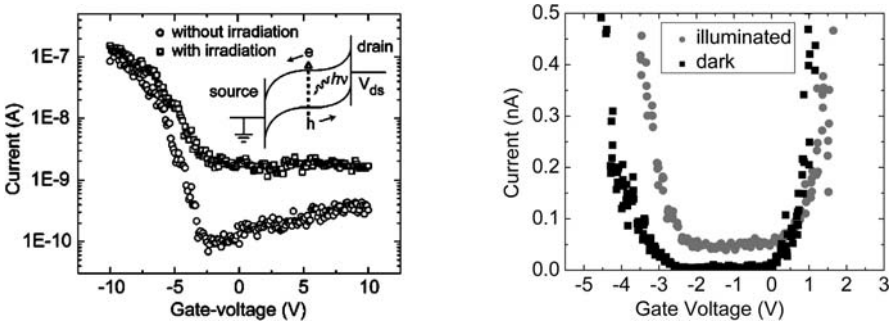

Fig. 7. Current vs. gate voltage for two CNTFETs in the dark and illuminated with infrared light. (**a**) For a unipolar p-type device (Reprinted with permission from [17]. Copyright (2005) American Chemical Society.). (**b**) For an ambipolar device [73]. In both cases the excitation occurs at the E_{22}^S transition, the laser power is $1\,\mathrm{kW/cm^2}$, and the drain voltage is $|V_\mathrm{d}| = 1\,\mathrm{V}$

In resonance, the polarization dependence follows a cosine-square law and is maximized at a polarization along the direction of the CNT (Fig. 8a). The photon-energy dependence of the photocurrent peaks at the expected E_{22} transition (Fig. 8b). The light is indeed absorbed in the carbon nanotube and the generated carriers are collected at the source and drain contacts. A thermal effect can be ruled out for CNTs in contact with a dielectric because the Raman Stokes/anti-Stokes intensity ratios of the radial breathing modes and G-bands of CNTs are not power dependent at the moderate power levels used here, [78], and a photovoltage is produced when the laser spot is focused to subdevice dimensions (see later in this contribution) [79].

In addition to the strong main peak in the spectrum that stems from the E_{22}^S-derived, dipole-active exciton, a weak side peak is visible 200 meV higher in energy. This peak has the same polarization as the main peak [17]. The energy difference between the peaks coincides with the energy of the optical phonons in CNTs that have been shown to be important sources of electron scattering in CNTFETs. Note that photocurrent spectroscopy allows the observation of the spectrum of a single CNT and phonon sidebands are unobscured, whereas absorption spectroscopy requires macroscopic quantities of CNTs, which are usually ensembles of CNTs with different chiralities and weak peaks can not be easily discerned. As we discussed in Sect. 2.3, the observation of these phonon sidebands is a strong argument for the generation of CNT excitons [17, 27]. The (internal) quantum efficiency η of a photoconductor is defined as the number of photogenerated electron–hole pairs per incident photon. The quantity that is directly accessible in an electro-optic measurement, however, is the external quantum efficiency, which is defined as the current produced by the device per incident photon. In our CNTFETs, we have measured external quantum efficiencies on the order of 1 % [72].

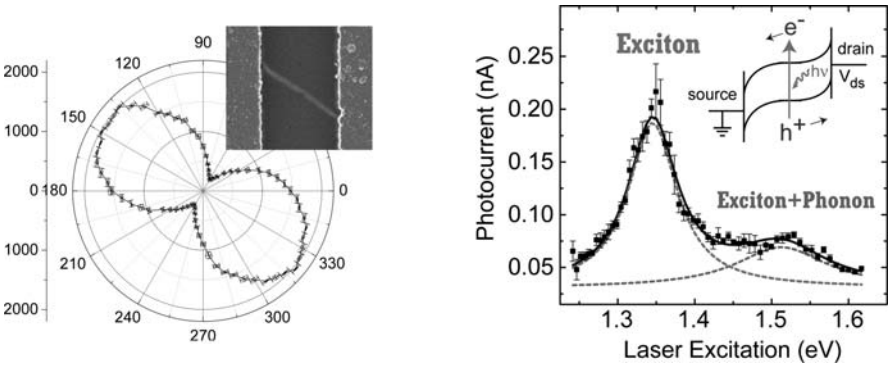

Fig. 8. Polarization and wavelength dependence of the photocurrent. (**a**) Polarization dependence of the photocurrent. The photocurrent is maximized for linearly polarized light along the length of the CNT. (**b**) Wavelength dependence of the photocurrent. The photocurrent peaks at the expected E_{22}^S exciton transitions. A side peak is visible about 200 meV higher in energy
. Reprinted with permission from [17]. Copyright (2005) American Chemical Society

An estimate of the internal quantum efficiency is complicated by the uncertainty in the size of absorption cross sections. These have only been measured on CNT ensembles that contain different chiralities of CNTs [80], and thus may underestimate the absorption in resonance. We have used modeling software [72] to estimate the internal quantum efficiency in resonance (e.g., at the E_{22} transition) and found $\eta \sim 10\,\%$, which means that about 10 % of the photons produce excitons and about 10 % of the excitons are separated and collected at the contacts. The latter number is sometimes referred to as the gain of the photoconductor.

The photocurrent and thus the external quantum efficiency increase linearly with drain bias up to about 1 to 2 V. Above this voltage, the Schottky barriers become quite transparent and the transport current dominates the measurement. Increasing Schottky barrier heights by using appropriate work-function metals or smaller-diameter CNTs could allow applying higher voltages and thus increasing the gain. Finally, excitation at higher energies, e.g., in the visible should further enhance the photocurrents, but with a loss of selectivity [81].

4.4 Photovoltage in Asymmetric CNTFETs – Schottky-Barrier Diodes

An example of the use of a CNTFET as a photovoltaic device is shown in Fig. 9 [70]. In the dark this nanotube photocell shows a rectifying diode I–V characteristic likely due to two different Schottky barriers at the source and

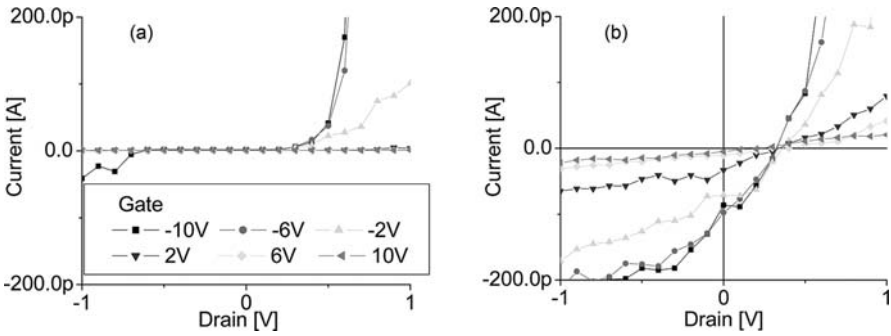

Fig. 9. Photovoltage in an asymmetric CNTFET. (**a**) Rectifying I–V characteristic acquired in the dark. (**b**) I–V characteristic of the same device for several gate voltages (see legend) under global IR irradiation [70]

drain. When uniform infrared light of about $1\,\mathrm{kW/cm^2}$ is incident on this device, an open-circuit photovoltage of $V_{\mathrm{OC}} = 300\,\mathrm{mV}$ is generated independent of the gate voltage that is applied at the backgate. The short-circuit photocurrent is on the order of $I_{\mathrm{SC}} = 100\,\mathrm{pA}$ and is maximized when the CNTFET is gated in the "on" state. (In the "off" state, the internal resistance along the CNT increases, which reduces the measured photocurrent.) In the previously discussed nanotube photoconductor, external fields were necessary to generate a current. Here, the internal fields at the Schottky barriers are able to separate electrons and holes even without an applied voltage. An important figure of merit for a photovoltaic device is the fill factor, defined as the ratio $\mathrm{FF} = (V_{\max} \times I_{\max})/(V_{\mathrm{OC}} \times I_{\mathrm{SC}})$, where $V_{\max}$ and $I_{\max}$ are the voltage and current that correspond to the maximum power that can be produced by the photovoltaic cell. From Fig. 9b we estimate $\mathrm{FF} \sim 0.4$ for this device.

In the example of Fig. 9 the two contacts were accidentally dissimilar and the mirror symmetry of the device was broken, enabling the generation of a photovoltage. It should be possible to use metals with different workfunctions for source and drain to achieve higher photovoltages. The limit of the photovoltage generated by a CNT device is given by the magnitude of its bandgap, $\sim 1\,\mathrm{V}$.

4.5 Photovoltage in a CNT p–n Junction

Another configuration in which a CNT can be used as a photovoltaic device is as part of a p–n junction [76]. This can be accomplished by a split gate that electrostatically dopes half of the tube p-type and the other half n-type [82]. It has been shown that CNT diodes with an abrupt p–n junction are very leaky due to band-to-band tunneling [83, 84]. The split gates are therefore separated by typically $0.5\,\mu\mathrm{m}$, which effectively produces a p–i–n diode with a depletion region of a few 100 nm. The I–V characteristic of a

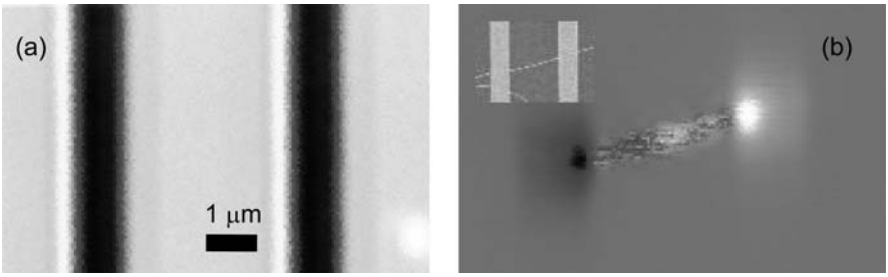

Fig. 10. Short-circuit photocurrent imaging of a CNTFET. (**a**) Reflected-light image of a CNTFET. The source and drain contacts are visible. The left contact is connected to GND and the right contact is grounded through a current amplifier. (**b**) Simultaneously acquired image of the short-circuit photocurrent as a function of the laser-spot position. Bright areas correspond to positive and dark areas to negative photocurrents. Inset: SEM image of the device

CNT p–i–n diode follows well the diode equation $I_{\mathrm{ds}} = I_0(e^{V_{\mathrm{DS}}}/nk_{\mathrm{B}}T - 1)$ with an ideality factor $n = 1.2$ [82]. (An ideality factor of 1 would imply that no recombination nor disorder are present, and $n = 2$ would mean complete recombination in the depletion region.) When the CNT is also suspended around the p–i–n junction, well-behaved diodes with an ideality factor close to 1 are produced [76].

4.6 Photovoltage Imaging

In a symmetric CNTFET under global illumination, no photovoltage is measured because the internal fields at the two Schottky barriers counteract each other. However, when the light is focused and only one SB is irradiated at a time, then a measurable photovoltage is obtained. Alternatively, in the short-circuit configuration the device generates a photocurrent at zero bias.

Figure 10 shows an image of the short-circuit photocurrent in a CNTFET as a function of the laser-spot position [85]. Similar images, albeit produced with applied bias, have been shown by the *Kern* and *Mews* groups [79, 86]. The strongest effect is seen where the internal fields that separate electrons and holes are strongest, namely at the two Schottky barriers. The sign of the photocurrent depends on the direction of local band bending in the CNT. The CNTFET in Fig. 10 is p-type and the bands bend upward on going from a contact toward the middle of the device. When photons are absorbed near a Schottky barrier, the electrons are accelerated toward the metal and the holes toward the CNT. This leads to a positive photocurrent for light incident at the right contact and a negative photocurrent for light incident on the left contact.

5 Electroluminescence

5.1 Ambipolar Mechanism

CNT excited states can be produced either by direct excitation, e.g., through light absorption, or through electron–hole association, e.g., in a p–n junction. Electron–hole pairs in semiconductors recombine by a variety of different mechanisms. In most cases, the energy will be released as heat (phonons), but a fraction of the recombination events may involve the emission of a photon. This process is termed "electroluminescence" (EL) and is widely used to produce solid-state light sources such as light-emitting diodes (LEDs). In order to produce LEDs or any other electroluminescent device, one must recombine significant populations of electrons and holes. Conventionally, this is achieved at an interface between a hole-doped and an electron-doped material. In ambipolar CNTFETs, at an appropriate bias, electrons and holes can be simultaneously injected at the opposite ends of the CNT channel. This allows radiative recombination to take place and electroluminescence to be emitted [71]. While the emission mechanism is the same as that in p–n junctions, ambipolar CNTFETs do not require any chemical doping, a significant simplification of the fabrication process.

CNT electroluminescence exhibits a variety of interesting properties. The emitted light is strongly polarized along the tube axis [71]. The radiation also has a characteristic energy that depends on the diameter and chirality of the excited SWNT, just as the optical bandgap does [87], and the length of the electroluminescent region is on the order of the recombination length, $l_{\mathrm{rec}} \leq 1\,\mu\mathrm{m}$. [88]

At a gate voltage halfway between source and drain voltages, $V_{\mathrm{g}} = (V_{\mathrm{d}} - V_{\mathrm{s}})/2$, equal numbers of electrons and holes are injected and while the total current is minimized, the amount of light generated due to ambipolar recombination is maximized [71]. In short devices ($L < l_{\mathrm{rec}}$, L is the channel length), the light emission encompasses the entire SWNT [71]. In long devices ($L \gg l_{\mathrm{rec}}$), where nonradiative electron–hole recombination is fast compared to carrier transit times through the channel, light emission originates from a small part of the CNT where electrons and holes coexist and can annihilate each other, i.e., the emission is localized wherever the concentrations of electrons and holes overlap most strongly [88]. In the regions above and below this recombination spot, transport is unipolar n-type and p-type. The overlap region can be physically moved using a gate electrode, since the relative contributions of electrons and holes to the total current are strongly gate dependent. Therefore, a CNT LED is a translatable light source; the gate bias V_{g} can smoothly and continuously position the site of emission [88, 89]. In Fig. 11 we demonstrate the translation of the emission spot between two electrodes by applying different gate voltages.

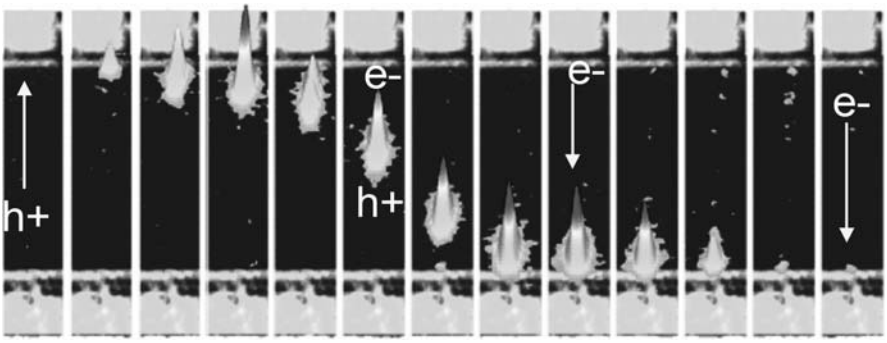

Fig. 11. Ambipolar infrared emission from a long-channel CNT FET (50 μm). Source and drain contacts are visible at the top and bottom. The recombination region, where electrons and holes overlap, produces light and can be translated along the CNT by an applied gate voltage

5.2 Mechanism of the Spot Movement in Ambipolar Transistors

In long CNTFETs, source–drain voltages of several tens of volts are applied and $V_s < V_g < V_d$, so both Schottky barriers are essentially transparent. Under these conditions a simple drift transport model can account for the main features of the movement of light emission [89]. The backgate effectively screens the source and drain voltages in long-channel CNTs and it couples capacitively to the CNT channel so that the potential along the CNT, $V(x)$, can be written as: $V(x) = V_g + C^{-1}[n_e(x) - n_h(x)]$, where C is the geometrical capacitance of the CNT and n_e and n_h are the number densities of electrons and holes, respectively. At the center of the recombination spot $n_e = n_h$, so that the potential is that of the gate V_g. It is clear then that if V_g is changed, the recombination (emission) spot would have to move. The current through the CNT is sustained by the electric field associated with the charge gradient in the CNT, rather than by the externally applied field, i.e., $I = -\mu \ n(x)\,\mathrm{d}V(x)/\,\mathrm{d}x$, where μ is the mobility and $n(x) = n_e(x) + n_h(x)$ is the sum of electron and hole number densities. In the long-channel limit where electron-hole recombination times are much shorter than carrier transport times through the device, the simple drift model can be solved analytically to obtain the position of the emission spot as a function of V_g and V_d. A comparison between experiment and the model's predictions is shown in Fig. 12. A reasonably good agreement between theory and experiment is evident. The S-shape movement of the spot with gate voltage is well reproduced. However, the gate-voltage range over which the spot moves is smaller in the experiment. This discrepancy is due to the voltage drop at the Schottky barriers. A hysteresis due to the production of charged traps in the thick gate oxide is also present in the experimental results. Numerical calculations on

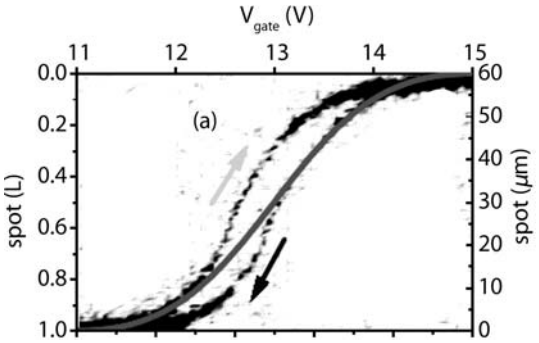

Fig. 12. Model of the spot movement in an ambipolar CNT FET overlaid over the actual data during forward and backward sweeps. A slight hysteresis is present in the experimental data

the light emission from intermediate-length devices were also performed by *Guo* and *Alam* [90].

5.3 Electroluminescence Spectrum and Efficiency of the Radiative Decay

Figure 13 shows the infrared electroluminescence spectra of two individual CNTs [87]. The short laser-ablation tube, biased with an average electric field of 100 kV/cm has a very broad spectrum with an exponential high-energy tail. The spectrum of the long CVD CNT at a much lower average field of 4 kV/cm is also much narrower. Both CNTs have a similar low-energy emission onset close to the position of the expected E_{11} transition below 0.6 eV. From a comparison of the experimental spectrum and the calculated optical conductivity we determined that the carrier distribution in the short CNT is quite hot (involves phonon excitation up to the energy of the optical phonon at about 200 meV).

The efficiency η of the radiative recombination process for electroluminescence can be determined by integrating over the spectrum in Fig. 13 and comparing it to the injected current. We find $\eta_{\mathrm{EL}} \sim 10^{-6}$ photons/electron–hole pair for the ambipolar process [87].

6 Unipolar Mechanism for Infrared Emission

In addition to the gate-translatable emission, localized electroluminescence is also observed from particular spots on a SWNT under unipolar transport conditions [45, 88, 91, 92]. In this case, the current is carried by only one type of carrier (electrons or holes). Since both types of carriers are necessary to produce light, these sites must be actively generating e–h pairs. This process

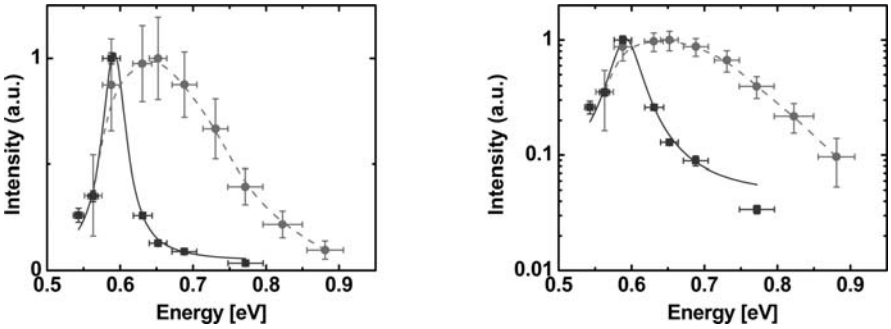

Fig. 13. Experimental spectrum of the electroluminescence for two different CNTs, one 50-μm long CVD-grown CNT with $V_d = -20\,V$, $V_g = -10\,V$, $I = 3.5\,\mu A$ (*squares*) and one 0.5 μm short laser-ablation CNT with $V_d = 5\,V$, $V_g = 2.5\,V$, $I = 5\,\mu A$ (*circles*). The *lines* are a guide to the eye. The low-energy onset is similar for both CNTs and corresponds to the energy of the E_{11}^S transition. (**a**) Plot on a linear scale. (**b**) Same data on a log scale

occurs near defects, trapped charges in the insulator, CNT–CNT contacts, or any other inhomogeneities that produce voltage drops along the CNT and generate large, local electric fields [91]. For example, in Fig. 14, in addition to the ambipolar emission spot, there are at least three additional stationary spots, that is, light spots that do not move with V_g. Each one appears once the ambipolar spot has moved across their position, and the corresponding nanotube segment has become n-type. They disappear on the reverse sweep as soon as the ambipolar spot has passed them again. The experimental evidence suggests that local electron–hole generation and recombination under n-type conduction is due to pockets of trapped electrons in the SiO_2 gate oxide that dope a nearby nanotube segment p-type and thus locally invert the carrier type under n-type conduction. Trapped charges (electrons or holes) are known to be responsible for hysteretic electronic characteristics in CNTFETs. [93,94] The electrons are extracted from the nanotube at high gate fields due to the field focusing at the nanometer-sized radius of the nanotube and get trapped in the SiO_2. The monitoring of localized electroluminescence provides a new tool for detecting defects in CNT devices.

Artificial structures can also be fabricated that locally create the conditions, i.e., sudden change in the potential, that generate e–h pairs and light emission [45]. An example of such a structure is shown in Fig. 15a. It consists of a backgated CNTFET in which a trench has been cut in the gate oxide by etching so that a portion of the CNT channel is suspended. The difference in the coupling to the gate of the oxide-supported and suspended part of the CNT leads to band bending at the interface of the two segments. Carriers reaching this interface are accelerated and through impact excitation can produce excitons or e–h pairs that recombine radiatively (Fig. 15b).

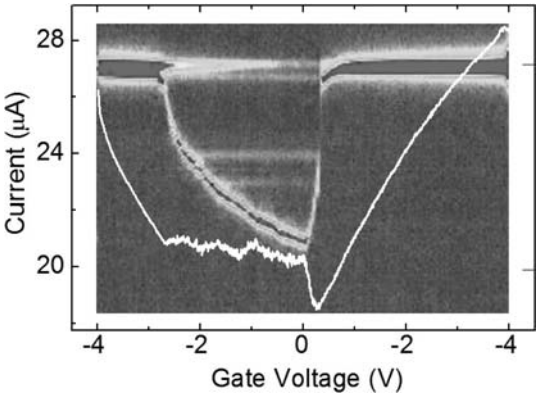

Fig. 14. Electroluminescence from a CNTFET during a gate-voltage sweep. p-doped segments along a CNT become optically active after the ambipolar spot has moved across them and the surrounding CNT turned n-type

Unlike the ambipolar device emission the light intensity of the unipolar devices depends exponentially on the current (Fig. 15c), there is a threshold voltage needed for the emission to occur and the emitting site is associated with a local voltage drop. While the current varies linearly with the applied voltage, the light emission intensity varies exponentially: $I(\text{photon}) \sim \exp(-F_{\text{th}}/F)$, where F_{th} is a threshold field and F the applied field. These findings support the proposed impact excitation mechanism. Furthermore, impact excitation is not subject to the same selection rules as photoexcitation so that impact-excited spectra can be different from that produced by photons [42]. For example, the spectrum of a $\sim 1.6\,\text{nm}$ CNT shown in Fig. 15d consists of two peaks, one at 0.67 eV and another weaker and broader peak at $\sim 0.92\,\text{eV}$. The first peak is the familiar E_{11} transition seen in photoluminescence, while the second band may be ascribed to the first interband transition of the CNT, in agreement with the findings of *Dukovic* et al. [26]. While interband transitions are suppressed in favor of exciton transitions in photoexcitation, impact excitation does produce free e–h pairs [27]. Thus, using internal impact excitation, both exciton and bandgap CNT emission can be observed. In suspended metallic tubes under high bias conditions, thermal light emission centered in the middle of the tube (hottest point) was also observed [95].

7 Conclusions – Future

The study of the optical and electro-optical properties of nanotubes and indeed of 1D systems in general is still in its infancy. For example, fundamental properties such as the absorption cross sections and radiative and nonradiative lifetimes of individual nanotubes are still a matter of debate. The role

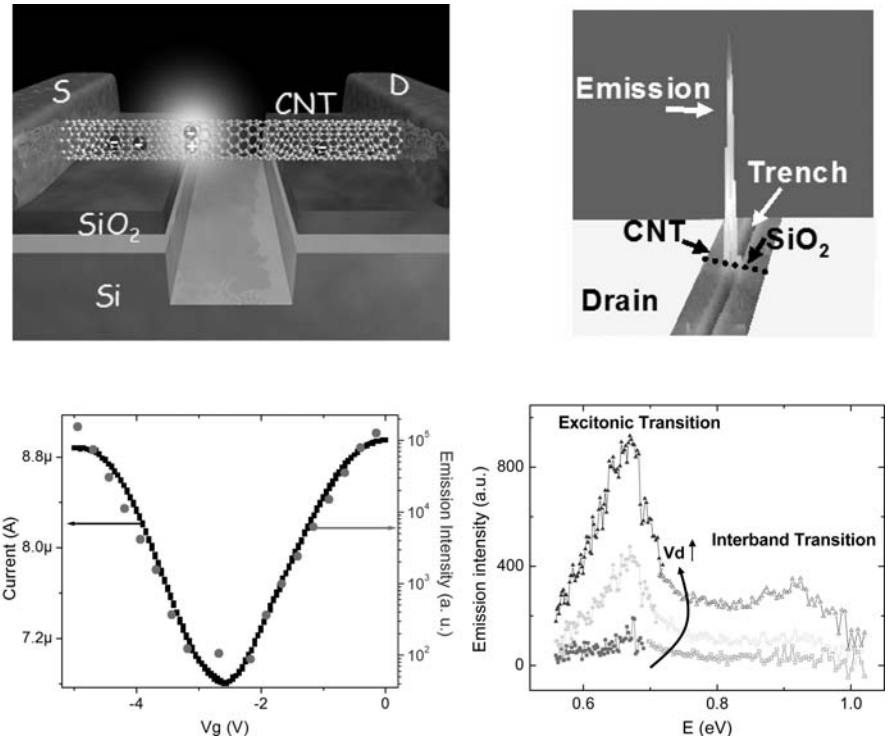

Fig. 15. Unipolar electroluminescence from a suspended CNT. (*top left*) Schematic of the CNTFET with a trench cut into the gate oxide. (*top right*) Spatially resolved infrared emission from a device. (*bottom left*) Current and IR emission intensity as a function of the back-gate voltage. Note the logarithmic scale for the IR intensity. (*bottom right*) IR spectra for increasing drain voltage. Exciton and band-to-band transitions at $\sim 0.67\,\mathrm{eV}$ and $\sim 0.92\,\mathrm{eV}$ are visible

of deviations from the perfect nanotube structure in the optical properties of nanotubes has not been adequately resolved. The reason for this lack of information is partly the unavailability of CNT samples of unique structure that prevent detailed studies with results that can be reproduced by several laboratories, and partly the scarcity of analytical techniques that have the sensitivity and the spatial resolution required. More near-field optical studies of CNTs [96] are obviously going to be of great value in this respect (see the contribution by Hartschuh). CNTs themselves may provide a powerful optical probe. Nanotubes in wraparound metal-gate configurations, i.e., surrounded by a thin dielectric layer followed by a metal layer, as in CNTFETs, can be used as the ultimately miniaturized (subwavelength) optical fiber and such could be used in molecular-scale optics and spectroscopy, interchip optical communications, and numerous other applications.

As we have seen above, simple, FET-like structures containing individual CNTs can emit light, detect light and generate photovoltages. The applied voltages in the same structure can also induce electroabsorption modulation. Selective synthesis or separation of single-type CNT would allow the fabrication of mesoscopic or even macroscopic devices involving arrays of CNTs with greatly enhanced light or current outputs. Lasing may also be achieved. Obviously, there is a need to better understand energy flow in excited CNTs to find conditions to optimize their emission properties. The role of the substrate, doping, surrounding ambient, defect-induced localization, and hot phonons needs to be understood. Nonlinear optical properties would also be interesting to explore. However, the most important characteristics of CNTs that make them appealing for electro-optics applications are not their high luminescence yields or size of electro-optical modulation, but rather their nm diameter, long length, flexibility, and the wide spectral response range and polarized nature of their absorption. CNT optics in conjunction with CNT electronics [58, 97, 98] can form the basis of a unified carbon-based optoelectronic technology. Finally, CNTs have provided the ideal model systems to study the optics of 1D systems. They have already significantly improved our understanding of excitons, impact excitation and hot carrier effects in confined systems.

References

[1] J. W. Mintmire, B. I. Dunlap, C. T. White: Are fullerene tubules metallic?, Phys. Rev. Lett. **68**, 631 (1992) 423

[2] X. Blase, L. X. Benedict, E. L. Shirley, S. G. Louie: Hybridization effects and metallicity in small radius carbon nanotubes, Phys. Rev. Lett. **72**, 1878 (1994) 423

[3] M. S. Dresselhaus, G. Dresselhaus, R. Saito: Carbon fibers based on C_{60} and their symmetry, Phys. Rev. B **45**, 6234 (1992) 423

[4] N. Hamada, S. Sawada, A. Oshiyama: New one-dimensional conductors: Graphitic microtubules, Phys. Rev. Lett. **68**, 1579 (1992) 423

[5] R. Saito, M. Fujita, G. Dresselhaus, M. S. Dresselhaus: Electronic structure of chiral graphene tubules, Appl. Phys. Lett. **60**, 2204 (1992) 423

[6] T. Ando: Excitons in carbon nanotubes, J. Phys. Soc. Jpn **66**, 1066 (1997) 423

[7] C. D. Spataru, S. Ismail-Beigi, L. X. Benedict, S. G. Louie: Excitonic effects and optical spectra of single-walled carbon nanotubes, Phys. Rev. Lett. **93**, 077402 (2004) 423, 424, 425

[8] C. D. Spataru, S. Ismail-Beigi, L. X. Benedict, S. G. Louie: Quasiparticle energies, excitonic effects and optical absorption spectra of small-diameter single-walled carbon nanotubes, Appl. Phys. A-Mater. **78**, 1129 (2004) 423, 424, 425

[9] V. Perebeinos, J. Tersoff, P. Avouris: Scaling of excitons in carbon nanotubes, Phys. Rev. Lett. **92**, 257402 (2004) 423, 424, 425, 426, 429, 433

[10] E. Chang, G. Bussi, A. Ruini, E. Molinari: Excitons in carbon nanotubes: An ab initio symmetry-based approach, Phys. Rev. Lett. **92**, 196401 (2004) 423
[11] T. G. Pedersen: Variational approach to excitons in carbon nanotubes, Phys. Rev. B **67**, 073401 (2003) 423
[12] C. L. Kane, E. J. Mele: Ratio problem in single carbon nanotube fluorescence spectroscopy, Phys. Rev. Lett. **90**, 207401 (2003) 423, 424
[13] H. Zhao, S. Mazumdar: Electron–electron interaction effects on the optical excitations of semiconducting single-walled carbon nanotubes, Phys. Rev. Lett. **93**, 157402 (2004) 423, 425
[14] C. L. Kane, E. J. Mele: Electron interactions and scaling relations for optical excitations in carbon nanotubes, Phys. Rev. Lett. **93**, 197402 (2004) 424
[15] F. Wang, G. Dukovic, L. E. Brus, T. F. Heinz: The optical resonances in carbon nanotubes arise from excitons, Science **308**, 838 (2005) 424
[16] J. Maultzsch, R. Pomraenke, S. Reich, E. Chang, D. Prezzi, A. Ruini, E. Molinari, M. S. Strano, C. Thomsen, C. Lienau: Exciton binding energies in carbon nanotubes from two-photon photoluminescence, Phys. Rev. B **72**, 241402R (2005) 424
[17] X. Qiu, M. Freitag, V. Perebeinos, P. Avouris: Photoconductivity spectra of single-carbon nanotubes: Implications on the nature of their excited states, Nano Lett. **5**, 749 (2005) 424, 430, 438, 439
[18] F. Plentz, H. B. Ribeiro, A. Jorio, M. S. Strano, M. A. Pimenta: Direct experimental evidence of exciton–phonon bound states in carbon nanotubes, Phys. Rev. Lett. **95**, 247401 (2005) 424, 430
[19] M. Jones, C. Engtrakul, W. K. Metzger, R. J. Ellingson, A. J. Nozik, M. J. Heben, G. Rumbles: Analysis of photoluminescence from solubilized single-walled carbon nanotubes, Phys. Rev. B **71**, 115426 (2005) 424, 427, 430
[20] S. G. Chou, F. Plentz, J. Jiang, R. Saito, D. Nezich, H. B. Ribeiro, A. Jorio, M. A. Pimenta, G. G. Samsonidze, A. P. Santos, M. Zheng, G. B. Onoa, E. D. Semke, G. Dresselhaus, M. S. Dresselhaus: Phonon-assisted excitonic recombination channels observed in DNA-wrapped carbon nanotubes using photoluminescence spectroscopy, Phys. Rev. Lett. **94**, 127402 (2005) 424, 430
[21] H. Htoon, M. J. O'Connell, S. K. Doorn, V. I. Klimov: Single carbon nanotubes probed by photoluminescence excitation spectroscopy: The role of phonon-assisted transitions, Phys. Rev. Lett. **94**, 127403 (2005) 424, 430
[22] Y. Miyauchi, S. Maruyama: Identification of an excitonic phonon sideband by photoluminescence spectroscopy of single-walled carbon-13 nanotubes, Phys. Rev. B. **74**, 035415 (2006) 424, 430
[23] V. Perebeinos, J. Tersoff, P. Avouris: Effect of exciton–phonon coupling in the calculated optical absorption of carbon nanotubes, Phys. Rev. Lett. **94**, 027402 (2005) 424, 429, 430, 431, 434
[24] H. Haug, S. W. Koch: *Quantum Theory of the Optical and Electronic Properties of Semiconductors* (World Scientific, London 2005) 424, 433
[25] P. Avouris, J. Chen, M. Freitag, V. Perebeinos, J. C. Tsang: Carbon nanotube optoelectronics, Phys. Stat. Sol. B **243**, 3197 (2006) 424, 425, 426, 428
[26] G. Dukovic, F. Wang, D. Song, M. Y. Sfeir, T. F. Heinz, L. E. Brus: Structural dependence of excitonic optical transitions and band-gap energies in carbon nanotubes, Nano Lett. **5**, 2314 (2005) 425, 446

[27] V. Perebeinos, J. Tersoff, P. Avouris: Radiative lifetime of excitons in carbon nanotubes, Nano Lett. **5**, 2495 (2005) 425, 427, 428, 430, 438, 446
[28] C. D. Spataru, S. Ismail-Beigi, R. B. Capaz, S. G. Louie: Theory and ab initio calculation of radiative lifetime of excitons in semiconducting carbon nanotubes, Phys. Rev. Lett. **95**, 247402 (2005) 425
[29] T. Ando: Effects of valley mixing and exchange on excitons in carbon nanotubes with Aharonov-Bohm flux, J. Phys. Soc. Jpn. **75**, 024707 (2006) 425
[30] E. Chang, D. Prezzi, A. Ruini, E. Molinari: Dark excitons in carbon nanotubes URL: `cond-matt/0603085` 425
[31] Y. Z. Ma, J. Stenger, J. Zimmermann, S. M. Bachilo, R. E. Smalley, R. B. Weisman, G. R. Fleming: Ultrafast carrier dynamics in single-walled carbon nanotubes probed by femtosecond spectroscopy, J. Chem. Phys. **120**, 3368 (2004) 427
[32] F. Wang, G. Dukovic, L. E. Brus, T. F. Heinz: Time-resolved fluorescence of carbon nanotubes and its implication for radiative lifetimes, Phys. Rev. Lett. **92**, 177401 (2004) 427
[33] A. Hagen, G. Moos, V. Talalaev, J. W. Tomm, T. Hertel: Electronic structure and dynamics of optically excited single-wall carbon nanotubes, Appl. Phys. A **78**, 1137 (2004) 427
[34] J. Lefebvre, D. G. Austing, J. Bond, P. Finnie: Photoluminescence imaging of suspended single-walled carbon nanotubes, Nano Lett. **6**, 1603 (2006) 427
[35] H. Htoon, P. J. Cox, V. I. Klimov: Structure of excited-state transitions of individual semiconductor nanocrystals probed by photoluminescence excitation spectroscopy, Phys. Rev. Lett. **93**, 187402 (2004) 428
[36] J. Lefebvre, P. Finnie, Y. Homma: Temperature-dependent photoluminescence from single-walled carbon nanotubes, Phys. Rev. B **70**, 045419 (2004) 428, 430
[37] A. Hagen, M. Steiner, M. B. Raschke, C. Lienau, T. Hertel, H. Qian, A. J. Meixner, A. Hartschuh: Exponential decay lifetimes of excitons in individual single-walled carbon nanotubes, Phys. Rev. Lett. **95**, 197401 (2005) 428
[38] J. Shaver, J. Kono, O. Portugall, V. Krstic, G. L. J. A. Rikken, Y. Miyauchi, S. Maruyama, V. Perebeinos: Magnetic brightening of carbon nanotube photoluminescence through symmetry breaking, Nano Lett. **7**, 1851 (2007) 428
[39] V. Perebeinos, J. Tersoff, P. Avouris: Electron–phonon interaction and transport in semiconducting carbon nanotubes, Phys. Rev. Lett. **94**, 086802 (2005) 429
[40] Y. Toyozawa: Prog. Theor. Phys. **25**, 59 (1964) 429
[41] J. C. Tsang, M. Freitag, V. Perebeinos, J. Liu, P. Avouris: Doping and phonon renormalization in carbon nanotubes, Nature Nano **2**, 725–730 (2007) 430
[42] V. Perebeinos, P. Avouris: Impact excitation by hot carriers in carbon nanotubes, Phys. Rev. B **74**, 121410R (2006) 431, 432, 446
[43] E. Pop, D. Mann, J. Cao, Q. Wang, K. Goodson, H. Dai: Negative differential conductance and hot phonons in suspended nanotube molecular wires, Phys. Rev. Lett. **95**, 155505 (2005) 432, 434
[44] M. Lazzeri, S. Piscanec, F. Mauri, A. C. Ferrari, J. Robertson: Electron transport and hot phonons in carbon nanotubes, Phys. Rev. Lett. **95**, 236802 (2005) 432

[45] J. Chen, V. Perebeinos, M. Freitag, J. Tsang, Q. Fu, J. Liu, P. Avouris: Bright infrared emission from electrically induced excitons in carbon nanotubes, Science **310**, 1171 (2005) 432, 444, 445
[46] F. Wang, G. Dukovic, E. Knoesel, L. E. Brus, T. F. Heinz: Observation of rapid Auger recombination in optically excited semiconducting carbon nanotubes, Phys. Rev. B **70**, 241403(R) (2004) 432
[47] J. Kono, G. N. Ostojic, S. Zaric, M. S. Strano, V. C. Moore, J. Shaver, R. H. Hauge, R. E. Smalley: Ultra-fast optical spectroscopy of micelle-suspended single-walled carbon nanotubes, Appl. Phys. A **78**, 1093 (2004) 432
[48] Y. Z. Ma, L. Valkunas, S. L. Dexheimer, S. M. Bachilo, G. R. Fleming: Femtosecond spectroscopy of optical excitations in single-walled carbon nanotubes: Evidence for exciton-exciton annihilation, Phys. Rev. Lett. **94**, 157402 (2005) 432
[49] W. Z. Franz: Influence of an electrical field on an optical absorption edge, Naturforsch. **13A**, 484 (1958) 433
[50] L. V. Keldysh: Influence of a strong electric field on the optical characteristics of nonconducting crystals, Zh. Eksp. Teor. Fiz. **34**, 1138 (1958) 433
[51] L. V. Keldysh: Influence of a strong electric field on the optical characteristics of nonconducting crystals, Sov. Phys. JETP **7** (1958) 433
[52] D. A. B. Miller, D. S. Chemla, T. C. Damen, A. C. Gossard, W. Wiegmann, T. H. Wood, C. A. Burrus: Band-edge electroabsorption in quantum well structures: The quantum-confined stark effect, Phys. Rev. Lett. **53**, 2173 (1984) 433
[53] D. A. B. Miller, D. S. Chemla, S. Schmitt-Rink: Relation between electroabsorption in bulk semiconductors and in quantum wells: The quantum-confined Franz–Keldysh effect, Phys. Rev. B **33**, 6976 (1986) 433
[54] V. Perebeinos, P. Avouris: Exciton ionization, Franz–Keldysh, and stark effects in carbon nanotubes, Nano Lett. **7**, 609 (2007) 433, 434
[55] H. Zhao, S. Mazumdar: Elucidation of the electronic structure of semiconducting single-walled carbon nanotubes by electroabsorption spectroscopy, Phys. Rev. Lett. **98**, 166805 (2007) 433
[56] H. A. Bethe, E. E. Salpeter: in *Quantum Mechanics of One- and Two- Electron Atoms* (Academic, New York 1957) 434
[57] C. Manzoni, A. Gambetta, E. Menna, M. Meneghetti, G. Lanzani, G. Cerullo: Intersubband exciton relaxation dynamics in single-walled carbon nanotubes, Phys. Rev. Lett. **94**, 207401 (2005) 434
[58] P. Avouris: Carbon nanotube electronics, Phys. World **20**, 40 (2007) 435, 448
[59] S. J. Tans, A. R. M. Verschueren, C. Dekker: Room-temperature transistor based on a single carbon nanotube, Nature **393**, 49 (1998) 435
[60] R. Martel, T. Schmidt, H. R. Shea, T. Hertel, P. Avouris: Single- and multi-wall carbon nanotube field-effect transistors, Appl. Phys. Lett. **73**, 2447 (1998) 435
[61] F. Leonard, J. Tersoff: Novel length scales in nanotube devices, Phys. Rev. Lett. **83**, 5174 (1999) 435
[62] M. S. Fuhrer, J. Nygård, L. Shih, M. Forero, Y. G. Yoon, M. S. C. Mazzoni, H. J. Choi, J. Ihm, S. G. Louie, A. Zettl, P. L. McEuen: Crossed nanotube junctions, Science **288**, 494 (2000) 435

[63] M. Freitag, M. Radosavljevic, Y. Zhou, A. T. Johnson: Controlled creation of a carbon nanotube diode by a scanned gate, Appl. Phys. Lett. **79**, 3326 (2001) 435
[64] R. Martel, V. Derycke, C. Lavoie, J. Appenzeller, K. K. Chan, J. Tersoff, P. Avouris: Ambipolar electrical transport in semiconducting single-wall carbon nanotubes, Phys. Rev. Lett. **87**, 256805 (2001) 435
[65] S. Heinze, J. Tersoff, R. Martel, V. Derycke, J. Appenzeller, P. Avouris: Carbon nanotubes as schottky barrier transistors, Phys. Rev. Lett. **89**, 106801 (2002) 435
[66] T. Nakanishi, A. Bachtold, C. Dekker: Transport through the interface between a semiconducting carbon nanotube and a metal electrode, Phys. Rev. B **66**, 073307 (2002) 435
[67] M. Radosavljevic, S. Heinze, J. Tersoff, P. Avouris: Drain voltage scaling in carbon nanotube transistors, Appl. Phys. Lett. **83**, 2435 (2003) 435
[68] J. Appenzeller, J. Knoch, V. Derycke, R. Martel, S. Wind, P. Avouris: Field-modulated carrier transport in carbon nanotube transistors, Phys. Rev. Lett. **89**, 126801 (2002) 435
[69] S. J. Wind, J. Appenzeller, R. Martel, V. Derycke, P. Avouris: Vertical scaling of carbon nanotube field-effect transistors using top gate electrodes, Appl. Phys. Lett. **80**, 3817 (2002) 435
[70] P. Avouis, A. Afzali, J. Appenzeller, J. Chen, M. Freitag, C. Klinke, Y.-M. Lin, J. C. Tsang: Carbon nanotube electronics and optoelectronics, IEDM Tech. Digest pp. 525–529 (2004) 435, 437, 439, 440
[71] J. A. Misewich, R. Martel, P. Avouris, J. C. Tsang, S. Heinze, J. Tersoff: Electrically induced optical emission from a carbon nanotube fet, Science **300**, 783 (2003) 435, 442
[72] M. Freitag, Y. Martin, J. A. Misewich, R. Martel, P. Avouris: Photoconductivity of single carbon nanotubes, Nano Lett. **3**, 1067 (2003) 436, 437, 438, 439
[73] X. Cui, M. Freitag, R. Martel, L. Brus, P. Avouris: Controlling energy-level alignments at carbon nanotube/Au contacts, Nano Lett. **3**, 783 (2003) 436, 438
[74] R. J. Chen, N. R. Franklin, J. Kong, J. Cao, T. W. Tombler, Y. Zhang, H. Dai: Molecular photodesorption from single-walled carbon nanotubes, Appl. Phys. Lett. **79**, 2258 (2001) 436
[75] M. E. Itkis, F. Borondics, A. Yu, R. C. Haddon: Bolometric infrared photoresponse of suspended single-walled carbon nanotube films, Science **312**, 413 (2006) 436
[76] J. U. Lee: Photovoltaic effect in ideal carbon nanotube diodes, Appl. Phys. Lett. **87**, 073101 (2005) 437, 440, 441
[77] J. Guo, M. A. Alam, Y. Yoon: Theoretical investigation on photoconductivity of single intrinsic carbon nanotubes, Appl. Phys. Lett. **88**, 133111 (2006) 437
[78] J. C. Tsang, M. Freitag: Private communications 438
[79] K. Balasubramanian, Y. Fan, M. Burghard, K. Kern, M. Friedrich, U. Wannek, A. Mews: Photoelectronic transport imaging of individual semiconducting carbon nanotubes, Appl. Phys. Lett. **84**, 2400 (2004) 438, 441
[80] M. F. Islam, D. E. Milkie, C. L. Kane, A. G. Yodh, J. M. Kikkawa: Direct measurement of the polarized optical absorption cross section of single-wall carbon nanotubes, Phys. Rev. Lett. **93**, 037404 (2004) 439

[81] P. T. Araujo, S. K. Doorn, S. Kilina, S. Tretiak, E. Einarsson, S. Maruyama, H. Chacham, M. A. Pimenta, A. Jorio: Third and fourth optical transitions in semiconducting carbon nanotubes, Phys. Rev. Lett. **98**, 067401 (2007) 439
[82] J. U. Lee, P. P. Gipp, C. M. Heller: Carbon nanotube p-n junction diodes, Appl. Phys. Lett. **85**, 145 (2004) 440, 441
[83] J. Appenzeller, Y. M. Lin, J. Knoch, P. Avouris: Band-to-band tunneling in carbon nanotube field-effect transistors, Phys. Rev. Lett. **93**, 196805 (2004) 440
[84] K. Bosnik, N. Gabor, P. McEuen: Transport in carbon nanotube p-i-n diodes, Appl. Phys. Lett. **89**, 163121 (2006) 440
[85] M. Freitag, J. C. Tsang, A. Bol, D. Yuan, J. Liu, P. Avouris: Imaging of the schottky barriers and charge depletion in carbon nanotube transistors, Nano Lett. **7**, 2037 (2007) 441
[86] K. Balasubramanian, M. Burghard, K. Kern, M. Scolari, A. Mews: Photocurrent imaging of charge transport barriers in carbon nanotube devices, Nano Lett. **5**, 507 (2005) 441
[87] M. Freitag, V. Perebeinos, J. Chen, A. Stein, J. C. Tsang, J. A. Misewich, R. Martel, P. Avouris: Hot carrier electroluminescence from a single carbon nanotube, Nano Lett. **4**, 1063 (2004) 442, 444
[88] M. Freitag, J. Chen, J. Tersoff, J. C. Tsang, Q. Fu, J. Liu, P. Avouris: Mobile ambipolar domain in carbon-nanotube infrared emitters, Phys. Rev. Lett. **93**, 076803 (2004) 442, 444
[89] J. Tersoff, M. Freitag, J. C. Tsang, P. Avouris: Device modeling of long-channel nanotube electro-optical emitter, Appl. Phys. Lett. **86**, 263108 (2005) 442, 443
[90] J. Guo, M. A. Alam: Carrier transport and light-spot movement in carbon-nanotube infrared emitters, Appl. Phys. Lett. **86**, 023105 (2005) 444
[91] M. Freitag, J. C. Tsang, J. Kirtley, A. Carlsen, J. Chen, A. Troeman, H. Hilgenkamp, P. Avouris: Electrically excited, localized infrared emission from single carbon nanotubes, Nano Lett. **6**, 1425 (2006) 444, 445
[92] L. Marty, E. Adam, L. Albert, R. Doyon, D. Menard, R. Martel: Exciton formation and annihilation during 1D impact excitation of carbon nanotubes, Phys. Rev. Lett. **96**, 136803 (2006) 444
[93] M. S. Fuhrer, B. M. Kim, T. Dürkop, T. Brintlinger: High-mobility nanotube transistor memory, Nano Lett. **2**, 755 (2002) 445
[94] M. Radosavljevic, M. Freitag, K. V. Thadani, A. T. Johnson: Nonvolatile molecular memory elements based on ambipolar nanotube field effect transistors, Nano Lett. **2**, 761 (2002) 445
[95] D. Mann, Y. K. Kato, A. Kinkhabwala, E. Pop, J. Cao, X. Wang, L. Zhang, Q. Wang, J. Guo, H. Dai: Electrically driven thermal light emission from individual single-walled carbon nanotubes, Nature Nanotech. **2**, 33 (2007) 446
[96] L. Novotny, B. Hecht: *Principles of Nano-Optics* (Cambridge University Press, Cambridge 2006) 447
[97] P. Avouris, J. Appenzeller, R. Martel, S. J. Wind: Carbon nanotube electronics, Proc. IEEE **91**, 1772 (2003) 448
[98] H. Dai, A. Javey, E. Pop, D. Mann, W. Kim, Y. Lu: Electrical transport properties and field-effect transistors of carbon nanotubes, NANO **1**, 1 (2006) 448

Index

Ultrafast Spectroscopy of Carbon Nanotubes

Ying-Zhong Ma[1,2], Tobias Hertel[3], Zeev Valy Vardeny[4], Graham R. Fleming[1,2], and Leonas Valkunas[5,6]

[1] Department of Chemistry, University of California, Berkeley, CA 94720-1460, USA
yzma@berkeley.edu
[2] Physical Biosciences Division, Lawrence Berkeley National Laboratory, Berkeley, CA 94720-1460, USA
GRFleming@lbl.gov
[3] Department of Physics and Astronomy, Vanderbilt University, Nashville, TN 37235, USA
tobias.hertel@vanderbilt.edu
[4] Department of Physics, University of Utah, 1400 East 115 South, Salt Lake City, Utah 84112, USA
val@nova.physics.utah.edu
[5] Institute of Physics, Vilnius University, Savanoriu Ave. 231, 02300 Vilnius, Lithuania
Leonas.Valkunas@ff.vu.lt
[6] Theoretical Physics Department, Faculty of Physics of Vilnius University, Sauletekio Ave. 9, build. 3, 10222 Vilnius, Lithuania

Abstract. Time-domain spectroscopic studies provide a unique perspective on the materials properties and the microscopic processes underlying them in carbon nanotubes. Ultrafast spectroscopy is used to study the dynamics and kinetics of scattering and relaxation processes from the femtosecond ($1\,\mathrm{fs} \equiv 10^{-15}\,\mathrm{s}$) to the picosecond timescale. This provides crucial information on carrier and exciton dynamics that underpin a variety of potential applications of carbon nanotubes, from their use as current-carrying quantum wires, through light-emitting or detecting nanodevices, to their use in light-harvesting technologies and photovoltaics. Background information on the ultrafast spectroscopic techniques of greatest applicability to nanotubes is also provided.

1 Introduction[1]

The remarkable advances in the generation and characterization of tunable, intense, ultrashort light pulses and in optoelectronic detection have made ultrafast spectroscopy a powerful tool for studies of electronic and vibrational excitations in complex systems. By exciting a given system perturbatively it is now possible to follow various dynamical processes by means of diverse techniques with high spectral and temporal resolution. Studies of the excitation dynamics in carbon nanotubes began only a few years ago and have been almost entirely focused on the population relaxation of electronic excited

[1] Ying-Zhong Ma and Tobias Hertel have contributed equally to this contribution.

A. Jorio, G. Dresselhaus, M. S. Dresselhaus (Eds.): Carbon Nanotubes,
Topics Appl. Physics **111**, 321–352 (2008)

states. Despite its infancy, this rapidly developing field has been particularly fruitful for the identification of several fundamental properties and has seen a continuous emergence of fascinating discoveries. In this contribution, we will review the major advances in this field.

This review begins in Sect. 2 with an introduction to the experimental and theoretical background for nonlinear optical spectroscopy. We will first in Sect. 2.1 introduce typical instrumentation for ultrafast spectroscopy. Subsequently, we will describe briefly in Sect. 2.2 some of the fundamentals of nonlinear optics and spectroscopy with an emphasis on connecting the physical quantities of interest to the experimental observables. In Sect. 3, we will discuss pioneering work on metallic nanotubes, which represents the historic origins of this exciting field. This is followed by an overview of exciton dynamics in semiconducting nanotubes in Sect. 4. Following a general discussion of exciton dynamics, we will review separately studies conducted under low and high excitation intensities. In Sect. 5, we will discuss some similarities between semiconducting nanotubes and π-conjugated polymers. The review concludes in Sect. 6 with a summary and an outlook for future directions. In addition to the contributions to this book cited above, the authors also note a discussion of measurements of the dynamics of radial breathing and the G-band Raman-active modes in the contribution by Kono et al. as measured by impulsive excitation techniques.

2 Background

2.1 Instrumentation for Ultrafast Spectroscopy

The key component of any ultrafast spectroscopic setup is a light source that can deliver femtosecond pulses at desired wavelengths. Today's Ti:sapphire mode-locked laser technology has become a standard for such applications and is commercially available, allowing routine generation of sub-100 fs pulses near 800 nm with pulse energies from a few nJ to over 1 mJ [1] at repetition rates from 80 MHz to 1 kHz, respectively. Frequency-conversion technology allows extension of the Ti:sapphire output from the near-ultraviolet (UV), through the visible to the near- and mid-infrared regions [1, 2] (see Fig. 1). This provides unique opportunities for experimental studies of ultrafast dynamics in single-walled carbon nanotubes (SWNTs) and other systems.

The techniques used for ultrafast optical studies can coarsely be divided into directly time-resolved schemes that employ fast detectors and into gated- or pump-probe detection schemes that can be performed with slow detectors.

Transient or synchronized differential absorption spectroscopy is one specific type of a variety of femtosecond time-resolved pump-probe spectroscopies, wherein an initial pump pulse excites a sample, and the resulting change of sample absorbance at the frequency ω is measured by a probe pulse at a specific time delay Δt [3–5]. The resulting differential absorbance

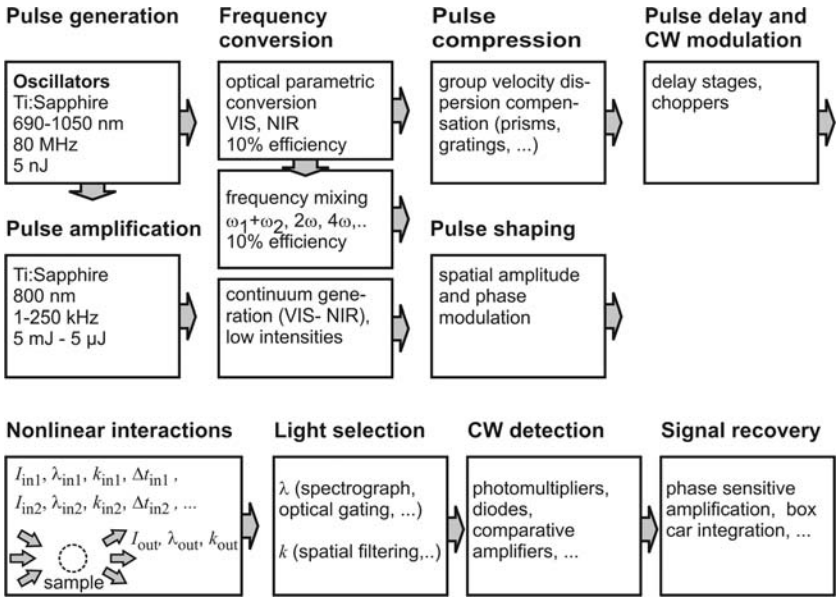

Fig. 1. Block diagram of the components of a generic time-resolved experiment. One or more components from each stage may be combined in a specific setup. *Numbers* for frequencies and pulse energies reflect approximate values

$\Delta\alpha(\omega, \Delta t)$ is then recorded as a function of the time delay between the pump and probe pulses, which is controlled by an optical delay line. The intensity of the probe and/or reference beams may be detected spectrally integrated or frequency resolved by a single-channel photodiode or by multichannel detection using CCD cameras or diode arrays. Phase-sensitive amplification is frequently used in conjunction with single-channel detection schemes to enhance the sensitivity down to 10^{-6}. Different variants of this technique are distinguished from one another based on the specific choice of the frequencies of the pump and probe beams (ω_{p} and ω_{pr}), their propagation direction (k_{p} and k_{pr}, which can be collinear or skewed), and their respective polarizations (ϵ_{p} and ϵ_{pr}). The resulting schemes are referred to as nondegenerate or degenerate, interferometric or polarization anisotropy pump-probe spectroscopy, to name only the most commonly used pump-probe varieties.

Another pump-probe detection scheme is time-resolved photoemission (TRPE) where a visible pump pulse creates a nonequilibrium electron distribution and a UV probe pulse monitors the state of the electronic system by photoemission of electrons from the sample. Energy-selective detection of photoemitted electrons can be realized using hemispherical analyzers or by the time-of-flight technique. The photoelectron intensity within a certain energy interval is then recorded as a function of Δt, allowing the extraction of dynamical information on changes of the nonequilibrium electron distribu-

tion f_{ne} [6–11]. Due to the small mean free path of low-energy photoelectrons, this technique is mostly limited to the exploration of carrier dynamics in the vicinity of vacuum/solid interfaces.

Time-integrating detectors can also be used to measure the ultrafast dynamics of photoluminescence (PL) decay by means of optical gating techniques, such as Kerr gating or fluorescence upconversion [4, 12–15]. The latter technique involves mixing of the fluorescence signal with an intense gate pulse in a nonlinear crystal. The resulting sum-frequency signal is measured as a function of the time delay between an ultrafast pump pulse used for the excitation and the gate pulse. The emission wavelength to be probed is selected simply by means of the angle at which the nonlinear crystal is aligned with respect to the fluorescence and gate beams. The upconverted signal is usually detected by a photomultiplier connected to a photon counter.

The pump-probe and gating techniques described above typically allow one to achieve sub-100 fs time resolution but they can occasionally also reach 10 fs or less. Direct measurements of time-resolved fluorescence with a time resolution of up to about 10 ps, on the other hand, are routinely achievable with fast detectors, e.g., photomultipliers (PMs), avalanche photodiodes (APDs) or streak cameras. Time-correlated single photon counting (TCSPC) for example, refers to the measurement of fluorescence signals using single photon detectors, such as APDs or PMs in combination with fast time-to-amplitude converters that can achieve an overall time resolution of a few tens of picoseconds [12, 16]. The high detection sensitivity of TCSPC, moreover, allows the study of individual SWNTs [17]. A time resolution of 1 ps can be achieved by some streak cameras, which enable simultaneous detection of both spectral and temporal information [12, 18].

2.2 Basics of Nonlinear Optics

The basis of practically all time-resolved pump-probe techniques is the nonlinear response of a medium to excitation with light. Light–matter interactions result in frequency-dependent changes of the radiation field as a consequence of elastic or inelastic scattering and/or absorption by the illuminated system. The resulting polarization P of the dielectric medium is coupled to the external transverse electromagnetic field $E(\boldsymbol{r}, t)$ according to the wave equation [19]:

$$\Delta E(\boldsymbol{r}, t) - \frac{1}{c^2}\frac{\partial^2}{\partial t^2}E(\boldsymbol{r}, t) = -\frac{4\pi}{c^2}\frac{\partial^2}{\partial t^2}P(\boldsymbol{r}, t)\,, \tag{1}$$

where c is the speed of light. Generally, internal electric fields between and within atoms are on the order of 10^{10} V/cm and are strong in comparison with even the most intense laser fields used for spectroscopic applications [20, 21]. To distinguish between linear ($P^{(1)}$) and nonlinear (P_{NL}) effects in the re-

sponse of the polarization, one commonly expands P in powers of the electric field strength $E(\boldsymbol{r},t)$:

$$P(\boldsymbol{r},t) = P^{(1)}(\boldsymbol{r},t) + P^{(2)}(\boldsymbol{r},t) + P^{(3)}(\boldsymbol{r},t) + \cdots \equiv P^{(1)}(\boldsymbol{r},t) + P_{\mathrm{NL}}(\boldsymbol{r},t)\,. \quad (2)$$

The nonlinear polarization P_{NL} carries the complete information needed for the description of any nonlinear optical process. To calculate P_{NL}, one needs to solve equations that describe the microscopic light–matter interactions. A semiclassical procedure is usually employed: the external field is treated classically, whereas the polarization of the system is calculated quantum mechanically. Thus, the system is characterized by the Hamiltonian H_0 and its interaction with the external electromagnetic field is described by the term [22]:

$$V_{\mathrm{int}} = -\boldsymbol{\mu}E(t)\,, \quad (3)$$

where $\boldsymbol{\mu}$ is the dipole moment of the system and $E(t)$ is the time-dependent electric-field component of the incident light. The evolution of the system perturbed by an external electromagnetic field can be determined by solving the Liouville–von Neumann equation [23]:

$$\frac{\partial\rho}{\partial t} = \frac{1}{i\hbar}[H_0 + V_{\mathrm{int}}, \rho] + \dot{\rho}_{\mathrm{diss}}\,, \quad (4)$$

where ρ is the density matrix of the system, $[H_0 + V_{\mathrm{int}}, \rho]$ designates the commutator between the Hamiltonian of the unperturbed system plus the interaction with the electromagnetic field V_{int} and the density matrix ρ, and $\dot{\rho}_{\mathrm{diss}}$ refers to dissipative processes, such as radiative and nonradiative decay. If the electric field is small compared to the internal fields of the system, we can expand the density matrix operator $\rho(t)$ in powers of the electric field:

$$\rho(t) = \rho^{(0)}(t) + \rho^{(1)}(t) + \rho^{(2)}(t) + \cdots\,, \quad (5)$$

where $\rho^{(n)}(t)$ is the nth-order contribution. The corresponding polarization $P^{(n)}$ is given by the expectation value of the dipole-moment operator $P^{(n)}(t) = \langle\boldsymbol{\mu}|\rho^{(n)}(t)\rangle$. Introducing the nonlinear response function $S^{(n)}$ the nth-order polarization $P^{(n)}$ can be written as:

$$P^{(n)}(t) = \int_0^\infty \mathrm{d}t_n \int_0^\infty \mathrm{d}t_{n-1} \cdots \int_0^\infty \mathrm{d}t_1 S^{(n)}(t_n, t_{n-1}, \ldots, t_1) \times E(t-t_n)E(t-t_n-t_{n-1})\cdots E(t-t_n-t_{n-1}-\cdots-t_1)\,. \quad (6)$$

The derivation of this equation and the functional forms of the first, second- and third-order response functions can be found in the literature (see, for instance, [22]). For centrosymmetric systems or isotropic media,

all even-order polarization terms vanish, and therefore the lowest term in P_{NL} is $P^{(3)}$. The third-order polarization dominates most nonlinear spectroscopies, such as photon-echo, transient grating, pump-probe, Raman scattering, two-dimensional (2D) electronic spectroscopy, etc. [22, 24]. The pump-probe signal, for example, is given by [25]:

$$I_{\mathrm{PP}}(\omega_{\mathrm{pr}}, \Delta t) = 2\omega_{\mathrm{pr}} \mathrm{Im} \int_{-\infty}^{+\infty} \mathrm{d}t' E_{\mathrm{pr}}(t') P^{(3)^*}(0, \Delta t, t') \,, \tag{7}$$

where ω_{pr} and E_{pr} are the carrier frequency and the electric-field envelope of the probe pulse, respectively, and Δt denotes the time delay between the pump and probe pulses. Here, E_{pr} also acts as a local oscillator, and a significantly amplified signal is achieved through intrinsic optical heterodyne detection (OHD) by coherently mixing it with a weak signal field along the same direction. An advantage of OHD is that the signal is linear with the third-order polarization $P^{(3)}$. Since $P^{(3)}$ is proportional to the third power of the electric field, the pump-probe signal should be linearly dependent on the intensity of the pump and probe pulses.

If the timescales on which the charge- and energy-transfer processes occur are large with respect to the dephasing times of the system, however, the optical transients can be described semiclassically using the frequency-dependent absorption coefficient $\alpha(\omega)$:

$$\alpha(\omega) = \frac{\omega \epsilon_2(\omega)}{n(\omega) c} \,. \tag{8}$$

Changes of α in transient spectra can thus be traced to changes of ϵ_2, the imaginary part of the dielectric function, which can be written as:

$$\epsilon_2(\omega) = \frac{2\pi e}{m_e \omega} \sum_{\mathrm{i,f}} \sum_{k} |M_{\mathrm{fi}}|^2 \rho_{\mathrm{ii}} (1 - \rho_{\mathrm{ff}}) \delta(E_{\mathrm{f}}(k) - E_{\mathrm{i}}(k) - \hbar\omega) \,, \tag{9}$$

in which the summation runs over all initial i and final f states with momentum k, and over the corresponding state populations ρ_{ii} and ρ_{ff} that are coupled to the electromagnetic field by the transition dipole matrix element M_{fi}. For transitions between two specific states $|1\rangle$ and $|2\rangle$ the change of the absorption coefficient measured in the transient spectra can then be related to:

$$\Delta\epsilon_2(\omega) = \frac{2\pi e}{m_e \omega} |M_{21}|^2 [(1 - \rho_{22}) \Delta\rho_{11} - \rho_{11} \Delta\rho_{22}] \,, \tag{10}$$

where $\Delta\rho_{11}$ and $\Delta\rho_{22}$ denote the population changes. Combining (8) and (10) for small excitation densities $\rho_{22} \ll \rho_{11}$, we finally obtain the semiclassical expression for the transient absorption signal in the incoherent limit:

$$\Delta\alpha(\omega) = \frac{2\pi e}{m_e n(\omega) c} |M_{21}|^2 [\Delta\rho_{11} - \Delta\rho_{22}] \,. \tag{11}$$

This incoherent limit is frequently used as a basis for the interpretation of optical transients.

3 Metallic Tubes

The electron–phonon (el–ph) interaction in metallic carbon nanotubes (see also the contribution by Saito et al.) plays a key role for several critical materials properties such as the temperature dependence of the electrical conductivity [26], their thermoelectric power [27], and possibly superconductivity [28]. Electron–phonon interactions can also induce subtle changes in the electronic band structure and open a small bandgap at the Fermi level of metallic SWNTs [29, 30]. Metallic SWNTs have, furthermore, been found to carry exceedingly large current densities of 10^7–$10^8\,\mathrm{Acm}^{-2}$ at room temperature without suffering current-induced damage [31, 32]. This is indicative of weak el–ph interactions that facilitate ballistic electron transport over long distances. We discuss here the first experiment studying carrier dynamics in metallic SWNTs using TRPE spectroscopy [33], which allows study of the carrier dynamics in the vicinity of the Fermi level in real time. For a brief description of the TRPE technique see Sect. 2.1.

Differential photoelectron spectra are recorded as a function of pump-probe delay. The kinetic energy of the photoemitted electrons here allows the observed transient spectra to be identified with the carrier dynamics in metallic tubes because semiconducting tubes do not contribute to the density of states near the Fermi level. The initial electron-gas thermalization is found to proceed on a 200 fs timescale. The evolution of the effective electron gas temperature from the moment of excitation up to time delays of 6 ps is shown in Fig. 2. The observed electron-gas cooling can here solely be attributed to the coupling of electronic and lattice degrees of freedom. The coupling of a thermalized electron distribution with temperature T_e to a lattice at temperature T_l is generally described by the so-called two-temperature model of *Anisimov* et al. [34]:

$$C_\mathrm{e}\frac{\mathrm{d}T_\mathrm{e}}{\mathrm{d}t} = \nabla(\kappa\nabla T_\mathrm{e}) - H(T_\mathrm{e}, T_\mathrm{l}) + S(t)\,, \tag{12}$$

$$C_\mathrm{l}\frac{\mathrm{d}T_\mathrm{l}}{\mathrm{d}t} = H(T_\mathrm{e}, T_\mathrm{l})\,, \tag{13}$$

where C_e and C_l refer to the electron and lattice specific heat capacities, respectively, κ is the electronic heat diffusion coefficient, $S(t)$ is the source term describing the energy deposited in the electronic system by the pump pulse and $H(T_\mathrm{e}, T_\mathrm{l})$ is the coupling term that describes the coupling strength between electronic and lattice degrees of freedom. In the low-temperature limit with electronic temperatures similar to or smaller than the Debye temperature Θ_D, the coupling term can be written as [35]:

$$H(T_\mathrm{e}, T_\mathrm{l}) = \frac{144\zeta(5)k_\mathrm{B}\gamma}{\pi\hbar}\frac{\lambda}{\Theta_\mathrm{D}^2}(T_\mathrm{e}^5 - T_\mathrm{l}^5)\,, \tag{14}$$

where $\zeta(5) = 1.0369\ldots$ is the Riemann zeta function, γ is the electronic heat capacity coefficient and λ is the el–ph mass enhancement factor [36]. By

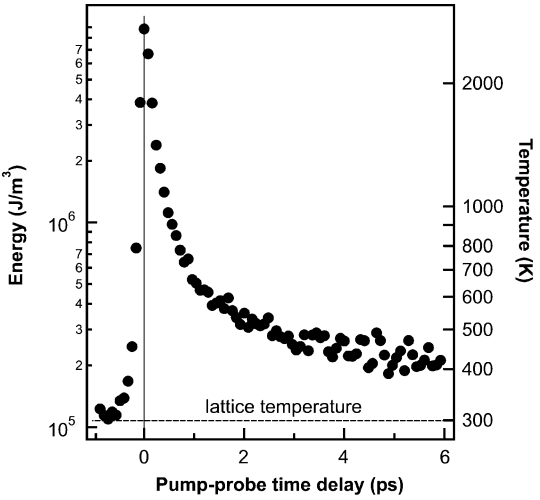

Fig. 2. Kinetic energy of the photoemitted electrons vs. time delay shows the laser heating and successive cooling back to the lattice temperature as driven by the electron–phonon coupling. (From [7])

assuming T_l fixed, a fit of (12) to experimental data yields an extraordinarily low el–ph mass enhancement factor on the order of $(4 \pm 1) \times 10^{-4}$ that can be used to estimate a room-temperature el–ph scattering time of 15 ps [33, 35]. TRPE experiments thereby provide a direct time-domain view of the extraordinary current-carrying capacity and long ballistic electron mean-free paths found in metallic or semiconducting SWNTs [31, 37].

4 Semiconducting Tubes

As discussed in the contributions by Spataru et al., Ando, Saito et al., and Lefebvre et al., the optical properties of semiconducting SWNTs are governed by excitons, with exciton binding energies being substantial fractions of the bandgap energies. Measurements on a range of structurally distinct nanotube species using two-photon excitation spectroscopy (see the contribution by Lefebvre et al.) further showed that both the exciton binding energy and the corresponding bandgap energy scale inversely with the tube diameter [38]. A detailed understanding of the photophysics including spectral properties, exciton dynamics and their potential correlation with the geometrical structure of SWNTs are of interest from both a fundamental perspective and novel applications, in particular, in optoelectronics [39] (see also the contribution by Avouris et al.). For instance, the diameter-tunable PL emission from semiconducting SWNTs is particularly attractive for developing nanometer-sized near-infrared light emitters, and the realization would be greatly facilitated if the quantum efficiencies could be significantly enhanced. A detailed study

of various competing relaxation pathways with ultrafast spectroscopy should enable the elucidation of the physical reason for the extremely low quantum efficiency (see the contribution by Lefebvre et al.). Similarly, the application of ultrafast spectroscopy will also allow the quantification of the response time of semiconducting nanotube-based photodetectors and solar cells [39].

4.1 Exciton Dynamics

The dynamics of excitons is governed by their interactions with phonons, surface defects and impurities, charged carriers, as well as other excitons [12]. These interactions cause a variety of generally competing dynamical processes including intra- and intersubband relaxation, exciton dephasing and migration, trapping at defect and impurity states, as well as nonlinear exciton–exciton annihilation. A detailed study of exciton dynamics will thus provide fundamental insights into the microscopic aspects of these interactions and their influences on macroscopic properties, such as spectral lineshape, relaxation timescale and PL quantum yield, etc.

Resonant excitation of a semiconducting nanotube with femtosecond optical pulses creates a delocalized exciton whose length scale is determined by the extent of the wavefunction spread over the system under consideration. Ideally, the coherence size of the exciton is determined by the wavelength of the excitation field, but a reduction of the size is found in practice due to the scattering by phonons. Direct excitation of a higher-lying excitonic state of semiconducting SWNTs such as E_{22}^S with pulses that are either in electronic resonance or non-resonance will undergo rapid intersubband relaxation to the energetically lowest excitonic state, the E_{11}^S state, as a result of exciton–phonon interaction [5, 40, 41]. As recent calculations showed that each of the exciton states, such as E_{11}^S, E_{22}^S and so on, corresponds to an exciton manifold [42], this will further lead to intrasubband relaxation.

Exciton recombination, one of the possible interband relaxation processes, can be either radiative or nonradiative. If one denotes the corresponding rate constants as k_{r} and k_{nr}, respectively, the PL quantum yield can be written as $\Phi = k_{\mathrm{r}}/(k_{\mathrm{r}} + k_{\mathrm{nr}})$. Given the typical Φ value of 10^{-3}–10^{-4} found for semiconducting SWNTs dispersed individually with different surfactants at room temperature [15, 40, 43], it is immediately clear that the exciton dynamics probed by ultrafast optical spectroscopy must be dominated by nonradiative relaxation processes. This inference is fully consistent with the long radiative lifetime, with a timescale of the order of tens of nanoseconds [15, 44–46]. While it remains to be explored what kind of processes are involved in the nonradiative relaxation and whether they are intrinsic or extrinsic, the observation of a significantly increased PL yield from free-standing, individual nanotubes suggests that some extrinsic factors may play a substantial role [47] (see also the contribution by Lefebvre et al.).

When the intensity of the excitation pulse reaches a level such that the probability of creating two or more excitons per nanotube is no longer neg-

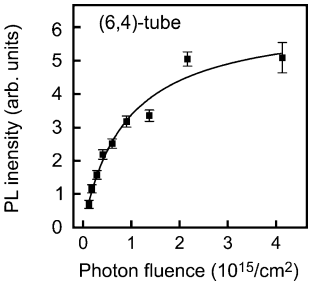

Fig. 3. Power dependence of the photoluminescence from a single confocally imaged (6,4) tube. The tube is excited off-resonantly at 800 nm and emission is detected in the 1110-nm range (from [17])

ligible, the interaction between excitons comes into play. This interaction is usually termed exciton–exciton annihilation in the language of molecular systems, and opens up an additional nonradiative decay channel. As a result, an accelerated kinetic decay and a decreased Φ value will be observed. The study of this nonlinear phenomenon provides information on the exciton motion in this one-dimensional (1D) system [48–53].

The discussion in the following will be divided into two subsections according to the excitation intensities employed in the experiments. The excitation density, i.e., the number of initial electron–hole (el–h) pair excitations per tube length, can be estimated, for example, using experimental or calculated photoabsorption cross sections of polyaromatic hydrocarbons [54, 55] as well as some recent experimental data from ropey and polydisperse SWNTs [54]. Due to the enhancement of exciton oscillator strengths in 1D systems both data sets probably underestimate the resonant photoabsorption cross sections σ and suggest that σ is in the $10^{-18}\,\mathrm{cm}^2\,\mathrm{atom}^{-1}$ range. For SWNTs with about 1 nm diameter, this implies an on-resonance photoabsorption cross section per nm of tube length well in excess of $10^{-16}\,\mathrm{cm}^2$. Experimentally, one finds that the power dependence of the PL signal from an individual (6,4) tube saturates around 5×10^{15} photons cm^{-2} if excited off-resonantly at 800 nm (see Fig. 3) [17]. This intensity corresponds to the excitation of 100 to 500 excitons per micrometer of tube length. In the following, low excitation densities are thus defined as the fluence range below 2×10^{14} photons cm^{-2} where the magnitude of optical transients as well as PL intensities scale linearly and the dynamics do not depend on excitation power.

4.2 Low Excitation Densities

As mentioned above, exciton dynamics in S-SWNTs depend on the excitation density, i.e., on the number of excitons generated on the tube per unit length [50, 53]. However, even low excitation densities – as identified by the linear dependence of transients and PL intensities on laser power – often correspond to the promotion of several excitons per tube. In fact, pump fluences at which only one exciton is excited per tube are experimentally difficult to realize simply because of the large number of atoms within a single tube

and due to the resulting large photoabsorption cross sections. Hence, our following discussion will be focused on the results obtained under the lowest excitation possible, in particular, on the data collected using streak cameras and TCSPC techniques. The high sensitivity of these techniques permits measurements at substantially lower excitation intensities than generally needed for other time-resolved experiments.

4.2.1 Intersubband Relaxation

Availability of tunable pulses with durations of < 50 fs allows one to resolve directly the intersubband exciton relaxation processes such as from the E_{22}^S to the E_{11}^S states. *Manzoni* et al. [56] reported so far the only study based on two-color pump-probe measurements on the SWNTs embedded in a polymethylmethacrylate matrix. The authors employed sub-10 fs visible pulses to excite the E_{22}^S states of S-SWNTs resonantly, and the subsequent relaxation was probed at the corresponding E_{11}^S states at 0.92 eV. The detected kinetics of induced transmission initiates with an instantaneous rise owing to the ground-state photobleaching, followed by a slower rise with a timescale of 40 fs corresponding to the relaxation from the E_{22}^S to E_{11}^S states. Similarly, a time constant of 65 fs was determined for the relaxation from the E_{33}^S to the E_{11}^S states.

As currently available samples are mostly polydisperse, usually with overlapping absorption spectra for at least some of the tube species, separate determination of the intersubband relaxation times for structurally distinct S-SWNTs remains to be explored. Future ensemble studies require either time-resolved PL measurements with an exceptionally high sensitivity and a time resolution better than sub-50 fs, or, perhaps more straightforwardly, transient absorption experiments with tunable sub-10 fs pulses provided that samples containing single tube types are available. The information gained from these studies will further enable verification of the predicted dependence of the intersubband relaxation times on nanotube chiralities [41].

4.2.2 Radiative Lifetime

Experimental determination of the radiative lifetime of S-SWNTs was first reported by *Hagen* et al. [46] and *Wang* et al. [15] based on time-resolved PL measurements on aqueous suspensions of SWNTs wrapped with surfactants. The experiments were performed by exciting the samples with ~ 100 fs pulses around 800 nm and by detecting the PL emission from various tube types with either a streak camera or by means of Kerr gating. These studies showed that the initial PL decay occurs on the 10-ps timescale with some variations from one study to the next. Given the low measured PL quantum yields of 10^{-3} or less [15, 40, 46, 57], it was concluded that nonradiative relaxation dominates the decay of the lowest optically active exciton. The radiative

lifetime was further estimated to be on the order of 10 and 110 ns, respectively. Even longer lifetimes of 260 ns [43] and 3.2 μs [58] were reported later by other groups based on time-resolved PL and transient absorption measurements. In comparison, theoretical calculations of *Spataru* et al. [44] and *Perebeinos* et al. [45] predicted, at room temperature, a radiative lifetime of the order of ~ 10 ns or ~ 50 ns, depending on whether only singlet excitonic states or both singlet and triplet states are assumed in the thermalization (see also the contributions by Spataru et al. and Avouris et al.).

It should be pointed out that a significantly increased PL yield up to ~ 0.07 was reported recently based on measurements on free-standing, individual tubes [47] (see also the contribution by Lefebvre et al.). Whether or not this will remarkably alter the radiative lifetime still needs to be tested by determining the PL lifetime.

4.2.3 Correlation of the PL Decay Timescales with the Tube Diameter

Selective detection of structurally distinct S-SWNTs, one at a time, with time-resolved PL spectroscopy at low excitation densities have allowed one to establish correlation of the PL decay time with the nanotube diameter (d_t). *Hertel* et al. [59] first reported a weak correlation based on the measurements on 6 small-diameter SWNTs and DWNT cores. In this experiment, several tube types were excited non-resonantly with sub-100 fs pulses at 795 nm and the emission from each tube type was spectrally selected and detected with a streak camera. The authors found that the decay time varies from ~ 10 ps for the tubes with $d_t = 0.76$ nm to 30 ps for those with $d_t = 0.88$ nm. Very recently, *Jones* et al. [60] reported a detailed time-resolved PL study of 15 different S-SWNT types with d_t ranging from 0.76 to 1.04 nm. In this experiment, each desired tube type was separately measured using TCSPC by exciting resonantly its E_{22}^S excitonic state and detecting the emission from the corresponding E_{11}^S state. The electronic resonance in both the excitation and detection permits the exclusive probing of the tube type of interest. The authors found that in a 10-ns detection window, the PL decays can be accurately fitted to a biexponential function with two characteristic time constants. The dominant decay component τ_1 increases from 60 to 200 ps with increasing d_t, while the lesser component τ_2 increases from 200 ps to 4.8 ns. As shown in Fig. 4, strong linear correlations with d_t are clearly evident for both time constants. The authors further proposed an extrinsic and an intrinsic model to explain the observed biexponential decay behavior.

One of the major discrepancies among the results reported so far is the dramatic differences in the time constant determined by different groups, even for the same type of tube coated with the same surfactant. For instance, the lifetime obtained for the (7,5) tube using SDS-solubilized samples varies from below 10 ps [59] to 29 ps [61] and further to 140 ps [43]. Another discrepancy is

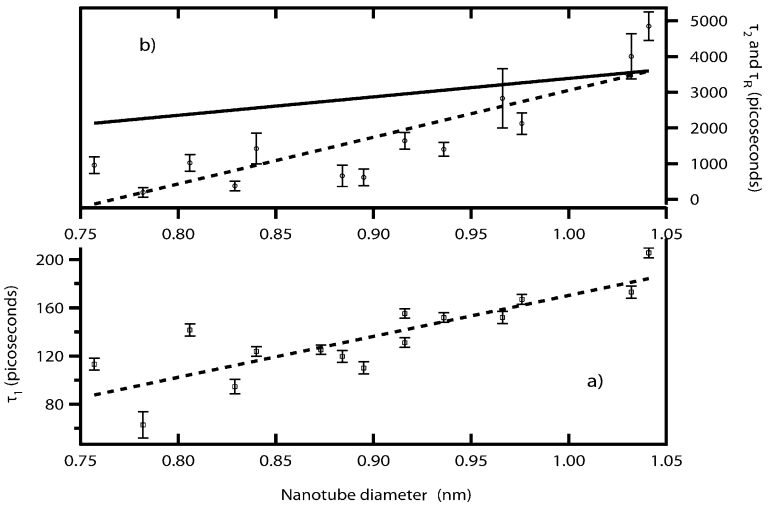

Fig. 4. Plot of decay times for (**a**) τ_1 and (**b**) τ_2 against nanotube diameter d_t for 15 SWNT species, with *dotted lines* provided as a guide to the eye. The *solid line* in (**b**) corresponds to the theoretical prediction of the natural radiative lifetime, τ_R vs. d_t, for these SWNTs according to [45] (from [60])

the functional form needed to adequately describe the PL decay, either mono- [61], bi- [43, 60] or nonexponential [62], which further connects to a general lack of understanding of the underlying relaxation processes and relevant physical mechanisms. The discrepancies may arise from differences in time resolution, detection window, excitation intensity and sample preparation. Future experimental studies with better time resolution and sensitivity are highly desirable. Systematic measurements of PL decays at low temperatures and using samples dispersed with different surfactants are likely to be crucial for understanding the physical mechanism underlying the linear correlation of the PL decay times with d_t.

4.2.4 Environmental and Temperature Effects on Exciton Population Dynamics

As objects with large surface area, SWNTs are expected to be highly sensitive to their environment, which may strongly affect their electronic properties and excited-state dynamics. Ensemble and single-tube time-resolved studies at low excitation densities have enabled study of environmental effects on the dynamics underlying radiative and nonradiative decay from S-SWNTs. *Hertel* et al. [59] found that the PL decay time is highly sensitive to the surfactants used to suspend the nanotubes. Figure 5 shows the dependence of the PL decay of a (7,5) tube in different environments as measured using a streak camera. Here, the PL lifetime is found to increase from below 10 ps (i.e.,

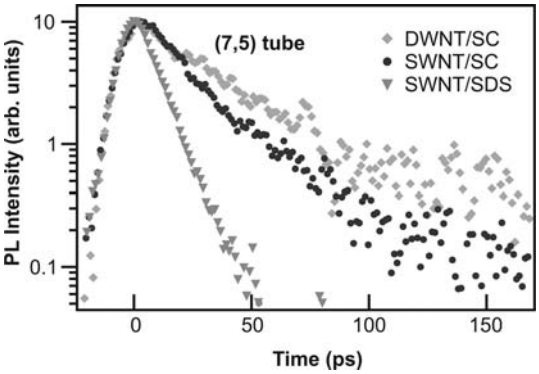

Fig. 5. E_{11}^{S} photoluminescence decay in a (7,5) tube at room temperature for SWNTs in different environments. The longest lifetimes are here found for core tubes of the semiconducting (7,5) tube within double-wall carbon nanotubes (DWNTs) suspended by sodium cholate (SC), while the shortest lifetimes are observed in sodium-dodecyl sulfate (SDS)-suspended SWNTs (from [59])

the instrument response function) to 17 ps when the tube is suspended in SDS, sodium cholate, and 22 ps if it is the core of another larger tube in a DWNT. Such a sensitivity of the dynamics to the tube environments was also reported by *Ostojic* et al. [63] in an earlier pump-probe study. The authors found that the dynamics is strongly dependent on the pH of the aqueous solution of the SWNTs suspension. The detailed mechanisms that cause these effects still await future work, and possibilities may include variation of the exciton mobility and binding energy induced by environmental changes.

The aforementioned sensitivity of the dynamics to environmental factors observed from ensemble measurements was also found in single-tube TCSPC studies at cryogenic temperatures. *Hagen* et al. [17] found that there are considerable heterogeneities of the PL decay time that was found to vary by almost one order of magnitude from 20 ps to about 200 ps at 87 K (see Fig. 6). The heterogeneities in this study were attributed to the sensitivity to environmental effects or on-tube defects. Specifically, local variations of the dielectric environment, arising from inhomogeneities in the surfactant coating, for example, may be linked to changes in the alignment of exciton states. In the same study the authors also reported on the temperature dependence of single-tube PL lifetimes, which increase with decreasing temperature until a constant value is reached at around 60 K. In line with the large variation of the PL decay time found in the single-tube experiment, the kinetics obtained from recent ensemble measurements using time-resolved PL [62] and pump-probe measurements [64] at different temperatures exhibit more complex decay behavior. For instance, *Berger* et al. [62] found that the PL decay measured for the (9,4) tube type contains an initial fast component, which is temperature independent and is attributed to the presence of small residual

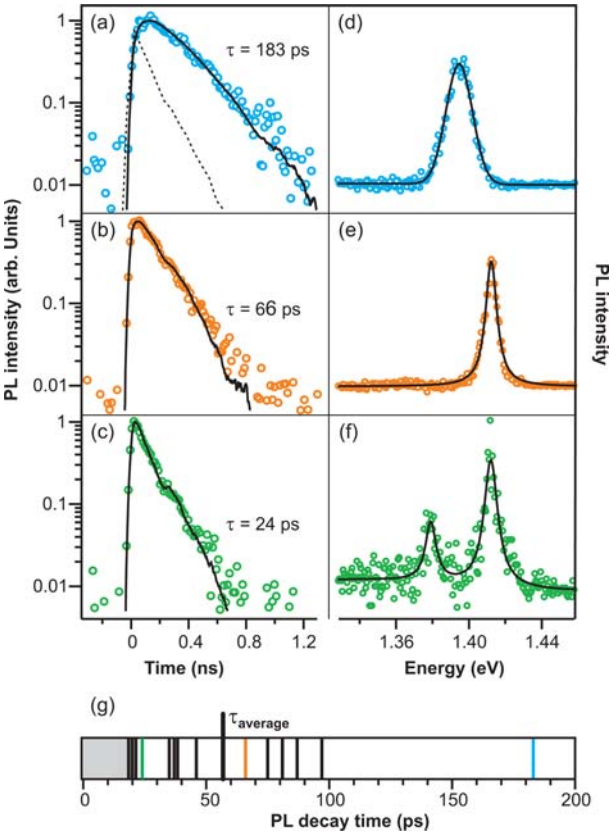

Fig. 6. Photoluminescence transients (**a**–**c**) and corresponding spectra (**d**–**f**) of three different single (6,4) SWNTs observed for excitation at 800 nm. Excited-state lifetimes at a sample temperature of 87 K for (**a**) and (**b**) and 67 K for (**c**) vary strongly from one tube to the next. (**g**) Bar graph of the distribution of all measured lifetimes at 87 K. The *gray area* on the *left* is the region not accessible due to the limited time resolution of the instrument (from [17])

bundles, and a slow component that is strongly dependent on temperature and is dominated by nonradiative processes down to 40 K. The observations from the ensemble and single-tube studies can either be attributed to the temperature dependence of the nonradiative decay rate or – as proposed recently – to the different emission strengths and temperature-dependent population distributions between the bright and slightly lower-lying dark excitons [65].

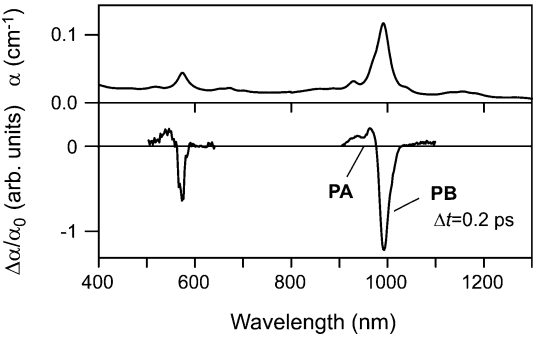

Fig. 7. Absorption spectrum (*upper panel*) and optical transient for E_{22}^S excitation at 572 nm of an isopycnically (6,5)-enriched SWNT suspension (adapted from [66])

4.2.5 Transient Absorption of a Chirality-Enriched SWNT Preparation

Pump-probe spectroscopy provides a complementary means to explore the dynamics of optically excited states. Optical transients in the absorption spectra, however, are generally more difficult to assign to specific electronic processes if compared to PL studies, which in effect simply probe the excited-state population as given by ρ_{ex}, the diagonal elements of the density matrix. If the dephasing times, however, are short with respect to the timescale of the energy and charge transfer or relaxation processes, we can use (11) for the analysis of transient spectra of optically active excitons in SWNT suspensions.

Figure 7 shows the absorption spectrum and transient spectrum of a chirality-enriched DNA-stabilized SWNT suspension in the visible and near-infrared regions [66]. The absorption spectrum is dominated by the optically active E_{11}^S and E_{22}^S states of the (6,5) tube at 993 nm and 572 nm, respectively. Analysis of absorption spectra suggests that roughly 35 % of the semiconducting tubes in this sample are of the (6,5) type. The high content of one specific species ensures that the dynamics observed in transient spectra are likewise dominated by the optical response of this particular species and to a much lesser extent by other tubes whose spectral features may overlap with the (6,5) tube. Resonant excitation of either the optically active E_{11}^S or E_{22}^S excitons, furthermore, allows mitigation of the influence of transients from other tubes by at least a factor of 5 due to resonantly increased absorption at the E_{11}^S or E_{22}^S energies [66].

The wavelength dependence of $\Delta\alpha(\omega)$ is shown in Fig. 8, from which it becomes evident that the spectral overlap of distinct photobleach (PB) and photoabsorption (PA) transients can be used to account for the seemingly complex wavelength dependence of optical transients. The same decomposition of the transient spectra into two similarly intense PB and PA components suggests that the PA component is due to a slightly blue-shifted (7.5 meV)

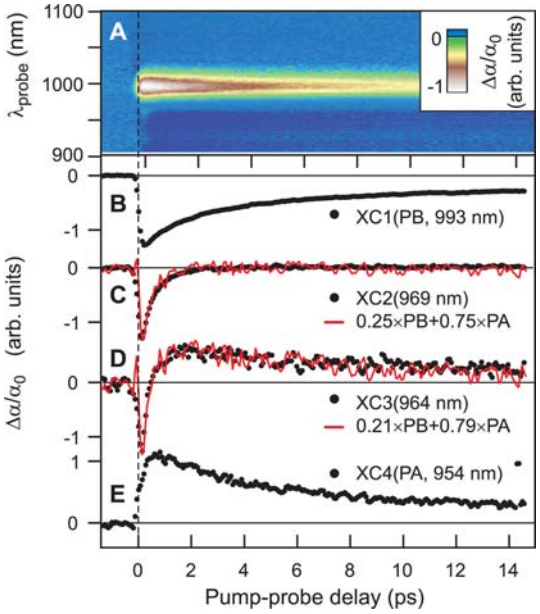

Fig. 8. (**A**) Optical transients as a function of probe wavelength and pump-probe delay for a DNA-stabilized (6,5)-enriched SWNT suspension. (**B**) Photobleach and (**E**) photoabsorption crosscorrelation traces at 993 nm and at 954 nm, respectively. The appropriately weighted sum of these two traces is shown to be able to account for the complex wavelength dependence of optical transients in (**C**) and (**D**). This illustrates that PB and PA represent two distinct but spectrally overlapping processes (adapted from [66])

transition [66]. The nature of this transition is currently still subject to debate [67, 68].

The nonexponential optical transients at longer pump-probe time delays (see Fig. 8) are found to exhibit power-law scaling in time with $\Delta\alpha(\omega) \approx t^{\gamma}$, where γ is found to be -0.45 ± 0.03 [66]. The power-law scaling can be interpreted as being due to some diffusion-limited relaxation process such as trapping in a disordered system [66] that is possibly associated with some type of exciton trapping mechanism. Pump-probe spectra from metallic carbon nanotubes, on the other hand, do not exhibit the power-law scaling type decay and return to the ground state significantly faster than their semiconducting counterparts [69].

4.3 High Excitation Densities

4.3.1 Spectroscopic and Dynamic Signatures of High-Intensity Excitation

When the intensity of an excitation pulse reaches a level where the probability of creating two or more excitons per nanotube is no longer negligible, one has to consider the effects induced by this high excitation intensity. In such an intensity regime, the interaction between two excitons results in a nonlinear exciton–exciton annihilation process, which involves rapid relaxation of one exciton by releasing its energy to the second exciton, and consequently promoting the latter to a higher-energy excited state [70,71]. The occurrence of this nonlinear process opens up an additional relaxation channel, which in turn strongly affects the exciton population dynamics detected using femtosecond fluorescence upconversion and pump-probe techniques.

Exciton–exciton annihilation in semiconducting nanotubes was first reported by *Fleming* and coworkers [50]. By employing a femtosecond fluorescence upconversion technique and an aqueous solution of micelle-dispersed HiPco nanotubes, the authors succeeded in measuring time-resolved fluorescence kinetics with sub-100 fs resolution. The measurements were performed on five structurally distinct nanotube species, namely, (8,3), (6,5), (7,5), (7,6) and (9,5) nanotubes. As an example, Fig. 9a shows the fluorescence kinetics detected at 1244 nm upon excitation at 660 nm for five different excitation densities. This combination of the excitation and emission wavelength selects exclusively the (9,5) tube type. As is clearly evident from Fig. 9a, the fluorescence decays show a strong intensity dependence, with faster decays as the excitation intensity increases. At the highest excitation intensity, the majority of excited population disappears within the first 500 fs. In addition, a nonlinear dependence of the maximum amplitude of the fluorescence signal on the excitation intensity is observed (Fig. 9b). A plot of the maximum amplitude versus the square root of excitation intensity shows a clear linear dependence (see inset in Fig. 9b). A similar decay behavior was observed for all other selected tube species, i.e., (8,3), (6,5), (7,5) and (7,6) (data not shown), which emit at 950, 975, 1024 and 1119 nm, respectively.

The strong excitation intensity dependence of the fluorescence decay in conjunction with the nonlinear correlation between the maximum fluorescence amplitude and the excitation intensity are indicative of the occurrence of exciton–exciton annihilation processes. Quantitative analysis of the fluorescence decays obtained at different excitation intensities further confirms this consideration. *Ma* et al. [50] found that the fluorescence decays can be satisfactorily described by the solution of a simple rate equation:

$$\frac{\mathrm{d}n_{\mathrm{ex}}(t)}{\mathrm{d}t} = -\frac{1}{2}\gamma n_{\mathrm{ex}}^2(t)\,, \tag{15}$$

where $n_{\mathrm{ex}}(t)$ denotes the population of excitons, and γ represents a time-independent rate constant.

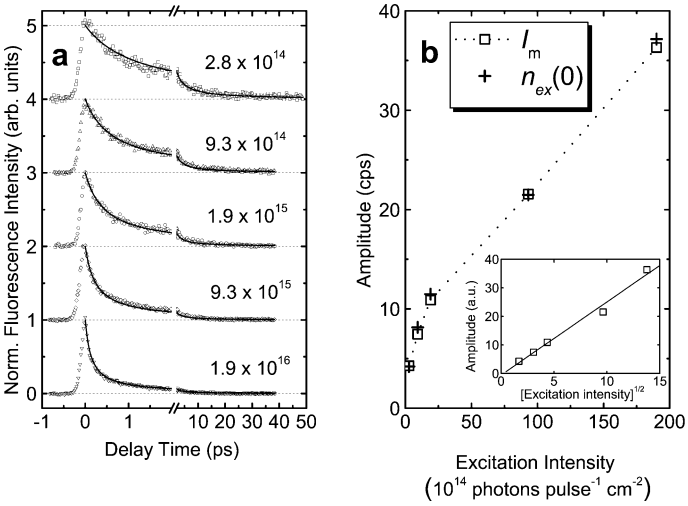

Fig. 9. (**a**) Normalized time-resolved fluorescence intensity vs. delay time for the (9,5) tube structure at different excitation intensities (in photons pulse^{-1} cm^{-2}) detected at 1244 nm upon excitation at 660 nm. The *solid lines* represent global fits according to the solution of (15). (**b**) Plot of the maximum fluorescence intensity I_{m} and the fitted parameter $n_{\mathrm{ex}}(0)$ vs. the excitation intensities. The *dotted line* is drawn to guide the eye. The *inset* shows I_{m} plotted vs. the square root of the excitation intensity, and the *solid line* represents a linear fit to the data points. After [49]

The occurrence of exciton–exciton annihilation in semiconducting nanotubes was subsequently observed by *Wang* et al. [51]. In this study, the authors employed 150-fs laser pulses centered at a wavelength of 810 nm to excite an aqueous-solution sample of HiPco tubes dispersed individually with poly(acrylic acid). The fluorescence emission from various nanotube species was time resolved by an optical Kerr gating technique. Although the detection was not tube-type selective, the observed fluorescence kinetics shows a clear dependence on excitation intensity. Under high excitation intensity, a fast decay component emerges and its amplitude increases linearly with intensity. The annihilation rate, or the coefficient for the Auger recombination of two el–h pairs as termed by these authors, was estimated to be 0.8 ps^{-1}.

A similar intensity dependence of the kinetics was also observed using femtosecond pump-probe spectroscopy at wavelengths corresponding to the E_{11}^S transitions of selective nanotube species [50, 51]. Evidently, frequency-resolved transient absorption spectroscopy appears particularly useful for elucidating the exciton–exciton annihilation phenomenon, and its application has led to identification of unique spectroscopic and dynamic signatures. As demonstrated by *Ma* et al. [48], electronically resonant excitation of the E_{11}^S state of the (8,3) tube at 953 nm induces an instantaneous spectral re-

sponse at 660 nm, the location of the corresponding E_{22}^S transition. The assignment of this response to the E_{22}^S transition was confirmed by the similarity between the kinetics probed at 660 nm for excitation of the E_{11}^S state and by direct E_{22}^S excitation. On the other hand, the dependence of the amplitude of the transient absorption signal on the intensity of pump pulses at 953 nm differs for the kinetics probed at 660 and 953 nm. The former exhibits a linear dependence on pump fluence, whereas a saturating behavior is seen for the data obtained with a 953-nm probe pulse (Fig. 10a). Furthermore, the kinetics probed at 660 and 953 nm upon resonant excitation of the E_{11}^S transition (Fig. 10b) are strongly correlated with each other. This correlation is manifested by an excellent match between the squared profile of the kinetics recorded at 953 nm and the kinetics measured at 660 nm (Fig. 10c).

The pump-intensity dependence of transient absorption spectra and of kinetics have been also observed by others [68, 72–74]. *Chou* et al. [72] reported two-color pump-probe experiments on an aqueous-solution sample of DNA-wrapped nanotubes synthesized by the CoMoCAT process, which is abundant in the (6,5) tube type. Upon excitation at 791 nm where an abundance of a large density of D-band phonons were excited, the kinetics probed at 990 nm, which is resonant with the E_{11}^S state of the (6,5) tube type, can be satisfactorily described by a model function consisting of three exponential components. The corresponding timescales were determined to be ~ 0.7, 2–3 and 50 ps for the fast, intermediate and slow decay components, respectively, and the intermediate decay component was identified with the decay of these phonons. The authors further found that the timescales associated with the intermediate and slow decay components decrease substantially with increasing pump intensity. Two-color pump-probe measurements were also performed by *Huang* and *Krauss* [73] on a D_2O solution of sodium dodecylbenzene sulfonate (SDBS) micelle-dispersed HiPco nanotubes under different pump fluences ranging from 2×10^{13} to 5×10^{15} photons/pulse cm^2. Following a procedure described in [75], the authors extracted time constants of 3.2 and 1.9 ps for the two and three el–h pairs states, respectively (see Fig. 11). Very recently, *Russo* et al. [74] reported a two-color pump-probe study on an aqueous solution of SDBS micelle-dispersed HiPco nanotubes at quite high excitation fluences corresponding to hundreds of excitons per micrometer length of a tube. Analysis of the kinetics obtained for the (8,6) and (7,6) tube types showed a power-law $1/\sqrt{\Delta t}$ dependence, where Δt denotes the time delay between the pump and probe pulses. The authors ascribed this behavior to an exciton population relaxation via 1D diffusion-limited two-body recombination. However, such a time dependence was not observed in any previous studies, and the reason for the clear discrepancy between this result and others is currently unknown.

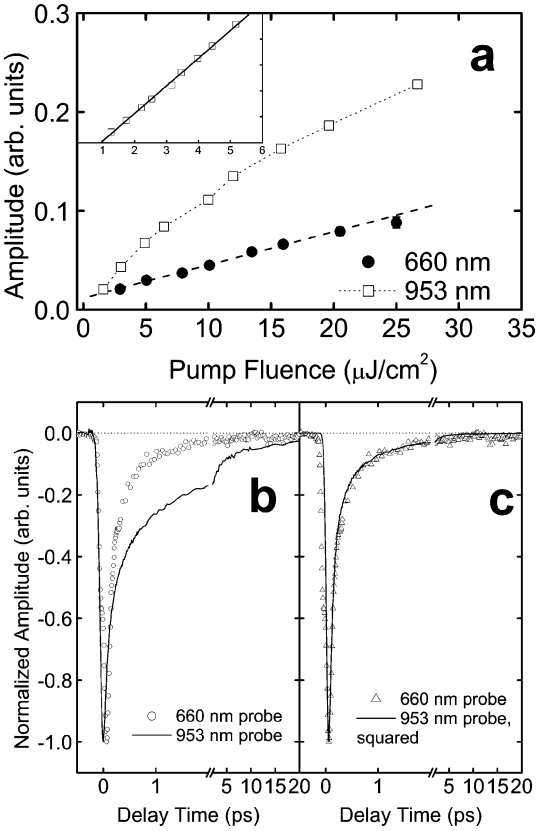

Fig. 10. (**a**) Plot of the maximum amplitude of the transient absorption kinetics probed at 660 nm (*filled circles*) and 953 nm (*open squares*) versus the intensity of the pump pulses at 953 nm. The *dashed line* is the linear fit of the data obtained with a 660-nm probe, and the *dotted line* is drawn to guide the eye for the data obtained with a 953-nm probe. The *inset* shows the 953-nm data, plotted vs. the scale of the square root of the pump intensity. The *solid line* represents the linear fit. (**b**) Kinetics probed at 660 (*open circles*) and 953 nm upon resonant excitation of the E_{11}^{S} transition of the (8,3) tube at 953 nm. (**c**) Comparison of the squared profile at 953 nm (*solid line*) and the kinetics at 660 nm, both data being recorded with the 953-nm excitation. All kinetics shown in (**b**) and (**c**) are normalized at the signal maxima, after [49]

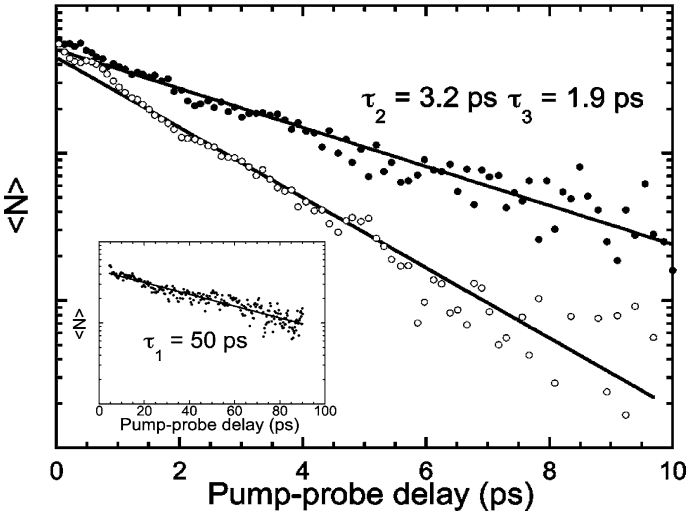

Fig. 11. The 1 el–h pair state dynamics (*inset*) and 2 (*solid circles*) and 3 (*open circles*) el–h pair dynamics extracted from transient absorption data probed at 1323 nm and fitted to a single exponential decay (*solid line*) (after [73])

4.3.2 Theoretical Advances

The need for describing and understanding the dynamics under high excitation intensities further stimulated theoretical interests. *Wang* et al. [51] first introduced a stochastic model of carrier dynamics for analyzing their experimental data obtained by time-resolved fluorescence measurements under different excitation intensities. The model explicitly includes Auger interactions and discrete occupancy of nanotubes by carriers, and numerical calculations showed good quantitative agreement with the experimental data. An analytical solution of this model was obtained later by *Barzykin* and *Tachiya* [52]. Very recently, *Wang* et al. [53], by attributing the process of the nonlinear exciton relaxation to exciton–exciton scattering, further derived an approximate expression for the Auger recombination (exciton annihilation) rate in terms of the exciton binding energy, optical matrix element and reduced carrier mass.

One major problem concerning the applicability of (15) to 1D systems was solved by *Valkunas* et al. [49] by considering explicitly the origin of the relaxation channels and exciton motion. This problem arises from the fact that (15) or its generalized form, with one or more linear terms in the right-hand side, is applicable to exciton–exciton annihilation in an extended system whose size is comparable with or larger than the exciton diffusion radius [70, 71]. For such systems, it is generally assumed that exciton–exciton annihilation is diffusion limited, and the corresponding annihilation rate depends on the dimensionality of the system. Use of a time-independent annihilation rate is

appropriate only for a system with a dimensionality (d) that is equal to or greater than 2. For systems with reduced dimension such as a SWNT, the annihilation rate limited by exciton diffusion becomes time dependent, given by $\gamma = \gamma_0/t^{1-(d/2)}$. However, it has been shown that an equation based on such an annihilation rate does not provide an appropriate description of the kinetics measured using fluorescence upconversion and transient absorption methods (with the exception of recent work by *Russo* et al. [74]). Thus, 1D diffusion as a limiting step for exciton–exciton annihilation does not provide the basis for a theoretical description of this process. *Valkunas* et al. [49] solved this problem by assuming that the nonlinear annihilation process predominantly proceeds between the coherent excitons within the SWNTs. Within this concept the results of *Russo* et al. may be considered as an indication of exciton–exciton annihilation defined by exciton migration from remote regions of the tube.

4.3.3 Exciton Dissociation

The annihilation of two E_{11}^S excitons and the subsequent rapid relaxation from the high-lying excited state back to the E_{11}^S state creates an exciton with a large excess energy. If this excess energy is greater than the exciton binding energy, exciton dissociation may occur. Such a dissociation was indeed identified previously in conjugated polymers [76]. Using the femtosecond transient absorption technique, *Ma* et al. [77] demonstrated the occurrence of exciton dissociation in semiconducting SWNTs. Employing pump pulses centered at 660 and 953 nm, the authors observed a new bleaching band in the transient absorption spectra, which peaks at 730 nm. This band cannot be assigned to the exciton transitions of the (8,3) tube type that was intentionally selected by the wavelength of the pump pulses, nor to those species that were unintentionally excited. Most importantly, the dependence of the kinetics detected at 730 nm on the intensity of 953-nm pump pulses indicates the occurrence of nonlinear relaxation, and a satisfactory description of the 730-nm kinetics probed under the highest pump intensity was obtained with a model involving Auger recombination of charge carriers. This strongly suggests that the 730-nm band does not originate from an exciton but instead from an el–h continuum [75, 78, 79]. Knowing the nature of this new band, it is straightforward to calculate an exciton binding energy of 0.41 eV for the (8,3) nanotube. This value is very close to the experimental results obtained using two-photon fluorescence excitation spectroscopy [80, 81], and this determination does not require any assumption for the model for the el–h interaction.

Since observation of this phenomenon was reported so far only for the (8,3) tube type, further studies on different semiconducting SWNT species under similar experimental conditions are highly desirable. Use of chirality-enriched SWNT samples will be particularly helpful in avoiding ambiguity.

5 Comparison of S-SWNTs with π-Conjugated Polymers

The π-conjugated polymers are the first quasi-1D systems that have been studied extensively over the last 25 years. π-conjugated polymers possess quasi-1D electronic states and consequently also a 1D density of states. The lateral quantization may result in structured conduction and valence bands with subbands and van Hove singularities. The properties of such electronic systems are determined by the ratio of two characteristic energies, namely the electron–electron Coulomb interaction, (E_{Coul}) and the confinement energy, ΔE of lateral quantization (energy separation, ΔE between the van Hove singularities). In many π-conjugated systems $E_{\mathrm{Coul}} > \Delta E$. Under these conditions it is not possible to consider electrons and holes as independent, noninteracting particles, as in semiconductor quantum dots or nanorods.

Unsubstituted π-conjugated polymers usually possess inversion symmetry, and thus their eigenstates are classified as having either even-parity nA_{g} or odd-parity $n'B_{\mathrm{u}}$, where both the n and n' are integers that denote the order within an exciton band. Two important singlet exciton levels (1^1B_{u} and m^1A_{g}) and a double-excitation-type singlet level (k^1A_{g}) are shown in Fig. 12 [82]; their electron configurations are also shown for clarity. The m^1A_{g} is a specific excited state above the 1^1B_{u} level, whereas the k^1A_{g} excited state may be due to a biexciton state, i.e., a bound state of two 1^1B_{u} excitons. The m^1A_{g} level is known to have strong dipole moment coupling to $1B_{\mathrm{u}}$, as deduced from the various optical nonlinear spectra of π-conjugated polymers analyzed in terms of the "four essential states" model [83]. It is therefore expected that two strong optical transitions form following the 1^1B_{u} photogeneration: PA_1 and PA_2, as shown in Fig. 12a, where PA denotes photoinduced absorption. As the m^1A_{g} state is below the continuum band threshold state n^1B_{u}, the energy of the PA_1 band gives the lower limit of exciton binding energy. A similarly calculated electronic structure of an S-SWNT is shown in Fig. 12b, which exhibits multiple energy manifolds $n = 1, 2, \ldots$, etc. Within each n, there occur optically dark excitons Dn a few $k_{\mathrm{B}}T$ below the optically allowed exciton Exn. The occurrence of these dark excitons represents one of the differences between S-SWNTs and π-conjugated polymers.

Vardeny and coworkers [84] found that the transient absorption spectra obtained using films of S-SWNTs and two π-conjugated semiconducting polymers, poly(dioctyloxy)para-phenylene vinylene (DOO-PPV) and poly(9,9-dioctylfluorene) (PFO), are quite similar. As an example, Fig. 13 shows the spectra collected at $\Delta t = 0$, and it is clear that all the spectra contain both negative PA and positive photobleaching (PB) or stimulated emission (SE) bands. In neither sample do the authors obtain a PA spectrum that increases at low energy in the shape of free-carrier absorption, viz., $\Delta\alpha \sim \omega^2$. Instead, the PA spectra are in the form of distinct photoinduced bands PA_1 and PA_2 associated with specific optical transitions of the primary photoexcitations in the samples, which are therefore not free carriers. The authors

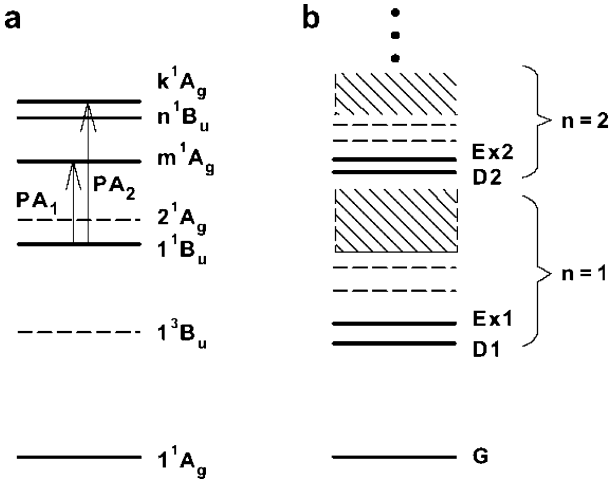

Fig. 12. Schematics of the excitonic electronic structures of (**a**) a light-emissive π-conjugated polymer and (**b**) an S-SWNT. In (**a**) the lowest triplet exciton 1^3B_u occurs below the lowest singlet exciton 1^1B_u. The lowest two-photon state 2^1A_g is composed of two triplets and plays a weak role in nonlinear absorption. Transient PA (photoabsorption) is from the 1^1B_u to the m^1A_g two-photon exciton that occurs below the continuum band threshold state n^1B_u, and to a high-energy k^1A_g state that occurs deep inside the continuum band. In (**b**), Exn and Dn are dipole-allowed and dipole-forbidden excitons, respectively (after [84])

further found, through measurements of the kinetics at selected probe wavelengths, that the PA and their respective PB (or SE) bands in both polymers and S-SWNTs are correlated to each other. This correlation is manifested by very similar dynamics and therefore they should share a common origin, namely, the same primary excitation, which is the photogenerated exciton. A similar correlation was also observed by *Hertel* and coworkers [66] on a chirality-enriched DNA-stabilized SWNT suspension.

Based on the analysis of the similarities between the transient absorption spectra and kinetics measured on the films of S-SWNTs and π-conjugated polymers, *Vardeny* and coworkers [84] concluded that the origin of the low-energy PA_1 in S-SWNTs is the excited-state absorption from Ex1 and D1 to higher-energy two-photon excitons. The broad nature of the PA_1 band in the S-SWNTs arises from the inhomogeneity of the experimental sample, with SWNT bundles that contain a distribution of S-SWNTs with different diameters and exciton binding energies. The authors also speculated that the n =1 continuum band lies between the peaks of the PA_1 and PA_2 bands. This analysis further enabled the authors to construct the vertical dashed line in Fig. 13c, which identifies the threshold of the continuum band for the S-SWNTs with the largest diameter in the film. Exciton binding energies of ca. 0.4 eV are then predicted for those S-SWNTs in the film that dominate

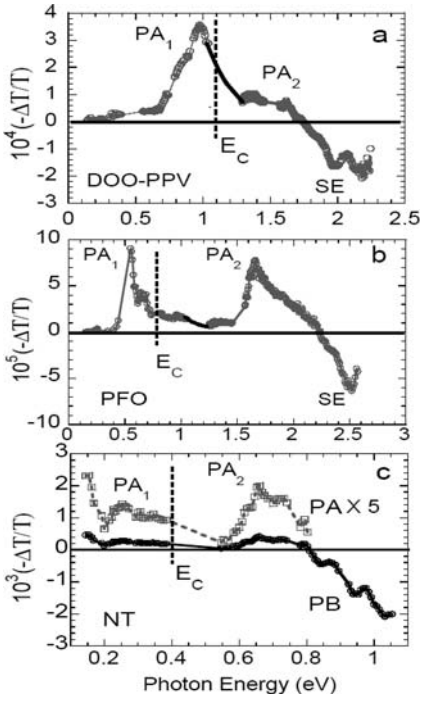

Fig. 13. Transient absorption spectra at $t = 0$ of films of DOO-PPV (**a**), PFO (**b**), and isolated SWNT in polyvinyl alcohol matrix (**c**). Various PA, PB, and SE bands are assigned. The *vertical dashed lines* at E_C between PA_1 and PA_2 denote the estimated continuum band onset. In (**a**) and (**b**), the *vertical dashed lines* were drawn based on the information obtained from two-photon absorption and electroabsorption experiments [84]. The *corresponding line* in (**c**) was drawn by scaling the result shown in (**b**) according to the ratio of their PA_1 peak energies (after [84])

the nonlinear absorption, which is similar to the results of two-photon PL excitation [80, 81] and femtosecond transient absorption [77] spectroscopy. The successful transferability of the parameters from PPV to S-SWNTs then suggests that the Coulomb interaction parameters as well as the background dielectric constants in these two classes of materials are close in magnitude. This in turn justifies the use of π-electron models for the S-SWNTs, at least for the S-SWNTs with the largest diameter, which dominate the nonlinear absorption.

6 Summary

Even though this field of carbon-nanotube research has been in existence for only a few years, progress in studies of carrier and exciton dynamics with ultrafast spectroscopy has been both rapid and fascinating. Application of TRPE, time-resolved fluorescence and femtosecond transient absorption spectroscopy has enabled elucidation in real time of the el–ph interactions in metallic tubes, and exciton relaxation processes and the underlying physical mechanisms in semiconducting SWNTs. It is now clear that excitation of semiconducting SWNTs with intense ∼100 fs laser pulses leads to dynamics dominated by a remarkable exciton–exciton annihilation process. Studies

employing low excitation intensity allow the timescales of the intersubband and radiative relaxation processes to be determined, along with the intrinsic spectral and dynamical properties, and the profound extrinsic effects of tube environment and temperature.

On the other hand, there are still significant inconsistencies and/or discrepancies between the results and their interpretations reported by different laboratories, which require further experimental and theoretical studies. Besides implementation of more sophisticated spectroscopic techniques, we believe that it is crucial to have samples with well-characterized purities and distribution of tube lengths. This will enable more precise quantification of the level of excitation intensity used for experiments. Another, perhaps equally important, area to explore via controlled studies concerns the potential effects arising from defects and/or unintentional doping during synthesis or post-growth processing.

We envision the emergence of several new research directions in the near future. These will include direct assessment of exciton coherence and relevant dephasing timescales, elucidation of the role of phonon and dark excitonic states in the exciton relaxation processes, quantification of exciton dissociation and discrimination of intrinsic dynamical processes from those induced by external factors. These new studies will involve time-resolved mid-infrared, terahertz, two-photon and 2D electronic spectroscopies. Besides these ensemble studies, time-resolved single-tube spectroscopy with various time-resolution and detection sensitivities will be also increasingly exploited. It is likely that the level of research activity in this field will continue to increase.

Acknowledgements

The work at Berkeley was supported by the NSF. Y.-Z. Ma thanks M. W. Graham for help with LaTeX, Drs. G. Rumbles, Libai Huang and T. D. Krauss for providing eps files of Figs. 4 and 11. L. Valkunas acknowledges the Lithuanian Science and Studies Foundation. T. Hertel acknowledges support by the NSF under grants #DMR0606505 and #DGE0333392 and by the Petroleum Research Fund under grant #PRF 44479-AC10. Z. V. Vardeny wishes to acknowledge Drs. O. Korovyanko and C.-X. Sheng for the transient absorption measurements, Prof. Baughman for the SWNT samples, and Prof. S. Mazumdar for fruitful discussions.

References

[1] C. Rullière (Ed.): *Femtosecond Laser Pulses: Principles and Experiments*, 2nd ed. (Springer, New York 2005) please provide place of printing for [1]. 322, 347

[2] J.-C. Diels, W. Rudolph: *Ultrashort Laser Pulse Phenomena* (Academic Press, San Diego, New York 1996) 322

[3] H. van Amerongen, R. van Grondelle: Transient absorption spectroscopy in study of processes and dynamics in biology, Method. Enzymol. **246**, 201–226 (1995) 322
[4] R. Jimenez, G. R. Fleming: Ultrafast spectroscopy of photosynthetic systems, in J. Amesz, A. J. Hoff (Eds.): *Biophysical Techniques in Photosynthesis* (Kluwer, Dordrecht 1996) pp. 63–73 322, 324
[5] Y.-Z. Ma, L. Valkunas, S. L. Dexheimer, G. R. Fleming: Ultrafast exciton dynamics in semiconducting single-walled carbon nanotubes, Mol. Phys. **104**, 1179–1189 (2006) 322, 329
[6] H. Petek, S. Ogawa: Femtosecond time-resolved two-photon photoemission studies of electron dynamics in metals, Prog. Surf. Sci. **56**, 239–310 (1998) 324
[7] T. Hertel, R. Fasel, G. Moos: Charge-carrier dynamics in single-walled carbon nanotube bundles: A time-domain study, Appl. Phys. A **75**, 449–465 (2002) 324, 328
[8] M. Bauer: Femtosecond ultraviolet photoelectron spectroscopy of ultrafast surface processes, J. Phys. D Appl. Phys. **38**, R253–R267 (2005) 324
[9] M. Wolf: Femtosecond dynamics of electronic excitations at metal surfaces, Surf. Sci. **377**, 343–349 (1997) 324
[10] P. M. Echenique, R. Berndt, E. V. Chulkov, T. H. Fausterd, A. Goldmann, U. Höfer: Decay of electronic excitations at metal surfaces, Surf. Sci. Rep. **52**, 219–317 (2004) 324
[11] R. W. Schoenlein, W. Z. Lin, J. G. Fujimoto, G. L. Eesley: Femtosecond studies of nonequilibrium electronic processes in metals, Phys. Rev. Lett. **58**, 1680–1683 (1987) 324
[12] J. Shah: *Ultrafast Spectroscopy of Semiconductors and Semiconductor Nanostructures*, 2nd ed., Springer series in solid-state sciences (Springer, Berlin, Heidelberg 1999) 324, 329
[13] M. A. Kahlow, W. Jarzeba, T. P. DuBruil, P. F. Barbara: Ultrafast emission spectroscopy in the ultraviolet by time-gated upconversion, Rev. Sci. Instrum. **59**, 1098–1109 (1988) 324
[14] J. Shah: Ultrafast luminescence spectroscopy using sum frequency generation, IEEE J. Quantum Electron. **24**, 276–288 (1988) 324
[15] F. Wang, G. Dukovic, L. E. Brus, T. F. Heinz: Time-resolved fluorescence of carbon nanotubes and its implication for radiative lifetimes, Phys. Rev. Lett. **92**, 177401 (2004) 324, 329, 331
[16] D. V. O'Connor, D. Phillips: *Time-Correlated Single Photon Counting* (Academic Press, London, Orlando 1984) 324
[17] A. Hagen, M. Steiner, M. B. Raschke, C. Lienau, T. Hertel, H. Qian, A. J. Meixner, A. Hartschuh: Exponential decay lifetimes of excitons in individual single-walled carbon nanotubes, Phys. Rev. Lett. **95**, 197401 (2005) 324, 330, 334, 335
[18] G. R. Fleming: *Chemical Applications of Ultrafast Spectroscopy*, The International series of monographs on chemistry (Oxford University Press, New York 1985) 324
[19] J. D. Jackson: *Classical Electrodynamics*, 3rd ed. (Wiley, New York 1999) 324
[20] N. Bloembergen: *Nonlinear Optics* (Benjamin, New York 1965) 324
[21] M. Born, E. Wolf: *Principles of Optics*, 6th ed. (Pergamon, Oxford 1980) 324

[22] S. Mukamel: *Principles of Nonlinear Optical Spectroscopy* (Oxford University Press, New York 1995) 325, 326
[23] K. Blum: *Density Matrix Theory and Applications* (Plenum, New York 1981) 325
[24] M. Cho, H. M. Vaswani, T. Brixner, J. Stenger, G. R. Fleming: Exciton analysis in 2D electronic spectroscopy, J. Phys. Chem. B **109**, 10542–10556 (2005) 326
[25] T. Joo, Y. Jia, J.-Y. Yu., M. J. Lang, G. R. Fleming: Third-order nonlinear time domain probes of solvation dynamics, J. Chem. Phys. **104**, 6089–6108 (1996) 326
[26] J. E. Fischer, H. Dai, A. Thess, R. Lee, N. M. Hanjani, D. L. Dehaas, R. E. Smalley: Metallic resistivity in crystalline ropes of single-wall carbon nanotubes, Phys. Rev. B **55**, R4921–R4924 (1997) 327
[27] J. Hone, I. Ellwood, M. Muno, A. Mizel, M. L. Cohen, A. Zettl, A. G. Rinzler, R. E. Smalley: Thermoelectric power of single-walled carbon nanotubes, Phys. Rev. Lett. **80**, 1042–1045 (1998) 327
[28] L. X. Benedict, V. H. Crespi, S. G. Louie, M. L. Cohen: Static conductivity and superconductivity of carbon nanotubes: Relations between tubes and sheets, Phys. Rev. B **52**, 14935–14940 (1995) 327
[29] J. W. Mintmire, B. I. Dunlap, C. T. White: Are fullerene tubules metallic?, Phys. Rev. Lett. **68**, 631–634 (1992) 327
[30] R. A. Jishi, M. S. Dresselhaus, G. Dresselhaus: Electron–phonon coupling and the electrical conductivity of fullerene nanotubules, Phys. Rev. B **48**, 11385–11389 (1993) 327
[31] S. Frank, P. Poncharal, Z. L. Wang, W. A. de Heer: Carbon nanotube quantum resistors, Science **280**, 1744–1746 (1998) 327, 328
[32] P. Avouris, T. Hertel, R. Martel, T. Schmidt, H. R. Shea, R. E. Walkup: Carbon nanotubes: Nanomechanics, manipulation, and electronic devices, Appl. Surf. Sci. **141**, 201–209 (1999) 327
[33] T. Hertel, G. Moos: Electron–phonon interaction in single-wall carbon nanotubes: A time-domain study, Phys. Rev. Lett. **84**, 5002–5005 (2000) 327, 328
[34] S. I. Anisimov, B. L. Kapeliov, T. L. Perel'man: Electron-emission from surface of metals induced by ultrashort laser pulses, Zh. Eksp. Teor. Fiz. **66**, 776–781 (1974) 327
[35] G. Moos, R. Fasel, T. Hertel: Temperature dependence of electron to lattice energy-transfer in single-wall carbon nanotube bundles, J. Nanosci. Nanotechnol. **3**, 145–149 (2003) 327, 328
[36] P. B. Allen: Theory of thermal relaxation of electrons in metals, Phys. Rev. Lett. **59**, 1460–1463 (1987) 327
[37] T. Durkop, S. A. Getty, E. Cobas, M. S. Fuhrer: Extraordinary mobility in semiconducting carbon nanotubes, Nano Lett. **4**, 35–39 (2004) 328
[38] G. Dukovic, F. Wang, D. Song, M. Y. Sfeir, T. F. Heinz, L. E. Brus: Structural dependence of excitonic optical transitions and band-gap energies in carbon nanotubes, Nano Lett. **5**, 2314–2318 (2005) 328
[39] P. Avouris, J. Chen, M. Freitag, V. Perebeinos, J. C. Tsang: Carbon nanotube optoelectronics, Phys. Stat. Sol. B **243**, 3197–3203 (2006) 328, 329

[40] M. J. O'Connell, S. M. Bachilo, C. B. Huffman, V. C. Moore, M. S. Strano, E. H. Haroz, K. L. Rialon, P. J. Boul, W. H. Noon, C. Kittrell, J. P. Ma, R. H. Hauge, R. B. Weisman, R. E. Smalley: Band gap fluorescence from individual single-walled carbon nanotubes, Science **297**, 593–596 (2002) 329, 331

[41] Y. Oyama, R. Saito, K. Sato, J. Jiang, G. Samsonidze, A. Grüneis, Y. Miyauchi, S. Maruyama, A. Jorio, G. Dresselhaus, M. S. Dresselhaus: Photoluminescence intensity of single-wall carbon nanotubes, Carbon **44**, 873–879 (2006) 329, 331

[42] Y.-Z. Ma, C. D. Spataru, L. Valkunas, S. G. Louie, G. R. Fleming: Spectroscopy of zigzag single-walled carbon nanotubes: Comparing femtosecond transient absorption spectra with ab initio calculations, Phys. Rev. B **74**, 085402 (2006) 329

[43] M. Jones, C. Engtrakul, W. K. Metzger, R. J. Ellingson, A. J. Nozik, M. J. Heben, G. Rumbles: Analysis of photoluminescence from solubilized single-walled carbon nanotubes, Phys. Rev. B **71**, 115426 (2005) 329, 332, 333

[44] C. D. Spataru, S. Ismail-Beigi, R. B. Capaz, S. G. Louie: Theory and ab initio calculation of radiative lifetime of excitons in semiconducting carbon nanotubes, Phys. Rev. Lett. **95**, 247402 (2005) 329, 332

[45] V. Perebeinos, J. Tersoff, P. Avouris: Radiative lifetime of excitons in carbon nanotubes, Nano Lett. **5**, 2495–2499 (2005) 329, 332, 333

[46] A. Hagen, G. Moos, V. Talalaev, T. Hertel: Electronic structure and dynamics of optically excited single-walled carbon nanotubes, Appl. Phys. A **78**, 1137–1145 (2004) 329, 331

[47] J. Lefebvre, D. G. Austing, J. Bond, P. Finnie: Photoluminescence imaging of suspended single-walled carbon nanotubes, Nano Lett. **6**, 1603–1608 (2006) 329, 332

[48] Y.-Z. Ma, L. Valkunas, S. L. Dexheimer, S. M. Bachilo, G. R. Fleming: Femtosecond spectroscopy of optical excitations in single-walled carbon nanotubes: Evidence for exciton-exciton annihilation, Phys. Rev. Lett. **94**, 157402 (2005) 330, 339

[49] L. Valkunas, Y.-Z. Ma, G. R. Fleming: Exciton-exciton annihilation in single-walled carbon nanotubes, Phys. Rev. B **73**, 115432 (2006) 330, 339, 341, 342, 343

[50] Y.-Z. Ma, J. Stenger, J. Zimmermann, S. M. Bachilo, R. E. Smalley, R. B. Weisman, G. R. Fleming: Ultrafast carrier dynamics in single-walled carbon nanotubes probed by femtosecond spectroscopy, J. Chem. Phys. **120**, 3368–3373 (2004) 330, 338, 339

[51] F. Wang, G. Dukovic, E. Knoesel, L. E. Brus, T. F. Heinz: Observation of rapid Auger recombination in optically excited semiconducting carbon nanotubes, Phys. Rev. B **70**, 241403 (2004) 330, 339, 342

[52] A. V. Barzykin, M. Tachiya: Stochastic models of carrier dynamics in single-walled carbon nanotubes, Phys. Rev. B **72**, 075425 (2005) 330, 342

[53] F. Wang, Y. Wu, M. S. Hybertsen, T. F. Heinz: Auger recombination of excitons in one-dimensional systems, Phys. Rev. B **73**, 245424 (2006) 330, 342

[54] M. F. Islam, D. E. Milkie, C. L. Kane, A. G. Yodh, J. M. Kikkawa: Direct measurement of the polarized optical absorption cross section of single-wall carbon nanotubes, Phys. Rev. Lett. **93**, 037404 (2004) 330

[55] G. Malloci, G. Mulas, C. Joblin: Electronic absorption spectra of PAHs up to vacuum UV – towards a detailed model of interstellar PAH photophysics, Astron. Astrophys. **426**, 105–117 (2004) 330
[56] C. Manzoni, A. Gambetta, E. Menna, M. Meneghetti, G. Lanzani, G. Cerullo: Intersubband exciton relaxation dynamics in single-walled carbon nanotubes, Phys. Rev. Lett. **94**, 207401 (2005) 331
[57] J. Crochet, M. Clemens, T. Hertel: Quantum yield heterogeneities of aqueous single-wall carbon nanotube suspensions, J. Am. Chem. Soc. **129**, 8058–8059 (2007) 331
[58] C.-X. Sheng, Z. V. Vardeny, A. B. Dalton, R. H. Baughman: Exciton dynamics in single-walled nanotubes: Transient photoinduced dichroism and polarized emission, Phys. Rev. B **71**, 125427 (2005) 332
[59] T. Hertel, A. Hagen, V. Talalaev, K. Arnold, F. Hennrich, M. Kappes, S. Rosenthal, J. McBride, H. Ulbricht, E. Flahaut: Spectroscopy of single- and double-wall carbon nanotubes in different environments, Nano Lett. **5**, 511–514 (2005) 332, 333, 334
[60] M. Jones, W. K. Metzger, T. J. McDonald, C. Engtrakul, R. J. Ellingson, G. Rumbles, M. J. Heben: Extrinsic and intrinsic effects on the excited-state kinetics of single-walled carbon nanotubes, Nano Lett. **7**, 300–306 (2007) 332, 333
[61] S. Reich, M. Dworzak, A. Hoffmann, C. Thomsen, M. S. Strano: Excited-state carrier lifetime in single-walled carbon nanotubes, Phys. Rev. B **71**, 033402 (2005) 332, 333
[62] S. Berger, C. Voisin, G. Cassabois, C. Delalande, P. Roussignol, X. Marie: Temperature dependence of exciton recombination in semiconducting single-wall carbon nanotubes, Nano Lett. **7**, 398–402 (2007) 333, 334
[63] G. N. Ostojic, S. Zaric, J. Kono, M. S. Strano, V. C. Moore, R. H. Hauge, R. E. Smalley: Interband recombination dynamics in resonantly excited single-walled carbone nanotubes, Phys. Rev. Lett. **92**, 117402 (2004) 334
[64] Y.-Z. Ma, L. Valkunas, S. M. Bachilo, G. R. Fleming: Temperature effects on femtosecond transient absorption kinetics of semiconducting single-walled carbon nanotubes, Phys. Chem. Chem. Phys. **8**, 5689–5693 (2006) 334
[65] I. B. Mortimer, R. J. Nicholas: Role of bright and dark excitons in the temperature-dependent photoluminescence of carbon nanotubes, Phys. Rev. Lett. **98**, 027404 (2007) 335
[66] Z. P. Zhu, J. Crochet, M. S. Arnold, M. C. Hersam, H. Ulbricht, D. Resasco, T. Hertel: Pump-probe spectroscopy of exciton dynamics in (6,5) carbon nanotubes, J. Phys. Chem. C **111**, 3831–3835 (2007) 336, 337, 345
[67] G. N. Ostojic, S. Zaric, J. Kono, V. C. Moore, R. H. Hauge, R. E. Smalley: Stability of high-density one-dimensional excitons in carbon nanotubes under high laser excitation, Phys. Rev. Lett. **94**, 097401 (2005) 337
[68] O. J. Korovyanko, C.-X. Sheng, Z. V. Vardeny, A. B. Dalton, R. H. Baughman: Ultrafast spectroscopy of excitons in single-walled carbon nanotubes, Phys. Rev. Lett. **92**, 017403 (2004) 337, 340
[69] Z. Zhu, M. S. Arnold, M. C. Hersam, T. Hertel: unpublished 337
[70] L. Valkunas, G. Trinkunas, V. Liuolia: Exciton annihilation in molecular aggregates, in D. L. Andrews, A. A. Demidov (Eds.): *Resonance Energy Transfer* (Wiley, Chichester 1999) pp. 244–307 338, 342

[71] H. van Amerongen, L. Valkunas, R. van Grondelle: *Photosynthetic Excitons* (World Scientific, Singapore, New Jersey, London, Hongkong 2000) 338, 342
[72] S. G. Chou, M. F. DeCamp, J. Jiang, G. G. Samsonidze, E. B. Barros, F. Plentz, A. Jorio, M. Zheng, G. B. Onoa, E. D. Semke, A. Tokmakoff, R. Saito, G. Dresselhaus, M. S. Dresselhaus: Phonon-assisted exciton relaxation dynamics for a (6,5)-enriched DNA-wrapped single-walled carbon nanotube sample, Phys. Rev. B **72**, 195415 (2005) 340
[73] L. Huang, T. D. Krauss: Quantized bimolecular Auger recombination of excitons in single-walled carbon nanotubes, Phys. Rev. Lett. **96**, 057407 (2006) 340, 342
[74] R. M. Russo, E. J. Mele, C. L. Kane, I. V. Rubtsov, M. J. Therien, D. E. Luzzi: One-dimensional diffusion-limited relaxation of photoexcitations in suspensions of single-walled carbon nanotubes, Phys. Rev. B **74**, 041405(R) (2006) 340, 343
[75] V. I. Klimov, A. A. Mikhailovsky, D. W. McBranch, C. A. Leatherdale, M. G. Bawendi: Quantization of multiparticle Auger rates in semiconductor quantum dots, Science **287**, 1011–1013 (2000) 340, 343
[76] M. A. Stevens, C. Silva, D. M. Russell, R. H. Friend: Exciton dissociation mechanisms in the polymeric semiconductors poly(9,9-dioctylfluorene) and poly(9,9-dioctylfluorene-co-benzothiadiazole), Phys. Rev. B **63**, 165213 (2001) 343
[77] Y.-Z. Ma, L. Valkunas, S. M. Bachilo, G. R. Fleming: Exciton binding energy in semiconducting single-walled carbon nanotubes, J. Phys. Chem. B **109**, 15671–15674 (2005) 343, 346
[78] M. Ghanassi, M. C. Schanne-Klein, F. Hache, A. I. Ekimov, D. Ricard, C. Flytzanis: Time-resolved measurements of carrier recombination in experimental semiconductor-doped glasses: Confirmation of the role of Auger recombination, Appl. Phys. Lett. **62**, 78–80 (1993) 343
[79] H. Htoon, J. A. Hollingsworth, R. Dickerson, V. I. Klimov: Effect of zero- to one-dimensional transformation on multiparticle Auger recombination in semiconductor quantum rods, Phys. Rev. Lett. **91**, 227401 (2003) 343
[80] F. Wang, G. Dukovic, L. E. Brus, T. F. Heinz: The optical resonances in carbon nanotubes arise from excitons, Science **308**, 838–841 (2005) 343, 346
[81] J. Maultzsch, R. Pomraenke, S. Reich, E. Chang, D. Prezzi, A. Ruini, E. Molinari, M. S. Strano, C. Thomsen, C. Lienau: Exciton binding energies in carbon nanotubes from two-photon photoluminescence, Phys. Rev. B **72**, 241402(R) (2005) 343, 346
[82] S. N. Dixit, D. Guo, S. Mazumdar: Essential-states mechanism of optical nonlinearity in π-conjugated polymers, Phys. Rev. B **43**, 6781–6784 (1991) 344
[83] S. V. Frolov, Z. Bao, M. Wohlgenannt, Z. V. Vardeny: Excited-state relaxation in π-conjugated polymers, Phys. Rev. B **65**, 205209 (2001) 344
[84] H. Zhao, S. Mazumdar, C.-X. Sheng, M. Tong, Z. V. Vardeny: Photophysics of excitons in quasi-one-dimensional organic semiconductors: Single-walled carbon nanotubes and π-conjugated polymers, Phys. Rev. B **73**, 075403 (2006) 344, 345, 346

Index

Rayleigh Scattering Spectroscopy

Tony F. Heinz

Departments of Physics and Electrical Engineering,
Columbia University, New York, NY 10027, USA,
tony.heinz@columbia.edu

Abstract. Single-wall carbon nanotubes can be probed optically by elastic light scattering. This effect forms the basis of a technique, termed Rayleigh scattering spectroscopy, for the study of individual nanotubes. Spectroscopic information on the electronic transitions of both semiconducting and metallic nanotubes is obtained by measuring the elastic scattering cross section as a function of photon energy. In this contribution, we describe the basic principles of the Rayleigh scattering method and its experimental implementation for the rapid and precise measurement of nanotube electronic spectra. The capabilities of the technique are illustrated with several examples of its application. The method offers a natural approach to investigate polarization effects and the persistence of the chiral structure of an individual nanotube, as well as a means to probe nanotube–nanotube interactions. Rayleigh scattering spectroscopy is also well suited for combination with other experimental techniques for the characterization of individual nanotubes. This possibility is illustrated by measurements of the Rayleigh spectra of individual nanotubes with chiral indices independently determined by electron-diffraction measurements.

1 Introduction

The ability to probe the properties of an individual single-wall carbon nanotube (SWNT) using optical spectroscopy is attractive for many investigations. Measurement at the individual nanotube level yields great simplification of the optical spectra. Unlike the situation for ensemble measurements, one is then dealing with just a single, defined nanotube structure. Further, the sensitivity of carbon nanotubes to their local environment can be examined with increased precision when probing individual carbon nanotubes. As discussed elsewhere in this volume (see the contribution by Hartschuh), the use of near-field optical techniques can further enhance this sensitivity to the local conditions by providing improvement in spatial resolution compared with that of conventional far-field techniques. Optical characterization of individual nanotubes is also of great value in connecting spectroscopic data with information obtained by complementary characterization techniques, such as electron diffraction and transport measurements, that must necessarily be carried out on individual structures.

These compelling motivations for optical spectroscopy at the level of single nanotubes have stimulated researchers to develop several experimental ap-

A. Jorio, G. Dresselhaus, M. S. Dresselhaus (Eds.): Carbon Nanotubes,
Topics Appl. Physics **111**, 353–369 (2008)

proaches that provide the required sensitivity. Two purely optical techniques are based on inelastic scattering of photons: photoluminescence spectroscopy (see the contribution by Lefebvre et al. and [1]) and Raman spectroscopy (see the contribution by Saito et al. and [2, 3]). In the former, light is emitted by the lowest-lying excitonic state and the method is limited to semiconducting nanotubes. Using photoluminescence excitation (PLE) spectroscopy, we can also determine the energies of excited states. The Raman technique provides information on the phonon structure of nanotubes. With the aid of enhancement by electronic resonances, resonance Raman scattering (RRS) can be applied to probe both individual semiconducting and metallic nanotubes. For fixed excitation photon energy, the spectral shifts between the incident and scattered photons provide a map of the accessible vibrational energies. By tuning the incident energy, Raman excitation spectroscopy can provide information about the location of electronic resonances. Both of these methods are extensively discussed elsewhere in the volume. In addition to these purely optical techniques, researchers have recently demonstrated the possibility of obtaining information about the electronic transitions in semiconducting nanotubes by means of the photocurrent spectroscopy for an optically excited nanotube under an electrical bias [4, 5].

In this contribution, we describe an additional experimental approach that has recently been introduced for the spectroscopy of individual single-wall carbon nanotubes [6–9]. The method consists of measurement of the spectral dependence of the cross section for *elastic* light scattering. Since the nanotube is an object much smaller than the wavelength of light, this method has been termed Rayleigh scattering spectroscopy. The advantages of the approach include its applicability to both semiconducting and metallic nanotubes, the simple interpretation of the information that the method yields, and the high data collection rate that it can provide at the individual nanotube level. The principal limitation of the method concerns the influence of background scattering and the associated restrictions on the experimental geometry. Through the use of freely suspended nanotubes, this complication can be eliminated.

2 Elastic Light Scattering

From a fundamental perspective, Rayleigh scattering relies on the same basic optical response as the absorption process, i.e., the linear optical susceptibility χ or the dielectric function ϵ of the nanotube. However, since the optical absorption of an individual nanotube is very weak ($< 10^{-4}$ for a tightly focused laser beam), it is more convenient to measure the response in a scattering or dark-field geometry. We can consider the interaction of the nanotube with the incident laser beam as giving rise to an induced dipole moment oscillating at the optical frequency. The radiation emitted in the forward direction interferes with the transmitted optical beam. This corresponds to the absorp-

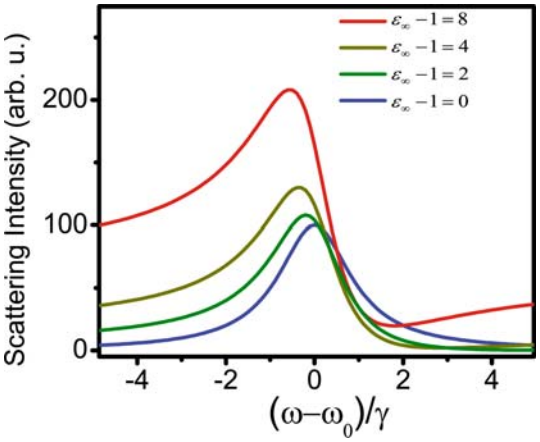

Fig. 1. Simulated lineshapes in a Rayleigh scattering measurement, described by $|\epsilon(\omega) - 1|^2$, for a Lorentzian absorption feature. The curves correspond to differing levels of a frequency-independent nonresonant contribution to $\Re(\epsilon)$. Here $(\omega - \omega_0)/\gamma$ represents the detuning from the resonance at ω_0 in units of the Lorentzian half-width γ. The absorption lineshape follows the Rayleigh spectrum for $\epsilon_\infty = 1$

tion process. The strength of the absorption is determined by the imaginary part of the dielectric function ϵ, since only this phase of the emitted radiation interferes with the transmitted beam.

For Rayleigh scattering, we detect this same dipole emission from the nanotube, but in a background-free direction. Consequently, the scattering signal, which varies as the square of the radiated electric field, scales quadratically with the magnitude of the induced dipole moment, i.e., as $|\epsilon - 1|^2$, where ϵ is the effective dielectric function of the nanotube. By recording the strength of Rayleigh scattering as a function of the frequency of the optical radiation, we obtain a spectrum that reflects the behavior of ϵ as a function of the photon energy. Since electronic transitions in the nanotubes give rise to strong peaks in the dielectric function ϵ, Rayleigh scattering permits ready identification of the electronic transitions in the system.

Before turning to issues involving the signal strength and radiation behavior, we wish to make a brief note about the expected lineshape of features in Rayleigh scattering spectroscopy. Unlike absorption measurements, in the scattering configuration the real part of the dielectric function also contributes to the signal strength. While this distinction is of no particular fundamental significance, it is important to bear in mind in considering experimental lineshapes. The influence of the real part of the dielectric function can lead to differences in the shape and center of resonances in the Rayleigh spectrum compared with those in an absorption measurement (or any other measurement that scales with absorption, such as photoluminescence excitation spectroscopy). We illustrate this effect in Fig. 1. The figure shows a series

of simulated Rayleigh spectra for a Lorentzian absorption line, but with the inclusion of differing nonresonant (spectrally flat) contributions to the real part of dielectric function ϵ. Such a contribution is present because of the off-resonance electronic transitions. As can be seen from the figure, despite a fixed behavior for the resonant transitions, there can be significant changes in the observed lineshape, as well as a modest shift in the frequency of the peak of the feature. This effect can easily be incorporated into modeling of the spectral line shapes, which is necessary for the most precise determination of the line center of a given transition.

To be more quantitative about the radiation process, we describe the elastic light scattering in terms of the interaction of a plane electromagnetic wave with a nanotube. The nanotube is modeled as a long cylinder of diameter d and a relative dielectric function $\epsilon(\omega)$, where ω is the angular frequency of the light. The elastic scattering cross section per unit length is then given by [10]

$$\sigma_{\mathrm{el}}(\omega) = (\pi^2/64)(\omega d/c)^3 |\epsilon(\omega) - 1|^2 d\,, \tag{1}$$

where c denotes the speed of light. We assume here that the polarization of the pump radiation is parallel to the axis of the nanotube and that we are detecting radiation also polarized parallel to the axis. Under these conditions, the emission is isotropic with respect to the azimuthal direction and the cross section includes emission at all angles.

From the expression above, we see that only a relatively low laser power is needed to obtain an adequate elastic scattering rate from an individual nanotube. If we assume, for example, an effective dielectric function of $\epsilon = 6$ for the response of a nanotube of diameter $d = 2\,\mathrm{nm}$, we find for Rayleigh scattering of light of wavelength of 500 nm a value of $\sigma_{\mathrm{el}} = 1.2 \times 10^{-7}\,\mu\mathrm{m}$. For a source with a power of, say, $100\,\mu\mathrm{W}$ focused to a width of $1\,\mu\mathrm{m}$, we then produce scattered photons at a rate of $3 \times 10^7\,\mathrm{s}^{-1}$. Allowing for an overall collection and detector quantum efficiency of 10^{-2}, this yields a count rate of $\sim 10^5$–$10^6\,\mathrm{s}^{-1}$. Such a signal level clearly permits rapid data-acquisition for scattering by an individual SWNT.

3 Experimental Technique

Figure 2 shows a schematic representation of the dark-field configuration appropriate for Rayleigh scattering spectroscopy. To optimize the signal, one naturally wishes to achieve both tight focusing of the pump laser beam and collection of a large solid angle of the elastically scattered light. This can be accomplished with a pair of matched microscope objectives, with the detection direction arranged to exclude any transmitted laser radiation.

Two distinctive features were incorporated into the initial experimental demonstration of the Rayleigh technique that allowed it to provide high-quality spectra with very short data-acquisition times [6]. The first was

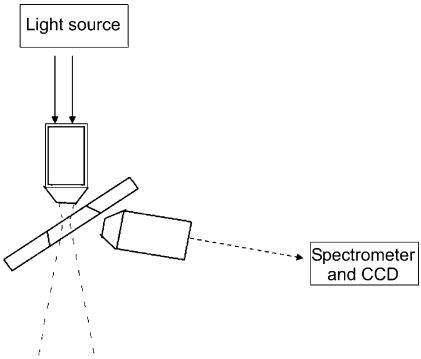

Fig. 2. Schematic diagram for a Rayleigh scattering measurement. Microscope objectives focus the incident light on a suspended nanotube and collect the radiation scattered light. Using a supercontinuum source, we can detect different wavelengths simultaneously with a spectrometer and multichannel (CCD) camera

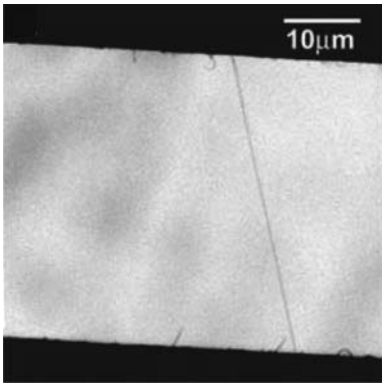

Fig. 3. Electron micrograph of an individual suspended SWNT. The sample is prepared by CVD using a substrate with a slit etched in it. Typical slit widths are tens of micrometers and slit lengths are up to 1 mm (after [6])

probing freely suspended nanotubes, an arrangement for which there was no background scattering of light; the second was the use of a laser-based supercontinuum source that permitted spectra to be collected in parallel over a wide range of wavelengths.

Samples of freely suspended nanotubes for the Rayleigh scattering measurements are prepared by means of chemical vapor deposition (CVD) on a silicon substrate into which a completely open slit has been etched by standard microfabrication techniques. Figure 3 shows an electron microscope image of an individual suspended SWNT crossing such a slit. The width of the slit can be varied depending on experimental requirements, but is typically chosen in the range of tens of micrometers to ensure that there is no appreciable scattering from accidental illumination of the substrate by stray pump light. The length of the slit (perpendicular to the nanotubes) can be as great as 1 mm, so that a single substrate can provide many individual SWNTs for study. By scanning the position of the sample relative to the probe beam, one can access different nanotubes or a given nanotube at different positions along its axis.

The preparation of the samples does not require any delicate manipulation of the nanotubes to make them bridge the slit. In the CVD growth, one simply places an appropriate metal catalyst for nanotube growth on the substrate at a distance from the slit. The nanotubes are then grown with the reactor gas flow directed from the catalyst towards the slit. As the nanotubes grow, they follow the reactor gas stream, remaining above the substrate. When the gas flow ceases, the nanotubes fall onto the substrate and, if sufficiently long, spontaneously cross the slit. Samples have been prepared using several distinct catalysts, such as Fe and Co thin films, and various feedstock gases, such as ethanol and methane [11, 12]. Adjustments of the feedstock gases and catalyst are made to ensure that the nanotubes are sufficiently sparse in the region of the slit so that only one SWNT will normally fall within the spot size ($\sim 1\,\mu\mathrm{m}$) of the focused optical pump radiation. That this condition is met can be verified by the characteristics of the observed Rayleigh spectrum. One can thus perform single-nanotube spectroscopy without the complexity of near-field optical techniques. Of course, the spatial resolution along the nanotube is limited to the size of the focused pump beam. As discussed elsewhere in this volume (see the contribution by Hartschuh), near-field methods can significantly improve upon this longitudinal resolution.

The second experimental feature that facilitates collection of Rayleigh scattering spectra is the use of an optimized light source for the measurement. To obtain spectroscopic information from Rayleigh scattering, we must scan the wavelength of the light undergoing scattering. This can certainly be accomplished by means of a tunable laser source, as is done for photoluminescence excitation spectroscopy or Raman excitation spectroscopy at the single-nanotube level. This process is, however, relatively slow and somewhat tedious when one wishes to cover a broad spectral range. Since the power needed to observe the elastically scattered light is low, researchers have shown the possibility of making use of a broadband laser-based source for the simultaneous measurement of Rayleigh scattering over a range of wavelengths. With an appropriate high-brightness broadband source, one can use parallel, multichannel detection to obtain the entire (excitation) spectrum at once. It should be noted that this method implicitly assumes that the strength of elastically scattered light dominates all inelastic contributions. This is a very good approximation for the concurrent Raman scattering process, since the vibrational coupling is weak and Raman scattering is inefficient compared with elastic light scattering. The only condition under which one must exercise some care would be for detection in the vicinity of the E_{11} transition in semiconducting nanotubes where fluorescent emission may be strong enough to compete with elastic scattering.

Bright continuum radiation with a spectrum extending from photon energies below 1 eV to approximately 3 eV can be obtained by passing femtosecond mode-locked laser pulses through an optimized nonlinear fiber [13]. Such sources may either be constructed in the laboratory from standard mode-locked oscillators or purchased as integrated commercial units. In either case,

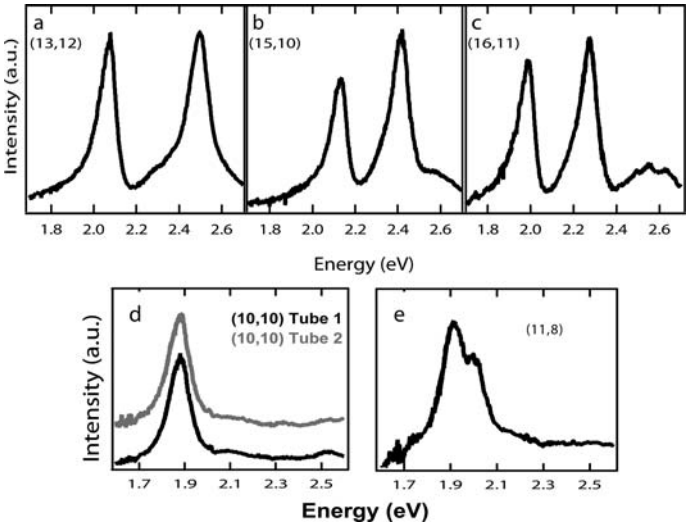

Fig. 4. Experimental Rayleigh scattering spectra for individual SWNTs of the specified chiral indices. The nanotubes (**a**–**c**) are different semiconducting structures; those of (**d**) and (**e**) are metallic nanotubes. The two sets of data for the (10,10) structure (displaced for clarity) correspond to completely independent measurements of different nanotubes. The chiral indices of all the nanotubes were determined independently by electron diffraction (after [7])

the radiation emerges from an optical fiber, which facilities its efficient focusing by a microscope objective. A suitable level of optical radiation for the Rayleigh spectroscopy measurements is typically a fraction of a mW of optical power. Such focused continuum radiation provides a reasonable level for the Rayleigh scattering signal without significant heating of the nanotube. As for the precision of the measured spectra, this is controlled entirely by the arrangement of the multichannel-detection scheme, i.e., by the dispersion of the spectrometer and the number of channels of the detector. For a suitable choice of grating dispersion, a spectral resolution of a few meV can be achieved over a broad energy range using a standard CCD camera. This level of performance fully resolves the features of electronic transitions of SWNTs, particularly for the higher E_{nn} transitions, which exhibit increased widths compared with the E_{11} transition.

Figure 4 displays results of Rayleigh scattering from several individual semiconducting and metallic SWNTs. The observed transitions are the E_{33}^S and E_{44}^S for the semiconducting nanotubes and the E_{11}^M for the metallic nanotubes. Note that there are two separate traces in Fig. 4d for (10,10) nanotubes. These are data from measurements of different individual SWNTs. The high level of reproducibility is apparent.

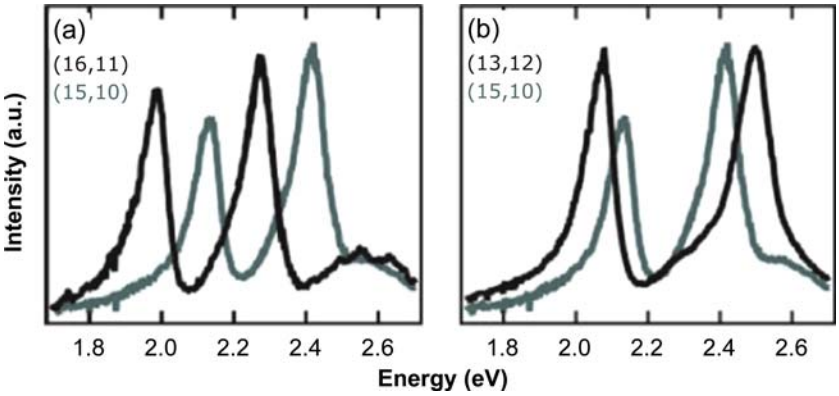

Fig. 5. Comparison of Rayleigh scattering spectra of similar semiconducting nanotubes from the data in Figs. 4a–c. The peaks correspond to the E_{33}^S and E_{44}^S transitions. The comparison in (**a**) corresponds to two nanotubes of the same $(2n + m)$ mod 3 type, but different diameter; the comparison in (**b**) involves two nanotubes of different type, but similar diameter (after [7])

4 Application of the Technique

Despite the relatively recent introduction of the method of Rayleigh scattering spectroscopy, the approach has already provided several interesting results about the optical properties and interactions of SWNTs [6–9]. Here, we review some representative studies to illustrate the possibilities provided by this method for single nanotube spectroscopy.

4.1 Electronic Transitions of Nanotubes of Independently Determined Structure

Figure 4 illustrates the capability of Rayleigh spectroscopy to provide high-quality spectra of individual SWNTs. The spectra are taken under favorable conditions in terms of having nanotubes unaffected by their environment, since the nanotubes are well isolated from one another and suspended in air. The spectra of the electronic transitions thus provide an attractive point for a rigorous comparison with theory. To do so, however, we have to overcome a fundamental limitation in a purely optical measurement, namely, that we do not have direct and independent knowledge of the structure of the material under study. Once appropriate assignments of spectroscopic features have been made, optical measurements can, of course, yield such structural information. Such careful assignments have been made of the optical transitions in ensemble samples containing nanotubes of various chiral indices using predicted theoretical trends and a wealth of experimental data [14].

Since accurate calculations of the transition energies, particularly for large-diameter or low-symmetry nanotubes, remain difficult, there is a mo-

tivation to obtain transition energies of individual nanotubes whose structure has been determined independently of any spectroscopic analysis. This goal can be met by combining the Rayleigh scattering data with direct structural analysis by electron diffraction at the individual nanotube level [7]. The diffraction data provide an unambiguous structural assignment of individual nanotubes with optical spectra previously measured by Rayleigh scattering spectroscopy. In Fig. 4, the indicated chiral indices have been obtained from such analysis by electron diffraction. We note that an analogous study was recently performed in which electron diffraction of individual carbon nanotubes was combined with single-nanotube Raman spectroscopy to obtain information on the frequencies of Raman features for nanotubes of independently defined structure [15].

A detailed comparison of the Rayleigh spectra for semiconducting nanotubes in Figs. 4a–c is instructive. In Fig. 5, we show the Rayleigh spectrum of the (15,10) nanotube in comparison with the (16,11) nanotube in the left panel and with the (13,12) nanotube in the right panel.

For the case of the (16,11) nanotube, we have a structure with the same $(2n+m)$ mod $3 = 1$ value (type I) as the (15,10) reference nanotube. The diameter of the (16,11) nanotube of 1.83 nm is 0.12 nm greater than the 1.71 nm diameter of the (15,10) nanotube. We consequently see a significant shift (of about 150 meV) towards lower energies in the transitions of the larger (16,11) nanotube. The ratio of the E_{44}^S to E_{33}^S transition energies is, however, quite similar – 1.150 for the larger (16,11) nanotube versus 1.135 for the smaller (15,10) nanotube – for these two nanotubes of the same type.

A comparison of the (13,12) nanotube with the (15,10) reference nanotube shows a different behavior. In this case, the average energies of the two transitions of the (15,10) and (13,12) nanotubes are very similar, differing only by ~ 10 meV. This might be anticipated given the nearly identical respective diameters of 1.71 nm and 1.70 nm for the two nanotubes. For this pair of nanotubes, however, the (13,12) nanotube is a type II ($(2n+m)$ mod $3 = 2$) structure, while the reference (15,10) nanotube is type I. This difference is manifested in dissimilar ratios of the E_{44}^S to E_{33}^S transition energies: 1.206 versus 1.135 for the (13,12) and (15,10) chiral indices, respectively. While the numerical values differ from those predicted by simple tight-binding models [16], the trend is exactly as predicted for nanotubes of type I and type II structure. Detailed examination of the Rayleigh data also permitted confirmation of the predicted trends for different chiral angles [7].

4.2 Polarization Dependence of Nanotube Electronic Transitions

In any ensemble optical measurement of nanotubes, the measurement necessarily averages over a variety of angular orientations of the nanotube. This severely complicates the study of the polarization properties of the optical transitions, which can be addressed only through achieving partial orientation of the nanotubes [17] or through measurements involving two distinct

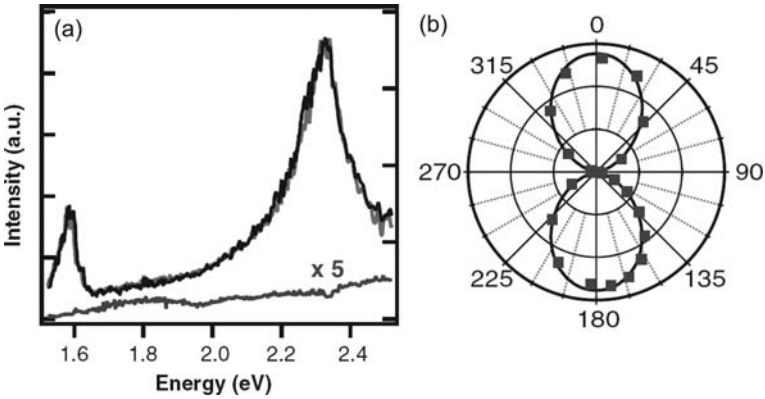

Fig. 6. Polarization effects observed in the Rayleigh spectrum of an individual SWNT. The polar plot (**b**) shows the nearly dipolar variation of the Rayleigh scattering with the polarization of the probe beam. The spectrum (**a**) displays the response parallel (large) and perpendicular (small) to the nanotube axis. The parallel spectrum is comprised of two traces, obtained at a separation of 30 μm from one another along the nanotube axis, a result indicating that no structural change occurs (after [6])

electronic transitions [18]. At the single-nanotube level, these complications disappear. Figure 6 presents an example of the strong polarization effects for the optical transitions in SWNTs manifested in Rayleigh scattering spectra. The local-field or "antenna" effect strongly reduces the response when the electric-field vector of the optical radiation lies perpendicular to the nanotube axis [19]. Indeed, the response is essentially that of a dipole ($\cos^2\theta$) intensity pattern, as shown in Fig. 6b. Close inspection of the spectra for excitation along and perpendicular to the nanotube axis reveals, however, the existence of a weak, but measurable response from the perpendicular configuration. This response arises from electronic transitions of the type $E_{n,n-1}$ and $E_{n-1,n}$ that contribute to the optical response perpendicular to the nanotube axis (see the contribution by Ando and [18]). The electromagnetic screening mentioned above, however, sharply reduces the observed strength of these transitions, particularly when an electronic resonance is approached.

4.3 Structural Stability Along the Nanotube Axis

The ability to grow long nanotubes by chemical vapor deposition combined with the possibility of rapid characterization of the electronic transitions (and, hence, physical structure) of the nanotubes permits study of the structural stability of the nanotube. Analysis of many CVD-grown nanotubes has shown that changes in chiral index are infrequent, with most nanotubes of lengths of tens of micrometers exhibiting no change in structure along the length of the tube. A representative set of data is displayed in Fig. 6a. Here,

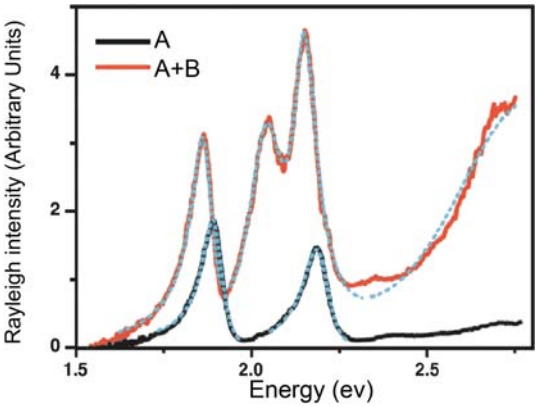

Fig. 7. Rayleigh spectra of an isolated nanotube A and of a bundle consisting of nanotube A and a second nanotube (A+B). The peaks of nanotube A can be seen in the bundle, together with additional peaks from nanotube B. The peaks of nanotube A are shifted to the red by tens of meV when they appear in the bundle (after [8])

precisely the same Rayleigh spectrum (and, hence, the same nanotube structure) is observed at a displacement of 30 μm along an individual SWNT.

Because of its rapid data-collection rate, Rayleigh spectroscopy allows convenient characterization of large numbers of nanotubes. This has permitted the infrequent spontaneous changes of the chiral index of a nanotube along its axis to be identified and the site of this structural transformation to be determined to optical resolution. A method has also been introduced that permits suspended nanotubes to be transferred onto a solid substrate at a desired location [20]. With the aid of this technique, one can first characterize the nanotube by Rayleigh spectroscopy and then place it in a convenient location for complementary analysis by other experimental methods. Initial experiments of this type have been performed in which the electrical transport properties of optically characterized nanotubes have been determined [9].

4.4 Nanotube–Nanotube Interactions

The ability to probe individual nanotubes provides a controlled approach for the investigation of the effect of the environment on nanotube properties. Since SWNTs are only one monolayer in thickness, one expects that the effect of the external environment can be significant. Such interactions are, of course, quite diverse in character, ranging from chemical modification to physical deformation.

Figure 7 illustrates the use of Rayleigh scattering spectroscopy to probe one class of change induced by the local environment [8]. In this case, we are able to probe an individual SWNT in its isolated form and as a part of a

bundle with a second SWNT. This structure was formed spontaneously in the CVD growth process. One nanotube extended fully across the slit, while a second nanotube formed a bundle over half the width of the slit. The Rayleigh spectra of the isolated nanotube A and of the bundled structure (A+B) are shown. In the bundle, one can clearly identify the peaks associated with nanotube A, in addition to new features arising from electronic transitions in nanotube B. The noteworthy feature in the spectra is that the transitions in nanotube A (the E_{33}^S and E_{44}^S transitions in a semiconducting nanotube) are clearly shifted in energy when they appear in the two-nanotube bundle. The peaks are displaced to lower energy by tens of meV when an adjacent nanotube is present in a bundle. In other data sets for similar configurations, the shifts are consistently to lower energy upon bundling. In addition, in some cases the nanotubes spontaneously form Y-junctions. It is then possible to measure the spectra of each of the two isolated constituents of the bundle separately and to determine the shifts undergone by each component in forming the bundle [8]. Again, we see redshifts for all transition energies. This observation suggests that possible strain effects are not significant, since the influence of strain would generally push some transition energies up and some down.

We can understand a redshift induced by bundling as a consequence of dielectric screening of the strong carrier–carrier interactions in a nanotube. The presence of an adjacent dielectric medium (nanotube B in Fig. 7) reduces the carrier–carrier interactions within the nanotube being probed (nanotube A in Fig. 7). The importance of such carrier–carrier interactions has been predicted theoretically by several researchers [21–26] and established experimentally by the observation of strong excitonic effects in semiconducting nanotubes [27–29]. Screening of this carrier–carrier interaction leads to a reduced quasiparticle bandgap (because of decreased electron–electron repulsion). Although this effect is partially offset by a reduced exciton binding energy, the net shift in the transition energy of the exciton caused by the dielectric screening is still expected to be towards lower energy. Spectral shifts of nanotube transitions from bundling and other environmental effects have been widely reported in previous ensemble measurements [30, 31]. As shown here, access to optical measurements at the single-nanotube level permits these interesting phenomena to be examined with a degree of control difficult to match in an ensemble measurement.

5 Outlook

Elastic light scattering from individual nanotubes is strong enough to be readily observed in the absence of background signals. Spectroscopy of the electronic transitions in nanotubes can thus be obtained by measuring the cross section for elastic scattering as a function of the photon energy, which provides direct information on the linear optical properties of the nanotube

under study. The resulting technique of Rayleigh scattering spectroscopy, when applied with a continuum light source, allows for rapid and precise measurement of the optical transitions in individual SWNTs of both semiconducting and metallic character.

The principal limitation in application of the method of Rayleigh scattering spectroscopy is, in some sense, the counterpoint of its strength. All types of nanotubes provide an elastic light-scattering response, making the method applicable to metallic, as well as semiconducting nanotubes, small bundles, and nanotubes with high defect densities, and so on. By the same token, however, any material other than the nanotube that is illuminated by the probe beam can also yield elastically scattered light, radiation that may be difficult to separate from the nanotube signal. By probing nanotubes suspended in air, this complication is eliminated. However, for a more general sample geometry, the role of background scattering must be considered, since such background signals can be far stronger than the nanotube response. While the distinctive spectral and polarization characteristics of the nanotube response can be identified in the presence of a spectrally unstructured background, this becomes difficult if the relative strength of the background signal is too great compared with the signal of interest. It should be noted, however, that an ideal planar surface does not give rise to diffuse scattering and would thus be compatible with Rayleigh scattering measurements from individual SWNTs. Understanding the practical limitations of the method in such cases and perhaps developing suitable spatial, spectral, or polarization modulation techniques to discriminate against undesired background signals is an interesting area for future development.

Rayleigh scattering spectroscopy provides a useful addition to the established techniques of Raman and photoluminescence spectroscopy that are based on inelastic light scattering. While all three methods permit access to spectroscopy of individual SWNTs, the methods are largely complementary to one another. Rayleigh spectroscopy extends photoluminescence measurements in its applicability to all nanotubes, including metallic species and semiconducting nanotubes for which fluorescence emission is weak (high level of defects) or difficult to detect (at long wavelengths). Rayleigh spectroscopy is also complementary to Raman and photoluminescence measurements in its ability to provide broadband excitation spectra rapidly at the single-nanotube level. This attribute makes it particularly convenient to combine Rayleigh and Raman spectroscopy for the study of individual SWNTs. By performing the Rayleigh spectroscopy first, one obtains information to ensure a choice of laser photon energy that benefits from the desired resonant enhancement of the Raman process. Further, the usual instrumentation for Rayleigh scattering serves for Raman (or photoluminescence) measurements simply by replacing the continuum source with the appropriate monochromatic laser excitation. Beyond the experimental convenience of performing Rayleigh and Raman spectroscopy jointly, the information from the two measurements,

electronic and vibrational spectra, are complementary and together provide a very complete characterization of any nanotube under study.

In addition to combining Rayleigh scattering with other single nanotube optical spectroscopies, Rayleigh spectroscopy can be fruitfully used, as illustrated in our earlier discussion of electron diffraction, in conjunction with entirely different experimental methods. This direction, while not unique to the Rayleigh scattering technique, will certainly become increasingly important in the future. From this perspective, Rayleigh scattering is attractive because of its short measurement time and its applicability to all types of nanotubes. A further frontier for measurements of individual nanotubes is accessing dynamics directly in the time domain. Impressive results have been demonstrated in time-resolved photoluminescence at the individual nanotube level [32]. To expand these measurements to a range of pump-probe techniques with the full femtosecond time resolution of current laser techniques requires a sensitive probe of the response of individual SWNTs. Rayleigh scattering, with its high signal strength, appears to be a promising optical probe for such measurements.

Acknowledgements

The author wishes to thank M. S. Dresselhaus, J. Maultzsch, and Y. Wu for help in preparing this chapter; to express appreciation to L. Brus, J. Hone, and S. O'Brien and their research groups for fruitful scientific collaboration; and to acknowledge support from the Nanoscale Science and Engineering Initiative of the U.S. National Science Foundation under grants CHE-0117752 and ECS-05-07111, the New York State Office of Science, Technology, and Academic Research (NYSTAR), and the Office of Basic Energy Sciences, U.S. Department of Energy under grant DE-FG02-03ER15463.

References

[1] A. Hartschuh, H. N. Pedrosa, J. Peterson, L. Huang, P. Anger, H. Qian, A. J. Meixner, M. Steiner, L. Novotny, T. D. Krauss: Single carbon nanotube optical spectroscopy, Chem. Phys. Chem. **6**, 577 (2005) 354

[2] M. S. Dresselhaus, G. Dresselhaus, A. Jorio, A. G. Souza-Filho, G. G. Samsonidze, R. Saito: Science and applications of single nanotube Raman spectroscopy, J. Nanosci. Nanotech. **3**, 19 (2003) 354

[3] M. S. Dresselhaus, G. Dresselhaus, R. Saito, A. Jorio: Raman spectroscopy of carbon nanotubes, Phys. Rep. **409**, 47 (2005) 354

[4] J. U. Lee, P. J. Codella, M. Pietrzykowski: Direct probe of excitonic and continuum transitions in the photocurrent spectroscopy of individual carbon nanotube p-n diodes, Appl. Phys. Lett. **90**, 053103 (2007) 354

[5] X. Qiu, M. Freitag, V. Perebeinos, P. Avouris: Photoconductivity spectra of single-carbon nanotubes: Implications on the nature of their excited states, Nano Lett. **5**, 749 (2005) 354

[6] M. Y. Sfeir, F. Wang, L. Huang, C.-C. Chuang, J. Hone, S. P. O'Brien, T. F. Heinz, L. E. Brus: Probing electronic transitions in individual carbon nanotubes by Rayleigh scattering, Science **306**, 1540 (2004) 354, 356, 357, 360, 362
[7] M. Y. Sfeir, T. Beetz, F. Wang, L. Huang, X. M. H. Huang, M. Huang, J. Hone, S. O'Brien, J. A. Misewich, T. F. Heinz, L. Wu, Y. Zhu, L. E. Brus: Optical spectroscopy of individual single-walled carbon nanotubes of defined chiral structure, Science **312**, 554 (2006) 354, 359, 360, 361
[8] F. Wang, M. Y. Sfeir, L. Huang, X. M. H. Huang, Y. Wu, J. Kim, J. Hone, S. O'Brien, L. E. Brus, T. Heinz: Interactions between individual carbon nanotubes studied by Rayleigh scattering spectroscopy, Phys. Rev. Lett. **96**, 167401 (2006) 354, 360, 363, 364
[9] B. Chandra, R. Caldwell, M. Huang, L. Huang, M. Y. Sfeir, S. P. O'Brien, T. F. Heinz, J. Hone: Electrical transport measurements of nanotubes with known (n, m) indices, Phys. Stat. Sol. B **243**, 3359 (2006) 354, 360, 363
[10] C. F. Bohren, D. R. Huffman: *Absorption and Scattering of Light by Small Particles* (Wiley, New York 1983) 356
[11] L. Huang, S. Wind, S. P. O'Brien: Controlled growth of single-walled carbon nanotubes from an ordered mesoporous silica template, Nano Lett. **3**, 299 (2003) 358
[12] L. Huang, X. Cui, B. White, S. P. O'Brien: Long and oriented single-walled carbon nanotubes grown by ethanol chemical vapor deposition, J. Phys. Chem. B **108**, 16451 (2004) 358
[13] J. M. Dudley, G. Genty, S. Coen: Supercontinuum generation in photonic crystal fiber, Rev. Mod. Phys. **78**, 1135 (2006) 358
[14] S. M. Bachilo, M. S. Strano, C. Kittrell, R. H. Hauge, R. E. Smalley, R. B. Weisman: Structure-assigned optical spectra of single-walled carbon nanotubes, Science **298**, 2361 (2002) 360
[15] J. C. Meyer, M. Paillet, T. Michel, A. Moréac, A. Neumann, G. S. Duesberg, S. Roth, J.-L. Sauvajol: Raman modes of index-identified freestanding single-walled carbon nanotubes, Phys. Rev. Lett. **95**, 217401 (2005) 361
[16] R. Saito, G. Dresselhaus, M. S. Dresselhaus: *Physical Properties of Carbon Nanotubes* (Imperial College Press, London 1998) 361
[17] M. F. Islam, D. E. Milkie, C. L. Kane, A. Yodh, J. Kikkawa: Direct measurement of the polarized optical absorption cross section of single-wall carbon nanotubes, Phys. Rev. Lett. **93**, 037404 (2004) 361
[18] Y. Miyauchi, M. Oba, S. Maruyama: Cross-polarized optical absorption of single-walled nanotubes by polarized photoluminescence excitation spectroscopy, Phys. Rev. B **74**, 205440 (2006) 362
[19] H. Ajiki, T. Ando: Aharonov-Bohm effect in carbon nanotubes, Physica B **201**, 349 (1994) 362
[20] X. M. H. Huang, R. Caldwell, L. Huang, S. C. Jun, M. Huang, M. Y. Sfeir, S. P. O'Brien, J. Hone: Controlled placement of individual carbon nanotubes, Nano Lett. **5**, 1515 (2005) 363
[21] T. Ando: Excitons in carbon nanotubes, J. Phys. Soc. Jpn. **66**, 1066 (1997) 364
[22] C. L. Kane, E. J. Mele: Electron interactions and scaling relations for optical excitations in carbon nanotubes, Phys. Rev. Lett. **93**, 197402 (2004) 364

[23] C. D. Spataru, S. Ismail-Beigi, L. X. Benedict, S. G. Louie: Excitonic effects and optical spectra of single-walled carbon nanotubes, Phys. Rev. Lett. **92**, 077402 (2004) 364
[24] V. Perebeinos, J. Tersoff, P. Avouris: Scaling of excitons in carbon nanotubes, Phys. Rev. Lett. **92**, 257402 (2004) 364
[25] H. Zhao, S. Mazumdar: Femtosecond spectroscopy of optical excitations in single-walled carbon nanotubes: Evidence for exciton–exciton annihilation, Phys. Rev. Lett. **93**, 157402 (2004) 364
[26] E. Chang, G. Bussi, A. Ruini, E. Molinari: Excitons in carbon nanotubes: An ab initio symmetry-based approach, Phys. Rev. Lett. **92**, 196401 (2004) 364
[27] F. Wang, G. Dukovic, L. E. Brus, T. Heinz: The optical resonances in carbon nanotubes arise from excitons, Science **308**, 838 (2005) 364
[28] J. Maultzsch, R. Pomraenke, S. Reich, E. Chang, D. Prezzi, A. Ruini, E. Molinari, M. S. Strano, C. Thomsen, C. Lienau: Exciton binding energies in carbon nanotubes from two-photon photoluminescence, Phys. Rev. B **72**, 241402(R) (2005) 364
[29] Y. Ma, L. Valkunas, S. Bachilo, G. Fleming: Exciton binding energy in semiconducting single-walled carbon nanotubes, J. Phys. Chem. B **109**, 15671 (2005) 364
[30] C. Fantini, A. Jorio, M. Souza, M. S. Strano, M. S. Dresselhaus, M. A. Pimenta: Optical transition energies for carbon nanotubes from resonant Raman spectroscopy: Environment and temperature effects, Phys. Rev. Lett. **93**, 147406 (2004) 364
[31] M. J. O'Connell, S. Sivaram, S. K. Doorn: Near-infrared resonance Raman excitation profile studies of single-walled carbon nanotube intertube interactions: A direct comparison of bundled and individually dispersed HiPco nanotubes, Phys. Rev. B **69**, 235415 (2004) 364
[32] A. Hagen, M. Steiner, M. B. Raschke, C. Lienau, T. Hertel, H. Qian, A. J. Meixner, A. Hartschuh: Exponential decay lifetimes of excitons in individual single-walled carbon nanotubes, Phys. Rev. Lett. **95**, 197401 (2005) 366

Index

Electrical Transport in Single-Wall Carbon Nanotubes

Michael J. Biercuk[1,3], Shahal Ilani[2], Charles M. Marcus[3], and Paul L. McEuen[2]

[1] Booz Allen Hamilton
Arlington, VA 22203, USA
[2] Laboratory of Atomic and Solid State Physics, Cornell University
Ithaca, NY 14853, USA
shahal.ilani@cornell.edu
mceuen@ccmr.cornell.edu
[3] Department of Physics, Harvard University
Cambridge, MA 02138, USA
marcus@harvard.edu

Abstract. We review recent progress in the measurement and understanding of the electrical properties of individual metal and semiconducting single-wall carbon nanotubes. The fundamental scattering mechanisms governing the electrical transport in nanotubes are discussed, along with the properties of p–n and Schottky-barrier junctions in semiconductor tubes. The use of advanced nanotube devices for electronic, high-frequency, and electromechanical applications is discussed. We then examine quantum transport in carbon nanotubes, including the observation of quantized conductance, proximity-induced supercurrents, and spin-dependent ballistic transport. We move on to explore the properties of single and coupled carbon-nanotube quantum dots. Spin and orbital (isospin) magnetic moments lead to fourfold shell structure and unusual Kondo phenomena. We conclude with a discussion of unanswered questions and a look to future research directions.

1 Introduction and Basic Properties

Since the discovery of single-wall carbon nanotubes (SWNTs) fifteen years ago [1], electrical measurements of individual SWNTs have proven to be one of the most powerful probes of this novel 1D system. Figure 1 shows a schematic of a standard device geometry. A SWNT is directly connected to two metallic contacts (labeled source and drain), and is capacitively coupled to a third gate terminal that can change the charge density on the tube (or equivalently, shift the energy bands in the conducting channel). Measurements are performed by applying ac or dc voltages to the various terminals and measuring the resulting currents between source and drain.

The first transport measurements in nanotube devices were reported in 1997–1998 [2–5], and since then there have been thousands of papers published on the subject. Scientists and engineers have built upon the simple three-terminal device geometry presented above to produce increasingly com-

A. Jorio, G. Dresselhaus, M. S. Dresselhaus (Eds.): Carbon Nanotubes,
Topics Appl. Physics **111**, 455–493 (2008)

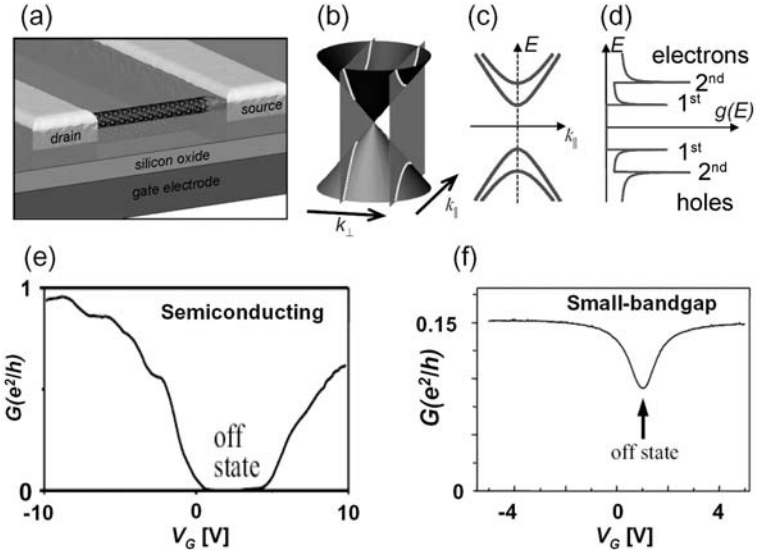

Fig. 1. (**a**) Schematic view a nanotube field-effect transistor (**b**) The Dirac energy dispersion cone of graphene near the K point in reciprocal space showing cutting lines for a semiconducting tube. (**c**) The dispersion relation of the semiconducting nanotube 1D subbands derived by slicing the cone at quantized values of the momentum along the circumference of the tube, $k_{\perp}$. (**d**) The corresponding 1D density of states. (**e**) Measured conductance of a semiconducting tube, G, as a function of gate voltage, V_{g}. (**f**) Same for small-bandgap metallic nanotube. Reference: McEuen group, unpublished

plex devices and to address questions of both device performance and fundamental physics. A decade later, a remarkably complete and consistent picture of transport in this novel 1D system has emerged. The power of transport measurements in elucidating the basic electronic properties of this material system has been truly remarkable. In this review, we summarize many of the major accomplishments, focusing on topics where a broad consensus has emerged and ones that were not covered in the previous book [6, 7]. We start with a discussion of the basic band structure and transport properties of nanotubes. In Sect. 2, we address the properties of nanotubes operating in the "classical", or incoherent, transport regime, and in Sect. 3 we discuss devices operating in this regime. In Sect. 4, we address the quantum properties of nanotube electrical transport and turn to nanotube quantum dots in Sect. 5. We end in Sect. 6 with a discussion of future research directions.

1.1 Band Structure

The transport properties of nanotubes are intimately related to their electronic band structure (see the contribution by Spataru et al.). The band

structure is composed of multiple 1D subbands sliced from the Dirac dispersion cone of graphene (Fig. 1b). These subbands have relativistic dispersion relations, which for the ith electron–hole subband are given by:

$$E_i(k) = \pm\left[(\hbar v_{\mathrm{F}} k)^2 + (E_{\mathrm{g}}^i/2)^2\right]^{1/2} . \tag{1}$$

Here, E and k are measured from the center of the Dirac cone of graphene, $v_{\mathrm{F}} \approx 8 \times 10^5\,\mathrm{m/s}$ is the Fermi velocity, and E_{g}^i are the individual energy gaps determined by the distance of the quantized k states to the center of the Dirac cone. The corresponding density of states, $g(E)$, has distinctive 1D van Hove singularities (Fig. 1d), and is given by:

$$g(E) = \sum_i g_i(E)\,, \qquad g_i(E) = \frac{4}{\pi\hbar v_{\mathrm{F}}}\left[1 - (E_{\mathrm{g}}^i/2E)^2\right]^{-1/2} . \tag{2}$$

The factor 4 in (2) comes from the fourfold degeneracy of each of these subbands at zero magnetic field, due to both the spin degeneracy and the orbital or "isospin" degeneracy associated with the band structure of graphene which is further discussed in the contribution by Charlier et al. This latter effect can be pictured as the separate left- and right-handed electron states spiraling down the tube. This fourfold degeneracy is lifted in a magnetic field by the orbital and spin Zeeman effects:

$$\Delta E_{\mathrm{g}}^i = -(\boldsymbol{\mu}_0 + \boldsymbol{\mu}_{\mathrm{s}}) \cdot \boldsymbol{B} = \pm\frac{d_{\mathrm{t}} e v_{\mathrm{F}} B_{\parallel}}{4} \pm \tfrac{1}{2}\, g\mu_b B_{\mathrm{tot}}\,, \tag{3}$$

where $B_{\parallel}$ is the field parallel to the tube axis, d_t is the tube diameter, g is the electrons' g-factor and B_{tot} is the total field. Nanotubes fall into three distinct electronic classes according to their fundamental bandgap, E_{g}^0, or simply E_{g}:

Semiconducting nanotubes, with a bandgap predicted by band theory to be $E_{\mathrm{g}} \approx 0.7\,\mathrm{eV}/d_{\mathrm{t}}(\mathrm{nm})$.
Small-bandgap nanotubes, which are nominally metallic tubes with a small bandgap (typically less than 100 mV) due to perturbations, such as curvature, strain, twist, etc.
True metallic nanotubes, where $E_{\mathrm{g}} = 0$. This class is rare, since nearly all tubes possess some small bandgap due to curvature, strain, or twist. These are often lumped together with small bandgap tubes, with the combined set called "metallic."

Three-terminal conductance measurements provide a direct means for identifying members of the different classes outlined above. The lower panels of Fig. 1 show the conductance measured at room temperature as a function of applied gate voltage for a semiconducting and a small-bandgap tube. When the Fermi level is tuned into the bandgap, the semiconducting tube shows

a broad region of near-zero conductance since $E_g \gg k_B T$, while the small-bandgap tube shows only a moderate dip since its bandgap is comparable to the thermal energy, $E_g \sim k_B T$.

Measurement of the nanotube capacitance to the gate can directly probe the subband structure [8] as shown in Fig. 2. The inverse capacitance C_{tot}^{-1} is the proportionality constant between the change in the electrochemical potential and the amount of charge added to the nanotube, and consists of both an electrostatic term, C_{elec}, and a "quantum" or density-of-states term:

$$C_{tot}^{-1} = C_{elec}^{-1} + [e^2 g(E)]^{-1} . \tag{4}$$

The observed gate-voltage dependence of the capacitance in Fig. 2a results from the density-of-states given in (2) manifesting itself in the capacitance via (4). In the figure, the bandgap is clearly visible as a large dip in the measured capacitance, followed by features that correspond to the first and second 1D electron and hole subbands. Fitting (2) and (4) to the experimental data gives the electrostatic capacitance and bandgap of the nanotube, which are in good agreement with calculated values based on the device geometry and the tube diameter.

While the capacitance shows clear electron–hole symmetry around the bandgap, the conductance measured on the same device (Fig. 2b) does not. This reflects the fact that the capacitance depends only on the thermodynamic density of states while the conductance depends also on the carriers' scattering rates and the contact resistances. Thus, the capacitance gives us a clear picture of the nanotube band structure and the amount of charge carriers present at a given gate voltage. Transport, on the other hand, measures the transmission of electrons through the device, as discussed below.

1.2 1D Transport in Nanotubes

To fully understand the transport characteristics of carbon nanotubes, we start with the Landauer formula, which states that the conductance of a quasi-1D system is given by:

$$G = \frac{4e^2}{h} \sum_i \int_{-\infty}^{\infty} \frac{\mathrm{d}f[(E - E_F)/k_B T]}{\mathrm{d}E} \Im_i(E)\, \mathrm{d}E , \tag{5}$$

where $\Im_i(E_F)$ is the transmission of the ith 1D subband state at the Fermi energy and $\mathrm{d}f/\mathrm{d}E$ is the energy derivative of the Fermi function. Conductance is thus a measure of the transmission of electrons through the entire device at the Fermi energy, broadened by the finite thermal width of the Fermi function.

When the Fermi energy is in the bandgap, $\Im_i(E_F) = 0$ and the conductance is governed by thermal activation from the tails of the Fermi function. When E_F lies within an electron or hole subband, the transmission properties

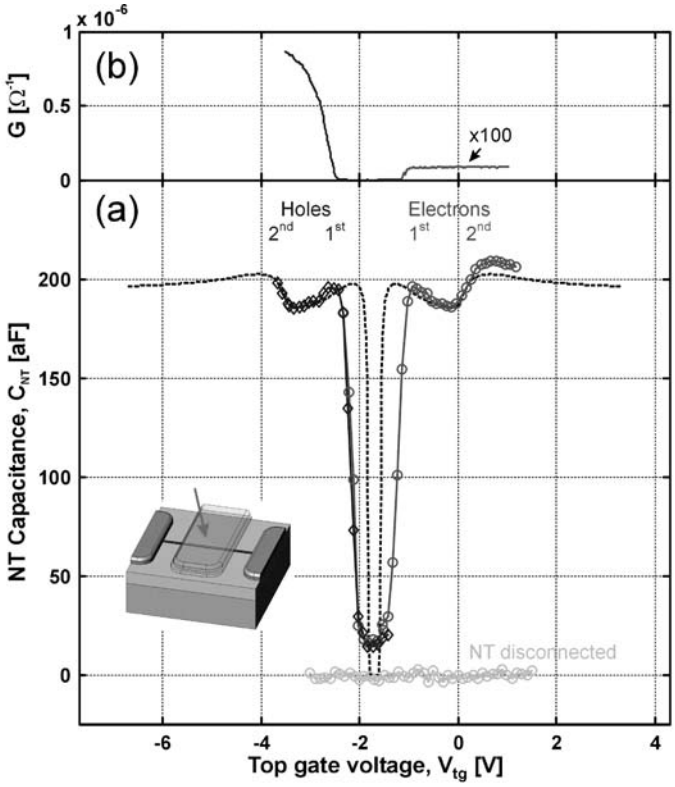

Fig. 2. Density dependence of the capacitance of a single SWNT. (**a**) Measured capacitance between an individual semiconducting SWNT and a metallic top-gate separated by 10 nm of SiO_x (scheme is shown in the *inset*). The *top trace* shows the dependence of the capacitance on the top-gate voltage. The *bottom trace* is the reference capacitance measured with the nanotube disconnected. The *dashed line* is a fit to a theory that includes elctrostatic and density-of-states contributions to the capacitance (2) and (4). (**b**) The conductance, G, measured on the same device. Adapted from [8]

of the entire device – tube plus contacts – determine the conductance. If the transport is ballistic and the tube has perfect contacts, this equation predicts a quantized conductance of $4e^2/h$ associated with each 4-fold degenerate 1D subband. Metallic nanotubes very often approach this quantized conductance value even at room temperature [9, 10]. Semiconducting nanotube devices have come within 25 % of this theoretical limit at room temperature [10, 11] and to within a few per cent at low temperatures [10–12], as discussed further in Sect. 4.

Conductance less than the quantized value can arise from additional resistance due to either the contacts or the tube. At or near room temperature, these two resistive contributions add incoherently, and are discussed sepa-

rately in Sect. 2 below. At lower temperatures, coherence effects and the Coulomb blockade become important. This quantum regime is discussed in Sect. 4.

2 Classical (Incoherent) Transport in Nanotubes

If we neglect coherence effects, the total resistance $R = G^{-1}$ of a nanotube device with a uniform channel can be written as:

$$R = R_{\text{contacts}} + R_{\text{tube}}\,, \tag{6}$$

where the contact resistance obeys $R_{\text{contacts}} \geq h/4e^2$, and for a uniform tube with diffusive scattering:

$$R_{\text{tube}} = (h/4e^2)(L/\ell)\,, \tag{7}$$

where L is the tube length, ℓ is the electron mean-free path for momentum relaxation, and we assume $L \gg \ell$. The measured device properties thus reflect the incoherent addition of the resistance of the tube and the contacts. A variety of measurements have been used to sort out the relative importance of these contributions in a given device. For example, electric force microscopy can measure the potential drop along the tube under current bias [13–15], directly probing the relative contributions. Devices where the contacts dominate [16] and ones where the tube properties dominate [11, 15] have been studied, as discussed below.

2.1 Contacts to Nanotubes: Schottky Barriers

Two types of barriers can form at the metal/tube interface and increase the contact resistance beyond the ideal $h/4e^2$ value. The first is a barrier created by an imperfect interface between the contact metal and the nanotube. Its resistance is a function of the cleanliness of the interface and the overlap of the metal–nanotube electronic states. Au and Pd have proven to make the best contacts to nanotubes, with near-perfect transmission frequently obtained [11].

More fundamental is the Schottky barrier that can form at the interface of a metal and a semiconducting nanotube. The properties of the Schottky barrier will depend on the band alignment at the interface (Fig. 3a). In the absence of interface states believed to be a good approximation for the metal/tube interface [17], the heights of the Schottky barriers for hole and electron injection are given by the work function of the metal contacts, ϕ_{M}, the work function of the nanotube, ϕ_{NT}, and its energy gap, E_{g} (see Fig. 3a):

$$\phi^{p}_{\text{SB}} = \phi_{\text{NT}} + E_{\text{g}}/2 - \phi_{\text{M}}\,, \qquad \phi^{n}_{\text{SB}} = \phi_{\text{M}} - \phi_{\text{NT}} + E_{\text{g}}/2\,. \tag{8}$$

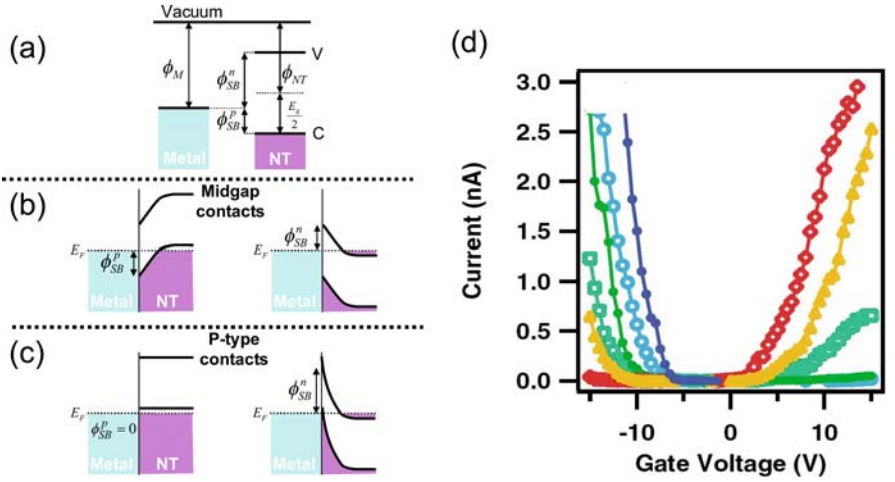

Fig. 3. Schottky-barrier height at the metal/nanotube interface. (**a**) A schematic of the nonaligned metal and nanotube energy levels depicting the relation between the Schottky-barrier heights for hole (/electron) injection, ϕ^p_{SB} (ϕ^n_{SB}) and the work-function of the metal, ϕ_{M}, the work function of the tube, ϕ_{NT}, and its energy gap E_{g}. When both are put in contact, band bending at the interface occurs to compensate for the work-function difference. (**b**) The case for contacts with the work function at the nanotube midgap. (**c**) p-type contacts. (**d**) Tuning the Schottky barrier from n- to p-type contacts using O_2. The *red curve* is the measured I–V with no exposure to oxygen. The remaining curves in order of increasing exposure to O_2 are colored *orange*, *light* and *dark green*, *light* and *dark blue*. Adapted from [16]

When the Fermi level of the metal lies at the midgap of the nanotube (Fig. 3b) there will be a Schottky barrier for both n and p carrier injection, whereas when it aligns with the hole band (Fig. 3c) there would be no barrier to hole injection but a large barrier to electron injection. This case corresponds to the semiconductor device in Fig. 2, where the on-state resistance in the n-regime far exceeds that of the p-regime. Thus, while the nanotube bands are electron–hole symmetric near the Dirac point, the contact properties generally are not.

A series of experiments, primarily by the IBM and Stanford groups, clarified the importance of Schottky barriers in SWNT transistors. Figure 3d shows measurements where the work function of the contact metal was adjusted for the same device by the adsorption of oxygen [16]. The device started out with predominantly n-type conduction, but as adsorbed oxygen increased the work function, the contacts changed to ambipolar, and finally to p-type. Other experiments on many different contact metals [11, 16, 18, 19] support this basic picture: high work function metals like Pd or Rh make good p-type contacts to tubes, while low work function metals like Al yield better n-type contacts. In all cases, adsorbed dipoles can strongly shift the metal work

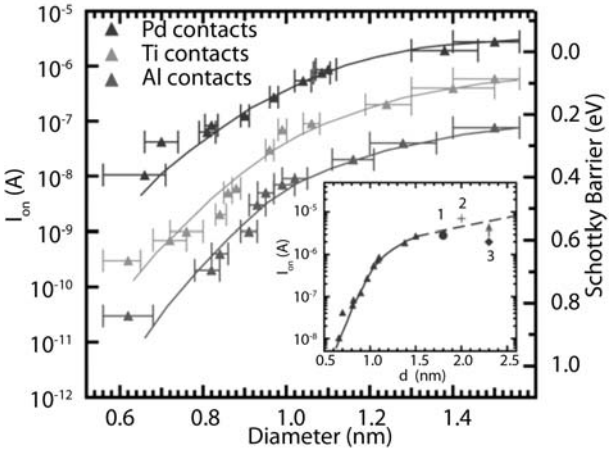

Fig. 4. On-state current and Schottky-barrier height as a function of SWNT diameter and contact metal. *Curves* from *top* to *bottom* correspond to Pd, Ti and Al. The right axis is the Schottky barrier, extracted from I_{on} using a self-consistent Poisson–Schrödinger model of the band bending near the contacts. *Inset* includes data points for Pd-contacted nanotube FETs from other publications. Adapted from [19]

functions, thus making the contact properties very sensitive to the ambient environment and device history. It was also noted [11] that a high work function by itself is not sufficient to assure ohmic contacts. For example, Pt has a larger work function than Pd but forms more resistive contacts, probably due to additional tunneling barriers formed as a result of poor wetting of the tube by the contact metal.

Since the energy gap grows with decreasing diameter ($E_g \sim 1/d_t$) it is clear from (8) that for every metal there exists a critical nanotube diameter below which a Schottky barrier with finite height will form and the height of this barrier will increase with decreasing diameter. Figure 4 shows the measured on-state current in the p-regime for nanotube transistors of different diameters and contact metals, along with the inferred Schottky barrier height. This height is seen to systematically grow with decreasing diameter. Ohmic p-type contacts are obtained only with Pd contacts to tubes of diameters > 1.5 nm.

These measurements provide a consistent picture of contact properties of semiconducting nanotubes. A major remaining challenge is to make good ohmic contacts to tubes with diameters 1.5 nm and smaller. Surprisingly, even small-bandgap/metallic tubes show significant barriers in this range [20]. The origin of this behavior is still not understood.

2.2 The Effect of Disorder

With an understanding of the role of contacts on nanotube conductance, we turn to examine the scattering properties of the nanotube channel itself and start by considering the effect of disorder. The major sources of disorder in nanotubes are:

Localized lattice defects, such as vacancies, substitutions, pentagon-heptagon defects and heterojunctions between nanotubes of different chiralities. Such defects are typically formed during nanotube growth, by volatile processing, or by intentional damage [21]. The atomically sharp nature of these defects leads to large momentum scattering.

Electrostatic potential fluctuations, created by a random distribution of charges in the substrate, by molecules adsorbed on the nanotube or by processing residues. These can induce both short- and long-range disorder.

Mechanical deformations, these include local strains and twists, which affect the local bandgap [22] as well as kinks that act as conductance barriers [23].

The coexistence of multiple sources of disorder in nanotube devices as well as the large variability in their properties makes it hard to make wide generalizations on the effects of disorder. Nevertheless, some understanding has emerged.

Experimentally, the effect of disorder is determined by extracting the nanotube corresponding mean-free paths from the conductivity (7) or by direct spatial imaging. Nanotubes with strong disorder show marked effects already at room temperature, whereas in cleaner nanotubes, disorder becomes the dominant scattering mechanism only at low temperatures. Low-temperature measurements of metallic tubes routinely show mean-free paths that are many micrometers long, as determined from their conductance [3, 24], from measured sizes of quantum dots [2, 3] and from scanned probe measurements [13, 25]. Semiconducting tubes, often show stronger sensitivity to disorder and shorter mean-free paths [4, 5]. However, they have also clearly demonstrated μm-long mean-free paths at low temperatures [26–30].

Disorder affects the transport in nanotubes in two distinct ways depending on its spatial scale, owing to two distinct backscattering processes – nanotubes have two degenerate dispersion branches originating from the K and K' points, each has left- and right-moving electrons. Backscattering can be either between the two branches or within the same branch. The first involves large momentum transfer, comparable to the inverse lattice constant and therefore occurs only from atomically sharp disorder. The latter requires small momentum transfer and is therefore caused by long-range disorder. It was further shown [31, 32], that due to the symmetries of the electronic wavefunctions, metallic tubes are affected only by short-range disorder, whereas

semiconducting tubes are affected by both short- and long-range disorder (see also contributions by Ando and by Spataru et al. in this book).

Scattering off atomic defects has been extensively studied theoretically [33–41], but the experimental situation is less clear. While localized scattering centers have certainly been observed in experiments [42–44], to date it has not been possible to probe the atomic-scale nature of the defect and to correlate it unambiguously with the observed transport properties.

Long-range disorder, e.g., from the electrostatic/mechanical interaction of a nanotube with the substrate is also known to be important, especially at low carrier densities in semiconducting nanotubes. The potential fluctuations break up the tube into a series of electronic puddles, with transport dominated by hopping between the puddles [45], as determined by a number of scanned probe measurements [13,14,25,46]. One manifestation of this is seen in the data of Fig. 2: The experimentally measured conductance and capacitance drop to zero well before the theoretical band edge is reached. At low carrier densities, the nanotube stops conducting before it runs out of carriers, as they become localized by a disorder potential along the nanotube length. We note that suspended nanotubes have shown dramatically improved transport characteristics, confirming this viewpoint, and allowing one to observe the first few electrons/holes added to a single-nanotube quantum dot. These will be discussed in Sect. 4.

2.3 Electron–Phonon Scattering in Nanotubes

In clean, high-quality metallic SWNTs at room temperature, the dominant scattering mechanism is well known to be electron–phonon scattering. Scattering by acoustic phonons dominates the resistances at small source–drain biases [47–49], whereas scattering by optical and zone-boundary phonons sets a limit on the maximal current carried by individual SWNT at large bias [49–51]. The latter is shown in Fig. 5 for a metallic nanotube. The slope of the current–voltage characteristic decreases for increasing bias, and, if the tube is suspended, can even become negative. This dramatic increase in resistance and saturation of the current at high electron energies was first explained by *Yao* et al. [50]: the electron rapidly emits a phonon as soon as it has an excess energy equal to the optical-phonon energy, $\hbar\omega_0 \sim 160\,\mathrm{meV}$. Recent experiments [49,51] have measured the phonon emission rate directly and confirm it to be very fast ($< 0.1\,\mathrm{ps}$). This emission process limits the current in all but the shortest nanotubes to currents less than $I_{\max} \sim (4e^2/h)(\hbar\omega_0/e) \sim 25\,\mu\mathrm{A}$. Metallic devices with short channels ($L \sim 10$–$15\,\mathrm{nm}$) comparable to the optical-phonon mean-free path [49, 51] ($l_{\mathrm{op}} \approx 10\,\mathrm{nm}$) have demonstrated sustained currents up to $110\,\mu\mathrm{A}$ in the high-field regime ($V_{\mathrm{SD}} \sim 1.5\,\mathrm{V}$) at room temperature [52].

The excess energy created by this phonon emission can be substantial, heating the tube significantly, particularly for suspended tubes. The phonons created can scatter additional electrons increasing the resistance even further.

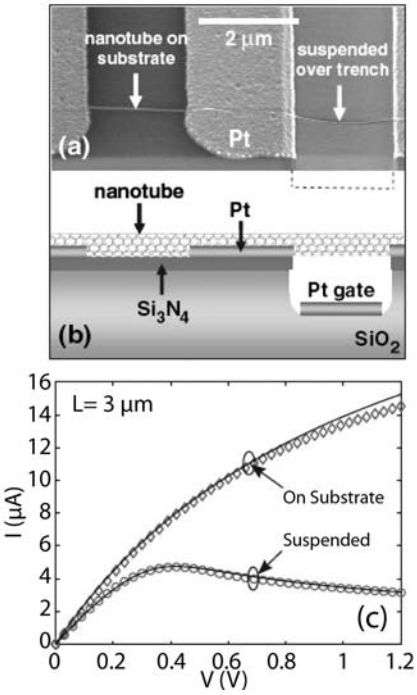

Fig. 5. Suspended tube I–Vs demonstrating the effect of optical-phonon scattering. (**a**) SEM image, taken at a 45° angle, of the nonsuspended (on nitride) and suspended (over a $\sim 0.5\,\mu$m deep trench) segments of the tube. (**b**) A schematic of the device cross section. (**c**) Current–voltage (I–V) characteristics of the same-length ($L \sim 3\,\mu$m) suspended and nonsuspended portions of a SWNT ($d_t \sim 2.4\,$nm) at room temperature measured in vacuum. The *symbols* represent experimental data; the *lines* are calculations based on average tube temperature (similar within $\sim 5\,\%$ to that based on actual tube-temperature profile and resistance integrated over the $\sim 3\,\mu$m tube length). Adapted from [53]

For suspended tubes, this effect is so strong as to lead to negative differential resistance [53] (Fig. 5), and the observed characteristics are in good agreement with a model [53] that accounts for the heat flow along the nanotube. The temperature can rise up to $\sim$ 1000 K, even creating significant light emission [54].

Recent measurements have shown that phonon scattering also limits the ultimate performance of semiconducting nanotube devices. Figure 6 shows the temperature dependence of the linear conductance of a clean nanotube device with good contacts [30]. The on-state resistance grows linearly with temperature, indicative of scattering by acoustic phonons, whose occupation also grows linearly with temperature; the mobility $\mu = (L^2/C_\mathrm{G})\,\mathrm{d}G/\,\mathrm{d}V_\mathrm{G}$ behaves in a similar way. Measurements on many semiconducting devices

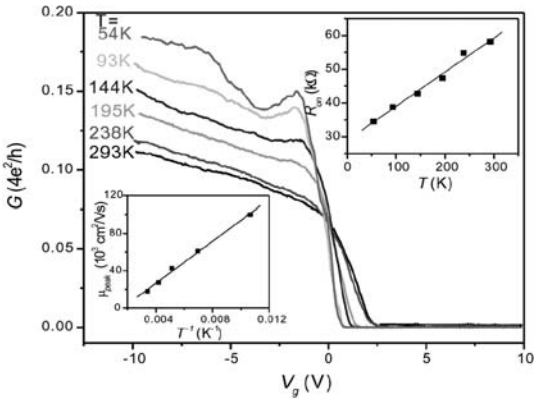

Fig. 6. Conductance and mobility of a p-type semiconducting nanotube transistor vs. temperature. *Main figure:* The conductance vs. gate voltage at different temperatures for a device with diameter $d_t = 4\,\text{nm}$ and length $L = 4\,\mu\text{m}$. *Upper inset:* R_{on} as a function of T. *Lower inset:* measured peak mobility as a function of T^{-1}. Both are shown with linear fitting. Adapted from [30]

yield the following approximate expression for the on-state mean-free path and the mobility:

$$l_{ap}(\text{on}) \approx 0.3\,\mu\text{m}\ \ d_t(\text{nm})\ \ \frac{300\,\text{K}}{T}\,,$$
$$\mu_{ap}(\text{max}) \approx 1000\frac{\text{cm}^2}{\text{Vs}}\ \ (d_t(\text{nm}))^2\ \ \frac{300\,\text{K}}{T}\,. \tag{9}$$

The peak mobility depends quadratically on the diameter of the nanotube, in agreement with theoretical predictions [55–57]. This dependence results from a decrease of both the effective mass and the scattering rate with increasing diameter.

The mobilities of clean semiconducting tubes are very high [26–30]. For the device in Fig. 6 $\mu_{peak} \sim 15\,000\,\text{cm}^2/\text{Vs}$ at room temperature, growing to $> 100\,000\,\text{cm}^2/\text{Vs}$ at $T = 50\,\text{K}$. These mobilities far surpass those found in silicon MOSFETs, fueling interest in nanotube transistor devices. This is discussed in the following section.

3 Nanotube Devices and Advanced Geometries

The high mobilities, long mean-free paths, and large current-carrying capacities of nanotubes have inspired many groups to explore a broad spectrum of electronic, high-frequency, optoelectronic, and nanomechanical applications of nanotubes as discussed also in the contribution by Endo et al. In this section we describe representative examples.

3.1 High-Performance Transistors

Since the first nanotube transistors were reported [4, 5], researchers have worked steadily to improve device performance through innovations such as improved contacts, shorter channels, and high-κ/thin dielectrics for improved gating, where κ refers to the dielectric constant. Figure 7 shows the I–V_{SD} characteristics of a nanotube transistor created using the high-κ dielectric, ZrO_2, and a top-gate electrode [58]. The I–V curves resemble those of a standard MOSFET, but show dramatically improved performance relative to Si or to previous backgated nanotube devices. The transconductance $\mathrm{d}I/\mathrm{d}V_G$ in the saturation regime of the transistor is $\sim 10\,\mu S$ at $V_{SD} = 1.2\,V$, and experiments on 50-nm channel length devices have achieved $30\,\mu S$ [59]. Normalized to the width of the tube, these transconductances are significantly larger than those obtained in Si MOSFETs. Furthermore, there is still room to improve: the theoretical limit, when the capacitance is governed by the quantum capacitance and the tube is in the ballistic-transport regime, is: $\mathrm{d}I/\mathrm{d}V_G = 4e^2/h \sim 155\,\mu S$.

Top-gated devices have also shown dramatic improvements in device subthreshold swing, $S = \ln(10)[\mathrm{d}V_G/\mathrm{d}\ln(I_{SD})]$, a key parameter in evaluating transistor performance that indicates how effectively the device turns off with gate voltage. Backgated nanotube transistors exhibited values of $S \sim 1$–$2\,V$/decade indicating a slow turn-off with V_G. This value should be compared with the theoretical limit of $k_B T \ln(10) = 60\,mV$/decade at room temperature, arising from thermal smearing of the Fermi distribution of carriers in the device. In contrast, top-gated nanotube transistors with thin or high-κ dielectrics routinely yield [58–61] $S \sim 70$–$130\,mV$/decade.

A final key device property is the ratio between the current through the transistor in its "on" state and the leakage current in the "off" state (the on/off ratio). Values in the range $\sim 10^6$–10^3 are common. Since, for an ambipolar device, this ratio depends exponentially on the bandgap [$\sim \exp(-E_g/2k_B T)$] smaller-diameter tubes give larger on/off ratios. However, smaller-diameter tubes have lower mobilities and are more prone to Schottky barrier effects, as discussed above. There is therefore a tradeoff between on/off ratio and the on-state current of the transistor.

The integration of multiple nanotube transistors into simple circuits has also begun. Perhaps the most sophisticated device yet created is shown in Fig. 8, where multiple transistors were created on the same long nanotube and connected into a ring-oscillator circuit, where transistors connected in a ring topology turn each other on/off sequentially in a looping domino effect [62]. The circuit oscillated at 50 MHz, limited not by the intrinsic performance of the nanotube transistors, but rather by the interconnect parasitics. The ultimate limits on frequency, device performance and circuit complexity remain to be explored, and are an active area of research, as discussed in the next section.

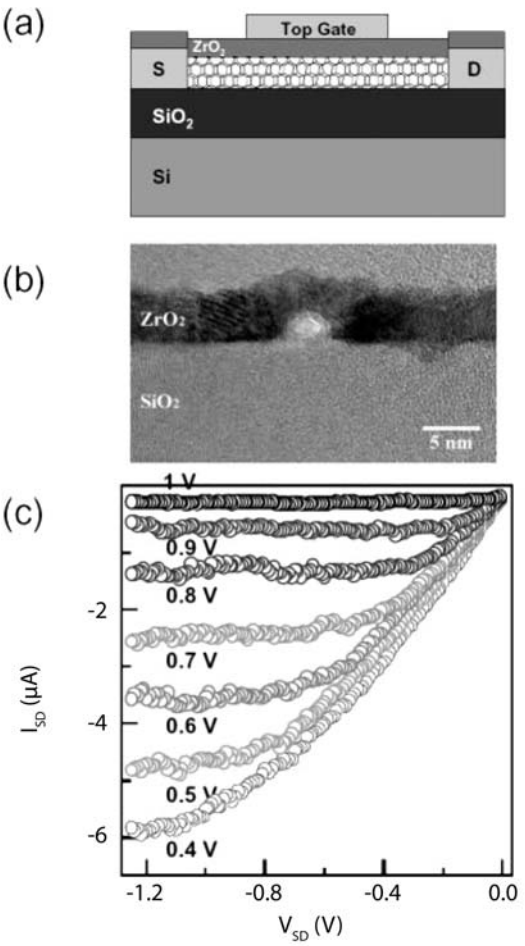

Fig. 7. High-κ nanotube transistor. (**a**) Sideview schematics of a SWNT-FET with ALD-ZrO_2 as the gate dielectrics (S and D represent the source and drain electrodes). The nominal thickness of ZrO_2 used is 8 nm. (**b**) TEM image of the cross section of a SWNT on SiO_2 with conformal coating of 4-nm thick ZrO_2. The circular region at the ZrO_2/SiO_2 interface is the cross section of a nanotube that exhibits light contrast in the TEM. (**c**) I–V curves of the FET recorded for various top-gate voltages. Adapted from [58]

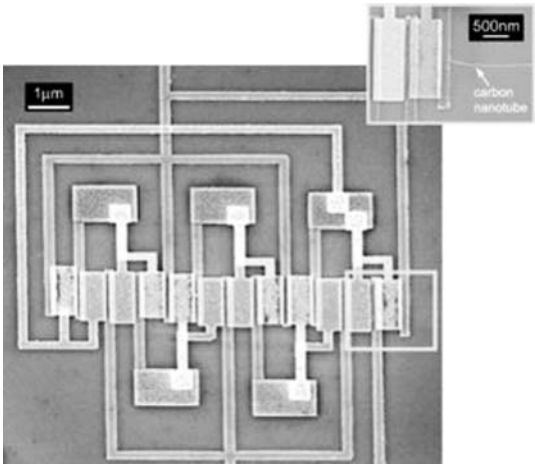

Fig. 8. An SEM image of a SWNT ring oscillator consisting of five CMOS inverter stages. Adapted from [62]

3.2 Radio-Frequency and Microwave Devices

In principle, nanotube transistors may operate up to the terahertz regime, but measurements of the high-frequency properties are difficult. The relatively high input impedance of a nanotube device ($R > h/4e^2 = 6.5\,\mathrm{k}\Omega$) limits device coupling efficiency into $50\,\Omega$ transmission lines, and this has served as a major impediment to device testing at RF/microwave frequencies. Nevertheless, a number of approaches have met with success. The most straightforward are measurements of the S-matrix, which characterizes the high-frequency transmission and reflection of a nanotube device. Changes in the nanotube impedance result in very small but measurable changes in the transmission/reflection coefficients. Both the resistive [63] and kinetic inductive portions [64] of a metallic nanotube impedance have been inferred. A measurement of a semiconducting tube in an FET geometry demonstrated a differential conductance at 1 GHz nearly identical to that at dc, indicating the potential for efficient operation at microwave frequencies [65].

Another approach is to use standard RF impedance-matching techniques to couple effectively to the nanotube. Several nanotube experiments have recently used the parasitic capacitance of the nanotube device itself in series or parallel with an external inductance in order to form a resonant circuit at $\omega_0 = 1/\sqrt{LC}$ with characteristic impedance matched to a 50-Ω transmission line [66, 67]. Variations in device resistance are mapped to modulation of the resonant circuit Q-factor, and hence to changes in the reflection or transmission of radiation at an applied carrier frequency (tuned to the circuit resonance). These techniques have been used to examine both transistor behavior and single-charge dynamics on microsecond timescales.

A third approach uses the nanotube transistor itself as the high-frequency signal detector. A transistor is a nonlinear device element since the conductance is a function of the applied gate or source drain voltage. Accordingly, it will rectify high-frequency signals to produce a dc response, or "mix" two high-frequency signals to produce sum and difference frequencies. Rectification and mixing using nanotube transistors at frequencies up to 50 GHz have been demonstrated by a number of groups [68–71]. Similarly, microwave detection and heterodyne detection exploiting nonlinearity in the I–V response of metallic nanotubes have recently been reported [72].

An interesting application of nanotube mixing has been to detect the motion of a vibrating nanotube in an electromechanical resonator device [68, 73, 74], as shown in Fig. 9. Nanotubes have among the highest Young's modulus known (see the contribution by Yamamoto et al. in this book), and can easily be prepared in suspended geometries, thus making them ideal candidates for use as electromechanical resonators and switches. In this device, the nanotube transistor was used as an electromechanical mixer. The vibration of the nanotube with respect to the gate changes the conductance at the vibration frequency f_0. An ac voltage is applied to the source-drain at a nearby frequency $f = f_0 + \Delta f$, resulting in a low-frequency output at Δf proportional to the amplitude of the mechanical vibration. Furthermore, the vibration frequency f_0 could be broadly tuned by the application of a dc gate voltage V_G, as shown in the figure.

While these initial results indicate the promise of nanotubes for high-frequency electronics, this field is only just beginning. For traditional applications requiring matching to 50 Ω, reducing the impedance of the device is critical. Devices incorporating multiple nanotubes in oriented arrays [75] or randomly oriented mats [76] have been shown to provide many parallel conductance channels, and hence reduce the device impedance. Single-tube devices, on the other hand, are naturally matched to the high impedances of the nanoscale electronic world and may prove useful as local detectors to read out the high-frequency behavior of other nanoscale devices.

3.3 P–N Junction Devices

Bipolar nanotube devices, where both electron- and hole-doped regions are present in the same device, are garnering increasing attention both for electronic and optoelectronic applications (see also the contribution by Avouris et al.). An example of a p–n junction device [77] is shown in Fig. 10. Separate gates are used to dope adjacent sections of the tube p- and n-type, coupled by an intrinsic region. The I–V_{SD} curves for this device show excellent rectification characteristics, with an exponential turn-on in forward bias and a reverse-bias breakdown voltage in excess of 10 V. Thermal measurements [78] show that the on-state conductance is thermally activated, and the parameters of the junction, from the bandgap to the transmission prob-

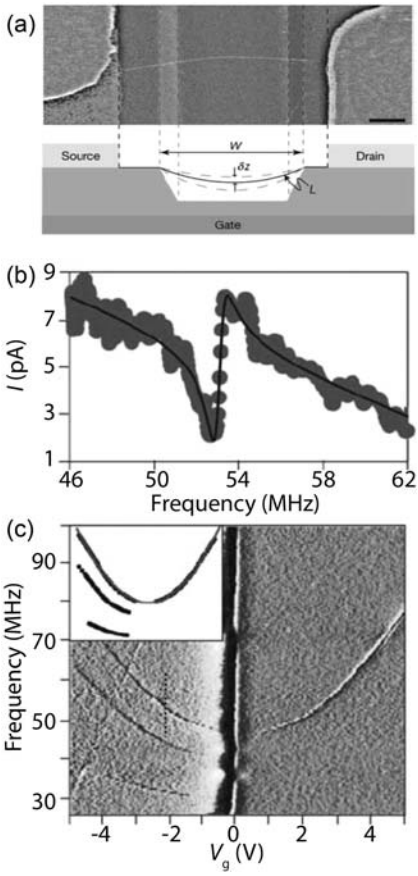

Fig. 9. Nanotube electromechanical resonantor. (**a**) An SEM image of a suspended device (*top*) and a schematic of device geometry (*bottom*). *Scale bar,* 300 nm. The sides of the trench, typically 1.2–1.5 μm wide and 500 nm deep, are marked with *dashed lines.* A suspended nanotube can be seen bridging the trench. (**b**) Detected current as a function of driving frequency. The *solid black line* is a Lorentzian fit to the data with an appropriate phase shift between the driving voltage and the oscillation of the tube. The fit yields the resonance frequency $f_0 = 55$ MHz, and quality factor $Q = 80$. (**c**) Detected current as a function of gate voltage V_G and frequency. The resonances in this figure are plotted as a function of gate voltage in the *inset.* Adapted from [68]

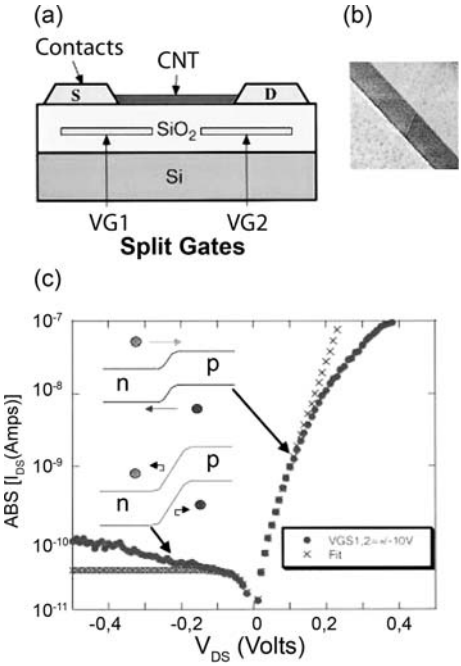

Fig. 10. Split-gate p–n junction device. (**a**) Schematic cross section of the device. The split gates V_{G1} and V_{G2} are used to electrostatically dope a SWNT. For example, a p–n junction with respect to the S contact can be formed by biasing $V_{g1} < 0$ and $V_{g2} > 0$. (**b**) SEM of a SWNT over a 1-μm split gate. (**c**) I–V curve plotted in absolute magnitude of the current. The band diagram illustrates the band structures during forward and reverse bias near the vicinity of the p–n junction. The fit is to the diode equation given with an ideality factor of $n = 1.2$ and $I_0 = 3 \times 10^{-11}$ A. Adapted from [77]

ability, can be inferred. Similar devices are proving to be ideal for studies of the photoconductivity in nanotubes.

p–n–p and n–p–n geometries are also easily created by separately gating different portions of the nanotube. To date, no one has demonstrated three-terminal bipolar transistor operation due to the difficulty of properly contacting the central or "base" region of the nanotube. Nevertheless, these devices have proven useful for a number of fundamental studies. One example [79] is shown in Fig. 11a, where a nanotube is partially suspended over a substrate. While the oxide-bound segments are p-doped by the substrate, the suspended section is intrinsic and thus forms a barrier for transport. A back-gate can offset the energy bands of the suspended section and as a result change the height of the transport barrier. Just before an n-type region is formed in the suspended segment (Fig. 11b), the height of the barrier is equal to the energy gap. Figure 11c shows thermal activation measurements across

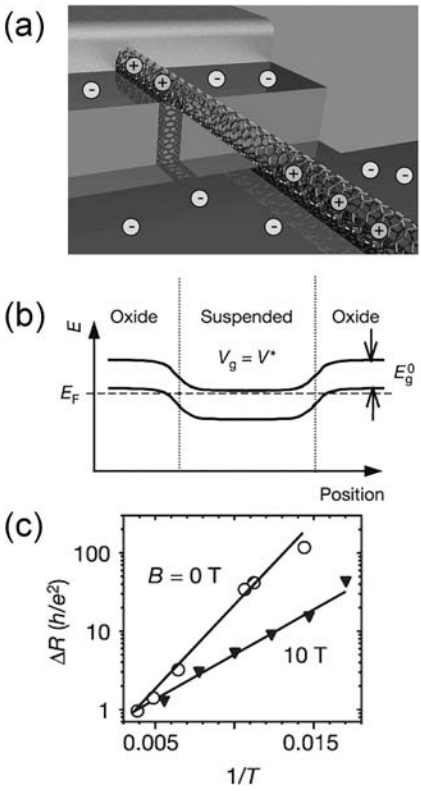

Fig. 11. p–n–p geometry for measuring bandgaps. (**a**) Schematics of a SWNT device partially suspended over a Si/SiO_2 substrate and contacted by source and drain electrodes (only one is shown). Charges on the substrate dope the oxide-bound segments p-type and a buried backgate is used to electrostatically dope the tube. For small positive gate voltages the suspended segment of the tube become n-type, while the oxide-bound segments remain p-type. (**b**) Energy-band diagram corresponding to a gate voltage just before an n-type region is formed in the suspended segment. At this gate voltage the number of thermally activated carriers is minimized, there is no n-type region to facilitate tunneling processes and the tube shows its highest resistance, $R_{\max}$. (**c**) Plot of the maximum resistance after subtracting the contact resistance $\Delta R = R_{\max} - R_{\text{contacts}}$ as a function of the inverse temperature for the nanotube in a magnetic field of 10 T and in zero magnetic field. Adapted from [79]

this barrier from which the bandgap can be directly deduced. These measurements demonstrate that the bandgap decreases linearly with magnetic field at a rate predicted by (3) above. The size of the inferred orbital magnetic moment is an order of magnitude larger than in atoms due to the large radius of the nanotube. Both the orbital and (smaller) spin magnetic moments will play important roles in the nanotube quantum dot measurements presented in the following sections.

4 Quantum Transport

At low temperature, a variety of quantum effects appear in transport in nanotubes. Because the energy scales for these quantum effects typically increase with decreasing system size, the "low-temperature" regime is often more readily reached in nanotubes than in other mesoscopic electronic devices, making nanotubes an attractive system to investigate basic quantum transport effects.

Quantum transport effects include the Coulomb blockade of conduction associated with charge quantization, interference effects associated with coherent wave properties of the charge carriers, periodic shell-filling signatures associated with resonant tunneling through orbital energy levels, Kondo effects associated with a spin degree of freedom on a confined nanotube hybridizing with the continuum of states in the metallic leads, and effects of ferromagnetism and superconductivity in the leads.

Effects of confinement and electron–electron interaction unique to one dimension, and associated with the separation of spin and charge degrees of freedom in excitations, can be identified in transport as power-law dependences of conduction on temperature and source–drain voltage.

Figure 12, showing differential conductance as a function of gate voltage and source–drain bias, provides an overview of various quantum transport regimes for a single tube connected to metallic leads, depending on the coupling of the tube to metallic leads. Evident are the crossovers from Coulomb-blockaded transport, to a fourfold shell-filling structure, to standing-wave (Fabry–Perot) resonances as the conduction between the nanotube and its metallic leads is altered by gross changes in backgate voltage [80].

4.1 Quantum Transport in One Dimension

4.1.1 Luttinger Liquid

In two and three spatial dimensions, the metallic state of interacting electrons is a Fermi liquid, with elementary excitations carrying charge e and spin 1/2, and behaving as weakly interaction fermions. In one dimension, interacting electrons cannot be described as Fermi liquids; spin and charge excitations are described as bosonic modes, are separable, and propagate at different velocities. The Fermi surface is not abrupt, even at zero temperature, and various power-law dependencies are expected in transport. This state is referred to as a Luttinger liquid [81,82]. Nanotubes are a nearly ideal realization of interacting electrons or holes in one dimension, and so provide an excellent testing ground for theoretical predictions of the behavior of Luttinger liquids, particularly in transport.

Power-law scaling of the conductance $G = \mathrm{d}I/\mathrm{d}V_{\mathrm{Sd}}$ with temperature T and source–drain bias V_{Sd}, distinctive features of transport through a Luttinger liquid, has been observed in nanotubes in several experiments [8, 42,

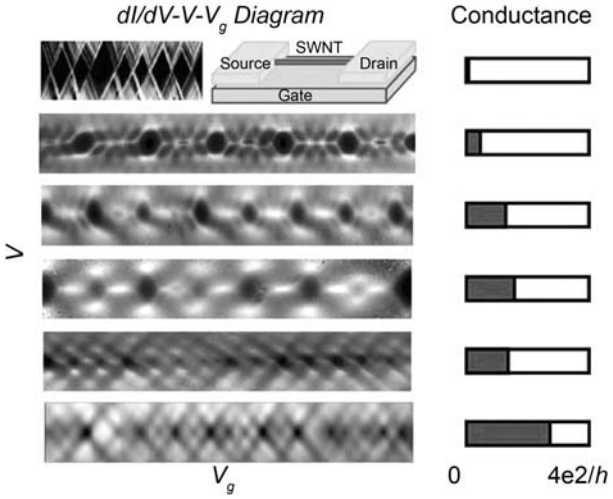

Fig. 12. As the tunnel barrier between nanotube and metallic leads goes from being highly reflecting (*top panels*) to being highly transmitting (*bottom*), the pattern of conductance (*gray scale*) as a function of gate voltage V_g and source–drain voltage V transforms from Coulomb-blockade diamonds, marking the addition of one charge to the nanotube dot per diamond (stripes in the conducting region reflect excited states of the dot) to a fourfold-degenerate pattern, marking the filling of degenerate manifolds (two spin states, two orbital states), to a one-dimensional standing-wave (Fabry–Perot) interference pattern in the nearly open (conductance $\sim 4e^2/h$) regime. *Upper right inside* shows device schematic. Adapted from [80]

83, 84]. For instance, *Bockrath* et al. [83] measured SWNTs contacted either from the top (effectively ending the tube at the contact) or from below (contacting the tube along its bulk), and in both cases find a power law $G(T) \propto T^{\alpha}$ for the zero-bias conductance, with α depending on the fabrication details ($\alpha_{\text{end}} \sim 0.6$, $\alpha_{\text{bulk}} \sim 0.3$) and a similar power law for the differential conductivity at finite bias, $\mathrm{d}I/\mathrm{d}V_{\text{SD}} \propto V_{\text{SD}}^{\alpha}$ yielding comparable values for α. The Luttinger parameter, g, which characterizes the strength and sign of the electron interaction, can be related to readily measured nanotube parameters E_{C}, the charging energy, and Δ the mean orbital level spacing by $g = (1 + 2E_{\text{C}}/\Delta)^{-1/2}$. Estimates and previous measurements give $E_{\text{C}}/\Delta \sim 6$ yielding a theoretical value $g \sim 0.28$, independent of tube length. For a SWNT with four conducting modes, theory also relates α to g: $\alpha_{\text{end}}(\text{theory}) \sim (g^{-1} - 1)/4$, $\alpha_{\text{bulk}}(\text{theory}) \sim (g^{-1} + g - 2)/8$, giving $\alpha_{\text{end}}(\text{theory}) \sim 0.65$ and $\alpha_{\text{bulk}}(\text{theory}) \sim 0.24$, in good agreement with experiment.

4.1.2 Ballistic Transport

Several experiments [11, 13, 51, 85–87] have demonstrated ballistic 1D transport in nanotubes, where the mean-free path of charge excitations exceeds the tube length. The four modes of a SWNT (two for spin, two for orbital degeneracy) give an expected intrinsic conductance of $4e^2/h \sim 6.5\,\mathrm{k}\Omega^{-1}$ for a ballistic nanotube, not including any additional extrinsic resistance at the contacts. Recent measurements on SWNTs with nearly ideal Pd contacts and local, gate-controlled depletion regions, show that the four 1D modes can be depleted one at a time, yielding quantized conductance plateaus [12] as a function of a gate voltage, as shown in Fig. 13. Surprisingly, even in zero applied magnetic field, the plateaus are spaced by e^2/h rather than the expected $2e^2/h$ for spin-degenerate states. The number and spacing of the plateaus, their energy spacing, and their evolution under applied source–drain bias [88] suggest that both orbital and spin degeneracy are lifted during the gate-depletion process. Similar effects have recently been observed in various semiconductor nanowire [89] and bulk heterostructure devices [90–92], and may also be related to the unexpected (but ubiquitious) appearance of an extra conductance plateau as a function of gate voltage, appearing much like a spin-split feature, though at zero magnetic field, at a conductance around $0.7(2e^2/h)$ in semiconductor quantum point contacts [93].

In ballistic nanotubes, conductance oscillations arising from 1D standing-wave-like quantum interference [9] of charge carriers are seen, comparable to Fabry–Perot oscillations in an optical cavity as a function of wavelength or cavity length. These are shown, as an example, in the bottom two panels of Fig. 12.

4.2 Superconducting Proximity Effect

When nanotubes are contacted with superconducting electrodes, signatures of proximity-effect superconductivity can appear [24, 94]. In a recent experiment [95], metallic carbon nanotubes were contacted with multilayer Ti/Al electrodes in a four-probe geometry in order to mitigate the effect of series contact resistance. Below a critical temperature, zero-resistance supercurrents are observed as long as the normal-state conductance is sufficiently high ($\sim 2e^2/h$), indicating highly transparent contacts.

Imperfect transmission at the interfaces produces broadened zero-dimensional (standing-wave) states in the energy-level structure. In normal-state devices, this leads to Fabry–Perot oscillations [9] as a function of gate voltage V_G as seen in the bottom panels of Fig. 12. In the case of the superconducting proximity effect, the broadened zero-dimensional states lead to periodic modulation of the critical current, I_C, as a function of V_G, as seen in Fig. 14. Finite-length Fabry–Perot effects, however, were not able to explain the magnitude of the fluctuations in I_C. Rather, Josephson dynamics indicating multiple reflections were demonstrated by correlating I_C with

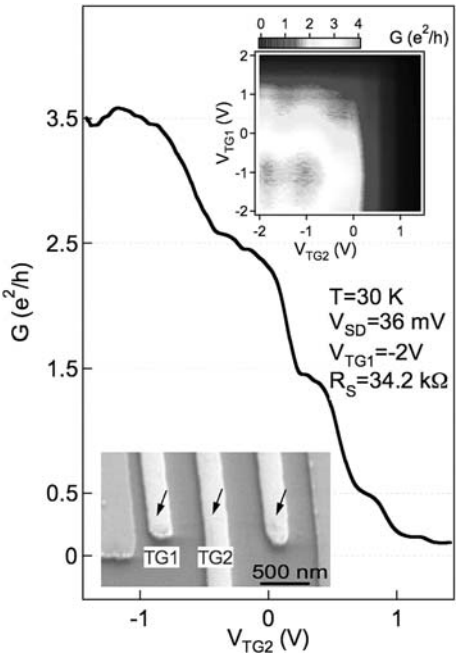

Fig. 13. Evidence of four-step conductance quantization in a single-wall nanotube with highly transparent Pd contacts, in units of the spin-resolved quantum of conductance, e^2/h, at the high-bias half-plateaus. No external magnetic field is applied: $B = 0$. Valley degeneracy can be broken by deformation of the tube, but where is spin degeneracy? *Lower inset* shows the device, with top gates passing over the tube. *Upper inset* shows conductance as a function of two top gates, demonstrating independent gating (*square gray scale pattern*) and a plateau structure for each gate. R_s is the extracted series resistance. Adapted from [12]

the normal-state conductance [95]. Additionally, the differential resistance, $\mathrm{d}V_{\mathrm{sd}}/\,\mathrm{d}I$, measured for current biases in excess of the gate-voltage-dependent $I_{\mathrm{C}}(V_{\mathrm{G}})$ shows modulation on the same voltage scale as that for I_{C}. Multiple Andreev reflections appear as peaks in $\mathrm{d}V_{\mathrm{sd}}/\,\mathrm{d}I$ as a function of applied current bias.

Following this work, more complex device geometries using the gate-tunable supercurrents in nanotubes have been realized. Nanotubes embedded in superconducting devices have been used as tunable Josephson junctions, displaying many of the dc and RF characteristics of standard junctions [96]. A recent experiment demonstrated the formation of a nanotube-based superconducting quantum interference device (SQUID) containing two carbon-nanotube sections connected to an Al loop [97].

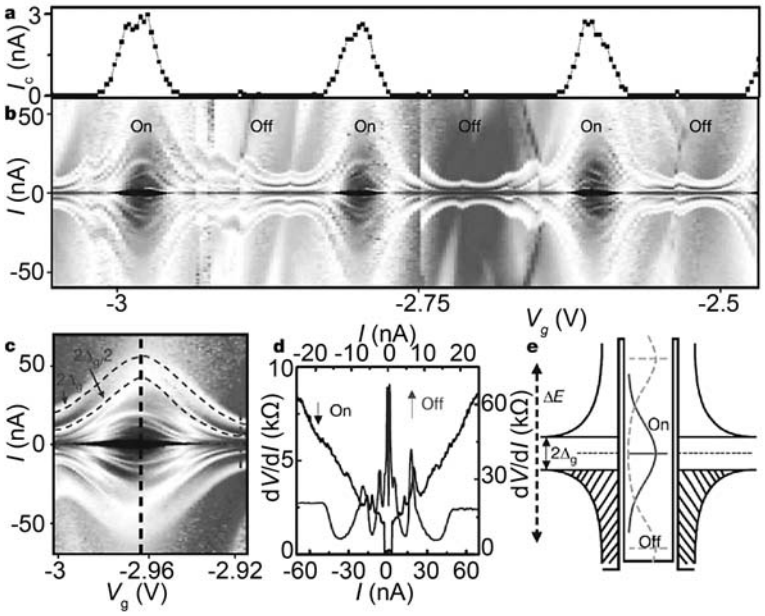

Fig. 14. (**a**) Dependence of critical current I_C on gate voltage, V_g. (**b**) Grayscale of dV/dI, with black representing zero. (**c**) High-resolution plot of dV/dI vs V_g, emphasizing multiple Andreev ridges. (**d**) Cuts through (**c**) at *dashed vertical lines*. (**e**) schematic energy-space diagram showing strongly coupled dot between superconducing leads. *Solid curve* in the central dot region shows "on" state; *dashed curve* shows off state. Adapted from [95]

4.3 Quantum Transport with Ferromagnetic Contacts

Experiments on multiwall carbon nanotubes with ferromagnetic contacts demonstrate the capability of nanotubes to sustain coherent spin transport [98–100]. This was observed through a modification of the device current dependent upon reversing the relative contact magnetizations, with antiparallel (AP) alignment typically producing higher device resistance than parallel (P), and hence a positive magnetoresistance, defined as $[(R_{AP} - R_P)/R_P]$.

Single-wall nanotubes contacted with highly transparent ferromagnetic PdNi leads display Fabry–Perot interference at 4.2 K [101, 102]. It was found that the magnetoresistance oscillated with the conductance, as shown in Fig. 15. These observations are well explained by a spin-dependent Landauer–Büttiker model [103] that independently accounts for the transmission probabilities of majority and minority carriers.

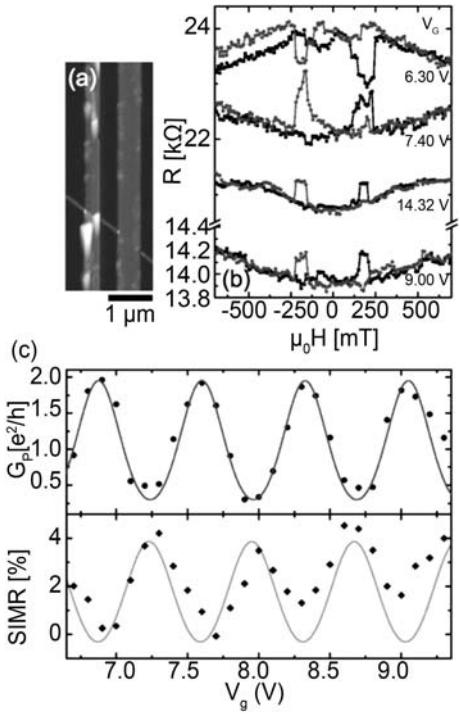

Fig. 15. (**a**) Atomic force micrograph of SWNT with asymmetric PdNi ferromagnetic leads, with the size scale indicated. (**b**) Two-terminal resistance traces as a function of applied magnetic field $\mu_0 H$. Usually, oppositely oriented magnetization leads to higher resistance. In some cases, it leads to a decrease in resistance (e.g., $V_g = 6.30\,\mathrm{V}$). (**c**) Comparison with experiment of theoretical predictions based on a spin-dependent Laudauer–Büttiker approach for calculating the gate-voltage-dependent conductance, and amplitude of spin-induced magnetoresistance (SIMR). Adapted from [101]

5 Nanotube Quantum Dots

A small conducting island – termed a quantum dot or a single-electron transistor – coupled via tunneling to the rest of a circuit, can show signatures of single-electron charging in transport at moderately low temperatures [104]. The requirement of tunneling implies contact resistances in excess of $h/e^2 \sim 26\,\mathrm{k}\Omega$. In addition, the energy required to add a single electron to the island, $e^2/2C$, where C is the island capacitance, must exceed the thermal energy $k_\mathrm{B}T$. Quantum confinement effects may also be observed as a discrete-level structure with orbital spacing Δ. Given the total capacitance values of the order of attofarads ($10^{-18}\,\mathrm{F}$) and energy scales E_C, Δ up to the meV range, single-electron charging effects are most commonly manifested at cryogenic temperatures $< 4\,\mathrm{K}$. Transport measurements are typically performed

as a function of source–drain bias V_{SD} across the island and gate voltage V_G, which shifts the energy levels of the dot. Such measurements permit a full mapping of discrete charge states (manifested as the Coulomb blockade), the excited-state energy spectrum, and exotic multibody interactions, since transport is allowed only when a single-particle energy level is aligned with the chemical potential of the leads [105].

5.1 Single Dots

Highly resistive contacts to carbon nanotubes have proved to be effective tunnel barriers for defining quantum dots. In such a geometry, the bulk of the nanotube forms the zero-dimensional island that is tunnel-coupled to metal leads. In a standard backgated configuration, the Si wafer serves as a gate electrode, which is capacitively coupled to the island [3].

In nanotube quantum dots, E_C is generally of the order of a few meV, and is set by the capacitance of the device. Approximating the capacitance per unit length from the formula for a coaxial cable $C/L = 2\pi\kappa\varepsilon_0 \ln(2h/r)$, where $\kappa \sim 2.5$ is the average of the dielectric constants of SiO_2 and vacuum, h the tube to backgate distance, and $r \sim 1\,\text{nm}$ the tube radius, we find a capacitance per unit length, $C/L \sim 19\,\text{aF}/\mu\text{m}$, and a charging energy, $E_C \sim 8\,\text{meV}/\mu\text{m}$, for a 1-μm gate oxide (a fairly standard value for thermally oxidized wafers).

The zero-dimensional energy-level spacing, Δ, may also be calculated for a carbon nanotube quantum dot of length L. In addition to the quantization of transverse momentum along the circumferential direction, the finite extent of a carbon-nanotube quantum dot leads to the quantization of momentum along the tube axis as $\Delta k = \pi/L$. Linearity of the bands near the Fermi level suggests that one may write

$$\Delta = \frac{h v_F \Delta k}{2 \times 2} \tag{10}$$

with Fermi velocity $v_F = 8.1 \times 10^5\,\text{m/s}$, which gives $\Delta \sim 0.4\,\text{meV}/\mu\text{m}$. The factors of two account for the band and spin degeneracy of the 1D subbands, and should be included when these degeneracies are lifted.

5.2 Band and Spin Effects in Single Quantum Dots

5.2.1 Shell Filling in Nanotube Dots

Transport in nanotube quantum dots shows the familiar characteristics of Coulomb blockade and bias spectroscopy down to individual electrons and holes. A number of experiments have demonstrated even–odd spin filling, where electrons are added to a single orbital level in pairs, occupying states of opposite spin. Experimentally [106] this filling scheme appears as an alternating large–small spacing between the narrow peaks of the conductance that

separate regions of Coulomb-blockaded transport, reflecting a corresponding alternation of addition energy between E_C and $E_C + \Delta$.

The interplay of spin and orbital degeneracies and the energetics of filling a 1D dot with interacting, spatially correlated electrons can lead to interesting filling patterns [107,108], as seen in the middle panels of Fig. 12. Experiments on clean isolated quantum dots, in both suspended and standard carbon nanotubes, show a fourfold periodicity in the addition energy spectrum [109], corresponding to the fourfold degeneracy of the nanotube levels [108, 110–112].

5.2.2 Nanotube Dots with Ferromagnetic Contacts

For experiments on nanotube quantum dots coupled to ferromagnetic leads, the relevant quantity to characterize coherent spin transport is the tunneling magnetoresistance (TMR), defined as TMR $= (R_{AP} - R_P)/R_P$ with subscripts AP and P denoting antiparallel and parallel contact magnetic moments, respectively. If spin transport can be modified *in situ*, it is possible to reverse the sign of the measured TMR. In transport experiments this is accomplished under the influence of an applied gate potential, producing a voltage-controlled spin valve.

Using single- and multiwall nanotube quantum dots contacted with NiPd [100] the Basel group demonstrated sign reversal of the TMR as a function of V_G [102, 113], comparable to the open-transport data [95] in Fig. 15. For SWNT devices the TMR signal oscillates with the same period as the Coulomb-blockade features in transport. The oscillation period, lineshape, and inversion magnitude of the TMR signal are consistent with a model of spin-dependent transmission through localized states on the nanotube dot.

5.3 Kondo Effects in Nanotube Dots

The Kondo effect arises from the hybridization of a localized spin (or any degeneracy within a localized system that can serve as a two-level system) with a continuum of conduction electrons below a characteristic temperature, T_K [114]. When the leads of a two-terminal device are the continua with which the localized spin hybridizes, characteristic transport features appear [115]. These can be readily understood as reflecting a density of states (for the hybridized state) within the dot at the Fermi energy of the lead participating in the hybridization. The Kondo effect in nanotubes was first investigated in 2000 by *Nygard* et al. [116] and shows all of the familiar Kondo-transport features, along with some unique to nanotubes, such as fourfold shell filling [116]. Novel Kondo-related phenomena have appeared in carbon nanotubes owing to both their unique band structure and the ability to produce nanotube quantum dots with non-Fermi liquid leads (e.g., superconducting leads). We highlight a few recent results in the following subsections.

5.3.1 Nonequilibrium Singlet–Triplet Kondo Effect

The Kondo effect is generally observed as a conductance peak at zero bias that appears for $T < T_K$ when the dot is occupied by an odd number of electrons. It was recently shown [117] that the lifted degeneracy between the singlet (spin = 0) and triplet (spin = 1) configurations of a nanotube dot occupied by an *even* number of electrons – somewhat similar to a spin 1/2 system in a magnetic field, though at zero field the triplet is threefold degenerate – also is described by a Kondo effect that appears at a finite source–drain bias V, corresponding to an energy splitting of singlet and triplet energies. In this case, applying an external magnetic field lifts the degeneracy of the triplet state, splitting the single peak in the differential conductance at finite bias into three distinct finite-bias peaks, separated in bias voltage by $\Delta V = g\mu_B B/e$. The splitting provides a straightforward measurement of the electron g factor, which is found to be $g \sim 2$. It was also found that the narrow conduction peaks at finite bias could only be modeled theoretically using a full Kondo treatment.

5.3.2 Orbital and SU(4) Kondo

Kondo correlations can also arise when an orbital degree of freedom serves as the localized two-level system. Since carbon nanotubes possess both band and spin degeneracies, it becomes possible to realize a higher-order Kondo system comprising both spin and orbital degrees of freedom. This system is described by a four-component vector and accordingly an SU(4) symmetry group.

The orbital Kondo effect was realized experimentally [110] in a nanotube quantum dot with an applied field parallel to the tube axis. This field couples to the magnetic moments of the clockwise and counterclockwise circulating electrons (the two isospin states) and tunes the degeneracy between isospin levels. Kondo ridges with appropriate temperature dependences appear at finite values of parallel field in the Coulomb valleys.

The full SU(4) Kondo symmetry appears at zero magnetic field in a regime of gate voltage that displays fourfold symmetry [110]. In Coulomb valleys with unpaired spins, an unusually strong Kondo enhancement is apparent at zero bias, consistent with theory (Fig. 16). As a function of applied magnetic field and source–drain voltage, the Kondo SU(4) resonance splits into four components.

An interesting interplay [118] between the Kondo effect and multiple Andreev reflections (MAR) was investigated in nanotube quantum dots with strong tunnel coupling to superconducting Au/Al leads [119]. This device satisfies the criterion for observing MAR: $E_C \leq \Gamma \sim \Delta_G \leq \Delta$, where E_C is the charging energy, Γ the level broadening due to coupling to the leads, Δ_G is half the superconducting gap of the leads and Δ the mean level spacing of the dot. These processes appear as transport resonances when the

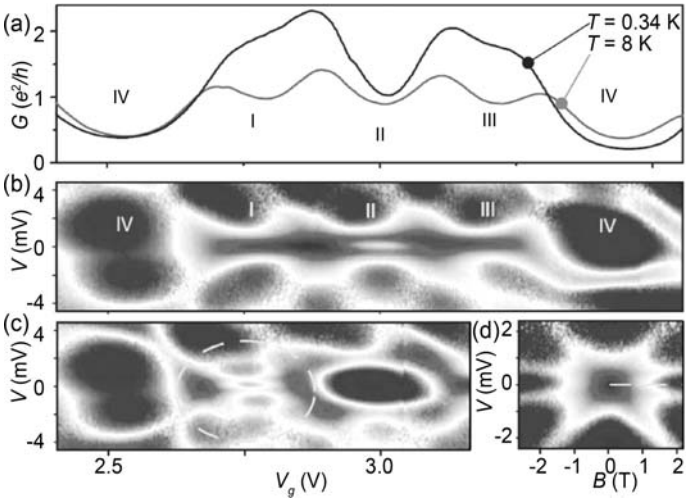

Fig. 16. (**a**) Conductance G as a function of backgate voltage V_g at 8 K and 0.34 K. Signature of the Kondo effect in valleys I and III is the rising conductance at decreased temperature. (**b**) Conductance (grayscale) as a function of V_g and source–drain voltage V at 0.24 K and $B = 0$. (**c**) Same as (**b**) except at 1.5 T. *Circle* marks fourfold splitting region. (**d**) Fourfold splitting of the Kondo peak as a function of field. Adapted from [110]

source–drain bias satisfies $V_{sd} = 2\Delta_G/ne$, with n an integer. Subsequent experiments demonstrating asymmetric device structures with one normal and one superconducting lead have also been performed in the presence of Kondo correlations [120].

5.4 Multiple Quantum Dots

The standard nanotube quantum dot device geometry, with two contacting leads and a single backgate, is ideal for making single quantum dots, but is not well suited for multidot structures since each dot usually requires independent control of tunneling and electrostatics in order to make interesting devices.

Experimental demonstrations of electrostatic depletion regions [12, 121] in a nanotube formed by the application of a voltage to a narrow topgate electrode were reported in [12, 121]. Based on this method, multidot structures were defined by several depletion gates on a single nanotube with transparent Pd electrodes [122]. A series of barrier gates produced local depletion regions in the tube, which served as tunable tunnel barriers, while plunger gates were used to shift the energy levels of the dots formed between the barrier gates (Fig. 17a). Double quantum dots produced in this way are fully tunable, as shown in Fig. 17. Several groups produced devices in similar configurations with comparable behavior [123–125]. Transport measurements on these tunable double quantum dots have now demonstrated signatures of fourfold

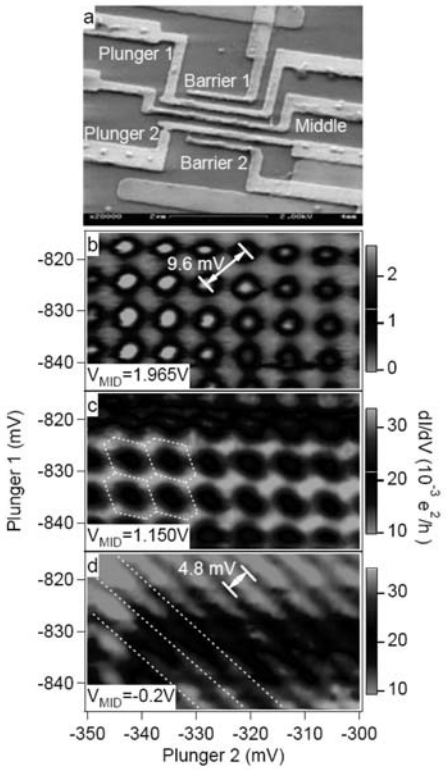

Fig. 17. (**a**) Electron micrograph of top-gated double quantum dot device. Barrier gates define the dots, plunger gates tune the electrostatics of the dots. (**b**) Square array pattern of Coulomb-blockade peaks in the conductance (*grayscale*) as a function of two plunger-gate voltages in the regime of small tunnel coupling and capacitive coupling of the two dots. Each peak marks a transition in the electron number of both of the dots. (**c**) As the middle gate separating the dots becomes less positive, tunneling of holes between the two dots as well as dot–dot crosscapacitance is increased, resulting in a hexagonal pattern of Coulomb-blockade conductance peaks. (**d**) At still lower gate voltage, the two dots merge, and the Coulomb-blockade pattern appears as a series of diagonal bands, where one plunger gate compensates the other, acting on the same large single dot. Adapted from [122]

shell filling in both the honeycomb charge-stability diagram and finite-bias triangles [123].

6 Future Directions

This chapter has presented an overview of the most significant advances in nanotube transport measurements over the past several years. We expect

that transport measurements on nanotubes will continue to produce fruitful experimental studies of basic physical phenomena.

We anticipate that hybrid devices [67], incorporating nanotubes and other nanoelectronics elements will become more common. We also anticipate that the weak hyperfine coupling [126] in carbon will make nanotubes a material system of choice for spin-based quantum information systems.

We anticipate high-frequency phenomena [70, 127] such as quantized vibrational modes or plasmons to become more widely investigated as techniques to measure nanotubes in the terahertz–far-infrared frequency regime are developed. We also expect that optoelectronic devices – structures where electrons and holes are converted to photons (or vice versa) – will open up new vistas for fundamental physics and device applications. While many of the basic transport phenomena in nanotubes are now understood, endless opportunities await the utilization of this unique system to explore the science of the nanoscale world.

References

[1] S. Iijima: Helical microtubules of graphitic carbon, Nature **354**, 56–58 (1991) 455

[2] S. J. Tans, M. H. Devoret, H. J. Dai, A. Thess, R. E. Smalley, L. J. Geerligs, C. Dekker: Individual single-wall carbon nanotubes as quantum wires, Nature **386**, 474–477 (1997) 455, 463

[3] M. Bockrath, D. H. Cobden, P. L. McEuen, N. G. Chopra, A. Zettl, A. Thess, R. E. Smalley: Single-electron transport in ropes of carbon nanotubes, Science **275**, 1922–1925 (1997) 455, 463, 480

[4] S. J. Tans, A. R, M. Verschueren, C. Dekker: Room-temperature transistor based on a single carbon nanotube, Nature **393**, 49–52 (1998) 455, 463, 467

[5] R. Martel, T. Schmidt, H. R. Shea, T. Hertel, P. Avouris: Single- and multi-wall carbon nanotube field-effect transistors, Appl. Phys. Lett. **73**, 2447–2449 (1998) 455, 463, 467

[6] S. G. Louie: in *Carbon Nanotubes* (Springer, Berlin, Heidelberg 2001) pp. 113–145 456

[7] Z. Yao, C. Dekker, P. Avouris: in *Carbon Nanotubes* (Springer, Berlin, Heidelberg 2001) pp. 147–171 456

[8] S. Ilani, L. A. K. Donev, M. Kindermann, P. L. McEuen: Measurement of the quantum capacitance of interacting electrons in carbon nanotubes, Nature Phys. **2**, 687–691 (2006) 458, 459, 474

[9] W. J. Liang, M. Bockrath, D. Bozovic, J. H. Hafner, M. Tinkham, H. Park: Fabry–Perot interference in a nanotube electron waveguide, Nature **411**, 665–669 (2001) 459, 476

[10] J. Kong, E. Yenilmez, T. W. Tombler, W. Kim, H. J. Dai, R. B. Laughlin, L. Liu, C. S. Jayanthi, S. Y. Wu: Quantum interference and ballistic transmission in nanotube electron waveguides, Phys. Rev. Lett. **87**, 106801 (2001) 459

[11] A. Javey, J. Guo, Q. Wang, M. Lundstrom, H. J. Dai: Ballistic carbon nanotube field-effect transistors, Nature **424**, 654–657 (2003) 459, 460, 461, 462, 476
[12] M. J. Biercuk, N. Mason, J. Martin, A. Yacoby, C. M. Marcus: Anomalous conductance quantization in carbon nanotubes, Phys. Rev. Lett. **94**, 026801 (2005) 459, 476, 477, 483
[13] A. Bachtold, M. S. Fuhrer, S. Plyasunov, M. Forero, E. H. Anderson, A. Zettl, P. L. McEuen: Scanned probe microscopy of electronic transport in carbon nanotubes, Phys. Rev. Lett. **84**, 6082–6085 (2000) 460, 463, 464, 476
[14] S. J. Tans, C. Dekker: Molecular transistors – potential modulations along carbon nanotubes, Nature **404**, 834–835 (2000) 460, 464
[15] Y. Yaish, J. Y. Park, S. Rosenblatt, V. Sazonova, M. Brink, P. L. McEuen: Electrical nanoprobing of semiconducting carbon nanotubes using an atomic force microscope, Phys. Rev. Lett. **92**, 046401 (2004) 460
[16] S. Heinze, J. Tersoff, R. Martel, V. Derycke, J. Appenzeller, P. Avouris: Carbon nanotubes as Schottky barrier transistors, Phys. Rev. Lett. **89**, 106801 (2002) 460, 461
[17] F. Leonard, J. Tersoff: Role of Fermi-level pinning in nanotube Schottky diodes, Phys. Rev. Lett. **84**, 4693–4696 (2000) 460
[18] X. D. Cui, M. Freitag, R. Martel, L. Brus, P. Avouris: Controlling energy-level alignments at carbon nanotube/Au contacts, Nano Lett. **3**, 783–787 (2003) 461
[19] Z. H. Chen, J. Appenzeller, J. Knoch, Y. M. Lin, P. Avouris: The role of metal-nanotube contact in the performance of carbon nanotube field-effect transistors, Nano Lett. **5**, 1497–1502 (2005) 461, 462
[20] W. Kim, A. Javey, R. Tu, J. Cao, Q. Wang, H. J. Dai: Electrical contacts to carbon nanotubes down to 1 nm in diameter, Appl. Phys. Lett. **87**, 173101 (2005) 462
[21] C. Gomez-Navarro, P. J. D. Pablo, J. Gomez-Herrero, B. Biel, F. J. Garcia-Vidal, A. Rubio, F. Flores: Tuning the conductance of single-walled carbon nanotubes by ion irradiation in the Anderson localization regime, Nature Mater. **4**, 534–539 (2005) 463
[22] E. D. Minot, Y. Yaish, V. Sazonova, J. Y. Park, M. Brink, P. L. McEuen: Tuning carbon nanotube band gaps with strain, Phys. Rev. Lett. **90**, 156401 (2003) 463
[23] H. W. C. Postma, T. Teepen, Z. Yao, M. Grifoni, C. Dekker: Carbon nanotube single-electron transistors at room temperature, Science **293**, 76–79 (2001) 463
[24] A. Y. Kasumov, R. Deblock, M. Kociak, B. Reulet, H. Bouchiat, I. Khodos, Y. B. Gorbatov, V. T. Volkov, C. Journet, M. Burghard: Supercurrents through single-walled carbon nanotubes, Science **284**, 1508–1511 (1999) 463, 476
[25] M. T. Woodside, P. L. McEuen: Scanned probe imaging of single-electron charge states in nanotube quantum dots, Science **296**, 1098–1101 (2002) 463, 464
[26] M. Shim, A. Javey, N. W. S. Kam, H. J. Dai: Polymer functionalization for air-stable *n*-type carbon nanotube field-effect transistors, J. Am. Chem. Soc. **123**, 11512–11513 (2001) 463, 466

[27] S. Rosenblatt, Y. Yaish, J. Park, J. Gore, V. Sazonova, P. L. McEuen: High performance electrolyte gated carbon nanotube transistors, Nano Lett. **2**, 869–872 (2002) 463, 466
[28] S. D. Li, Z. Yu, C. Rutherglen, P. J. Burke: Electrical properties of 0.4 cm long single-walled carbon nanotubes, Nano Lett. **4**, 2003–2007 (2004) 463, 466
[29] T. Durkop, S. A. Getty, E. Cobas, M. S. Fuhrer: Extraordinary mobility in semiconducting carbon nanotubes, Nano Lett. **4**, 35–39 (2004) 463, 466
[30] X. J. Zhou, J. Y. Park, S. M. Huang, J. Liu, P. L. McEuen: Band structure, phonon scattering, and the performance limit of single-walled carbon nanotube transistors, Phys. Rev. Lett. **95**, 146805 (2005) 463, 465, 466
[31] T. Ando, T. Nakanishi: Impurity scattering in carbon nanotubes – absence of back scattering, J. Phys. Soc. Jpn. **67**, 1704–1713 (1998) 463
[32] P. L. McEuen, M. Bockrath, D. H. Cobden, Y. G. Yoon, S. G. Louie: Disorder, pseudospins, and backscattering in carbon nanotubes, Phys. Rev. Lett. **83**, 5098–5101 (1999) 463
[33] J. C. Charlier, T. W. Ebbesen, P. Lambin: Structural and electronic properties of pentagon–heptagon pair defects in carbon nanotubes, Phys. Rev. B **53**, 11108–11113 (1996) 464
[34] L. Chico, L. X. Benedict, S. G. Louie, M. L. Cohen: Quantum conductance of carbon nanotubes with defects, Phys. Rev. B **54**, 2600–2606 (1996) 464
[35] L. Chico, V. H. Crespi, L. X. Benedict, S. G. Louie, M. L. Cohen: Pure carbon nanoscale devices: Nanotube heterojunctions, Phys. Rev. Lett. **76**, 971–974 (1996) 464
[36] V. H. Crespi, M. L. Cohen, A. Rubio: In situ band gap engineering of carbon nanotubes, Phys. Rev. Lett. **79**, 2093–2096 (1997) 464
[37] L. Chico, M. P. L. Sancho, M. C. Munoz: Carbon-nanotube-based quantum dot, Phys. Rev. Lett. **81**, 1278–1281 (1998) 464
[38] T. Kostyrko, M. Bartkowiak, G. D. Mahan: Reflection by defects in a tight-binding model of nanotubes, Phys. Rev. B **59**, 3241–3249 (1999) 464
[39] T. Kostyrko, M. Bartkowiak, G. D. Mahan: Localization in carbon nanotubes within a tight-binding model, Phys. Rev. B **60**, 10735–10738 (1999) 464
[40] M. Igami, T. Nakanishi, T. Ando: Conductance of carbon nanotubes with a vacancy, J. Phys. Soc, Jpn. **68**, 716–719 (1999) 464
[41] H. J. Choi, J. Ihm, S. G. Louie, M. L. Cohen: Defects, quasibound states, and quantum conductance in metallic carbon nanotubes, Phys. Rev. Lett. **84**, 2917–2920 (2000) 464
[42] Z. Yao, H. W. C. Postma, L. Balents, C. Dekker: Carbon nanotube intramolecular junctions, Nature **402**, 273–276 (1999) 464, 474
[43] M. Ouyang, J. L. Huang, C. L. Cheung, C. M. Lieber: Atomically resolved single-walled carbon nanotube intramolecular junctions, Science **291**, 97–100 (2001) 464
[44] H. Kim, J. Lee, S. J. Kahng, Y. W. Son, S. B. Lee, C. K. Lee, J. Ihm, Y. Kuk: Direct observation of localized defect states in semiconductor nanotube junctions, Phys. Rev. Lett. **90**, 216107 (2003) 464
[45] B. Gao, D. C. Glattli, B. Placais, A. Bachtold: Cotunneling and one-dimensional localization in individual disordered single-wall carbon nanotubes: Temperature dependence of the intrinsic resistance, Phys. Rev. B **74**, 085410 (2006) 464

[46] J. Zhu, M. Brink, P. L. McEuen: Frequency shift imaging of quantum dots with single-electron resolution, Appl. Phys. Lett. **87**, 242102 (2005) 464
[47] C. L. Kane, E. J. Mele, R. S. Lee, J. E. Fischer, P. Petit, H. Dai, A. Thess, R. E. Smalley, A. R. M. Verschueren, S. J. Tans, C. Dekker: Temperature-dependent resistivity of single-wall carbon nanotubes, Europhys. Lett. **41**, 683–688 (1998) 464
[48] J. Appenzeller, R. Martel, P. Avouris, H. Stahl, B. Lengeler: Optimized contact configuration for the study of transport phenomena in ropes of single-wall carbon nanotubes, Appl. Phys. Lett. **78**, 3313–3315 (2001) 464
[49] J. Y. Park, S. Rosenblatt, Y. Yaish, V. Sazonova, H. Ustunel, S. Braig, T. A. Arias, P. W. Brouwer, P. L. McEuen: Electron–phonon scattering in metallic single-walled carbon nanotubes, Nano Lett. **4**, 517–520 (2004) 464
[50] Z. Yao, C. L. Kane, C. Dekker: High-field electrical transport in single-wall carbon nanotubes, Phys. Rev. Lett. **84**, 2941–2944 (2000) 464
[51] A. Javey, J. Guo, M. Paulsson, Q. Wang, D. Mann, M. Lundstrom, H. J. Dai: High-field quasiballistic transport in short carbon nanotubes, Phys. Rev. Lett. **92**, 106804 (2004) 464, 476
[52] A. Javey, P. F. Qi, Q. Wang, H. J. Dai: Ten- to 50-nm-long quasi-ballistic carbon nanotube devices obtained without complex lithography, Proc. Nat. Acad. Sci. USA **101**, 13408–13410 (2004) 464
[53] E. Pop, D. Mann, J. Cao, Q. Wang, K. Goodson, H. J. Dai: Negative differential conductance and hot phonons in suspended nanotube molecular wires, Phys. Rev. Lett. **95**, 155505 (2005) 465
[54] D. Mann, Y. K. Kato, A. Kinkhabwala, E. Pop, J. Cao, X. R. Wang, L. Zhang, Q. Wang, J. Guo, H. J. Dai: Electrically driven thermal light emission from individual single-walled carbon nanotubes, Nature Nanotechnol. **2**, 33–38 (2007) 465
[55] H. Suzuura, T. Ando: Phonons and electron-phonon scattering in carbon nanotubes, Phys. Rev. B **65**, 235412 (2002) 466
[56] G. Pennington, N. Goldsman: Semiclassical transport and phonon scattering of electrons in semiconducting carbon nanotubes, Phys. Rev. B **68**, 045426 (2003) 466
[57] V. Perebeinos, J. Tersoff, P. Avouris: Electron–phonon interaction and transport in semiconducting carbon nanotubes, Phys. Rev. Lett. **94**, 086802 (2005) 466
[58] A. Javey, H. Kim, M. Brink, Q. Wang, A. Ural, J. Guo, P. McIntyre, P. McEuen, M. Lundstrom, H. J. Dai: High-kappa dielectrics for advanced carbon-nanotube transistors and logic gates, Nature Mater. **1**, 241–246 (2002) 467, 468
[59] A. Javey, J. Guo, D. B. Farmer, Q. Wang, E. Yenilmez, R. G. Gordon, M. Lundstrom, H. J. Dai: Self-aligned ballistic molecular transistors and electrically parallel nanotube arrays, Nano Lett. **4**, 1319–1322 (2004) 467
[60] S. J. Wind, J. Appenzeller, R. Martel, V. Derycke, P. Avouris: Vertical scaling of carbon nanotube field-effect transistors using top gate electrodes, Appl. Phys. Lett. **80**, 3817–3819 (2002) 467
[61] A. Javey, J. Guo, D. B. Farmer, Q. Wang, D. W. Wang, R. G. Gordon, M. Lundstrom, H. J. Dai: Carbon nanotube field-effect transistors with integrated ohmic contacts and high-k gate dielectrics, Nano Lett. **4**, 447–450 (2004) 467

[62] Z. H. Chen, J. Appenzeller, Y. M. Lin, J. Sippel-Oakley, A. G. Rinzler, J. Y. Tang, S. J. Wind, P. M. Solomon, P. Avouris: An integrated logic circuit assembled on a single carbon nanotube, Science **311**, 1735–1735 (2006) 467, 469
[63] Z. Yu, P. J. Burke: Microwave transport in metallic single-walled carbon nanotubes, Nano Lett. **5**, 1403–1406 (2005) 469
[64] J. J. Plombon, K. P. O'Brien, F. Gstrein, V. M. Dubin, Y. Jiao: High-frequency electrical properties of individual and bundled carbon nanotubes, Appl. Phys. Lett. **90**, 063106 (2007) 469
[65] Z. Yu, C. Rutherglen, R. J. Burke: Microwave nanotube transistor operation at high bias, Appl. Phys. Lett. **88**, 233115 (2006) 469
[66] S. D. Li, Z. Yu, S. F. Yen, W. C. Tang, P. J. Burke: Carbon nanotube transistor operation at 2.6 GHz, Nano Lett. **4**, 753–756 (2004) 469
[67] M. J. Biercuk, D. J. Reilly, T. M. Buehler, V. C. Chan, J. M. Chow, R. G. Clark, C. M. Marcus: Charge sensing in carbon-nanotube quantum dots on microsecond timescales, Phys. Rev. B **73**, 201402 (2006) 469, 485
[68] V. Sazonova, Y. Yaish, H. Ustunel, D. Roundy, T. A. Arias, P. L. McEuen: A tunable carbon nanotube electromechanical oscillator, Nature **431**, 284–287 (2004) 470, 471
[69] J. Appenzeller, D. J. Frank: Frequency dependent characterization of transport properties in carbon nanotube transistors, Appl. Phys. Lett. **84**, 1771–1773 (2004) 470
[70] S. Rosenblatt, H. Lin, V. Sazonova, S. Tiwari, P. L. McEuen: Mixing at 50 GHz using a single-walled carbon nanotube transistor, Appl. Phys. Lett. **87**, 153111 (2005) 470, 485
[71] A. A. Pesetski, J. E. Baumgardner, E. Folk, J. X. Przybysz, J. D. Adam, H. Zhang: Carbon nanotube field-effect transistor operation at microwave frequencies, Appl. Phys. Lett. **88**, 113103 (2006) 470
[72] F. Rodriguez-Morales, R. Zannoni, J. Nicholson, M. Fischetti, K. S. Yngvesson, J. Appenzeller: Direct and heterodyne detection of microwaves in a metallic single wall carbon nanotube, Appl. Phys. Lett. **89**, 083502 (2006) 470
[73] H. B. Peng, C. W. Chang, S. Aloni, T. D. Yuzvinsky, A. Zettl: Ultrahigh frequency nanotube resonators, Phys. Rev. Lett. **97**, 087203 (2006) 470
[74] B. Witkamp, M. Poot, H. S. J. van der Zant: Bending-mode vibration of a suspended nanotube resonator, Nano Lett. **6**, 2904–2908 (2006) 470
[75] S. J. Kang, C. Kocabas, T. Ozel, M. Shim, N. Pimparkar, M. A. Alam, S. V. Rotkin, J. A. Rogers: High-performance electronics using dense, perfectly aligned arrays of single-walled carbon nanotubes, Nature Nanotechnol. **2**, 230–236 (2007) 470
[76] E. S. Snow, J. P. Novak, P. M. Campbell, D. Park: Random networks of carbon nanotubes as an electronic material, Appl. Phys. Lett. **82**, 2145–2147 (2003) 470
[77] J. U. Lee, P. P. Gipp, C. M. Heller: Carbon nanotube p–n junction diodes, Appl. Phys. Lett. **85**, 145–147 (2004) 470, 472
[78] K. Bosnick, N. Gabor, P. McEuen: Transport in carbon nanotube p–i–n diodes, Appl. Phys. Lett. **89**, 163121 (2006) 470

[79] E. D. Minot, Y. Yaish, V. Sazonova, P. L. McEuen: Determination of electron orbital magnetic moments in carbon nanotubes, Nature **428**, 536–539 (2004) 472, 473
[80] W. J. Liang, M. Bockrath, H. Park: Transport spectroscopy of chemical nanostructures: The case of metallic single-walled carbon nanotubes, Ann. Rev. Phys. Chem. **56**, 475–490 (2005) 474, 475
[81] F. D. M. Haldane: 'Luttinger liquid theory' of one-dimensional quantum fluids. I. Properties of the Luttinger model and their extension to the general 1D interacting spinless Fermi gas, J. Phys. C **14**, 2585–609 (1981) 474
[82] J. Voit: One-dimensional Fermi liquids, Rep. Prog. Phys. **57**, 977 (1994) 474
[83] M. Bockrath, D. H. Cobden, J. Lu, A. G. Rinzler, R. E. Smalley, T. Balents, P. L. McEuen: Luttinger-liquid behaviour in carbon nanotubes, Nature **397**, 598–601 (1999) 475
[84] H. W. C. Postma, M. de Jonge, C. Dekker: Electrical transport through carbon nanotube junctions created by mechanical manipulation, Phys. Rev. B **62**, R10653–6 (2000) 475
[85] D. Mann, A. Javey, J. Kong, Q. Wang, H. Dai: Ballistic transport in metallic nanotubes with reliable Pd ohmic contacts, Nano Lett. **3**, 1541 (2003) 476
[86] C. Berger, Y. Yi, Z. L. Wang, W. A. de Heer: Multiwalled carbon nanotubes are ballistic conductors at room temperature, Appl. Phys. A-Mater. **A74**, 363–5 (2002) 476
[87] C. Berger, P. Poncharal, Y. Yi, W. de Heer: Ballistic conduction in multiwalled carbon nanotubes, J. Nanosci. Nanotechnol. **3**, 171–7 (2003) 476
[88] H. van Houten, C. Beenakker, B. van Wees: in M. A. Reed (Ed.): *Nanostructured Systems* (Academic Press, San Diego 1992) pp. 9–112 476
[89] W. Liu, J. Xiang, B. P. Timko, Y. Wu, C. M. Lieber: One-dimensional hole gas in germanium/silicon nanowire heterostructures, Proc. Nat. Acad. Sci. **102**, 10046 (2005) 476
[90] D. J. Reilly, T. M. Buehler, J. L. O'Brien, A. R. Hamilton, A. S. Dzurak, R. G. Clark, B. E. Kane, L. N. Pfeiffer, K. W. West: Density-dependent spin polarization in ultra-low-disorder quantum wires, Phys. Rev. Lett. **89**, 246801/1–4 (2002) 476
[91] K. J. Thomas, J. T. Nicholls, M. Y. Simmons, M. Pepper, D. R. Mace, D. A. Ritchie: Possible spin polarization in a one-dimensional electron gas, Phys. Rev. Lett. **77**, 135–8 (1996) 476
[92] G. Scappucci, L. D. Gaspare, E. Giovine, A. Notargiacomo, R. Leoni, F. Evangelisti: Conductance quantization in etched Si/SiGe quantum point contacts, Phys. Rev. B **74**, 035321 (2006) 476
[93] S. M. Cronenwett, H. J. Lynch, D. Goldhaber-Gordon, L. P. Kouwenhoven, C. M. Marcus, K. Hirose, N. S. Wingreen, V. Umansky: Low-temperature fate of the 0.7 structure in a point contact: A Kondo-like correlated state in an open system, Phys. Rev. Lett. **88**, 226805/1–4 (2002) 476
[94] A. F. Morpurgo, J. Kong, C. M. Marcus, H. Dai: Gate-controlled superconducting proximity effect in carbon nanotubes, Science **286**, 263–5 (1999) 476
[95] P. Jarillo-Herrero, J. A. van Dam, L. P. Kouwenhoven: Quantum supercurrent transistors in carbon nanotubes, Nature **439**, 953 (2006) 476, 477, 478, 481
[96] J. P. Cleuziou, W. Wernsdorfer, S. Andergassen, S. Florens, V. Bouchiat, T. Ondarcuhu, M. Monthioux: Gate-tuned high frequency response of carbon nanotube Josephson junctions, arXiv (2007) URL: `0705.2033` 477

[97] J. P. Cleuziou, W. Wernsdorfer, H. Bouchiat, T. Ondarcuhu, M. Monthioux: Carbon nanotube superconducting quantum interference device, Nature Nanotechnol. **1**, 53 (2006) 477

[98] S. Chakraborty, K. M. Walsh, B. W. Alphenaar, L. Liu, K. Tsukagoshi: Temperature-mediated switching of magnetoresistance in co-contacted multiwall carbon nanotubes, Appl. Phys. Lett. **83**, 1008–10 (2003) 478

[99] K. Tsukagoshi, B. W. Alphenaar, H. Ago: Coherent transport of electron spin in a ferromagnetically contacted carbon nanotube, Nature **401**, 572–4 (1999) 478

[100] S. Sahoo, T. Kontos, C. Schonenberger, C. Surgers: Electrical spin injection in multiwall carbon nanotubes with transparent ferromagnetic contacts, Appl. Phys. Lett. **86**, 112109 (2005) 478, 481

[101] H. T. Man, I. J. W. Wever, A. F. Morpurgo: Spin-dependent quantum interference in single-wall carbon nanotubes with ferromagnetic contacts, Phys. Rev. B **73**, 241401(R) (2006) 478, 479

[102] A. Cottet, T. Kontos, S. Sahoo, H. T. Man, M.-S. Choi, W. Belzig, C. Bruder, A. F. Morpurgo, C. Schonenberger: Nanospintronics with carbon nanotubes, Semicond. Sci. Technol. **21**, S78 (2006) 478, 481

[103] C. Beenakker, H. van Houten: in *Solid State Physics – Advances in Research and Applications* (Academic, San Diego, CA 1991) pp. 1–228 478

[104] L. Kouwenhoven, C. Marcus: Quantum dots, Phys. World **11**, 35–9 (1998) 479

[105] L. P. Kouwenhoven, C. Marcus, P. L. McEuen, S. Tarucha, R. M. Westervelt, N. S. Wingreen: Electron transport in quantum dots, in L. P. Kouwenhoven, G. Schon, L. L. Sohn (Eds.): *NATO ASI conference proceedings* (Kluwer, Dordrecht 1997) 480

[106] D. H. Cobden, M. Bockrath, P. L. McEuen, A. G. Rinzler, R. E. Smalley: Spin splitting and even-odd effects in carbon nanotubes, Phys. Rev. Lett. **81**, 681–4 (1998) 480

[107] D. H. Cobden, J. Nygard: Shell filling in closed single-wall carbon nanotube quantum dots, Phys. Rev. Lett. **89**, 046803 (2002) 481

[108] W. Liang, M. Bockrath, H. Park: Shell filling and exchange coupling in metallic single-walled carbon nanotubes, Phys. Rev. Lett. **88**, 126801/1–4 (2002) 481

[109] S. Sapmaz, P. Jarillo-Herrero, J. Kong, C. Dekker, L. P. Kouwenhoven, H. S. J. van der Zant: Electronic excitation spectrum of metallic carbon nanotubes, Phys. Rev. B **71**, 153402 (2005) 481

[110] P. Jarillo-Herrero, J. Kong, H. S. J. van der Zant, C. Dekker, L. P. Kouwenhoven, S. D. Franceschi: Orbital Kondo effect in carbon nanotubes, Nature **434**, 484 (2005) 481, 482, 483

[111] A. Makarovski, J. Liu, G. Finkelstein: Evolution of SU(4) transport regimes in carbon nanotube quantum dots, arXiv (2006) URL: `cond-mat/0608573` 481

[112] S. Moriyama, T. Fuse, M. Suzuki, Y. Aoyagi, K. Ishibashi: Four-electron shell structures and an interacting two-electron system in carbon nanotube quantum dots, Phys. Rev. Lett. **94**, 186806 (2005) 481

[113] S. Sahoo, T. Kontos, J. Furer, C. Hoffmann, M. Graber, A. Cottet, C. Schonenberger: Electric field control of spin transport, Nature Phys. **1**, 99 (2005) 481

[114] A. C. Hewson: *The Kondo Problem to Heavy Fermion* (Cambridge University Press, Cambridge 1993) 481
[115] L. Kouwenhoven, L. Glazman: Revival of the Kondo effect, Phys. World **14**, 33–38 (2001) 481
[116] J. Nygard, D. H. Cobden, P. E. Lindelof: Kondo physics in carbon nanotubes, Nature **408**, 342–6 (2000) 481
[117] J. Paaske, A. Rosch, P. Wolfle, N. Mason, C. Marcus, J. Nygard: Non-equilibrium singlet–triplet Kondo effect in carbon nanotubes, Nature Phys. **2**, 460 (2006) 482
[118] A. A. Clerk, V. Ambegaokar, S. Hershfield: Andreev scattering and the Kondo effect, Phys. Rev. B **61**, 3555–62 (2000) 482
[119] M. R. Buitelaar, W. Belzig, T. Nussbaumer, B. Babic, C. Bruder, C. Schonenberger: Multiple Andreev reflections in a carbon nanotube quantum dot, Phys. Rev. Lett. **91**, 057005 (2003) 482
[120] M. Graber, T. Nussbaumer, W. Belzig, C. Schonenberger: Quantum dot coupled to a normal and a superconducting lead, Nanotechnol. **15**, S479 (2004) 483
[121] M. J. Biercuk, N. Mason, C. M. Marcus: Locally addressable tunnel barriers within a carbon nanotube, Nano Lett. **4**, 2499–2502 (2004) 483
[122] M. J. Biercuk, S. Garaj, N. Mason, J. M. Chow, C. M. Marcus: Gate-defined quantum dots on carbon nanotubes, Nano Lett. **5**, 1267 (2005) 483, 484
[123] S. Sapmaz, C. Meyer, P. Beliczynski, P. Jarillo-Herrero, L. P. Kouwenhoven: Excited state spectroscopy in carbon nanotube double quantum dots, Nano Lett. **6**, 1350 (2006) 483, 484
[124] M. Graber, T. Nussbaumer, W. Belzig, C. Schonenberger: Molecular states in carbon nanotube double quantum dots, Phys. Rev. B **74**, 075427 (2006) 483
[125] H. I. Grove-Rasmussen, J. R. Hauptmann, P. E. Lindelof: Single wall carbon nanotube double quantum dot, Appl. Phys. Lett. **89**, 232113 (2006) 483
[126] Y. G. Semenov, K. W. Kim, G. J. Iafrate: Electron spin relaxation in semiconducting carbon nanotubes: The role of hyperfine interaction, Phys. Rev. B **75**, 045429 (2007) 485
[127] P. J. Burke: Solid State Electronics **48**, 2013 (2004) 485

Index

Introduction to the Important and Exciting Aspects of Carbon-Nanotube Science and Technology

David Tománek[1], Ado Jorio[2,3], Mildred S. Dresselhaus[4], and Gene Dresselhaus[5]

[1] Physics and Astronomy Department, Michigan State University, East Lansing, Michigan 48824-2320, USA
[2] Departamento de Física, Universidade Federal de Minas Gerais, Belo Horizonte, MG, 30.123-970, Brazil
adojorio@fisica.ufmg.br
[3] Diviso de Metrologia de Materiais, Instituto Nacional de Metrologia, Normalizao e Qualidade Industrial (INMETRO), Duque de Caxias, RJ, 25250-020, Brazil
[4] Department of Physics and Department of Electrical Engineering and Computer Science, Massachusetts Institute of Technology, Cambridge, MA, 02139-4307, USA
millie@mgm.mit.edu
[5] Francis Bitter Magnet Laboratory, Massachusetts Institute of Technology, Cambridge, MA, 02139-4307, USA
gene@mgm.mit.edu

Abstract. The 21 contributions of this book cover advanced topics on the application, synthesis, structure and properties of carbon nanotubes and related materials. These topics are linked to one another in this introductory contribution. By describing the book structure and highlighting advances in the field since the publication of the first volume (Carbon Nanotubes: Synthesis, Structure, Properties and Applications, edited by M. S. Dresselhaus. G. Dresselhaus and P. Avouris, Vol. 80, Topics in Applied Physics Series, Springer, Berlin, 2000), it seems clear that the carbon nanotube field is on the verge of approaching a "phase-transition critical point". Carbon nanotubes have been a model system for studying physics and for developing new measurement tools. The field is now mature for making the transition from nanoscience to nanotechnology, as we show here.

1 Introduction

Over the past 15 years, carbon nanotubes have evolved into one of the most intensively studied materials of this decade. The field has changed substantially since the publication of the first edition [Carbon Nanotubes: Synthesis, Structure, Properties and Applications, edited by M. S. Dresselhaus. G. Dresselhaus and P. Avouris, Vol. 80, Topics in Applied Physics Series, Springer,

A. Jorio, G. Dresselhaus, M. S. Dresselhaus (Eds.): Carbon Nanotubes,
Topics Appl. Physics **111**, 1–12 (2008)

Berlin, 2000]. The present volume focuses on advanced topics and applications, built on the generic aspects of the first volume that stresses some of the fundamentals of carbon-nanotube science. It is important to recognize that while the last contribution of the first volume was devoted to applications, in the present volume applications come in the first contribution, as well as being spread over many other contributions. The development of nanometrology, important for achieving reliability and industrial quality for the new generation of nanomaterials as they enter into nanotechnology, is the second topic in this book. The other 19 contributions in this volume were selected to reflect areas that have grown most rapidly since the first volume, and many of these chapters devote a section for specific applications of the science featured in the contribution. Areas like graphene, other carbon-like and other tube-like materials, not so much discussed in the 2000 volume, are now more prominently featured because these fields are likely to affect and influence developments in nanotubes in the next 5 years. The role of carbon nanotubes as a model system for studying low dimensional physics and for developing new measurement tools is likely to increase in concert with developments in graphene.

Due to their unique structural, chemical, mechanical, thermal, optical, optoelectronic and electronic properties, the interest in the fundamental properties of carbon nanotubes and their exploitation through a wide range of applications continues to increase. Regarding the synthesis of single-wall carbon nanotubes (SWNTs), the growth of a single tube at a specific location and in a given direction, and the growth of a huge amount of millimeter-long tubes with nearly 100 % purity have been achieved. Regarding nanotube processing, substantial success with the separation of nanotubes by metallicity and length has been achieved and advances have been made with doping nanotubes for the modification of their properties. Studies on nanotube optics, transport and electrochemistry have exploded, revealing many rich and complex fundamental excitonic phenomena. The magnetic properties have now been accessed experimentally, revealing many novel effects including symmetry-breaking phenomena leading to the investigation of dark states. Quantum transport phenomena, including quantum information, spintronics and superconducting effects have also been explored. Major advances have been achieved in the study of double-wall carbon-nanotube physics, greatly advancing our understanding of multiwall carbon nanotubes and intertube interactions. Finally, a comparison between recent findings related to carbon nanotubes, graphene, other carbon-like or tube-like materials have strongly enriched all of these fields, thereby opening up many new routes for exciting and unexpected developments.

This is an important time to review what we have learned in the past decade and, most important, to look into the future of the carbon nanotube and related fields. Carbon nanotubes are often held responsible for co-triggering the nanotechnology revolution. To gain a deeper understanding of

the meaning of this nanotechnology revolution, each section of this chapter presents a preview of the exciting things you will find in this book.

2 Applications and Metrology

After a decade and a half of intense activity in carbon-nanotube research, more and more attention is now focusing on the practical applications of the many unique and special properties of carbon nanotubes. The overwhelming interest in applications of carbon nanotubes has motivated the editors to feature applications in the chapter of the book by Endo et al. In developing this topic, we consider, on the one hand, applications for which carbon nanotubes have already entered the commercial market place. Some of these applications are growing rapidly. Following closely behind are a host of applications with promise for commercialization in the coming decade now under development in laboratories worldwide, some in a university setting, others in national research laboratories where many special facilities are available. Much activity is occurring as expected in industrial research laboratories, including startup companies, large established corporations, and everything in between. Finally, there are many longer-term applications-oriented efforts emanating from fundamental discoveries at one end of the spectrum or from needs-driven R&D at the other end. Besides the chapter by Endo et al., interesting applications are found in many other chapters of the book, especially in the contribution by Terrones et al. on doping nanotubes, in the contribution on carbon nanohorns and nanocones by Yudasaka et al. add comma here and on inorganic nanotubes and fullerene-like structures by Tenne et al.

For applications to have broad impact on society they have to be based on metrology, standardization and industrial quality control. Metrology is important for nanomaterials in general, and single-wall carbon nanotubes (SWNTs) are of special importance for nanometrology science. A review on nanotube metrology in support of these applications is presented in the chapter by Jorio et al. and is a new review article feature for this volume. Although various tools and approaches towards advancing nanotube metrology will be found in many of the chapters of this book, the chapter by Jorio et al. is the keynote metrology chapter, especially devoted to the research aspects of metrology. The special challenges of nanotube metrology arise from many factors: 1. the very small diameter of nanotubes, 2. the paucity of instruments with sufficient resolution to measure accurately and reproducibly specific properties of objects on such a small length scale, 3. the diverse properties of different (n, m) tubes differing from one another by only small differences in diameter or chiral angle (where (n, m) denotes the tube chiral indices), 4. the difficulty in controlling the nanotube (n, m) chirality at the synthesis stage, 5. the importance of environmental effects on the detailed properties of nanostructured materials. On one hand, research in the metrology of carbon nanotubes promises to be a challenging intellectual endeavor, which is expected to im-

pact the overall nanoscience and nanotechnology revolution. Such research is also vital to provide a basis for establishing standards, metrics, and the industrial quality control that will be necessary for large-scale production of products conforming to controlled specifications. Safety and public-health issues are also important concerns for large-scale commercialization of nanostructures such as carbon nanotubes.

3 Synthesis

Synthesis remains a central focus, since we are still far from gaining a reliable control over synthesis methods to produce the desired (n, m) carbon nanotube at a given location, growing in a desired direction over a controlled length. The chapter by Joselevich et al. on nanotube synthesis is the second longest chapter in the book (after applications), reflecting the fact that nanotube synthesis is the most popular and most challenging research area of nanotube research, and results in the largest relative number of publications. The coverage includes topics such as synthesis methods and mechanisms, scaleup, purification, sorting by metallicity, diameter and length, nanotube alignment and epitaxy organization into fibers, films, and other structures. Scientific advances and practical applications are both critically dependent on the success in advancing the broad front of challenges now being addressed by this large research community, now being joined by an even larger user community seeking the utilization of nanotubes for their own applications, both scientifically and commercially.

All common methods to synthesize carbon nanotubes involve high temperatures, including the carbon arc (CA) discharge, pulsed-laser vaporization (PLV) of graphite, thermal or plasma-assisted chemical vapor deposition (CVD), high-pressure CO (HipCO) decomposition. The treatment of a system out of equilibrium is always a challenge for physics. These high-temperature processes are rather efficient and robust, but yield a mixture of metallic and semiconducting tubes, and a mixture of (n, m) nanotube chiral indices. Although amazing advances in the placement of nanotubes in specific positions and in shaping nanotube ensembles into fancy arrangements have been achieved, the (n, m) polymorphism in carbon nanotubes remains a largely unresolved problem that currently limits molecular electronics applications of nanotubes. Structural defects and their control are also an issue. Other interesting nanotube-like structures, such as the nanohorns and nanocones, and inorganic nanotubes (discussed elsewhere in the book) also present challenging synthesis problems. The synthesis on n-layer graphene samples has become a new major synthesis challenge.

4 Defect Control

The important topic of defects in carbon nanotubes has started to receive more and more attention. Defects in nanomaterials not only drastically influence their optical, mechanical and thermal properties, but defects are likely to play an essential role in nanomaterials-based devices. As in other nanostructures, the conductance and other properties of nanotubes are strongly influenced by defects. The presence of defects brings benefits, including the introduction of anchor points for chemical functionalization, charge injection, and symmetry-breaking effects, thus facilitating spectroscopic characterization. On the other hand, the suitability of nanotubes for future large-scale applications depends on developing successful strategies to control the defects needed for specific applications, while limiting their negative influence on other nanotube properties. Since the lifetime of electronic excitations, which significantly change the force field in nanotubes, extends over several phonon periods, photochemical processes offer a unique possibility to selectively reconnect broken bonds, or selectively desorb impurities. Nanotubes thus appear as promising candidates for the nanomanipulation of atomic-scale defects using monochromatic light or electrons, with no adverse effects on the defect-free nanotube regions, and leaving no chemical residue. Challenging opportunities are being pursued in the detailed characterization of specific defects in nanotubes. The utilization of these specific interactions to better control nanotube properties is expected to have a major impact on the future applications of carbon nanotubes. Therefore, structural defects are an issue that is important to all the articles in this book, and defects will have to be deeply explored before we can understand and utilize the ultimate properties of carbon nanotubes.

5 Mechanical and Thermal Properties

Vital to the applications of carbon nanotubes are their unusual mechanical and thermal properties, which are reviewed in the chapter by Yamamoto et al. On a per-bond basis, the graphitic sp^2 bond is 33% stronger than the sp^3 bond of diamond, the hardest substance in nature. The high tensile strength of nanotubes is closely related to that of graphene. In contrast to planar graphene, the cylindrical shape provides nanotubes with structural stability also under compression. The Young's modulus of nanotube bundles, when considered as a uniform material, exceeds 1 TPa. This is particularly beneficial for the high-strength properties of composites based on nanotubes. Major challenges are achieving a uniform dispersion and alignment of nanotubes in a matrix, and matrix-to-nanotube load transfer. An intriguing way to harness the toughness of nanotubes is to spin them into yarns and fibers. Current emphasis is on advancing both the science and applications stemming from these mechanical properties. Since defects strongly influence the mechanical

properties of nanotubes, researchers come back continuously to facing the challenges of controlling the synthesis process.

Until recently, the thermal conductivity of isotopically pure diamond was unsurpassed in nature due to the combination of a high speed of sound, high Debye temperature, and a long phonon mean-free path. The thermal conductivity of nanotubes along their axis appears superior to that of all materials, including diamond, due to the benefits derived from the strength and toughness of the sp^2 bond and from the 1D character of nanotubes that strongly limits their allowed scattering processes. Due to their relationship to graphene, carbon nanotubes remain stable up to very high temperatures, close to the melting point of graphite near 4000 K. Similar to other polymers and low-dimensional structures, nanotubes maximize their configurational and vibrational entropy at little energy cost, giving rise to thermal contraction in length and volume up to temperatures of several hundred degrees Celsius. Only at higher temperatures, corresponding to a significant fraction of their high melting point, do anharmonicities start to dominate and induce thermal expansion.

The opportunities for applications emanating from the remarkable thermal and mechanical properties of carbon nanotubes are extraordinary. These great mechanical properties have been envisaged theoretically and experimentally, but some unknowns still impede achievement of the ultimate thermal and mechanical performance expected for carbon nanotubes. While the connection between the chapter by Endo et al. on applications and the chapter by Yamamoto et al. on mechanical and thermal properties is now clear, actual applications are likely to be based on developments in the area of metrology and carbon nanotube synthesis.

6 Electronic Structure and Atomic Arrangement

The basis for the development of carbon-nanotube theory comes from the fact that the electronic structure of carbon nanotubes is closely related to that of graphene. The very special Fermi surface of graphene consists of the corner points of the hexagonal Brillouin zone, labeled the K point (and the K' point related to point K by time-reversal symmetry). Only those nanotubes, where a K point lies on one of the momentum quantization lines, turn out to be conducting, for which $n - m$ is a multiple of 3. Other carbon nanotubes are semiconducting at room temperature. As in other 1D systems, the electronic density of states is dominated by van Hove singularities. In metallic nanotubes, the nearly linear π-band dispersion near the Fermi wavevector K gives rise to a constant density of states in-between the pair of van Hove singularities closest to the Fermi level. In semiconducting nanotubes, the chirality-dependent fundamental energy gap is on the order of 1 eV and spans the region between the van Hove singularities for filled

and empty states. The related field of graphene, which is now growing explosively, will greatly benefit from and be beneficial to advances taking place in the nanotube field.

The huge advance in carbon-nanotube science in the past five years is the development of our knowledge about the nanotube structure. While the morphology of nanotubes has been established, from the earliest times, as intimately related to that of graphene, recent years have shown the increasing importance of chirality (helicity) effects. These effects are actually intimately related to the deviation of the carbon-nanotube structure from that of graphene, i.e., to curvature effects. These curvature effects have been shown, both theoretically and experimentally, to be chirality dependent, influencing many carbon-nanotube properties when the nanotube diameter is small, i.e., below 2 nm. This diameter and chirality dependence generates an interesting structural aspect of nanotubes that was demonstrated by the study of small-diameter (large curvature) tubes, i.e., the importance of structurally defined categories and families in delineating the physical properties of carbon nanotubes. The mapping of the (n, m) physical properties of small-diameter carbon nanotubes shows patterns that are distinguished by their three categories, defined by $\mathrm{mod}[(2n + m), 3] = 1, 2, 3$ and their three kinds of families $(n - m) =$ constant, $(2n + m) =$ constant and $(n + 2m) =$ constant. The $(2n + m) =$ constant families define single-wall carbon nanotubes of similar diameter but different chiral angle, or $(n - m) =$ constant defines tubes with similar chiral angles but having different diameters. The three categories define semiconducting tubes of type 1 and type 2 ($\mathrm{mod}\,[(2n + m), 3] = 1$ and 2, respectively) and metallic tubes ($\mathrm{mod}[(2n + m), 3] = 0$). These three categories can alternatively be defined by $\mathrm{mod}[(n - m), 3]$, resulting in an exchange of type 1 and type 2 in the definition of the semiconducting tubes. The importance of these structural aspects is discussed in numerous places in this book through the different physical properties associated with the various tube categories and families. Control of the nanotube structure serves as a target for future development of this field.

While all these advances have pushed the experimental work on the materials science of carbon nanotubes to its limits, it is clear that theory has often been ahead of experiment and predicted many new things that were later discovered experimentally. The chapters on theory by Spataru et al. and by *Ando* are central to achieving the objectives of this book. These two chapters are both pedagogic with respect to advancing topics covered in the book and predictive, offering challenges to experimentalists to test these predictions. The chapter by Spataru et al. addresses quasiparticle and excitonic phenomena in the optical response of nanotubes and graphene nanoribbons from an *ab-initio* point of view, providing a firm basis for the very active present activity in transport and photophysics studies on both carbon nanotubes and graphene as well as on nanoribbons, which bridge these two categories of carbon materials. In the chapter by Ando, the Aharanov–Bohm phase is discussed first on a tutorial basis and is then developed to predict

and explain three different phenomena: 1. novel aspects of excitons in optical experiments, 2. phenomena occurring in crosspolarized light, and 3. optical phonons in metallic nanotubes.

7 Advances in Photophysics

The important role of measurements at the single-nanotube level is emphasized in many chapters of this book. Besides the chapters by Jorio et al. and Yamamoto et al., already discussed above, very detailed (n, m)-dependent experimental work has been carried out with resonance Raman spectroscopy (described in the contribution by Saito et al.), photoluminescence (contribution by Lefevre et al.), time-resolved spectroscopy (in the contribution by Ma et al.), Rayleigh scattering (in the contribution by Heinz), and other advanced techniques, like near-field optical microscopy, inelastic electron tunneling and coherent phonon generation see contribution by Hartschuh.

The importance that nanotube photophysics has achieved is reflected in the number of chapters devoted to this topic, and is a consequence of the high accuracy of the experimental results, clearly showing the presence of rich (n, m)-, defect-, and environmental-dependent effects. Similar to other sp^2-bonded carbon nanostructures, the optical properties of carbon nanotubes are dominated by a π plasmon at $h\nu \approx 6\,\mathrm{eV}$ and a σ plasmon at $h\nu \approx 15$ to$-20\,\mathrm{eV}$. However, for energies in the visible and infrared range, the optical properties depend sensitively on (n, m) due to quantum-confinement effects. Optics has become a powerful practical tool to identify the distribution of nanotube chiralities in a sample. The (n, m) identification of nanotubes can be performed even at the single-nanotube level by using photoluminescence, resonant Raman scattering and Rayleigh scattering. The measurements are nondestructive, so that other in-situ experiments can be performed on (n, m)-assigned tubes. Photophysics has offered a very accurate, massless and chargeless probe for single-nanotube study.

The recent rapid development related to excitonic behavior has split the photophysics field wide open, with many research opportunities now available for studying dark excitons, phonon-assisted phenomena, decay dynamics and many-body behavior of very small diameter tubes, together with the challenge of developing applications for the many new properties offered by these systems. Powerful new tools are part of the expanding interest in this research area, and they also trigger the development of the metrology for nanomaterials. The contribution by Saito et al. brings theory and experiment together in a discussion of Raman scattering phenomena, advancing the fundamental understanding of the role of excitons in one-dimensional systems, and expanding our knowledge in the interpretation of the Raman spectra and in the use of Raman techniques to characterize carbon nanotubes. Photoluminescence (in the contribution by Lefebore et al.) is a new subject not covered in the first book, along with fast optics (the contribution by Ma et al.) and

Rayleigh scattering (the contribution by Heinz), which are also here reviewed for the first time. The review gives insights about where we now are in the fast optics field, which is expected to develop quickly in the future. Rayleigh scattering has been shown to be very powerful at the single-nanotube level, because it can access both metallic and semiconducting tubes. The chapter on new techniques (by Hartschuh) is aimed at pointing out new frontiers for nanoscience research in general and for nanotubes in particular. Although the field is still very young, the examples given indicate the potential impact of these and other to-be-discovered techniques.

Another new feature of this book is the high magnetic field chapter (by Kono et al.), which brings together magnetotransport and magneto-optics, and shows the power of theory and new experimental techniques to work together in an exciting way, utilizing the Aharanov–Bohm effect. These new approaches allow exploration of symmetry-breaking effects and dark-exciton states at the cutting edge of the photophysics of carbon nanotubes.

8 Transport Properties

The transport effects in SWNTs are now attracting great interest, especially from the device community who are now exploring a possible role for nanotubes in the next generation of information-technology devices. IBM, Intel and NEC now have sizeable groups working in these areas, and efforts such as these are bringing many new entrants with broader interests into the carbon-nanotube research field. Some of the most pioneering aspects of recent developments in the optoelectronics and quantum-transport research of SWNTs are found in the two chapters on optoelectronics and photoconductivity (by Avouris et al.), and on quantum transport (by Biercuk et al.).

The observation of photoluminescence from carbon nanotubes in 2002 opened a huge avenue of possibilities for the characterization and applications of nanotubes. The controlled occurrence of photoemission, induced by the recombination of electrons injected from one end and holes injected from the other end of an ambipolar nanotube during transport, suggests the suitability of nanotubes for a variety of optoelectronics applications contribution by Avouris et al.

Due to the low defect density and the absence of backscattering, metallic SWNTs are ballistic conductors with an exceptionally long electron mean free path. In the ballistic regime, the nanotube conductance G is quantized in multiples of the fundamental conductance quantum G_0, and $G = 2G_0$ is observed in all metallic nanotubes at low bias voltages. The question, to what degree are multiwall nanotubes ballistic or diffusive conductors, still awaits a conclusive answer. Independent of the conduction type and intrinsic to nanotubes, it is the nature of the contacts that ultimately determines their conductance behavior in a circuit. Exciting developments in transport in the nanotube field are now occurring through improvements in superconducting

and magnetic contacts to nanotubes, and through recent advances in the spintronics of carbon nanotubes add "(see contribution by Biercuk et al.)".

9 Double-Wall Carbon Nanotubes

Double-wall carbon nanotubes (DWNTs) are the simplest archetypical manifestation of multiwall nanotubes (MWNTs) and as such combine the outstanding properties of SWNTs with the possibility to study coaxial intertube interactions with high precision. The contribution on double-wall carbon nanotubes (DWNTs) by Pfeiffer et al. is a new chapter in this active area, of particular interest to both fundamental science (because it allows investigation of intertube interactions in detail) and to applications (since DWNTs behave somewhat like SWNTs in their physical properties, but are more sturdy mechanically).

10 Chemical Reactivity

Doping is one technique for controlling nanotube properties, and it also relates to electrochemistry, gating and intercalation. Due to their close relationship to graphite, carbon nanotubes are mostly inert chemically. Chemical reactions involving the formation of strong covalent or ionic bonds occur preferentially near defect sites and near the nanotube ends. The intrinsic hydrophobicity of carbon nanotubes can be modified by surfactants, which are frequently used to disperse nanotubes. The small dependence of nanotube reactivity on their conductive properties has been used with some success in the separation of metallic from semiconducting nanotubes (see the contribution by Joselevich et al.). The functionalization of carbon nanotubes for specific applications is a major growth area at present. Substitutional (in-plane) doping of carbon nanotubes not only changes their chemical reactivity, but also their mechanical, thermal and transport properties. This is a promising direction for applications, but presently requires further developments both in synthesis approaches and in characterization methods. These new topics were not discussed in the first volume and appear here in two chapters, one on chemical doping by Terrones et al. and another on electro-chemical doping by Kavan et al.

11 Related Structures

Chapters by Yudasaka et al. and by Tenne et al. deal with materials related to carbon nanotubes. Single-wall carbon nanohorns and nanocones are discussed in the contribution by Yudasaka et al., and inorganic nanotubes and fullerene-like structures in the contribution by Tenne et al. These materials

have recently taken a big step toward bringing applications to the marketplace, and their development is likely to both influence and be influenced by the carbon-nanotube field.

Inorganic nanotubes based on WS_2 and MoS_2 and a wide variety of other materials are starting to attract a lot of attention because of their outstanding applications potential. These materials are exceptional insofar as the speed at which they were commercialized. Using materials other than carbon as feedstock, many of the growth techniques yield nanotubes with a different chemical composition, such as BN, in inorganic nanotubes like MoS_2, WS_2, and a variety of other species. The interior space in open-ended or defective nanotubes may be filled by substances ranging from small molecules, including fullerenes, to metals and other species, which form 1D quantum wires. These quantum wires typically order in a different way from their bulk counterparts. A prominent example is a chain of fullerenes within a single-wall nanotube, often called a "peapod" that, when appropriately heat treated, becomes a precursor for the synthesis of DWNTs (as described in the chapter by Pfeiffer et al.). Synthesis and characterization of nanotubes from different chemical species remain important research growth areas, as does the growth of one-dimensional chains of novel materials within nanotube cores.

12 Graphene

Finally, the book ends with a chapter on graphene by Charlier et al., which is a brief review of recent developments in the study of graphene, denoting one sheet of carbon atoms with sp^2 bonding (or an unfolded single-wall nanotube). Surprisingly, this very basic system, which had been studied for many decades, suddenly appeared with many novel properties that were not even imagined until someone synthesized a single graphene sheet, and until an anomalous quantum Hall effect was found in graphene. This is now a very hot research field in its own right. The graphene chapter emphasizes those developments in graphene that are strongly related to carbon nanotubes. Correlation between theoretical and experimental techniques, as well as achievements in the understanding of new effects in these two fields, is likely to help advance both carbon-nanotube and graphene science and applications.

13 Outlook

As stated above, this is an important time to review what has been learned during the last decade and, most important, to look into the future of carbon nanotubes and related fields. Carbon nanotubes are held responsible for cotriggering the nanotechnology revolution. To gain a deeper understanding of the meaning of this nanotechnology revolution, we invite you to read this

book and learn about the exciting open path that has been forged for making this revolution a reality.

Acknowledgements

D. Tomanek was partly supported by the NSF NIRT grant ECS-0506309, the NSF NSEC grant EEC-0425826, and a Alexander-von-Humboldt award. A. Jorio acknowledges the Rede Nacional de Pesquisa em Nanotubos de Carbono - MCT and CNPq, CAPES and FAPEMIG, Brazil. M. S. Dresselhaus and G. Dresselhaus acknowledge support from NSF/DMR 04-05538.

Index

Electron and Phonon Properties of Graphene: Their Relationship with Carbon Nanotubes

J.-C. Charlier[1], P. C. Eklund[2] J. Zhu[2], A. C. Ferrari[3]

[1] Unité de Physico-Chimie et de Physique des Matériaux
Université Catholique de Louvain
1 Place Croix du Sud, 1348 Louvain-la-Neuve, Belgium
jean-christophe.charlier@uclouvain.be
[2] Department of Physics, The Pennsylvania State University
104 Davey Lab, University Park, PA 16802-6300, USA
pce3@psu.edu, jzhu@phys.psu.edu
[3] Engineering Department, Cambridge University
9 JJ Thomson Avenue, Cambridge CB3 OFA, UK
acf26@eng.cam.ac.uk

Abstract. The discovery of *Novoselov* et al. (2004) of a simple method to transfer a single atomic layer of carbon from the c-face of graphite to a substrate suitable for the measurement of its electrical and optical properties has led to a renewed interest in what was considered to be before that time a prototypical, yet theoretical, two-dimensional system. Indeed, recent theoretical studies of graphene reveal that the linear electronic band dispersion near the Brillouin zone corners gives rise to electrons and holes that propagate as if they were massless fermions and anomalous quantum transport was experimentally observed. Recent calculations and experimental determination of the optical phonons of graphene reveal Kohn anomalies at high-symmetry points in the Brillouin zone. They also show that the Born–Oppenheimer principle breaks down for doped graphene. Since a carbon nanotube can be viewed as a rolled-up sheet of graphene, these recent theoretical and experimental results on graphene should be important to researchers working on carbon nanotubes. The goal of this contribution is to review the exciting news about the electronic and phonon states of graphene and to suggest how these discoveries help understand the properties of carbon nanotubes.

1 Introduction

The fundamental building block of both a graphite crystal and a carbon nanotube is the graphene layer shown schematically in Fig. 1a. Such an atomic structure is characterized by two types of C–C bonds (σ, π) constructed from the four valence orbitals (2s, $2p_x$, $2p_y$, $2p_z$), where the z-direction is perpendicular to the sheet. Three σ-bonds join a C atom to its three neighbors. They are quite strong, leading to optical-phonon frequencies much higher than observed in diamond. In addition, the C–C bonding is enhanced by a fourth bond associated with the overlap of p_z (or π) orbitals. Graphite is comprised of coherently stacked layers of graphene. Two layers (A and B) are needed to define the unit cell in graphite. The three-dimensional (3D)

A. Jorio, G. Dresselhaus, M. S. Dresselhaus (Eds.): Carbon Nanotubes,
Topics Appl. Physics **111**, 673–709 (2008)
Springer-Verlag Berlin Heidelberg 2008

structure of graphite is therefore held together by a weak interlayer van der Waals (vdW) force. A single-wall carbon nanotube (SWNT), on the other hand, is a seamless cylinder of graphene. SWNTs are analogously bound in a bundle by the vdW force. The electronic properties of graphene, graphite and carbon nanotubes are determined by the bonding π- and antibonding π^*-orbitals that form wide electronic valence and conduction bands (Fig. 1b). As the tube diameter decreases, the bond angle between the σ and π orbitals increases slightly, introducing curvature effects into the electronic and phonon properties of SWNTs.

Theoretical calculations show that the π-band overlap in graphite disappears as the layers are further separated over their equilibrium distance in graphite. This leads to decoupled graphene layers that can be described as a zero-gap semiconductor. The π-band electronic dispersion for graphene near the six corners of the 2D hexagonal Brillouin zone is found to be linear. Thus, "cones" of carriers (holes and electrons) appear in the corners of a 2D Brillouin zone whose points touch at the Fermi energy, as shown in Fig. 1c. The linear electronic band dispersion leads to the term "massless Dirac fermions" for these carriers. The six points where the cones touch are referred to as the "Dirac" points in the graphene literature.

Graphene, because of its structural simplicity (two atoms per unit cell), has been extensively investigated in theory for the past 60 years [1]. However, only recently has it been possible to produce ultrathin films containing a countable number (n) of graphene layers (i.e., $1 < n < 20$). The synthetic techniques fall into two categories. The first approach exploits the weak bonding between the graphene layers by pealing off an n-graphene layer (nGL) by chemical means [2–6] or by mechanical means [7, 8]. Mechanical separation of nGLs from the parent crystal involves rubbing the freshly cleaved quasi-2D system against a smooth substrate. This technique has allowed graphene and nGLs to be studied in the laboratory for the first time [7]. It is simple, inexpensive and produces graphene and nGL flakes of very high quality. However, this approach lacks the scalability required by mass device production. The second approach grows epitaxial graphitic films by thermal decomposition of SiC [9–12]. This technique has the potential of producing large-area lithography-compatible films and is rapidly advancing at the moment.

In this contribution, we review the connection between the electron and phonon states in graphene (nGLs) and SWNTs. We begin with a discussion of the electronic states. Recent theoretical arguments and experiments are converging on a picture of free carriers in graphene near the Fermi energy behaving as massless Dirac fermions propagating at $\sim 1/100$ the speed of light, i.e., they do not behave as simple electrons or holes with an effective mass. Experimental observations of an anomalous integer quantum Hall effect in graphene has been reported recently and has created a lot of attention [13, 14]. These and other interesting experimental electronic transport results are reviewed as well [15] with further discussion provided in the contributions in this volume by *Ando* and by *Spataru* et al. We then discuss

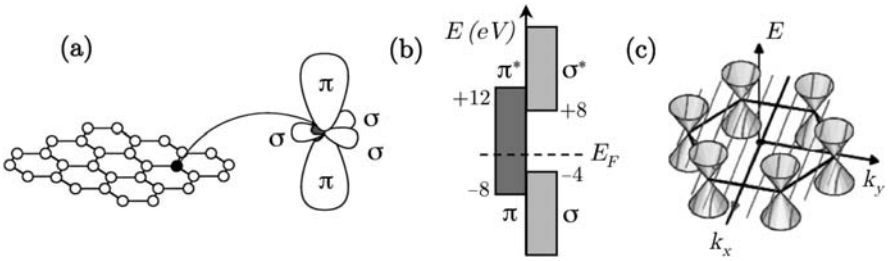

Fig. 1. Illustration of the carbon valence orbitals. (**a**) The three inplane σ (s, p_x, p_y) orbitals in graphene and the π (p_z) orbital perpendicular to the sheet. The inplane σ and the π bonds in the carbon hexagonal network strongly connect the carbon atoms and are responsible for the large binding energy and the elastic properties of the graphene sheet. The π orbitals are perpendicular to the surface of the sheet. The corresponding bonding and the antibonding σ bands are separated by a large energy gap of $\sim 12\,\mathrm{eV}$ (**b**), while the bonding and antibonding π states lie in the vicinity of the Fermi level (E_F). Consequently, the σ bonds are frequently neglected for the prediction of the electronic properties of graphene around the Fermi energy. Dirac cones located at the six corners of the 2D Brillouin zone are illustrated in (**c**)

the optical phonons in graphene that are directly accessible by Raman spectroscopy and give rise to the most prominent Raman peaks when graphene is folded into nanotubes. We focus on their coupling to electrons, which is key to understanding many phenomena in graphene and nanotubes.

For example, it was recently argued that in doped graphene, the adiabatic Born–Oppenheimer approximation [16], valid in many solid-state systems, breaks down [17]. The electron–phonon interaction in graphene has also been carefully re-examined and has been recently shown to give rise to Kohn anomalies in the phonon dispersion at important points (Γ, K) in the Brillouin zone where the phonons can be studied by Raman spectroscopy [18–21]. Many of these new ideas proposed for graphene and nGLs carry over to nanotubes. Kohn anomalies are responsible for the different Raman spectra of metallic and semiconducting nanotubes, and non-Born–Oppenheimer effects strongly shape the Raman spectra of doped and annealed nanotubes [19, 22]. These connections are also discussed in this review.

2 Electronic Properties and Transport Measurements

2.1 Graphene

2.1.1 Electronic Band Structure

Figure 2 shows the *ab-initio* calculations of the electronic bands of graphene along the high-symmetry M–Γ–K directions [23]. Its space group ($P3m$)

contains a mirror-plane symmetry, allowing symmetric σ and antisymmetric π states to be distinguishable. In a 2D crystal, a parallel mirror symmetry operation separates the eigenstates for the whole Brillouin zone, and not only along some high-symmetry axis. The π and π^* bands touch at the corners of the hexagonal Brillouin zone. Such corners are labeled by their momentum vector usually denoted by K and K'. Consequently, graphene is a special semimetal or zero-gap semiconductor, whose intrinsic Fermi surface is reduced to the six points at the corners of the 2D hexagonal Brillouin zone. Close to the Fermi energy, the π and π^* bands are quasilinear (linear very close to K, K') (Fig. 1c), in contrast with the usual quadratic energy–momentum relation obeyed by electrons at band edges in conventional semiconductors. When several interacting graphene planes are stacked, as in nGLs or in a perfect graphite crystal, the former antisymmetric π bands are split (owing to bonding or antibonding patterns), whereas the σ bands are much less affected by the stacking.

The graphene sheet is thus highly specific for this linear energy–momentum relation. The electronic group velocity, estimated at the Dirac points, is quite high: $\sim 1\times10^6$ m/s. Consequently, graphene exhibits electronic properties for a 2D gas of charged particles described by an equation of the form of the relativistic Dirac equation rather than the nonrelativistic Schrödinger equation with an effective mass. Indeed, in graphene, charge carriers mimic particles with zero mass and an effective "speed of light" $c^* \sim 1 \times 10^6$ m/s. Recently, graphene has revealed a variety of unusual transport phenomena characteristic of two-dimensional Dirac fermions, such as an anomalous integer quantum Hall effect, a "minimum" conductivity of order $4e^2/h$ even when the carrier concentration tends to zero, a cyclotron mass m_c of massless carriers with an energy E described by $E = m_c c^{*2}$, and Shubnikov–de Haas oscillations that exhibit a phase shift of π due to Berry's phase [13, 14]. These remarkable properties will be described in the next section.

The electronic structure of graphene can be reasonably well described using a rather simple tight-binding Hamiltonian, leading to analytical solutions for their energy dispersion and related eigenstates [23]. Since the bonding and antibonding σ bands are well separated in energy ($> 10\,\mathrm{eV}$ at Γ), they are frequently neglected in semiempirical calculations since they are too far away from the Fermi level to play a role. Only the remaining two π bands are thus needed to describe the electronic properties of graphene.

When the atoms are placed onto the graphene hexagonal lattice (Fig. 1a), the electronic wavefunctions from different atoms overlap. However, such an overlap between the $\mathrm{p}_z(\pi)$ orbitals and the s or the p_x and p_y orbitals is strictly zero by symmetry. Consequently, the p_z electrons, which form the π bands in graphene, can be treated independently from the other valence electrons. Within this π-band approximation, it is easy to describe the electronic

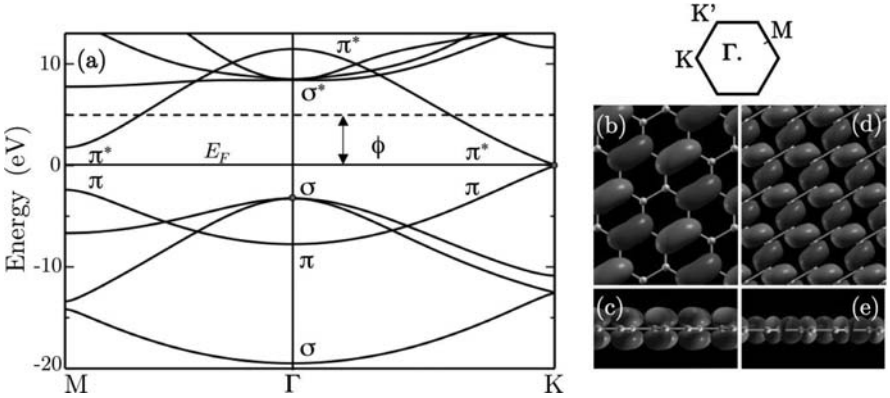

Fig. 2. (**a**) Electronic band structure of graphene from *ab-initio* calculations [23]. The bonding σ and the antibonding σ^* bands are separated by a large energy gap. The bonding π (highest valence band) and the antibonding π^* (lowest conduction band) bands touch at the $K(K')$ points of the Brillouin zone. The Fermi energy ($E_{\rm F}$) is set to zero and ϕ indicates the work function (by the *dashed horizontal line*). Above the vacuum level ϕ, the states of the continuum are difficult to describe and merge with the σ^* bands. The 2D hexagonal Brillouin zone is illustrated with the high-symmetry points Γ, M, K and K'. (**b**,**c**) π state at K and (**d**,**e**) σ-state at Γ seen, respectively, from above and from the side of the graphene plane. Note that the π wavefunction cancels on a hexagonal sublattice due to the $e^{(iK\ \ r)}$ phase factor. The π (σ) state is odd (even) with respect to the graphene plane reflection. Courtesy of Zanolli, 2007, unpublished

spectrum of the total Hamiltonian and to obtain the dispersion relations restricted to first-nearest-neighbor interactions only:

$$E^{\pm}(k_x, k_y) = \pm\gamma_0 \sqrt{1 + 4\cos\frac{\sqrt{3}k_x a}{2}\cos\frac{k_y a}{2} + 4\cos^2\frac{k_y a}{2}}\,, \tag{1}$$

where $a = \sqrt{3}a_{\text{C-C}}$ ($a_{\text{C-C}} = 1.42$ Å is the carbon–carbon distance in graphene) and γ_0 is the transfer integral between first-neighbors π orbitals (typical values for γ_0 are 2.9–3.1 eV). The $\boldsymbol{k} = (k_x, k_y)$ vectors that belong to the first hexagonal Brillouin zone (BZ) constitute the ensemble of available electronic momenta.

With one p_z electron per atom in the π-π^* model (the three other s, p_x, p_y electrons fill the low-lying σ band), the ($-$) band (negative energy branch) in (1) is fully occupied, while the ($+$) branch is totally empty. These occupied and unoccupied bands touch at the K and K' points. The Fermi level $E_{\rm F}$ (or charge-neutrality point) is chosen as the zero-energy reference in Fig. 2 and the Fermi surface is defined by the set of K and K' points. Since the occupied and unoccupied bands touch at the zone corners, the graphene sheet displays a semimetallic, or zero-gap semiconducting character.

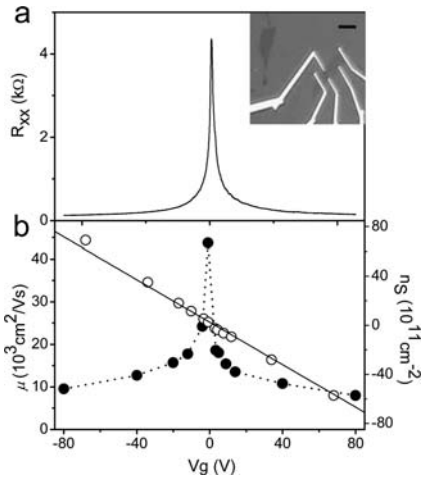

Fig. 3. Resistivity, mobility and carrier density as a function of gate voltage V_g in a single-layer graphene field-effect transistor device. (**a**) V_g-dependent R_{xx} showing a finite value at the Dirac point. The resistivity ρ_{xx} can be calculated from R_{xx} using the geometry of the device. The *inset* is an image of a graphene device on a Si:SiO_2 substrate. The Si is the bottom gate; five top electrodes formed via e-beam lithography are shown in the *inset*. Scale bar 5 μm. (**b**) Mobility μ and carrier density n_s as a function of V_g. The mobility (*dotted curve*) diverges artificially at the Dirac point due to a finite resistivity. Adapted from [14]

Expanding (1) at $K(K')$ yields the linear π and π^* bands for Dirac fermions:

$$E^{\pm}(\boldsymbol{\kappa}) = \pm\hbar v_{\mathrm{F}}|\boldsymbol{\kappa}|\,, \tag{2}$$

where $\boldsymbol{\kappa} = \boldsymbol{k} - K$, and v_{F} is the electronic group velocity given by:

$$v_{\mathrm{F}} = \sqrt{3}\gamma_0 a/2\hbar\,. \tag{3}$$

In graphene, $v_{\mathrm{F}} \approx 1 \times 10^6$ m/s. The resulting cone structure at the six Brillouin zone corners is shown in Fig. 1c.

The linear dispersion given by (2) is the solution to the following effective Hamiltonian at the $K(K')$ point [24]:

$$\boldsymbol{H} = \hbar v_{\mathrm{F}}(\boldsymbol{\sigma}\ \ \boldsymbol{\kappa})\,, \tag{4}$$

where $\boldsymbol{\kappa} = -i\nabla$, and $\boldsymbol{\sigma}$'s are the pseudospin Pauli matrices operating in the space of the electron amplitude on the A–B sublattices of graphene.

In the next section, we briefly describe some of the unusual properties of graphene [15] derived from the linear dispersion and the "chiral" nature of the quasiparticles defined by (2) and (4).

2.1.2 Transport Measurements in Single-Layer Graphene

Figure 3 shows the resistivity ρ_{xx}, density n_s and mobility μ of 2D carriers in a single-layer graphene field-effect transistor (FET) as a function of gate voltage [14]. Graphene FETs are fabricated with standard lithography and etching techniques using mechanically cleaved graphene flakes [25]. A degenerately doped silicon substrate with a thin oxide overlayer serves as an

insulated gate electrode that can continuously tune E_F, and therefore the 2D carrier density n_S across the charge-neutrality point, covers a range of roughly $\pm 1 \times 10^{13}/\mathrm{cm}^2$. The conduction is symmetric about the Dirac point as shown in Fig. 3a, indicating that the electron and hole mobilities are approximately equal. In the high carrier density regime, the mobility is found to be roughly carrier-density independent and temperature independent. Reported mobility values span a wide range $2000 < \mu < 20\,000\,\mathrm{cm}^2/(\mathrm{Vs})$, with the high end representing a long mean-free path of $\sim 0.3\,\mu\mathrm{m}$, comparable to that of SWNTs. The weak temperature dependence found for μ indicates that impurity or defect scattering is the dominant scattering mechanism and provides room for future device improvement [13, 26]. Possible sources for scattering centers include adsorbents, defects in the graphene lattice and ionized impurities in the SiO_2 substrate. The carrier-density dependence of the conductivity (not shown) near the Dirac point is found to sensitively depend upon the range of the scatterers [27] and varies from device to device.

Figure 3 also reveals a remarkable property of 2D carriers in graphene. Although the carrier density approaches zero at the Dirac point, the 2D resistivity ρ_{xx} or conductivity σ_{xx} remains finite. Such behavior, dubbed the "minimum" conductivity, has been observed experimentally in many graphene devices with ρ_{xx} ranging from 2 to $7\,\mathrm{k}\Omega$ at low temperature [13, 14]. A slightly larger value of ρ_{xx} from 6 to $9\,\mathrm{k}\Omega$ is also reported for bilayer graphene [28]. The origin of this finite conductivity $\sim 4e^2/h$ remains unclear at the moment. In a real device, ionized impurities in the SiO_2 substrate or the rippling of the graphene sheet [29] may lead to local puddles of electrons and holes with finite densities and result in finite conduction through the device [30]. On the other hand, calculations show that a minimum quantum conductivity (often $4e^2/h\pi$) can also arise intrinsically from the linear excitation spectrum of Dirac fermions and/or the chiral nature of the quasiparticles (for a more detailed review, see [15]). However, present experiments seem to converge at $4e^2/h$. More experiments, particularly with cleaner substrates or suspended devices, are needed to clarify this intriguing issue.

In a magnetic field perpendicular to the graphene plane, the linear excitation spectrum of Dirac fermions evolves into discrete Landau levels (LLs) whose energies are given [31, 32] in terms of the LL index by:

$$E_n = \pm v_F \sqrt{2e\hbar|n|B}\,. \tag{5}$$

The $\sqrt{B}$ dependence of E_n, which distinguishes graphene from conventional 2D semiconductors (that have LLs linear in B), has been confirmed by recent spectroscopic measurements [33–35]. The large splitting in graphene ($\Delta E_{0,1} = 240\,\mathrm{meV}$ at $45\,\mathrm{T}$) leads to the observation of the quantum Hall effect at room temperature [36].

Including spin and sublattice degeneracy, the number of states for each LL is $4eB/h$. In graphene, because of the touching bands at the $K(K')$ points, the $n = 0$ LL is shared equally between electrons and holes. This counting scheme

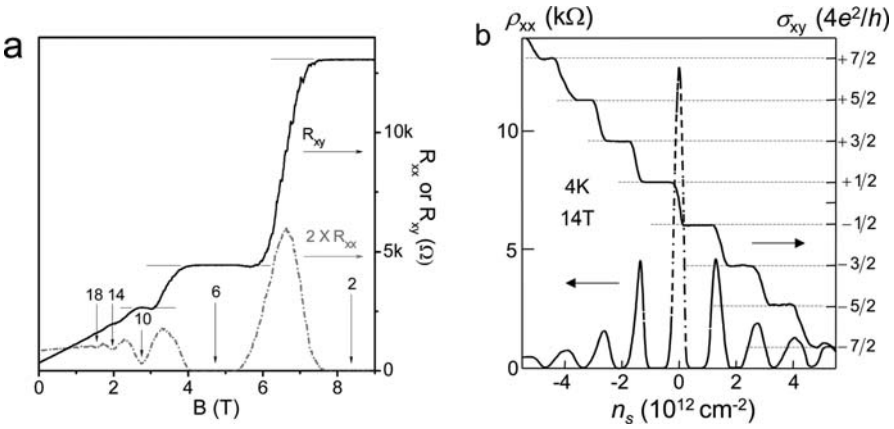

Fig. 4. Anomalous-integer quantum Hall effect in single-layer graphene. (**a**) Magnetic-field sweeps of Hall resistance R_{xy} (*solid*) and longitudinal resistance R_{xx} (*dash-dotted*) at fixed carrier density (or V_g) showing plateaus in R_{xy} quantized at $h/e^2\nu$ and the corresponding zero-resistance minima in R_{xx}. *Arrows* indicate filling factor $\nu = n_s h/eB = 4(n+1/2)$, where n_s is the carrier density and n the LL index. Adapted from [14]. (**b**) Hall conductivity σ_{xy} (*solid*) and longitudinal resistivity ρ_{xx} (*dashed*) as a function of carrier density at $B = 14\,\mathrm{T}$. Here, σ_{xy} is calculated as $\sigma_{xy} = \rho_{xy}/(\rho_{xx}^2 + \rho_{xy}^2)$ and is observed to be quantized as $\sigma_{xy} = 4(n+1/2)e^2/h$. Adapted from [13]

gives rise to the occurrence of the quantum Hall effect at half-integer LL indices (Fig. 4), which can also be viewed as the result of a conventional integer sequence with a phase shift of π known as Berry's phase [37]. This π phase shift arises from the linear dispersion of the Dirac fermions and serves as a sensitive indicator of the existence of such an excitation spectrum. It persists to lower magnetic fields, where quantum Hall states turn into magnetoresistance (Shubnikov–de Haas or SdH) oscillations [38]. The magnitude of the phase shift can be accurately extracted from the LL fan diagrams (Fig. 5a) [13,14].

Although the light-like linear electronic band dispersion implies massless particles, Dirac fermions moving in a magnetic field are characterized by a finite cyclotron mass m_c. Values for m_c can be extracted from the thermal damping of SdH oscillations via the same expression as in conventional 2D systems [38]: $R_{xx} \propto T/\sinh(2\pi^2 kTm_c/\hbar eB)$. Experiments find the carrier-density dependence of m_c to be well described by:

$$m_c = E_F/v_F^2 = (h^2 n_S/4\pi v_F^2)^{1/2}\,. \tag{6}$$

Equation (6) is behind the use of m_c as the "relativistic" mass of Dirac fermions, where v_F plays the role of c^*. Here, v_F is found to be $\approx 1.0 \times 10^6$ m/s experimentally [13,14,34,35], in good agreement with band-structure calculations for m_c/m_0 (Fig. 5b). As E_F approaches zero, i.e., the charge-

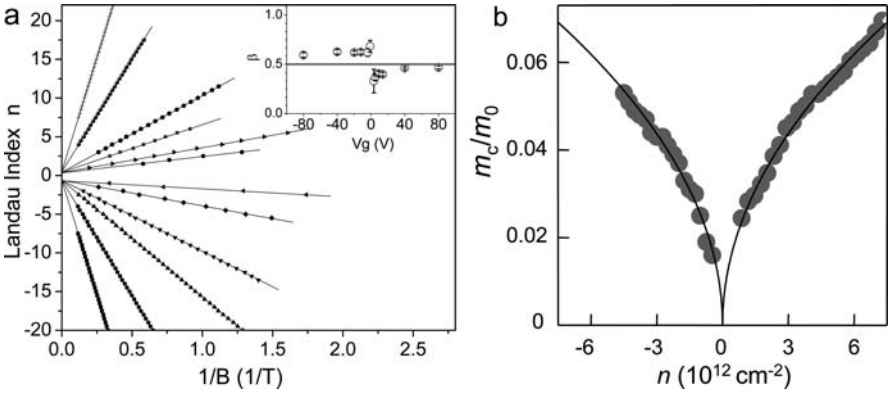

Fig. 5. Berry's phase π and the cyclotron mass of Dirac fermions in single-layer graphene. (**a**) LL fan diagram plotting the positions of the resistance minima in SdH oscillations against the LL index n. Different lines correspond to different carrier densities produced by the backgate. The n-axis intercept yields Berry's phase $2\pi\beta$. Analysis in single-layer graphene consistently yields $\beta = 0.5$ (*inset*), providing convincing evidence for Dirac fermions. Adapted from [14]. (**b**) Cyclotron mass obtained from temperature-dependent low-field SdH oscillations. m_c scales with $\sqrt{n_S}$ and vanishes near the Dirac point. The theoretical fit using (6) (*solid line*) yields $v_F \approx 1 \times 10^6$ m/s. Adapted from [13]. Values of m_c as low as $0.007m_0$ (for $n_S \sim 2 \times 10^{11}/\text{cm}^2$) have been reported [14]

neutrality point, m_c vanishes accordingly. Values of m_c as low as $0.007m_e$ ($n_S \sim 2 \times 10^{11}$ /cm^2) have been reported [14].

Graphene in ultrahigh magnetic fields up to 45 T displays additional plateaus in σ_{xy} at filling factors $\nu = 0, \pm 1, \pm 4$ [39, 40]. Whereas the single-particle Zeeman splitting was identified as the origin of the $\nu = \pm 4$ plateaus [39], the nature of the $\nu = 0, \pm 1$ states is still unclear. The underlying mechanisms of these quantum Hall states are the focus of many recent theoretical discussions (see a review by [41]), where a variety of interaction-driven ground states and novel charge and spin excitations have been predicted by combining quantum Hall physics with graphene's unique linear excitation spectrum and four-fold degeneracy. Reducing disorder in the present samples is crucial to the examination of these exciting ideas.

2.2 Graphene Nanoribbons

Among carbon nanostructures based on graphene, ribbons a few nanometers in width have also been extensively studied [42–54]. Since graphene nanoribbons (GNRs) are just geometrically terminated graphene, their electronic structure has been modeled by imposing appropriate boundary conditions (i.e., standing waves) on the Schrödinger equation within the present simple

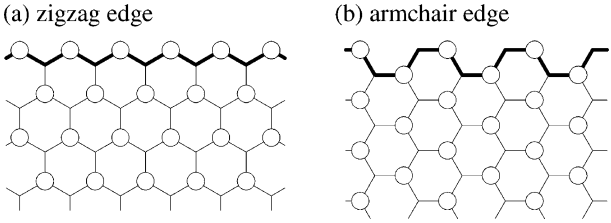

Fig. 6. GNR edges. (**a**) Zigzag edge, (**b**) armchair edge

tight-binding approximations based on the π-states of carbon [42, 43, 48] or on a two-dimensional Dirac equation with an effective speed of light ($c^* \sim 1 \times 10^6$ m/s) [49–51].

Within these models, it is predicted that GNRs with "armchair" edges (AGNR) can be either metallic or semiconducting depending on their widths [42, 43, 48–51], and that GNRs with "zigzag" edges (ZGNR) are metallic with peculiar edge states on both sides of the ribbon regardless of their widths [42–51] (Fig. 6). This edge state stems not from graphene nor from the dangling bonds at the edge, but from the topology of the π-electron networks across a significant part of the Brillouin zone and has no counterpart in an armchair edge. The corresponding energy bands are almost flat at the Fermi level, inducing a sharp peak in the density of states at E_F. The charge density of the edge state is strongly localized on the zigzag edge sites. Although a general GNR is often characterized by a mixture of zigzag and armchair sites [42, 44], theory predicts that a GNR edge with three or four zigzag sites per sequence is sufficient to exhibit the characteristics of a zigzag edge state [42]. Indeed, STM and STS measurements [55] have observed evidence of this edge state near E_F at zigzag edge sites and at defect sites of armchair edges, but not at sites along a homogeneous armchair edge.

Although the tight-binding approximation based on π-states of carbon is known to accurately describe the energy dispersion of the carbon sheet, a careful consideration of edge effects in GNRs only a few nanometers in width is required to determine their band structures accurately [45, 48]. Recent *ab-initio* calculations [52–54] reveal that all GNRs with hydrogen-passivated armchair- or zigzag-shaped edges have nonzero direct bandgaps. The gap size decreases as the width of the GNR increases, approaching zero in graphene in the limit of infinite width. The origins of the bandgaps for the different types of homogeneous edges vary.

The bandgaps of GNRs with armchair edges originate from quantum confinement, but edge effects play a crucial role [52, 53]. Hydrogen passivation introduces C–H σ bonds (or other types of terminations in general) at the edge, causing the C–C bond length and the on-site energy of the C atoms at the armchair edge to be different from those in the interior of the GNR. The decrease of the C–C bond length induces an increase of $\sim 12\,\%$ in the hopping integral between π-orbitals. This physical deformation at the edge is

responsible for the presence of a bandgap even for the armchair GNRs [52,53], which are predicted to be metallic in tight-binding calculations.

In the case of GNRs with zigzag edges, bandgaps arise upon the inclusion of the spin degrees of freedom [47, 52–54]. The existence of the narrow-band edge states at the Fermi level implies possible magnetization at the edges [43, 46, 47, 52–54]. The difference in total energy per atom on the edge between non-spin-polarized and spin-polarized edge states is found to be of the order of a few tens of meV [52, 53]. Spin-polarization effects in the electronic structure are discussed in the contribution to this volume by *Spataru* et al. Indeed, the zigzag GNRs are predicted to have a magnetic insulating ground state with ferromagnetic ordering at each zigzag edge and antiparallel spin orientation between the two edges. Because the two edge states with opposite spins occupy different sublattices, magnetic ordering leads to staggered sublattice potentials, which introduce bandgaps for electrons on a honeycomb hexagonal lattice [56]. Since the strength of the staggered potentials in the interior of the ribbon decreases as the ribbon width increases, the bandgaps of zigzag GNRs are inversely proportional to the width.

Similar to carbon nanotubes, optical spectra of GNRs are affected by self-energy and many-body corrections to the single-particle excitation spectrum and are characterized by bound excitons, with binding energies ~ 0.5–$1\,\mathrm{eV}$ for ribbons of a width comparable to the circumference of a typical SWNT [57]. The exciton binding energy scales inversely with the ribbon width [57].

Experimental exploration of GNRs is at a very early stage. Recently, GNRs with 10–500 nm width have been patterned lithographically using hydrogen silsesquioxane as an etch mask and oxygen plasma etching [58, 59]. Such an approach most likely produces mixed zigzag and armchair edges terminated by carboxyl groups. It was shown by *Han* et al. [58] that lateral confinement indeed leads to energy gaps with a ribbon width W dependence given by $E_{\mathrm{gap}} = \alpha/(W - W^*)$, where $\alpha = 0.2\,\mathrm{eV}$ nm and $W^* = 16\,\mathrm{nm}$ represents the offset in the active ribbon width determination. This empirical relation is consistent with DFT calculations presented in [52, 53]. Furthermore, unlike the closed structure of carbon nanotubes, the dangling bonds at the edges of a GNR may be chemically functionalized to perform selective chemical/biological sensing. Edge functionalisation and atomic substitutions can indeed modify the electronic and spin properties of the GNRs [60]. This whole new direction awaits experimentation.

In conclusion, the role of the edges is crucial in determining the values and scaling rules for the bandgaps in both armchair and zigzag GNRs. In addition, although the spin-orbit interaction is very small in graphite [61], the coexistence of electrons with opposite spin orientations in GNRs could open up a new path to the exploration of spintronics at the nanometer scale (when the electrical current is completely spin polarized) [54]. The ability to selectively create specific edge types on demand is essential to test GNR theories and evaluate GNR-based devices.

2.3 Graphite and *n*-Graphene Layer Systems

Bulk graphites consist of a tridimensional (3D) stacking of graphene sheets with an interlayer spacing around 3.35–3.4 Å. However, various graphites differ in the stacking sequence of the carbon planes, such as simple hexagonal graphite ($AAA\ldots$); Bernal graphite ($ABAB\ldots$); and rhombohedral graphite ($ABCABC\ldots$). These graphene-based 3D crystals exhibit specific semimetallic properties that depend directly on the geometry of the stacking between layers [62–65]. Consequently, the nature of the charge carriers strongly depends on the particular stacking of the graphene sheets and the corresponding Fermi surfaces exhibit a complex shape around the H–K–H line at the edge of the 3D hexagonal Brillouin zone [62–65].

In contrast to the corresponding 3D bulk structures, electrons in an n-graphene layer (nGL, n = a small integer) are confined along the crystallographic direction perpendicular to the graphene sheets, offering a genuine 2D character to the nGL electronic states. However, the linear dispersion of the electronic bands near the Fermi level that appears in monolayer graphene is lost, as a consequence of the interaction between layers.

Recent *ab-initio* electronic calculations [66] have revealed that nGLs belong to an intermediate case between bulk graphite and a graphene sheet. The corresponding band structures of nGLs will be reminiscent of both cases. The weak interlayer interaction that creates the c-axis band dispersion in 3D graphites is now responsible for band mixing of states otherwise associated with isolated graphene bands. The number of layers and the stacking order are key factors influencing the transport properties of nGLs [66, 67]. Indeed, depending on these factors, an nGL can behave as a 2D metal (with a single or mixed-carrier type) or a narrow-gap 2D semiconductor. For example, amongst 3- and 4-layer nGLs, $ABAC$ stacking is found to lead to a narrow-gap semiconductor (with a bandgap $\sim 9\,\text{meV}$) [66]. Other stackings can exhibit a metallic behavior with different signatures: the rhombohedral family (ABC, $ABCA$) displays a very small ($< 3\,\text{meV}$) overlap between electron and hole bands, while the Bernal family (ABA, $ABAB$) shows overlaps of a few tens of meV (from 5–20 meV) in agreement with experimental measurements [66]. Besides perfectly stacked ABAB structures, nGLs might also be made to exhibit a turbostratic random stacking, leading to a weak band overlap [66, 68].

Among nGLs, the simplest and arguably most interesting case may be bilayer graphene (2GL). A calculated band structure of 2GL is given in Fig. 7a together with angle-resolved photoemission spectroscopy (ARPES) measurements by *Ohta* et al. [11]. A gap of $\sim 0.8\,\text{eV}$ appears for the high-energy bands due to the interlayer interaction. This splitting is predicted to be independent of carrier concentration in the two layers [69]. The splitting of the low-energy bands, however, arises from the broken inversion symmetry of the two constituent layers and sensitively depends upon the strength of the interlayer electric field. The experiments of *Ohta* et al. [11] used potassium

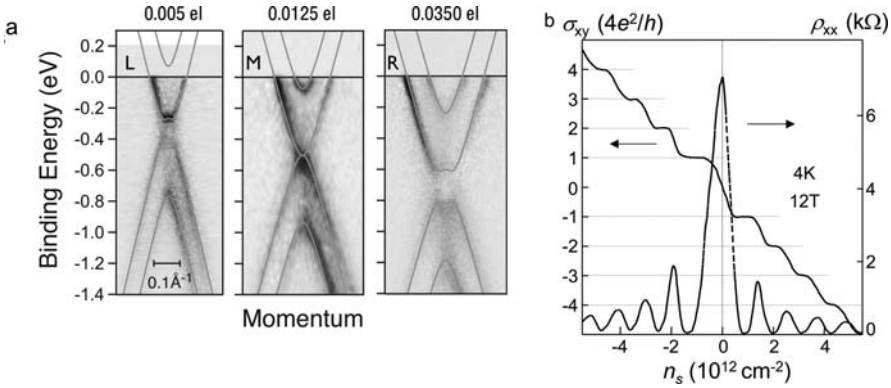

Fig. 7. Band structure and quantum Hall effect of bilayer graphene. (**a**) Band structure measured by angle-resolved photoemission spectroscopy. From *left* to *right:* Tuning the bandgap of the low-energy bands by increasing the amount of potassium doping. Calculations [69] are shown for comparison (*solid lines*). Adapted from [11]. (**b**) Quantum Hall effect in bilayer graphene showing quantized steps of σ_{xy} at $4ne^2/h$. σ_{xy} jumps from $-4e^2/h$ to $4e^2/h$ across the charge-neutrality Dirac point. Adapted from [28]

atoms to continuously and preferentially dope the top layer of the bilayer graphene, allowing a continuous tuning of the gap opening in the low-energy bands. The resulting band structures are shown in Fig. 7a. More recently, *Castro* et al. [70] demonstrated that by combining chemical doping and field-effect doping imposed by a backgate, the gap splitting and the Fermi level of bilayer graphene can be independently controlled. This gap-tuning capability may have important implications in the development of graphene-based electronics.

Bilayer graphene (2GL) with parabolic but degenerate bands at the Dirac point (middle panel of Fig. 7a) exhibits a distinctive quantum Hall effect. The LLs of these massive, chiral quasiparticles are described by [69]:

$$E_n = \frac{\hbar eB}{m^*}\sqrt{n(n-1)}\,. \tag{7}$$

The conventional integer quantum Hall sequence $\sigma_{xy} = 4ne^2/h$ is restored for the 2GL. However, the merging of the $n = 1$ and the $n = 0$ LLs leads to an eightfold degeneracy at the charge-neutrality point and the absence of the $\nu = 0$ plateau σ_{xy}. These features are signatures of a bilayer graphene sample and have been observed recently by *Novoselov* et al. [28] (Fig 7b).

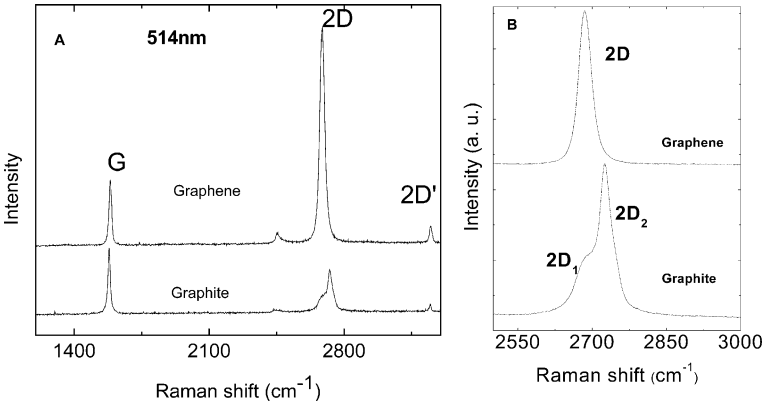

Fig. 8. (**A**) Comparison of the Raman spectra of graphene and graphite measured with 514.5-nm excitation. (**B**) Comparison of the 2D peaks in graphene and graphite (also measured with 514.5-nm excitation)

3 Optical Phonons and Raman Spectroscopy

Presently, the widely used micromechanical cleavage method produces nGL flakes with varying n and the yield of low-n graphene flakes is low. A simple method to locate these flakes and determine the number of layers is much needed for the studies of these materials. nGLs are optically invisible on most substrates. Their optical detection requires an optimal combination of detection wavelength and oxide thickness [71] and so far all the successful observations of single- and bilayer graphene are made with Si substrates with a specific oxide thickness of $\sim 300\,\text{nm}$ [7]. Alternatively, an atomic force microscope (AFM) may be used to identify nGLs. This approach has two drawbacks. First, AFM suffers from low throughput. Secondly, instead of the expected graphite interlayer spacing 0.34 nm, AFM height measurements report an apparent step height of 0.5–1 nm between a graphene flake and the SiO_2 substrate due to their difference in chemical composition. This variable offset can present problems for the AFM identification of 1GL and 2GL films. Here, we show that an nGL's electronic structure is uniquely captured in its Raman spectrum. Raman fingerprints for single-, bi- and few-layer graphene allow unambiguous, high-throughput, nondestructive identification of the number of layers.

3.1 Raman D and G Bands, Double Resonance and Kohn Anomalies

Figure 8 compares the Raman spectra of graphene and bulk graphite collected with 514-nm (2.41 eV) excitation [72]. In general, the main features in the first order Raman spectra of graphitic carbons are the so-called G and D bands,

which lie at ~ 1580 and $\sim 1360\,\mathrm{cm}^{-1}$, respectively, for visible excitation [73]. The assignment of these bands is straightforward in the "molecular" picture of carbon materials. They are present in all polyaromatic hydrocarbons [74, 75]. The G band is due to the bond stretching of all pairs of sp^2-bonded atoms in both rings and chains. The D band is due to the breathing modes of sp^2-bonded atoms in rings [74, 76, 77]. However, this molecular approach to the interpretation of these Raman bands in graphitic carbons has undergone a debate that has lasted several decades. The D band was first attributed to a breathing mode for phonons with wavevectors near the (K, K') points, activated by disorder (D). This relaxes the fundamental Raman selection rule, which states that only phonons near the Γ point can be seen in first order Raman scattering [76]. The D band was then linked to maxima in the vibrational density of states of graphite at the M and K points of the Brillouin zone [78, 79]. However, this does not account for the dispersion of the Raman D-peak position with photon excitation energy [80, 81], or why the D-peak overtone (2D band) at $\sim 2710\,\mathrm{cm}^{-1}$ can be observed even in the absence of the D peak, or why the intensity ratio $I(\mathrm{D})/I(\mathrm{G})$ is dispersive (i.e., a function of the incident photon energy) [80, 81]. Phonon confinement does not explain why the D mode is more intense than other modes closer to Γ, nor why it is seen in disordered graphite with an in-plane correlation length, L_a, as large as 30 nm [82].

Pocsik et al. [81] proposed that the D band arises due to a resonant Raman coupling in which there is a strong enhancement of the Raman cross section of a phonon of wavevector $\boldsymbol{q}$, when $\boldsymbol{q} = \boldsymbol{k}$, the wavevector of the vertical electronic transition excited by the incident photon ("quasi-selection rule") [77]. However, this "quasi-selection rule" does not explain why, amongst all phonons satisfying this condition, only those on one particular optical branch are seen. *Thomsen* and *Reich* [83] and *Baranov* et al. [84] proposed double resonance (DR) as the activation mechanism. Within DR, Raman scattering is a fourth-order process involving four virtual transitions: 1. excitation of an electron–hole pair; 2. electron–phonon scattering with an exchanged momentum $\boldsymbol{q} \sim \boldsymbol{K}$, where $\boldsymbol{K}$ is the K point Brillouin zone vector; 3. defect scattering; 4. electron–hole recombination. The DR condition is reached when the energy is conserved over all these four transitions [83]. A similar "intravalley" process is possible. This activates phonons with a small $\boldsymbol{q}$, resulting in the so-called D$'$ peak, that appears at $\sim 1620\,\mathrm{cm}^{-1}$ in graphite with defects [78].

The phonon dispersion around the K point is also crucial for the correct interpretation of the Raman D band. Graphene has four frequencies at the K point, originating from six phonon branches around K (three are shown in Fig. 9 that focus of the longitudinal optical (LO) and transversal optical (TO); a fourth lower-lying optical branch crossing the K point at $\sim 800\,\mathrm{cm}^{-1}$ also exists). All these branches should be Raman active if their electron–phonon couplings (EPCs) are ignored [81, 83, 86–88]. However, only a single D band is observed [76]. In the molecular approach [74, 75, 77, 89], the

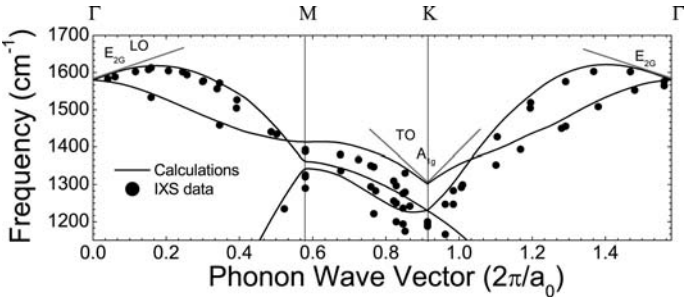

Fig. 9. Phonon dispersion of graphene calculated by DFPT [18] compared with the inelastic X-ray scattering data of [85]. The *lines* emphasize the presence of the two Kohn anomalies at $\boldsymbol{\Gamma}$ and $\boldsymbol{K}$

D band was assigned to the highest optical branch near $\boldsymbol{K}$. This assignment is based on symmetry and on the large Raman cross section of large aromatic molecules. However, this assignment was initially disputed [81, 83, 86–88]. In fact, the measured linear D band dispersion with excitation energy [81] seemed at odds with the flat, or even negative, slope of the highest optical branch near K given by previous calculations [90–94]. Many authors [81, 83, 86–88] therefore initially attributed the D band to the doubly degenerate, linearly dispersive 1200 cm^{-1} E′ mode at the K point. *Piscanec* et al. [18] finally confirmed the attribution of the D band to the highest optical (A_1) branch near K ($\boldsymbol{K}$–A_1') [76, 77, 89, 90]. Indeed, theoretical calculations have shown that the A_1' branch has by far the biggest EPC amongst all the K point phonons [20]. Secondly, the $\boldsymbol{K}$–A_1' branch exhibits linear dispersion near the K point (Fig. 9). A Kohn anomaly at K is the physical origin of this linear dispersion, which is in quantitative agreement with the measured D-band dispersion [81].

In general, atomic vibrations are partially screened by filled electronic states. In a metal, this screening is determined by the shape of the Fermi surface and can change rapidly from one point to another in the Brillouin zone (BZ). The consequent anomalous behavior of the phonon dispersion is called a Kohn anomaly [95]. Kohn anomalies may occur only for phonon wavevectors $\boldsymbol{q}$ such that there are two electronic states $\boldsymbol{k_1}$ and $\boldsymbol{k_2}$ on the Fermi surface, where $\boldsymbol{k_2} = \boldsymbol{k_1} + \boldsymbol{q}$ [95]. In graphene, the gap between occupied and empty electronic states is zero at the six corners of the BZ ($\boldsymbol{K}$ and $\boldsymbol{K}'$). These points are connected by a vector of length K. Thus, Kohn anomalies can occur for $\boldsymbol{q} = 0(\Gamma)$ or $\boldsymbol{q} = \boldsymbol{K}$ (Fig. 9 [18]). The cusps in $\omega(\boldsymbol{q})$ calculated at $\boldsymbol{q} = 0$ or $\boldsymbol{q} = \boldsymbol{K}$ cannot be described by a finite set of interatomic force constants [18]. Interestingly, for a given value of $\boldsymbol{q}$, the Kohn anomalies are present only in the highest optical branches. This can be understood from the details of the EPC [18–21].

3.2 Electron–Phonon Coupling from Phonon Dispersions and Raman Linewidths

Electron–phonon coupling (EPC) is important to the properties of graphene and nanotubes. Ballistic transport, superconductivity, excited-state dynamics, Raman spectra and phonon dispersions all fundamentally depend on it. In nanotubes, the EPC of the optical phonon is also extremely relevant, since electron scattering by optical phonons sets the ultimate limit to high-field ballistic transport [21, 96–99]. Many contradicting tight-binding calculations of EPC for optical phonons in graphene and nanotubes are in the literature [97, 100–103] (see Table II of Ref. [19] for a summary).

References [18,20] presented DFT calculations of graphene optical phonons and the EPC, as well as a strategy for their experimental determination. The presence of the Kohn anomalies is revealed by two sharp kinks in the phonon dispersion $\omega(\boldsymbol{q})$ (Fig. 9). Their slope S is proportional to the ratio of the square of the EPC and the electronic π band slope β [18]:

$$S_{\boldsymbol{\Gamma}}^{\mathrm{LO}} = \frac{\sqrt{3}\hbar a_0^2}{8M\omega_{\boldsymbol{\Gamma}}\beta}\,\mathrm{EPC}(\Gamma)^2\,, \tag{8}$$

and

$$S_{\boldsymbol{K}}^{\mathrm{TO}} = \frac{\sqrt{3}\hbar a_0^2}{8M\omega_{\boldsymbol{K}}\beta}\,\mathrm{EPC}(K)^2\,, \tag{9}$$

where $\beta = \hbar v_{\mathrm{F}} = 5.52\,\text{Å eV}$, M is the carbon atomic mass, and $\omega_{\boldsymbol{\Gamma}}$ and $\omega_{\boldsymbol{k}}$ are, respectively, the frequency of the E_{2g} phonon at Γ and the $\boldsymbol{K}$–A_1' phonon. The experimental phonon dispersion therefore can be used to measure the EPC [18–20].

An alternative strategy for the EPC measurement is based on the analysis of the G-peak linewidths. The EPC is the major source of broadening for the Raman G band in graphite, graphene and for the G^- peak in metallic nanotubes [19, 20].

In a perfect crystal, the Raman linewidth γ, or inverse phonon lifetime, is determined by the anharmonic terms in the interatomic potential and the EPC, i.e., $\gamma = \gamma^{\mathrm{an}} + \gamma^{\mathrm{EPC}}$, in which γ^{an} is always present and γ^{EPC} is important only in metals since the carrier density interacting with phonons would be very low for semiconductors. If γ^{an} is negligible or otherwise known, measuring the linewidth is a simple way to determine the contribution from EPC. This is the case in graphene, graphite and metallic carbon nanotubes, where γ^{an} is much smaller than γ^{EPC} [20].

From Fermi's golden rule, γ_0^{EPC} can be described by a simple analytical formula [20]:

$$\gamma_0^{\mathrm{EPC}} = \frac{\sqrt{3}\hbar^2 a_0^2}{4M\beta^2}\left[\mathrm{EPC}(\Gamma)\right]^2\,, \tag{10}$$

provided that the conservation of energy and momentum is fulfilled (i.e., $\boldsymbol{q} \leq \hbar\omega_{\boldsymbol{\Gamma}}/\beta$). Otherwise, $\gamma_0^{\mathrm{EPC}} = 0$. This condition is satisfied by the Raman G peak of undoped graphite and graphene. On the other hand, the double-resonant D′ mode close to G does not satisfy this criterion. Indeed, the D′ peak is sharper than the G peak [104]. The experimental G bandwidth full width at half-maximum (FWHM(G)) of graphite and undoped graphene is $\sim 13\,\mathrm{cm}^{-1}$ [20, 105]. Temperature-dependent measurements show no increase of FWHM(G) in the $2 - 900\,\mathrm{K}$ range [105]. Accounting for a Raman spectrometer resolution of $\sim 1.5\,\mathrm{cm}^{-1}$, this implies that the anharmonic contribution is lower than the spectral resolution. Thus, $\gamma_0^{\mathrm{EPC}}(\mathrm{G}) \sim 11.5\,\mathrm{cm}^{-1}$. Then, from (10), $[EPC(\Gamma)]^2 \sim 47\,(\mathrm{eV/\AA})^2$. This compares very well with DFT calculations [19, 20], further supporting a small γ^{an}.

Finally, [17, 106] extended (10) to finite doping ($\epsilon_{\mathrm{F}} \neq 0$, ϵ_{F} being the Fermi level):

$$\gamma^{\mathrm{EPC}} = \gamma_0^{\mathrm{EPC}} \left[f\left(-\frac{\hbar\omega_0}{2} - \epsilon_{\mathrm{F}}\right) - f\left(\frac{\hbar\omega_0}{2} - \epsilon_{\mathrm{F}}\right) \right], \tag{11}$$

where $f(E)$ is the Fermi–Dirac distribution. Note that, even for zero doping, (11) predicts a significant decrease of γ^{EPC} with temperature. Since the anharmonic contribution to the FWHM is much smaller than γ^{EPC}, (11) predicts a net decrease of FWHM(G) with temperature, in contrast to what happens in most materials. This unusual trend was indeed observed recently [105].

3.3 The Raman Spectrum of Graphene and *n*-Graphene Layer Systems

Figure 8 shows that the two most intense features in the Raman spectrum of graphene are the G peak at $\sim 1580\,\mathrm{cm}^{-1}$ and a band at $\sim 2700\,\mathrm{cm}^{-1}$, historically named G′, since it is the second most prominent band always observed in graphite samples [80]. However, we now know that the G′ band is due to second-order Raman scattering at $\omega = \omega_1(\boldsymbol{q}) + \omega_2(-\boldsymbol{q})$, where $\boldsymbol{q} \sim \boldsymbol{K}$ and $\omega_1 = \omega_2 = \omega_D$. Thus, we refer to the G′ band as the 2D band. Figure 8 also shows another peak at $\sim 3250\,\mathrm{cm}^{-1}$. Its frequency is higher than double the G-peak frequency, thus it is not the second-order scattering of G phonons. This peak has been identified with the second-order scattering of the intravalley D′ band discussed above. Thus, for consistency, we call it the 2D′ band. Figure 8b shows a significant change in the shape and intensity of the 2D band of graphene compared to bulk graphite. The 2D band in bulk graphite consists of two components $2\mathrm{D}_1$ and $2\mathrm{D}_2$ [78, 80], roughly 1/4 and 1/2 of the intensity of the G band, respectively. Graphene has a single, sharp 2D peak, roughly 4 times more intense than the G peak.

Figure 10 shows the evolution of the 2D band in nGLs as a function of the number of layers for 514.5 nm excitation [72]. Bilayer graphene ($n = 2$)

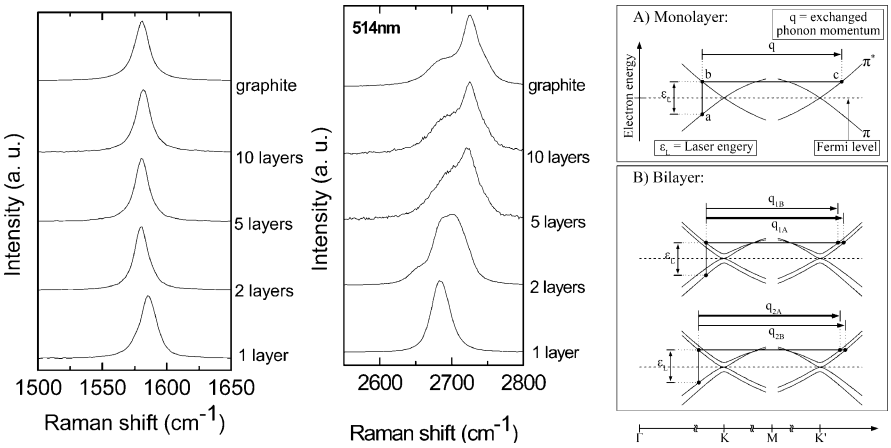

Fig. 10. Left and Center: Raman spectra for the G band (left) and for the 2D-band (right) of nGL with varying n. **Right:** The DR process for the 2D peak in (**A**) graphene and (**B**) bilayer graphene

has a much broader and upshifted 2D band with respect to graphene. The shape of this band is quite different from that of bulk graphite. It can be well fitted by 4 components, $2D_{1B}$, $2D_{1A}$, $2D_{2A}$, $2D_{2B}$, two of which, $2D_{1A}$ and $2D_{2A}$, are more intense than the other two, as indicated in Fig. 11. Increasing the number of layers further leads to a significant decrease of the relative intensity of the lower-frequency $2D_1$ peaks. The Raman spectrum of an nGL of more than 5 layers becomes hardly distinguishable from that of bulk graphite [72]. In contrast, the shape of the G band does not change with the number of layers. However, a slight frequency upshift can be seen in the case of graphene. This is due to a combination of self-doping [17], as discussed later, and the fact that the frequency of the Raman active phonon in graphene is slightly higher than in graphite, due to mode splitting (see lower panel of Fig. 1 in [18]).

Figure 12 shows the effect of laser excitation energy on the shape and position of the 2D band [107]. Spectra for $n = 1$–4 are shown in three panels corresponding to excitations at 785 nm (left), 514.5 nm (middle) and 488 nm (right). These spectra are fitted to four Lorentzian components ($2D_{1A}$, $2D_{1B}$, $2D_{2A}$, $2D_{2B}$) as described above. The relative intensities of these components within the 2D manifold change with laser excitation energy. The simple, near-Lorentzian lineshape of the $n = 1$ band is preserved and a shift in peak position of $\sim 100\,\mathrm{cm}^{-1}/\mathrm{eV}$ with increasing excitation energy is observed [72, 83, 89, 108].

Figure 13 shows the peak-position shift with layer number n for the 3rd-order Raman band near $4270\,\mathrm{cm}^{-1}$ [109]. The spectra were collected with a 514.5-nm excitation and the $\sim 4270\,\mathrm{cm}^{-1}$ band is identified with a three-

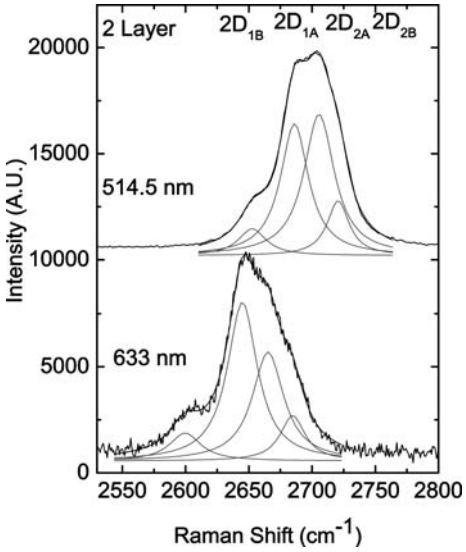

Fig. 11. The four components of the 2D peak in bilayer graphene at two laser-excitation wavelengths [72]

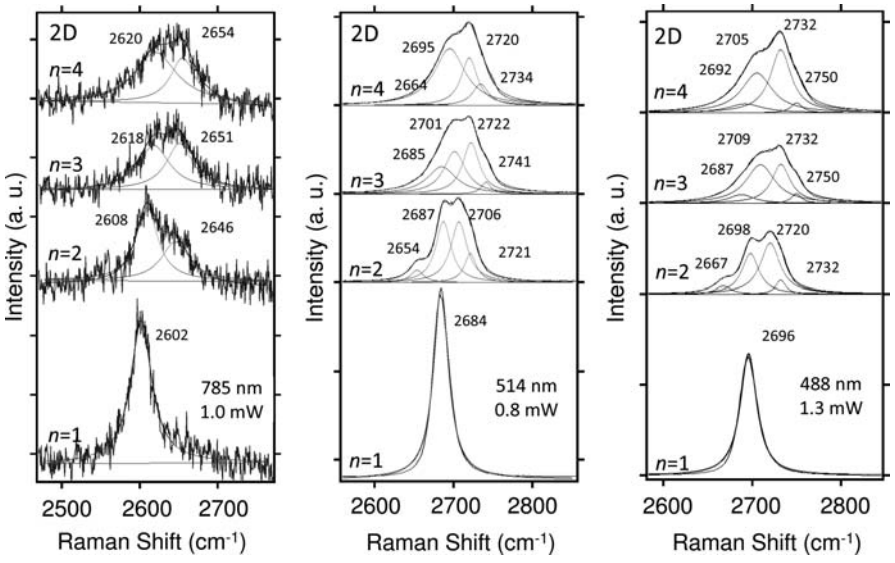

Fig. 12. Excitation dependence of the 2D band for $n = 1$–4 nGLs supported on SiO_2:Si

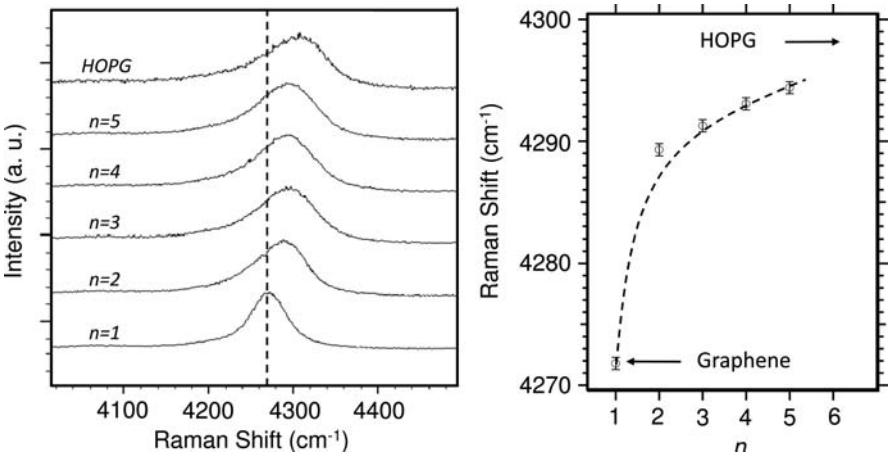

Fig. 13. 3rd-order Raman bands assigned to 2D+G phonons. **Left:** HOPG and $n = 1$–5 supported on SiO_2:Si. **Right:** Band position vs. n. Data collected with 514.5-nm excitation

phonon process in which 2D phonons ($\sim 2 \times 1350\,\mathrm{cm}^{-1}$) and one G phonon ($\sim 1580\,\mathrm{cm}^{-1}$) are created simultaneously in the scattering process. We call this band 2D+G. The left panel shows the n dependence of the lineshape and the right panel displays the n dependence of the band maximum. As can be seen in the left panel, graphene exhibits a nearly symmetric 2D+G band that asymmetrically broadens to lower frequency and upshifts with increasing n. The shape of the band remains simple in character. This 3rd-order band appears to afford a means to determine the number of layers in the nGL (as shown in the right panel). Therefore, for low n, the frequency rises steeply and then crosses over to an almost linear upshift with further increases in n (the dashed curve in the figure is a guide to the eye).

The excitation-energy dependence of the 3rd-order (2D+G) band is shown in Fig. 14 for 514-nm (left panel) and 488-nm (right panel) excitation. In both panels, the 3rd-order Raman band shifts to higher frequency with increasing layer number. The band dispersion of $93\,\mathrm{cm}^{-1}/\mathrm{eV}$ with excitation energy is consistent with its identification as a 3-phonon 2D+G process. That is, the frequency upshift with increasing excitation energy tracks that of the 2nd-order 2D band (the G-band remains fixed, independent of excitation). Other overtones up to $\sim 6000\,\mathrm{cm}^{-1}$ were also identified [110].

Ferrari et al. [72] explained why graphene (1GL) has a single 2D band, and why this band splits into four components in bilayer graphene and evolves into two distinguishable components in bulk graphite (see Fig. 10b). The 2D Raman band in graphene is due to two phonons with opposite momenta in the highest optical branch near the K point [18, 76, 77]. The resulting 2D frequency is twice that of the scattering phonons, whose $\boldsymbol{q}$ is determined

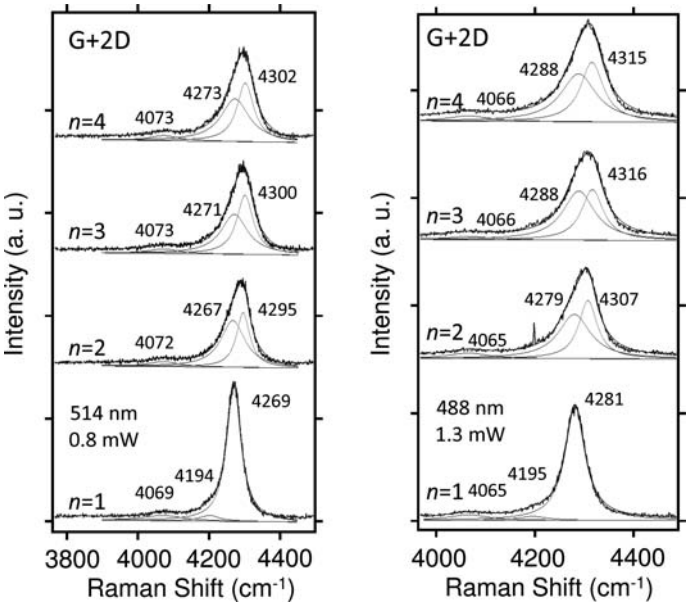

Fig. 14. Excitation dependence of the 2D+G band for $n = 1$–4. nGLs supported on SiO_2:Si

by the DR condition (Fig. 10B). In bilayer graphene, the interlayer interaction causes the π and π^* bands to divide into two hole and two electron bands, with a different splitting for electrons and holes (Fig. 10B). Amongst the 4 possible optical transitions, the incident light couples more strongly the two transitions shown in Fig. 10B. The two almost degenerate phonons in the highest optical branch couple all electron bands amongst them. The resulting four scattering processes involve phonons with momenta $\boldsymbol{q}_{1B}$, $\boldsymbol{q}_{1A}$, $\boldsymbol{q}_{2A}$, and $\boldsymbol{q}_{2B}$, as shown in Fig. 10B. These wavevectors correspond to phonons with different frequencies, due to the strong phonon dispersion around $\boldsymbol{K}$ [18]. They produce four different peaks in the Raman spectrum of bilayer graphene [72].

3.4 Doped Graphene: Breakdown of the Adiabatic Born–Oppenheimer Approximation

Doping moves ϵ_F and changes the Fermi surface of graphene. The Kohn anomaly then moves away from $\boldsymbol{q} = 0$. Thus, since first-order Raman scattering probes $\boldsymbol{q} = 0$ phonons, intuitively we might expect the G peak to stiffen with electron or hole doping. Indeed, this response is reported in [17, 111]. There, the graphene sheet was supported on a SiO_2:Si substrate and the doping level was controlled by applying a gate voltage. The G peak upshifts for both hole and electron doping. Figure 15 plots the G-peak position

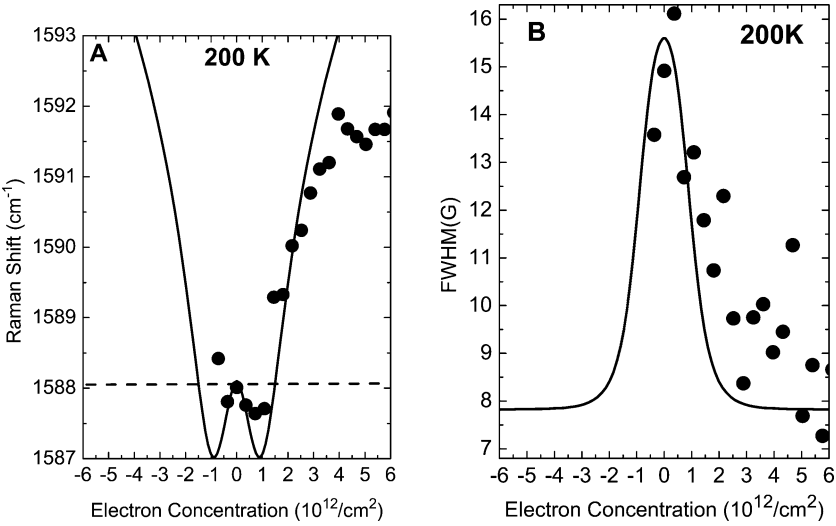

Fig. 15. (**A**) G peak position as a function of electron concentration at 200 K. (*dots*) measurements; (*horizontal-dashed line*) adiabatic Born–Oppenheimer; (*line*) finite-temperature nonadiabatic calculation. The minimum observed in the calculations at $\sim 10^{12}/\mathrm{cm}^2$ occurs when the Fermi energy equals half of the phonon energy. (**B**) FWHM(G) at 200 K as a function of electron concentration. (*dots*) measurements; (*line*) theoretical FWHM of a Voigt profile obtained from a Lorentzian component given by (11), and a constant Gaussian component of $\sim 8\,\mathrm{cm}^{-1}$ [17]

and FWHM measured at 200 K as a function of electron doping. The trends in Fig. 15 are similar to those reported in [111] at 10 K.

The trend in the FWHM is fully consistent with the prediction of (11). The upshift of the G peak with doping can be understood by extending the DFT calculations of [18] to include beyond-Born–Oppenheimer corrections to the dynamical matrix [17]. The detailed theoretical analysis of this case is reported in [106, 112, 113].

The adiabatic Born–Oppenheimer approximation (ABO) has been standard in describing the interaction between electrons and nuclei since the early days of quantum mechanics [16]. ABO assumes that the lighter electrons adjust adiabatically to the motion of the heavier nuclei, remaining in their instantaneous ground states. ABO is well justified when the energy gap between the ground and excited electronic states is larger than the energy scale of the nuclear motion. The use of ABO to describe lattice motion in metals is, therefore, questionable. Nonetheless, the ABO has proven effective for the determination of chemical reactions, molecular dynamics and phonon frequencies in a wide range of metallic systems.

Quite remarkably ABO fails in graphene [17]. Indeed, the inverse of the G-peak pulsation is ~ 3 fs, which is much smaller than the typical electron-momentum relaxation time, which was estimated to be a few hundred fs

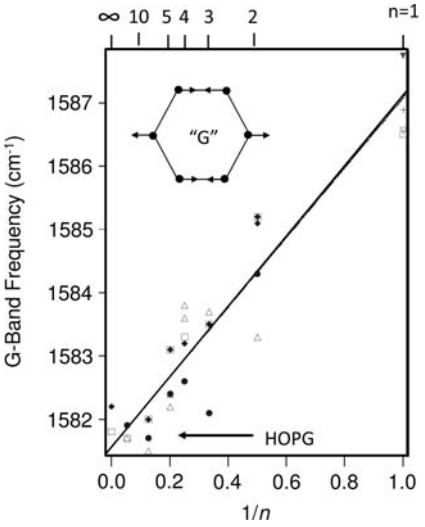

Fig. 16. G-band frequency vs. $1/n$. Spectra excited with 5 14.5-nm light and collected from nGLs supported on a single SiO_2:Si substrate. The *straight line* is obtained by a least-squares fit. Data on the same set of nGLs were collected from several spots well removed from the edge of the flake

from the electron mobility in graphene [39] and ultrafast spectroscopy in graphite [114, 115]. Thus, electrons do not have time to relax their momenta to reach the instantaneous adiabatic ground state, as assumed in ABO. The nonadiabatic Born–Oppenheimer calculation for the G-band shift $\Delta\omega$ with ϵ_F can be described analytically [106]:

$$\hbar\Delta\omega = \frac{\hbar A\langle D_{\boldsymbol{I}}^2\rangle_F}{\pi M\omega_0(\hbar v_F)^2}\left[|\epsilon_F| + \frac{\hbar\omega_0}{4}\ln\left(\left|\frac{|\epsilon_F| - \frac{\hbar\omega_0}{2}}{|\epsilon_F| + \frac{\hbar\omega_0}{2}}\right|\right)\right], \tag{12}$$

where $A = 5.24\,\text{Å}^2$ is the graphene unit-cell area and ω_0 is the frequency of the G peak in the undoped case. This equation is derived for $T = 0$. However, the result of (12) can be extended to any finite temperature T [17, 106], giving reasonable agreement with the experimental data shown in Fig. 15.

A systematic upshift in the position of the G band with increasing $1/n$ was reported for nGLs supported on SiO_2:Si substrates [72, 116, 117]. This behavior is plotted in Fig. 16. Shown there are the results of many spectra collected from nGLs on the same substrate. In most of the cases, a single nGL was measured several times, but with the laser focused on a spot of $\sim 1\,\mu\text{m}^2$ at different locations on the film. n was determined via atomic force microscope z-scans [116]. Although there is a significant amount of scatter in the G-band position for a fixed n, a $1/n$ dependence of the G-band frequency is evident. The solid line in the plot is a least-squares fit to the data, which indicates a 5-cm^{-1} upshift of the G band from its location

in highly oriented pyrolytic graphite (HOPG) to that for $n = 1$ graphene. Gupta et al. proposed that the upshift may be due to an n-dependent bending of the nGL as it is attracted to the oxide surface and tries to conform to the surface roughness of the substrate, which is about 2 nm. However, as discussed above, this trend might be due to the diminishing influence of self-doping with increasing n [118, 119]. Indeed, measurements on a variety of single layer graphene have shown a G peak position variation of 13 cm^{-1}, much bigger than that reported between single and multi-layer graphene [118, 119]. Another consequence of doping is the significant decrease of $I(2D)/I(G)$, with respect to the undoped case [120].

4 Implications for Phonons and Raman Scattering in Nanotubes

4.1 Adiabatic Kohn Anomalies

Graphene has been used as a model for the calculations of the electronic and vibrational properties of carbon nanotubes. However, a SWNT can be either metallic or semiconducting, whereas graphene is a semimetal/zero-gap semiconductor. The differences between graphene and SWNTs can be explained in terms of curvature and confinement [19]. Curvature effects arise because in a nonplanar geometry the C–C bonds in SWNTs assume a mixed σ–π character. Confinement effects arise because the electronic wavefunctions in a SWNT have to be commensurate to the tube circumference, resulting in the quantization of the electronic momentum component perpendicular to the tube axis.

Neglecting the effects of curvature, it is thus possible to map the electronic states of a SWNT onto those of graphene. It has been shown that folding the electronic structure of graphene to describe the band structure of SWNTs produces accurate results for tubes with diameters larger than 0.8 nm [121, 122]. This technique is known as electronic zone folding (EZF). In the past, a similar technique had also been applied to phonons. This goes under the name of phonon zone folding (PZF). However, as discussed in Sect. 3.1, phonon dispersions of graphene are affected by two Kohn anomalies, which occur only in metals. Thus, Kohn anomalies cannot be present in semiconducting SWNTs, while they can be enhanced in metallic SWNTs because of their reduced dimensionality [19, 20]. As a consequence, PZF may not be suitable for the description of the phonon dispersion of metallic SWNTs close to the Kohn anomalies. Even for semiconducting SWNTs, PZF of graphene may not be precise, since PZF does not have Kohn anomalies [19]. However, neglecting the effects of curvature, phonons of SWNTs can be obtained from the phonons of a flat graphene sheet, if the calculation is done by performing the electronic Brillouin-zone integration on the lines of the electronic zone

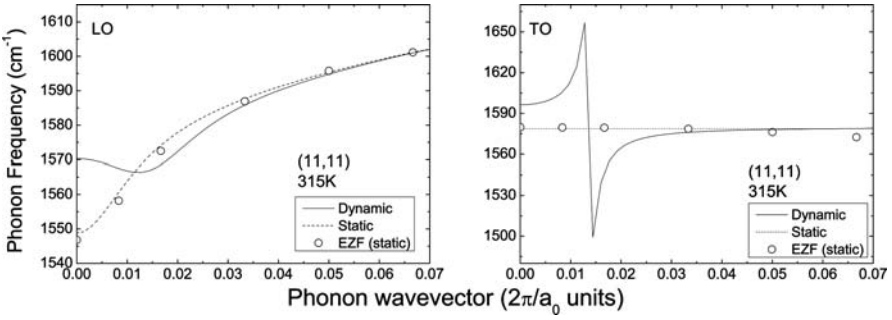

Fig. 17. Phonon dispersion of the modes for a (11,11) SWNT derived from the graphene E_{2g} branch. The dots are the results of static PZF calculations. The *dotted* and *solid lines* are obtained with analytical models based, respectively, on the adiabatic and nonadiabatic description of phonons [19]

folding [19,20]. This approach allows the description of all the effects of quantum confinement, and can be used to compute phonon dispersions of tubes with a diameter larger than 0.8 nm, which are typical in experiments.

4.2 Nonadiabatic Kohn Anomalies

Nonadiabatic effects lead to a deep modification in the description of the Kohn anomalies (KAs) [17, 19, 106]. Using the zone-folding approach of [19, 20], it is possible to obtain the theoretical description of the KAs in metallic SWNTs within the adiabatic (static) and nonadiabatic (dynamic) approaches. These results should then be corrected for curvature effects, as shown by [19]. Figure 17 compares the modes derived from the graphene E_{2g} in a (11,11) metallic SWNT, calculated using a static and a dynamic description of the phonons. In the first case, only the LO mode is affected by a Kohn anomaly, centered at $\boldsymbol{q} = 0(\Gamma)$. On the other hand, calculations performed with the dynamic, time-dependent approach show the presence of the anomalies for both the LO and the TO modes, respectively, and predict the anomalies to be shifted from $\boldsymbol{\Gamma}$ [19].

4.3 The Raman G Peak of Nanotubes

In SWNTs, the doubly degenerate Raman-active E_{2g} mode of graphene splits into two dominant phonons. As shown in Fig. 18, such modes are polarized, respectively, along the tube axis (longitudinal mode) and along the tube circumference (tangential mode), and are usually referred to as the LO and the TO modes [19].

In the 1550–1590 cm^{-1} region, the Raman spectra of SWNTs are characterized by the presence of two distinct features: the so-called G^{+} and G^{-}

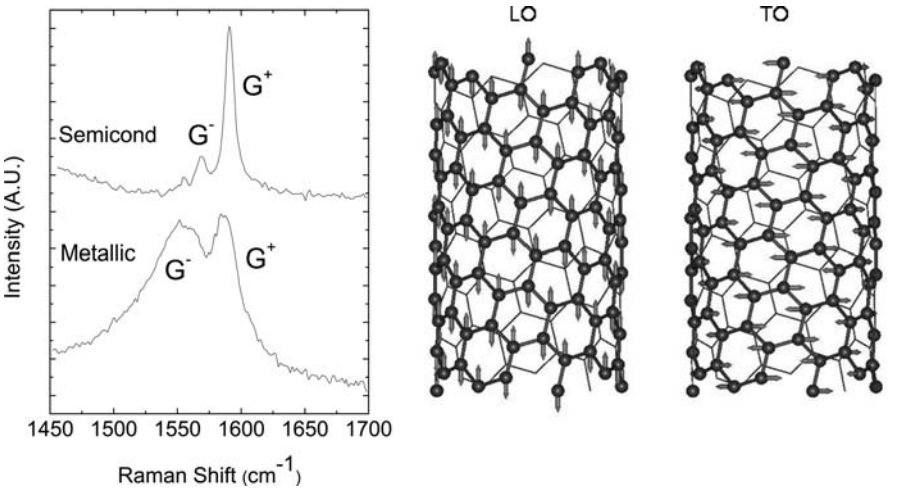

Fig. 18. Left: G-band of semiconducting and metallic SWNTs. Semiconducting tubes are characterized by two sharp peaks. Metallic tubes show a characteristic broad, downshifted G^- peak [123]. **Right:** LO and TO phonon modes of SWNTs derived from the E_{2g} phonon of graphene

peaks. These peaks are due to the LO and TO modes, and their shape and position strongly depend on the electronic properties of the tubes. The G band of a metallic and of a semiconducting SWNT [123] are compared in Fig. 18. In semiconducting tubes, both the G^+ and the G^- peaks appear as sharp Lorentzians, centered, respectively, at $\sim 1590\,\mathrm{cm}^{-1}$ and $\sim 1570\,\mathrm{cm}^{-1}$. The G^+ peak is usually more intense than the G^-, and its position is nearly independent of the tube's diameter, whereas the position of the G^- peak decreases for decreasing tube diameter. On the other hand, in metallic tubes, the G^- peak is usually rather intense, very broad, and downshifted with respect to its counterpart in semiconducting tubes.

In semiconducting tubes, the splitting between the LO and the TO modes is usually explained in terms of curvature. Indeed, the σ–π mixing of the C–C bonds along the circumference results in a softening of the TO mode with respect to the LO, accounting for both the splitting of the peaks and the diameter dependence of the G^- position.

For metallic tubes, different theories have been proposed. The first attempt to explain the broadened, downshifted G^- in metallic SWNTs was based on a Fano resonance between the TO phonon and the plasmons in metallic tubes [124, 125]. However, this model neglects both the presence of Kohn anomalies in the phonon dispersion of metallic SWNTs, and the role of the electron–phonon interaction. Indeed, it is possible to show, as discussed in Sect. 4, that the G^- peak of metallic SWNTs is strongly influenced by the effects of EPC [19, 20]. Modeling the EPC in metallic SWNTs by using the

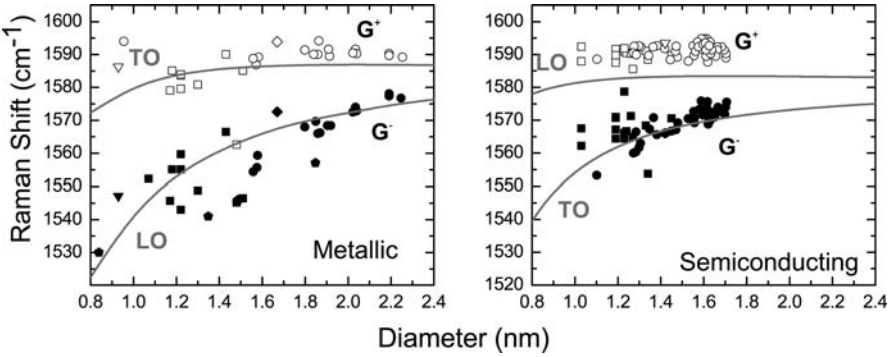

Fig. 19. Comparison between the computed frequency of the LO and the TO phonon in SWNTs (*lines*) and the experimental position of the G^+ and the G^- Raman peak in metallic and semiconducting tubes as measured by various authors [19]. Calculations include the dynamic effects and a correction for the curvature effects [19]

same tight–binding model as was used for graphene, it is possible to show that the EPC affects the LO mode only and acts in two different ways. First, it is responsible for the onset of a Kohn anomaly resulting in a strong downshift of the LO frequency. Secondly, in agreement with the Fermi golden rule, it reduces the LO–phonon lifetime, resulting in an increase of the phonon linewidth. Consistent with this view, the G^- peak in metallic tubes does not originate from a curvature-downshifted TO phonon, as in semiconducting tubes, but is derived from an EPC-affected LO mode [19, 20]. The prediction given by the dynamic, time-dependent model can be compared with the data from Raman spectroscopy. Figure 19 shows that the calculated frequencies of the TO and LO modes in metallic SWNTs are in reasonable agreement with the position of the G^+ and G^- Raman peaks. This suggests that the G^+ and G^- peaks of metallic nanotubes should be assigned to TO (tangential) and LO (axial) modes, the opposite of semiconducting nanotubes [19, 20].

In SWNTs, due to the reduced dimensionality, the nonadiabatic contributions are essential to describe the phonons [19] and they should be more important in the case of doped SWNTs [22]. Thus, the shape of the G peak will be affected by doping in a similar fashion to doped graphene. Furthermore, due to energy conservation, measuring a metallic nanotube off resonance can result in a sharp G^- feature. We can thus simply understand the reason for the large variety of G^- lineshapes reported in the literature. Finally, the nonadiabatic Kohn anomaly at Γ also explains the observed electronic temperature dependence of the Raman spectra [19].

It is important to note the following on the shape of the G^- peak [20]. The peak shape observed in an actual experiment depends on the coupling between the experimental probe and the system, as discussed in the seminal paper by *Fano* [126]. Indeed, if the laser couples not only to the G^- phonon,

but also to the continuum that broadens the phonon, the Raman spectrum shows an asymmetric Fano profile [126]. Thus, the detection of an asymmetric Fano profile in a Raman measurement gives information on how the electromagnetic radiation couples to the system, but not on the origin of the broadening. Here, we discussed how the broadening of the G^- peak in metallic nanotubes can be mainly attributed to the coupling of the LO phonon to the continuum of the electron–hole excitations, not to phonon–plasmon coupling. This does not imply that a Fano-like profile cannot be observed in experiments.

5 Outlook

In the past two years, tens of papers have been published and more than 600 papers have been posted on graphene. Thus, by no means could we give a comprehensive review of this fast-moving field in the limited space available here. So, we have focused on the basic electronic and phonon properties of graphene and their relation to nanotubes.

Even if graphene research is at the beginning, scientists can now exploit the large amount of expertise acquired in the study of carbon nanotubes. Almost all the experiments reported on nanotubes are now being performed on graphene. These range from transistor fabrication, to nanoelectromechanical assemblies, to spin transport to optoelectronics. Furthermore, bilayer and few-layer graphene samples could lead to a variety of interesting new physics and applications. A research area that is still largely unexplored is the growth of graphene layers on a substrate of choice. Large-scale deposition of graphene is the needed breakthrough to make this new material viable for electronic applications. Once this is achieved, standard top-down processes could be utilized for large-area production of devices. This is a major advantage compared to nanotubes, for which on-demand chirality is still a dream.

Acknowledgements

J. C. Charlier acknowledges the National Fund for Scientific Research [FNRS] of Belgium for financial support. A. C. Ferrari acknowledges support from The Royal Society and The Leverhulme Trust. P. C. Eklund and J. Zhu acknowledge support from the National Science Foundation NIRT program, and we thank A. Gupta and T. J. Russin for helpful discussions and assistance with preparing figures.

References

[1] P. R. Wallace: The band theory of graphite, Phys. Rev. **71**, 622 (1947) 674
[2] L. M. Viculis, J. J. Mack, R. B. Kaner: A chemical route to carbon nanoscrolls, Science **299**, 1361 (2003) 674

[3] L. M. Viculis, J. J. Mack, O. M. Mayer, H. T. Hahn, R. B. Kaner: Intercalation and exfoliation routes to graphite nanoplatelets, J. Mater. Chem. **15**, 974 (2005) 674
[4] S. Niyogi, E. Bekyarova, M. E. Itkis, J. L. McWilliams, M. A. Hammon, R. C. Haddon: Solution properties of graphite and graphene, J. Am. Chem. Soc. **128**, 7720 (2006) 674
[5] S. Stankovich, D. A. Dikin, G. H. B. Dommett, K. M. Kohlhass, E. J. Zimmey, E. A. Stach, R. D. Piner, S.-B. T. Nguyen, R. S. Ruoff: Graphene-based composite materials, Nature **442**, 282 (2006) 674
[6] S. Stankovich, R. D. Piner, X. Chen, N. Wu, T. Nguyen, R. S. Ruoff: Stable aqueous dispersions of graphitic nanoplatelets via the reduction of exfoliated graphite oxide in the presence of poly(sodium 4-styrenesulfonate), J. Mater. Chem. **16**, 155 (2006) 674
[7] K. S. Novoselov, A. K. Geim, S. V. Morozov, D. Jiang, S. V. Dubonos, I. V. Girgorieva, A. A. Firsov: Electric field effect in atomically thin carbon films, Science **306**, 666 (2004) 674, 686
[8] Y. B. Zhang, J. P. Small, W. V. Pontius, P. Kim: Fabrication and electric-field-dependent transport measurements of mesoscopic graphite devices, Appl. Phys. Lett. **86**, 073104 (2005) 674
[9] I. Forbeaux, J. M. Themlin, J. M. Debever: High-temperature graphitization of the 6H-SiC (000(1)over-bar) face, Surf. Sci. **442**, 9 (1999) 674
[10] C. Berger, Z. M. Song, T. B. Li, X. B. Li, A. Y. Ogbazghi, R. Feng, Z. T. Dai, A. N. Marchenkov, E. H. Conrad, P. N. First, W. A. de Heer: Ultrathin epitaxial graphite: 2D electron gas properties and a route toward graphene-based nanoelectronics, J. Phys. Chem. B **108**, 19912 (2004) 674
[11] T. Ohta, A. Bostwick, T. Seyller, K. Horn, E. Rotenberg: Controlling the electronic structure of bilayer graphene, Science **313**, 951 (2006) 674, 684, 685
[12] E. Rolling, G. H. Gweon, S. Y. Zhou, B. S. Mun, J. L. McChesney, B. S. Hussain, A. Fedorov, P. N. First, W. A. de Heer, A. Lanzara: Synthesis and characterization of atomically thin graphite films on a silicon carbide substrate, J. Phys. Chem. Solids **67**, 2172 (2006) 674
[13] K. S. Novoselov, A. K. Geim, S. V. Morozov, D. Jiang, M. I. Katsnelson, I. V. Girgorieva, S. V. Dubonos, A. A. Firsov: Two-dimensional gas of massless Dirac fermions in graphene, Nature **438**, 197 (2005) 674, 676, 679, 680, 681
[14] Y. Zhang, Y. W. Tan, H. L. Stormer, P. Kim: Experimental observation of the quantum Hall effect and Berry's phase in graphene, Nature **438**, 201 (2005) 674, 676, 678, 679, 680, 681
[15] A. K. Geim, K. S. Novoselov: The rise of graphene, Nature Mater. **6**, 183 (2007) 674, 678, 679
[16] M. Born, R. Oppenheimer: Ann. Phys. **84**, 457 (1927) 675, 695
[17] S. Pisana, M. Lazzeri, C. Casiraghi, K. Novoselov, A. K. Geim, A. C. Ferrari, F. Mauri: Breakdown of the adiabatic Born–Oppenheimer approximation in graphene, Nature Mater. **6**, 198 (2007) 675, 690, 691, 694, 695, 696, 698
[18] S. Piscanec, M. Lazzeri, F. Mauri, A. Ferrari, J. Robertson: Kohn anomalies and electron–phonon interactions in graphite, Phys. Rev. Lett. **93**, 185503 (2004) 675, 688, 689, 691, 693, 694, 695

[19] S. Piscanec, M. Lazzeri, J. Robertson, A. C. Ferrari, F. Mauri: Optical phonons in carbon nanotubes: Kohn anomalies, Peierls distortions, and dynamic effects, Phys. Rev. B **75**, 035427 (2007) 675, 688, 689, 690, 697, 698, 699, 700

[20] M. Lazzeri, S. Piscanec, F. Mauri, A. C. Ferrari, J. Robertson: Phonon linewidths and electron–phonon coupling in graphite and nanotubes, Phys. Rev. B **73**, 155426 (2006) 675, 688, 689, 690, 697, 698, 699, 700

[21] M. Lazzeri, S. Piscanec, F. Mauri, A. C. Ferrari, J. Robertson: Electron transport and hot phonons in carbon nanotubes, Phys. Rev. Lett. **95**, 236802 (2005) 675, 688, 689

[22] N. Caudal, A. M. Saitta, M. Lazzeri, F. Mauri: Kohn anomalies and nonadiabaticity in doped carbon nanotubes, Phys. Rev. B **75**, 115423 (2007) 675, 700

[23] J.-C. Charlier, X. Blase, S. Roche: Electronic and transport properties of nanotubes, Rev. Mod. Phys. **79**, 677–732 (2007) 675, 676, 677

[24] J. C. Slonczewski, P. R. Weiss: Band structure of graphite, Phys. Rev. **109**, 272 (1958) 678

[25] K. S. Novoselov, D. Jiang, F. Schedin, T. J. Booth, V. V. Khotkevich, S. V. Morozov, A. K. Geim: Two-dimensional atomic crystals, Proc. Nature Acad. Sci. USA **102**, 10451 (2005) 678

[26] C. Berger, Z. Song, X. Li, X. Wu, N. Brown, C. Naud, D. Mayou, T. Li, J. Hass, A. N. Marchenkov, E. H. Conrad, P. N. First, W. A. De Heer: Electronic confinement and coherence in patterned epitaxial graphene, Science **312**, 1191 (2006) 679

[27] K. Nomura, A. H. MacDonald: Quantum transport of massless Dirac fermions, Phys. Rev. Lett. **98**, 076602 (2007) 679

[28] K. S. Novoselov, E. McCann, S. V. Morozov, V. I. F. M. I. Katsnelson, U. Zeitler, D. Jiang, F. Schedin, A. K. Geim: Unconventional quantum Hall effect and Berry's phase of 2 pi in bilayer graphene, Nature Phys. **2**, 177 (2006) 679, 685

[29] S. V. Morozov, K. S. Novoselov, M. I. Katsnelson, F. Schedin, L. A. Ponomarenko, D. Jiang, A. K. Geim: Strong suppression of weak localization in graphene, Phys. Rev. Lett. **97**, 016801 (2006) 679

[30] V. M. Galitski, S. Adam, S. D. Sarma: Statistics of random voltage fluctuations and the low-density residual conductivity of graphene, arXiv Url: cond-mat/0702117 679

[31] F. D. M. Haldane: Model for a quantum Hall effect without Landau levels: Condensed-matter realization of the "parity anomaly", Phys. Rev. Lett. **61**, 2015 (1988) 679

[32] Y. S. Zheng, T. Ando: Hall conductivity of a two-dimensional graphite system, Phys. Rev. B **65**, 245420 (2002) 679

[33] M. L. Sadowski, G. Martinez, M. Potemski, C. Berger, W. A. de Heer: Landau level spectroscopy of ultrathin graphite layers, Phys. Rev. Lett. **97**, 266405 (2006) 679

[34] Z. Jiang, E. A. Henriksen, L. C. Tung, Y.-J. Wang, M. E. Schwartz, M. Y. Han, P. Kim, H. L. Stormer: Infrared spectroscopy of Landau levels of graphene, Phys. Rev. Lett. **98**, 197403 (2007) 679, 680

[35] R. S. Deacon, K.-C. Chuang, R. J. Nicholas, K. S. Novoselov, A. K. Geim: Cyclotron resonance study of the electron and hole velocity in graphene monolayers, Phys. Rev. B **76 (8)**, 081406 (2007) 679, 680
[36] K. S. Novoselov, Z. Jiang, Y. Zhang, S. V. Morozov, H. L. Stormer, U. Zeitler, J. C. Maan, G. S. Boebinger, P. Kim, A. K. Geim: Room-temperature quantum Hall effect in graphene, Science **315**, 1379 (2007) 679
[37] M. Berry: Quantal phase-factors accompanying adiabatic changes, Proc. R. Soc. Lond. A **392**, 45 (1984) 680
[38] D. Shoenberg: *Magnetic Oscillations in Metals* (Cambridge University Press, Cambridge 1984) 680
[39] Y. Zhang, Z. Jiang, J. P. Small, M. S. Purewal, Y. W. Tan, M. Fazlollahi, J. D. Chudow, J. A. Jaszczak, H. L. Stormer, P. Kim: Landau-level splitting in graphene in high magnetic fields, Phys. Rev. Lett. **96**, 136806 (2006) 681, 696
[40] D. A. Abanin, K. S. Novoselov, U. Zeitler, P. A. Lee, A. K. Geim, L. S. Levitov: Dissipative quantum Hall effect in graphene near the Dirac point, Phys. Rev. Lett. **98**, 196806 (2007) 681
[41] K. Yang: Spontaneous symmetry breaking and quantum Hall effect in graphene, Solid State Comm. **143**, 27 (2007) 681
[42] K. Nakada, M. Fujita, G. Dresselhaus, M. S. Dresselhaus: Edge state in graphene ribbons: Nanometer size effect and edge shape dependence, Phys. Rev. B **54**, 17954 (1996) 681, 682
[43] K. Wakabayashi, M. Fujita, H. Ajiki, M. Sigrist: Electronic and magnetic properties of nanographite ribbons, Phys. Rev. B **59**, 8271 (1999) 681, 682, 683
[44] Y. Miyamoto, K. Nakada, M. Fujita: First-principles study of edge states of H-terminated graphitic ribbons, Phys. Rev. B **59**, 9858 (1999) 681, 682
[45] T. Kawai, Y. Miyamoto, O. Sugino, Y. Koga: Graphitic ribbons without hydrogen-termination: Electronic structures and stabilities, Phys. Rev. B **62**, R16349 (2000) 681, 682
[46] S. Okada, A. Oshiyama: Magnetic ordering in hexagonally bonded sheets with first-row elements, Phys. Rev. Lett. **87**, 146803 (2001) 681, 682, 683
[47] H. Lee, Y.-W. Sun, N. Park, S. Han, J. Yu: Magnetic ordering at the edges of graphitic fragments: Magnetic tail interactions between the edge-localized states, Phys. Rev. B **72**, 174431 (2005) 681, 682, 683
[48] M. Ezawa: Peculiar width dependence of the electronic properties of carbon nanoribbons, Phys. Rev. B **73**, 045432 (2006) 681, 682
[49] L. Brey, H. A. Fertig: Electronic states of graphene nanoribbons studied with the Dirac equation, Phys. Rev. B **73**, 235411 (2006) 681, 682
[50] K.-I. Sasaki, S. Murakami, R. Saito: J. Phys. Soc. Jpn. **75**, 074713 (2006) 681, 682
[51] D. A. Abanin, P. A. Lee, L. S. Levitov: Spin-filtered edge states and quantum Hall effect in graphene, Phys. Rev. Lett. **96**, 176803 (2006) 681, 682
[52] Y.-W. Son, M. L. Cohen, S. G. Louie: Energy gaps in graphene nanoribbons, Phys. Rev. Lett. **97**, 216803 (2006) 681, 682, 683
[53] Y.-W. Son, M. L. Cohen, S. G. Louie: Erratum: Energy gaps in graphene nanoribbons, Phys. Rev. Lett. **98**, 089901 (2007) 681, 682, 683
[54] Y.-W. Son, M. L. Cohen, S. G. Louie: Half-metallic graphene nanoribbons, Nature **444**, 347 (2006) 681, 682, 683

[55] Y. Kobayashi, K. Fukui, T. Enoki, K. Kusakabe, Y. Kaburagi: Observation of zigzag and armchair edges of graphite using scanning tunneling microscopy and spectroscopy, Phys. Rev. B **71**, 193406 (2005) 682
[56] C. L. Kane, E. J. Mele: Z(2) topological order and the quantum spin Hall effect, Phys. Rev. Lett. **95**, 146802 (2005) 683
[57] D. Prezzi, D. Varasano, A. Ruini, E. Molinari: Optical properties of graphene nanoribbons: The role of many-body effects, arXiv:0706.0916 (2007) 683
[58] M. Y. Han, B. Özyilmaz, Y. Zhang, P. Kim: Energy band-gap engineering of graphene nanoribbons, Phys. Rev. Lett. **98**, 206805 (2007) 683
[59] Z. Chen, Y.-M. Lin, M. J. Rooks, P. Avouris: Graphene nano-ribbon electronics, arXiv URL: `cond-mat/0701599` 683
[60] F. Cervantes-Sodi, G. Csanyi, S. Piscanec, A. C. Ferrari: Edge functionalised and substitutional doped graphene nanoribbons: electronic and spin properties, Cond Mat 0711.2340 (2007) 683
[61] G. Dresselhaus, M. S. Dresselhaus: Spin-orbit interaction in graphite, Phys. Rev. **140**, 401 (1965) 683
[62] J.-C. Charlier, X. Gonze, J.-P. Michenaud: First-principles study of the electronic properties of graphite, Phys. Rev. B **43**, 4579 (1991) 684
[63] J.-C. Charlier, X. Gonze, J.-P. Michenaud: First-principles study of the electronic properties of simple hexagonal graphite, Phys. Rev. B **46**, 4531 (1992) 684
[64] J.-C. Charlier, X. Gonze, J.-P. Michenaud: First-principles study of the stacking effect on the electronic properties of graphite(s), Carbon **32**, 289–299 (1994) 684
[65] J.-C. Charlier, X. Gonze, J.-P. Michenaud: Graphite interplanar bonding: electronic delocalization and van der Waals interaction, Europhys. Lett. **28**, 403–408 (1994) 684
[66] S. Latil, L. Henrard: Charge carriers in few-layer graphene films, Phys. Rev. Lett. **97**, 036803 (2006) 684
[67] F. Guinea, A. H. Castro-Neto, N. M. R. Peres: Electronic states and Landau levels in graphene stacks, Phys. Rev. B **73**, 245426 (2006) 684
[68] J.-C. Charlier, J.-P. Michenaud, P. Lambin: Tight-binding density of electronic states of pregraphitic carbon, Phys. Rev. B **46**, 4540 (1992) 684
[69] E. McCann, V. I. Fal'ko: Landau-level degeneracy and quantum Hall effect in a graphite bilayer, Phys. Rev. Lett. **96**, 086805 (2006) 684, 685
[70] E. V. Castro, K. S. Novoselov, S. V. Morozov, N. M. R. Peres, J. M. B. L. dos Santos, J. Nilsson, F. Guinea, A. K. Geim, A. H. Castro-Neto: Biased bilayer graphene: Semiconductor with a gap tunable by electric field effect, arXiv URL: `cond-mat/0611342` 685
[71] C. Casiraghi, A. Hartschuh, E. Lidorikis, H. Qian, H. Harutyunyan, T. Gokus, K. S. Novoselov, A. C. Ferrari: Rayleigh imaging of graphene and graphene layers, Nano Lett. **7**, 2711 (2007) 686
[72] A. C. Ferrari, J. C. Meyer, V. Scardaci, C. Casiraghi, M. Lazzeri, F. Mauri, S. Piscanec, D. Jiang, K. S. Novoselov, S. Roth, A. K. Geim: Raman spectrum of graphene and graphene layers, Phys. Rev. **97**, 187401 (2006) 686, 690, 691, 692, 693, 694, 696
[73] A. C. Ferrari, J. Robertson: Raman spectroscopy in carbons: From nanotubes to diamond, Philos. Trans. Roy. Soc. A **362**, 2267–2565 (2004) 687

[74] C. Castiglioni, F. Negri, M. Rigolio, G. Zerbi: Raman activation in disordered graphites of the $A_1^{'}$ symmetry forbidden k $\neq$ 0 phonon: The origin of the D line, J. Chem. Phys. **115**, 3769 (2001) 687
[75] C. Castiglioni, M. Tommasini, G. Zerbi: Raman spectroscopy of polyconjugated molecules and materials: Confinement effect in one and two dimensions, Philos. Trans. R. Soc. Lond. A **362**, 2425 (2004) 687
[76] F. Tuinstra, J. Koenig.: Raman spectrum of graphite, J. Chem. Phys. **53**, 1126 (1970) 687, 688, 693
[77] A. C. Ferrari, J. Robertson: Interpretation of Raman spectra of disordered and amorphous carbon, Phys. Rev. B **61**, 14095 (2000) 687, 688, 693
[78] R. J. Nemanich, S. A. Solin: First- and second-order Raman scattering from finite-size crystals of graphite, Phys. Rev. B **20**, 392 (1979) 687, 690
[79] R. Al-Jishi, G. Dresselhaus: Lattice-dynamical model for graphite, Phys. Rev. B, **26**, 4514 (1982) 687
[80] R. P. Vidano, D. B. Fishbach, L. J. Willis, T. M. Loehr: Observation of Raman band shifting with excitation wavelength for carbons and graphites, Solid State Commun. **39**, 341 (1981) 687, 690
[81] I. Pocsik, M. Hundhausen, M. Koos, L. Ley: DC electrical properties of amorphous carbon with different bonding hybridization, J. Non-Cryst. Solids **227–230**, 1087 (1998) 687, 688
[82] P. Lespade, A. Marchard, M. Couzi, F. Cruege: Caracterisation de materiaux carbones par microspectrometrie Raman, Carbon **22**, 375 (1984) 687
[83] C. Thomsen, S. Reich: Double resonant Raman scattering in graphite, Phys. Rev. Lett. **85**, 5214 (2000) 687, 688, 691
[84] A. V. Baranov, A. N. Bekhterev, Y. S. Bobovich, V. I. Petrov: Interpretation of some peculiarities in Raman spectra of graphite and glassy carbon, Opt. Spektrosk. **62**, 1036 (1987) 687
[85] J. Maultzsch, S. Reich, C. Thomsen, H. Requardt: Phonon dispersion in graphite, P. Ordejón. Phys. Rev. Lett. **92**, 075501 (2004) 688
[86] M. J. Matthews, M. A. Pimenta, G. Dresselhaus, M. S. Dresselhaus, M. Endo: Origin of dispersive effects of the Raman D band in carbon materials, Phys. Rev. B **59**, 6585 (1999) 687, 688
[87] A. Gruneis, R. Saito, T. Kimura, L. G. Cançado, M. A. Pimenta, A. Jorio, A. G. S. Filho, G. Dresselhaus, M. S. Dresselhaus: Determination of two-dimensional phonon dispersion relation of graphite by Raman spectroscopy, Phys. Rev. B **65**, 155405 (2002) 687, 688
[88] R. Saito, A. Jorio, A. G. S. Filho, G. Dresselhaus, M. S. Dresselhaus, M. A. Pimenta: Probing phonon dispersion relations of graphite by double resonance Raman scattering, Phys. Rev. Lett. **88**, 027401 (2002) 687, 688
[89] A. C. Ferrari, J. Robertson.: Resonant Raman spectroscopy of disordered, amorphous, and diamondlike carbon, Phys. Rev. B, **64**, 075414 (2001) 687, 688, 691
[90] C. Mapelli, C. Castiglioni, G. Zerbi, K. Mullen: Common force field for graphite and polycyclic aromatic hydrocarbons, Phys. Rev. B **60**, 12710 (1999) 688
[91] G. Kresse, J. Furthmuller, J. Hafner: Ab initio force constant approach to phonon dispersion relations of diamond and graphite, Europhys. Lett. **32**, 729 (1995) 688

[92] P. Pavone, R. Bauer, K. Karch, O. Schütt, S. Vent, W. Windl, D. Strauch, S. Baroni, S. de Gironcoli: Ab initio phonon calculations in solids, Physica B, **219–220**, 439 (1996) 688
[93] L. Wirtz, A. Rubio: The phonon dispersion of graphite revisited, Solid. State Commun. **131**, 141 (2004) 688
[94] O. Dubay, G. Kresse: Accurate density functional calculations for the phonon dispersion relations of graphite layer and carbon nanotubes, Phys. Rev. B **67**, 035401 (2003) 688
[95] W. Kohn: Image of the Fermi surface in the vibration spectrum of a metal, Phys. Rev. Lett. **2**, 393 (1959) 688
[96] A. Javey, J. Guo, M. Paulsson, Q. Wang, D. Mann, M. Lundstrom, H. Dai: High-field quasiballistic transport in short carbon nanotubes, Phys. Rev. Lett. **92**, 106804 (2004) 689
[97] J. Y. Park, S. Rosenblatt, Y. Yaish, V. Sazonova, H. Ustunel, S. Braig, T. A. Arias, P. W. Brouwer, P. L. McEuen: Electron–phonon scattering in metallic single-walled carbon nanotubes, Nano Lett. **4**, 517 (2004) 689
[98] V. Perebeinos, J. Tersoff, P. Avouris: Electron–phonon interaction and transport in semiconducting carbon nanotubes, Phys. Rev. Lett. **94**, 086802 (2005) 689
[99] Z. Yao, C. L. Kane, C. Dekker: High-field electrical transport in single-wall carbon nanotubes, Phys. Rev. Lett. **84**, 2941 (2000) 689
[100] J. Jiang, R. Saito, A. Gruneis, G. Dresselhaus, M. S. Dresselhaus: Electron–phonon interaction and relaxation time in graphite, Chem. Phys. Lett. **392**, 383 (2004) 689
[101] J. Jiang, R. Saito, A. Grüneis, S. G. Chou, G. G. Samsonidze, A. Jorio, G. Dresselhaus, M. S. Dresselhaus: Photoexcited electron relaxation processes in single-wall carbon nanotubes, Phys. Rev. B **71**, 045417 (2005) 689
[102] G. Pennington, N. Goldsman: Semiclassical transport and phonon scattering of electrons in semiconducting carbon nanotubes, Phys. Rev. B **68**, 045426 (2004) 689
[103] G. D. Mahan: Electron–optical phonon interaction in carbon nanotubes, Phys. Rev. B **68**, 125409 (2003) 689
[104] P. H. Tan, C. Y. Hu, J. Dong, W. C. Shen, B. F. Zhang: Polarization properties, high-order Raman spectra, and frequency asymmetry between Stokes and anti-Stokes scattering of Raman modes in a graphite whisker, Phys. Rev B **64**, 214301 (2000) 690
[105] V. Scardaci, P. H. Tan, A. C. Ferrari, et al.: unpublished 690
[106] M. Lazzeri, F. Mauri: Nonadiabatic Kohn anomaly in a doped graphene monolayer, Phys. Rev. Lett. **97**, 266407 (2006) 690, 695, 696, 698
[107] A. Gupta, P. C. Eklund: unpublished 691
[108] Y. Wang, D. C. Aolsmeyer, R. L. McCreery: Raman spectroscopy of carbon materials: Structural basis of observed spectra, Chem. Mater. **2**, 557 (1990) 691
[109] A. Gupta, P. C. Eklund: unpublished 691
[110] P. H. Tan, C. Casiraghi, A. C. Ferrari: unpublished 693
[111] J. Yan, Y. Zhang, P. Kim, A. Pinczuk: Electric field effect tuning of electron–phonon coupling in graphene, Phys. Rev. Lett. **98**, 166802 (2007) 694, 695
[112] T. Ando: Anomaly of optical phonon in monolayer graphene, J. Phys. Soc. Jpn. **75**, 124701 (2006) 695

[113] A. H. Castro-Neto, F. Guinea.: Electron–phonon coupling and Raman spectroscopy in graphene, Phys. Rev. B **75**, 045404 (2007) 695
[114] G. Moos, C. Gahl, R. Fasel, M. Wolf, T. Hertel: Anisotropy of quasiparticle lifetimes and the role of disorder in graphite from ultrafast time-resolved photoemission spectroscopy, Phys. Rev. Lett. **87**, 267402 (2001) 696
[115] T. Kampfrath, L. Perfetti, F. Schapper, C. Frischkorn, M. Wolf: Strongly coupled optical phonons in the ultrafast dynamics of the electronic energy and current relaxation in graphite, Phys. Rev. Lett. **95**, 187403 (2005) 696
[116] A. Gupta, G. Chen, P. Joshi, S. Tadigadapa, P. C. Eklund: Raman scattering from high-frequency phonons in supported n-graphene layer films, Nano Lett. **6**, 2667 (2006) 696
[117] D. Graf, F. Molitor, K. Ensslin, C. Stampfer, A. Jungen, C. Hierold, L. Wirtz: Spatially resolved Raman spectroscopy of single- and few-layer graphene, Nano Lett. **7**, 238 (2007) 696
[118] C. Casiraghi, S. Pisana, K. S. Novoselov, A. K. Geim, A. C. Ferrari: Raman fingerprint of charged impurities in graphene, Cond-Mat 0709.2566 (2007) 697
[119] C. Casiraghi, S. Pisana, K. S. Novoselov, A. K. Geim, A. C. Ferrari: Raman fingerprint of charged impurities in graphene, Appl. Phys. Lett. in press. 697
[120] A. Das, S. Pisana, S. Piscanec, B. Chakraborty, S. K. Saha, U. V. Waghmare, R. Yiang, H. R. Krishnamurhthy, A. K. Geim, A. C. Ferrari, A. K. Sood: Electrochemically gated graphene: Monitoring dopants by Raman scattering, cond mat 0709.1174 (2007) 697
[121] V. Zolyomi, J. Kurti: First-principles calculations for the electronic band structures of small diameter single-wall carbon nanotubes, Phys. Rev. B, **70**, 085403 (2004) 697
[122] D. Connétable, D., G.-M. Rignanese, J.-C. Charlier, X. Blase: Room temperature Peierls distortion in small diameter nanotubes, Phys. Rev. Lett. **94**, 015503 (2005) 697
[123] A. Jorio, R. Saito, M. S. Dresselhaus, G. Dressselhaus: One contribution of 13 to a theme 'Raman spectroscopy in carbons: from nanotubes to diamond', Trans. Roy. Soc. A **362**, 2311 (2004) 699
[124] S. D. M. Brown, A. Jorio, P. Corio, M. S. Dresselhaus, G. Dresselhaus, R. Saito, K. Kneipp: Origin of the Breit–Wigner–Fano lineshape of the tangential g-band feature of metallic carbon nanotubes, Phys. Rev. B **63**, 155414 (2001) 699
[125] K. Kempa: Gapless plasmons in carbon nanotubes and their interactions with phonons, Phys. Rev. B **66**, 195406 (2002) 699
[126] U. Fano: Effects of configuration interaction on intensities and phase shifts, Phys. Rev. **124**, 1866 (1961) 700, 701

Index

Potential Applications of Carbon Nanotubes

Morinobu Endo[1], Michael S. Strano[2], and Pulickel M. Ajayan[3]

[1] Department of Electrical and Electronic Engineering, Shinshu University, 4-17-1 Wakasato, Nagano-shi 380-8553, Japan
endo@endomorinobu.shinshu.ac.jp
[2] Department of Chemical Engineering, Massachusetts Institute of Technology, Cambridge, MA 02139-4301, USA
strano@mit.edu
[3] Department of Materials Science and Engineering, Rensselaer Polytechnic Institute, Troy, New York 12180-3590, USA
ajayan@rpi.edu

Abstract. This review explores the state-of-the-art applications of various kinds of carbon nanotubes. We will address the uniqueness of nanotubes that makes them better than their competitors for specific applications. We will discuss several examples of the already existing commercial uses of nanotubes and then point out feasible nanotube applications for the near term (within ten years) and the long term (beyond ten years). In our discussions of the applications, we will distinguish between the various kinds of nanotubes in play today, ranging from multiwall nanotubes having different degrees of perfection to the near-perfect molecular single-wall nanotubes. The last decade of research in this field points to several possible applications for these materials; electronic devices and interconnects, field emission devices, electrochemical devices, such as supercapacitors and batteries, nanoscale sensors, electromechanical actuators, separation membranes, filled polymer composites, and drug-delivery systems are some of the possible applications that have been demonstrated in the laboratories. We further discuss the status of this field and point out the value-added applications that exist today versus the revolutionary applications that will ensue in the distant future. The opportunities, challenges and the major bottlenecks, including large-scale manufacturing for nanotube material, will be identified as we define the applications space for nanotubes. We will also consider some of the recent concerns regarding health, environment as well as handling and safety protocols for carbon nanotubes.

1 Introduction

The combination of structure, topology, and dimensions creates a host of physical properties in carbon nanotubes that are unparalleled by most known materials. After a decade and a half of research efforts, these tiny quasi-one-dimensional structures show great promise for a variety of applications areas, such as nanoprobes, molecular reinforcements in composites, displays, sensors, energy-storage media, and molecular electronic devices [1–3]. There have been great improvements in synthesis and purification techniques, which can now produce good-quality nanotubes in large quantities. There is a vast and enticing database from theoretical calculations and experiments that

A. Jorio, G. Dresselhaus, M. S. Dresselhaus (Eds.): Carbon Nanotubes,
Topics Appl. Physics **111**, 13–62 (2008)

predicts several unique opportunities for nanotube applications based on their properties. At this juncture, when one looks at the applications landscape for nanotubes and nanotube-based products, it seems appropriate to divide this landscape into three categories based on timelines: present applications that are already in the marketplace, near-term applications that will succeed in the marketplace in the next ten years, and long-term applications beyond the ten-year horizon. In the next several sections of this review we will deal with various applications where nanotubes have shown promise, within the perspective of this timeline. The summary at the end of this review (see Sect. 3) captures the big picture of carbon-nanotube applications. At the outset we would like to state that beyond these clearly visible practical uses there have been tremendous advances in the understanding of the physics and chemistry of carbon systems and this material has acted as a front runner for the whole field of nanotechnology, attracting much attention from the academic community and industry alike.

In some sense, carbon nanotubes came following the footsteps of what was a unique discovery in carbon science, the C_{60} fullerene molecule [4]. Although the fullerenes could stimulate and motivate the large scientific community, their applications remain at large to date. On the other hand, graphite and carbon fibers [5], the larger analogs of nanotubes, have been commercially used for decades. Their applications range from use as conductive fillers and mechanical structural reinforcements in composites (e.g., in the aerospace industry) to electrode materials (e.g., in batteries) (see Table 1). Although the primary bonding in graphite, carbon fibers and nanotubes is the same (the sp^2-hybridized, hexagonal honeycomb lattice); nanotubes are distinguished from the other carbon forms by their unique morphology, dimensions and defects. Carbon nanotubes approach the theoretical inplane properties of graphite, which, based on the defect-free carbon–carbon bond, provide the strongest bonding in nature. The exceptionally high modulus, electrical and thermal conductivity and elasticity of planar graphite are all reflected in the inherent properties of nanotubes, and several of the other contributions in this book have been devoted to describing these. The issues we want to discuss in this review are different; after a few decades of research and development of the nanotube material (starting from early reports by *Endo* and coworkers [6]), where do we now stand in terms of applications and what are the real commercial prospects for this material? What are the real challenges that still impede progress towards applications for nanotubes? Will the promises of the early days of nanotube reporting hold out and will nanotubes actually emerge as the leading material in the nanotechnology revolution that we foresee?

To discuss the above issues, it is imperative that we identify what we call nanotubes today with some discrimination. There are essentially two categories of nanotubes that are prevalently used today [7]. The multiwall carbon nanotubes (MWNTs), which have shown the most promising appearance to the marketplace in recent times, date back to early reports of Endo in the late

Table 1. Some of the main applications of traditional graphite-based materials including carbon fibers

Traditional graphite material	Commercial applications
Graphite and graphite-based products	Materials-processing applications such as furnaces/crucibles, large electrodes in metallurgical processes, electrical and electronic devices such as electric brushes, membrane switches, variable resistors, etc., electrochemical applications for electrode materials in primary and secondary cells, separators for fuel cells, nuclear fission reactors, bearings and seals (mechanical) and dispersions such as inks. (Estimated market: 13 billions USD)
Carbon-fiber-based products	Carbon-fiber composites (Total market: $\sim$ 1 billion USD: Aerospace (70 %), sporting goods (18 %), industrial equipment (7 %), marine (2 %), miscellaneous (3 %))
Carbon–carbon composites	High-temperature structural materials, Aerospace applications such as missile nose tips, re-entry heat shields, etc., Brake-disc applications (lightweight, thermal conductivity, stability), Rotating shafts, pistons, bearings (low coefficient of friction), Biomedical implants such as bone plates (biocompatibility) (Estimated market: 202 million USD).

1970s. These were catalytically grown (by chemical vapor deposition; CVD) multilayer graphitic tubular structures that could be further annealed to decrease their defect density. The dimensions of these were typically several tens of nanometers in diameter, but occasionally smaller structures including single-layer tubular structures were also observed. In the early 1990s, *Iijima* and others [8, 9] showed that the high-temperature arc-discharge process could produce smaller, highly graphitized multiwall structures. Then came the discovery of single-wall nanotubes (SWNTs) [10, 11] in 1993 by the NEC and IBM groups that suggested that catalytic vapor deposition can be controlled to make single-layer tubular structures of graphene with diameters as small as 1 nm. The ability to grow such small defect-free graphene tubes prompted people to suggest various applications for these structures, including that of electronic devices; features such as chirality, defect-free structure and small dimensions showed possibilities of their use as quantum wires.

Carbon-based fibrillar structures at that point crossed over from the traditional graphite-like material to molecular structures with an applications domain expanding into nontraditional areas like nanoelectronics. Today, we are able to make nanotubes with a precisely tuned number of layers, such as SWNTs and double-wall nanotubes (DWNTs) and a lot of progress has occurred in the scalable synthesis of this material. It is also possible these days to synthesize in large quantitites carbon nanotubes that are uniformly doped with elements such as nitrogen and these hold promise for specific applications (see the contribution by *Terrones* et al.). When the applications of nanotubes are considered, they divide between the traditional (where nanotubes provide value addition compared to carbon fibers and other carbons) and nontraditional (where nanotube applications provide unique applications) uses, often delineating the timeline expected for applications.

2 Applications of Carbon Nanotubes

The last couple of decades of work in fullerenes and nanotubes promised an amazing range of applications for these materials [1–3]. However, these new concepts and ideas for applications of carbon nanomaterials have had a limited success in the marketplace, mainly due to issues in processing, scaleup and more importantly due to the inability to properly assess the time frame that is needed to take new products to market, in particular if these products result in disruptive technologies. Many of the applications of fullerenes and nanotubes conform to this class, be it drug delivery using fullerenes or nanoelectronics using nanotubes. In addition, there are intrinsic challenges at the nanoscale (assembly, role of interfaces, contacts, etc.) which have also slowed the pace of progress in the applications of these new materials.

At the same time, there are a few applications of nanotubes that are indeed commercialized today. The best examples of present bulk applications of CNTs are the use of CVD-grown large multiwall nanotubes in lithium-ion batteries and in plastics for electrostatic discharge applications. Both of these applications do not utilize the spectacular mechanical or electronic properties of perfect nanotubes, but function as additives that add value to the products (mechanical stabilizing in batteries and dissipation of static electric charges in plastics). These applications cater to large volumes of nanotubes and the need has driven large-scale manufacturing of this material in the last few years. Today, the bulk volumes of manufactured MWNTs reach a few hundred tons per year. The situation of SWNTs is different with the volume of material produced per year not exceeding a few kilos. There are some indications that suggest that there could be a quantum leap in the production of SWNTs in the next few years but the drive towards this will depend on demand for this material in specific areas of applications. One potential application for SWNTs that would require large quantities of material is the field emission display, which has been widely talked about as the first major application of

SWNTs; and prototypes have been demonstrated by large companies such as Samsung and Motorola. However, the product has not been commercialized yet, for reasons that are unknown.

This section in this chapter will deal with important application areas of both MWNTs and SWNTs. The major applications that arise from the intrinsic advantage of nanotubes will be considered in the broad areas of electronics, energy, composites, sensors, field emission, biology and other miscellaneous fields. In each of these distinct areas, the prospects of nanotubes will be described based on their known attributes, demonstrated abilities and state-of-the-art efforts that have been invested in these materials. The main theme of this chapter will be described in these subsections, pointing out whether the applications are imminent or long term. We hope that the readers gain a better understanding of carbon nanotube applications, including current challenges and potential uses in future technologies. In the final sections, some of the health and environmental effects of nanotubes will be considered. There has been a lot of scrutiny in recent times on the adverse effects of nanotubes (and nanomaterials in general) to health. Although the issue still needs systematic and long-term evaluation to properly understand the effects, it is worth pointing out what the thinking is on this issue at the present time. In the concluding section, we will make a conscious effort to list nanotube applications from two separate points of view; bulk vs. limited-volume applications and short-term versus long-term applications. These will act as a guide for readers to follow the application pathways for nanotubes in the years to come. The success of these possibilities will depend on whether some of the technical challenges described in this and other reviews elsewhere in the book can be addressed and solved within realistic time frames.

2.1 Carbon Nanotubes in Electronics

It should be pointed out that the integration of nanotubes into electronic devices still is a long-term application with the prospect of commercial products beyond the ten-year time frame. However, nanotubes (in particular, SWNTs) have emerged as a promising class of electronic materials due to their nanoscale dimensions and outstanding properties, such as ballistic electronic conduction [12, 13] and insensitivity to electromigration [14, 15]. Both metallic and semiconducting SWNTs are found to possess electrical characteristics that compare favorably with the best electronic materials presently available. The recent advances in the separation [16, 17] of SWNTs with different electronic properties has enabled the nanotube community to develop the field-effect transistors (FET) and interconnects on a large scale (Fig. 1).

In hot pursuit of Moore's law, semiconductor giants like Intel, IBM, AMD, UMC and TSMC are commercially manufacturing silicon-based transistors at the 65-nm technology node (Q1, 2007). Intel intends to commercialize transistors at the 45-nm technology node by the end of 2007 or early 2008 [19]. By an evolutionary process, a conservative estimate for the smallest conceivable

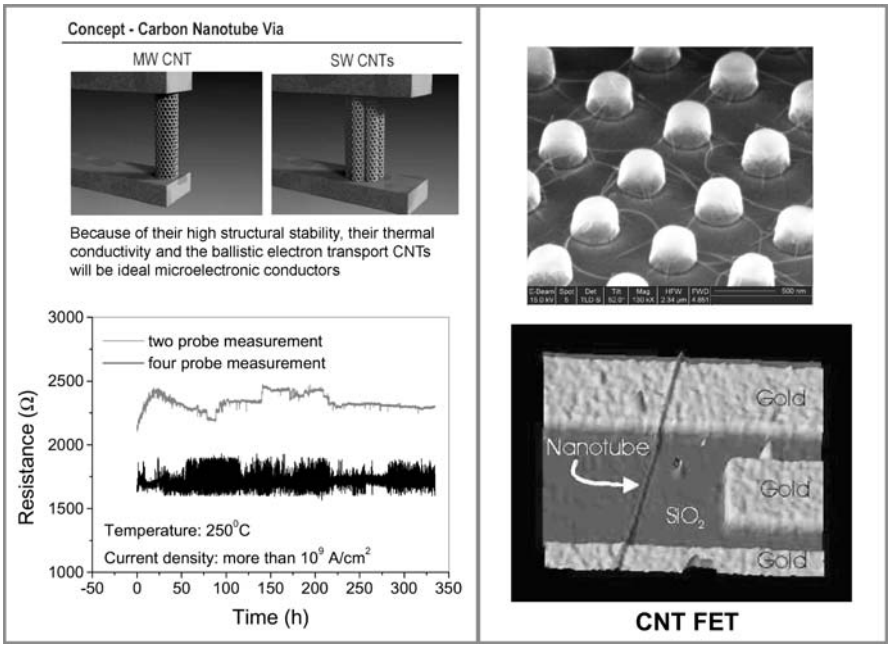

Fig. 1. *Left Panel: Top schematic* shows the possibility of using carbon nanotubes (both MWNT and SWNT bundles) as via interconnects (Courtesy of Georg Duesberg at Infineon Corporation). The problems that copper faces, such as electromigration may be overcome by using nanotubes in the vertical configuration. *Bottom figure* presents an experimental test showing electromigration studies of a single multiwall nanotube contacted by two probes [18]. The current-carrying capacity of nanotubes is exceptionally high. *Right Panel:* The *top image* shows the possibility of growing horizontal networks of single-wall nanotubes on silicon surfaces by CVD and the *bottom panel* shows a FET device that can be constructed from such a SWNT after properly contacting them with metal in a three-terminal configuration (*bottom image,* courtesy of Phaedon Avouris of the IBM Corporation)

silicon transistor at this point is 16 nm, expected to hit markets not prior to 2018. A revolutionary speedup of this process can be realistically envisioned only if nanotechnology can be controlled on a large scale. Single-wall carbon nanotubes, with a diameter of $\sim$ 1 nm, have been demonstrated to operate as field-effect transistors almost a decade ago, and since then, the FETs have steadily grown in versatility and promise for future nanometer-scale electronics.

The earliest works on room-temperature carbon-nanotube transistors were done simultaneously by the Delft [20] and the IBM groups [21]. They demonstrated that semiconducting single-wall nanotubes have a channel conductance that can be modified by orders of magnitude ($\sim 10^5$) by an exter-

nally applied gate voltage, very similar to that of a MOSFET. These tube-FETs or CNT-FETs were generally p-type, and the charge transport was modulated by the modification of the Schottky barrier height at the electrical contact between the nanotube and the metal electrodes upon application of a gate voltage. Since then, a number of groups have made progressive improvements in building n-type as well as ambipolar CNT-FETs. By 2001, further important progress was made in the integration of nanotubes from simple transistors to logic circuits. One-, two-, and three-transistor circuits that exhibit a range of digital logic operations, were demonstrated such as an inverter, a logic NOR, a static random-access memory cell, and an ac ring oscillator [22]. The IBM team developed a technique to produce arrays of carbon-nanotube transistors, bypassing the need to meticulously separate metallic and semiconducting nanotubes [23]. The next half a decade saw a flurry of technological advances that demonstrated the usefulness of CNT-FETs in diverse ways. CNT power transistors were demonstrated to have 20 times less switching resistance and 200 times more current-handling capability than conventional power MOSFETs. A University of Maryland team has recently demonstrated that CNTs can have enormous carrier mobility ($\sim 10^5\,\mathrm{cm}^2/\mathrm{Vs}$) [23]. Other researchers were able to push the feasibility of using nanotube FETs at the GHz and THz frequency range. Other innovations like using nanotube Y-junctions to form switches [24], and chemical functionalization to modify nanotube conductance have given more flexibility in design consideration for the final chip-making process.

In addition to transistors, nanotubes can also function as interconnects due to their metallic characteristics. As interconnect feature sizes shrink, copper resistivity increases due to surface and grain-boundary scatterings and also due to surface roughness [25]. In contrast, carbon nanotubes exhibit a ballistic flow of electrons with electron mean-free paths of several micrometers, and are capable of conducting very large current densities [26]. Carbon nanotubes have been shown to withstand current densities up to $10^{10}\,\mathrm{A/cm}^2$, exceeding copper by a factor of 1000. A bundle of closely packed parallel metallic carbon nanotubes, or a large defect-free MWNT are proposed to be used for the next generation of interconnects. A bundle of 400 SWNTs can be as narrow as 20 nm in diameter since making a bundle and connecting the tubes in parallel serves two main purposes. Firstly, connecting in parallel helps in overcoming the problem of the high value of the contact resistance of a single nanotube and secondly bundles ensure a lower capacitance comparable to that of a single nanotube, as opposed to the high value for a monolayer of nanotubes [27]. Moreover, with respect to resistance, nanotubes are favorable in high aspect ratio structures like vias, where also the highest current densities are expected [27]. In addition to the onchip (short as well as via) interconnects, due to the mechanical flexibility and compliance of nanotube bundles, they are also being considered for back-end (die to package, in packaging) flexible interconnects and these may be realized in a time frame faster than the integration of onchip nanotube-based structures. The intrinsic elec-

tromechanical properties of nanotubes can also be useful in the creation of probe arrays that have several uses in the microelectronics industry.

As indicated before, many groups have now successfully made FETs with semiconducting carbon nanotubes as the channel in their transistors [28, 29]. Semiconducting carbon-nanotube FETs have successfully shown an ON to OFF ratio of conductance, $G_{\mathrm{ON}}/G_{\mathrm{OFF}} \sim 10^5$ [30]. Moreover, thin films of high-dielectric materials, such as ZrO_2 and HfO_2 ($\kappa \sim 15$–25), are highly desirable for gate dielectric integration in field-effect transistors as they enable high ON-state current densities (speed) and low operating power consumptions. The integration of high-κ dielectrics, however, has been a challenge in planar MOSFETs because of the inherent mobility degradation of the Si channels. A unique advantage of carbon nanotubes is their compatibility with high-κ dielectrics. The lack of dangling bonds at the nanotube/high-κ interface and the weak noncovalent bonding interactions between the two materials prevent any perturbation to the electron transport in nanotubes.

Another important achievement is the development of an electromechanical memory device by Nanterro Inc., a startup company focused on bringing on the first major electronic application of nanotubes. Owing to their mechanical resilience and electrical conductivity, CNTs (carbon nanotubes) can perform as sensitive nanoelectromechanical devices such as nonvolatile memory. Using a crossbar layered architecture, Nanterro is developing a bistable memory device that can be actuated electrostatically [31]. Since direct growth of such structures is challenging, the structure is made from thin membranes that are suspended above prefabricated electrodes and it seems that these devices can be operated at low voltages for millions of cycles at high switching speed. This device, which is being codeveloped by LSI Logic, is poised to enter the market in the next few years.

Invisible circuits based on transparent transistors have found broad potential applications in consumer, military, and industrial electronic systems. The quest for flexible and transparent transistors made from SWNTs has resulted in several noteworthy achievements [31]. SWNTs have recently been used to make all of the conducting (i.e., source, drain, and gate electrodes) and semiconducting layers, respectively, of a transparent, mechanically flexible, thin-film transistor (TFT) [32]. These devices are fabricated on plastic substrates using layer-by-layer transfer printing of SWNT networks grown using optimized chemical vapor deposition (CVD) procedures. The unique properties of the SWNT networks lead to electrical (good performance on plastic), optical (transparent at visible wavelengths), and mechanical (extremely bendable) characteristics in these TFTs that would be difficult, or impossible, to achieve with conventional materials. Similar work [33] has shown integration of transparent SWNT electrodes with organic semiconductors to form flexible TTFTs (transparent thin-film transistors) on plastic substrates. These devices have shown good electrical properties including negligible contact resistances, mobilities larger than $0.5\,\mathrm{cm^2V^{-1}s^{-1}}$, mechanical flexibility (radii of curvature $< 5\,\mathrm{mm}$) and optical transparency (70 %). In addition,

there have also been successful attempts at manufacturing ultrathin, transparent, optically homogeneous, electrically conducting films of pure SWNTs and DWNTs and transferring those films to various substrates [34]. These films exhibit conductivity and transparency performances equivalent to the commercially used transparent conductor indium tin oxide (ITO) but have better transparency in the important infrared bandwidth range. One day, the transparent nanotube films could replace ITO, at least in applications such as displays and touch screens and even LEDs at a later stage. The challenge here is to get relatively high transparency ($> 90\,\%$) simultaneously with high conductance.

Some of the existing and near-term electrical applications of nanotubes are in areas where the high aspect ratio, and high electrical conductivity of nanotubes with good dispersion (at a few wt % loadings) in polymer matrices enables excellent electrical percolation leading to electrostatic discharge (ESD) and electrical-shielding applications [35]. For ESD applications, the nanotubes prevent charge buildup on the surface of the insulating plastic. Today, large (tonnage) quantities of multiwall nanotubes and nanofibrils are manufactured by the company Hyperion Catalysis International and supplied as premixed material in thermoplastics to the General Electric (GE) company for use in their engineering plastics that are employed in automobile body parts. This remains as one of the biggest bulk application of nanotubes today. The first commercial applications for MWNTs make use of their properties to address electrostatic discharge. The applications also include high-end microelectronics products where static electric discharge from packaging components can destroy electronic chip components. In addition to the ESD application, electromagnetic interference (EMI) shielding applications have also been pursued [5] for nanotubes at high loadings, utilizing the extremely high conductivity of nanotubes. Carbon fibers have been used in this area and unless nanotubes offer significant advantages compared to the traditional fillers, it is not clear if nanotube-based plastics would outperform conventional materials in EMI shielding.

Another area where nanotubes could bring in change (in the 5–10 year time frame) is in the area of onchip thermal management. High power consumption and the corresponding problem of heat dissipation is one of the biggest issues in high-performance microprocessors today. There have been several reports pointing out the record axial thermal conductivity of individual nanotubes. It has been recently shown by several groups that efficient cooling can be achieved on silicon chips using aligned carbon nanotube arrays (MWNTs) [36]. Tiny cooling elements can be fabricated and mounted on chips to enable significantly enhanced power dissipation from the heated chips and hot spots (Fig. 2). The cooling performance observed for nanotube structures makes them viable candidates for onchip thermal management. The issue here is that of thermal interfaces where scattering leads to dissipation of thermal energy. For efficient application, the thermal contact resistance needs to be decreased. The high thermal anisotropy of nanotube

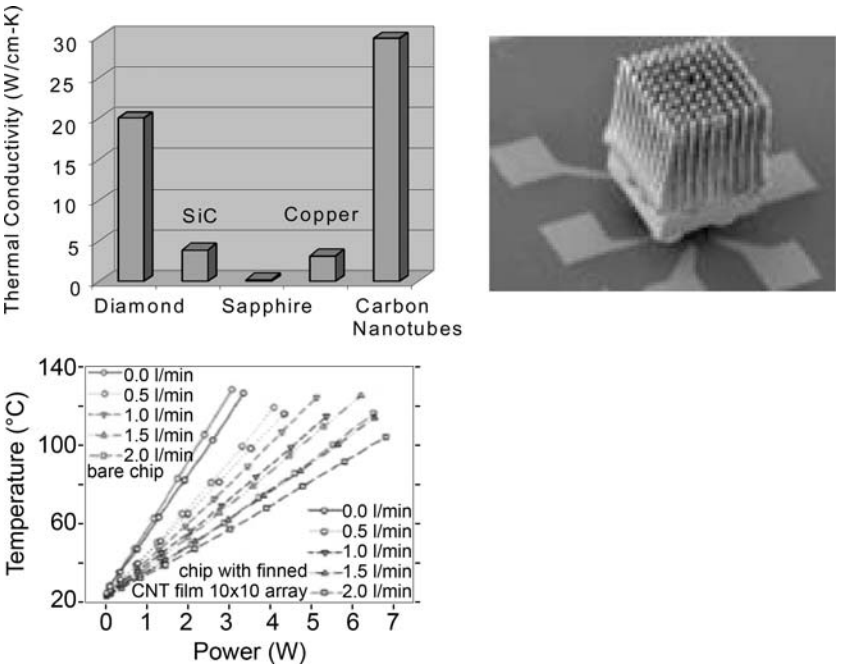

Fig. 2. *Clockwise from top left:* Plot shows the comparison of the thermal conductivity of nanotubes with the best (thermally conducting) materials. The high thermal conductivity along the tube axis (conductivity is highly anisotropic due to the structure) allows the material to be used in thermal management, for example, onchip cooling. The SEM image shows a fin structure constructed from a uniformly aligned array of MWNTs using laser machining. The fin structure is flipchip bonded to a silicon substrate on a thermocouple device that has been printed for temperature measurements. *Graph* in the *bottom panel* shows chip temperatures measured for chip-on-substrate and for the corresponding MWNT 10×10 fin array-on-chip-on-substrate assemblies under various heating powers and N_2 flow rates. It was seen that with the MWNT fin attachment, the cooling efficiency under forced flow improved by about 20 % [36]

structures (high axial conductivity versus poor transverse conductivity) can be a challenge or an advantage when designing cooling architectures based on aligned nanotube structures.

2.2 Carbon Nanotubes in Energy Applications

Conventional carbon materials have been utilized either as the electrode materials themselves or the conductive filler for the active materials in various electrochemical energy-storage systems due to their good chemical stability and high electrical conductivity. Therefore, it is natural that carbon nanotubes have been adopted as the preferred alternative electrode mate-

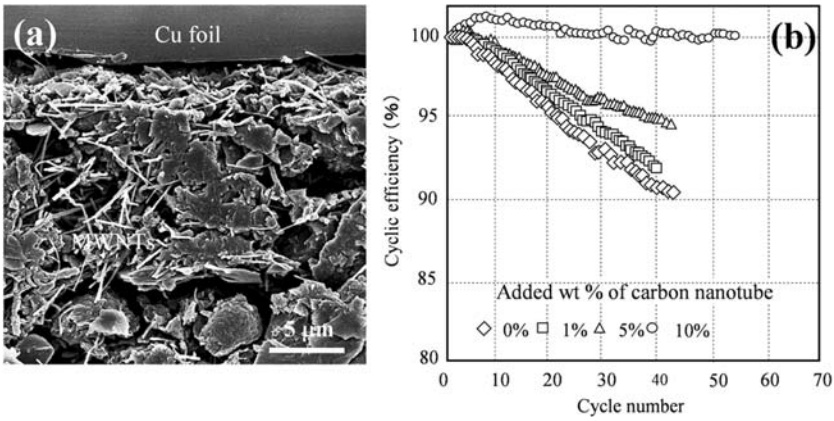

Fig. 3. (**a**) FE-SEM micrographs of the anode sheet containing carbon nanofibers/nanotubes in a commercial Li-ion battery, and (**b**) the cyclic efficiency of synthetic graphite, heat treated at 2800 °C, for samples with various weight per cent nanotubes, in the range 0 to 1.5 V, with a current density of 0.2 mA/cm^2 [44]

rial because they have unique electrical and electronic properties, a wide electrochemical-stability window, and a highly accessible surface area. With regard to energy generation and storage, nanotubes show great promise in supercapacitors, Li-ion batteries, solar cells and fuel cells; and energy applications could become the largest applications domain in the bulk application of nanotubes. At the same time, one major energy application that initially generated a lot of interest for nanotubes, namely hydrogen-storage, is now considered as not viable because careful studies have shown that the hydrogen-storage capacity of nanotubes at room temperature is far too low to generate any practical interest.

The high potential of carbon nanotubes as the electrodes in lithium-ion batteries (LIBs) has been suggested [37–40] because carbon nanotubes exhibited an increased reversible capacity up to 1000 mA h/g [41]. Unfortunately, the large reversible capacity, the absence of a voltage plateau, and the large hysteresis, that are observed in a typical hard carbon [42], limited the use of nanotubes as the electrode material in LIBs. On the other hand, carbon nanotubes have been commercialized as the filler of choice for the anode materials used in LIBs [43]. Homogeneously dispersed carbon nanotubes in synthetic graphite (ca. 3 wt %) give rise to a continuous conductive network as well as a mechanically strong electrode, resulting in a doubled energy efficiency of LIBs (see Fig. 3) [44]. Nitrogen-doped CNTs and nanofibers have also shown efficient reversible energy storage in LIBs (480 mA h/g), higher compared to commercial carbon materials used for LIBs (330 mA h/g).

For energy-storage devices other than batteries, supercapacitors have been extensively and actively investigated because they are able to store and deliver energy rapidly and efficiently for a long life cycle via a simple charge-

separation process [45]. In addition, their wide range of power capability makes it possible to hybridize them with other energy-storage devices, such as batteries and fuel cells. Even though they are being used now in various types of electronic devices (e.g., memory backup), from computers to vehicles, their intrinsic low energy density has blocked the maturation of their market. In this context, supercapacitors with carbon-nanotube electrodes have been evaluated to increase their energy density [46, 47]. For example, a SWNT electrode exhibited the maximum reported capacitance of ca. 180 F/g and a power density in the range of 6.5–7 Wh/kg [47]. Also, chemically modified MWNTs are in the early stage of commercialization for use as a conductive filler for porous carbon materials for high-power supercapacitors [48].

Silicon-based photovoltaics have reached solar-energy conversion efficiencies of $\sim 25\,\%$; however, this technology requires environmentally hazardous processing and has proven to be too expensive to replace nonrenewable energy sources for widespread application. A different option is to use organic thin films of conjugated polymers, which, although having relatively low conversion efficiencies ($\sim 5\,\%$), would be lower in cost compared to silicon-based technologies. Conjugated polymers are able to absorb a photon and generate an exciton that can dissociate into an electron–hole pair under the strong electric field found at polymer/metal interfaces. The most efficient design for organic solar cells uses a bulk heterojunction composite of a conjugated polymer with nanoscale electron acceptors forming a percolating network through the thin film. This maximizes the interfacial area between the metal filler material and the polymer, which promotes charge separation and allows conduction of the electrons through the percolating network to be collected at the electrode. For an organic solar cell to be commercially viable and to compete with silicon-based technologies it will need to reach an energy conversion efficiency of 5–10 %, have a lifetime of at least 5 years and cost less than 1/peak watt.

Carbon nanotubes can be a good material for forming bulk heterojunctions in organic solar cells (Fig. 4). Their high aspect ratio allows formation of a percolating network of nanotubes at low doping levels in a polymer composite [49, 50]. As one-dimensional nanostructures, nanotubes are also ideal for electron transport as they exhibit quasiballistic features [51, 52]. The general device design for a bulk heterojunction organic solar cells is a sandwich structure (Fig. 4) consisting of a transparent conducting electrode, typically indium tin oxide (ITO) or fluoride tin oxide (FTO), coated on a glass or PET substrate, a layer of Poly(3,4-ethylenedioxythiophene) (PEDOT):poly(styrenesulfonate) (PSS), a layer of the composite material, and a thermally evaporated electrode on the top of the composite layer, typically aluminum. Ultrasonication is used to disperse nanotubes in the conjugated polymer, followed by centrifugation to remove large aggregates. The composite solution is then deposited on the transparent electrode either by drop casting or spin casting.

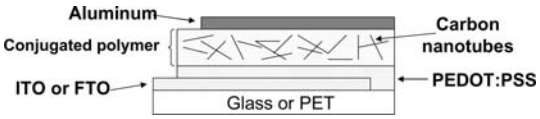

Fig. 4. Sandwich structure of bulk heterojunction organic thin-film photovoltaic cell. Glass or PET substrate is first coated with ITO or FTO, which is transparent and conductive. PEDOT:PSS is spin coated on top of the ITO to promote hole mobility into the electrode. The bulk heterojunction nanotube composite is then layered onto the device and an aluminum electrode is thermally evaporated on top of the nanotube composite [50, 51, 53–57]

Kymakis and coworkers [53, 54] first demonstrated in 2002 that SWNTs dispersed in poly(3-octylthiophene) (P3OT) showed an increase in short-circuit current, I_{SC}, by 2 orders of magnitude compared to P3OT alone in an ITO/composite/aluminum sandwiched device. As the light intensity increases the device also yields larger photocurrents, as expected from an increase in the formation of excitons in the composite materials. In 2005 they were able to improve the device performance by coating the ITO electrode with PEDOT:PSS that helps to promote hole injection into the ITO [55]. This device had an increase in power conversion efficiency from 2.5×10^{-5} to 0.1 % compared to P3OT alone. By varying the percentage of SWNTs in the composite the maximum efficiency was found at 1 % SWNTs, as higher loading limited the photocurrent due to a lower photogeneration rate from the polymer.

Carbon nanotubes have also been utilized in different conjugated polymer matrices with improvement in charge separation and transport. Various research groups have achieved a 2–6 fold increase in the photoresponse of the composite compared to the pure polymer [51, 58–65]. Devices of composites with water-soluble conducting polymers have the potential to lead to more environmentally benign processing and reduced production costs [59, 64]. The efficiencies of these devices are not high enough to be of much commercial interest at this point, but this enhancement is promising for long-term development.

Bulk heterojunctions of nanotubes in organic conjugated polymers have led to improved exciton dissociation and charge transport; however, these devices are not optimized to absorb light over the entire solar spectrum. The solar spectrum has a maximum in light intensity between 500–800 nm, but many semiconducting polymers do not absorb strongly in this region. One approach to improving the absorption of light in this region is to incorporate organic dyes with high absorption coefficients at the nanotube/polymer interface that absorb strongly in the peak intensity region of the solar spectra [66, 67]. Several groups have demonstrated an improvement in SWNT- or MWNT-based solar cells with this approach. *Bhattacharyya* et al. [56] reported the enhancement in device performance by incorporating a dye with aromatic

pyrenyl groups N-(1-pyrenyl)maleimide (PM) into a SWNT/P3OT device. Naphthalocyanine (NaPc) was used by *Kymakis* and *Amaratunga* [57] as the sensitizer in a SWNT/P3OT device. For this particular device there was an enhancement by a factor of 20 of the photocurrent with the dye compared to the dark. Naphthalocyanine has also been used in MWNT-poly(3-hexylthiophene) composites to drastically improve the absorption in the visible region, promoting a higher generation rate of excitons.

Nanotube-based hybrids can also be designed to aid exciton generation and charge separation using quantum dots and nanoparticles. In 2005, quantum dot-SWNT hybrid devices were designed by the *Landi* group to take advantage of the QD (quantum dot) electron affinity and the low doping levels of SWNTs [49]. Photovoltaic performance from this composite demonstrated a V_{OC} similar to the previous SWNT/P3OT but had a limited efficiency, which was attributed to interfacial defects at the device junctions. Titania nanoparticles can also be used to enhance the device performance using electrostatic linking. *Feng* et al. [68] used acid-functionalized MWNTs to attach TiO_2 nanoparticles and observed a twofold photocurrent increase over a device without nanotubes.

Semiconducting carbon nanotubes can generate excitons upon absorption of near-infrared light, which can increase overall exciton generation in the device as well as expand the range of light that can be absorbed simultaneously [69, 70]. The science of excitons in carbon nanotubes is discussed in the contributions by *Spataru* et al. [69], *Ando* and *Kono* et al. *Kazaoui* et al. [71] has demonstrated, using a SWNT/poly[2-methoxy, 5-(2-ethylhexoxy)-1,4-phenylene vinylene] (MEHPPV) or SWNT/P3OT composite with Al and ITO electrodes in a sandwich structure, that the range of photoresponse can be extended past the visible to a range of 300–1600 nm. The photocurrent response from the devices in a range from 900–1500 nm matches the optical absorbance features of semiconducting SWNTs. Below 900 nm the photocurrent is dominated by exciton generation from MEHPPV of P3OT. The science of carbon nanotubes optoelectronics is discussed in detail in the contribution by *Avouris* et al.

Carbon nanotubes have proven to be promising materials for bulk heterojunctions in organic thin-film solar cells. These devices have shown improvement in charge separation and transport but currently perform at relatively low efficiencies. Even with these efficiencies there is interest to move forward with commercialization for low-power applications in the next few years. With further enhancement and optimization of the nanotube/polymer interface these materials are expected to be able to reach energy-conversion efficiencies of 15–20 % in the next ten years. The focus in present development must be to improve device efficiency as well as the lifetime of the cell in order to be a competitive technology with silicon cells. At this point the most promising routes forward are in dye sensitization and nanoparticle hybrids to improve exciton generation and charge separation.

In the field of fuel-cell systems, carbon nanotubes are very promising as supporting materials for Pt catalyst [72, 73]. Experimentally, stacked-cup carbon nanotubes [74] and nanohorns [75] with a large portion of reactive edge sites were effective to anchor homogeneously distributed small-sized Pt catalysts, and this resulted in a doubled fuel-cell performance [76]. The National Institute of Standards and Technology (NIST) in collaboration with Carbon Nanotechnologies, Inc., Motorola, Inc. and Johnson Matthey Fuel Cells, Inc. is planning to develop "free-standing" carbon-nanotube electrodes for microfuel cells in order to meet the ever-growing demand for more power and longer run times in portable microelectronics. In particular, higher efficiency for proton-exchange membrane fuel cells (PEMFC) have been demonstrated using Pt catalysts supported on MWNTs [77]. This application looks very promising and could find a marketplace in less than 5 years.

2.3 Carbon Nanotubes for Mechanical Applications

The mechanical and structural applications of carbon nanotubes also hold potential to be the biggest large-scale application for the material. The mechanical, and thermal properties of carbon nanotubes are discussed in detail in the contribution by *Yamamoto* et al. Nanotubes are considered to be the ideal form of fibers with superior mechanical properties compared to the best carbon fibers, the latter of which already has fifty times the specific strength (strength/density) of steel and are excellent load-bearing reinforcements in composites [1]. Carbon fibers have been used as reinforcements in high strength, light weight, high-performance composites; one can typically find these in a range of products ranging from expensive tennis rackets to spacecraft and aircraft body parts (see Table 1). Ideally, nanotubes should perform far better than these fibers in mechanical applications. The observed tensile strength of individual nanotubes could come close to a few 100 GPa and their elastic modulus in the terapascal range [78–80], far better than traditional carbon fibers. Nanotubes can sustain large strains under compression. The reversibility of deformations, such as buckling, has been studied [81]. Flexibility and compliance of nanotubes depends on the geometric parameters of the nanotubes, which can be tailored. Such flexibility of nanotubes under mechanical loading is important for their potential application as nanoprobes and in electromechanical applications [82]. The near-ideal properties of nanotubes have prompted several groups, the most prominent among them being NASA, to invest large amounts of resources in developing carbon-nanotube-based composites for applications in aerospace (Fig. 5). Although nanotubes have near perfect structures and high aspect ratios, there are stiff challenges in adapting these materials for structural applications. Needless to say, there has not been significant progress, even after a decade of research, in developing nanotube (as load-bearing filler material)-based composites that outperform the best carbon-fiber composites.

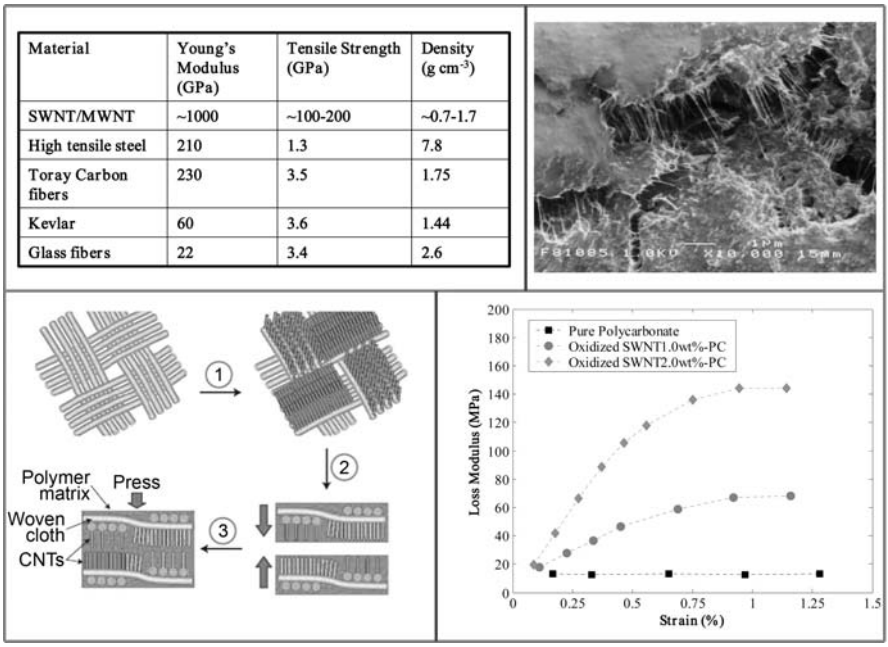

Fig. 5. *Top panel: Left table* shows a comparison of the mechanical properties of nanotubes compared with other structural materials, making them attractive for composite applications. *Right figure* is an SEM image showing the fracture surface of an epoxy-SWNT composite, exposing the stretched nanotubes in the crack [83]. Processing of nanotube composites is a challenging task due to poor dispersions obtained in most cases. *Bottom panel: Left schematic* (from [84]) shows the possibility of taking traditional stacked fiber panel composites and adding an interfacial layer of nanotubes that bridges the panels that hold the oriented fibers (SiC or carbon fiber, for example). The interfacial nanotube layer acts like a velcro, stiffening the adjacent stacks and helping to improve the through-thickness properties of 3D composites. *Right plot* shows loss modulus of SWNT-polycarbonate composites, showing the excellent improvement in vibrational damping properties (measured by the loss modulus) with the addition of nanotubes [85]

Although nanotube-filled polymer composites could have obvious advantages, the main problem seems to be in creating a good interface between nanotubes and the polymer matrix and attaining good load transfer from the matrix to the nanotubes during loading [83, 86]. The reason for this is that nanotubes are atomically smooth and unless properly engineered, the interface between nanotubes and the polymer matrix remains weak. Secondly, nanotubes are almost always organized into aggregates (concentric arrangement within MWNTs and as bundles in SWNTs) that behave differently in response to a load, as compared to individual nanotubes. Earlier studies of load transfer using Raman spectroscopy suggested that simply mixing

nanotubes into a polymer does not guarantee good load transfer [86]. Hence, recent approaches have all been based on chemically modifying the surface functionalities of nanotubes so that strong interfaces can be created [87]. In addition to these intrinsic problems, processing of nanotube-filled polymers (e.g., epoxy) remains difficult since even a low wt % of the nanotubes ($< 5\,\%$) increases viscosity prohibitively, making processing difficult. Finally, one needs to appreciate the fact that even with the very high aspect ratios, nanotubes essentially belong to the category of short fibers, which are not ideal structural reinforcements compared to continuous fiber reinforcements in composites. The role of nanotubes in composites may turn out to be a different one compared to what had been initially envisioned; more than as active load-bearing fibers in the composites, nanotubes could play the role of matrix additives, providing multifunctional properties to the composite. Even with these challenges, there are several companies in the USA (e.g., Zyvex corporation) and Japan (e.g., Mistui Corporation, Toray) who are developing nanotube-blended plastics for making superior sporting goods and some of the products promising better performance are already in the market. These utilize the CVD-grown MWNTs and nanofibrils as their nanotube additive. Once again, nanotubes in these products act more as matrix enhancers rather than as the primary load-bearing structures.

In a very different approach, it has been shown recently that nanotubes can improve properties of 3D composite [84] (Fig. 5). Here again, nanotubes are not the main load-bearing fibers, but add value to the composite in the direction normal to the plane of the fibers. Traditional fiber-reinforced composite materials made of oriented fiber stacks embedded in a polymer have excellent inplane properties but fare poorly in through-thickness (normal to the stacks and fiber direction) properties. There have been several approaches, particularly via new fiber-packing designs, but all these have had only limited success. Aligned interlaminar carbon-nanotube arrays (CVD grown directly onto SiC fiber stacks) provide enhanced multifunctional properties along the thickness direction. The carbon-nanotube arrays allow the fastening of adjacent plies in the 3D composite, providing the much-needed interlaminar strength and toughness under various loading conditions. For the fabricated 3D composites in which nanotubes are incorporated, remarkable improvements in the interlaminar fracture toughness, delamination resistance, through-thickness mechanical properties and damping, were observed. Furthermore, the inplane properties of the composites were not compromised at the same time. Such value-added propositions using nanotubes incorporated in unique geometries to traditional composites are welcome applications of nanotubes in the area of structural polymer composites.

The interfacial weakness when one adds nanotubes to polymer matrices can be converted to a strength in terms of application in the area of vibration damping. Damping alleviation is a major issue in aerospace as well as automobile applications, and the successful implementation of nanotubes for vibration damping has been recently demonstrated [85, 88, 89] (Fig. 5). Work

has shown that the nanotube-matrix sliding energy-dissipation mechanism can induce a nearly three orders of magnitude increase in loss modulus of a polymer matrix with a relatively small (1–2 %) weight fraction of well-dispersed SWNT fillers. Impressive damping increases in epoxy as well as other high-temperature resins have been shown using SWNT fillers. If large-scale manufacturing of nanotube-based composites can be implemented in a scalable way, nanotube fillers as damping elements in composites could become a real bulk application. These applications of nanotubes in composites are still in the developmental stage and although the composite application of nanotubes was taken for granted, it will take several more years to evaluate the effectiveness of nanotube composite systems versus traditionally fiber-reinforced composites. In the best scenario, nanotubes in composites would provide multifunctionality (matrix stiffness, damping, conductivity, ESD, etc.) rather than simply acting as mechanical reinforcements.

Given that pristine nanotubes provide poor interfaces between polymers, there have been attempts to use doped nanotube structures for better interfacial strength, which is crucial in composites. Preliminary studies on the preparation of epoxy composites using N-doped MWNTs revealed a substantial increase in the glass-transition temperature with incorporation of small amounts (2.5 wt %) of nitrogen-doped MWNTs. More recently, it has been demonstrated that it is possible to grow polystyrene (PS) on the surface of N-doped MWNTs [90] and nitroxide-mediated radical polymerization [91] without using any acid treatment that is now typically done on carbon tubes to create defects. This demonstrates that inplane doping is important in the establishment of covalent bonds between the nanotube surfaces and polymer chains. Recent mechanical and electrical tests have demonstrated that PS-grafted doped nanotubes exhibit enhanced properties when compared to mixtures of PS and pristine doped nanotubes. These studies are motivating further work in the fabrication of strong, conducting composites. Terrones et al. and *Kavan* et al. discuss the chemical and electro-chemical doping of carbon nanotubes in their respective contributions.

The potential uses of nanotube-filled polymers in the medical field, such as the microcatheter, have been explored [92]. Homogeneously dispersed carbon nanotubes in nylon polymer enable microcatheters to have small-sized (0.53 mm) outer diameters, two times greater mechanical strength, black color, and highly reduced thrombogenicity and blood coagulability, as compared with a pure polymer microcatheter (Fig. 6). In addition, stable biological responses of nanotube-filled microcatheters were confirmed by measuring the systematic T-cells and a histopathological study [93]. Thus, it is clear that the carbon-nanotube-filled composite-derived catheter exhibited outstanding properties when compared with a neat polymer-derived catheter, and it is envisaged that these systems will be widely utilized in various medical devices.

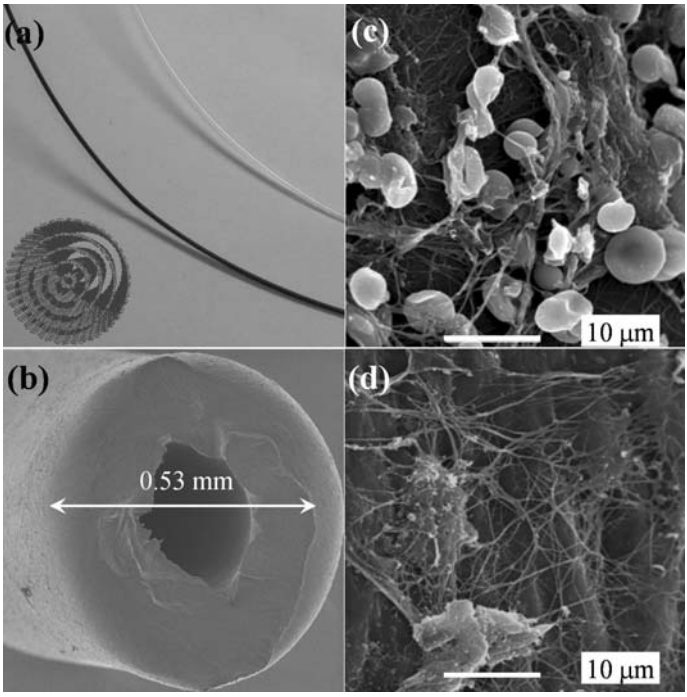

Fig. 6. (**a**) SEM photographs of transparent nylon-derived and opaque black nanotube-filled nanocomposite-derived microcatheters, (**b**) cross section of microcatheter with a hollow core, SEM images of the extraluminal surface for (**c**) control and (**d**) nanotube-filled microcatheters, respectively (taken from [92, 93])

2.4 Carbon-Nanotube Sensors

Carbon nanotubes have been effective as sensing elements utilizing their electrical, electrochemical and optical properties (Fig. 7). Detecting a low concentration of toxic gases is important for environmental purposes and chemical safety. SWNTs have been highlighted as promising gas-sensing elements due to the 1-dimensional electronic structure with all the atoms residing only on the surface. SWNTs have advantages over conventional metal-oxide-based sensors in terms of power consumption, sensitivity, miniaturization, and reliable mass production [94]. In 2000 *Kong* et al. [95] reported a conductance change of up to three orders of magnitude from individual semiconducting SWNTs within several seconds of exposure to NH_3 and NO_2 gas. This prototype SWNT gas sensor, including most up-to-date follow-ups, had an arrangement based on a field-effect transistor (FET). The conductance change of a back-gated SWNT channel upon analyte adsorption is monitored via source/drain electrodes. The untreated SWNT-FET typically shows a p-type behavior, with threshold voltages being shifted upon gas exposure.

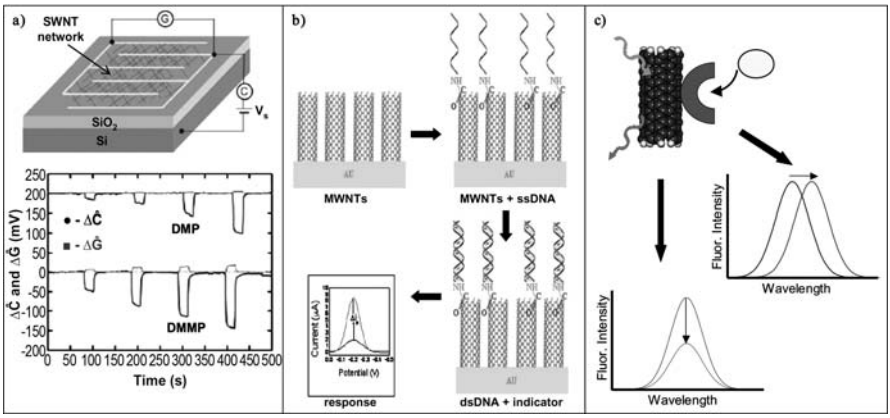

Fig. 7. (**a**) Gas sensors: Most SWNT gas sensors have an electrically contacted nanotube network on a SiO_2 layer, where the array conductance (G) is monitored upon exposure to the gas-phase analyte. It can be backgated for characterization or modification of the sensor. *Snow* et al. recently demonstrated that the capacitance (C) between the SWNT network and Si substrate can be monitored simultaneously. Normalized capacitance and conductance responses to dimethyl phosphite (DMP) and dimethyl methylphosphonate (DMMP) are shown [34]; (**b**) Electrochemical sensors: There is a wide variety of electrochemical sensors utilizing CNTs. In the DNA-hybridization sensor shown, DNA is covalently attached to MWNTs on a gold substrate. After hybridization, either methylene blue or duanomycin can be used to induce a current change [42]; (**c**) Optical sensors: The near-infrared fluorescence of noncovalently functionalized SWNTs is exploited for biological detection. Binding of the analyte to the immobilized target results in a SWNT surface event that modulates the SWNT fluorescence. In the glucose-detection system, the fluorescence intensity is modulated [96]. In the DNA hybridization and metal-cation detection systems, the energy of the fluorescence maxima gets shifted in wavelength [97, 98]

Electron charge transfer between a SWNT and an adsorbed analyte was shown to occur both theoretically [99] and experimentally [100]. However, it has been unclear as to how the signal transduction occurs in a SWNT-FET. A general thought is that exposure to electron-donating gases such as NH_3 shifts the Fermi level away from the valence band, causing hole depletion and conductance decrease. For electron-withdrawing gases (i.e., NO_2), conversely, the Fermi level shifting closer to the valence band creates more hole carriers and increases the conductance. Since *Heinze* et al. [101] showed that a SWNT-FET operates as an unconventional Schottky barrier transistor, several studies have been reported on the role of the SWNT–metal contact. *Bradley* and coworkers [102] first showed experimentally that the signal was not from the contact, by exposing contact-passivated sensors to NH_3 and polyethyleneimine (PEI). Similar results were obtained for thionyl

chloride [100] However, a recent study by *Zhang* et al. [103] verified that NO_2 sensing occurs primarily at the interface between the nanotube and electrodes. Thorough studies on various analytes are required to clarify the sensing mechanism.

Most effort so far has been on improving the sensitivity and selectivity. A common approach is to functionalize the nanotube surface with selectively binding ligands such as polymers. NO_2 at the parts-per-trillion level was detected selectively over NH_3 from a PEI-functionalized SWNT array, whereas selectivity for NH_3 was achieved by nafion-functionalization [94]. SWNT arrays become n-type upon functionalization with electron-rich PEI, and this provides higher binding affinity for the electron-withdrawing NO_2. The array was decorated with transition-metal nanoparticles for the analytes with little electron donor or acceptor properties (i.e., CH_4, CO) [104]. It is proposed that the formation of a transition metal-analyte complex facilitates the charge transfer between the nanotube and metal nanoparticle. *Staii* et al. [105] recently utilized DNA-decorated SWNTs for various analytes with the sensitivity being tuned by varying the DNA sequences.

Robustness of the sensor is a critical factor for long-term applications. It is noticed for many analytes that the sensor signal is not restored to its initial value, which is caused by irreversible analyte adsorption on the nanotube surface. Hence, the array has to be regenerated from these analytes. *Kong* et al. [95] were able to thermally desorb the analyte. A molecular photodesorption via UV irradiation [106] as well as a gate bias [107] were shown to effectively regenerate the surface. Hydrolysis can be a facile method for moisture-sensitive analytes [100].

In 2005 *Snow* et al. [108] demonstrated a novel SWNT chemicapacitor for gas sensing. An optically transparent but electrically continuous SWNT network was grown on thermal silicon oxide by CVD, and interdigitated electrodes were patterned on the SWNT layer. Analytes are polarized by an electric field from the SWNT network, causing an increase in capacitance. This chemicapacitor is highly sensitive, fast, and completely reversible. Functionalization with chemoselective polymers enabled ppb-level detection of dimethyl methylphosphonate (DMMP), a simulant for the nerve agent sarin. Another advantage of this configuration is that the capacitance and conductance can be monitored simultaneously. The follow-up study revealed the ratio of the conductance to capacitance response to be analyte specific and concentration independent [109]. This result suggests an unknown gas can be identified by this ratio.

Commercial carbon-nanotube gas sensors are already on the market. One sensor, from Nanomix, is for industrial-level hydrogen detection where nanotube networks were grown on a silicon substrate and electrically contacted. A top recognition layer designed for selective hydrogen binding was then applied to the array. A significant improvement in cross-sensitivity, compared to other commercialized products based upon catalytic beads or metal oxides, has been demonstrated with common interferants such as CO, CO_2, H_2S,

NH_3, and CH_4. Tuning the recognition layer enabled a CO_2-detection device for breath analysis as well. Synthesis of robust selective binding ligands, in conjunction with a recent achievement in nanotube separation by electronic structure, is critical for further development in this area.

Carbon nanotubes are excellent materials for use as electrodes in electrochemical sensors due to fast electron-transfer kinetics from a number of electroactive species. A wide range of sensor architectures have been developed ranging from carbon-nanotube paste electrodes (CNTPE), glassy carbon electrodes (GCE) modified by CNTs, metal nanoparticle-modified CNT electrodes, to CNTs embedded in a conducting polymer matrix. Many sensing methodologies involve immobilizing enzymes at the CNT electrode, either through electrostatic forces or through covalent attachment. Glucose sensing has been a major thrust of electrochemical biosensor development. The majority of electrochemical glucose sensors utilize the enzyme glucose oxidase (GOx), which catalyzes the oxidation of β-D-glucose to D-glucono-1,5-lactone with hydrogen peroxide (H_2O_2) as a reaction byproduct. The generated H_2O_2 is then oxidized at the electrode and detected by measuring current flow. The first sensor to use such a configuration was made by *Sotiropoulou* and *Chaniotakis* [36] using multiwall carbon nanotubes (MWNTs) grown directly on a Pt electrode. The device was fabricated by adsorbing GOx to carboxylic acid groups functionalized to the MWNTs. *Wang* and *Musameh* [110] encapsulated MWNTs in a Teflon matrix along with GOx on a GCE, and demonstrated a marked increase in sensitivity of glucose detection compared to an analogous device made with graphite. Similarly, *Gao* et al. [111] embedded MWNTs and GOx in a conducting matrix of polypyrrole and showed a roughly linear response to glucose in the range of 0–20 mM. *Tang* et al. employed a different sensing architecture by incorporating Pt nanoparticles in a Nafion/GOx/MWNT electrode [112]. The use of Pt nanoparticles was extended to SWNT by *Hrapovic* et al. for Nafion/GOx/SWNT on a GCE and demonstrated a sensitivity of 0.5 μM [113]. The sensitivity of the device was further increased through the use of Cu nanoparticles to 250 μM [114]. The major drawback to such devices is that the linear response range usually does not cover a large enough range of glucose concentrations.

In addition to glucose, a large number of devices have been made for the electrochemical detection of DNA. Single-stranded DNA (ssDNA) is immobilized on the electrode and current changes are monitored upon DNA hybridization with a complementary strand. Usually, a redox indicator that has higher affinity for double-stranded DNA (dsDNA) is used to change the electrochemical response. The first such sensor was fabricated by *Cai* et al. [115] using a MWNT/GCE and the intercalating agent duanomycin (Dmc). Methylene blue has also been used as a redox indicator for DNA detection [116]. Methods for reagentless DNA detection by monitoring oxidation of guanine have also been developed [117, 118]. A number of other analytes have been detected using electrochemical means. The first instance of using carbon nanotubes as electrochemical sensors was by *Ajayan* and coworkers [119],

who observed reversible oxidation of dopamine at a multiwall carbon nanotube electrode. A number of groups have reported direct electron transfer to nanotube electrodes from redox enzymes such as GOx [120, 121] and Cytochrome c. [122] Other detected analytes include NAD+ [123], cholesterol [124] and indole acetic acid [125]. Because electrochemical sensors utilizing nanotubes are the most mature CNT-based biosensing technology, commercialization is expected to happen sooner than for any of the biosensors discussed below. However, utilization of CNTs in commercial biosensors faces a number of hurdles and as such are not expected to be available in the near term.

Semiconducting SWNTs have been fabricated into field-effect transistor (FET) devices. Such devices have been found to be very sensitive to adsorption events on the nanotube surface [95]. The first SWNT-FET for biosensing was developed by *Besteman* et al. [126] by attaching GOx, via a linker, to single SWNTs, demonstrating a slight conductance change upon addition of glucose. *Chen* et al. [127] demonstrated specific protein detection by first functionalizing the nanotubes with a target ligand, either biotin, staphylococcal protein A or U1A antigen, and showed a measurable conductance change upon protein binding to the ligand. However, further work by the same group pointed to protein adsorption at the gold electrodes as the mechanism of sensing, as after passivation of the electrodes there was no longer any detectable conductance change upon protein binding [128]. *Star* et al. fabricated a SWNT-FET based DNA hybridization sensor and demonstrated detection of a single nucleotide polymorphism, a major cause of many diseases [129]. Similar work by *Tang* et al. showed that the mechanism of DNA hybridization detection on SWNT-FETs was that of hybridization on the gold electrodes, drawing into question the ability of SWNT-FETs to detect DNA hybridization [130]. Thus, many questions remain regarding the ability of SWNT-FETs to detect specific biomolecular interactions and as such any commercialization of this technology will happen only in the long term.

The most recent type of nanotube biosensor to be developed is based on semiconducting SWNT photoluminescence (PL). The science of carbon nanotubes photoluminescence is discussed in the contribution by *Lefebvre* et al. For biomedical applications, SWNTs have a number of advantages over conventional fluorophores; they fluoresce in a region of the electromagnetic spectrum where blood and tissue are most transparent, they will not photobleach and they are sensitive to changes in the local dielectric environment. *Strano* et al. adsorbed GOx and a reaction mediator, which quenched SWNT PL, to individually solubilized SWNT. Hydrogen peroxide produced by glucose oxidation would then react with the mediator and restore SWNT PL [96]. A DNA hybridization sensor was also fabricated by the same group, by first adsorbing a target DNA strand to the SWNT. Hybridization with the complement resulted in up to a 2 meV blueshift in the emission maximum [97]. Finally, addition of divalent metal cations to DNA-suspended SWNT resulted in a redshift of the SWNT PL. This was even detectable with the SWNT en-

capsulated in living cells [98]. While the use of SWNT PL opens new avenues of sensing, any commercially available sensor is not expected to be available for > 10 years.

In addition to the FET-based sensors that were described above, there have also been attempts to make sensors based on nanotubes functioning as electrodes, utilizing the field-ionization properties of nanotubes for gases. An example of this is the gas-ionization sensor, where the transition-metal state electrodes are replaced by arrays of nanotubes [131]. The sharp tips of nanotubes generate very high electric fields at relatively low voltages, lowering breakdown voltages several-fold in comparison to traditional electrodes, and thereby enabling compact, battery-powered and safe operation for such sensors. The sensors show good sensitivity and excellent selectivity, and are unaffected by extraneous factors such as temperature, humidity, and gas flow. These simple, low-cost, sensor electrodes based on vertically aligned MWNTs could be deployed for a variety of gas-sensor applications, such as environmental monitoring and in the chemical industry. Vertically aligned nanotubes, due to their high elastic compressibility, allow for building electromechanical pressure sensors. The resistivity measured in phase with the applied cyclic compressive strain on vertically aligned nanotube arrays has been found to be very sensitive to small strain levels [132]. Such strain sensors could be useful in MEMS devices. The response of the nanotube conductivity to pressure has also been utilized in flow sensing but the challenge remains in factoring out the effects of pressure alone (compared to temperature, adsorption, etc.) in influencing the nanotube conductance.

Electromechanical actuators have been proposed using sheets of MWNTs and SWNTs [133, 134]. Nanotube sheets infiltrated with polymer binders have been shown to perform as excellent electrochemical actuators, mimicking the actuator mechanism present in natural muscles. The nanotube actuators are superior to conducting polymer-based devices, since in the former no ion intercalation (which limits actuator life) is required. Several applications have been proposed including nanotube-based microcantilevers and artificial muscles that are stable at high temperatures. The electromechanical and electrochemical applications of nanotubes are being developed but face stiff challenges due to inherent limitations as well as competition from new ferroelectric and organic materials.

2.5 Carbon Nanotubes in Field Emission and Lighting Applications

CNTs have been considered as preferred field emitters due to their low threshold voltage, good emission stability and long emitter lifetime [135–138]. The contribution by *Ma* et al. discusses the electron relaxation processes in carbon nanotubes. These characteristics make them useful in the fabrication of cathode-ray lighting elements and flatpanel displays. The prototype cathode-ray tube (CRT) lighting elements using arc-derived MWNTs as cold electron

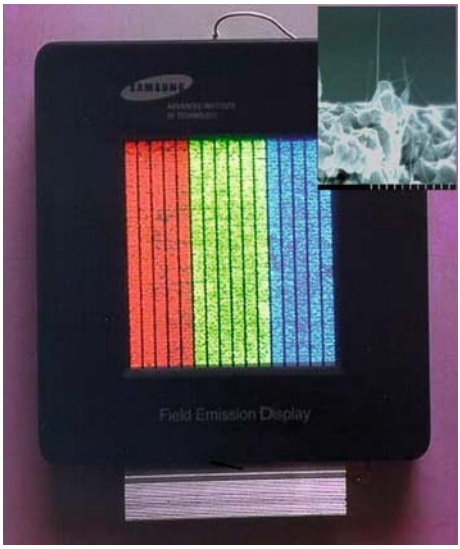

Fig. 8. A prototype 4.5 in FED using a printing method. Inset is an SEM image of single-wall carbon nanotubes projecting out of the nanotube layer. (Courtesy of Dr. W. Choi of Samsung Advanced Institute of Technologies)

sources exhibited stable electron emission, adequate luminance, and long life of the emitters [139]. Also, Samsung released the fabrication of a 4.5 in diode-type flat panel display using arc-based SWNTs [140] (Fig. 8). Even though SWNTs were shown to have excellent emitting performance [140], they were simply degraded at high emission current [141]. In this sense, DWNTs and or thin MWNTs have been examined as the best field emitting materials because they were shown to have a low threshold voltage comparable to SWNTs and a better structural stability compared to SWNTs, almost comparable to that of MWNTs [142–144]. Very recently, *Hiraoka* et al. [145] successfully fabricated a DWNT forest using Ni-based alloys with Cr or Fe as catalysts, and then measured the field emission from such a CNT/buckypaper cathode to an anode. They claimed that the homogeneous emission from the DWNT electrode is a result of the good electrical contact between the DWNTs and the grid substrate. Printable DWNT or thin MWNT-based field emitters are quite competitive for fabricating large-area FEDs (field emission displays) at relatively low cost. Even though technical problems have to be solved, it is certain that nanotube-based large-area color FEDs will appear on the market. This application seems to be clearly poised for commercial appearance in the next five years. The science of DWNTs is discussed in detail in the contribution by *Pfeiffer* et al.

Doping of nanotubes might also help field emission. *Charlier* et al. [146] have demonstrated experimentally and theoretically that B-doped MWNTs exhibit enhanced field emission (turn-on voltages at ca. 1.4 V/μm) when com-

pared to pure carbon MWNTs (turn on voltages at ca. 3 V/μm). This phenomenon is thought to be due to the presence of B atoms at the nanotube tips, which results in an increased density of states close to the Fermi level. Theoretical tight-binding and *ab-initio* calculations demonstrate that the work function of B-doped SWNT is much lower (1.7 eV) than that observed in pure carbon MWNTs. Similarly, it has been demonstrated that bundles of N-doped MWNTs are able to emit electrons at relatively low turn-on voltages (2 V/μm) and high current densities (0.2–0.4 A/cm^2) [147]. More recently, individual N-doped MWNTs have also shown excellent field emission properties at 800 K; experimental work functions of 5 eV and emission currents of ca. 100 nA were obtained at ±10 V [148].

2.6 Carbon Nanotubes for Biological Applications

The optical properties of nanotubes impart promising advantages to their use in imaging applications within live cells and tissues. The unique photostability of SWNT photoluminescence allows for longer excitation time at higher laser fluence than either organic fluorophores or quantum dots. Also, in the range of 700–1400 nm, visibly opaque tissue exhibits greatly attenuated absorption, autofluorescence, and scattering characteristics. This range overlaps with the fluorescence profiles of many semiconducting nanotubes, allowing their observation in whole blood and thick tissue [149]. *Cherukuri* et al. [150] directly imaged nanotubes after incorporation by macrophages, observing no photobleaching – a phenomenon that plagues conventional biological imaging. Nanotube fluorescence was also used to image SWNT in tissue sections as well as measure their concentration in blood [151]. The extremely large resonance-enhanced Raman scattering profile of nanotubes is also available for detection in cells and can be applied to tissues as resonance enhancement occurs at near-infrared wavelengths [152]. The science of resonance Raman scattering is discussed in the contribution by *Saito* et al. Additionally, *Heinz* discussed Rayleigh scattering in carbon nanotubes, and *Hartschuh* discusses complementary techniques, such as near-field optics.

The therapeutic effect of drugs is constantly being increased through the development of new delivery vehicles. Previously, these vehicles included viral vectors, liposomes, cationic lipids, polymers, and nanoparticles. While viral vectors have an inbuilt transfection capability, there have been safety concerns surrounding their use, opening the door for other vehicles [153]. Although nonviral vehicles have versatility of shape, size and materials, one issue of concern is the poor penetration of some therapeutic agents into cells. Carbon nanotubes are readily internalized by cells; and after surface modification, they exhibit low cytotoxicity over the period of a few days [154–161]. In addition, they have a higher surface area to volume ratio than spheres, giving nanotubes the potential to be conjugated with more functional agents than spheres [159] and to accommodate higher loadings of therapeutic agents [161]. For these reasons, nanotubes have received a lot of attention as potential

vehicles for drug delivery. This section will address much of the work that has been done toward the successful use of carbon nanotubes to effectively deliver therapeutic agents into cells.

A suitable scheme to conjugate the drug and the nanotube is required to make CNTs into viable delivery vehicles. The nanotubes are hydrophobic and therefore insoluble in liquid biological media, so various methods have been exploited to functionalize the nanotubes, both covalently and noncovalently to make them soluble. In the noncovalent methods, molecules with hydrophobic groups, including RNA [157], DNA [162], Triton-X-100 [163], and 1-pyrenebutanoic acid [164], adsorbed reversibly to the nanotube surface, while the hydrophilic groups rendered the conjugates soluble. Covalent functionalization remains the more common method with various chemistries based on the creation of carboxyl [165, 166] and amino [159] groups on the ends and walls of the nanotubes. At the carboxyl sites, researchers have attached amine [159, 160, 167–169] and thiol [161] groups, to link various biomolecules [154–156, 158] to the nanotubes. Another critical step for nanotube drug delivery is to conjugate the nanotubes in such a way that the functionality of the biomolecules is maintained. The ability of covalently functionalized nanotubes to act as condensation sites for plasmid DNA has been demonstrated as a precursor to nanotube gene-delivery vehicles [169]. Proteins such as Biliverdin/Xbeta reductase enzyme have also been shown to form conjugates with functionalized nanotubes [163]. *Salvador-Morales* et al. [170] also report that nanotubes can activate a response in the complement, part of the human immune system, as evidenced by the adsorption of specific fibrinogen and apolipoproteins.

More recently, researchers have shown that nanotube conjugates can enter a cell and release the therapeutic agents for successful drug delivery. *Wu* et al. [159] reported the use of passive cellular uptake to deliver multiwall carbon nanotubes conjugated with amphotericin B (AmB), an antibiotic that is effective in treating fungal infections, but toxic to mammalian cells when it is free in solution. Functionalization of the nanotubes with AmB reduced the toxicity towards Jurkat cells, but still maintained (and in some instances increased) its functionality to inhibit visible growth of C. parapsilosis, C. albicans, and C. neoformans.

The introduction of foreign DNA to cells is another major area for therapeutic delivery using carbon nanotubes. *Cai* et al. [156] used nanotube spearing, utilizing the magnetic properties of nickel-embedded single-wall carbon nanotubes (SWNTs), to deliver DNA plasmid vectors containing the sequence for EGFP (a fluorescent protein) to Bal17 and Mouse splenic B cells, which are nondividing cells, and therefore notoriously difficult to transfect. They observed expression of EGFP in the cells, whereas a vector without EGFP did not show any detectable fluorescence. Furthermore, the use of a commercial product, Lipofectamine 2000, did not lead to any detectable fluorescence from EGFP, indicating the high efficiency of the nanotube-spearing method. *Cai* et al. also note that the small size of the nanotubes allows for penetration

with only minor perturbations to the cell, and the magnetic spearing may be gentler than the ballistic method for mechanical delivery. Plasmid DNA vector-multiwall nanotubes have also employed a passive transport mechanism through the cell membrane, resulting in DNA uptake and gene expression of β-galactosidase in CHO cells [160]. *Kam* et al. [171] used this passive delivery mechanism, which led to the formation of endosomes containing oligonucleotide-single walled nanotubes, and followed with a second step to rupture the endosomes with pulses of a NIR (near-infrared) laser. Single-wall nanotubes absorb strongly at NIR wavelengths and exhibit local heating upon NIR absorption. This work showed that NIR radiation caused the nanotubes to release the DNA, allowing for its translocation into the cell nucleus. This technique was also used in the same study to cause cell death. Nanotubes were functionalized using a folate moiety that allowed them to be selectively internalized by cells that had been labeled with folate receptor tumor markers. Upon NIR irradiation, the cells were killed due to local heating caused by the nanotubes. In a separate study, *Kam* et al. [161] employed a technique that used a disulfide linker to conjugate oligonucleotide-SWNT and siRNA-SWNT. The conjugated nanotubes were passively endocytosed into the cell, and the disulfide bond was subsequently cleaved by the presence of thiol-reducing enzymes and the acidic environment in the liposome. The siRNA sequence they used caused silencing of the gene encoding for lamin A/C protein in HeLa cells, and they observed a transfection level that was twice as high as that of lipofectamine, a commonly used agent. Nanotubes have also been used to deliver proteins, such as cyt-c, to cells to induce apoptosis, or programmed cell death [69]. In this work, cyt-c-SWNT were endocytosed NIH-3T3 cells. The cyt-c-SWNTs were subsequently released by adding chloroquine to the cell medium, resulting in an increased rate of apoptosis.

While significant progress has been made in the area of carbon-nanotube delivery of therapeutic agents, there are still many issues left to resolve before clinical use of these materials can be realized. The field would be greatly advanced with the development of a noninvasive means to release nanotubes from endosomes into cells. Although passive methods allow for consistent uptake of nanotubes by cells, a controlled, yet nondestructive, method of nanotube transport with specificity to a target area would broaden the therapeutic potential for these materials. A more efficient means of unloading the cargo would also improve the efficacy. Further investigation is also needed to determine the long-term effects of conjugated nanotubes in-vivo, with issues such as toxicity, and interaction with biologic components like blood and tissue. Also of importance is the metabolism of these materials, and the possibility of in-vivo nanotube excretion after the therapeutic agent has been delivered. While these issues may take years to resolve, this field remains promising, with nanotubes already demonstrating high and versatile loading capacity for therapeutic agents, some selective cargo unloading, and better cell penetration than many other delivery materials.

For both biomedical applications mentioned above, the transport of nanotubes into cells is of central importance. The central question in the cellular transport of carbon nanotubes is the transportation mechanism. Understanding this process will help further drug and gene delivery, as well as enable precise cellular targeting for bioimaging applications. As yet, there exists a significant amount of controversy and confusion about the way in which nanotubes enter cells. In the case of SWNTs, *Dai* et al. [155] have reported that acid-functionalized SWNTs can enter the cells via the endocytosis pathway; however, *Bianco* et al. [160] suggests a passive, endocytosis-independent mechanism for ammonium-functionalized SWNTs and MWNTs. In the case of MWNTs, which are beyond the size limit of an endocytosis pathway, another suggested mechanism is one where the lipid molecules of the membrane are flipped, allowing entry into the cell [154, 172].

The coating on the nanotube surface is one factor that governs the nanotube–cell interaction. Serum in cell media contains various proteins, such as albumin, fibronectin and transferrin, that will adsorb to the nanotube surface. Even for systems without serum, the cell rapidly produces sufficient protein to coat the nanotube. These proteins are also present in vivo and almost immediately coat any foreign material introduced to the body. In either case, the actual surface presented to the cell is the protein-modified surface [173], and this has been confirmed in the case of gold nanoparticles [174].

The size and shape of a particle also affect the interaction of particles with cells. Phage cells in the primary immune system "eat" foreign particles (phagocytosis) that are above several hundreds of nm (Fig. 9a), and is one cellular uptake pathway suggested for CNTs [150]. Another potential mechanism is receptor-mediated endocytosis (Fig. 9b). For nanotube cellular transport, clathrin-mediated endocytosis is one of the most studied receptor-mediated pathways [175]. The molecular structure of clathrin is such that there is a natural size limit (about 150 nm) for the cages formed during endocytosis on the membrane, which suggests a size cutoff for particles [175]. Also, direct physical forces, including van der Waals, electrostatic, and hydrophobic effects that lead particles to be attracted to cells and affect the uptake process. For example, the presence of positive charges on a nanoparticle pushes the optimal wrapping size of the clathrin layer to nanoparticles larger than 25 nm [176]. If the adhesion free energy between the nanoparticles and the cell membrane is larger than that of typical receptor-ligand binding, the critical size of wrapping may also decrease [177]. However, MWNTs, that have a 10 nm radius and 200 nm length, are suggested not to have an endocytotic pathway, but possibly one of spontaneous switching of lipid molecules in the membrane (Fig. 9c) [160, 172]. Another unanswered question is the fate of nanotubes once they have entered the cell. For most biological applications it would be advantageous if the nanotubes were subsequently expelled from the cell; however, as yet this has not been reported in the literature. Much work is needed on nanotube cellular transport before these discrepancies will begin to be solved, allowing true understanding and control of nanotube placement

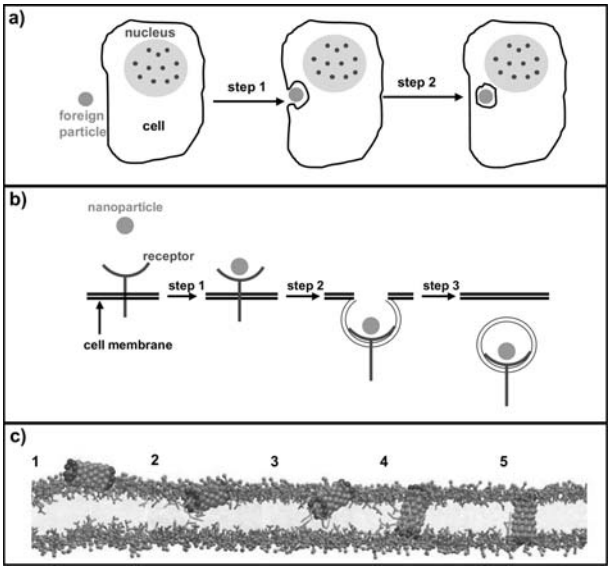

Fig. 9. (**a**) Phagocytosis of a foreign particle into a phage cell. *Step 1:* The membrane surrounds the particle. *Step 2:* The foreign particle is internalized. (**b**) Receptor-mediated endocytosis *Step 1:* A nanoparticle binds to a receptor on the cell membrane. *Step 2:* The receptor wraps the nanoparticle, forming an invagination on the cell membrane. *Step 3:* The nanoparticle is completely internalized into the cell. (**c**) Spontaneous lipid flipping *Step 1:* Spontaneous adsorption of a nanotube to the cell membrane. *Step 2:* The nanotube is partially inserted parallel to the membrane. *Step 3:* Random thermal fluctuations force one end of the nanotube toward the hydrophobic membrane core. *Step 4:* The end of the nanotube is directed, by the attached membrane lipids, to the opposite side of the membrane. *Step 5:* The final nanotube location is perpendicular to the plane of the lipid membrane (taken from [82])

inside cells. As such, using nanotubes for the aforementioned biological applications is not expected to yield any products for the foreseeable future and can be seen as a long-term project.

2.7 Carbon Nanotubes in Miscellaneous Applications

One of the applications of nanotubes that is in the market today is that of nanotube-based probe tips. With extremely small sizes, high conductivity, high mechanical strength and elasticity, nanotubes have shown their potential to be useful nanoprobes [178–180]. The nanotube-based tips provide better resolution for imaging and have better durability because of their elasticity, unlike conventional silicon tips that suffer from frequent tip crashes. Today, nanotube-based (mainly good-quality multiwall) AFM probe tips can be bought from scanning-probe instrument manufacturers. These still cost

dearly (few hundred dollars per tip) and can be considered as a low-volume specialty application. There have been lots of proposals for the use of nanotube tips in future technology, for example in imaging, nanolithography [181] and as nanoelectrodes. The nanotube tips have been used in the imaging of surfaces as well as biological species such as DNA at high resolution. The nanotube tips have the advantage that they are conducting, and they can be chemically modified for use in chemical imaging as well as in the manipulation of molecular species on surfaces. The future of nanotube probes will depend on how reliably these tips can be fabricated (either grown directly or transferred on to conventional tips) at high yield.

Another interesting application that has been touted for nanotubes is their use as membrane filters. Several groups have published papers in recent years suggesting that membranes made from aligned nanotube arrays (both SWNTs and MWNTs) could be used for selective transport of species [182–184]. Activated and porous carbons have been traditionally used as filters (e.g., water purification) but the advantage of nanotubes is that the pore sizes are very uniform and small, so that separation of really small molecules becomes possible. Although the pore size is small, the flow rate is not reduced due to the unique nature of the flow of solvents through the nanotube cavities. Another advantage could be that the nanotube surfaces may be chemically modified to make the separation very selective. Although several groups are working to develop nanotube-based membranes for filtration, molecular as well as gas separation, these are still far from commercial products and their development could take more than a decade.

In recent years, work has progressed in getting stable dispersions of nanotubes in various solvents (nanotube inks) [185] (Fig. 10), which can be directly spun or printed onto various substrates. Easily printable (e.g., inkjet printing) circuits and films are extremely useful for a range of applications ranging from flexible electronics to antennas. Nanotubes have also been spun into fibers using various techniques ranging from extrusion of nanotube slurries to drawing from aligned arrays. High weight percentage dispersions of SWNTs have been spun directly or using polymer binders to continuous fibers reaching macroscopic lengths [186, 187] (Fig. 10). The fibers can be also assembled into sheets, membranes and other products. Several applications have been demonstrated for such nanotube fibers and their products, for example as high-brightness incandescent bulbs [188], reinforcements in polymers, shielding elements and in ballistic protection. Direct growth of aligned nanotubes can be used to make distinct products, such as brushes [189] (Fig. 10). The tiny brushes with nanotube bristles have been demonstrated for use in a variety of applications including cleaning of microscale spaces, conducting contact brushes, and probe arrays. Another possibility is the use of aligned nanotube arrays as dry adhesive tape; one recent study shows that properly engineered nanotube arrays could have adhesive strengths even rivaling gecko feet [190]. The variety of assembled and dispersed products from nanotubes could feed various industrial applications in the future and could allow

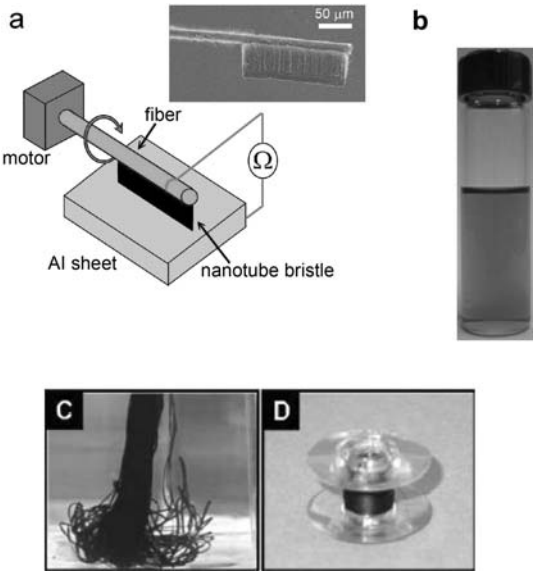

Fig. 10. A few miscellaneous applications that have been demonstrated using nanotubes. (**a**) Nanotube-based microbrushes have been synthesized and can be used in various instances including as a brush contact (seen in the schematic). (**b**) Nanotube inks: fully dispersed SWNTs in water, using a surfactant. Such dispersions in water or organic solvents and polymer binders have been used for printing structures using inkjet printers on various substrates, for example to make conducting nanotube lines. (**c**,**d**) Fibers of nanotubes and polymers have been spun in a continuous fashion. The SEM images show SWNT-PVA fibers that have been spun using a coagulation-based spinning method [191]. These nanotube-polymer fibers could be useful in composites, membranes, etc.

continuous and roll-to-roll manufacturing incorporating nanotubes. Many of these products (in particular the spun fibers) could come to the marketplace within the ten-year time frame.

Research on carbon nanotubes has also provided avenues in developing novel carbon nanostructures, which could have specific applications. Nanotubes filled with various materials have been made using approaches such as capillarity infiltration [192, 193]. Hybrid nanowire–nanotube structures have been designed and even branched nanostructures have been synthesized [194, 195]. All these structures provide the range of building blocks that could one day be used in nanotechnology applications, but these are clearly beyond the ten-year time frame we have considered. However, there are some structures, such as carbon nanohorns (larger fullerene-like structures with low density and high surface area) as described in detail in the contribution by *Yudasaka* et al. [196] that have been shown as useful in applications related to electrodes and supercapacitors and a variety of other applications.

These materials can be easily produced in bulk by the pyrolysis of carbon precursors and could be commercialized within the ten-year period. Additionally, *Yudasaka* et al. discuss in this volume the science and application of nanohorns, *Tenne* et al. discuss inorganic nanotubes, and *Charlier* et al. discuss the science of graphene.

2.8 Environmental and Health Effects of Carbon Nanotubes

As we have seen in the previous sections, carbon nanotubes hold great potential in electronics, environment, energy, and bio/medical fields. One uncertain issue that still remains unsolved is the safety and biocompatibility of the nanotube material [197–205]. Recently, it has been suggested that a simple and effective method can be used to evaluate the toxicity and biocompatibility of carbon nanotubes through a measurement of $CD4^+$ and $CD8^+$ T-cells in peripheral blood and their histopathological study on carbon-nanotube-implanted tissues [201] because $CD4^+$ (a coreceptor for MHCII) and $CD8^+$ (a coreceptor for MHCI) give us important antigen information of T-cells. Interestingly, in the protocol demonstrated, the mortality of animals was negligible, and no chronological changes of body weight were observed among nanotube-implanted mice versus control over three months postimplantation (Fig. 11a). Time-dependent changes in peripheral T-cells, which involved into carbon nanotubes in situ, were well correlated with a processing phase of granuloma formation (Fig. 11b). Even though their potential toxic nature was probed to be significantly lower for CVD-grown MWNTs, more detailed and systematic (long-term) studies with regard to the toxic natures of various types of carbon nanotubes (including direct aspiration of the tubes in lungs) have to be carried out to address the safety of carbon nanotubes.

Nanotube cytotoxic properties appear situational, depending highly on the degree and type of functionalization, aggregation state, and the presence of metal-catalyst particles remaining from synthesis. Pristine nanotubes are reported to cause oxidative stress and decrease cell viability [206,207], though there is some indication that leftover catalyst particles contribute to this effect [208]. The cytoxicity can be greatly attenuated via functionalization. *Sayes* et al. [209] reports that the high cytotoxicity of pristine SWNTs can be reduced to zero with increasing coverage with a covalently attached polar functional group. The choice of functional group can impart a range of cell responses including the activation of primary immune cells by polyethylene glycol-coated SWNTs [210]. The toxicity of noncovalently functionalized carbon nanotubes similarly depends on the nature of the adsorbate. Successfully individually encapsulated DNA-wrapped SWNTs leave cells viable upon internalization of the complex [211]. Toxicity studies are also reported in the contribution by *Terrones* et al. on nitrogen doped nanotubes.

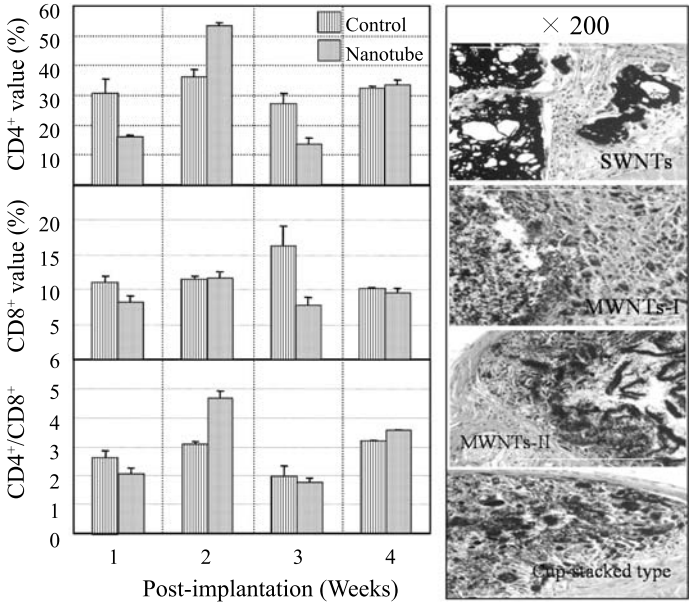

Fig. 11. (**a**) Time-dependent changes in $CD4^+$, $CD8^+$ and $CD4^+/CD8^+$ after the subcutaneous implantation of high-purity carbon nanotubes, (**b**) light microscopic pictures of skin tissue after three months implantation of SWNTs, MWNTs-I, MWNTs-II and cup-stacked-type carbon nanotubes, respectively (from [201])

3 Conclusions

It is important to summarize the applications of nanotubes in terms of the timeline we discussed in the beginning of this chapter. In addition, it would be useful to separate applications that rely on large-scale manufacturing (bulk applications) from those that are based on controlled fabrication. We will discuss the challenges, that are involved in the successful transfer of knowledge to commercial applications. The great promise with which nanotubes has fascinated the scientific and technological community needs to bear fruit at this juncture. For this to happen, it is important to address the realistic potential of nanotubes as a commercial commodity. In Table 2 we group the applications of nanotubes, that we discussed in earlier sections, in two categories; one, based on the timeline of commercialization and two, based on their scale (bulk vs. limited volume).

It would seem incomplete if we do not discuss some of the issues and challenges that have faced carbon-nanotube applications from the very beginning. These challenges have slowed down the pace of nanotube commercialization. The foremost among these is the manufacturing issue. The bulk applications of nanotubes necessarily will rely on the ability to manufacture nanotubes in high volume, on the industrial scale. For the case of CVD-grown MWNTs

Table 2. Shows applications of nanotubes grouped as present (existing), near term (to appear in the market within ten years) and long term (beyond ten-year horizon) and as categories belonging to bulk (requiring large amounts of material) and limited volume (small volume and organized nanotube structure) applications

	Large-volume applications	Limited-volume applications (mostly based on engineered nanotube structures)
Present	– Battery electrode additives (MWNT) – Composites (sporting goods; MWNT) – Composites (ESD* applications; MWNT)	– Scanning probe tips (MWNT) – Specialized medical appliances (catheters) (MWNT)
Near term (less than ten years)	– Battery and supercapacitor electrodes – Multifunctional composites (3D, damping) – Fuel-cell electrodes (catalyst support) – Transparent conducting films – Field emission displays/ lighting – CNT-based inks for printing	– Single-tip electron guns – Multitip array X-ray sources – Probe array test systems – CNT brush contacts – CNT sensor devices – Electromechanical memory device – Thermal-management systems
Long term (beyond ten years)	– Power transmission cables – Structural composites (aerospace and automobile, etc.) – CNT in photovoltaic devices	– Nanoelectronics (FET, interconnects) – Flexible electronics – CNT-based biosensors – CNT fitration/separation membranes – Drug-delivery systems

* ESD stands for electrostatic discharge

(so-called Endo fibers) large-scale manufacturing has been reasonably successful. Companies such as Hyperion in the USA and Mitsui Corporation and Showa-denko in Japan have built manufacturing facilities that can produce up to a hundred tons of material per year. This has happened over the last decade and in particular the last few years, essentially to supply the demand for nanotubes arising mainly from the ESD and battery applications. Even this volume is tiny in comparison to carbon fibers and other carbons that are commercially used. In the case of SWNTs the situation is not the same. Even after a decade and a half of research in this area, no technique can yet manufacture this material in reasonable volume. The amounts are still restricted to gram quantities, limiting any real bulk application for the material. There have been bold undertakings by several companies in the USA, Canada and China recently promising a SWNT supply in comparable

volumes to the MWNT availability in the next decade or so, but these claims remain to be demonstrated. In addition to availability there are also other issues such as cost (SWNTs still sell at around 100 USD per gram, compared to a few dollars/kg for the CVD-grown MWNTs) as well as fundamental materials-science problems and compatibility. For example, we have already discussed the issue of interfaces when we discussed polymer composites and more work needs to be done in engineering to solve these problems. In the meanwhile, the promising applications in the near term will come from value-added uses, such as application of nanotubes as additives in battery electrodes to help mechanical stabilization.

For applications that require organized nanotube structures there has been a clear lack of emphasis on integration schemes. The revolutionary applications of nanotubes, for example nanotube electronics, need much more focus on controlled assembly and integration. There are still holy grails in this path, for example the selective growth of nanotubes with specific chirality or diameter. There are still challenges in obtaining nanotubes with controlled length, precise alignment, control of location, etc. Processing is also an issue. For example, the temperatures that are used to grow nanotubes today are far higher than what is acceptable in today's silicon semiconductor processing and hence integration of nanotubes into existing processes in the industry is challenging. Perhaps such high-value applications with nanotubes will take several more decades to happen. In the near term, there could be nanotube-based devices in more forgiving applications such as field emission displays, sensors, membranes, coatings, etc. Good examples are the electromechanical memories and transparent conductive films that are based on random assemblies of nanotubes. For even these to be commercially viable, they need to be manufactured with consistency and in a cost-effective manner, so that they compete with other material choices available in the market. The contribution by *Joselevich* et al. gives a survey on the synthesis and processing of carbon nanotubes.

There are also other issues that need to be carefully considered as we go ahead with applications of nanotubes. Of utmost importance are the environmental and health-safety issues related to nanomaterials. There simply have not yet been enough studies that could unequivocally prove either way (regarding safety) and for all practical purposes the jury is still out. Isolated experiments have shown that the nanotubes are not toxic. Whatever is the final word, we need to be aware of protocols on how to handle these materials, both in the laboratory and in an industrial setting. Well-defined regulatory controls need to be in place when large quantities of the material are handled routinely. The long-term impact of these on health should be studied. There needs to be standard procedures established on how to package and transport nanotube materials and how to handle them.

The next decade will be the decade of nanotechnology thus requiring research in nanometrology (see contribution by *Jorio* et al.). Carbon nanotubes and their products will have a seminal role to play. Large amounts of

resources have been invested for understanding and developing the carbon-nanotube material. The last several years have been extremely exciting. The new scientific discoveries and new knowledge base developed with nanotubes have been enormous and satisfying. We are now at the critical juncture where the demonstrations of applications need to get translated into product lines. Some of these endeavors will be successful and some will fail. The test for the nanotube material will be whether it will live up to the expectations and promises that have been flouted based on its amazing physical properties.

Acknowledgements

We thank Prof. Mauricio Terrones for the information regarding the relevance and applications of doped carbon nanotubes. The parts in this chapter on doped nanotubes were provided by Prof. Terrones and in some cases are further discussed in the contribution to this volume by *Terrones* et al. PMA acknowledges the Focus Center New York for Interconnects supported by NYSTAR for sponsoring the research. MSS acknowledges Paul W. Barone, Esther S. Jeng, Rachel A. Graff, Chang Young Lee, Hong Jin, and Daniel A. Heller for contributions to this review ME acknowledges support from the CLUSTER of Ministry of Education, Culture, Sports, Science and Technology of Japan.

References

[1] R. H. Baughman, A. A. Zakhidov, W. A. Zakhidov: Carbon nanotubes – the route toward applications, Science **297**, 787–792 (2002) 13, 16, 27
[2] B. I. Yakobson, R. E. Smalley: Fullerene nanotubes: C1,000,000 and beyond, Am. Sci. **85**, 324 (1997) 13, 16
[3] P. M. Ajayan: Nanotubes from carbon, Chem. Rev. **99**, 1787–1800 (1999) 13, 16
[4] H. W. Kroto, J. R. Heath, S. C. O'Brien, S. C. Curl, R. E. Smalley: C_{60}: buckministerfullerene, Nature **318**, 162–163 (1985) 14
[5] M. S. Dresselhaus, G. Dresselhaus, K. Sugihara, I. L. Spain, H. A. Goldberg: *Graphite Fibers and Filaments* (Springer, Berlin, Heidelberg 1988) 14, 21
[6] A. Oberlin, M. Endo, T. Koyama: Filamentous growth of carbon through benzene decomposition, J. Cryst. Growth **32**, 335–349 (1976) 14
[7] R. Saito, G. Dresselhaus, M. S. Dresselhaus: *Physical Properties of Carbon Nanotubes* (Imperial College Press, London 1998) 14
[8] S. Iijima: Helical microtubules of graphitic carbon, Nature **354**, 56–58 (1991) 15
[9] T. W. Ebbesen, P. M. Ajayan: Large scale synthesis of carbon nanotubes, Nature **358**, 220 (1992) 15
[10] S. Iijima, T. Ichihashi: Single shell carbon nanotubes of 1-nm diameter, Nature **363**, 603–605 (1993) 15

[11] D. S. Bethune, C. H. Klang, M. S. deVries, G. Gorman, R. Savoy, J. Vazquez, R. Beyers: Cobalt catalysed growth of carbon nanotubes with single atomic layer wells, Nature **363**, 605–607 (1993) 15
[12] C. Dekker: Carbon nanotubes as molecular quantum wires, Phys. Today **52**, 22–28 (1999) 17
[13] A. Javey: Ballistic carbon nanotube field-effect transistors, Nature **424**, 654–657 (2003) 17
[14] P. L. McEuen, M. S. Fuhrer, H. K. Park: Single-walled carbon nanotube electronics, IEEE Transact. Nanotechnol. **1**, 78–85 (2002) 17
[15] F. Kreup, A. P. Graham, M. Liebau, G. S. Duesberg, R. Seidel, E. Unger: Carbon nanotubes for interconnect applications, IEDM pp. 683–686 (2004) 17
[16] M. S. Arnold, A. A. Green, J. F. Hulvat, S. I. Stupp, M. C. Hersam: Sorting carbon nanotubes by electronic structure using density differentiation, Nature Nanotechnol. **1**, 60–65 (2006) 17
[17] G. Y. Zhang: Selective etching of metallic carbon nanotubes by gas-phase reaction, Science **314**, 974–977 (2006) 17
[18] B. Q. Wei, R. Vajtai, P. M. Ajayan: Reliability and current carrying capacity of carbon nanotubes, Appl. Phys. Lett. **79**, 1172 (2001) 18
[19] URL `http://en.wikipedia.org/wiki/45nm` URL: `http://en.wikipedia.org/wiki/65nm` 17
[20] S. J. Tans, A. R. M. Verschueren, C. Dekker: Room-temperature transistor based on a single carbon nanotube, Nature **393**, 49–52 (1998) 18
[21] R. Martel, T. Schmidt, H. R. Shea, T. Hertel, P. Avouris: Single- and multi-wall carbon nanotube field-effect transistors, Appl. Phys. Lett. **73**, 2447 (1998) 18
[22] A. Bachtold, P. Hadley, T. Nakanishi, C. Dekker: Reports, logic circuits with carbon nanotube transistors, Science **294**, 1317–1320 (2001) 19
[23] P. G. Collins, M. S. Arnold, P. Avouris: Engineering carbon nanotubes and nanotube circuits using electrical breakdown, Science **292**, 706–709 (2001) 19
[24] C. Klinke, J. B. Hannon, A. Afzali, P. Avouris: Field effect transistors assembled from functionalized nanotubes, Nano Lett. **6**, 906–910 (2006) 19
[25] S. M. Rossnagel, T. S. Kaun: Alteration of Cu conductivity in the size effect regime, J. Vac. Sci. Technol. B **22**, 240–247 (2004) 19
[26] C. T. White, T. N. Todorov: Quantum electronics – nanotubes go ballistic, Nature **411**, 649–651 (2001) 19
[27] A. R. Naeemi, R. Sarvari, J. D. Meindl: Performance comparison between carbon nanotube and copper interconnects for gigascale integration (GSI), IEEE Electron. Device Lett. **26**, 84–86 (2005) 19
[28] Y. M. Lin, J. Appenzeller, Z. Chen, Z. G. Chen, H. M. Cheng, P. Avouris: High-performance dual-gate carbon nanotube FETs with 40-nm gate length, IEEE Electron. Device L. **26**, 823–825 (2005) 20
[29] A. Javey, J. Guo, D. B. Farmer, Q. Wang, E. Yenilmez, R. G. Gordon, M. Lundstrom, H. Dai: Self-aligned ballistic molecular transistors and electrically parallel nanotube arrays, Nano Lett. **4**, 1319–1322 (2004) 20

[30] A. Javey, H. S. Kim, M. Brink, Q. Wang, A. Ural, J. Guo, P. McIntyre, P. McEuen, M. Lundstrom, H. Dai: High-kappa dielectrics for advanced carbon-nanotube transistors and logic gates, Nature Mater. **1**, 241–246 (2002) 20

[31] 20
URL: `http://www.nantero.com/`

[32] Q. Cao, S. H. Hur, Z. T. Zhu, Y. G. Sun, C. J. Wang, M. A. Meitl, M. Shim, J. A. Rogers: Highly bendable, transparent thin-film transistors that use carbon-nanotube-based conductors and semiconductors with elastomeric dielectrics, Adv. Mater. **18**, 304–309 (2006) 20

[33] Q. Cao, Z. T. Zhu, M. G. Lemaitre, M. G. Xia, M. S. J. A. Rogers: Transparent flexible organic thin-film transistors that use printed single-walled carbon nanotube electrodes, Appl. Phys. Lett. **88**, 113511 (2006) 20

[34] Z. Wu, Z. Chen, X. Du, J. M. Logan, J. Sippel, M. Nikolou, K. Kamaras, J. R. Reynolds, D. B. Tanner, A. F. Hebard, A. G. Rinzler: Transparent, conductive carbon nanotube films, Science **305**, 1273–1276 (2004) 21, 32

[35] 21
URL: `http://www.fibrils.com/`

[36] K. Kordás, G. Tth, P. Moilanen, M. Kumpumki, J. Vhkangas, A. Uusimki, R. Vajtai, P. M. Ajayan: Chip cooling with integrated carbon nanotube microfin architectures, Appl. Phys. Lett. **90**, 123105 (2007) 21, 22, 34

[37] F. Leroux, K. Metenier, S. Gautier, E. Frackowiak, S. Bonnamy, F. Beguin: Electrochemical insertion of lithium in catalytic multi-walled carbon nanotubes, J. Power Sources **81**, 317–322 (1999) 23

[38] A. S. Claye, J. E. Fischer, C. B. Huffman, A. G. Rinzler, R. E. Smalley: Solid-state electrochemistry of the Li single wall carbon nanotube system, J. Electrochem. Soc. **147**, 2845–2852 (2000) 23

[39] H. Shimoda, et al.: Lithium intercalation into opened single-wall carbon nanotubes: storage capacity and electronic properties, Phys. Rev. Lett. **88**, 015502 (2002) 23

[40] W. Lu, D. D. L. Chung: Anodic performance of vapor-derived carbon filaments in lithium-ion secondary battery, Carbon **39**, 493–496 (2001) 23

[41] B. Gao, A. Kleinhammes, X. P. Tang, C. Bower, L. Fleming, Y. Wu, O. Zhou: Electrochemical intercalation of single-walled carbon nanotubes with lithium, Chem. Phys. Lett. **307**, 153–157 (1999) 23

[42] M. Sato, A. Noguchi, N. Demachi, N. Oki, M. Endo: A mechanism of lithium storage in disordered carbons, Science **264**, 556–558 (1994) 23, 32

[43] M. Endo, C. Kim, K. Nishimura, T. Fujino, K. Miyashita: Recent development of carbon materials for Li ion batteries, Carbon **38**, 183–197 (2000) 23

[44] M. Endo, Y. A. Kim, T. Hayashi, K. Nishimura, T. Matsushita, K. Miyashita, M. S. Dresselhaus: Vapor-grown carbon fibers (VGCFs) basic properties and battery application, Carbon **39**, 1287–1297 (2001) 23

[45] B. E. Conway: *Electrochemical Supercapacitors-Scientific Fundamentals and Technological Applications* (Kluwer, New York 1999) 24

[46] C. Niu, E. K. Sickel, R. Hoch, D. Moy, H. Tennent: High power electrochemical capacitors based on carbon nanotube electrodes, Appl. Phys. Lett. **70**, 1480–1482 (1997) 24

[47] K. H. An, W. S. Kim, Y. S. Park, J. M. Moon, D. J. Bae, S. C. Lim, Y. S. Lee, Y. H. Lee: Electrochemical properties of high-power supercapacitors using single-walled carbon nanotube electrodes, Adv. Funct. Mater. **11**, 387–392 (2001) 24

[48] Y. J. Kim, Y. A. Kim, T. Chino, H. Suezaki, M. Endo, M. S. Dresselhaus: Chemically modified multi-walled carbon nanotubes as an additive for supercapacitors, Small **2**, 339–345 (2006) 24

[49] B. J. Landi, S. L. Castro, H. J. Ruf, C. M. Evans, S. G. Bailey, R. P. Raffaelle: CdSe quantum dot-single wall carbon nanotube complexes for polymeric solar cells, Sol. Energ. Mater. Sol. C. **87**, 733–746 (2005) 24, 26

[50] E. Kymakis, G. A. J. Amaratunga: Electrical properties of single-wall carbon nanotube-polymer composite films, J. Appl. Phys. **99**, 084302 (2006) 24, 25

[51] Z. H. Xu, Y. Wu, B. Hu, I. N. Ivanov, D. B. Geohegan: Carbon nanotube effects on electroluminescence and photovoltaic response in conjugated polymers, Appl. Phys. Lett. **87**, 263118 (2005) 24, 25

[52] A. Bachtold, M. S. Fuhrer, S. Plyasunov, M. Forero, E. H. Anderson, A. Zettl, P. L. McEuen: Scanned probe microscopy of electronic transport in carbon nanotubes, Phys. Rev. Lett. **84**, 6082–6085 (2000) 24

[53] E. Kymakis, I. Alexandrou, G. A. J. Amaratunga: High open-circuit voltage photovoltaic devices from carbon-nanotube-polymer composites, J. Appl. Phys. **93**, 1764–1768 (2003) 25

[54] E. Kymakis, G. A. J. Amaratunga: Single-wall carbon nanotube/conjugated polymer photovoltaic devices, Appl. Phys. Lett. **80**, 112–114 (2002) 25

[55] E. Kymakis, G. A. J. Amaratunga: Carbon nanotubes as electron acceptors in polymeric photovoltaics, Rev. Adv. Mater. Sci. **10**, 300–305 (2005) 25

[56] S. Bhattacharyya, E. Kymakis, G. A. J. Amaratunga: Photovoltaic properties of dye functionalized single-wall carbon nanotube/conjugated polymer devices, Chem. Mater. **16**, 4819–4823 (2004) 25

[57] E. Kymakis, G. A. J. Amaratunga: Photovoltaic cells based on dye-sensitisation of single-wall carbon nanotubes in a polymer matrix, Sol. Energ. Mater. Sol. C. **80**, 465–472 (2003) 25, 26

[58] G. M. A. Rahman, D. M. Guldi, R. Cagnoli, A. Mucci, L. Schenetti, L. Vaccari, M. Prato: Combining single wall carbon nanotubes and photoactive polymers for photoconversion, J. Am. Chem. Soc. **127**, 10051–10057 (2005) 25

[59] R. P. Raffaelle, B. J. Landi, J. D. Harris, S. G. Bailey, A. Hepp: Carbon nanotubes for power applications, Mater. Sci. Eng. B-Solid **116**, 233–243 (2005) 25

[60] A. J. Miller, R. A. Hatton, S. R. P. Silva: Water-soluble multiwall-carbon-nanotube-polythiophene composite for bilayer photovoltaics, Appl. Phys. Lett. **89**, 123115 (2006) 25

[61] A. J. Miller, R. A. Hatton, S. R. P. Silva: Interpenetrating multiwall carbon nanotube electrodes for organic solar cells, Appl. Phys. Lett. **89**, 133117 (2006) 25

[62] S. B. Lee, T. Katayama, H. Kajii, H. Araki, K. Yoshino: Electrical and optical properties of conducting polymer-C-60-carbon nanotube system, Synth. Met. **121**, 1591–1592 (2001) 25

[63] B. J. Landi, R. P. Raffaelle, S. L. Castro, S. G. Bailey: Single-wall carbon nanotube-polymer solar cells, Prog. Photovoltaics **13**, 165–172 (2005) 25

[64] J. A. Rud, L. S. Lovell, J. W. Senn, Q. Qiao, J. T. Mcleskey: Water soluble polymer/carbon nanotube bulk heterojunction solar cells, J. Mater. Sci. **40**, 1455–1458 (2005) 25
[65] L. Valentini, J. M. Kenny: Novel approaches to developing carbon nanotube based polymer composites: fundamental studies and nanotech applications, Polymer **46**, 6715–6718 (2005) 25
[66] S. Spiekermann, G. Smestad, J. Kowalik, L. M. Tolbert, M. Grtzel: Poly(4-undecyl-2,2'-bithiophene) as a hole conductor in solid state dye sensitized titanium dioxide solar cells, Synth. Met. **121**, 1603–1604 (2001) 25
[67] M. Gratzel: Photoelectrochemical cells, Nature **414**, 338–344 (2001) 25
[68] W. Feng, Y. Feng, Z. Wu, A. Fujii, M. Ozaki, K. Yoshino: Optical and electrical characterizations of nanocomposite film of titania adsorbed onto oxidized multiwalled carbon nanotubes, J. Phys.-Condens. Matter. **17**, 4361–4368 (2005) 26
[69] C. D. Spataru, S. Ismail-Beigi, L. X. Benedict, S. G. Louie: Quasiparticle energies, excitonic effects and optical absorption spectra of small-diameter single-walled carbon nanotubes, Appl. Phys. A-Mater. **78**, 1129–1136 (2004) 26, 40
[70] M. Ichida, S. Mizuno, Y. Tani, Y. Saito, A. Nakamura: Exciton effects of optical transitions in single-wall carbon nanotubes, J. Phys. Soc. Jpn. **68**, 3131–3133 (1999) 26
[71] S. Kazaoui, N. Minami, B. Nalini, Y. Kim, K. Hara: Near-infrared photoconductive and photovoltaic devices using single-wall carbon nanotubes in conductive polymer films, J. Appl. Phys. **98**, 084314 (2005) 26
[72] P. J. Britto, K. S. V. Santhanam, A. Rubio, A. Alonso, P. M. Ajayan: Improved charge transfer at carbon nanotube electrodes, Adv. Mater. **11**, 154–157 (1999) 27
[73] G. Che, B. B. Lakshmi, E. R. Fisher, C. R. Martin: Carbon nanotube membranes for electrochemical energy storage and production, Nature **393**, 346–349 (1999) 27
[74] M. Endo, Y. A. Kim, M. Ezaka, K. Osada, T. Yanagisawa, T. Hayashi, M. Terrones, M. S. Dresselhaus: Selective and efficient impregnation of metal nanoparticles on cup-stacked-type nanofibers, Nano Lett. **3**, 723–726 (2003) 27
[75] T. Yoshitake, Y. Shimakawa, S. Kuroshima, H. Kimura, T. Ichihashi, Y. Kubo, D. Kasuya, K. Takahashi, F. Kohai, M. Yudasaka, S. Iijima: Preparation of fine platinum catalyst supported on single-wall carbon nanohorns for fuel cell application, Physica B **323**, 124–126 (2002) 27
[76] C. Kim, Y. J. Kim, Y. A. Kim, T. Yanagisawa, M. Endo, M. S. Dresselhaus: Pt/Ru supported on Cup-stack typed carbon nanotubes as an electrode for fuel cell applications, J. Appl. Phys. **96**, 5903–5905 (2004) 27
[77] C. Wang, M. Waje, X. Wang, J. M. Tang, R. C. Haddon, Y. S. Yan: Proton exchange membrane fuel cells with carbon nanotube based electrodes, Nano Lett. **4**, 345–348 (2004) 27
[78] M. M. J. Treacy, T. W. Ebbesen, J. M. Gibson: Exceptionally high Young's modulus observed for individual carbon nanotubes, Nature **381**, 678–681 (1996) 27

[79] M. Yu, O. Lourie, M. J. Dyer, K. Moloni, T. F. Kelly, R. S. Ruoff: Strength and breaking mechanism of multiwalled carbon nanotubes under tensile load, Science **287**, 637–640 (2000) 27
[80] H. D. Wagner, O. Lourie, Y. Feldman, R. Tenne: Stress – induced fragmentation of multiwall carbon nanoutbes in a polymer matrix, Appl. Phys. Lett. **72**, 188–190 (1998) 27
[81] B. I. Yakobson: Mechanical relaxation and intramolecular plasticity in carbon nanotubes, Appl. Phys. Lett. **72**, 918 (1998) 27
[82] A. Cao, D. L. Dickrell, W. G. Sawyer, M. N. Ghasemi-Nejhad, P. M. Ajayan: Super-compressible foamlike carbon nanotube films, Science **310**, 1307–1310 (2005) 27, 42
[83] P. M. Ajayan, L. S. Schadler, C. Giannaris, A. Rubio: Single-walled carbon nanotube-polymer composites: Strength and weakness, Adv. Mater. **12**, 750 (2000) 28
[84] V. P. Veedu, A. Cao, X. Li, K. Ma, C. Soldano, S. Kar, P. M. Ajayan, M. N. Ghasemi-Nejhad: Multifunctional composites using reinforced laminae with carbon-nanotube forests, Nature Mater. **5**, 457–462 (2006) 28, 29
[85] J. Suhr, W. Zhang, P. M. Ajayan, N. A. Koratkar: Temperature-activated interfacial friction damping in carbon nanotube polymer composites, Nano Lett. **6**, 219–223 (2006) 28, 29
[86] L. S. Schadler, S. C. Giannaris, P. M. Ajayan: Load transfer in carbon nanotube epoxy composites, Appl. Phys. Lett. **73**, 3842 (1998) 28, 29
[87] A. Eitan, K. Y. Jian, D. Dukes, R. Andrews, L. S. Schadler: Surface modification of multiwalled carbon nanotubes: Toward the tailoring of the interface in polymer composites, Chem. Mater. **15**, 3198–3201 (2003) 29
[88] J. Suhr, N. Koratkar, P. Keblinski, P. M. Ajayan: Viscoelasticity in carbon nanotube composites, Nature Mater. **4**, 134 (2005) 29
[89] R. F. Gibson, E. O. Ayorinde, Y.-F. Wen: Vibrations of carbon nanotubes and their composites: A review, Compos. Sci. Technol. **67**, 1–28 (2007) 29
[90] B. Fragneaud, K. Masenelli-Varlot, A. González-Montiel, M. Terrones, J. Y. Cavaillé: Efficient coating of N-doped carbon nanotubes with polystyrene using atomic transfer radical polymerization, Chem. Phys. Lett. **419**, 567 (2005) 30
[91] M. Dehonor, K. M. Varlot, A. G. Montiel, C. Gauthier, J. Y. Cavaillé, H. Terrones, M. Terrones: Nanotube brushes: Polystyrene grafted covalently on CNx nanotubes by nitroxide-mediated radical polymerization, Chem. Commun. **42**, 5349–5351 (2005) 30
[92] M. Endo, S. Koyama, Y. Matsuda, T. Hayashi, Y. A. Kim: Thrombogenicity and blood coagulation of a micro-catheter prepared from carbon nanotube-nylon based composite, Nano Lett. **5**, 101–106 (2005) 30, 31
[93] S. Koyama, H. Haniu, K. Osaka, H. Koyama, N. Kuroiwa, M. Endo, Y. A. Kim, T. Hayashi: Medical application of carbon nanotube-filled nanocomposites: microcatheter, Small **2**, 1406–1411 (2006) 30, 31
[94] P. Qi, O. Vermesh, M. Grecu, A. Javey, Q. Wang, H. Dai, S. Peng, K. J. Cho: Toward large arrays of multiplex functionalized carbon nanotube sensors for highly sensitive and selective molecular detection, Nano Lett. **3**, 347–351 (2003) 31, 33

[95] J. Kong, N. R. Franklin, C. Zhou, M. G. Chapline, S. Peng, K. Cho, H. Dai: Nanotube molecular wires as chemical sensors, Science **287**, 622–625 (2000) 31, 33, 35
[96] P. W. Barone, S. Baik, D. A. Heller, M. S. Strano: Near-infrared optical sensors based on single-walled carbon nanotubes, Nature Mater. **4**, 86–92 (2005) 32, 35
[97] E. S. Jeng, A. E. Moll, A. C. Roy, J. B. Gastala, M. S. Strano: Detection of DNA hybridization using the near-infrared band-gap fluorescence of single-walled carbon nanotubes, Nano Lett. **6**, 371–375 (2006) 32, 35
[98] D. A. Heller, E. S. Jeng, T. K. Yeung, B. M. Martinez, A. E. Moll, J. B. Gastala, M. S. Strano: Optical detection of DNA conformational polymorphism on single-walled carbon nanotubes, Science **311**, 508–511 (2006) 32, 36
[99] S. Peng, K. J. Cho: Chemical control of nanotube electronics, Nanotechnol. **11**, 57–60 (2000) 32
[100] C. Y. Lee, S. Baik, J. Zhang, R. I. Masel, M. S. Strano: Charge transfer from metallic single-walled carbon nanotube sensor arrays, J. Phys. Chem. B **110**, 11055–11061 (2006) 32, 33
[101] S. Heinze, J. Tersoff, R. Martel, V. Derycke, J. Appenzeller, P. Avouris: Carbon nanotubes as Schottky barrier transistors, Phys. Rev. Lett. **89**, 106801 (2002) 32
[102] K. Bradley, J. C. P. Gabriel, A. Star, G. Grüner: Short-channel effects in contact-passivated nanotube chemical sensors, Appl. Phys. Lett. **83**, 3821–3823 (2003) 32
[103] J. Zhang, A. Boyd, A. Tselev, M. Paranjape, P. Barbara: Mechanism of NO_2 detection in carbon nanotube field effect transistor chemical sensors, Appl. Phys. Lett. **88**, 123112 (2006) 33
[104] Y. Lu, J. Li, J. Han, H. T. Ng, C. Binder, C. Partridge, M. Meyyappan: Room temperature methane detection using palladium loaded single-walled carbon nanotube sensors, Chem. Phys. Lett. **391**, 344–348 (2004) 33
[105] C. Staii, A. T. Johnson: DNA-decorated carbon nanotubes for chemical sensing, Nano Lett. **5**, 1774–1778 (2005) 33
[106] R. J. Chen, N. R. Franklin, J. Kong, J. Cao, T. W. Tombler, Y. Zhang, H. Dai: Molecular photodesorption from single-walled carbon nanotubes, Appl. Phys. Lett. **79**, 2258–2260 (2001) 33
[107] J. P. Novak, E. S. Snow, E. J. Houser, D. Park, J. L. Stepnowski, R. A. McGill: Nerve agent detection using networks of single-walled carbon nanotubes, Appl. Phys. Lett. **83**, 4026–4028 (2003) 33
[108] E. S. Snow, F. K. Perkins, E. J. Houser, S. C. Badescu, T. L. Reinecke: Chemical detection with a single-walled carbon nanotube capacitor, Science **307**, 1942–1945 (2005) 33
[109] E. S. Snow, F. K. Perkins: Capacitance and conductance of single-walled carbon nanotubes in the presence of chemical vapors, Nano Lett. **5**, 2414–2417 (2005) 33
[110] J. Wang, M. Musameh: Carbon nanotube/teflon composite electrochemical sensors and biosensors, Anal. Chem. **75**, 2075–2079 (2003.) 34
[111] M. Gao, L. M. Dai, G. G. Wallace: Biosensors based on aligned carbon nanotubes coated with inherently conducting polymers, Electroanal. **15**, 1089–1094 (2003) 34

[112] H. Tang, J. Chen, S. Yao, L. Nie, G. Deng, Y. Kuang: Amperometric glucose biosensor based on adsorption of glucose oxidase at platinum nanoparticle-modified carbon nanotube electrode, Anal. Biochem. **331**, 89–97 (2004) 34
[113] S. Hrapovic, Y. Liu, K. B. Male, J. H. T. Luong: Electrochemical biosensing platforms using platinum nanoparticles and carbon nanotubes, Anal. Chem. **76**, 1083–1088 (2004) 34
[114] K. B. Male, S. Hrapovic, Y. Liu, W. Dashan, J. H. T. Luong: Electrochemical detection of carbohydrates using copper nanoparticles and carbon nanotubes, Anal. Chim. Acta **516**, 35–41 (2004) 34
[115] H. Cai, X. Cao, Y. Jiang, P. He, Y. Fang: Carbon nanotube-enhanced electrochemical DNA biosensor for DNA hybridization detection, Anal. Bioanal. Chem. **375**, 287–293 (2003) 34
[116] S. G. Wang, R. Wang, P. J. Sellin, Q. Zhang: DNA biosensors based on self-assembled carbon nanotubes, Biochem. Biophys. Res. Comm. **325**, 1433–1437 (2004) 34
[117] K. Kerman, Y. Morita, Y. Takamura, M. Ozsoz, E. Tamiya: DNA-directed attachment of carbon nanotubes for enhanced label-free electrochemical detection of DNA hybridization, Electroanal. **16**, 1667–1672 (2004) 34
[118] J. Wang, G. Liu, M. R. Jan: Ultrasensitive electrical biosensing of proteins and DNA: Carbon-nanotube derived amplification of the recognition and transduction events, J. Am. Chem. Soc. **126**, 3010–3011 (2004) 34
[119] P. J. Britto, K. S. V. Santhanam, P. M. Ajayan: Carbon nanotube electrode for oxidation of dopamine, Bioelectroch. Bioener. **41**, 121–125 (1996) 34
[120] A. Guiseppi-Elie, C. H. Lei, R. H. Baughman: Direct electron transfer of glucose oxidase on carbon nanotubes, Nanotechnol. **13**, 559–564 (2002) 35
[121] Y.-D. Zhao, W.-D. Zhang, H. Chen, Q.-M. Luo: Direct electron transfer of glucose oxidase molecules adsorbed onto carbon nanotube powder microelectrode, Anal. Sci. **18**, 939–941 (2002) 35
[122] J. Wang, M. Li, Z. Shi, N. Li, Z. Gu: Direct electrochemistry of cytochrome c at a glassy carbon electrode modified with single-wall carbon nanotubes, Anal. Chem. **74**, 1993–1997 (2002) 35
[123] M. Musameh, J. Wang, A. Merkoci, Y. Lin: Low-potential stable NADH detection at carbon-nanotube-modified glassy carbon electrodes, Electrochem. Commun. **4**, 743–746 (2002) 35
[124] G. Li, J. M. Liao, G. Q. Hu, N. Z. Ma, P. J. Wu: Study of carbon nanotube modified biosensor for monitoring total cholesterol in blood, Biosens. Bioelectron. **20**, 2140–2144 (2005) 35
[125] K. Wu, Y. Sun, S. Hu: Development of an amperometric indole-3-acetic acid sensor based on carbon nanotubes film coated glassy carbon electrode, Sens. Actuators B-Chem. **96**, 658–662 (2003) 35
[126] K. Besteman, J. Lee, F. G. M. Wiertz, H. A. Heering, C. Dekker: Enzyme-coated carbon nanotubes as single-molecule biosensors, Nano Lett. **3**, 727–730 (2003) 35
[127] R. J. Chen, S. Bangsaruntip, K. A. Drouvalakis, N. W. S. Kam, M. Shim, Y. Li, W. Kim, P. J. Utz, H. Dai: Noncovalent functionalization of carbon nanotubes for highly specific electronic biosensors, Proc. Nat. Acad. Sci. USA **100**, 4984–4989 (2003) 35

[128] R. J. Chen, et al.: An investigation of the mechanisms of electronic sensing of protein adsorption on carbon nanotube devices, J. Am. Chem. Soc. **126**, 1563–1568 (2004) 35
[129] A. Star, et al.: Label-free detection of DNA hybridization using carbon nanotube network field-effect transistors, Proc. Nat. Acad. Sci. USA **103**, 921–926 (2006) 35
[130] X. W. Tang, et al.: Carbon nanotube DNA sensor and sensing mechanism, Nano Lett. **6**, 1632–1636 (2006) 35
[131] A. Modi, N. Koratkar, E. Lass, B. Q. Wei, P. M. Ajayan: Miniaturized gas ionization sensors using carbon nanotubes, Nature **424**, 171 (2003) 36
[132] P. Victor, et al.: Electromechanical properties of a macroscale carbon nanotube block, Appl. Phys. Lett. (2007) in review 36
[133] R. H. Baughman, C. Cui, A. A. Zhakhidov, Z. Iqbal, J. N. Barisci, G. M. Spinks, G. G. Wallace, A. Mazzoldi, D. D. Rossi, A. G. Rinzler, O. Jaschinski, S. Roth, M. Kertesz: Carbon nanotube actuators, Science **284**, 1340 (1999) 36
[134] M. W. Hamberg, et al.: An electrochemical micro actuator, in *Micro Electro Mechanical Systems*, Proc. IEEE **106** (1995) 36
[135] A. G. Rinzler, et al.: Unraveling nanotubes: Field emission from an atomic wire, Science **269**, 1550–1553 (1995) 36
[136] W. A. D. Heer, A. Chatelain, D. Ugarte: A carbon nanotube field emission electron source, Science **270**, 1179–1180 (1995) 36
[137] Y. Saito, S. Uemura: Field emission from carbon nanotubes and its applications to electron sources, Carbon **38**, 169–182 (2000) 36
[138] S. S. Fan, M. G. Chaplind, N. R. Franklin, T. W. Tombler, A. M. Cassel, H. Dai: Self oriented regular arrays of carbon nanotubes and their field emission properties, Science **283**, 512–514 (1999) 36
[139] Y. Saito, S. Uemura, K. Hamaguchi: Cathode ray tube lighting elements with carbon nanotube field emitters, Jpn. J. Appl. Phys. **37**, L346–L348 (1998) 37
[140] W. B. Choi, D. S. Chung, J. H. Kang, H. Y. Kim, Y. W. Jin, I. T. Han, Y. H. Lee, J. E. Jung, N. S. Lee, G. S. Park, J. M. Kim: Fully sealed high brightness carbon nanotube field emission display, Appl. Phys. Lett. **75**, 3219–3231 (1999) 37
[141] J. M. Bonard, J. P. Salvetat, T. Stockli, W. A. Deheer, L. Forro, A. Chatelain: Field emission from single-wall carbon nanotube film, Appl. Phys. Lett. **73**, 918–920 (1998) 37
[142] H. Kurachi, S. Uemura, J. Yotani, T. Nagasako, H. Yamada, H. Ezaki, T. Maesoba, R. Loutfy, A. Moravsky, T. Nakazawa, Y. Saito: in *Proc. 21st Int. Display Res. Conf./8th Int. Display Workshops: Soc. Inf. Display* (2001) pp. 1245–1248 37
[143] K. Seko, J. Kinoshita, Y. Saito: In situ transmission electron microscopy of field-emitting bundles of double wall carbon nanotubes, Jpn. J. Appl. Phys. **44**, L743–L745 (2005) 37
[144] Y.-W. Son, S. Oh, J. Ihm, S. Han: Field emission properties of double-wall carbon nanotubes, Nanotechnol. **16**, 125–128 (2005) 37
[145] T. Hiraoka, T. Yamada, K. Hata, D. N. Futaba, H. Kurachi, S. Uemura, M. Yumura, S. Iijima: Synthesis of single and double walled carbon nanotubes forests on conducting metal foils, J. Am. Chem. Soc. **128**, 13338–13339 (2006) 37

[146] J.-C. Charlier, M. Terrones, M. Baxendale, V. Meunier, T. Zacharia, N. L. Rupesinghe, W. K. Hsu, N. Grobert, H. Terrones, G. A. J. Amaratunga: Enhanced electron field emission in B-doped carbon nanotubes, Nano Lett. **2**, 1191 (2002) 37
[147] D. Golberg, P. S. Dorozhkin, Y. Bando, Z. C. Dong, C. C. Tang, Y. Uemura, N. Grobert, M. Reyes-Reyes, H. Terrones, M. Terrones: Structure, transport and field-emission properties of compound nanotubes: CNx vs. BNCx (x < 0.1), Appl. Phys. A-Mater. **76**, 499 (2003) 38
[148] M. Doytcheva, M. Kaiser, M. Reyes-Reyes, M. Terrones, N. de Jonge: Electron emission from individual nitrogen-doped multi-walled carbon nanotubes, Chem. Phys. Lett. **396**, 126 (2004) 38
[149] D. A. Heller, et al.: Optical detection of DNA conformational polymorphism on single-walled carbon nanotubes, Science **311**, 508–511 (2006) 38
[150] P. Cherukuri, et al.: Near-infrared fluorescence microscopy of single-walled carbon nanotubes in phagocytic cells, J. Am. Chem. Soc. **126**, 15638–15639 (2004) 38, 41
[151] P. Cherukuri, et al.: Mammalian pharmacokinetics of carbon nanotubes using intrinsic near-infrared fluorescence, Proc. Nat. Acad. Sci. USA **103**, 18882–18886 (2006) 38
[152] D. A. Heller, et al.: Single-walled carbon nanotube spectroscopy in live cells: Towards long-term labels and optical sensors, Adv. Mater. **17**, 2793–2799 (2005) 38
[153] C. Klumpp, et al.: Functionalized carbon nanotubes as emerging nanovectors for the delivery of therapeutics, BBA-Biomembranes **1758**, 404–412 (2006) 38
[154] D. Pantarotto, et al.: Translocation of bioactive peptides across cell membranes by carbon nanotubes, Chem. Commun. **2004**, 16–17 (2004) 38, 39, 41
[155] N. W. S. Kam, et al.: Nanotube molecular transporters: Internalization of carbon nanotube-protein conjugates into mammalian cells, J. Am. Chem. Soc. **126**, 6850–6851 (2004) 38, 39, 41
[156] D. Cai, et al.: Highly efficient molecular delivery into mammalian cells using carbon nanotube spearing, Nature Method. **2**, 449–454 (2005) 38, 39
[157] Q. Lu, et al.: RNA polymer translocation with single-walled carbon nanotubes, Nano Lett. **4**, 2473–2477 (2004) 38, 39
[158] N. W. S. Kam, H. J. Dai: Carbon nanotubes as intracellular protein transporters: Generality and biological functionality, J. Am. Chem. Soc. **127**, 6021–6026 (2005) 38, 39
[159] W. Wu, et al.: Targeted delivery of amphotericin B to cells by using functionalized carbon nanotubes, Angew. Chem. Int. Edit. **44**, 6358–6362 (2005) 38, 39
[160] D. Pantarotto, et al.: Functionalized carbon nanotubes for plasmid DNA gene delivery, Angew. Chem. Int. Edit. **43**, 5242–5246 (2004) 38, 39, 40, 41
[161] N. W. S. Kam, Z. Liu, H. J. Dai: Functionalization of carbon nanotubes via cleavable disulfide bonds for efficient intracellular delivery of siRNA and potent gene silencing, J. Am. Chem. Soc. **127**, 12492–12493 (2005) 38, 39, 40
[162] Zheng, et al.: Structure-based carbon nanotube sorting by sequence-dependent DNA assembly, Science **302**, 1545–1548 (2003) 39

[163] M. I. H. Panhuis, et al.: Characterization of an interaction between functionalized carbon nanotubes and an enzyme, J. Nanosci. Nanotechnol. **3**, 209–213 (2003) 39
[164] R. J. Chen, et al.: Noncovalent sidewall functionalization of single-walled carbon nanotubes for protein immobilization, J. Am. Chem. Soc. **123**, 3838–3839 (2001) 39
[165] J. Liu, et al.: Fullerene pipes, Science **280**, 1253–1256 (1998) 39
[166] H. Hu, et al.: Chemically functionalized carbon nanotubes as substrates for neuronal growth, Nano Lett. **4**, 507–511 (2004) 39
[167] Y. Liu, et al.: Polyethylenimine-grafted multiwalled carbon nanotubes for secure noncovalent immobilization and efficient delivery of DNA, Angew. Chem. Int. Ed. **44**, 4782–4785 (2005) 39
[168] G. Pastorin, et al.: Double functionalisation of carbon nanotubes for multimodal drug delivery, Chem. Commun. **11**, 1182–1184 (2006) 39
[169] R. Singh, et al.: Binding and condensation of plasmid DNA onto functionalized carbon nanotubes: Toward the construction of nanotube-based gene delivery vectors, J. Am. Chem. Soc. **127**, 4388–4396 (2005) 39
[170] C. Salvador-Morales, et al.: Complement activation and protein adsorption by carbon nanotubes, Mol. Immunol. **43**, 193–201 (2006) 39
[171] N. W. S. Kam, et al.: Carbon nanotubes as multifunctional biological transporters and near-infrared agents for selective cancer cell destruction, Proc. Nat. Acad. Sci. USA **102**, 11600–11605 (2005) 40
[172] C. F. Lopez, et al.: Understanding nature's design for a nanosyringe, Proc. Nat. Acad. Sci. USA **101**, 4431–4434 (2004) 41
[173] I. Lynch: Are there generic mechanisms governing interactions between nanoparticles and cells? Epitope mapping the outer layer of the protein-material interface, Physica A **373**, 511–520 (2007) 41
[174] B. D. Chithrani, A. A. Ghazani, W. C. W. Chan: Determining the size and shape dependence of gold nanoparticle uptake into mammalian cells, Nano Lett. **6**, 662–668 (2006) 41
[175] N. W. S. Kam, Z. A. Liu, H. J. Dai: Carbon nanotubes as intracellular transporters for proteins and DNA: An investigation of the uptake mechanism and pathway, Angew. Chem. Int. Ed. **45**, 577–581 (2006) 41
[176] F. Osaki, et al.: A quantum dot conjugated sugar ball and its cellular uptake on the size effects of endocytosis in the subviral region, J. Am. Chem. Soc. **126**, 6520–6521 (2004) 41
[177] Gao, H. J., W. D. Shi, L. B. Freund: Mechanics of receptor-mediated endocytosis, Proc. Nat. Acad. Sci. USA **102**, 9469–9474 (2005) 41
[178] A. T. Woolley, C. Guillemette, C. L. Cheung, D. E. Housman, C. M. Lieber: Direct haplotyping of kiobase size DNA using carbon nanotube probes, Nature Biotechnol. **18**, 760–763 (2000) 42
[179] J. H. Hafner, C. L. Cheung, A. T. Woolley, C. M. Lieber: Structural and functional imaging with carbon nanotube AFM probes-review, Prog. Biophys. Mol. Bio. **77**, 73–110 (2001) 42
[180] 42
URL: `http://www.xidex.com`
[181] H. Dai, N. Franklin, J. Han: Exploiting the properties of carbon nanotubes for nanolithography, Appl. Phys. Lett. **73**, 1508–1510 (1998) 43

[182] B. J. Hinds, N. Chopra, T. Rantell, R. Andrews, V. Gavalas, L. G. Bachas: Aligned multiwalled carbon nanotube membranes, Science **303**, 62–65 (2004) 43
[183] J. K. Holt, H. G. Park, Y. M. Wang, M. Stadermann, A. B. Artyukhin, C. P. Grigoropoulos, A. Noy, O. Bakajin: Fast mass transport through sub-2-nanometer carbon nanotubes, Science **312**, 1034–1037 (2006) 43
[184] A. Srivastava, O. N. Srivastava, S. Talapatra, R. Vajtai, P. M. Ajayan: Carbon nanotube filters, Nature Mater. **3**, 610–614 (2004) 43
[185] K. Kordas, et al.: Inkjet printing of electrically conductive patterns of carbon nanotubes, Small **2**, 1021–1025 (2006) 43
[186] L. M. Ericson, et al.: Macroscopic, neat, single-walled carbon nanotube fibers, Science **305**, 1447–1450 (2004) 43
[187] Y.-L. Li, I. A. Kinloch, A. H. Windle: Direct spinning of carbon nanotube fibers from chemical vapor deposition synthesis, Science **304**, 276–278 (2004) 43
[188] J. Wei, H. Zhu, D. Wu, B. Wei: Carbon nanotube filaments in household light bulbs, Appl. Phys. Lett. **84**, 4869–4871 (2004) 43
[189] A. Cao, V. P. Veedu, X. Li, Z. Yao, M. N. Ghasemi-Nejhad, P. M. Ajayan: Multifunctional brushes made from carbon nanotubes, Nature Mater. **4**, 540–545 (2005) 43
[190] B. Yurdumakan, N. R. Raravikar, P. M. Ajayan, A. Dhinojwala: Synthetic gecko foot-hairs from multiwalled carbon nanotubes, Chem. Commun. **30**, 3799–3801 (2005) 43
[191] A. B. Dalton, et al.: Continuous carbon nanotube composite fibers: Properties, potential applications and problems, J. Mater. Chem. **14**, 1 (2004) 44
[192] L. Sun, F. Banhart, A. V. Krasheninnikov, J. A. Rodriguez-Manzo, M. Terrones, P. M. Ajayan: Carbon nanotubes as high-pressure cylinders and nanoextruders, Science **312**, 1199–1202 (2006) 44
[193] P. M. Ajayan, O. Stephan, P. Redlich, C. Colliex: Carbon nanotubes as removable templates for metal oxide nanocomposites and nanostructures, Nature **375**, 564 (1995) 44
[194] F. S. Ou, M. M. Shaijumon, L. Ci, D. Benicewicz, R. Vajtai, P. M. Ajayan: Multisegmented one-dimensional hybrid structures of carbon nanotubes and metal nanowires, App. Phys. Lett. **89**, 243122 (2006) 44
[195] G. W. Meng, Y. J. Jung, A. Cao, R. Vajtai, P. M. Ajayan: Controlled fabrication of hierarchically branched nanopores, nanotubes and nanowires, Proc. Nat. Acad. Sci. **102**, 7074 (2005) 44
[196] N. Sano: Low cost synthesis of singlewalled carbon nanohorns using the arc in water method using gas injection, J. Phys. D: Appl. Phys. **37**, L17–L20 (2004) 44
[197] A. A. Shvedova, V. Castranova, E. R. Kisin, D. Schwegler-Berry, A. R. Murray, V. Z. Gandelsman, A. Maynard, P. Baron: Exposure to carbon nanoutbe material: assessment of nanotube cytoxicity using human keratinocyte cell, J. Toxicol. Environ. Health **66**, 1909–1926 (2003) 45
[198] C. W. Lam, J. T. James, R. McCluskey, R. L. Hunter: Pulmonary toxicity of single-wall carbon nanotubes in mice 7 and 90 days after intratracheal instillation, Toxicol. Sci. **77**, 126–134 (2004) 45

[199] D. B. Warheit, B. R. Laurence, K. L. Reed, D. H. Roach, G. A. Reynolds, T. R. Webb: Comparative pulmonary toxicity assessment of single-wall carbon nanotubes in rats, Toxicol. Sci. **77**, 117–125 (2004) 45
[200] A. D. Maynard, O. P. A. Baron, M. Foley, A. A. Shvedova, E. R. Kisin, V. Castranova: Exposure to carbon nanotube material: aerosol release during the handling of unrefined single walled carbon nanotube material, J. Toxicol. Environ. Heath **67**, 87–107 (2004) 45
[201] S. Koyama, M. Endo, Y. A. Kim, T. Hayashi, T. Yanagisawa, K. Osaka, H. Koyama, H. Haniu, N. Kuroiwa: Role of systemic T-cells and histopathological aspects after subcutaneous implantation of various carbon nanotubes in mice, Carbon **44**, 1079–1092 (2006) 45, 46
[202] G. Jia, H. Wang, L. Yan, X. Wang, R. Pei, T. Yan, Y. Zhao, X. Guo: Cytoxicity of carbon nanomaterials: Single wall nanotube, multi-wall nanotube, and fullerene, Environ. Sci. Technol. **39**, 1378–1383 (2005) 45
[203] D. Cui, F. Tian, C. Ozkan, M. Wang, H. Gao: Effect of single wall carbon nanotubes on human HEK293 cells, Toxicol. Lett. **155**, 73–85 (2005) 45
[204] Y. Sato, K. Shibata, H. Kataoka, S. Ogino, F. Bunshi, A. Yokoyama, K. Tamura, T. Akasaka, M. Uo, K. Motomiya, B. Jeyadevan, R. Hitakeyama, F. Watari, K. Tohji: Mol. BioSyst. **1**, 142–145 (2005) 45
[205] R. F. Service: Science policy: Priorities needed for nano-risk research and development, Science **314**, 45 (2006) 45
[206] D. X. Cui, et al.: Effect of single wall carbon nanotubes on human HEK293 cells, Toxicol. Lett. **155**, 73–85 (2005) 45
[207] S. K. Manna, et al.: Single walled carbon nanotube induces oxidative stress and actiaves nuclear transcription factor – kappa B in human keratinocytes, Nano Lett. **55**, 1676–1684 (2005) 45
[208] V. E. Kagan, et al.: Direct and indirect effects of single walled carbon nanotubes on RAW 264.7 macrophages: Role of iron, Toxicol. Lett. **165**, 88–100 (2006) 45
[209] C. M. Sayes, et al.: Functionalization density dependence of single-walled carbon nanotubes cytotoxicity in vitro, Toxicol. Lett. **161**, 135–142 (2006) 45
[210] H. Dumortier, et al.: Functionalized carbon nanotubes are non-cytotoxic and preserve the functionality of primary immune cells, Nano Lett. **6**, 1522–1528 (2006) 45
[211] N. W. S. Kam, et al.: Carbon nanotubes as multifunctional biological transporters and near-infrared agents for selective cancer cell destruction, Proc. Nat. Acad. Sci. USA **102**, 11600–11605 (2006) 45

Index

Carbon-Nanotube Metrology

Ado Jorio[1,2], Esko Kauppinen[3], and Abdou Hassanien[4]

[1] Departamento de Física, Universidade Federal de Minas Gerais (UFMG), Belo Horizonte, MG, 30.123-970, Brazil
adojorio@fisica.ufmg.br
[2] Divisão de Metrologia de Materiais, Instituto Nacional de Metrologia, Normalização e Qualidade Industrial (INMETRO), Duque de Caxias, RJ,25250-020 Brazil
[3] NanoMaterials Group, Laboratory of Physics and Center for New Materials (CNM), Helsinki University of Techology (HUT) and VTT Biotechnology, Espoo, Finland
esko.kauppinen@vtt.fi
[4] Nanotechnology Research Institute, AIST, 1-1-1 Umezono, Tsukuba, Ibaraki 305-8568, Japan
abdou.hassanien@aist.go.jp

Abstract. Scientific and industrial metrology provided tools for technological growth and innovation, by fostering competitiveness and creating a favorable environment for scientific and industrial development. Every major country has its own metrology institute to support companies in increasing their productivity and the quality of their goods and services. The fast development of carbon-nanotube science and applications urged studies on metrology, standardization and industrial quality control. Development of protocols for the definition of sample parameters like structural metrics, physical properties and stability are important for both research and applications of single-, double- and multiwall carbon nanotubes. This work discusses some of the experimental techniques that are broadly used for carbon-nanotube characterization, including scanning probe microscopy and spectroscopy, electron microscopy and diffraction, and optical spectroscopies, from the molecular level to bulk properties, addressing achievements, limitations and directions where further research is needed for the development of standards and protocols for metrology, standardization and industrial quality control of carbon nanotubes.

1 Introduction

The worldwide adoption of a democratic process is guaranteed in science through the rigid review processes and the setting of impact parameters of the scientific journals. When turning to applications, the Metrology Institutes take over this responsibility, following the regulations of society, aimed at defending both the citizen and the environment. Historically, the diffusion of a coherent measurement system, based on invariant physical properties, was the consequence of a radical transformation in the world [1]. Before the 19th century, the number of different measurement systems in use basically reflected the number of different economical activities, and also societal and

A. Jorio, G. Dresselhaus, M. S. Dresselhaus (Eds.): Carbon Nanotubes,
Topics Appl. Physics **111**, 63–100 (2008)

technological practices from one location to another on our planet. In 1889, as a result of the work of many scientists over many decades (including names like Lagrange and Lavoisier), a standardization document was approved at the Weights and Length General Conference in Paris [2]. The fundamental metrology determination of the national and international prototypes for the meter and kilogram were defined, based on platinum irradiated by iridium. The equations relating national and international standards for the meter and kilogram were within the limits of ± 0.01 mm and ± 1 mg. Even though technology has improved substantially and the international system of units is now well established, nanoscience promises a revolution in technology. The development of nanotechnology is now bringing us back to the very basic problem of defining metrics and measurement systems, back to the basics of metrology.

The fast development of nanotube science and applications urges emphasis to be given to studies on their metrology, standardization and industrial quality control [3–8]. The development of protocols for the definition of sample parameters like structural metrics (carbon–carbon distance, nanotube diameter, chiral angle, surface area), physical properties (optical, thermal, mechanical), morphology (isomer population, purity, homogeneity) and stability (dispersability, biocompatibility and health effects) are important both for advancing future research and for stimulating future applications of nanotubes. These protocols are expected to be applicable not only to carbon nanotube metrology, but also to influencing developments in the exploding field of nanomaterials, where metrology issues will also drive technological growth and innovation.

The problem of carbon nanotube metrology could be addressed using two approaches, by focusing on 1. carbon nanotube properties, or 2. advances in experimental metrology techniques. Although the description by materials properties is sometimes more convenient for practical uses, the discussion by technique allows a deeper understanding of the metrology capabilities and limitations, and it is more broadly applicable to nanometrology overall. For this reason, this work focuses on the experimental techniques that are broadly used for carbon nanotube characterization, from the molecular level to bulk properties, addressing the achievements, limitations and directions where further research is needed for the development of standards and protocols for metrology, standardization and industrial quality control of carbon nanotubes. Through understanding of the characterization capabilities of nanomaterials, it is possible to establish parameters and protocols, and to address some of the challenging tasks that await future applications of nanotubes. The basis for the development of novel materials can also be fostered by these efforts.

Section 2 focuses on electron microscopies, including operational principles along with recent developments in instrumentation. Section 3 describes scanning probe microscopy and spectroscopy, going down to the atomic structure of carbon nanotubes towards defect characterization. Section 4 dis-

cusses optical characterization, important to extract physical properties in the "nanoworld" by using a massless and contactless probe. Section 5 is the summary where we elaborate on the future of the nanometrology of nanotubes.

2 Electronic Microscopy

2.1 Introduction

Among the various analytical techniques for carbon nanotubes, transmission electron microscopy (TEM) is the one by which carbon nanotubes were discovered when observing carbon soot produced in an electric arc between graphite electrodes [9]. In a transmission electron microscope, the electron wave mainly experiences two basic processes during its propagation from the specimen to the image: interaction with the specimen and modulation by the electron-optical lens system [10]. During the first process, the electron wave picks up the structure information of the specimen. In the second process, the structure information is transferred in the microscope. Due to the unique design of the TEM, the electron wave carrying the structure information forms an electron-diffraction pattern (EDP) on the back focal plane of the objective lens and an image on the imaging plane. Therefore, the EDP and the image can be simultaneously observed in the TEM. By using an aperture at the back focal plane of the objective lens to select the transmitted electron beam for imaging, a bright-field (BF) image is formed. A dark-field (DF) image is created by using one of the diffracted beams in the EDP for imaging. If a large aperture is selected to allow both the transmitted electron beam and a set of diffracted beams to pass through, a high-resolution TEM (HRTEM) image is formed. Mainly due to the spherical aberration (Cs) of the objective lens in the microscope, the contrast of an HRTEM image is seriously affected by the focusing conditions, and the image resolution is limited. As a result, a HRTEM image is usually not straightforward to interpret and it is hard to directly observe the atomic structure of carbon nanotubes (CNTs). Due to the recent development of the Cs-corrected HRTEM [11], the resolution of the microscope has dramatically improved to the sub-Å level. It is worth remembering that to minimize spherical aberration, the microscope is preferably operated at an acceleration voltage lower than 120 kV to minimize the knock-on atomic displacement damage of the CNTs by high-energy electrons, and to increase the image contrast.

Scanning electron microscopes (SEM) are frequently used to observe carbon nanotubes due to their wider availability, relative ease of use, as well as simpler sample preparation methods compared to TEM and scanning tunneling microscopy (STM). Both nanotube powder samples as well as individual tubes on a bulk substrate (e.g., silicon wafer) can be observed by SEM. A fine

electron probe is scanned across the sample surface while recording the current of the electrons emitted from the sample surface due to beam–surface interactions. The image is the intensity of the emitted electron current versus beam location at the sample. An image can be formed by the secondary electrons emitted from the sample surface as well as by the backscattered primary electrons. In modern, field emission electron-source-based instruments, the energy filtering of emitted electrons is also possible. Several electron detectors, including standard chamber detectors, in-lens (or semi-in-lens) and backscattered detectors can be used in parallel. The energy of the primary electrons is varied from 100 V to 30 keV. The secondary electron imaging resolution of the state-of-the-art field emission source SEMs vary from 0.4 nm at 30 kV to 1.6 nm at 1 kV acceleration voltage. Accordingly, the walls of the single and multiwall nanotubes cannot be observed with SEM. Similarly, whether small tubes are isolated or bundled cannot be resolved.

2.2 Sample Preparation

The preparation of carbon-nanotube samples for electron microscopy study is dependent on the type of CNTs, the analytical methods and the purpose of the analysis. For TEM study of a CNT powder sample, usually a small amount of the powder is dissolved in ethanol or acetone. The concentration of the solution is estimated by its color. A light-gray solution is just right for TEM observation (with the tip of the tweezers, pick up a very tiny amount of CNT blacks and put them into 0.5 ml ethanol until you see the solution changing from colorless to some color). One drop of such a solution is then dropped onto a holey carbon film on a copper TEM grid. When the carbon nanotubes are produced in the gas phase by a floating catalyst method, direct collection of CNTs onto conventional TEM holy-carbon grids by applying an electric field, diffusion or thermophoresis is convenient [12]. The concentration of the carbon nanotubes on the grid is controlled by the collection time. For structural determination of SWNTs or DWNTs, the concentration of the nanotubes should be carefully controlled so that individual carbon nanotubes can be found. When the carbon nanotubes are produced on bulk solid substrates, like Si with its native oxide, one can scratch the CNTs off the substrate surface with a knife, or alternatively make a cross section with for example focused ion beam (FIB) methods. For SEM observation, basically all samples that are suitable for TEM observation are also ready for study by SEM. In addition, CNTs grown on substrates can be directly observed by SEM without preparation. In order to reduce the hydrocarbon contamination of the nanotubes in the microscope, especially for high-magnification observation, it is preferable to pretreat the sample by heating the specimen in vacuum at 150 °C for 30 min to one hour.

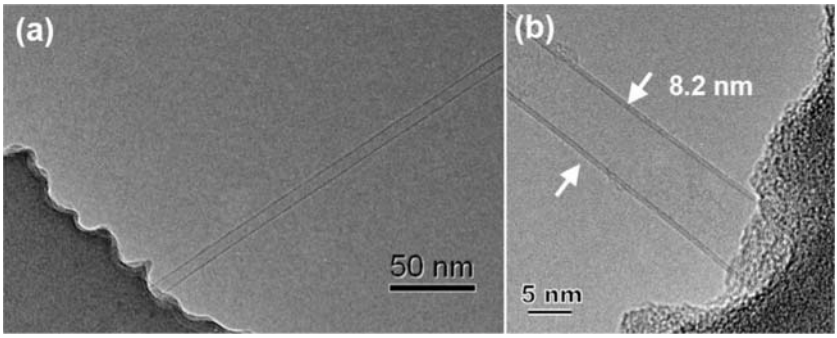

Fig. 1. TEM images of a large-diameter DWNT produced from CO by supported CVD process on Si_3N_4-membrane substrate: (**a**) at a low magnification; (**b**) at a high magnification

2.3 Morphology

SEM and TEM are both effective for observation of the morphology of CNT products. TEM has an obvious advantage over SEM in that its high-resolution capacity enables distinguishing the carbon nanotube types, i.e., single wall, or double wall, or multi-wall, and if the carbon nanotubes are in bundles or not. Even with high-resolution TEM, a high enough magnification is needed to resolve the number of walls. Figures 1a and b are TEM images of the same double-wall carbon nanotube that is produced by a CVD process on a Si_3N_4-membrane substrate [13]. It looks very much like an individual single-wall carbon nanotube in Fig. 1a since the magnification is too low to resolve the wall structure. Besides conventional morphology observation, HRTEM is required to see the atomic structure of carbon nanotubes directly. Generally from TEM images it is rather direct to tell the purity and quality of a carbon-nanotube sample. Software packages for image analysis can give quantitative information about purity for larger nanotube ensembles. However, other methods like differential scanning calorimetry or near-infrared spectroscopy can give such a quantitative analysis more easily [5–8].

SEM is very useful for observing the overall structure of both the nanotube powder and individual nanotubes, prior to TEM and STM observation. In particular, SEM imaging at low voltages is frequently used to locate individual tubes at the silicon wafer with a native oxide, due to enhanced secondary electron emission induced by the tube at the oxide surface. Figures 2a–d show low-voltage secondary-electron images of about 2 nm diameter SWNTs on the thin, holey SiO_2 film. When imaging the tube on a silica surface with 2 kV, secondary electrons are emitted from about a 100-nm wide area, whereas the tube at the hole (i.e., in the vacuum) appears to be below 5 nm in diameter. When reducing the voltage to 0.3 kV, the apparent diameter of the tube on a silica surface is reduced to about 50 nm. When imaging at 0.1 kV voltage, the tube diameter appears to be the same both in vacuum and at the silica

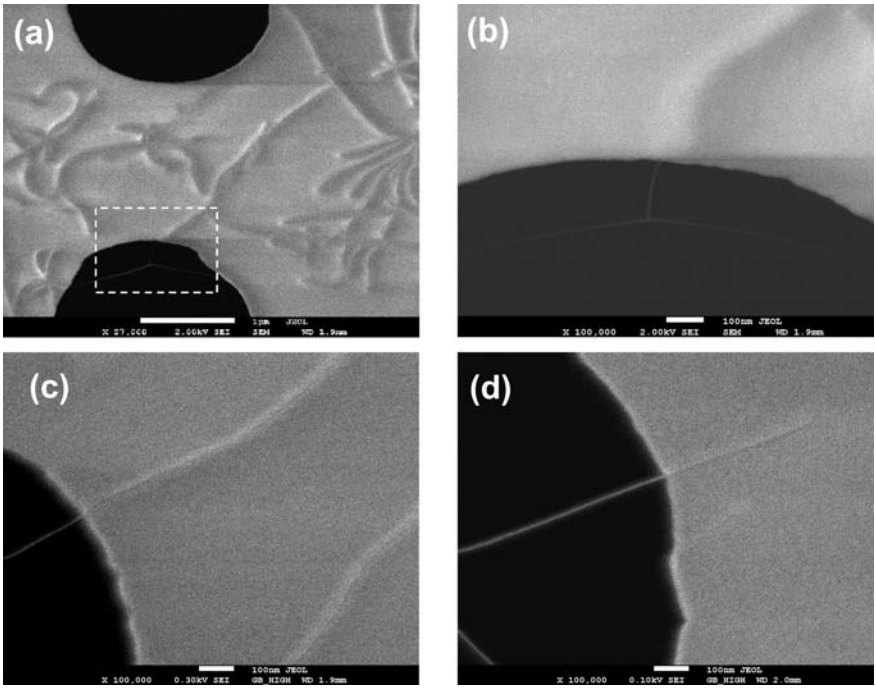

Fig. 2. The effect of the acceleration voltage on the secondary-electron images of SWNTs on a holey, thin SiO_2 film. Images (**a**) and (**b**) were recorded with 2 kV electron beam energy, (**c**) with 0.3 kV and (**d**) with 0.1 kV. *Scale bar* in image (a) is 1 μm and in (b–d) 100 nm

surface. Figures 3a–d show the effect of the emitted-electron-energy filtering on the apparent size of the SWNT. The low-energy secondary electrons, emitted from the large area surrounding the tube, are responsible for the bright appearance of SWNTs at a silica surface. Low-energy SEM imaging, electron-beam lithography and ion-beam deposition introduce significant damage to the nanotube structure [14].

2.4 Atomic Structure by HRTEM

Due to the resolution limit in conventional transmission electron microscopes, HRTEM images of SWNTs usually appear as a pair of dark lines without useful contrast in between. By carefully tuning the focusing condition, and accordingly the contrast transfer function of the TEM, and working at a low accelerating voltage (120 kV), one can obtain Moiré fringes from the rolled-up graphene layers between the two intense dark lines [15]. Fourier transform of such an image will produce a pattern that is similar to the EDP, based on which the nanotube chiral indices (n, m) can be determined. Since the Fourier transform pattern is usually rather indistinct, and on the other hand the tube

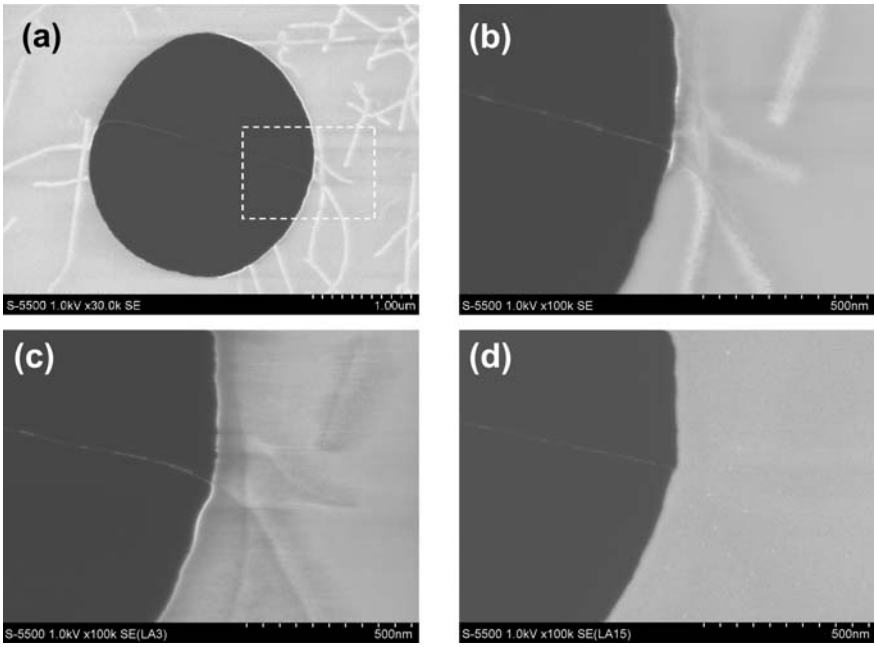

Fig. 3. The effect of energy filtering on the secondary-electron images of SWNTs at a holey, thin SiO_2 film, as observed with 1-keV primary electrons: (**a**) and (**b**) no filtering of emitted-electron energy, i.e., the image with mainly the low-energy secondary electrons, (**c**) lowest-energy secondary electrons are removed, (**d**) with backscattered electrons only. *Scale bar* in image (a) is 1 μm and in (b–d) 500 nm

axis may not be perpendicular to the incident electron beam, a trial-and-error image-simulation procedure is needed for (n, m) determination. This method was practically confined to small-diameter nanotubes, "because the smaller one has only a few possible solutions due to a specific diameter" even though the useful signal from images of small tubes "appear more diffused than those of the larger one." [16]

In the Cs-corrected TEM, the spherical aberration of the objective lens is compensated electron-optically by using an additional set of electromagnetic hexapoles, called the Cs corrector. The improvement in spatial resolution enables direct observation of the carbon atom arrangements, and accordingly the determination of (n, m). Though the Cs-corrected electron microscopy is a rather promising technique for structural determination of single-wall carbon nanotubes [17, 18], the stability of the nanotube under the electron beam is a practical limitation of this method, in addition to the present high cost of a Cs-corrected microscope.

2.5 Chiral Indices Determination by Electron Diffraction

Electron diffraction was the first technique used to characterize SWNTs at the time when they were discovered [9, 19], and it is still one of the most powerful methods for their structural analysis. Advanced nanobeam electron-diffraction techniques uniquely allow direct probing of individual nanotubes and characterization of their atomic structure. The chiral angle can also be calculated from the distance ratios between the diffraction layerlines [20], and the tube diameter can be evaluated from the equatorial layerline profile of the diffraction pattern. The intensity distribution of the equatorial layerline is described by a zero-order Bessel function $J_0(\pi D_0 R)$, based on which the tube diameter is determined. The determination of the chiral angle by the above-mentioned method is more or less independent of the tilt angle of the nanotube with respect to the incident electron beam. However, the evaluation of the tube diameter depends sensitively on the tilting of the tube unless the diffraction patterns are intrinsically calibrated with standard materials, which are typically unavailable in the experiment. In the absence of such standards, absolute calibration of a SWNT EDP depends on the value of the carbon–carbon (C–C) bonding distance, which has an uncertainty between 0.142 nm and 0.144 nm (i.e., 2 pm). Also, calibration of the EDP by using the C–C bonding distance is either tilt sensitive or complicated by the curvature of the tube. Two independent techniques have been used recently for the direct determination of chiral indices (n, m) of single-wall carbon nanotubes from their electron-diffraction patterns, as described below.

2.5.1 Bessel-Function Analysis [21]

For the normal-incidence condition, the intensity modulation along a diffracted layerline in the EDP is dominated by a single squared Bessel function (hereafter termed the Bessel factor) of a certain order n that is simply associated with the (n, m) indices [22, 23]. This enables direct evaluation of the chiral indices of carbon nanotubes. Unambiguous determination of (n, m) then depends on reliably retrieving the Bessel orders from the corresponding Bessel factor plots. By comparing the ratios measured from the intensity profile along a given layerline in the EDP with the characteristic ratios, the Bessel order can be retrieved, which can then be ascribed to the chiral indices (n, m) of the nanotube. For a more confident (n, m) determination, a full consideration of the tilt effect should be included in the electron-diffraction analysis of SWNTs.

2.5.2 Intrinsic Layerline Distance Analysis [24]

For this purpose, we introduce a novel nondimensional "intrinsic layerline spacing" concept for electron-diffraction analysis of SWNTs. The intrinsic layerline spacing (ξ_i) corresponding to each nonequatorial layerline

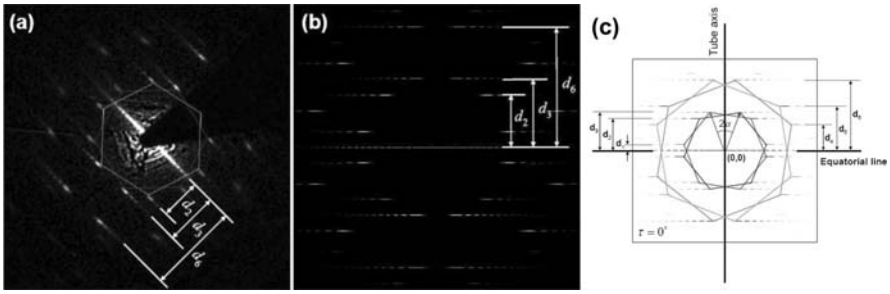

Fig. 4. (**a**) An experimental electron-diffraction pattern of an individual SWNT; (**b**) the corresponding simulated EDP of a (23,10) nanotube at a tilt angle of 10°; (**c**) a simulated EDP from a (12,7) SWNT in normal incidence ($\tau = 0°$) showing the layerline structure [24]

is defined by $\xi_i = D_0\ d_i$. By geometrical considerations, expressions for ξ_i of the six most important layerlines (d_i, $i = 1, 2, \ldots, 6$, Fig. 4) are given by $\xi_1 = (n - m)/\sqrt{3}\pi$, $\xi_2 = (n + 2m)/\sqrt{3}\pi$, $\xi_3 = (2n + m)/\sqrt{3}\pi$, $\xi_4 = (\sqrt{3}m)/\pi$, $\xi_5 = (\sqrt{3}n)/\pi$, $\xi_6 = [\sqrt{3}(n + m)]/\pi$. Simultaneous solutions of any two expressions of ξ_i give directly the chiral indices (n, m). When the (n, m) are determined, the tilt angle can simply be evaluated by, for instance, $\cos\tau = \xi_3/\xi_3^\tau = (2n+m)/(\sqrt{3}\pi\ \ \xi_3^\tau)$, where ξ_3^τ represents the actual measured value of the intrinsic layerline spacing under the tilt effect, and τ is the tilt angle of the nanotube. This method does not require any calibration of the EDP and the effect of the tilt is compensated for the (n, m) determination.

In Fig. 4 an example of an analysis of the EDP for a SWNT prepared by ethanol aerosol precursors is given using the two methods comparatively to yield $(n, m) = (25, 10)$ for a tube with a tilt angle τ of about 10°. Without taking the tilt angle into account, the nanotube was previously evaluated to be a (21,9) metallic tube [22].

The diameter measured directly from HRTEM typically has up to 10% error. The "intrinsic layerline distance analysis" method is aimed at unambiguous structural determination of single-wall carbon nanotubes by electron diffraction. Since only the layerline spacing and the interval between the zeros along the equatorial line are involved in the measurement, this method has no significant limitations for the (n, m) determination with EDP.

3 Scanning Probe Microscopy

3.1 Introduction

Scanning probe microscopy (SPM) refers to a large family of microscopies that use a sharp needle to sense material properties [25–27]. Currently, scanning tunneling microscopy (STM) and atomic force microscopy (AFM) are

the most widely used techniques in the real-space mapping of carbon nanotubes (CNTs) properties. Ever since its invention in 1982 [28], STM continues to be a very versatile tool in surface science and technology. The principle behind the STM relies on the tunneling of electrons between a sample and a sharp tip. In the normal STM spectroscopic mode of operation (STS), the tip is stabilized around 1 nm above the sample and the current is recorded as the bias voltage, V_{bias}, which is ramped (normally $-3\,\text{V} \leq V_{\text{bias}} \leq +3\,\text{V}$) across the sample–tip barrier. Under these conditions, electrons tunnel across the gap from the sample to the tip or vice versa (depending on the bias polarity). In the imaging mode, STM keeps the current constant through the feedback loop and records the changes in the gap distance as the tip rasters over the sample. By using this mode of operation, we obtain a direct 3D image of the sample surface structure [28]. The STM owes its high vertical resolution to the exponential dependence of the tunnel current (I) on the gap distance (d), (an increase of 0.1 nm in d_{t} causes I to decrease by one order of magnitude). However, the lateral resolution at an atomic scale is largely determined, amongst other factors, by the tip quality and tip–sample interactions. Tips are usually made of hard metals to withstand prolonged imaging without changing their electronic properties. Metals like tungsten or platinum–iridium alloys (e.g., $\text{Pt}_{0.90}\text{Ir}_{0.10}$) are the most suitable for this purpose. As a crucial check before imaging, the tip quality must be verified by acquiring STS data of a known sample, such as Au(111) or graphite. Most of the electrons tunnel elastically, and therefore the tunneling current features several signatures of the molecular energy levels. The signatures of these excited states can be seen clearly as peaks in the plot of differential conductance as a function of sample bias. The full width of the peak at half-maximum (FWHM) intensity is an important quantity to measure as it gives many details about the nature of the excited states of the sample and their coupling to the perturbation by the tip electric field and substrate interactions. If the FWHM of successive peaks is smaller than their energy-level spacing, then each state can be mapped directly by STM. As we shall see in section 3.4, even single-electron states can be imaged one by one. The rest of the electrons, less than 10 %, inelastically tunnel (IET) from the tip to the sample due to coupling with phonons, thus allowing us to probe and excite vibrational modes of single molecules at surfaces [29–31]. The IET process manifests itself as a conductance enhancement at the characteristic energy of the vibrational modes [30], and can be easily seen in the first derivative of the differential conductance (see the contribution by *Hartschuh*). Unlike Raman spectroscopy, the selection rules are more relaxed in inelastic electron spectroscopy (IETS) [32]. For example, optically forbidden modes may be active in IETS and even appear as strong bands [33]. In that regard, the high-resolution power of STM, both in space and energy, has allowed us not only to confirm the interplay between structural and local electronic properties, but also to identify the influence of electron–phonon interactions on the electronic band structure. In this section we highlight the

usefulness of SPM techniques in characterizing the mesoscopic structure and properties of carbon nanotubes.

3.2 Sample Preparation

For SPM studies on single molecules, making a suitable density of SWNTs on a clean surface is the most crucial step for acquiring meaningful data. Ideally one desires that 10 % or more of the deposited tubes be isolated individual tubes with a density of one tube per $200 \times 200\,\mathrm{nm}^2$, because the process of finding the individual CNTs can be time consuming. There are several methods to deposit individual SWNTs on substrates. Here, we will briefly discuss two methods that are very suitable for subsequent characterization by SPM techniques. The first one uses a stamping technique developed by *Hones*' group at Columbia University [34]. This method is especially suitable to study a CVD-grown CNT, since it requires no further treatments of the raw soot to yield individual tubes. Moreover, it allows individual SWNTs to be transferred to different substrates, thus giving us the opportunity to perform various complementary measurements on the same structure [35]. The second method uses the sonication of a purified or raw CNT soot to disperse the material into individual tubes and small ropes. Typically, a small amount (a few micrograms) of SWNT soot is sonicated in 5 mL of dichloroethane until the material is totally dispersed (for laser-ablation-produced nanotubes a sonication power of 60 W for about 30 min would be enough to disperse the nanotubes). A 3 μL of the sonicated CNTs solution is cast on the Au(111) substrates, then briefly washed with a few droplets of isopropanol alcohol and blow dried with pure nitrogen gas. To ensure surface cleanliness, and therefore reliable STS spectroscopy, samples are immediately introduced into a high-vacuum chamber and preferably annealed at 100 °C for a few hours to ensure the total removal of a water layer or any residues of organic solvents. Finally, the samples are loaded into the ultra high vacuum (UHV) STM system, which can be cooled to liquid-helium temperature for atomically resolved spectroscopic measurements. This method is relatively faster and easier than other methods but has the disadvantages of being invasive and produces a low yield of individual SWNTs.

3.3 Imaging the Structure and Electronic Properties of SWNTs

Soon after the discovery of SWNTs [36], several groups [37–41] reported the structure of CNTs using STM and AFM but these results were not correlated with their electronic properties. It was not until 1998 when several research groups [42–44] confirmed the interplay between the structure and the electronic properties. This was a crucial finding as it gave direct proof of the most important prediction for nanotubes, namely that the tubes can be either metallic or semiconducting depending on their structural parameters. In

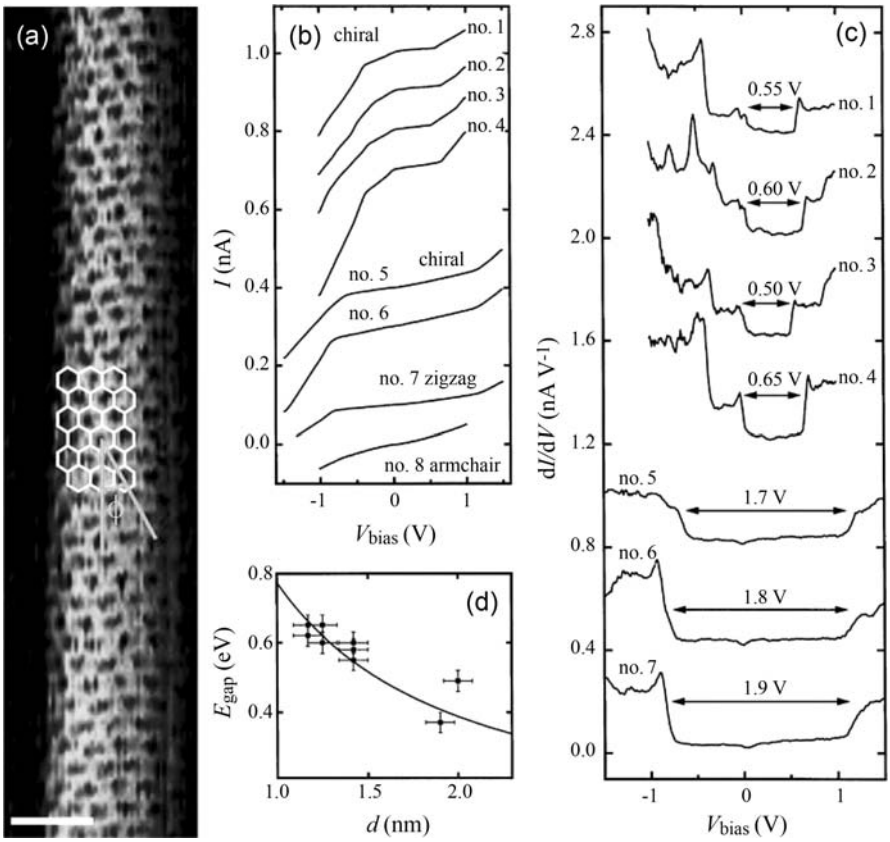

Fig. 5. STM topography and spectroscopy on SWNTs. (**a**) An atomically resolved image of a zigzag SWNT; $\theta = 0^\circ$ and $d_t = 1.2\,\text{nm}$. The *scale bar* is 1 nm. Reproduced from [45]. (**b**) I–V curves with kinks below $\pm 1\,\text{V}$ are semiconducting, the rest are metallic with a finite density of states. (**c**) Differential conductance as a function of sample bias. The peaks are due to van Hove singularities characteristic of one-dimensional bands. (**d**) The energy gaps scale inversely with the diameter of semiconducting NTs. Reproduced from [42]

Fig. 5a we show an atomically resolved SWNT image taken at room temperature [45]. The hexagonal arrangements of carbon hexagons on the CNT wall are clearly visible, which allow the precise determination of the chirality. The easiest way to determine the chirality is to measure the angle between raw hexagons and the CNT axis (see Fig. 5a).

Due to tip–tube convolution effects, the apparent tube diameter is exaggerated by a factor of 2 or more. A better estimate of the CNT diameter can be obtained by measuring its height. In the ideal case, height resolution in an STM is very high, something better than 0.01 nm due to the logarithmic

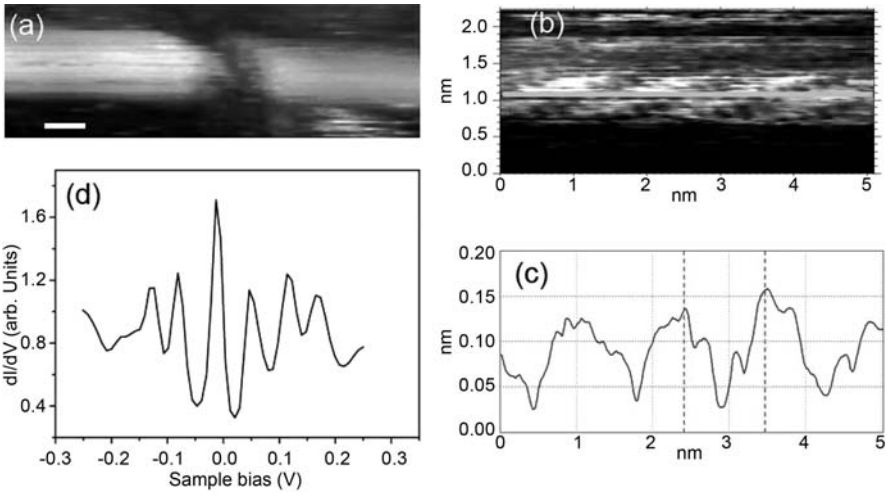

Fig. 6. Single-electron states on SWNT. (**a**) An individual CNT is cut by applying a voltage pulse of 5 V. (**b**) Atomically resolved image on a 20-nm long CNT showing two different oscillations; one is due to the lattice and the other is due to the interference of electrons on SWNT lattice. (**c**) A line profile along the *highlighted line* in (**b**). (**d**) the $\mathrm{d}I/\mathrm{d}V$ *curve* shows peaks due to single-electron states as electrons enter the dot one by one

dependence between the tunneling current and the tip–sample distance. This resolution can be achieved on atomically flat substrates like highly ordered pyrolytic graphite (HOPG) or MoS_2. In a nanotube, however, there are other factors that must be considered. Tip–tube topology tends to show elongated deformation in the hexagon centers on the lateral directions, making it difficult to decide where exactly the tube axis is. Tube–STM-tip interaction might underestimate the height due to local deformations. This problem can be reduced dramatically by restricting the bias window to values around 1 eV and currents within 100 pA. Substrate–tube van der Waals interaction is expected to deform the tubes, influencing also the STS results for tubes larger than 2 nm [46]. This is of course less relevant for small diameter nanotubes (below 1 nm).

The spacing between the first van Hove singularities is given by $E_\mathrm{g} = 2\gamma_0 a_{\mathrm{C\text{–}C}}/d_\mathrm{t}$ (γ_0 is the nearest-neighbor tight-binding overlap integral and $a_{\mathrm{C\text{–}C}}$ is the carbon–carbon distance [47]), so that we can also estimate d_t from E_g [41]. The electronic properties can be obtained by mapping the current–voltage (I–V) characteristics at different locations on the CNT and on the bare substrate [42–44]. Figure 5b shows typical examples of STS I–V curves taken on different SWNTs. Some of these curves show metallic behavior as I increases linearly with the applied sample bias, while others display semiconducting behavior as I is nearly zero up to a certain threshold above

which I increases rapidly. To investigate the electronic band structure, we need to measure the differential conductance as a function of applied sample bias. This is usually determined by numerical differentiation of the I–V curves or is more conveniently measured directly using lock-in techniques. Figure 5c shows the measured $\mathrm{d}I/\mathrm{d}V$ versus V_{bias}. Peaks reflect the van Hove singularities characteristic of the one-dimensional energy bands of CNTs. All CNTs with a zero density of states inside the gap are semiconductors, and the rest are metallic. The semiconducting gap is typically $< 1\,\mathrm{eV}$ and is inversely proportional to d_{t}, as expected (see Fig. 5d).

By any scanning probe means, diameter measurements for supported SWNT with d_{t} above 2 nm are a challenge. The radial deformations are expected to dramatically modify the LDOS (local density of states). In Fig. 5d the fit (solid line) gives $\gamma_0 = 2.7 \pm 0.1\,\mathrm{eV}$, but deviations between the solid line and the data points go up to 60 meV for a $\sim$ 2-nm diameter tube. Several factors can contribute to this deviation. The data were taken on a flat Au substrate, and interaction effects (plus electronic noise) cause broadening of the linewidth [42]. Inhomogeneities in substrate–nanotube interactions may occur due to local defects or imperfect contact "roughness". Finally, the $\gamma_0 = 2.7\,\mathrm{eV}$ value is inconsistent with optical results that indicate much larger values for E_{g} [47]. The discrepancy between optics and STS are partially due to the fact that STM is a local technique, which does not require a large assembly of atoms to probe the energy gap. On the other hand, the optics will see collective effects and local defects may not be seen due to low signal intensity (see chapter by *Ando*). Near-field optics (see the chapter by *Hartschuh*) is expected to shed some light on such differences. To minimize the interaction, one should consider suspending the nanotube over trenches; in this case the E_{g}, and thereby the diameter determination, would be more accurately determined.

3.4 Single-Electron States of SWNTs

The previous results focused on the overall band structure of SWNTs ($\sim 1\,\mu\mathrm{m}$) in a high-energy range ($\sim 3\,\mathrm{eV}$). However, in order to understand the full picture of the band structure, we need to study low-level excitations. These details are easily accessed by looking at single-electron excitation in the vicinity of the Fermi level.

To access low-level excitations experimentally we need to increase the energy-level spacing, ΔE, to a value larger than the FWHM of single states. This can be achieved by confining the electron waves to smaller lengths ($< 30\,\mathrm{nm}$). A rough estimate of ΔE is given by $hv_{\mathrm{F}}/2L$ eV, where h is Planck's constant, v_{F} is the Fermi velocity and L is the CNT length. In the case of a 20-nm long CNT, $\Delta E = 0.08\,\mathrm{eV}$, which allows easy resolution of single states at moderately low temperature (77 K or below) [48]. In Fig. 6 the CNT is shortened to 20 nm by applying a single voltage pulse of 5 V at the

desired location (see Fig. 6a). Higher-resolution images show two periodicities: one is due to atomic lattice corrugations (see Fig. 6b top) and the other due to interference of electron waves as they bounce off the tube edges in a fashion similar to a particle in a box (see Fig. 6b bottom). The low-bias STS $\mathrm{d}I/\mathrm{d}V$ curve shows peaks, which are due to single-electron states (Coulomb blockade, see Fig. 6d). As electrons enter the dot one by one, we can easily map single-electron excited state profiles by plotting $\mathrm{d}I/\mathrm{d}V$ as a function of position on the CNT [48].

3.5 Defects

The structural quality of SWNTs is of prime importance when it comes to electronic applications since some defects cause degradation to device performance. Generally speaking, any deviation from the prescribed hexagonal carbon arrangement is considered as a defect. However, not all defects are undesirable; for example, two CNTs of different electronic character can join together via heptagon–pentagon pair to form an intramolecular junction (IMJ). Such structures are quite interesting for electronic applications since the junction can function as a diode (in the case of a metallic–semiconductor IMJ). Both transport and atomically resolved STM spectroscopy studies have confirmed the expected behavior of these devices [49–51].

STM also offers the potential to study the influence of structural defects on the electronic properties [52, 53]. In Fig. 7a we show one type of defect in the form of a void due to missing hexagons from the SWNT lattice. Features associated with defects can usually be seen in high-resolution images as bright spots due to the scattering of electron waves in their vicinity. If we sample the tunneling currents within a narrow bias window, $< 75\,\mathrm{mV}$, an interference pattern can be observed (as peak paring, Fig. 7b and c). By analyzing the decay of the interference signal, we can study the effect of electron–electron (e–e) or electron–phonon (e–ph) interactions. Figure 7b shows an atomically resolved image of a Fermi-electron wavepacket as it scatters on the edge of an armchair lattice [52]. The signal intensity of the interference pattern decays within 8 nm away from the edge, indicating coupling with a dephasing process due to e–e and e–ph interactions. In the proximity of the Fermi level of a suspended SWNT, the e–ph interaction is less relevant [54] and the dephasing process is mainly due to an intratube e–e interaction [55]. Indeed the range of the interference signals becomes larger for suspended CNTs as a result of the reduced coupling to the substrate [55].

However, due to scattering (as well as screening) of electron waves in the vicinity of defects, the interference patterns can mask the local atomic structure, thereby making it difficult to identify the atomic structure of local defects. Increasing the bias window is expected to decrease the interference signal intensity and the signal due to atomic structure can be more pronounced. *Ishigami* et al. [56] used a novel technique in which they iterated

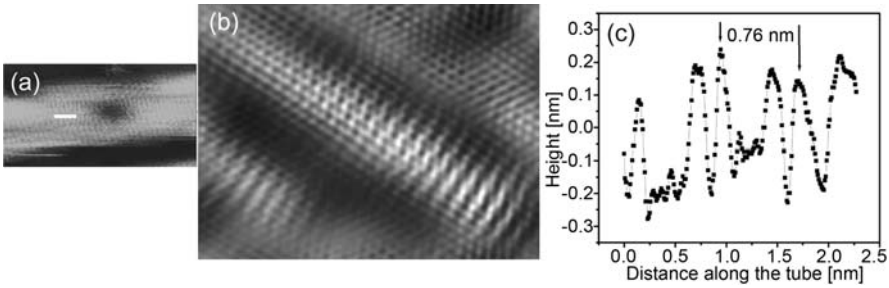

Fig. 7. Defects on a SWNT lattice. (**a**) Missing hexagons on a SWNT. Reproduced from [55]. (**b**) Interference pattern due to Fermi electrons near the CNT edge. (**c**) A line profile near the edge in (b) showing a peak-pairing behavior with a periodicity 0.76 nm. Reproduced from [52]

a model structure of an intermolecular junction, containing a pentagon–heptagon pair, obtaining a good match between theoretical and experimental data of both STS and topographic STM images. In principle, their approach can be used to identify other types of defects on CNTs, although it is clearly desirable to probe the structure directly without the need for elaborate theoretical modelling. This is a challenge for future research.

3.6 Local Vibrational Spectroscopy in SWNTs

The high lateral resolution of STM can be utilized to probe the local vibrational modes of SWNTs by detecting inelastic tunneling processes, especially near defects. Unlike conventional optical spectroscopy, which requires averaging over an area of the surface, inelastic tunneling spectroscopy with STM (IETS-STM) can probe the vibrational spectroscopy with a lateral resolution approaching atomic dimensions [30]. Combining IETS with ETS gives us the opportunity to investigate the correlation between phonon modes, structural deformation and local electronic properties. Among the vibrational modes of a SWNT, the RBM of SWNTs ($\sim$ 10–45 meV), in particular is sensitive not only to defects and local environment but also to local deformation such as bends, twists or radial distortion. *Vital* et al. [57] have studied the local phonon spectroscopy of SWNTs and confirmed the predicted relation between the diameter (d_t) and radial breathing mode frequency (ω_{RBM}), $\omega_{RBM} = C/d_t$; where C is a constant (see also the chapter by *Hartschuh*). They have demonstrated an elegant method to characterize the influence of topological defects and mechanical deformation on the electronic properties by monitoring the spatial variation of the RBM energy near the intermolecular junction, cap region and crossed CNT junctions [57, 58]. The mechanical interaction between crossed CNTs can cause a radial distortion and induce dramatic changes in the electronic properties. For example, a

semiconducting gap can totally disappear in the crossing region. As expected, pronounced variations in the ω_{RBM} were also detected, which reflect the reliability of IETS to monitor local mechanical interactions in CNTs. Signatures of electrically excited phonons can also be seen as additional small peaks around the main elastic tunneling peaks in the plot of the differential conductance versus sample bias voltage. These extra peaks are due to the opening of IET channels at certain characteristic energies in which phonon-assisted tunneling occurs. Only certain phonon modes can participate in the IET process. The necessary condition is that their decay rate must be much slower than the electron-injection rate. This means that, previously excited phonons can exchange energy with successive tunneling electrons and thereby cause electrons to gain (or lose) energy. In a remarkable experiment *LeRoy* et al. [59] have demonstrated that the tunneling of single electrons can populate and detect the low-k optical-phonon mode (RBM) on suspended SWNTs. A key factor in these experiments is how to minimize CNT-substrate interactions in order to reduce the lifetime broadening of ET that otherwise would mask the IET peaks. Interestingly, the e–ph interaction has also been confirmed in transport experiments where equally spaced low-level excitations occur parallel to the Coulomb diamond edges [60]. More detailed discussion about this technique is presented in the contribution by *Hartschuh*.

4 Optics

4.1 Basic Principles

Optical techniques have been largely used to characterize carbon nanotubes. The advantages of optics rely on both experimental and fundamental aspects. Experimentally, the techniques are readily available, relatively simple to perform, quick, and can be performed at room temperature and under ambient pressure. Fundamentally, the optical techniques are nondestructive and noninvasive because they use the photon, a massless and chargeless particle, as a probe. Furthermore, optical experiments can be carried out at the single-nanotube level [61–63] due to the unusually high optical response of nanotubes, which is a consequence of the one-dimensional confinement of their electronic structure [64].

Despite the specificity of each optical technique, the basis for the understanding of the optical responses from carbon nanotubes is common to all optical spectroscopies and can be represented by the so-called Kataura plot, proposed by *Kataura* et al. in 1999 [65]. This plot was presented in the first volume [47], but the knowledge behind it has developed largely in the past 4 years. A Kataura plot is shown in Fig. 8a. Each point in this plot represents one optical transition energy E_{ii} ($i = 1, 2, 3, \ldots$) for a specific (n, m) SWNT plotted as a function of nanotube diameter (d_{t}). A specific (n, m) carbon

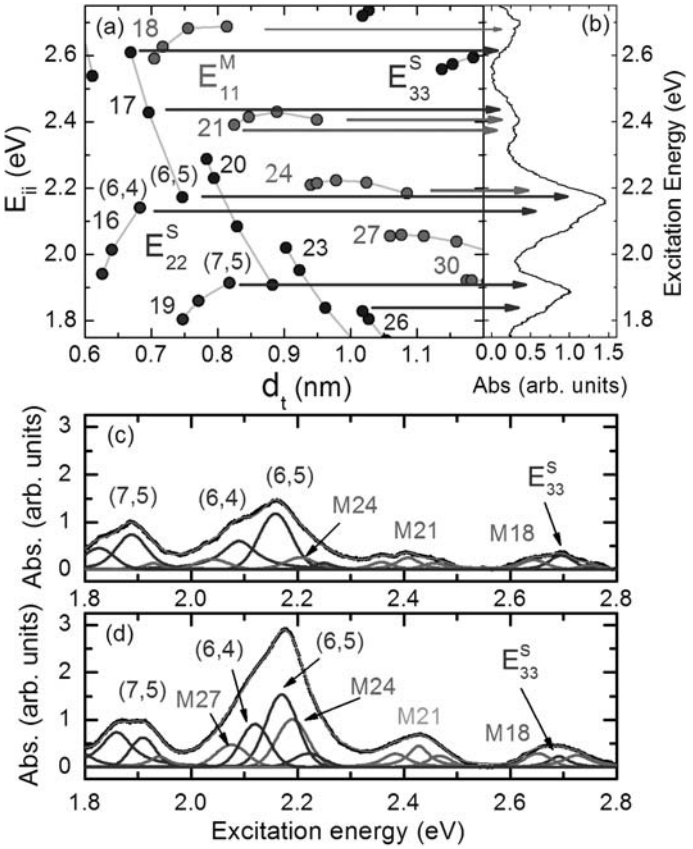

Fig. 8. (**a**) The Kataura plot in the diameter range of tubes in a CoMoCAT SWNT sample. (**b**) The optical absorption in the CoMoCAT SWNT sample dispersed in aqueous solution with SDS, within the energy range shown in (a). (**c**) Shows the optical absorption spectrum for the CoMoCAT SWNT sample wrapped by DNA and (**d**) shows the same spectrum as in (b). (c) and (d) have been analyzed for their (n,m) contents. *Gray* and *black* Lorentzians indicate metallic and semiconducting tubes, respectively [66]

nanotube will absorb light, and reveal the many different optical responses, when it is illuminated resonantly by photons with energy E_{ii}.

Important geometrical trends, as discussed in the contribution by D. *Tománek* et al., are observed and drive the observed optical processes in terms of: 1. families of $(2n + m) = \text{const}$, which group tubes with similar d_t and different θ (light gray lines connecting points in Fig. 8a), and families $(n-m) = \text{const}$, which group tubes with similar θ and different d_t; 2. the three categories with $\text{mod}\,[(2n+m), 3] = 0, 1, 2$. The $\text{mod}\,0$ denotes metallic tubes (dark gray bullets in Fig. 8a), while the $\text{mod}\,1$ and 2 denote the lower or up-

per branches in semiconducting tubes (black bullets Fig. 8a). Whether mod 1 or 2 will be the upper or lower branch inside a given E_{ii} subband depends on the level (i subindex), alternating with i. Tubes with $\mathrm{mod}[(2n+m),3] = 1$ and 2 are called type 1 and type 2 semiconducting tubes, respectively. These categories have been also defined using $\mathrm{mod}[(n-m),3] = 0,1,2$, but the type 1 and type 2 definition will in this case be reversed relative to the definition based on $\mathrm{mod}[(2n+m),3]$. Notation is important for metrology, and one must be careful when defining categories whether it is the $(2n+m)$-type or $(n-m)$-type that is used.

An enormous number of experimental and theoretical studies have been done in order to establish the Kataura plot [67], i.e., to establish the (n,m) dependence for E_{ii}. The first and second optical levels for semiconducting tubes, E_{11}^{S} and E_{22}^{S}, respectively, are related to strongly bound excitons (see contributions by *Spataru* et al. and by *Ando*, and [67]) while for the higher-lying levels E_{ii}^{S}, $i > 3$, the electronic continuum might decrease the exciton binding energies [68]. E_{11}^{M} is the lowest set of transition energies for metallic SWNTs. Good agreement between experimental and theoretical values for E_{ii} has been obtained by using an extended (nonorthogonal, symmetry-adapted) tight-binding model [69, 70] plus diameter–dependent many-body corrections [71]. A simple expression for E_{ii}, that can be used to build a Kataura plot, has been introduced recently [68]:

$$E_{ii}(p,d_{\mathrm{t}},\theta) = \left\{ a\frac{p}{d_{\mathrm{t}}}\left[1 + b\log\frac{c}{p/d_{\mathrm{t}}}\right] + \beta_p \cos 3\theta/d_{\mathrm{t}}^2 \right\} + \gamma/d_{\mathrm{t}}\,, \tag{1}$$

with $a = 1.049\,\mathrm{eVnm}$, $b = 0.456$ and $c = 0.812\,\mathrm{nm}^{-1}$ and $p = 1$, 2, 3, 4, 5 for E_{11}^{S}, E_{22}^{S}, E_{11}^{M}, E_{33}^{S}, E_{44}^{S}, respectively. The experimental β_p values for the lower(upper) E_{ii} branches are $-0.07(0.05)$, $-0.19(0.14)$, -0.19(not observed), $-0.42(0.42)$ and $-0.4(0.4)$ for $p = 1$, 2, 3, 4 and 5, respectively. Each term has its physical origin, as discussed in [68], and the last term (outside the curly brackets) applies only for the E_{ii} levels with $p > 3$, and $\gamma = (0.305 \pm 0.004)\,\mathrm{eVnm}$ was found.

This functional is consistent with experimental results on CoMoCAT and HiPco tubes in SDS aqueous solution, alcohol-grown aligned SWNT samples and isolated SWNTs suspended on Si trenches, measured by resonance Raman spectroscopy, photoluminescence excitation and Rayleigh scattering, as discussed in [68]. However, the E_{ii} values are expected to change with changes in the environment (within 1–10 %, e.g., see [72] for bundling, and contributions by *Spataru* et al. and *Lefebvre* et al. for temperature- and pressure-dependent effects). Environmental effects are a big challenge for metrology, and advances are obtained by taking the same nanotube and putting it in different environments. Controlled and systematic experiments are needed.

4.2 Optical Absorption

Optical absorption (OA) is the simplest optical technique, from both an experimental and analytic point of view. OA can be used easily to show the presence of SWNTs in the sample [3], from the observation of absorption peaks related to the first and second optical transition from semiconducting tubes (E_{11}^{S} and E_{22}^{S}), and the first optical level of metallic tubes (E_{11}^{M}). For higher optical levels, the optical absorption response gets buried due to the absorption by σ-bonded electrons [65]. OA can also be used to characterize the metal vs. semiconducting SWNT separation process, or just the separation of tube bundles into isolated SWNTs (dispersability) (see the contribution by Lefebvre et al. and [5]). A detailed discussion, including sample preparation and step-by-step procedures has been established by *Arepalli* et al. [5].

Figures 8a and b show the relation between the OA profile of a CoMoCAT sample [66] and the Kataura plot. Basically, light will be absorbed when in resonance with E_{ii} values for the (n, m) nanotubes in the sample. The resonance width depends strongly on sample environment, and the broad peaks observed in Fig. 8b are actually related to groups of unresolved absorption profiles for different (n, m) SWNTs with similar E_{ii} values. For example, the peak centered at 1.9 eV is mostly due to absorption at the E_{22}^{S} level for semiconducting SWNTs with $(2n + m) = 19$ and 23. The peak centered at 2.1 eV has a strong contribution from the absorption of the E_{22}^{S} from the $(6, 5)$ tube, known to be very abundant when using this special growth technique [73], but also from the E_{22}^{S} from other (n, m) tubes, plus the contribution from metallic tubes (E_{11}^{M}) with $(2n + m) = 24$. The peak centered at 2.4 eV has a contribution mostly from E_{11}^{M} for metallic SWNTs with $(2n + m) = 21$.

As discussed above, in OA it is difficult to resolve the spectra from tubes with different (n, m) that have similar E_{ii}. Figures 8c and d show the spectral analysis for the optical absorption spectra of two CoMoCAT SWNT samples, one dispersed in an SDS aqueous solution, Fig. 8c, and the other wrapped with DNA, Fig. 8d. The black and gray Lorentzians (FWHM 80 meV) are associated with semiconducting and metallic SWNTs, respectively. This analysis is only possible if you know *a priori* the E_{ii} values in the sample. A small change in E_{ii} would compromise the analysis of the abundance of specific (n, m) SWNTs. This is the challenge introduced by environmental effects.

However, the presence of groups absorbing at similar frequencies can be used, for example, to characterize the separation between metallic and semiconducting tubes. From the spectra in Figs. 8c and d one can see a subtraction of the signal related to metallic tubes in the DNA-wrapped sample, indicating a DNA-induced separation between metallic and semiconducting tubes. The (n, m)-dependent OA spectra can be resolved when a sample has a small diameter distribution, and this approach is effective mainly for smaller-diameter tubes. For larger-diameter tubes the number of different (n, m) with similar E_{ii} increases. As a rule of thumb, when the bands in the Kataura plot are well separated from one another, the distinction between one $(2n + m)$

family and another can be effectively done, and for small diameter tubes, individual (n, m) can be identified from the absorption spectra (as for Raman scattering, as discussed in the next section).

Comparative analysis performed on different samples, like for Figs. 8c and d can be made accurately [66]. For an absolute population analysis, however, like defining how many per cent of one given sample is metallic and semiconducting, or is related to a given (n, m) species, it is important to know the optical absorption efficiency as a function of (n, m), E_{ii} and the environemt. For example, while the results in Fig. 8 indicate a DNA-induced separation between metallic and semiconducting tubes, studies have to be performed to assure that what is changing is really the sample population, and not the optical response. There is no procedure available considering calibration standards from, for example, known salts. For the (n, m) dependence, there are theoretical predictions available for the density of states and electron–photon matrix elements (see the contribution by *Saito* et al.). Experiments should be performed on a sample with population known *a priori*, or at the single-nanotube level. Optical absorption measurements on isolated SWNTs are difficult, since the amount of light absorbed from the light source will in general be hard to measure. Such a measurement has been achieved recently by using photothermal heterodyne detection to record absorption images and spectra of individual SWNTs. [74].

4.3 Resonance Raman Spectroscopy

Raman spectroscopy is commonly used for characterizing SWNTs because it is one of the most sensitive characterization tools for these nanostructures [75, 76] and requires very little work (or no work) on sample preparation. The Raman spectra from carbon nanotubes (see Fig. 9) is very rich and can be used to characterize several aspects of isolated, bundled and processed samples. Generally speaking, the Raman spectra depend strongly on the excitation laser energy (E_{laser}) because only nanotubes in resonance with E_{laser} exhibit a strongly enhanced Raman signal. For this reason, resonance Raman spectroscopy (RRS) is a dominant optical characterization technique. The Raman intensity also depends strongly on the light polarization, since absorption occurs mostly for light polarized along the nanotube axis. This polarization effect, which is characteristic of nanotubes, can be used for the characterization of different aspects related to SWNT orientation.

Carbon nanotubes bundled or isolated (in contact with the substrate or crossing trenches) can be synthesized by different methods (see the contribution by *Joselevich* et al.) and can be measured directly, as grown. For isolated-tube measurements, low-density sample (less than 1 SWNT/μm^2) guarantees that single SWNTs will be measured in a micro-Raman system and that one will not get a Raman signal from two or more SWNTs within the same light spot. Sonication of SWNT-bundle samples in solution can also form isolated SWNTs to be measured in large quantity (many isolated tubes

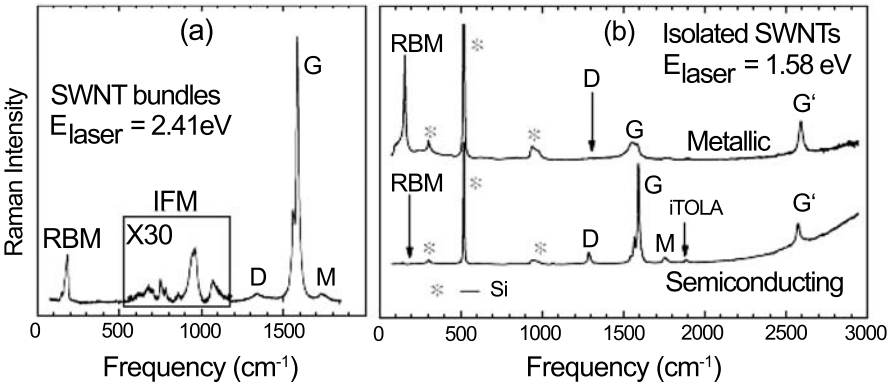

Fig. 9. (**a**) Raman spectrum from HiPco SWNT bundles [75]. (**b**) Raman spectra from a metallic (*top*) and a semiconducting (*bottom*) SWNT at the single-nanotube level. The spectra show the radial breathing modes (RBM), D-band, G-band and G′ band features, in addition to weak double-resonance features associated with the M-band and the iTOLA second-order modes [77]. The isolated carbon nanotubes are sitting on an oxidized silicon substrate that provides contributions to the Raman spectra denoted by '*', and these Si features are used for calibration purposes [75]

under the light spot). Wrapping nanotubes with, for example, SDS (sodium dodecyl sulfate) surfactant guarantees that tubes previously separated by sonication will not subsequently agglomerate [78].

Figure 9a gives a general view of the Raman spectra from a sample of SWNT bundles. The two dominant Raman features are the radial breathing mode (RBM) at low frequencies and the tangential (G band) multifeature at higher frequencies. Other weak features, such as the disorder-induced D band is also shown, and when the background intensity is increased, a rich Raman spectrum is observed for the intermediate-frequency phonon modes (IFM) that lie between the RBM and G-band features.

Usually, the weak point of Raman spectroscopy is the low-signal intensity as compared to PL, for example. In the process of measuring the Raman spectra from isolated SWNTs on a Si/SiO_2 substrate using a fixed laser energy E_{laser} (see Fig. 9b), one focuses the laser spot on the substrate surface and scans the sample until the Raman signal from an isolated SWNT is observed. A similar procedure can be used for measuring the PL signal from isolated SWNTs suspended on trenches in the substrate, enhanced by the stronger PL signal (see next section). The Raman intensity from SWNTs is usually buried under the noise, except for a few (n, m) SWNTs for which the resonance with the given E_{laser} occurs strongly for the electronic states confined within van Hove singularities (vHSs). The observation of the weak Si feature at $303\,\text{cm}^{-1}$ is a useful guide for knowing whether the radial breathing Raman mode from an isolated SWNT can be measured. On a well-aligned single

monochromator, usually 4 s of accumulation time is enough to identify this Si feature and the RBM from a resonant SWNT. Figure 9b shows an example of Raman signals from two resonant SWNTs at two different spots on the Si/SiO_2 surface. The upper spectrum shows an unusually strong RBM signal, while the lower spectrum shows a more typical RBM result. The opposite is observed for the G band, that is unusually strong in the lower spectrum. Such a result is related to resonance with the scattered light (see the contribution by *Saito* et al.). We now focus on the details for the three most important carbon-nanotube Raman features for SWNT characterization purposes.

4.3.1 The Radial Breathing Mode (RBM)

The RBM is unique to carbon nanotubes and is not observed in other carbon materials. It has the very important property that is the RBM mode frequency is proportional to the inverse tube diameter. As discussed in Sect. 2, absolute calibration of a SWNT electron-diffraction pattern depends on the value of the carbon–carbon (C–C) bonding distance, which has an uncertainty of 2 pm. By considering that common Raman instruments have a spectral accuracy of about $1\,\mathrm{cm}^{-1}$, and that the RBM frequencies (ω_{RBM}) from typical samples (diameters d_{t} around 0.5–5.0 nm) range from 500–50 cm^{-1}, Raman spectra can determine the tube diameter with a 1 Å accuracy for a $d_{\mathrm{t}} = 5.0\,\mathrm{nm}$ tube, the accuracy increasing with decreasing diameter, reaching 1 pm accuracy for a $d_{\mathrm{t}} = 0.5\,\mathrm{nm}$ tube. The use of a triple monochromator can get this resolution to $0.1\,\mathrm{cm}^{-1}$ in frequency, i.e., up to 0.1 pm resolution in the diameter determination.

The big problem is the determination of the precise relation between ω_{RBM} and d_{t} [71]. Although the RBM frequency has been shown to be weakly dependent on doping (charge transfer) or laser heating (temperature-dependent effects), there are many different ω_{RBM} vs. d_{t} relations in the literature, probably due to the different environmental conditions on each particular measurement (see the contribution by *Saito* et al.). Simple force-constant calculations predict a linear dependence between ω_{RBM} and the inverse diameter ($1/d_{\mathrm{t}}$), and this has been confirmed experimentally in some regimes. For smaller-diameter tubes, where the accuracy is larger, ω_{RBM} is expected to also show a small dependence on the chiral angle θ because of chirality-dependent curvature effects. For DWNTs the innertube frequency depends on the outer tubes, as discussed in the contribution by *Pfeiffer* et al.

The room-temperature natural RBM linewidth (γ_{RBM}) has been established as $3\,\mathrm{cm}^{-1}$ for isolated SWNTs on Si/SiO_2 substrates [75]. A d_{t} dependence on γ_{RBM} has been observed, showing that for even larger diameter tubes (above 5 nm), the RBM feature gets broad and cannot be resolved experimentally. This characteristic, and the $1/d_{\mathrm{t}}$ dependence of the Raman cross section limits the use of the RBM feature to study the geometry of large-diameter multiwall carbon nanotubes. The RBM from MWNTs is only

observed when they have very small innertubes (below 3 nm), for which the RBM feature can be observed.

Analysis of the RBM resonance profiles (RBM intensity as a function of laser energy E_{laser}) can be used to measure the E_{ii} for specific (n, m) tubes on bundles, isolated in aqueous solution [68, 72] or on Si substrates [75, 76]. Figure 10 shows a two-dimensional plot built from many RBM spectra obtained with different laser lines [68]. Since (E_{laser}, ω_{RBM}) and (E_{ii},$1/d_{\text{t}}$) can be directly related, the plot in Fig. 10 is a direct measure of the Kataura plot displayed as a function of $1/d_{\text{t}}$. A plot can be used to measure the effect of temperature, pressure, stress, bundling, substrate interaction, etc. on the E_{ii} optical levels. The resonance profile linewidth (γ_{r}) ranges from 8 meV on isolated tubes on a Si substrate [75, 76] up to 160 meV for SWNTs in bundles [72], giving information on the interactions of SWNTs with their environments. The intensity analysis reveals the (n, m)-dependent population in a sample. As for optical absorption, the use for comparative analysis can be easily performed, but for absolute (n, m) population assignments, the resonance Raman cross-section dependence on (n, m) has to be established. Theory shows that there is a very strong (n, m) dependence on the electron–phonon coupling (see the contribution by *Saito* et al. and [79]). The overall predictions (like a larger Raman cross section for smaller chiral angle tubes or a mod$[(2n + m), 3]$ dependence, both changing intensities by about 1 order of magnitude) have been observed experimentally [68]. However, theory still has to be fully validated by a reliable determination of the (n, m) populations in carbon-nanotube samples using resonance Raman spectroscopy. Again, measurements on isolated tubes might be necessary, although great care with environmental effects will be necessary. Comparative analyses (Raman vs. photoluminescence, Raman vs. optical absorption) have already shed some light on this problem, showing that the calculations have to include the excitonic nature of the optical levels to account for the strong diameter dependence of the Raman cross section [79, 80].

As for the tube–environmental interaction, a clear effect is observed when the resonance profiles are obtained for the RBMs in the bundled sample and when compared with the SWNTs dispersed in solution. A redshift in the optical transition energies is observed, as well as a broadening in the resonance profiles [72]. It has been shown experimentally that the redshift depends on the aggregation state of the carbon-nanotube bundle and is larger when the intertube contact surface is larger [81]. Environmental effects have been observed also when the nanotubes are dispersed in different surfactants due to the different dielectric constants of the nanotube surrounding. For example, a small shift in E_{ii} is observed when SDS-wrapped nanotubes are compared with DNA-wrapped nanotubes [66, 82]. Environment effects have been observed also in the intensities of the resonance Raman profiles that are associated with the relative population of the different (n, m) nanotubes present in the sample [83]. Besides the bundling, temperature-dependent effects on the carbon nanotubes have been observed by Raman spectroscopy. An increase

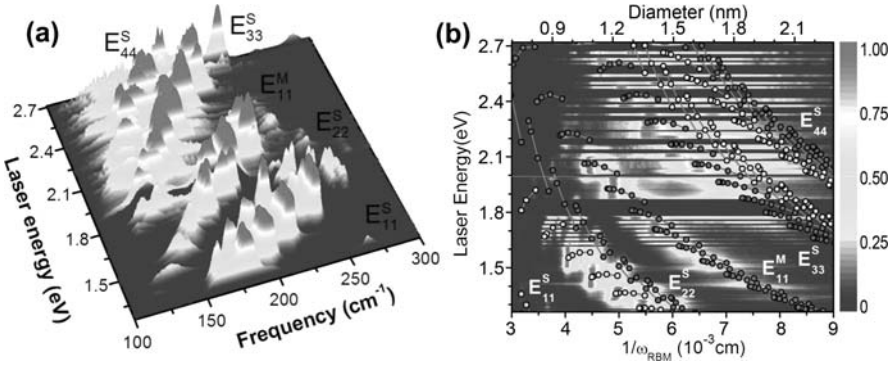

Fig. 10. Resonance Raman spectra as a function of E_{laser} [68]. The Kataura plot was superimposed on the experimental data in the *right panel* for which an intensity scale is provided

in linewidths of different features in the Raman spectra of SWNTs has been observed by increasing the sample temperature T especially for $T > 400\,\text{K}$, while small changes are observed for $T < 400\,\text{K}$ [84]. Changes in the relative intensities of the RBM spectra as a function of T are also observed and are related to changes in E_{ii} when the nanotube temperature is varied. All these effects can also be measured with photoluminescence spectroscopy (see Sect. 4.4).

4.3.2 The Tangential Modes (G Band)

While the G band in graphite has a single peak at $1582\,\text{cm}^{-1}$, the G band in SWNTs is composed basically of two stronger peaks (G^+ and G^-) related to the circumferential (TO) and axial (LO) atomic vibrations [85]. The splitting for these two peaks depends on the tube-wall curvature, so that the G has a small frequency dependence on d_t that can be used to corroborate the diameter information obtained from the RBM. The G-band TO and LO peaks also have an intensity dependence on chiral angle, for both metallic and semiconducting tubes, but the exact functional relating intensity and chiral angle has not yet been established experimentally.

However, the most important characteristic is the strong lineshape dependence of the G^- peak on the tube type and doping. While in semiconducting tubes the circumferential TO mode has a lower frequency when compared to the axial LO mode, the opposite happens in metallic tubes. The LO mode in metallic tubes shows up at a much lower frequency than the G^- peak (TO) from semiconducting tubes, and it exhibits a broad and asymmetric (Fano-like) lineshape (see Fig. 11). This broad features have been largely used to distinguish between metallic and semiconducting tubes, although the assignment is not that simple (see the contribution by *Saito* et al.). Metallic tubes

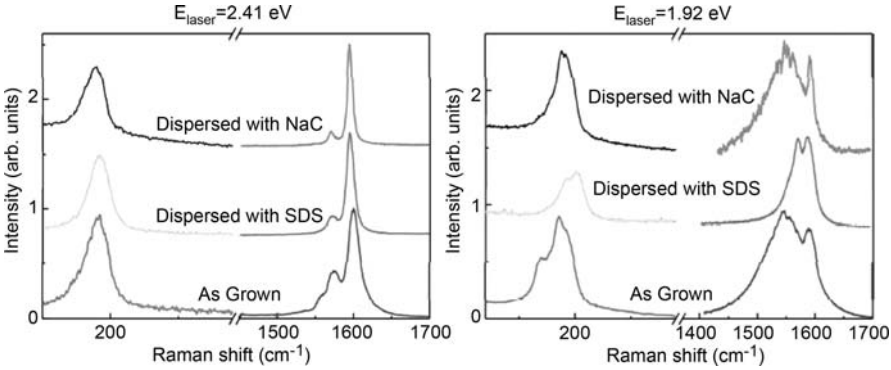

Fig. 11. Raman spectra of SWNTs in bundles as-grown, and dispersed in aqueous solution with two different surfactants (SDS and NaC), obtained with two different excitation laser energies [86]. In the *right panel* metallic SWNTs are in resonance, while in the *left panel* semiconducting SWNTs are in resonance

can indeed exhibit a "semiconducting-like" G band. The Fano-like G^- band in metallic tubes has been used to identify doping effects, since the band broadens/sharpens and increases/decreases in intensity due to changes in the Fermi level. The G^+ peak does not change lineshape, but shifts in frequency with doping for both semiconducting and metallic tubes, positively for donor doping and negatively for acceptor doping, although the frequency shift vs. doping behavior is not yet established quantitatively, or even well understood. The natural G-band linewidth (FWHM) was measured to be $\gamma_{G^\pm} = 5\,\mathrm{cm}^{-1}$, which appears to be smaller than in graphene ($\sim 12\,\mathrm{cm}^{-1}$), except for the BWF-like feature, that is broader, and shows a dependence on tube diameter [84].

As for the RBM, other interesting effects occur in the G band when changing the tube environment. The left panel in Fig. 11 shows a linewidth broadening when comparing isolated and bundled semiconducting tubes, and this effect can be used for dispersability characterization [86]. More systematic work is needed to establish procedures for accurate lineshape-related quantitative analysis. However, a considerable broadening of the G^+ band, achieving FWHM values larger than $\gamma_{G^+} \sim 20\,\mathrm{cm}^{-1}$, is a clear indication of the presence of defective material and/or amorphous carbon. This effect is always related to the observation of the so-called disorder-induced D band, discussed below. Although all the effects discussed here are clearly established, the literature is very poor on standards for quantitative analysis of metal/semiconducting, doping and dispersability characterizations based on the G-band profile.

4.3.3 The Disorder-Induced Feature (D Band)

The D band add (1350 cm^{-1}, see Fig. 8) is observed when there is symmetry breaking on the hexagonal sp^2-bonding lattices for graphite and nanotubes, and the D band has been widely used for the characterization of carbon samples. The observation of a D band in the Raman spectra is, therefore, related to either the presence of defects in the tube walls (e.g., vacancies, 7–5 pairs, dopants or just the presence of tube ends) or to the presence of amorphous-carbon material in the sample. As a metric for the internal calibration procedure, the analysis is typically made based on the I_D/I_G intensity ratio. The more defective the material, the larger and broader the D band, and the larger the I_D/I_G ratio. For comparative I_D/I_G analysis on different samples, one has to consider also the strong dependence of the I_D/I_G ratio on the excitation laser energy (E_{laser}). This dependence is well established for nanographite, depending on E_{laser}^{-4} [87]. For SWNTs, the D-band intensity depends on the analysis of the Kataura plot, diameter distribution in the sample, and it is usually stronger for metallic tubes [88].

The D band was shown to increase by B doping [89] (inducing defects) and also by tube-length shortening (the smaller the tube-length, the more important are the edge effects [90]). More systematic work is needed for quantitative analysis of sample purity and quality using the Raman D band. Furthermore, near-field Raman spectroscopy (spectroscopy with spatial resolution of $\sim$ 20 nm) shows that the D-band scattering is localized at specific sites along a single tube and the D-band intensity profiles vary strongly among single tubes grown by different synthesis methods (see contribution by *Hartschuh*). The D-band intensity has been shown to display even more sophisticated properties, like the dependence on the atomic edge structure observed at graphene edges [91]. Because of this strong potential for very sophisticated characterization of nanocarbons, more detailed theoretical and experimental studies of the D-band problem are now in progress [92].

4.3.4 Other Raman Features

Finally, the Raman spectra of nanotubes still have many other first-order, combination and overtone features with strong potential for playing an important role in carbon-nanotube characterization. For example, the intermediate-frequency modes (IFM, see Fig. 9) are very rich and strongly dependent on sample type [93]. Recent work showed a systematic dependence on tube length, some IFMs increasing intensity with decreasing tube length, and some others not [94]. The second order of the D band (G′ band) is known to depend on the carbon-nanotube electronic structure. Interestingly, this band was shown recently to depend on the number of graphene layers in a graphite sample with a few layers (below 5 layers) and it is now largely used as a fingerprint for a nondestructive, quick and easy identification of single- and

double-layer graphene samples on a substrate (see [95, 96] and the contribution by *Charlier* et al.). For more information, see the contribution by *Saito* et al.

The Raman features are analyzed by a Lorentzian fit of the spectra, with the exception of the lower-frequency G-band feature for metallic SWNTs, denoted by G^-, which is observed to have a Breit–Wigner–Fano (BWF) lineshape (that is broad and asymmetric), though the G^- feature for semiconducting SWNTs remains Lorentzian. Although it is known that the disorder-induced bands appear in the Raman spectra of graphite-like materials through a double-resonance process [97, 98] where inhomogeneous broadening occurs, we use the Lorentzian lineshape fit as an approximation to interpret the behavior of these Raman features.

4.4 Photoluminescence

Among the optical techniques, photoluminescence has the strongest signal. Nano-PL Inc., the first company specializing in producing instruments for carbon-nanotube sample characterization, performs an (n, m)-dependent PL intensity characterization of a given sample within 1 min. One strong limitation, however, is the sample preparation. Nanotubes contained in bundles do not luminesce, nor can metallic tubes within a sample be measured.

The photoluminescence signal from SWNTs can only be measured on isolated semiconducting SWNTs. Isolated SWNTs should be grown suspended on Si/SiO_2 substrates, crossing over lithographically prepared trenches [63], using a CVD method. Alternatively, sonication of SWNT-bundle samples in solution also produces isolated SWNTs, and wrapping each nanotube with surfactants guarantees that tubes previously separated by sonication will not rejoin subsequently [78]. There are some studies on the PL signal from DWNTs, but it is not yet clear whether or not the signal in these measurements comes from SWNT impurities contained in the DWNT sample.

Similar to Raman spectroscopy, photoluminescence can be used to measure the effect of temperature, pressure, strain, etc., on the E_{ii} optical levels of isolated tubes, as well as for the (n, m) population analysis (see the contribution by *Lefebvre* et al.). While Raman has a unique signature $(E_{ii}, \omega_{\mathrm{RBM}})$ for each (n, m) tube, photoluminescence excitation spectra (PL emission as a function of the excitation energy) provide another unique signature, that is obtained by measurement of the $(E_{22}^{\mathrm{S}}, E_{11}^{\mathrm{S}})$ for each specific (n, m) tube. Such an experiment is shown in Fig. 12. Each darker gray dot represents a strong emission at E_{11}^{S}, stimulated by a prior strong absorption at a higher E_{ii}^{S} level, for one specific (n, m) species. The $(E_{22}^{\mathrm{S}}, E_{11}^{\mathrm{S}})$ pairs can be well established when a full photoluminescence excitation map is performed, like in Fig. 12, and they show nice $(2n+m)$ and $(n-m)$ family patterns that yield the (n, m) assignment for each PL feature [73, 78]. If using only a small set of excitation laser energies, like the work by Nano-PL Inc., the (n, m) population can be rapidly extracted by PL-lineshape analysis (Lorentzian fit of the spectra,

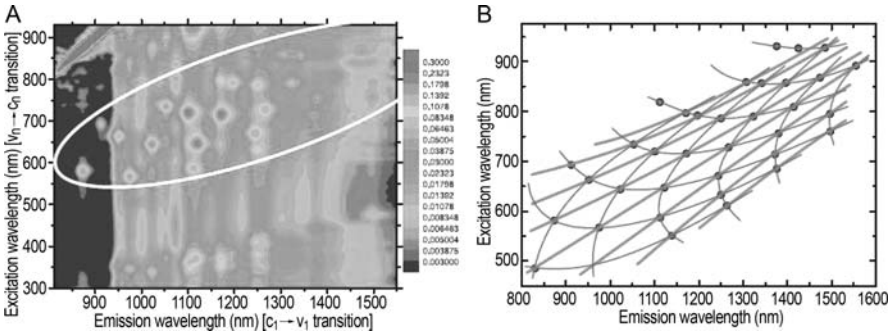

Fig. 12. (**A**) Photoluminescence excitation map [78]. Each *darker gray dot* represents the absorption at E_{ii}^{S} $(i > 1)$ on the Y-axis and emission at the E_{11}^{S} on the X-axis for a given (n, m) SWNT. (**B**) Schematic of the PL pattern formed by the $(2n + m)$ and $(n - m)$ SWNT families within the E_{22}^{S} absorption and E_{11}^{S} emission peaks contained within the *white ellipse* in (A) [78]

although asymmetric bands have also been measured [63]). In this case the E_{ii} values have to be known *a priori* with a high precision (within meVs). Proper metrological conditions require consideration of the environmental conditions seen by the SWNTs, which can affect the E_{ii} levels by tens of meV, which means that good standards have to be developed. For absolute population analysis, one has to consider that the cross section for the PL efficiency for specific tubes depends strongly on their (n, m) values. Theoretical work has been developed trying to address the (n, m) dependence of the PL signal as well [99, 100], but again, experimental work is needed to validate these theoretical predictions, so that the actual population of specific (n, m) SWNTs in a sample can be determined. Imaging techniques discussed in the contribution by *Lefebvre* et al. may be important for developing a counting procedure that may also help establishing standards for comparison. Such a counting procedure has been developed for resonance Raman measurements as well [101].

5 Summary and Outlook

In this work we discussed state-of-the-art capabilities and limitations of electron microscopies, electron-diffraction, scanning probe microscopies, scanning probe spectroscopy, optical absorption, resonance Raman and photoluminescence spectroscopies for the development of carbon-nanotube metrology. This work is far from being a complete discussion about the metrological issues related to carbon nanotubes. Development of standards and protocols require much more detailed discussion about procedures. Many other techniques like near-infrared spectroscopy, thermogravimetric analysis, differential scan-

ning calorimetry, small-angle X-ray dispersion and others are important for carbon-nanotube bulk-sample characterization, mainly with respect to purity (presence of noncarbon and amorphous/disordered carbon), microdispersion (distribution of nanotube bundles) and nanodispersion (splitting of bundles into individual tubes) characterization. These basic parameters on the carbon-nanotube production process have been systematically discussed in the metrology community [6, 7], and were not addressed in this work. We here focused on some specific forefront problems of nanometrology [8].

As we have described in this work, high-resolution STM and TEM measurements can be utilized to study in detail the interplay between structure, electronic properties and local perturbations. Optics promises a powerful trend in nanotube research as a fast and reliable characterization method, as demanded for applications. Very fruitful outcomes should be achieved when combining SPM and TEM with optical spectroscopy techniques. This will give us the opportunity to correlate vibrational modes with local changes in the microscopic structure or chemical attachment of functional groups on individual SWNTs. For example, the inelastic tunneling spectroscopy (IETS-STM) technique offers the possibility to detect local variation in vibrational modes due to sidewall chemical functionalization or encapsulation of molecules inside SWNTs. For a precise determination of optical intensities, for example, the analysis of the effect of defects is extremely important, since defects can completely change the optical response of nanotubes. There is also a trend in the scientific community to use IETS to investigate the microscopic origin of the Raman-active intermediate–frequency modes of SWNTs so that a complete picture of the vibrational spectrum can be achieved.

Although a lot of work has been done in this field, there is still a lot remaining to be done. A good feeling for the problem can be obtained by looking at well-established bulk-material parameters, like for example for GaAs, GaP, InAs, and InP in [102]. 38 parameters are well established, e.g., lattice constant, density, thermal expansion, Γ, L, Δ point bandgaps (plus spin orbit), electron mass (light hole), (heavy hole), (spin orbit hole), dielectric constant – static ϵ_s and optic ϵ_∞, ionicity, elastic constants, Young's modulus, bulk modulus, piezoelectric coupling, deformation potentials, donor binding, thermal conductivity, electron mobility ... This long list of unknowns in carbon-nanotube materials confirms what we have pointed out at the beginning of this work: developing the nanometrology is a big task for a consistent transformation of nanoscience into nanotechnology. In the case of nanotubes the complexity is enhanced by the important dependence on diameter, chiral angle and environmental effects, as well as a problem common to other nanostructures, which concerns the perturbation of the nanostructure by the measurement probe.

Acknowledgements

The authors of the contribution strongly acknowledge Prof. Dresselhaus and Dr. Hua Jiang for their help in writing this work.A.J. acknowledges financial support under Universal Grants (CNPq and Fapemig) and by Rede Nacional de Pesquisa em Nanotubos de Carbono-MCT.

References

[1] Dias, J. L. de Matos: *Medidas, normalização e qualidade: aspectos da história da metrologia no Brasil* (Ilustrações, Rio de Janeiro 1998) 63
[2] *Conférence Générale des Poids et Measures. Comptes Rendus des Séances* (Gauthier-Villars, Paris 1889) 64
[3] A. G. Rinzler, J. Liu, H. Dai, P. Nikolaev, C. B. Huffman, F. G. Rodrigues, et al.: Large-scale purification of single-walled carbon nanotubes: process, product, and characterization, Appl. Phys. A. **67**, 29–37 (1998) 64, 82
[4] I. W. Chiang, B. E. Brinson, R. E. Smalley, J. L. Margrave, R. H. Haure: Purification and characterization of single-wall carbon nanoutbes, J. Phys. Chem. B **105**, 1157–1161 (2001) 64
[5] S. Arepalli, P. Nikolaev, O. Gorelik, V. G. Hadjiev, W. Holmes, B. Files, L. Yowell: Protocol for the characterization of single-wall carbon nanotube material quality, Carbon **42**, 1783–1791 (2004) 64, 67, 82
[6] *2nd Joint Workshop on Measurement Issues in Single Wall Carbon Nanotubes: Purity and Dispersion Part II* (NIST Gaithersburg 2005) URL: `http://www.msel.nist.gov/Nanotube2/Carbon_Nanotubes.htm` 64, 67, 92
[7] *Third NASA-NIST Workshop on Nanotube Measurements* (NIST Gaithersburg 2007) URL: `http://polymers.nist.gov/Nanotube3/Workshop3.htm` 64, 67, 92
[8] *First International Forum on the Metrology, Standardization and Industrial Quality of Carbon Nanotubes* (INMETRO Rio de Janeiro 2007) URL: `http://www.inmetro.gov.br/msin07` 64, 67, 92
[9] S. Iijima: Helical microtubules of graphitic carbon, Nature **354**, 56 (1991) 65, 70
[10] H. Jiang, F. H. Li, E. I. Kauppinen: (Springer, Netherlands 2004) 65
[11] M. Haider, S. Uhlemann, E. Schwan, H. Rose, B. Kabius, K. Urban: Electron microscopy image enhanced, Nature **392**, 768 (1998) 65
[12] A. G. Nasibulin, A. Moisala, D. P. Brown, H. Jiang, E. I. Kauppinen: A novel aerosol method for single walled carbon nanotube synthesis, Chem. Phys. Lett. **402**, 227–232 (2005) 66
[13] P. Queipo, A. G. Nasibulin, D. Gonzalez, U. Tapper, H. Jiang, T. Tsuneta, K. Grigoras, J. A. Duenas, E. I. Kauppinen: Novel catalyst particle production method for cvd growth of single- and double-walled carbon nanotubes, Carbon **44(8)**, 1604–1608 (2006) 67
[14] S. Suzuki, K. Kanzaki, Y. Homma, S. Fukuba: Jpn. J. Appl. Phys. **43**, 1118–1120 (2004) 68
[15] A. Hashimoto, K. Suenaga, A. Gloter, K. Urita, S. Iijima: Direct evidence for atomic defects in graphene layers, Nature **430**, 870–873 (2004) 68

[16] A. Hashimoto, K. Suenaga, K. Urita, T. Shimada, T. Sugai, S. Bandow, H. Shinohara, S. Iijima: Atomic correlation between adjacent graphene layers in double-wall carbon nanotubes, Phys. Rev. Lett. **94**, 045504 (2005) 69
[17] N. Tanaka, J. Yamasaki, T. Kawai, H. Pan: Nanotechnol. **15**, 1779–1784 (2004) 69
[18] K. Hirahara, K. Saitoh, J. Yamasaki, N. Tanaka: Direct observation of six-membered rings in the upper and lower walls of a single-wall carbon nanotube by spherical aberration-corrected HRTEM, Nano Lett. **6(8)**, 1778–1783 (2006) 69
[19] S. Iijima, T. Ichihashi: Single-shell carbon nanotubes of 1-nm diameter, Nature **363**, 603–605 (1993) 70
[20] M. Gao, J. Zuo, R. D. Twesten, I. Petrov, L. A. Nagahara, R. Zhang: Structure determination of individual single-wall carbon nanotubes by nanoarea electron diffraction, Appl. Phys. Lett. **82(16)**, 2703–2705 (2003) 70
[21] H. Jiang, D. P. Brown, A. G. Nasibulin, E. I. Kauppinen: Robust bessel-function-based method for determination of the (n,m) indices of single-walled carbon nanotubes by electron diffraction, Phys. Rev. B **74**, 035427 (2006) 70
[22] A. Lucas, P. Lambin: Diffraction by DNA, carbon nanotubes and other helical nanostructures, Rep. Prog. Phys. **68**, 1181–1249 (2005) 70, 71
[23] Z. Liu, Q. Zhang, L.-C. Qin: Determination and mapping of diameter and helicity for single-walled carbon nanotubes using nanobeam electron diffraction, Phys. Rev. B **71**, 245413 (2005) 70
[24] H. Jiang, A. G. Nasibulin, D. P. Brown, E. I. Kauppinen: Unambiguous atomic structural determination of single-walled carbon nanotubes by electron diffraction, Carbon **45(3)**, 662–667 (2006) 70, 71
[25] E. Meyer, H. J. Hug, R. Bennewitz: *Scanning Probe Microscopy: The Lab on a Tip* (Springer, Berlin, Heidelberg 2003) 71
[26] H. J. Guntherodt, R. Wiesendanger (Eds.): *Scanning Tunnelling Microscopy II: Further Applications and Related Scanning Techniques*, 2nd ed., Springer Series in Surface Sciences (Springer, Berlin, Heidelberg 1995) 71
[27] S. Morita, R. Wiesendanger, E. Meyer: *Noncontact Atomic Force Microscopy* (Springer, Berlin, Heidelberg 2002) 71
[28] G. Binning, H. Rohrer, C. Gerber, E. Weibel: Surface studies by scanning tunneling microscopy, Phys. Rev. Lett. **49**, 57–61 (1982) 72
[29] J. W. Gadzuk: Inelastic resonance scattering, tunneling, and desorption, Phys. Rev. B **44**, 13446–13477 (1991) 72
[30] B. C. Stipe, M. A. Rezaei, W. Ho: Inducing and viewing the rotational motion of a single molecule, Science **279**, 1907–1909 (1998) 72, 78
[31] B. C. Stipe, M. A. Rezaei, W. Ho, S. Gao, M. Persson, B. I. Lundqvist: Single molecule dissociation by tunneling electrons, Phys. Rev. Lett. **78**, 4410–4413 (1997) 72
[32] N. Lorente, M. Persson, L. J. Lauhon, W. Ho: Symmetry selection rules for vibrationally inelastic tunneling, Phys. Rev. Lett. **86**, 2593–2596 (2001) 72
[33] S. Nolen, S. T. Ruggiero: Tunneling spectroscopy of fullerene/Ge multilayer systems, Chem. Phys. Lett. **300**, 656–660 (1999) 72
[34] X. M. H. Huang, R. Caldwell, L. Huang, S. C. Jun, M.Huang, M. Y. Sfeir, S. P. O'Brien, J. Hone: Controlled placement of individual carbon nanotubes, Nano Lett. **5**, 1515–1518 (2005) 73

[35] M. Y. Sfeir, T. Beetz, F. Wang, L. Huang, X. M. H. Huang, M. Huang, J. Hone, S. O'Brien, J. A. Misewich, T. F. Heinz, L. Wu, Y. Zhu, L. E. Brus: Optical spectroscopy of individual single-walled carbon nanotubes of defined chiral structure, Science **312**, 554 (2006) 73
[36] Understanding carbon nanotubes: From basics to applications, in A. Loiseau, P. Launois, P. Petit, S. Roche, J.-P. Salvetat (Eds.): *Lecture Notes in Physics*, vol. 677 (Springer 2006) 73
[37] Z. Zhang, C. M. Lieber: Nanotube structure and electronic properties probed by scanning tunneling microscopy, Appl. Phys. Lett. **62**, 2792–2794 (1993) 73
[38] C. H. Olk, J. P. Heremans: Scanning tunneling spectroscopy of carbon nanotubes, J. Mater. Res. **9**, 259–262 (1994) 73
[39] M. Ge, K. Sattler: Vapor-condensation generation and STM analysis of fullerene tubes, Science **260**, 515–518 (1993) 73
[40] D. L. Carroll, P. Redlich, P. M. Ajayan, J. C. Charlier, X. Blase, A. De Vita, R. Car: Electronic structure and localized states at carbon nanotube tips, Phys. Rev. Lett. **78**, 2811–2814 (1997) 73
[41] M. Ge, K. Sattler: Scanning tunneling microscopy of single-shell nanotubes of carbon, Appl. Phys. Lett. **65**, 2284–2286 (1994) 73, 75
[42] J. W. G. Wilder, L. C. Venema, A. G. Rinzler, R. E. Smalley, C. Dekker: Electronic structure of atomically resolved carbon nanotubes, Nature **391**, 59–62 (1998) 73, 74, 75, 76
[43] T. W. Odom, J.-L. Huang, P. Kim, C. M. Lieber: Atomic structure and electronic properties of single-walled carbon nanotubes, Nature **391**, 62–64 (1998) 73, 75
[44] A. Hassanien, M. Tokumoto, Y. Kumazawa, H. Kataura, Y. Maniwa, S. Suzuki, Y. Achiba: Atomic structure and electronic properties of single-wall carbon nanotubes probed by scanning tunneling microscope at room temperature, Appl. Phys. Lett. **73**, 3839–3841 (1998) 73, 75
[45] A. Mrzel, A. Hassanien, Z. Liu, K. Suenaga, Y. Miyata, K. Yanagi, H. Kataura: Effective, fast, and low temperature encapsulation of fullerene derivatives in single wall carbon nanotubes, Surface Science, in press URL: `http://dx.doi.org/10.1016/j.susc.2007.04.236` 74
[46] R. S. Ruoff, J. Tersoff, D. C. Lorents, S. Subramoney, B. Chan: Radial deformation of carbon nanotubes by van der Waals forces, Nature **364**, 514–516 (1993) 75
[47] M. S. Dresselhaus., G. Dresselhaus, P. Avouris (Eds.): *Carbon Nanotubes: Synthesis, Structure, Properties and Applications*, Top. Appl. Phys. **80** (Springer, Berlin, Heidelberg 2000) 75, 76, 79
[48] E. C. Venema, J. W. G. Wildoer, J. W. Janssen, S. J. Tans, H. L. J. T. Tuinstra, L. P. Kouwenhoven, C. Dekker: Imaging electron wave functions of quantized energy levels in carbon nanotubes, Science **283**, 52–55 (1999) 76, 77
[49] Z. Yao, H. W. C. Postma, L. Balents, C. Dekker: Carbon nanotube intramolecular junctions, Nature **402**, 273–276 (1999) 77
[50] M. Ouyang, J.-L. Huang, C. L. Cheung, C. M. Lieber: Atomically resolved single-walled carbon nanotube intramolecular junctions, Science **291**, 97–100 (2001) 77

[51] A. Hassanien, M. Holzinger, A. Hirsch, , M. Tokumoto, P. Venturini: Ropes of carbon nanotube intramolecular junction, Synth. Met. **137**, 1203–1204 (2003) 77
[52] A. Hassanien, M.Tokumoto, P. Umek, D. Mihailovic, A. Mrzel: Fermi electron wave packet interference images on carbon nanotubes at room temperature, Appl. Phys. Lett. **78**, 808–810 (2001) 77, 78
[53] R. A. Jishi, M. S. Dresselhaus, G. Dresselhaus: Electron–phonon coupling and the electrical conductivity of fullerene nanotubules, Phys. Rev. B **48**, 11385 (1993) 77
[54] T. Hertel, G. Moos: Influence of the excited electron lifetime on the electronic structure of carbon nanotubes, Chem. Phys. Lett. **320**, 359 (2000) 77
[55] A. Hassanien, M. Tokumoto: The electronic properties of suspended single wall carbon nanotubes, Carbon **12–13**, 2649–2653 (2004) 77, 78
[56] L. Vitali, M. Burghard, M. A. Schneider, L. Liu, S. Y. Wu, C. S. Jayanthi, K. Kern: Phonon spectromicroscopy of carbon nanostructures with atomic resolution, Phys. Rev. Lett. **93**, 136103 (2004) 77
[57] L. Vitali, M. Burghard, P. Wah, M. A. Schneider, K. Kern: Local pressure-induced metallization of a semiconducting carbon nanotube in a crossed junction, Phys. Rev. Lett. **96**, 086804 (2006) 78
[58] M. Ishigami, H. J. Choi, S. Aloni, S. G. Louie, M. L. Cohen, A. Zettl: Identifying defects in nanoscale materials, Phys. Rev. Lett. **93**, 196803 (2004) 78
[59] B. J. LeRoy, S. G. Lemay, J. Kong, C. Dekker: Electrical detection and control of phonons in carbon nanotubes, Nature **432**, 371–374 (2004) 79
[60] S. Sapmaz, P. Jarillo-Herrero, L. P. Kouwenhoven, H. S. J. van der Zant: Quantum dots in carbon nanotubes, Semicond. Sci. Technol. **21(11)**, S52–S63 (2006) 79
[61] A. Jorio, R. Saito, J. H. Hafner, C. M. Lieber, M. Hunter, T. McClure, G. Dresselhaus, M. S. Dresselhaus: Structural (n,m) determination of isolated single-wall carbon nanotubes by resonant Raman scattering, Phys. Rev. Lett. **86**, 1118–1121 (2001) 79
[62] M. Y. Sfeir, T. Beetz, F. Wang, L. Huang, X. M. H. Huang, M. Huang, J. Hone, S. O'Brien, J. A. Misewich, T. F. Heinz, L. Wu, Y. Zhu, L. E. Brus: Optical spectroscopy of individual single-walled carbon nanotubes of defined chiral structure, Science **312**, 554–556 (2006) 79
[63] J. Lefebvre, J. M. Fraser, P. Finnie, Y. Homma: Photoluminescence from an individual single-walled carbon nanotube, Phys. Rev. B **69**, 075403 (2004) 79, 90, 91
[64] A. Jorio, R. Saito, T. Hertel, R. B. Weisman, G. Dresselhaus, M. S. Dresselhaus: Carbon nanotube photophysics, MRS Bull. **29**, 276 (2004) 79
[65] H. Kataura, Y. Kumazawa, Y. Maniwa, I. Umezu, S. Suzuki, Y. Ohtsuka, Y. Achiba: Optical properties of single-wall carbon nanotubes, Synthetic Met. **103**, 2555–2558 (1999) 79, 82
[66] C. Fantini, A. Jorio, A. P. Santos, V. S. T. Peressinotto, M. A. Pimenta: Characterization of DNA-wrapped carbon nanotubes by resonance Raman and optical absorption spectroscopies, Chem. Phys. Lett. **439**, 138–142 (2007) 80, 82, 83, 86
[67] M. S. Dresselhaus, G. Dresselhaus, R. Saito, A. Jorio: Exciton photophysics of carbon nanotubes, Ann. Rev. Phys. Chem. **58**, 719–747 (2007) 81

[68] P. T. Araujo, S. K. Doorn, S. Kilina, D. Tretiak, III, E. Einarsson, S. Maruyama, H. Chacham, M. A. Pimenta, A. Jorio: The third and fourth optical transitions in semiconducting carbon nanotubes, Phys. Rev. Lett. **98**, 067401 (2007) 81, 86, 87

[69] G. G. Samsonidze, R. Saito, N. Kobayashi, A. Grüneis, J. Jiang, A. Jorio, S. G. Chou, G. Dresselhaus, M. S. Dresselhaus: Family behavior of the optical transition energies in single-wall carbon nanotubes of smaller diameters, Appl. Phys. Lett. **85**, 5703–5705 (2004) 81

[70] V. N. Popov, L. Henrard: Comparative study of the optical properties of single-walled carbon nanotubes within orthogonal and nonorthogonal tight-binding models, Phys. Rev. B **70**, 115407 (2004) 81

[71] A. Jorio, C. Fantini, M. A. Pimenta, R. B. Capaz, G. G. Samsonidze, G. Dresselhaus, M. S. Dresselhaus, J. Jiang, N. Kobayashi, A. Grüneis, R. Saito: Resonance Raman spectroscopy (n, m) dependent effects in small diameter single-wall carbon nanotubes, Phys. Rev. B **71**, 075401 (2005) 81, 85

[72] C. Fantini, A. Jorio, M. Souza, M. S. Strano, M. S. Dresselhaus, M. A. Pimenta: Optical transition energies for carbon nanotubes from resonant Raman spectroscopy: Environment and temperature effects, Phys. Rev. Lett. **93**, 147406 (2004) 81, 86

[73] S. M. Bachilo, L. Balzano, J. E. Herrera, F. Pompeo, D. E. Resasco, R. B. Weisman: Narrow (n,m)-distribution of single-walled carbon nanotubes grown using a solid supported catalyst, J. Am. Chem. Soc. **125**, 11186 (2003) 82, 90

[74] S. Berciaud, L. Cognet, P. Poulin, R. B. Weisman, B. Lounis: Absorption spectroscopy of individual single-walled carbon nanotubes, Nano Lett. (2007) 83

[75] M. S. Dresselhaus, G. Dresselhaus, R. Saito, A. Jorio: Raman spectroscopy of carbon nanotubes, Physics Reports **409**, 47–99 (2005) 83, 84, 85, 86

[76] A. Jorio, M. A. Pimenta, A. G. Souza Filho, R. Saito, G. Dresselhaus, M. S. Dresselhaus: Characterizing carbon nanotube samples with resonance Raman scattering, New J. Phys. **5**, 1.1–1.17 (2003) 83, 86

[77] V. W. Brar, G. G. Samsonidze, G. Dresselhaus, M. S. Dresselhaus, R. Saito, A. K. Swan, M. S. Ünlü, B. B. Goldberg, A. G. Souza Filho, A. Jorio: Second-order harmonic and combination modes in graphite, single-wall carbon nanotube bundles, and isolated single-wall carbon nanotubes, Phys. Rev. B **66**, 155418 (2002) 84

[78] S. M. Bachilo, M. S. Strano, C. Kittrell, R. H. Hauge, R. E. Smalley, R. B. Weisman: Structure-assigned optical spectra of single-walled carbon nanotubes, Science **298**, 2361–2366 (2002) 84, 90, 91

[79] J. Jiang, R. Saito, K. Sato, J. S. Park, G. G. Samsonidze, A. Jorio, G. Dresselhaus, M. S. Dresselhaus: Exciton–photon, exciton–phonon matrix elements, and resonant Raman intensity of single-wall carbon nanotubes, Phys. Rev. B **75**, 035405 (2007) 86

[80] A. Jorio, C. Fantini, M. A. Pimenta, D. A. Heller, M. S. Strano, M. S. Dresselhaus, Y. Oyama, J. Jiang, R. Saito: Carbon nanotube population analysis from Raman and photoluminescence intensities, Appl. Phys. Lett. **88**, 023109 (2006) 86

[81] D. A. Heller, P. W. Barone, J. P. Swanson, R. M. Mayrhofer, M. S. Strano: Using Raman spectroscopy to elucidate the aggregation state of single-walled carbon nanotubes, J. Phys. Chem. B **108**, 6905–6909 (2004) 86

[82] S. G. Chou, H. B. Ribeiro, E. Barros, A. P. Santos, D. Nezich, G. G. Samsonidze, C. Fantini, M. A. Pimenta, A. Jorio, F. P. Filho, M. S. Dresselhaus, G. Dresselhaus, R. Saito, M. Zheng, G. B. Onoa, E. D. Semke, A. K. Swan, M. S. Ünlü, B. B. Goldberg: Optical characterization of DNA-wrapped carbon nanotube hybrids, Chem. Phys. Lett. **397**, 296–301 (2004) 86

[83] A. Jorio, A. P. Santos, H. B. Ribeiro, C. Fantini, M. Souza, J. P. M. Vieira, C. A. Furtado, J. Jiang, L. Balzano, D. E. Resasco, M. A. Pimenta: Quantifying carbon-nanotube species with resonance Raman scattering, Phys. Rev. B **72**, 075207–1–5 (2005) 86

[84] A. Jorio, C. Fantini, M. S. S. Dantas, M. A. Pimenta, A. G. Souza Filho, G. G. Samsonidze, V. W. Brar, G. Dresselhaus, M. S. Dresselhaus, A. K. Swan, M. S. Ünlü, B. B. Goldberg, R. Saito: Linewidth of the Raman features of individual single-wall carbon nanotubes, Phys. Rev. B **66**, 115411 (2002) 87, 88

[85] A. Jorio, A. G. Souza Filho, G. Dresselhaus, M. S. Dresselhaus, A. K. Swan, M. S. Ünlü, B. Goldberg, M. A. Pimenta, J. H. Hafner, C. M. Lieber, R. Saito: G-band resonant Raman study of 62 isolated single wall carbon nanotubes, Phys. Rev. B **65**, 155412 (2002) 87

[86] A. P. G. Pereira, V. S. T. Peressinotto, A. P. Santos, A. Jorio, M. A. Pimenta: Debundling effects on the tangential modes of carbon nanotubes, unpublished (2007) 88

[87] L. Cançado, K. Takai, T. Enoki, M. Endo, Y. A. Kim, H. Mizusaki, A. Jorio, L. N. Coelho, R. Magalhães-Paniago, M. A. Pimenta: Appl. Phys. Lett. **88**, 163106 (2006) 89

[88] J. Maultzsch, S. Reich, C. Thomsen: Chirality-selective Raman scattering of the D mode in carbon nanotubes, Phys. Rev. B **64**, 121407(R) (2001) 89

[89] K. McGuire, N. Gothard, P. L. Gai, M. S. Dresselhaus, G. Sumanasekera, A. M. Rao: Synthesis and Raman characterization of boron-doped single-walled carbon nanotubes, Carbon **43**, 219 (2005) 89

[90] S. G. Chou, H. Son, J. Kong, A. Jorio, R. Saito, M. Zheng, G. Dresselhaus, M. S. Dresselhaus: Length characterization of DNA-wrapped carbon nanotubes using Raman spectroscopy, Appl. Phys. Lett. **90**, 131109 (2007) 89

[91] L. G. Cançado, M. A. Pimenta, B. R. A. Neves, M. S. S. Dantas, A. Jorio: General equation for the determination of the crystallite size L_a of nanographite by Raman spectroscopy, Phys. Rev. Lett. **93**, 247401 (2004) 89

[92] M. A. Pimenta, G. Dresselhaus, M. S. Dresselhaus, L. G. Cançado, A. Jorio, R. Saito: Studying disorder in graphite-based systems by Raman spectroscopy, Phys. Chem. Chem. Phys. **9**, 1276–1291 (2007) 89

[93] C. Fantini, A. Jorio, M. Souza, R. Saito, G. G. Samsonidze, M. S. Dresselhaus, M. A. Pimenta: Intermediate frequency Raman modes in metallic and semiconducting carbon nanotubes, in *Proc. Int. Winterschool on Electronic Properties of Novel Mater.* (2005) 89

[94] S. G. Chou, H. Son, M. Zheng, R. Saito, A. Jorio, G. Dresselhaus, M. S. Dresselhaus: Finite length effects in DNA-wrapped carbon nanotubes, Chem. Phys. Lett. **443**, 328–332 (2007) 89

[95] A. C. Ferrari, J. C. Meyer, V. Scardaci, C. Casiraghi, M. Lazzeri, F. Mauri, S. Piscanec, D. Jiang, K. S. Novoselov, S. Roth, A. K. Geim: Raman spectrum of graphene and graphene layers, Phys. Rev. Lett. **97**, 187401 (2006) 90
[96] A. Gupta, G. Chen, P. Joshi, S. Tadigadapa, P. C. Eklund: Nano Lett. (2006) 90
[97] C. Thomsen, S. Reich: Double resonant Raman scattering in graphite, Phys. Rev. Lett. **85**, 5214 (2000) 90
[98] R. Saito, A. Jorio, A. G. Souza Filho, G. Dresselhaus, M. S. Dresselhaus, M. A. Pimenta: Probing phonon dispersion relations of graphite by double resonance Raman scattering, Phys. Rev. Lett. **88**, 027401 (2002) 90
[99] Y. Oyama, R. Saito, K. Sato, J. Jiang, G. G. Samsonidze, A. Grueneis, Y. Miyauchi, S. Maruyama, A. Jorio, G. Dresselhaus, M. S. Dresselhaus: Photoluminescence intensity of single-wall carbon nanotubes, Carbon **44**, 873–879 (2006) 91
[100] S. Reich, C. Thomsen, J. Robertson: Exciton resonances quench the photoluminescence of zigzag carbon nanotubes, Phys. Rev. Lett. **95**, 077402 (2005) 91
[101] H. B. Son, A. Reina, M. S. Dresselhaus, J. Kong: Characterizing the chirality distribution of single-walled carbon nanotube materials with tunable Raman spectroscopy. Physica Status Solidi B-Basic, Solid State Physics **243(13)**, 3161–3165 (2006) 91
[102] O. Madelung: *Semiconductors Data Handbook*, 3rd ed. (Springer 2004) ISBN 10-354040880 92

Index

Carbon Nanotube Synthesis and Organization

Ernesto Joselevich[1], Hongjie Dai[2], Jie Liu[3], Kenji Hata[4], and Alan H. Windle[5]

[1] Department of Materials and Interfaces, Weizmann Institute of Science, Rehovot 76100, Israel
ernesto.joselevich@weizmann.ac.il
[2] Department of Chemistry, Stanford University Stanford, CA 94305, USA
hdai1@stanford.edu
[3] Department of Chemistry, Duke University Durham, NC 27708, USA
j.liu@duke.edu
[4] Research Center for Advanced Carbon Materials, National Institute of Advanced Industrial Science and Technology (AIST) 1-1-1 Higashi, Tsukuba, Ibaraki 305-8565, Japan
kenji-hata@aist.go.jp
[5] Department of Materials Science and Metallurgy, University of Cambridge Pembroke Street, Cambridge CB2 3QZ, UK
ahw1@cam.ac.uk

Abstract. The synthesis, sorting and organization of carbon nanotubes are major challenges toward future applications. This chapter reviews recent advances in these topics, addressing both the bulk production and processing of carbon nanotubes, and their organization into ordered structures, such as fibers, and aligned arrays on surfaces. The bulk synthetic methods are reviewed with emphasis on the current advances toward mass production and selective synthesis. New approaches for the sorting of carbon nanotubes by structure and properties are described in the context of the specific physical or chemical interactions at play, and referring to the characterization methods described in the contribution by *Jorio* et al. Recent advances in the organization of carbon nanotubes into fibers are reviewed, including methods based on spinning from solution, from dry forests, and directly from the gas phase during growth. The organization of carbon nanotubes on surfaces, as a critical prerequisite toward future applications in nanoelectronics, is reviewed with particular emphasis given to the synthesis of both vertically and horizontally aligned arrays. Vertically aligned growth has been recently boosted by the development of highly efficient catalytic processes. Horizontally aligned growth on surfaces can yield a whole new array of carbon-nanotube patterns, with interesting physical properties and potential applications. Different mechanisms of horizontally aligned growth include field- and flow-directed growth, as well as recently developed methods of surface-directed growth on single-crystal substrates by epitaxial approaches. The proposed mechanisms pertinent to each technique are discussed throughout this review, as well as their potential applications and critical aspects toward future progress.

A. Jorio, G. Dresselhaus, M. S. Dresselhaus (Eds.): Carbon Nanotubes,
Topics Appl. Physics **111**, 101–164 (2008)

1 Introduction

Carbon nanotubes can have different individual structures, morphologies and properties, as well as different collective arrangements and emerging properties, all of which are determined by the method of preparation and further processing. Hence, a wide variety of synthetic methods have been developed to produce the desired materials and properties for specific scientific studies or technological applications. The first growth of high-quality and milligram quantities of multiwall carbon nanotubes (MWNTs) [1] and single-wall carbon nanotubes (SWNTs) [2, 3] marked important milestones that enabled the study of the intrinsic properties of nanotubes. Chemical vapor deposition (CVD) for high-quality SWNTs [4–6] further opened up new routes for controlled synthesis and device integration. It is clear that future developments in nanotube-based science and technology will continue to rely on the further improved highly controlled synthesis of nanotubes. Some of the long-standing problems in the nanotube area are due to the lack of control in the synthesis and chemical processing of SWNTs, in chirality control that determines whether a nanotube is metallic or semiconducting, in diameter control that determines the bandgap of a semiconducting SWNT, and in the placement and orientation control on large substrates that is needed for scalable production of nanotube electronics and other devices. Currently, there are four main challenges in the field of nanotube synthesis: 1. Mass production, i.e., the development of low-cost, large-scale processes for the synthesis of high-quality nanotubes, including SWNTs; 2. Selective production, i.e., control over the structure and electronic properties of the produced nanotubes; 3. Organization, i.e., control over the location and orientation of the produced nanotubes on a flat substrate; and 4. Mechanism, i.e., the development of a thorough understanding of the processes of nanotube growth. For applications such as composites and hydrogen storage, it is desired to obtain high-quality nanotubes at the kilogram or ton level using bulk-growth methods that are simple, efficient and inexpensive. For devices such as nanotube-based electronics, which require highly organized arrays, scaleup will unavoidably rely on self-assembly techniques or controlled growth strategies on surfaces combined with microfabrication techniques.

In this review, we present an overview of the current state-of-the-art methods and understanding in the synthesis of carbon nanotubes, following this rational order from bulk production to organized production, namely from methods involving large amounts of material and a low level of organization, to methods yielding higher levels of organization in smaller amounts. Thus, we start with bulk production methods (Sect. 2), with emphasis on mass production and selective synthesis, followed by purification (Sect. 3) and sorting (Sect. 4). Then we describe current methods for the production of nanotubes organized into fibers (Sect. 5) and into vertical and horizontal arrays on surfaces (Sect. 6), the latter representing the highest level of organization. Relevant mechanisms are briefly referred to throughout this re-

view, and the general perspectives of nanotube synthesis are summarized in the last section (Sect. 7). For the synthesis of doped carbon nanotubes and double-walled carbon nanotubes, see contributions by *Terrones* et al. and *Pfeiffer* et al., respectively.

2 Bulk Production Methods

The preparation of high-quality carbon nanotubes with high yield has been the goal of many research endeavors. So far, arc discharge, laser ablation, and chemical vapor deposition (CVD) are the three main methods for SWNT production. In the following subsections, we discuss the various methods for the bulk synthesis of carbon nanotubes, first describing their general principles, and then focusing specifically on mass production and selective synthesis. In addition, some of the recent methods of vertical growth on surfaces (Sect. 6.1) can also yield bulk quantities of carbon nanotubes.

2.1 Arc Discharge and Laser Vaporization

Arc discharge and laser ablation were the first methods that allowed synthesis of SWNTs in relatively large (gram) amounts [7]. Both methods involve the condensation of hot gaseous carbon atoms generated from the evaporation of solid carbon. In 1992, a breakthrough in MWNT growth by arc discharge was first achieved by Ebbesen and Ajayan who demonstrated growth and purification of high-quality MWNTs at the gram level [1]. For the growth of single-wall tubes, a metal catalyst is needed in the arc–discharge system. The first success in producing substantial amounts of SWNTs by arc discharge was achieved by *Bethune* and coworkers in 1993 [2]. The growth of high-quality SWNTs at the 1–10 g scale was achieved by *Smalley* and coworkers using a laser-ablation (laser oven) method [3]. Nevertheless, the equipment requirements and the large amount of energy consumed by these methods make them less favorable for nanotube production. With the arc and laser methods, only powdered samples with nanotubes tangled into bundles can be produced. Controlled synthesis on substrates with ordered nanotube structures has not been possible by these methods.

2.2 Chemical Vapor Deposition (CVD)

The CVD method involves the decomposition of a gaseous or volatile compound of carbon, catalyzed by metallic nanoparticles, which also serve as nucleation sites for the initiation of carbon-nanotube growth. This method, which can be easily scaled up to industrial production levels, has become the most important commercial method for SWNT production [7–9]. Chemical vapor deposition is the term used to describe heterogeneous reactions

in which both solid and volatile products are formed from a volatile precursor through chemical reactions, and the solid products are deposited on a substrate. Both MWNT and SWNT synthesis have been well developed using CVD. Another advantage of CVD methods is that they allow more control over the morphology and structure of the produced nanotubes. With the CVD methods, one can produce well-separated individual nanotubes either supported on flat substrates or suspended across trenches [7–9]. These nanotubes can be directly used to fabricate nanoscale electronics.

Over the last ten years, several methods have been developed that have the potential for industrial-scale preparation of nanotubes. All of them are based on CVD methods. Among these methods, five different approaches have been shown to be the most promising: methane CVD, HiPCO, CO CVD, alcohol CVD and PECVD (plasma-enhanced CVD). Methane CVD was developed by *Dai*'s group at Stanford; they first reported the synthesis of bulk amounts of SWNTs by CVD from methane at 900 °C [5, 10, 11]. *Su* et al. significantly improved the yield of this method using Al_2O_3 aerogels impregnated with Fe/Mo nanoparticles as a catalyst [12]. Several groups used other hydrocarbons and catalysts to prepare SWNTs. For example, *Hafner* et al. prepared SWNTs using an extremely small amount of C_2H_4 diluted by Ar and an Fe/Mo bimetallic catalyst with an Al_2O_3 support. Both single- and double-wall nanotubes were observed for reaction temperatures from 700 °C to 750 °C [6].

HiPCO, which stands for high-pressure catalytic decomposition of carbon monoxide [13], is a method for the preparation of SWNTs using high-pressure CO as the carbon source. The catalysts used in a HiPCO process are formed in the gas phase from a volatile organometallic catalyst precursor introduced into the reactor. The organometallic species decompose at high temperature, forming metal clusters on which SWNTs nucleate and grow. The HiPCO process was originally developed by Smalley's research group at Rice University. Currently, the HiPCO process is the only process that can make SWNTs on a kilogram per day scale. CO was actually the first feed gas used for the growth of SWNTs. *Dai* et al. performed the first CVD synthesis of SWNTs by Mo-catalyzed disproportionation of CO at 1200 °C in 1996 [4]. It was reported that most of the resulting SWNTs had catalytic particles attached to the ends, indicating that the growth of SWNTs was catalyzed by preformed nanoparticles. The use of CO as a feed gas does offer certain advantages over hydrocarbons. Compared with samples made using the same catalyst and methane, the amount of amorphous carbon can be reduced. An important advance in the CO CVD method that makes it potentially commercial is the development of the Co-MoCat process by *Resasco*'s group at the University of Oklahoma, who used Co-Mo bimetallic catalysts and a fluidized-bed CVD reactor to produce a large quantity of SWNTs [14].

A recent addition to the family of CVD methods for SWNT production is the alcohol CVD method [15]. *Maruyama* and coworkers recently reported the synthesis of high-purity SWNTs using alcohols such as methanol and

ethanol as a carbon source. TEM and SEM showed that the products are very clean SWNTs without any amorphous carbon coating. It is hypothesized that the OH radical formed at high temperature from alcohols can remove the amorphous carbon efficiently during nanotube growth, leaving only pure SWNTs as a product.

Plasma-enhanced CVD (PECVD) methods have also been widely used for making carbon materials including MWNTs. PECVD for high-quality SWNT synthesis is only recent and has been reported by several groups [16–20]. The reactive species in the plasma system could affect the growth of very small diameter tubes, with implications to both diameter control and selective etching of metallic SWNTs (Sect. 4.3). PECVD growth of large multiwall structures has also been studied extensively and has been discussed in review articles [21].

2.3 Mass Production

Mass production of CNTs is the key factor to realize a viable CNT industry. Among the various approaches to produce CNTs, including laser ablation [3] and arc discharge [22], CVD [4] possesses promising characteristics, such as scalability and controllability and thus is regarded as the most promising approach for mass production. Table 1 compares the relative advantages of some of the CVD methods for mass production. For MWNTs, industrial scale and economical mass production has been commercially realized by a floating-catalyst CVD method. However, low-cost mass production of high-quality and high-purity SWNTs still remains a big challenge. Some approaches based on floating-catalyst [23] or catalyst-supported CVD methods have launched the market, but generally the cost is too high and the purity is not yet sufficient. The difficulty for mass production of SWNTs stems from the fact that a single MWNT is thousands of times heavier than a single SWNT, and thus to make the same amount of SWNTs, thousands of times more SWNTs in number have to be synthesized. In the floating-catalyst CVD method, catalytic metal nanoparticles are injected into a vertical furnace with a carbon source and SWNTs precipitate from the nanoparticles. Floating-catalyst CVD is an ideal system for MWNT growth because 1. CNTs can grow laterally by deposition of carbon on the sidewalls, and 2. catalyst particles are allowed to aggregate, enabling high-density catalyst injection into the furnace. Thus, the furnace is scalable in three dimensions. These features make the floating-catalyst CVD method highly productive for MWNT synthesis. On the other hand, the situation is very different for SWNT growth because neither lateral growth nor catalyst aggregation are acceptable. Also, the catalyst size has to be small, in the range of a few nanometers. As such, the general strategy to synthesize SWNTs is to dilute the catalyst density in order to avoid aggregation and to shorten the growth time in order to avoid lateral growth. Therefore, scalability has a tendency to become two-dimensional, and

Table 1. Comparison of different CVD methods for mass production

CVD method	Temperature	Scalability	Efficiency	Purity	Quality	Alignment
Floating catalyst	High	○ (3D→2D)	○	○	◎	–
Fluidized bed*	Medium	◎ (3D)	○	×	○	×
Supergrowth	Medium	– (2D)	◎	◎	○	◎

Notes: *Rotary kiln with supported catalyst. Quality: ◎ Excellent.
○ Good. × Bad. – Unknown or depends.

thus the productivity of SWNTs is diminished significantly when compared to MWNT synthesis.

Another well-pursued approach is to synthesize SWNTs on supported catalysts in systems such as a fluidized bed or a rotary kiln. Generally, these approaches have high scalability. For example, metal furnaces can be used since the growth temperature is typically below 900 °C, while most furnaces for floating-catalyst CVD growth are made of quartz or a ceramic because the growth temperature is usually above 1000 °C. The weak point of supported-catalyst CVD is the low purity of the growth product, because the support material intrinsically remains as an impurity. At this moment, there seems to be no promising approach to address this key issue. Another emerging approach is to grow massive vertically aligned SWNT forests on substrates. For example, water-assisted CVD (denoted by "supergrowth", Sect. 6.1) has a very high growth efficiency (10 min growth on a 29.7 cm × 21 cm metal foil produces more than 1 g) and can provide the purest SWNT material ever made. However, at this moment it is not obvious if this process is scalable or not. Several key points, such as large area and continuous CVD growth, need to be addressed, not to mention the issue of reducing the cost of the substrate. Finally, for SWNTs to become a widely used industrial material, eventually the cost must be reduced to the level of classic carbons, such as activated carbon or carbon fibers. This means a cost reduction of factors of hundreds to thousands must be realized in the future. All in all, so far, every existing synthetic approach has its specific weak points that need to be solved to realize mass production of high-quality, high-purity and cheap SWNTs. Only time will show which way will be the best.

2.4 Toward Selective Synthesis

Controlling SWNT growth by selectively forming nanotubes with desirable (n, m) indices is important to obtain pure metallic or semiconducting materials needed for electronics applications, such as interconnects or transistors. Unfortunately, most of the synthesis methods produce mixtures of SWNTs with random (n, m). In a few rare cases, selective synthesis phenomena have been observed. *Li* et al. [16] reported that a low-temperature PECVD growth method selectively grew ∼ 85–90 % of semiconducting SWNTs, as opposed

to $\sim 67\,\%$ of semiconductors expected for random (n, m) distribution. The selective growth was attributed to the relative low heat of formation energy of semiconducting vs. metallic nanotubes, especially for SWNTs in the very small diameter range [24]. Later, *Zhang* et al. [25] reported selective plasma etching of metallic SWNTs over semiconducting ones, raising the possibility of plasma playing a role in selective formation of semiconducting nanotubes.

Resasco and coworkers reported SWMT synthesis with highly enriched (6,5) species using a CoMo binary catalyst and CO feedstock [26]. Recently, they suggested that the (n, m) distribution of the SWNT product can be reproducibly altered by varying the reaction temperature, the gaseous feed, or the cluster surface morphology [27]. The main effect of increasing the reaction temperature is to increase the metal-particle size during the SWNT growth, and consequently the nanotube diameter. By varying the support one affects the resulting morphology of the metal cluster, and as a result, the chiral angle of the nanotube produced. The interaction of the metal and the support plays an important role in the size and morphology of the cluster. It may be possible that by the appropriate selection of the growth parameters (support, gas, temperature, etc.) one can have a relatively narrow control of the (n, m) distribution [27]. However, much work remains to be done to selectively grow SWNTs with specific (n, m) over a wide range of diameters and chiralities.

3 Purification

"Purification" of carbon nanotubes is a process that separates nanotubes from non-nanotube impurities included in the raw products, or from nanotubes with undesired numbers of walls. These impurities generally include amorphous carbon, catalysts, catalyst supports, carbon nanoparticles, and unwanted nanotubes such as a small amount of MWNTs in a raw SWNT sample, or SWNTs in DWNT samples. Generally, the purification methods can be separated into dry methods and wet methods. However, the separation method varies dramatically for nanotubes produced using different methods described above, since the type of impurities included in the raw samples are quite different depending on the production methods.

Purification has been an important synthetic effort since the discovery of carbon nanotubes, and there are hundreds, if not thousands, of publications discussing different aspects of the purification process. Here, we just intend to give a brief overview of the principles with a few examples. Good review articles on the purification of nanotubes are available in the recent literature [28, 29].

3.1 Dry Methods

The dry methods of purification refer to methods that can selectively remove, through gas-phase oxidation, amorphous-carbon species due to their

higher reactivity compared to that of carbon nanotubes. The simplest method is air oxidation at selected temperature, originally developed for the purification of MWNTs produced by either CVD or arc-discharge methods [30]. For SWNTs, due to their higher reactivity than MWNTs, the reaction conditions need to be adjusted from simple air oxidation to improve the selectivity of oxidation and to improve the purification yield. For example, *Zimmerman* et al. [31] reported a gas-phase purification method incorporating Cl_2, H_2O, and HCl gaseous mixtures for SWNTs grown from pulsed-laser vaporization. SWNTs grown from the arc discharge method can be purified by oxidizing in air at 350 °C or 470 °C, as described in different reports [32, 33]. For CVD and HiPCO nanotubes, there are also many reports on their purification. For example, HiPCO nanotubes can be purified using wet air (or wet Ar–O_2) oxidation, at 180–300 °C [34]. A scalable method to effectively purify HiPCO nanotubes was also developed by *Smalley*'s group at Rice University by adding a step to convert metal oxide in raw samples after mild oxidation to $C_2H_2F_4$ or SF_6 to form a metal fluoride that can be easily removed by HCl treatment [35]. Many more reports on gas-phase purification are available in the literature [28, 29].

3.2 Wet Methods

The wet methods treat nanotubes in solution for purification purposes, and can be used alone or together with dry methods. Actually, most dry methods of purification are also followed by a step of acid treatment to dissolve metal catalyst and/or metal oxides formed during the gas-phase oxidation step. Use of nitric acid (HNO_3) is the most common wet method for purification, as it is straightforward, inexpensive, and effective in removing metal catalysts and amorphous carbon from large quantities of raw material. For example, as-prepared SWNTs grown by laser-ablation techniques are known to have long bundles of SWNTs with few defects. They can be purified using nitric acid treatment [36–43]. In a typical run [41, 43], raw SWNTs are refluxed in 2.6 M HNO_3 for 45 h. After repeated filtration steps and maybe also centrifugation steps, highly purified nanotubes can be obtained. This method is also widely adapted for the purification of nanotubes prepared by other methods with a small variation in acid concentrations. Wet purification methods can also be combined with dry oxidation methods. For example, *Dillon* et al. [37] have reported a nondestructive, scalable, three-step purification process that yields materials with 98 % purity. Their method contains a dilute nitric acid (3 M HNO_3) reflux for 16 h, functionalized, and redistributes the nonnanotube fractions, so as to form a uniform and reactive coating on the SWNTs. This coating is selectively removed by oxidation in stagnant air. In addition, they investigated the effect of this procedure on arc discharge SWNTs, and found that a relatively long-period exposure consumed a significant fraction of the nanotubes themselves, due to the presence of a larger metal content.

Additionally, other methods, including different chromatography methods [44–46] and centrifugation methods [47, 48], were also demonstrated to be very useful for the purification of carbon nanotubes. For example, Haddon's group at UC Riverside discovered that ultracentrifugation at different speeds can be a very effective method for the purification of SWNTs made by the arc method [47]. The method is capable of large scaleup at low cost.

4 Sorting

Although there has been promising progress toward the selective synthesis of carbon nanotubes of specific structure or electronic type (Sect. 2.4), all synthesis methods reported to date produce mixtures of carbon nanotubes of different structures and types. Therefore, significant research is currently being devoted to developing methods for sorting these mixtures into specific structures or types [29, 49]. By "sorting", one ideally refers to the partition of a mixture into physically separated ensembles of carbon nanotubes of a particular type (metallic or semiconducting) or structure (length, diameter, chirality), or, even more ideally, a specific pair of (n, m) indices. Less ideally, but often more realistically, one can also refer to partial sorting or "enrichment" of samples having a higher proportion of a particular type, or "fractionation" into ensembles having a narrower distribution of diameters or lengths.

During the last five years, significant progress in carbon nanotube sorting has been enabled by the development of new methods of dispersing carbon nanotubes in solution [50], as well as by new methods of carbon nanotube metrology (see contribution by *Jorio* et al.), which are critical for determining the distribution of structures in carbon nanotube samples. The dispersion of discrete carbon nanotubes in solution and their systematic population analysis have also enabled the study of selective interactions between external forces or chemical species and carbon nanotubes of different structures and/or types. Any of these selective interactions can in principle be exploited for the sorting of carbon nanotubes. This section reviews the different methods of carbon nanotube sorting, and also the different selective interactions, which could in principle become the basis for future sorting methods. Rather than sequentially reviewing the more than 70 reports related to the topic of carbon nanotube sorting, we shall first attempt to classify them in a rational way by their operating principles. We then describe some of the most promising methods of sorting reported so far, and finally try to draw some conclusions and perspectives toward the ideal sorting of carbon nanotubes.

4.1 Classification of Sorting Methods and Selective Processes

The different methods of carbon nanotube sorting, and selective interactions or processes, which could eventually lead to new methods of sorting, may be rationally classified by the following aspects:

1. *Parameter of selectivity* (from more general to more specific): length (L), electronic type (M/S), diameter (d_t), chirality (θ), and structure (n, m).
2. *Type of selective force or interaction* (from weaker to stronger, or from longer to shorter range): gravity (e.g., in sedimentation), inertial forces (e.g., in centrifugation), volume-exclusion forces (e.g., in size-exclusion chromatography), electric-field (e.g., dielectrophoresis), selective noncovalent adsorption (e.g., by van der Waals forces, charge-transfer, π-stacking, etc.), reversible covalent functionalization, irreversible chemical reaction, and finally, a selective elimination by a chemical (e.g., etching) or physical (e.g., electrical breakdown) process.
3. *Type of medium* (from less to more condensed): vacuum, plasma, gas, organic solvent, aqueous solution, gel, and solid.
4. *Degree of separation* (from lower to higher): selective orientation (e.g., by electric field), selective modification (e.g., adsorption, reaction, etc.), microscopic selection (e.g., selective deposition of individual nanotubes), bulk enrichment, and finally, complete bulk separation.
5. *Production scale* or *scalability*, namely, what amount of nanotubes are sorted, or can be sorted, using a particular method.

Combinations of different selection parameters, types of interactions, or types of medium are also possible.

Table 2 summarizes different reported methods of sorting and selective processes, with their respective references, classified by the parameter of selectivity and the type of selective force or interaction. Specific subgroups of interactions are listed in italics. The type of medium is indicated in parentheses, unless it is an aqueous dispersion with common ionic or nonionic surfactants, such as sodium dodecylsulfate (SDS), sodium dodecylbenzenesulfonate (SDBS) or Triton X-100, assuming that the interaction with the surfactants is not the main selective agent. In each field, the different items are listed by increasing degree of separation (4). Items in black indicate actual sorting or enrichment methods, which are in principle scaleable, whereas items in gray are selective processes not attaining a physical separation of the different types of nanotubes. Specific remarks are listed below the table.

4.2 Nondestructive Sorting

Four exemplary nondestructive methods of carbon nanotube sorting selected from Table 2 are schematically represented in Fig. 1, and explained below (other methods have been described in recent reviews [29, 49]).

Dielectrophoresis (Fig. 1a)

This was the first demonstrated method of sorting by electronic type [59]. In this method, a surfactant-stabilized aqueous suspension of single-wall carbon nanotubes is placed onto an array of interdigitated electrodes, across

Table 2. Classification of sorting methods and selective processes

	L	M/S	d_t
Gravity		Precipitation[1]	
Inertial forces		Centrifugation[1]	
Hydrodynamic forces	Field-flow fractionation [43, 51]		
Volume-exclusion forces	Size-exclusion chromatography [44, 45, 52–56]	Filtration[1]	
Electric field	Electrophoresis [57, 58]	Dielectrophoresis [59–67]	Electrophoresis [58]
Noncovalent adsorption		RNH_2 $(THF)^2$ + filtration [68, 69]; + centrifugation [70, 71]	
Van der Waals	Extraction TOAB $(H_2O/EA)^3$ [72]		Encapsulation of metallocenes [73] Reversible cyclic peptides + centrifugation [74]
Charge transfer		Br_2 + centrifugation [75]	Electrochemical doping [76] $FeCl_3$ [77, 78] K [77, 78]
π *stacking*		Porphyrins + centrifugation [79]	DNA + centrifugation [80]
Reversible covalent functionalization		$RN_2^+ + e^-$ [66] $RN(CH_2)_2^-$ + precipitation [81]	
Chemical reaction		$OsO_4 + h\nu$ [82]	
Chemical decomposition		RN_2^+ (l/s) [83] H_2O_2 [84] H plasma [85] CH_4 plasma (g) [86]	HNO_3 [87] O_2 (g) [87] H_2SO_4/H_2O_2 [88]
Physical destruction		Electrical breakdown (g/s) [89, 90]	

Notes: [1] These processes are not selective per se, but are used for physical separation in combination with the selective processes listed below. [2] THF = tetrahydrofurane. [3] TOAB = tetraoctylammonium bromide, EA = ethyl acetate

Table 2. continued

	M/S + d_t	θ	n, m
Gravity			
Inertial forces			
Hydrodynamic forces			
Volume-exclusion forces			
Electric field	Dielectrophoresis field-flow fractionation [91]		
Noncovalent adsorption	RNH_2 $(THF)^2$ + filtration [92]		
Van der Waals			Bile salts + density-gradient centrifugation [93]
Charge transfer	$Fe(CN)_6^{3-}$ [94]		
π stacking			DNA + ion-exchange chromatography [95–98]
Reversible covalent functionalization	H^+ [99] RN_2^+ [100–102] RN_2^+ + filtration [103] RN_2^+ + dielectrophoresis [104]	RN_2^+ [105]	
Chemical reaction	CCl_2 [106]		
Chemical decomposition	NO_2^+ [107, 108] F_2 (g) [109]	H_2SO_4/H_2O_2 [110]	
Physical destruction			

Notes: [1] These processes are not selective per se, but are used for physical separation in combination with the selective processes listed below. [2] THF = tetrahydrofurane. [3] TOAB = tetraoctylammonium bromide, EA = ethyl acetate

which an ac voltage of 10 V at 10 MHz is applied for a few minutes. The dielectrophoretic force acting on a particle is proportional to the field square gradient and the Clausius–Mossotti factor $(\varepsilon_p - \varepsilon_m)/(\varepsilon_p + 2\varepsilon_m)$, where ε_p and ε_m are the dielectric constants of the particles and the medium, respectively. The dielectric constant of metallic SWNTs is larger than that of water, whereas that of semiconducting nanotubes is actually smaller, so the Clausius–Mossotti factor is positive for metallic nanotubes but negative for semiconducting ones. Hence, only the metallic carbon nanotubes are attracted toward the electrodes, and selectively deposited onto them, while the semiconducting nanotubes remain in the suspension. This method can yield $\sim$ 100 pg quantities of carbon nanotubes enriched with 80 % metallic nanotubes. Interestingly, the Clausius–Mossotti factor can be modified by varying the frequency [61] or by chemical functionalization [104], thus allowing different sorting possibilities. The method can be used for depositing thin films of aligned metallic nanotubes [67], and can in principle be scaled up using macroscopic electrodes [64], filtration [62], and microfluidics. Dielectrophoretic field-flow fractionation is an interesting way of combining the advantages of dielectrophoresis and field-flow fractionation [91], which also allows sorting by diameter. In any case, the fact that dielectrophoresis requires an inhomogeneous field means that its scaling up for mass production may not be trivial.

Covalent Functionalization (Fig. 1b)

This is a more classically chemical approach to type and diameter sorting. Diazonium ions (RN_2^+, where R is an aromatic group, such as 4-chlorophenyl) were shown to react selectively with metallic carbon nanotubes of small diameters [100]. Similar selective functionalization with diazonium ions having the bulky group R = 4 tert-butylphenyl enabled subsequent separation by filtration on silica gel [103]. After separation, the metal-enriched functionalized SWNTs could be defunctionalized into pristine SWNTs by thermal treatment. This process can in principle be performed in a chemical reactor, so it could be massively scaled up.

DNA-Assisted Dispersion (Fig. 1c)

This is an interesting pathway for type and diameter sorting [95]. Single-stranded DNA was shown to wrap around SWNTs, allowing their dispersion in aqueous solutions. The DNA-wrapped SWNTs are negatively charged, and can then be fractionated by ion-exchange chromatography, yielding a fraction enriched in metallic or semiconducting SWNTs with different diameter ranges. The use of a specific DNA sequence consisting of a $d(GT)_{10–45}$ repeat (i.e., 10 to 45 alternate G and T bases) significantly enhances the structure-based sorting of SWNTs, producing highly enriched fractions of

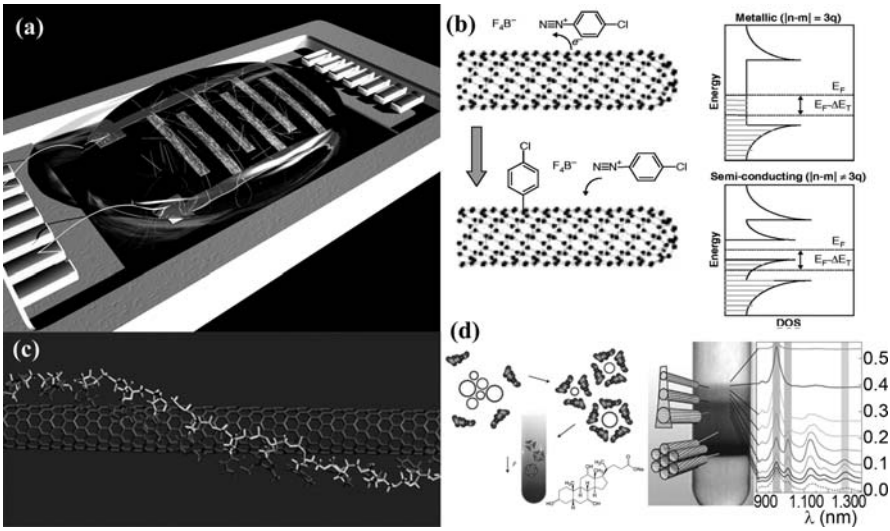

Fig. 1. Exemplary nondestructive methods of carbon nanotube sorting. (**a**) Dielectrophoresis [59]. (**b**) Covalent functionalization [100] (E_F: Fermi energy; ΔE_T: charge-transfer energy). (**c**) Ion-exchange chromatography with DNA. Model of a DNA-wrapped SWNT [95]. (**d**) Density-gradient centrifugation with bile salts (e.g., sodium cholate) [93]

specific (n, m) [96]. This process is scalable in principle, but relatively expensive due to the high price of oligonucleotides.

Density Differentiation with Bile Salts (Fig. 1d)

This is a very promising recent approach for (n, m) sorting [93]. Bile salts are relatively bulky and rigid surfactants that are naturally derived from cholesterol. They encapsulate SWNTs in such an arrangement that the density of the supramolecular assembly depends on the nanotube diameter. Hence, ultracentrifugation in a density gradient leads to separation by type and diameter. Using narrowly dispersed starting materials, such as CoMoCAT-grown SWNTs, and repeating the separation with the right combination of surfactants, allow the production of highly enriched fractions with single (n, m) structures. The fact that bile salts are abundant byproducts of the meat-processing industry, and the relative simplicity of the centrifugation technique, could make this sorting method highly scalable and inexpensive.

4.3 Selective Elimination

The last two rows of Table 2 show different sorting methods based on selective elimination. Such methods may be especially important for the elimina-

tion of metallic nanotubes from nanotube-based electronic circuits in situ, in order have only semiconducting nanotubes to operate as field-effect transistors (FETs). Selective physical destruction of metallic nanotubes by electrical breakdown has been used for this purpose [89, 90]. However, this method requires the nanotubes to be connected to electrodes, which is a limitation for large-scale integration of nanocircuits. *Dai* and coworkers [25] have recently developed a process of methane plasma followed by annealing, to selectively etch or hydrocarbonate M-SWNTs and retain S-SWNTs in the 1–2 nm diameter window. It is revealed that diameter is an important factor in the chemical reactivity of a SWNT towards hydrocarbonation and etching. Smaller-diameter SWNTs (below ~ 1.2 nm) are preferentially etched over larger ones due to the higher radius of curvature and higher strain in the C–C bonding configuration. In a certain diameter range, metallic tubes are selectively etched over semiconducting ones due to more abundant delocalized electronic states. The difference in chemical reactivity diminishes for SWNTs with large diameters (~ 2 nm and larger) without selectivity [25].

The gas-phase etching method is reliable and can provide 100 % yield of semiconductors in an ensemble of SWNTs. The retained S-SWNTs are free of covalent alterations upon thermal treatment and thus exhibit electrical properties similar to pristine materials. The distribution of diameters of the S-SWNTs is narrowed down to a window (~ 1.3–1.6 nm) that provides sufficient bandgaps for high on/off ratios and allows for good electrical contacts, both of which are important for high-performance electronics [25]. The dual effects of selective metal removal and diameter-distribution narrowing combined with compatibility with microfabrication technology make the method promising for large-scale SWNT electronics. This method was used to demonstrate FETs with large numbers of S-SWNTs in parallel by selectively etching metallic SWNTs in a large ensemble of tubes. About 20 intact semiconducting SWNTs in parallel in SWNT devices were obtained without any metallic short [25].

4.4 General Principles and Perspectives of Sorting

By looking at Table 2 and considering the selected examples, one can learn several interesting principles: *Length*-sorting methods are usually based on relatively weak and long-range forces, such as in field-flow fractionation [43, 51], size-exclusion chromatography [44, 45, 52–56], and electrophoresis [57, 58]. One interesting exception is the length-dependent extraction in a two-phase liquid–liquid system using a phase-transfer chemical agent [72]. In contrast, methods for sorting by *type* and *diameter* (and combinations thereof) are usually based on stronger or shorter-range forces, from electric fields to covalent bonding. Nondestructive selective interactions with chemical species cannot by themselves lead to sorting, unless they are combined with an additional weaker or longer-range force, which is used to physically

separate the different nanotubes, for example by precipitation [81], centrifugation [70, 71, 74, 75, 79, 80, 93], filtration [68, 69, 92, 103] or chromatography [95–98]. In these cases, the selective interaction with chemical species will lead to a physical separation based on chemically induced differences in solubility [68,69,74,81,92,103], density [75,93] or charge [95–98]. It is interesting to note that type and diameter selectivity often come together. This can often be attributed to the fact that smaller-diameter nanotubes have a larger bandgap and a higher strain. Hence, the diameter also affects the physical and chemical properties of the nanotubes. In general, metallic carbon nanotubes are more reactive than semiconducting ones toward covalent functionalization due to their higher density of states near the Fermi energy [100], resulting in stronger orbital interactions [111, 112]. However, semiconducting-selective reactions have also been reported [79]. Smaller-diameter nanotubes are generally more reactive toward covalent functionalization due to their higher strain and sp^2-orbital pyramidalization [113]. On the other hand, their doping or charge-transfer functionalization is more favorable for large-diameter nanotubes due to their smaller bandgap [76, 77, 113]. Interestingly, there are very few reports of *chirality*-dependent processes [105, 110], and their chiral dependence can actually be attributed to a combination of type and diameter selectivity. The lack of intrinsically chirality-dependent processes may indicate that chirality per se does not strongly affect the chemical or physical properties of the nanotubes, but rather their type and diameter. Moreover, there is currently no method for chirally resolving left-handed from right-handed nanotubes. One could envisage a chiral-dependent process by a commensurate interaction between the rolled graphene sheet and a chiral crystalline surface or a helical overlayer of chiral molecules, but such resolution has not yet been reported. Finally, the ultimate sorting of unique (n, m) structures has so far been achieved by highly type- and diameter-selective processes using narrowly distributed starting materials [93, 95]. From these principles, it may be concluded that the most promising pathway for the production of pure (n, m) samples could be a skillful combination of a selective synthetic method (Sect. 2.4) with a highly type- and diameter-selective sorting method, based in turn on a combination of chemical modification with an effective means of physical separation. Amplification of (n, m)-sorted SWNT "seeds" by continued growth [114–116] could make the sorting process even more scalable in an analogous way as the synthesis of DNA has been boosted by the invention of a polymerase chain reaction (PCR). If progress continues at a good pace, the day when one can order carbon nanotubes with specific (n, m) and length from a catalog may not be too far away.

5 Organization into Fibers

Carbon nanotubes, both single wall and multiwall have beguiling axial properties. Mechanically, they have been shown to be very strong and stiff, elec-

trically they are conducting, and in the case of single-wall tubes, the nature of the conductivity, ranging from metallic to a large-band-gap semiconductivity, depends critically on how the graphene sheet is joined up to make the tube, in fact on its chirality. They also show promise as thermal conductors.

The challenge is to organize these individual nanotubes into a material that will transfer their individual properties into an exploitable material form. In the case of the axial properties of carbon nanotubes, the obvious material form is a fiber in which the nanotubes are well aligned with the axis and as closely packed as possible. There is a broad spectrum of research aimed at maximizing the property transfer from the nano- to the macroscale, and it reflects one of the central themes of materials science, namely the organization of atomic, molecular, nano- and microscales of structure to realize desired properties at the macroscale. The properties of the individual nanotubes, the building blocks for the fiber, are crucial in determining the final properties, for it is all but impossible that these will be enhanced on fiber forming, and in general they will be degraded.

This section focuses on the developing technologies that are providing routes to the production of fibers consisting of carbon nanotubes. However, there are many options for incorporating varying amounts of a second material, typically a polymer, within the fiber. Of course there is a continuous range of compositions here, ranging from pure nanotube fibers, through property-modified nanotube fibers, through composites, through to what are really no more than nanotube-filled polymer fibers, and finally through to pure polymer fibers themselves. An arbitrary limit is set in this section, in that only fibers with concentrations greater than 20 % carbon nanotubes are discussed, and where the nanotubes are the minority component, then the descriptions are limited to processes that can also make quite pure nanotube fibers. Hence, coagulation spinning of composite fibers is included, but not melt extrusion and drawing of a polymer containing carbon nanotubes as a filler, as in this latter case the enhancement of the melt viscosity by the nanotubes makes such processing difficult above concentrations of 10–20 %. There is also another focus, and most attention is given to processes that have the ability to spin fibers continuously.

5.1 Processing Principles

The task is clear, we have to start with carbon nanotubes in some form, and organize these into a fiber, while at the same time, as far as is possible, align them perfectly with the fiber axis. Carbon nanotubes are long and thin, and in the case of single-wall tubes, their diameter is similar to that of many polymer molecules (e.g., the PMMA molecule is ~ 0.7 nm in diameter). They are, however, very stiff compared with even the stiffest polymer molecules. Computational modeling [117] indicates that the persistence length of even a small-diameter single-wall carbon nanotube (7,7) is some tens of micrometers, which would make it some 100 times stiffer than DNA. While such a

value may be surprising, it should be remembered that a thin-walled tube is amongst the stiffest, per unit mass, of all engineering structures, and in the case of carbon nanotubes bending requires the stretching and compression of the strong carbon–carbon bonds. A direct consequence of this stiffness is that assemblies of carbon nanotubes are not expected to melt to form any free-flowing phase. The melting point of any crystal is given by $T_{\mathrm{m}} = \Delta H/\Delta S$. In the case of nanotubes, the ΔS term is vanishingly small on two counts. Firstly, their intrinsic stiffness means they are all but as rigid in the disorganized state than when packed parallel on an hexagonal net; secondly they are large compared with individual atoms so the entropy of mixing is correspondingly very small. The melting point is thus effectively "off scale", and melt-processing routes are not available. It is therefore necessary to look at other options. There are two: creating free-flowing suspensions in a low molecular weight liquid or applying mechanical fields to dilute assemblies of nanotubes in a gas phase. In each gas the dilution of the nanotubes will enable them to be oriented by the field as it forms the fiber. These two approaches, which may be classified as "wet" and "dry", form the basis of all the successful process strategies for the formation of carbon nanotube fibers. A final method, which is currently being reduced to practice, involves the extension of an existing fiber by continual synthesis and deposition of carbon nanotubes onto its end [115]. In the descriptions below, the wet routes will be explored first, and then the dry.

5.2 Liquid Suspensions of Carbon Nanotubes

With so little entropy to be gained through distributing nanotubes in a liquid medium, it has to be achieved by treating the system so that there is a clearly negative heat of mixing (ΔH_{mix}), or in other words, there needs to be a preference for bonds to be formed between the nanotube surface and the molecules of the liquid. Such a favorable heat of mixing can be achieved either by a very careful choice of solvent [118], or by surface treating the carbon nanotubes so that they are compatible with the suspending liquid [119] or through the use of surfactants, i.e., small molecules that have a liquid compatible part and a carbon nanotube-compatible part [52]. These strategies continue to evolve. A key aspect of liquid suspensions of long rigid rods is that they can organize in two ways, they can assume random orientations (bag of nails) but with very inefficient packing so that such structures will be associated with high dilutions. Alternatively, the rods can pack parallel, but with solvent molecules still between them. Such a phase is a solvent stabilized, or, specifically a lyotropic, liquid-crystalline phase. The relationship between the concentration of rigid rods in a suspending medium, and either the heat of mixing (ΔH_{mix}), or the temperature, is shown as a schematic phase diagram in Fig. 2, first predicted by *Flory* [120]. *Song* et al. [121], first demonstrated nanotube liquid crystallinity using aqueous suspensions of multiwall nanotubes. They extended the study to topological defects in the

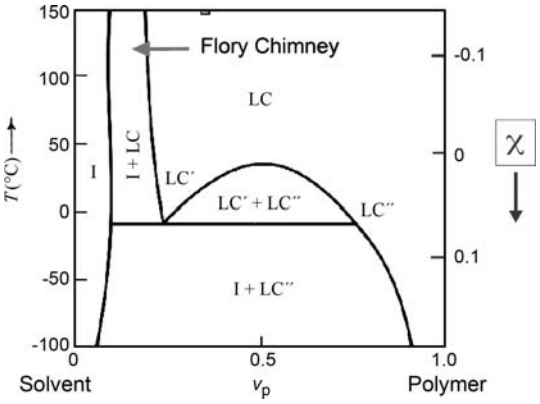

Fig. 2. Schematic phase diagram for a system consisting of a liquid containing rigid rods in suspension. It shows isotropic and liquid-crystalline phase fields (I) and (LC). The diagram does not allow for the possibility of crystallization of the rods at high concentrations. The diagram is drawn here as a function of temperature and χ, which is a variable related to the heat of mixing, ΔH_{mix}

director fields relating these back to the precepts of liquid-crystal science. Incidentally, where there is a distribution of lengths and perfection amongst any suspension of carbon nanotubes, it has been shown that, for concentrations within the two-phase region or "Flory chimney", the longer, straighter tubes partition into the liquid-crystalline phase, with the poorer material being rejected into the isotropic phase. Such partition has recently been exploited in a fractionation process [122], which has relevance as the longer, straighter nanotubes are known to form stronger fibers, as is discussed further below. Liquid crystallinity is an example of self-organization, and such phases are known to be an excellent precursor for obtaining high orientation in fibers spun from the liquid, the process for making aramid fibers being the most important example, e.g., [123].

5.3 Spinning Carbon Nanotube Fibers from Liquid-Crystalline Suspensions

The first successful spinning of a continuous single-wall carbon nanotube fiber from a liquid-crystalline suspension was reported in 2004 by *Ericson* et al. [124] from Rice University. The suspending medium for an 8 % dispersion single-wall nanotube, which had been synthesized from carbon monoxide in the HiPCO method, was 102 % sulfuric acid (2 wt% excess SO_3). The suspension was stabilized by the formation of a charge-transfer complex as the acid protonated the nanotubes. The solution, which had to be kept completely dry, was extruded into an aqueous coagulation bath where the sulfuric acid was removed, leaving a fiber of the order of 50 µm diameter. Figure 3 shows a WAXS diffraction pattern of the fiber (fiber axis vertical)

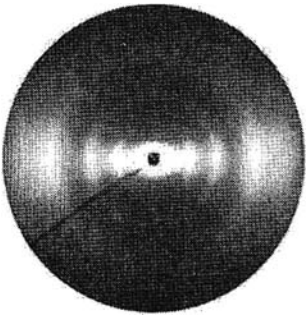

Fig. 3. Wide-angle X-ray diffraction picture of a single-wall carbon nanotube fiber drawn from a liquid-crystalline suspension in concentrated sulfuric acid. The *pattern* indicates high-quality alignment of the nanotubes with the fiber axis [124]

and an azimuthal scan yielded a peak width of 31° (at half-maximum). The fibers showed a strength of 0.16 GPa and a stiffness of 120 GPa.

Two other pieces of work have explored the production of fibers by essentially the same route as the Rice work, but using rather more amenable solvents. *Steinmetz* et al. [125] spun from a stabilized aqueous suspension of arc-grown single-wall nanotubes into a coagulation bath of either ethylene glycerol or ethylene glycol, to which 1 % SDS had been added to act as a surfactant. The fibers were then washed to remove the surfactant. By way of comparison, *Zhang* et al. [126] spun from an ultrasonically stabilized suspension of multiwall nanotubes in glycol into a coagulation bath of ether. The processes produced fibers of strengths of ~ 0.1 GPa (inferred) and 0.20 GPa, respectively. The elastic moduli, however, were 2 GPa and 130 GPa for the two processes. The electrical conductivities were also very different, being 700 S/m and 8000 S/m. *Zhang* et al. also measured the quality of the alignment in a way that permits comparison with the sulfuric acid spinning of [124]. The Zhang value was 20° width at half-height for the azimuthal peak, indicating somewhat better alignment for the multiwall nanotube specimen.

It would appear that all three of these spinning processes were from lyotropic liquid-crystalline suspensions, although *Steinmetz* et al. do not say so explicitly. The strengths, and in the case of the single-wall surfactant dispersed tubes, the elastic modulus, are disappointing. Various authors across the field have commented that a central factor in maximizing strength will be the lengths of the individual nanotubes [127, 128], in much the same way as the strength of polymeric fibers is optimized at high molecular weights. Strengths are also likely to be enhanced by crosslinks between individual nanotubes [125].

5.4 Wet Spinning of CNT Composite Fibers

It appears that the first successful spinning of a carbon nanotube-bearing fiber was by Vigolo, Poulin and coworkers in a sequence of papers stemming from *Vigolo* et al. in 2000 [129]. In [130] the team reports the spinning of continuous lengths of a composite fiber consisting of a significant concentration

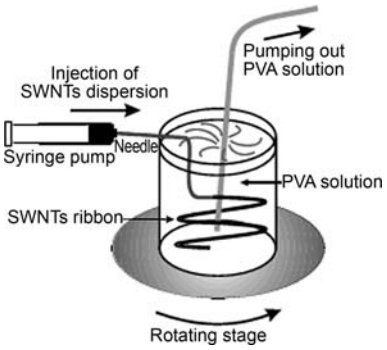

Fig. 4. The wet spinning method developed by *Vigolo*, *Poulin* and co-workers [130]. An aqueous suspension of carbon nanotubes, stabilized by a surfactant, is injected into a flowing solution of polyvinyl alcohol which causes the fiber to coagulate. It is then removed from the bath and washed to remove excess polymer. The resultant fiber is a composite, typically 50/50 of carbon nanotubes and polymer

of nanotubes in polyvinyl alcohol (PVA). They set the work in the context of other alignment methods such as electrophoretic nanotube alignment for short fiber lengths [131], and also provided a good basis for the use of surfactants to achieve the dispersions. Figure 4 [130], shows the essence of the process. A dilute surfactant-stabilized aqueous suspension of single-wall carbon nanotubes, (CNT concentration $< 1\,\%$, surfactant, SDS, concentration $< 5\,\%$) is injected into a flowing bath of PVA solution in water. The PVA replaces the water causing the fiber to coagulate. The fibers had a strength of 0.15 GPa and a stiffness of 15 GPa. The work sparked a development process involving stretching of "rewetted" fibers [132], to give a strength of 0.2 GPa and a stiffness of 40 GPa.

Further developments have followed by the French group [133, 134], who have shown that for SWNT PVA ratios in the region of 50/50, that in addition to improved strength and stiffness, very high toughness fibers can be obtained. In particular, the process of hot drawing of the composite [133] seems to provide an exciting enhancement of toughness at low strains, with a strength of 1.5 GPa and a toughness (at 11 % fracture strain), of 55 J/g. The orientation of the PVA molecules in such samples is of a particularly high order. Figure 5 shows the stress/strain data from [133] correlated with the WAXS patterns indicating the degree of alignment in the fibers. In a parallel development involving coaxial flow, fibers of strengths as high as 1.8 GPa [135] have been seen. Salt routes for nanotube dispersion, where a sodium salt is made in association with the nanotube that then carries charge, possibly as much as one unit per ten carbon atoms, are a further important step [136]. When placed in a polar solvent the charged nanotubes form a suspension without the need for sonication and the possible consequence of a reduction in fiber lengths. Applying this suspension route to the coagulation process [127], produced mechanical properties close to those for the SDS-spun material, even with only 15 % CNT loading compared with 50 % for the surfactant suspensions. Wet-spun composite fibers are unlikely to be good candidates for high electrical conductivity owing to the insulating polymer separating the nanotubes, and there are correspondingly only sparse reports

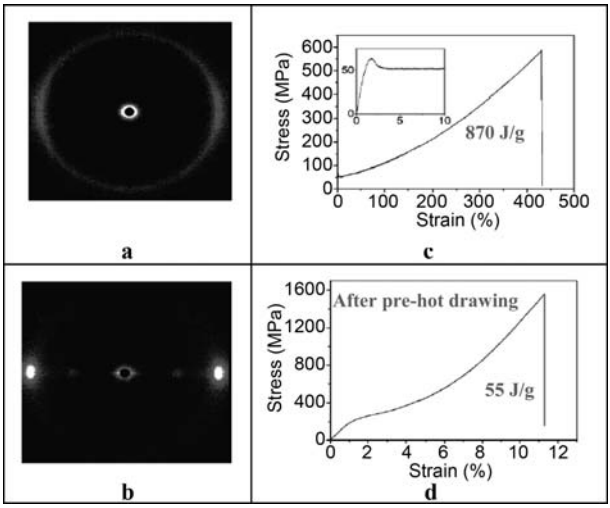

Fig. 5. More recent results from the wet-spinning method showing X-ray and stress-strain data from wet-spun composite fibers (SWNT/polyvinyl alcohol), incorporating additional alignment procedure during spinning, (**a**) to give a remarkable tough fiber by any comparative standard, albeit measured up to a breaking strain of 430 % and (**b**), the result of hot drawing the fiber, giving much better orientation of both the nanotubes and the matrix polymer molecules, and a resultant increased fracture stress, whilst retaining a significant energy to break for only 11 % elongation [133]

of such measurements. However, values in the range of 4–300 S/m, have been quoted for SDS wet-spun CNT fiber.

The coagulation spinning technique is versatile, and has been used by several workers to generate fibers with a wide range of polymers with comparatively low nanotube loadings for specific purposes. References [137–140], for example, cover polyanaline, polyacronitrile and UHMW polyethylene.

5.5 Dry Spinning from Carbon Nanotube Forests

Carbon nanotubes, especially multiwall ones, can be grown as "forests" from a flat substrate with comparative ease (Fig. 6a). The nanotubes are relatively straight and thus have only modest levels of entanglement. *Jiang* et al. [141] first demonstrated that for forests grown under the right conditions, the nanotubes can be drawn away from the forest edgeways to form a very thin coherent film that can then be twisted into a fiber.

A process established for continuous wind-up [142] has provided an excellent basis for determining the influence of twist on strength, where the relationships between twist angle and nanotube lengths can be analyzed using the precepts of yarn technology, as it applies to the creation of continuous yarn from twisted short fibers (staple) [143]. Figure 6b shows the process in operation. The twisted yarn in this example is in fact very fine (2 µm diameter),

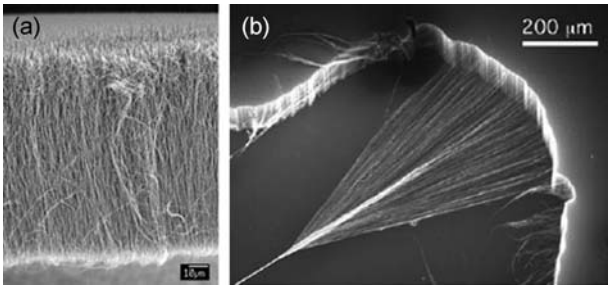

Fig. 6. Dry spinning from carbon nanotube forests. (**a**) A typical "forest" of multiwall carbon nanotubes grown from a substrate, in this case a silica plate. (**b**) Photograph of the spinning of a carbon nanotube fiber from a forest of multiwall nanotubes. The fiber is drawn at right angles to the direction of the nanotubes in the forest [142]

and could be difficult to see with the naked eye. The mechanical properties first reported were tensile strengths in the range of 0.3–0.8 GPa and stiffnesses up to 25 GPa. The electrical conductivity reported was 30×10^3 S/m (compared to Cu: 60×10^6 S/m). With the twist optimized, one route towards increased mechanical and electrical properties is likely to be the growth of forests of ever-increasing length [128, 144]. There is also the possibility of exploiting the thin films drawn as they first emerge from the forest. They are exceptionally thin and transparent; they also show amazingly high strengths on a mass per unit area basis [145].

5.6 Direct Spinning from Carbon Nanotube Fibers from the CVD Reaction Zone

In all the techniques described so far, the carbon nanotubes have to be synthesized in one stage, and the fibers spun as a second distinct step. The method of spinning nanotube fibers directly from the CVD reaction zone was introduced by *Li* and coworkers [146]. There have been numerous reports in the literature of fibrous-like deposits in CVD reaction chambers. Of these *Zhu* et al. [147] were the first to measure mechanical properties of 20 cm strands, which they found were significant with elastic moduli of the order of 50 GPa and strengths of 1 GPa. The Cambridge process [146] took the significant step of realizing that the carbon plume formed in the reaction chamber, where the floating catalyst of iron was introduced into the furnace as ferrocene dissolved in the liquid hydrocarbon feedstock, had elastic properties owing to the entanglement of the long nanotubes. This elastic smoke can be "hooked" and wound up continually either within the furnace or outside. The geometry can be varied to form either a fiber or a film (Figs. 7 and 8). The elastic smoke is technically an aerogel. Its condensation into fiber or film geometries is either achieved through the particular wind-up geometry em-

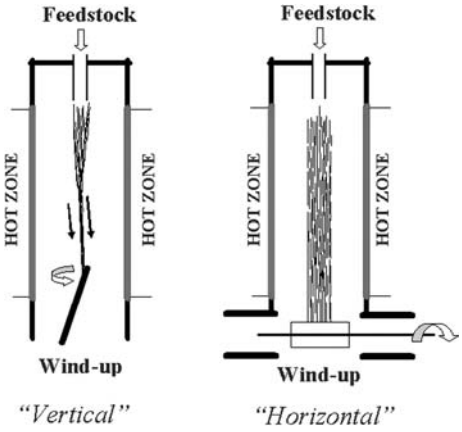

Fig. 7. Schematic diagrams of the process by which carbon nanotube fibers are spun directly from the CVD reaction zone. Two wind-up schemes are illustrated here, one to produce fiber, the other thin film

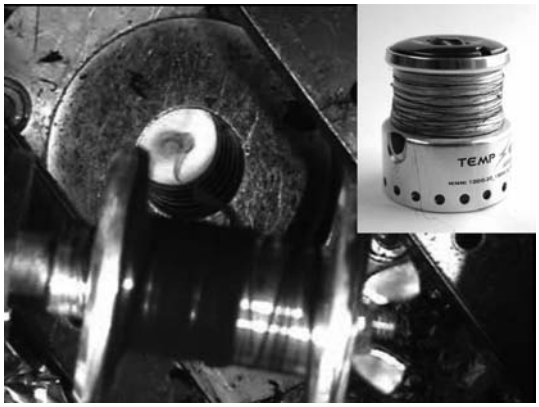

Fig. 8. Fiber being spun directly from the furnace via a gas valve that separates the hydrogen in the furnace from the air. The fiber condensation, at an intermediate level is achieved by the rotary motion of the gas. The *inset* shows a fiber after full condensation using acetone evaporation

ployed, or by subsequent twisting or wetting with an appropriate solvent. The process is enhanced through the addition of a sulfur-containing compound, typically thiophene, to the feed stock. Optimization of the process depends on the achievement of the right balance of feedstock composition, including catalyst and sulfur concentration, injection rate, hydrogen carrier gas flow rate, furnace temperature and wind-up speed [148, 149].

Fibers can be routinely spun with strengths of the order of 1 N/tex (if the specific gravity of the fiber is assumed to be unity, then these numbers equate to GPa) and if the conditions are taken to the limits of spinnability, then strengths of double this are seen. The elastic moduli are in the region of 70 N/tex [150] (Note: "tex" is a unit of measure for the linear mass den-

sity of fibers, defined as the mass in grams per 1000 m, i.e. 1 tex is equal to 10^{-6} kg/m in S.I. units). Typical stress-strain curves of continuously spun material that has not been subjected to any post-treatment except for condensation are shown in Fig. 9. Very much higher values have been seen on short sections of the fiber, approaching 8 N/tex strength and 200 N/tex elastic modulus (values about three times those of Kevlar), which indicate not only the potential of the process but the directions for future development. The fibers are also tough, absorbing 60 J/g at $\sim 10\,\%$ extension. Adjustment of the process parameters can control the type of nanotubes comprising the fiber, whether they are single wall, thin wall or multiwall, and their mean diameter. The fibers with the best mechanical performance appear to comprise mainly double-wall nanotubes of unusually large diameter, so that many of them have undergone autocollapse to give "dog-bone" cross sections. The fibers also show a readiness to absorb polymer solutions, which opens up one of several routes to the further enhancement of their properties. Their electrical conductivity, without any optimization, is 0.3×10^6 S/m and their thermal conductivity between 1000 and 1500 $\mathrm{Wm^{-1}K^{-1}}$. As with the fibers made by dry spinning of nanotube forests, the fiber has yarn-like qualities. It is tough, flexible and has a knot strength of 80 %.

Of the three spinning methods described, the liquid route appears to produce the best-ordered fibers and quite stiff ones (up to 130 GPa), although the strengths were low, at around 0.2 GPa. Fibers dry-spun from multiwall nanotube forests have reported strengths up to 0.8 GPa, and stiffness of the order of 25 GPa. Fibers spun directly from the CVD reaction zone reach strengths considerably above 1 GPa, and stiffnesses equal to, or in excess of, the liquid-crystalline spun material, while much higher strengths and stiffness have been demonstrated on occasions, underlining the huge potential of the process. A key parameter is the length of the component nanotubes, which can now reach > 1 mm by "supergrowth" (Sect. 6.1). Electrical conductivity is also promising in pure dry-spun fibers, with values approaching 1 % of copper, or 8 % on a weight basis. Nanotube–polymer coagulation spun fibers show high energy absorption at fracture. Ultimately, the process that succeeds to win a substantial portion of the high-performance fiber market (2 B p.a.) will be the one that is the most industrially scalable, cheaper and better. See also the contribution in this volume by *Endo* et al.

6 Organization on Surfaces

The organization of carbon nanotubes on surfaces is an important issue toward many different future applications. Organization into vertical arrays (Sect. 6.1) may be especially important for field emitters in display technology (see contribution by *Endo* et al.), as well as a source for dry spinning of nanotube fibers (Sect. 5), whereas organization into horizontal arrays (Sects. 6.2 and 6.3) is a critical prerequisite for large-scale integration into

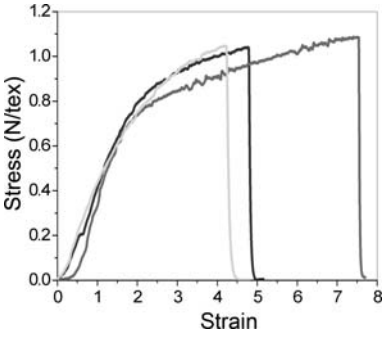

Fig. 9. Stress–strain curves from standard fibers that can be spun in the laboratory by the km. Higher strengths can also be achieved

nanocircuits [151]. An important difference exists between the organization of SWNTs and MWNTs on surfaces, due to their different mechanical properties. MWNTs are relatively rigid, and their growth is more naturally directional. Therefore, significant progress in the organization of MWNTs on surfaces was achieved relatively earlier [152–154]. In contrast, SWNTs are relatively flexible, making their organization especially challenging. This section focuses on the recent progress in the organization of SWNTs on surfaces. Such organization can be achieved during nanotube formation by vertically or horizontally aligned growth (Sects. 6.1 and 6.3, respectively), or by organized assembly of pre-formed nanotubes (Sect. 6.2).

6.1 Vertically Aligned Growth and Supergrowth

With arc discharge or laser-ablation techniques, only tangled nanotubes mixed randomly with various impurities are obtainable. Research in CVD nanotube growth has also been initiated by the idea that aligned and ordered nanotube structures can be grown on surfaces with control, as first demonstrated by *Ren* and coworkers by growing large-diameter MWNTs forming oriented "forests" on glass substrates by PECVD [155], and by *Fan* and coworkers by CVD on uniform and catalytically patterned substrates [156]. Carbon nanotubes can self-assemble into aligned structures during CVD growth into vertically aligned films or patterns perpendicular to the substrate surface. The mechanism of nanotube self-orientation typically involves the nanotube base-growth mode substrates. During CVD growth, nanotubes interact with their neighbors via van der Waals forces to gain rigidity, which allows the nanotubes to self-orient and grow perpendicular to the substrate [7].

6.1.1 Supergrowth

Most growth methods based on CVD, such as those mentioned above, are seriously limited by the low activity and short life time of the catalyst. The resulting low catalytic activity of CNT synthesis has not only reduced the availability of SWNTs, but the dead catalysts remain in the as-grown material

as impurities. Addition of a controlled amount of water vapor in the growth ambient can dramatically enhance the activity and lifetime of the catalysts and address these problems [157–161]. This new CVD approach denoted as "supergrowth", works best on substrates with catalytic nanoparticles. With the assistance of water, dense, vertical-standing, and aligned SWNT forests with millimeter-scale height can be synthesized. Figure 10a shows a 2.5-mm high SWNT forest that was grown in ten minutes [157]. The SWNT/catalyst weight ratio exceeds 50,000 %, more than 100 times higher than for other processes, illuminating the remarkable efficiency of water-assisted nanotube synthesis. A close examination (Fig. 10b) at the ledge of the SWNT forest illustrates that the nanotubes are well aligned vertically relative to the substrate. High-resolution transmission electron microscopy (TEM) studies (Fig. 10c) show that the nanotubes are clean SWNTs free from amorphous carbon. Low-resolution TEM studies (Fig. 10d) of the as-grown forest reveal the presence of only thin nanotubes and the absence of metallic particles and supporting materials that usually comprise a major constituent of as-grown SWNT material. Raman spectra showed clear radial breathing mode peaks that correspond well with the diameter of the SWNTs measured by TEM. Thermogravimetric analysis (TGA) on pure SWNT material using N_2 gas with water shows that SWNT combustion in the presence of water starts at about 950 °C, indicating that the water does not oxidize or damage the nanotubes at the growth temperature.

Characterization of the structure of SWNT forests provided interesting insights into the growth mechanism [162]. For a typical SWNT forest, the SWNT area density is 5.2×10^{11} tubes/cm^2, the mass density of the forest is 0.037 g/cm^3, the average SWNT size is 3.0 nm, and the SWNT area density is 5.2×10^{11} tubes/cm^2. The catalyst activity was estimated to be 84 % (±6 %), the highest value ever reported for SWNT growth. On average, there exists one 3-nm diameter SWNT in a substrate area of 190 nm^2 and the average distance between tubes is 14 nm. SWNTs occupy 3.6 % of the total volume, and more that 96 % is empty space. Interestingly, other SWNT forests synthesized by different methods and catalysts also show a similar sparseness, and the density of the CNTs is roughly in the range of a few to 10 % [163]. The sparseness of the forest is thought to be essential for growing SWNT forests by CVD with root growth. This is because excessively high densities inhibit carbon diffusion to the catalysts (diffusion limited); whereas, for insufficiently high densities, the SWNTs would fail to grow vertically and would instead form a mat and quickly suffocate the catalysts as observed in normal CVD growth. With this sparseness, vast amounts of SWNTs can be grown on a substrate while not restricting the delivery of the carbon feedstock.

The SWNT forest structure can be easily removed from the substrate using, for example, a razor blade. After removal, the substrate is still catalytically active to grow SWNT forests again, which means that growth by a root-growth mode with catalysts remaining on the substrate after removal of

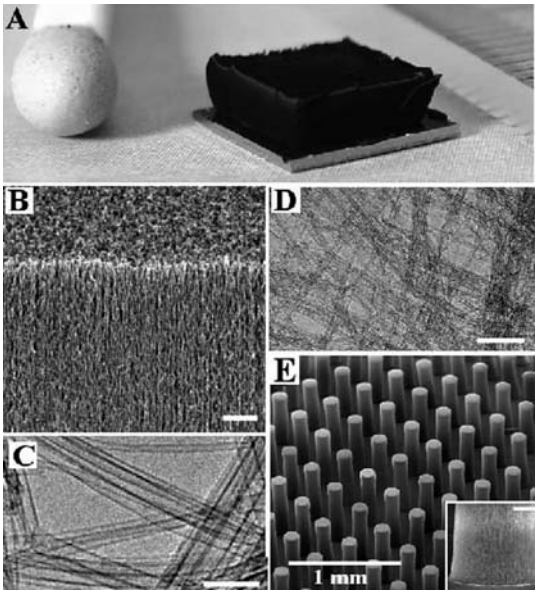

Fig. 10. (**a**) Picture of a single-walled carbon nanotube (SWNT) forest. (**b**) Scanning electron microscopy (SEM) image of the SWNT forest ledge. (**c**) High-resolution transmission electron microscopy (TEM) image of SWNTs. (**d**) A large-area TEM image. (**e**) SEM image of SWNT cylindrical pillars with 150 μm radius, 250 μm pitch, and 1 nm height. *Inset*, SEM image of a root of a pillar. *Scale bar,* 50 μm [157]

the forest. The high SWNT/catalyst weight ratio, the clean TEM images in Fig. 10, and the easy removal of the forests suggest that the as-grown SWNT material is highly pure. Thermogravimetric analysis (TGA) showed no measurable residue after heating above 750 °C, indicative of a carbon purity above 99 %. Quantitative elemental analysis with X-ray fluorescence spectrometry detected 0.013 % Fe as the only impurity, meaning a carbon purity over 99.98 %, i.e., the purest SWNT material ever made.

Realization of large-scale organized SWNT structures of [157] desired shape and form is important for obtaining scaled-up functional devices. With the assistance of water, SWNTs grow easily from lithographically patterned catalyst islands into well-defined vertical-standing organized structures, as demonstrated by the large-scale arrays of macroscopic cylindrical pillars (Fig. 10e). The cross section of the SWNT structure corresponds well with the patterned catalyst (inset of Fig. 10e), and thus it is possible to fabricate arbitrary shapes of organized SWNT structures where the base is lithographically defined and the height is controlled by the growth time.

The effect of water can be revealed by [157] formulating a numerical growth model that describes the time evolution of the supergrowth [164]. The

time evolution of the forest heights (yield) (Fig. 11a) showed that the growth rate gradually decreased over the subsequent 20 min, and finally terminated with a height of 970 μm. The time evolution of the height $H(t)$ of the forest growth rate could be expressed, as $H(t) = \beta\tau_0[1 - \exp(-t/\tau_0)]$, by assuming that the catalysts lose their activity in a similar fashion to radioactive decay. Important physical meaning can be assigned to the two fitting parameters: β is the initial growth rate (IGR) and τ_0 is the characteristic catalyst lifetime. Fitting the growth equation to the experimental time-evolution data yielded excellent agreement (Fig. 11a), and the fitting parameters were: IGR (β) of 207 μm/min and lifetime (τ_0) of 4.74 min, respectively. According to the growth equation, the product of the two fitting parameters, $\beta\tau_0$ gives the theoretical maximum height, $H_{\max}$, that was calculated to be 980 μm, matching well with the experimentally obtained height of 970 μm. A family of time-evolution data of the supergrowth was obtained at different ethylene flow rates at a fixed water level. From each growth equation curve, the initial growth rate β and the characteristic catalyst lifetime τ_0 was calculated and plotted as a function of the ethylene flow rate (Fig. 11b). Overall, the lifetime and IGR followed divergent trends, i.e., the IGR monotonically increases while the lifetime decreases with the ethylene level. The existence of these crossings among growth equation curves is a direct result of this divergent trend: slower initial growth with long lifetimes achieves higher maximum heights than rapid initial growth but with short lifetimes. Furthermore, despite this divergent trend, the theoretical maximum height (Fig. 11b, shown as a histogram), being the product of the two fitting parameters, $\beta\tau_0$ exhibits a peak representing the optimum ethylene flow rate for this water level. The divergent trends are easily explainable: 1. IGR monotonically increases with ethylene flow rate because the carbon source for SWNT growth increases, 2. the lifetime decreases since the catalyst is poisoned faster by rapid accumulation of an amorphous-carbon coating, a factor known to kill the catalyst activity.

Further analysis was carried out by the two-dimensional mapping of the dependence of the lifetime, initial growth rate, and theoretical maximum height on water and ethylene. Rearranging the data into a plot of the maximum height as a function of the water/ethylene ratio revealed a clear trend. The maximum height initially increased with the water/ethylene ratio, peaked at a value of about 1/1000, then decreased with further increase of the water/ethylene ratio. The water-assisted enhanced growth efficiency is reflected in the initial increase of the maximum height, and the peak represents the optimum growth conditions of the supergrowth. This result demonstrates the existence of a scaling relation between ethylene and water, and that the balance of the ethylene and water is the most critical factor for controlling the supergrowth. The same maximum height can be achieved by both a slow growth with a long lifetime and a fast growth with a short lifetime, given that the water/ethylene ratio is the same. Furthermore, the existence of this scaling law suggests that the catalysts consume a specific number of ethylene

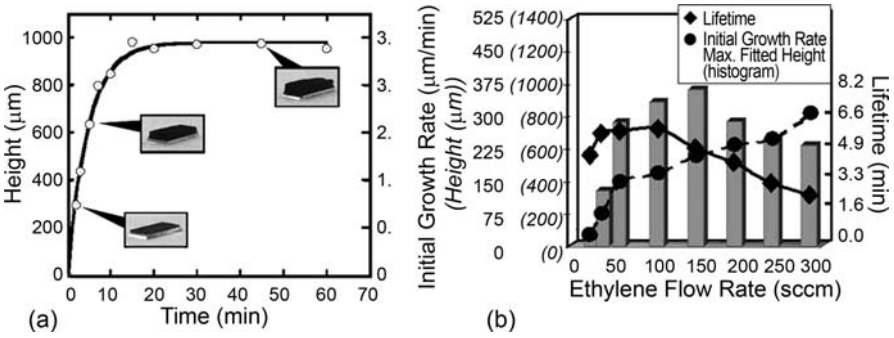

Fig. 11. Time evolution of SWNT forest growth. (**a**) Plot of the SWNT forest height as a function of the growth time. (**b**) Overlaid plots of the lifetime, initial growth rate, and maximum height (*histogram*), as derived from each growth curve [164]

and water molecules before they die, and this specific number is determined by the water/ethylene ratio. This implies that the rate-limiting process of the SWNT growth is the supply of carbon to catalysts from the gas phase.

Synthesis of catalyst-free DWNT forests with millimeter-scale height is also possible by using catalyst nanoparticles tailored to achieve maximum DWNT selectivity [165] (see more on DWNTs in the contribution by *Pfeiffer* et al.) Catalyst engineering is the key point for selective DWNT synthesis and was achieved by determining the optimum mean tube diameter for selective DWNT synthesis and by growing CNTs with this optimum mean diameter by precisely controlling the thickness of the Fe catalyst film. To understand and control CNT synthesis, the relationship between the tube type (single, double or multiwall) and diameter was studied by constructing a phase diagram (Fig. 12a) of the relative populations of SWNTs, DWNTs, MWNTs vs. the tube diameter. The phase diagram clearly shows that DWNTs occupy the majority of the nanotube population within a distinct diameter range sandwiched between the SWNT and MWNT regions. The existence of this distinct DWNT region affords selective DWNT growth via tuning the tube diameter into this DWNT region. Importantly, the mean CNT diameter was found to increase approximately linearly with the thickness of the Fe thin-film thickness (Fig. 12b). This finding enabled control of the mean CNT diameter accurately into the DWNT region. The maximum DWNT selectivity achieved with this approach was 85 %. This DWNT selectivity is one of the highest reported, and it is worth noting that it was achieved on an as-grown sample without any additional processes implemented to improve selectivity. Supergrowth was implemented to demonstrate highly efficient DWNT syntheses from these engineered catalyst particles, demonstrating that it is possible to

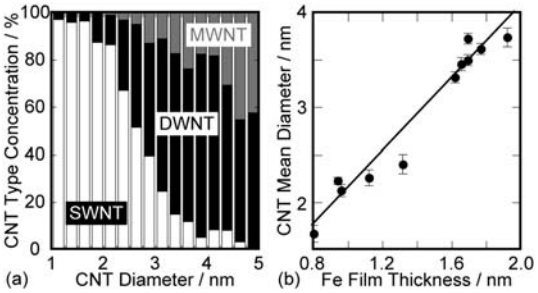

Fig. 12. Trends in CNT type and diameter. (**a**) Phase diagram of the relative concentration of SWNTs, double-wall carbon nanotubes (DWNTs) and multiwall carbon nanotubes as a function of the CNT diameter. (**b**) Plot of CNT mean diameter as a function of Fe film thickness [165]

grow DWNT forests with the same quality, yield and purity as the SWNT forests.

Generally, SWNT syntheses have been implemented on insulating substrates, such as Si wafers or quartz. In many cases, growths on conducting substrates are desired but have resulted in the formation of multiwalled carbon nanotubes (MWNTs) or graphite films. Ni-based alloys with Cr or Fe were found to possess both high durability to the CVD ambient and the ability to support highly efficient SWNT (DWNT) synthesis [166]. Successful syntheses of SWNT forests were achieved on various alloy substrates such as, Inconel 601, YEF 426, NiCr , YEF 50, SUS 310S, covering a wide range of Ni–Fe–Cr compositions (Fig. 13a). The growth product was mainly SWNTs with a selectivity of 95 %, and the growth yield and quality was comparable to the level of growth on Si wafers. To demonstrate an easy one-step assembly of CNT devices by this approach, a short DWNT forest was grown on a 1-cm diameter YEF 426 metal cathode (Fig. 13b) as a field electron emitter. The emission current increased exponentially with increasing electric field (Fig. 13c), following the Fowler–Nordheim equation. The spatial mapping of the emission current showed an excellent homogeneity that is evidence of good electrical contact between DWNTs and the grid substrate. Metal foils are much more economical and scalable than Si wafers or quartz substrates. Therefore, this approach would open up an economical route towards the mass production of SWNT and DWNT forests, and will facilitate flexible design of device architectures and fabrication processes for CNT devices.

6.1.2 SWNT-Solid

The intrinsic excellent properties of individual CNTs are frequently lost in macroscopic forms of CNTs. To address this matter, various CNT forms have been demonstrated ranging from fibers and yarns (Sect. 5), mats, vertically aligned CNTs (forests), powders, pellets, foams, and sheets. Yet, it is dif-

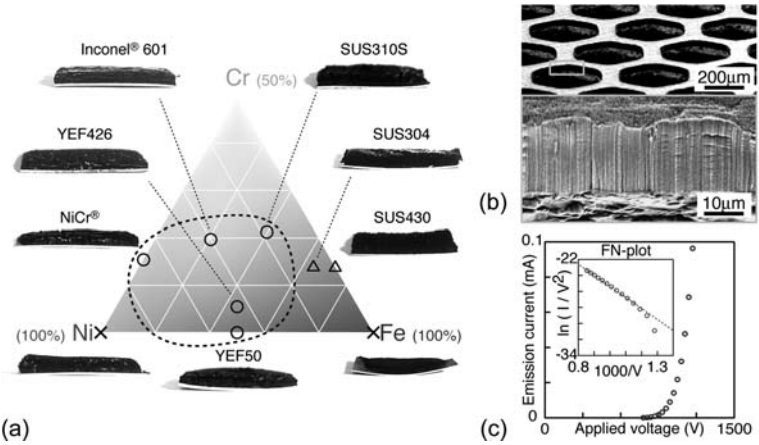

Fig. 13. (**a**) Correlation between components of Ni–Cr–Fe alloys and photographs of CNT forests grown on them. *Symbols* indicate the level of SWNT selectivity (○ high selectivity; △ medium selectivity; × low selectivity). (**b**) Double/YEF 426 as an electron field emitter. SEM images of a DWNT forest directly grown on a YEF 426 grid. (**c**) Emission current versus applied voltage profile (the *inset* shows a Fowler–Nordheim plot and fit) [166]

ficult to simultaneously retain the fundamental SWNT properties, such as high surface area and electrical conductivity on a macroscopic scale and have versatility in creating different shapes. A macroscopic bulk form of CNT material called the "SWNT solid" addresses this issue and has aligned densely packed SWNTs, while retaining the intrinsic properties of SWNTs [167]. When liquids are introduced into the sparse as-grown SWNT forest and dried, the surface tension of liquids, and the strong van der Waals interaction effectively "zippers" the SWNTs together in a nearly ideal graphitic spacing. Liquid-induced collapse shows a 4.5-fold decrease in the two lateral dimensions with no detectable change in the height, producing a $\sim$ 20-fold increase in mass density (Fig. 14a). This indicates that alignment of the as-grown forest is critical in triggering an efficient liquid-induced collapse, which is understandable because the aligned nature of the growth provides an ideal condition for optimum van der Waals overlap. The initial 97 % empty space in forests is here reduced to $\sim$ 50 %, and the intertube and innertube volumes become equivalent. The Vickers hardness of the SWNT solid increases over 70-fold to 7–10, which is comparable with that of highly oriented pyrolytic graphite (HOPG). The zippering action proceeds without damaging the tubes. The above characterization highlights the solidness and unity of the liquid-induced collapsed material, and thus this form was denoted as a "SWNT-solid".

The SWNT solid concept can be extended to create a variety of unique solid structures from as-grown forest material with diverse shapes by con-

trolling the parameters that influence the collapse process, such as the forest aspect ratio, the initial liquid contact point, and substrate–forest interaction. For example, lithographically defined as-grown SWNT circular pillars with [167] a high aspect ratio collapsed from the tip creates well-defined and patterned SWNT solid needles with a high aspect ratio (Fig. 14b). Another approach to extend the ability to engineer the shape of the solid is to employ moderate external forces, such as very light pressure, to direct the direction of the collapse. For example, applying light pressure in one lateral direction suppresses collapse in one lateral dimension and creates a bar (Fig. 14d). Similar application of light pressure at a shearing angle to the alignment induces a vertical collapse, without any collapse in both lateral dimensions, results in a solid sheet (Fig. 14c). Because the SWNTs are directed to lie like a field of corn stalks flattened by a tractor, the solid sheets maintain a comparable degree of alignment of the forest. This approach is easily extendable to fabricate strongly adhered solid sheets on desired flat substrates without the use of bonding agents by simply transferring the forest onto a target substrate and implementing the collapse process. The ability to engineer the shapes of solids is beneficial for a multitude of applications requiring high surface area, high density, aligned, conducting, and flexible or rigid CNT material. The SWNT solids represent substantial progress towards producing a macroscopic scale, high-density SWNT material, engineered in both shape and structure, thus opening diverse functionality that is advantageous for numerous applications, such as energy storage.

6.2 Organized Assembly of Preformed Nanotubes

The controlled deposition of preformed nanotubes from solution onto a substrate with well-defined structures has been a topic of intense research for several years [168]. To be able to control the structure of deposited nanotubes, external forces, such as electrical, mechanical and chemical interactions, are needed to provide guidance toward the desired structures. One of the earliest examples of the controlled deposition of nanotubes on a substrate was developed by *Smalley*'s group at Rice University, where surface patterns with chemically different functional groups are used to guide the structure of deposited nanotubes [169]. More recently, the affinity of nanotubes to Al_2O_3 was used as a way to guide nanotubes to specific locations to form nanotube devices in large numbers (Fig. 15) [170].

Surface patterns with different hydrophobic/hydrophilic functional groups is another common method to provide forces needed for guided deposition of nanotubes. A representative example for the use of such methods was developed by *Rao* et al. [171] where individual nanotubes or small bundles of nanotubes were deposited onto a substrate with precise control of their location and orientation (Fig. 16). More recently, *Mirkin* and coworkers [172, 173] used the edge of a hydrophilic pattern on a hydrophobic background to

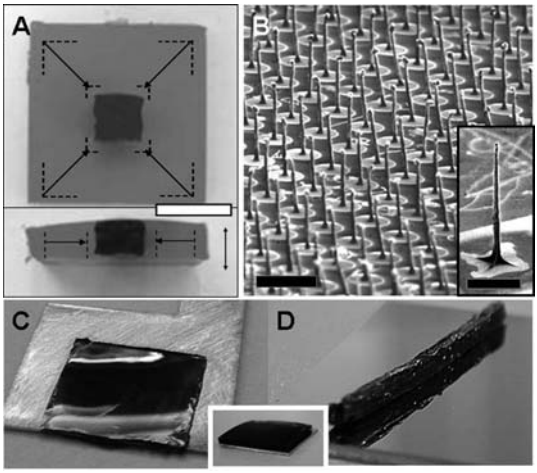

Fig. 14. (**a**) Overlaid pictures illustrating the decrease in lateral dimensions before (*gray*) and after (*black*) collapse. The *double-ended arrow* indicates tube alignment direction. (**b**) Engineerable shape: SEM image of an array of lithographically designed solid needles. *Scale bar*, 500 µm *Inset*, magnified individual needle. *Scale bar*, 60 µm. (**c**) Flexible SWNT solid, engineered into a flattened sheet adhered to a copper sheet. *Inset*, Photograph of the as-grown forest. (**d**) SWNT solid, engineered into a rigid bar [167]

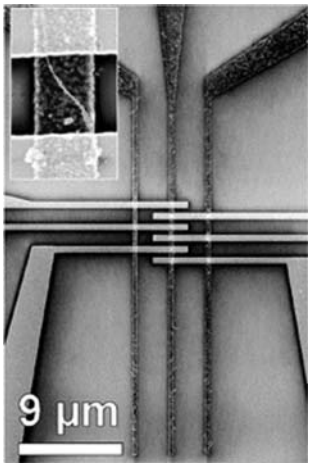

Fig. 15. SEM image of a CNT field-effect transistor [170]. Functionalized CNTs were assembled by their chemical affinity for the Al_2O_3 gate oxide, then contacted with evaporated gold source and drain electrodes [170]

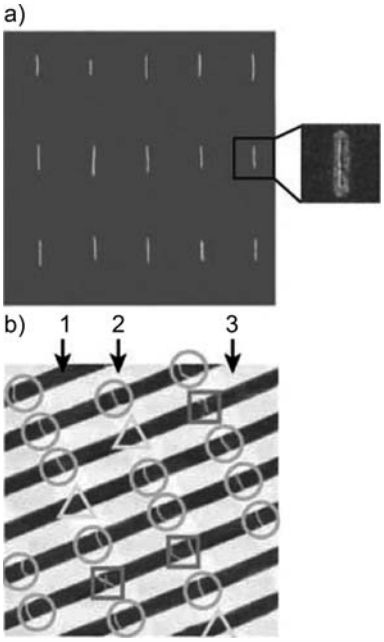

Fig. 16. AFM images showing large-scale self-assembly of SWNTs: (**a**) Topography ($30 \times 30\,\mu m^2$) of an array of individual nanotubes covering about $1\,cm^2$ of a Au surface. The friction-force image (*inset*) shows a single nanotube (*dark line*), and the regions containing 2-mercaptoimidazole (*bright area*) and octadecyltrichlorosilane (ODT; used to passivate the SiO_2 surface; *dark area*). (**b**) Topography ($20 \times 20\,\mu m^2$) of an array of junctions with no nanotube (△), one nanotube (○), or two nanotubes (□) covering an area of about $1\,cm^2$. *Arrows* 1, 2, and 3 indicate ODT, 2-mercaptoimidazole on Au, and ODT on Au, respectively [171]

organize nanotubes on a substrate into rings with well-controlled diameters and locations.

Electric and magnetic forces are also used to align nanotubes into desired structures. There are many reports on the formation of aligned nanotube structures under such forces. For example, *Smalley* and coworkers used a very strong magnetic field to form films with aligned nanotubes [174–178]. Mechanical force introduced by liquid flow was also demonstrated to align nanotubes into parallel structures [179]. However, it is the electric forces that showed the most promising advances in organizing nanotubes into desired structures. Both dc and ac dielectrophoresis have been used to deposit nanotubes from a suspension onto a substrate with good control of the alignment [59–61, 180–183]. *Krupke* and coworkers [60] used ac dielectrophoresis forces to precisely align nanotubes into parallel arrays of electrodes (Fig. 17), and provide a convenient way to make nanotube devices under good control. The same approach was used to separate metallic and semiconducting nanotubes [59] (Sect. 4).

Assembly of premade, chemically processed SWNTs on substrates is also a promising approach for the placement of densely aligned nanotubes. Langmuir–Blodgett (LB) films have been known for decades as an effective method for making well-organized organic monolayer patterns. Recently, *Dai* and coworkers [184] produced LB films of SWNTs on a large scale using HiPCO nanotubes as well as laser-ablation-grown nanotubes (Fig. 18). Suspensions of as-grown laser-ablation and HiPCO SWNTs in 1,2-dichloro-

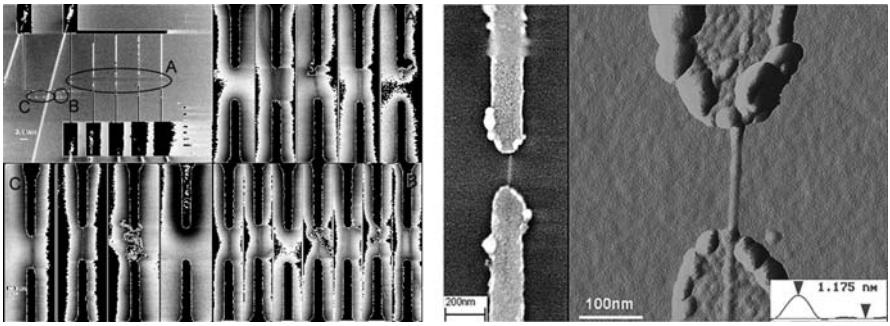

Fig. 17. SEM and AFM images of metallic nanotube bundles deposited on electrode arrays by dielectrophoresis [60] (the *right-bottom corner inset* shows a topographic section of a nanotube)

ethane (DCE) solutions of poly(m-phenylenevinylene-co-2,5-dioctoxy-p-phenylenevinylene) (PmPV) were prepared by sonication, ultra-centrifugation and filtration. The suspension contained mostly individual nanotubes well solubilized in DCE without free unbound PmPV. PmPV binds to SWNT sidewalls via π stacking of its conjugated backbone and thus imparts solubility to nanotubes in an organic solvent. Importantly, DCE was found to be the only solvent in which PmPV-bound SWNTs remained stably suspended when free unbound PmPV molecules were removed. The PmPV-treated SWNTs exhibited no aggregation in DCE over several months. An LB film of SWNTs was made by adding SWNT DCE solutions to water in a LB trough to form a layer of SWNTs floating on a water surface upon vaporization of DCE. An aligned SWNT film was then formed by compressing the SWNTs on a water surface using two barriers. Such a film was then transferred to a substrate by simple dipping. AFM microscopy and Raman spectroscopy characterization revealed high-quality, densely aligned SWNTs (normal to the compression and substrate pulling direction) formed uniformly over large substrates for both HiPCO and laser-ablation-derived SWNTs. The height of the film relative to the nanotube-free regions of the substrate was < 2 nm under AFM, suggesting a monolayer of packed SWNTs [184].

Aligned SWNT LB monolayers on oxide substrates can be treated as carbon nanotube on insulator (CNT-OI) materials for patterning and integration into potential devices, much like how Si on insulator (SOI) has been used for electronics. Lithographic patterning techniques and oxygen plasma etching can be used to remove unwanted nanotubes and form patterned arrays for device integrations. The LB assembly of densely aligned SWNTs can be combined with chemical separation and selective chemical reaction methods to yield purely metallic or semiconducting SWNTs in a massively parallel configuration, useful for interconnection or high-speed transistor ap-

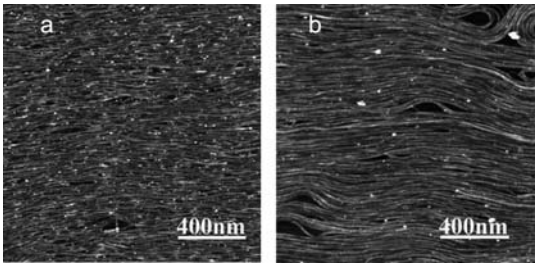

Fig. 18. Langmuir–Blodgett (LB) monolayer assembly of aligned SWNTs. (**a**) AFM image of a LB film of HiPCO SWNTs on a SiO_2 substrate. (**b**) AFM image of a LB film of laser-ablation-grown SWNTs [184]

plications on a large scale. The method is generic in terms of the type of nanotube materials and substrates.

6.3 Horizontally Aligned Growth

An attractive approach for the organization of carbon nanotubes into horizontal arrays is the directed growth on surfaces by CVD [185], under the influence of an aligning force, such as an applied electric or magnetic field, the gas flow or the surface. One can envisage the creation of a variety of carbon nanotube arrays by defining the growth of the nanotubes on the surface in the form of a vector, having an origin, a direction, and a length. The origin can be defined by patterning the catalyst nanoparticles at specific locations, while the direction is defined by the aligning force, and the length is controlled by the growth time and rate. Successive or simultaneous steps of such "vectorial growth" [186] in different directions could yield different carbon nanotube architectures on surfaces.

6.3.1 Field-Directed Growth

Electric fields can orient carbon nanotubes owing to their large and highly anisotropic polarizability [187] (as seen in Sect. 4). This can be exploited for the alignment of carbon nanotubes during their growth. The growth of SWNTs suspended across lithographic ridges was observed by *Dai* and coworkers to be directed into parallel arrays by an electric field, which was applied by a pair of electrodes outside the ridges on a dielectric substrate during CVD growth [188], as shown in Fig. 19a. In the absence of an electric field, the SWNTs grow into random suspended networks (Fig. 19b).

Similar field-directed growth of SWNTs but lying on the surface was also observed by *Joselevich* et al. [186, 189] on thermally oxidized silicon wafers (Fig. 20a). In this case, the nanotubes are believed to grow up from the surface, and to be aligned by the electric field before they settle down and get

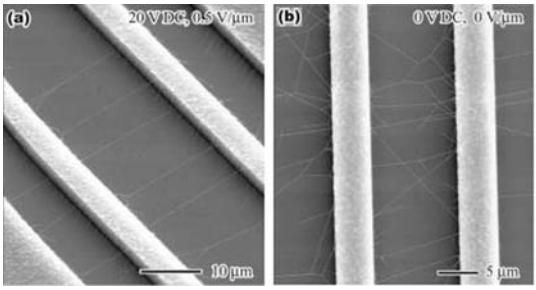

Fig. 19. Field-directed suspended SWNTs grown between two posts under an electric field (**a**) and in the absence of an electric field (**b**) [188]. The field intensity in (a) was 0.5 V/μm. The substrate is quartz. The distance between the poly-Si suspending ridges is 20 μm, and the distance between the outer poly-Si electrodes is 40 μm

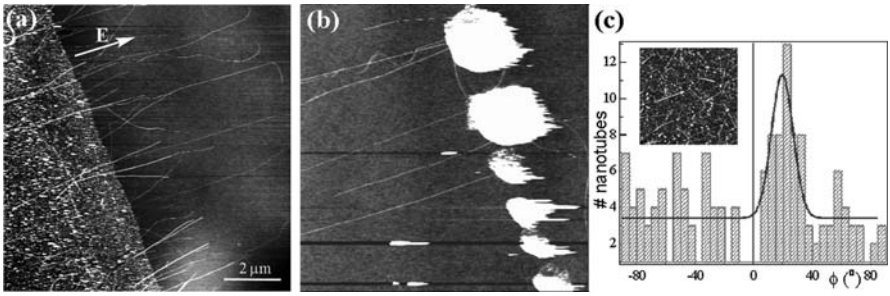

Fig. 20. Field-directed growth of SWNTs on oxidized Si wafers [186]. (**a**) Aligned array of SWNTs. The field intensity was 2×10^6 V/m. (**b**) Vectorial growth of SWNT arrays by field-directed growth from Al_2O_3-supported catalyst islands on the oxidized Si. (**c**) Bimodal angular distribution of field-directed short SWNTs (L = 200–600 nm). The *solid line* indicates a narrow Gaussian distribution around the direction of the field, which may be attributed to the metallic nanotubes, plus a broad distribution, which may be attributed to the semiconducting nanotubes. The *inset* (scale 2.5 μm) shows the partially aligned SWNTs

pinned to the surface by van der Waals forces. Vectorial growth of SWNTs from patterned islands of catalyst was used to produce ordered arrays of parallel 5–20 μm long SWNTs on oxidized silicon wafers (Fig. 20b) [186]. Interestingly, the angular distribution of short SWNTs (L < 200 nm) grown under the same electric-field is not normal but bimodal (Fig. 20c). This can be attributed to the selective alignment of metallic carbon nanotubes, due to their higher polarizability compared to that of semiconducting ones.

Attempts to organize SWNTs into crossbar architectures by electric field-directed growth in two dimensions actually led mainly to looped struc-

tures [190]. This was attributed to the complex shape of the field lines, and showed the limitations of purely field-directed growth. Crossbar architectures using field-directed growth were successfully achieved by *Joselevich* and coworkers [191] in combination with surface-directed growth (vide infra). Field-directed growth was also used to grow SWNTs between electrodes to produce self-assembled field-effect transistors [192]. A different interesting approach combining field-directed growth with surface-directed growth is the oriented growth of SWNTs using lithographic alumina patterns, which created a local electric field due to static charging [193], without the need for electrodes and applied voltage. In this case, the SWNTs tend to lie perpendicular to the straight or curved edges of the alumina islands. Yet another approach for the generation of aligned arrays that is somehow related to electric-field-directed growth is the orientationally selective ablation of random networks with a planarly polarized laser [194]. SWNTs lying with a component parallel to the plane of polarization were selectively ablated, leaving on the surface only those nanotubes that are perpendicular to the plane of polarization.

Magnetic fields were also used to direct the growth of carbon nanotubes on surfaces in a few cases. Magnetic-field-directed growth of MWNTs was attributed to the interaction of the magnetic field with the ferromagnetic Fe catalyst [195]. Magnetic fields were also used to preorient the magnetite (Fe_3O_4) nanoparticles from a magnetic bacterium, which were subsequently used as catalyst for CVD growth [196]. (See contribution by *Kono* et al.)

Overall, field-directed growth seems to be a useful tool for the organization of carbon nanotubes into horizontally aligned arrays. However, a practical limitation is that the electric field has to be generated by lithographic electrodes or charging islands, which impose size limitations and could interfere with other elements in functional devices. Also, silicon can significantly screen the electric field, producing complicated field lines, which are not parallel to the surface. Therefore, field-directed growth works fine on dielectric substrates, but is not ideal for large-scale organization on silicon wafers.

6.3.2 Flow-Directed Growth

Another promising approach to orient SWNTs is to use the feeding gas to align SWNTs along the flow direction. This method was originally discovered by *Liu* and coworkers [197–200] using a fast-heating CVD method, in which the Si wafer containing catalysts patterns were heated quickly to the reaction temperature by inserting the substrate into the center of a heated furnace. Figure 21 is a typical SEM image of the nanotubes from the new "fast-heating" process using Fe/Mo catalyst nanoparticles and CO/H_2 as the feeding gas. AFM height measurements show that the diameters of the nanotubes range from 0.8 nm to 2.5 nm, with an average diameter around 1.25 nm. Note that not all the nanotubes under "fast-heating" are long and oriented. In the catalyst area there are still many short random nanotubes, relating to

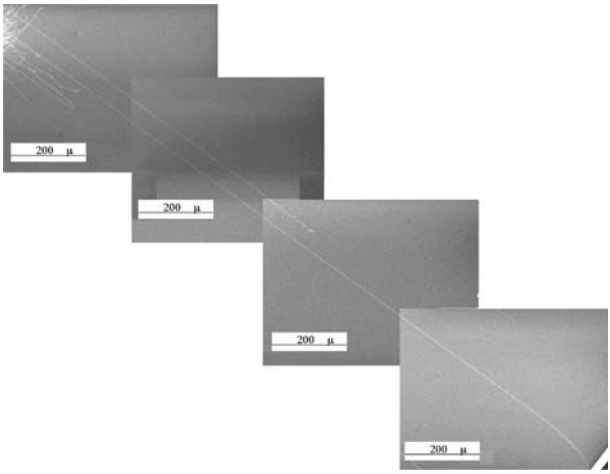

Fig. 21. SEM image of SWNTs grown with the flow-aligned CVD method

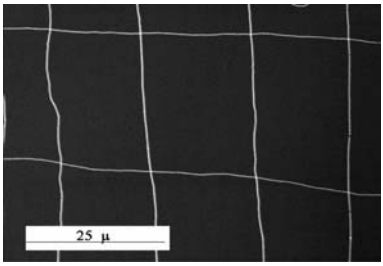

Fig. 22. SEM image of a 2D nanotube network grown using multistep growth [197]

different growth mechanisms, which will be discussed later. So, some of the nanotubes grown by the "fast-heating" process, using monodispersed Fe/Mo nanoparticles as a catalyst and CO/H_2 as the feeding gas, are long (up to a centimeter scale), well-oriented, and individual SWNTs. The orientation of nanotubes was found to be determined by the gas flow.

It has been proved that such a "fast-heating" process is a general method for growing superlong well-oriented SWNTs on a surface. Such superstructures of SWNTs can be generated by using different catalysts, other than Fe/Mo nanoparticles (e.g., pure Fe nanoparticles, Fe/Pt nanoparticles, and water-soluble molecular Fe/Mo clusters), and different carbon sources other than CO (e.g., CH_4, CH_3OH, etc.). It is believed that fast heating is also suitable for other SWNT growth systems. Such a big window provides a chance to control the SWNTs growth for different purposes.

As mentioned above, the long nanotubes from the "fast-heating" process are well oriented and the direction is determined by gas flow without using any external forces like a strong electric field. Figure 22 shows an SEM image of crossed nanotube arrays by a two-times patterning catalyst and a

two-times growth using Fe/Mo nanoparticles as catalysts and CO/H_2 as the feeding gas. A growth mechanism was proposed by the researchers, where a key component is that the nanotubes grow above the substrate surface. The fast-heating process was believed to cause convection of the gas flow due to the temperature difference between the substrate and feed gas. Such convection flow of the feed gas lifted the nanotubes upward and kept them floating and waving in the gas until they were caught by the laminar flow and came to the substrate. The actively growing nanotubes then floated in the feeding gas and grew along the flow direction. More recently, a variation of the fast-heating method, and even methods without the need of the fast-heating step, were developed for the growth of aligned nanotubes with their growth directions controlled by the gas flow. For example, *Burke* and coworkers [201, 202] discovered that the growth of nanotubes from catalysts deposited on a high platform fabricated on a flat Si wafer can grow long nanotubes not only along the gas flow but also against the direction of the gas flow. Additionally, no fast-heating step is needed in these studies. At first sight, the results seem to contradict the proposed growth mechanism. However, after a closer look, the nanotube alignment can be explained by the formation of reversed gas flow reflected by the high platform, and the platform serves as a mechanism to lift the catalysts and the growing nanotubes above the substrate, which are two of the key components of the mechanism: nanotubes growing above the substrate and the existence of a gas-flow current to direct the growth direction. More recently, *Kim* and coworkers [203] also demonstrated the use of a small quartz tube inside a large tube to achieve better alignment. It is believed that the small tubes can achieve better laminar flow of the feeding gas. *Li* and coworkers [204] also demonstrated the growth of well-aligned nanotubes with their directions controlled by gas flow using different catalysts. Overall, the use of gas flow to determine the growth directions of nanotubes not only produces aligned nanotubes, but the nanotubes grown in this way are almost always produced with extremely long lengths. A Raman study along individual long nanotubes revealed that the majority of the nanotubes showed a uniform radial breathing mode spectrum along their whole length, which is very encouraging for future use of the nanotubes in nanoelectronic devices.

6.3.3 Surface-Directed Growth: "Nanotube Epitaxy"

A promising new approach to carbon nanotube horizontal organization, which has developed rapidly during the last three years, is the growth of carbon nanotubes directed by well-defined crystal surfaces, or "nanotube epitaxy". Epitaxy generally refers to the "growth of a crystal of one material on the crystal base of another material in such a manner that its crystalline orientation is the same as that of the substrate". Epitaxy of inorganic materials is very important in the semiconductor industry, as well as in many other fields of technology. Molecular epitaxy [205], which refers to the formation of organized molecular layers on crystalline surfaces, has a more complex

nature than the classical commensurate epitaxy of inorganic crystals, and has been recognized to exist in a hierarchy of different modes: Commensurate, semicommensurate (or "coincident") and incommensurate (or "orientational") epitaxy, taking place on atomically flat surfaces; ledge-directed epitaxy, taking place on vicinal surfaces, which are terminated with atomic steps; and graphoepitaxy, taking place on nanostructured surfaces. *Joselevich* and coworkers [206] have recently developed different nanotube analogs to some of these epitaxial modes, followed by other groups. These orientational heteroepitaxial modes of nanotube growth should not be confused with the continued growth of SWNTs [114–116] (Sects. 4.4 and 5.1), which may be considered as a mode of nanotube homoepitaxy.

Different phenomena that can now be considered as early manifestations of carbon nanotube epitaxy include the aligned electrophoretic deposition of SWNTs on highly oriented pyrolytic graphite C (0001) [43], the aligned growth of short SWNTs along the low-index directions of Si (100), Si (111) [207] and Au (111) [208] surfaces, the catalyst-free formation of SWNTs along or across step edges of 6H-SiC (0001) [209], and the aligned dry deposition of SWNTs on GaAs (110) [210, 211]. In all these cases, however, the nanotubes lay in different directions and were often too short to be considered as organized arrays. The formation of highly aligned, unidirectional and dense arrays of long SWNTs on surfaces was first observed to form by CVD growth on low-quality C-plane sapphire [212]. The cheap C-plane sapphire wafers turned out to be miscut a few degrees off the C-plane, and the SWNT grew along the atomic steps of the vicinal α-Al_2O_3 (0001) surfaces (vide infra). This mode of surface-directed growth could thus be related to ledge-directed epitaxy. Later, SWNTs were also shown to grow along well-defined directions of a variety of other crystal surfaces by different epitaxial modes. Following a rational order from smaller to larger aligning features, three different modes of carbon nanotube epitaxy have been identified so far [206]: lattice-directed epitaxy (by atomic rows), ledge-directed epitaxy (by atomic steps) and graphoepitaxy (by nanofacets).

Lattice-Directed Nanotube Epitaxy by Atomic Rows

Following the first reports of atomic-step-templated growth of SWNTs on miscut C-plane sapphire [212], two independent groups reported the observation of aligned SWNT growth on singular A-plane and R-plane sapphire, i.e., α-Al_2O_3 $(11\bar{2}0)$, α-Al_2O_3 $(1\bar{1}02)$, respectively [213, 214], where the SWNTs grow along the $[2\bar{2}01]$ and $[1\bar{1}0\bar{1}]$ directions, respectively [215, 216]. The preferential growth of SWNTs along these lattice directions was attributed to higher charge densities along these atomic rows due to electrostatic and van der Waals forces. The lattice-directed epitaxial growth of SWNTs on A-plane and R-plane sapphire was recently used for building field-effect transistors, and a nanotube-on-insulator technology of registry-free nanocircuits

was proposed [217]. Lattice-directed epitaxial growth of SWNTs will probably take place on other atomically flat single-crystal substrates. Recently, for instance, SWNTs were observed to grow on MgO (001) preferentially along the [110] and [1$\bar{1}$0] directions [218].

Ledge-Directed Nanotube Epitaxy by Atomic Steps

SWNT produced by CVD on miscut C-plane sapphire were shown to grow along the 0.2-nm high atomic steps of the vicinal α-Al_2O_3 (0001) surfaces [212]. This atomic-step-templated mode of nanotube growth leads to the formation of dense arrays of highly parallel arrays of SWNTs, as shown in Fig. 23. The miscut is characterized by an inclination angle θ and an azimuth angle ϕ, as defined in Fig. 23b. The degree of alignment correlates mainly with the miscut inclination angle θ, while the straightness of the nanotubes correlates with the azimuth angle ϕ: When the step direction is along a low-index direction, such as [11$\bar{2}$0] or [10$\bar{1}$0], the nanotubes tend to be straight. However, when the steps run along a high-index direction, then the nanotubes tend to be kinked, with straight segments parallel to the nearest low-index directions. Some nanotubes present sharp kinks of exactly 30°, which could be attributed to single pentagon-heptagon defects induced by kinked steps. These defects may involve structural changes along the nanotubes, constituting interesting metallic–semiconducting intramolecular junctions and superlattices. Single-nanotube Raman spectra from these samples exhibit a high intensity of D-band peaks, which indicates a significant loss of translational symmetry, consistent with this picture [219]. Polarized Raman measurements confirm the preferred orientation of the SWNTs along low-index directions [220]. A "wake-growth mechanism" has been proposed [212], where the catalyst nanoparticle slides along the step leaving the nanotube behind as a wake. Recent AFM images of SWNTs grown on well-defined vicinal α-Al_2O_3 (0001) surfaces (Fig. 23d), succeeded to resolve the densely packed atomic steps, and confirmed that the SWNTs continuously follow the atomic steps [220].

Ledge-directed nanotube epitaxy was recently observed also on miscut quartz [221]. In this case, the surface consists of vicinal α-SiO_2 (1$\bar{1}$01) with steps running along the [$\bar{2}$1$\bar{1}$0] direction. SWNTs grown on this surface by CVD form along the steps, similarly as on vicinal α-Al_2O_3 (0001). The parallel arrays of SWNTs on quartz were used as thin-film transistors. Patterning of the catalyst allowed the formation of spatially selective arrays of SWNTs, and their integration into submillimeter thin-film transistors [222].

Nanotube Graphoepitaxy by Nanofacets

"Graphoepitaxy" is a mode of incommensurate epitaxy that generally refers to the orientation of crystals or periodic molecular assemblies by relief features of the substrate, such as steps or grooves, which can be significantly

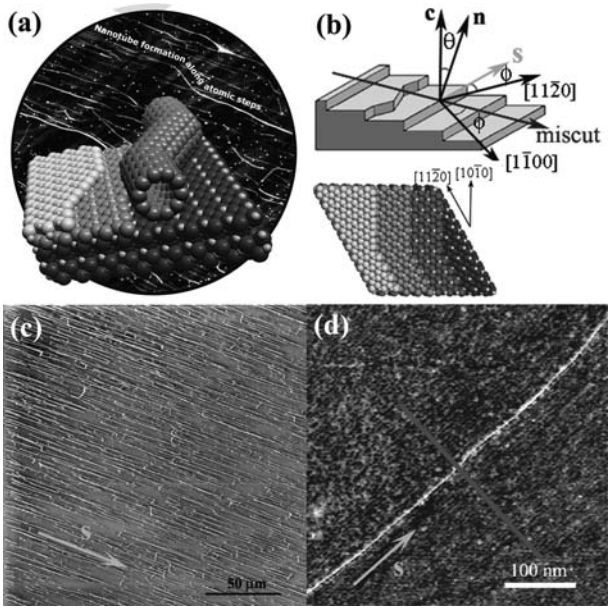

Fig. 23. Nanotube formation along the atomic steps of miscut C-plane sapphire, i.e., vicinal α-Al_2O_3 (0001) [212]. (**a**) Model of a kinked SWNT grown along an atomic step on the background of an AFM topographic image of a real sample. (**b**) Definition of the step vector $\boldsymbol{s} = (\boldsymbol{c}/c) \times \boldsymbol{n}$, miscut inclination θ, and miscut azimuth ϕ, where $\boldsymbol{c}$ is the principal lattice vector and $\boldsymbol{n}$ is a unit vector normal to the surface. A top-view model of the vicinal surface is shown below. (**c**) Large-scale SEM micrograph of SWNTs grown on a vicinal α-Al_2O_3 (0001) surface. (**d**) High-resolution AFM topographic image providing a direct observation of the atomic steps on the surface, and a SWNT tightly following one of the steps [220]

larger than the lattice parameter [223, 224]. Graphoepitaxy of SWNTs was demonstrated on thermally annealed miscut C-plane sapphire [206]. When the vicinal α-Al_2O_3 (0001) surfaces are annealed at 1100 °C, the thermodynamically unstable atomic steps of 0.2 nm height bunch together into periodic nanosteps of 1.3 nm to 4 nm height. SWNTs grown by CVD on these periodically faceted surfaces generate a variety of morphologies, depending on the shape and surface energy of the nanofacets. As shown in Fig. 24, annealing of a C-plane sapphire miscut in different directions can yield nanofacets with a variety of morphologies (straight or sawtooth) and different surface energies. SWNTs produced on these nanofaceted surfaces (Fig. 25d) can have different morphologies (straight, wavy and ultrastraight). SWNTs grown on metastable nanofacets are especially straight, with angular deviations of less than ±0.5°, for lengths of up to 100 μm (Figs. 25a and b). This can be attributed to the high surface energy of these nanofacets, which makes them particularly sticky toward the nanotubes.

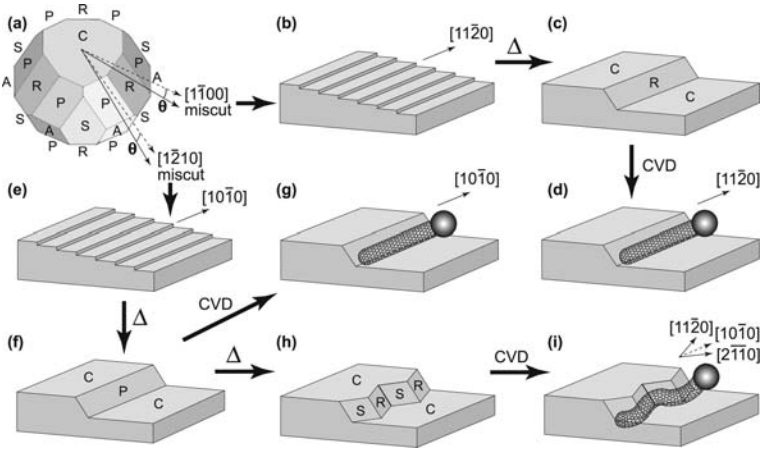

Fig. 24. Flow chart describing the formation of possible morphologies of carbon nanotube graphoepitaxy by miscut of C-plane sapphire, annealing, and CVD [206]. (**a**) Equilibrium shape of α-Al_2O_3, with facets C{0001}, R{1$\bar{1}$02}, S{10$\bar{1}$1}, P{11$\bar{2}$3}, and A{11$\bar{2}$0}, in order of increasing surface energy. The same drawing is used to show the different miscut directions. (**b**) Miscut toward [1$\bar{1}$00] produces a vicinal α-Al_2O_3 (0001) surface with atomic steps along [11$\bar{2}$0]. (**c**) Annealing leads to R-faceted nanosteps. (**d**) SWNTs grow straight along [11$\bar{2}$0] (the ball represents the catalyst nanoparticle). (**e**) Miscut toward [1$\bar{2}$10] produces a vicinal α-Al_2O_3 (0001) with atomic steps along [10$\bar{1}$0]. (**f**) Annealing initially leads to metastable P-faceted nanosteps. (**g**) SWNTs grow straight along [10$\bar{1}$0]. (**h**) Further annealing from (**f**) leads to sawtooth-shaped S/R-faceted nanosteps. (**i**) SWNTs grow loosely conformal to the sawtooth-shaped nanosteps, with segments along [11$\bar{2}$0] and [2$\bar{1}\bar{1}$0]

Nanotube Epitaxy Combined with External Forces

Combinations of nanotube epitaxy with field-directed or flow-directed growth offer the possibility of generating more complex carbon nanotube patterns. For instance, crossbar architectures are especially desired for nanoelectronics, as they constitute the basis of most logic and memory elements in computing devices [225]. Crossbar arrays of single-wall carbon nanotubes were spontaneously produced in a single CVD step by simultaneous graphoepitaxy and field-directed growth, perpendicular to each other [191], as shown in Fig. 26. The two alignment mechanisms take place selectively on miscut C-plane sapphire and patterned amorphous SiO_2 islands, respectively, without mutual interference, producing dense nanotube grids, with up to 12 junctions per μm^2. This one-step method of orthogonal self-assembly may open up new possibilities for nanotube circuit integration. In principle, nanotube epitaxy should also be compatible with other external forces, such as in flow-directed growth (vide supra).

Judging by these examples, nanotube epitaxy seems to be rapidly evolving into an efficient approach for the organization of aligned arrays of SWNTs

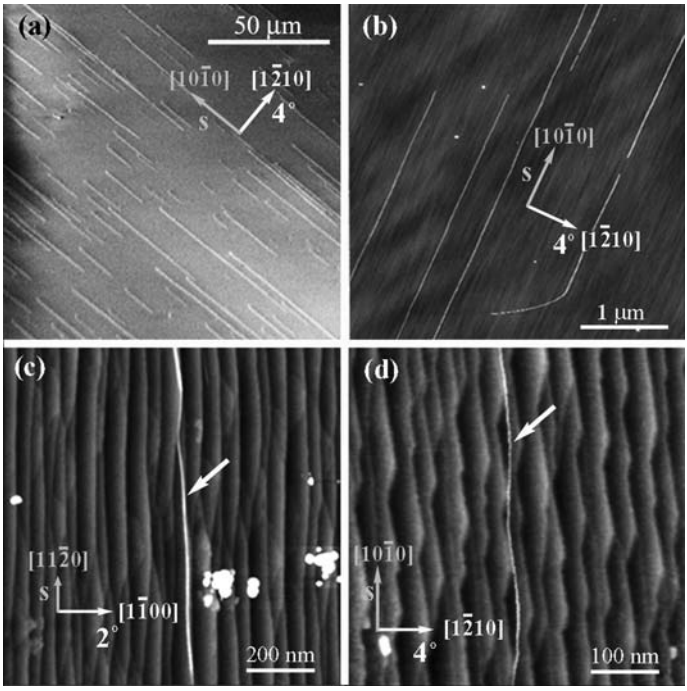

Fig. 25. Graphoepitaxial SWNTs on different annealed miscut C-plane sapphire [206]: (**a**) Straight nanosteps along [10$\bar{1}$0], as in Fig. 24g, observed by SEM. (**b**) AFM image of (a), showing the nanosteps. (**c**) Nanosteps along [11$\bar{2}$0], as in Fig. 24d. (**d**) Highly faceted sawtooth-shaped nanosteps along [10$\bar{1}$0], as in Fig. 24i

with a variety of morphologies, including highly straight, kinked, wavy and crossed. Some of these arrays have been already integrated into thin-film transistors. An intriguing open question that remains is whether all of these modes of nanotube epitaxy are indeed incommensurate, or may there be at least some degree of commensurism or registry between the surface lattice or the ledges, and the curved graphene lattice of the nanotubes. If this were the case, then one could expect a certain degree of control over the chirality and handedness of the nanotubes. Another question of greater practical implications toward future applications of nanotube epitaxy in nanoelectronics concerns the degree of atomic perfection and the electronic properties of the epitaxial nanotubes. Moreover, it is not yet clear whether or not the atomic steps and rows or nanofacets perturb the electronic properties of the nanotubes. The fact that these epitaxial substrates are bulk dielectric materials has also made their integration and electrical characterization difficult. A possible solution would be to develop a procedure for transferring the organized nanotubes from the epitaxial templates onto silicon wafers, or onto predefined

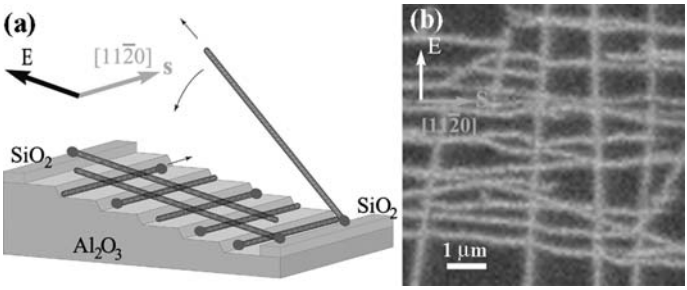

Fig. 26. Orthogonal self-assembly of SWNT crossbar architectures by simultaneous graphoepitaxy and field-directed growth, in a single step of CVD [191]. (**a**) Schematic representation of the process, showing the annealed miscut C-plane sapphire with nanosteps along the [11$\bar{2}$0] direction, while the electric field is applied perpendicularly to the steps. The nanotubes originating from catalyst nanoparticles lying on the sapphire (Al_2O_3) grow along the faceted nanosteps, while the nanotubes emerging from the catalyst on patterned amorphous SiO_2 stripes grow freely without interacting with the surface, in a way that allows their alignment by the electric field, eventually falling across the nanotubes grown on the sapphire. (**b**) SEM image of a dense SWNT grid obtained by simultaneous graphoepitaxy and field-directed growth (miscut inclination angle $\theta = 4°$, field intensity $E = 2 \times 10^6$ V/m)

target structures. Progress in these directions may enable the realization of many applications.

6.3.4 Patterned Growth on Surfaces

Another important aspect of the organization of carbon nanotubes on surfaces is not only their orientation, but also their location. One approach to control the placement of SWNTs is to control the sites from which nanotubes are grown by patterning catalyst particles on a substrate [5]. The initial idea of such patterned growth was demonstrated with micrometer-scale islands of catalyst patterned on SiO_2/Si wafers (Fig. 27a). Approximate location control of SWNTs (without orientation control) was obtained by chemical vapor deposition (CVD) growth of nanotubes from the catalyst islands. Since the initial patterned CVD growth demonstration, single-catalyst particle ($\sim$ 2 nm Fe clusters) patterning on substrates and orientation control of SWNTs grown by CVD have been actively pursued [226]. Single catalyst-nanoparticle patterning (Fig. 27b) for SWNTs growth by CVD was recently achieved (Fig. 27c).

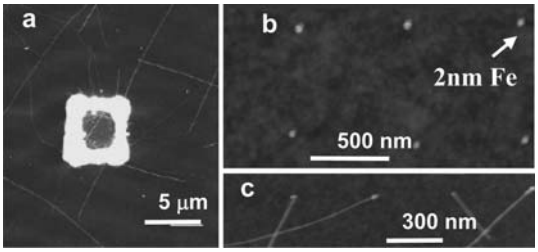

Fig. 27. Patterned growth of SWNTs. (**a**) Previous growth from micrometer-sized catalyst island (*white structure*) [5]. (**b**) AFM image of a recently made regular array of individual Fe clusters [226]. (**c**) SWNTs grown from the single-particle array

7 Summary and Outlook

Mass production, selective production, and organization of carbon nanotubes continue to be major synthetic challenges toward future applications. Significant advances during the last five years include the development of new CVD methods for mass production and for aligned growth on surfaces, both vertically and horizontally. Mass production and vertically aligned growth by CVD have been significantly boosted by the discovery of "supergrowth", adding small amounts of water to the CVD precursor or using alcohol as the carbon feedstock, to inhibit the formation of amorphous carbon, and thus to enhance the formation of clean carbon nanotubes. A fundamental key to further increase the control of carbon nanotube synthesis is understanding the different mechanisms of formation of carbon nanotubes, which determine their structure, electronic properties and arrangement. Since the mechanisms of CVD growth are not yet fully understood, further mechanistic insight will probably have an impact on the yield, purity and selectivity of CVD growth. An important development in this direction has been the direct observation of nanotube growth under the TEM [227].

We have seen promising advances in the selective production of carbon nanotubes, as well as in the continued growth of carbon nanotubes with conservation of their initial (n, m) structure. Single-wall carbon nanotubes have been sorted by length, electronic type and diameter using a variety of physical and chemical methods. Combinations of these methods promise to enable the production of nanotube fractions with progressively narrower (n, m) distribution. However, the selective production of pure nanotube samples with a unique (n, m) structure is a challenge yet to be met.

An important synthetic advance toward application of carbon nanotubes as structural and textile materials has been the development of new methods for spinning carbon nanotube fibers, either from liquid suspension, from dry forests, or directly from the CVD zone during growth. The mechanical properties of these carbon nanotube fibers are remarkable, but are still inferior to

those of individual carbon nanotubes. Approaching the nanoscopic properties at a macroscopic scale will probably require a better control, not only of the nanotube length and alignment, but also of the nanotube–nanotube interactions. Textile processing of carbon nanotubes into ultrastrong or "smart" clothing could be an exciting outcome to be seen soon.

Finally, the organization of carbon nanotubes into horizontally aligned arrays on surfaces, which continues to be a major challenge toward integration into nanocircuits, has been significantly advanced by the development field-directed, flow-directed and surface-directed growth. Flow-directed growth has allowed the controlled production of macroscopically long carbon nanotubes on surfaces. More recently, aligned growth by orientational epitaxy on well-defined crystal surfaces, directed by atomic steps, nanofacets or atomic rows, has opened up new ways of organizing nanotubes on surfaces into perfectly aligned arrays, as well as more complex morphologies. In addition to the control of nanotube orientation, there is still a need for better control of the nanotube location. This requires a reliable method for patterning catalyst nanoparticles that nucleate carbon nanotubes with a 100 % yield. Thanks to encouraging advances in this direction, the combination of patterned growth with orientational control is a promising prospect, which could greatly advance nanotube electronics in the next few years.

References

[1] T. W. Ebbesen, P. M. Ajayan: Large-scale synthesis of carbon nanotubes, Nature **358**, 220–222 (1992) 102, 103

[2] D. S. Bethune, C. H. Kiang, M. DeVries, G. Gorman, R. Savoy, J. Vazquez, R. Beyers: Cobalt-catalysed growth of carbon nanotubes with single-atomic-layer walls, Nature **363**, 605–607 (1993) 102, 103

[3] A. Thess, R. Lee, P. Nikolaev, H. J. Dai, P. Petit, J. Robert, C. H. Xu, Y. H. Lee, S. G. Kim, A. G. Rinzler, D. T. Colbert, G. E. Scuseria, D. Tomanek, J. E. Fischer, R. E. Smalley: Crystalline ropes of metallic carbon nanotubes, Science **273**, 483–487 (1996) 102, 103, 105

[4] H. Dai, A. G. Rinzler, A. Thess, P. Nikolaev, D. T. Colbert, R. E. Smalley: Single-wall carbon nanotubes produced by metal-catalyzed disproportionation of carbon monoxide, Chem. Phys. Lett. **260**, 471–475 (1996) 102, 104, 105

[5] J. Kong, H. Soh, A. Cassell, C. F. Quate, H. Dai: Synthesis of individual single-walled carbon nanotubes on patterned silicon wafers, Nature **395**, 878–881 (1998) 102, 104, 147, 148

[6] J. Hafner, M. Bronikowski, B. Azamian, P. Nikolaev, D. Colbert, R. Smalley: Catalytic growth of single-wall carbon nanotubes from metal particles, Chem. Phys. Lett. **296**, 195–202. (1998) 102, 104

[7] H. Dai: Carbon nanotubes: opportunities and challenges, Surf. Sci. **500**, 218–241 (2002) 103, 104, 126

[8] H. Dai: Carbon nanotubes: synthesis, integration, and properties, Acc. Chem. Res. **35**, 1035–1044 (2002) 103, 104

[9] H. Dai, J. Kong, C. Zhou, N. Franklin, T. Tombler, A. Cassell, S. Fan, M. Chapline: Controlled chemical routes to nanotube architectures, physics and devices, J. Phys. Chem. **103**, 11246–11255 (1999) 103, 104
[10] J. Kong, A. M. Cassell, H. Dai: Chemical vapor deposition of methane for single-walled carbon nanotubes, Chem. Phys. Lett. **292**, 567–574 (1998) 104
[11] A. Cassell, J. Raymakers, J. Kong, H. Dai: Large scale single-walled nanotubes by CVD synthesis, J. Phys. Chem. **103**, 6484–6492 (1999) 104
[12] M. Su, B. Zheng, J. Liu: A scalable CVD method for the synthesis of single-walled carbon nanotubes with high catalyst productivity, Chem. Phys. Lett. **322**, 321–326 (2000) 104
[13] P. Nikolaev, M. J. Bronikowski, R. K. Bradley, F. Rohmund, D. T. Colbert, K. A. Smith, R. E. Smalley: Gas-phase catalytic growth of single-walled carbon nanotubes from carbon monoxide, Chem. Phys. Lett. **313**, 91–97 (1999) 104
[14] B. Kitiyanan, W. E. Alvarez, J. H. Harwell, D. E. Resasco: Controlled production of single-wall carbon nanotubes by catalytic decomposition of CO on bimetallic Co-Mo catalysts, Chem. Phys. Lett. **317**, 497–503 (2000) 104
[15] S. Maruyama, R. Kojima, Y. Miyauchi, S. Chiashi, M. Kohno: Low-temperature synthesis of high-purity single-walled carbon nanotubes from alcohol, Chem. Phys. Lett. **360**, 229–234 (2002) 104
[16] Y. M. Li, D. Mann, M. Rolandi, W. Kim, A. Ural, S. Hung, A. Javey, J. Cao, D. W. Wang, E. Yenilmez, Q. Wang, J. F. Gibbons, Y. Nishi, H. J. Dai: Preferential growth of semiconducting single-walled carbon nanotubes by a plasma enhanced CVD method, Nano Lett. **4**, 317–321 (2004) 105, 106
[17] G. F. Zhong, T. Iwasaki, K. Honda, Y. Furukawa, I. Ohdomari, H. Kawarada: Low temperature synthesis of extremely dense and vertically aligned single-walled carbon nanotubes, Jpn. J. App. Phys. 1 **44**, 1558–1561 (2005) 105
[18] G. Y. Zhang, D. Mann, L. Zhang, A. Javey, Y. M. Li, E. Yenilmenz, Q. Wang, J. McVittie, Y. Nishi, J. Gibbons, H. Dai: Ultra-high-yield growth of vertical single-walled carbon nanotubes: Hidden roles of hydrogen and oxygen, Proc. Nat. Acad. Sci. **102**, 16141–16145 (2005) 105
[19] W. L. Wang, X. D. Bai, Z. Xu, S. Liu, E. G. Wang: Low temperature growth of single-walled carbon nanotubes: Small diameters with narrow distribution, Chem. Phys. Lett. **419**, 81–85 (2006) 105
[20] T. Kato, R. Hatakeyama, K. Tohji: Diffusion plasma chemical vapour deposition yielding freestanding individual single-walled carbon nanotubes on a silicon-based flat substrate, Nanotechnol. **17**, 2223–2226 (2006) 105
[21] A. V. Melechko, V. I. Merkulov, T. E. McKnight, M. A. Guillorn, K. L. Klein, D. H. Lowndes, M. L. Simpson: Vertically aligned carbon nanofibers and related structures: Controlled synthesis and directed assembly, J. Appl. Phys. **97**, 041301 (2005) 105
[22] C. Journet, W. K. Maser, P. Bernier, A. Loiseau, M. L. delaChapelle, S. Lefrant, P. Deniard, R. Lee, J. E. Fischer: Large-scale production of single-walled carbon nanotubes by the electric-arc technique, Nature **388**, 756–758 (1997) 105
[23] P. Nikolaev, M. J. Bronikowski, R. K. Bradley, F. Rohmund, D. T. Colbert, K. A. Smith, R. E. Smalley: Gas-phase catalytic growth of single-walled carbon nanotubes from carbon monoxide, Chem. Phys. Lett. **313**, 91–97 (1999) 105

[24] Y. Li, S. Peng, D. Mann, J. Cao, R. Tu, K. J. Cho, H. Dai: On the origin of preferential growth of semiconducting single-walled carbon nanotubes, J. Phys. Chem. B **109**, 6968–6971 (2005) 107

[25] G. Y. Zhang, P. F. Qi, X. R. Wang, Y. R. Lu, X. L. Li, R. Tu, S. Bangsaruntip, D. Mann, L. Zhang, H. J. Dai: Selective etching of metallic carbon nanotubes by gas-phase reaction, Science **314**, 974–977 (2006) 107, 115

[26] S. M. Bachilo, L. Balzano, J. E. Herrera, F. Pompeo, D. E. Resasco, R. B. Weisman: Narrow (n,m)-Distribution of Single-Walled Carbon Nanotubes Grown Using a Solid Supported Catalyst, J. Am. Chem. Soc. **125**, 11186–11187 (2003) 107

[27] G. Lolli, L. A. Zhang, L. Balzano, N. Sakulchaicharoen, Y. Q. Tan, D. E. Resasco: Tailoring (n,m) structure of single-walled carbon nanotubes by modifying reaction conditions and the nature of the support of CoMo catalysts, J. Phys. Chem. B **110**, 2108–2115 (2006) 107

[28] T. J. Park, S. Banerjee, T. Hemraj-Benny, S. S. Wong: Purification strategies and purity visualization techniques for single-walled carbon nanotubes, J. Mater. Chem. **16**, 141–154 (2006) 107, 108

[29] R. C. Haddon, J. Sippel, A. G. Rinzler, F. Papadimitrakopoulos: Purification and separation of carbon nanotubes, MRS Bull. **29**, 252–259 (2004) 107, 108, 109, 110

[30] T. W. Ebbesen, P. M. Ajayan, H. Hiura, K. Tanigaki: Purification of Nanotubes, Nature **367**, 519–519 (1994) 108

[31] J. L. Zimmerman, R. K. Bradley, C. B. Huffman, R. H. Hauge, J. L. Margrave: Gas-phase purification of single-wall carbon nanotubes, Chem. Mater. **12**, 1361–1366 (2000) 108

[32] J. M. Moon, K. H. An, Y. H. Lee, Y. S. Park, D. J. Bae, G. S. Park: High-yield purification process of singlewalled carbon nanotubes, J. Phys. Chem. B **105**, 5677–5681 (2001) 108

[33] Z. J. Shi, Y. F. Lian, F. H. Liao, X. H. Zhou, Z. N. Gu, Y. G. Zhang, S. Iijima: Purification of single-wall carbon nanotubes, Solid State Commun. **112**, 35–37 (1999) 108

[34] I. W. Chiang, B. E. Brinson, A. Y. Huang, P. A. Willis, M. J. Bronikowski, J. L. Margrave, R. E. Smalley, R. H. Hauge: Purification and characterization of single-wall carbon nanotubes (SWNTs) obtained from the gas-phase decomposition of CO (HiPco process), J. Phys. Chem. B **105**, 8297–8301 (2001) 108

[35] Y. Q. Xu, H. Q. Peng, R. H. Hauge, R. E. Smalley: Controlled multistep purification of single-walled carbon nanotubes, Nano Lett. **5**, 163–168 (2005) 108

[36] I. W. Chiang, B. E. Brinson, R. E. Smalley, J. L. Margrave, R. H. Hauge: Purification and characterization of single-wall carbon nanotubes, J. Phys. Chem. B **105**, 1157–1161 (2001) 108

[37] A. C. Dillon, T. Gennett, K. M. Jones, J. L. Alleman, P. A. Parilla, M. J. Heben: A simple and complete purification of single-walled carbon nanotube materials, Adv. Mater. **11**, 1354–1358 (1999) 108

[38] E. Dujardin, T. W. Ebbesen, A. Krishnan, M. M. J. Treacy: Purification of single-shell nanotubes, Adv. Mater. **10**, 611–613 (1998) 108

[39] D. Chattopadhyay, I. Galeska, F. Papadimitrakopoulos: Complete elimination of metal catalysts from single wall carbon nanotubes, Carbon **40**, 985–988 (2002) 108

[40] M. Monthioux, B. W. Smith, B. Burteaux, A. Claye, J. E. Fischer, D. E. Luzzi: Sensitivity of single-wall carbon nanotubes to chemical processing: an electron microscopy investigation, Carbon **39**, 1251–1272 (2001) 108

[41] A. G. Rinzler, J. Liu, H. Dai, P. Nikolaev, C. B. Huffman, F. J. Rodriguez-Macias, P. J. Boul, A. H. Lu, D. Heymann, D. T. Colbert, R. S. Lee, J. E. Fischer, A. M. Rao, P. C. Eklund, R. E. Smalley: Large-scale purification of single-wall carbon nanotubes: process, product, and characterization, Appl. Phys. A-Mater. **67**, 29–37 (1998) 108

[42] C. Bower, A. Kleinhammes, Y. Wu, O. Zhou: Intercalation and partial exfoliation of single-walled carbon nanotubes by nitric acid, Chem. Phys. Lett. **288**, 481–486 (1998) 108

[43] J. Liu, A. G. Rinzler, H. J. Dai, J. H. Hafner, R. K. Bradley, P. J. Boul, A. Lu, T. Iverson, K. Shelimov, C. B. Huffman, F. Rodriguez-Macias, Y. S. Shon, T. R. Lee, D. T. Colbert, R. E. Smalley: Fullerene pipes, Science **280**, 1253–1256 (1998) 108, 111, 115, 142

[44] Y. L. Yang, L. M. Xie, Z. Chen, M. H. Liu, T. Zhu, Z. F. Liu: Purification and length separation of single-walled carbon nanotubes using chromatographic method, Synth. Met. **155**, 455–460 (2005) 109, 111, 115

[45] X. Y. Huang, R. S. McLean, M. Zheng: High-resolution length sorting and purification of DNA-wrapped carbon nanotubes by size-exclusion chromatography, Anal. Chem. **77**, 6225–6228 (2005) 109, 111, 115

[46] S. Niyogi, H. Hu, M. A. Hamon, P. Bhowmik, B. Zhao, S. M. Rozenzhak, J. Chen, M. E. Itkis, M. S. Meier, R. C. Haddon: Chromatographic purification of soluble single-walled carbon nanotubes (s-SWNTs), J. Am. Chem. Soc. **123**, 733–734 (2001) 109

[47] A. P. Yu, E. Bekyarova, M. E. Itkis, D. Fakhrutdinov, R. Webster, R. C. Haddon: Application of centrifugation to the large-scale purification of electric arc-produced single-walled carbon nanotube, J. Am. Chem. Soc. **128**, 9902–9908 (2006) 109

[48] H. B. Jia, Y. F. Lian, M. O. Ishitsuka, T. Nakahodo, Y. Maeda, T. Tsuchiya, T. Wakahara, T. Akasaka: Centrifugal purification of chemically modified single-walled carbon nanotube, Sci. Technol. Adv. Mater. **6**, 571–581 (2005) 109

[49] R. Krupke, F. Hennrich: Separation techniques for carbon nanotubes, Adv. Eng. Mater. **7**, 111–116 (2005) 109, 110

[50] M. J. O'Connell, S. M. Bachilo, C. B. Huffman, V. C. Moore, M. S. Strano, E. H. Haroz, K. L. Rialon, P. J. Boul, W. H. Noon, C. Kittrell, J. P. Ma, R. H. Hauge, R. B. Weisman, R. E. Smalley: Band gap fluorescence from individual single-walled carbon nanotubes, Science **297**, 593–596 (2002) 109

[51] B. L. Chen, J. P. Selegue: Separation and characterization of single-walled and multiwalled carbon nanotubes by using flow field-flow fractionation, Anal. Chem. **74**, 4774–4780 (2002) 111, 115

[52] G. S. Duesberg, M. Burghard, J. Muster, G. Philipp, S. Roth: Separation of carbon nanotubes by size exclusion chromatography, Chem. Commun. pp. 435–436 (1998) 111, 115, 118

[53] K. Arnold, F. Hennrich, R. Krupke, S. Lebedkin, M. M. Kappes: Length separation studies of single walled carbon nanotube dispersions, Phys. Stat. Sol. B **243**, 3073–3076 (2006) 111, 115
[54] G. S. Duesberg, J. Muster, V. Krstic, M. Burghard, S. Roth: Chromatographic size separation of single-wall carbon nanotubes, Appl. Phys. A-Mater. **67**, 117–119 (1998) 111, 115
[55] G. S. Duesberg, W. Blau, H. J. Byrne, J. Muster, M. Burghard, S. Roth: Chromatography of carbon nanotubes, Synthetic Met. **103**, 2484–2485 (1999) 111, 115
[56] E. Farkas, M. E. Anderson, Z. H. Chen, A. G. Rinzler: Length sorting cut single wall carbon nanotubes by high performance liquid chromatography, Chem. Phys. Lett. **363**, 111–116 (2002) 111, 115
[57] X. Y. Xu, R. Ray, Y. L. Gu, H. J. Ploehn, L. Gearheart, K. Raker, W. A. Scrivens: Electrophoretic analysis and purification of fluorescent single-walled carbon nanotube fragments, J. Am. Chem. Soc. **126**, 12736–12737 (2004) 111, 115
[58] A. A. Vetcher, S. Srinivasan, I. A. Vetcher, S. M. Abramov, M. Kozlov, R. H. Baughman, S. D. Levene: Fractionation of SWNT/nucleic acid complexes by agarose gel electrophoresis, Nanotechnol. **17**, 4263–4269 (2006) 111, 115
[59] R. Krupke, F. Hennrich, H. von Lohneysen, M. M. Kappes: Separation of metallic from semiconducting single-walled carbon nanotubes, Science **301**, 344–347 (2003) 110, 111, 114, 135
[60] R. Krupke, F. Hennrich, H. B. Weber, M. M. Kappes, H. von Lohneysen: Simultaneous deposition of metallic bundles of single-walled carbon nanotubes using ac-dielectrophoresis, Nano Lett. **3**, 1019–1023 (2003) 111, 135, 136
[61] R. Krupke, F. Hennrich, M. M. Kappes, H. V. Lohneysen: Surface conductance induced dielectrophoresis of semiconducting single-walled carbon nanotubes, Nano Lett. **4**, 1395–1399 (2004) 111, 113, 135
[62] D. S. Lee, D. W. Kim, H. S. Kim, S. W. Lee, S. H. Jhang, Y. W. Park, E. E. B. Campbell: Extraction of semiconducting CNTs by repeated dielectrophoretic filtering, Appl. Phys. A-Mater. **80**, 5–8 (2005) 111, 113
[63] Z. B. Zhang, X. J. Liu, E. E. B. Campbell, S. L. Zhang: Alternating current dielectrophoresis of carbon nanotubes, J. Appl. Phys. **98**, 056103 (2005) 111
[64] T. Lutz, K. J. Donovan: Macroscopic scale separation of metallic and semiconducting nanotubes by dielectrophoresis, Carbon **43**, 2508–2513 (2005) 111, 113
[65] C. W. Marquardt, S. Blatt, F. Hennrich, H. V. Lohneysen, R. Krupke: Probing dielectrophoretic force fields with metallic carbon nanotubes, Appl. Phys. Lett. **89**, 183117 (2006) 111
[66] Z. Chen, Z. Y. Wu, L. M. Tong, H. P. Pan, Z. F. Liu: Simultaneous dielectrophoretic separation and assembly of single-walled carbon nanotubes on multigap nanoelectrodes and their thermal sensing properties, Anal. Chem. **78**, 8069–8075 (2006) 111
[67] R. Krupke, S. Linden, M. Rapp, F. Hennrich: Thin films of metallic carbon nanotubes prepared by dielectrophoresis, Adv. Mater. **18**, 1468–1470 (2006) 111, 113

[68] D. Chattopadhyay, L. Galeska, F. Papadimitrakopoulos: A route for bulk separation of semiconducting from metallic single-wall carbon nanotubes, J. Am. Chem. Soc. **125**, 3370–3375 (2003) 111, 116

[69] G. G. Samsonidze, S. G. Chou, A. P. Santos, V. W. Brar, G. Dresselhaus, M. S. Dresselhaus, A. Selbst, A. K. Swan, M. S. Unlu, B. B. Goldberg, D. Chattopadhyay, S. N. Kim, F. Papadimitrakopoulos: Quantitative evaluation of the octadecylamine-assisted bulk separation of semiconducting and metallic single-wall carbon nanotubes by resonance raman spectroscopy, Appl. Phys. Lett. **85**, 1006–1008 (2004) 111, 116

[70] Y. Maeda, S. Kimura, M. Kanda, Y. Hirashima, T. Hasegawa, T. Wakahara, Y. F. Lian, T. Nakahodo, T. Tsuchiya, T. Akasaka, J. Lu, X. W. Zhang, Z. X. Gao, Y. P. Yu, S. Nagase, S. Kazaoui, N. Minami, T. Shimizu, H. Tokumoto, R. Saito: Large-scale separation of metallic and semiconducting single-walled carbon nanotubes, J. Am. Chem. Soc. **127**, 10287–10290 (2005) 111, 116

[71] Y. Maeda, M. Kanda, M. Hashimoto, T. Hasegawa, S. Kimura, Y. F. Lian, T. Wakahara, T. Akasaka, S. Kazaoui, N. Minami, T. Okazaki, Y. Hayamizu, K. Hata, J. Lu, S. Nagase: Dispersion and separation of small-diameter single-walled carbon nanotubes, J. Am. Chem. Soc. **128**, 12239–12242 (2006) 111, 116

[72] K. J. Ziegler, D. J. Schmidt, U. Rauwald, K. N. Shah, E. L. Flor, R. H. Hauge, R. E. Smalley: Length-dependent extraction of single-walled carbon nanotubes, Nano Lett. **5**, 2355–2359 (2005) 111, 115

[73] L. J. Li, A. N. Khlobystov, J. G. Wiltshire, G. A. D. Briggs, R. J. Nicholas: Diameter-selective encapsulation of metallocenes in single-walled carbon nanotubes, Nature Mater. **4**, 481–485 (2005) 111

[74] A. Ortiz-Acevedo, H. Xie, V. Zorbas, W. M. Sampson, A. B. Dalton, R. H. Baughman, R. K. Draper, I. H. Musselman, G. R. Dieckmann: Diameter-selective solubilization of single-walled carbon nanotubes by reversible cyclic peptides, J. Am. Chem. Soc. **127**, 9512–9517 (2005) 111, 116

[75] Z. H. Chen, X. Du, M. H. Du, C. D. Rancken, H. P. Cheng, A. G. Rinzler: Bulk separative enrichment in metallic or semiconducting single-walled carbon nanotubes, Nano Lett. **3**, 1245–1249 (2003) 111, 116

[76] L. Kavan, L. Dunsch: Diameter-selective electrochemical doping of HiPco single-walled carbon nanotubes, Nano Lett. **3**, 969–972 (2003) 111, 116

[77] A. Kukovecz, T. Pichler, R. Pfeiffer, H. Kuzmany: Diameter selective charge transfer in p- and n-doped single wall carbon nanotubes synthesized by the HiPCO method, Chem. Commun. pp. 1730–1731 (2002) 111, 116

[78] A. Kukovecz, T. Pichler, R. Pfeiffer, C. Kramberger, H. Kuzmany: Diameter selective doping of single wall carbon nanotubes, Phys. Chem. Chem. Phys. **5**, 582–587 (2003) 111

[79] H. P. Li, B. Zhou, Y. Lin, L. R. Gu, W. Wang, K. A. S. Fernando, S. Kumar, L. F. Allard, Y. P. Sun: Selective interactions of porphyrins with semiconducting single-walled carbon nanotubes, J. Am. Chem. Soc. **126**, 1014–1015 (2004) 111, 116

[80] M. S. Arnold, S. I. Stupp, M. C. Hersam: Enrichment of single-walled carbon nanotubes by diameter in density gradients, Nano Lett. **5**, 713–718 (2005) 111, 116

[81] C. Menard-Moyon, N. Izard, E. Doris, C. Mioskowski: Separation of semiconducting from metallic carbon nanotubes by selective functionalization with azomethine ylides, J. Am. Chem. Soc. **128**, 6552–6553 (2006) 111, 116
[82] S. Banerjee, S. S. Wong: Selective metallic tube reactivity in the solution-phase osmylation of single-walled carbon nanotubes, J. Am. Chem. Soc. **126**, 2073–2081 (2004) 111
[83] L. An, Q. A. Fu, C. G. Lu, J. Liu: A simple chemical route to selectively eliminate metallic carbon nanotubes in nanotube network devices, J. Am. Chem. Soc. **126**, 10520–10521 (2004) 111
[84] Y. Miyata, Y. Maniwa, H. Kataura: Selective oxidation of semiconducting single-wall carbon nanotubes by hydrogen peroxide, J. Phys. Chem. B **110**, 25–29 (2006) 111
[85] A. Hassanien, M. Tokumoto, P. Umek, D. Vrbanic, M. Mozetic, D. Mihailovic, P. Venturini, S. Pejovnik: Selective etching of metallic single-wall carbon nanotubes with hydrogen plasma, Nanotechnol. **16**, 278–281 (2005) 111
[86] G. Y. Zhang, P. F. Qi, X. R. Wang, Y. R. Lu, X. L. Li, R. Tu, S. Bangsaruntip, D. Mann, L. Zhang, H. J. Dai: Selective etching of metallic carbon nanotubes by gas-phase reaction, Science **314**, 974–977 (2006) 111
[87] E. Borowiak-Palen, T. Pichler, X. Liu, M. Knupfer, A. Graff, O. Jost, W. Pompe, R. J. Kalenczuk, J. Fink: Reduced diameter distribution of single-wall carbon nanotubes by selective oxidation, Chem. Phys. Lett. **363**, 567–572 (2002) 111
[88] E. Menna, F. D. Negra, M. D. Fontana, M. Meneghetti: Selectivity of chemical oxidation attack of single-wall carbon nanotubes in solution, Phys. Rev. B **68**, 193412 (2003) 111
[89] P. C. Collins, M. S. Arnold, P. Avouris: Engineering carbon nanotubes and nanotube circuits using electrical breakdown, Science **292**, 706–709 (2001) 111, 115
[90] R. Seidel, A. P. Graham, E. Unger, G. S. Duesberg, M. Liebau, W. Steinhoegl, F. Kreupl, W. Hoenlein: High-current nanotube transistors, Nano Lett. **4**, 831–834 (2004) 111, 115
[91] H. Q. Peng, N. T. Alvarez, C. Kittrell, R. H. Hauge, H. K. Schmidt: Dielectrophoresis field flow fractionation of single-walled carbon nanotubes, J. Am. Chem. Soc. **128**, 8396–8397 (2006) 112, 113
[92] S. N. Kim, Z. T. Luo, F. Papadimitrakopoulos: Diameter and metallicity dependent redox influences on the separation of single-wall carbon nanotubes, Nano Lett. **5**, 2500–2504 (2005) 112, 116
[93] M. S. Arnold, A. A. Green, J. F. Hulvat, S. I. Stupp, M. C. Hersam: Sorting carbon nanotubes by electronic structure using density differentiation, Nature Nanotechnol. **1**, 60–65 (2006) 112, 114, 116
[94] L. J. Li, R. J. Nicholas: Bandgap-selective chemical doping of semiconducting single-walled carbon nanotubes, Nanotechnol. **15**, 1844–1847 (2004) 112
[95] M. Zheng, A. Jagota, E. D. Semke, B. A. Diner, R. S. Mclean, S. R. Lustig, R. E. Richardson, N. G. Tassi: DNA-assisted dispersion and separation of carbon nanotubes, Nature Mater. **2**, 338–342 (2003) 112, 113, 114, 116
[96] M. Zheng, A. Jagota, M. S. Strano, A. P. Santos, P. Barone, S. G. Chou, B. A. Diner, M. S. Dresselhaus, R. S. McLean, G. B. Onoa, G. G. Samsonidze, E. D. Semke, M. Usrey, D. J. Walls: Structure-based carbon nanotube sorting

by sequence-dependent DNA assembly, Science **302**, 1545–1548 (2003) 112, 114, 116

[97] M. S. Strano, M. Zheng, A. Jagota, G. B. Onoa, D. A. Heller, P. W. Barone, M. L. Usrey: Understanding the nature of the DNA-assisted separation of single-walled carbon nanotubes using fluorescence and raman spectroscopy, Nano Lett. **4**, 543–550 (2004) 112, 116

[98] S. R. Lustig, A. Jagota, C. Khripin, M. Zheng: Theory of structure-based carbon nanotube separations by ion-exchange chromatography of DNA/CNT hybrids, J. Phys. Chem. B **109**, 2559–2566 (2005) 112, 116

[99] M. S. Strano, C. B. Huffman, V. C. Moore, M. J. O'Connell, E. H. Haroz, J. Hubbard, M. Miller, K. Rialon, C. Kittrell, S. Ramesh, R. H. Hauge, R. E. Smalley: Reversible, band-gap-selective protonation of single-walled carbon nanotubes in solution, J. Phys. Chem. B **107**, 6979–6985 (2003) 112

[100] M. S. Strano, C. A. Dyke, M. L. Usrey, P. W. Barone, M. J. Allen, H. W. Shan, C. Kittrell, R. H. Hauge, J. M. Tour, R. E. Smalley: Electronic structure control of single-walled carbon nanotube functionalization, Science **301**, 1519–1522 (2003) 112, 113, 114, 116

[101] M. L. Usrey, E. S. Lippmann, M. S. Strano: Evidence for a two-step mechanism in electronically selective single-walled carbon nanotube reactions, J. Am. Chem. Soc. **127**, 16129–16135 (2005) 112

[102] C. J. Wang, Q. Cao, T. Ozel, A. Gaur, J. A. Rogers, M. Shim: Electronically selective chemical functionalization of carbon nanotubes: Correlation between Raman spectral and electrical responses, J. Am. Chem. Soc. **127**, 11460–11468 (2005) 112

[103] C. A. Dyke, M. P. Stewart, J. M. Tour: Separation of single-walled carbon nanotubes on silica gel. Materials morphology and Raman excitation wavelength affect data interpretation, J. Am. Chem. Soc. **127**, 4497–4509 (2005) 112, 113, 116

[104] S. Baik, M. Usrey, L. Rotkina, M. Strano: Using the selective functionalization of metallic single-walled carbon nanotubes to control dielectrophoretic mobility, J. Phys. Chem. B **108**, 15560–15564 (2004) 112, 113

[105] M. S. Strano: Probing chiral selective reactions using a revised Kataura plot for the interpretation of single-walled carbon nanotube spectroscopy, J. Am. Chem. Soc. **125**, 16148–16153 (2003) 112, 116

[106] K. Kamaras, M. E. Itkis, H. Hu, B. Zhao, R. C. Haddon: Covalent bond formation to a carbon nanotube metal, Science **301**, 1501–1501 (2003) 112

[107] K. H. An, J. S. Park, C. M. Yang, S. Y. Jeong, S. C. Lim, C. Kang, J. H. Son, M. S. Jeong, Y. H. Lee: A diameter-selective attack of metallic carbon nanotubes by nitronium ions, J. Am. Chem. Soc. **127**, 5196–5203 (2005) 112

[108] C. M. Yang, J. S. Park, K. H. An, S. C. Lim, K. Seo, B. Kim, K. A. Park, S. Han, C. Y. Park, Y. H. Lee: Selective removal of metallic single-walled carbon nanotubes with small diameters by using nitric and sulfuric acids, J. Phys. Chem. B **109**, 19242–19248 (2005) 112

[109] C. M. Yang, K. H. An, J. S. Park, K. A. Park, S. C. Lim, S. H. Cho, Y. S. Lee, W. Park, C. Y. Park, Y. H. Lee: Preferential etching of metallic single-walled carbon nanotubes with small diameter by fluorine gas, Phys. Rev. B **73**, 075419 (2006) 112

[110] T. W. Odom, J. L. Huang, P. Kim, C. M. Lieber: Structure and electronic properties of carbon nanotubes, J. Phys. Chem. B **104**, 2794–2809 (2000) 112, 116
[111] E. Joselevich: Chemistry and electronics of carbon nanotubes go together, Angew. Chem. Int. Ed. **43**, 2992–2994 (2004) 116
[112] E. Joselevich: Electronic structure and chemical reactivity of carbon nanotubes: A chemist's view, Chem. Phys. Chem. **5**, 619–624 (2004) 116
[113] Z. F. Chen, W. Thiel, A. Hirsch: Reactivity of the convex and concave surfaces of single-walled carbon nanotubes (SWCNTs) towards addition reactions: Dependence on the carbon-atom pyramidalization, Chem. Phys. Chem. **4**, 93–97 (2003) 116
[114] R. E. Smalley, Y. B. Li, V. C. Moore, B. K. Price, R. Colorado, H. K. Schmidt, R. H. Hauge, A. R. Barron, J. M. Tour: Single wall carbon nanotube amplification: En route to a type-specific growth mechanism, J. Am. Chem. Soc. **128**, 15824–15829 (2006) 116, 142
[115] Y. H. Wang, M. J. Kim, H. W. Shan, C. Kittrell, H. Fan, L. M. Ericson, W. F. Hwang, S. Arepalli, R. H. Hauge, R. E. Smalley: Continued growth of single-walled carbon nanotubes, Nano Lett. **5**, 997–1002 (2005) 116, 118, 142
[116] M. J. Kim, E. Haroz, Y. Wang, H. Shan, N. Nicholas, C. Kittrell, V. C. Moore, Y. Jung, D. Luzzi, R. Wheeler, T. BensonTolle, H. Fan, S. Da, W. F. Hwang, T. J. Wainerdi, H. Schmidt, R. H. Hauge, R. E. Smalley: Nanoscopically flat open-ended single-walled carbon nanotube substrates for continued growth, Nano Lett. **7**, 15–21 (2007) 116, 142
[117] M. Hamm, J. A. Elliott, H. J. Smithson, A. H. Windle: Mater. Res. Soc. Symp. Proc. **788** (2004) 117
[118] S. Giordani, S. D. Bergin, V. Nicolosi, S. Lebedkin, M. M. Kappes, W. J. Blau, J. N. Coleman: Debundling of single-walled nanotubes by dilution: Observation of large populations of individual nanotubes in amide solvent dispersions, J. Phys. Chem. B. **110**, 15708–15718 (2006) 118
[119] M. S. P. Shaffer, X. Fan, A. H. Windle: Dispersion and packing of carbon nanotubes, Carbon **36**, 1603–1612 (1998) 118
[120] P. J. Flory, P. R. Soc.: Phase equilibria in solutions of rod-like particles, London A **234**, 73–89 (1956) 118
[121] W. H. Song, I. A. Kinloch, A. H. Windle: Nematic liquid crystallinity of multiwall carbon nanotubes, Science **302**, 1363–1363 (2003) 118
[122] S. J. Zhang, I. A. Kinloch, A. H. Windle: Mesogenicity drives fractionation in lyotropic aqueous suspensions of multiwall carbon nanotubes, Nano Lett. **6**, 568–572 (2006) 119
[123] H. G. Chae, S. Kumar: Rigid-rod polymeric fibers, J. Appl. Polym. Sci. **100**, 791–802 (2006) 119
[124] L. M. Ericson, H. Fan, H. Q. Peng, V. A. Davis, W. Zhou, J. Sulpizio, Y. H. Wang, R. Booker, J. Vavro, C. Guthy, A. N. G. Parra-Vasquez, M. J. Kim, S. Ramesh, R. K. Saini, C. Kittrell, G. Lavin, H. Schmidt, W. W. Adams, W. E. Billups, M. Pasquali, W. F. Hwang, R. H. Hauge, J. E. Fischer, R. E. Smalley: Macroscopic, neat, single-walled carbon nanotube fibers, Science **305**, 1447–1450 (2004) 119, 120

[125] J. Steinmetz, M. Glerup, M. Paillet, P. Bernier, M. Holzinger: Production of pure nanotube fibers using a modified wet-spinning method, Carbon **43**, 2397–2400 (2005) 120

[126] S. Zhang, K. K. K. Koziol, I. A. Kinloch, A. H. Windle: Carbon (2007) submitted 120

[127] A. Penicaud, L. Valat, A. Derre, P. Poulin, C. Zakri, O. Roubeau, M. Maugey, P. Miaudet, E. Anglaret, P. Petit, A. Loiseau, S. Enouz: Mild dissolution of carbon nanotubes: Composite carbon nanotube fibres from polyelectrolyte solutions, Compos. Sci. Technol. **67**, 795–797 (2007) 120, 121

[128] L. X. Zheng, M. J. O'Connell, S. K. Doorn, X. Z. Liao, Y. H. Zhao, E. A. Akhadov, M. A. Hoffbauer, B. J. Roop, Q. X. Jia, R. C. Dye, D. E. Peterson, S. M. Huang, J. Liu, Y. T. Zhu: Ultralong single-wall carbon nanotubes, Nature Mater. **3**, 673–676 (2004) 120, 123

[129] B. Vigolo, A. Penicaud, C. Coulon, C. Sauder, R. Pailler, C. Journet, P. Bernier, P. Poulin: Macroscopic fibers and ribbons of oriented carbon nanotubes, Science **290**, 1331–1334 (2000) 120

[130] P. Poulin, B. Vigolo, P. Launois: Films and fibers of oriented single wall nanotubes, Carbon **40**, 1741–1749 (2002) 120, 121

[131] H. H. Gommans, J. W. Alldredge, H. Tashiro, J. Park, J. Magnuson, A. G. Rinzler: Fibers of aligned single-walled carbon nanotubes: Polarized Raman spectroscopy, J. Appl. Phys. **88**, 2509–2514 (2000) 121

[132] B. Vigolo, P. Poulin, M. Lucas, P. Launois, P. Bernier: Improved structure and properties of single-wall carbon nanotube spun fibers, Appl. Phys. Lett. **81**, 1210–1212 (2002) 121

[133] P. Miaudet, S. Badaire, M. Maugey, A. Derre, V. Pichot, P. Launois, P. Poulin, C. Zakri: Hot-drawing of single and multiwall carbon nanotube fibers for high toughness and alignment, Nano Lett. **5**, 2212–2215 (2005) 121, 122

[134] V. Pichot, S. Badaire, P. A. Albouy, C. Zakri, P. Poulin, P. Launois: Structural and mechanical properties of single-wall carbon nanotube fibers, Phys. Rev. B **74**, 245416 (2006) 121

[135] A. B. Dalton, S. Collins, E. Munoz, J. M. Razal, V. H. Ebron, J. P. Ferraris, J. N. Coleman, B. G. Kim, R. H. Baughman: Super-tough carbon-nanotube fibres - These extraordinary composite fibres can be woven into electronic textiles, Nature **423**, 703–703 (2003) 121

[136] A. Penicaud, P. Poulin, A. Derre, E. Anglaret, P. Petit: Spontaneous dissolution of a single-wall carbon nanotube salt, J. Am. Chem. Soc. **127**, 8–9 (2005) 121

[137] T. V. Sreekumar, T. Liu, B. G. Min, H. Guo, S. Kumar, R. H. Hauge, R. E. Smalley: Polyacrylonitrile single-walled carbon nanotube composite fibers, Adv. Mater. **16**, 58–61 (2004) 122

[138] C. Y. Wang, V. Mottaghitalab, C. O. Too, G. M. Spinks, G. G. Wallace: Polyaniline and polyaniline-carbon nanotube composite fibres as battery materials in ionic liquid electrolyte, J. Power Sources **163**, 1105–1109 (2007) 122

[139] B. G. Min, T. V. Sreekumar, T. Uchida, S. Kumar: Oxidative stabilization of PAN/SWNT composite fiber, Carbon **43**, 599–604 (2005) 122

[140] Y. P. Wang, R. L. Cheng, L. L. Liang, Y. M. Wang: Study on the preparation and characterization of ultra-high molecular weight polyethylene-carbon nanotubes composite fiber, Compos. Sci. Technol. **65**, 793–797 (2005) 122
[141] K. L. Jiang, Q. Q. Li, S. S. Fan: Nanotechnology: Spinning continuous carbon nanotube yarns - Carbon nanotubes weave their way into a range of imaginative macroscopic applications, Nature **419**, 801–801 (2002) 122
[142] M. Zhang, K. R. Atkinson, R. H. Baughman: Multifunctional carbon nanotube yarns by downsizing an ancient technology, Science **306**, 1358–1361 (2004) 122, 123
[143] J. W. S. Hearle, P. Grosberg, S. Becker: *Structural Mechanics of Fibres, Yarns and Fabrics* (Wiley, New York 1969) 122
[144] Q. Li, X. Zhang, R. F. DePaula, L. X. Zheng, Y. H. Zhao, L. Stan, T. G. Holesinger, P. N. Arendt, D. E. Peterson, Y. T. Zhu: Poster presentation preprint, MRS Fall Meeting, Boston (2006) 123
[145] M. Zhang, S. L. Fang, A. A. Zakhidov, S. B. Lee, A. E. Aliev, C. D. Williams, K. R. Atkinson, R. H. Baughman: Strong, transparent, multifunctional, carbon nanotube sheets, Science **309**, 1215–1219 (2005) 123
[146] Y. L. Li, I. A. Kinloch, A. H. Windle: Direct spinning of carbon nanotube fibers from chemical vapor deposition synthesis, Science **304**, 276–278 (2004) 123
[147] H. W. Zhu, C. L. Xu, D. H. Wu, B. Q. Wei, R. Vajtai, P. M. Ajayan: Direct synthesis of long single-walled carbon nanotube strands, Science **296**, 884–886 (2002) 123
[148] M. Motta, A. Moisala, I. A. Kinloch, V. Premnath, M. Pick, A. H. Windle: The parameter space for the direct spinning of fibres and films of carbon nanotubes, Physica E **37**, 40–43 (2007) 124
[149] M. Motta, Y. L. Li, I. Kinloch, A. Windle: Mechanical properties of continuously spun fibers of carbon nanotubes, Nano Lett. **5**, 1529–1533 (2005) 124
[150] M. Motta, A. Moisala, I. Kinloch, A. H. Windle: High performance fibres from dog bone carbon nanotubes, Adv. Mater. **19**, 3721–3726 (2007) 124
[151] R. F. Service: Assembling nanocircuits from the bottom up, Science **293**, 782–785 (2001) 126
[152] S. M. Huang, L. M. Dai, A. W. H. Mau: Patterned growth and contact transfer of well-aligned carbon nanotube films, J. Phys. Chem. B. **103**, 4223–4227 (1999) 126
[153] B. Q. Wei, R. Vajtai, Y. Jung, J. Ward, R. Zhang, G. Ramanath, P. M. Ajayan: Organized assembly of carbon nanotubes - Cunning refinements help to customize the architecture of nanotube structures, Nature **416**, 495–496 (2002) 126
[154] L. M. Dai, A. Patil, X. Y. Gong, Z. X. Guo, L. Q. Liu, Y. Liu, D. B. Zhu: Aligned nanotubes, Chem. Phys. Chem. **4**, 1150–1169 (2003) 126
[155] Z. F. Ren, Z. P. Huang, J. W. Xu, J. H. Wang: Synthesis of large arrays of well-aligned carbon nanotubes on glass, Science **282**, 1105–1107 (1998) 126
[156] S. Fan, M. Chapline, N. Franklin, T. Tombler, A. Cassell, H. Dai: Self-oriented regular arrays of carbon nanotubes and their field emission properties, Science **283**, 512–514 (1999) 126

[157] K. Hata, D. N. Futaba, K. Mizuno, T. Namai, M. Yumura, S. Iijima: Water-assisted highly efficient synthesis of impurity-free single-waited carbon nanotubes, Science **306**, 1362–1364 (2004) 127, 128
[158] Y. H. Yun, V. Shanov, Y. Tu, S. Subramaniam, M. J. Schulz: Growth mechanism of long aligned multiwall carbon nanotube arrays by water-assisted chemical vapor deposition, J. Phys. Chem. B. **110**, 23920–23925 (2006) 127
[159] Q. W. Li, X. F. Zhang, R. F. DePaula, L. X. Zheng, Y. H. Zhao, L. Stan, T. G. Holesinger, P. N. Arendt, D. E. Peterson, Y. T. T. Zhu: Sustained growth of ultralong carbon nanotube arrays for fiber spinning, Adv. Mater. **18**, 3160–3163 (2006) 127
[160] H. Ago, N. Uehara, N. Yoshihara, M. Tsuji, M. Yumura, N. Tomonaga, T. Setoguchi: Gas analysis of the CVD process for high yield growth of carbon nanotubes over metal-supported catalysts, Carbon **44**, 2912–2918 (2006) 127
[161] S. Chakrabarti, T. Nagasaka, Y. Yoshikawa, L. J. Pan, Y. Nakayama: Growth of super long aligned brush-like carbon nanotubes, Jpn. J. Appl. Phys. 2 **45**, L720–L722 (2006) 127
[162] D. N. Futaba, K. Hata, T. Namai, T. Yamada, K. Mizuno, Y. Hayamizu, M. Yumura, S. Iijima: 84 % Catalyst activity of water-assisted growth of single walled carbon nanotube forest characterization by a statistical and macroscopic approach, J. Phys. Chem. B **110**, 8035–8038 (2006) 127
[163] G. F. Zhong, T. Iwasaki, H. Kawarada: Semi-quantitative study on the fabrication of densely packed and vertically aligned single-walled carbon nanotubes, Carbon **44**, 2009–2014 (2006) 127
[164] D. N. Futaba, K. Hata, T. Yamada, K. Mizuno, M. Yumura, S. Iijima: Kinetics of water-assisted single-walled carbon nanotube synthesis revealed by a time-evolution analysis, Phys. Rev. Lett. **95**, 056104 (2005) 128, 130
[165] T. Yamada, T. Namai, K. Hata, D. N. Futaba, K. Mizuno, J. Fan, M. Yudasaka, M. Yumura, S. Iijima: Size-selective growth of double-walled carbon nanotube forests from engineered iron catalysts, Nature Nanotechnol. **1**, 131–136 (2006) 130, 131
[166] T. Hiraoka, T. Yamada, K. Hata, D. N. Futaba, H. Kurachi, S. Uemura, M. Yumura, S. Iijima: Synthesis of single- and double-walled carbon nanotube forests on conducting metal foils, J. Am. Chem. Soc. **128**, 13338–13339 (2006) 131, 132
[167] D. N. Futaba, K. Hata, T. Yamada, T. Hiraoka, Y. Hayamizu, Y. Kakudate, O. Tanaike, H. Hatori, M. Yumura, S. Iijima: Shape-engineerable and highly densely packed single-walled carbon nanotubes and their application as supercapacitor electrodes, Nature Mater. **5**, 987–994 (2006) 132, 133, 134
[168] Y. H. Yan, M. B. Chan-Park, Q. Zhang: Advances in carbon-nanotube assembly, Small **3**, 24–42 (2007) 133
[169] J. Liu, M. J. Casavant, M. Cox, D. A. Walters, P. Boul, W. Lu, A. J. Rimberg, K. A. Smith, D. T. Colbert, R. E. Smalley: Controlled deposition of individual single-walled carbon nanotubes on chemically functionalized templates, Chem. Phys. Lett. **303**, 125–129 (1999) 133
[170] C. Klinke, J. B. Hannon, A. Afzali, P. Avouris: Field-Effect Transistors Assembled from Functionalized Carbon Nanotubes, Nano Lett. **6**, 906–910 (2006) 133, 134
[171] S. G. Rao, L. Huang, W. Setyawan, S. H. Hong: Large-scale assembly of carbon nanotubes, Nature **425**, 36–37 (2003) 133, 135

[172] Y. H. Wang, D. Maspoch, S. L. Zou, G. C. Schatz, R. E. Smalley, C. A. Mirkin: Controlling the shape, orientation, and linkage of carbon nanotube features with nano affinity templates, Proc. Nat. Acad. Sci. **103**, 2026–2031 (2006) 133

[173] S. Zou, D. Maspoch, Y. Wang, C. A. Mirkin, G. C. Schatz: Rings of Single-Walled Carbon Nanotubes: Molecular-Template Directed Assembly and Monte Carlo Modeling, Nano Lett. **7**, 276–280 (2007) 133

[174] A. L. Bassi, M. G. Beghi, C. S. Casari, C. E. Bottani, A. Podesta, P. Milani, A. Zakhidov, R. Baughman, D. A. Walters, R. E. Smalley: Inelastic light scattering from magnetically aligned single-walled carbon nanotubes and estimate of their two-dimensional Young's modulus, Diam. Relat. Mater. **12**, 806–810 (2003) 135

[175] M. J. Casavant, D. A. Walters, J. J. Schmidt, R. E. Smalley: Neat macroscopic membranes of aligned carbon nanotubes, J. Appl. Phys. **93**, 2153–2156 (2003) 135

[176] J. E. Fischer, W. Zhou, J. Vavro, M. C. Llaguno, C. Guthy, R. Haggenmueller, M. J. Casavant, D. E. Walters, R. E. Smalley: Magnetically aligned single wall carbon nanotube films: Preferred orientation and anisotropic transport properties, J. Appl. Phys. **93**, 2157–2163 (2003) 135

[177] D. A. Walters, M. J. Casavant, X. C. Qin, C. B. Huffman, P. J. Boul, L. M. Ericson, E. H. Haroz, M. J. O'Connell, K. Smith, D. T. Colbert, R. E. Smalley: In-plane-aligned membranes of carbon nanotubes, Chem. Phys. Lett. **338**, 14–20 (2001) 135

[178] B. W. Smith, Z. Benes, D. E. Luzzi, J. E. Fischer, D. A. Walters, M. J. Casavant, J. Schmidt, R. E. Smalley: Structural anisotropy of magnetically aligned single wall carbon nanotube films, Appl. Phys. Lett. **77**, 663–665 (2000) 135

[179] M. D. Lay, J. P. Novak, E. S. Snow: Simple route to large-scale ordered arrays of liquid-deposited carbon nanotubes, Nano Lett. **4**, 603–606 (2004) 135

[180] J. Q. Li, Q. Zhang, N. Peng, Q. Zhu: Manipulation of carbon nanotubes using AC dielectrophoresis, Appl. Phys. Lett. **86**, 153116 (2005) 135

[181] J. Tang, G. Yang, Q. Zhang, A. Parhat, B. Maynor, J. Liu, L. C. Qin, O. Zhou: Rapid and reproducible fabrication of carbon nanotube AFM probes by dielectrophoresis, Nano Lett. **5**, 11–14 (2005) 135

[182] J. Tang, B. Gao, H. Z. Geng, O. D. Velev, L. C. Qin, O. Zhou: Assembly of ID nanostructures into sub-micrometer diameter fibrils with controlled and variable length by dielectrophoresis, Adv. Mater. **15**, 1352–1355 (2003) 135

[183] R. Krupke, F. Hennrich, H. B. Weber, D. Beckmann, O. Hampe, S. Malik, M. M. Kappes, H. V. Lohneysen: Contacting single bundles of carbon nanotubes with alternating electric fields, Appl. Phys. A-Mater. **76**, 397–400 (2003) 135

[184] X. Li, L. Zhang, X. Wang, I. Shimoyama, X. Sun, W.-S. Seo, H. Dai: Langmuir-Blodgett assembly of densely aligned single-walled carbon nanotubes from bulk materials, J. Am. Chem. Soc. **129**, 4890–4891 (2007) 135, 136, 137

[185] J. Kong, H. T. Soh, A. M. Cassell, C. F. Quate, H. J. Dai: Synthesis of individual single-walled carbon nanotubes on patterned silicon wafers, Nature **395**, 878–881 (1998) 137

[186] E. Joselevich, C. M. Lieber: Vectorial growth of metallic and semiconducting single-wall carbon nanotubes, Nano Lett. **2**, 1137–1141 (2002) 137, 138

[187] L. X. Benedict, S. G. Louie, M. L. Cohen: Static Polarizabilities of Single-Wall Carbon Nanotubes, Phys. Rev. B **52**, 8541–8549 (1995) 137
[188] Y. G. Zhang, A. L. Chang, J. Cao, Q. Wang, W. Kim, Y. M. Li, N. Morris, E. Yenilmez, J. Kong, H. J. Dai: Electric-field-directed growth of aligned single-walled carbon nanotubes, Appl. Phys. Lett. **79**, 3155–3157 (2001) 137, 138
[189] A. Ural, Y. M. Li, H. J. Dai: Electric-field-aligned growth of single-walled carbon nanotubes on surfaces, Appl. Phys. Lett. **81**, 3464–3466 (2002) 137
[190] A. Nojeh, A. Ural, R. F. Pease, H. J. Dai: Electric-field-directed growth of carbon nanotubes in two dimensions, J. Vac. Sci. Technol. B **22**, 3421–3425 (2004) 139
[191] A. Ismach, E. Joselevich: Orthogonal self-assembly of carbon nanotube crossbar architectures by simultaneous graphoepitaxy and field-directed growth, Nano Lett. **6**, 1706–1710 (2006) 139, 145, 147
[192] S. Dittmer, J. Svensson, E. E. B. Campbell: Electric field aligned growth of single-walled carbon nanotubes, Curr. Appl. Phys. **4**, 595–598 (2004) 139
[193] I. Radu, Y. Hanein, D. H. Cobden: Oriented growth of single-wall carbon nanotubes using alumina patterns, Nanotechnol. **15**, 473–476 (2004) 139
[194] C. Kocabas, M. A. Meitl, A. Gaur, M. Shim, J. A. Rogers: Aligned arrays of single-walled carbon nanotubes generated from random networks by orientationally selective laser ablation, Nano Lett. **4**, 2421–2426 (2004) 139
[195] K. H. Lee, J. M. Cho, W. Sigmund: Control of growth orientation for carbon nanotubes, Appl. Phys. Lett. **82**, 448–450 (2003) 139
[196] N. Kumar, W. Curtis, J. I. Hahm: Laterally aligned, multiwalled carbon nanotube growth using Magnetospirillium magnetotacticum, Appl. Phys. Lett. **86**, 173101 (2005) 139
[197] S. M. Huang, X. Y. Cai, J. Liu: Growth of millimeter-long and horizontally aligned single-walled carbon nanotubes on flat substrates, J. Am. Chem. Soc. **125**, 5636–5637 (2003) 139, 140
[198] S. M. Huang, Q. Fu, L. An, J. Liu: Growth of aligned SWNT arrays from water-soluble molecular clusters for nanotube device fabrication, Phys. Chem. Chem. Phys. **6**, 1077–1079 (2004) 139
[199] S. M. Huang, B. Maynor, X. Y. Cai, J. Liu: Ultralong, well-aligned single-walled carbon nanotube architectures on surfaces, Adv. Mater. **15**, 1651–1655 (2003) 139
[200] S. M. Huang, X. Y. Cai, C. S. Du, J. Liu: Oriented long single walled carbon nanotubes on substrates from floating catalysts, J. Phys. Chem. B **107**, 13251–13254 (2003) 139
[201] S. D. Li, Z. Yu, C. Rutherglen, P. J. Burke: Electrical properties of 0.4 cm long single-walled carbon nanotubes, Nano Lett. **4**, 2003–2007 (2004) 141
[202] Z. Yu, S. D. Li, P. J. Burke: Synthesis of aligned arrays of millimeter long, straight single-walled carbon nanotubes, Chem. Mater. **16**, 3414–3416 (2004) 141
[203] B. H. Hong, J. Y. Lee, T. Beetz, Y. M. Zhu, P. Kim, K. S. Kim: Quasi-continuous growth of ultralong carbon nanotube arrays, J. Am. Chem. Soc. **127**, 15336–15337 (2005) 141
[204] W. W. Zhou, Z. Y. Han, J. Y. Wang, Y. Zhang, Z. Jin, X. Sun, Y. W. Zhang, C. H. Yan, Y. Li: Copper catalyzing growth of single-walled carbon nanotubes on substrates, Nano Lett. **6**, 2987–2990 (2006) 141

[205] D. E. Hooks, T. Fritz, M. D. Ward: Epitaxy and molecular organization on solid substrates, Adv. Mater. **13**, 227–241 (2001) 141
[206] A. Ismach, D. Kantorovich, E. Joselevich: Carbon nanotube graphoepitaxy: Highly oriented growth by faceted nanosteps, J. Am. Chem. Soc. **127**, 11554–11555 (2005) 142, 144, 145, 146
[207] M. Su, Y. Li, B. Maynor, A. Buldum, J. P. Lu, J. Liu: Lattice-oriented growth of single-walled carbon nanotubes, J. Phys. Chem. B **104**, 6505–6508 (2000) 142
[208] M. Tominaga, A. Ohira, A. Kubo, I. Taniguchi, M. Kunitake: Growth of carbon nanotubes on a gold(111) surface using two-dimensional iron oxide nano-particle catalysts derived from iron storage protein, Chem. Commun. pp. 1518–1519 (2004) 142
[209] V. Derycke, R. Martel, M. Radosvljevic, F. M. R. Ross, P. Avouris: Catalyst-free growth of ordered single-walled carbon nanotube networks, Nano Lett. **2**, 1043–1046 (2002) 142
[210] L. B. Ruppalt, P. M. Albrecht, J. W. Lyding: Atomic resolution scanning tunneling microscope study of single-wailed carbon nanotubes on GaAs(110), J. Vac. Sci. Technol. B. **22**, 2005–2007 (2004) 142
[211] L. B. Ruppalt, P. M. Albrecht, J. W. Lyding: UHV-STM study of single-walled carbon nanotubes applied to the GaAs(110) and InAs(110) surfaces, J. Phys. IV **132**, 31–34 (2006) 142
[212] A. Ismach, L. Segev, E. Wachtel, E. Joselevich: Atomic-step-templated formation of single wall carbon nanotube patterns, Angew. Chem. Int. Ed. **43**, 6140–6143 (2004) 142, 143, 144
[213] S. Han, X. L. Liu, C. W. Zhou: Template-free directional growth of single-walled carbon nanotubes on a- and r-plane sapphire, J. Am. Chem. Soc. **127**, 5294–5295 (2005) 142
[214] H. Ago, K. Nakamura, K. Ikeda, N. Uehara, N. Ishigami, M. Tsuji: Aligned growth of isolated single-walled carbon nanotubes programmed by atomic arrangement of substrate surface, Chem. Phys. Lett. **408**, 433–438 (2005) 142
[215] H. Ago, N. Uehara, K. Ikeda, R. Ohdo, K. Nakamura, M. Tsuji: Synthesis of horizontally-aligned single-walled carbon nanotubes with controllable density on sapphire surface and polarized Raman spectroscopy, Chem. Phys. Lett. **421**, 399–403 (2006) 142
[216] Q. K. Yu, G. T. Qin, H. Li, Z. H. Xia, Y. B. Nian, S. S. Pei: Mechanism of horizontally aligned growth of single-wall carbon nanotubes on R-plane sapphire, J. Phys. Chem. B **110**, 22676–22680 (2006) 142
[217] X. L. Liu, S. Han, C. W. Zhou: Novel nanotube-on-insulator (NOI) approach toward single-walled carbon nanotube devices, Nano Lett. **6**, 34–39 (2006) 143
[218] M. Maret, K. Hostache, M. C. Schouler, B. Marcus, F. Roussel-Dherbey, M. Albrecht, P. Gadelle: Oriented growth of single-walled carbon nanotubes on a MgO(001) surface, Carbon **45**, 180–187 (2007) 143
[219] M. Souza, A. Jorio, C. Fantini, B. R. A. Neves, M. A. Pimenta, R. Saito, A. Ismach, E. Joselevich, V. W. Brar, G. G. Samsonidze, G. Dresselhaus, M. S. Dresselhaus: Single- and double-resonance Raman G-band processes in carbon nanotubes, Phys. Rev. B **69**, 241403 (2004) 143

[220] A. Ismach, D. Kantorovich, J. Berson, N. Geblinger, L. Segev, E. Wachtel, H. Son, A. Jorio, M. S. Dresselhaus, G. Dresselhaus, E. Joselevich: Epitaxial Modes of Carbon Nanotube Growth on Vicinal a-Al2O3 (0001) Surfaces, unpublished 143, 144
[221] C. Kocabas, S. H. Hur, A. Gaur, M. A. Meitl, M. Shim, J. A. Rogers: Guided growth of large-scale, horizontally aligned arrays of single-walled carbon nanotubes and their use in thin-film transistors, Small **1**, 1110–1116 (2005) 143
[222] C. Kocabas, M. Shim, J. A. Rogers: Spatially selective guided growth of high-coverage arrays and random networks of single-walled carbon nanotubes and their integration into electronic devices, J. Am. Chem. Soc. **128**, 4540–4541 (2006) 143
[223] H. I. Smith, D. C. Flanders: Oriented Crystal-Growth on Amorphous Substrates Using Artificial Surface-Relief Gratings, Appl. Phys. Lett. **32**, 349–350 (1978) 144
[224] R. A. Segalman, H. Yokoyama, E. J. Kramer: Graphoepitaxy of spherical domain block copolymer films, Adv. Mater. **13**, 1152–1155 (2001) 144
[225] T. Rueckes, K. Kim, E. Joselevich, G. Y. Tseng, C. L. Cheung, C. M. Lieber: Carbon nanotube-based nonvolatile random access memory for molecular computing, Science **289**, 94–97 (2000) 145
[226] A. Javey, H. J. Dai: Regular arrays of 2 nm metal nanoparticles for deterministic synthesis of nanomaterials, J. Am. Chem. Soc. **127**, 11942–11943 (2005) 147, 148
[227] S. Helveg, C. Lopez-Cartes, J. Sehested, P. L. Hansen, B. S. Clausen, J. R. Rostrup-Nielsen, F. Abild-Pedersen, J. K. Norskov: Atomic-scale imaging of carbon nanofibre growth, Nature **427**, 426–429 (2004) 148

Index

Mechanical Properties, Thermal Stability and Heat Transport in Carbon Nanotubes

Takahiro Yamamoto[1], Kazuyuki Watanabe[1], and Eduardo R. Hernández[2]

[1] Department of Physics, Tokyo University of Science
1-3 Kagurazaka, Shinjuku-ku, Tokyo 162-8601, Japan
takahiro@rs.kagu.tus.ac.jp, kazuyuki@rs.kagu.tus.ac.jp
[2] Institut de Ciencia de Materials de Barcelona (ICMAB–CSIC),
Campus de Bellaterra, 08193 Barcelona, Spain
ehe@icmab.es

Abstract. Ever since the discovery of carbon nanotubes (CNTs) in the early 1990s, it was anticipated that these nanostructures would have truly remarkable mechanical and heat-transport properties, given the strength of the carbon-carbon bond within graphene layers in graphite. Nowadays, there is growing evidence, coming from both experimental and theoretical studies, that CNTs do indeed have an outstandingly high Young's modulus, high thermal stability and thermal conductivity. In this contribution, we provide an overview of the current state of knowledge on these properties in CNTs and related nanostructures.

1 Introduction

In this contribution we present an overview of the mechanical, the thermal stability and heat-transport properties of carbon nanotubes (CNTs). Ultimately, all these seemingly different aspects of CNTs are a direct consequence of the nature of the carbon–carbon chemical bond and of the particular geometrical arrangement of such bonds in CNTs; it is therefore natural to consider them together. These properties have led to the expectation that CNTs and related nanostructures may be used in many different kinds of applications, such as reinforcement of composite materials (a field that is already in very active development; for a recent review, see [1]), lubrication [2], fabrication of nanoelectromechanical devices (NEMS) [3], heat-dissipation components of such devices [4], etc., see also the contribution by *Endo*, *Strano* and *Ajayan* in this volume.

In spite of the common denominators existing between the mechanical and thermal properties of CNTs, it is nevertheless true that the state-of-the-art of research into these different aspects has not reached a uniform level of development. The mechanical properties of CNTs are, we feel, on the whole well understood, and have posed no major conceptual difficulty. The theory of elasticity [5] provides an appropriate conceptual framework for understanding the mechanical properties of CNTs, and although its use in the nanoscale world requires some care, there is no significant difficulty involved. The situation is different, however, in what concerns the heat-transport properties

A. Jorio, G. Dresselhaus, M. S. Dresselhaus (Eds.): Carbon Nanotubes,
Topics Appl. Physics **111**, 165–195 (2008)

of CNTs. Firstly, the body of experimental work on this problem is much less than that probing the mechanical properties, so the picture is as yet far from complete. Secondly, and perhaps more importantly, the microscopic theory of heat transport is still under development, so the conceptual framework that the theory of elasticity provides for understanding the mechanical properties of CNTs is still not there, or is only partially there, when it comes to the heat-transport properties. It is not surprising that this is so, since heat-transport phenomena are intrinsically more subtle than is the plain strength of chemical bonds, given that both electrons and phonons may separately contribute to the conduction of heat. These different levels of development in our understanding of the mechanical and thermal properties of CNTs have imposed slightly different styles in the way we address these two topics in what follows below. The mechanical properties are covered in a fairly descriptive fashion, referring mostly to published work, both experimental and theoretical, which we consider to be particularly illustrative of the current state–of–the–art regarding these properties. Concerning the heat transport, although we also provide a brief summary of both experimental and theoretical work already available in the literature, the focus is put on recent developments in the microscopic theory of heat transport and its application to the characterization of the thermal conductivity of CNTs.

It is not our objective to produce an exhaustive review of the literature on mechanical and thermal properties of CNTs here. Given the large number of publications on these different aspects, to write such a review would be a daunting task, beyond the scope of this work. We have instead set ourselves the more modest aim of providing a bird's eye view of these topics, illustrating them with examples of research taken from the literature. Inevitably, some important relevant literature, necessary for a comprehensive understanding of the mechanical and thermal properties of nanotubes, will not be cited here due to lack of space. Nevertheless, it is our hope that this bird's eye view of the important topics related to the mechanical and thermal properties of CNTs may serve as a useful introduction for readers interested in these properties, who, from here may be able to move on to the relevant articles and detailed reviews [6–10] that are already available in the literature.

The contents of this contribution are as follows: in Sect. 2 we discuss the mechanical and thermal properties of nanotubes; with the term thermal properties we loosely refer to the behavior of nanotubes under a variety of external factors, such as temperature, pressure, irradiation by an electron or ion beam, etc. In Sect. 3, we discuss heat–transport phenomena of CNTs over the whole temperature range. The contribution concludes with a brief summary and outlook section.

2 Mechanical Properties and Thermal Stability of Nanotubes

2.1 Elasticity at the Nanoscale

The classical theory of elasticity [5] defines a series of moduli (Young's modulus, bulk modulus, elastic constants, etc.) that characterize the response of a material when subject to a perturbation that changes its shape and/or volume from that of its equilibrium configuration. For example, the Young's modulus, Y, which defines the response of the system when it is strained along a particular axis, is given by

$$Y = \frac{1}{V_{\mathrm{eq}}} \left(\frac{\partial^2 E}{\partial \epsilon^2} \right)_{\epsilon=0} , \tag{1}$$

where E is the (free) energy of the system, ϵ is the axial strain, defined as $(L - L_{\mathrm{eq}})/L_{\mathrm{eq}}$, L being the length of the system along the strain axis, and V_{eq} is the equilibrium volume of the system; other elastic moduli are defined in similar ways. Since the (free) energy is an extensive property (it grows with the size of the system), the factor of V_{eq}^{-1} is introduced in (1) so as to make the Y intensive (i.e., size independent). However, the definition of V_{eq} can be problematic in nanoscaled objects, as is the case for SWNTs, because there is no obvious way of defining the thickness of a shell that is one atom thick. This difficulty is frequently overcome by assigning an arbitrary thickness to the wall of SWNTs (e.g., the interlayer spacing in graphite, ca. 0.35 nm), but there is no universally followed convention. A more generally useful definition would be [11, 12]

$$\hat{Y} = \frac{1}{N} \left(\frac{\partial^2 E}{\partial \epsilon^2} \right)_{\epsilon=0} , \tag{2}$$

where N is the number of atoms. This definition has the advantage of not requiring any convention, and can be used regardless of the actual geometry of the system. When a system volume can be unambiguously defined, the conventional definition of the Young's modulus (1) can be recovered by multiplying $\hat{Y}$ by the equilibrium particle density, $\rho_{\mathrm{eq}} = N/V_{\mathrm{eq}}$.

There are quite a number of publications containing seemingly contradictory results obtained from similar computer simulations, where the difference arises because a different convention in the definition of the elastic properties has been used, a situation that leads to some confusion as to what the actual value of, e.g., the Young's modulus really is. In order to avoid this situation, we strongly encourage the use of the definition (2), originally proposed by *Robertson* et al. [11].

2.2 Mechanical Properties of Nanotubes: Elastic Regime

Probably the first theoretical study on the energetics and elastic properties of SWNTs was that due to *Robertson* et al. [11], published in 1992.

These authors performed calculations on models of SWNTs using two different empirical potentials, namely those of *Tersoff* [13] and *Brenner* [14]; for a selected subset of nanotubes calculations were also performed employing first-principles techniques as a check on the reliability of the empirical potentials. This study established that the strain energy, defined as the energy difference (per atom) of a given nanotube and an infinite flat graphene sheet, scales as the inverse of the squared radius of the nanotube, in agreement with what had been predicted by classical elasticity theory [15]. This is so even down to very narrow nanotube radii. Concerning the Young's modulus, the calculations show that in the limit of large radii the stiffness of the tube corresponds directly to the C_{11} elastic constant of graphite calculated with the same model. The accepted experimental value for C_{11} of graphite is 1.06 TPa [16, 17], and the empirical potential of *Brenner* [14] gave a value in close agreement with this result, while that of *Tersoff* [13] slightly overestimated it. Another interesting result to be derived from this study was that both empirical models predicted that the Young's modulus should decrease for very narrow (radius ≤ 4 Å) nanotubes. This result is physically intuitive, because as the curvature strain is increased, the C–C bonds are weakened, and this effect should be reflected in the mechanical properties.

The first experimental report of the measurement of the Young's modulus of multiwall carbon nanotubes was that of *Treacy* et al. [18] in 1996. In this article the Young's modulus of a series of anchored nanotubes was obtained. The authors employed transmission electron microscopy (TEM) to locate tubes that were embedded in amorphous material at one end, having the other end standing in free space. It was then possible to monitor the amplitude of the thermally induced oscillations of the free-standing tip as a function of the ambient temperature. From such measurements the Young's modulus could be inferred if the nanotubes were supposed to behave as hollow cylinders with a given wall thickness. *Treacy* et al. obtained an average value of 1.8 TPa out of a sample of 11 different nanotubes, for which individual values ranged from 0.4 to 4.15 TPa. The scatter of the data is relatively large, reflecting the experimental difficulties in obtaining accurate measurements of the amplitude of the oscillations, the internal and external diameter of the tubes, their length, etc. Nevertheless, these results provided the first proof that carbon nanotubes possessed remarkable elastic properties.

The same experimental approach was later used by *Krishnan* et al. [19] to measure the Young's modulus of single-wall nanotubes. In this case a larger sample of nanotubes (27 in total) was used, and the mean value obtained was 1.25 TPa, which is very similar to the value of the C_{11} elastic constant of graphite, characterizing the inplane deformation of graphene layers. Likewise, *Chopra* and *Zettl* [20] obtained a Young's modulus of 1.22 TPa for a boron nitride (BN) nanotube, using the same approach. This was the first measurement of the Young's modulus of noncarbon nanotubes, and these results indicated that the Young's modulus of BN nanotubes was also very high, and

even competitive with that of carbon nanotubes (see also the contribution by *Tenne* et al. in this volume).

Shortly after the experimental measurements of *Treacy* and coworkers, a different procedure to probe the mechanical properties of nanotubes was employed by *Wong* et al. [21]. Instead of relying on thermal effects to induce oscillations on the free tips of anchored nanotubes, these authors employed an atomic force microscope (AFM) to laterally bend the nanotubes, and simultaneously record the restoring force exerted by the bent nanotube on the AFM tip as a function of the nanotube deflection. Because the deformations inflicted on the nanotubes in this kind of experiment were much larger than the amplitude of the thermal oscillations monitored in the experiments of *Treacy* et al., it was necessary to actually pin the nanotubes by one end on a substrate before they could be bent. This was done by first dispersing the nanotubes on a cleaved MoS_2 substrate, and then depositing on top a square grid of SiO_x pads. The experimental setup and procedure are illustrated in Fig. 1.

Firstly, and in order to test the reliability of the experimental procedure, measurements were carried out on SiC nanorods, for which a Young's modulus ranging between 600–660 GPa was obtained, in good agreement with both theoretical calculations and previous measurements performed in micro-scaled SiC objects. Subsequently, the authors measured the Young's modulus of 6 multiwall nanotubes of varying diameters, obtaining an average value of the Young's modulus of 1.28 ± 0.6 TPa, which was insensitive to the nanotube diameter.

The experiments of *Treacy* et al. [18] and *Wong* et al. [21] confirmed the expectation that indeed carbon nanotubes possess truly remarkable mechanical properties. But not only did nanotubes have the highest ever measured Young's modulus (twice as large as that of SiC rods); they were also shown to be extremely flexible in the experiments of *Falvo* et al. [22]. In these experiments multiwall nanotubes were laterally bent on a substrate using an AFM probe until they twisted over themselves, without any sign of failure being observed. Furthermore, it was possible to make the tubes reversibly recover their original configuration, thus providing visible proof of their resilience, toughness and flexibility.

Salvetat et al. [23, 24] also used an AFM tip to probe the mechanical properties of nanotubes. Their approach consisted of depositing bundles of single-wall nanotubes [23] or individual multiwall nanotubes [24] on an ultrafiltration membrane with a regular pattern of holes having a diameter of approximately 0.4 μm. When a nanotube or bundle was found lying across one such hole, the AFM tip was used to apply a load on the suspended length of the tube, measuring at the same time the restoring force as a function of the deflection. The assumption was made that the tubes were pinned to the substrate by means of dispersion forces, so that they could not slide on the surface of the membrane when the load was applied. For multiwall nanotubes measurements were carried out on both tubes grown by the arc-discharge

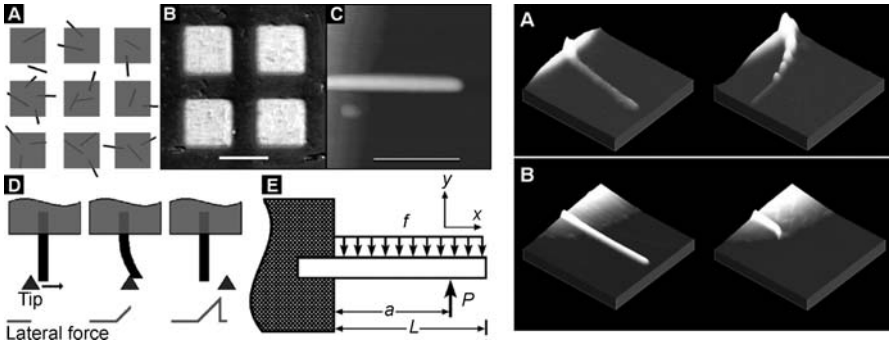

Fig. 1. The *left panel* shows a schematic overview of the experimental procedure followed by *Wong* et al. [21] to measure the mechanical properties of SiC nanorods and MWNTs. (**A**) SiC rods or MWNTs are deposited on a substrate, and then pinned by the deposition of a grid of squared SiO pads, shown in the optical micrographic image in (**B**). (**C**) An AFM image of a SiC nanorod protruding from a SiO pad. (**D**) Diagram illustrating the use of the AFM tip to bend the SiC nanorods or MWNTs and the restoring force. (**E**) Schematic of a pinned rod or nanotube protruding from a patch. The beam of length L is subject to a load P at point a distance a from the surface of the patch and to a friction force f distributed along the length of the beam. The *right panel* shows images of MWNTs and SiC nanorods before and during distortion by the AFM tip. In (A) a MWNT of diameter 4.4 nm in its equilibrium position prior to bending (*left*) and the bent nanotube (*right*) on which the buckling induced by the distortion on the surface of the nanotube is clearly visible. In (B) similar images are shown for a SiC nanorod of 21.5 nm in diameter. The rod is seen in its equilibrium configuration (*left*), but in this case applying the load by the AFM tip resulted in fracture of the beam at the base of the pinning (*right*)

method, as well as on catalytically grown nanotubes, which were structurally much less perfect that the first ones. For the arc-discharge-grown nanotubes, measurements were performed on both as-grown nanotubes and on a series of thermally annealed nanotubes; the measured value of the Young's modulus ranged from an average of 0.87 TPa for as-grown nanotubes to an average of 0.755 TPa for thermally treated nanotubes. While these values are somewhat lower than those previously obtained by *Treacy* et al. [18] and *Wong* et al. [21], they are still very high. The differences could be due either to a higher concentration of structural defects in the nanotubes used in these experiments, or else to a partial breakdown of the assumption of pinning of the nanotubes to the substrate. What was most remarkable in this study, however, was that it clearly showed how much the mechanical properties of nanotubes were affected by the presence of structural defects. Indeed, for the catalytically grown nanotubes the value of the Young's modulus was on average as low as 27 GPa, ranging between 10 to 50 GPa. Their measurements

on bundles of SWNTs uncovered the fact that such bundles have a very low shear modulus ($\approx 1\,\mathrm{GPa}$), implying that nanotubes in a bundle easily slide against each other, a fact perhaps not unexpected in view of the ease with which graphite can be exfoliated. This situation can, however, be ameliorated by using electron or ion irradiation to promote the formation of bonds between the different SWNTs in the bundle, as recently demonstrated by *Kis* et al. [25]. The electron or ion bombardment kicks a percentage of carbon atoms out of their lattice position, and such atoms are sometimes able to form bonds with atoms of neighboring nanotubes. It is possible that similar treatments may be used in nanotube–polymer composites in order to improve the binding between the nanotubes and the polymer matrix.

In parallel to the above experimental studies on the mechanical properties of nanotubes, several research groups were working on simulation studies aimed at complementing the experimental picture that was beginning to emerge. Using the empirical potential due to *Brenner* [14], *Yakobson* et al. [26] performed a series of atomistic molecular dynamics simulations of nanotubes subject to large compressive strains, and to bending or torsional distortions. For nanotubes under compressive strain it was found that the tubes began to buckle at critical strain values at which the energy of the system displayed a slope discontinuity. The appearance of these buckles was rationalized in terms of a continuum shell model with appropriately fitted parameters of flexural rigidity and inplane stiffness. This model was also able to account for the buckling observed under bending and torsional deformations. The atomistic simulations of this study confirmed that SWNTs could sustain large structural distortions without any indication of bond breaking or rearrangement of the bonding pattern, demonstrating the high elasticity of nanotubes. The experimental observation [27] of similarly distorted nanotubes served as a confirmation of the conclusions derived from this study.

A detailed study of the mechanical properties of nanotubes was carried out by *Lu* [28]. In this work, the Young's modulus, the Poisson ratio (defined as minus the radial strain divided by the axial strain) and other elastic constants were calculated for a series of SWNTs, MWNTs and crystalline ropes of SWNTs, using an empirical force field fitted to reproduce the vibrational frequencies and elastic constants of graphite. It was found that the Young's modulus of SWNTs was insensitive to the nanotube diameter and chiral angle. The lack of sensitivity to the nanotube diameter, even for narrow nanotubes, was in contradiction with the earlier finding of *Robertson* et al. [11]; the reason for this disagreement can be ultimately traced to the simplicity of the model used by Lu, which included only harmonic springs to represent carbon–carbon bonds and pairwise Lennard–Jones type potentials to model the interlayer interaction in MWNTs. In the case of bundles of SWNTs it was found that the Young's modulus decreases as the diameter of the nanotubes forming the bundle is increased. However, this does not reflect a weakening of the C–C bonds in these bundles, but simply is a consequence of the fact that the unit-cell volume grows more rapidly than the

number of atoms. Therefore, the decreasing value of Y is a consequence of the peculiar geometry of the system. The values of Y reported by Lu varied between 1.11 TPa for MWNTs to 0.97 TPa for isolated SWNTs.

Other theoretical studies on the mechanical properties of nanotubes conducted at this time were those of *Hernández* et al. [29,30] and *Sánchez-Portal* and coworkers [12]. In the first one, the mechanical properties of SWNTs of different compositions, including C, BN, BC_2N, C_3N_4 and BC_3, were obtained employing a tight-binding model [31] parametrized on density functional theory (DFT). This study confirmed that, among the different compositions considered, carbon nanotubes have the highest Young's modulus, with a value of 1.26 TPa for the widest tubes, although this value was largely insensitive to the nanotube diameter except for very narrow nanotubes, where the high curvature resulted in a weakening of the chemical bonds and consequently in a reduction of the Young's modulus. BN nanotubes were calculated to have a Young's modulus of 0.8 TPa, which, although lower than that of carbon nanotubes, is still very high (higher than that of SiC nanorods, for example). In the second investigation [12], an extensive study of the vibrational and mechanical properties of SWNTs was conducted, both in isolated and bundle geometries, employing DFT calculations with the SIESTA [32] code. *Sánchez-Portal* and coworkers obtained values of the Young's modulus of 1 TPa for SWNTs in an isolated geometry, while in a bundle geometry this value came down to 0.5 TPa for a bundle of (10,10) nanotubes. The results of *Lu* [28], *Hernández* et al. [29,30] and *Sánchez-Portal* et al. [12] essentially agree on the finding that the Young's modulus is insensitive to the diameter and chiral angle of nanotubes (except for very low diameters), and provide similar values of the Young's modulus when the same convention is used to define the thickness of the nanotube shell ($\delta = 0.34$ nm). These theoretical results are also in good agreement with the the experimental measurements of *Wong* et al. [21] and those of *Krishnan* et al. [19] for MWNTs and SWNTs.

2.3 Beyond the Elastic Regime

The Young's modulus measures the response of nanotubes to axial distortion within the linear, elastic, regime. However, for practical applications and also for fundamental reasons, it is crucial to understand and characterize the mechanical properties of nanotubes beyond this linear regime, when plastic (nonreversible) deformation begins to occur. It is desirable to know what is the stress that should be applied on a given nanotube in order to break it, that is, its strength, and how much strain it will sustain before failure sets in, or in other words, what is the breaking strain. The first experiments aiming at measuring the breaking stress and strain of nanotubes were conducted by the group of Ruoff. Firstly, experiments were carried out on MWNTs [33]. Tensile-loading experiments were carried out by attaching MWNTs simultaneously to two opposing AFM tips (see Fig. 2). The nanotubes were attached to the tips with the electron beam of a scanning electron microscope (SEM), a procedure

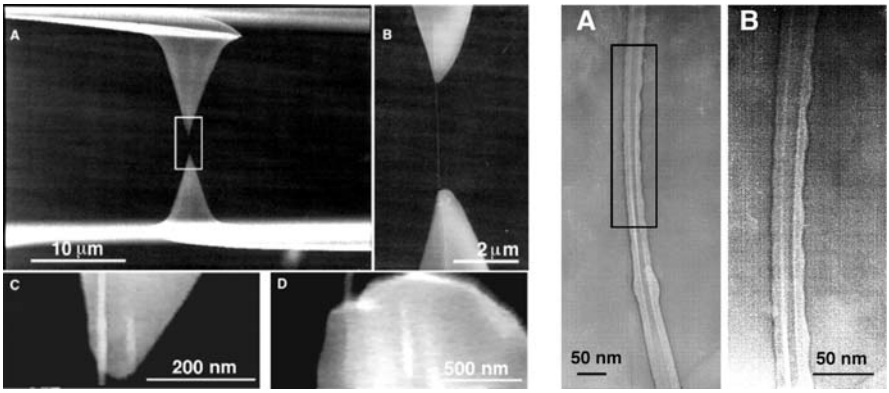

Fig. 2. The *left panel* shows an individual MWNT attached to two opposing AFM tips. In (**A**) a SEM image providing a general view of the experimental setup can be seen, while in (**B**) a closeup of the tips with the tube visible between them is shown. (**C**) and (**D**) show details of the MWNT attachment to the upper and lower AFM tips, respectively. The *right panel* shows TEM images of different MWNTs after fracture has taken place. Images taken from [33]

that transforms residual organic species present in the SEM chamber into a carbonaceous solid film that binds the nanotube to the AFM tip. Once the nanotubes had been attached to the AFM tips as described, the two tips were pulled apart until failure was observed. The technical difficulties in carrying out these experiments are illustrated by the fact that in about 50 % of the attempted load experiments, the nanotube detached itself from one of the two tips before failure was observed. Nevertheless, *Yu* et al. [33] managed to carry out 19 successful load experiments where failure of the tubes was indeed monitored. In all such experiments the tubes were observed to break in the so-called sword-in-sheath mechanism; failure was probably restricted to the outer shell of the MWNT, i.e., that which was directly attached to the AFM tips, while the inner shells were seemingly unaffected, and simply slid out as a sword pulled from its sheath once the outer tube failed. The experiments made possible the simultaneous measure of the load and the strain of the nanotubes up to their breaking point. From the stress vs. strain curves the Young's modulus of the outer tube could be derived, obtaining values that ranged between 270 to 950 GPa. The breaking strain ranged between 3 and 12 %, and the strengh from 11 to 63 GPa. The variability in this data probably reflects different contents in number of structural defects in the outer shells of the MWNTs.

Similar experiments were conducted by the same group on bundles of SWNTs [34]. Like in the case of MWNTs, it was found that the load was essentially transmitted only to the tubes lying on the outer side of the bundle, so that when yield was observed the inner tubes remained largely

intact, and simply slid against the broken outer tubes. The average value of the breaking strength was 30 GPa, with individual values ranging from 13 to 50 GPa; the average breaking strain was found to be 3.1 %, with individual values reaching up to 5.3 %.

Thus, the experiments of *Yu* et al. [33,34] demonstrate that both MWNTs and bundles of SWNTs are brittle, at least at ambient conditions. The question then arises as to how the fracture mechanism depends on temperature. Indeed, experiments have been recently reported [35] in which a SWNT is stretched at high temperatures ($T \geq 2000\,^{\circ}\mathrm{C}$), and is observed to display a superplastic behavior, sustaining strains of up to 280 % with a concomitant 15-fold reduction of diameter from 12 down to 0.8 nm. Similar behavior has been reported for double-wall and even MWNTs [36]. Thus, it seems that, although in normal conditions carbon nanotubes are brittle, at sufficiently high temperatures they become extremely ductile. This superplastic behavior seems to be a consequence of the ease of formation of dislocation kinks at these conditions, a behavior that had been theoretically predicted by *Yakobson* [37, 38] in the late 1990s.

Long before this superplastic behavior had been experimentally observed, theoretical and simulation studies had been conducted in order to gain insight into the possible yield mechanisms of nanotubes under axial strain. *Nardelli* et al. [39, 40] found, by means of molecular-dynamics simulations, a possible mechanism for stress release in tensioned nanotubes. This mechanism consisted of the formation of a so-called 5/7/7/5 cluster defect, in which two pentagonal and two heptagonal rings appear in the otherwise hexagonal ring pattern of the nanotube through a *Stone–Wales* [41] bond rotation. At zero stress the formation of such defects is endothermic, but as the stress increases beyond a certain threshold ($\approx$ 5 % strain) the formation energy becomes exothermic, although it is still necessary to overcome an activation barrier in order to form the defect. However, once formed, the 5/7/7/5 constitutes a dislocation dipole, which can split into two 5–7 pairs that are really dislocation cores. The continued migration apart of these two dislocation cores eventually results in the appearance of a neck in the nanotube, which will have a different symmetry, and hence possibly different electronic properties.

A second possible yield mechanism has been uncovered by simulations, which may be relevant for brittle fracture [42] at low temperatures and high stress. In recent work, *Dumitrică* and coworkers [43] have developed a strength theory of nanotubes incorporating both the plastic and brittle yield mechanisms, analyzing how these different mechanisms are affected by the nanotube symmetry, the imposed strain and the temperature. This theory, combined with the possibility of direct sublimation of carbon atoms, or their direct kick-out by the electron beam, seem to explain all the observed features of the superplastic behavior [44].

2.4 Thermal Stability of Nanotubes

Nanotubes, both MWNTs and SWNTs, are metastable with respect to graphite. From the earliest theoretical studies of nanotubes [11] it is known that the strain energy (the curvature-induced energy of a nanotube, see Sect. 2.2), scales as the inverse of the nanotube radius squared, in agreement with what is predicted by classical elasticity theory [15]. In other words, the wider the nanotube, the more stable it is. Since MWNTs are normally wider than SWNTs, we can expect that the former will be generally the more stable of the two. Furthermore, since the intershell spacing in MWNTs is similar to that observed in graphite, we can expect that dispersion-type forces between shells further stabilize this kind of nanotube. We can thus foresee the following hierarchy of stability in carbon nanoscaled objects: graphite > MWNTs > SWNTs > fullerenes, where the > sign is to be read as "more stable than". It therefore may be asked if it is possible to observe the transition between these different forms of carbon; in some cases such transitions have indeed been observed. One example of this is the coalescence of fullerene molecules trapped inside a SWNT, the so-called nanopeapods [45], (see the contribution by *Pfeiffer* et al. in this volume) to form a tubular-like structure inside the original encapsulating tube [46, 47]. The dynamics of this process has been studied using molecular-dynamics simulations by *Hernández* et al. [48].

In a similar way, pairs of SWNTs have also been observed to coalesce forming either a wider SWNT (with the consequent reduction of strain energy) [49], and entire bundles of SWNTs can merge to form an individual MWNT [50]. The fusion of two individual SWNTs into a wider one was observed using TEM [49] (see Fig. 3); while the driving force for this coalescence of nanotubes is the reduction of strain energy thus achieved, it seems that the process itself is catalyzed by the formation of vacancies on the nanotubes due to the electron bombardment. It is known that the electron beam can kick out carbon atoms from the nanotube framework, forming defects that can act as nucleation sites for the coalescence, which has been suggested to take place via a zipper-like effect [49, 51]. The energy provided by an electron beam can also be used to induce the welding of nanotubes to form molecular junctions of different kinds and shapes, as demonstrated by *Terrones* et al. [52]. The atomistic details of these coalescence processes have not been experimentally resolved, although it is thought that the presence of defects such as vacancies as well as *Stone–Wales* [41] transformations will play a role [53, 54].

The effects of external pressure on the stability of nanotubes have also been investigated, both experimentally and employing simulation techniques. An early example of this is the work of *Venkateswaran* and coworkers [55], who studied the pressure dependence of the Raman-active modes in bundles of SWNTs subject to external pressure. *Reich* et al. [56] have used first-principles techniques to obtain the bulk modulus and its pressure derivative

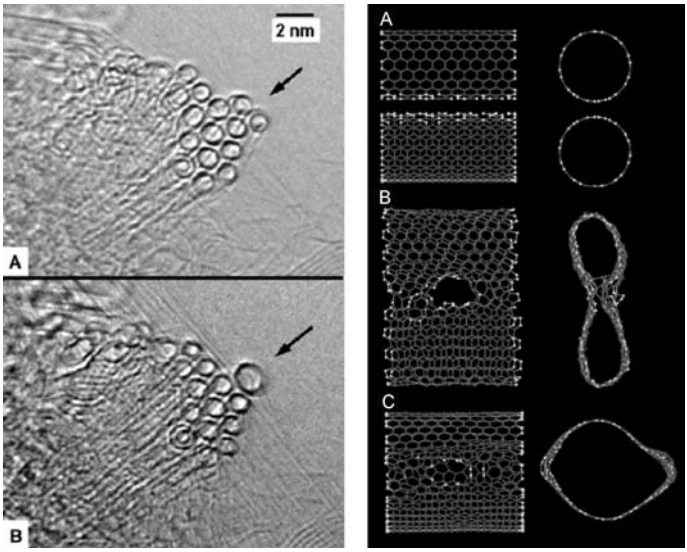

Fig. 3. The *left panel* shows high-resolution TEM images of the cross section of a bundle of SWNTs. In (**A**) the bundle is seen in its starting configuration, and (**B**) shows the bundle a few seconds later, after being subject to high-intensity electron irradiation (1.25 MeV) at a temperature of 800 °C. The two rightmost tubes in the bundle in image A have coalesced after the electron irradiation, as can be seen in image B [49]. The *right panel* shows a molecular-dynamics simulation of the coalescence of two (10,10) nanotubes with 2.5 % vacancy density. Figures reproduced from [49]

of bundles of SWNTs up to pressures of 8.5 GPa, obtaining a bulk modulus of 37 GPa, identical to the value for graphite. Simulations of nanotubes subject to external pressure have also served to provide a picture of the transformations that nanotubes undergo at sufficiently high pressure. *Reich* et al. [57] have reported simulations in which bundles of (6,6) SWNTs are observed to squash and form links among nanotubes in the regions of higher curvature; similar work, albeit using empirical potentials, has also been reported by *Zhang* et al. [58] or *Baltazar* et al. [59], among others.

In 2000 *Cumings* and *Zettl* [60] demonstrated that it was possible to telescopically extend MWNTs. Their experiment consisted of first opening the tip of the MWNT by selectively eliminating some of the outer caps at the nanotube end, thus exposing the inner shells. A nanomanipulator was then brought into contact with the tip of the exposed inner tubes, and welded to them by means of a short pulse of current. It was then possible to pull the core of inner tubes out of the external shells in a sword-in-sheath fashion (recall the experiments of *Yu* et al. [33] discussed in Sect. 2.3). The inner core of tubes can be repeatedly pulled in and out as illustrated in Fig. 4, without any apparent sign of wear or fatigue. The inner tubes could also

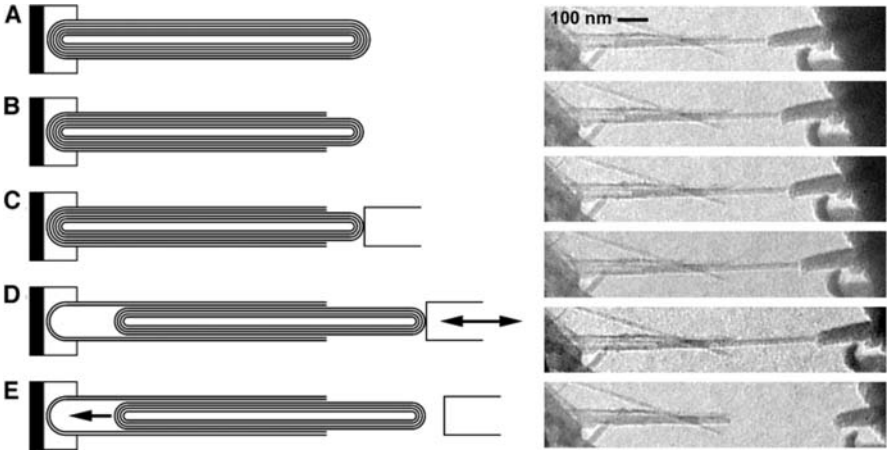

Fig. 4. The *left panel* shows a schematic representation of the sword-pulling experiment of *Cumings* and *Zettl* [60]; the MWNT is shown in its original configuration in (**A**); external caps are selectively removed in (**B**), exposing the core tubes; in (**C**) a nanomanipulator is approached and welded to the internal tubes, which are then pulled out and as in (**D**), or released as in (**E**). The *right panel* shows TEM images of a real nanotube undergoing the sequence of steps schematically illustrated in the *left panel*

be released from the nanomanipulator at the point of largest telescopic extension. It was then observed that they rapidly (on a timescale of less than 4.6 ns) retracted into the outer shell, due to the pull of the van der Waals force. These experiments provided proof of the possibility of nanoengineering MWNTs to construct NEMS such as nanobearings subject to low friction and wear. A further step in the direction of constructing nanoscaled machines was the impressive development of an electromechanical rotational actuator by *Fennimore* et al. [3], in which a metal plate attached to a MWNT serving as bearing was made to rotate around it.

The experimental work of *Cumings* and *Zettl* [60] on nanobearings inspired the proposal of constructing nanotube-based oscillators of similar geometry [61], suggesting that such nano-oscillators could reach frequencies in the GHz regime. Several atomistic simulations of such devices have been reported [62–64], and models of nanoresonators of this kind have been taken as prototypical models on which to study the nature of friction at the nanoscale [65–68].

2.5 Summary of Mechanical Properties and Thermal Stability

Significant advances have been achieved in the characterization of the mechanical properties of both SWNTs and MWNTs within the elastic limit.

Progress has also been substantial in studying the response of CNTs under large stresses (i.e., in the plastic regime). Much work has also been directed at probing the behavior of CNTs when subject to external perturbations such as temperature, pressure and electronic or ionic radiation. Electronic radiation has been used to improve the mechanical properties of bundles of SWNTs, to cause welding of individual nanotubes resulting in Y junctions, or to cause the fusion of separate tubes into wider ones. Local thermal or radiation treatments may be able in the future to shape and twist NEMS components, and in particular CNTs, to give them their desired functionality. At this stage most of these examples of nanomanipulation constitute proofs of principle, but they certainly pave the way and may become routine strategies for future nanotechnologies.

3 Heat-Transport Properties

As well as mechanical stiffness and thermal stability, CNTs possess a high thermal conductivity, surpassing diamond's value $\sim 2000\,\mathrm{W/m\text{-}K}$, due to the strong carbon–carbon chemical bonding (for example, see [69]). On account of their high thermal conductivity, the heat transport in CNTs has attracted much attention from both theoretical and experimental points of view [10]. Their high thermal conductivity has very recently been exploited to develop a CNT-based heat-removal device that efficiently dissipates the heat generated by an integrated circuit [4]. Besides their high thermal conductivity, various other interesting heat-transport properties of CNTs have been discovered in recent years. In the following subsections, we present a comprehensive review of recent advances in theoretical and experimental studies of heat transport in CNTs.

3.1 Ballistic Heat Transport in SWNTs

3.1.1 Landauer Theory for Phonon Transport

The phonon mean-free path (MFP) L_0 of SWNTs is estimated to be of the order of μm at low temperatures, both experimentally [70, 71] and theoretically [72]. Thus, SWNTs can be regarded as quasi-one-dimensional ballistic phonon conductors at low temperatures [73] because typical lengths of CNTs used in devices are much smaller than L_0 at these temperatures. Depite the long-standing theoretical interest that it has raised, going back to *Peierls'* early work [74], little progress has been achieved toward elucidating ballistic phonon transport in mesoscopic or nanoscale systems. This is because the conventional transport theories for bulk systems, such as Kubo's linear-response theory, are not suitable for phonon transport in small systems far from equilibrium. We discuss the ballistic phonon transport in SWNTs at low temperatures using the Landauer theory for phonon conduction [75, 76].

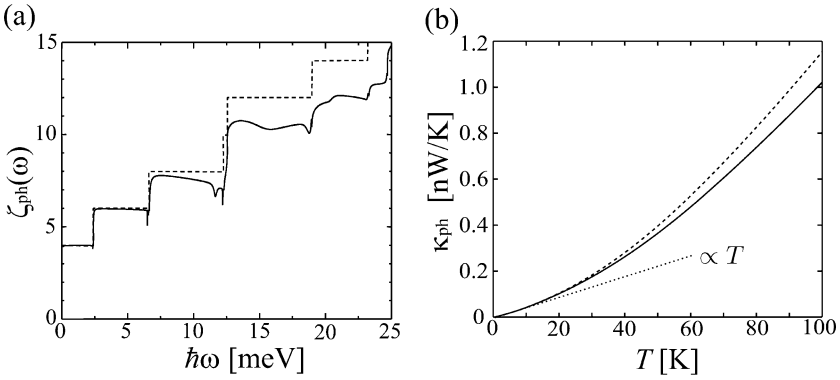

Fig. 5. (**a**) Phonon transmission functions and (**b**) thermal conductances of the (8,8) SWNT with no defects (*dashed curve*) and with a single-atom vacancy defect (*solid curve*) [77]. The *dotted line* in (b) is an asymptotic linear curve with gradient $4\pi^2 k_B^2/3h = 4 \times (9.465 \times 10^{-13})$W/K at low temperatures

Here, we consider a SWNT connected to hot and cold heat reservoirs at temperatures T_h and $T_c (< T_h)$, respectively. We also assume an infinitesimal temperature difference, $T_h - T_c \to 0$, between the hot and cold heat reservoirs. In this situation, the thermal conductance $\kappa_{ph}(T)$ is given by

$$\kappa_{ph}(T) = \frac{k_B}{2\pi} \int_0^\infty d\omega \left(\frac{\hbar\omega}{k_B T}\right)^2 \frac{e^{\hbar\omega/k_B T}}{\left(e^{\hbar\omega/k_B T} - 1\right)^2} \zeta_{ph}(\omega), \tag{3}$$

where T is defined as the averaged temperature $T = (T_h + T_c)/2$ and $\zeta_{ph}(\omega)$ is the transmission function for phonons at energy $\hbar\omega$ [75, 76]. There are several alternative methods for calculating $\zeta_{ph}(\omega)$ for nanoscale objects with complex atomic structures: the Green's function method [77–79], the phonon wavepacket scattering method [80, 81], and the scattering boundary method [82]. For perfect SWNTs, $\zeta_{ph}(\omega)$ shows a stepwise structure giving the number of phonon branches at an energy $\hbar\omega$, as shown by the dashed curve in Fig. 5a. Below 2.4 meV, that is, below the bottom of the lowest optical-phonon branch, the dashed curve has a constant value, $\zeta_{ph}(\omega) = 4$, equal to the number of acoustic branches (longitudinal, twisting, and doubly degenerate flexural modes). If the SWNT contains defects (e.g., vacancies, Stone–Wales defects, isotope impurities, etc.), then $\zeta_{ph}(\omega)$ deviates from the stepwise structure because of the phonon scattering with defects. In Fig. 5a, the $\zeta_{ph}(\omega)$ phonon transmission function for an (8,8) SWNT containing a single-atom vacancy defect is shown by the solid curve. It can be seen that this curve deviates dramatically from the dashed curve, particularly at high energies. However, it remains unchanged in the low-energy region. This is because long-wavelength phonons in SWNTs are not scattered by the single-atom vacancy, which has a size much smaller than the phonon wavelength.

3.1.2 Quantization of Thermal Conductance

According to experiments performed on crystalline ropes of SWNTs [70], the measured thermal conductances $\kappa_{\rm ph}(T)$ (or conductivities) vary linearly with temperature T at low temperatures and go to zero at $T = 0$, a signature of quantum transport in one dimension. However, the gradient of the T-linear behavior was not determined in [70] because of experimental difficulties. Another interesting observation is that the temperature range where $\kappa_{\rm ph}$ shows a linear behavior increases with decreasing tube diameter [83].

The thermal conductance $\kappa_{\rm ph}(T)$ can be obtained theoretically by substituting the calculated $\zeta_{\rm ph}(\omega)$ into (3). Figure 5b represents the calculated $\kappa_{\rm ph}(T)$ for an (8,8) SWNT with no defects (dashed curve) and with a single-atom vacancy defect (solid curve), as a function of temperature T. At low temperatures, where the optical phonons are frozen out, the thermal conductance displays a T-linear behavior with a gradient of $4 \times (\pi^2 k_{\rm B}^2/3h) = 4 \times (9.465 \times 10^{-13})\,{\rm W/K}$, which is independent of the tube geometry (diameter and chirality), as shown by the dotted line in Fig. 5b. The factor 4 in the gradient of the T-linear behavior represents the number of acoustic branches. This means that the thermal conductance of CNTs is quantized in terms of the universal value of $\kappa_0 = (\pi^2 k_{\rm B}^2/3h) \times T$ per acoustic mode at low temperatures. Recently, quantization of the thermal conductance $\kappa_{\rm ph}(T)$ has been observed in individual CNTs [84].

With increasing temperature, the thermal conductance (solid and dashed curves) deviates upward from the T-linear behavior, as seen in Fig. 5b, signalling that the optical phonons begin to contribute to the heat transport. The solid curve for the defective SWNT with a single-atom vacancy decreases from the curve for the defect-free SWNT. The influence of structural defects on the thermal-transport properties of CNTs will be discussed in Sect. 3.2.2. Here, we focus on the tube-geometry dependence of $\kappa_{\rm ph}(T)$ for defect-free SWNTs. Figure 6a shows the thermal conductances $\kappa_{\rm ph}(T)$ of SWNTs with various chiralities normalized by the quantum of thermal conductance κ_0. We found that the quantization plateau (the T-linear region) in the thermal-conductance curve extends to higher temperatures in SWNTs with smaller diameters. The extent of the quantization plateau increases because the energy gap $\Delta E_{\rm op}$ of the lowest optical-phonon modes increases as $\sim 1/d^2$ with decreasing tube diameter d [85]. This trend has also been verified by experiments [83].

Another interesting feature is that the different curves of $\kappa_{\rm ph}/\kappa_0$ in Fig. 6a exhibit a universal behavior when the scaled temperature $\tau = k_{\rm B}T/\Delta E_{\rm op}$ is introduced. Taking account of the four acoustic and doubly degenerate lowest optical modes, (3) can be rewritten in a simple form:

$$\kappa_{\rm ph}(\tau) = 4\kappa_0 \left\{ 1 + \frac{3}{\pi^2} e^{-1/\tau} \left(1 + \frac{1}{\tau} + \frac{1}{2\tau^2} \right) \right\}, \tag{4}$$

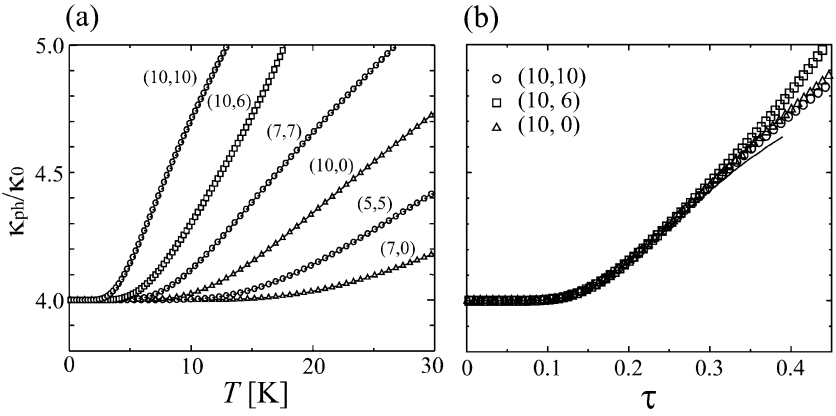

Fig. 6. Thermal conductance $\kappa_{\rm ph}$ normalized by the quantum of thermal conductance κ_0 as a function of (**a**) temperature T and (**b**) the dimensionless temperature $\tau = k_{\rm B}T/\Delta E_{\rm op}$ scaled by the energy gap $\Delta E_{\rm op}$ of the lowest optical-phonon modes [76]. The *solid curve* represents (4) in the text

under the conditions of $\zeta_{\rm ph}(\omega) = 1$ and at low temperature. The curves in Fig. 6a are replotted against the dimensionless temperature τ in Fig. 6b. It is evident that all curves (only three curves are shown for clarity) collapse onto the universal curve of (4) in the low-temperature region below $\tau \sim 0.3$, i.e., $T \sim 0.3 \times \Delta E_{\rm op}/k_{\rm B}$. Therefore, the low-temperature thermal conductance depends only on the tube diameter, but not on the details of the atomic geometry such as chirality. The temperature width of the quantization plateau $T_{\rm qp}$ is estimated to be $T_{\rm qp} \sim 0.14 \times \Delta E_{\rm op}/k_{\rm B}$ from Fig. 6b.

3.1.3 Electron Contribution to the Thermal Conductance

SWNTs can be either metallic or semiconducting, depending on the chirality [85]. For semiconducting SWNTs, the electron contribution to heat conduction is negligible for moderate temperatures because of the large electronic bandgap. For metallic SWNTs, on the other hand, heat is carried by conduction electrons as well as phonons. However, according to the simultaneous measurement of the thermal conductivity $\lambda_{\rm tot}$ and the electrical conductivity σ using SWNTs with an average diameter of $d = 1.4\,{\rm nm}$, the measured ratio $\lambda_{\rm tot}/\sigma T$ is at least two orders of magnitude larger than the Lorentz number

$$\frac{\lambda_{\rm el}}{\sigma T} = \frac{\pi^2}{3}\left(\frac{k_{\rm B}}{e}\right)^2 = 2.45 \times 10^{-8}\,({\rm V/K})^2 \tag{5}$$

for electrons over the wide temperature range from 10 to 350 K [70]. This means that the heat in SWNTs is predominantly carried by phonons over this temperature range. At low temperatures, the electrical conductance G

of SWNTs is quantized by the universal quantum of conductance $G = 2 \times (2e^2/h)$ because two (π and π^*) bands cross the Fermi level [85]. According to the Wiedemann–Franz law (5), the electron-derived thermal conductance is also quantized by the same value as the phonon conductance, namely $\kappa_{el} = 4\pi^2 k_B^2 T/3h$. Here, we use the relation $\lambda_{el} = (L/S)\kappa_{el}$ and $\sigma = (L/S)G$, where L and S are the length and cross section of SWNTs, respectively. The total thermal conductance of metallic SWNTs is given by $\kappa_{tot} = \kappa_{el} + \kappa_{ph} = 8\kappa_0$ at low temperatures [76].

A significant difference has been recognized between the widths of the quantization plateaus of κ_{ph} and κ_{el} in metallic SWNTs. The energy gap of the lowest electronic subband is of the order of an electronvolt, while the energy gap of the lowest optical phonon branch is typically less than 0.01 eV. Consequently, the electron-derived thermal conductance is $\kappa_{el} = 4\kappa_0$ over the whole temperature range from $T = 0$ to 1000 K, while the phonon-derived thermal conductance begins to deviate from the plateau (at $\sim$ 3 K for a (10,10) SWNT with $d = 1.4$ nm), as shown in Fig. 6a. Thus, the electron contribution to the heat transport becomes vanishingly small with increasing temperature [76].

3.2 Quasiballistic Heat Transport in SWNTs

3.2.1 Length Effect of the Thermal Conductivity

For the purely ballistic phonon transport in SWNTs discussed in Sect. 3.1, the phonon-derived thermal conductivity λ_{ph} behaves linearly with respect to the tube length L because the phonon mean-free path (MFP) L_0 is bound by L. However, L_0 decreases as the temperature increases and eventually becomes comparable to the tube length L. In this quasiballistic region ($L \sim L_0$ or $L < L_0$), the thermal conductivity is no longer proportional to L. Recent molecular dynamics simulations show that the room-temperature thermal conductivity λ_{ph} of SWNTs with finite length L exhibits a power-law dependence $\lambda_{ph} \propto L^{\alpha}$ [86,87]. Figure 7 shows the length dependence of the thermal conductivity of a (5,5) SWNT at 300 K, calculated by the nonequilibrium molecular dynamics method on the basis of two different thermostats: the phantom (circle) and Nosé–Hoover (asterisk) thermostats, respectively [87]. For short lengths below $L \sim 20$ nm, the thermal conductivity λ_{ph} is proportional to L owing to the purely ballistic phonon transport. With increasing L, λ_{ph} deviates downward from the L-linear behavior and exhibits a power-law behavior ($\lambda_{ph} \propto L^{\alpha}$) in the region $L > 100$ nm. The exponent α is estimated to be approximately $\alpha = 0.25$ for the (5,5) SWNT at 300 K [87].

The power-law behavior of the thermal conductivity in finite-length SWNTs is reminiscent of the anomalous heat transport in one-dimensional nonlinear lattice models, where the thermal conductivity diverges with L as L^{α} [88]. However, the thermal conductivity λ_{ph} of SWNTs should not diverge, but rather be an intensive quantity independent of L in the diffusive

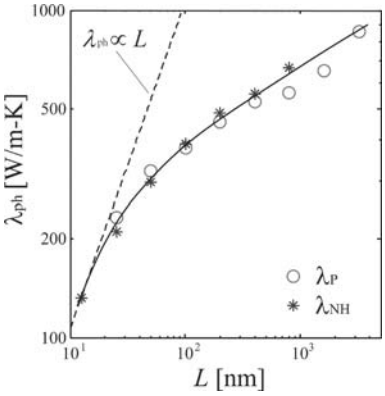

Fig. 7. The length dependence of the thermal conductivity of (5,5) SWNTs at 300 K calculated by molecular dynamics simulations based on the phantom (*circles*) and Nosé–Hoover (*asterisks*) thermostats [87]. The *dashed curve* represents the asymptotic linear curve in the short-length region

region ($L \gg L_0$). According to theoretical analyses based on the Boltzmann–Peierls phonon transport equation, the thermal conductivity $\lambda_{\rm ph}$ of a SWNT saturates to a finite value in the thermodynamic limit $L \to \infty$ if 3-phonon scattering processes are considered to second or higher order [89]. Therefore, the exponent α for SWNTs becomes zero ($\alpha \to 0$) in the thermodynamic limit $L \to \infty$. Thus, we should note that the exponent α for SWNTs is an effective exponent and valid within the limited quasiballistic region where ballistic and diffusive phonons coexist, rather than the asymptotic exponent at $L \to \infty$.

In the quasiballistic region, the phonon transmission function $\zeta_{\rm ph}(\omega)$ in the Landauer formula (3) is approximately given by the phenomenological expression [90]:

$$\zeta_{\rm ph}(\omega) = \frac{L_0(\omega)}{L_0(\omega) + L}\,, \tag{6}$$

where $L_0(\omega)$ is the phonon MFP. If the frequency dependence of $L_0(\omega)$ is assumed to be $L_0(\omega) = A\omega^{-r}$, the thermal conductivity $\lambda_{\rm ph} = (L/S)\kappa_{\rm ph}$ is given by

$$\lambda_{\rm ph} \sim \int_0^\infty \frac{{\rm d}\omega}{\omega^r + A/L} \propto L^{(r-1)/r} \tag{7}$$

at low frequencies $\hbar\omega/k_{\rm B}T \ll 1$. Thus, we obtain the power-law dependence $\lambda_{\rm ph} \propto L^\alpha$ with the exponent $\alpha = (r-1)/r$ in the quasiballistic region [90].

From the previous analysis, we find that the exponent α is closely related to the phonon-scattering mechanism. The phonon-scattering mechanism in CNTs is not yet well understood. In the quasiballistic region, the

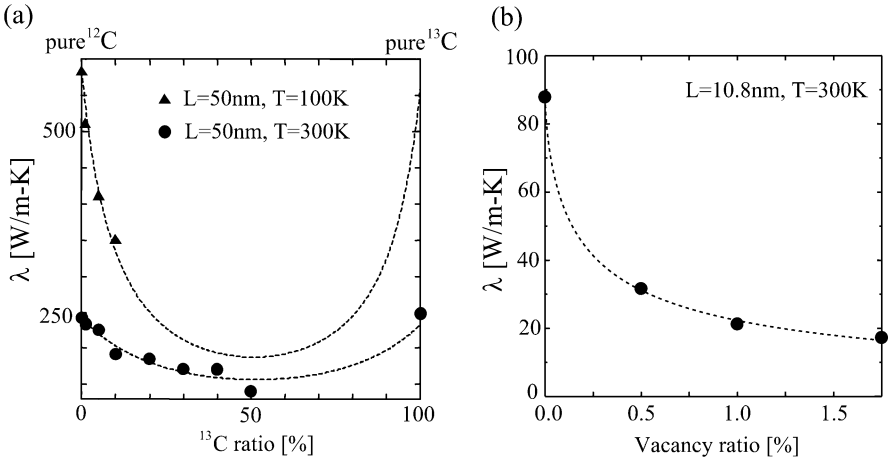

Fig. 8. (**a**) Dependence of the thermal conductivity of a (5,5) SWNT on ^{13}C isotope concentration in percentage [92]. The *triangles* and *circles* are the thermal conductivities of the (5,5) SWNT with $L = 50$ nm at 100 K and 300 K, respectively. (**b**) The calculated thermal conductivity of an (8,0) SWNT with 10.8 nm measured at 300 K as a function of the single-atom vacancy concentration in % [93]

dominant mechanism is expected to be Umklapp phonon–phonon scattering. Umklapp phonon–phonon scattering yields $\alpha = 0.5$ because the phonon MFP behaves as $L_0 \propto \omega^{-2}$. However, this is not consistent with the nonequilibrium molecular dynamics result of $\alpha = 0.25$ for the (5,5) SWNT. One reason for this is that the Brenner potential [14], which was used in the molecular dynamics simulations in [87], underestimates the strength of the binding. As we will see in Sect. 3.3, other scattering processes become important at higher temperatures (above room temperature). Clearly, more experimental and theoretical work is required to determine the exponent α for SWNTs and fully understand the phonon-scattering mechanisms in CNTs.

3.2.2 Influence of Defects on the Thermal Conductivity

Theoretical studies suggest that the room-temperature thermal conductivity of CNTs could be higher than that of diamond [69]. However, there is concern that the high thermal conductivity is diminished by defects (e.g., a vacancy defect, an isotope impurity, or a Stone–Wales defect) generated during the CNT synthesis, or by artificial operations such as ion/electron irradiation. Indeed, these defects have been observed directly using high-resolution transmission electron microscopy (HR-TEM) [91]. The influence of defects on the heat transport in the low-dimensional structure of CNTs could be anomalously high, much larger than in bulk materials [92, 93].

Figure 8a shows the molecular dynamics results of the thermal conductivities of (5,5) SWNTs with $L = 50\,\text{nm}$ at an averaged temperature of 100 K (triangles) and 300 K (circles), as a function of ^{13}C isotope concentrations [92]. With 50 % ^{13}C isotopes, the thermal conductivity at 300 K (circles) has decreased by 40 %. Similarly, the thermal conductivity at 100 K (triangles) affects sensitively ^{13}C isotopes. The isotope effect on thermal conductivity has not yet been studied experimentally in CNTs, but it has been studied in boron nitride nanotubes (BNNTs) [94]. It is known experimentally that the thermal conductivity of isotopically pure BNNTs is comparable to that of pure CNTs and is also sensitively decreased by isotopic substitution [94].

We found from Fig. 8a that the thermal conductivity at 100 K (triangles) is lower than that at 300 K (circles). This contradicts experimental observations that the thermal conductivity increases monotonically with increasing temperature up to room temperature [71] and then decreases due to Umklapp phonon–phonon scattering [95]. This is because the Brenner potential underestimates the spring constants between carbons or the lattice temperature. We note that the thermal conductivity (triangles) at 100 K would not be realistic because the classical molecular dynamics simulation cannot reproduce the quantum effect in the thermal conductivity at low temperatures [87].

On the other hand, Fig. 8b represents the dependence of the thermal conductivity of an (8,0) SWNT with $L = 10.8\,\text{nm}$ on the single-atom vacancy defect concentration, which was obtained by molecular dynamics simulations [93]. With a vacancy concentration of only 1 %, the thermal conductivity of CNTs is reduced to approximately 25 %. In contrast to isotope impurities, single-atom vacancy defects decrease the thermal conductivity dramatically because they locally disrupt the hexagonal network of CNTs. Since the single-atom vacancy in SWNTs is energetically metastable, a rebonding of two dangling-bond atoms occurs and only one dangling-bond atom remains (i.e., rearrangement of the single-atom vacancy) as a result of thermal treatments [96,97]. Thus, the thermal conductivity is expected to recover somewhat. However, the room-temperature thermal conductivity is not dramatically increased by the structural rearrangement because the stable structure after rearrangement also disrupts the hexagonal network. In view of this, defect-repair techniques other than thermal annealing are required to restore the thermal conductivity by any appreciable amount. High-quality CNTs are desirable to retain the intrinsic high thermal conductivity of CNTs.

3.3 Diffusive Heat Transport in SWNTs

Figure 9 shows the measured thermal conductivity of an isolated suspended single-wall CNT with length $L = 2.6\,\mu\text{m}$ and diameter $d = 1.7\,\text{nm}$ from $T = 300$ to 800 K [95]. In this temperature range, the thermal-conductivity decays with temperature as $T^{-\beta}$. We can obtain information on what scattering processes are dominant for the thermal-conductance decay by estimating the exponent β. The dashed curve shows the T^{-1} behavior expected

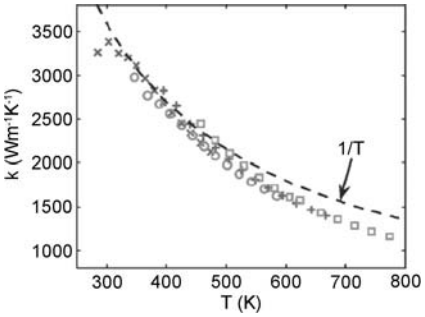

Fig. 9. The measured thermal conductivity of an isolated suspended single-wall CNT with a length $L = 2.6\,\mu\text{m}$ and diameter $d = 1.7\,\text{nm}$ in the temperature range of $T = 300$ to $800\,\text{K}$ [95]. The *dashed curve* indicates the $1/T$ behavior expected from the Umklapp phonon–phonon scattering

from the three-phonon Umklapp scattering. Thus, the three-phonon Umklapp scattering is found to be dominant for the thermal-conductivity decay in the temperature range below 400 K. However, at higher temperatures, above 400 K, the decay of the thermal conductivity is faster than T^{-1}. This is attributed to four-phonon scattering processes. Consequently, the thermal conductivity scales as $(aT + bT^2)^{-1}$ where the parameters a and b are chosen as $a = 3.7 \times 10^{-7}\,\text{m/W}$ and $b = 9.7 \times 10^{-10}\,\text{m/(WK)}$ by fitting to the experimental data [95].

3.4 Heat Transport in MWNTs

As in the case of SWNTs, the heat flow in MWNTs is predominantly carried by phonons [10]. In contrast to SWNTs, MWNTs with a large diameter cannot be regarded as simple one-dimensional phonon systems, and exhibit complex heat-transport phenomena because of the interwall interaction.

Figure 10 shows the measured thermal conductance of an individual MWNT with diameter $d = 14\,\text{nm}$ and length $L = 2.5\,\mu\text{m}$. In the temperature range from $T = 8$ to $50\,\text{K}$, the thermal conductance increases as $\sim T^{2.5}$, which is different from that in SWNTs, showing the T-linear quantization behavior [98]. In order to observe the quantization of the thermal conductance of MWNTs, we need to lower the temperature to $T \sim 1\,\text{K}$ for typical MWNTs [10]. Over the intermediate temperature range, from $T = 50$ to 150 K, the thermal conductivity increases as $\sim T^2$. Above 150 K, it deviates from the quadratic temperature dependence, reaching a maximum of approximately $1.6 \times 10^{-7}\,\text{W/K}$ at 320 K. In terms of the thermal conductivity, the maximum value is over $3000\,\text{W/(mK)}$. This value is comparable to that of a SWNT (see Fig. 9). Beyond the peak, it decreases rapidly because of strong phonon–phonon Umklapp scattering.

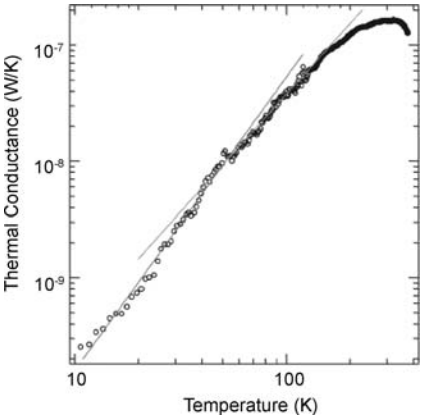

Fig. 10. Measured thermal conductance of an individual MWNT of diameter 14 nm [98]

We now explain the temperature dependence of the thermal conductivity of MWNTs. According to the Boltzmann–Peierls phonon-transport equation in the relaxation-time approximation, the thermal conductivity is given by

$$\lambda_{\mathrm{ph}} = \sum_{\nu,k} v_{\nu,k} l_{\nu,k} C_{\nu,k} \,, \tag{8}$$

where $v_{\nu,k}$, $l_{\nu,k}$, and $C_{\nu,k}$ is the phonon group velocity, the phonon MFP, and the specific heat of a phonon with wave number k on a branch ν [99]. The phonon MFP consists of a normal and an Umklapp scattering length. At low temperature, Umklapp scattering is negligible in the heat transport in MWNTs, and the normal scattering is temperature independent. Thus, the temperature dependence of the low-temperature thermal conductivity follows that of the specific heat. The low-temperature specific heat in a d-dimensional phonon system is known to vary as $T^{d/n}$ for acoustic phonons obeying the dispersion relation $\omega \propto k^n$ in the long-wavelength limit. Thus, the temperature dependence of the thermal conductivity at low temperatures contains information about the dimensionality of the system and the phonon-dispersion relations. Although the phonon-dispersion relation of MWNTs has not yet been elucidated, it is expected to be similar to that of bulk graphite, due to the interwall phonon coupling except at extremely low temperatures below $\Theta_{\mathrm{LOP}} \sim 1\,\mathrm{K}$.

Below the interwall Debye temperature $\Theta_{\mathrm{D}}^{\perp}$ determined by the van der Waals interaction between the walls of a MWNT, the thermal conductivity has a three-dimensional nature, and consequently the thermal conductivity at low temperatures ($< 50\,\mathrm{K}$) increases as $\lambda_{\mathrm{ph}} \sim T^{2.5}$, similar to the $T^{2.3}$ behavior in graphite fibers at low temperatures [100]. For $T > \Theta_{\mathrm{D}}^{\perp}$, where the weak interwall interaction is negligible, MWNTs behave as a two-dimensional phonon material because of their large diameter, and the thermal

conductivity increases as T^2. The T^2 behavior has also been observed in the thermal conductivity of millimeter-sized mats of MWNTs with 20–30 nm diameter [73]. From the crossover between the two- and three-dimensional regimes, the interwall Debye temperature is estimated to be $\Theta_{\mathrm{D}}^{\perp} = 50\,\mathrm{K}$.

3.5 Summary of Heat Transport

Heat-transport properties of CNTs have been reviewed from the standpoint of the phonon-conduction mechanisms on the basis of the thermal conductance and/or thermal conductivity. At low temperatures, phonon conduction is ballistic through the entire body of the SWNT, leading to universal quantization in the thermal conductance. The quantized nature persists despite the presence of structural defects. As the temperature is increased, the length of the phonon mean-free path becomes comparable to that of SWNTs, and phonon conduction ceases to be ballistic. As such, a marked reduction is observed in the thermal conductivity due to defects. The heat-transport behavior changes from quasiballistic to diffusive at temperatures above room temperature. MWNTs further show the characteristic temperature dependence of the thermal conductivity due to the van der Waals interaction between the tube walls. CNTs are unique nanoscale materials that exhibit a variety of interesting heat-transport phenomena.

4 Summary and Outlook

In this contribution, we have provided an overview of the current state of knowledge on the mechanical, thermal and heat-transport properties of CNTs. The characterization of these properties of CNTs has inspired some remarkable feats of nanoengineering and nanomanipulation on the experimental side, paving the way for future advances in the practical and commercial exploitation of the nanoscale as foreseen by Richard P. Feynman in his visionary talk "There is plenty of room at the bottom" at the end of the 1950s [101]. On the theoretical side, research on CNTs is fueling the development of novel simulation techniques, and perhaps more importantly, the development of the theoretical basis of the microscopic theory of heat transport, which will be useful in other branches of physics and materials science. The picture is as yet far from complete, but new experiments and theoretical work will no doubt give us a more complete picture in the not so distant future. There is no doubt that exciting times lie ahead for both theory and experiment, for basic and applied research, in the realm of the nanoscale.

Acknowledgements

T. Y. and K. W. acknowledge partial financial support from the Japan Science and Technology Corporation (JST-CREST), and from the Ministry of Edu-

cation, Culture, Sports, Science and Technology of Japan through Grants-in-Aid (No. 30408695 and No. 19540411) and Holistic Computational Science (HOLCS) of the Tokyo University of Science. They thank Professor Satoshi Watanabe, Professor Shigeo Maruyama, and Dr. Junichiro Shiomi for helpful discussions on the heat transport in CNTs. Some of the numerical calculations were performed on the Hitachi SR11000s at ISSP, The University of Tokyo.

E. R. H. acknowledges support from the Spanish Ministry of Science and Education (MEC) through Grant No. BFM2003-03372-C03 and from the Catalan Regional Government through Grant No. 2005SGR683. This author also wishes to thank the Tokyo University of Science for its hospitality during a visit in which part of this contribution was written.

References

[1] J. N. Coleman, U. Khan, W. J. Blau, Y. K. Gun'ko: Small but strong: a review of the mechanical properties of carbon nanotube-polymer composites, Carbon **44**, 1624 (2006) 165

[2] R. Tenne: Inorganic nanotubes and fullerene-like nanoparticles, Nature Nanotechnol. **1**, 103 (2006) 165

[3] A. M. Fennimore, T. D. Yuzvinsky, W. Q. Han, M. S. Fuhrer, J. Cumings, A. Zettl: Rotational actuators based on carbon nanotubes, Nature London **424**, 408 (2003) 165, 177

[4] T. Iwai, H. Shioya, D. Kondo, S. Hirose, A. Kawabata, S. Sato, M. Nihei, T. Kikkawa, K. Joshin, Y. Awano, N. Yokoyama: Thermal and source bumps utilizing carbon nanotubes for flip-chip high power amplifiers, IEEE IEDM Tech. Digest **257** (2005) 165, 178

[5] L. D. Landau, E. M. Lifshitz: *Theory of Elasticity* (Pergamon, Oxford 1986) 165, 167

[6] B. I. Yakobson, P. Avouris: in M. Dresselhaus, G. E. Dresselhaus, P. Avouris (Eds.): *Carbon Nanotubes, Synthesis, Structure, Properties and Applications*, Top. Appl. Phys. **80** (Springer, Berlin, Heidelberg 2001) pp. 287–328 166

[7] M. S. Dresselhaus, G. Dresselhaus, J. C. Charlier, E. Hernández: Electronic, thermal and mechanical properties of carbon nanotubes, Philos. Trans. R. Soc. Lond. A **362**, 2065 (2004) 166

[8] J. P. Salvetat, S. Bhattacharyya, R. B. Pipes: Progress on mechanics of carbon nanotubes and derived materials, J. Nanosci. Nanotechnol. **6**, 1857 (2006) 166

[9] S. Reich, C. Thomsen, J. Maultzsch: *Carbon Nanotubes, Basic Concepts and Physical Properties* (Wiley-VCH 2004) 166

[10] J. Hone: in M. Dresselhaus, G. E. Dresselhaus, P. Avouris (Eds.): *Carbon Nanotubes, Synthesis, Structure, Properties and Applications*, Top. Appl. Phys. **80** (Springer, Berlin, Heidelberg 2001) pp. 287–328 166, 178, 186

[11] D. H. Robertson, D. W. Brenner, J. W. Mintmire: Progress on mechanics of carbon nanotubes and derived materials, Phys. Rev. B **45**, 12592 (1992) 167, 171, 175

[12] D. Sánchez-Portal, E. Artacho, J. M. Soler, A. Rubio, P. Ordejón: Ab initio structural, elastic and vibrational properties of carbon nanotubes, Phys. Rev. B **59**, 12678 (1999) 167, 172
[13] J. Tersoff: New empirical-approach for the structure and energy of covalent systems, Phys. Rev. B **37**, 6991 (1988) 168
[14] D. W. Brenner: Empirical potential for hydrocarbons for use in simulating the chemical vapor deposition of diamond films, Phys. Rev. B **42**, 9458 (1990) 168, 171, 184
[15] G. G. Tibbets: Why are carbon filaments tubular, J. Cryst. Growth **66**, 632 (1983) 168, 175
[16] B. T. Kelly: *Physics of Graphite* (Applied Science, London 1981) 168
[17] M. S. Dresselhaus, G. Dresselhaus, K. Sugihara, I. L. Spain, H. A. Goldberg: *Graphite Fibers and Filaments* (Springer, Berlin, Heidelberg 1988) 168
[18] M. M. Treacy, T. W. Ebbesen, J. M. Gibson: Exceptionally high Young's modulus observed for individual carbon nanotubes, Nature (London) **381**, 678 (1996) 168, 169, 170
[19] A. Krishnan, E. Dujardin, T. W. Ebbesen, P. N. Yianilos, M. M. J. Treacy: Young's modulus of single-walled nanotubes, Phys. Rev. B **58**, 14013 (1998) 168, 172
[20] N. G. Chopra, A. Zettl: Measurement of the elastic modulus of a multi-wall boron nitride nanotube, Solid State Commun. **105**, 297 (1998) 168
[21] E. W. Wong, P. E. Sheehan, C. M. Lieber: Nanobeam mechanics: elasticity, strength and toughness of nanorods and nanotubes, Science **277**, 1971 (1997) 169, 170, 172
[22] M. R. Falvo, G. J. Clary, R. M. Taylor, V. Chi, F. P. Brooks, S. Washburn, R. Superfine: Bending and buckling of carbon nanotubes under large strain, Nature (London) **389**, 582 (1997) 169
[23] J. P. Salvetat, G. A. D. Briggs, J. M. Bonard, R. R. Bacsa, A. J. Kulik, T. Stoeckli, N. A. Burnham, L. Forró: Elastic and shear moduli of singlewalled carbon nanotube ropes, Phys. Rev. Lett. **82**, 944 (1999) 169
[24] J. P. Salvetat, A. J. Kulik, J. M. Bonard, G. A. D. Briggs, T. Stoeckli, K. Méténier, S. Bonnamy, F. Béguin, N. A. Burnham, L. Forró: Elastic modulus of ordered and disordered multiwalled carbon nanotubes, Adv. Mater. **11**, 161 (1999) 169
[25] A. Kis, G. Csányi, J. P. Salvetat, T. N. Lee, E. Couteau, A. J. Kulik, W. Benoit, J. Brugger, L. Forró: Reinforcement of single-walled carbon nanotube bundles by intertube bridging, Nature Mater. **3**, 153 (2004) 171
[26] B. I. Yakobson, C. J. Brabec, J. Bernholc: Nanomechanics of carbon tubes: instabilities beyond linear regime, Phys. Rev. Lett. **76**, 2511 (1996) 171
[27] S. Iijima, C. J. Brabec, A. Maiti, J. Bernholc: Structural flexibility of carbon nanotubes, J. Chem. Phys. **104**, 2089 (1996) 171
[28] J. P. Lu: Elastic properties of carbon nanotubes and nanoropes, Phys. Rev. Lett. **79**, 1297 (1997) 171, 172
[29] E. Hernández, C. Goze, P. Bernier, A. Rubio: Elastic properties of C and $B_xC_yN_z$ composite nanotubes, Phys. Rev. Lett. **80**, 4502 (1998) 172
[30] E. Hernández, C. Goze, P. Bernier, A. Rubio: Elastic properties of singlewall nanotubes, Appl. Phys. A **68**, 287 (1999) 172

[31] D. Porezag, T. Frauenheim, T. Koehler, G. Seifert, R. Kaschner: Construction of tight-binding-like potentials on the basis of density-functional theory: application to carbon, Phys. Rev. B **51**, 12947 (1995) 172
[32] J. M. Soler, E. Artacho, J. D. Gale, A. García, J. Junquera, P. Ordejón, D. Sánchez-Portal: The SIESTA method for ab initio order-n materials simulation, J. Phys. Condens. Matter **14**, 2745 (2002) 172
[33] M. F. Yu, O. Lourie, M. J. Dyer, K. Moloni, T. F. Kelly, R. S. Ruoff: Strength and breaking mechanism of multiwalled carbon nanotubes under tensile load, Science **287**, 637 (2000) 172, 173, 174, 176
[34] M. F. Yu, B. S. Files, S. Arepalli, R. S. Ruoff: Tensile loading of ropes of single wall carbon nanotubes and their mechanical properties, Phys. Rev. Lett. **84**, 5552 (2000) 173, 174
[35] J. Y. Huang, S. Chen, Z. Q. Wang, K. Kempa, Y. M. Wang, S. H. Jo, G. Chen, M. S. Dresselhaus, Z. F. Ren: Superplastic carbon nanotubes, Nature (London) **439**, 281 (2006) 174
[36] J. Y. Huang, S. Chen, Z. F. Ren, Z. Q. Wang, D. Z. Wang, M. Vaziri, Z. Suo, G. Chen, M. S. Dresselhaus: Kink formation and motion in carbon nanotubes at high temperatures, Phys. Rev. Lett. **97**, 075501 (2006) 174
[37] B. I. Yakobson: in *Proceedings of the Recent Advances in the Chemistry and Physics of Fullerenes and Related Materials*, vol. 97 (Electrochem. Soc., Pennington 1997) p. 549 174
[38] B. I. Yakobson: Mechanical relaxation and intramolecular plasticity in carbon nanotubes, Appl. Phys. Lett. **72**, 918 (1998) 174
[39] M. B. Nardelli, B. I. Yakobson, J. Bernholc: Mechanism of strain release in carbon nanotubes, Phys. Rev. B **57**, R4277 (1998) 174
[40] M. B. Nardelli, B. I. Yakobson, J. Bernholc: Brittle and ductile behavior in carbon nanotubes, Phys. Rev. Lett. **81**, 4656 (1998) 174
[41] A. J. Stone, D. J. Wales: Theoretical studies of icosahedral C_{60} and some related species, Chem. Phys. Lett. **128**, 501 (1986) 174, 175
[42] T. Dumitrică, T. Belytschko, B. I. Yakobson: Bond-breaking bifurcation states in carbon nanotube fracture, J. Chem. Phys. **118**, 9485 (2003) 174
[43] T. Dumitrică, M. Hua, B. I. Yakobson: Symmetry, time and temperature dependent strength of carbon nanotubes, PNAS **103**, 6105 (2006) 174
[44] F. Ding, K. Jiao, M. Wu, B. I. Yakobson: Pseudoclimb and dislocation dynamics in superplastic nanotubes, Phys. Rev. Lett. **98**, 075503 (2007) 174
[45] B. W. Smith, M. Monthioux, D. E. Luzzi: Encapsulated C_{60} in carbon nanotubes, Nature (London) **396**, 323 (1998) 175
[46] B. W. Smith, D. E. Luzzi: Formation mechanism of fullerene peapods and coaxial tubes: a path to large scale synthesis, Chem. Phys. Lett. **321**, 169 (2000) 175
[47] S. Bandow, M. Takizawa, K. Hirahara, M. Yudasaka, S. Iijima: Raman scattering study of double-wall carbon nanotubes derived from the chains of fullerenes in sigle-wall carbon nanotubes, Chem. Phys. Lett. **337**, 48 (2001) 175
[48] E. Hernández, V. Meunier, B. W. Smith, R. Rurali, H. Terrones, M. B. Nardelli, M. Terrones, D. E. Luzzi, J.-C. Charlier: Fullerene coalescence in nanopeapods: a path to novel tubular carbon, Nano Lett. **3**, 1037 (2003) 175

[49] M. Terrones, H. Terrones, F. Banhart, J.-C. Charlier, P. M. Ajayan: Coalescence of single-walled carbon nanotubes, Science **288**, 1226 (2000) 175, 176
[50] M. J. López, A. Rubio, J. A. Alonso, S. Lefrant, K. Méténier, S. Bonnamy: Patching and tearing single-wall carbon nanotube ropes into multiwall carbon nanotubes, Phys. Rev. Lett. **89**, 255501 (2002) 175
[51] M. Yoon, S. Han, G. Kim, S. B. Lee, S. Berber, E. Osawa, J. Ihm, M. Terrones, F. Banhart, J.-C. Charlier, N. Grobert, H. Terrones, P. M. Ajayan, D. Tománek: Zipper mechanism for nanotube fusion: theory and experiment, Phys. Rev. Lett. **92**, 075504 (2004) 175
[52] M. Terrones, F. Banhart, N. Grobert, J.-C. Charlier, H. Terrones, P. M. Ajayan: Molecular junctions by joining single-walled carbon nanotubes, Phys. Rev. Lett. **89**, 075505 (2002) 175
[53] Y. F. Zhao, B. I. Yakobson, R. E. Smalley: Dynamic topology of fullerene coalescence, Phys. Rev. Lett. **88**, 185501 (2002) 175
[54] Y. F. Zhao, R. E. Smalley, B. I. Yakobson: Coalescence of fullerene cages: topology, energetics and molecular dynamics simulation, Phys. Rev. B **66**, 195409 (2002) 175
[55] U. D. Venkateswaran, A. M. Rao, E. Richter, M. Menon, A. Rinzler, R. E. Smalley, P. C. Eklund: Probing the single-wall carbon nanotube bundle: Raman scattering under high pressure, Phys. Rev. B **59**, 10928 (1999) 175
[56] S. Reich, C. Thomsen, P. Ordejón: Elastic properties of carbon nanotubes under hydrostatic pressure, Phys. Rev. B **65**, 153407 (2004) 175
[57] S. Reich, C. Thomsen, P. Ordejón: Elastic properties and pressure-induced phase transitions of single-walled carbon nanotubes, Phys. Stat. Sol. B **235**, 354 (2003) 176
[58] X. H. Zhang, D. Y. Sun, Z. F. Liu, X. G. Gong: Structure and phase transitions of single-wall carbon nanotube bundles under hydrostatic pressure, Phys. Rev. B **70**, 035422 (2004) 176
[59] S. E. Baltazar, A. H. Romero, J. L. Rodríguez, R. Martoňák, J. Phys.: Finite singlewall capped carbon nanotubes under hydrostatic pressure, Condens. Matter **18**, 9119 (2006) 176
[60] J. Cumings, A. Zettl: Low-friction nanoscale linear bearing realized from multiwall carbon nanotubes, Science **289**, 602 (2000) 176, 177
[61] Q. Zheng, Q. Jiang: Multiwalled carbon nanotubes as gigahertz oscillators, Phys. Rev. Lett. **88**, 045503 (2002) 177
[62] S. B. Legoas, V. R. Coluci, S. F. Braga, P. Z. Coura, S. O. Dantas, D. S. Galvão: Molecular-dynamics simulations of carbon nanotubes as gigahertz oscillators, Phys. Rev. Lett. **90**, 055504 (2003) 177
[63] W. Guo, Y. Guo, H. Gao, Q. Zheng, W. Zhong: Energy dissipation in gigahertz oscillators from multiwalled carbon nanotubes, Phys. Rev. Lett. **91**, 125501 (2003) 177
[64] Y. Zhao, C. Ma, G. Hua, Q. Jiang: Energy dissipation mechanisms in carbon nanotube oscillators, Phys. Rev. Lett. **91**, 175504 (2003) 177
[65] J. Servantie, P. Gaspard: Methods of calculation of a friction coefficient: application to nanotubes, Phys. Rev. Lett. **91**, 185593 (2003) 177
[66] J. Servantie, P. Gaspard: Translational dynamics and friction in doublewalled carbon nanotubes, Phys. Rev. B **73**, 125428 (2006) 177

[67] P. Tangney, S. G. Louie, M. L. Cohen: Dynamic sliding friction between concentric carbon nanotubes, Phys. Rev. Lett. **93**, 065503 (2004) 177
[68] P. Tangney, M. L. Cohen, S. G. Louie: Giant wave-drag enhancement of friction in sliding carbon nanotubes, Phys. Rev. Lett. **97**, 195901 (2006) 177
[69] S. Berber, Y.-K. Kwon, D. Tománek: Unusally high thermal conductivity of carbon nanotubes, Phys. Rev. Lett. **84**, 4613 (2000) 178, 184
[70] J. Hone, M. Whitney, C. Piskoti, A. Zettl: Thermal conductivity of single-walled carbon nanotubes, Phys. Rev. B **59**, R2514 (1999) 178, 180, 181
[71] C. Yu, L. Shi, Z. Yao, D. Li, A. Majumdar: Thermal conductance and thermopower of an individual single-wall carbon nanotube, Nano Lett. **5**, 1842 (2005) 178, 185
[72] N. Mingo, D. A. Broido: Carbon nanotube ballistic thermal conductance and its limits, Phys. Rev. Lett. **95**, 096105 (2005) 178
[73] W. Yu, L. Lu, Z. Dian-lin, Z. W. Pan, S. Xie: Linear specific heat of carbon nanotubes, Phys. Rev. B **59**, R9015 (1999) 178, 188
[74] R. E. Peierls: *Quantum Theory of Solid* (Oxford University Press, New York 1955) 178
[75] L. G. C. Rego, G. Kirczenow: Quantized thermal conductance of dielectric quantum wires, Phys. Rev. Lett **81**, 232 (1998) 178, 179
[76] T. Yamamoto, S. Watanabe, K. Watanabe: Universal features of quantized thermal conductance of carbon nanotubes, Phys. Rev. Lett. **92**, 075502 (2004) 178, 179, 181, 182
[77] T. Yamamoto, K. Watanabe: Nonequilibrium Green's function approach to phonon transport in defective carbon nanotubes, Phys. Rev. Lett. **96**, 255503 (2006) 179
[78] N. Mingo: Anharmonic phonon flow through molecular-sized junctions, Phys. Rev. B **74**, 125402 (2006) 179
[79] J.-S. Wang, J. Wang, N. Zeng: Nonequilibrium Green's function approach to mesoscopic thermal transport, Phys. Rev. B **74**, 033408 (2006) 179
[80] P. K. Schelling, S. R. Phillpot, P. Keblinski: Phonon wave-packet dynamics at semiconductor interfaces by molecular-dynamics simulation, Appl. Phys. Lett. **80**, 2484 (2002) 179
[81] N. Kondo, T. Yamamoto, K. Watanabe: Phonon wavepacket scattering dynamics in defective carbon nanotubes, Jpn. J. Appl. Phys. **45**, L963 (2006) 179
[82] J. Wang, J.-S. Wang: Mode-dependent energy transmission across nanotube junctions calculated with a lattice dynamics approach, Phys. Rev. B **74**, 054303 (2006) 179
[83] J. Hone, M. C. Llaguno, M. J. Biercuk, A. T. Johnson, B. Batlogg, Z. Benes, J. E. Fischer: Thermal properties of carbon nanotubes and nanotube-based materials, Appl. Phys. A **74**, 339 (2002) 180
[84] H.-Y. Chiu, V. V. Deshpande, H. W. C. Postma, C. N. Lau, C. Mikó, L. Forró, M. Bockrath: Ballistic phonon thermal transport in multiwalled carbon nanotubes, Phys. Rev. Lett. **95**, 226101 (2005) 180
[85] R. Saito, G. Dresselhaus, M. S. Dresselhaus: *Physical Properties of Carbon Nanotubes* (Imperial College, London 1998) 180, 181, 182
[86] S. Maruyama: A molecular dynamics simulation of heat conduction of a finite length SWNTs, Physica B **323**, 193 (2002) 182

[87] S. Maruyama: A molecular dynamics simulation of heat conduction of a finite length single-walled carbon nanotube, Microscale Thermophys. Eng. **7**, 41 (2003) 182, 183, 184, 185
[88] R. Livi, S. Lepri: Thermal physics: heat in one dimension, Nature **421**, 327 (2003) 182
[89] N. Mingo, D. A. Broido: Length dependence of carbon nanotube thermal conductivity and the "problem of long waves", Nano Lett. **5**, 1221 (2005) 183
[90] J. Wang, J.-S. Wang: Carbon nanotube thermal transport: ballistic to diffuse, Appl. Phys. Lett. **88**, 111909 (2006) 183
[91] A. Hashimoto, K. Suenaga, A. Gloter, K. Urita, S. Iijima: Direct evidence for atomic defects in graphene layers, Nature (London) **430**, 870 (2004) 184
[92] S. Maruyama, Y. Igarashi, Y. Taniguchi, J. Shiomi: Anisotropic heat transfer of single-walled carbon nanotubes, J. Therm. Sci. Tech. **1**, 138 (2006) 184, 185
[93] N. Kondo, T. Yamamoto, K. Watanabe: Molecular-dynamics simulations of thermal transport in carbon nanotubes with structural defects, e-J. Surf. Sci. Nanotech. **4**, 239 (2006) 184, 185
[94] C. W. Chang, A. M. Fennimore, A. Afanasiev, D. Okawa, T. Ikuno, H. Garcia, D. Li, A. Majumdar, A. Zettl: Isotope effects on the thermal conductivity of boron nitride nanotubes, Phys. Rev. Lett. **97**, 085901 (2006) 185
[95] E. Pop, D. Mann, Q. Wang, K. Goodson, H. Dai: Thermal conductance of an individual single-wall carbon nanotube above room temperature, Nano Lett. **6**, 96 (2006) 185, 186
[96] Y. Miyamoto, S. Berber, M. Yoon, A. Rubio, D. Tománek: Onset of nanotube decay under extreme thermal and electronic excitations, Physica B **323**, 78 (2002) 185
[97] A. V. Krasheninnikov, K. Nordlund: Stability of irradiation-induced point defects on walls of carbon nanotubes, J. Vac. Sci. Technol. B **20**, 728 (2002) 185
[98] P. Kim, L. Shi, A. Majumdar, P. L. McEuen: Thermal transport measurements of individual multiwalled nanotubes, Phys. Rev. Lett. **87**, 215502 (2001) 186, 187
[99] J. M. Ziman: *Electrons and Phonons* (Oxford University Press, London 1960) 187
[100] J. Heremans, C. P. Beetz, Jr.: Thermal conductivity and thermopower of vapor-grown graphite fibers, Phys. Rev. B **32**, 1981 (1985) 187
[101] R. P. Feynman: There is plenty of room at the bottom, Eng. Sci. (Feb. 1960) 188

Index

Quasiparticle and Excitonic Effects in the Optical Response of Nanotubes and Nanoribbons

Catalin D. Spataru[1], Sohrab Ismail-Beigi[2], Rodrigo B. Capaz[3,4], and Steven G. Louie[5,6]

[1] Center for Integrated Science and Engineering
and Center for Electron Transport in Molecular Nanostructures,
Columbia University, New York, NY 10027, USA
dcs2113@columbia.edu
[2] Department of Applied Physics, Yale University,
New Haven, Connecticut 06520, USA
sohrab.ismail-beigi@yale.edu
[3] Instituto de Física, Universidade Federal do Rio de Janeiro,
Caixa Postal 68528, Rio de Janeiro, RJ 21941-972, Brazil
capaz@if.ufrj.br
[4] Divisão de Metrologia de Materiais, Instituto Nacional de Metrologia,
Normalização e Qualidade Industrial - Inmetro,
R. Nossa Senhora das Graças 50, Xerém, Duque de Caxias, RJ 25245-020, Brazil
[5] Department of Physics, University of California at Berkeley,
Berkeley, CA 94720, USA
sglouie@berkeley.edu
[6] Materials Science Division, Lawrence Berkeley National Laboratory,
Berkeley, CA 94720, USA

Abstract. This chapter discusses the effects of many-electron interactions in the photophysics of nanotubes and their consequences on measured properties. The basic theory and key physical differences between two common types of electronic excitations are developed: single-particle excitations (quasiparticles) measured in transport or photoemission experiments, and electron–hole pair excitations (excitonic states) measured in optical experiments. We show, through first-principles calculations, that both quasiparticle and excitonic effects are crucial in understanding the optical response of the carbon nanotubes. These effects change qualitatively the nature of the photoexcited states, leading to extraordinarily strongly bound excitons in both semiconducting and metallic nanotubes and explaining the so-called "ratio problem" in carbon-nanotube spectroscopy. Using simplified models parameterized by the first-principles results, the diameter and family dependences of the exciton properties in carbon nanotubes are further elucidated. We also analyze the symmetries of excitons and their selection rules for one- and two-photon spectroscopy. A method for calculating the radiative lifetime of excitons in carbon nanotubes is also described. In addition, we briefly discuss the effects of pressure and temperature on optical transitions. Finally, we show that many-electron effects are equally dominant in the excitation spectra of other quasi-one-dimensional systems, including the boron-nitride nanotubes, semiconductor nanowires, and graphene nanoribbons.

A. Jorio, G. Dresselhaus, M. S. Dresselhaus (Eds.): Carbon Nanotubes,
Topics Appl. Physics **111**, 195–227 (2008)

1 Introduction

Optical transitions in single-wall carbon nanotubes (SWNTs) were initially interpreted as arising from band-to-band transitions. This interpretation was very succesful in describing overall trends and providing a comparative and even semiquantitative picture of the transition energies for a variety of tubes [1]. Indeed, essentially correct (n, m) chiral indices assignments were made using simple band-to-band transitions as a guide to the experimental data [1, 2]. However, it was precisely the possibility of such assignments that revealed irreconcilable differences between band-to-band transition energies and experimental ones. A particularly striking manifestation of these discrepancies was posed as the "ratio problem" [2]: As described in the contribution by Ando, the ratio between E_{22}^S and E_{11}^S transition energies did not converge to 2 in the limit of large-diameter tubes, as any single-particle description required.

Reconciliation came through the excitonic description of optical transition energies. Early model calculations anticipated the possible importance of many-body effects in systems with reduced dimensions [3], and full *ab-initio* calculations [4–6] provided, with no fitting parameters, unquestionable proof of the importance of many-electron effects and excellent agreement between theory and experiment. The *ab-initio* studies predicted extraordinarily large exciton binding energies for the semiconducting SWNTs and the existence of bound excitons in the metallic SWNTs. [4, 5] One year later, the direct evidence for the excitonic nature of the optical transitions in SWNTs, by means of two-photon absorption measurements [7, 8], was the crowning achievement of a successful interplay between theory and experiment in the field of carbon-nanotube optics.

In this chapter, we focus on many aspects of the theory of excitons in SWNTs. Section 2 provides an overview on the methodology for calculating quasiparticle and excitonic effects using *ab-initio* techniques. Section 3 presents the results for such calculations for a few semiconducting and metallic SWNTs. Section 4 discusses how one can use model calculations to extrapolate the results of the previous section to many SWNTs of various diameters and chiralities. Section 5 presents a group-theory analysis of the symmetries and selection rules of excitons. Section 6 presents calculations of the radiative lifetime of excitons, where temperature and dark-exciton effects are taken into account. Section 7 discusses the effects of pressure, strain and temperature on the optical transition energies. Finally, Sect. 8 presents results on related systems (BN nanotubes and carbon nanoribbons), and Sect. 9 summarizes our main conclusions and our vision on open issues that should guide future work in this field.

2 Methodology

Our overall approach for describing the electronic and optical properties of crystals and nanostructures such as carbon nanotubes and nanoribbons is based on a combination of first-principles or *ab-initio* theoretical methods, each suitable for describing the relevant set of experimental observables (for a general review, see for example [9]). *Ab-initio* approaches do not use fitting parameters or simplifications that apply to restricted types of situations. We attempt to describe the quantum-mechanical and many-particle interactions among electrons and atomic nuclei as generally and accurately as possible. Hence, this approach requires some computational effort but delivers results that should be reliable and accurate for many situations.

Our investigation requires us to start with the proper atomic geometry for carbon nanotubes or other nanostructures in their electronic ground-state (i.e., prior to excitation). For this we employ density-functional theory (DFT) [10, 11], the most widely used framework for *ab-initio* solid-state and materials-physics calculations. DFT allows one, in principle, to find the ground-state energy and electron density of an interacting many-electron system by solving a set of effective, self-consistent, single-body equations. Optimization of the total energy versus the atomic coordinates then yields the stable atomic geometry. The single-particle eigenvalue equations are the Kohn–Sham equations

$$\left[-\frac{\hbar^2\nabla^2}{2m} + V_{\text{ion}}(\boldsymbol{r}) + V_{\text{H}}(\boldsymbol{r}) + V_{\text{xc}}(\boldsymbol{r})\right]\phi_j(\boldsymbol{r}) = \epsilon_j\phi_j(\boldsymbol{r})\,. \tag{1}$$

Here, V_{ion} is the Coulombic attractive potential felt by electrons due to the atomic nuclei, V_{H} is the repulsive electrostatic Hartree field generated by the average electronic distribution, and V_{xc} is an exchange-correlation potential that encodes the complex, quantum electron–electron interactions. In practice, some approximation is needed to make exchange and correlation tractable: we use the standard local-density approximation (LDA) [11]. (Approximations including effects of density gradients are also standard [12–14].) In addition, we describe electronic states using a plane-wave (Fourier) basis that is a general, bias-free, and complete basis set. Furthermore, atomic pseudopotentials remove the tightly bound core electrons from the calculation and allow us to focus only on the physically active valence electrons. For details, reviews are available [15]. DFT with the LDA provides accurate ground-state properties for a large variety of systems. These include atomic geometries, lattice constants, cohesive or surface energies, reconstructions, defect states, vibrational spectra, etc. [15]. For our cases, the main output of DFT is the atomic structure as well as a mean-field Kohn–Sham description of the electronic states.

Unfortunately, DFT has problems in predicting electronic excitations. This is not surprising because it is a ground-state and not an excited-state theory. If one interprets the electronic states ϕ_j and energies ϵ_j as the *bona*

fide band structure, one finds serious errors and underestimations [16, 17]. Aside from these problems with band structures, ground-state DFT can not describe optical excitations properly: an optically excited state or exciton is comprised of (at least) one excited electron and hole. This is a two-particle problem since both are charged and interact. A single-body theory such as ground-state DFT does not contain such a description.

Therefore, we must go beyond DFT to describe excitations properly. Our approach is based on many-body perturbation theory: we calculate response functions or Green's functions that yield experimental observables. Here, there are two Green's functions of interest: 1. the one-particle Green's function provides the properties of quasiparticles, namely electron and hole band energies and wavefunctions, and 2. the two-particle Green's function provides us with the energies and transition strengths for optical excitations.

For the single-particle response, the key quantities are the quasiparticle energies ϵ_j and amplitudes $\psi_j(\boldsymbol{r})$ that rigorously describe the energies and amplitudes for adding or removing electrons to a material. For example, these are the excitations involved in charge transport where quasiparticles propagate through the system and we seek their energies and quantum amplitudes. These quantities are determined by the self-consistent Dyson equation

$$\left[-\frac{\hbar^2\nabla^2}{2m} + V_{\text{ion}}(\boldsymbol{r}) + V_{\text{H}}(\boldsymbol{r})\right]\psi_j(\boldsymbol{r}) + \int \mathrm{d}\boldsymbol{r}'\Sigma_{\text{xc}}(\boldsymbol{r},\boldsymbol{r}',\epsilon_j)\psi_j(\boldsymbol{r}') = \epsilon_j\psi_j(\boldsymbol{r})\,. \quad (2)$$

The self-energy $\Sigma_{\text{xc}}(\boldsymbol{r},\boldsymbol{r}',\omega)$ encodes the exchange-correlation potential an excited quasiparticle feels due to the surrounding electronic medium, and it is nonlocal and energy dependent. For example, Hartree–Fock has a nonlocal but energy-independent exchange self-energy. While in principle this description yields the exact band energies and quasiparticle amplitudes, in practice Σ_{xc} must be approximated. The "*GW*" approximation to the self-energy includes the effects of dynamic and position-dependent screening by the surrounding electronic medium on the dynamics of the quasiparticle under consideration [17, 18]. The typical accuracy in band energies is ~ 0.1–$0.2\,\text{eV}$ when compared to experiment. In retrospect, the failure of DFT is not surprising: the true nonlocal and energy-dependent effects in $\Sigma_{\text{xc}}(\boldsymbol{r},\boldsymbol{r}',\omega)$ are approximated by a local and energy-independent potential $V_{\text{xc}}(\boldsymbol{r})$.

We emphasize that the above band energies and amplitudes are for excitations involving a single added or removed electron, whereas optical excitations have a pair of particles (an electron and hole) added to the ground state. Describing an optical excitation as a simple interband transition, i.e., a pair of noninteracting electron and hole, means that excitation energies should equal the sum of electron and hole quasiparticle energies, i.e., the differences between occupied and unoccupied ϵ_j. Such an interband approximation is reasonable only when electron–hole interactions are relatively weak, e.g., when exciton binding energies are much smaller than the quasiparticle

bandgap. As we show below, this view is qualitatively and quantitatively incorrect for excitons in nanostructures: low-energy excitations are strongly bound excitons and electron–hole interactions dominate.

To describe excitons, we use a two-particle Green's function approach. For each exciton (excited state) labeled by S, we seek the energy Ω_S required to create it and the quantum amplitude $\chi_S(\boldsymbol{r}_\mathrm{e}, \boldsymbol{r}_\mathrm{h})$ to find the excited electron at position $\boldsymbol{r}_\mathrm{e}$ and the hole at position $\boldsymbol{r}_\mathrm{h}$. Within the Tamm–Dancoff approximation [19–25], the amplitude is given by

$$\chi_S(\boldsymbol{r}_\mathrm{e}, \boldsymbol{r}_\mathrm{h}) = \langle 0|\hat{\Psi}(\boldsymbol{r}_\mathrm{h})^\dagger \hat{\Psi}(\boldsymbol{r}_\mathrm{e})|S\rangle = \sum_{\mathrm{cv}} A^S_{\mathrm{cv}} \psi_\mathrm{c}(\boldsymbol{r}_\mathrm{e}) \psi_\mathrm{v}(\boldsymbol{r}_\mathrm{h})^* \,. \tag{3}$$

Here, the kets $|0\rangle$ and $|S\rangle$ are the ground and excited states so the excitation energy is $\Omega_S = E_S - E_0$, $\hat{\Psi}(\boldsymbol{r})/\hat{\Psi}(\boldsymbol{r})^\dagger$ are annihilation/creation operators that remove/add an electron at $\boldsymbol{r}$, and c and v label unoccupied and occupied (conduction and valence) quasiparticle states, respectively. The states ψ_j and energies ϵ_j are from the GW calculation. The amplitude χ_S is a coherent sum over free electron–hole pairs: the A^S_{cv} coefficients allow for correlation and entanglement of the electron and hole and the formation of *bona fide* excitons. We find Ω_S and A^S_{eh} by solving the Bethe–Salpeter equation (BSE)

$$(\epsilon_\mathrm{c} - \epsilon_\mathrm{v}) A^S_{\mathrm{cv}} + \sum_{c'v'} K(\Omega_S)_{cv,c'v'} A^S_{c'v'} = \Omega_S \, A^S_{\mathrm{cv}} \,. \tag{4}$$

The electron and hole interact via the dynamic kernel $K(\omega)$ that, physically, includes an attractive long-range screened Coulomb interaction as well as a short-range repulsive "exchange" interaction [19–21]. The combined GW-BSE approach predicts well both transition energies and optical transition strengths: typical agreement for transition energies is $\sim$ 0.1–0.2 eV [22–25]. Armed with Ω_S and transition amplitudes χ_S, we can calculate the linear response of a system to external electromagnetic fields.

In summary, there are three distinct steps to our approach: 1. the ground state is described using DFT that provides the atomic structure and a mean-field description of electronic states that includes the realistic potential from the atomic nuclei, 2. the GW approximation to the self-energy accounts for the electronic correlations needed to describe quasiparticle excitation energies corresponding to the addition of single electrons or holes, and 3. the BSE accounts for electron–hole interactions and correlations and yields exciton states (both bound and unbound) and optical transition strengths.

3 First-Principles Studies of the Optical Spectra of SWNTs

Using the first-principles techniques outlined in the previous section, we have computed the optical absorption spectra of several SWNTs, both semiconducting and metallic, with diameters ranging from 0.4 to 1.4 nm. Because

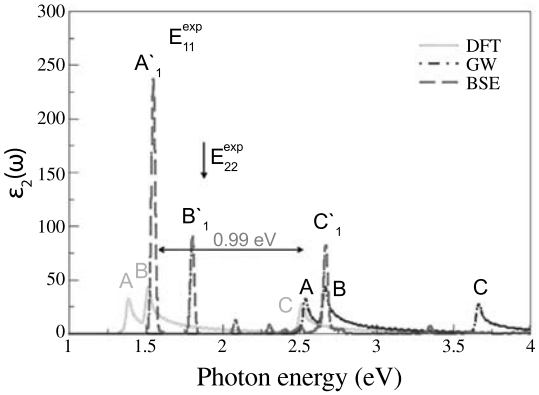

Fig. 1. Absorption spectrum and excitonic effects of a (8,0) SWNT calculated in three ways: using optically allowed interband transitions from DFT eigenvalues and wavefunctions (*solid curve*), without electron–hole interaction but including self-energy effects at the *GW* level (*dot-dashed curve*), and with electron–hole interaction at the BSE level (*dashed curve*). The polarization of the light is parallel to the nanotube axis. Adapted from [4, 5]

our calculations scale as the number of atoms to the fourth power (given the plane-wave basis set), we have restricted our *ab-initio* studies to armchair and zigzag SWNTs, which have smaller unit cells.

Figure 1 shows the optical absorption spectrum, for light parallel to the nanotube axis, of the semiconducting (8,0) SWNT calculated at three different levels of approximation. First, we compute the absorption spectrum at the DFT level, using Kohn–Sham energies and velocity matrix elements between occupied and unoccupied wavefunctions from an LDA calculation, neglecting the self-energy corrections and the electron–hole interaction. In this case (shown in solid curve), three main peaks appear in $\epsilon_2(\omega)$ in the photon energy range up to 4 eV, labeled A, B and C. The peaks correspond to optically allowed interband transitions between DFT bands.

Next, we correct the Kohn–Sham eigenvalues for single-particle excitations using the *GW* approximation to the self-energy, while continuing to neglect the electron–hole interaction. The absorption spectrum (dot-dashed curve) is dramatically blueshifted due to an increase in bandgaps due to self-energy effects. We find that a "scissor" shift of ≈ 1.15 eV approximately describes the *GW* quasiparticle corrections to the Kohn–Sham energies.

Finally, we take into account both self-energy *GW* corrections and the electron–hole interaction. For the (8,0) tube, the overall electron–hole interaction is strongly attractive and leads to a dramatic qualitative change in the absorption spectrum with respect to that calculated at the *GW* level. After solving the Bethe–Salpeter equation, the absorption spectrum (dashed curve) is redshifted with respect to the independent quasiparticle result, and each peak corresponds to an excitonic (two-particle electron–hole) state. From

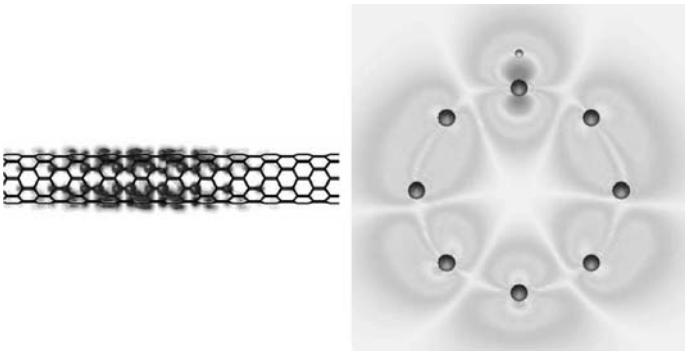

Fig. 2. Wavefunction squared of the lowest-energy bright exciton in the (8,0) SWNT showing isosurfaces of the electron probability distribution with the hole fixed at the position indicated by the *small dot*. From [4, 5, 26]

these calculated shifts, the binding energy of excitons in (8,0) SWNTs can be seen to be as large as $\approx 1\,\mathrm{eV}$. This huge binding energy (compared to the case of bound excitons in bulk semiconductors of similar bandgap) is due to the enhancement of Coulomb effects [3–5] in these quasi-one-dimensional systems.

It is interesting to note that the initial blueshift (at the *GW* level) and subsequent redshift (at the Bethe–Salpeter level) tend to cancel each other. However, this cancelation is not complete and there still remains a notable blueshift between the absorption spectrum obtained from the BSE and the one calculated from the ground-state DFT. Moreover, the physical nature of the excitations and the shape of the optical spectra are dramatically different in the two cases. A similar observation can be made for the other (n,0) semiconducting tubes we studied: (7,0), (10,0) and (11,0).

Figure 2 shows the exciton wavefunction of the lowest bright exciton in the (8,0) tube (labeled A_1' in Fig. 1). In the upper panel one can see several isosurfaces of the electron–hole probability distribution of finding the electron about the hole that is fixed on top of a carbon atom as indicated by the green star. The calculated root mean square size of the exciton along the tube axis is 0.86 nm. The lower panel shows a cross-sectional plot of the exciton wavefunction squared, in a plane that passes through carbon atoms. The exciton is delocalized along the circumference of the tube, due to the fact that there is only one pair of valence and conduction bands that mainly contributes to this exciton. As we shall see in Sect. 8, the situation in boron-nitride tubes is quite different, the wavefunction being localized in both the axial and circumferential coordinates.

Table 1 shows our *ab-initio* results for 4 different semiconducting SWNTs, compared with those deduced from resonant fluorescence spectroscopy [2]. We compare the lowest two optical transition energies E_{11}^S and E_{22}^S, as well as their ratio. We see that we have excellent agreement between theory and ex-

Table 1. Lowest two optical transition energies of four semiconducting SWNTs. From [4, 5, 28]

	E_{11}^S (eV)		E_{22}^S (eV)		E_{22}^S / E_{11}^S	
Tube	Theory	Exp.[a]	Theory	Exp.[a]	Theory	Exp.[a]
(7,0)	1.20	1.29	3.00	3.14	2.50	2.43
(8,0)	1.55	1.60	1.80	1.88	1.16	1.17
(10,0)	1.00	1.07	2.39	2.31	2.39	2.16
(11,0)	1.21	1.20	1.74	1.66	1.44	1.38

[a] [2]

periment, not only for the E_{22}^S/E_{11}^S ratio but also for the absolute value of the excitation energies. In the limit of large-diameter tubes, the experimental fits provide a ratio of $E_{22}^S/E_{11}^S = 1.85$, while a traditional tight-binding model in the noninteracting framework gives a ratio of 2. Our *ab-initio* calculations explain the deviation of E_{22}^S/E_{11}^S from 2 as a consequence of three important physical effects: band-structure effects, quasiparticle self-energy effects and excitonic effects. All three need to be taken into account for a proper qualitative and quantitative understanding. Moreover, the predicted large binding energies of excitons have recently been verified experimentally using two-photon spectroscopy and other techniques [7, 8, 27].

We have also studied several metallic SWNTs, such as the small-diameter tubes (3,3) and (5,0) [4, 5], as well as the larger-diameter tubes (12,0) and (10,10) [29]. Except for the (5,0) tube, we found that optical absorption spectra of these metallic tubes are also dictated by bound exciton states. This is a novel predicted phenomenon that has not been seen in other metallic systems. Normally, one does not find bound excitons in bulk metallic systems because the long-range part of the electron–hole interaction is screened out completely by the available carriers.

Due to the screening in metallic SWNTs, the *GW* quasiparticle corrections to the LDA Kohn–Sham energies in large-diameter metallic tubes should resemble those in a single graphene layer. We find that for the (12,0) and (10,10) tubes, the slope in the dispersion relation of the quasiparticle bands increases by approximately 25 % when compared to the LDA result. In the smaller-diameter tubes (3,3) and (5,0), we find that the metallic screening is more enhanced, leading to self-energy corrections of about 15 %, which is similar to those we find in graphite [30].

In a quasi-1D system, all k-states along a band can have well-defined symmetry, which causes optical transitions to obey well-defined selection rules across entire bands. In armchair and zigzag metallic tubes, the bands that meet at the Fermi level, giving rise to the metallic character of the tubes, do not allow optical transitions between them. As a consequence, the optical spectra in these metallic systems show a symmetry gap. Figure 3 shows the optical absorption spectra for the first allowed transition in the (10,10) tube.

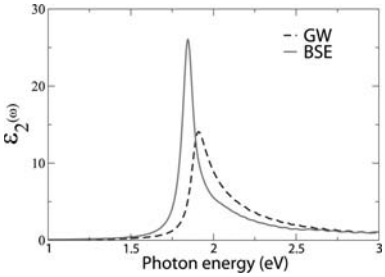

Fig. 3. The calculated first absorption peak in the (10,10) SWNT. The imaginary part of the dielectric function is calculated in two ways: without electron–hole interaction but including self-energy effects at the *GW* level (*dashed curve*), and with electron–hole interaction at the BSE level (*full curve*). The curves are broadened by convolving with a Lorenzian function with width 80 meV. From [29]

When neglecting electron–hole interactions (but including *GW* self-energy effects), we find no dipole-allowed electron–hole transitions with energy below the prominent peak at 1.89 eV. When including the electron–hole interaction, which is dominated by the attractive (direct) term, we see that the prominent peak in the noninteracting spectrum gives rise to one bound exciton with a binding energy of 50 meV. The surprising result of having a bound exciton in a metallic nanotube stems from several factors owing to reduced dimensionality: incomplete screening of Coulomb interactions in quasi-1D systems, the existence of symmetry gaps, and the ease of trapping a quantum state in an attractive 1D potential well [29]. The existence of a sole bound exciton is due to the metallic screening and the weakness of the repulsive exchange term in the electron–hole kernel: the effective electron–hole interaction along the tube axis resembles an attractive $\delta(z)$ function, and in 1D, the Hamiltonian $H = -\frac{1}{2m^*}\frac{\mathrm{d}^2}{\mathrm{d}z^2} - |V_0|\delta(z)$ has a single bound eigenstate.

It is found that the optical absorption spectra of the metallic (3,3) and (12,0) tubes are also dictated by bound exciton states. The binding energy associated with the first optical transition is 86 meV for the (3,3) tube and about 50 meV for the (12,0) tube. For the (5,0) tube, however, we found that the electron–hole interactions do not create bound excitons: the symmetry of the bands in the (5,0) tube diminishes the attractive (direct) interaction term, which is dominated by the repulsive (exchange) interaction term and is thus unable to bind excitons.

Table 2 shows our *ab-initio* results for the excitation energies of the four metallic tubes we studied, in comparison with measurements. The theoretical results for the lowest optical transition energy are shown at three different levels of approximation: LDA, *GW* and Bethe–Salpeter (BS). At the Bethe–Salpeter level the agreement with experiment is excellent. Moreover, as seen in Fig. 3, a detailed analysis of the lineshape of the absorption spectrum should

Table 2. Lowest optical transition energy of four metallic SWNTs. From [4, 5, 29]

Tube	Theory			Exp.	References
	LDA	*GW*	BS		
(5, 0)	1.13	1.30	1.33	1.37	[31]
(3, 3)	2.83	3.26	3.17	3.1	[31]
(12, 0)	1.84	2.30	2.25	2.16	[32]
(10,10)	1.51	1.89	1.84	1.89	[32, 33]

provide a means to experimentally measure the properties of the predicted bound excitons in metallic nanotubes.

4 Diameter and Chirality Dependence of Exciton Properties

As discussed in the previous section, substantial reduction in the computational effort of *ab-initio* calculations of excitons is achieved if they are restricted to achiral and/or small-diameter tubes [4–6]. However, in carbon-nanotube physics, understanding the diameter and chirality trends of a given property is often as important as the accurate determination of that property for a limited set of tubes. Usually, trends have to be determined from model calculations. But, when a reliable model for trends is coupled with an accurate *ab-initio* theory that determines its parameters, the model acquires quantitative and predictive powers. We describe in this section how one can follow this procedure to extract the full diameter and chirality dependences of several exciton properties in carbon nanotubes [34]. Similar studies along these lines have been made by *Perebeinos* et al. [35], who obtained scaling relations of binding energies and exciton sizes with diameter from model calculations, as described in the contribution by Avouris et al.

We employ a symmetry-based, variational, tight-binding method, based on the effective mass and envelope-function approximations [34]. Gaussian envelope functions impose the localization of the exciton wavefunction in the relative coordinate between electron and hole. The Gaussian width σ is then a good measure of the exciton size and it is the only variational parameter in the problem. We focus on binding energies and spatial extents for excitons associated with the so-called E_{11}^S transitions.

We minimize the exciton energy that is composed of three terms: direct, exchange and kinetic energies, written in a tight-binding basis [34]. We treat singlet excitons only and the Coulomb integrals between atomic orbitals are parametrized by the Ohno formula [36]. The onsite Coulomb repulsion $U_0 = 16\,\text{eV}$ and the dielectric constant $\epsilon = 1.846$ are chosen to reproduce the *ab-initio* values discussed in the previous section for the binding energy and

Table 3. *Ab-initio* and model binding energies for E_{11}^S and E_{22}^S excitons for a few small-diameter SWNTs. From [34]

Tube	E_b^{11} (eV)		E_b^{22} (eV)	
	Ab-initio	Model	*Ab-initio*	Model
(7,0)	0.89	0.87	1.13	1.61
(8,0)	0.99	1.03	0.86	0.92
(10,0)	0.76	0.68	0.95	1.09
(11,0)	0.76	0.76 (fitted)	0.72	0.75

bright–dark exciton splittings for the (11,0) tube and kept constant for all other tubes.

As a test of our model, we compare in Table 3 our variational binding energies with *ab-initio* ones obtained from solving the Bethe–Salpeter equation [4, 5] for a few zigzag tubes. The agreement is excellent, except for the E_{22}^S exciton in the (7,0) SWNT, for which exciton size becomes extremely small ($\sigma = 0.53\,\mathrm{nm}$), owing to the large effective masses, and therefore the envelope-function approximation is not expected to be valid. Notice also that our model correctly captures the distinct family oscillations in the binding energy.

Figure 4a shows the binding energy of the E_{11}^S bright exciton as a function of diameter for 38 SWNTs covering the full range of chiralities. The $(2n+m)$ family indices are indicated in the figure. Notice the appearance of a clear family pattern. As expected, binding energies decrease with tube diameter, but chirality effects are also strong, contributing to about 20 % spread in the binding energies for nanotubes with 1 nm diameter. Excitons in $(2n + m)$ mod 3 = 1 (MOD1) tubes have generally larger binding energies than in $(2n + m)$ mod 3 = 2 (MOD2) tubes, an effect that can be traced to the chirality dependence of the effective masses.

Figure 4b shows the exciton sizes as a function of diameter. Again, as expected, exciton sizes increase with diameter and they show the opposite MOD1-MOD2 trends as compared to the binding energies. Notice that even for tubes as small as 0.5 nm in diameter the E_{11}^S exciton sizes are already several times larger than the carbon–carbon bond, thus justifying the use of the envelope-function approximation.

We provide analytical expressions for diameter and chirality dependences of both binding energies and sizes:

$$E_\mathrm{b} = \frac{1}{d_\mathrm{t}}\left(A + \frac{B}{d_\mathrm{t}} + C\xi + D\xi^2\right) \qquad \sigma = d_\mathrm{t}(E + F\xi + G\xi^2)\,, \tag{5}$$

where d_t is the tube diameter in nm and $\xi = (-1)^\nu \cos 3\theta/d_\mathrm{t}$ captures the chirality dependence. The best fits are given by $A = 0.6724\,\mathrm{eVnm}$, $B = -4.910\times10^{-2}\,\mathrm{eVnm}^2$, $C = 4.577\times10^{-2}\,\mathrm{eVnm}^2$, $D = -8.325\times10^{-3}\,\mathrm{eVnm}^3$, $E = 1.769$, $F = -2.490\times10^{-1}\,\mathrm{nm}$ and $G = 9.130\times10^{-2}\,\mathrm{nm}^2$. These analyti-

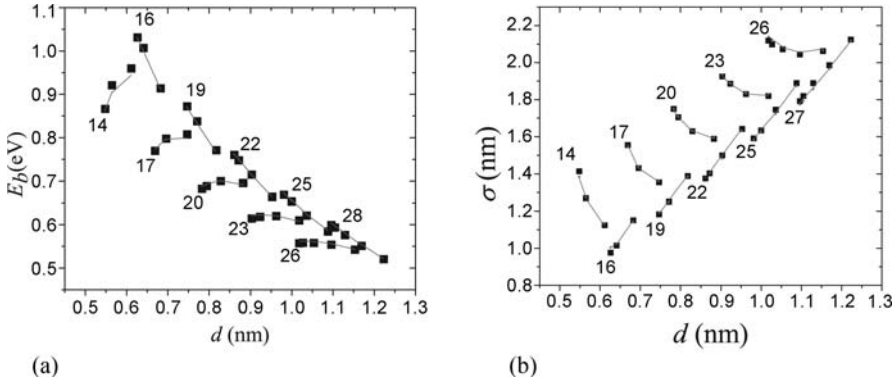

Fig. 4. Binding energies (**a**) and sizes (**b**) for the lowest-energy bright excitons in 38 SWNTs with varying diameter and chirality. The *dots* are our model results and the *lines* represent the analytical fit using (5). The *labels* indicate the $(2n + m)$ families. From [34]

cal fits are the lines in Figs. 4a and b. The agreement between the numerical results and the analytical fit is nearly perfect.

We now compare our results to the available experimental determinations of the exciton binding energies to date. Two-photon spectroscopy has been performed for SWNTs in a polymeric matrix [7, 27] and in D_2O solution wrapped by a surfactant [8]. These environments provide extra screening, so these results should not be directly compared with *ab-initio* theory for isolated tubes. However, in our variational scheme, it is very easy to investigate the influence of screening and to adjust the dielectric constant ϵ to match the experimental results. In fact, we find that binding energies follow very nicely the scaling $E_b \propto \epsilon^{-1.4}$ proposed by *Perebeinos* et al. [35]. Therefore, it is straightforward to apply (5) for SWNTs in *any* environment, provided that one scales the binding energies by using the appropriate phenomenological dielectric constant. For instance, taking $\epsilon = 3.049$ gives binding energies in excellent agreement (standard deviation of 0.02 eV) for all 13 SWNTs measured by *Dukovic* et al. [27]. Similarly, the results of *Maultzsch* et al. [8] for 6 different SWNTs are reproduced with a standard deviation of 0.03 eV using a slightly larger dielectric constant $\epsilon = 3.208$. Such good agreements indicate that the use of a single dielectric constant for all tubes, although certainly not correct, may not be a bad approximation for the exciton ground state of tubes in a narrow range of diameters.

5 Symmetries and Selection Rules of Excitons

An analysis of exciton symmetries in SWNTs is crucial to understand in greater detail many aspects of their optical properties, especially the nature

Table 4. Irreducible representations ($\mathcal{D}$) relevant to the exciton problem for chiral and achiral nanotubes. GWV and LG stand for "group of the wavevector" and "line group" notations, respectively. The dimension (d) of each representation is shown on the *right* for both GWV and LG formalisms. The *last column* describes the wavevector (k), quasiangular momentum ($\tilde{\mu}$) and parity quantum numbers (Π). For chiral tubes, the relevant parity is related to the C_2 operation (Π^{C_2}), whereas for achiral tubes the parity Π is also related to $\sigma_{\rm h}$, $\sigma_{\rm v}$ reflections and inversion i. The GWV notation chooses the parity under i as a quantum number and the LG notation chooses the parity under $\sigma_{\rm h}$ as a quantum number, thus making the translation between the two notations somewhat cumbersome. A zero parity quantum number means that the representation does not have a well-defined parity. From [37]

	GWV		LG		
Chiral	$\mathcal{D}$	d	$\mathcal{D}$	d	$(k, \tilde{\mu}, \Pi^{C_2})$
	$A_1(0)$	1	${}_0A_0^+$	1	$(0, 0, +1)$
	$A_2(0)$	1	${}_0A_0^-$	1	$(0, 0, -1)$
	$(E_{\tilde{\mu}}(k) + E_{-\tilde{\mu}}(-k))$	1	${}_kE_{\tilde{\mu}}$	2	$(\pm k, \pm\tilde{\mu}, 0)$
Achiral	$\mathcal{D}$	d	$\mathcal{D}$	d	$(k, \tilde{\mu}, \Pi^{\sigma_{\rm v}}, \Pi^{\sigma_{\rm h}}, \Pi^{i}, \Pi^{C_2})$
	$A_{1u}(0)$	1	${}_0B_0^-$	1	$(0, 0, -1, -1, -1, +1)$
	$A_{2u}(0)$	1	${}_0A_0^-$	1	$(0, 0, +1, -1, -1, -1)$
	$A_{1g}(0)$	1	${}_0A_0^+$	1	$(0, 0, +1, +1, +1, +1)$
	$A_{2g}(0)$	1	${}_0B_0^+$	1	$(0, 0, -1, +1, +1, -1)$
	$E_{\|\tilde{\mu}\|u}(0)$	2	${}_0E_{\|\tilde{\mu}\|}^{\Pi^{\sigma_{\rm h}}}$	2	$(0, \tilde{\mu}, 0, (-1)^{\tilde{\mu}+1}, -1, 0)$
	$E_{\|\tilde{\mu}\|g}(0)$	2	${}_0E_{\|\tilde{\mu}\|}^{\Pi^{\sigma_{\rm h}}}$	2	$(0, \tilde{\mu}, 0, (-1)^{\tilde{\mu}}, +1, 0)$
	$(B'(k) + B'(-k))$	1	${}_kE_n^A$	2	$(\pm k, n, +1, 0, 0, 0)$
	$(B''(k) + B''(-k))$	1	${}_kE_n^B$	2	$(\pm k, n, -1, 0, 0, 0)$
	$(E_{\|\tilde{\mu}\|}(k) + E_{\|\tilde{\mu}\|}(-k))$	2	${}_kG_{\tilde{\mu}}$	4	$(\pm k, \tilde{\mu}, 0, 0, 0, 0)$

of dark (optically inactive) states and the selection rules for 1-photon and 2-photon transitions, which are used to measure exciton binding energies. [7, 8] In this section, we describe the symmetries of the excitonic states in SWNTs, as well as the selection rules for optical absorption and emission [37].

Two different but equivalent formalisms can be used for describing the symmetry properties of carbon nanotubes: the group of the wavevector and the line groups. Complete descriptions of all symmetry operations, quantum numbers and irreducible representations labeling are available elsewhere, both for the group of the wavevector [38] and line-group [39, 40] formalisms. In this work, we focus on the irreducible representations that are relevant for the exciton problem, described in Table 4. Despite its technical aspect, this table is presented here for a clear definition of the symmetry-related quantum numbers in both group-theory formalisms used in the literature.

The exciton wavefunction can be written as a linear combination of products of conduction (electron) and valence (hole) eigenstates, as shown in (3). For moderately small-diameter nanotubes, the separation between singularities in the single-particle JDOS is large and it is reasonable to consider, as a

first approximation, that only the electronic bands contributing to a given singularity will mix to form the excitonic states [4,5]. This is the ideal situation for employing the usual effective-mass and envelope-function approximations, as we have done in the previous section:

$$\psi^{\mathrm{EMA}}(\boldsymbol{r}_{\mathrm{e}}, \boldsymbol{r}_{\mathrm{h}}) = \sum_{\mathrm{cv}}{}' A_{\mathrm{cv}} \phi_{\mathrm{c}}(\boldsymbol{r}_{\mathrm{e}}) \phi_v^*(\boldsymbol{r}_{\mathrm{h}}) F_\nu(z_{\mathrm{e}} - z_{\mathrm{h}}) \,, \tag{6}$$

where the coefficients A_{cv} are dictated by symmetry. It is important to emphasize that the approximate wavefunctions ψ^{EMA} have the same symmetries as the full wavefunctions ψ. The use of such envelope functions serves merely as a physically grounded guess for the ordering in which the different exciton states appear. The envelope function $F_\nu(z_{\mathrm{e}} - z_{\mathrm{h}})$ provides an ad-hoc localization of the exciton in the relative coordinate $z_{\mathrm{e}} - z_{\mathrm{h}}$ along the axis, as described in the previous section, and ν labels the levels in the 1D hydrogen series [41]. The envelope functions will be either even ($\nu = 0, 2, 4, \ldots$) or odd ($\nu = 1, 3, 5, \ldots$) upon $z \to -z$ operations. The irreducible representation of the excitonic state $\mathcal{D}(\psi^{\mathrm{EMA}})$ is given by the direct product:

$$\mathcal{D}(\psi^{\mathrm{EMA}}) = \mathcal{D}(\phi_{\mathrm{c}}) \otimes \mathcal{D}(\phi_{\mathrm{v}}) \otimes \mathcal{D}(F_\nu) \,, \tag{7}$$

where $\mathcal{D}(\phi_{\mathrm{c}})$, $\mathcal{D}(\phi_{\mathrm{v}})$ and $\mathcal{D}(F_\nu)$ are the irreducible representations of the conduction state, valence state and envelope function, respectively [42]. We applied (7) to study the symmetry of excitons in chiral and achiral (zigzag and armchair) carbon nanotubes [37]. In this review, we will illustrate our procedure with the case of the first optical transition (E_{11}^S) in the most common type of nanotubes, the chiral tubes. We refer the reader to the original article for a description of zigzag and armchair tubes [37].

Figure 5a shows a schematic diagram of the electronic valence and conduction bands with a quasiangular momentum $|\tilde{\mu}|$, for a general chiral SWNT, where the electron and hole states at the band edge are labeled according to their irreducible representations [38]. One can see that there are two electronic bands in chiral tubes, one with the band edge at $k = k_0$ and the other one at $k = -k_0$. In order to evaluate the symmetry of the excitonic states, it is necessary to consider that the Coulomb interaction will mix the two inequivalent states in the conduction band (electrons) with the two inequivalent states in the valence band (holes). These electron and hole states at the van Hove singularities (vHSs) transform as the 1D representations $E_{\tilde{\mu}}(k_0)$ and $E_{-\tilde{\mu}}(-k_0)$ of the C_N point group [38], where we have considered that conduction- and valence-band extrema occur at the same $k = k_0$. Taking this into consideration, the symmetries of the exciton states with the $\nu = 0$ envelope function, which transforms as the $A_1(0)$ representation, can be obtained using the direct product in (7):

$$\begin{aligned} \big(E_{\tilde{\mu}}(k_0) + E_{-\tilde{\mu}}(-k_0)\big) \otimes \big(E_{-\tilde{\mu}}(-k_0) + E_{\tilde{\mu}}(k_0)\big) \otimes A_1(0) \\ = A_1(0) + A_2(0) + E_{\tilde{\mu}'}(k') + E_{-\tilde{\mu}'}(-k') \,, \end{aligned} \tag{8}$$

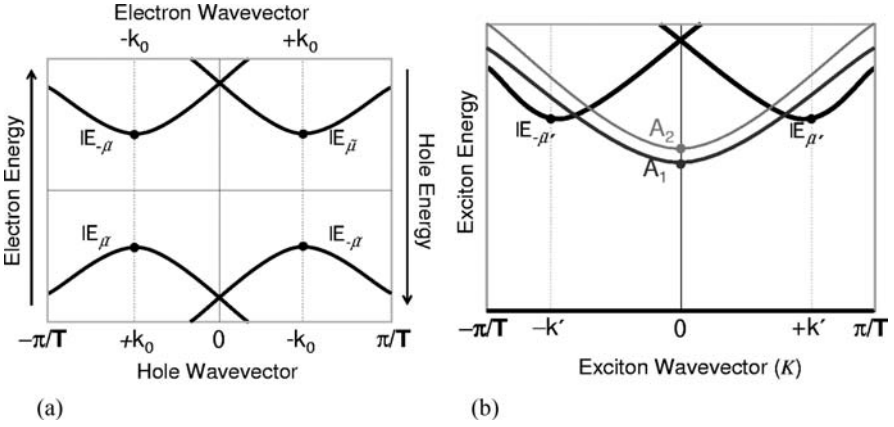

Fig. 5. Diagrams for the electronic bands and symmetries for (**a**) chiral SWNTs and for (**b**) their respective excitonic bands. The electron, hole and exciton states at the band edges are indicated by a *solid circle* and labeled according to their irreducible representation. The electronic and excitonic band structures shown here are only pictorial. Group theory does not order the values for the eigenenergies. From [37]

where k' and $\tilde{\mu}'$ are the exciton linear momenta and quasiangular momenta, respectively. Therefore, group theory shows that the lowest-energy set of excitons is composed of four exciton bands, shown schematically in Fig. 5b. The mixing of electron and hole states with opposite quantum number k ($k_\mathrm{e} = \pm k_0$, $k_\mathrm{h} = \mp k_0$) will give rise to excitonic states that transform as the A_1 and A_2 representations of the D_N point group. These representations correspond, respectively, to states even and odd under the C_2 rotation. These excitons will have a band minimum at the Γ point. The excitonic states formed from electrons and holes with $k_\mathrm{e} = k_\mathrm{h} = \pm k_0$ will transform as the $E_{\tilde{\mu}'}(k')$ and $E_{-\tilde{\mu}'}(-k')$ 1D irreducible representations of the C_N point group, with an angular quantum number $\tilde{\mu}' = 2\tilde{\mu}$. These exciton states will have a band edge at $k' = 2k_0$ if $2k_0$ is within the 1st Brillouin zone (1BZ).

Let us now consider higher-energy exciton states $\nu > 0$ for the E_{11} JDOS (joint density of states) in chiral tubes. For ν even, the resulting decomposition is the same as for $\nu = 0$, since the envelope function also has A_1 symmetry. For odd values of ν, the envelope function will transform as A_2, but that will also leave the decomposition in (8) unchanged. The result is still the same if one now considers higher-energy exciton states derived from higher singularities in the JDOS (E^S_{22} or E^S_{33} transitions). Therefore, (8) describes the symmetries of all exciton states in chiral nanotubes associated with E^S_{ii} transitions.

To obtain the selection rules for the optical absorption of the excitonic states, it is necessary to consider that the ground state of the nanotube transforms as a totally symmetric representation (A_1) and that only $K = 0$

excitons can be created due to linear momentum conservation. For light polarized parallel to the nanotube axis, the interaction between the electric field and the electric dipole moment in the nanotube transforms as the A_2 representation for chiral nanotubes [38]. Therefore, from the 4 excitons obtained for each envelope function ν, only the A_2 symmetry excitons are optically active for parallel polarized light, the remaining three being edark states. For 2-photon excitation experiments, the excitons with A_1 symmetry are accessed ($A_2 \otimes A_2 = A_1$), and thus, there will also be one bright exciton for each ν envelope function. Thus, the explanation of the results obtained in 2-photon excitation experiments [7, 8] does not rely on symmetry-selection rules and should rather be related to oscillator-strength arguments. For instance, the bright exciton associated with odd ν states in chiral tubes can be understood as a product between an even Bloch function and an odd envelope function. Therefore, although being formally bright, we expect a very low oscillator strength for these excitons, since an odd envelope function should give a very low probability for finding an electron and a hole at the same position for recombination.

6 Radiative Lifetime

We now consider the radiative lifetimes of excitons in carbon nanotubes. This topic has been addressed in the literature both from theoretical [43, 44] (see also the contribution by Avouris et al.) and experimental perspectives [45–47] (see also the contribution by Ma et al.). We begin with the intrinsic radiative lifetime, i.e., exciton decay into emitted photons due to the coupling to the electromagnetic field. An exciton in a structurally perfect and very long nanotube has a well-defined center of mass crystal momentum $\hbar Q$ along the nanotube axis. Let $|S(Q);0\rangle$ be the state where the nanotube is excited into exciton S with momentum $\hbar Q$ and the electromagnetic field is in its vacuum. Let $|0;\boldsymbol{q}\lambda\rangle$ denote the state with the nanotube in its ground state and an emitted photon of momentum $\mathbf{q}$ and polarization λ. The transition rate is given by the Fermi golden rule expression

$$\gamma_S(Q) = \frac{2\pi}{\hbar} \sum_{\boldsymbol{q},\lambda} |\langle 0;\boldsymbol{q}\lambda|\hat{H}^{\text{int}}|S(Q);0\rangle|^2 \delta(\hbar\Omega_S(Q) - \hbar c|\boldsymbol{q}|)\,. \tag{9}$$

The expression $\Omega_S(Q)$ means that the exciton energy is momentum dependent. In the Coulomb gauge, $\hat{H}^{\text{int}} = -\frac{1}{c}\hat{A}\ \ \hat{J}$ is the coupling of the electromagnetic vector potential operator $\hat{A}$ to the electron current operator $\hat{J}$.

To proceed, we use the following facts: 1. during decay, only momentum along the nanotube axis is conserved: this means that the component of the photon $\boldsymbol{q}$ along the nanotube axis equals Q; 2. for optical photons, the wavelength is large compared to interatomic distances, and we use the dipole

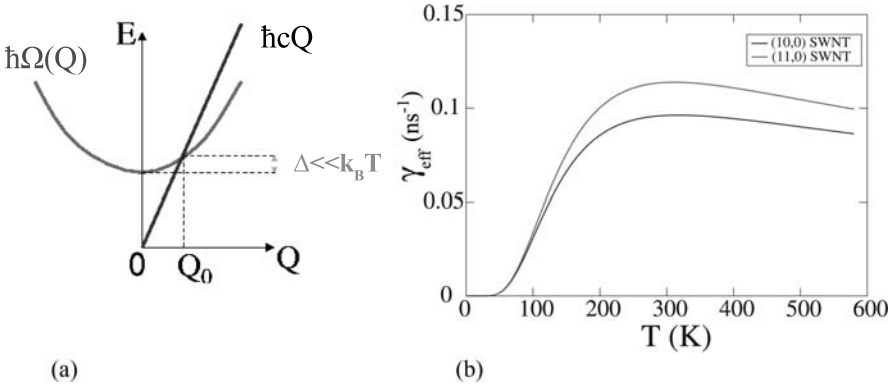

Fig. 6. (**a**) Exciton energy relation versus momentum $\hbar Q$ (*parabolic curve*) and photon light line (*straight line*). The momentum Q_0 is where the two cross. Only excitons with $|Q| \leq Q_0$ can decay into photons while conserving energy and momentum. Δ is the corresponding range of exciton energies and is much smaller than thermal energies at room temperature. (**b**) Exciton effective radiative decay rate versus temperature including phase-space considerations (radiative zone effect) and dark excitons. The *upper light grey curve* is for (11,0) and the *lower dark grey curve* for (10,0). From [43]

approximation for transition matrix elements; and 3. due to strong depolarization effects in nanotubes, only transition dipoles parallel to the nanotube axis have appreciable size. After some manipulations [43], we arrive at the decay rate

$$\gamma_S(Q) = \begin{cases} \dfrac{2\pi e^2 \Omega_S(0)^2}{\hbar c^2} \dfrac{\mu_S^2}{a} \dfrac{\Omega_S(Q)^2 - c^2 Q^2}{\Omega_S(Q)^2} & \text{if } |Q| \leq Q_0 \\ 0 & \text{if } |Q| > Q_0 \end{cases} . \tag{10}$$

The intensive quantity μ_S^2/a is the squared exciton transition dipole matrix element along the nanotube per unit length of the nanotube (a is the nanotube unit cell size). As shown in Fig. 6a, the wavevector Q_0 is defined by the light cone crossing condition $\hbar\Omega_S(Q_0) = \hbar c Q_0$: it is the maximum momentum allowed for an exciton that can decay radiatively, while obeying both energy and momentum conservation. Clearly, the decay rate, or its inverse the lifetime, is momentum dependent. This reflects the phase-space for decay: for $|Q| < Q_0$, the photon has momentum $\boldsymbol{q}_\perp$ in the orthogonal directions in order to satisfy energy conservation $\hbar\Omega_S(Q) = \hbar c\sqrt{\boldsymbol{q}_\perp{}^2 + Q^2}$. The magnitude of $\boldsymbol{q}_\perp$ and hence the number of final states varies with Q.

Table 5 shows the calculated intrinsic radiative lifetimes for a set of small-diameter semiconducting carbon nanotubes. Lifetimes are on the order of tens of ps, ∼1000 times smaller than those of typical molecules. The reason is that excitons in ideal nanotubes are coherent quantum states: while their

Table 5. Lowest-energy bright exciton lifetimes in semiconducting carbon nanotubes. μ^2/a is the dipole transition strength per unit length, $\hbar\Omega(0)$ is the exciton energy for the zero momentum ($Q = 0$) exciton, $\tau_{\rm i}$ is the intrinsic radiative lifetime, $\tau^b_{\rm eff}$ is the lifetime including thermal exciton distribution effects at 300 K, and $\tau_{\rm eff}$ is the effective lifetime including, in addition, the effect of dark excitons. From [43]

Tube	μ^2/a (a.u.)	$\hbar\Omega(0)$ (eV)	$\tau_{\rm i}(0)$ (ps)	$\tau^b_{\rm eff}$ (ns)	$\tau_{\rm eff}(0)$ (ns)
(7,0)	2.8	1.20	12.8	1.1	—
(8,0)	2.8	1.55	8.1	1.0	—
(10,0)	2.8	1.00	19.1	1.8	10.4
(11,0)	2.5	1.21	14.3	1.7	8.8

dipole strengths per unit length (see Table 5) are rather typical of molecular systems, a decaying exciton has these dipoles radiating in phase over a length scale set by the photon wavelength λ. This enhances emission rates by $\sim \lambda/a$, which is ~ 1000 for optical wavelengths.

There are many reasons why this intrinsic lifetime is much shorter than what will be observed experimentally. Clearly the presence of defects will reduce the length scale of exciton coherence thus reducing intrinsic decay rates and increasing lifetimes. Even in defect-free nanotubes, thermal atomic vibrations reduce the coherence length. If spin-flip mechanisms exist (e.g., through magnetic defects or multiple exciton collisions), spin singlet excitons can be converted into triplet excitons that can not decay due to spin-selection rules (in practice, spin-orbit perturbations make triplet lifetimes finite but very long).

Here, however, we will be considering two significant effects operative for singlet excitons in perfect nanotubes and excluding atomic vibrations. First, we have seen above that excitons can couple to photons only inside the radiative region $|Q| \leq Q_0$: this is true for decaying excitons as well as those created by radiation. A simple estimate of Q_0 based on an effective mass expansion comes from $\hbar\Omega(Q_0) \cong \hbar\Omega(0) + \hbar^2 Q_0^2/2M^* = \hbar c Q_0$ (see Fig. 6a). Due to the large value of the speed of light c, Q_0 is quite small and is $\sim$ 1/100th the size the first Brilouin zone for a reasonable effective mass. Thus, excitons are created inside the small region $|Q| \leq Q_0$, and if we assume that they thermalize on a timescale faster than the intrinsic radiative lifetime $\tau_{\rm i} \sim$ 10 ps, then most excitons leave the radiative region and are effectively dark. Only excitons that "wander" into the radiative region $|Q| \leq Q_0$ can decay. An actual calculation uses a Boltzmann distribution of exciton momenta and averages the decay rate of (10) over the thermal distribution [43]. For a temperature of 300 K, one arrives at the lifetimes $\tau^{\rm b}_{\rm eff}$ in Table 5. The lifetimes are increased by roughly a factor of ~ 100.

Secondly, so far we have only discussed optically bright excitons, i.e., excitons that have nonzero dipole transition matrix elements. We have seen that spin-singlet excitons with zero transition dipole (dark excitons) exist by

reasons of symmetry. Our first-principle calculations together with symmetry considerations show that in semiconducting nanotubes, there is always at least one dark singlet exciton below the singlet bright exciton [37, 43]. The calculated energy spacings are roughly 30 meV for the (10,0) and (11,0) nanotubes and have a strong dependence on diameter [34]. Hence, if excitons thermalize faster than the intrinsic lifetime, most will inhabit the lower-energy dark states and be radiatively inactive. This lifetime correction is straightforward to calculate using a weighted sum over decay rates multiplying thermal occupation factors. The final effective lifetimes in Table 5 are τ_{eff} and include the dark excitons at 300 K. Lifetimes increase further by a factor of ~ 10.

The main reason that these dark excitons are generically lower in energy than the bright ones is due to the nature of the exchange contribution to exciton energies. For any exciton, the exchange-energy contribution is

$$E_S^x = 2 \int \mathrm{d}\boldsymbol{r} \int \mathrm{d}\boldsymbol{r}' \frac{\chi_S(\boldsymbol{r},\boldsymbol{r})^* \chi_S(\boldsymbol{r}',\boldsymbol{r}')}{|\boldsymbol{r}-\boldsymbol{r}'|} \,. \tag{11}$$

This is a positive Coulombic self-energy where $\chi_S(\boldsymbol{r},\boldsymbol{r})$ plays the role of a density. Now $\chi_S(\boldsymbol{r},\boldsymbol{r})$, given by (3), is the amplitude to find the electron and hole at the same position $\boldsymbol{r}$. The orthogonality of electron and hole states means that the integral of $\chi_S(\boldsymbol{r},\boldsymbol{r})$ is zero so that it represents a neutral distribution. Hence, the dominant part of the exchange contribution comes from the dipole–dipole term in the integral. Interestingly, this dipole is the same as the transition dipole μ_S given by

$$\mu_S = -e\langle 0|\hat{\boldsymbol{r}}|S\rangle = -e \int \mathrm{d}r\, \boldsymbol{r}\, \chi(\boldsymbol{r},\boldsymbol{r}) \,. \tag{12}$$

For a bright exciton, the exciton transition dipole μ_S is nonzero and we then expect a positive and significant exchange energy. A dark exciton has $\mu_S = 0$ and will have a small or vanishing exchange energy. As described in the contribution by Kono et al., recent experimental determinations of bright–dark energy splittings employ a combination of magnetic brightening of the dark excitons and temperature tuning of the exciton populations in each level [48, 49]. The measured splittings for nanotubes in solution are somewhat smaller than the *ab-initio* values for isolated SWNTs.

Finally, we can compute the full temperature dependence of exciton decay rates including both effects as shown in Fig. 6b. The decay rate first increases and then decreases with temperature due to competition between the above two effects. The phase-space effect stemming from the small size of the radiative zone $|Q| \leq Q_0$ makes for decreasing decay rates with increasing temperature as the thermal distribution spreads out in Q. The effect of low-energy dark excitons leads to increasing decay rates with increasing temperature as the bright exciton becomes thermally occupied. Each effect dominates the respective temperature regime. (See also the contribution by Kono et al.)

7 Pressure, Strain and Temperature Effects

Understanding the temperature, hydrostatic pressure, strain shifts of optical (excitonic) transition energies in carbon nanotubes provides important information about the nature of the band-edge electronic states and their coupling to static and dynamic lattice distortions. Likely, the most important contribution to the excitonic energy shifts under pressure, strain and temperature comes from the shifts in the bandgap (E_{g}). Strain [50–54], pressure [52] and temperature [55, 56] shifts of the bandgap have recently been theoretically predicted for isolated single-wall carbon nanotubes (SWNTs). A number of experiments have also addressed these issues [53, 54, 56–61] (see also the contribution by Lefebvre et al.).

Both in the case of pressure and temperature, clear "family behaviors" (i.e., SWNTs with the same value of $(n-m)$ behaving similarly) have been observed and explained. In particular, it is found that the pressure induced bandgap shifts have different signs for different nanotube families, in contrast with traditional semiconductors. Similar results occur for the temperature induced shifts at low temperatures.

Figure 7 summarizes the calculated results for the pressure coefficients of the bandgap in the linear regime ($\mathrm{d}E_{\mathrm{g}}/\mathrm{d}P$) for several SWNTs with various diameters and chiralities. Density-functional theory (DFT) is used to obtain the diameter-dependent elastic constants (and therefore the atomic relaxations under hydrostatic pressure conditions) and tight-binding (TB) electronic structure calculations to calculate $\mathrm{d}E_{\mathrm{g}}/\mathrm{d}P$. Details of the methodology are described in [52]. Figure 7a shows that $\mathrm{d}E_{\mathrm{g}}/\mathrm{d}P$ displays a very strong family behavior and Fig. 7b shows that such an apparently complicated dependence on diameter and chirality can be described by a simple phenomenological equation:

$$\frac{\mathrm{d}E_{\mathrm{g}}}{\mathrm{d}P} = A + B(-1)^{\nu} d_{\mathrm{t}} \cos(3\theta)\,, \tag{13}$$

where d_{t} and θ are the SWNTs diameter and chiral angle, respectively, $\nu = (n-m) \bmod 3$, and A and B are constants. Analytical expressions for A and B can be obtained within a single-orbital TB model. In fact, in a subsequent study [56], (13) is generalized to describe the energy shift of any E_{ii} transition with respect to a general combination of radial (ϵ_{r}) and axial (ϵ_{z}) strains:

$$\Delta E_{ii} = -2E_{ii}\epsilon_{\mathrm{r}} - 3\gamma_0(-1)^{i}(-1)^{\nu}(\epsilon_{\mathrm{r}} - \epsilon_{\mathrm{z}})\cos(3\theta)\,, \tag{14}$$

where γ_0 is the hopping energy between p orbitals, $i = 1, 2, 3, 4, \ldots$ for E_{11}^{S}, E_{22}^{S}, E_{11}^{M}, E_{33}^{S}, etc., and ν can be extended to metallic tubes: $\nu = 1$ and 2 for the lower and upper metallic transitions, respectively.

The two terms in the expression (13) for $\mathrm{d}E_{\mathrm{g}}/\mathrm{d}P$ can be explained in terms of the interplay of the anisotropic deformations introduced by hydrostatic pressure and the anisotropy of the band-edge states themselves. Carbon

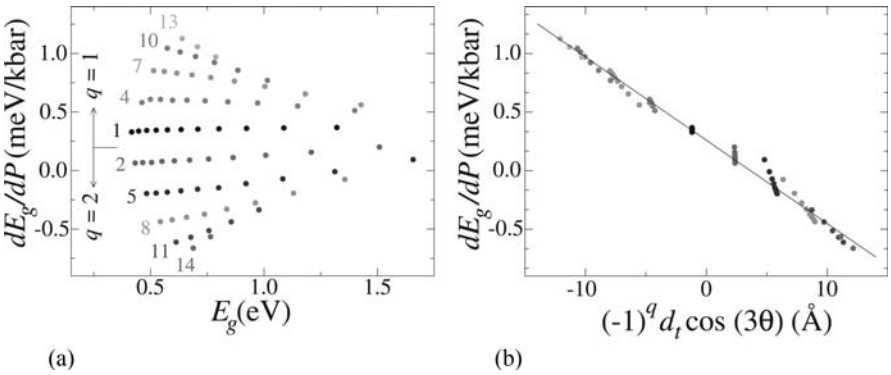

Fig. 7. (**a**) Bandgap pressure coefficient as a function of the energy gap for a large number of semiconducting SWNTs. Tubes are grouped into different shades of grey according to their $(n - m)$ family. The values of $(n - m)$ for each family are also shown in the figure. (**b**) Collapse of $\mathrm{d}E_\mathrm{g}/\mathrm{d}P$ values to a single line when plotted against $(-1)^\nu d_\mathrm{t} \cos(3\theta)$. From [52]

nanotubes have different elastic constants along the circumferential and axial directions: Upon hydrostatic pressure conditions, the radial strains are larger than axial ones [52]. An isotropic compression of the tubes would lead, according to (14) to a constant and positive $\mathrm{d}E_\mathrm{g}/\mathrm{d}P$ for all tubes, due to the overall increase in the Fermi velocity of graphene. This is the meaning of the first term, that we can now call the "isotropic contribution" to $\mathrm{d}E_\mathrm{g}/\mathrm{d}P$. However, since circumferential deformations are larger, gap shifts will be more sensitive to the circumferential character (bonding or antibonding) of the band-edge states. For the $\nu = 1$ SWNTs, circumferential compression will lead to the valence (conduction) band state shifting down (up) in energy due to its bonding (antibonding) character along the circumference. Therefore, this effect will lead to a gap increase in the $\nu = 1$ SWNTs. The situation for $\nu = 2$ SWNTs is precisely the opposite, leading to a gap decrease. This is the physics behind the second term in (13) that we can now call the "anisotropic contribution" to $\mathrm{d}E_\mathrm{g}/\mathrm{d}P$.

We now turn to the analysis of temperature induced shifts. Figure 8 shows the calculated thermal shifts of the bandgap for 18 different SWNTs, with varying diameter and chirality. The shifts are calculated using a "frozen-phonon" technique to obtain the electron–phonon couplings [55]. Although the high-temperature behavior shows a universal decrease of the bandgap with temperature (just like in 3D semiconductors), the low-temperature behavior shows a strong family dependence, with unusual nonmonotonic gap shifts for some tubes. This behavior can be traced to the contribution of a few low-frequency phonon branches ("shape-deformation modes") to the thermal shift [55] and the family dependence of the temperatures shifts at such low

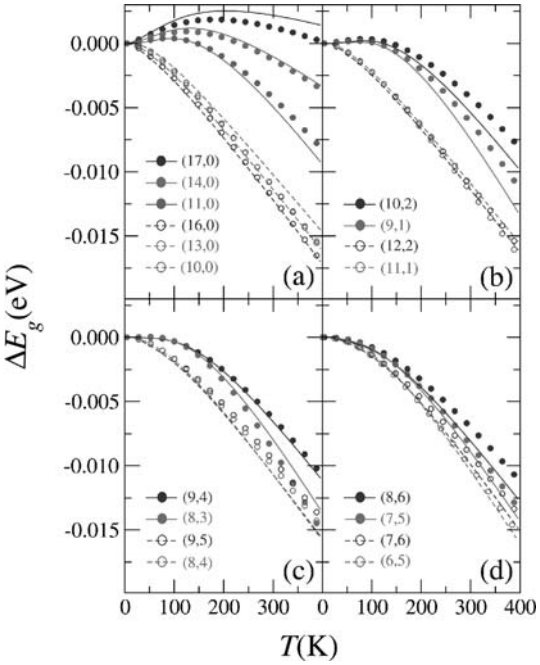

Fig. 8. Calculated $\Delta E_{\mathrm{g}}(T)$ for 18 different SWNTs with varying diameters and chiralities. *Full dots* and *lines* correspond to $\nu = 2$ SWNTs, whereas *open dots* and *dashed lines* correspond to $\nu = 1$ SWNTs. *Dots* are numerical results and *lines* are fits to model expressions. From [55]

temperatures share the same physical origin that we have just described for the pressure shifts, i.e., the anisotropy of bonding and antibonding character of the band-edge states [62]. (See also the contribution by Lefebvre et al.)

8 Related Structures: Boron-Nitride Nanotubes and Graphene Nanoribbons

Many-electron effects are found to be similarly dominant in the quasiparticle excitation and optical spectra of other quasi-one-dimensional systems such as the boron-nitride nanotubes, small-diameter Si nanowires, and graphene nanoribbons. Figure 9 shows the calculated optical spectrum of a (8,0) BN nanotube [26]. As in the case of the carbon nanotubes, electron–hole interactions give rise to a series of sharp lines in the absorption spectrum due to strongly bound exciton states, and the optical strength is virtually completely shifted to these exciton states from the continuum part of the spectrum. For the (8,0) BN nanotube, which has the same diameter as the (8,0) carbon SWNT, the binding energy of the lowest-energy exciton is over

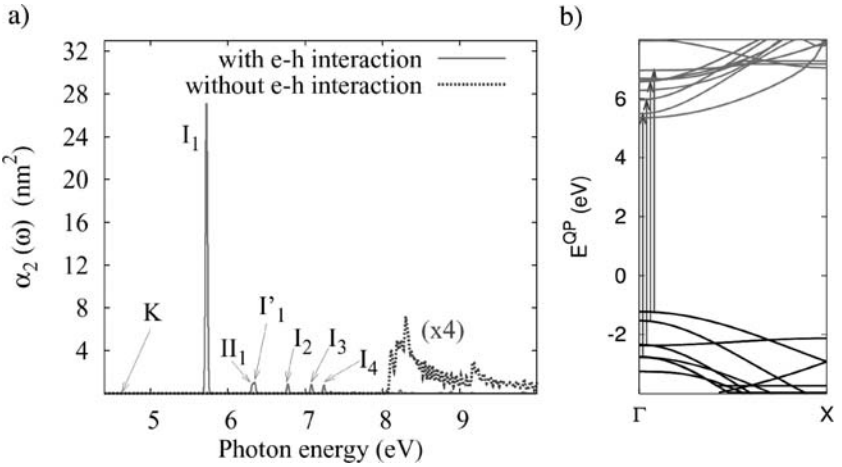

Fig. 9. (**a**) Absorption α_2 spectrum of a (8,0) single-walled BN nanotube. The imaginary part of the polarizability per tube is shown, with a Gaussian broadening factor of 0.0125 eV. (**b**) Quasiparticle band structure, showing the different sets of interband transitions contributing to the lowest-energy excitons. From [26]

2 eV. This is consistent with the fact that the BN nanotubes are wide-gap insulators. Unlike the carbon SWNT case, the lowest-energy exciton here is, however, composed almost in equal weight of 4 sets of interband transitions, as indicated on Fig. 9b.

Figure 10 shows the exciton wavefunction of the lowest-energy exciton of the (8,0) BN nanotube. It has a root-mean-square radius along the tube axis that is only 0.37 nm. This is to be compared to a root-mean-square radius of 0.86 nm for the lowest-energy exciton in the (8,0) carbon nanotube (see Fig. 2), consistent with the larger binding energy in the BN nanotube. Further, as seen in Fig. 10c, the exciton wavefunction for the BN case does not extend around the circumference of the tube. This spatial localization of the electron–hole separation around the circumference is a consequence of the mixing of different subband transitions into forming the exciton state. Experimentally, there have been only limited studies on the optical response of the BN nanotubes [63, 64]. These measurements are inconclusive in terms of comparing with each other and with theory. On the other hand, similarly large quasiparticle and electron–hole interaction effects in the optical spectra of small-diameter Si nanowires have been found. For example, for a 1.2-nm diameter hydrogen-passivated Si nanowire, the excitonic binding energy is again very large, with a value of nearly 1 eV [65].

Another related class of quasi-one-dimensional systems is the graphene nanoribbons. As emphasized throughout this volume, graphene (a single atomic layer of graphite) is a zero-gap semiconductor whose electronic structure near the Fermi energy is given by linear dispersing bands that cross at

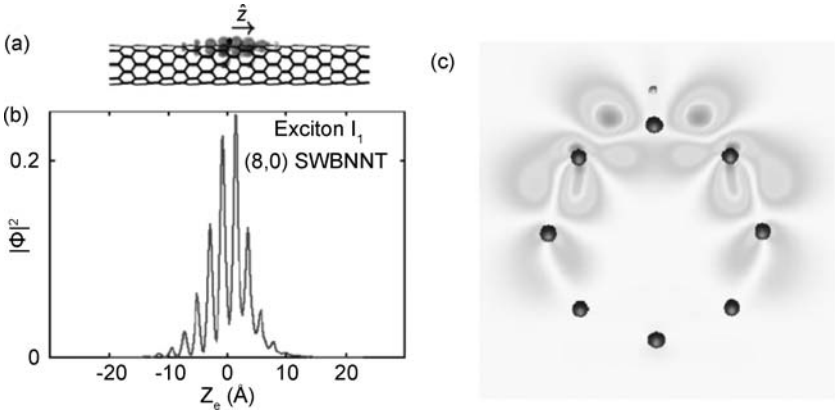

Fig. 10. Wavefunction squared of the lowest-energy bright exciton in the (8,0) BN SWNT, showing the electron probability distribution for a fixed hole. (**a**) Definition of the electron axial coordinate z_e, as measured from the hole position (*small dot*). (**b**) Wavefunction squared along the axis. (**c**) Cross-sectional electron probability isosurfaces. From [26]

two inequivalent points, K and K', in the hexagonal Brillouin zone (see the contribution by Charlier et al.). This unique feature makes the low-energy electrons of graphene behave like a system of two-dimensional (2D) massless Dirac fermions and explains many of the electronic properties of SWNTs. In fact, single-layer graphene has been fabricated and measured recently. These measurements confirmed the 2D massless Dirac fermion behavior and showed novel properties such as new spacing in the integer quantum Hall effect and a Berry-phase contribution to transport properties [66, 67]. One expects that nanoscale ribbons of graphene would also possess interesting properties and have the promise of useful applications.

We consider here nanoribbons of graphene with the dangling σ bonds passivated by hydrogen or other atoms or molecules. As in the case of carbon nanotubes, graphene nanoribbons of different widths and edge shapes are possible. Of the homogeneous edged graphene nanoribbons, there are two common types – one is with armchair-shaped edges (the armchair graphene nanoribbons AGNR), and the other is with zigzag-shaped edges (the zigzag graphene nanoribbons ZGNR). These nanoribbons are labeled as n-AGNR for an armchair-shaped ribbon with n dimer rows forming the width of the ribbon, and n-ZGNR for a zigzag ribbon with n zigzag chains forming its width. Within simple tight-binding theory [68–71] or the free massless Dirac fermion model [72–74], the armchair graphene nanoribbons are metals if $n = 3p + 2$, where p is an integer; otherwise it is a semiconductor. For the zigzag nanoribbons, these models yield a metallic system with very special edge states on both sides of the ribbon regardless of its width [68–78].

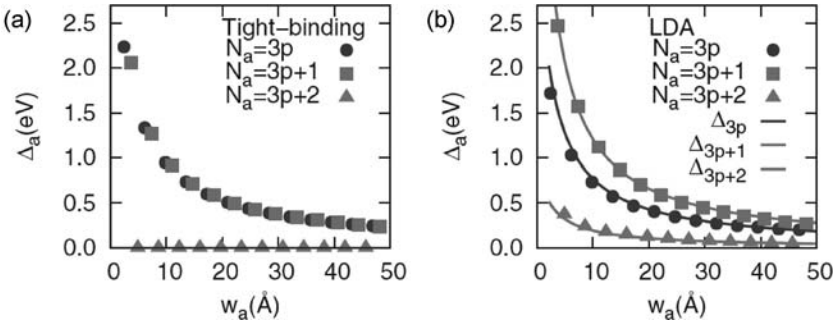

Fig. 11. Calculated bandgaps of Na-AGNRs as a function of the width (w_a) obtained (**a**) from tight-binding calculations and (**b**) from density-functional calculations. From [79]

Calculations based on DFT show, however, that GNRs with hydrogen-passivated armchair- or zigzag-shaped edges both always have nonzero and direct bandgaps. The origins of the bandgaps for the different types of homogeneous edges vary. The bandgaps of AGNRs originate from quantum confinement, and edge effects play a crucial role [79–81]. For the ZGNRs, the bandgaps arise from a staggered sublattice potential due to spin-ordered states at the edges [79, 80]. Although the ribbon widths W_a and energy bandgaps Δ_a of the GNRs are related to each other primarily in inverse proportion, there is a rich structure in the ratio of the proportionalities as in the behavior of carbon nanotubes, as shown in Fig. 11. For the AGNRs, analytic scaling rules for the size of the bandgaps as a function of width have been obtained [79]. The results from the analytical expressions are in good agreement with first-principles calculations, and are useful in analyzing experiments and in studying trends. As in the nanotubes, many-electron effects are expected to be very important in the quasiparticle and optical excitation spectra of the graphene nanoribbons. These effects need to be considered for quantitative understanding of the properties of the nanoribbons. As seen in Fig. 12, *GW* calculations of the quasiparticle bandgaps in the AGNRs show significant enhancements as compared to the DFT Kohn–Sham bandgaps, very similar to the effects observed in carbon nanotubes [82].

Another interesting and potentially useful phenomenon associated with the GNRs is that the ZGNRs have been predicted to become half-metals under a transverse external electric field [80]. In this state, the carriers at the Fermi energy are 100 % spin-polarized, and the spin could be tuned with an external electric field. As mentioned above, if one neglects magnetic effects, the ZGNRs are found to be metals due to the existence of a half-filled, doubly degenerate edge-state band at the Fermi energy, with one state localized on each of the edges. Inclusion of spin effects in local spin-density approximation (LSDA) calculations, however, shows that the ZGNRs have a magnetic ordered insulating ground state that is ferromagnetically coupled along one

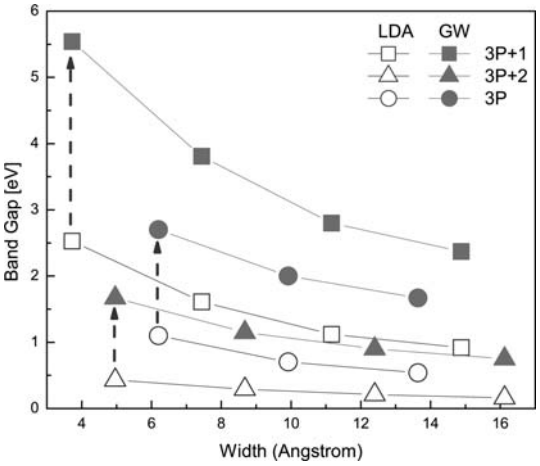

Fig. 12. Calculated bandgaps of AGNRs obtained from Kohn–Sham eignvalues within LDA (*open symbols*) and from quasiparticle energies within GW approximation (*closed symbols*). From [82]

edge and antiferromagnetically coupled across the edges, with a bandgap of about a few tenths of an eV depending on the width of the ribbon. Application of an external electric field transverse to the ribbon length splits the antiferromagnetic spin-up/spin-down degeneracy of the edge states, resulting in the occupied and unoccupied states of one spin type moving toward the middle of the gap and the occupied and unoccupied states of the opposite spin type moving away from the middle of the gap, as shown in Fig. 13. Above a certain critical field strength (that depends on the ribbon width), the gap for one spin type closes, resulting in a metallic state with 100 % spin-polarized carriers or half-metallicity. One can also envision achieving half-metallicity at a lower field by doping the system with carriers. Moreover, the spin polarization of the carriers may be reversed by reversing the direction of the applied electric field.

The physical origin of this phenomenon is associated with the potential drop across the ribbon induced by the external electric field. Because the edge states are ferromagnetically coupled along one edge and antiferromagnetically coupled across the ribbon, in the presence of a transverse electric field, the energies of the occupied (α-spin) and unoccupied (β-spin) edge states on one side are shifted relative to the energies of the occupied (β-spin) and unoccupied (α-spin) edge states on the other side. This shift in energies results in the closing of the gap for one spin type and the opening of the gap for the other spin type. Since the effect is due to the induced potential drop across the ribbon, it should exhibit a systematic behavior as a function of the applied field strength and the width of the ribbon. This is illustrated in Fig. 13b where the bandgaps of ZGNRs with three different widths ($n = 8$, 16 and 32)

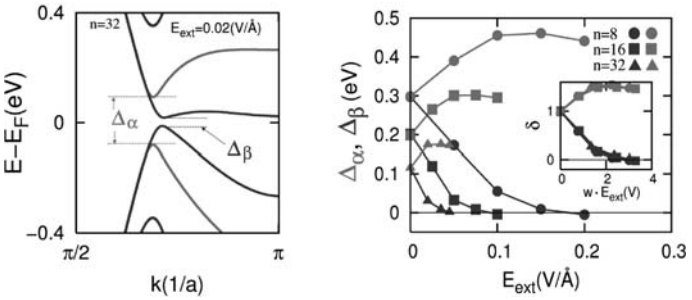

Fig. 13. Energy bands of n-ZGNRs in a transverse electric field obtained from LSDA calculations. Δ_α and Δ_β denote the bandgaps of the two spin types. *Left panel:* energy bands of a 32-ZGNR in a field of 0.2 V/nm. *Right panel:* energy gaps as a function of the electric field strength. The *inset* shows the normalized gap δ as a function of the potential drop wE_{ext} across the ribbon. From [80]

are shown as a function of the external field strength. As expected, it is proportionally easier to make the system into a half-metal for wider ribbons. In particular, as shown in the inset, the normalized bandgaps Δ (defined as the bandgap in the presence of the field divided by the gap without the field) as a function of the potential-drop collapse to a single universal curve, confirming this physical picture.

9 Conclusion

We conclude this chapter with a brief mention of several topics that are of considerable interest and warrant further exploration. A more comprehensive understanding of exciton binding and binding energies, particularly in metallic nanotubes, requires further experimental work. Theory has shown that spin-singlet dark excitons are ubiquitous in nanotubes and can drastically affect quantum yields and luminescent properties. Extending the experimental study employing methods that break symmetry to "brighten" the dark excitons (thermal vibrations, magnetic fields, or controlled introduction of defects) can play an important role. Another topic that we have not emphasized is the spin-triplet excitons. *Ab-initio* theoretical results are available on these exciton states [43, 44]. Triplet excitons have lower energies, extremely long lifetimes, and provide a separate reservoir of dark states. Singlet–triplet conversion can be affected by magnetic defects as well as multiexciton collision processes. Exploration of splitting and tuning of triplet exciton energies with magnetic fields would provide a separate avenue for control. In a related note, first-principles work on exciton–phonon interactions is needed to further the understanding of exciton and luminescent dynamics. Another wide-open field is the *ab-initio* studies and experimental probes of exciton–exciton interactions in the SWNTs. Other interesting avenues of inquiry involve going

beyond the single-wall nanotubes. Experiment and theory on photoexcitations in multiwall nanotubes is a largely unexplored area and may provide complementary or new physics. Similarly, detailed studies of the photophysics in graphene nanoribbons remain to be carried out, both in theory and experiment; and one expects strong and rich many-electron effects in these systems also.

Acknowledgements

We thank our collaborators E. B. Barros, L. X. Benedict, M. L. Cohen, J. Deslippe, C.-H. Park, D. Prendergast, Y.-W. Son, P. Tangney and L. Yang. C. D. Spataru acknowledgements support from the Nanoscale Science and Engineering Initiative of the National Science Foundation under NSF Award Numbers CHE-0117752 and CHE-0641523, and by the New York State Office of Science, Technology, and Academic Research (NYSTAR). R. B. Capaz acknowledgements financial support from Brazilian agencies CNPq, FAPERJ, Instituto de Nanociências and Rede Nacional de Pesquisa em Nanotubos de Carbono. This work was supported by National Science Foundation Grant No. DMR04-39768 and by the Director, Office of Science, Office of Basic Energy Sciences, Division of Materials Sciences and Engineering Division, U.S. Department of Energy under Contract No. DE- AC02-05CH11231. Computational resources have been provided by NPACI and NERSC.

References

[1] A. Jorio, C. Fantini, M. A. Pimenta, R. B. Capaz, G. G. Samsonidze, G. Dresselhaus, M. S. Dresselhaus, J. Jiang, N. Kobayashi, A. Gruneis, R. Saito: Resonance Raman spectroscopy (n,m)-dependent effects in small-diameter single-wall carbon nanotubes, Phys. Rev. B **71**, 075401 (2005) 196

[2] S. M. Bachilo, M. S. Strano, C. Kittrell, R. H. Hauge, R. E. Smalley, R. B. Weisman: Structure-assigned optical spectra of single-walled carbon nanotubes, Science **298**, 2361 (2002) 196, 201, 202

[3] T. Ando: Excitons in carbon nanotubes, J. Phys. Soc. Jpn. **66**, 1066 (1997) 196, 201

[4] C. D. Spataru, S. Ismail-Beigi, L. X. Benedict, S. G. Louie: Excitonic effects and the optical spectra of single-walled carbon nanotubes, Phys. Rev. Lett. **92**, 077402 (2004) 196, 200, 201, 202, 204, 205, 208

[5] C. D. Spataru, S. Ismail-Beigi, L. X. Benedict, S. G. Louie: Quasiparticle energies, excitonic effects and optical absorption spectra of small-diameter single-walled carbon nanotubes, Appl. Phys. A-Mater. **78**, 1129 (2004) 196, 200, 201, 202, 204, 205, 208

[6] E. Chang, G. Bussi, A. Ruini, E. Molinari: Excitons in carbon nanotubes: An ab-initio symmetry-based approach, Phys. Rev. Lett. **92**, 196401 (2004) 196, 204

[7] F. Wang, G. Dukovic, L. E. Brus, T. F. Heinz: The optical resonances in carbon nanotubes arise from excitons, Science **308**, 838 (2005) 196, 202, 206, 207, 210
[8] J. Maultzsch, R. Pomraenke, S. Reich, E. Chang, D. Prezzi, A. Ruini, E. Molinari, M. S. Strano, C. Thomsen, C. Lienau: Exciton binding energies in carbon nanotubes from two-photon photoluminescence, Phys. Rev. B **72**, 241402(R) (2005) 196, 202, 206, 207, 210
[9] S. G. Louie: Predicting materials and properties: Theory of the ground and excited state, in S. G. Louie, M. L. Cohen (Eds.): *Conceptual Foundations of Materials: A Standard Model for Ground- and Excited-State Properties* (Elsevier, Amsterdam 2006) p. 9 197
[10] P. Hohenberg, W. Kohn: Inhomogeneous electron gas, Phys. Rev. **136**, B864 (1964) 197
[11] W. Kohn, L. J. Sham: Self-consistent equations including exchange and correlation effects, Phys. Rev. **140**, A1133 (1965) 197
[12] J. P. Perdew, W. Yue: Accurate and simple density functional for the electronic exchange energy – Generalized gradient approximation, Phys. Rev. B **33**, 8800 (1986) 197
[13] J. P. Perdew, Y. Wang: Correlation hole of the spin-polarized electron gas, with small-wave-vector and high-density scaling, Phys. Rev. B **44**, 13298 (1991) 197
[14] J. P. Perdew, K. Burke, M. Ernzerhof: Generalized gradient approximation made simple, Phys. Rev. Lett. **77**, 3865 (1996) 197
[15] M. C. Payne, M. P. Teter, D. C. Allan, T. A. Arias, J. D. Joannopoulos: Iterative minimization techniques for ab-initio total-energy calculations – molecular dynamics and conjugate gradients, Rev. Mod. Phys. **64**, 1045 (1992) 197
[16] S. Lundqvist, N. H. March (Eds.): *Theory of the Inhomogeneous Electron Gas* (Plenum, N.Y. 1983) see the references therein 198
[17] M. S. Hybertsen, S. G. Louie: Electron correlation in semiconductors and insulators – Band-gaps and quasi-particle energies, Phys. Rev. B **34**, 5390 (1986) 198
[18] L. Hedin: New method for calculating 1-particle Green's function with application to electron-gas problem, Phys. Rev. **139**, A796 (1965) 198
[19] G. Strinati: Dynamical shift and broadening of core excitons in semiconducotrs, prl **49**, 1519 (1982) 199
[20] G. Strinati: Effects of dynamical screening on resonances at inner-shell thresholds in semiconductors, Phys. Rev. B **29**, 5718 (1984) 199
[21] G. Strinati: Application of the Green's-functions method to the study of the optical-properties of semiconductors, Riv. Nuovo Cimento **11**, 1 (1988) 199
[22] S. Albrecht, L. Reining, R. D. Sole, G. Onida: Ab-initio calculation of excitonic effects in the optical spectra of semiconductors, Phys. Rev. Lett. **80**, 4510 (1998) 199
[23] L. X. Benedict, E. L. Shirley, R. B. Bohn: Optical absorption of insulators and electron-hole interaction: An ab-initio calculation, Phys. Rev. Lett. **80**, 4514 (1998) 199
[24] M. Rohlfing, S. G. Louie: Electron-hole excitations in semiconductors and insulators, Phys. Rev. Lett. **81**, 2312 (1998) 199
[25] M. Rohlfing, S. G. Louie: Electron-hole excitations and optical spectra from first principles, Phys. Rev. B **62**, 4927 (2000) 199

[26] C.-H. Park, C. D. Spataru, S. G. Louie: Excitons and many-electron effects in the optical response of single-walled boron nitride nanotubes, Phys. Rev. Lett. **96**, 126105 (2006) 201, 216, 217, 218
[27] G. Dukovic, F. Wang, D. Song, M. Y. Sfeir, T. F. Heinz, L. E. Brus: Structural dependence of excitonic optical transitions and band-gap energies in carbon nanotubes, Nano Lett. **5**, 2314 (2005) 202, 206
[28] Y.-Z. Ma, C. D. Spataru, L. Valkunas, S. G. Louie, G. R. Fleming: Spectroscopy of zigzag single-walled carbon nanotubes: Comparing femtosecond transient absorption spectra with ab-initio calculations, Phys. Rev. B **74**, 085402 (2006) 202
[29] J. Deslippe, C. D. Spataru, D. Prendergast, S. G. Louie: Bound excitons in metallic single-walled carbon nanotubes, Nano Lett. **7**, 1626 (2007) 202, 203, 204
[30] S. G. Louie: in C. Y. Fong (Ed.): *Topics in Computational Materials Science* (World Scientific, Singapore 1997) p. 96 202
[31] Z. M. Li, Z. K. Tang, H. J. Liu, N. Wang, C. T. Chan, R. Saito, S. Okada, G. D. Li, J. S. Chen, N. Nagasawa, S. Tsuda: Polarized absorption spectra of single-walled 4 angstrom carbon nanotubes aligned in channels of an AlPO4-5 single crystal, Phys. Rev. Lett. **87**, 127401 (2001) 204
[32] C. Fantini, A. Jorio, M. Souza, M. S. Strano, M. S. Dresselhaus, M. A. Pimenta: Optical transition energies for carbon nanotubes from resonant Raman spectroscopy: Environment and temperature effects, Phys. Rev. Lett. **93**, 147406 (2004) 204
[33] H. Telg, J. Maultzsch, S. Reich, F. Hennrich, C. Thomsen: Chirality distribution and transition energies of carbon nanotubes, Phys. Rev. Lett. **93**, 177401 (2004) 204
[34] R. B. Capaz, C. D. Spataru, S. Ismail-Beigi, S. G. Louie: Diameter and chirality dependence of exciton properties in carbon nanotubes, Phys. Rev. B **74**, 121401 (2006) 204, 205, 206, 213
[35] V. Perebeinos, J. Tersoff, P. Avouris: Scaling of excitons in carbon nanotubes, Phys. Rev. Lett. **92**, 257402 (2004) 204, 206
[36] K. Ohno: Some remarks on the Pariser–Parr–Pople method, Theor. Chim. Acta **2**, 219 (1964) 204
[37] E. B. Barros, R. B. Capaz, A. Jorio, G. G. Samsonidze, A. G. Souza, S. Ismail-Beigi, C. D. Spataru, S. G. Louie, G. Dresselhaus, M. S. Dresselhaus: Selection rules for one- and two-photon absorption by excitons in carbon nanotubes, Phys. Rev. B **73**, 241406 (2006) 207, 208, 209, 213
[38] E. B. Barros, A. Jorio, G. G. Samsonidze, R. B. Capaz, A. G. Souza, J. Mendes, G. Dresselhaus, M. S. Dresselhaus: Review on the symmetry-related properties of carbon nanotubes, Phys. Rep. **431**, 261 (2006) 207, 208, 210
[39] M. Damnjanović, I. Milosevic, T. Vukovic, R. Sredanovic: Full symmetry, optical activity, and potentials of single-wall and multiwall nanotubes, Phys. Rev. B **60**, 2728 (1999) 207
[40] M. Damnjanović, T. Vukovic, I. Milosevic: Modified group projectors: Tight-binding method, J. Phys. A **33**, 6561 (2000) 207
[41] R. Loudon: One-dimensional hydrogen atom, Am. J. Phys. **27**, 649 (1959) 208
[42] R. S. Knox: *Theory of Excitons*, Solid State Physics **5** (Academic, N.Y. 1963) 208

[43] C. D. Spataru, S. Ismail-Beigi, R. B. Capaz, S. G. Louie: Theory and ab-initio calculation of radiative lifetime of excitons in semiconducting nanotubes, Phys. Rev. Lett. **95**, 247402 (2005) 210, 211, 212, 213, 221

[44] V. Perebeinos, J. Tersoff, P. Avouris: Radiative lifetime of excitons in carbon nanotubes, Nano Lett. **5**, 2495 (2005) 210, 221

[45] A. Hagen, G. Moos, V. Talalaev, T. Hertel: Electronic structure and dynamics of optically excited single-wall carbon nanotubes, Appl. Phys. A **78**, 1137 (2004) 210

[46] F. Wang, G. Dukovic, L. E. Brus, T. F. Heinz: Time-resolved fluorescence of carbon nanotubes and its implication for radiative lifetimes, Phys. Rev. Lett. **92**, 177401 (2004) 210

[47] A. Hagen, M. Steiner, M. B. Raschke, C. Lineau, T. Hertel, H. H. Qian, A. J. Meixner, A. Hartschuh: Exponential decay lifetimes of excitons in individual single-walled carbon nanotubes, Phys. Rev. Lett. **95**, 197401 (2005) 210

[48] I. B. Mortimer, R. J. Nicholas: Role of bright and dark excitons in the temperature-dependent photoluminescence of carbon nanotubes, Phys. Rev. Lett. **98**, 027404 (2007) 213

[49] J. Shaver, J. Kono, O. Portugall, V. Krstic, G. L. J. A. Rikken, Y. Miyauchi, S. Maruyama, V. Perebeinos: Magnetic brightening of carbon nanotube photoluminescence through symmetry breaking, arXiv URL: `cond-mat/0702036` 213

[50] L. Yang, M. P. Anantram, J. Han, J. P. Lu: Band-gap change of carbon nanotubes: Effect of small uniaxial and torsional strain, Phys. Rev. B **60**, 13874 (1999) 214

[51] Y. N. Gartstein, A. A. Zakhidov, R. H. Baughman: Mechanical and electromechanical coupling in carbon nanotube distortions, Phys. Rev. B **68**, 115415 (2003) 214

[52] R. B. Capaz, C. D. Spataru, P. Tangney, M. L. Cohen, S. G. Louie: Hydrostatic pressure effects on the structural and electronic properties of carbon nanotubes, Phys. Stat. Sol. B **241**, 3352 (2004) 214, 215

[53] S. B. Cronin, A. K. Swan, M. S. Unlu, B. B. Goldberg, M. S. Dresselhaus, M. Tinkham: Resonant Raman spectroscopy of individual metallic and semiconducting single-wall carbon nanotubes under uniaxial strain, Phys. Rev. B **72**, 035425 (2005) 214

[54] A. G. Souza, N. Kobayashi, J. Jiang, A. Gruneis, R. Saito, S. B. Cronin, J. Mendes, G. G. Samsonidze, G. Dresselhaus, M. S. Dresselhaus: Strain-induced interference effects on the resonance Raman cross section of carbon nanotubes, Phys. Rev. Lett. **95**, 217403 (2005) 214

[55] R. B. Capaz, C. D. Spataru, P. Tangney, M. L. Cohen, S. G. Louie: Temperature dependence of the band gap of semiconducting carbon nanotubes, Phys. Rev. Lett. **94**, 036801 (2005) 214, 215, 216

[56] S. B. Cronin, Y. Yin, A. Walsh, R. B. Capaz, A. Stolyarov, P. Tangney, M. L. Cohen, S. G. Louie, A. K. Swan, M. S. Unlu, B. B. Goldberg, M. Tinkham: Temperature dependence of the optical transition energies of carbon nanotubes: The role of electron-phonon coupling and thermal expansion, Phys. Rev. Lett. **96**, 127403 (2006) 214

[57] J. Wu, W. Walukiewicz, W. Shan, E. Bourret-Courchesne, J. W. Ager, K. M. Yu, E. E. Haller, K. Kissell, S. M. Bachilo, R. B. Weisman, R. E. Smalley: Structure-dependent hydrostatic deformation potentials of individual single-walled carbon nanotubes, Phys. Rev. Lett. **93**, 017404 (2004) 214
[58] L. J. Li, R. J. Nicholas, R. S. Deacon, P. A. Shields: Chirality assignment of single-walled carbon nanotubes with strain, Phys. Rev. Lett. **93**, 156104 (2004) 214
[59] J. Lefebvre, P. Finnie, Y. Homma: Temperature-dependent photoluminescence from single-walled carbon nanotubes, Phys. Rev. B **70**, 045419 (2004) 214
[60] R. S. Deacon, K.-C. Chuang, J. Doig, I. B. Mortimer, R. J. Nicholas: Photoluminescence study of aqueous-surfactant-wrapped single-walled carbon nanotubes under hydrostatic pressure, Phys. Rev. B **74**, 201402 (2006) 214
[61] D. Karaiskaj, C. Engtrakul, T. McDonald, M. J. Heben, A. Mascarenhas: Intrinsic and extrinsic effects in the temperature-dependent photoluminescence of semiconducting carbon nanotubes, Phys. Rev. Lett. **96**, 106805 (2006) 214
[62] R. B. Capaz, C. D. Spataru, P. Tangney, M. L. Cohen, S. G. Louie: Family behavior of the pressure and temperature dependences of the band gap of semiconducting carbon nanotubes, in *XIX International Winterschool/Euroconference on Electronic Properties of Novel Materials*, Proc. AIP **786** (2005) p. 411 216
[63] R. Arenal, O. Stephan, M. Kociak, D. Taverna, A. Loiseau, C. Colliex: Electron energy loss spectroscopy measurement of the optical gaps on individual boron nitride single-walled and multiwalled nanotubes, Phys. Rev. Lett. **95**, 127601 (2005) 217
[64] J. S. Lauret, R. Arenal, F. Ducastelle, A. Loiseau, M. Cau, B. Attal-Tretout, E. Rosencher, L. Goux-Capes: Optical transitions in single-wall boron nitride nanotubes, Phys. Rev. Lett. **94**, 037405 (2005) 217
[65] L. Yang, C. D. Spataru, S. G. Louie, M. Y. Chou: Enhanced electron-hole interaction and optical absorption in a silicon nanowire, Phys. Rev. B **75**, 201304 (2007) 217
[66] K. S. Novoselov, A. K. Geim, S. V. Morozov, D. Jiang, M. I. Katsnelson, I. V. Grigorieva, S. V. Dubonos, A. A. Firsov: Two-dimensional gas of massless Dirac fermions in graphene, Nature **438**, 197 (2005) 218
[67] Y. B. Zhang, Y. W. Tan, H. L. Stormer, P. Kim: Experimental observation of the quantum Hall effect and Berry's phase in graphene, Nature **438**, 201 (2005) 218
[68] M. Fujita, K. Wakabayashi, K. Nakada, K. Kusakabe: Peculiar localized state at zigzag graphite edge, J. Phys. Soc. Jpn. **65**, 1920 (1996) 218
[69] K. Nakada, M. Fujita, G. Dresselhaus, M. S. Dresselhaus: Edge state in graphene ribbons: Nanometer size effect and edge shape dependence, Phys. Rev. B **54**, 17954 (1996) 218
[70] K. Wakabayashi, M. Fujita, H. Ajiki, M. Sigrist: Electronic and magnetic properties of nanographite ribbons, Phys. Rev. B **59**, 8271 (1999) 218
[71] M. Ezawa: Peculiar width dependence of the electronic properties of carbon nanoribbons, Phys. Rev. B **73**, 045432 (2006) 218
[72] L. Brey, H. A. Fertig: Electronic states of graphene nanoribbons studied with the Dirac equation, Phys. Rev. B **73**, 235411 (2006) 218
[73] K.-I. Sasaki, S. Murakami, R. Saito: Gauge field for edge state in graphene, J. Phys. Soc. Jpn **75**, 074713 (2006) 218

[74] D. A. Abanin, P. A. Lee, L. S. Levitov: Spin-filtered edge states and quantum hall effect in graphene, Phys. Rev. Lett. **96**, 176803 (2006) 218
[75] S. Okada, A. Oshiyama: Magnetic ordering in hexagonally bonded sheets with first-row elements, Phys. Rev. Lett. **87**, 146803 (2001) 218
[76] H. Lee, Y. W. Son, N. Park, S. W. Han, J. J. Yu: Magnetic ordering at the edges of graphitic fragments: Magnetic tail interactions between the edge-localized states, Phys. Rev. B **72**, 174431 (2005) 218
[77] Y. Miyamoto, K. Nakada, M. Fujita: First-principles study of edge states of H-terminated graphitic ribbons, Phys. Rev. B **59**, 9858 (1999) 218
[78] T. Kawai, Y. Miyamoto, O. Sugino, Y. Koga: Graphitic ribbons without hydrogen-termination: Electronic structures and stabilities, Phys. Rev. B **62**, R16349 (2000) 218
[79] Y.-W. Son, M. L. Cohen, S. G. Louie: Energy gaps in graphene nanoribbons, Phys. Rev. Lett. **97**, 216803 (2006) 219
[80] Y.-W. Son, M. L. Cohen, S. G. Louie: Half-metallic graphene nanoribbons, Nature (London) **444**, 347 (2006) 219, 221
[81] V. Barone, O. Hod, G. E. Scuseria: Electronic structure and stability of semiconducting graphene nanoribbons, Nano Lett. **6**, 2748 (2006) 219
[82] L. Yang, C.-H. Park, Y.-W. Son, M. L. Cohen, S. G. Louie: Quasiparticle energies and band gaps of graphene nanoribbons, Phys. Rev. Lett. accepted for publication 219, 220

Index

Role of the Aharonov–Bohm Phase in the Optical Properties of Carbon Nanotubes

Tsuneya Ando

Department of Physics, Tokyo Institute of Technology,
2–12–1 Ookayama, Meguro-ku, Tokyo 152-8551, Japan

Abstract. A brief review is given on the electronic and optical properties of carbon nanotubes with emphasis on Aharonov–Bohm effects. The topics include an effective-mass description of the electronic states, optical absorption and excitons, their fine structure, optical absorption for perpendicular polarization, and optical phonons.

1 Introduction

Carbon nanotubes (CN) are either a metal or semiconductor, depending on their diameters and helical arrangement. This condition can be obtained based on the band structure of a two-dimensional (2D) graphite sheet and periodic boundary conditions along the circumference direction [1]. This result was predicted first by means of a tight-binding model and also by a $\boldsymbol{k}\ \boldsymbol{p}$ method or an effective-mass approximation [2]. The cylindrical shape leads to a strong Aharonov–Bohm (AB) effect in the band structure due to a magnetic field parallel to the axis [3, 4]. The purpose of this chapter is to give a brief review of the AB effect on the electronic and optical properties of carbon nanotubes, predicted in the $\boldsymbol{k}\ \boldsymbol{p}$ scheme.

2 Effective-Mass Description

A monolayer graphite (graphene) sheet is a zero-gap semiconductor in which the conduction and valence bands consist of π states that cross at the K and K′ points of the Brillouin zone [5]. The structure is shown in Fig. 1 together with the first Brillouin zone and coordinate systems to be used in the following. Electronic states near a K point are described by the $\boldsymbol{k}\ \boldsymbol{p}$ equation [2, 6, 7]:

$$\gamma(\boldsymbol{\sigma}\ \ \hat{\boldsymbol{k}})\boldsymbol{F}(\boldsymbol{r}) = \varepsilon\boldsymbol{F}(\boldsymbol{r})\,, \quad \boldsymbol{F}(\boldsymbol{r}) = \begin{pmatrix} F_{\mathrm{A}}(\boldsymbol{r}) \\ F_{\mathrm{B}}(\boldsymbol{r}) \end{pmatrix}\,, \tag{1}$$

where γ is the band parameter, $\hat{\boldsymbol{k}} = (\hat{k}_x, \hat{k}_y) = -i\boldsymbol{\nabla}$ is a wavevector operator, ε is the energy, and σ_x and σ_y are the Pauli spin matrices. Two components

A. Jorio, G. Dresselhaus, M. S. Dresselhaus (Eds.): Carbon Nanotubes,
Topics Appl. Physics **111**, 229–250 (2008)

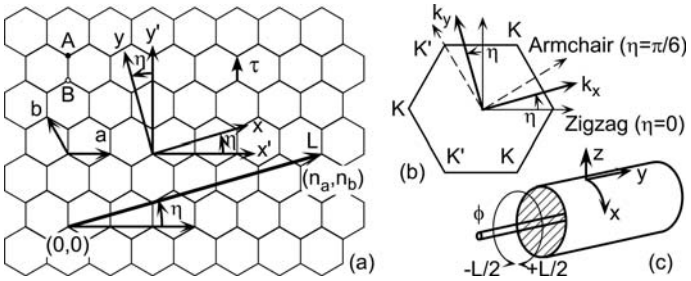

Fig. 1. (**a**) Lattice structure of a two-dimensional graphite (graphene) sheet. The coordinates (x', y') are fixed on the graphite sheet and (x, y) are chosen in such a way that x is along the circumference and y is along the axis. (**b**) The first Brillouin zone showing the K and K′ points. (**c**) The coordinates for the nanotube. An Aharonov–Bohm flux ϕ is applied along the y-axis direction of the nanotube

of the wavefunction $\boldsymbol{F}(\boldsymbol{r})$ correspond to the amplitude at A and B sites in a unit cell. Equation (1) has the form of Weyl's equation for neutrinos. If we use a nearest-neighbor tight-binding model with hopping integral $-\gamma_0$, the band parameter becomes

$$\gamma = \frac{\sqrt{3}}{2} a\gamma_0 \,, \tag{2}$$

where a is the lattice constant.

An important feature of the Weyl equation is the presence of a topological singularity at $\boldsymbol{k} = 0$. A neutrino has a helicity and its spin is quantized into the direction of its motion. The spin eigenfunction changes its signature due to Berry's phase under a 2π rotation [8]. Correspondingly, the wavefunction acquires a phase $-\pi$ when $\boldsymbol{k}$ is rotated around the origin along a closed contour [9, 10]. The signature change occurs only when the closed contour encircles the origin $\boldsymbol{k} = 0$ but not when the contour does not contain $\boldsymbol{k} = 0$. This topological anomaly leads to the absence of backward scattering and the perfect conductance in metallic nanotubes even in the presence of scatterers unless their potential range is smaller than the lattice constant a [9, 10]. When the Fermi level lies in higher bands, there is a perfectly conducting channel [11]. This unique property can be affected by various symmetry-breaking perturbations [12–14].

A singularity at $\varepsilon = 0$ manifests itself in a magnetic field B. Semiclassically, the Landau levels can be obtained as $\varepsilon_n = \sqrt{|n| + (1/2)}\,\mathrm{sgn}(n)(\sqrt{2}\gamma/l)$ with integer n ($n = 0, \pm 1, \dots$), where l is the magnetic length given by $l = \sqrt{c\hbar/eB}$ and $\mathrm{sgn}(t)$ stands for the sign of t. There can be no Landau level at $\varepsilon = 0$. However, a full quantum-mechanical treatment gives $\varepsilon_n = \sqrt{|n|}\,\mathrm{sgn}(n)(\sqrt{2}\gamma/l)$ due to Berry's phase, leading to the formation of the Landau level $n = 0$ at $\varepsilon = 0$ [15].

The structure of a nanotube is specified by a chiral vector $\boldsymbol{L}$ corresponding to the circumference as shown in Fig. 1. In the following we shall choose the

x-axis in the circumference direction and the y-axis in the axis direction, i.e., $\boldsymbol{L} = (L, 0)$ with $L = |\boldsymbol{L}|$. The angle η between $\boldsymbol{L}$ and the horizontal axis is called the chiral angle.

The electronic states can be obtained by imposing the periodic boundary condition in the circumference direction $\psi(\boldsymbol{r} + \boldsymbol{L}) = \psi(\boldsymbol{r})$ except in extremely thin tubes. The Bloch functions at a K point change their phase by $\exp(\mathrm{i}\boldsymbol{K}\ \boldsymbol{L}) = \exp(2\pi\mathrm{i}\nu/3)$, where $\nu = 0$ or ± 1, determined by $\boldsymbol{L}$. Because $\psi(\boldsymbol{r})$ is written as a product of the Bloch function and the envelope function, i.e., the neutrino wavefunction $\boldsymbol{F}(\boldsymbol{r})$, this phase change should be canceled by that of the envelope functions and the boundary conditions are given by $\boldsymbol{F}(\boldsymbol{r} + \boldsymbol{L}) = \boldsymbol{F}(\boldsymbol{r}) \exp(-2\pi\mathrm{i}\nu/3)$.

A nonzero curvature causes a shift in the origin of $\hat{k}_x$ and $\hat{k}_y$ in the $\boldsymbol{k}\ \boldsymbol{p}$ Hamiltonian. The shift in the y-direction is irrelevant and that in the x-direction can be replaced by an effective flux ϕ_c. The flux was estimated as [7, 16]

$$\frac{\phi_c}{\phi_0} = \frac{2\pi}{4\sqrt{3}} \frac{a}{L} p \cos 3\eta \,, \tag{3}$$

with $\phi_0 = ch/e$ being the flux quantum, $p = 1 - (3/8)\gamma'/\gamma$, $\gamma = -(\sqrt{3}/2)V_{pp}^{\pi} a$, and $\gamma' = -(\sqrt{3}/2)(V_{pp}^{\sigma} - V_{pp}^{\pi})a$, where V_{pp}^{π} $(= -\gamma_0)$ and V_{pp}^{σ} are the conventional tight-binding parameters for neighboring p orbitals [16]. The curvature effect is largest in zigzag nanotubes with $\eta = 0$ and absent in armchair nanotubes with $\eta = \pi/6$. The above flux is different from that given in [17] in which V_{pp}^{σ} was neglected.

The presence of a lattice distortion $\boldsymbol{u} = (u_x, u_y, u_z)$ also causes an effective flux. It is estimated as [18]

$$\frac{\phi_s}{\phi_0} = \frac{L g_2}{2\pi\gamma} [(u_{xx} - u_{yy}) \cos 3\eta - 2u_{xy} \sin 3\eta] \,, \tag{4}$$

where $u_{\mu\nu}$ $(\mu, \nu = x, y)$ denotes the strain tensor given by

$$u_{xx} = \frac{\partial u_x}{\partial x} + \frac{2\pi u_z}{L} \,, \quad u_{yy} = \frac{\partial u_y}{\partial y} \,, \quad 2u_{xy} = \frac{\partial u_x}{\partial y} + \frac{\partial u_y}{\partial x} \,, \tag{5}$$

and g_2 is the interaction energy given by $g_2 = (\alpha/2)\gamma_0$ with $\alpha \sim 1$ [18]. This shows that twist and stretch deformation give rise to nonzero flux in armchair and zigzag nanotubes, respectively. The coupling constant g_2 is about a factor of three smaller than that discussed using a tight-binding model [19, 20].

In summary, the electronic states in nanotubes can be specified by a single parameter φ_e defined by

$$\varphi_e = -\frac{\nu}{3} + \varphi_c + \varphi_s \,, \quad \varphi_c = \frac{\phi_c}{\phi_0} \,, \quad \varphi_s = \frac{\phi_s}{\phi_0} \,, \tag{6}$$

and energy levels for the K point are obtained by putting $k_x = \kappa_{\varphi_e}(n)$ with $\kappa_{\varphi_e}(n) = (2\pi/L)(n + \varphi_e)$ and $k_y = k$ in the above $\boldsymbol{k}\ \boldsymbol{p}$ equation

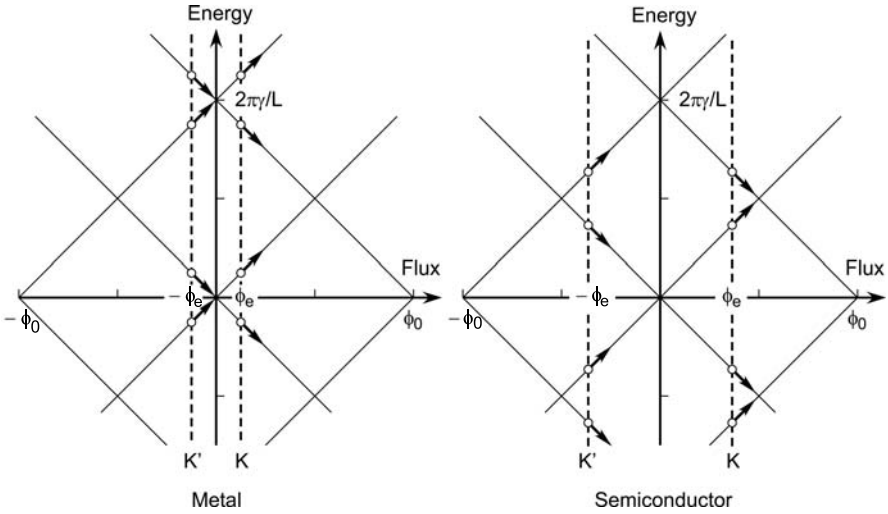

Fig. 2. The band edges $\pm(2\pi\gamma/L)|n-(\phi/\phi_0)|$ as a function of ϕ for metallic and semiconducting tubes. In the presence of an effective flux ϕ_e due to curvature and/or strain, we have $\phi=\phi_e$ for the K point and $\phi=-\phi_e$ for the K′ point. An AB magnetic flux shifts ϕ in the positive direction as shown by *arrows*

as $\varepsilon^{(\pm)}_{\varphi_e}(n,k)=\pm\gamma\sqrt{\kappa_{\varphi_e}(n)^2+k^2}$, where n is an integer ($n=0,\pm1,\dots$) and the upper (+) and lower (−) signs represent the conduction and valence bands, respectively. For the K′ point, the Schrödinger equation is given by replacing $\boldsymbol{\sigma}$ with complex conjugate $\boldsymbol{\sigma}^*$ and the boundary condition gives an effective flux $-\varphi_e$ leading to $k_x=\kappa_{-\varphi_e}(n)$. When $\phi_c=\phi_s=0$, a nanotube becomes metallic for $\nu=0$ and semiconducting with gap $\varepsilon_G=4\pi\gamma/3L$ for $\nu=\pm1$.

When a magnetic field is applied parallel to the axis, i.e., in the presence of a magnetic flux ϕ passing through the cross section, the AB flux leads to the change in the boundary condition $\psi(\boldsymbol{r}+\boldsymbol{L})=\psi(\boldsymbol{r})\exp(+2\pi\mathrm{i}\varphi)$, where $\varphi=\phi/\phi_0$. Consequently, $\kappa_{\varphi_e}(n)$ is replaced with $\kappa_{\varphi+\varphi_e}(n)$ for the K point and $\kappa_{-\varphi_e}(n)$ with $\kappa_{\varphi-\varphi_e}(n)$ for the K′ point. The energy bands are given by $\varepsilon^{(\pm)}_{\varphi+\varphi_e}(n,k)$ and $\varepsilon^{(\pm)}_{\varphi-\varphi_e}(n,k)$ for the K and K′ points, respectively. Figure 2 shows a schematic illustration of the band edges $\varepsilon^{(\pm)}_{\varphi\pm\varphi_e}(n,0)$. The gap exhibits an oscillation between 0 and $2\pi\gamma/L$ with a period ϕ_0 with the change in the AB flux ϕ [2]. This giant AB effect on the bandgap is a unique property of nanotubes. In summary, the boundary conditions become $\psi(\boldsymbol{r}+\boldsymbol{L})=\psi(\boldsymbol{r})\exp[2\pi\mathrm{i}(\varphi+\varphi_c+\varphi_s)]$ or $\boldsymbol{F}(\boldsymbol{r}+\boldsymbol{L})=\exp[2\pi\mathrm{i}(\mp\nu/3+\varphi+\varphi_c+\varphi_s)]$ with the upper and lower signs for the K and K′ points, respectively.

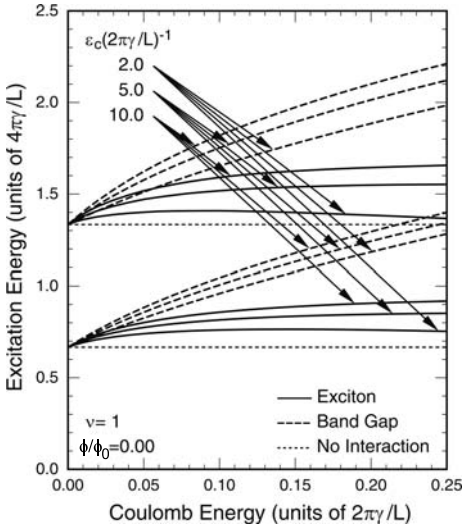

Fig. 3. Calculated bandgaps (*dashed lines*) and exciton absorption energies (*solid lines*) of the first and second bands as a function of the effective Coulomb energy in the absence of flux for various cutoff energies

3 Excitons

A carbon nanotube has characteristic optical properties. In fact, the absorption of light polarized perpendicular to the axis is known to be suppressed considerably because of a strong depolarization effect in comparison with that of light polarized parallel to the axis [21, 22], and the Coulomb interaction plays a crucial role. Interaction effects on the band structure were evaluated within a conventional screened Hartree–Fock approximation and were shown to enhance the bandgap considerably [23]. It was shown further that the exciton effect is extremely important because of the one-dimensional nature of the nanotube [23].

A later calculation of quasiparticle energies using a full dynamical random-phase approximation [24, 25], which is often called the GW approximation [26–28], showed that the screened Hartree-Fock approximation works sufficiently well in semiconducting nanotubes and in metallic nanotubes apart from bands with a linear dispersion. It was demonstrated that the self-energy shift depends on the cutoff energy, leading to an extra logarithmic dependence on the diameter. The energy bands and excitons were calculated carefully including this cutoff dependence [29].

Within the effective-mass approximation, the strength of the electron–electron interaction is characterized by the dimensionless parameter $(e^2/\kappa L)(2\pi\gamma/L)^{-1}$ independent of L, where κ is a static dielectric constant describing the effects of the polarization of electrons of core states, σ bands, π bands away from the K and K′ points, and the surrounding material. In bulk graphite we have $\kappa \approx 2.4$ [30]. Although the exact value of κ is unknown in nanotubes, the interaction parameter is expected to lie in the range $0.1 \lesssim (e^2/\kappa L)(2\pi\gamma/L)^{-1} \lesssim 0.2$.

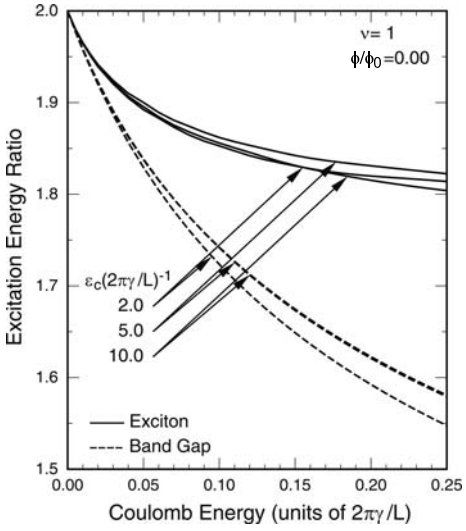

Fig. 4. The ratio of the absorption energies (*solid lines*) and bandgaps (*dashed lines*) between the first and second bands as a function of the effective Coulomb energy

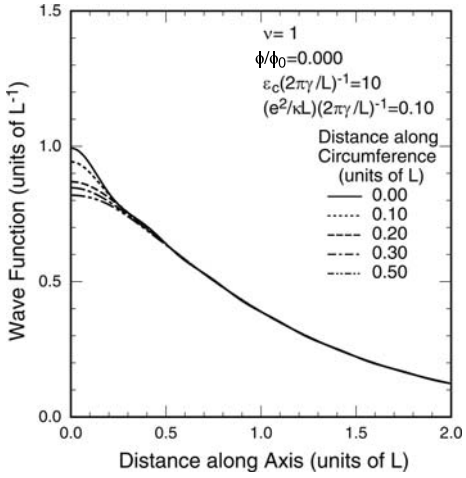

Fig. 5. Calculated amplitude of the wavefunction of an exciton as a function of the distance between an electron and a hole along the axis direction for a fixed distance in the circumference direction

Figure 3 shows the bandgaps and the lowest exciton absorption energies associated with the fundamental and second gaps as a function of the effective Coulomb energy $(e^2/\kappa L)\,(2\pi\gamma/L)^{-1}$ in the absence of magnetic flux. A dominant feature is the enhancement of the bandgaps with the increase of the interaction strength. The binding energy of excitons increases with the interaction but remains smaller than the bandgap enhancement. As a result, the absorption energies become higher than the bandgap without interaction. Further, interaction effects on the bandgap and the exciton binding energy are larger for the second band than for the first band.

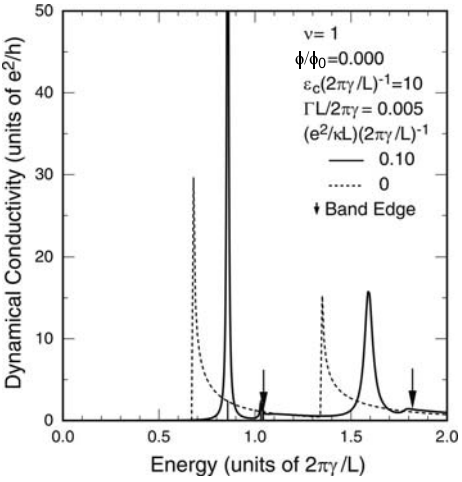

Fig. 6. Calculated optical absorption spectrum of a semiconducting nanotube. The *solid* and *dotted lines* represent spectra in the presence and absence of interaction, respectively. The band edges are indicated by *vertical arrows*

The cutoff energy ε_c is of the order of half the π bandwidth $\sim 3\gamma_0$. This leads to $\varepsilon_c(2\pi\gamma/L)^{-1} \sim (\sqrt{3}/\pi)(L/a)$, i.e., $\varepsilon_c(2\pi\gamma/L)^{-1} \sim 10$ for typical CNs with diameter $\sim 1.4\,\mathrm{nm}$. Figure 4 shows the ratio of the excitation energies of the second gap and that of the first gap. The ratio is essentially independent of the cutoff energy and therefore of the diameter. Further, the ratio of the exciton energies decreases from two in the absence of interaction to about 1.8 in the presence of the interaction. This explains the feature of the experimental results quite well.

Figure 5 shows an example of the exciton wavefunctions. The position of a hole is fixed at the origin $(x, y) = (0, 0)$ and the amplitude for an electron is shown along the x-direction parallel to the axis and for several values of y along the circumference. The amplitude is independent of the distance toward the circumference direction except in the extreme vicinity of the hole, showing that interband mixing effects are not important and that the exciton is uniformly extended in the circumference direction.

Some examples of the absorption spectra are shown in Fig. 6 for $\varepsilon_c (2\pi\gamma/L)^{-1} = 10$ and $(e^2/\kappa L)(2\pi\gamma/L)^{-1} = 0.1$. Most of the absorption intensity is transferred to the exciton ground state from the interband continuum for both the first and second gaps. In this figure the absorption for the second gap has a larger broadening than that for the first gap simply because a larger phenomenological broadening has been introduced due to the necessity in the calculation.

In the present scheme the relevant parameter γ is related to the nearest-neighbor hopping integral γ_0 through $\gamma = \sqrt{3}a\gamma_0/2$. Figure 7 shows the comparison of the calculated absorption energies with some of the existing experiments [31–33] for $\gamma_0 = 2.7\,\mathrm{eV}$. It is concluded that the overall dependence on the circumference and the diameter is in good agreement with the experiments. It should be noted that γ need not be the same as that of 2D graphite

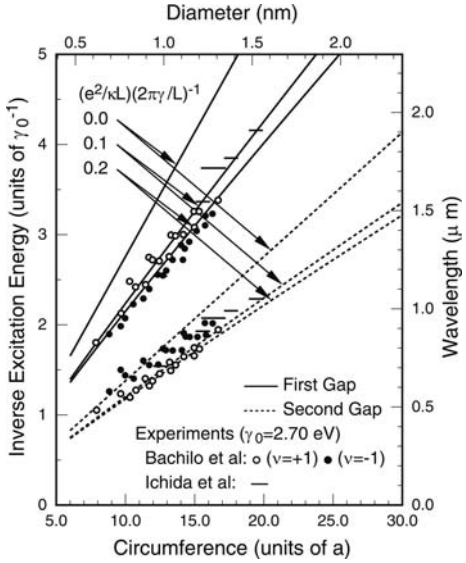

Fig. 7. The inverse of the absorption energies as a function of the circumference and the diameter. The experimental results (*Ichida* et al. [31, 33] and *Bachilo* et al. [32]) are plotted using $\gamma_0 = 2.7\,\mathrm{eV}$

obtained by inclusion of interaction effects. Experimental results depend on the chirality as well as the diameter (so-called family effect), in particular, for thin nanotubes. In thin nanotubes various effects, neglected completely in the present approximation scheme, start to manifest themselves.

Quasiparticle spectra of nanotubes were calculated using a first-principles GW method [34], and calculations were performed also for optical absorption spectra with the inclusion of excitonic final-state interactions [35–38]. There have also been some reports on a phenomenological description of excitons [39, 40].

4 Exciton Fine Structure and Aharonov–Bohm Effect

Because of the electron spin and the presence of K and K′ points, there are 16 exciton states. They can be written, for example, as $|KK'\rangle$, where an electron is in the conduction band at the K point and a hole in the valence band at the K′ point. Similar definitions can be made for other combinations. First, by a short-range part of the Coulomb interaction giving rise to scattering of an electron between the K and K′ points, the excitons $|KK\rangle$ and $|K'K'\rangle$ are coupled to form a bonding state $|KK\text{–}K'K'(+)\rangle$ with a lower energy and an antibonding $|KK\text{–}K'K'(-)\rangle$ with a higher energy. Because of the momen-

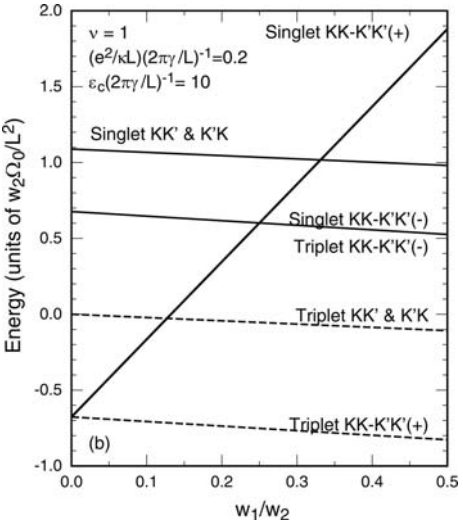

Fig. 8. The energy levels of excitons as a function of w_1/w_2. The singlet and triplet states are degenerate for $|KK\text{–}K'K'(-)\rangle$. The crossing of singlet $|KK\text{–}K'K'(+)\rangle$ (bright) and $|KK\text{–}K'K'(-)\rangle$ (dark) occurs around at $w_1/w_2 = 0.25$. $(e^2/\kappa L) \times (2\pi\gamma/L)^{-1} = 0.2$

tum conservation, the $|KK'\rangle$ and $|K'K\rangle$ excitons remain decoupled by this interaction. The matrix element of this interaction is given by [41]

$$V^{(2)}_{(K'2,K1)(K4,K'3)} = \Omega_0 w_2 \int \mathrm{d}\boldsymbol{r} \left[F_2^{K'A}(\boldsymbol{r})^* F_1^{KA}(\boldsymbol{r}) F_4^{KA}(\boldsymbol{r})^* F_3^{K'A}(\boldsymbol{r}) \right. \quad (7)$$

$$\left. + F_2^{K'B}(\boldsymbol{r})^* F_1^{KB}(\boldsymbol{r}) F_4^{KB}(\boldsymbol{r})^* F_3^{K'B}(\boldsymbol{r}) \right], \quad (8)$$

with

$$w_2 \approx \sum_{\boldsymbol{R}} V(\boldsymbol{R}) \mathrm{e}^{\mathrm{i}(\boldsymbol{K}-\boldsymbol{K}')\ \boldsymbol{R}}, \quad (9)$$

where $\Omega_0 = \sqrt{3}a^2/2$ is the area of a unit cell, $\boldsymbol{F}^K$ and $\boldsymbol{F}^{K'}$ are the two-component wavefunctions for the K and K′ points, respectively, and $V(\boldsymbol{R})$ stands for the Coulomb potential between π orbitals with lattice separation $\boldsymbol{R}$. A similar equation can be rewritten also for $V^{(2)}_{(K2,K'1)(K'4,K3)}$.

These excitons split into spin-singlet and triplet states due to the exchange interaction. Among them only the singlet $|KK\text{-}K'K'(+)\rangle$ exciton is optically allowed (bright) and all others do not contribute to absorption and emission (dark). The exchange interaction arises due to a short-range part of the Coulomb interaction within the K and K′ points, not included in the effective-mass approximation [41],

$$V^{(1)}_{(K2,K1)(K4,K3)} = \Omega_0 w_1 \int \mathrm{d}\boldsymbol{r} \left[\boldsymbol{F}_2^K(\boldsymbol{r})^\dagger \sigma_z \boldsymbol{F}_1^K(\boldsymbol{r}) \right] \left[\boldsymbol{F}_4^K(\boldsymbol{r})^\dagger \sigma_z \boldsymbol{F}_3^K(\boldsymbol{r}) \right], \quad (10)$$

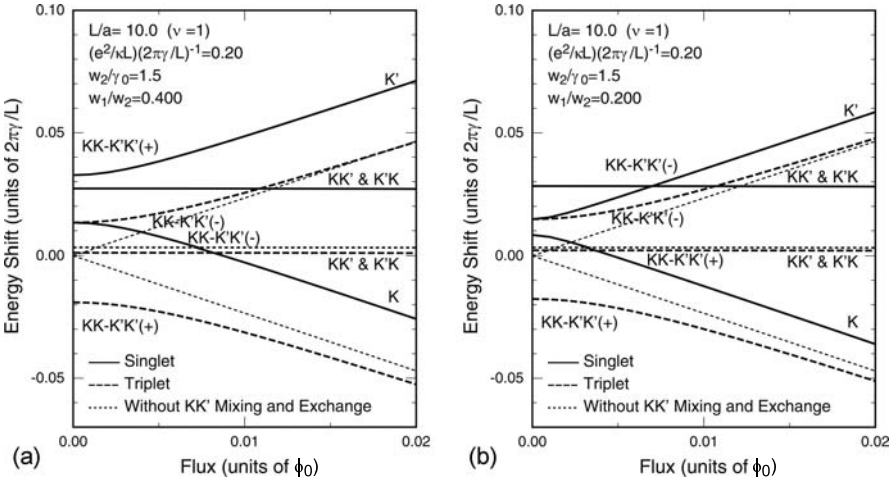

Fig. 9. Calculated energy levels of the singlet and triplet excitons as a function of the flux for the parameter $w_2/\gamma_0 = 1.5$ in semiconducting nanotubes with $\nu = 1$ and circumference $L/a = 10$. $(e^2/\kappa L)(2\pi\gamma/L)^{-1} = 0.2$. (**a**) $w_1/w_2 = 0.4$ and (**b**) 0.2

with

$$w_1 \approx \frac{1}{2}\sum_{\boldsymbol{R}}[V(\boldsymbol{R}) - V(\boldsymbol{R}-\boldsymbol{\tau})]\,, \tag{11}$$

where σ_z is the z-component of the Pauli matrix and $\boldsymbol{\tau}$ is a vector connecting nearest-neighbor atoms shown in Fig. 1. When we assume the simple Coulomb form $V(\boldsymbol{R}) \propto e^2/|\boldsymbol{R}|$ for $\boldsymbol{R} \neq 0$, we have

$$w_1 \approx \frac{1}{2}[V(0) - c_1 V(a)]\,, \quad w_2 \approx V(0) - c_2 V(a)\,, \tag{12}$$

where c_1 and c_2 are constants given by $c_1 = 2.67\ldots$ and $c_2 = 1.54\ldots$ determined by the lattice structure alone. This shows that $w_1 \lesssim w_2/2$. If we use the Ohno potential $V(\boldsymbol{R}) = U[(U|\boldsymbol{R}|/e^2)^2+1]^{-1/2}$ with $U \approx 11.3\,\mathrm{eV}$ [42,43], we have $w_1/w_2 \sim 0.17$.

The amount of the splitting and shift is of the order of $(a/L)^2 w_2$ or $(a/L)^2 w_1$, in contrast to $\propto a/L$ suggested in [44], and therefore becomes rapidly smaller with L. Figure 8 shows the exciton energy levels determined by w_1 and w_2 as a function of w_1/w_2. Except in the case of $w_1 = 0$, the triplet states are lower in energy and the bright exciton, i.e., singlet $|KK\text{–}K'K'(+)\rangle$, increases in energy with the increase of w_1/w_2. Around $w_1/w_2 = 0.25$ it becomes higher than the dark singlet exciton $|KK\text{–}K'K'(-)\rangle$.

This exciton fine structure is strongly affected by an Aharonov–Bohm magnetic flux because of the splitting of the K and K′ points as shown

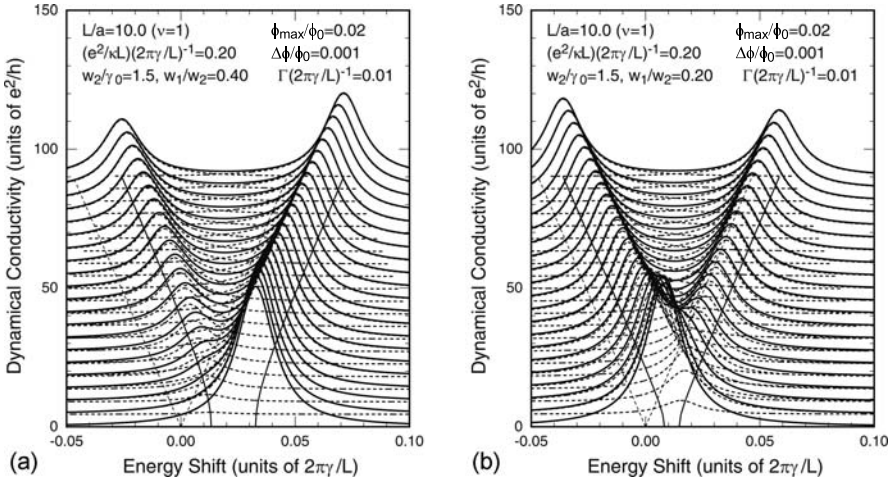

Fig. 10. Calculated dynamical conductivity describing the absorption spectra. The *solid lines* represent the conductivity and the *dotted lines* contributions of two singlet KK–$K'K'$ excitons. The flux ϕ is varied with interval $\Delta\phi/\phi_0 = 0.001$ up to $\phi_{\max}/\phi_0 = 0.02$. Curves of different ϕ are shifted in the vertical direction. The peak positions in the presence and absence of the short-range interaction are shown also. A phenomenological broadening $\Gamma(2\pi\gamma/L)^{-1} = 0.01$ is introduced. $L/a = 10$. $(e^2/\kappa L)(2\pi\gamma/L)^{-1} = 0.2$. (**a**) $w_1/w_2 = 0.4$ and (**b**) 0.2

in Fig. 2. This Aharonov–Bohm splitting was observed in recent experiments [45–50]. Figure 9 shows some examples of the energy levels of the singlet and triplet excitons as a function of the flux for the parameter $w_2/\gamma_0 = 1.5$ in nanotubes with circumference $L/a = 10$. For $w_1/w_2 = 0.4$ the highest-energy exciton is bright, while for $w_1/w_2 = 0.2$ the bright exciton has a lower energy than the antibonding states of singlet $|KK\rangle$ and $|K'K'\rangle$ excitons. Mixing between the K and K′ points diminishes rapidly with the increase of the flux and excitons for the K and K′ points become independent of each other for a sufficiently large AB flux. On the other hand, $|KK'\rangle$ and $|K'K\rangle$ excitons remain at the same energy because of the cancelation of flux effects between the conduction and valence bands.

Figure 10 shows some examples of the dynamical conductivity describing the absorption spectra. In the absence of flux, a single absorption peak appears only at the energy of the bonding combination of $|KK\rangle$ and $|K'K'\rangle$ excitons depending on the ratio w_1/w_2, as mentioned above. When $w_1/w_2 > 0.25$, the bright $|KK$–$K'K'(+)\rangle$ exciton lies higher in energy than the dark $|KK$–$K'K'(-)\rangle$ exciton and a new peak appears in the low-energy side. When $w_1/w_2 < 0.25$, on the other hand, the bright $|KK$–$K'K'(+)\rangle$ exciton lies lower than the dark $|KK$–$K'K'(-)\rangle$ exciton and a new peak appears in the high-energy side.

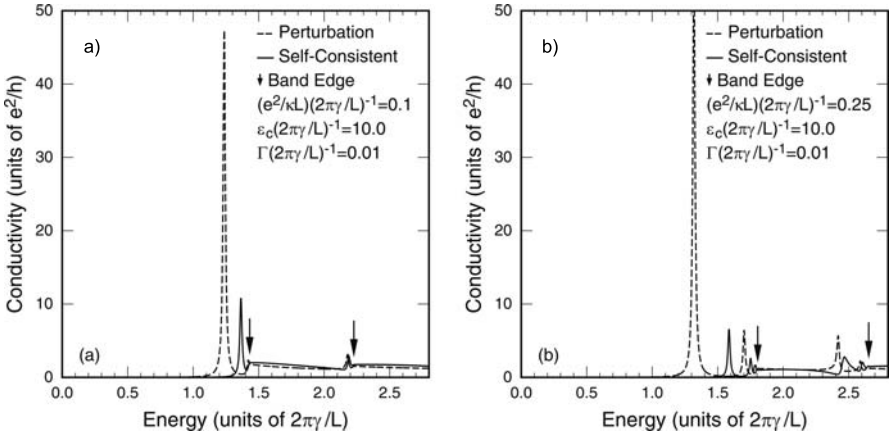

Fig. 11. Examples of calculated absorption spectra for light polarized perpendicular to the axis. The *dashed lines* turn into the *solid lines* by the depolarization effect. (**a**) $(e^2/\kappa L)(2\pi\gamma/L)^{-1} = 0.1$. (**b**) 0.25

An important characteristic feature of the experimental results of the Aharonov–Bohm splitting [45–50] is that the splitting does not seem to become observable until the magnetic flux reaches a certain critical value and then starts to increase with the flux. This is consistent with the above result that two peaks become observable only when the Aharonov–Bohm splitting exceeds the mixing between the $|KK\rangle$ and $|K'K'\rangle$ exciton due to the short-range Coulomb interaction. A detailed and careful experimental study of the Aharonov–Bohm effect on the exciton may be used to determine the relative ordering of bright and dark excitons.

The exciton fine structure has been discussed also in different methods, including first-principles [44, 51–53]. The Aharonov–Bohm effect on the dark and bright excitons was also suggested in [48] and recently observed in photoluminescence experiments [54].

5 Exciton Absorption for Crosspolarized Light

The interband absorption for perpendicular polarization is known to be suppressed considerably because of a strong depolarization effect in comparison with that of light polarized parallel to the axis [21, 22]. However, a peak appears when the strong exciton effect is taken into account [55].

When the depolarization effect is ignored completely, the dynamical conductivity giving the absorption spectrum is given by

$$\sigma_{xx}^{l}(\omega) = \frac{2\hbar e^2}{AL} \sum_{KK'} \sum_{u} \frac{-2i\hbar\omega |\langle u, l|\hat{v}_x^l|g\rangle|^2}{\varepsilon_u[\varepsilon_u^2 - (\hbar\omega)^2 - 2i\hbar\omega\Gamma]}\,, \tag{13}$$

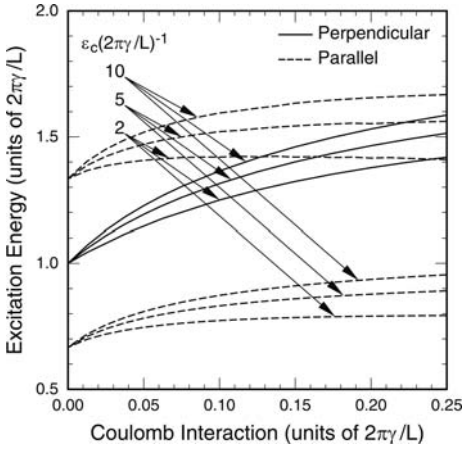

Fig. 12. The exciton energies for the perpendicular (*solid lines*) and parallel polarization (*dashed lines*). The dependence is larger for the perpendicular polarization

where ε_u and $|u,l\rangle$ represent the energy and the wavefunction of the electron–hole pair, $|g\rangle$ is the ground-state wavefunction, $\hat{v}_x^l$ is the velocity in the circumference direction corresponding to the wave number $2\pi l/L$ ($l = \pm 1$), and Γ is a phenomenological energy broadening.

The depolarization effect can be included in a self-consistent manner by considering the electric field corresponding to the polarization [21, 22]. As a result, the effective dynamical conductivity becomes

$$\tilde{\sigma}_{xx}^{l}(\omega) = \frac{\sigma_{xx}^{l}(\omega)}{\varepsilon_{xx}^{l}(\omega)}\,, \quad \varepsilon_{xx}^{l}(\omega) = 1 + \frac{4\pi^2 \mathrm{i}|l|}{\kappa L \omega}\sigma_{xx}^{l}(\omega)\,. \tag{14}$$

The absorption is proportional to the real part of $\tilde{\sigma}_{xx}(\omega)$ given by

$$\tilde{\sigma}_{xx}(\omega) = \frac{1}{2}\left[\tilde{\sigma}_{xx}^{l=1}(\omega) + \tilde{\sigma}_{xx}^{l=-1}(\omega)\right]. \tag{15}$$

This shows that the excitation energy is given by a zero point of the dielectric function $\varepsilon_{xx}^{l=\pm 1}(\omega)$. Actually, we have $\sigma_{xx}^{l=1}(\omega) = \sigma_{xx}^{l=-1}(\omega)$ within the present effective-mass scheme and therefore $\varepsilon_{xx}^{l=1}(\omega) = \varepsilon_{xx}^{l=-1}(\omega)$. In the presence of a slight asymmetry between the conduction and valence bands, $\sigma_{xx}^{l=1}(\omega) \neq \sigma_{xx}^{l=-1}(\omega)$ and therefore the absorption peak splits into two.

Figure 11 shows some examples of calculated absorption spectra. The dashed lines change into the solid lines by the depolarization effect. The absorption intensity is reduced by the depolarization effect, but the exciton manifests itself due to its large binding energy. Figure 12 shows the exciton energies for both parallel and perpendicular polarization. In the absence of interaction, the excitation energy for the perpendicular polarization is at the middle of those of the first and second gaps in the case of the parallel polarization. For the interaction strength $(e^2/\kappa L)(2\pi\gamma/L)^{-1} \gtrsim 0.1$ corresponding to actual systems, however, the exciton energy for the perpendicular polarization is closer to the second gap.

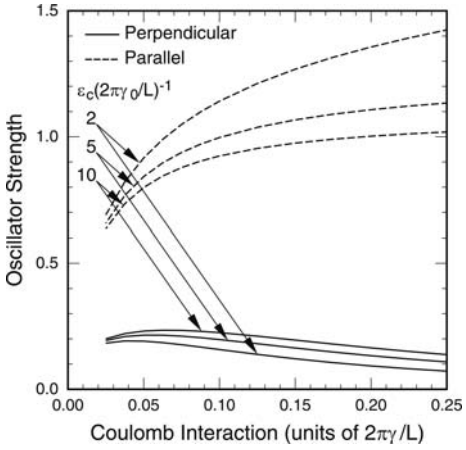

Fig. 13. The oscillator strength of the exciton absorption for the perpendicular (*solid lines*) and parallel polarization (*dashed lines*)

Figure 13 compares the oscillator strength of the exciton absorption between the case of the parallel and perpendicular polarization. The strength for the perpendicular polarization is about 10–20 % of that for the parallel polarization. In spite of this weakening of the intensity, it is certainly possible to observe exciton peaks for the perpendicular case.

Photoluminescence spectra of single-wall nanotubes were decomposed into those associated with absorption of parallel and perpendicular light [56]. The obtained spectra for perpendicular polarization showed that a peak with intensity about an order-of-magnitude smaller than that for parallel polarization appears at a position closer to that of the second lowest peak for parallel polarization. This result seems to be consistent with the theoretical prediction of the exciton absorption and emission of perpendicularly polarized light. The exciton peaks for perpendicular polarization were theoretically discussed in very thin nanotubes [36, 53].

6 Optical Phonons

Long-wavelength phonons play important roles in electron–phonon interaction and are usually described well by a continuum model. An equation of motion for optical phonons of two-dimensional graphite in the long-wavelength limit has been derived based on a valence-force-field model [18]. In nanotubes the wavevector becomes discrete in the circumference direction $q_x = 2\pi j/L$ with integer j and remains continuous in the axis direction (q). In the following we shall confine ourselves to the long-wavelength limit, $j = 0$ and $qL \ll 1$. Then, the phonon Hamiltonian is written as

$$\mathcal{H}_{\rm ph} = \sum_{q,\mu} \hbar\omega_0 \left(b^\dagger_{q\mu} b_{q\mu} + \frac{1}{2} \right), \tag{16}$$

where μ denotes the mode ($\mu = l$ for the longitudinal mode with the displacement in the axis direction and $\mu = t$ for the transverse mode with the displacement in the circumference direction), and $b^{\dagger}_{q\mu}$ and $b_{q\mu}$ are the creation and destruction operators, respectively [57].

The lattice displacement can be expanded as

$$\boldsymbol{u}(\boldsymbol{r}) = \sum_{q\mu} \sqrt{\frac{\hbar}{2NM\omega_0}} (b_{q\mu} + b^{\dagger}_{-q\mu}) \boldsymbol{e}_{q\mu} e^{iqy} \,, \tag{17}$$

where N is the number of unit cells, M is the mass of a carbon atom, and

$$\boldsymbol{e}_{ql} = i(0, q/|q|) \,, \quad \boldsymbol{e}_{qt} = i(q/|q|, 0) \,. \tag{18}$$

The interaction between optical phonons and electrons is described by the Hamiltonian

$$\mathcal{H}_{\rm int} = -\sqrt{2} \frac{\beta\gamma}{b^2} \boldsymbol{\sigma} \times \boldsymbol{u}(\boldsymbol{r}) \,, \tag{19}$$

where $b = a/\sqrt{3}$ is the equilibrium bond length and $\beta = -d \ln \gamma_0 / d \ln b$ with γ_0 being the resonance integral between nearest-neighbor carbon atoms appearing in a tight-binding model related to γ through $\gamma = (\sqrt{3}a/2)\gamma_0$ with $a = 2.46$ Å being the lattice constant [57]. The corresponding results for the K′ point are obtained by replacing $\boldsymbol{\sigma}$ by $\boldsymbol{\sigma}^*$.

Because the interaction is weak, the shift $\Delta\omega$ and the broadening Γ of the phonon frequency are given by the lowest-order perturbation. They are given by

$$\Delta\omega_\mu = \frac{1}{\hbar} \Re \Pi_\mu(q, \omega_0) \,, \quad \Gamma_\mu = -\frac{1}{\hbar} \Im \Pi_\mu(q, \omega_0) \,, \tag{20}$$

where $\Pi_\mu(q, \omega)$ is the self-energy of the phonon Green's function. For the contribution of the K point, for example, we have

$$\begin{aligned} \Pi_\mu(q, \omega) = -g_{\rm s} \sum_{s,s'} \sum_n \int \frac{dk}{2\pi} \left(\frac{\beta\gamma}{b^2} \right)^2 \frac{\hbar}{NM\omega_0} \\ \times \frac{1}{2} \left(1 \pm \frac{ss'[\kappa_{\nu\varphi}(n)^2 - k(k-q)]}{\sqrt{\kappa_{\nu\varphi}(n)^2 + k^2} \sqrt{\kappa_{\nu\varphi}(n)^2 + (k-q)^2}} \right) \\ \times \frac{f[\varepsilon^s_{\nu\varphi}(n,k)] - f[\varepsilon^{s'}_{\nu\varphi}(n,k-q)]}{\hbar\omega - \varepsilon^s_{\nu\varphi}(n,k) + \varepsilon^{s'}_{\nu\varphi}(n,k-q) + i0} \,, \end{aligned} \tag{21}$$

where $f(\varepsilon)$ is the Fermi distribution function and the upper and lower signs correspond to $\mu = l$ and t, respectively. The factor two comes from the electron spin. The correct self-energy is obtained by subtracting from the above the contribution in 2D graphite, which is obtained by the summation over a discrete wavevector in the circumference direction $\kappa_{\nu\varphi}(n)$ replaced with a continuous integration.

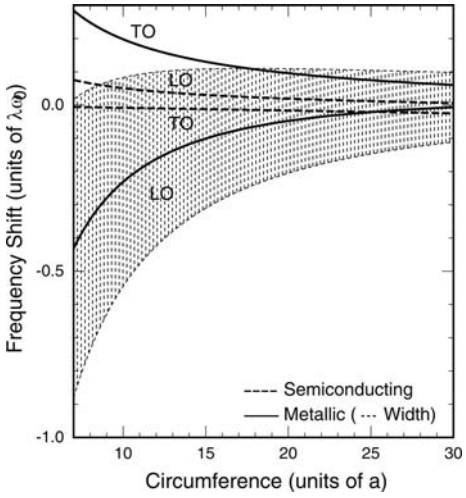

Fig. 14. Calculated frequency shifts of the optical phonons. The transverse and longitudinal modes are denoted by TO and LO, respectively. The *shadowed region* shows the broadening. The longitudinal mode is lowered in frequency and has large broadening in metallic nanotubes

The self-energy shows that a singular behavior occurs when the denominator vanishes. Because the phonon frequency is usually much smaller than bandgaps in semiconducting nanotubes, this occurs in metallic nanotubes with/without an Aharonov–Bohm magnetic flux and strain or in narrow-gap semiconductors with a small gap due to curvature. In fact, the most notable feature appears in the broadening.

$$\Gamma_t = \alpha(L)\omega_0 \frac{g_\mathrm{v} g_\mathrm{s} \pi \varphi^2}{\tilde{\omega}\sqrt{\tilde{\omega}^2 - 4\varphi^2}}\,, \tag{22}$$

$$\Gamma_l = \alpha(L)\omega_0 \frac{g_\mathrm{v} g_\mathrm{s} \pi}{4}\sqrt{1 - \left(\frac{2\varphi}{\tilde{\omega}}\right)^2}\,, \tag{23}$$

$$\alpha(L) = \lambda\frac{a}{L}\,, \tag{24}$$

with $\tilde{\omega} = \hbar\omega_0(2\pi\gamma/L)^{-1}$, where λ is the dimensionless parameter

$$\lambda = \frac{27}{\pi}\beta^2\gamma_0\frac{\hbar^2}{2Ma^2}\left(\frac{1}{\hbar\omega_0}\right)^2. \tag{25}$$

For the parameter $\hbar\omega_0 = 0.196\,\mathrm{eV}$, $\gamma_0 = 2.63\,\mathrm{eV}$, and $\beta = 2$, the parameter becomes $\lambda = 0.08$, but can be larger or smaller depending on β.

Figure 14 shows the frequency shift as a function of the circumference L. The broadening appears only in the longitudinal mode in metallic nanotubes and is shown by the dark region in the figure. In metallic nanotubes, the frequency decreases for the longitudinal mode and increases for the transverse mode. In semiconducting nanotubes, the behavior is completely opposite although the shift itself is much smaller.

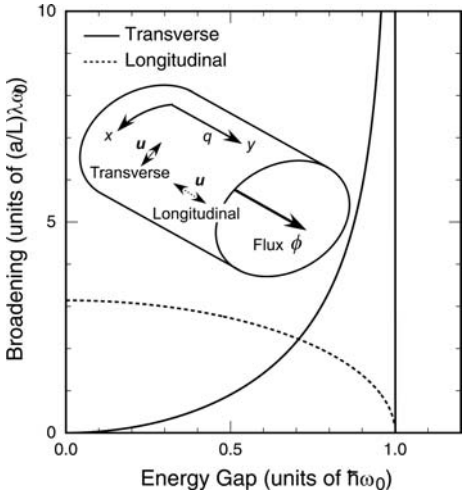

Fig. 15. The broadening of optical phonons in metallic nanotubes as a function of the bandgap induced by Aharonov–Bohm flux. When the gap reaches the optical-phonon energy $\hbar\omega_0$, the broadening disappears for the longitudinal mode and becomes infinite for the transverse mode

Figure 15 shows the broadening as a function of the Aharonov–Bohm gap $4\pi\gamma|\varphi|/L$. For the transverse mode, with the increase of the gap, the broadening increases in proportion to φ^2, diverges when the gap reaches the optical-phonon energy $\hbar\omega_0$, and vanishes when the gap exceeds the phonon energy. For the longitudinal mode, on the other hand, the broadening gradually decreases with the magnetic flux and vanishes when the gap reaches the phonon energy $\hbar\omega_0$.

The magnetic field required for the observation of this anomaly is about 200 T for typical single-wall nanotubes with diameter ~ 1.5 nm. This Aharonov–Bohm effect can be used for the determination of a narrow gap present in chiral nanotubes or in strained nanotubes, because this gap is also a result of an effective flux [7] as has been discussed in Sect. 2. Further, this effect can be sensitive to carrier doping.

Optical-phonon modes in nanotubes were studied theoretically using various methods such as the zone-folding scheme [58], force-constant models [59,60], first-principles methods [61–68] and some combinations [69]. Some of the features are in agreement with the results of these calculations, but there seem to remain significant disagreements among them and with the present results. The results can be compared with the G^+ and G^- peaks experimentally obtained [70]. The amount of the peak splitting seems to be in good agreement with the experiments for metallic nanotubes, but is smaller than the experiments for semiconducting nanotubes. The broadening of the longitudinal mode in metallic nanotubes predicted theoretically has the same order of magnitude as that of the G^- peak observed experimentally.

Acknowledgements

The author acknowledges collaboration with H. Ajiki, H. Suzuura, H. Sakai, S. Uryu, and K. Ishikawa. This work has been supported in part by a 21st Century COE Program at Tokyo Tech "Nanometer-Scale Quantum Physics" and by a Grant-in-Aid for Scientific Research from the Ministry of Education, Culture, Sports, Science and Technology, Japan.

References

[1] R. Saito, G. Dresselhaus, M. S. Dresselhaus: *Physical Properties of Carbon Nanotubes* (Imperial College Press, London 1998) 229
[2] H. Ajiki, T. Ando: Electronic states of carbon nanotubes, J. Phys. Soc. Jpn. **62**, 1255 (1993) 229, 232
[3] H. Ajiki, T. Ando: Magnetic properties of carbon nanotubes, J. Phys. Soc. Jpn. **63**, 4267 (1994) 229
[4] H. Ajiki, T. Ando: Magnetic properties of carbon nanotubes, J. Phys. Soc. Jpn. **62**, 2470 (1993) 229
[5] P. R. Wallace: The band theory of graphite, Phys. Rev. **71**, 622 (1947) 229
[6] J. C. Slonczewski, P. R. Weiss: Band structure of graphite, Phys. Rev. **109**, 272 (1958) 229
[7] T. Ando: Theory of electronic states and transport in carbon nanotubes, J. Phys. Soc. Jpn. **74**, 777 (2005) 229, 231, 245
[8] M. V. Berry: Quantum phase factors accompanying adiabatic changes, Proc. Roy. Soc. London, **A392**, 45 (1984) 230
[9] T. Ando, T. Nakanishi: Impurity scattering in carbon nanotubes – absence of back scattering –, J. Phys. Soc. Jpn. **67**, 1704 (1998) 230
[10] T. Ando, T. Nakanishi, R. Saito: Berry's phase and absence of back scattering in carbon nanotubes, J. Phys. Soc. Jpn. **67**, 2857 (1998) 230
[11] T. Ando, H. Suzuura: Presence of perfectly conducting channel in metallic carbon nanotubes, J. Phys. Soc. Jpn. **71**, 2753 (2002) 230
[12] T. Ando, K. Akimoto: Effects of short-range scatterers on perfect channel in metallic carbon nanotubes, J. Phys. Soc. Jpn. **73**, 1895 (2004) 230
[13] K. Akimoto, T. Ando: Effects of trigonal warping on perfect channel in metallic carbon nanotubes, J. Phys. Soc. Jpn. **73**, 2194 (2004) 230
[14] T. Ando: Aharonov-Bohm effect and symmetry crossover in carbon nanotubes, J. Phys. Soc. Jpn. **75**, 054701 (2006) 230
[15] J. W. McClure: Diamagnetism of graphite, Phys. Rev. **104**, 666 (1956) 230
[16] T. Ando: Spin-orbit interaction in carbon nanotubes, J. Phys. Soc. Jpn. **69**, 1757 (2000) 231
[17] C. L. Kane, E. J. Mele: Size, shape, and low energy electronic structure of carbon nanotubes, Phys. Rev. Lett. **78**, 1932 (1997) 231
[18] H. Suzuura, T. Ando: Phonons and electron-phonon scattering in carbon nanotubes, Phys. Rev. B **65**, 235412 (2002) 231, 242
[19] L. Yang, M. P. Anantram, J. Han, J. P. Lu: Band-gap change of carbon nanotubes: Effect of small uniaxial and torsional strain, Phys. Rev. B **60**, 13874 (1999) 231

[20] L. Yang, J. Han: Electronic structure of deformed carbon nanotubes, Phys. Rev. Lett. **85**, 154 (2000) 231
[21] H. Ajiki, T. Ando: Aharonov-Bohm effect in carbon nanotubes, Physica B **201**, 349 (1994) 233, 240, 241
[22] H. Ajiki, T. Ando: Carbon nanotubes: Optical absroption in Aharonov-Bohm flux, Jpn. J. Appl. Phys. Suppl. **34-1**, 107 (1995) 233, 240, 241
[23] T. Ando: Excitons in carbon nanotubes, J. Phys. Soc. Jpn. **66**, 1066 (1997) 233
[24] H. Sakai, H. Suzuura, T. Ando: Effective-mass theory of electron correlations in band structure of semiconducting carbon nanotubes, J. Phys. Soc. Jpn. **72**, 1698 (2003) 233
[25] H. Sakai, H. Suzuura, T. Ando: Effective-mass approach to interaction effects on electronic structure in carbon nanotubes, Physica E **22**, 704 (2004) 233
[26] L. Hedin: New method for calculating the one-particle green's function with application to the electron-gas problem, Phys. Rev. **139**, A796 (1965) 233
[27] A. W. Overhauser: Simplified theory of electron correlations in metals, Phys. Rev. B **3**, 1888 (1971) 233
[28] L. Hedin, S. Lundqvist: *Effects of Electron-electron and Electron-phonon Interactions on the One-electron States of Solids, Solid State Physics*, vol. 23 (Academic, New York 1969) p. 1 233
[29] T. Ando: Excitons in carbon nanotubes revisited: Dependence on diameter, Aharonov-Bohm flux, and strain, J. Phys. Soc. Jpn. **73**, 3351 (2004) 233
[30] E. A. Taft, H. R. Philipp: Optical properties of graphite, Phys. Rev. **138**, A197 (1965) 233
[31] M. Ichida, S. Mizuno, Y. Saito, H. Kataura, Y. Achiba, A. Nakamura: Coulomb effects on the fundamental optical transition in semiconducting single-walled carbon nanotubes: Divergent behavior in the small-diameter limit, Phys. Rev. B **65**, 241407 (2002) 235, 236
[32] S. M. Bachilo, M. S. Strano, C. Kittrell, R. H. Hauge, R. E. Smalley, R. B. Weisman: Structure-assigned optical spectra of single-walled carbon nanotubes, Science **298**, 2361 (2002) 235, 236
[33] M. Ichida, S. Mizuno, Y. Tani, Y. Saito, A. Nakamura: Exciton effects of optical transitions in single-wall carbon nanotubes, J. Phys. Soc. Jpn. **68**, 3131 (1999) 235, 236
[34] T. Miyake, S. Saito: Quasiparticle band structure of carbon nanotubes, Phys. Rev. B **68**, 155424 (2003) 236
[35] C. D. Spataru, S. Ismail-Beigi, L. X. Benedict, S. G. Louie: Quasiparticle energies, excitonic effects and optical absorption spectra of small-diameter single-walled carbon nanotubes, Appl. Phys. A **78**, 1129 (2004) 236
[36] E. Chang, G. Bussi, A. Ruini, E. Molinari: Excitons in carbon nanotubes: An ab initio symmetry-based approach, Phys. Rev. Lett. **92**, 196401 (2004) 236, 242
[37] R. B. Capaz, C. D. Spataru, S. Ismail-Beigi, S. G. Louie: Diameter and chirality dependence of exciton properties in carbon nanotubes, Phys. Rev. B **74**, 121401 (2006) 236
[38] C. D. Spataru, S. Ismail-Beigi, L. X. Benedict, S. G. Louie: Excitonic effects and optical spectra of single-walled carbon nanotubes, Phys. Rev. Lett. **92**, 077402 (2004) 236

[39] T. G. Pedersen: Variational approach to excitons in carbon nanotubes, Phys. Rev. B **67**, 073401 (2003) 236
[40] V. Perebeinos, J. Tersoff, P. Avouris: Scaling of excitons in carbon nanotubes, Phys. Rev. Lett. **92**, 257402 (2004) 236
[41] T. Ando: Effects of valley mixing and exchange on excitons in carbon nanotubes with Aharonov-Bohm flux, J. Phys. Soc. Jpn. **75**, 024707 (2006) 237
[42] K. Ohno: Some remarks on the Pariser–Parr–Pople method, Theoret. Chim. Acta **2**, 219 (1964) 238
[43] I. Ohmine, M. Karplus, K. Schulten: Renormalized configuration interaction method for electron correlation in the excited states of polyenes, J. Chem. Phys. **68**, 2298 (1978) 238
[44] V. Perebeinos, J. Tersoff, P. Avouris: Radiative lifetime of excitons in carbon nanotubes, Nano Lett. **5**, 2495 (2005) 238, 240
[45] S. Zaric, G. N. Ostojic, J. Kono, J. Shaver, V. C. Moore, R. H. Hauge, R. E. Smalley, X. Wei: Estimation of magnetic susceptibility anisotropy of carbon nanotubes using magnetophotoluminescence, Nano Lett. **4**, 2219 (2004) 239, 240
[46] L. J. Li, R. J. Nicholas: Magnetophotoluminescence of chirality-characterized single-walled carbon nanotubes, Internat. J. Mod. Phys. B **18**, 3509 (2004) 239, 240
[47] S. Zaric, G. N. Ostojic, J. Shaver, J. Kono, X. Wei, M. Furis, S. A. Crooker, O. Portugall, P. H. Frings, G. L. J. A. Rikken, V. C. Mooree, R. H. Haugee, R. E. Smalley: Magneto-optical spectroscopy of carbon nanotubes, Physica E **29**, 469 (2005) 239, 240
[48] S. Zaric, G. N. Ostojic, J. Shaver, J. Kono, O. Portugall, P. H. Frings, G. L. J. A. Rikken, M. Furis, S. A. Crooker, X. Wei, V. C. Moore, R. H. Hauge, R. E. Smalley: Excitons in carbon nanotubes with broken time-reversal symmetry, Phys. Rev. Lett. **96**, 016406 (2006) 239, 240
[49] H. Yokoi, N. Kuroda, Y. Kim, N. Minami, S. Kazaoui, K. Uchida, S. Takeyama: Magneto-optical study of Aharonov-Bohm effect on second subbands in single-walled carbon nanotubes, in J. Kono, J. Leotin (Eds.): *Narrow Gap Semiconductors* 2005 (*Institute of Physics Conference Series Number* 187) (Taylor & Francis, London 2006) p. 278 239, 240
[50] S. Zaric, G. N. Ostojic, J. Kono, J. Shaver, V. C. Moore, M. S. Strano, R. H. Hauge, R. E. Smalley, X. Wei: Optical signatures of the Aharonov-Bohm phase in single-walled carbon nanotubes, Science **304**, 1129 (2004) 239, 240
[51] V. Perebeinos, J. Tersoff, P. Avouris: Electron-phonon interaction and transport in semiconducting carbon nanotubes, Phys. Rev. Lett. **94**, 086802 (2005) 240
[52] C. D. Spataru, S. Ismail-Beigi, R. B. Capaz, S. G. Louie: Theory and ab inito calculation of radiative lifetime of excitons in semiconducting carbon nanotubes, Phys. Rev. Lett. **95**, 247402 (2005) 240
[53] H. Zhao, S. Mazumdar: Electron-electron interaction effects on the optical excitations of semiconducting single-walled carbon nanotubes, Phys. Rev. Lett. **93**, 157402 (2004) 240, 242
[54] I. B. Mortimer, R. J. Nicholas: Role of bright and dark excitons in the temperature-dependent photoluminescence, Phys. Rev. Lett. **98**, 027404 (2007) 240

[55] S. Uryu, T. Ando: Exciton absorption of perpendicularly polarized light in carbon nanotubes, Phys. Rev. B **74**, 155411 (2006) 240
[56] Y. Miyauchi, M. Oba, S. Maruyama: Cross-polarized optical absorption of single-walled nanotubes probed by polarized photoluminescence excitation spectroscopy, Phys. Rev. B **74**, 205440 (2006) 242
[57] K. Ishikawa, T. Ando: Optical phonon interacting with electrons in carbon nanotubes, J. Phys. Soc. Jpn. **75**, 084713 (2006) 243
[58] R. A. Jishi, L. Venkataraman, M. S. Dresselhaus, G. Dresselhaus: Phonon modes in carbon nanotubules, Chem. Phys. Lett. **209**, 77 (1993) 245
[59] R. Saito, T. Takeya, T. Kimura, G. Dresselhaus, M. S. Dresselhaus: Raman intensity of single-wall carbon nanotubes, Phys. Rev. B **57**, 4145 (1998) 245
[60] J. Maultzsch, S. Reich, C. Thomsen, E. Dobardzic, I. Milosevic, M. Damnjanovic: Phonon dispersion of carbon nanotubes, Solid State Commun. **121**, 471 (2002) 245
[61] O. Dubay, G. Kresse, H. Kuzmany: Phonon softening in metallic nanotubes by a Peierls-like mechanism, Phys. Rev. Lett. **88**, 235506 (2002) 245
[62] O. Dubay, G. Kresse: Accurate density functional calculations for the phonon dispersion relations of graphite layer and carbon nanotubes, Phys. Rev. B **67**, 035401 (2003) 245
[63] D. Sanchez-Portal, E. Artacho, J. M. Soler, A. Rubio, P. Ordejon: Ab initio structural, elastic, and vibrational properties of carbon nanotubes, Phys. Rev. B **59**, 12678 (1999) 245
[64] S. Reich, C. Thomsen, P. Ordejon: Phonon eigenvectors of chiral nanotubes, Phys. Rev. B **64**, 195416 (2001) 245
[65] K.-P. Bohnen, R. Heid, H. J. Liu, C. T. Chan: Lattice dynamics and electron-phonon interaction in (3,3) carbon nanotubes, Phys. Rev. Lett. **93**, 245501 (2004) 245
[66] D. Connetable, G.-M. Rignanese, J.-C. Charlier, X. Blase: Room temperature Peierls distortion in small diameter nanotubes, Phys. Rev. Lett. **94**, 015503 (2005) 245
[67] R. Barnett, E. Demler, E. Kaxiras: Electron-phonon interaction in ultrasmall-radius carbon nanotubes, Phys. Rev. B **71**, 035429 (2005) 245
[68] I. Milosevic, E. Dobardzic, M. Damnjanovic: Phonons in narrow carbon nanotubes, Phys. Rev. B **72**, 085426 (2005) 245
[69] M. Lazzeri, S. Piscanec, F. Mauri, A. C. Ferrari, J. Robertson: Phonon linewidths and electron-phonon coupling in graphite and nanotubes, Phys. Rev. B **73**, 155426 (2006) 245
[70] A. Jorio, A. G. S. Filho, G. Dresselhaus, M. S. Dresselhaus, A. K. Swan, M. S. Unlu, B. B. Goldberg, M. A. Pimenta, J. H. Hafner, C. M. Lieber, R. Saito: g-band resonant Raman study of 62 isolated single-wall carbon nanotubes, Phys. Rev. B **65**, 155412 (2002) 245

Index

Excitonic States and Resonance Raman Spectroscopy of Single-Wall Carbon Nanotubes

Riichiro Saito[1], Cristiano Fantini[2], and Jie Jiang[3]

[1] Department of Physics, Tohoku University and CREST JST, Sendai 980-8578, Japan
rsaito@flex.phys.tohoku.ac.jp
[2] Departamento de Física, Universidade Federal de Minas Gerais, Belo Horizonte, MG, 30123-970, Brazil
cfleite@fisica.ufmg.br
[3] Department of Physics, NC State University, Raleigh, NC 27695-7518, USA
jiang@chips.ncsu.edu

Abstract. This chapter includes both experimental and theoretical results on Raman spectroscopy of carbon nanotubes. Raman-scattering measurements are reported on the effect of using different kinds of carbon nanotube samples. Resonance Raman profiles (intensity vs. excitation energy), associated with different types of carbon nanotubes have been obtained from a quasicontinuous change of the excitation energy. Experimental plots of optical transition energies as a function of the nanotube diameter have been obtained from the experiments and can be directly compared with theoretical calculations. In the theory part, we have investigated the Raman spectra of the first-order Raman process in terms of excitonic states and their interaction with photons and phonons. We compare these results with former theoretical results obtained on the basis of the electron–hole pair picture. We show that the Raman intensity shows a unique chiral-angle and diameter dependence for single-wall carbon nanotubes.

1 Introduction

1.1 Outline

In this chapter, we present recent progress on resonance Raman spectroscopy (RRS) of single-wall carbon nanotubes (SWNTs), which has been investigated intensively since the first observation of RRS from a single individual SWNT [1]. RRS is widely used for the sample evaluation and characterization of carbon nanotubes because it is a noncontact and nondestructive measurement, operated at room temperature and in air (see the contribution by Yamamoto et al., and the contribution by Jorio et al.). By changing the laser excitation energies, we can observe resonance-enhancement phenomena associated with the Raman intensity from which we can assign (n, m) values to individual SWNTs precisely. Now we know that the RRS intensity for an

A. Jorio, G. Dresselhaus, M. S. Dresselhaus (Eds.): Carbon Nanotubes,
Topics Appl. Physics **111**, 251–286 (2008)

(n, m) SWNT has a strong chirality and diameter dependence. Thus, we can determine the population of specific (n, m) nanotubes in the sample by combining experiment and theory. Thus, an understanding of the Raman spectra of SWNTs is important from both a scientific and an applications point of view.

An important concept in RRS is the exciton picture in which a photoexcited electron and hole pair is combined into an exciton. In semiconductor physics, the exciton normally has a binding energy on the order of a few meV and is observed only at a low temperature. However, for one-dimensional (1D) materials, the exciton binding energy (0.3–0.5 eV) is much larger than the thermal energy $k_{\mathrm{B}}T$ at room temperature (see the contribution by Spataru et al.) and thus exciton effects can be obtained even at room temperature. Because of the localized wavefunction of an exciton, the intensity of the optical process is enhanced significantly, and thus, Raman spectroscopy in SWNTs is dominated by excitons from photoexcited electron–hole pairs.

In this contribution, we give an overview of both observations and calculations of RRS phenomena in SWNTs. In Sect. 2, we review the Raman spectra observed for the various spectral features, including the radial breathing modes (RBM), G-band, G'-band, and so on. In Sect. 3, the resonance Raman profile is discussed. In Sect. 4 we discuss Raman intensity calculations using exciton wavefunctions. The results for the exciton Raman intensity are compared with the corresponding results obtained for free electron–hole pairs. Finally, in Sect. 5, topics of special interest are briefly discussed and future directions for the field are suggested.

1.2 Overview of Resonance Raman Measurements

Resonance Raman spectra of SWNTs are usually acquired using a triple-monochromator micro-Raman setup in a backscattering configuration. The fore-monochromator stage is used to eliminate the light originating from elastic scattering processes and the spectrograph is responsible for the dispersion of the light originating from the inelastic scattering. Alternatively, a single-monochromator micro-Raman system can be used. In this case the scattered light goes directly from the sample to the spectrograph stage passing by a notch filter that blocks the elastic scattered light. A more intense Raman signal is obtained with a single monochromator. However, when many laser excitation energies are used in the experiment, such as in a tunable laser, a triple-monochromator setup is necessary.

Most of the experiments described here were performed using both discrete excitation energies from Ar:Kr and He:Ne lasers, and tunable Ti:sapphire and dye lasers. Both Ti:sapphire and dye lasers are usually pumped by an Ar ion laser in a multiline mode, with output power ≥ 5 W. The Ti:sapphire laser provides output wavelengths in the near-infrared (NIR) range from (1080 to 700 nm) and the dye laser allows us to change the output wavelengths in the visible region and the specific wavelength range depends on

the kind of dye solution used. Usually, three different dyes are used in the experiments described here: DCM special[1], rhodamine 590, and rhodamine 560, whose output wavelengths range from 680 to 520 nm. For wavelengths in the range from 520 to 458 nm, several discrete lines of the Ar:Kr laser are frequently used.

In micro-Raman measurements, an optical microscope is attached to the system so that we can get a spatial resolution up to the wavelength of the light. Usually the samples are focused using 10×, 50× and 100× objectives for SWNTs in solution, in bundles and isolated on a SiO_2 substrate, respectively. In experiments with carbon-nanotube samples on SiO_2 substrates or suspended in aqueous solution, high laser power density (up to 40 $mW/\mu m^2$) can be used without heating or damaging the samples. For nanotube samples in bundles or as isolated SWNTs suspended in air, a low power density ($< 1\,mW/\mu m^2$) must be used. For polarized Raman experiments, an analyzer is placed after the microscope and two half-wave plates are placed, one before and another after the microscope, to rotate the polarization of the incident and scattered light in relation to the nanotube axis. Alternatively, only one half-wave plate that rotates both the incident and scattered light can be used.

1.3 Overview of the Raman Intensity Calculation

The resonance Raman intensity calculation is based on several other computational programs, such as that of 1. the electronic structure, 2. the phonon dispersion, 3. the electron–photon interaction, and 4. the electron–phonon interaction. The first-order Raman process (Fig. 1) consists of optical absorption ($M^{\mathrm{op}}(\mu,k)$), phonon emission ($M^{\mathrm{el-ph}}(\mu,k)$), and photon emission ($M^{\mathrm{op}}(\mu,k)$), which are calculated by the following intensity formula for each phonon mode at the center of the Brillouin zone with energy E_{ph} and for the μth cutting line[2] and for a given laser energy E_{L}

$$I^{\mu}(E_{\mathrm{L}}) = \sum_{\mu} \int \left| \frac{M^{\mathrm{op}}(\mu,k) M^{\mathrm{el-ph}}(\mu,k) M^{\mathrm{op}}(\mu,k)}{[E_{\mathrm{L}} - E_{\mu}(k) - i\gamma]\,[E_{\mathrm{L}} - E_{\mu}(k) - E_{\mathrm{ph}} - i\gamma]} \right|^2 dk. \qquad (1)$$

Here, the integration on k is taken for the μth cutting line that is relevant to the ith optical transition (E_{ii}) [2, 4]. In the second-order resonance Raman spectra, two-phonon scattering (instead of one) occurs in the Raman processes [5, 6]. For defect-induced Raman features such as the D-band, we need to consider the elastic scattering of an electron in one of the two possible sequences of scattering processes in a second-order Raman process [7].

[1] DCM special is a 1 : 1 mixture of the dyes DCM (4-dicyanomethylene-2-methyl-6-p-dimethylaminostyryl-4H-pyran [$C_{19}H_{17}N_3$]) and sulphorhodamine B ($C_{27}H_{30}N_2S_2O_3$).

[2] The cutting line is defined by the one-dimensional Brillouin zone lines of a SWNT in the two-dimensional Brillouin zone of graphite [2, 3].

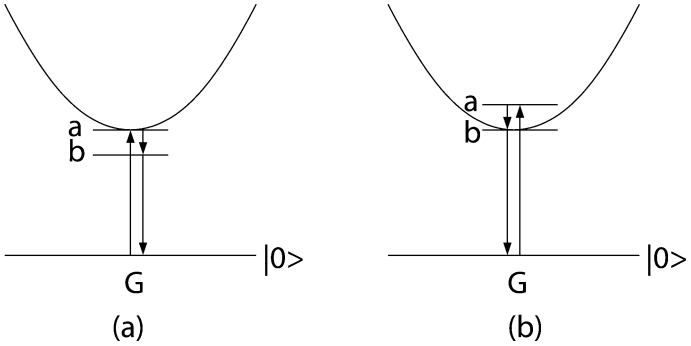

Fig. 1. First-order resonance Raman processes, (**a**) incident resonance process and (**b**) scattered resonance process. G, a and b denote, respectively, the ground state and the intermediate states

In second-order Raman processes, the scattering of a phonon can have a finite k value since an electron can go back to its original position to recombine with the hole [5]. The electronic and phonon structures are calculated by the extended tight-binding method in which up to 20th nearest-neighbor parameters are fitted to the first-principles calculation to reproduce the interatomic potential and the energy dispersion of the electrons and phonons [8].

When we consider many-body effects such as the Coulomb interaction between a photoexcited electron and valence electrons, the electron–hole wavefunction is localized in real space to form an exciton by mixing different k states. The exciton wavefunction is calculated by solving the Bethe–Salpeter equation within the extended tight-binding method [9]. The exciton wavefunction is used for calculating the exciton–photon and exciton–phonon interactions as well as the Raman intensity [10, 11].

In a real RRS process, we do not expect a singular resonance response at $E_{\mathrm{L}} = E_{\mu}(k)$ (Fig. 1a) or $E_{\mathrm{L}} = E_{\mu}(k) + E_{\mathrm{ph}}$ (Fig. 1b), but rather a finite response because of the resonance width γ. The γ values in resonance Raman spectra appear in the denominators $(E_{\mathrm{L}} - E(k) - i\gamma)$ or $(E_{\mathrm{L}} - E(k) - E_{\mathrm{ph}} - i\gamma)$ of (1) that give an energy width of γ in the resonance Raman profile. The origin of γ is associated with the finite lifetime of the scattering event that is expressed as an energy by the uncertainty relation of quantum mechanics [12]. Since the phonon emission lifetime is less than 1 ps, the corresponding energy width is about 0.1 eV. Thus, for intensity calculations, the explicit consideration of γ values is essential.

2 Measurement of Raman Spectra

2.1 Raman Spectra of SWNTs

In Fig. 2, we show the Raman spectrum for bundled SWNT samples. The low-frequency features (100–400 cm^{-1}) show the radial breathing mode (RBM), associated with vibrations of carbon atoms in a radial direction from the nanotube axis associated with all SWNTs within the resonance window of E_L. The band observed between 1500 and 1600 cm^{-1} is associated with the highest-frequency optical phonon modes at the Γ-point in the Brillouin zone. This band is also denoted by the graphite-like band or simply the G band, because these modes originate from the even parity E_{2g} Raman mode of graphite, which in the case of nanotubes splits into G^+ and G^- peaks. In addition to the G-band, we can see in the spectrum of Fig. 2 the defect-induced band (also denoted by the D-band) at $\sim 1300\,\mathrm{cm}^{-1}$ that is induced by the presence of amorphous carbon remaining from the synthesis or by symmetry-breaking defects in the nanotube structure and this Raman feature originates from a double-resonance process [5]. The overtone of the D-band called the G′-band (also seen in highly oriented graphite) is observed at around 2600 cm^{-1}. The inset (a) in Fig. 2 represents a zoom of the spectral range between the RBM and the D-band, from 600 to 1100 cm^{-1}. We can see in the zoom the presence of several low-intensity features, and since their frequency occurs between the low- and the high-frequency regions, we call these modes intermediate-frequency modes (IFMs). Most of these modes are associated with second-order (two phonon) Raman processes. Other weak features observed in Fig. 2 with frequencies above the G-band also originate from a two-phonon process. The so-called M (2oTO) and iTOLA features are enlarged in the inset (b) in Fig. 2.

In the following sections we discuss in some detail all of these features in the Raman spectra and the recent advances in the understanding of the nanotube physics provided from RRS.

2.2 The Radial Breathing Mode

The radial breathing mode is a totally symmetric vibrational mode associated with the vibration of carbon atoms in a radial direction in relation to the nanotube axis. Theoretical and experimental results show that the RBM frequency (ω_{RBM}) is inversely proportional to the nanotube diameter, following the equation, $\omega_{\mathrm{RBM}} = A/d_{\mathrm{t}} + B$. The parameters A ($\mathrm{cm}^{-1}\mathrm{nm}$) and B (cm^{-1}) are determined experimentally and different values have been obtained for 1. nanotubes on a SiO_2 substrate [1] ($A = 248$, $B = 0$), 2. bundled nanotubes[3] [13] ($A = 239$, $B = 0$), 3. dispersed in aqueous solution [14] ($A = 218$, $B = 16$) or 4. free-standing nanotubes [15] ($A = 204$, $B = 27$).

[3] Based on the formula for an (n, m) tube, $\omega_{\mathrm{RBM}} = \{239 - 5(n - m)/n\}/d_{\mathrm{t}}$.

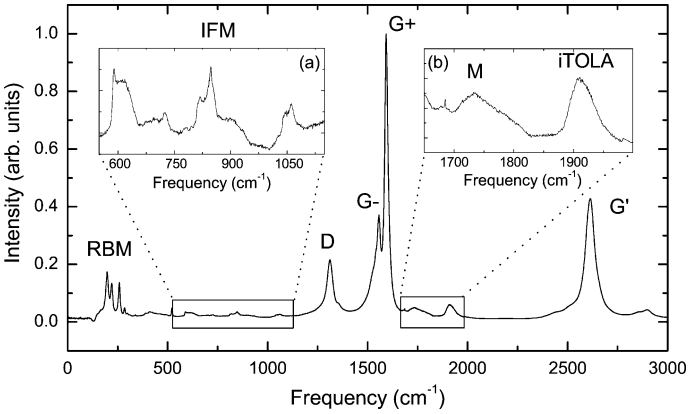

Fig. 2. Raman spectrum of SWNT bundles (HiPco) obtained with excitation laser energy $E_{\mathrm{L}} = 1.96\,\mathrm{eV}$. The radial breathing mode (RBM), the disorder-induced (D) band, the graphite-like (G^{+} and G^{-}) band, the intermediate-frequency modes (IFMs), G′-band, M and iTOLA bands are observed in the figure. The ranges associated with the IFM (600–1100 cm^{-1}) and the M and iTOLA bands (1650–2000 cm^{-1}) are enlarged in the *insets* (**a**) and (**b**), respectively

Because of its dependence on the nanotube diameter, the spectra of this mode is largely used for the characterization of the diameter distribution in a carbon-nanotube sample. The Raman intensity for the RBM is strongly enhanced when the incident or scattered light is in resonance with an excitonic transition according to (1). Thus, the Raman spectra of the RBMs for a sample composed of an ensemble of different nanotube chiralities is strongly dependent on E_{L} because for each value of E_{L}, the optical transition energies (E_{ii}) for different SWNTs are in resonance, and thus, the intensity of the RBM for these nanotubes is resonantly enhanced. Figures 3a and b show the RBM spectra obtained using different laser excitation energies (E_{L}) for two SWNT samples produced by the HiPco [16] and arc-discharge [17] methods, respectively (see the description of these synthesis methods in the contribution by Joselevich et al.). We can see in Fig. 3 the strong dependence of the RBM spectra on E_{L} and on the synthesis method and synthesis conditions used in the growth process, because of the different distribution of nanotube diameters in the two samples. The arc-discharge sample shows RBM peaks at lower frequencies than the RBMs observed for the HiPco sample, showing that the HiPco synthesis method produces smaller-diameter nanotubes.

The strong resonance enhancement in the RBM Raman spectra makes it possible to observe the Raman spectrum of one single nanotube when the energy of the incident or the scattered light is in resonance with the energy of an optical transition to an excitonic level. The observation of the RBM for single nanotubes allows us to get the (n, m) assignment for the nanotube observed as described in [1]. Figure 3c shows some RBM spectra for isolated

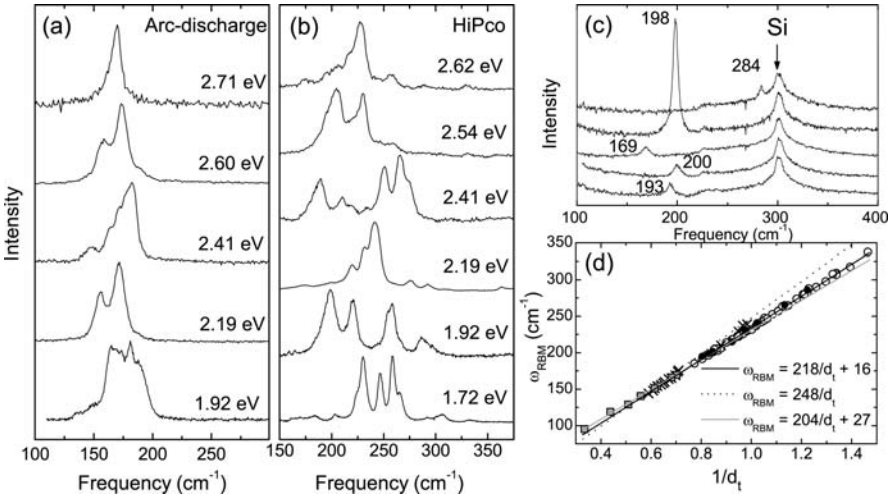

Fig. 3. RBM Raman spectra, obtained with different laser excitation energies, of bundled carbon nanotube samples prepared by the (**a**) arc-discharge and (**b**) HiPco methods. (**c**) RBM Raman spectra, obtained with $E_{\mathrm{L}} = 2.19\,\mathrm{eV}$, for 5 different isolated SWNTs grown by the HiPco method on an SiO_2 substrate. (**d**) a ω_{RBM} vs. d_{t} plot and their fitting functions. CVD SWNTs on SiO_2 (×), HiPco SWNTs on SiO_2 (*solid circles*), HiPco SWNTs in solution [14] (*open circles*), free-standing SWNTs [15] (*gray squares*), whose data is fitted, respectively, to $\omega_{\mathrm{RBM}} = A/d_{\mathrm{t}} + B$, with $(A, B) = (248, 0)$ for CVD [1], (218,16) for HiPco [14], and (204,17) for free-standing [15] samples

carbon nanotubes prepared by the HiPco method on a SiO_2 substrate. The sample has a density ≤ 1 SWNT/$\mu\mathrm{m}^2$, and therefore, only one nanotube is probed in each spectrum. The spectra were obtained with $E_{\mathrm{L}} = 2.19\,\mathrm{eV}$ and the (n, m) assignment is obtained from the observed RBM frequency. From the (n, m) assignment, the nanotube diameters are obtained and the resulting RBM frequencies are plotted in Fig. 3d as a function of the inverse of the nanotube diameter. Experimental results obtained for different kinds of samples (see figure caption) are shown in Fig. 3d. The three curves presented here become close to one another for large (1.5–2.5 nm) d_{t} compared with the shift due to the environment. In the contribution by Jorio et al., more discussion on sample dependence is given.

2.3 G-Band

The graphite-like band (G-band) in carbon nanotubes is directly related to the G-band in graphite that is identified with an in-plane tangential optical phonon involving the stretching of the bond between the two atoms in the graphene unit cell. While the G-band in graphite exhibits a single Lorentzian

feature of E_{2g} symmetry at $\sim 1582\,\mathrm{cm}^{-1}$, the G-band of carbon nanotubes is composed of several peaks originating from the quantum confinement of the wavevector along the SWNT circumferential direction, and the folding of the graphite Brillouin zone into the SWNT Brillouin zone. The G-band of a chiral (achiral) SWNT is composed of phonon modes of symmetries $A(A_{1g})$, $E_1(E_{1g})$ and $E_2(E_{2g})$ originating from a first-order Raman process. Two phonons of each symmetry are both predicted [18] and observed [19]. However, for defective samples other phonons of different symmetries can also be observed due to the double-resonance Raman process [20]. The G-band feature has been extensively studied for both bundled and isolated carbon nanotubes and the differences in the spectral features for semiconducting and metallic nanotubes, as well as the diameter dependence of their peak frequencies is well established. Moreover, the identification of the phonon symmetries and the assignment of single- and double-resonance features in the G-band have been obtained by polarized Raman experiments [6, 21–23].

The right panels of Fig. 4a show the G-band Raman spectra of isolated semiconducting SWNTs, where two main features, the so-called G^- and G^+ components, are observed with frequencies at ~ 1570 and $\sim 1590\,\mathrm{cm}^{-1}$, respectively. These two features are associated, respectively, with vibrations of the carbon atoms along the circumferential direction (TO phonon) and along the nanotube axis (LO phonon). The G^- feature is strongly sensitive to whether the nanotube is metallic or semiconducting, showing a Breit–Wigner–Fano (BWF) lineshape in the case of metallic nanotubes, as described in [24, 25]. The diameter dependence of the frequencies of the G^+ and G^- features are obtained from measurements of the RBM [Fig. 4a left panels] and G-band spectra [Fig. 4a right panels] for the same SWNT. Such measurements reveal that the frequency of the G^+ feature is both diameter and chiral-angle independent, while the G^- feature shows a dependence on the nanotube diameter. The frequencies of the G^- and G^+ features are plotted in Fig. 4b as a function of $1/d_t$ for 46 isolated semiconducting (solid circles) and 16 isolated metallic (open circles) SWNTs. The frequency of the G^- feature can be very well fitted with the equation $\omega_G^- = \omega_G^+ - C/d_t^2$, with the constants $\omega_G^+ = 1591\,\mathrm{cm}^{-1}$ and $C = 47.7\ (79.5)\,\mathrm{cm}^{-1}\mathrm{nm}^2$ for semiconducting (metallic) SWNTs [19].

According to the resonance Raman selection rules for chiral (achiral) SWNTs, A (A_{1g}) symmetry modes must be observed when both the incident and scattered light are polarized parallel to each other (VV configuration), and, on the other hand, E_1 (E_{1g}) modes must be observed when the polarizations for incident and scattered light are perpendicular to each other (VH configuration). However in the case of bundled nanotubes, they must be aligned so that polarization effects can be observed, although both A_1 and E_1 modes will be observed in the VV and VH polarizations. The E_2 (E_{2g}) symmetry phonons are only observed when the polarization of the incident and scattered light are both polarized perpendicular to the nanotube axis. The E_2 phonons can be clearly distinguished from the other ones in the experiments

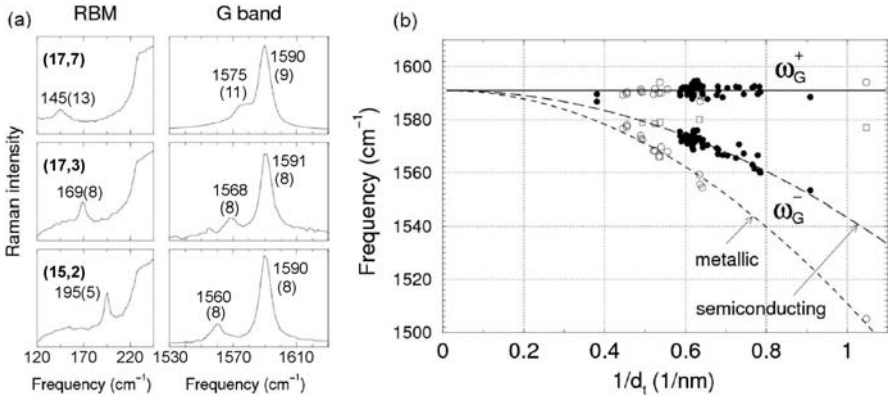

Fig. 4. (**a**) G-band spectra for some isolated, semiconducting SWNTs. (**b**) Diameter dependence of the G^- and G^+ frequencies [19]

on aligned bundled SWNTs, while the A and E_1 can not be clearly separated because their frequencies overlap [22]. The E_2 symmetry modes are observed for crosspolarized light in resonance with optical transitions from the E_μ^v to $E_{\mu\pm2}^c$ excitonic states [23]. However, a strong reduction in the Raman intensity is observed, especially for metallic nanotubes, when both the incident and scattered light are polarized perpendicular to the nanotube axis [26, 27] due to the antenna effect [28]. Thus, the optical spectra of carbon nanotubes are dominated by the absorption/emission of light polarized parallel to the nanotube axis and, consequently, by A symmetry modes.

Recent studies show that the properties of the BWF lineshapes for metallic SWNTs, i.e., its low-frequency and broad aspect, are related to the electron–phonon coupling near the Fermi energy [10, 29–31]. Because of the electron–phonon interaction, the phonon mode frequency at a certain wavevector is downshifted (Kohn anomaly) for one of the two G-modes of SWNTs. In this case, the assignment for TO (G^+) and LO (G^-) phonon modes in metallic SWNTs is opposite to the assignment for TO (G^-) and LO (G^+) phonon modes in semiconducting SWNTs [31]. This effect demonstrates the importance of the electron–phonon interaction for the high-energy optical phonons in nanotubes, important for the electronic properties (see the contribution by *Charlier* et al.).

Several theoretical studies have proposed that the BWF lineshape of the G^- peak of metallic nanotubes is the result of a Kohn anomaly (KA) at the Γ point [10, 29–31]. In accordance with the KA, the LO phonon distorts the lattice in such a way that a dynamic bandgap is induced in the electronic band structure [32, 33]. This effect on the electron–phonon (el–ph) interaction lowers the energy of the valence electrons near the Fermi point that in turn

lowers the energy required to distort the lattice, hence softening the phonon (see the contribution by *Charlier* et al.).

Since it is the LO phonon that is softened by the KA, the TO(G^+) and LO(G^-) assignment in metallic SWNTs is opposite to that of semiconducting nanotubes, where the TO phonon is at a lower energy due to the curvature of the rolled up graphene sheet. This assignment is supported by experiments on individual metallic nanotubes in which the el–ph coupling is observed to be weakened by tuning the Fermi level away from the Dirac point [34, 35]. As the interaction between electrons and phonons is reduced, the LO frequency increases and eventually becomes higher than the TO frequency, resulting in the recovery of the LO(G^+) and TO(G^-) frequency ordering found in semiconducting tubes.

Experiments at the single-nanotube level have also reported an assortment of G-band lineshapes [36]. By correlating the (n, m) assignment of metallic tubes with their G-band lineshape, *Maultzsch* et al. show that the degree of phonon softening depends on the diameter and chiral angle, likely because of differences in the el–ph matrix elements. Raman selection rules also contribute to the assortment of G^--band lineshapes that are observed. For instance, in zigzag(armchair) nanotubes the TO(LO) Raman mode is not allowed. This chirality dependence explains the absence of the BWF feature in the Raman spectra of certain individual metallic nanotubes.

2.4 D-Band

In contrast to the first-order process, where only phonons near the Γ point of the Brillouin zone are probed, in second-order Raman spectra it is possible to probe features identified with phonons associated with interior points in the Brillouin zone. This becomes possible because the selection rules for the second-order features are relaxed with respect to the first-order features. The most common example of a second-order feature in the Raman spectra of carbon nanotubes is the disorder-induced D-band, observed in the ∼1300–1400 cm^{-1} range (see Fig. 2). The D-band, common to all sp^2-hybridized disordered carbon materials, originates from phonons close to the K point of the graphite Brillouin zone, and becomes active in carbon nanotubes due to the presence of defects, such as impurities or missing atoms, finite-size effects and molecules linked to the nanotube sidewalls. In graphite, the frequency of this band shows a strong linear dependence on the excitation laser energy, presenting a dispersion $\Delta\omega_{\mathrm{D}}/\Delta E_{\mathrm{L}} \sim 53\,\mathrm{cm}^{-1}/\mathrm{eV}$. This strong E_{L} dependence is caused by a softening of the LO phonons near the K(K') point due to the electron–phonon coupling, i.e., the Kohn anomaly [37, 38]. The dispersive behavior of this band has been explained by a double-resonance process involving a phonon and a defect [5, 7, 39]. In this process an electron–hole pair is created when the incident photon is absorbed. After that, the electron is scattered by a phonon (or a defect) with wavevector q and scattered back

by a defect (or phonon) with wavevector $-q$, recombining with the hole and emitting a scattered photon.

The E_{L} dependence of the D-band has been largely investigated for both bundled and isolated carbon nanotube samples. In both cases, a dispersion in ω_{D} as a function of E_{L} has been observed, but, with some marked differences. In the case of bundled carbon nanotube samples, it has been observed for a given value of E_{L} that the D-band frequency is always smaller by about $\sim 20\,\mathrm{cm}^{-1}$, as compared with other sp^2 carbon materials. The ω_{D} for SWNT bundles is observed to follow the relation $\omega_{\mathrm{D}} = 1210 + 53E_{\mathrm{L}}$, with ω_{D} in cm^{-1} and E_{L} in eV [40]. For bundled nanotubes an oscillation is observed in the E_{L} dependence of ω_{D}. Such an oscillation is not observed for other sp^2 carbon materials [40].

For a given E_{L}, the different isolated SWNTs actually exhibit different ω_{D} values, because the double-resonance condition must be satisfied for each tube [41, 42]. It is also observed for isolated nanotubes that ω_{D} decreases with decreasing nanotube diameter [41, 43, 44]. Thus, the D-band spectra observed for a sample composed of an ensemble of nanotubes is a sum of different features originating from different (n, m) species of nanotubes and for resonances with different E_{ii}, which together give rise to the oscillatory behavior discussed above.

2.5 G′-Band

The most intense feature in the second-order Raman spectra of SWNTs is the overtone of the D-band feature discussed above, the so-called G′-band, whose frequency is $2\omega_{\mathrm{D}}$ (see Fig. 2) and its frequency dispersion is twice the D-band frequency dispersion. While the D-band originates from a double-resonance process involving a phonon and a defect, in the G′-band, instead of a defect, another phonon is responsible for the momentum conservation in the double-resonance process.

In contrast to what happens in graphene, where the G′-band is a single Lorentzian feature, sometimes two features are observed for the G′-band in isolated carbon nanotubes [45]. The presence of two peaks in the G′-band of a single nanotube indicates the resonance with two different van Hove singularities, one in (space) resonance with the incident photon of energy E_{L} and another inresonance with the scattered photon $E_{\mathrm{L}} \pm E'_{\mathrm{G}}$. The signals + and − correspond to the anti-Stokes and Stokes processes, respectively. The two peaks observed in the G′-band are associated with phonons corresponding to the wavevectors $q_i = 2k_i$ where i represents the ith optical transition energy E_{ii}. In the case of semiconducting nanotubes where the resonance occurs with the optical transition energies E^S_{33} and E^S_{44}, the difference in the phonon wavevectors is $q_4 - q_3 \simeq 4d_{\mathrm{t}}/3$. Thus, the two different features observed in the G′-band are related to phonons with different wavevectors in the phonon dispersion around the K point.

In the case of metallic nanotubes, the two peaks observed in the G′-band originate from the splitting in the van Hove singularities caused by the trigonal warping effect [46, 47]. The electron wavevector, and consequently also the phonon wavevectors, for the two resonance states in this case show almost the same magnitude but opposite signs in the wavevector relative to the K point. Thus, the two peaks observed in the G′-band are caused by an anisotropy of the phonon dispersion around the K point, known as the phonon trigonal warping effect [48].

2.6 Intermediate-Frequency Modes

In the spectral range between the RBM and the D-band, we observe some low-intensity features, the so-called intermediate-frequency modes (IFMs) as we can see in the inset (a) to Fig. 2. It was observed that these modes exhibit a strong dependence on the laser excitation energy, and a dispersion of their frequency with E_{laser} has been reported [49]. However, the dispersive behavior is not monotonic, as observed for many features in graphite-like materials due to energy-selective double-resonance Raman-scattering processes [5, 7], but it rather occurs in "steps", and we refer to this effect as a "step-like dispersive behavior" [50, 51]. Figures 5a and b show the Raman spectra of bundled SWNT samples grown by the arc-discharge and HiPco methods, respectively, obtained in the frequency range 600–1100 cm^{-1}, and measured using many laser energies (E_{laser}) in the range 1.62–2.71 eV. The shaded areas represent some nondispersive peaks that can be assigned as first-order Raman features [51], in particular, the central peak arises from the out-of-plane transverse optical (oT0) phonon of graphite, and its frequency is $\omega_{\text{oT0}} \sim$ 860 and 845 cm^{-1} for the arc-discharge and HiPco samples, respectively. This difference in the oTO frequency is due to the different diameter distributions of the two samples. The arrows in Figs. 5a and b clearly show well-resolved step-like dispersive IFM peaks appearing and disappearing in the spectra while E_{laser} is varied. A lineshape analysis of the spectra reveals the same effect for peaks above ω_{oTO}. It is important to emphasize that the number of IFM peaks below and above ω_{oTO} and their frequencies are different for the two samples discussed here.

The dispersion of the IFMs can be described by considering the creation of both an optic and an acoustic-like phonon (positive dispersion), or considering the creation of an optic phonon and the annihilation of an acoustic-like phonon (negative dispersion).[4] Thus, the IFM frequency can be written as

$$\omega_{\text{IFM}}^{\pm} = \omega_{\mathcal{O}}^{\pm} \pm \omega_{\mathcal{A}} \,, \tag{2}$$

where $\omega_{\mathcal{O}}$ and $\omega_{\mathcal{A}}$ correspond, respectively, to the frequencies of the optic and acoustic-like phonon [50]. The frequency of the acoustic phonon can be writ-

[4] We call these modes acoustic-like because they originate from an acoustic branch for 2D graphite, but, in SWNTs, they are actually optic modes.

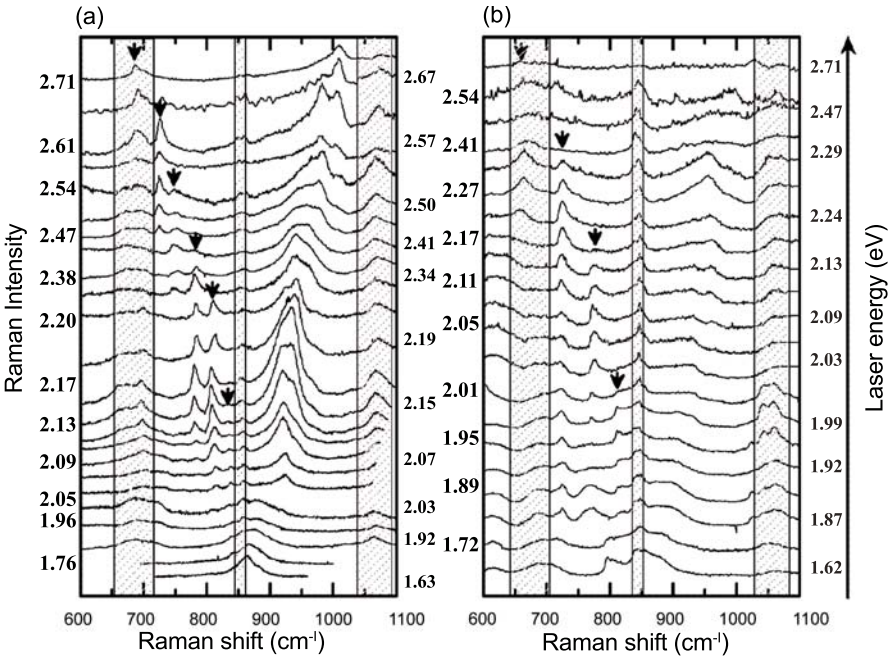

Fig. 5. Raman spectra of the IFMs for arc-discharge (**a**) and HiPco (**b**) samples obtained by changing the laser energy between 1.63 and 2.71 eV. The arrows in the figure represent the well-resolved and step-like dispersive IFM peaks below the first-order peak at $\omega_{\mathrm{oTO}} \sim 860\,\mathrm{cm}^{-1}$ in (a) and at $\omega_{\mathrm{oTO}} \sim 845\,\mathrm{cm}^{-1}$ in (b). The *shaded areas* mark the nondispersive features [51]

ten as $\omega_{\mathcal{A}} = v_{\mathcal{A}} q_{\perp}$ where $v_{\mathcal{A}}$ is its dispersion and $q_{\perp}$ is the wavevector perpendicular to the nanotube axis. However, this two-phonon coupling assumption does not by itself explain the resonance-selective process responsible for the step-like dispersion that is observed. Both the nanotube electronic structure and a double-resonance process must be considered in the discussion.

The IFM can be explained considering a double-resonance process where two electronic states E_i and E_j are connected by two phonons, e.g., an optical and an acoustic-like phonon. In this case, both the incident and scattered photon are in resonance with different electronic states, connected to one another by phonons with symmetry E_{μ} that follow the selection rule ($\mu_{\mathrm{phonon}} = \mu_j - \mu_i$). In the case of the arc-discharge sample, the E_{33}^S and E_{44}^S optical transition energies are resonant, and the electronic states E_4^S and E_3^S are connected by phonons with symmetry E_3, and in this case $q_{\perp} = 6/d_{\mathrm{t}}$, showing an explicit diameter dependence of the IFM frequencies. The proposed model to explain the IFM in semiconducting nanotubes [50] can also be applied to explain the electronic transitions associated with metallic SWNTs [51], by just changing the phonon symmetry. The diameter depen-

dence of the IFM features has been confirmed in experiments with DWNTs where the inner and outer tubes show distinctly distinguishable bands in the IFM region [52]. The explanations above have been made considering free electron–hole pairs. The IFM spectra have not been explained yet considering excitons. Another unexplained point about the IFMs is their dependence on the nanotube length and on the presence of defects in the nanotubes.

2.7 Other Two-Phonon Modes

Beside the G' band and the IFMs discussed above, several other two-phonon modes present in the Raman spectra of carbon nanotubes have been assigned and deserve to be mentioned here. Some low-intensive modes observed with frequencies above the G-band (see inset (b) to Fig. 2) have recently received some attention. One set of modes is the so-called M-band observed at $\sim 1750\,\mathrm{cm}^{-1}$, and is assigned as an overtone of the out-of-plane (oTO) phonon in graphite [53]. The M-band is composed of a nondispersive M^{+} feature associated with an intravalley $q = 0$ scattering process, and an M^{-} feature associated with an intervalley $q = 2k$ process, that exhibits a small negative dispersion of $-23\,\mathrm{cm}^{-1}/\mathrm{eV}$. Another low-intensity second-order feature is observed at $\sim 1900\,\mathrm{cm}^{-1}$. This band, which shows a very large dispersion ($\sim 200\,\mathrm{cm}^{-1}/\mathrm{eV}$) in its frequency as E_{L} is changed and has been assigned as a combination of the iTO + LA phonons in graphite [53]. These modes are usually strong when using FT-Raman at $E_{\mathrm{L}} = 1.16\,\mathrm{eV}$. The intensity of these and other double-resonance features is a very important open issue.

Another two-phonon mode observed in the Raman spectra is a weak feature at around $2450\,\mathrm{cm}^{-1}$. This feature was assigned to the $q = 0$ scattering of optic-phonon modes [5] and a weak dispersion of its frequency with laser excitation energy has been observed [54]. However, recently, the $2450\,\mathrm{cm}^{-1}$ mode has been assigned to other Raman combination modes of TO and LA at $q = 2k$ along the K-Γ direction near the K point [55].

3 Resonance Raman Profile

3.1 Experimental Optical Transition Energies

Because of the strong dependence of the Raman intensity on the density of electronic states, the resonance Raman profiles of the RBM, i.e., the RBM Raman intensity as a function of E_{L}, are very useful in the study of the nanotube electronic structure. When E_{L} is continuously changed in the measurements of the RBM, it is possible to observe a change in the intensity of the RBM when it comes in and out of the resonance condition. The resonance Raman profile for an RBM was first observed for an isolated SWNT grown by the CVD method on a SiO_2 substrate, and from the experimental spectra the joint density of states associated with that SWNT was obtained [56]. For

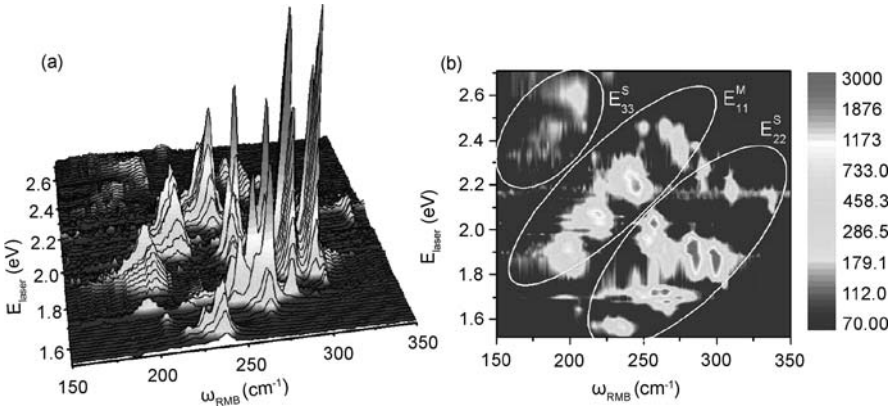

Fig. 6. (**a**) RBM resonance Raman measurements of HiPco SWNTs dispersed in a sodium dodecyl sulfate (SDS) aqueous solution, measured with 76 different laser lines E_{L} [14]. The nonresonance Raman spectrum from a separated CCl_4 solution is acquired after each RBM measurement, and the CCl_4 features are used to calibrate the spectral intensities and to check the frequency calibration with high resolution (better than $0.5\,\mathrm{cm}^{-1}$). (**b**) Top view of (a). The intensity scale is given on the right

a sample composed of an ensemble of different (n, m) nanotube species, the resonance behavior for the RBMs associated with different (n, m) nanotubes is observed.

Figure 6 presents Stokes resonance Raman measurements of carbon nanotubes, grown by the HiPco process and dispersed in a sodium dodecyl sulfate (SDS) [$CH_3(CH_2)_{11}$–$NaSO_4$] aqueous solution [57], in the frequency region of the RBM features. In these experiments a tunable laser system that allows an almost continuous change of the excitation laser energies (E_{L}) in the range between 1.52 eV up to 2.71 eV was used [14]. This quasicontinuous variation of E_{L} allows us to obtain detailed information about the evolution of the RBM Raman spectra as a function of E_{L}. Several RBM peaks appear in Fig. 6, each peak corresponding to a carbon nanotube in resonance with E_{L}, thereby delineating for each nanotube the resonance profile. This experiment can be used to determine, from resonance Raman spectroscopy measurements, the two sets of information $(E_{ii}, \omega_{\mathrm{RBM}})$ for each (n, m) nanotube. The frequency determination ω_{RBM} is directly given in the Raman spectra with $0.5\,\mathrm{cm}^{-1}$ accuracy. The electronic transition energy determination E_{ii} is obtained by analyzing the resonance profile for each RBM peak, as discussed below.

From these measurements, plots of the Stokes and anti-Stokes Raman peak intensities for each RBM frequency versus E_{L} are determined (see Fig. 7a). Stokes and anti-Stokes resonance profiles are shifted in energy due to the difference in the emission and absorption energies, given by the $\pm E_{\mathrm{ph}}$

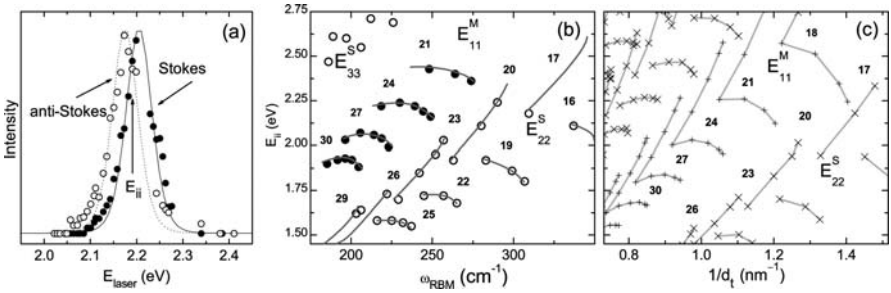

Fig. 7. (**a**) Stokes (*solid symbols*) and anti-Stokes (*open symbols*) experimental resonance windows obtained for the RBM of an SDS-wrapped nanotube [14]. (**b**) Electronic transition energies E_{ii} vs. ω_{RBM} for 41 different (n, m) carbon nanotubes measured by resonance Raman spectroscopy [14]. *Open* and *solid circles* denote, respectively, semiconducting and metallic SWNTs wrapped with SDS in aqueous solution. *Solid lines*, delineate nanotubes belonging to families of constant values of $(2n + m)$ (**c**) A theoretical plot similar to (b) of E_{ii} vs. $1/d_{\mathrm{t}}$ based on the ETB model [2, 8, 58]

term in (1) for the E_{L}-dependent resonance Raman intensity. From the fitting of the resonance windows, the γ values for the different (n, m) nanotubes are determined. The γ values for SDS-wrapped nanotubes in solution are between 40 and 80 meV depending on the (n, m). This (n, m) dependence of the γ values is further discussed later in this review.

The intersection points between the Stokes and anti-Stokes resonance windows [see arrows in Fig. 7a] give the transition energies E_{ii} accurately (to ± 5 meV). The intensity for the anti-Stokes resonant windows is normalized by the relation $I_{\mathrm{AS}}/I_{\mathrm{S}} = n(E_{\mathrm{ph}})/[n(E_{\mathrm{ph}}) + 1]$, where $n(E_{\mathrm{ph}}) = 1/[\exp(E_{\mathrm{ph}}/k_{\mathrm{B}}T) - 1]$ is the Bose–Einstein thermal factor. For the SWNTs in solution, $T = 300$ K in the Boltzmann factor normalizes the Stokes and anti-Stokes resonance windows, so that heating due to laser power need not be considered in the analysis.

Figure 7b plots the experimental results obtained for E_{ii} vs. ω_{RBM} for each (n, m) nanotube. Open and solid circles represent, respectively, semiconducting and metallic HiPco nanotubes wrapped in SDS. Different E_{ii} electronic transitions for semiconducting (E_{22}^S and E_{33}^S) and metallic (E_{11}^M) tubes are clearly seen. The geometrical patterns for carbon-nanotube families with $(2n + m) =$ constant (solid lines) for E_{22}^S and E_{11}^M can be seen in the figure, and for each family the corresponding value of $2n + m$ is shown. The $(E_{ii}, \omega_{\mathrm{RBM}})$ results (Fig. 7a) can be compared with extended tight-binding (ETB) predictions (Fig. 7c), where curvature effects and $\sigma - \pi$ rehybridization are considered [8, 58].

The electronic transition energies for metallic SWNTs, not observed in the photoluminescence studies, are also determined by RRS (black circles in

Fig. 7b), and the formation of families of constant $(2n + m)$ is also observed for these nanotubes. Surprisingly, the expected splitting in the E_{11}^{M} van Hove singularities (see Fig. 7c) caused by the trigonal warping effect [59, 60] was not observed in this experiment, and only the lower-energy component of E_{11}^{M} for each (n, m) SWNT was observed (Fig. 7a). The observation of only one E_{11}^{M} peak arises because the electron–phonon coupling matrix elements for the E_{11}^{M+} are very weak as compared with the E_{11}^{M-} ones [61, 62]. Some RBM Raman peaks associated with resonances with E_{ii}^{M+} were recently observed for individual SWNTs grown by the CVD method [63] and the observation confirms the very weak intensities predicted for resonances with these higher-energy optical transitions. The maximum intensities for the observed RBM peaks associated with the E_{11}^{M+} resonances are about 7 times lower than that associated with E_{11}^{M-} resonances. The families observed in the geometrical pattern for the metallic nanotube data are also used to find the (n, m) assignment for metallic nanotubes. From the (n, m) assignment the relation $\omega_{\mathrm{RBM}}(\mathrm{cm}^{-1}) = 218/d_{\mathrm{t}}(nm) + 16$ between the RBM frequency and the nanotube diameter (open circles and black solid curve in Fig. 3d) was obtained, with a deviation of the experimental points from this relation that is smaller than $\pm 2\,\mathrm{cm}^{-1}$. A more detailed description of the determination of the (n, m) assignment and the use of RRS for nanotubes characterization is presented in the contribution by *Jorio* et al. of this book.

A comparison between Figs. 7b and 7c reveals an up to 240 meV shift to lower energies in the theoretical plot, obtained from the ETB model [8, 58] when compared with the experimental plot obtained by resonance Raman spectroscopy [14]. This discrepancy between the experimental and theoretical results, 10 times larger than the experimental accuracy, is corrected when many-body effects originating from both electron–electron and electron–hole interactions are considered and such corrections have been applied to ETB calculations [64].

4 Electron–Phonon and Electron–Photon Matrix Elements

Starting from a discussion of the early calculations (ETB) that showed the origin of $(2n + m)$ family behavior, we explain here why we need the more recent work on the exciton and how to calculate the resonance Raman intensity (1) by the ETB model and the excitonic wavefunctions.

4.1 Extended Tight-Binding Method for Electrons and Phonons

The extended tight-binding (ETB) method is a tight-binding (TB) method for calculating the electronic and phonon structure in which we consider long-distance carbon–carbon interactions and σ–π interactions as TB parameters [8]. We adopted the TB parameters given by the Porezag function

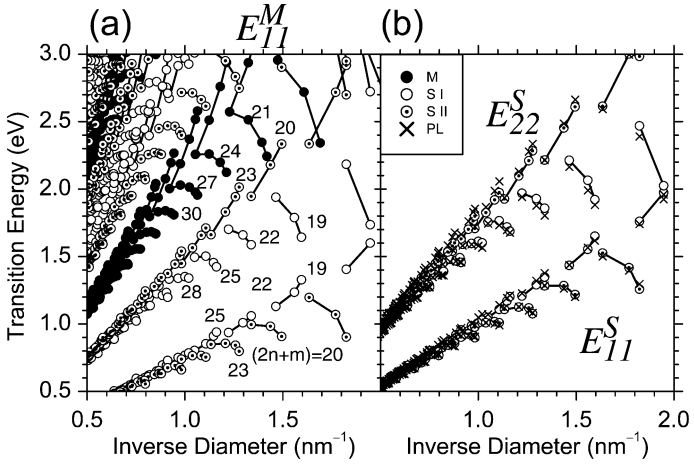

Fig. 8. (**a**) Extended tight-binding results of E_{ii} as a function of inverse diameter d_t^{-1}, (**b**) comparison of theory with photoluminescence energy measurements [8]

for the interatomic distance between two carbon atoms that are fitted either to first-principles calculations or to experimental results [65]. In the ETB method, we consider both 2s and 2p orbitals of a carbon atom within the Slater–Koster scheme so that we can take into account the curvature effect of a small-diameter (less than 1 nm) SWNT. In the phonon-structure calculation, we construct the dynamical matrix elements in which we use force constants up to 20 nearest neighbors fitted to the phonon dispersions $\omega(q)$ based on inelastic X-ray [55] and electron energy-loss spectroscopy [66] and first-principles calculations [30].

For the phonon-dispersion calculation, we use the symmetry of the SWNT, to help solve for each cutting line, a 6×6 dynamical matrix for each k [67]. Thus, the calculation of the phonon dispersion for a given (n, m) SWNT is very quick. By calculating the electronic density of states, we obtain the energy separation E_{ii} of two van Hove singularities between the ith conduction and ith valence energy bands. The plot of E_{ii} as a function of the diameter of SWNTs (d_t or d_t^{-1}) is called the Kataura plot within the ETB scheme (see the contribution by *Jorio* et al.). The ETB calculation reproduces well the experimental Kataura plot (see Fig. 8) provided that we add the empirical many-body effect [64].

In Fig. 8a, E_{ii} values for metallic (solid circles), type I (open circle), type II (open-dot circles) semiconducting nanotubes are plotted as a function of d_t^{-1}. In Fig. 8b, we also plot the experimental photoluminescence (PL) energy values (crosses). We can see that the calculated values reproduce PL energies well. Here, type I and II semiconducting SWNTs are defined by $\mathrm{mod}(2n + m, 3) = 1$ or 2, respectively, for an (n, m) semiconducting SWNT. The SWNTs with the same $2n + m$ value are identified as a $(2n + m)$ family

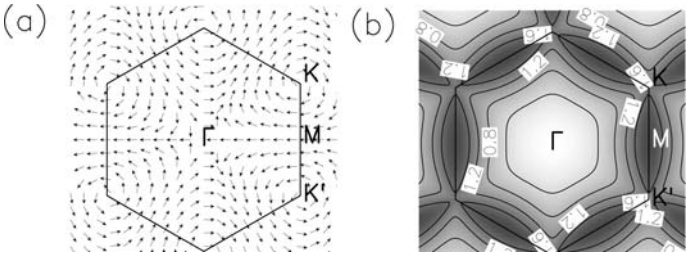

Fig. 9. (**a**) The normalized dipole vector is plotted as a function of $\boldsymbol{k}$ over the 2D BZ. (**b**) The oscillator strength is plotted over the 2D BZ in units of atomic dipole vector m_{opt} as a function of $\boldsymbol{k}$ (by A. Gruneis, Thesis, Tohoku Univ. 2004)

that is shown in Fig. 8a by lines connecting appropriate circles. Since (n, m) SWNTs with the same $2n + m$ family values have similar diameters to one another, the variation of E_{ii} within the $2n + m$ family shows the chiral-angle dependence. In RRS, for a given E_{L}, we can find the resonance (n, m) value and its d_{t} (or ω_{RBM}) from the Kataura plot. Since the frequency of the RBM is inversely proportional to d_{t}, the plot of E_{ii} as a function of ω_{RBM} is given purely by experiment, which we call the experimental Kataura plot.

From the Kataura plot, we can assign the (n, m) value of the PL or Raman spectra for a given laser energy. However, in actual experiments, the E_{ii} values shift by up to 80 meV depending on the surrounding materials of a SWNT (environmental effect, as discussed in the contribution by *Jorio* et al.). This is due to the screening of the Coulomb interaction by dielectric materials. Nevertheless, the shift by the environmental effect is systematic, so that if we can get experimental information on a set of E_{ii} for a given family (and the family pattern), we can determine the (n, m) values without difficulty.

4.2 Dipole Approximation for the Optical Matrix Element

In order to estimate the optical absorption and emission, we usually adopt the dipole approximation for optical transitions in which the optical matrix element is proportional to the inner product of the polarization vector $\boldsymbol{P}$ of light and the dipole vector, $\boldsymbol{D} \equiv < \Psi_{\mathrm{f}} | \nabla | \Psi_{\mathrm{i}} >$, where Ψ_{i} and Ψ_{f} are the initial and final electronic states, respectively.

When we plot the direction of $\boldsymbol{D}$ as a function of $\boldsymbol{k}$ using a single-particle wavefunction in the two-dimensional Brillouin zone (Fig. 9a), $\boldsymbol{D}$, which lies in the two-dimensional plane, rotates around the high symmetry K and K' points. When the polarization vector $\boldsymbol{P}$ rotates in the two-dimensional plane of graphene, the k points that contribute to the optical transition on the equienergy line moves. This effect has been observed in the nanographite system [68]. Further calculations show that this polarization dependence should also be observable in a SWNT [69]. This is a reason for the chirality dependence of the Raman and PL intensity [70].

The absolute values of $\boldsymbol{D}$, which is proportional to the oscillator strength (Fig. 9b), has larger values along the K–M lines compared with those along the K–Γ lines. Thus, dipole vectors are anisotropic with regard to both direction and intensity. This result is relevant to the fact that for type I semiconducting SWNTs the E_{22}^S absorption is larger than the type II E_{22}^S absorption, since the corresponding cutting line for type I E_{22}^S lies along the K–Γ line while that for type II E_{22}^S lies along the K–Γ line. As for E_{11}^S the situation for type I and II SWNTs is exchanged with each other. Since E_{22}^S gives a larger type I and II difference, the PL intensity is generally larger for type I tubes of similar diameter, as is also observed experimentally [71].

4.3 Electron–Phonon Matrix Element Calculation

The electron–phonon (el–ph) matrix element is calculated by an inner product of the deformation potential vector $\langle \Psi_{\boldsymbol{k}'}(\boldsymbol{r})|\delta V|\Psi_{\boldsymbol{k}}(\boldsymbol{r})\rangle$ and the vibration amplitude vector [67]. When we expand the ETB electron wavefunction $\Psi_{\boldsymbol{k}}$, the calculated deformation potentials δV are the sum of atomic deformation potentials that are defined by the three-center integrals of atoms for two atom wavefunctions and a one atom deformation potential. When the two atom wavefunctions are for the same atom, the atomic deformation potential gives an onsite el–ph interaction that modifies the on-site energy by the deformation of the other atom. When the two atomic wavefunctions come from different atoms, the atomic deformation potential gives an off-site electron–phonon interaction that modifies the transfer energy by the deformation of the atom. Both on-site and off-site el–ph interactions give important contributions to the phonon-scattering processes.

In graphene, we need to consider only the π orbital atomic deformation potential, which has a direction along the bond direction connecting the two carbon atoms. Since the atomic deformation potential vector lies in the graphene plane, the out-of-plane modes do not contribute to the el–ph coupling of graphene. The atomic deformation potential has a maximum value ($\approx 7.8\,\mathrm{eV/\AA}$) when the two electron centers are at the same site and the potential center is on a nearest-neighbor site, and it has a second maximum value ($\approx 3.2\,\mathrm{eV/\AA}$) when one electron has the same center as the potential and another electron center is on a nearest-neighbor site [67].

Due to curvature-induced rehybridization, π, σ and s orbitals are mixed with one another for the π band in SWNTs, although the π orbital is the dominant component in the wavefunction coefficient. It thus follows that we need to consider all orbitals in the atomic deformation-potential calculation. The atomic deformation-potential vector is either along or perpendicular to the bond connecting two atoms, so that the component of the vector perpendicular to the SWNT side wall is not zero, which contributes to the el–ph coupling for both the RBM and out-of-plane optic-phonon modes. For the LO and A_1 modes, where the vibration is basically in the nanotube side wall,

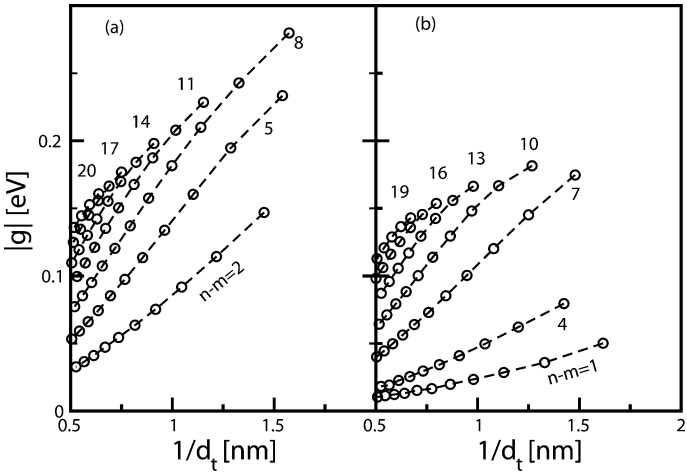

Fig. 10. Family patterns in the el–ph matrix element $|g|$ vs. inverse tube diameter at E_{22}^{S} transitions for the RBM, for (**a**) type I and (**b**) type II tubes. The numbers denote $n - m$ families [67]

the el–ph coupling is dominated by the π orbital since its atomic deformation potential is also basically in the nanotube sidewall.

Another important concept that must be considered is the intravalley and intervalley scattering processes. Since the equi-energy surfaces exist at the K and K' points, energy-momentum conserved phonon scattering consists of: 1. within the same K (or K') point (intravalley scattering) and 2. from the K to K' (or from K' to K) point (intervalley scattering). The intravalley (intervalley) scattering consists of $\boldsymbol{q}$ vectors around the Γ (or K) points. The phonon modes in first-order Raman processes are Γ point phonons, while not only zone-center phonon modes around the Γ point but also zone-edge phonon modes around the K point contribute to second-order Raman processes.

In Fig. 10, we plot the absolute value of the el–ph matrix element $|g|$ for the RBM for semiconductor SWNTs that shows strong type (type I or II), diameter and chiral-angle dependences [67]. M^{el-ph} in (1) equals to $-\sqrt{n/N_u}g$ with n and N_u the phonon number and the number of graphene unit cells in a SWNT, respectively. The matrix element generally decreases with d_{t} and chiral angle θ [2]. Similar to the electron–photon matrix element, the el–ph matrix element is sensitive to the position of the vHS, i.e., the $K\Gamma$ or KM sides [62]. The matrix element is larger on the KM side (E_{22}^S for type I) than the $K\Gamma$ side (E_{22}^S for type II). Moreover, the matrix element on the $K\Gamma$ side has nodes for θ close to 27°. Keeping the above rules in mind, we can draw the following conclusions. 1. Type I SWNTs have a larger matrix element than type II SWNTs at the transitions E_{22}^S, E_{44}^S, ..., while type II SWNTs have a larger matrix element than type I SWNTs at the transitions E_{11}^S, E_{33}^S, ..., 2. The matrix element for RBM modes becomes very small around a large

chiral angle ($\theta \sim 30°$) for type I SWNTs at the transitions E_{11}, E_{33}, ... and for type II SWNTs at the transitions E_{22}, E_{44}, ..., 3. The matrix element has a larger value around the zigzag SWNTs while it has a small value around the armchair SWNTs, 4. When we connect SWNTs with the same $(n - m)$ value (similar θ) in the matrix element vs $1/d_t$ plot, we can also see family patterns (see Fig. 10).

4.4 Extension to the Exciton Matrix Element Calculation

Recent theories and experiments on carbon nanotubes support a picture where excitonic effects are important to optical spectroscopy. Strongly bound excitons are predicted for small-diameter S-SWNTs and confirmed by experiments (see more detail in the contributions by *Spataru* et al. and by *Ando*).

The exciton energies and wavefunctions have been calculated by solving the Bethe–Salpeter equation within the simple and extended tight-binding models (STB and ETB) [9, 11]. The π electron screening effect is calculated within the random phase approximation (RPA) and the static screening approximation [72, 73]. The quasiparticle energies are calculated by including the self-energy corrections. A static dielectric constant κ is introduced to describe the effects of electrons in core states, σ bands, and the external environment of the SWNT. The value of $\kappa = 2$ will be used here unless otherwise mentioned.

Optical transitions are relevant to the electrons and holes around the K or K' regions of 2D graphene. If both the electron ($\boldsymbol{k}_c$) and hole ($\boldsymbol{k}_v$) lie on the same cutting line, the center-of-mass momentum $2\bar{\boldsymbol{K}} = \boldsymbol{k}_c - \boldsymbol{k}_v$ lies on the cutting line passing through the Γ point and the corresponding exciton is an A symmetry exciton. If the electron and hole are from two different cutting lines, the corresponding exciton is an E_μ symmetry exciton with an index $\mu = \mu_c - \mu_v$, where μ_c (μ_v) is the electron (hole) cutting-line index. The A excitons can further be classified into A_1 and A_2 excitons, which are symmetric and antisymmetric under the C_2 rotation around the axis perpendicular to the nanotube axis. For an achiral (armchair or zigzag) SWNT, exciton wavefunctions are either even or odd functions of z (z is along the tube axis) because of the inversion center in the SWNT. Thus, we use A_{2u} or A_{2g} to label an A_2 exciton in an achiral SWNT, which is symmetric or antisymmetric under a σ_h reflection ($z \to -z$), respectively. In the case of parallel polarization, an A_2-symmetry exciton for a chiral tube or an A_{2g} exciton for an achiral tube is a bright exciton and other excitons are dark (see details in the contributions by *Spataru* et al. and by *Ando*). In the case of perpendicular polarization, an E_1 or E_{-1} exciton is a bright exciton and other excitons are dark ones. We label exciton states by considering both the notation E_{ii} used for the optical-level designation and the exciton symmetries. For example, $E_{ii}(A)$ means that the electron and hole for an A exciton lie, respectively, on the ith cutting line with respect to the K point of the 2D BZ of graphene.

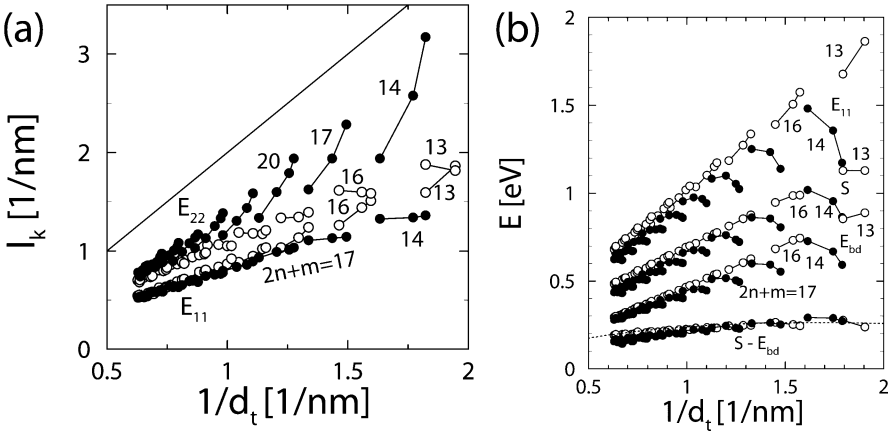

Fig. 11. (**a**) The half-width ℓ_k of the wavefunctions in 1D k space for $E_{11}(A_2^0)$ and $E_{22}(A_2^0)$ states. The cutting-line spacing $2/d_t$ is shown by the *solid line* for comparison. (**b**) The excitation energy E_{11}, self-energy Σ, binding energy $E_{\rm bd}$ and energy corrections $\Sigma - E_{\rm bd}$ based on the ETB for $E_{11}(A_2^0)$ states. The *dashed line* is calculated by (3) with $p = 1$. In both (a) and (b), *open* and *filled circles* are for type I and II SWNTs, respectively, and integers denote $2n + m$ values [9]

For $E_{ii}(A^n)$[5] $(n = 0, 1, 2, \dots)$ excitons, n is the number of nodes in the wavefunction along the tube axis. Here, we use the index $n = 1, 2, \dots$ to indicate the exciton excited states. Information on the wavefunction half-width (ℓ_k) in 1D k space, which is the width of k at a half-maximum amplitude of $\Psi(\boldsymbol{k})$, is especially important for discussing the chirality dependences of the exciton–photon and exciton–phonon matrix elements [11]. We find that (see Fig. 11a): 1. ℓ_k is always smaller than the cutting-line spacing $2/d_{\rm t}$ and the $E_{ii}(A_2^0)$ state has a larger ℓ_k than the $E_{ii}(A_2^\nu)$ states with $\nu = 1, 2, \dots$, indicating that one cutting line is sufficient to describe the $E_{ii}(A)$ states. 2. ℓ_k decreases with increasing $d_{\rm t}$ and the $E_{22}(A_2^0)$ have a larger ℓ_k than the $E_{11}(A_2^0)$. 3. ℓ_k shows a tube type (type I or II) dependence and $(2n+m)$-family patterns. For E_{11} states, type I SWNTs have a longer ℓ_k than type II SWNTs. For E_{22} states, in contrast, type II SWNTs have a longer ℓ_k than type I SWNTs.

It is well known that the excitation energy E_{ii} exhibits regular family patterns. It is interesting that the exciton binding energy $E_{\rm bd}$ for an $E_{11}(A_2^0)$ exciton shows family patterns similar to the excitation energy E_{11} (see Fig. 11b). Moreover, for the low energy transitions E_{11} and E_{22}, the family spread of the exciton binding energy is almost cancelled by the family

[5] A^n is an A symmetry exciton with n nodes.

spread of the self-energy correction to the quasiparticle energy Σ, leading to a logarithmic energy correction as a function of d_t (see Fig. 11b),

$$E^{\log} = 0.55(2p/3d_t)\log[3/(2p/3d_t)]\,. \tag{3}$$

Here, $p = 1, 2$ denote E_{11}^S, E_{22}^S respectively. The large family spread in the Kataura plot then comes from the single-particle spectra, which is contributed by the curvature effect and the C–C bond-length optimization in small d_t SWNTs. The many-body correction to E_{11} and E_{22} follows a logarithmic behavior by (3) and the magnitude of the correction is around 0.2 eV (see Fig. 11b). For the high energy transitions E_{11}^M, E_{33} and E_{44}, many body corrections make a contribution to the family spread in the Kataura plot and the magnitude of the correction can be as large as 0.6 eV.

The exciton–photon (ex–op) and exciton–phonon (ex–ph) matrix elements can be derived with the help of the exciton wavefunction and the el–op and el–ph matrix elements. As we mentioned in Sect. 4.2, we calculate the el–op matrix element M^{op} in the dipole approximation [74–76], i.e., $M^{op} \propto \boldsymbol{D}(\boldsymbol{k}', \boldsymbol{k})\ \boldsymbol{P}$. In the case of parallel polarization, the selection rule for $\boldsymbol{k}$ gives $\boldsymbol{k}' = \boldsymbol{k}$ and so $M^{op} \propto D_{\boldsymbol{k}}$ with D the z-component of $\boldsymbol{D}$. The exciton wavefunction $|\Psi_{\boldsymbol{q}}^n>$ with a center-of-mass momentum $\boldsymbol{q}$ can be expressed as

$$|\Psi_{\boldsymbol{q}}^n\rangle = \sum_{\boldsymbol{k}} Z^n_{\boldsymbol{k}c,(\boldsymbol{k}-\boldsymbol{q})v} c^+_{\boldsymbol{k}c} c_{(\boldsymbol{k}-\boldsymbol{q})v} |0\rangle, \tag{4}$$

where $Z^n_{\boldsymbol{k}c,(\boldsymbol{k}-\boldsymbol{q})v}$ is the eigenvector of the nth ($n = 0, 1, 2, \ldots$) state of the Bethe–Salpeter equation, and $|0\rangle$ is the ground state. The summation on $\boldsymbol{k}$ is taken for the 2D BZ. However, as we have mentioned, the summation on a single cutting line of a k state is sufficient [9]. Due to momentum conservation, the photon-excited exciton is an exciton with $\boldsymbol{q} = 0$. The ex–op matrix element is a summation over $\boldsymbol{k}$ of the el–op matrix element $D_{\boldsymbol{k}}$ weighted by the exciton wavefunction coefficient $Z^{n*}_{\boldsymbol{k}c,\boldsymbol{k}v}$,

$$M_{\text{ex–op}} = \sum_{\boldsymbol{k}} D_{\boldsymbol{k}} Z^{n*}_{\boldsymbol{k}c,\boldsymbol{k}v}\,. \tag{5}$$

When we use the relation $D_{\boldsymbol{k}} = D_{-\boldsymbol{k}}$, the ex–op matrix elements for the A_1 and A_2 excitons are given by

$$M_{\text{ex–op}}(A_1^n) = 0, \text{ and } M_{\text{ex–op}}(A_2^n) = \sqrt{2}\sum_{\boldsymbol{k}} D_{\boldsymbol{k}} Z^{n*}_{\boldsymbol{k}c,\boldsymbol{k}v}\,. \tag{6}$$

Here, $\boldsymbol{k}$ is either around K or K' of the 2D BZ. Equation (6) directly indicates that A_1 excitons are dark and only A_2 excitons are bright, which is consistent with the predictions by group theory [77].

An ex–ph scattering process involves both el–ph and hole–phonon (hl–ph) processes. Thus, ex–ph matrix elements have two terms,

$$M^{\text{ex–ph}}_{\boldsymbol{k},\boldsymbol{k}+\boldsymbol{q}} = \sum_{\boldsymbol{k}} \left[M^{\nu}(c) Z^{n2*}_{\boldsymbol{k}+\boldsymbol{q},\boldsymbol{k}-\boldsymbol{q}1} Z^{n1}_{\boldsymbol{k},\boldsymbol{k}-\boldsymbol{q}1} - M^{\nu}(v) Z^{n2*}_{\boldsymbol{k}+\boldsymbol{q}2,\boldsymbol{k}} Z^{n1}_{\boldsymbol{k}+\boldsymbol{q}2,\boldsymbol{k}+\boldsymbol{q}}\right], \tag{7}$$

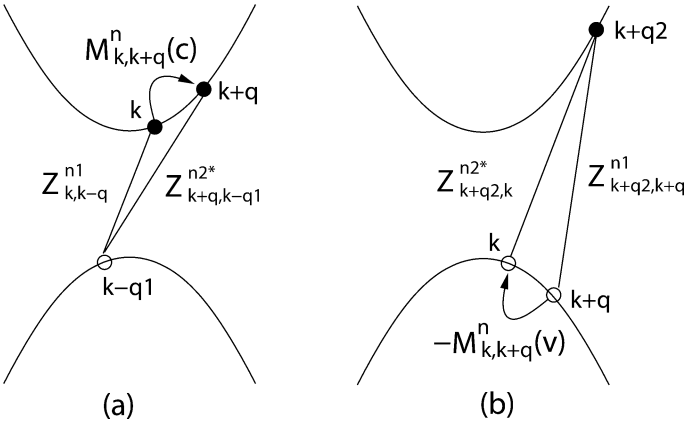

Fig. 12. (**a**) Electron- and (**b**) hole-scattering processes in the exciton–phonon matrix element for the first and second terms of (7). The matrix element for (a) and (b) is determined by the electron and hole matrix elements weighted by the wavefunction coefficients from the initial and final states

with $\boldsymbol{q} = \boldsymbol{q}2 - \boldsymbol{q}1$ giving the momentum conservation. The energy conservation gives $E^{n2}_{\boldsymbol{q}2} - E^{n1}_{\boldsymbol{q}1} = E_{\rm ph}$ for phonon absorption, and $E^{n1}_{\boldsymbol{q}1} - E^{n2}_{\boldsymbol{q}2} = E_{\rm ph}$ for phonon emission. In the following, we will consider only the Stokes (phonon emission) process and we will not explicitly write the phonon number in $|\Psi^n_{\boldsymbol{q}}\rangle$. Figure 12 schematically illustrates the electron- and hole-scattering processes in the ex–ph matrix element, which corresponds to the first and second terms in (7), respectively.

4.5 Raman Intensity Calculation

In the resonance Raman processes as shown in Fig. 1, by absorbing a photon the system is excited from the ground state ($|0\rangle$) to an A_2 excitonic state $|a\rangle$. The exciton then scatters by a phonon from $|a\rangle$ to $|b\rangle$ and is annihilated by emitting a photon. In the real calculation, the wavefunction for the virtual state ($|b\rangle$ in Fig. 1a and $|a\rangle$ in Fig. 1b) is replaced by that of the real state (($|a\rangle$ in Fig. 1a and $|b\rangle$ in Fig. 1b) as an approximation. Thus, the ex–ph matrix element for the resonance Raman processes is that between $|\Psi^n_0(A_2)\rangle$ and $|\Psi^n_0(A_2)\rangle$ states and the matrix element of (8) is simplified as

$$M_{\rm ex\text{–}ph} = \sum_{\boldsymbol{k}} \left[M^{\nu}_{\boldsymbol{k},\boldsymbol{k}}(c) - M^{\nu}_{\boldsymbol{k},\boldsymbol{k}}(v)\right] |Z_{\boldsymbol{k},\boldsymbol{k}}|^2. \tag{8}$$

After we calculate the exciton energy spectra, and the ex–op and ex–ph matrix elements, we can calculate the resonance Raman intensity in an

excitonic picture. For the first-order resonance Raman process, with the help of Fig. 1, the Stokes Raman intensity, $I_{\rm ex}$, can be written as

$$I_{\rm ex} = \left| \sum_a \frac{M_{\rm ex-op}(a) M_{\rm ex-ph}(a \to b) M_{\rm ex-op}(b)}{(E - E_a + i\gamma)(E - E_a - E_{\rm ph} + i\gamma)} \right|^2$$
$$= \left| \sum_a \frac{M_{\rm ex-op}(a)^2 M_{\rm ex-ph}(a \to a)}{(E - E_a + i\gamma)(E - E_a - E_{\rm ph} + i\gamma)} \right|^2 , \quad (9)$$

where γ is a broadening factor. Here, we assume that γ is a constant (0.06 eV) [62, 64]. In the second expression of (9), we replace the wavefunction of the virtual state $|b\rangle$ by that of the real state $|a\rangle$. The reason is that the virtual state $|b\rangle$ is a combination of all the A_2 real states with a zero center-of-mass momentum, and the real state $|a\rangle$ has a dominant component because the energy difference $|E_b - E_a|$ is the smallest in this case. Thus, we can set $|b\rangle = |a\rangle$ in (9). The summation in (9) is taken for all A_2 states that have a center-of-mass momentum $\boldsymbol{q} = 0$.

In the free-particle picture, the free e–h pair excited by a photon is that with the electron and hole at the same wavevector $\boldsymbol{k}$. Thus, the first-order Raman intensity in the free-particle picture $I_{\rm el}$ turns out to be (1).

4.6 RBM and G-Band: Length, Type, Chirality, and Diameter Dependence

The A_2^0 state has a much larger optical matrix element $M_{\rm ex-op}$ than the other excited exciton $A_2^n (n > 1)$ states. The large matrix element in A_2^0 is mainly due to the special shape of its $Z_{\boldsymbol{k}}$, which has no node. For the A_0^n state with $n = 2, 3, \ldots$ the contribution to $M_{\rm ex-op}$ from the positive and negative parts of $Z_{\boldsymbol{k}}$ are either cancelled or partially cancelled, leading to a zero or small matrix element value.

The matrix element $M_{\rm ex-op}$ increases with tube length L and $M_{\rm ex-op}$ follows the relationship $M_{\rm ex-op} \propto 1/\sqrt{L}$. Thus, when we consider the matrix element per unit length we should calculate $M_{\rm ex-op}/\sqrt{L}$. We find that the ex–op matrix element per two carbon atoms $M_{\rm ex-op}/\sqrt{N}$ is proportional to $1/d_{\rm t}$ (see Fig. 13). Since the el–op matrix element is weakly dependent on $d_{\rm t}$, the exciton effect enhances the optical matrix element diameter dependence. The $M_{\rm ex-op}/\sqrt{N} \propto 1/\sqrt{d_{\rm t}}$ dependence is from the $\ell_{\boldsymbol{k}} \propto 1/\sqrt{d_{\rm t}}$ dependence in the wavefunction delocalization length (Fig. 11a). Moreover, the exciton effects tend to decrease the chirality dependence of the optical matrix element (Fig. 13). The reason for this is that the family spread in $M_{\rm el-op}$ is partially cancelled by that in $\ell_{\boldsymbol{k}}$.

We next calculate the ex–ph matrix elements $M_{\rm ex-ph}$ for the RBM and G-band modes by using (8). We find that for the RBM and LO modes $M_{\rm el-ph}$ in the free-particle picture has a maximum at k_{ii} and it decreases slowly in the

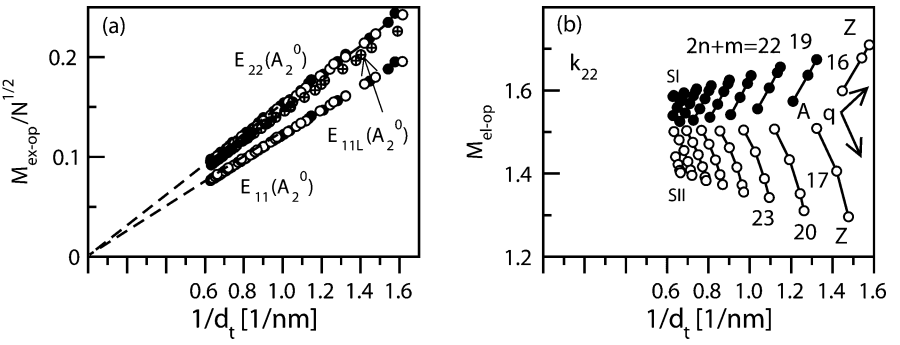

Fig. 13. Tube-diameter dependence of $M_{\text{ex–op}}/N^{1/2}$, and M^{op} (el–op) in SWNTs with $0.5\,\text{nm} < d_t < 1.6\,\text{nm}$. *Filled, open* and *crossed circles* are for type I, II semiconducting and for metallic SWNTs, and (**a**) $M_{\text{ex–op}}$ for $E_{22}(A_2^0)$ of S-SWNTs and $E_{11L}(A_2^0)$ of M-SWNTs, (**b**) $M_{\text{el–op}}$ at k_{22}. The *arrows* in (b) indicate the directions along which θ is decreasing (A: armchair side, Z: zigzag side)

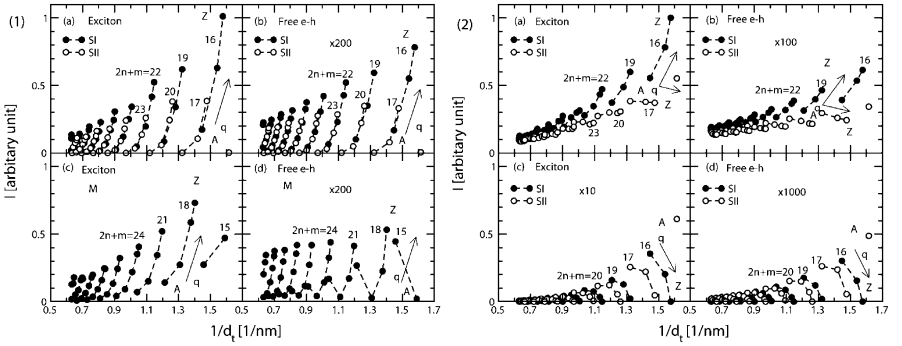

Fig. 14. (**1**) RBM and (**2**) G-band Raman intensity per length for SWNTs with $0.5\,\text{nm} < d_t < 1.6\,\text{nm}$. For both intensities, (**a**) and (**b**) are for $E_{22}(A_2^0)$ and free e–h at k_{22} in S-SWNTs, respectively. *Filled* and *open circles* are for type I and II tubes. (**c**) and (**d**) are for $E_{11L}(A_2^0)$ and free e-h at k_{11L} in M-SWNTs, respectively. The intensity in the free el–ph case has been multiplied by (1b) 200, (1d) 200, (2b) 100, and (2d) 1000. The *arrows* indicate the θ-decreasing direction (A: armchair side, Z: zigzag side). For the G-band mode, (a) and (b) are for the LO (G^+) phonon mode, while (c) and (d) are for the TO (G^-) phonon mode

$|Z_{\boldsymbol{k}}|^2$ delocalized region. As a result, for the RBM and G modes, the matrix elements $M_{\text{ex–ph}}$ for $E_{ii}(A_2^0)$ and $M_{\text{el–ph}}$ at k_{ii} are very similar to each other. For the TO mode, the $M_{\text{ex–ph}}$ and $M_{\text{el–ph}}$ are also similar to each other while the excitonic effect slightly decreases the matrix element for SWNTs with a large chiral angle.

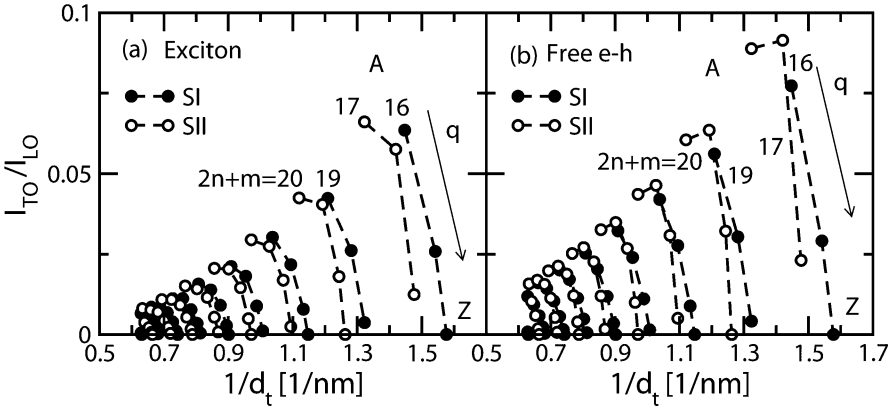

Fig. 15. The Raman intensity ratio between the TO and LO modes, $I_{\mathrm{TO}}/I_{\mathrm{LO}}$, in S-SWNTs with $0.5\,\mathrm{nm} < d_{\mathrm{t}} < 1.6\,\mathrm{nm}$. (**a**) and (**b**) are for the exciton and free e–h pictures, respectively. The *arrows* indicate the θ-decreasing direction (A: armchair side, Z: zigzag side)[11]

We calculate the resonance Raman intensity for the RBM by using (9). The intensities per length for the $E_{22}(A_2^0)$ and $E_{11\mathrm{L}}(A_2^0)$ in S-SWNTs and M-SWNTs are shown in Figs. 14(1a) and (1c), respectively. The intensities for the corresponding free e–h by (1) are also shown in Figs. 14(1b) and (1d). We can see that the exciton and free-particle pictures yield the same tube type and similar chiral-angle dependences, and as expected the excitonic effect enhances the diameter dependence. Moreover, the excitonic effect enhances the magnitude of the intensity by enhancing the optical matrix element. Furthermore, Fig. 14(1) shows the same order of magnitude for the RBM Raman intensity for M-SWNTs and S-SWNTs, which is consistent with experiments. The reason is that the optical matrix elements for an M-SWNT and an S-SWNT with a similar d_{t} have a similar value.

The Raman intensity for the G-band modes for S-SWNTs are also calculated. The results are shown in Fig. 14(2). Similar to the RBM case, the shapes of the curves in Figs. 14(2a) and (2c) for the excitonic model are similar to those of Figs. 14(2b) and (2d) for the free-particle model, respectively. The excitonic effect also enhances the diameter dependence and magnitude of the intensity. From Figs. 14(2a), and (2c), it is seen that the LO mode has a weaker chiral-angle dependence compared to the RBM and TO modes. Moreover, Fig. 14(2a) shows a family pattern similar to that in the excitation energy Kataura plot [8].

Motivated by the experimental facts that the G^- (TO) mode has a weaker intensity than the G^+ (LO) mode, we calculate the Raman intensity ratio $I_{\mathrm{TO}}/I_{\mathrm{LO}}$ [11] and the results are shown in Fig. 15. We can see that $I_{\mathrm{TO}}/I_{\mathrm{LO}}$ in the exciton picture is generally smaller than that in the free e–h picture [78].

Moreover, $I_{\mathrm{TO}}/I_{\mathrm{LO}}$ is the largest for the SWNTs with a chiral angle closest to the armchair tubes and it becomes zero for zigzag SWNTs. The intensity ratio in Fig. 15 also shows clear family patterns. In view of the experiments, the environmental dielectric constants can be varied from close to 1 to a large value by putting the SWNT samples in air or water. Thus, the excitonic effect varies in the different SWNT samples and the Raman intensity ratio $I_{\mathrm{TO}}/I_{\mathrm{LO}}$ is expected to be smaller for the SWNT samples with a smaller environmental dielectric constant.

From Fig. 14, we can see that for calculating the resonance Raman intensity, the exciton and free-particle models generally yield the same tube type and a similar chirality dependence. The excitonic effect increases the diameter dependence and the absolute value of the intensity. Within the excitonic picture, the diameter dependence for the RBM intensity within the diameter range observed experimentally in [26] is about 4 times stronger than within the free electron–hole picture. Therefore, our calculations now predict the observed intensity-diameter-dependent trend shown in [26].

We should mention that the general conclusions for the diameter and chirality dependence of the el–ph matrix elements shown in Sect. 4 are also valid for the diameter and chirality dependence of the resonance Raman intensity. The ex–op matrix elements change the detailed family patterns in the intensity, and especially enhance the diameter dependence of the resonance Raman intensity.

5 Future Directions, Summary

In this review, we mainly show the first-order Raman intensity as a function of E_{L}, which is compared with the experimental Raman excitation profile. The dependence of length, family, chirality, and diameter can be well explained by exciton theory and thus such dependences can be an important tool for characterizing the (n, m) assignment, the relative intensity, and the population of specific (n, m) SWNTs in the sample. The characterization of SWNT samples by using Raman spectroscopy becomes a standard in the field of nanotubes.

An important issue for Raman spectroscopy that is not covered in this chapter is the effect of various types of external fields around a SWNT, such as magnetic field, electric field, pressure and stress on the RRS spectra. The environmental effects due to wrapping agents, peapod insertions, the outer (inner)-shell interaction for DWNTs, also give rise to important modifications to the observed RRS. The symmetry-breaking effect due to doping, caps, edges and defects may induce new Raman signals, which are also important for characterizing sample properties.

Most of the dependence of RRS on external fields, the environmental conditions and symmetry-breaking effects imposed on SWNTs can be understood by the response of the SWNT electronic structures, which will be

ongoing subjects of Raman spectroscopy. Understanding the higher-order Raman spectra, energy transfer between two nanotubes, handling dark excitons, and understanding Kohn anomalies in metallic tubes are hot topics, which await solution in the near future.

Acknowledgements

R. Saito acknowledges a Grant-in-Aid (No. 16076201) from the Ministry of Education, Japan. C. Fantini acknowledges the fellowship from CAPES, Ministry of Education, Brazil.

References

[1] A. Jorio, R. Saito, J. H. Hafner, C. M. Lieber, M. Hunter, T. McClure, G. Dresselhaus, M. S. Dresselhaus: Structural (n, m) determination of isolated single-wall carbon nanotubes by resonant Raman scattering, Phys. Rev. Lett. **86**, 1118 (2001) 251, 255, 256, 257

[2] R. Saito, G. Dresselhaus, M. S. Dresselhaus: *Physical Properties of Carbon Nanotubes* (Imperial College Press, London 1998) 253, 266, 271

[3] G. G. Samsonidze, R. Saito, A. Jorio, M. A. Pimenta, A. G. Souza Filho, A. Grüneis, G. Dresselhaus, M. S. Dresselhaus: The concept of cutting lines in carbon nanotube science, J. Nanosci. Nanotechnol. **3**, 431 (2003) 253

[4] S. Reich, C. Thomsen, J. Maultzsch: *Carbon Nanotubes, Basic Concepts and Physical Properties* (Wiley-VCH, Berlin 2004) 253

[5] R. Saito, A. Jorio, A. G. Souza Filho, G. Dresselhaus, M. S. Dresselhaus, M. A. Pimenta: Probing phonon dispersion relations of graphite by double resonance Raman scattering, Phys. Rev. Lett. **88**, 027401 (2002) 253, 254, 255, 260, 262, 264

[6] M. S. Dresselhaus, G. Dresselhaus, R. Saito, A. Jorio: Raman spectroscopy of carbon nanotubes, Phys. Rep. **409**, 47 (2005) 253, 258

[7] C. Thomsen, S. Reich: Symmetry of the high-energy modes in carbon nanotubes, Phys. Rev. Lett. **85**, 5214 (2000) 253, 260, 262

[8] G. G. Samsonidze, R. Saito, N. Kobayashi, A. Grüneis, J. Jiang, A. Jorio, S. G. Chou, G. Dresselhaus, M. S. Dresselhaus: Family behavior of the optical transition energies in single-wall carbon nanotubes of smaller diameters, Appl. Phys. Lett. **85**, 5703 (2004) 254, 266, 267, 268, 278

[9] J. Jiang, R. Saito, G. G. Samsonidze, A. Jorio, S. G. Chou, G. Dresselhaus, M. S. Dresselhaus: Chirality dependence of the exciton effects in single-wall carbon nanotubes, Phys. Rev. B **75**, 035407 (2007) 254, 272, 273, 274

[10] V. N. Popov, P. Lambin: Radius and chirality dependence of the radial breathing mode and the G-band phonon modes of single-walled carbon nanotubes, Phys. Rev. B **73**, 085407 (2006) 254, 259

[11] J. Jiang, R. Saito, K. Sato, J. S. Park, G. G. Samsonidze, A. Jorio, G. Dresselhaus, M. S. Dresselhaus: Exciton-photon, exciton-phonon matrix elements and resonance Raman intensity, Phys. Rev. B **75**, 035405 (2007) 254, 272, 273, 278

[12] J. S. Park, Y. Oyama, R. Saito, W. Izumida, J. Jiang, K. Sato, C. Fantini, A. Jorio, G. Dresselhaus, M. S. Dresselhaus: Raman resonance window of single-wall carbon nanotubes, Phys. Rev. B **74**, 165414 (2006) 254
[13] M. Milnera, J. Kürti, M. Hulman, H. Kuzmany: Periodic resonance excitation and intertube interaction from quasi-continuous distributed helicities in single-wall carbon nanotubes, Phys. Rev. Lett. **84**, 1324 (2000) 255
[14] C. Fantini, A. Jorio, M. Souza, M. S. Strano, M. S. Dresselhaus, M. A. Pimenta: Optical transition energies for carbon nanotubes from resonant Raman spectroscopy: Environment and temperature effects, Phys. Rev. Lett. **93**, 147406 (2004) 255, 257, 265, 266, 267
[15] J. C. Meyer, M. Paillet, T. Michel, A. Moreac, A. Neumann, G. S. Duesberg, S. Roth, J.-L. Sauvajol: Raman modes of index-identified freestanding single-walled carbon nanotubes, Phys. Rev. Lett. **95**, 217401 (2005) 255, 257
[16] A. V. Nilolaev, M. J. Bronikowski, R. K. Bradley, F. Rohmund, D. T. Colbert, K. A. Smith, R. E. Smalley: Gas-phase catalytic growth of single-walled carbon nanotubes from carbon monoxide, Chem. Phys. Lett. **313**, 91 (1999) 256
[17] S. Iijima, T. Ichihashi: Single shell carbon nanotubes of 1-nm diameter, Nature London **363**, 603 (1993) 256
[18] R. Saito, T. Takeya, T. Kimura, G. Dresselhaus, M. S. Dresselhaus: Raman intensity of single-wall carbon nanotubes, Phys. Rev. B **57**, 4145 (1998) 258
[19] A. Jorio, A. G. Souza Filho, G. Dresselhaus, M. S. Dresselhaus, A. K. Swan, M. S. Ünlü, B. Goldberg, M. A. Pimenta, J. H. Hafner, C. M. Lieber, R. Saito: G-band resonant Raman study of 62 isolated single wall carbon nanotubes, Phys. Rev. B **65**, 155412 (2002) 258, 259
[20] M. Souza, A. Jorio, C. Fantini, B. R. A. Neves, M. A. Pimenta, R. Saito, A. Ismach, E. Joselevich, V. Brar, G. G. Samsonidze, G. Dresselhaus, M. S. Dresselhaus: Single- and double-resonance Raman G-band processes in carbon nanotubes, Phys. Rev. B **69**, R15424 (2004) 258
[21] A. M. Rao, A. Jorio, M. A. Pimenta, M. S. S. Dantas, R. Saito, G. Dresselhaus, M. S. Dresselhaus: Polarized Raman study of aligned multiwalled carbon nanotubes, Phys. Rev. Lett. **84**, 1820 (2000) see also comment in Phys. Rev. Lett. **85**, 3545 258
[22] A. Jorio, G. Dresselhaus, M. S. Dresselhaus, M. Souza, M. S. S. Dantas, M. A. Pimenta, A. M. Rao, R. Saito, C. Liu, H. M. Cheng: Polarized Raman study of single-wall semiconducting carbon nanotubes, Phys. Rev. Lett. **85**, 2617 (2000) 258, 259
[23] A. Jorio, M. A. Pimenta, A. G. Souza Filho, G. G. Samsonidze, A. K. Swan, M. S. Ünlü, B. B. Goldberg, R. Saito, G. Dresselhaus, M. S. Dresselhaus: Resonance Raman spectra of carbon nanotubes by cross-polarized light, Phys. Rev. Lett. **90**, 107403 (2003) 258, 259
[24] S. D. M. Brown, A. Jorio, P. Corio, M. S. Dresselhaus, G. Dresselhaus, R. Saito, K. Kneipp: Origin of the Breit–Wigner–Fano Lineshape of the tangential G-band feature of metallic carbon nanotubes, Phys. Rev. B **63**, 155414 (2001) 258
[25] M. A. Pimenta, A. Marucci, S. Empedocles, M. Bawendi, E. B. Hanlon, A. M. Rao, P. C. Eklund, R. E. Smalley, G. Dresselhaus, M. S. Dresselhaus: Raman modes of metallic carbon nanotubes, Phys. Rev. B Rapid **58**, R16016 (1998) 258

[26] C. Fantini, M. A. Pimenta, M. S. S. Dantas, D. Ugarte, A. M. Rao, A. Jorio, G. Dresselhaus, M. S. Dresselhaus: Micro-Raman investigation of aligned single-wall carbon nanotubes, Phys. Rev. B **63**, 161405 (2001) 259, 279
[27] G. S. Duesberg, I. Loa, M. Burghard, K. Syassen, S. Roth: Polarized Raman spectroscopy on isolated single-wall carbon nanotubes, Phys. Rev. Lett. **85**, 5436 (2000) 259
[28] H. Ajiki, T. Ando: Physics of carbon nanotubes, Physica B Condens. Matter **201**, 349 (1994) 259
[29] O. Dubay, G. Kresse, H. Kuzmany: Accurate density functional calculations for the phonon dispersion relations of graphite layer and carbon nanotubes, Phys. Rev. Lett. **88**, 235506 (2002) 259
[30] O. Dubay, G. Kresse, M. Lazzeri, S. Piscanec, F. Mauri, A. C. Ferrari, J. Robertson: Accurate density functional calculations for the phonon dispersion, Phys. Rev. B **67**, 035401 (2003) 259, 268
[31] M. Lazzeri, S. Piscanec, F. Mauri, A. C. Ferrari, J. Robertson: Phonon linewidths and electron–phonon coupling in graphite and nanotubes, Phys. Rev. B **73**, 155426 (2006) 259
[32] G. G. Samsonidze, E. B. Barros, R. Saito, J. Jiang, G. Dresselhaus, M. S. Dresselhaus: Electron–Phonon coupling mechanism in in two-dimensional graphite and single-wall carbon nanotubes, Phys. Rev. B **75**, 155420 (2007) 259
[33] S. Roche, J. Jiang, L. E. F. F. Torres, R. Saito: Charge transport in carbon nanotubes: quantum effects of electron–phonon coupling, J. Phys. Condens. Matter **19**, 183203 (2007) 259
[34] H. Farhat, H. Son, G. G. Samsonidze, S. Reich, M. S. Dresselhaus, J.Kong: in *Phonon softening in individual metallic carbon nanotubes due to the kohn anomaly*, vol. 99, Phys.Rev. Lett. (2007) p. 145506 260
[35] Y. Wu, J. Maultzsch, E. Knoesel, B. Chandra, M. Huang, M. Y. Sfeir, L. E. Brus, J. Hone, T. Heinz: in *APS March meeting*, vol. 99, Phys. Rev. Lett. (2007) p. 027402 260
[36] Maultzsch, et al.: in *APS March meeting*, Phys. Rev. Lett. (2007) 260
[37] S. Piscanec, M. Lazzeri, M. Mauri, A. C. Ferrari, J. Robertson: Kohn anomalies and electron-phonon interaction in graphite, Phys. Rev. Lett. **93**, 185503 (2004) 260
[38] A. C. Ferrari, J. C. Meyer, V. Scardaci, C. Casiraghi, M. Lazzeri, M. Mauri, S. Piscanec, D. Jiang, K. S. Novoselov, S. Roth, A. K. Geim: Raman spectrum of graphene and graphene layers, Phys. Rev. Lett. **97**, 187401 (2006) 260
[39] R. Saito, A. Grüneis, G. G. Samsonidze, V. Brar, G. Dresselhaus, M. S. Dresselhaus, A. Jorio, L. G. Cançado, C. Fantini, M. A. Pimenta, A. G. Souza Filho: Double resonance Raman spectroscopy of single wall carbon nanotubes, New J. Phys. **5**, 157.1 (2003) 260
[40] M. A. Pimenta, E. B. Hanlon, A. Marucci, P. Corio, S. D. M. Brown, S. A. Empedocles, M. G. Bawendi, G. Dresselhaus, M. S. Dresselhaus: The anomalous dispersion of the disorder-induced and the second-order Raman bands, Brazil. J. Phys. **30**, 423 (2000) 261
[41] A. G. Souza Filho, A. Jorio, G. Dresselhaus, M. S. Dresselhaus, R. Saito, A. K. Swan, M. S. Ünlü, B. B. Goldberg, J. H. Hafner, C. M. Lieber, M. A. Pimenta: Effect of quantized electronic states on the dispersive Raman features in individual single-wall carbon nanotubes, Phys. Rev. B **65**, 035404 (2002) 261

[42] J. Kürti, V. Zólyomi, A. Grüneis, H. Kuzmany: Effect of quantized electronic states on the dispersive Raman features in individual single wall carbon nanotubes, Phys. Rev. B **65**, 165433 (2002) 261
[43] S. D. M. Brown, A. Jorio, G. Dresselhaus, M. S. Dresselhaus: The D-band feature of carbon nanotubes, Phys. Rev. B **64**, 073403 (2001) 261
[44] M. A. Pimenta, A. Jorio, S. D. M. Brown, A. G. Souza Filho, G. Dresselhaus, J. H. Hafner, C. M. Lieber, R. Saito, M. S. Dresselhaus: Diameter dependence of the Raman D-band in isolated single-wall carbon nanotubes, Phys. Rev. B **64**, 041401 (2001) 261
[45] A. G. Souza Filho, A. Jorio, A. K. Swan, M. S. Ünlü, B. B. Goldberg, R. Saito, J. H. Hafner, C. M. Lieber, M. A. Pimenta, G. Dresselhaus, M. S. Dresselhaus: Anomalous two-peak G'-band Raman effect in one isolated single-wall carbon nanotube, Phys. Rev. B **65**, 085417 (2002) 261
[46] R. Saito, G. Dresselhaus, M. S. Dresselhaus: Trigonal warping effect of carbon nanotubes, Phys. Rev. B **61**, 2981 (2000) 262
[47] A. G. Souza Filho, A. Jorio, G. G. Samsonidze, G. Dresselhaus, M. S. Dresselhaus, A. K. Swan, M. S. Ünlü, B. B. Goldberg, R. Saito, J. H. Hafner, C. M. Lieber, M. A. Pimenta: Probing the electronic trigonal warping effect in individual single-wall carbon nanotubes using phonon spectra, Chem. Phys. Lett. **354**, 62 (2002) 262
[48] G. G. Samsonidze, R. Saito, A. Jorio, A. G. Souza Filho, A. Grüneis, M. A. Pimenta, G. Dresselhaus, M. S. Dresselhaus: Phonon trigonal warping effect in graphite and carbon nanotubes, Phys. Rev. Lett. **90**, 027403 (2003) 262
[49] L. Alvarez, A. Righi, T. Guillard, S. Rols, E. Anglaret, D. Laplaze, J. L. Sauvajol: Excitation energy dependence of the Raman spectrum of single-walled carbon nanotubes, Chem. Phys. Lett. **316**, 186 (2000) 262
[50] C. Fantini, A. Jorio, M. Souza, L. O. Ladeira, M. A. Pimenta, A. G. Souza Filho, R. Saito, G. G. Samsonidze, G. Dresselhaus, M. S. Dresselhaus: One-dimensional character of combination modes in the resonance Raman scattering of carbon nanotubes, Phys. Rev. Lett. **93**, 087401 (2004) 262, 263
[51] C. Fantini, A. Jorio, M. Souza, R. Saito, G. G. Samsonidze, M. S. Dresselhaus, M. A. Pimenta: Step-like dispersion of the intermediate frequent Raman modes in semiconducting and metallic carbon Nanotubes, Phys. Rev. B **72**, 085446 (2005) 262, 263
[52] M. Kalbac, L. Kavan, M. Zukalova, L. Dunsch: The intermediate frequency modes of single- and double-walled carbon nanotubes: A Raman spectroscopic and In Situ Raman spectroelectrochemical study, Chem. Eur. J. **12**, 4451 (2006) 264
[53] V. Brar, G. G. Samsonidze, G. Dresselhaus, M. S. Dresselhaus, R. Saito, A. K. Swan, M. S. Ünlü, B. B. Goldberg, A. G. Souza Filho, A. Jorio: Second-order harmonic and combination modes in graphite, single-wall carbon nanotube bundles, and isolated single-wall carbon nanotubes, Phys. Rev. B **66**, 155418 (2002) 264
[54] T. Shimada, T. Sugai, C. Fantini, M. Souza, L. G. Cançado, A. Jorio, M. A. Pimenta, R. Saito, A. G. G. Dresselhaus, M. S. Dresselhaus, Y. Ohno, T. Mizutani, H. Shinohara: Origin of the 2450 cm^{-1} Raman bands in HOPG, single-wall and double-wall carbon nanotubes, Carbon **43**, 1049 (2005) 264

[55] J. Maultzsch, S. Reich, C. Thomsen, H. Requardt, P. Ordejon: Double-resonant Raman scattering in graphite: Interference effects, selection rules, and phonon dispersion, Phys. Rev. Lett. **92**, 075501 (2004) 264, 268
[56] A. Jorio, A. G. Souza Filho, G. Dresselhaus, M. S. Dresselhaus, R. Saito, J. H. Hafner, C. M. Lieber, F. M. Matinaga, M. S. S. Dantas, M. A. Pimenta: Joint density of electronic states for one isolated single-wall carbon nanotube studied by resonant Raman scattering, Phys. Rev. B **63**, 245416 (2001) 264
[57] M. J. O'Connell, S. M. Bachilo, X. B. Huffman, V. C. Moore, M. S. Strano, E. H. Haroz, K. L. Rialon, P. J. Boul, W. H. Noon, C. Kittrell, J. Ma, R. H. Hauge, R. B. Weisman, R. E. Smalley: Band gap fluorescence from individual single walled carbon nanotubes, Science **297**, 593 (2002) 265
[58] V. N. Popov: Curvature effects on the structural, electronic and optical properties of isolated single-walled carbon nanotubes within a symmetry-adapted non-orthogonal tight-binding model, New J. Phys. **6**, 17 (2004) 266, 267
[59] M. S. Dresselhaus, G. Dresselhaus, P. Avouris: *Carbon Nanotubes: Synthesis, Structure, Properties and Applications*, Top. Appl. Phys. **80** (Springer-Verlag, Berlin, Heidelberg 2001) 267
[60] P. Kim, T. Odom, J.-L. Huang, C. M. Lieber: Electronic properties, etc. – electronic density of states of atomically resolved single-walled carbon nanotubes: Van Hove singularities and end states, Phys. Rev. Lett. **82**, 1225 (1999) 267
[61] A. G. Souza Filho, N. Kobayasi, J. Jiang, A. Grüneis, R. Saito, S. B. Cronin, J. Mendes Filho, G. G. Samsonidze, G. Dresselhaus, M. S. Dresselhaus: Strain-induced interference effects on the resonant Raman cross section of carbon nanotubes, Phys. Rev. Lett. **95**, 217403 (2005) 267
[62] J. Jiang, R. Saito, A. Grüneis, S. G. Chou, G. G. Samsonidze, A. Jorio, G. Dresselhaus, M. S. Dresselhaus: Intensity of the resonance Raman excitation spectra of single-wall carbon nanotubes, Phys. Rev. B **71**, 205420 (2005) 267, 271, 276
[63] H. Son, A. Reina Cecco, G. G. Samsonidze, R. Saito, A. Jorio, J. Kong, M. S. Dresselhaus: Raman characterization of electronic transition energies of metallic single wall carbon nanotubes, Phys. Rev. B (Brief Report) **74**, 073406 (2006) 267
[64] A. Jorio, C. Fantini, M. A. Pimenta, R. B. Capaz, G. G. Samsonidze, G. Dresselhaus, M. S. Dresselhaus, J. Jiang, N. Kobayashi, A. Grüneis, R. Saito: Resonance Raman Spectroscopy (n, m) dependent effects in small diameter single-wall carbon nanotubes, Phys. Rev. B **71**, 075401 (2005) 267, 268, 276
[65] D. Porezag, T. Frauenheim, T. Köhler, G. Seifert, R. Kaschner: Construction of tight-binding-like potentials on the basis of density-functional theory: Application to carbon, Phys. Rev. B **51**, 12947 (1995) 268
[66] T. Aizawa, R. Souda, S. Otani, Y. Ishizawa, C. Oshima: Bond softening in monolayer graphite formed on transition-metal carbide surfaces, Phys. Rev. B **42**, 11469 (1990) 268
[67] J. Jiang, R. Saito, G. G. Samsonidze, S. G. Chou, A. Jorio, G. Dresselhaus, M. S. Dresselhaus: Electron–phonon matrix elements in Single-Wall Carbon Nanotubes, Phys. Rev. B **72**, 235408 (2005) 268, 270, 271
[68] L. G. Cançado, M. A. Pimenta, B. R. A. Neves, M. S. S. Dantas, A. Jorio: Influence of the atomic structure on the Raman spectra of graphite edges, Phys. Rev. Lett. **93**, 247401 (2004) 269

[69] J. Jiang, R. Saito, A. Grüneis, G. Dresselhaus, M. S. Dresselhaus: Optical absorption matrix elements in single-wall carbon nanotube, Carbon **42**, 3169 (2004) 269
[70] Y. Oyama, R. Saito, K. Sato, J. Jiang, G. G. Samsonidze, A. Gruneis, Y. Miyauchi, S. Maruyama, A. Jorio, G. Dresselhaus, M. S. Dresselhaus: Photoluminescence intensity of single-wall carbon nanotubes, Carbon **44**, 873 (2006) 269
[71] Y. Miyauchi, S. Chiashi, Y. Murakami, Y. Hayashida, S. Maruyama: Fluorescence spectroscopy of single-walled carbon nanotubes synthesized from alcohol, Chem. Phys. Lett. **387**, 198 (2004) 270
[72] T. Ando: Excitons in carbon nanotubes, J. Phys. Soc. Jpn. **66**, 1066 (1997) 272
[73] T. Ando: Excitons in carbon nanotubes revisited: Dependence on diameter, Aharonov–Bohm flux, and strain, J. Phys. Soc. Jpn. **73**, 3351 (2004) 272
[74] A. Grüneis, R. Saito, G. G. Samsonidze, T. Kimura, M. A. Pimenta, A. Jorio, A. G. S. Filho, G. Dresselhaus, M. S. Dresselhaus: Inhomogeneous optical absorption around the K point in graphite and carbon nanotubes, Phys. Rev. B **67**, 165402 (2003) 274
[75] J. Jiang, R. Saito, A. Grüneis, G. Dresselhaus, M. S. Dresselhaus: Electron–phonon interaction and relaxation time in graphite, Chem. Phys. Lett. **392**, 383 (2004) 274
[76] R. Saito, A. Grüneis, G. G. Samsonidze, G. Dresselhaus, M. S. Dresselhaus, A. Jorio, L. G. Cançado, M. A. Pimenta, A. G. Souza: Optical absorption of graphite and single-wall carbon nanotubes, Appl. Phys. A **78**, 1099 (2004) 274
[77] E. B. Barros, R. B. Capaz, A. Jorio, G. G. Samsonidze, A. G. Filho, S. Ismail-Beigi, C. D. Spataru, S. G. Louie, G. Dresselhaus, M. S. Dresselhaus: Selection rules for one- and two-photon absorption by excitons in carbon nanotubes, Phys. Rev. B Rapid **73**, 241406(R) (2006) 274
[78] R. Saito, A. Jorio, J. H. Hafner, C. M. Lieber, M. Hunter, T. McClure, G. Dresselhaus, M. S. Dresselhaus: Chirality-dependent G-band Raman intensity of carbon nanotubes, Phys. Rev. B **64**, 085312 (2001) 278

Index

Photoluminescence: Science and Applications

Jacques Lefebvre[1], Shigeo Maruyama[2], and Paul Finnie[1]

[1] Institute for Microstructural Sciences, National Research Council of Canada, 1200 Montreal Road, Ottawa, Ontario K1A 0R6, Canada
jacques.lefebvre@nrc-cnrc.gc.ca
[2] Department of Mechanical Engineering, The University of Tokyo, 7-3-1 Hongo, Bunkyo-ku, Tokyo 113-8656, Japan

Abstract. In the past five years photoluminescence (PL) of SWNTs has gone from discovery to one of the most actively researched areas, with broad impact on the basic science of SWNTs, as well as the promise of applications. The simplest free-carrier models of perfect semiconducting SWNTs in vacuum predict that they have direct bandgaps and therefore should be efficient light absorbers and emitters. Experimentally, isolating SWNTs from environmental interactions proves crucial to observing this strong PL. The Coulomb interaction enhanced by one-dimensional confinement requires that excitonic models be invoked to understand PL features. Prepared properly, SWNTs are strong PL emitters, with good quantum yield, showing principal PL peaks with characteristic lineshapes and (n, m)-dependent emission and absorption energies, as well as a rich absorption spectrum. PL has emerged as an important characterization tool for determining (n, m) and (n, m) distributions, albeit with some limitations. Extrinsic factors, such as chemical environment, temperature, electric and magnetic field, or intrinsic factors, such as phonons, are manifest in SWNT PL. Possible applications in sensing, biological markers, and optoelectronics are beginning to emerge from current research in SWNT PL.

1 Introduction

The first report of photoluminescence (PL) in single-wall carbon nanotubes (SWNTs) dates back to 2002 [1], and in the intervening half-decade there has been tremendous progress including a large number of fundamental studies of SWNT PL, the emergence of PL methods as basic characterization tools, and the early exploration of PL-related applications. The term "photoluminescence" describes any process in which light is absorbed by a medium, generating an excited state, and then light of lower frequency is re-emitted upon relaxation to a ground state. In nanotube optics the term fluorescence is used synonymously and is actually more precisely correct as it describes "allowed" PL processes for which the timescale between absorption and emission is few nanoseconds or less. In the currently accepted picture of SWNT PL, when a SWNT is photoexcited, electron–hole pairs are created in the form of excitons, which are subsequently annihilated with the emission of photons. Of special interest for fundamental science is the strong, one-dimensional confinement with its consequences for PL characteristics. The SWNT represents

A. Jorio, G. Dresselhaus, M. S. Dresselhaus (Eds.): Carbon Nanotubes,
Topics Appl. Physics **111**, 287–319 (2008)

a unique model system for which the range of diameters and chiralities available through synthesis allows for a nearly continuous tuning of exciton confinement energy and symmetry. The SWNT also constitutes a bridge between bulk crystals traditionally studied by physicists, and molecules traditionally studied by chemists, and as such its optical properties can be understood in terms of either as a starting point, and the methods of both disciplines can be applied.

The aim of this chapter is to outline the PL-related properties of SWNTs and how they are presently understood. The number of publications is large and growing rapidly, and cannot be fully explained in such a short review. Nonetheless, we hope the chapter will provide a good starting point for those interested in SWNT PL. Some important topics are treated very briefly because they are covered in detail in other contributions to this book. This contribution consists of the following sections: Sect. 2 gives the basic description of optical processes in SWNTs, including absorption, luminescence, photoluminescence excitation, effects of sample preparation, and excitonic effects. Section 3 presents the spectral characteristics of SWNT PL including linewidths, lineshapes, quantum efficiency, and phonon-related features. Section 4 gives an overview of the effects on the PL of various physical parameters such as temperature, strain, electric and magnetic fields, and chemical doping. Sect. 5 looks beyond the fundamental science to explore some of the possible PL-related applications of SWNTs that are currently under exploration. Finally, Sect. 6 provides a summary and outlook for the field of SWNT PL-related research in the next few years.

2 Basic Photoluminescence Spectroscopy of Isolated Nanotubes

2.1 Model

In SWNTs, the band structure is a series of one-dimensional subbands arising from the periodic boundary conditions imposed by wrapping the graphene sheet. The dominant "allowed" optical electronic transitions connect bands with the same index. These longitudinal transitions are labeled E_{11} and E_{22} (more generally E_{ii}, $i = 1, 2, 3, \ldots$) in Fig. 1, and are allowed for light polarized along the nanotube axis. In the simplest physical picture of PL, light absorption occurs at E_{ii}, and after some relaxation process, recombination occurs at E_{11}. A schematic of the band structure of a SWNT and the PL process at this level of approximation is shown in Fig. 1a. Absorption and

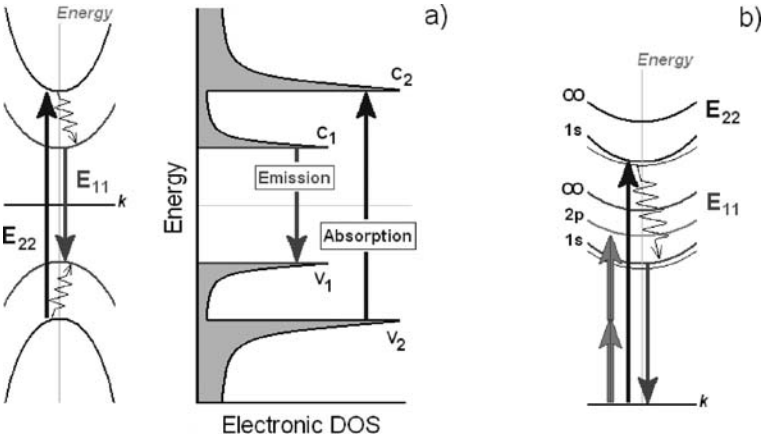

Fig. 1. Optical processes in SWNTs. (**a**) The band structure and optical transitions in a simplified single-particle picture and its corresponding density of states. Light absorption at E_{22} is shown with an *upward-pointing arrow* and light emission at E_{11} is shown with a *downward-pointing arrow*. The *thin jagged arrows* illustrate relaxation from E_{22} to E_{11}. (**b**) A simplified picture of the exciton band structure and optical transition. One-photon processes are shown as in (a) and a two-photon process is shown with two *gray upward-pointing arrows*. The ground state represents a vacuum state, that is, with no excitons

emission energies are intimately connected to the nanotube diameter and chirality. The longitudinal transitions can be described to leading order by:

$$E_{11} = 2\gamma_o a d^{-1} + (-1)^{\nu} \frac{t_{11} \cos(3\theta)}{d^2}\,, \tag{1}$$

$$E_{22} = 4\gamma_o^* a d^{-1} - (-1)^{\nu} \frac{t_{22} \cos(3\theta)}{d^2}\,, \tag{2}$$

where γ_o, γ_o^* (both between 2.6 and 3.0 eV), t_{11} and t_{22} are free parameters related to the onsite energy and to the hopping integrals, respectively, and a is the lattice parameter (2.42 Å), d is the nanotube diameter, and θ is the nanotube chiral angle. For polarization perpendicular to the tube axis, transitions are allowed between states belonging to bands that differ by one in band index. For example, an electron is promoted from the highest valence band (v_1 in Fig. 1a) to the second-lowest conduction band (c_2), an E_{12} transition. The large geometrical anisotropy of carbon nanotubes, and consequently its dielectric environment, leads to a strong suppression of transverse transitions (the "antenna effect", see the contribution by *Ando*) [2]. Within a noninteracting picture, the tranverse E_{12} (and E_{21}) transitions appear halfway in energy between E_{11} and E_{22}. Experimentally, the longitudinal and transverse configurations are most commonly probed. However, light propagation along the tube axis will also give rise to interesting optical transitions. For example, chiral tubes will show different responses to left- and right-circular

polarization for light propagation along the tube axis ("dichroic effects"). Such transitions should also be weak due to the antenna effect.

Although noninteracting pictures are useful models, the effect of the Coulomb interaction must be taken into account to properly describe SWNT PL. In one dimension, charged particles are compelled to interact more strongly, and the peaked DOS, the reduced charge screening, and the reduced phase space are all factors enhancing the effect of Coulomb interaction. This was already recognized in the earliest PL work on SWNTs [2], and it is PL experiments that have since provided the most direct evidence of these Coulomb effects. The contributions by *Ando* and by *Spataru* et al. provide full treatments of exciton theory. In particular, Fig. 3 of contribution by *Ando* shows how the bandgaps and the exciton absorption energies of the first and second bands evolves as the strength of Coulomb interaction is increased [3].

A basic description of interaction effects on peak positions is needed to understand PL data. First, positions of the free-particle E_{ii} transitions are pushed upward by a self-energy renormalization term. At the same time, an electron and a hole will bind together via their mutual Coulomb interaction, and these bound excitonic states lie well below ($\sim 0.5\,\mathrm{eV}$) the free-particle states, more or less counteracting the repulsive self-energy correction. Each optical transition (e.g., E_{11} or E_{22}) and its related bands in the single-particle picture generates a set of exciton bands with its own selection rules, as discussed in the contribution by *Spataru* et al. The unbound (or "continuum") states still exist, but the oscillator strength shifts from the free electron–hole pair to the optically allowed ground-state exciton. When using the notation E_{ij} in PL experiment now, one generally refers to the bound optically active excitonic bands.

Within the excitonic picture, experiment indicates that (1) and (2) remain a reasonable approximation, but with a different set of parameters for γ_o, γ_o^*, t_{11} and t_{22}. This can be understood in part because the exciton dispersion, though different from the single-particle dispersion, still must incorporate the same graphene-derived symmetries. Thus, measurement of PL transition energies can provide evidence for excitons in SWNTs.

2.2 Absorption

Absorption is the fundamental first step to any PL emission. Historically, optical absorption on SWNTs preceded PL measurements by several years [4,5], principally because, regardless of preparation, nanotubes can absorb light, while nanotubes must be specially prepared to be good PL emitters. These early samples consisted of large ensembles of SWNTs, which would typically be bundled into ropes and contain some level of impurities, for example catalyst residues and non-nanotube carbonaceous material. A typical absorption spectrum from SWNTs as compared to graphite is shown in Fig. 2a [6]. Above 2.0 eV, the spectrum is relatively featureless and generally similar to graphite. At lower energies, however, both spectra differ significantly, with

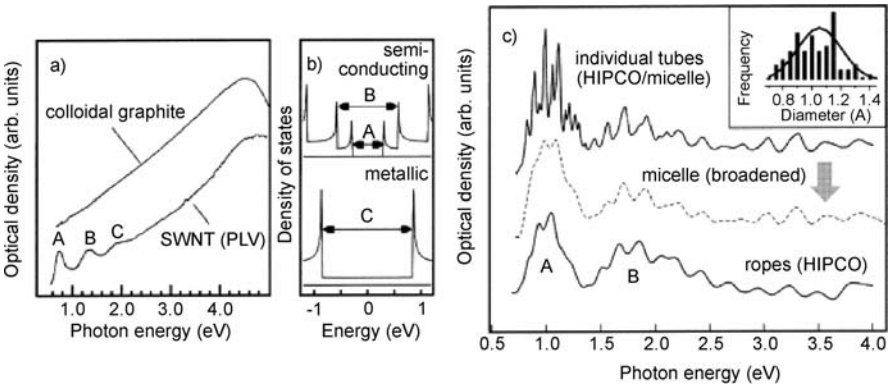

Fig. 2. Optical absorption from SWNT ensembles using different preparation methods. (**a**) Raw spectrum from SWNTs and graphite. (**b**) Illustration of interband process giving rise to the absorption peaks. (**c**) Effect of sample preparation on absorption resonances for a background subtracted spectrum. The *inset* shows the diameter distribution [6]

the SWNT sample showing three broad peaks labeled A, B and C (~ 0.1 to ~ 0.4 eV FWHM). The origin of these peaks was associated with the lowest allowed transition in semiconducting SWNTs (peak A, typically referred to as E_{11}), the second allowed transition of the same semiconducting SWNTs (peak B, or E_{22}), and the first peak in the JDOS of the metallic nanotubes (metallic according to $\mathrm{mod}(n - m, 3) = 0$). The corresponding transitions are labeled in Fig. 1.

Despite the fact that SWNTs have a sharply peaked density of states, the peaks found in the absorption spectra are broad. Beyond lifetime broadening, several factors affect the absorption linewidth for materials in general. Specifically for SWNTs, sample heterogeneity is a dominant factor. An ensemble of nanotubes most often consists of many different species (n, m), each with a different set of absorption peaks, adding up to produce the broad peak reflecting to first order a diameter distribution. In addition, even if the sample consisted of only a single nanotube species, interaction with the environment, either through bundling or contact with other material, can broaden the spectral features. Figure 2c illustrates how bundling severely broadens the series of narrow absorption peaks (~ 25 meV) obtained on ensembles of individual SWNTs.

2.3 Photoluminescence from Isolated SWNTs

The breakthrough that began the era of PL studies on SWNTs was at first one of purification, with isolated SWNTs being separated from bundled ones [1]. The absorption spectra of the separated SWNTs showed series of sharp peaks

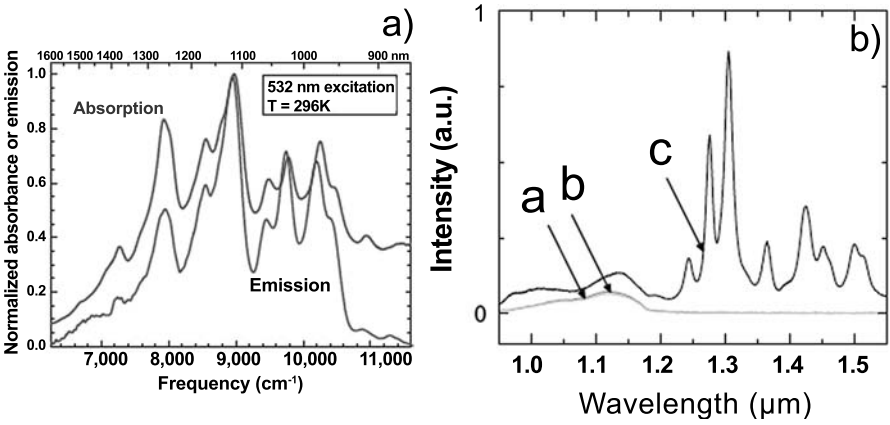

Fig. 3. (**a**) Optical emission and absorption from an ensemble of isolated SWNTs in a surfactant solution [1]. (**b**) PL from a small number of SWNTs suspended freely above a substrate. Samples without suspended SWNTs do not show SWNT PL (a,b), while areas with suspended SWNTs show sharp PL peaks (c) [7]

($\sim$ 25 meV), rather than the broad peaks seen for bundles. (see Figs. 3a and 2c). In stark contrast to bundle samples, these separated SWNTs in suspension also showed sharp PL peaks in the near-infrared when excited with laser illumination in the visible. Figure 3a shows the emission spectrum, which has virtually identical energies and similar linewidths ($\sim$ 25 meV) as the absorption spectrum. This led to the conclusion that the same states are responsible for both processes and that the luminescence involves transitions between band extrema in semiconductors (i.e., from E_{11}^S). Since this original work, many other recipes using a variety of surfactants have been tested by several groups. This is presently the dominant method to obtain PL spectra from SWNTs.

For basic studies and for many applications, it is useful to immobilize the nanotubes. The addition of PVP to the suspensions produced a solid with similar luminescence efficiencies to the aqueous suspension. There are also alternative methods of isolating individual SWNTs that predate these methods. One approach to isolating SWNTs from their surroundings and preventing bundling is to synthesize them on textured substrates, for instance on a substrate patterned with pillars or trenches [8]. Chemical vapor deposition was found to be an effective method to produce such samples, where large numbers of isolated single SWNTs bridging pillar to pillar can be synthesized [8, 9]. Apart from their supporting segments, nanotubes are surrounded only by gas ambient – there is no surfactant or solvent to interact with the nanotube surface. In a first experiment with such samples, laser illumination showed no NIR photoluminescence from the flat surfaces known to have abundant SWNTs [7]. But on pillars bridged by sparse networks of SWNTs, sharp

peaks were observed (Fig. 3b). Notably, these peaks are substantially sharper ($\sim 10\,\text{meV}$) than the micelle-wrapped SWNTs. Wavelength-dependent excitation confirmed that these peaks are the same E_{11}^S transitions observed for micelle-wrapped SWNTs. Such SWNTs have spectral properties which are arguably better than micelle-wrapped nanotubes (see Sect. 3.1 for details), and single nanotube studies [10] are no more difficult than ensemble studies. These freely suspended SWNTs, either in air or some other gas ambient, are ideal for spectroscopic studies.

2.4 Photoluminescence Excitation Map

SWNTs have a unique, species-dependent optical absorption spectrum. An alternative probe of the energy band structure that is closely related to optical absorption is photoluminescence excitation (PLE) spectroscopy. In PLE the PL intensity is recorded while the excitation wavelength is changed. A maximum in intensity is found whenever the excitation energy passes through an absorption resonance from which relaxation to a PL-emitting transition occurs. One can build up a three-dimensional "map" showing luminescent intensity vs. emission and excitation wavelength. An example of a PLE map is shown in Fig. 4a [11]. The intensity of luminescence is plotted on a grey scale, with the emission wavelength along the x-axis and the excitation wavelength along the y-axis. This particular PLE map is for rather large diameter nanotubes, and the excitation energy extends over a relatively large range.

A PLE map obtained from an ensemble of SWNTs produces an intriguing pattern of spots such as in Fig. 4a, each representing a single (n, m) species. The so-called "fingerprint region" is visible in the center of the plot. Each spot in this region comes from resonant absorption into E_{22}^S with emission at E_{11}^S, for a given (n, m) species of nanotube [12, 13]. The link between the $(E_{11}^S,\ E_{22}^S)$ spots on the photoluminescence excitation map and their connection to specific (n, m) represents one of the most fundamental results in nanotube photophysics and is discussed in detail in the contribution by *Jorio* et al. PLE mapping has already emerged as an important method of identifying the (n, m) species in a given sample. This (n, m) assignment provides an alternative way to construct a "Kataura plot" (Fig. 4b) [4], which is complementary to Raman-derived plots. In such a plot, E_{11}^S and E_{22}^S resonances are plotted versus the nanotube diameter.

That the PLE map shows (n, m)-dependent spots can be understood from the dispersion of graphene and the cutting lines associated with each (n, m) species. Conceptually, for a linear dispersion with no chiral-angle dependence, an excitation map would show up as a series of spots distributed along a straight line with slope 2. Deviations from linearity would not change the map qualitatively, but would only put E_{22}^S at some other factor away from E_{11}^S. The SWNT, however, possesses a trigonal symmetry of bonding similar to graphene, and therefore, the dispersion relation contains a trigonal warping term to reflect this distortion away from a circle. A PLE map including

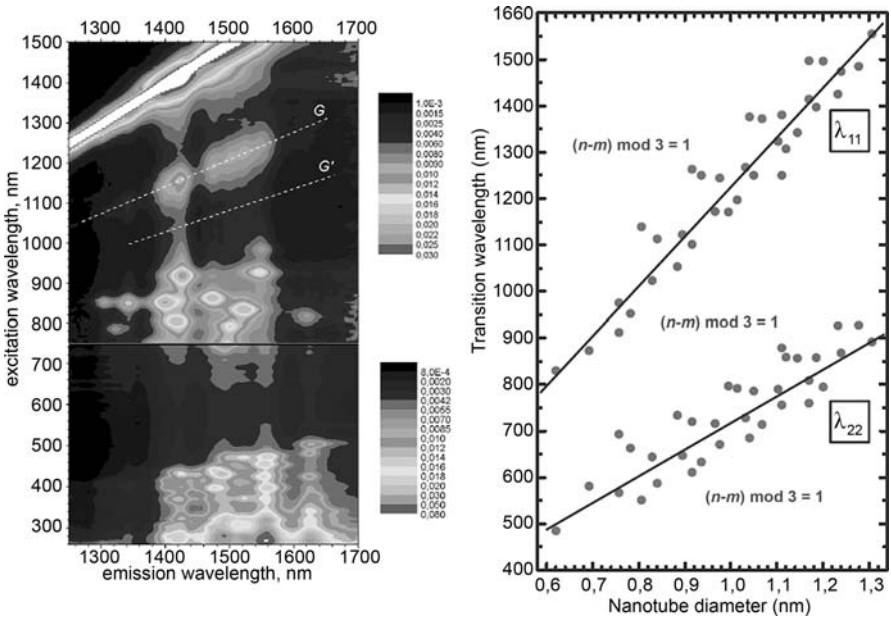

Fig. 4. (**a**) A photoluminescence excitation map from an ensemble of SWNTs in a surfactant solution [11]. (**b**) A Kataura plot derived from photoluminescence data from a SWNT solution [12]. The middle (n-m)mod3=1 should read (n-m)mod3=2.

trigonal warping effects would fan out compared with the linear case, with two sets of branches on either side of the slope 2 median. Small $n-m$ points (near armchair) sit close to the median line, and large $n-m$ (towards zigzag) are farther away. Points with the same $n-m$ are sometimes referred to as a "family", and each $n-m$ family is approximately linear on the Kataura plot. Geometrically, the $n-m$ value describes how far the chiral vector deviates from the armchair line. The set of spots below the median (small E_{22}^S energy for a given E_{11}^S) originate from SWNTs which are labelled "mod 2" (as defined by $\mathrm{mod}(n-m,3)=2$), and the upper set originates from SWNTs which are labelled "mod 1". This separation comes from the fact that mod 1 and mod 2 correspond to cutting lines on opposite sides of the K(K') points sample opposite sides of energy contours. The effect of the trigonal warping term is amplified in PLE maps since the E_{11}^S and E_{22}^S cutting lines sample opposite sides of the energy dispersion. Experimentally, the median line is found to be around 1.7, and the deviation from 2 is attributed to self-energy corrections to the energy dispersion as discussed in the contribution by *Spataru* et al.

Another important grouping is the $2n+m$ "family", and this family can also be seen on the Kataura plot (Fig. 4b). Each set of peaks peeling away from the central line in the Kataura plot belongs to a single $2n+m$ family.

The geometrical meaning of the $2n+m$ family is also simple and arises from the projection of the chiral vector onto the first primitive lattice vector, i.e., the projection of the chiral vector onto the zigzag line. SWNTs belonging to a given $2n+m$ family sample the full range of chiral angles, while remaining fairly similar in diameter.

Beyond (E_{11}^S, E_{22}^S) spots, a number of additional spectral features are evident in a PLE map. For example, the vertical streakiness in the map results from off-resonance absorption, which is typically a factor of ten or more weaker than on-resonance. Also, at the bottom right in Fig. 4a ($\lambda < 500\,\text{nm}$), a second "fingerprint" region appears as a kind of "echo" of the first fingerprint region. This corresponds to resonant excitation at E_{33}^S or E_{44}^S and emission at E_{11}^S. Like the first fingerprint, these resonances too, could be used for (n,m) assignment. Another kind of feature is the line labeled G, and also the much weaker line labelled G'. These show resonant absorption at levels that are a phonon frequency above E_{11}^S, in this case the G (or G') phonon. Many such phonon echoes are now known, originating both from E_{11}^S and E_{22}^S and will be discussed in the next section. Importantly, pure Raman features some phonon energy below the excitation energy are often seen in PLE maps when laser excitation is used, particularly as combination modes (e.g., $2D+2G$) [14]. Finally, the bright line along the top, where the excitation wavelength and emission wavelength are almost equal, is primarily an experimental artifact caused by the lack of rejection of the excitation source. However, some real structure is visible here, originating from E_{11}^S absorption resonances, which are broader than the rejection of the optical setup.

While PLE maps are qualitatively similar for SWNT samples prepared with various methods, detailed analysis can reveal some significant differences. For example, Fig. 5 shows a map from SWNTs in free space with the SDS-wrapped data of [12] plotted for comparison [14]. One immediately sees the same pattern of spots, and they can be related one-to-one to the surfactant-based assignment. The micelle-encapsulated emission peaks are slightly redshifted (28 meV on average for E_{11}^S). This shift is explained by dielectric screening produced by the solution surrounding the nanotubes [3]. The magnitude of the shift can be understood with reference to exciton models. However, it is not trivial, since two effects opposite in sign shift the energy peak position, namely the self-energy, which increases the energy, and the exciton binding energy, which decreases it. The overall redshift of optical resonances was predicted theoretically (see also the contributions by *Ando*, and *Saito* et al. of this volume).

Depending on the details of the sample preparation, PLE maps can evolve from well-resolved peaks to broad unresolved features. In some cases, light emission observed from bundles was attributed to nonradiative relaxation and blackbody emission accompanying transient heating [15]. Recently, detailed analysis of PLE maps revealed that excitons can transfer to a neighboring nanotube and emit light [16]. Structures closely related to individual, isolated

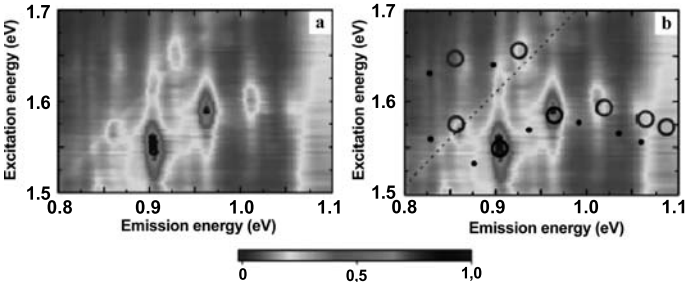

Fig. 5. A photoluminescence excitation map from an ensemble of freely suspended SWNTs. (**a**) shows the data only. In (**b**) corresponding surfactant nanotubes peaks are labeled as *black dots*, and *circles* show the surfactant peaks plus a fixed energy offset that provides the best fit with the air-suspended peak positions [14]

SWNTs are also likely to emit PL in some cases. For example, preliminary PL experiments on double-wall carbon nanotubes (DWNTs) have been performed, though with quite different results [17, 18].

2.5 Exciton Picture

In general, excitonic effects are important in low-dimensional systems and similarly, excitons are expected to be important in SWNT PL: early experimental work alludes to their importance [12], and at the time some excitonic effects were already predicted [2]. The excitonic picture is discussed in full detail in the contributions by *Ando* and by *Spataru* et al.

One early line of evidence for the need to use excitons to explain the PL data is the ratio problem [19, 20]. The ratio of E_{22}^S/E_{11}^S for linear energy dispersion within the simplest tight-binding model is 2. In more physical models of the single-particle dispersion, "trigonal warping", other trigonally symmetric terms and diameter-dependent curvature effects distort the shape of the dispersion and cause this ratio to deviate from 2. However, these distortions vanish in the limit of large SWNT radius (i.e., near the K-point of the graphene dispersion). Thus, the limit of E_{22}^S/E_{11}^S for large-diameter SWNTs should go to 2. Extrapolating from the PLE mapping data, the ratio rather goes to ~ 1.7 [12, 13].

The ratio problem can be understood if Coulomb interaction is included even in the simplest model with linear dispersion [20]. While the electronic (single-particle) bandgaps scale roughly as $1/d_t$, the Coulomb interaction has two contributions, excitonic and self-energy corrections. For large nanotube diameters, excitonic corrections become negligible but self-energy corrections present in graphene remain. These are repulsive contributions that increase the values of both E_{11}^S and E_{22}^S, in such a manner that the average ratio becomes smaller than 2. The magnitude of the deviation is determined by

the strength of the Coulomb interaction, and consequently is sensitive to the dielectric constant.

More evidence for excitons in SWNTs is provided by a two-photon PLE experiment [21, 22]. Conventional PL is a one-photon (linear) process and the absorption of a single-photon causes the transition from the ground state to an excited state. The emission is also usually a single photon-process: recombination occurs across the bandgap with the emission of a single photon. However, at high excitation power densities, two-photon absorption (TPA) can occur at an appreciable rate. TPA and one-photon absorption (OPA) obey different selection rules. In conventional semiconductor materials, the difference between OPA and TPA has been used to demonstrate excitonic effects. Two groups have performed this type of experiment on SWNTs, showing that the TPA data is incompatible with the single-particle picture of SWNT photoluminescence [21, 22], and is further discussed in the contribution by *Spataru* et al.

In one dimension, excitonic states can be described by a hydrogen-like Rydberg series $(s, p, d, \dots)$ of bands below the single-particle bandgap. For SWNTs, this is a somewhat simplified picture; nonetheless, this description provides some useful insights (for a more complete picture of excitonic states, see the contribution by *Spataru* et al.). Excitonic states have definite parity with respect to a plane perpendicular to the tube axis. For transitions polarized along the tube axis, which are usually dominant in SWNT photoluminescence, OPA selection rules dictate that the initial and final states have opposite parity. In TPA such transitions have the same parity. In the Rydberg model, OPA excites the lower-lying s-like exciton, while TPA excites the p-like excited exciton state. This simple model is used to describe TPA but proper account of symmetries is required to reflect the chirality of SWNTs. Excitation with two photons will result in an absorption peak higher in energy than the one-photon peak. The process of two-photon absorption followed by one-photon photoluminescence emission in the excitonic picture is illustrated schematically in Fig. 1b.

In contrast, the single-particle picture has only excitations into a continuum, and thus there is no selection rule to separate one- and two-photon processes. One- and two-photon absorption should both take place at the bandgap as measured by PL. A deviation of the two-photon absorption peak from the photoluminescence emission peak (or one-photon absorption peak) is a signature of excitonic effects. This is precisely what is observed in a PL experiment as shown in Fig. 6. The absorption peak for the single-particle picture would sit along a line at twice the emission wavelength. There is, however, an approximately $0.2-0.3\,\mathrm{eV}$ shift, representing the difference between the one- and two-photon states. The exciton binding energy can be estimated from this difference, but the exact number is model dependent. In any case, this represents a significant fraction of the electronic bandgap, and is much larger than found in bulk semiconductors or two-dimensional confined semiconductor heterostructures.

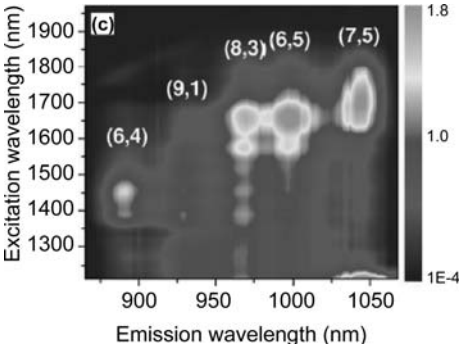

Fig. 6. A photoluminescence excitation map obtained from a two-photon absorption experiment [22]

3 Spectroscopic Properties of Nanotube Photoluminescence

3.1 Lineshape

As described in the previous section, the electronic DOS is strongly peaked at the band edge with the consequence of limited thermal broadening. Even if higher-energy states can become thermally occupied at finite temperature, the lower density for those states reduces their relative contribution to the PL intensity. This reduced dimensionality should be reflected in PL linewidths. Indeed, air-suspended SWNTs have emission linewidths at 300 K as small as 9 meV, significantly smaller than the thermal energy of 25 meV [10]. The early reports from surfactant SWNTs showed broader Lorentzian peaks of about 25 meV (FWHM) [1]. The broader linewidth of these surfactant SWNTs as compared to air-suspended SWNTs might by due to inhomogenous surfactant coatings, bundling effects, or due to damage or cutting due to the relatively aggressive suspension process. More recently, narrow linewidths have been obtained from individual surfactant SWNTs at room temperature [15].

For air-suspended SWNTs the lineshape is systematically asymmetric, with a sharper rise on the low-energy side and a more gradual falloff at high energy (Fig. 7) [10]. Some surfactant SWNTs with narrow PL linewidth also show this shape [15]. Interestingly, this shape qualitatively matches that of a 1D DOS, but the connection of the lineshape to the DOS has not been separately confirmed. Individual nanotubes prepared by drying a drop of dispersion on glass have a single Lorentzian lineshape with an approximately 25 meV linewidth [23].

It seems likely that the narrow linewidths are intrinsic. Clearly, lifetime broadening can be excluded since the PL radiative lifetime is estimated to be of the order of nanoseconds, which implies μeV linewidths. Since excitons in SWNTs are strongly bound (~ 0.4 eV), excitonic effects are important even

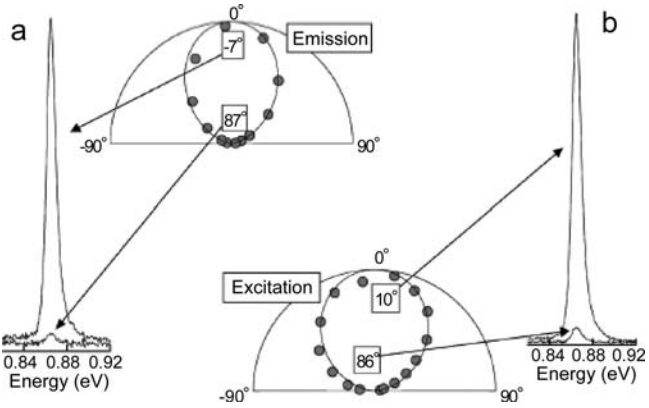

Fig. 7. Polarization dependence of PL emission (**a**) and excitation (**b**). In the polar plots, the angle is between the optical electric field and the nanotube axis [10]

at room temperature. One clue to the origin of the linewidths is the correlation between nanotube diameter and emission linewidth [24]: the linewidth is broader in smaller-diameter nanotubes at room temperature. A possibility is that this broadening originates from the dephasing time of excitons in the ground state due to exciton–phonon scattering, i.e., if the dephasing time is shorter for smaller-diameter SWNTs. The role of exciton–phonon scattering is also apparent in the temperature dependence of the linewidth, as described later in this chapter.

The absorption linewidth and shape is largely determined by the carrier relaxation timescale. In contrast with emission, the PLE profile even from an individual nanotube can show several resonances. However, the E_{22} resonance is strongly dominant, with a Lorentzian lineshape of FWHM measuring about 40 meV. This linewidth is consistent with lifetime broadening at the timescales (< 1 ps) measured in photobleaching experiments (See the contribution by *Ma* et al.). For E_{22}^S, no significant systematic trend in linewidths as a function of (n, m) has yet been reported.

3.2 Polarization

The optical response of SWNTs is strongly affected by its shape anisotropy, with both absorption and emission of photons having a strong polarization dependence. Anisotropic scattering was first demonstrated in Raman spectroscopy on individual nanotubes [25]. For surfactant SWNTs, the same effect was seen soon after the discovery of PL [23]. Figure 7 shows the polarization dependence of both light absorption and PL emission. Both emission at E_{11}^S and absorption at E_{22}^S have a maximum intensity for polarization parallel to the nanotube axis. The intensity fits a $\cos^2\theta$ polarization dependence, and the polarization anisotropy was found to be ~ 20 in emission, and ~ 10 in

absorption. Considering the enormous aspect ratio of these SWNTs, the measured anisotropy is actually quite small. However, those nanotubes deviated at least slightly from perfect straightness and any bend necessarily reduces the polarization anisotropy. Results of absorption anisotropy are now available on ensembles using post-growth alignment schemes or vertically grown nanotube forests [26, 27].

As discussed in Sect. 2, perpendicular excitations are expected to be strongly suppressed due to the antenna effect [2]. Still, PLE spectra reveal distinct absorption peaks for different polarization configurations. Anisotropy in the PL for micelle-suspended SWNTs was first reported and it was shown that the degree of anisotropy was different for different fixed excitation wavelengths [28]. Polarized photoluminescence excitation (PLE) spectroscopy (i.e., with tunable excitation wavelength) on ensembles of smaller-diameter nanotubes clearly showed crosspolarized absorption peaks [29]. In the crosspolarized configuration, excitation is transversely polarized with respect to emission. Using data obtained from the different configuration of polarization allows for "pure" components of parallel (longitudinal) and perpendicularly (transverse) excitations to be extracted. Figure 8a shows a PLE map in the usual longitudinal configuration, while Fig. 8b shows the transverse PL excitation map revealing resonances (horizontal arrows) attributed to E_{12}^S and E_{21}^S transitions. Those resonances appear close but at a different energy from the dominant E_{22}^S resonances. Within a noninteracting model, transition energies for the crosspolarized condition are expected halfway between E_{11}^S and E_{22}^S. However, the resonances observed in Fig. 8 appear close to E_{22}^S, thus at considerably higher energy than predictions within a single-particle theory. This result provides further evidence for excitons in SWNTs. A blueshift of excitonic E_{12}^S and E_{21}^S transitions relative to E_{11}^S is expected theoretically by correlated-electron calculations [30]. The amount of blueshift depends on the strength of the Coulomb interaction. Similarly, a large blueshift of an excitonic absorption peak for perpendicular polarization is expected on the basis of calculations that take into account the depolarization effect (see the contribution by *Saito* et al.) [31]. New polarized PLE imaging results on individual SWNTs clearly resolve E_{12}^S and other features, including their (n, m) dependence, and they can be explained in the context of these excitonic pictures [32].

3.3 Quantum Efficiency

The quantum efficiency (η) is a parameter of great interest from the point of view of basic physics as well as from the point of view of photonic and optoelectronic applications. It can be defined as the ratio of the number of photons emitted (n_{em}) to the number of photons absorbed (n_{abs}), so that $\eta = n_{\mathrm{em}}/n_{\mathrm{abs}}$. For SWNTs in a surfactant, early reports suggested $\eta \approx 0.1\,\%$, but much higher values have been measured recently. These numbers represent

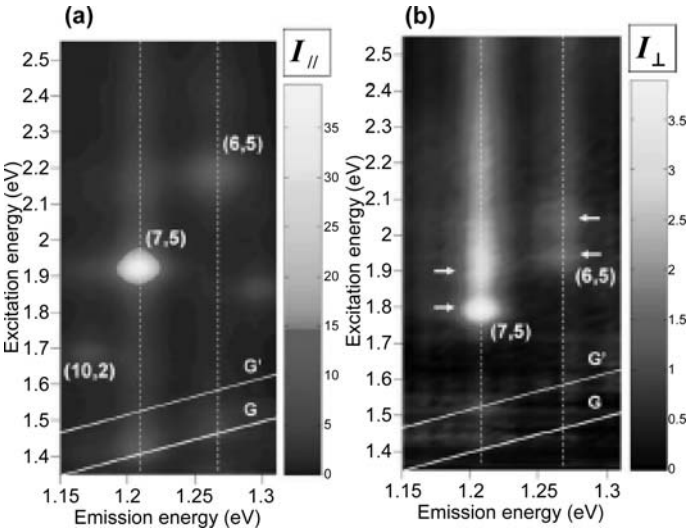

Fig. 8. Longitudinal (**a**) and transverse PL excitation maps. The resonances in (**b**) are attributed to absorption into E_{12} and E_{21}. *Horizontal arrows* indicate transverse resonances [29]

only estimates since either or both photon numbers (n_{em} and n_{abs}) have not been measured directly.

For nanotubes in solution, the number of absorbed photons at a given energy is straightforward and is measured simply by looking at the optical density of the solution. Solutions with optical density of order OD = 0.1 are often used (corresponding to transmission of 80 %). Non-SWNT absorbers must be negligible or accounted for in some way. Ideally, all absorbed photons excite SWNTs in the solution. If the nanotubes were pristine and perfect, PL would not be expected from the metallic fraction (so $\eta = 0$), and would be a maximum for semiconductors ($\eta = \eta_{\max}$). For bundles, or individual SWNTs that are defective, short with end effects, kinked or otherwise imperfect, the efficiency should be lower ($\eta < \eta_{\max}$). In ensemble measurements one is averaging over a distribution, and so can only determine a lower bound on the intrinsic η of pristine SWNTs. Of course, SWNT PL is possible over a large range of wavelengths, and the detector must be sensitive to all possible emitters in the sample. One must also be careful to take into account the collection efficiency of the optical system.

It is more straightforward to determine η for an individual SWNT of known diameter and length. In that case, in terms of experimentally accessible parameters, $\eta = P_{\mathrm{e}}\lambda_{\mathrm{e}}S/AP_{\mathrm{i}}\lambda_{\mathrm{i}}S_T$ where P_{i}, λ_{i} and S are, respectively, the incident laser power, wavelength and spot area, and A is the fraction of incident photons absorbed by the nanotube, P_{e} is the power emitted from the tube, λ_{e} the emission peak wavelength, and S_{T} is the surface area of

the SWNT. Like molecules, SWNTs are expected to be transparent to most incident photons, so that $A \ll 1$. Measurements of A are not available at the single-nanotube level, however, ensemble measurements yield an optical crossection of $1.6 \times 10^{-4}\,\mathrm{nm}^2$ per carbon atom [26], and with a surface density of carbon atoms in graphene of 37 carbon atoms/nm^2, the absorption coefficient of a SWNT is estimated at $A = 0.0059$ (i.e., a SWNT absorbs one out of 169 incident photons). With PL imaging and spectroscopy, all parameters except A are determined and the SWNT quantum efficiency is estimated at $\eta = 7\,\%$, a value significantly higher than previous reports [33].

A low η might be expected by comparison to similar materials. For example, in conjugated polymers a low η is understood to arise from optically dark states, which are lower in energy than the optically bright state. However, in SWNTs, these states are expected to be just below the bright exciton (about 7 meV below) and therefore only significant at low temperatures (of order 10 K) [34]. Loss of PL intensity has been seen in this temperature range [35], and recent temperature- and magnetic-field-dependent measurements strongly support this picture [36].

PL excitation maps suggest that the quantum efficiency might be (n, m) dependent and three factors may cause η to be (n, m) dependent: E_{22}^S absorption rates, E_{11}^S emission rates, and relaxation process between the two states. These may have intrinsic as well as extrinsic components. Intrinsic aspects have begun to be investigated theoretically [37, 38]. Within a nonexcitonic model, optical absorption at E_{22}^S is found to depend strongly on chiral angle, while the diameter dependence is weak. For emission at E_{11}^S the dominant dependence is on the diameter. On this basis, PL intensities would be greater for smaller-diameter nanotubes of the mod 2 family, with emission from near-zigzag angle SWNTs being most intense. In contrast, there is a virtual absence of signal from near-zigzag SWNTs in PLE maps. Experimentally however, (n, m) distributions are not likely to be uniform. In the model, the phonon-relaxation process from E_{22}^S to E_{11}^S results in lower η for mod 2 and near-zigzag SWNTs. For the mod 2 family with its smaller E_{22}^S/E_{11}^S ratio, interband splitting becomes less than the LO phonon energy, closing a relaxation pathway and so dramatically slowing relaxation to E_{11}^S (see also the contribution by *Saito* et al.).

A relaxation picture involving a process where two E_{11}^S excitons are created was used to explain weak PL in near-zigzag SWNTs [38]. This extra decay channel should be possible in mod 1 nanotubes for which $E_{22}^S > 2E_{11}^S$, but not for mod 2 nanotubes where mod 1 and mod 2 are defined in terms of (mod $(n - m)$,3) = 1 or 2. Independent experimental evidence, for example larger absorption linewidths for shorter decay times, has not yet been obtained.

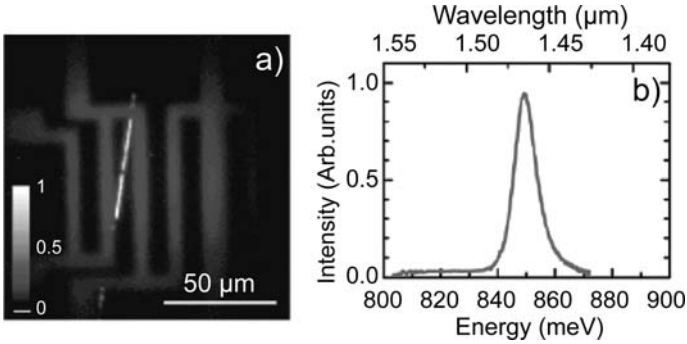

Fig. 9. (**a**) A PL image of an individual SWNT freely suspended in air above a patterned Si substrate. (**b**) The PL spectrum of the nanotube in (a) [33]

3.4 Photoluminescence Imaging

SWNTs are often grown to millimeter lengths or more. This means that despite their nanometer-scale diameters, they are macroscopic objects and they can produce an extended, resolvable optical image in the far field.

PL imaging of individual nanotubes in the far field has been reported for detection with near-infrared 2D detectors and laser illumination [15, 33, 39], as well as white-light illumination [40]. A PL image of a single SWNT suspended over a trench is shown in Fig. 9a, with the corresponding PL spectrum shown in Fig. 9b. Spatially resolved spectroscopy shows that for individual nanotubes in surfactant gels, PL linewidths are usually $\sim 30\,\text{meV}$, but occasionally only $\sim 12\,\text{meV}$, in line with air-suspended nanotubes [15]. On extended images, small spectral shifts ($\sim 2\,\text{meV}$) have been reported from end-to-end of a single such nanotube. Such shifts and broadening have been interpreted in terms of the different environmental effects along the length of the nanotube. On freely suspended SWNTs [33], while most nanotubes had fixed emission wavelengths, small shifts in emission were seen in some nanotubes, possibly attributable to changes in the local environment along the lengths of the single nanotubes. Large spectral shifts were also seen and attributed to (n, m) changes.

PL imaging with deep submicrometer resolution is also possible using scanning probe near-field techniques (see the contribution by *Hartschuh* on new techniques) [41]. For SDS-wrapped SWNTs on mica, "hotspots", $\sim 20\,\text{meV}$ shifts and significant linewidth variations have been observed with $\sim 15\,\text{nm}$ resolution on micrometer-length nanotubes [42]. These are presumably all environmental effects related to the micelle wrapping. Such methods have also been used to detect and spatially resolve nanotubes directly on glass [43].

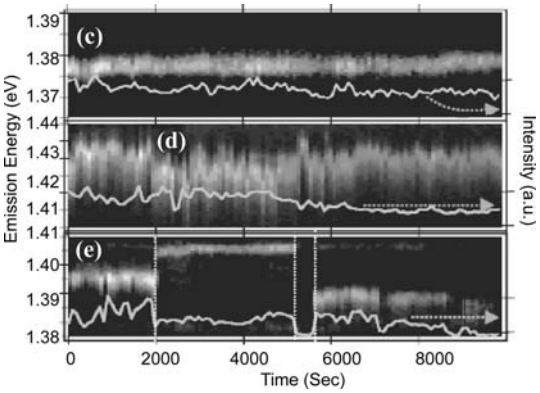

Fig. 10. Time evolution of photoluminescence spectrum from individual SWNTs on a substrate measured at low temperature. In (**c**), the emission is constant and the intensity fluctuates, while in (**d**) and (**e**) both emission energy and intensity fluctuate [44]

3.5 Time Dependence

Ultrafast optical studies (from ps to μs timescales) give detailed information about the dynamics of the PL process and are covered in detail in the contribution by *Ma* et al. Here, we discuss only very slow (ms to ks timescale) fluctuations in PL intensity that are sometimes observed. The experimental results are quite diverse and depend on experimental conditions. For SWNTs suspended above a substrate, stable PL is obtained, and this is sometimes the case in solution. Time-dependent PL can be caused by high excitation intensities, temperature fluctuations, fluctuations in ambient environment, pH changes, gas ambient changes and other effects. For surfactant-coated SWNTs deposited on substrates, random fluctuations of PL intensity (blinking) and/or PL wavelength (spectral diffusion) have been seen, especially at low temperatures (see Fig. 10) [44]. Presumably, these random fluctuations are the consequence of local defects on the nanotube or in its immediate surrounding, and these defects change the nanotube environment dynamically by trapping and releasing charged or neutral excitations. Blinking was observed even at room temperature in similar samples, and explained in the same way [45].

In contrast, the vast majority of air-suspended SWNTs show steady luminescence at low excitation power. However, some do show slow intensity variations and gradual dimming [33]. This phenomena is associated with the "pushing down" of suspended SWNTs by optically induced forces and was first seen by global Raman imaging [46]. In that case, SEM observation of the nanotubes showing losses of Raman intensities confirmed that they collapsed down onto the substrate. Of course, SWNTs may collapse onto the

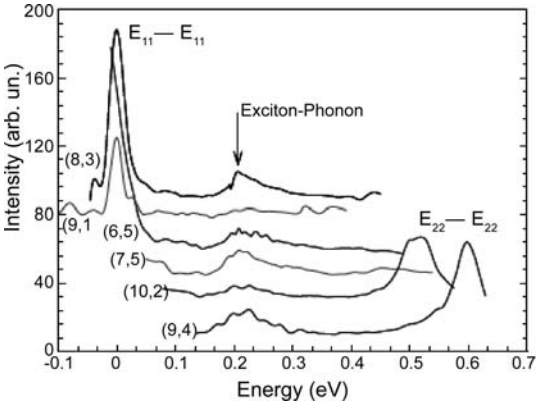

Fig. 11. PL excitation profile just above E_{11}^S showing phonon-assisted absorption (*peaks* around 200 meV). The energies have been offset by the corresponding E_{11}^S energy. Peaks visible at higher energy correspond to E_{22}^S absorption [48]

substrate for other reasons as well, for example because of simple electrostatic interactions.

3.6 Phonons

Optical processes described so far in this chapter involved solely electron–hole excitations. This is reasonable for a first description since they represent by far the strongest resonances in the PLE map. There are, however, a number of additional weaker features, some of which can be assigned to phonon-assisted processes. These appear as satellites of the main E_{11}^S and E_{22}^S resonances. In one spectacular example, several phonon sidebands including overtones are observed in low-temperature PLE on individual SWNTs [47]. Figure 11 shows an example of an E_{11}^S phonon sideband [48]. The excitation energies have been offset by the corresponding E_{11}^S emission energy to highlight the common-phonon feature. There is a clear peak around 200 meV above E_{11}^S that corresponds to the energy of the G-band phonon. This is described as an exciton–phonon complex and theory predicts that the strength of this sideband is much greater within an excitonic picture, and it would not be visible in a nonexcitonic picture [49].

Phonon sidebands are not limited to E_{11}^S excitons, but also originate in other exciton bands such as E_{22}^S. An experimental demonstration of the relation of an E_{22}^S sideband to phonons was provided by comparing PL of SWNTs made from different carbon isotopes [50]. A slight spectral shift occurs when ^{13}C is used instead of ^{12}C. The spectral weight of this sideband is of the order of a few per cent, in agreement with theory [49].

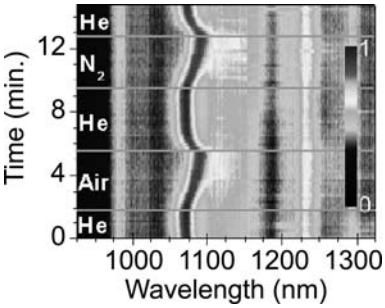

Fig. 12. Dynamics of the photoluminescence peak position upon cycling of the gas ambient [52]

4 Physical and Chemical Effects

4.1 External Environment

All atoms in SWNTs are surface atoms, and, furthermore, SWNTs are miniscule, so SWNT physical and chemical properties, including PL, depend greatly on the immediate surroundings. Effects of the environment are seen whether the luminescent nanotubes are in a surfactant solution – whether neutral or ionic – or a solid matrix, suspended in air or other ambient gas or in direct contact with a substrate or even contacting other nanotubes.

One way the environment can affect the nanotube properties is by changing its electrostatic surrounding. This may occur simply by dielectric screening, or through the transfer of electric charges. The effect of dielectric screening on the PLE map was discussed in Sect. 2.3, and the theory is discussed in detail in the contribution by *Spataru* et al. Briefly, the electron–hole dipole produced by photon absorption will displace surrounding charges, effectively reducing the Coulomb interaction between the electron and hole. Theory predicts that increased dielectric screening (i.e., weaker interaction) leads to a redshift of E_{11}^S and E_{22}^S transitions, because the self-energy correction (redshift with increasing screening) is generally greater than the exciton binding energy (blueshift with increasing screening). Simple scaling relationships have been found for the exciton binding energy as a function of dielectric constant [51]. Figure 5 shows the difference (of order 10 meV) in E_{11}^S and E_{22}^S energies for air ambient as compared to surfactant solutions. Sensitivity to ambient is also shown in Fig. 12 where shifts in E_{11}^S are attributed to molecular adsorption and desorption on the SWNT [52].

In environments where charge is transferred to the SWNT, the effects on the PL are more severe. For SWNTs in an ionic solution, changing the pH affects the charge state of the nanotube, leading to the suppression of both light emission and absorption [53]. This can be understood because the addition of charges shifts the Fermi energy from the midgap region toward and ultimately into the conduction or valence band. Light absorption in SWNTs

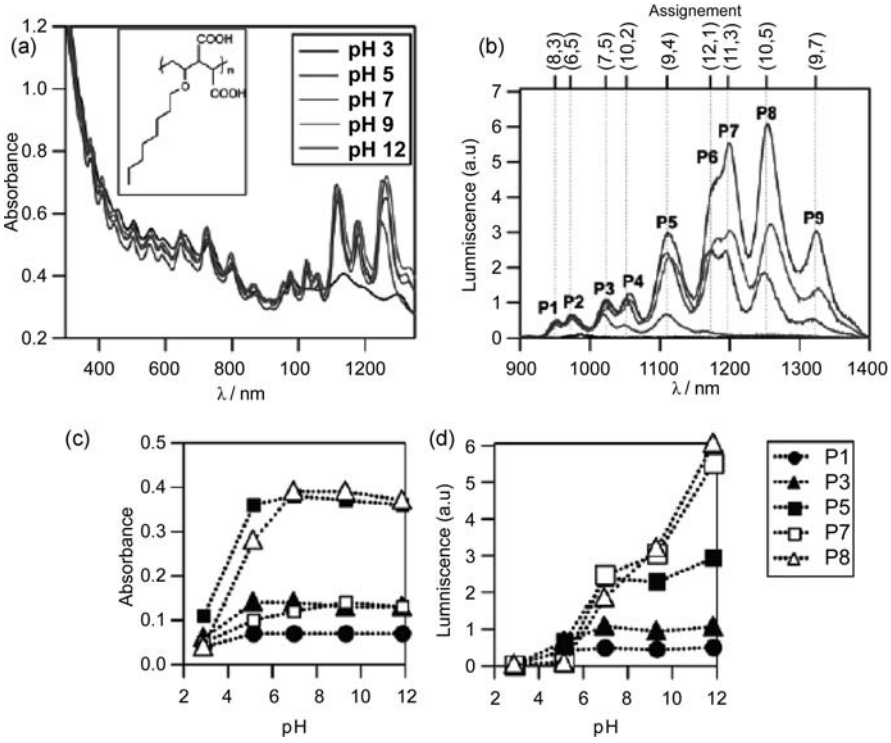

Fig. 13. The pH-dependence study of absorbance (a) and (c), and luminescence (b) and (d), in SWNT ensembles. A decrease in pH leads to a suppression of both light absorption and emission [53]

is strongly resonant, and electrostatic doping removes or adds electrons from those resonant states and light absorption is necessarily suppressed. In contrast with light absorption, which is mainly only sensitive to state filling, light emission can also be very sensitive to the presence of dopants as reactive centers. Indeed, pH-dependent PL studies show that the PL intensity diminishes, while absorption is largely unchanged (Fig. 13). Within their radiative lifetime (estimated at ns) E_{11}^S excitons can diffuse towards these reactive centers, where PL is quenched by nonradiative decay. A small number of charges can also quench PL through nonradiative Auger recombination [53]. These two processes are faster (taking only $\sim$ 10 ps) than radiative decay rates and therefore dramatically lower PL intensities. The charge state can also be changed through capacitive gating, described in Sect. 4.2.

The surrounding matrix, especially solids, can induce strain on an SWNT and so alter PL emission. An isotropic strain produces predominantly a radial stress on a long nanotube that can be viewed primarily as uniaxial stress on the graphene sheet [54]. Within a TB model, the anisotropic distortion

of the graphene sheet results solely in a shift of the Fermi points. For a metallic nanotube, this leads to the opening of a gap, while for semiconducting nanotubes it leads to an increase of E_{11}^S and a reduction of E_{22}^S energies for the mod 1 family, and to an opposite shift for mod 2 with a diameter-independent $\cos 3\theta$ functional form (see the contribution by *Spataru* et al.) [54]. This effect was observed in PL for SWNTs frozen in an ice matrix where the strain results in large shifts [55]. The large axial strain produced by mismatch of the thermal expansion coefficients was estimated at 0.5 % corresponding to a stress of 5 GPa. In contrast, PL experiments in liquid with hydrostatic pressures up to 1 GPa were found to decrease E_{11}^S and E_{22}^S energies, irrespective of the family [56]. This was attributed to a higher-order effect beyond the graphene-electronic energy band model. Recently, uniaxial strains have been applied, stretching individual SWNTs resulting in small shifts in PL peak position [57].

4.2 External Physical Parameters

The previous section showed that temperature can be used indirectly to affect the strain on the nanotube in a matrix. In such samples, intrinsic temperature effects are mixed with strain effects and the two contributions must be disentangled. For freely suspended SWNTs, matrix effects are minimized, and experiments have been carried out down to the single-nanotube level, with PL spectra obtained from 4 K to 700 K [35, 52]. At low temperatures, the ambient must be controlled since the condensation of atmospheric gases causes a quenching of SWNT PL. Figure 14 shows single-SWNT data with changes in emission energy and linewidth as well as the emergence of additional peaks near 5 K. Not shown here, intensity changes, shifts in absorption peak position, and the emergence of many otherwise unseen peaks also occur at low temperature.

The E_{11} PL emission peaks blueshift from 300 K down to low temperature, with a species-dependent magnitude ranging from almost zero to $\sim -50\,\mu\text{eV/K}$. This is an order of magnitude less than conventional bulk semiconductors, and is important in applications such as lasers, where heating can shift the bandgap and consequently reduce gain and efficiency. This data is well fitted theoretically by a TB model that includes only electron–phonon interaction, not excitonic effects [58]. The model predicts a family pattern for the shift, and for some species of the mod 2 family, the bandgap shows a more complex dependence, with a redshift at temperatures below 100 K. The temperature dependence of all E_{11}^S species is predicted by a "Vina"-type equation that includes two phonon energy scales with (n,m)-dependent coupling strength (see the contribution by *Spataru* et al.). A more complete experimental study measuring the temperature dependence of the PL for many (n, m) has not yet been reported.

Interestingly, at high temperatures a sudden shift in the PL peak position has been found to occur (a "bandgap shift transition") [52, 59]. This abrupt

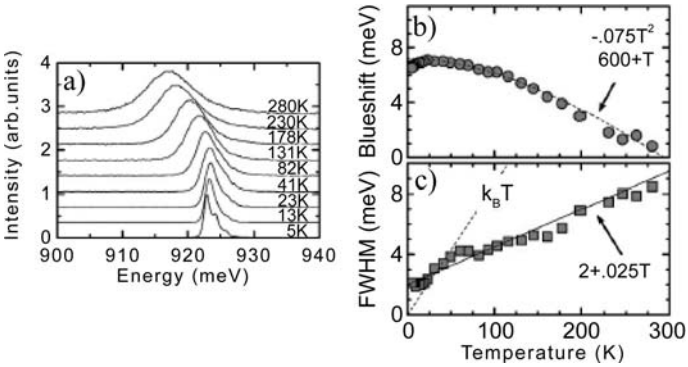

Fig. 14. Temperature dependence of the luminescence from a single freely suspended SWNT (**a**) PL spectra from 280 to 5 K. Evolution of (**b**) peak position (**c**) linewidth. In (c), the thermal energy k_BT is plotted for comparison [35]

blueshift (~ 30 meV) on heating, which can take place over a few degrees, is larger than the entire redshift that occurs between 5 K and room temperature. As described in Sect. 4.2, this effect is not thought to be intrinsic, but is rather interpreted as a result of the outgassing of atmospheric adsorbates from the SWNT surface.

The linewidth and the intensity of the PL peak can provide insight into the PL mechanism. In several reports on individual SWNTs and SWNT ensembles, the linewidth narrows linearly from 300 K to 4 K, while the integrated intensity increases modestly as temperature is reduced from 300 K to leveling off and ultimately decreasing from about 50 K to 4 K. The temperature dependence of the linewidth in Fig. 14 shows a linear drop from 9 meV to 2 meV between 280 and 4 K. Sub-meV linewidths have also been reported at low temperature for nanotubes in contact with a substrate [44]. It should be noted that in such samples blinking and spectral diffusion was also observed, suggesting that extrinsic factors, such as substrate-induced or ontube defects are important. It is worth noting that Raman features often have narrow linewidths overlapping the SWNT PL emission range, and care must be taken in assigning spectral features to radiative recombination.

Time-resolved PL decay experiments are essential complements to CW PL data, especially to help explain the trends observed in emission intensity and linewidth. Detailed discussion of time-resolved data can be found in the contribution by *Ma* et al. on fast optics). Briefly, for single SWNTs, a monoexponential decay is observed with timescales from order 10 ps to 100 ps. Variability of timescale is a sign of sample inhomogeneity [60]. In SWNT ensembles, this tube-to-tube variation in decay rates leads to multiple exponential decay curves. A detailed temperature study of the long-timescale component (~ 100 ps) shows a fivefold increase of the decay time from 300 K and a leveling off and decrease below 50 K [34]. This result correlates exactly with the

emission intensity, and is also consistent with the temperature dependence of the linewidth. The mechanisms attributed to the high- and low-temperature behavior are competing radiative and nonradiative channels of the bright and dark exciton states. Above 50 K, excitons in the lowest-energy dark states are thermally excited to the bright exciton state; therefore, the most significant and relevant decay channel at elevated temperatures is through the bright exciton state. For the bright state alone, both radiative and nonradiative processes compete, with the latter being phonon mediated. At low temperature, the dark exciton state becomes an effective nonradiative channel for exciton decay, as excitons trapped in those states can no longer be thermally excited to the bright state. These experiments allow for an estimate of ~ 4 meV for the dark–bright exciton splitting (see the contribution by *Kono* et al.).

Since the dark exciton–bright exciton energy splitting is small, weak symmetry-breaking perturbations can significantly change SWNT PL, either by altering the band ordering, or by changing state mixing. Brightening of PL intensities is observed when high magnetic fields (> 1 T) are applied along the SWNT axis, providing the most direct evidence of low-energy dark excitons in SWNTs [36, 61, 62]. This effect and its physical origin is described in detail in the contribution by *Kono* et al. The existence of dark excitons has been proposed to reduce SWNT PL quantum efficiencies. However, because of the small splitting this effect appears minimal at room temperature [36].

An electric field also affects PL, by breaking the symmetry or by changing the SWNT charge state. A suspended SWNT can be electrically connected in a nanotube field-effect transistor (FET) configuration (see the contributions by *Avouris* et al. and by *Biercuk* et al.). In such a device, the capacitive coupling to the conductive substrate allows for charges to be drawn in and out of the nanotube, and in addition to measuring electrical conductivity, PL spectra can be acquired. Figure 15 shows that the PL intensity reaches a maximum at negative gate voltages, while the spectral shape remains qualitatively unchanged [63]. The peak corresponds to the onset of hole conduction. It was also found that electric current suppresses PL intensity. The analysis is based on a free-electron and free-hole picture, and must be revised in the light of the excitonic picture. In analogy with pH-dependent studies, we might expect that excess charge in electrostatically doped nanotubes should also lead to a suppression of the luminescence, for example through the creation of new Auger-process decay channels.

5 Applications

5.1 Nanotube Research

The advance of research in any materials system is intimately linked to the ability to evaluate the outcome of synthesis and fabrication. While other

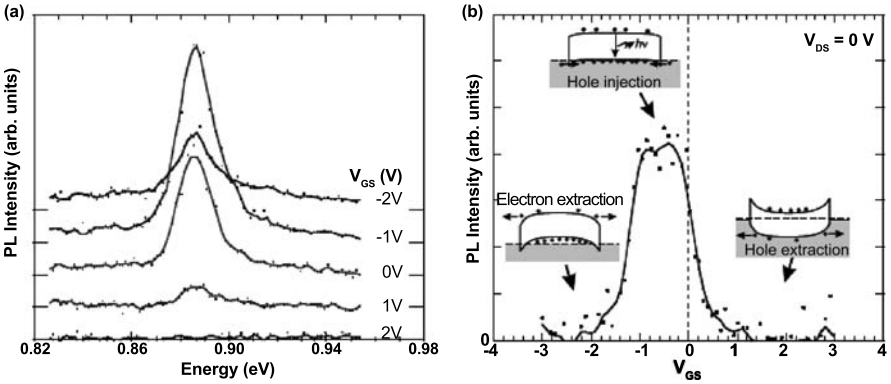

Fig. 15. Electric-field dependence of PL for a suspended SWNT in a nanotube field-effect transistor. (**a**) PL spectra taken at various gate voltages V_{GS}. (**b**) PL intensity versus gate voltage showing a maximum at a flat-band condition as illustrated in the *insets* [63]

methods, either direct like TEM, or indirect, like resonant Raman spectroscopy can provide structural information, the PLE mapping method has emerged as arguably the most effective way to determine (n, m) distributions for semiconducting SWNTs. Other methods can provide similar data, and even be more direct, but PLE mapping is rapid, relatively economical, and reliable, and can be used at the ensemble or even down to the single-nanotube level (see contribution by *Jorio* et al.). PLE mapping systems are already available commercially.

The weaknesses of PLE mapping are discussed in detail in the contribution by *Jorio* et al. Briefly, first, metallic nanotubes are not seen in PLE maps. Estimating the relative abundance of a given (n, m) species within a sample is a delicate undertaking if one does not simply count nanotubes. There is not yet a generally accepted calibration as to the relative brightness of different species. Selection effects are possible, especially in solution, as there may be extrinsic environmental effects that preferentially weaken the luminescence of certain species. If SWNTs are not well isolated, it is already clear that energy transfer between nearby isolated nanotubes or within bundles can occur [16], and this must be species dependent. Defects should reduce luminescence efficiency with their abundance or effect being likely (n, m) dependent. Despite its weaknesses, PLE mapping remains a very effective method of estimating (n, m) distributions, especially when comparing relative abundances of like samples.

5.2 Wider Applications

SWNTs are prime candidates for sensing applications, because interactions with the surface are a basis for sensing and for SWNTs, every carbon atom is on the surface and can potentially contribute. As described in Sect. 4, light emission in SWNTs is affected in several ways when the local environment changes. Potentially, the sensitivity of SWNT PL to the local environment could be used for sensing in a broad range of applications. At the present time, the challenge is to carefully characterize SWNT PL sensing, and determine whether or not this kind of sensing is competitive with existing technologies.

One can foresee that SWNT sensors based on light detection could have several advantages including ease of implementation (relative to electronic-based sensing), flexibility in the choice of embedding matrix (either free in solution or fixed on a substrate), the potential for ultrahigh packing density, and chemical specificity (through attachment of various functional groups). That SWNTs emit in the near-infrared may appear to be a drawback. However, detector sensitivity in the near-IR has improved significantly in recent years, and sensitive cameras are becoming less and less expensive. In addition, IR emission is desirable in specific applications where an emission background is present in the visible range.

A specific sensing application is fluorescent-dye labeling in biological systems. Biological activities from the organism level to the molecular level can be monitored by imaging PL from dyes. Dyes must be bio-compatible with the subject, alive or not, and should show strong PL in a fixed band. Some dye molecules (or "fluorophores") are not benign and for example may be toxic to a cell under investigation. The main weakness of common fluorophores is their sensitivity to photobleaching, meaning they can degrade under photoexcitation. SWNTs are very promising as fluorophores and are actively being investigated in this context. There is no evidence of blinking or photobleaching in SWNTs after prolonged exposure to excitation at high intensity [64]. SWNTs also have a reasonably high quantum efficiency [33], and many distinct species (and thus potentially many distinct fluorophores) emit in the portion of the near-infrared band that is largely transparent in biomaterials. The opacity of liquid water at long wavelength limits the usefulness of larger-diameter nanotubes for this application. It is quite possible that SWNTs, at least in small quantities may be benign in biological systems. For example, it has been demonstrated that cell division can occur in cells incorporating luminescent nanotubes [39]. However, much more research will be required to determine what effects SWNTs have on biological systems, good or bad, and what SWNT concentration would be required to cause such effects. It is presently unclear what health risks (or benefits) might be associated with SWNTs, if any.

Electronic applications of SWNTs are promising in large part because of their remarkable current-carrying capacity. Since the discovery of PL in SWNTs, interest has grown in their optoelectronic properties. In electrolu-

minescence (EL) light emission occurs with purely electrical excitation, as opposed to optical excitation in PL, as for example at the interface of a p–n junction, and by impact excitation with the creation of hot carriers [65, 66]. Likewise, light absorption by SWNTs can give rise to electrical signals, with photoconductivity [67, 68], and bolometry [69], now being actively explored. Thus, applications arise from PL alone, but also by characterizing SWNT luminescence and absorption, PL data motivates and assists in the development of nanotube-based optoelectronic devices.

6 Conclusion

The field of SWNT PL is in a rapid growth phase. Basic features of SWNT PL have been uncovered, and explained in the present review, but there is vastly more that is only beginning to be investigated. Preparing SWNTs such that they emit any significant PL at all was an early challenge, but now surfactant-liquid, surfactant-solid and air-suspended preparations are well established and successful. PL from SWNTs has such remarkable attributes as (n, m) dependence, high quantum efficiency (up to 7%), strong polarization dependence, sub-kT linewidths and characteristic lineshapes. The method of PLE mapping has emerged as a popular method for (n, m) assignment, and features in the PLE map beyond E_{11}^S and E_{22}^S are being systematically explored. In addition to purely spectroscopic study, PL imaging is also growing in importance. The effect of the dielectric environment, charge transfer, temperature, strain, electric field, magnetic field and similar effects have all been explored to some extent, but not in a comprehensive way. Over the past couple of years, the excitonic origin of SWNT PL has been explored extensively, with large bandgap-renormalization and exciton-binding effects seen and the role of dark excitons being uncovered. The SWNT is a model system for one-dimensional exciton physics. The exploration of systematic trends in PL as a function of (n, m) is becoming even more important, and is especially interesting because changing (n, m) allows one to "tune" diameter and chirality.

As has been the case for more-established materials systems, it is likely that much of the future work on SWNT PL will relate to improvements in sample preparation. Until recently, the SWNT has usually been viewed as an ideal, perfect lattice, in a perfectly featureless background. It is of course expected, and already there is considerable evidence, that SWNT PL is sensitive to many of the real-world deviations from this idealized picture. We can expect a systematic understanding, experimental and theoretical, of how deviations from ideality affect SWNT PL. For example, dopant densities, adsorbates, defects, end effects, chemical functionalization and surface effects remain to be systematically studied and the mechanisms underlying their effects remain to be fully elaborated. The collective effects on PL of combinations of SWNTs either in bundles, at crossings, at junctions or as shells of

DWNTs will be an important area of SWNT PL work in future years. We can expect better and better SWNT samples for PL, and in return PL will likely only grow in importance as a method of characterizing SWNT samples. Of course, there have already been surprises with almost every experiment and there is likely almost as much that is unpredictable in the road ahead.

It has largely been fundamental scientific interest that has been driving research into SWNT PL. However, SWNT PL studies have uncovered diverse phenomena that could be exploited technologically. New applications in biology, medicine, photonics and optoelectronics appear to hold promise as we look to the future, and we expect these applications to increasingly drive applied research in SWNT optics.

References

[1] M. J. O'Connell, S. M. Bachilo, C. B. Huffman, V. C. Moore, M. S. Strano, E. H. Haroz, K. L. Rialon, P. J. Boul, W. H. Noon, C. Kittrell, J. Ma, R. H. Hauge, R. B. Weisman, R. E. Smalley: Band gap fluorescence from individual single-walled carbon nanotubes, Science **297**, 593 (2002) 287, 291, 292, 298

[2] H. Ajiki, T. Ando: Carbon nanotubes: Optical absorption in Aharonov–Bohm flux, Jpn. J. Appl. Phys. Suppl. **34-1**, 107 (1995) 289, 290, 296, 300

[3] T. Ando: Excitons in carbon nanotubes, J. Phys. Soc. Jpn. **66**, 1066 (1997) 290, 295

[4] H. Kataura, Y. Kumazawa, Y. Maniwa, I. Umezu, S. Suzuki, Y. Ohtsuka: Optical properties of single-wall carbon nanotubes, Synth. Met. **103**, 2555 (1999) 290, 293

[5] O. Jost, A. A. Gorbunov, W. Pompe, T. Pichler, R. Friedlein, M. Knupfer, M. Reibold, H.-D. Bauer, L. Dunsch, M. S. Golden, J. Fink: Diameter grouping in bulk samples of single-walled carbon nanotubes from optical absorption spectroscopy, Appl. Phys. Lett. **75**, 2217 (1999) 290

[6] A. Hagen, T. Hertel: Quantitative analysis of optical spectra from individual single-wall carbon nanotubes, Nano Lett. **3**, 383 (2003) 290, 291

[7] J. Lefebvre, Y. Homma, P. Finnie: Bright bandgap photoluminescence from unprocessed single walled carbon nanotubes, Phys. Rev. Lett. **90**, 217401 (2003) 292

[8] J. Kong, A. M. Cassel, H. Dai: Chemical vapor deposition of methane for single-walled carbon nanotubes, Chem. Phys. Lett. **292**, 567 (1998) 292

[9] Y. Homma, Y. Kobayashi, T. Ogino, T. Yamashita: Growth of suspended carbon nanotube networks on 100-nm-scale silicon pillars, Appl. Phys. Lett. **81**, 2261 (2002) 292

[10] J. Lefebvre, J. M. Fraser, P. Finnie, Y. Homma: Photoluminescence from an individual single-walled carbon nanotube, Phys. Rev. B **69**, 075403 (2004) 293, 298, 299

[11] S. Lebedkin, K. Arnold, F. Hennrich, R. Krupke, B. Renker, M. M. Kappes: FTIR-luminescence mapping of dispersed single-walled carbon nanotubes, New J. Phys. **5**, 140 (2003) 293, 294

[12] S. M. Bachilo, M. S. Strano, C. Kittrell, R. H. Hauge, R. E. Smalley, R. B. Weisman: Structure-assigned optical spectra of single-walled carbon nanotubes, Science **298**, 2361 (2002) 293, 294, 295, 296
[13] S. Bachilo, R. B. Weisman: Dependence of optical transition energies on structure for single-walled carbon nanotubes in aqueous suspension: An empirical "Kataura Plot", Nano Lett. **3**, 1235 (2003) 293, 296
[14] J. Lefebvre, J. M. Fraser, Y. Homma, P. Finnie: Photoluminescence from single-walled carbon nanotubes: A comparison between suspended and micelle-encapsulated nanotubes, Appl. Phys. A: Mater. Sci. Proc. **78**, 1107 (2004) 295, 296
[15] D. A. Tsyboulski, S. M. Bachilo, R. B. Weisman: Versatile visualization of individual single-walled carbon nanotubes with near-infrared fluorescence microscopy, Nano Lett. **5**, 975 (2005) 295, 298, 303
[16] O. N. Torrens, D. E. Milkie, M. Zheng, J. M. Kikkawa: Photoluminescence from intertube carrier migration in single-walled carbon nanotube bundles, Nano Lett. **6**, 2864 (2006) 295, 311
[17] T. Hertel, A. Hagen, V. Talalaev, K. Arnold, F. Hennrich, M. Kappes, S. Rosenthal, J. McBride, H. Ulbricht, E. Flahaut: Spectroscopy of single- and double-wall carbon nanotubes in different environment, Nano Lett. **5**, 511 (2005) 296
[18] T. Okazaki, S. Bandow, G. Tamura, Y. Fujita, K. Iakoubovskii, S. Kazaoui, N. Minami, T. Saito, K. Suenaga, S. Iijima: Photoluminescence quenching in peapod-derived double-walled carbon nanotubes, Phys. Rev. B **74**, 153404 (2006) 296
[19] C. L. Kane, E. J. Mele: The ratio problem in single carbon nanotube fluorescence spectroscopy, Phys. Rev. Lett. **90**, 207401 (2003) 296
[20] E. J. Mele, C. L. Kane: Many body effects in carbon nanotubes fluorescence spectroscopy, Solid State Commun. **135**, 527 (2005) 296
[21] F. Wang, G. Dukovic, L. E. Brus, T. F. Heinz: The optical resonances in carbon nanotubes arise from excitons, Science **308**, 838 (2005) 297
[22] J. Maultzsch, R. Pomraenke, S. Reich, E. Chang, D. Prezzi, A. Ruini, E. Molinari, M. S. Strano, C. Thomsen, C. Lienau: Exciton binding energies in carbon nanotubes from two-photon photoluminescence, Phys. Rev. B **72**, 241402 (2005) 297, 298
[23] A. Hartschuh, H. N. Pedrosa, L. Novotny, T. D. Krauss: Simultaneous fluorescence and Raman scattering from single carbon nanotubes, Science **301**, 1354 (2003) 298, 299
[24] T. Inoue, K. Matsuda, Y. Murakami, S. Maruyama, Y. Kanemitsu: Diameter dependence of exciton–phonon interaction in individual single-walled carbon nanotubes studied by microphotoluminescence spectroscopy, Phys. Rev. B **73**, 233401 (2006) 299
[25] G. S. Duesberg, I. Loa, M. Burghard, K. Syassen, S. Roth: Polarized Raman spectroscopy on isolated single-wall carbon nanotubes, Phys. Rev. Lett. **85**, 5436 (2000) 299
[26] M. F. Islam, D. E. Milkie, C. L. Kane, A. G. Yodh, J. M. Kikkawa: Direct measurement of the optical absorption cross section of single-wall carbon nanotubes, Phys. Rev. Lett. **93**, 037404 (2004) 300, 302

[27] Y. Murakami, E. Einarsson, T. Edamura, S. Maruyama: Polarization dependence of the optical absorption of single-walled carbon nanotubes, Phys. Rev. Lett. **94**, 087402 (2005) 300
[28] S. Lebedkin, F. Hennrich, T. Skipa, M. M. Kappes: Near-infrared photoluminescence of single-walled carbon nanotubes prepared by the laser vaporization method, J. Phys. Chem. B **107**, 1949 (2003) 300
[29] Y. Miyauchi, M. Oba, S. Maruyama: Cross polarized optical absorption of single-walled nanotubes by polarized photoluminescence excitation spectroscopy, Phys. Rev. B **74**, 205440 (2006) 300, 301
[30] H. Zhao, S. Mazumdar: Electron–electron interaction effects on the optical excitations of semiconducting single-walled carbon nanotubes, Phys. Rev. Lett. **93**, 157402 (2004) 300
[31] S. Uryu, T. Ando: Exciton absorption of perpendicularly polarized light in carbon nanotubes, Phys. Rev. B **74**, 155411 (2006) 300
[32] J. Lefebvre, P. Finnie: Polarized photoluminescence excitation spectroscopy of single-walled carbon nanotubes, Phys. Rev. Lett. **98**, 167406 (2007) 300
[33] J. Lefebvre, D. G. Austing, J. Bond, P. Finnie: Photoluminescence imaging of suspended single-walled carbon nanotubes, Nano Lett. **6**, 1603–1608 (2006) 302, 303, 304, 312
[34] S. Berger, C. Voisin, G. Cassabois, C. Delalande, P. Roussignol, X. Marie: Temperature dependence of exciton recombination in semiconducting single-walled carbon nanotubes, Nano Lett. **7**, 398 (2007) 302, 309
[35] J. Lefebvre, P. Finnie, Y. Homma: Temperature dependent photoluminescence from single-walled carbon nanotubes, Phys. Rev. B **70**, 045419 (2004) 302, 308, 309
[36] I. B. Mortimer, R. J. Nicholas: Role of bright and dark excitons in the temperature-dependent photoluminescence of carbon nanotubes, Phys. Rev. Lett. **98**, 027404 (2007) 302, 310
[37] Y. Oyama, R. Saito, K. Sato, J. Jiang, G. G. Samsonidze, A. Grüneis, Y. Miyauchi, S. Maruyama, A. Jorio, G. Dresselhaus, M. S. Dresselhaus: Photoluminescence intensity of single-wall carbon nanotubes, Carbon **44**, 873 (2006) 302
[38] S. Reich, C. Thomsen, J. Robertson: Exciton resonances quench the photoluminescence of zigzag carbon nanotubes, Phys. Rev. Lett. **95**, 077402 (2005) 302
[39] P. Cherukuri, S. M. Bachilo, S. H. Litovsky, R. B. Weisman: Near-infrared fluorescence microscopy of single-walled carbon nanotubes in phagocytic cells, J. Am. Chem. Soc. **126**, 15638 (2004) 303, 312
[40] D. G. Austing, J. Lefebvre, J. Bond, P. Finnie: Carbon contacted nanotube field effect transistors, Appl. Phys. Lett. **90**, 103112 (2007) 303
[41] A. Hartschuh, H. Qian, A. J. Meixner, N. Anderson, L. Novotny: Nanoscale optical imaging of single-walled carbon nanotubes, J. Lumin. **119**, 204 (2006) 303
[42] H. Qian, T. Gokus, N. Anderson, L. Novotny, A. J. Meixner, A. Hartschuh: Near-field imaging and spectroscopy of electronic states in single-walled carbon nanotubes, Phys. Stat. Sol. B **243**, 3146 (2006) 303
[43] A. Hartschuh, H. N. Pedrosa, J. Peterson, L. Huang, P. Anger, H. Qian, A. J. Meixner, M. Steiner, L. Novotny, T. D. Krauss: Single carbon nanotube optical spectroscopy, ChemPhysChem **6**, 577 (2005) 303

[44] H. Htoon, M. J. O'Connell, P. J. Cox, S. K. Doorn, V. I. Klimov: Low temperature emission spectra of individual single-walled carbon nanotubes: Multiplicity of subspecies within single-species nanotube ensembles, Phys. Rev. Lett. **93**, 027401 (2004) 304, 309
[45] K. Matsuda, Y. Kanemitsu, K. Irie, T. Saiki, T. Someya, Y. Miyauchi, S. Maruyama: Photoluminescence intermittency in an individual single-walled carbon nanotube at room temperature, Appl. Phys. Lett. **86**, 123116 (2005) 304
[46] K. Kaminska, J. Lefebvre, D. G. Austing, P. Finnie: Real-time global Raman imaging and optical manipulation of suspended carbon nanotubes, Phys. Rev. B **73**, 235410 (2006) 304
[47] H. Htoon, M. J. O'Connell, S. K. Doorn, V. I. Klimov: Single carbon nanotubes probed by photoluminescence excitation spectroscopy: the role of phonon-assisted transitions, Phys. Rev. Lett. **94**, 127403 (2005) 305
[48] F. Plentz, H. B. Ribeiro, A. Jorio, M. S. Strano, M. A. Pimenta: Direct experimental evidence of exciton–phonon bound states in carbon nanotubes, Phys. Rev. Lett. **95**, 247401 (2005) 305
[49] V. Perebeinos, J. Tersoff, P. Avouris: Electron–phonon interaction and transport in semiconducting carbon nanotubes, Phys. Rev. Lett. **94**, 086802 (2005) 305
[50] Y. Miyauchi, S. Maruyama: Identification of an excitonic phonon sideband by photoluminescence spectroscopy of single-walled carbon-13 nanotubes, Phys. Rev. B **74**, 035415 (2006) 305
[51] V. Perebeinos, J. Tersoff, P. Avouris: Scaling of excitons in carbon nanotubes, Phys. Rev. Lett. **92**, 257402 (2004) 306
[52] P. Finnie, Y. Homma, J. Lefebvre: Band-gap shift transition in the photoluminescence of single-walled carbon nanotubes, Phys. Rev. Lett. **94**, 247401 (2005) 306, 308
[53] G. Dukovic, B. E. White, Z. Zhou, F. Wang, S. Jockusch, M. L. Steigerwald, T. F. Heinz, R. A. Friesner, N. J. Turro, L. E. Brus: Reversible surface oxidation and efficient luminescence quenching in semiconductor single-wall carbon nanotubes, J. Am. Chem. Soc. **126**, 15269 (2004) 306, 307
[54] L. Yang, J. Han: Electronic structure of deformed carbon nanotubes, Phys. Rev. Lett. **85**, 000154 (2000) 307, 308
[55] K. Arnold, S. Lebedkin, O. Kiowski, F. Hennrich, M. M. Kappes: Matrix-imposed stress-induced shifts in the photoluminescence of single-walled carbon nanotubes at low temperatures, Nano Lett. **4**, 2349 (2004) 308
[56] J. Wu, W. Walukiewicz, W. Shan, E. Bourret-Courchesne, J. W. Ager, K. M. Yu, E. E. Haller, K. Kissell, S. M. Bachilo, R. B. Weisman, R. E. Smalley: Structure-dependent hydrostatic deformation potentials of individual single-walled carbon nanotubes, Phys. Rev. Lett. **93**, 017404 (2004) 308
[57] H. Maki, T. Sato, K. Ishibashi: Direct observation of the deformation and the band gap change from an individual single-walled carbon nanotube under uniaxial strain, Nano Lett. **7**, 890 (2007) 308
[58] R. B. Capaz, C. D. Spataru, P. Tangney, M. L. Cohen, S. G. Louie: Temperature dependence of the band gap of semiconducting carbon nanotubes, Phys. Rev. Lett. **94**, 036801 (2005) 308

[59] D. E. Milkie, C. Staii, S. Paulson, S. E. Hindman, A. T. Johnson, J. M. Kikkawa: Controlled switching of optical emission energies in semiconducting single-walled carbon nanotubes, Nano Lett. **5**, 1135 (2005) 308
[60] A. Hagen, M. Steiner, M. B. Raschke, C. Lienau, T. Hertel, H. Qian, A. J. Meixner, A. Hartschuh: Exponential decay lifetimes of excitons in individual single-walled carbon nanotubes, Phys. Rev. Lett. **95**, 197401 (2005) 309
[61] L. J. Li, R. J. Nicholas: Magneto-photoluminescence of chirality-characterized single-walled carbon nanotubes, Int. J. Mod. Phys. B **18**, 3509 (2004) 310
[62] J. Shaver, J. Kono, O. Portugall, V. Krsti, G. L. J. A. Rikken, Y. Miyauchi, S. Maruyama, V. Perebeinos: Magnetic brightening of dark excitons in single-walled carbon nanotubes, Nano Lett. **7**, 1851 (2007) 310
[63] Y. Ohno, S. Kishimoto, T. Mizutani: Photoluminescence of single-walled carbon nanotubes in field-effect transistors, Nanotechnol. **17**, 549 (2006) 310, 311
[64] D. A. Heller, S. Baik, T. E. Eurell, M. S. Strano: Single-walled carbon nanotube spectroscopy in live cells: Towards long-term labels and optical sensors, Adv. Mater. **17**, 2793 (2005) 312
[65] J. A. Misewich, R. Martel, P. Avouris, J. C. Tsang, S. Heinze, J. Tersoff: Electrically induced optical emission from a carbon nanotube FET, Science **300**, 783 (2003) 313
[66] J. Chen, V. Perebeinos, M. Freitag, J. Tsang, Q. Fu, J. Liu, P. Avouris: Bright infrared emission from electrically induced excitons in carbon nanotubes, Science **310**, 1171 (2005) 313
[67] M. Freitag, Y. Martin, J. A. Misewich, R. Martel, P. Avouris: Photoconductivity of single carbon nanotubes, Nano Lett. **3**, 1067 (2003) 313
[68] I. A. Levitsky, W. B. Euler: Photoconductivity of single-wall carbon nanotubes under continuous-wave near-infrared illumination, Appl. Phys. Lett. **83**, 1857 (2003) 313
[69] M. E. Itkis, F. Borondics, A. Yu, R. C. Haddon: Bolometric infrared photoresponse of suspended single-walled carbon nanotube films, Science **312**, 413 (2006) 313

Index

Index